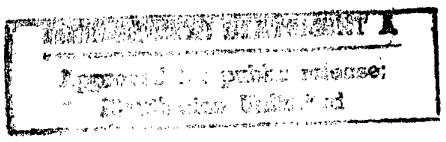
NINTH INTERNATIONAL SYMPOSIUM ON

APPLICATIONS OF LASER TECHNIQUES TO FLUID MECHANICS

VOLUME I

19980924 137



July 13th - 16th 1998
Lisbon, Portugal

DTIC QUALITY INSPECTED 1

AQ F98-12-2561

REPORT DOCUMENTATION PAGE

Form Approved OMB No. 0704-0188

Public reporting burden for this collection of information is estimated to average 1 hour per response, including the time for reviewing instructions, searching existing data sources, gathering and maintaining the data needed, and completing and reviewing the collection of information. Send comments regarding this burden estimate or any other aspect of this collection of information, including suggestions for reducing this burden to Washington Headquarters Services, Directorate for Information Operations and Reports, 1215 Jefferson Davis Highway, Suite 1204, Arlington, VA 22202-4302, and to the Office of Management and Budget, Paperwork Reduction Project (0704-0188), Washington, DC 20503.

1. AGENCY USE ONLY (Leave blank)	2. REPORT DATE	3. REPORT TYPE AND DATES COVERED
	10 July 1998	Conference Proceedings

4. TITLE AND SUBTITLE

Ninth Int'l Symposium on Applications of Laser Techniques to Fluid Mechanics

Vol. 1

5. FUNDING NUMBERS

F61775-98-WE015

6. AUTHOR(S)

Conference Committee

7. PERFORMING ORGANIZATION NAME(S) AND ADDRESS(ES)

Instituto Superior Tecnico
Av. Rovisco Pais
Lisboa Codex 1096
Portugal

8. PERFORMING ORGANIZATION REPORT NUMBER

N/A

9. SPONSORING/MONITORING AGENCY NAME(S) AND ADDRESS(ES)

EOARD
PSC 802 BOX 14
FPO 09499-0200

10. SPONSORING/MONITORING AGENCY REPORT NUMBER

CSP 98-1011

11. SUPPLEMENTARY NOTES

Two volumes.

12a. DISTRIBUTION/AVAILABILITY STATEMENT

Approved for public release; distribution is unlimited.

12b. DISTRIBUTION CODE

A

13. ABSTRACT (Maximum 200 words)

The Final Proceedings for Ninth Int'l Symposium on Applications of Laser Techniques to Fluid Mechanics, 13 July 1998 - 16 July 1998

Turbulent Flows; Unsteady Flows; Hydrodynamic and Aerodynamic Flows; Reacting Flows; Two Phase Flows and Related Instrumentation; Particle Sizing; Developments of Instrumentation for Laser Anemometry; Whole Field Velocimetry; Optical Methods for Temperature, Density, Concentration; Imaging Methods for Scalar Fields

14. SUBJECT TERMS

Combustion, Fluid Mechanics, Laser Measurements Techniques

15. NUMBER OF PAGES

Too many to count.

16. PRICE CODE

N/A

17. SECURITY CLASSIFICATION OF REPORT	18. SECURITY CLASSIFICATION OF THIS PAGE	19. SECURITY CLASSIFICATION OF ABSTRACT	20. LIMITATION OF ABSTRACT
UNCLASSIFIED	UNCLASSIFIED	UNCLASSIFIED	UL

NINTH INTERNATIONAL SYMPOSIUM ON APPLICATIONS OF LASER TECHNIQUES TO FLUID MECHANICS

VOLUME I

July 13 - 16, 1998

Lisbon, Portugal

PREFACE

These proceedings volumes I and II comprise the papers accepted for presentation at the ***Ninth International Symposium on Applications of Laser Techniques to Fluids Mechanics***, which is to be held at The Calouste Gulbenkian Foundation in Lisbon, during the period July 13 to 16, 1998. The prime objective of this Ninth Symposium is to provide a forum for the presentation of the most advanced research on laser techniques for flow measurements, and reveal significant results to fluid mechanics. The applications of laser techniques to scientific and engineering fluid flow research is emphasised, but contributions to the theory and practice of laser methods are also considered where they facilitate new improved fluid mechanics research. Attention is focused on laser-Doppler anemometry, particle sizing and other methods for the measurement of velocity and scalars, such as particle image velocimetry and laser induced fluorescence.

The papers comprising the formal record of the meeting were selected following high standard reviews, by members of the Advisory Committee, from approximately 300 extended abstracts submitted for presentation at this meeting.

Volume I comprises the papers to be presented in sessions 1 to 20 during the first and second days of the Symposium, namely July 13 and 16, while Volume II includes the papers included in sessions 21 to 39, which will occur in the following days, Wednesday, July 15, and Thursday, July 16.

We would like to take this opportunity to thank those who assisted in the Organization of the Symposium an in particular the members of Advisory Committee. We are highly indebted for the financial support provided by the Sponsoring Organisations that made this Symposium possible. Many thanks are also due to the Secretariat of the Symposium, Graça Pereira, Tibéria Valente, Luisa Martins, Anabela Almeida and Ana Nunes.

THE ORGANIZING COMMITTEE

ORGANIZING COMMITTEE

- **Ronald J. Adrian**
  Department of Theoretical and Applied Mechanics
  University of Illinois at Urbana - Champaign
  Urbana, Illinois 61801
  USA

- **Diamantino F. G. Durão**
  Department of Mechanical Engineering
  Instituto Superior Técnico
  Av. Rovisco Pais
  1096 Lisboa Codex
  PORTUGAL

- **Franz Durst**
  Lehrstuhl für Strömungsmechanik
  Erlangen Universität - Nurenberg
  Egerlandstraße 13
  D-8520 Erlangen
  GERMANY

- **Manuel V. Heitor**
  Department of Mechanical Engineering
  Instituto Superior Técnico
  Av. Rovisco Pais
  1096 Lisboa Codex
  PORTUGAL

- **Masanobu Maeda**
  Department of Mechanical Engineering
  Keio University
  1-14-1 Hioshi, Kohuku
  Yokohama 223
  Japan

- **James H. Whitelaw**
  Imperial College of Science, Technology and Medicine
  Department of Mechanical Engineering
  Exhibition Road
  London SW7 2BX
  England, United Kingdom

ADVISORY COMMITTEE

R. A. Antonia
C. Arcoumanis
W. D. Bachalo
A. Boutier
A. Cartallier
A. Cenedese
A. Coghe
W. J. A. Dahm
D. Dopheide
M. Escudier
L. Fingerson
J. Fitzpatrick
M. Gharib
G. Gouesbet
I. Grant
J. A. C. Humphrey
D. A. Jackson
T. Jacobsen
R. Karlsson
K. Hishida
J. Kompenhans
L. Lading
F. Lance
B. Lehmann
A.Leipertz
W.Lempert
A. Melling
W. Merzkirch
J. F. Meyers
E. A. Müller
T. Nakajima
N. Nakatani
A. Naqwi
K. Ohba
T. Obokata
J. C. Pereira
H. J. Pfeifer
F. Pinho
M. L. Riethmüller
D. Rockwell
X. Shen
R. L. Simpson
M. Sommerfeld
R. N. Syred
A. Taylor
E. P. Tomasini
M. Trinité
C. Tropea
J. E. S. Venart
G. Wigley
P. O. Witze
M. Yianneskis

SPONSORING ORGANISATIONS

- Calouste Gulbenkian Foundation
- European Research Office:
  United States Army,
  Navy and Air Force Departments
- Expo'98
- FCT – Fundação para a Ciência e Tecnologia, Portuguese Ministry of Science and Technology
- FLAD, Portuguese-American Foundation for the Development
- IST - Instituto Superior Técnico
- TAP, Air Portugal

LOCAL SECRETARIAT

Graça Pereira

Tibéria Valente

Anabela Almeida

Luisa Martins

Ana Paula Nunes

Instituto Superior Técnico

Department of Mechanical Engineering

Av. Rovisco Pais, 1096 Lisboa Codex

Portugal

Telephone: (351 1) 841 73 79

Fax: (351 1) 849 61 56

EMail: symp98@tercomb.ist.utl.pt

LIST OF CONTENTS

VOLUME I (SESSIONS 1-20)

SESSION 1. PLENARY SESSION

1.1 Instantaneous rotor wake measurements using Doppler global velocimetry
J. F. Meyers, G. A. Fleming, S. A. Gorton and J. D. Berry

1.2 Effect of sensor geometry on the performance of PIV interrogation
J. Westerweel

1.3 Effect of variable liquid properties on the flow structure within shear-driven liquid films
A. Elsässer, W. Samenfink, J. Ebner, K. Dullenkopf, S. Wittig

SESSION 2. WAKES

2.1 A Study of the near-wake region of a circular cylinder
R. Elavarasan, L. Djenidi and R.A. Antonia

2.2 LDV measurements in the near wake behind a egg-formed body close to a stationary and a moving wall
M. S. Kim and D. Geropp

2.3 LDA measurements and visualization of the supersonic flow around a longitudinal cylinder with different surface roughness
F. Leopold, E. Augenstein, S. Damp and F. Christnacher

2.4 Laser Doppler velocimetry (LDV) and particle image velocimetry (PIV) measurements of the time dependent flow behind a circular cylinder and comparison with results obtained by numerical simulation
O. Stenzel and C. Lund

2.5 The structure of subsonic air wakes at high Reynolds number
F. Barreras, A. Lozano, A. Yates and C. Dopazo

2.6 Characterization of a bluff body wake using LDV and DPIV techniques
Ö. Karatekin, F. Y. Wang, and J.-M. Charbonnier

2.7 LIF measurements in a turbulent far-wake
H.Rehab, L. Djenidi and R.A. Antonia

SESSION 3. COMBUSTION I

3.1 Three-dimensional LDA measurements in a turbulent precessing jet flame
G.M. Schneider, G.L. Nathan, R.E. Luxton and N. Syred

3.2 Quantitative characterisation of the precessing vortex core and the vortex breakdown phenomena using particle image velocimetry
W. Fick, A.J. Griffiths, G. Schoepf and T. O'Doherty

3.3 On the extension of a laser-Doppler anemometer to the analysis of oscillating flames
E. C. Fernandes and M. V. Heitor

3.4 Liquid-fuelled flames with imposed air oscillations
Y. Hardalupas, A. Selbach and J.H. Whitelaw

3.5 Phase locked velocity measurements in an excited transient pressure field
J. R. Dawson, A. Beale, T. O'Doherty and N. Syred

3.6 Measurements of unsteady combustion in a simple combustor configuration
S. Dawson and J.A. Fitzpatrick

SESSION 4. VORTICES

4.1 Experimental study by white light laser tomoscopy and P.I.V. of the interaction of a vortex ring with a flat wall
P. Dupont, O. Werquin, S. Le Mironet and M. Stanislas

4.2 Vorticity evolution of a vortex ring using high resolution CCDPIV
J. Cater, J. Soria and T.T. Lim

4.3 The application of laser diagnostics to cyclonic flow with vortex precession
A.J. Hoekstra, A.T. Israel. J.J. Derksen and H . E.A. van den Akker

4.4 On the advantages and pitfalls of statistical PIV analysis in the measurement of confined vortex breakdown
J.M.M. Sousa and C. Freek

4.5 Analysis of orderlines in higher instabilities towards the occurrence of chaos in a Taylor-couetter flow system
N. Ohmura, K. Matsumoto, T. Aoki and K. Kataoka

4.6 LDV measurements on baroclinic waves
B. Sitte and C. Egbers

SESSION 5. MANUFACTURER'S TECHNICAL PRESENTATION

SESSION 6. PIV OPTICS

6.1 Multilayer PIV technique with high power pulse laser diodes
M. Abe, N. Yoshida, K. Hishida, M. Maeda

6.2 Gas flow visualization by laser diode light sheet imaging
B. Nath, W. Löber, W. Baetz , W. Holzapfel

6.3 Fibre optic beam delivery of high peak power, short pulse laser light for PIV
D. P. Hand, D. P. Wiles, A. Kuhn, J. Jones, J. D. Entwistle and C.A. Greated

6.4 Diagnostic techniques for microfluids research
C. D. Meinhart, J. G. Santiago, S. T. Wereley, and R. J. Adrian

6.5 Design and calibration of a stereoscopic PIV system
D. C. Bjorkquist

6.6 Investigation of a turbulent boundary layer flow using LDV and PIV
S. Kerrigan, W. Lai, C. Tomkins, K. Sharp, Z.-C. Liu, R. Adrian

SESSION 7. SPRAYS IN ENGINES

7.1 LDA-based measurements of instantaneous and integrated flow rates in high-pressure gasoline injection system
M. Ismailov, T. Ishima, T. Obokata, M. Tsukagoshi and K. Kobayashi

7.2 Charateristics of sprays from gasoline injectors
C. Brehm, M . Posylkin and J. H. Whitelaw

7.3 Comparison of different drop sizing techniques on direct injection gasoline sprays
J.-F. Le Coz

7.4 Characterization of a diesel spray head by different laser based techniques
L. Araneo, A. Coghe, and G. E. Cossali

7.5 Application of two-component phase Doppler anemometry to the study of transient diesel spray impingement
H. G. C.-Góngora and M. Brun

7.6 Diesel spray-wall impingement characterization by means of PDA and high speed visualization
J.M. Desantes, J. Arregle, J.V. Pastor and U. Gonzalez

SESSION 8. COMPLEX FLOWS I

8.1 Laser velocimetry measurements in a cyclone separator
M. J. Fisher and R.D. Flack

8.2 Investigation of internal flows by means of the stereoscopic PIV method
J. Schabacker and A. Bolcs

8.3 Effects of centrebody rotation on the laminar flow of a shear-thinning liquid through an eccentric annulus
M. P. Escudier and I.W. Gouldson

8.4 Energy losses on a 90° tee junction
R. Maia, P. Miranda, F. T. Pinho and M. F. Proença

8.5 Microchannel flows: whole-field optical measurements of velocity and mixing after merging three laminar channel flows
D.R. McCluskey, J. A. van de Konijnenberg, J. J. Rasmussen and B. Stenum

8.6 3D LDV measurements in a rotating cooling channel
P. Gicquel, Y. Servouze and B. Tanguy

SESSION 9. 2-PHASE FLOWS INSTRUMENTATION I

9.1 Refractive index measurements with phase Doppler anemometry in the size range 0.3 to 20 um
P. Volkholz, A. Melling and F. Durst

9.2 Velocity, size and concentration in suspension measurements of cylindrical jets and spherical droplets
F. Onofri, L. Bergounoux, J-L. Firpo and J. M.-Ripault

9.3 Principle of statistical dependence and its application to sizing of irregular particles using phase Doppler technique
A. Naqwi and C. Fandrey

9.4 A high power, high resolution LDA/PDA system aplied to dense Gasoline Direct Injection Sprays
G. Wigley, G.K. Hargrave and J. Heath

9.5 A new approach to eliminate the measurement volume effect in PDA measurements
H. Qiu and C. T. Hsu

SESSION 10. PIV SIGNAL PROCESSING

10.1 Advanced evaluation algorithms for standard and dual plane particle image velocimetry
O. Ronneberger, M. Raffel and J. Kompenhans

10.2 Particle tracking velocimetry using an image relaxation method
K. Ohmi and D. H. Lam

10.3 Fast sub-pixel precision PIV using SSDA algorithm
T. Uemura, T. Tosiyasu and K. Katayama

10.4 A new algorithm for the evaluation of PTV data using point matching distance measures and deterministic annealing
A. Kuzmanovski and K. Obermayer

10.5 An advanced MQD tracking algorithm for PDIV
L. Gui and W. Merzkirch

10.6 Evaluation of the spring model tracking algorithm using standard images for PIV
K. Okamoto

SESSION 11. WALL FLOWS

11.1 Turbulent boundary layer investigations with convential and stereoscopic PIV
C.J. Kahler, R.J. Adrian and C.E. Willert

11.2 Experimental study of a high Reynolds number turbulent boundary layer using DPIV
J. M. Foucaut, P. Dupont, J. Carlier and M. Stanislas

11.3 Reynolds number dependence of near wall turbulent statistics in channel flows
M. Fischer, F. Durst and J. Jovanovic

11.4 LDV analysis of temporal intermittency in pipe flow
E. Nino and C. Serio

11.5 Streamwise vortex production by an array of inclined jets
X. Zhang and A. Rona

SESSION 12. 2-PHASE FLOWS INSTRUMENTATION II

12.1 PIV in two-phase flows: Simultaneous bubble sizing and liquid velocity measurements
I. Dias and M. L. Riethmuller

12.2 PIV application for spray characteristic measurement
Y. Ikeda, N. Yamada and N. Kawahara

12.3 Advanced measurement techniques for injector validation
W. Scheuerpflug and S. Funke

12.4 Measurement of particle size and velocity in two phase flows using PIV
W.T. Martin, J.R. Kadambi and M.P. Wernet

12.5 Directionally resolved two phase flow measurements using PIV with fluorescent particles and colour recording
D.P. Towers, C.E. Towers, C.H. Buckberry and M. Reeves

12.6 Multi-intensity-layer PIV for spray measurement
Y. Ikeda, N. Yamada and T. Nakajima

SESSION 13. PIV DATA PROCESSING

13.1 On the accuracy of a DIC-PIV system based on massive sampling
C. Freek, J . M. M. Sousa, W. Hentschel , W. Merzkirch and J.M.F. Raposo

13.2 Wavenumber Spectrum Estimation from Irregularly Spaced Data: Application to PIV Data Processing
W. Hubner, C. Tropea and J. Volkert

13.3 The Elimination of Correlation Errors in PIV Processing
D. P. Hart

13.4 Particle imaging velocimetry stadard images for transient three-dimensional flow
T. Kobayashi, T. Saga, S. Nishio and K. Okamoto

13.5 Measurement of velocity field spectra by means of PIV
L.M. Lourenco, M. B. Alkislar and R. Sen

13.6 International activities for cooperation, comparison, and standardization at the development and application of particle image velocimetry
J. Kompenhans, M. Stanislas, M. Gharib and T. Kobayashi

SESSION 14. MIXERS

14.1 A study of vorticity and dissipation around a Rushton turbine using particle image velocimetry
K.V. Sharp, K.C. Kim and R.J. Adrian

14.2 Visualisation of the trailing vortex system produced by a pitched blade turbine using a refractive index matched automated LDA-technique
M. Schafer, P. Wachter, F. Durst and M. Yianneskis

14.3 Measurement of the mixing characteristics of a stirred vessel with a liquid crystal technique
K.C. Lee

14.3 Laser pulsed holography applied to three-dimensional two-phase-flow in aerated stirred vessels
O. Feldmann and F. Mayinger

14.4 Phase-resolved three-dimensional LDA measurements in the impeller region of a turbulently stirred tank
J . J. Derksen, M. S. Doelman and H. E. A. van den Akker

14.5 Turbulence energy dissipation rate estimation in stirred vessels
P. Saarenrinne

14.6 Synchronised LDA and interfacial wave height measurements in a model of continuous casting moulds
M. Keicher, H. Morikita and A. M. K. P. Taylor

SESSION 15. LDV OPTICS I

15.1 Investigation of a two-component LDA using integrated optical devices
C . Resagk, J. Grabow and S. Voigt

15.2 A compact LDV System for high resolution flow measurements
L. Berkner and A. Naqwi

15.3 Compact achromatic laser Doppler anemometer employing novel powerful fiber lasers and diffraction optics
Jürgen W. Czarske, H. Zellmer, K. Plamann, H. Welling

15.4 Optical preamplification of 1064 nm LDA radiation
H. Tobben, H. Muller and D. Dopheide

15.4 Analysis of the three-dimensional fringe patterns formed by the interference of ideal and astigmatic Gaussian beams
E.B. Li and A.K. Tieu

SESSION 16. HOLOGRAPHIC PIV

16.1 Decomposition of Turbulent fields and Visualization of vortices
K.T. Christensen, R.J. Adrian, S.M. Soloff, C.D. Meinhart and Z.C. Liu

16.2 Instantaneous 3-D velocity measurement of a thermal plume using HPIV
K. Yamaguchi, M. Maeda and K. Hishida

16.3 Development of a low cost IROV holographic PIV using genetic algorithm data processing
J. Sheng and H. Meng

16.4 New advances in holographic interferometry as a fluid velocimetry technique
M .P. Arroyo, M. P. Alvarez, I. J. Sola and N. Andrés

16.5 Development and Application of a Defocusing Three Dimensional DPIV Technique for the Mapping of Two Phase Bubbly Flows
M. Gharib, D. Modares, D. Dabiri, F. Pereira and F. Taugwalder

SESSION 17. FREE FLOWS I

17.1 A PIV study of compressible shear layers
W. D. Urban and M. G. Mungal

17.2 Experimental determination of the turbulent kinetic energy and the dissipation rate in variable density turbulent jets
J. Pagé, B. Sarh and I. Gökalp

17.3 Turbulent scalar mixing in coaxial Jet flows
F. Caldas, P. Ferrão, M. V. Heitor and M. Matos

17.4 PIV and PLIF investigation of mixing by model filter-feeders
U. Ullmum, R. J. Adrian and P. S. Larsen

SESSION 18. 2-PHASE FLOWS INSTRUMENTATION II

18.1 Planar particle image analyzer
C. Hess

18.2 Droplet sizing by interferometric method based on Mie scattering
O. Pajot and C. Mounaïm-Rousselle

18.3 Aerosol size measurement using a laser Doppler probe and acoustic excitation of the fluid flow
V. Strunck, H. Muller, G. Grosche and D. Dopheide

18.4 Measurement of size and velocity of particles by optical based spatial filtering technique
D. Petrak, K. Rosenfeld and E. Przybilla

18.5 A new laser method for aerosol concentration measurements
G. Cognet, P. Falgayrettes and Y. Brenier

18.6 Rainbow thermometry with a pulsed laser
J.P.A.J. van Beeck and M. L. Riethmuller

18.7 Non-orthogonal optical spray pattern analysis
R. Sellens and R. Deljouravesh

SESSION 19. AERODYNAMIC FLOWS

19.1 LDV-measurements on a high-lift configuration with separation control
F. Tinapp and W. Nitsche

19.2 Flow measurements on a large delta wing using particle image velocimetry
L. Dieterle, J. Raffel, K. Ehrenfried and J. Kompenhans

19.3 Flow field in the vicinity of a thick cambered trailing edge
G. Pailhas, Y. Touvet, P. Sauvage and E. Coustols

19.4 Reconstruction of 3-D steady incompressible flow field out 2-D PIV measurements in wind tunnels
N. Lang and W. Limberg

19.5 Embedded LDV methodology for boundary-layer measurements on oscillating models
C. Allain, E. Berton, D. Favier and C. Maresca

19.6 Instantaneous flow field measurements for propeller Aircraft and Retorcraft research
M. Raffel, C.E. Willert, F. De Gregorio, K. Ehrenfried, J. Kompenhans K. Pengel and C. Kähler

SESSION 20. COMPLEX FLOWS II

20.1 Three-dimensional effects of turbulent flow in an in-line tube bundle
K. E. Meyer

20.2 Detailed LDV flow field measurements on a model of bayonet tube equipped with heat transfer augmenting devices
A. Cattanei, N. Elia, S. Razore, A. Sciacchitano, M. Ubaldi and P. Zunino

20.3 LDA and PIV measurements on thermal convection in spherical shells
C. Böhm, C. Egbers and H. J. Rath

20.4 Instantaneous 3D flow structures in the wake of a surface-mounted mixing tab measured by planar and holographic PIV
Y. Pu, Z. Huang, W. Yang and H. Meng

20.5 A Fence flow with periodic cross-flow forcing
H. A. Siller and H. H. Fernholz

20.6 Measurements in the shear-layer behind a surface-mounted obstacle for the determination of coherent structures
T. Baur and J. Köngeter

20.7 Measurements of the Spatial coherence of the flow around two cylinders
V. Valeau and J.A. Fitzpatrick

VOLUME II (SESSIONS 21-39)

SESSION 21. 2-PHASE FLOWS I

21.1 Molten metal atomization by inert gases: Off-line and on-line metal powder characterization by PDA
J. Raimann, G. Wolf, J. Domnick, G. Brenn and F. Durst

21.2 Investigation of rebounding droplets from a heated cylinder in spray cooling using PDA
H -H Qiu and Y. F. Yeung

21.3 Experimental study on the behaviour of a spray in the model of a fuel preparation duct
A.N. Barros and A.L.N. Moreira

21.3 Some aspects of electrohydrodynamic spraying in cone-jet mode
K. Ohba, P. H. Son and Y. Dakemoto

21.4 Characteristic measurement of electrostatic fuel spray
Y. Ikeda, J. H. Kim and T. Nakajima

SESSION 22. SEPARATED FLOWS

22.1 Reynolds number effect and laminarisation of turbulent flow in axisymmetric sudden-contraction pipe flow
K. T. Ajayi and F. Durst

22.2 A flow structure at reattachment region of a two dimensional backward-facing step
N. Furuichi, T. Hachiga, K. Hishida, and M. Kumada

22.3 A non-newtonian turbulent sudden expansion flow
A. S. Pereira and F. T. Pinho

22.4 PIV measurements of turbulence statistics in the three-dimensional flow over a surface-mounted obstacle
J.M.M. Sousa, C. Freek and J. C. F. Pereira

22.5 Turbulence analysis on the BFS with iterative multigrid PIV image processing
F. Scaramo and M. L. Riethmuller

SESSION 23. SCALAR MEASUREMENTS I

23.1 Evaluation of flowfield temperatures and pressures using broadband excitation and detection
J. Mendoza, I. Catton and M. Azzazy

23.2 Measuring water temperatures by means of Linear Raman spectroscopy
J. Karl, M Ottmann and D. Hein

23.3 Development of a fluorescence-based temperature measurement technique for two-phase flashing propane jets
J.T. Allen and R. J. Bettis

23.4 Combined measurement of velocity, temperature, and pressure in compressible gas flows using laser-induced iodine fluorescence
M. Havermann and A. E. Beylich

23.5 Density and temperature measurements in a nitrogen jet at supercritical pressures using spontaneous Raman scattering
M. Oschwald and A. Schik

SESSION 24. 2-PHASE FLOWS II

24.1 On the frequency analysis of the disintegration of planar liquid films
I. S. Carvalho, M.V. Heitor and D. Santos

24.2 The velocity field in an air-blasted liquid sheet
A. Lozano, I. Garcia Pallacin and F. Barreras

24.3 Measurements of film characteristics along a stationary Taylor bubble using laser induced fluorescence
J.P. Kockx, R. Delfos, J.L.J. Zijl, T.D. Tujeehut and R.V.A. Oliemans

24.4 Experimental analysis of a confined bluff body flow laden with polydispersed solid particles
T. Ishima, J. Boree, P. Fanouille and I. Four

24.5 Experimental analysis of spatial and temporal two-phase flows structures in circulating fluidized beds using particle images velocimetry and phase Doppler anemometry
F. Onofri, T. Van den Moortel, L. Tadrist and J. Pantaloni

24.6 Investigation of a particle laden wake flow by means of particle image velocimetry
T. J. Möller and K. A. Bütefisch

SESSION 25. COMBUSTION II

25.1 Experimental investigation of spatio-temporal correlation between aerodynamic and flame front location in an axisymetric non premixed bluff body burner flame
A. Susset, M. Trinite, D. Honore, D. Jaffre and M. Perrin

25.2 Simultaneous PIV and PLIF measurements in nonpremixed transverse jet flames
E. F. Hasselbrink, M. G. Mungal, and R. K. Hanson

25.3 Simultaneous PIV and OH planar LIF in the stabilization region of a lifted-turbulent jet flame
C. Maurey, A. Cessou and D. Stepowski

25.4 Detection of 3D temperature gradients in turbulent premixed flames with the dual-sheet laser Rayleigh scattering technique
A. Soika, F. Dinkelacker and A. Leipertz

25.5 On the effect of rotation on bluff-body stabilized flames
D. Duarte and P. Ferrão

25.6 Simultaneous planar OH and temperature measurements for the detection of lifted reaction zones in premixed bluff-body stabilized flames
D. Most, V. Holler, A. Soika, F. Dinkelacker and A. Leipertz

25.7 A laser-Doppler analysis of flame stabilisation in a lean premixed prevaporised research combustor
P. Anacleto and M.V. Heitor

SESSION 26. SCALAR MEASUREMENTS II

26.1 Measurement of free surface inclination using specklegram
K. Okamoto, G. Tanaka and H. Madarame

26.2 Non-linear effects in planar scattering techniques: Proofs of existence, simulations and numerical corrections of extinction and multiple scattering
P. Voigt

26.3 CT-type 2DLaser concentration meter with no rotating parts-Application of virtual-load method to an inverse problem
M. Hino and Y. Sato

26.4 Applications of laser in the study of thermodynamical properties of heavy oils and petroleum in water emulsions
G. Da Costa

26.5 Application of non-linear containing infrared spectrograph for researching of the methane flows
A.B. Britan, P.V. Kozlov, V.A. Levin, S.Y. Mitichkin and V.G. Testov

26.6 Concentration measurement by molecular absorption using narrow band tunable infra-red laser
T. Kawaguchi, K. Hishida and M. Maeda

SESSION 27. 2-PHASE FLOWS III

27.1 Thermocapillary Bubble Experiments Using Liquid Crystals
G. Wozniak

27.2 Simultaneous measurements of continous and dispersed phase in bubble columns by PDA
D. Bröder and M. Sommerfeld

27.3 The Determination of the Bubble Growth Rate in Boiling Heat Transfer by Phase-Doppler Anemometry
T. I . Nonn

27.4 3D measurements of wake interaction in a bubbly two-phase flow using Scanning PIV (SPIV) and Stereo-Imaging
Ch. Brücker

27.5 Investigation of three-dimensional bubbly flow measurement using displacement particle image velocimetry technique
Y.A. Hassan, W. D. Schmidt and J.Ortiz-Villafuerte

SESSION 28. LDV OPTICS II

28.1 Instantaneous velocity profile capturing by a scanning laser velocimeter
M. D. Matovic and O. LeRudulier

28.2 First breadboard study about the operation of miniaturized laser Doppler anemometry (LDA) in view of an application on test container level of the future fluid science laboratory (FSL)
J. Immohr, C. Egbers and H. J. Rath

28.3 Development of fiber optic laser Doppler velocimetry sensor for measurement of local blood velocity
K. Ohba, M. Nishiyama and K. Korenaga

28.4 Integrated laser Doppler velocimeter for wall friction measurements: new prototypes and performance
P.L. Auger, A. Cartallier, P. Bench and I. Schanen-Duport

SESSION 29. BIOLOGICAL FLOWS I

29.1 Visualizations of pulsatile flows in bifurcation and stenosis models
S. Yongda, Y. Lixin, G. Changsong, Y. Xianqiu, Z. Liubao and C. Jingui

29.2 DPIV measurements of pulsative flow in a constricted tube
A. Borg, J. Bolinder and L. Fuchs

29.3 Steady and unsteady LDV and PIV investigations of flow within lung bifurcation
A. Ramuzat, S. Day and M. L. Riethmuller

29.4 Spectral and instantaneous flow characteristics of vascular junctions using continuous DPIV
Y. Grad and S. Einav

29.5 Low coherence interferometry for flow measurement
A.G. Podoleanu, J.A. Rogers and D.A. Jackson

SESSION 30. OPEN FORUM

SESSION 31. ENGINES 1

31.1 Investigation of in-cylinder flow inside a small two stroke engine using PIV in conjunction with endoscopic optics
J. Gindele and U. Spicher

31.2 Application of cross correlation particle image velocimetry to the characterisation of unsteady rotating flow
M. Mouqallid , A. Belghit and M. Trinité

31.3 Visualization and PIV- Measurements inside the intake port an IC-Engine
G. Rottenkolber, K. Dullenkopf and S. Wittig

31.4 Influence of axial compression on a strongly swirling cylinder flow
J. Keller, C. Tropea and J. Volkert

31.5 Development of a 2 Colour PIV system for in-cylinder spark ignition engine flows
D.P. Towers, C.H. Buckberry and M. Reeves

SESSION 32. LDV SIGNAL PROCESSING

32.1 Correlation estimate for two-channel, non-coincidence laser Doppler anemometry
E. Muller, H. Nobach and C.Tropea

32.2 Improved reconstruction of turbulent velocity fluctuations from laser-Doppler anemometry data
H.R.E. van Maanen and F. J. Nijenboer

32.3 Determination of Doppler frequencies and characteristic frequency modulation phenomena in laser Doppler signals
P. Lehmann

32.3 Quadrature demodulation as advantageous Doppler signal processing technique
J. W. Czarske and O. Dölle

32.4The measurement of structure functions with laser Doppler anemometry
G. P. Romano

32.5Benchmark Tests for the Estimation of power spectra from LDA Signals
C. Tropea and L. Benedict

SESSION 33. COMPLEX FLOWS III

33.1 DPIV- Measurements for examination of transient flow Phenomena
J. Reuber and J. Köngeter

33.2 A comparison of velocity-field data behind a double-swirl nozzle measured by means of Doppler-global and conventional three-component LDA techniques
B. Lehmann and I. Röhle

33.3 Characteristics of transverse dispersion and fluid flow at the exit of short ceramic foams inside a pipe
J.C.F. Pereira and J. Raposo

33.4 Interaction of swirling flows from two adjacent coal burners
A. Aroussi, S. Tarr and S. J. Pickering

33.5 LDA measurements in a flash smelting furnace model
B . Chiné and A. Barrientos

33.6 Flow induced vibration of a scale model of the flow in a scale model of the Flixborough "by-pass" pipe
R. Teng-yang, K.F. Sollows and J. E.S. Venart

SESSION 34. MULTI-POINT METHODS

34.1 Quantitiative unseed molecular velocimetry imaging
P. A. Drbarber, L. A. Ribarov, J. A. Wehrmeyer, F. Batliwala and R. W. Pitz

34.2 Recent applications of three-component Doppler global velocimetry in turbo-machinery
I. Röhle, C. Willert, and R. Schodl

34.3 The use of diode array velocimetry for the measurement of turbulent pipe flow
E. Huckle, I. Catton and M. Azzazy

34.4 A novel approach to measuring the instantaneous velocity of flow density gradients
G. Papadopoulos and W. M. Pitts

34.5 Application of digital holographic interferometry to visualize buoyancy convection
B. Skarman, K. Wozniak and J. Becker

34.6 Measurement of the velocity distribution of turbulent flow by the laser photothermal effect with a CCD-LD-interferometer
N. Nakatani

34.7 Fluid image velocimetry for unseeded flow
Y. Levy, B. Golovanevsky and T. A. Kowalewski

SESSION 35. COMBUSTION III

35.1 PIV and OH LIF imaging of flame-vortex interactions in an opposed-jet burner
J. R. Gord, J. M . Donbar, G. J . Fiechtner, C. D. Carter and J. C. Rolon

35.2 Three-dimensional mapping of turbulent flame fronts
M. Lawes, C. G. W. Sheppard and R. Woolley

35.3 Application of new light collecting probe with spatial resolution to a spark-ignited spherical flames
S. Tsushima, F. Akamatsu and M. Katsuki

35.4 Size, Shape, velocity and temperature measurement of burning coal particles with a newly designed optical measurement technique - TOSCA
G . Hackert, S. Wirtz and H. Kremer

35.5 Devolatilization of Single Carbon Particles
B. Zhao, I. Kantorovich, and E. Bar-Ziv

35.6 Laser ignition of single particles
J. F. Zevenbergen, A. E. Dahoe, A. A. Pekalski and B. Scarlett

35.7 PIV in spherically expanding laminar cellular flames
C. G. W. Sheppard, R. Woolley and M. Lawes

SESSION 36. TURBO MACHINERY

36.1 Measurements of rotating machinery flows under steady and transient operating conditions using LDV and PIV
Rajan K. Menon, Wing T. Lai, Steve D. Hoff and Tim P. Mahon

36.2 Detailed measurements of the internal flow of a backswept centrifugal impeller
El Hajem M., Morel R., J. Y. Champagne and F. Spettel

36.3 Measurements of in instantaneous flow structures in turbomachinery using PIV
Draciana Udrea, M. Burnett, W. K. Lee and P. Bryanston-Cross

36.4 Unsteady boundary layers on the diffuser blades of a centrifugal stage due to rotor blade wake interaction
A. Cattanei, M. Ubaldi and P. Zunino

36.5 Experimental and numerical investigation of the unsteady flow in an axial turbine at different points of operation
C. Gentner, G. Lein and E. Göde

36.6 Secondary flow field measurements with a LDV in the vaned diffuser of a high subsonic centrifugal compressor
D. Stahlecker, E. Casartelli and G. Gyarmathy

36.7 Velocity measurement downstream an axial blade wheel using LDV-PIV
L. Girardot, F. Lanzetta, J. P. Prenel, J. Stefanini and R. Menon

SESSION 37. ENGINES II

37.1 PIV measurements during combustion in a reciprocating internal combustion engine
D. L . Reuss and M. Rosalik

37.2 In-cylinder measurements of mixture composition for investigation of residual gas scavenging
P. Miles

37.3 Laser diagnostics of nitric oxide inside a two-stroke DI diesel engine
G. Stoffels, E.van den Boom, C. Spaanjaars, N. Dam, W. Meerts and J.J. ter Meulen

37.4 Investigation of oil transport mechanisms in the piston ring pack of a single cylinder diesel engine, using two-dimensional laser induced fluorescence
B. Thirouard and D. P. Hart

SESSION 38. FREE FLOWS II

38.1 Weakly interacting two parallel plane jets
J. C. S. Lai and A. Nasr

38.2 An image processing approach to the study of turbulent structures with a jet in a crossflow
S. McCusker, N. Toy and E. Savory

38.3 PTV analysis of jets in cross-flow
G . Carlomagno, A. Cenedese and G. De Angelis

38.4 A 30o inclined wall jet
J. C. S. Lai and D. Lu

SESSION 39. COMPLEX FLOWS IV

39.1 Energy dissipation study of submerged breakwaters using velocity measurements
F. T. Pinto, M. F. Proença and F. V. Gomes

39.2 LDV measurements of turbulence length scales generated by swell downstream to a structure
A. Arsié, L. Maison and M. Bélorgey

39.2 Classification of tsunami wave to runup transition using laser-induced fluorescence technique
K.M. Mok and H. Yeh

39.3 Characterisation of the interaction between a boundary layer and a cavity using digital particle image velocimetry with optical flow
G. Quénot, A. Rambert, P. Gougat and T. Kowalevski

SESSION 1

Plenary Session

INSTANTANEOUS DOPPLER GLOBAL VELOCIMETRY MEASUREMENTS OF A ROTOR WAKE: LESSONS LEARNED

James F. Meyers and Gary A. Fleming

National Aeronautics and Space Administration
Langley Research Center
Hampton, Virginia 23681 USA

and

Susan Althoff Gorton and John D. Berry

Aeroflightdynamics Directorate (AVRDEC)
U. S. Army Aviation and Missile Command
Langley Research Center
Hampton, Virginia 23681 USA

ABSTRACT

A combined Doppler Global Velocimetry (DGV) and Projection Moiré Interferometry (PMI) investigation of a helicopter rotor wake flow field and rotor blade deformation is presented. The three-component DGV system uses a single-frequency, frequency-doubled Nd:YAG laser to obtain instantaneous velocity measurements in the flow. The PMI system uses a pulsed laser-diode bar to obtain blade bending and twist measurements at the same instant that DGV measured the flow. The application of pulse lasers to DGV and PMI in large-scale wind tunnel applications represents a major step forward in the development of these technologies. As such, a great deal was learned about the difficulties of using these instruments to obtain instantaneous measurements in large facilities. Laser speckle and other image noise in the DGV data images were found to be traceable to the Nd:YAG laser. Although image processing techniques were used to virtually eliminate laser speckle noise, the source of low-frequency image noise is still under investigation. The PMI results agreed well with theoretical predictions of blade bending and twist.

1. INTRODUCTION

The precise prediction of the helicopter main rotor wake has been cited as the driving factor for accurately predicting rotor loads, vibration, performance, and noise. It is widely accepted throughout the rotorcraft industry that correctly modeling the wake geometry and the tip vortex formation, size, strength, and position are essential to a numerical solution of the wake problem. Although there have been many efforts to characterize the rotor wake using various methods of flow visualization, these qualitative efforts are insufficient to validate and improve the numerical models of the rotor wake. Detailed, quantitative flowfield information is required.

The acquisition of the requisite flowfield measurements has been impeded by the harsh environment in which a rotor blade operates. Since the blades rotate, the flow environment is constantly changing, and each blade is affected by the wake structure shed from the preceding blades. Thus, investigations of this unsteady, vortex-dominated flow require measurement techniques that are: 1) nonintrusive, 2) instantaneous, 3) simultaneous three-component, and 4) correlated with rotor azimuth. Although fringe-type laser velocimetry satisfies the measurement requirements, the excessive acquisition time needed to obtain statistically-significant, azimuth-dependent results makes the technique impractical for surveying large areas within the rotor flowfield. Particle Image Velocimetry is limited to two dimensional measurements over relatively small measurement planes in large wind tunnel applications.

For the past several years, the NASA Langley Research Center has been developing Doppler Global Velocimetry (DGV) for use in large wind tunnels. DGV is a planar measurement technique capable of obtaining three-component flow field velocity data. Previous applications of DGV used a continuous-wave (CW) Argon-ion laser and produced flow velocity measurements that were temporally integrated over the 16.7 ms CCD camera exposure. Demonstrations of the instrument operating in this manner included the detailed measurement of wing tip vortices at focal distances of 18 m (Meyers (1996)). While these integration times were satisfactory for the measurement of stationary flows, they were unacceptable for the measurement of the unsteady flows found in rotorcraft applications. In anticipation of this limitation, the Northrop Research and Technology Center was contracted by the NASA Langley Research Center in 1990 (Komine *et al* (1994)) to conduct laboratory investigations to determine if a single-frequency, frequency-doubled Nd:YAG laser could be used in DGV applications to obtain instantaneous velocity measurements. This successful research program culminated

with the first instantaneous DGV measurements, as demonstrated by one-component velocity measurements in a 10-x 10-cm free jet.

The subject of this investigation was the rotor wake developed by an isolated rotor system consisting of a Mach-scaled, four bladed rotor with a rotor disk diameter of 1.7 m. A scaled, generic helicopter fuselage shell, independent of the rotor drive system and hub, could be raised from the tunnel floor to investigate its effect on the flow and nonlinear interactions with the rotor wake. The primary objective of the current investigation was to integrate the three-component DGV technology developed by NASA with the experience derived from the Northrop effort to create an instrumentation system capable of measuring the unsteady rotor wake flow field. Complete diagnostics of the rotor wake must include blade deformation and position data since the rotor wake geometry is largely affected by these parameters. A second objective was to use the newly advanced capabilities of a laser diode-based Projection Moiré Interferometer to obtain blade position, bending, and twist data at the same instant as the velocity field was measured with the DGV system.

2. EXPERIMENTAL FACILITIES

The experiment was performed in the Langley 14-by 22-Foot Subsonic Tunnel shown in Figure 1 (Gentry *et al* (1990)). This atmospheric, closed-circuit low-speed wind tunnel can be operated with a closed test section, or by raising the walls and ceiling, in an open test section mode. For this study, the tunnel was operated as a modified open test section with the walls raised for maximum optical access to the rotor wake, and the ceiling lowered to serve as a mounting platform for the isolated rotor drive system. The wind tunnel is equipped with propylene glycol vaporization/ condensation smoke generators that were mounted on a traversing mechanism located in the tunnel settling chamber.

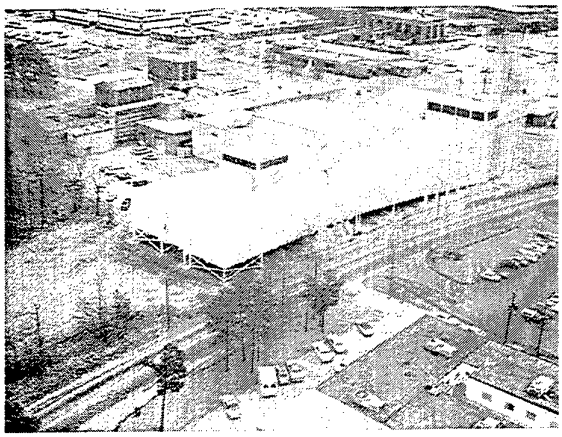


Figure 1 The Langley 14-by 22-Foot Subsonic Tunnel.

The isolated rotor test system (IRTS) is a general-purpose rotor testing system. The fully articulated hub holds a Mach-scaled, four-bladed, 1.7-meter diameter rotor. The rotor blades have a rectangular planform and an NACA 0012 airfoil section with a chord of 6.6 cm and a linear twist of -8 degrees, nose down. Note that the rotor blades are very stiff torsionally when compared with a full-scale rotor system. A digital 1024 pulse per revolution encoder was attached to the rotor shaft to monitor rotor speed and provide an azimuthal record for conditionally sampling the instrumentation systems. A helicopter fuselage model was mounted on a vertical strut below the rotor. The strut could be raised and lowered to locate the fuselage in proper position under the rotor, Figure 2, or fully lowered to be out of the influence of the rotor wake, Figure 3. The tunnel's conventional, 3-D Laser Velocimeter was also used during the test to acquire a limited number of velocity measurements in the rotor wake.

3. DOPPLER GLOBAL VELOCIMETER

The Doppler Global Velocimeter is an Iodine vapor cell based, three-component system utilizing a pulsed, single-frequency, frequency-doubled Nd:YAG laser to obtain instantaneous (10 ns) measurements. The description of DGV technology is given by Komine (1990) and Meyers (1995). The system consists of the Nd:YAG laser, light sheet forming optics, laser frequency monitoring system, and three receiver optical systems. The output laser beam was directed to the light sheet forming optics located on the wind tunnel test section floor, Figures 2 and 3. The receiver optical systems and the laser frequency monitoring system consisted of a linear polarizer, beamsplitter, an encased and insulated Iodine vapor cell, mirror, and two electronically shuttered CCD video cameras, Figure 4. Each system was enclosed to protect the optics from the wind tunnel environment and flow buffeting.

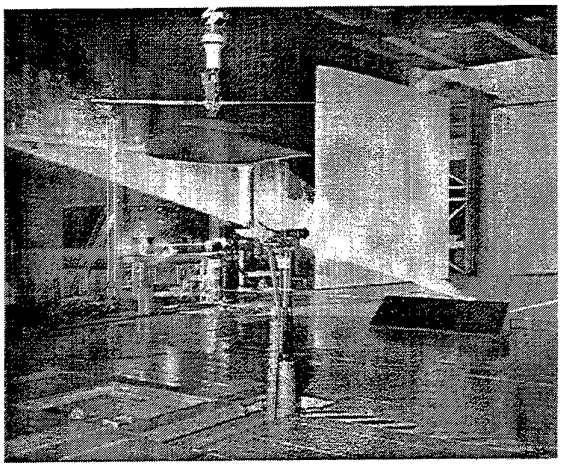


Figure 2 The 1.7-meter isolated rotor system with the fuselage placed below the rotor mounted in the 14-by 22-Foot Subsonic Tunnel.

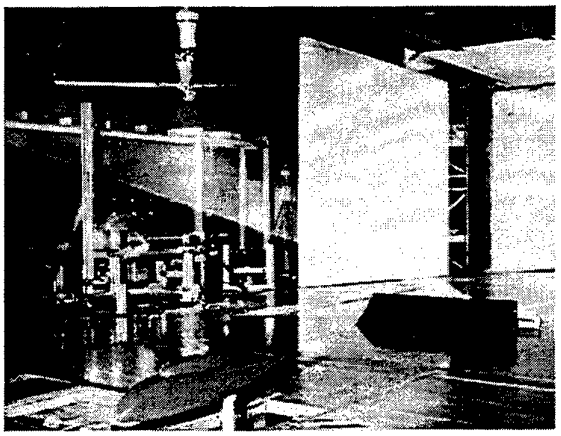


Figure 3 The 1.7-meter isolated rotor system with the fuselage placed out of the flow.

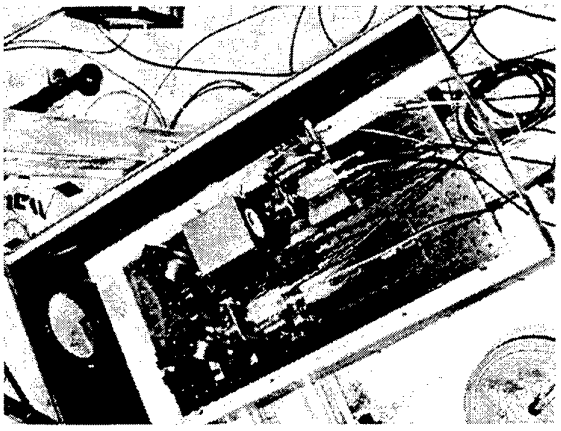


Figure 4 Doppler Global Velocimeter receiver optical system.

All three receiver optical systems were placed on the advancing side of the rotor to have an unobstructed view of the laser light sheet when the fuselage was in place, Figure 5. Their placement yielded an angle between the vector measured by component A and the vector measured by component B of 52 degrees, 47 degrees between the vectors measured by components A and C, and 41 degrees between the vectors measured by components B and C. These separation angles were sufficient to minimize trigonometric errors when translating the measurements to the streamwise, vertical, and crossflow velocity components. The common field of view was an area 1.02-by 1.14 meters.

The data acquisition system consists of a network of five PC compatible computers with one computer dedicated to each measurement component, the fourth obtaining data from the laser frequency monitor, and the fifth serving as the operator terminal and system controller. Each component computer contains two 10-bit frame grabbers to acquire single-field (512x256 pixels) images from the signal and reference cameras, respectively. The industry standard RS-170 cameras were electronically shuttered (0.1 ms) in synchronization with the Nd:YAG laser. While the cameras and data acquisition system were set to free run, images were only acquired when the rotor shaft encoder aligned with one of the selected azimuth angles: 0- to 90-degrees, in 10 ±0.7 degrees (±2 encoder steps) increments.

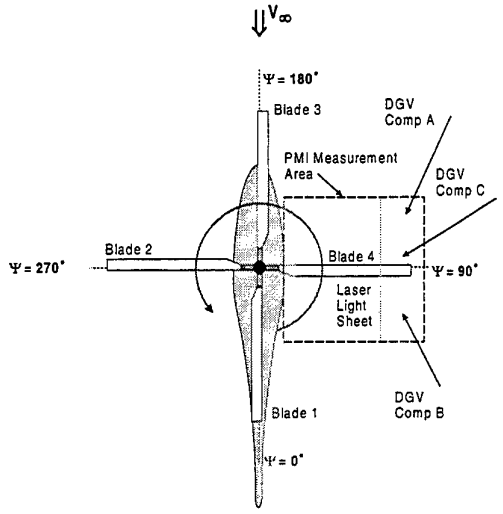


Figure 5.- Planview of the model, laser light sheet, DGV receiver optical systems, and PMI measurement area.

4. PROJECTION MOIRÉ INTERFEROMETER

Conventional projection moiré interferometry begins with the projection of a grid of equispaced, parallel lines onto the surface of a test object. With the object in the reference condition, a CCD video camera is used to acquire an image of the object illuminated by the lines. When the object is deformed, the grid line spatial arrangement changes. A second image is then acquired. Subtracting the reference image from the data image yields a pattern of moiré fringes tracing the contours of constant deformation amplitude. The measured deformation direction is along the bisector of the projection and viewing vector directions. The deformation amplitude between adjacent moiré fringes is proportional to the projected grid line spacing and the angle between the projection and viewing vectors.

The Projection Moiré Interferometry (PMI) system used in this study was a single-component, laser diode based system capable of obtaining instantaneous (0.1 ms) measurements. This system is described in detail by Fleming and Gorton (1998). The system consists of a pulsed 15 W laser diode bar (10 discrete emitters) operating at 800 nm, a Ronchi ruling, projecting optics, and an electronically shuttered CCD video camera. The laser diode bar was chosen as the light source because of its small size, high output power, single pulse operation, and infrared wavelength. The laser light passes through the Ronchi ruling (a diffracting grading with a square wave cross section) to a lens system that projected the resulting lines onto the underside of the rotor blades, Figure 6. The PMI optical system was placed below the test section floor to view a 1.2-x 1.2-meter area in the rotor

disk plane covering 50 degrees of rotor azimuth, Figure 5. The data acquisition system, a one-camera version of the DGV component acquisition system, and the laser diode bar were triggered by the DGV synchronization signal. Thus the DGV and PMI systems acquired data at the same instant with the same measurement window.

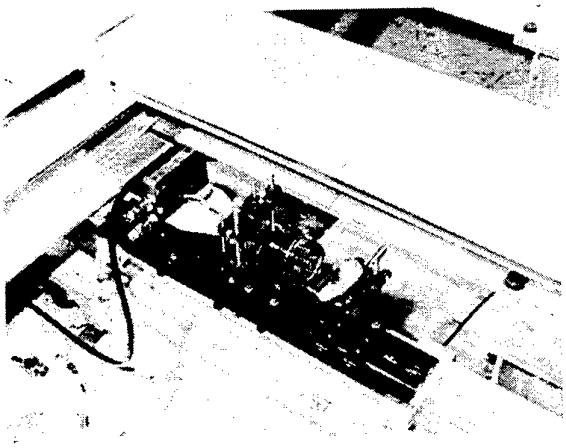


Figure 6 Projection Moiré Interferometer laser and transmission optical system.

The standard PMI reference image could not be obtained since the rotor blades continuously moved through the viewing area. An aluminum honeycomb plate was placed in the rotor disk plane at the rotor hub height to obtain a reference image. Subtraction of this image from the data images produced moiré fringe patterns representing height changes of the rotor blade above this reference plane. Additional processing, described by Fleming and Gorton (1998), yielded the location, bending, and twist of the imaged rotor blade at the instant of the DGV velocity measurement.

5. CALIBRATION PROCEDURES

As with most optical instrumentation systems, DGV and PMI required daily alignment and system calibration. Their use of video cameras as the measurement sensors eased alignment procedures, but increased the number of calibration techniques needed. The systems were aligned using a simple target of equispaced dots shown in Figure 7. Each DGV component receiver optical system was aligned using a custom electronics system to normalize the signal camera image by the reference camera image in real time. Adjusting the signal camera position and viewing angle to the proper alignment would extinguish the dots from the normalized image. Aligning the PMI was even simpler: align the viewing camera to keep the dot pattern as square as possible, then focus the projected grid lines to fill the viewing area and obtain optimal contrast.

Daily calibration of the instruments more extensive system alignment was necessary. Both techniques required optical calibrations to remove optical and perspective distortions from the acquired data images. Spatial distortions were determined using the alignment target, Figure 7, to establish a centroid map for each camera. The maps, which embodied the observed optical and perspective distortions, were used to compute the piecewise bilinear warping coefficients necessary to remove the distortions from the data images (Meyers (1992) and Meyers (1995)). Corrected DGV signal images could then be normalized by their respective corrected reference images to yield the component velocity data images. In addition, the warping procedures were sufficiently accurate to allow the determination of the orthogonal U, V, and W velocity components from the three measured components. Likewise, similar procedures were used to remove spatial distortions from the PMI data images.

Since DGV measurements are based on the ratio of image amplitudes, additional calibrations were required that

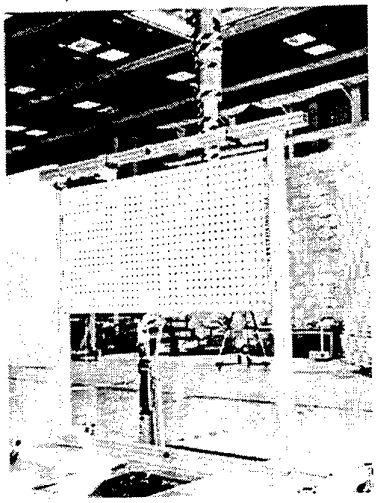


Figure 7 Alignment and spatial calibration target for DGV and PMI.

were not necessary for the spatially-based measurements of the PMI. The amplitude response of each DGV receiver system was flattened by determining the sensitivity of each camera pixel, and measuring any spatially dependent transmission losses through the optics. This process generated a pixel sensitivity correction image for each camera in the DGV system, and an optical transmission correction image for each receiver. When multiplying data images by their respective pixel sensitivity correction image, the overall camera response would be held constant. Likewise, by multiplying the normalized signal images by their respective optical transmission correction image, differences in the transmission of light through the signal and reference optical paths were removed (Meyers (1995)).

The final calibration for DGV determined the Iodine cell transfer function. The Nd:YAG laser output beam was redirected and split into three beams that were then directed to points on the tunnel structure, each within the field of view of their respective receiver optical system. The sampling of the output beam by the laser frequency monitor was also maintained. Tuning the laser frequency through the Iodine absorption line produced the simultaneous calibration of the

four cells. This procedure could be performed at any time, even during tunnel operation.

The PMI reference plane was established by replacing the dot target with an aluminum honeycomb plate painted flat white. The laser bar generated the grid of projected lines on the plate. A comparison of the camera image of the projected lines with the images of the dot target yielded the grid line spacing, and thus the sensitivity factor for the moiré fringes (Fleming and Gorton (1998)).

6. THE TEST

The Rotor Wake / Configuration Aerodynamics Test was conducted to investigate the three-component velocity flow field within the rotor wake with and without a fuselage placed below the rotor. The measurement of the trajectory and velocity of the rotor tip vortices as they moved downstream was of primary interest. Several instrumentation issues were in question since this was the first attempt at using global instrumentation to quantify the rotor wake. These included the integration of a pulsed, Nd:YAG laser into the DGV system, the ability of PMI to accurately measure instantaneous blade position, bending, and twist, and the logistics behind the simultaneous operation of the DGV and PMI systems with synchronized lasers (2), video cameras (9), and data acquisition systems (6 computers).

Velocity measurements of the rotor wake were desired at the 30-, 80-, 97-, 99-, 101-, and 103-percent span locations. Planar measurements at these spanwise locations would provide enough information to accurately determine the blade tip vortex structure and trajectory in the near rotor wake. The DGV laser light sheet was oriented vertically and directed upstream, Figure 2. An automated beam steering mechanism was devised to position the light sheet within the 97- to 103-percent span locations so that light sheet alignment changes could be made while the tunnel was operating. The 30- and 80-percent locations required realignment of the DGV optics.

Each day of testing began with the alignment of the DGV and PMI optical systems, followed by the spatial calibration of both systems at the desired span position. A rotor blade was removed during this process to allow unobstructed optical access to the measurement plane. The laser light sheet was then aligned to the span position. Once aligned, the laser beam was redirected to the tunnel structure to conduct the Iodine vapor cell calibrations. The rotor blade was then replaced and the tunnel test section sealed. The rotor was spun to 2,000 rpm and the laser beam redirected to form the light sheet. Note that the rotor was always spinning when the pulsed light sheet was crossing the blades; this technique protected the composite rotor blades from damage by the high-power light sheet. The tunnel speed was then set to 9.1 m/s and the smoke plume positioned to pass through the light sheet at the rotor wake.

Data acquisition began when the rotor system, wind tunnel velocity, and smoke plume position were stable. A portion of the Nd:YAG laser beam was sampled by a fast photodiode whose output was monitored with a high-speed digital oscilloscope. The shape of the photodiode amplitude vs. time trace was visually inspected to determine that the laser operated in single-frequency mode. If the photodiode output signal had a Gaussian amplitude profile, the laser was operating at a single frequency. A series of 100 conditionally sampled DGV and PMI image sets was acquired when single frequency operation was obtained. The laser beam was redirected to the tunnel walls and a sample of ten images was acquired. This provided a measurement of the Iodine vapor calibration stability. The light sheet was reformed and a second acquisition of 100 image sets obtained. Another calibration check was made followed by the acquisition of the third and final data set. The 300 image sets would yield approximately 30 image sets at each of the selected azimuth angles. This process was repeated at tunnel speeds of 27.7 m/s and 42.0 m/s with the fuselage in both high and low positions (Figures 2 and 3).

7. EFFECTS OF USING THE ND:YAG LASER IN DGV

Changing the DGV laser source from an Argon-ion laser to a pulsed, single-frequency, frequency-doubled Nd:YAG laser provided the capability to obtain conditionally-sampled rotor azimuth-dependent data. It also simplified Iodine vapor cell calibrations since the optical frequency was continuously tunable. Unfortunately, the change in laser also affected both image quality and frequency stability. Laser speckle was a far greater problem with the Nd:YAG laser than the Argon-ion laser. Although increased speckle might be expected from the narrower linewidth Argon-ion laser (10 MHz vs. 80 MHz for the Nd:YAG), the reverse was found. The level of laser speckle noise expected from the Argon-ion laser was reduced by temporal averaging the collected particle-scattered light during the 16.7 ms CCD camera integration time.

Classically laser speckle has been removed using low pass filtering techniques. These techniques include temporal averaging, spatial averaging, low frequency camera Modulation Transfer Functions (MTF) (Smith (1998)), data binning (McKenzie (1997)), and image convolution with a filtering kernel (Meyers (1995)). Temporal averaging of conditionally sampled instantaneous data requires an instrument satiability greater than that achieved in the present study. The other techniques have varying potential for removing laser speckle noise. They all low-pass filter the image data. Complete removal of laser speckle noise would require such a low filter bandwidth that the characteristics of flow structures would be masked. Since the data processing software developed for the Argon-ion based system used the image convolution technique, a new method was developed that would remove laser speckle noise without modifying the flow structure data such as for rotor vortices.

A nonlinear filtering technique developed to remove impulse noise without affecting the underlying image integrity is the median filter (Astola and Kuosmanen (1997)). Basically, the technique sorts pixel amplitudes within the processing kernel, e.g., 5x5 pixels, then selects the median amplitude as the filtered result. A median filter removes impulsive noise while the kernel based low pass filter passes an impulse, albeit wider with a lower amplitude. The effectiveness of this filter can be seen by comparing an original reference camera image with the image after filtering, Figure 8. Using this filtering method, laser speckle noise was virtually eliminated from the data images, revealing the rotor wake structures. It also revealed a low spatial-frequency modulation in the normalized signal image not found in the Argon-ion laser based system.

Laser frequency stability greatly deteriorated during the wind tunnel investigation though it was not identified as a

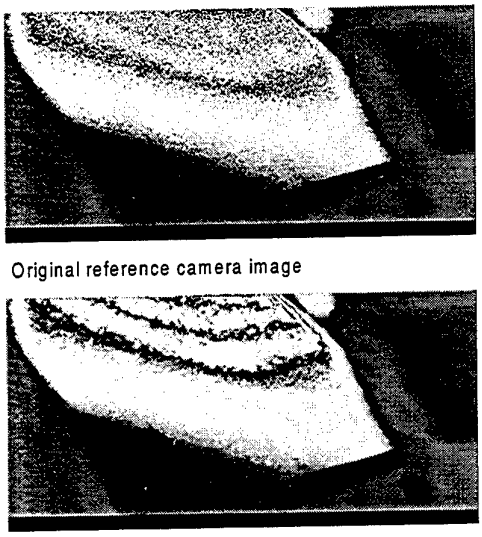


Figure 8 Removal of laser speckle noise with a median filter.

potential concern in the laboratory. This can be illustrated by comparing a series of ratio measurements obtained by the laser

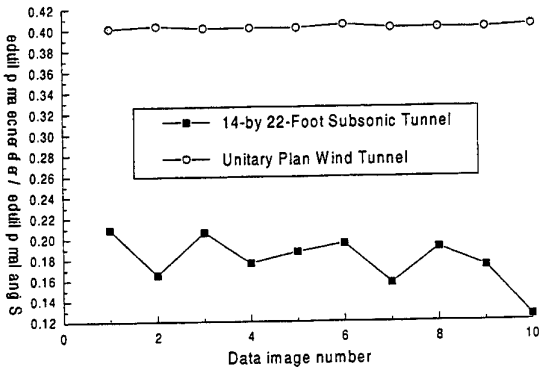


Figure 9 Comparison of Nd:YAG laser frequency stability during two wind tunnel tests.

frequency monitoring system during the rotor wake investigation with a similar series obtained during a subsequent investigation in the Langley Unitary Plan Wind Tunnel, Figure 9. A comparison of the two samples clearly shows a far more stable output frequency from the Nd:YAG laser during the UPWT investigation than the rotor wake test. The difference was traced to the sensitivity of the laser to vibration. The area adjacent to the UPWT test section was equivalent to a laboratory environment. However, the area adjacent to the open test section in the 14-by 22-Foot Subsonic Tunnel proved to be a very hostile. Floor vibration and wind tunnel shear layer buffeting caused the laser to lose frequency stability. Also, temperature variations, up to 30° C, during tunnel operation affected the Iodine vapor cell temperature stability, thus modifying its absorption characteristics.

8. IODINE VAPOR CELL STABILITY

The inability of the Iodine vapor cell heating system to compensate for large changes in environmental temperature was discovered during a previous DGV entry in the 14-by 22-Foot Subsonic Tunnel. In preparation for the current investigation, the cells were insulated and encased with a controlled heat sink on the stem to maintain a small, but constant positive heat transfer. Also the cell in the laser frequency monitor was modified to have a limited vapor pressure by reducing the amount of Iodine placed in the cell. In addition, calibrations were conducted before the tunnel run, once during the run between changes in tunnel velocity, and after the tunnel run, along with laser frequency measurements made between the acquisition of data sets. An overlay of these three Iodine cell calibrations for component C from a typical tunnel run is shown in Figure 10. The mismatch in calibration was a result of temperature variations in the cell from 47.4° C, to 48.0° C, to 53.0° C respectively. Since the environmental effects were not eliminated by insulating and encasing the cells, bias errors were present in the velocity measurements. Although the limited-vapor cell temperature also changed, 50.2° C, to 49.8° C, to 52.4° C with the corresponding calibrations shown in Figure 11, the affects on cell calibration were reduced.

9. SMOKE SYSTEM SEEDING

The seeding system for the DGV measurements used a superheated propylene glycol and water mixture. The smoke was injected using the standard flow visualization smoke generator for the tunnel and three additional portable smoke

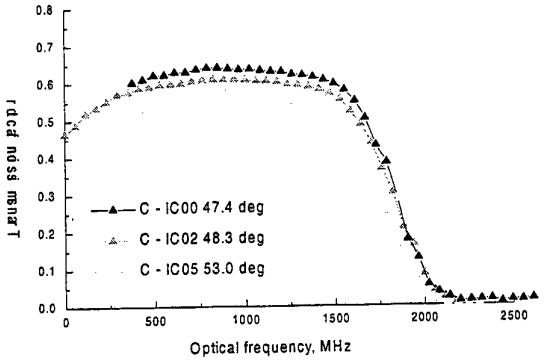


Figure 10 Iodine vapor cell calibrations for component C before, during, and after a typical tunnel run.

generators all located on a positioning system in the settling chamber of the tunnel. The smoke generators were mounted on an array as shown in Figure 12 which was upstream of the flow straightening honeycomb and four anti-turbulence screens, 26 m upstream from the test section. The smoke output for DGV in this wide field of view application was

marginal. Although each of the generators was producing the maximum volume of smoke, the smoke dispersion and distribution in the test section was unsatisfactory to seed the large planar viewing area. In addition, the heated smoke contained its own convective flow patterns at the lowest tunnel speeds. It was also difficult to locate the smoke plume in the vortex region since the laser could not be synchronized with rotor azimuth.

10. ROTOR WAKE MEASUREMENTS

The objective of the rotor wake measurements was to obtain measurements of the rotor tip vortex trajectory and

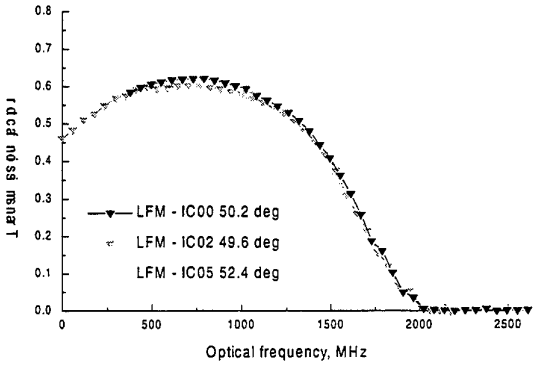


Figure 11 Iodine vapor cell calibrations for the laser frequency monitor obtained simultaneously with Figure 10.

velocity for several flight conditions, with and without the

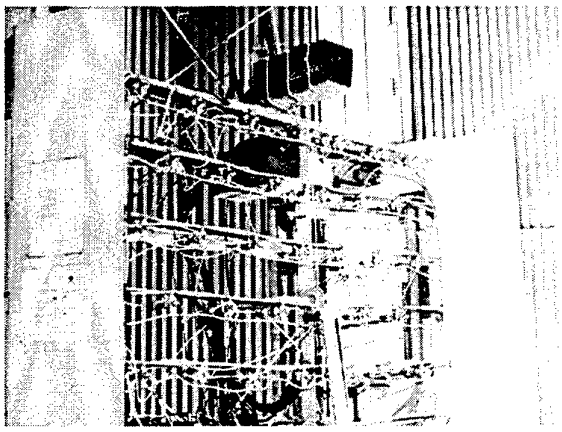


Figure 12 Vaporization/condensation smoke generators attached to the laser velocimeter particle generation nozzle array in the tunnel settling chamber.

presence of a fuselage beneath the rotor. The test conditions were chosen to match the conditions for which flow visualization data were reported by Ghee *et al* (1996) as well as to match the conditions for which rotor inflow data were obtained by Elliott *et al* (1988).

Although the bias error limits the usefulness of the DGV data, patterns appear to correlate to the expected behavior of the rotor wake system. The rotor wake can be described as a cylindrical column of accelerated flow which is skewed from the freestream direction by an angle determined from the downward velocity within the wake and the freestream velocity magnitude. The resulting angle from the vertical for the average wake trajectory is known as the skew angle, X. Using the analysis of Stepniewski and Keys (1984) a derivation of skew angle for a rotor in forward flight can be found as:

$$X = \tan^{-1}\left(V\cos(\alpha)/(v_f - V\sin(\alpha))\right) \qquad (1)$$

where V is the freestream velocity, α is the rotor shaft angle of attack, and v_f is a function of rotor thrust coefficient and freestream velocity.

For this rotor system, operating at a rotor thrust coefficient of 0.0064 and a rotational speed of 209 rad/s, the following table shows the skew angle calculated from the above reference for a rotor in forward flight. Also included in table 1 are the skew angles determined from the experimental data found by Ghee *et al* (1996) as well as the skew angle measured in the DGV data and discussed below the table.

Table 1 Experimental and theoretical skew angles.

Freestream Velocity, V, m/s	9	27.7	42
α, deg	0	-3	-3
v_f, m/s	10.6	3.7	2.5
X, deg Theoretical	40	79	84
X, deg Experimental Flow Vis (Ghee, et al (1996))	NA	77	79
X, deg DGV Experimental Images	57	78	83

Figures 13 and 14 show a DGV image of the freestream velocity component for a rotor position of zero degrees azimuth for the 27.7 and 42.0 m/s test conditions, respectively. The view in the image is from the right side of the model looking inboard at the 80-percent radial location. The flow is from right to left in the figures, and the rotor blade is rotating from left to right. The grayscale in the image indicates where the smoke was observed in the field of view. The black areas are the absence of the seeding smoke. In each image, the center of the hub is located by a small crosshair and the blades are overlaid at their forward and aft positions. The overlaid dot card pattern gives a sense of scale with 6.35 cm spacing between the dots.

The long dashed white line in each of the images highlights the skew angle seen in the DGV measurements. The boundary of the wake should convect downstream at the wake skew angle and should theoretically be along the short dashed lines. However, vortex positions obtained from the flow visualization data (symbols), (Ghee *et al* (1996)), show the location of the wake boundary to match the DGV results for these test conditions. Both theoretical and experimental data indicate good agreement in skew angle.

While the good agreement of skew angle is a positive indication for the DGV measurement, further comparisons with wind tunnel freestream data and with independent, three-component laser velocimetry data have been limited by the thermal variations in the Iodine calibrations and low frequency variations in the scattered light. Calibration corrections based

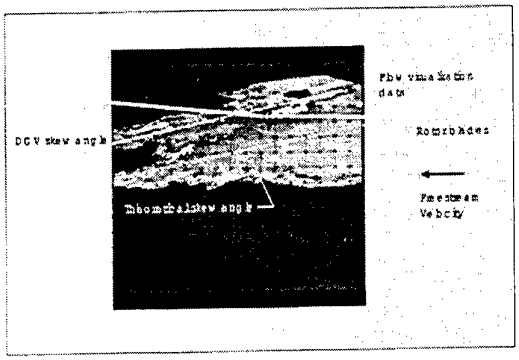


Figure 13 DGV measurement of the streamwise velocity with overlays of theoretical rotor wake skew angle and vortex positions obtained from flow visualization, freestream velocity = 27.7 m/s.

on cell temperature measurements obtained for every image are

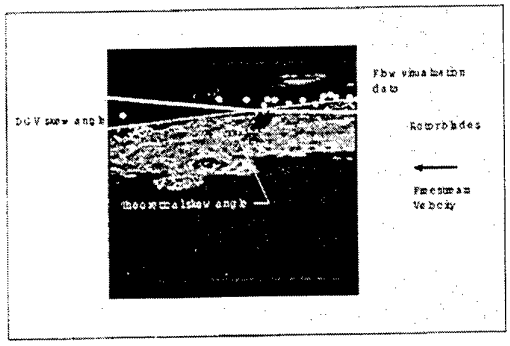


Figure 14 DGV measurement of the streamwise velocity with overlays of theoretical rotor wake skew angle and vortex positions obtained from flow visualization, freestream velocity = 42.0 m/s.

underway at this time to improve the DGV data for later comparisons. Also, laboratory investigations are underway to determine the source of the low frequency variations in the normalized signal image not found in the Argon-ion laser based system.

11. ROTOR BLADE DEFORMATION MEASUREMENTS

PMI was successfully used to measure the rotor blade deformation. Figure 15 shows the contours of the blade deformation for several test conditions, and differences in the blade shape are clearly visible. The blade shape deforms as would be expected for a rotor system undergoing changes in test condition; the most dramatic tip deformation relative to the horizontal reference plane occurred when the rotor shaft angle was tilted forward. Figure 16 shows the change in measured blade height with rotor azimuth for the rotor tip path plane tilted 3 degrees nose down. The measured 26 mm difference in the blade tip deflection between 70 and 110 degrees of azimuth corresponds well to the expected deflection due to the geometry of 32 mm.

12. LESSONS LEARNED

Three-component flow field investigations using DGV to conditionally sample an unsteady flow field in a large wind tunnel facility illustrates the vast differences between laboratory and large wind tunnel environments. The tasks

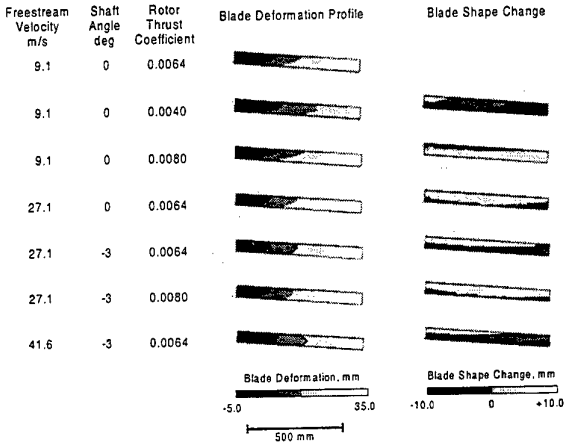


Figure 15 PMI measured blade deflection profiles for seven different flight conditions, blade #4.

where difficulties were anticipated such as combining the

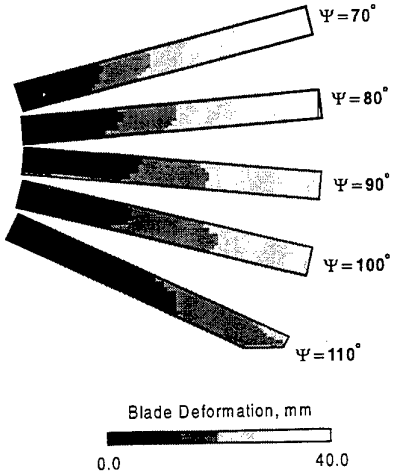


Figure 16 Azimuth dependent PMI measured blade deformation profiles, fuselage down, rotor shaft angle set to -3 degrees.

DGV and PMI systems, synchronizing the lasers, cameras, and data acquisition computers, and conditionally sampling the

measurements as a function of rotor azimuth, were very successful. Several areas have been identified where previous experience was insufficient to predict system characteristics. These included insufficient isolation of the Iodine vapor cells from the tunnel environment, laser speckle, and other noise sources originating from the Nd:YAG laser.

From these experiences, the following modifications to the system and procedures are recommended:

1. Procedures must be developed to prevent laser damage to wind tunnel models.
2. Vapor pressure limited Iodine vapor cells completely isolated from the wind tunnel environment need to be developed.
3. Vibration isolate the Nd:YAG laser and place it totally out of the flow field.
4. Develop a smoke generating system that will yield smoke plumes at least 1.5 m in diameter, preferably using cold injection.
5. Use the rotor synchronized Argon-ion based laser light sheet system to set the smoke plume position.

13. SUMMARY

The first attempt to use pulsed, three-component Doppler Global Velocimetry to measure unsteady rotor wake flow fields was presented. These conditionally sampled results were accompanied by the simultaneously acquired pulsed laser Projection Moiré Interferometry deformation and twist measurements of the moving rotor blades. While the PMI results were very successful, the DGV results suffered from environmental problems and image noise originating by the Nd:YAG laser. The vapor-limited Iodine cell was found to be less sensitive to the environmental changes than the standard cells. Median filtering techniques virtually eliminated laser speckle noise while preserving details of the vortex structures. Work continues on reducing noise sources and correcting the data for temperature induced calibration changes.

REFERENCES

Astola, J. and Kuosmanen, P. 1997, Fundamentals of Nonlinear Digital Filtering. CRC Press, New York.

Elliott, J.W.; Althoff, S.L.; and, Sailey, R.H. 1988, Inflow Measurement Made With a Laser Velocimeter on a Helicopter Model in Forward Flight. Volumes I-III, NASA TM 100541-100543, AVSCOM TM 88-B-004-006.

Fleming, G.A. and Gorton, S.A. 1998, Measurement of Rotorcraft Blade Deformation using Projection Moiré Interferometry. Proc. of the 3rd Int. Conf. on Vibration Measurements by Laser Techniques, Ancona, Italy.

Gentry, G.L., Jr.; Quinto, P.F.; Gatlin, G.M.; and, Applin, Z.T. 1990, The Langley 14-by 22-Foot Subsonic Tunnel — Description, Flow Characteristics, and Guide for Users. NASA TP-3008.

Ghee, T.A.; Berry, J.D.; Zori, L.A.J.; and, Elliott, J.W. 1996, Wake Geometry Measurements and Analytical Calculations on a Small-Scale Rotor Model. NASA TP 3584, ATCOM TR-96-A-007.

Komine, H. 1990, System for Measuring Velocity Field of Fluid Flow Utilizing a Laser -Doppler Spectral Image Converter, US Patent 4 919 536.

Komine, H.; Brosnan, S.J.; Long, W.H.; and Stappaerts, E.A. 1994, Doppler Global Velocimetry Development of a Flight Research Instrumentation System for Application to Non-intrusive Measurements of the Flow Field. NASA Report CR-191490.

McKenzie, R.L. 1997, Planar Doppler Velocimetry for Large-Scale Wind Tunnel Applications. AGARD Fluid Dynamics Panel 81st Meeting and Symposium on Advanced Aerodynamic Measurement Technology, paper 9, Seattle, WA.

Meyers, J.F. 1992, Doppler Global Velocimetry - The Next Generation? AIAA 17th Aerospace Ground Testing Conf., paper AIAA-92-3897, Nashville, TN.

Meyers, J.F. 1995, Development of Doppler Global Velocimetry as a Flow Diagnostics Tool. Measurement in Fluids and Combustion Systems, Special Issue, Measurement Science and Technology, vol 6, no. 6, pp. 769-783.

Meyers, J.F. 1996, Evolution of Doppler Global Velocimetry Data Processing. Eighth Int. Symp. on Applications of Laser Techniques to Fluid Mechanics, paper 11.1, Lisbon, Portugal.

Smith, M.W. 1998, Application of a Planar Doppler Velocimetry System to a High Reynolds Number Compressible Jet. AIAA 36th Aerospace Sciences Meeting & Exhibit, paper AIAA 98-0428, Reno, NV.

Stepniewski, W.Z.; and, Keys, C.N. 1984, Rotary-Wing Aerodynamics. Dover Publications, Inc., New York.

Effect of Sensor Geometry On the Performance of PIV Interrogation

J. Westerweel

Laboratory for Aero & Hydrodynamics
Delft University of Technology
Rotterdamseweg 145, 2628 AL Delft, the Netherlands

Abstract

This paper describes the mathematical investigation of the effect of the sensor geometry, i.e. the pixel size and pixel fill ratio, on the performance of PIV interrogation. Two sub-pixel estimators are investigated: the particle-image centroid, and the Gaussian peak fit. It is found that no bias errors occur when the particle-image diameter is at least two pixels, and the measurement error is determined by random errors only. When particle images are much smaller than one pixel, an irrecoverable signal loss deteriorates the measurement performance. For intermediate resolutions the bias errors are of the same magnitude as the random errors. It is demonstrated that image blurring by de-focussing reduces the bias error. The analysis shows that sensors with a high fill ratio have a better performance.

1 Introduction

In recent years the performance of PIV interrogation methods has improved considerably, and the resolution of the pixelization with respect to the particle-image diameter has been reduced substantially.

Originally, the pixelization of PIV images was done with a high resolution. When the discretization of the image matches the minimum sampling rate prescribed by the sampling theorem, the original continuous image can be reconstructed perfectly from the discrete samples. In that case the details of the sensor geometry are completely negligible, and typically occurs for the analysis of highly resolved PIV photographs. However, nowadays it is more common to record PIV images directly on electronic image sensors (viz., CCD arrays). The demand for PIV measurements with high spatial resolution often implies that the discretization no longer matches the Nyquist sampling criterion, and consequently, the measurement precision depends on the detailed geometry of the image sensor.

For example, an effect known as 'pixel locking' may interfere with the measurements when the size of the pixels is about the size of the particle images. This pixel locking is described as a biasing of the measured displacement towards integer values of the displacement in pixel units, as is illustrated in Figure 1. The effect is usually ascribed to the fact that the particle images become too small with respect to the size of the pixels. Also, it is conjectured that CCD sensor arrays with low fill ratio are more susceptible to pixel locking.

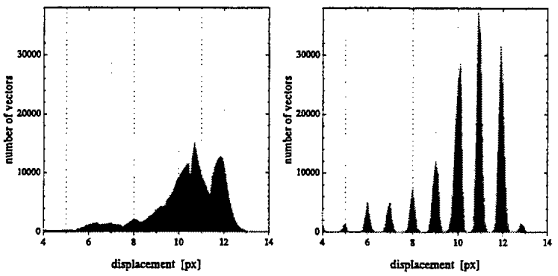


Figure 1: Histograms of the measured displacement for PIV in a turbulent pipe flow. An 'ideal' measurement (left), and a measurement that suffers from pixel locking (right).

In this paper the error for PIV interrogation is investigated mathematically as a function of the sensor geometry, which is characterized by the size d_τ of the pixels, and the relative fraction a^2 of the total pixel area that is light sensitive. Generally the measurement error is split into a random error component and a bias error component. The random error is proportional to the width of the particle images, whereas the bias error is associated with the finite size of the pixels. Other effects that may influence the interrogation performance are left out of consideration.

The next section consists of a concise review of the main characteristics of particle images, spatial correlation and pixelization. In Section 3 two estimators are investigated: (1) the particle-image centroid (which is commonly applied at low image density), and (2) the so-called *Gaussian peak fit* (which is applied at high image density). The analysis for the particle-image centroid is based on the work by Alexander and Ng (1991), and is extended to include the effect of blur. Altough the analysis is done mathematically, the results are incidentally compared with results obtained from the interrogation of synthetic PIV images, generated by means of Monte-Carlo methods. Section 4 contains the conclusions and a discussion on the valid range for PIV measurements that are restricted by the sensor characteristics.

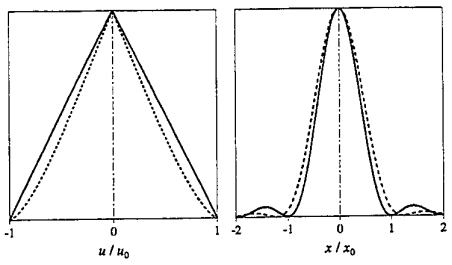


Figure 2: The optical transfer function (left) and diffraction-limited spot (right) for square (——) and circular (– – –) apertures.

2 characteristics of particle images

2.1 continuous domain

The image of a small tracer particle is given by the convolution of its geometrical image and the diffraction-limited spot of the imaging optics (Goodman 1968). The Fourier transform of the diffraction-limited spot is commonly referred to as the optical transfer function (OTF). The OTF for a lens with a square aperture is given by

$$F(u,v) = \Lambda(u/u_0)\Lambda(v/u_0), \tag{1}$$

with

$$\Lambda(u) = \begin{cases} 1-|u| & \text{for } |u|<1, \\ 0 & \text{elsewhere,} \end{cases} \tag{2}$$

and where u_0 is the cut-off spatial frequency, given by

$$u_0 = D/f\lambda(M+1), \tag{3}$$

where D is the aperture diameter, f the lens focal length, λ the light wavelength, and M the image magnification. The corresponding diameter d_s of the diffraction-limited spot is given by

$$d_s = 2(M+1)f\lambda/D = 2/u_0. \tag{4}$$

The OTF of a square aperture is separable in u and v, which makes it very convenient for mathematical analysis. It is also a good approximation of the OTF of a lens with a circular aperture, which has the same cut-off frequency, but is circularly symmetric. The diameter d_s of the diffraction-limited spot for a lens with a circular aperture is given by

$$d_s \cong 2.44(M+1)f\lambda/D. \tag{5}$$

The optical transfer function and diffraction-limited spot for a lens with a circular aperture and for a lens with a rectangular aperture are shown in Figure 2.

The diffraction-limited spot and geometric particle image are commonly approximated by two-dimensional Gaussian functions, so that the particle-image diameter d_τ is approximately given by (Adrian 1984)

$$d_\tau \cong \left(M^2 d_p^2 + d_s^2\right)^{\frac{1}{2}}, \tag{6}$$

where d_p is the diameter of the tracer particle. Hence, for small M the size of the particle images is determined by the diffraction-limited spot, i.e. $d_\tau \cong d_s$.

2.2 spatial correlation

At high image density the particle-image displacement is determined from the estimated location of the displacement-correlation peak in the spatial correlation of two image fields I_1 and I_2, taken with a small time delay. It was shown by Keane and Adrian (1992) that the spatial cross-correlation can be separated into three terms: $R_D + R_C + R_F$. The term R_D represents the spatial correlation of the image intensity fluctuations, and holds all information with regard to the motion of the particle images. The terms R_C and R_F vanish when the (local) mean image intensity is subtracted from the instantaneous image fields. The ensemble mean of the term R_D over all possible realizations of I_1 and I_2 for a given uniform velocity field $\boldsymbol{u}$ is given by (Keane and Adrian 1992)

$$\langle R_D(s)|\boldsymbol{u}\rangle \propto N_I F_I F_O F_\tau(s - s_D), \tag{7}$$

where N_I is the image density (i.e., the mean number of particle images in the interrogation window), F_I and F_O the loss-of-correlation due to in-plane and out-of-plane motion respectively of the tracer particles, F_τ is the self-correlation of the particle images, and s_D is the (in-plane) displacement of the particle-images. For Gaussian particle images with an e^{-2}-diameter d_τ, the displacement-correlation peak is also Gaussian, but with an e^{-2}-diameter of $\sqrt{2}d_\tau$.

2.3 discrete domain

The sensor geometry that was described in the Introduction can be represented by the spatial pixel sensitivity $p(x,y)$. For square pixels with a uniform sensitivity over the light sensitive area $p(x,y)$ is given by:

$$p(x,y) = \frac{1}{(ad_\tau)^2}\begin{cases} 1 & \text{for: } |x|,|y| \leqslant \frac{1}{2}ad_\tau, \\ 0 & \text{elsewhere.} \end{cases} \tag{8}$$

The discrete image field is given by the convolution of the continuous image intensity field and the pixel sensitivity, sampled at intervals d_τ, i.e.

$$I[i,j] = \iint p(x-x_i, y-y_j)I(x,y)dxdy, \tag{9}$$

with: $x_i = id_\tau$, $y_j = jd_\tau$.

The pixelization of an image $f(x,y)$ can be expressed in the two-dimensional spatial frequency domain as a double infinite series of the Fourier transform $F(u,v)$ of $f(x,y)$, multiplied by the Fourier transform of the spatial pixel sensitivity, denoted by $P(u,v)$, i.e.:

$$G(u,v) = \sum_{n=-\infty}^{\infty}\sum_{m=-\infty}^{\infty} F\left(u-\frac{n}{d_\tau}, v-\frac{m}{d_\tau}\right) P\left(u-\frac{n}{d_\tau}, v-\frac{m}{d_\tau}\right) \tag{10}$$

(Alexander and Ng 1991; Oppenheim et al. 1983). For $p(x,y)$ given in (8), $P(u,v)$ is equal to

$$P(u,v) = \mathrm{sinc}(ua/d_\tau)\,\mathrm{sinc}(va/d_\tau), \tag{11}$$

with $\mathrm{sinc}(u) = \sin(\pi u)/\pi u$.

The discrete spatial correlation is given by convolution of continuous spatial correlation and self-correlation of pixel sensitivity, sampled at intervals d_τ:

$$R_D[i,j] = \iint \Phi_{pp}(s - s_i, t - t_j) R_D(s,t) ds dt, \tag{12}$$

with

$$\Phi_{pp}(s,t) = \iint p(x,y) p(x+s, y+t) dx dy \tag{13}$$

(Westerweel 1993). For the pixel sensitivity defined in (8), the self-correlation $\Phi_{pp}(s,t)$ is given by

$$\Phi_{pp}(s,t) = \Lambda(s/ad_\tau)\Lambda(t/ad_\tau), \tag{14}$$

where $\Lambda(u)$ is defined in (2). Note that $\Phi_{pp}(s,t)$ is separable in s and t.

2.4 optimal sampling

The sampling theorem states that a bandlimited signal can be reconstructed from its discrete samples when the sampling rate is at least twice the bandwidth (Oppenheim et al. 1983). Optical systems are essentially bandlimited, for which the bandwidth is given by the OTF cut-off spatial frequency (Goodman 1968).

In the case of an aberration-free lens with a square aperture, the OTF cut-off frequency is given by (1). This means that an exact reconstruction of the continuous image intensity field from the discrete samples (viz., discrete image) could be achieved when the size of the pixels is less than $1/2u_0$. Given that d_s is equal to $2/u_0$, the Nyquist sampling criterion is satisfied when the pixel size d_τ is less than one quarter of the diffraction-limited spot diameter, i.e.

$$d_s/d_\tau \geqslant 4. \tag{15}$$

Hence, errors that are associated with the sensor geometry may be expected when the size of a pixel is larger than about one-quarter of the diffraction-limited spot diameter.

3 Analysis

Consider a particle image or a displacement-correlation peak located at a position (d_x, d_y). The measurement error is the difference between the estimated position (m_x, m_y) returned by the interrogation, and the actual position. Condider only the error in the x-coordinate:

$$\varepsilon_x = m_x - d_x. \tag{16}$$

It is convenient to separate ε_x into mean and fluctuating parts, and average over many identical measurements:

$$\langle \varepsilon_x \rangle = \delta_x, \quad \text{and:} \quad \langle \varepsilon_x^2 \rangle = \delta_x^2 + \sigma_x^2, \tag{17}$$

where δ_x is denoted as the *bias error*, and σ_x as the r.m.s. *random error*. The random error is generally associated with variations of individual particle images with respect to the average shape of the particle image, whereas the bias error is associated with the variation of the average shape with respect to ideal shape of the particle images. Typically, the bias error arises due to the change in shape of the particle image or displacement-correlation peak as a result of image pixelization.

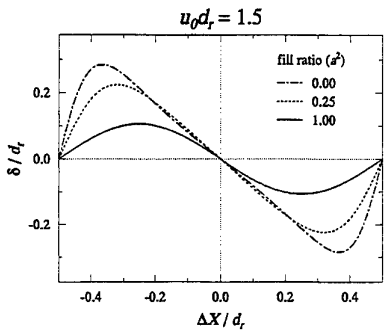


Figure 3: The bias error for the centroid of a diffraction-limited particle image as a function of the displacement, for $d_s/d_\tau = \frac{4}{3}$ and $a = 1.0$, 0.5 and 0.0.

3.1 random error

In the continuous domain the uncertainty to determine the location of a particle image or displacement-correlation peak is proportional to the width of the particle image (Adrian 1991)

$$\sigma_x \sim c\, d_\tau, \tag{18}$$

where c is a proportionality constant. This constant is about 0.05 to 0.1, as obtained from experimental data (Prasad et al. 1992). It was shown by Wernet and Pline (1993) that this relationship also holds for discrete images, and that the value for c is inversely proportional to the signal-to-noise ratio for the image intensity field. For low light levels the signal strength is determined by the photon count rate, so that the signal-to-noise ratio is proportional to the square root of the intensity (viz., photon count). Hence, the signal-to-noise ratio for a given light level will be proportional to the square root of the active pixel area, so that a reduction of the pixel fill ratio at a fixed light level implies a proportional increase of the random error. This can be compensated for by properly increasing the total illumination of the tracer particles. However, note that by this argument a sensor with 20% fill ratio requires a 5 times more powerfull illumination source in comparison with a 100% fill-ratio sensor.

3.2 particle-image centroid

Consider a single particle image, with an intensity distribution $\tau(x,y) = f(x - d_x, y - d_y)$, where (d_x, d_y) is the location of the particle image. The centroid m_x of the particle image in the direction of the x-coordinate is then given by

$$m_x = \frac{\iint x\tau(x,y) dx dy}{\iint \tau(x,y) dx dy}, \tag{19}$$

and *vice versa* for the centroid m_y of the particle image in the direction of the y-coordinate. The centroid bias error δ_x for the particle-image centroid in (19) can be written as

$$\delta_x = \frac{\iint x f(x,y) dx dy}{\iint f(x,y) dx dy} = \frac{\frac{dF}{du}(0,0)}{2\pi i F(0,0)}, \tag{20}$$

(Alexander and Ng 1991) where $F(u,v)$ is the Fourier transform of $f(x,y)$. It is easily proven that the centroid (m_x, m_y) yields the *exact* location of the particle image when $f(x,y)$ is symmetric (Alexander and Ng 1991).

The image pixelization is accounted for by substitution of $G(u,v)$ in (10) for $F(u,v)$ in (20). In order to keep the mathematics simple, it is assumed that $G(u,v)$ is separable, i.e.:

$$G(u,v) = G_u(u)G_v(v), \quad \text{and:} \quad \frac{dG}{du}(u,v) = G'_u(u)G_v(v) \tag{21}$$

This reduces the subsequent analysis to a one-dimensional problem.

Following the analysis of Alexander and Ng (1991) yields the following exact expression for the bias error δ_x:

$$\delta_x = \frac{\sum_{n=1}^{\infty} G'_u(n/d_\tau)\sin(2\pi d_x n/d_\tau)}{\pi\left[G_u(0) + \sum_{n=1}^{\infty} G_u(n/d_\tau)2\cos(2\pi d_x n/d_\tau)\right]}, \tag{22}$$

and *vice versa* for δ_y. Note that the error is zero when the cut-off frequency is smaller than $1/d_\tau$. This implies that it is not necessary to satisfy the Nyquist sampling rate—which is equal to 2 times the cut-off frequency—to obtain error-free estimates of the particle-image centroid. So, the pixel resolution d_τ should satisfy

$$d_s/d_\tau \geqslant 2. \tag{23}$$

This is a factor two smaller than the minimum sampling rate prescribed by (15).

3.2.1 *slight under-sampling*

If the OTF cut-off frequency is between $1/d_\tau$ and $2/d_\tau$ then (22) reduces to:

$$\delta_x = \frac{G'_u(1/d_\tau)\sin(2\pi d_x/d_\tau)}{\pi\left[G_u(0) + G_u(1/d_\tau)2\cos(2\pi d_x/d_\tau)\right]}. \tag{24}$$

So, the error is periodic with a period that is equal to the sample spacing d_τ.

Let us evaluate this result for a diffraction-limited particle image. Given that $G_u(u) = F_u(u)P_u(u)$, we have:

$$\begin{cases} G_u(0) = 1, \quad G_u(1/d_\tau) = (1 - 1/u_0 d_\tau)\,\mathrm{sinc}(a) \\ G'_u(1/d_\tau) = d_\tau(1 - 1/u_0 d_\tau)\cos(\pi a) - d_\tau\,\mathrm{sinc}(a) \end{cases} \tag{25}$$

Substitution in (24) yields the following expression for δ_x at $a = 0$:

$$\delta_x/d_\tau = -\frac{(1/u_0 d_\tau)\sin(2\pi d_x/d_\tau)}{\pi\left[1 + (1 - 1/u_0 d_\tau)2\cos(2\pi d_x/d_\tau)\right]} \tag{26}$$

and for δ_x at $a = 1$:

$$\delta_x/d_\tau = -\frac{1}{\pi}(1 - 1/u_0 d_\tau)\sin(2\pi d_x/d_\tau). \tag{27}$$

In Figure 3 the error δ_x is plotted for $a^2 = 0$, $\frac{1}{4}$ and 1, for a sampling rate $u_0 d_\tau = \frac{3}{2}$. This graph shows that the error for contiguous pixels (i.e., $a = 1$) is smaller than for infinitesimal pixels (i.e., $a = 0$).

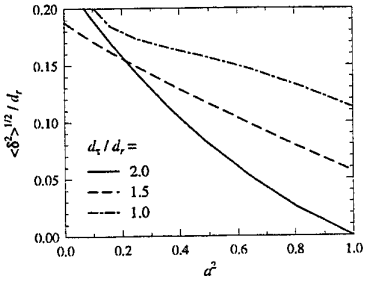


Figure 4: The root-mean-square amplitude $\langle\delta^2\rangle^{1/2}$ of the bias error for the diffraction-limited particle-image centroid as a function of the pixel fill ratio a^2, for $d_s/d_\tau = 1.0$, 1.5 and 2.0.

For the special case where $1/d_\tau$ exactly matches the cut-off frequency, the amplitude of δ_x is zero for $a^2 = 1$, whereas values of $a^2 < 1$ lead to a finite error amplitude. This demonstrates the importance of using CCD arrays with 100% fill ratio.

Note that the curves in Figure 3 have negative gradients at $d_x = 0$. This implies that the measured location for a particle image is biased towards the center of a pixel. Consequently, measurements of the location and displacement of a particle image favor integer pixel values. This effect is commonly referred to as *pixel locking*. The analysis presented here has demonstrated that this effect can be associated with an undersampling in the pixelization of the image scene.

3.2.2 *the effect of blur*

In the literature it is often reported that a slight blurring of the image improves the precision of the estimated location. In this section this will be investigated by considering the tracking error for slightly defocussed particle images. Since the tracking error is identical to zero for fully resolved pixelization, we consider the effect of blur for the case of slightly under-sampled pixelization. To keep the analysis concise only the case for contiguous pixels (i.e., $a^2 = 1$) will be considered.

The analysis in Section 3.2.1 showed that the shape and amplitude of the tracking error is determined by $G_u(1/d_\tau)$ and $G'_u(1/d_\tau)$, where $G_u(u)$ is the product of the optical transfer function (OTF) and the spatial pixel sensitivity. For an optical configuration that is not exactly in focus the OTF is given by (Goodman 1968):

$$G_u(u) = \Lambda(u/u_0)\,\mathrm{sinc}\left[8\frac{w}{\lambda}\frac{u}{u_0}\left(1 - \frac{|u|}{u_0}\right)\right] \tag{28}$$

where w is the *maximum path-length error*, defined as:

$$w = \left(\frac{1}{d_i} + \frac{1}{d_o} - \frac{1}{f}\right)\frac{D^2}{8} \tag{29}$$

where d_i and d_o are the image and object distances respectively. The maximum path-length error can be written as: $w/\lambda \approx -\frac{1}{2}h/\delta_z$, where h is the distance between the object

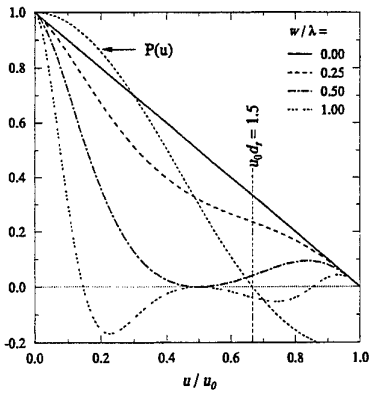


Figure 5: The optical transfer function for a (square aperture) optical system with different degrees of out-of-focus aberration. The dash-dotted line represents the transfer function of contiguous pixels ($a^2 = 1$) at a sampling rate of $u_0 d_\tau = \frac{3}{2}$.

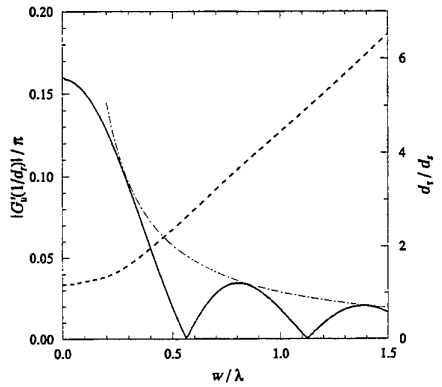


Figure 6: The amplitude of the bias error and e^{-2} width of the diffraction-limited spot, as a function the out-of-focus path length error w. The dashed dotted line represents the envelope of the curve for the bias-error amplitude.

plane and the plane of focus, and δ_z the object focal depth (Adrian 1991).

Figure 5 shows the optical transfer function (OTF) for an optical system with square aperture for different values of w, corresponding to an object plane that is located between zero ($w/\lambda = 0$) and twice ($w/\lambda = 1$) the focal depth from the true focal plane. Note that where the object plane is out of focus, the values of $G(u)$ and $G'(u)$ for $1 \leq 2u/u_0 \leq 2$ are generally *smaller* than for the case of perfect focus ($w/\lambda = 0$); this already indicates that one may expect a smaller tracking error for blurred particle images.

For the case of contiguous pixels, the pixelization transfer function is zero for $u = 1/d_\tau$; see (11). Consequently, the tracking bias error is a sinus function with an amplitude given by:

$$\frac{1}{\pi} G'(1/d_\tau) = -\frac{1}{\pi} \Lambda\left(\frac{1}{u_0 d_\tau}\right) \operatorname{sinc}\left[8 \frac{w}{\lambda} \frac{1}{u_0 d_\tau}\left(1 - \frac{1}{u_0 d_\tau}\right)\right]. \quad (30)$$

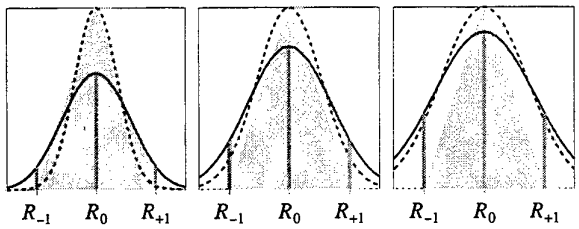
The absolute amplitude of the tracking error for pixelization with contiguous pixels with a sample spacing of $u_0 d_\tau = \frac{3}{2}$ is shown in Figure 6. This result indeed shows a considerable reduction for the tracking error for an increasing out-of-focus location of the object plane. The amplitude even becomes zero at $w/\lambda \cong 0.65$ and 1.25.

So, a slight blur can reduce the tracking error considerably, and for this particular example a properly chosen blur may even completely compensate for the tracking error. However, it should noted that blur *increases* the particle-image diameter, which also increases the random error and may cancel out the favorable effect of blur. This is illustrated by Figure 6, in which is also plotted the e^{-2}-diameter of the particle image as a function of w/λ; note that the particle-image diameter increases linearly for $w/\lambda > 0.5$. The envelope of the bias error amplitude (denoted by the dash-dotted line in Figure 6) is inversely proportional to w, and consequently the product of the envelope and the particle-image diameter is constant. Hence, for this particular case the *reduction* of the tracking bias error is replaced by a proportional *increase* of the random error.

3.3 Gaussian peak-fit

The observation that the shape of particle images and consequently the shape of the displacement-correlation peak is well approximated by a Gaussian curve has promoted the use of a Gaussian curve fit for the estimation of the particle-image or peak location (Willert and Gharib 1991; Westerweel 1993). For correlation peaks in the discrete domain it was shown that for small particle images, i.e. $d_\tau/d_\tau \sim$ 1-2, only the correlation maximum and it adjacent correlation values are significant with respect to the background random correlations (Westerweel 1993). Hence, each component of the location is estimated by fitting a Gaussian curve to the correlation maximum R_0, and its two neighbors, denoted by R_{-1} and R_{+1} respectively. The location is then given by:

$$m_x = i_0 d_\tau + \frac{1}{2} \frac{\ln R_{-1} - \ln R_{+1}}{\ln R_{-1} + \ln R_{+1} - 2 \ln R_0} d_\tau, \quad (31)$$



(a) 1.0 (b) 1.5 (c) 2.0

Figure 7: The continuous (– – –) and discrete (——) correlation peaks for Gaussian particle images with $d_\tau/d_\tau = 1.0$, 1.5 and 2.0, at zero fractional displacement with $a = 1$. The shaded triangle represents Φ_{pp}.

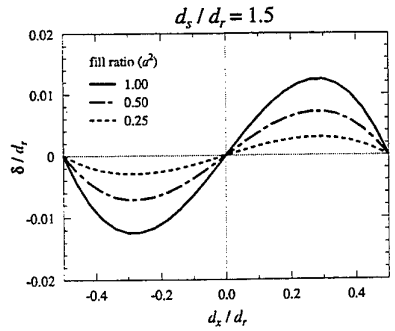


Figure 8: The bias error for the Gaussian peak fit for Gaussian particle images as a function of the displacement, for $d_\tau/d_r = 1.5$ and fill ratio $a^2 = 1.00$, 0.50 and 0.25.

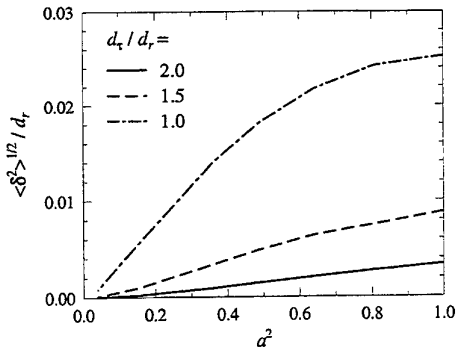


Figure 9: The root-mean-square amplitude $\langle \delta^2 \rangle^{1/2}$ of the bias error for the Gaussian peak fit as a function of the fill ratio a^2 for $d_\tau/d_r = 1.0$, 1.5 and 2.0.

with: $R_i = R_D[i_0 + i, j_0]$, where $[i_0, j_0]$ are the indices of the maximum correlation. For matter of simplicitly it is assumed that $i_0 = j_0 = 0$. When the correlation peak has an exact Gaussian shape, then the estimate returned by (31) would be exact. However, for digital image fields, the shape of the discrete correlation peak is given by (12); see also Figure 7. So, even for perfectly Gaussian particle images, the estimate (31) will deviate from the true location.

To determine the bias error as a function of the particle-image size and pixel fill ratio, the expression in (12) for the discrete correlation was substituted in (31). It was assumed that the continuous displacement-correlation peak was Gaussian with an e^{-2}-diameter of $\sqrt{2}d_\tau$. The result was determined by numerical integration of the substituted equations.

3.3.1 slight under-sampling

First, the bias error is considered for the range of particle-image sizes that can be considered as 'slightly under-sampled,' i.e. $1 \leqslant d_\tau/d_r \leqslant 2$.

In Figure 8 the bias error for the Gaussian peak fit is shown as a function of the displacement for $d_\tau/d_r = \frac{3}{2}$. Note that the derivative of the bias error at $d_x = 0$ is *positive*. Hence, in contrast with the bias error for the centroid, the Gaussian peak-fit estimate for the location of the displacement-correlation peak is biased *against* integer pixel values. This is opposite to what is observed in many practical situations, in which the Gaussian peak fit also suffers from a bias towards integer pixel values, rather than a bias against integer pixel values. This is further discussed in the next section.

The bias error amplitude is plotted in Figure 9 as a function of the fill ratio a^2 for different values of d_τ/d_r. Note that the bias error for the centroid estimate was increased when the fill ratio was decreased, whereas the result in Figure 9 for the Gaussian peak fit estimate shows that the bias error *decreases* for decreasing fill ratio. This is not very surprising, given that a Gaussian shape for the continuous displacement-correlation peak was chosen originally. In a practical situation the shape of the particle images is not exactly Gaussian, so it is expected that bias error does not decrease that rapidly. In addition, a reduction of the fill ratio will also increase the random error (unless the total illumination is increased proportionally; see Section 3.1). The error reduction only sets in when a^2 is substantially smaller than unity, so that the total illumination needs to be increased by a considerable amount before one can expect any benefit from such a low fill ratio.

The bias error for the Gaussian peak fit is plotted in Figure 10 as a function of d_τ/d_r for $a = 0.5$ and 1.0. The bias error is inversely proportional to d_τ/d_r. It increases very rapidly for $d_\tau/d_r < 1$, and it practically vanishes for $d_\tau/d_r > 2$. This complies with the result obtained for the centroid estimate. Note that the difference between the curves for different fill ratio only differ slightly, indicating that the fill ratio only marginally affects the bias error.

In Figure 10 are also plotted the total root-mean-square error obtained from the analysis of synthetic PIV images. The straight dashed line in Figure 10 corresponds to the emperical relationship in (18) with $c \cong 0.02$. This rather low value for c can be explained by the fact that these synthetic PIV images do not include any noise source, other than the local variation of the number of tracer particles, so that the SNR is likely to be substantially higher than

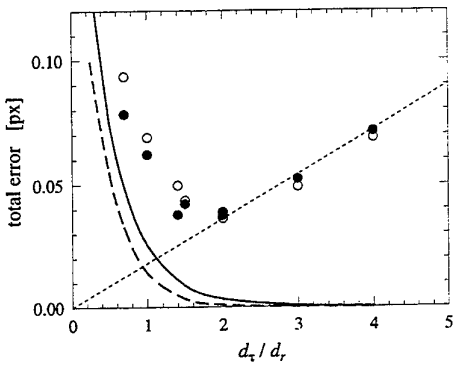
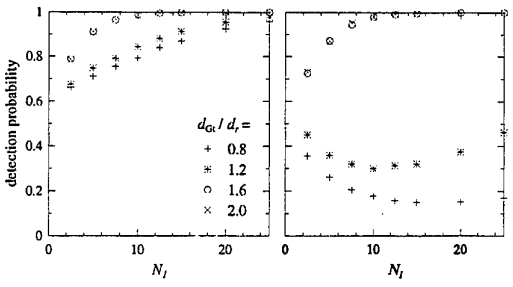


Figure 10: The total r.m.s. error for the Gaussian peak fit as a function of d_τ/d_r for $a = 1.0$ (—— and ●) and $a = 0.50$ (– – – and ○). The symbols represent results obtained from synthetic PIV images.



(a) $d_x/d_\tau = 0.0$ (b) $d_x/d_\tau = 0.5$

Figure 11: The detection probability for the displacement-correlation peak as a function of the image density N_I, for different values of d_τ/d_τ. (a) displacement is exact integer of pixels; (b) displacement is in between two integer pixel values.

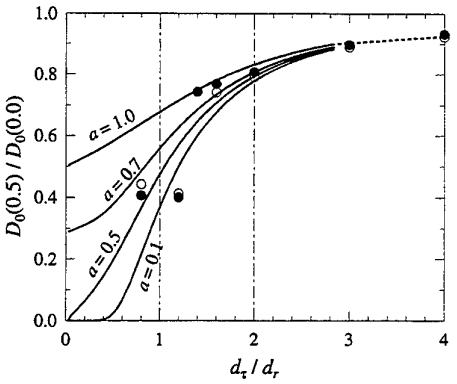


Figure 12: The ratio of the detectability D_0 for 0.5 and 0.0 fractional displacement as a function of d_τ/d_τ.

in most practical situations. Nonetheless, the minimum value for the total error occurs at about $d_\tau/d_\tau \sim 2$ with a value of about $0.04d_\tau$, which complies with simulation studies carried out by Willert (1996), and experimental data obtained by Prasad et al. (1992) and Westerweel et al. (1997).

3.3.2 serious under-sampling

The preceding analysis was done for values of the pixel size that correspond to a slight under-sampling of the image field. When the size of the particle images with respect to the pixels is further reduced, then another effect sets in that will be explained here.

Consider the expression (12) in the limit $d_\tau/d_\tau \to 0$. The shape of the discrete correlation peak is dominated by the self-correlation of the pixel sensitivity Φ_{pp}. Evidentely, the correlation amplitude is proportional to $\Phi_{pp}(d_x, d_y)$. So, the detectability of the displacement-correlation peak does not only depend on the image density, and the in-plane and out-of-plane loss-of-pairs, but also on the fractional part of the displacement. The lowest value of the detectability as a function of the fractional displacement occurs for $d_x/d_\tau = \pm\frac{1}{2}$. So, what happens is that the peak amplitude for non-zero fractional displacements is reduced, but the random correlations maintain the sample amplitude. Consequently, the probability that a random correlation peak is higher than the displacement-correlation peak is enhanced. The detection probability for fractional displacements of zero and $\frac{1}{2}$ is plotted as a function of the image density in Figure 11 for different d_τ/d_τ. Note that there is virtually no effect for large d_τ/d_τ, whereas there is almost a complete signal loss for small d_τ/d_τ.

In Figure 12 the ratio of the peak height at a fractional displacement of one-half and the peak height at zero fractional displacement is plotted as a function of d_τ/d_τ for different fill ratios. Assuming that the amplitude for the random correlations is the same for both values of the fractional displacement, this ratio is also a measure of the relative change in peak detectability.

For contiguous pixels (i.e., $a = 1$), the amplitude of the correlation peak drops by a factor 2 in the limit $d_\tau/d_\tau \to 0$ (i.e., $\Lambda(d_x/d_\tau) = \frac{1}{2}$ for $d_x/d_\tau = \frac{1}{2}$). However, when the pixel fill ratio is less than 0.25, the displacement-correlation peak vanishes completely (i.e., $\Lambda(d_x/ad_\tau) = 0$ for $a < d_x/d_\tau = \frac{1}{2}$). If one would plot a displacement histogram for such a situation, only displacements with a fractional displacement near zero yield valid measurements, whereas displacements with a fractional displacement near one-half result in a stong signal loss. This would explain why measurements obtained with the Gaussian peak fit display pixel locking at zero fractional displacements.

4 Discussion and Conclusions

The preceding analysis has shown that the effects of sensor geometry on the performance of PIV interrogation are negligible when the particle-image diameter is at least two pixels.

When the particle-images are slightly under-sampled, i.e. $1 \leqslant d_\tau/d_\tau \leqslant 2$, the bias errors are of the same order of magnitude as the random errors, so that measurements in this range of d_τ/d_τ are still feasible. However, the performance depends strongly on the pixel fill ratio, and it deteriorates substantially for both the centroid error and Gaussian peak fit when the fill ratio is much smaller than unity.

For slightly under-sampled images a blurring of the image by means of a slight de-focussing can reduce the bias error amplitude. However, this also increases the random error amplitude, so there is no real net improvement. For a substantial improvement of the measurement performance it is necessary to increase the signal bandwidth, whereas de-focussing only changes the shape of the OTF, but not its width.

When the particle images are less than one pixel in diameter, the bias errors dominate. For the Gaussian peak fit this implies an un-recoverable signal loss, that is proportional to the magnitude of the fractional part of the displacement. This leads to a higher probability to detect displacements that lie near an integer value

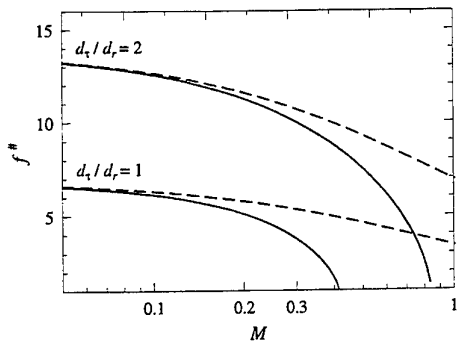


Figure 13: The minimum numerical aperture $f^{\#}$ $(= f/D)$ as a function of the image magnification M for 20 μm (——) and 2 μm (– – –) particles.

of in pixel units. Hence, the pixel locking effect for the Gaussian peak fit is more likely related to a signal loss, than a variation in peak shape as a function of the sensor parameters.

So, in what way does this affect how one can apply PIV with digital image sensors to measurements in flows? Given the experimental restriction $d_\tau/d_r \sim 1$–2, one may use (6) to determine a relation between the mimimum f-number and the image magnification for given tracer size d_p and pixel size d_τ.

For a PIV measurement in air the specific gravity of the tracer particles (or droplets) is much higher than that of the fluid, so that one is forced to use very small tracer particles. The typical diameter of oil droplets is 1–2 μm. Hence, for measurements in air the particle-image diameter is usually determined by the diffraction-limited spot of the imaging optics; at small image magnification one has to use high f-number lenses to match the particle-image diameter to the size of the pixels (and use correspondingly powerfull light sources to obtain a significant signal).

For experiments in water the situation is somewhat different. It is usually possible to match the specific gravity of the tracer particles with that of the fluid, so that one may use considerably larger particles in comparison with PIV measurements in air. Typical diameters for tracer particles in measurements in water lie in the range of 10–20 μm. So, for measurements in water it is more likely that the particle-image diameter is determined by the diameter of the geometric particle image, i.e. Md_p, when M is large.

These aspects are summarized in Figure 13, which shows the minimum required f-number for the imaging optics that correspond to $d_\tau/d_r = 1$ and 2 as a function of the image magnification M for $d_p = 2$ μm and 20 μm (representing PIV measurements in air and water respectively), and for a given pixel size of 12 μm (which is a typical value for CCD sensor arrays).

The image magnification for the typical small-scale laboratory experiment lies in the range between 0.25 and 1, which shows that low f-numbers can be used. However, for large-scale experiments, such as measurements in large wind tunnels, the image magnification may have a much lower value; imaging a 1 m^2 area on a 0.5 inch CCD array corresponds to $M = 0.012$, whereas imaging the same area on a large format 4"×5" film corresponds to $M = 0.1$. Hence, for such situations PIV measurements with CCD arrays at low f-numbers would typically suffer from pixel locking effects.

PIV measurements that lie near the corresponding curve for $d_\tau/d_r = 2$ are 'ideal' in the sense that the total error is minimal, whereas measurements that lie below the $d_\tau/d_r = 1$ curve suffer from an irreversible form of 'pixel locking'; between the two curves, the image field is slightly undersampled, and pixel locking only affects the measurements marginally.

Acknowledgement

The research of dr.ir. J. Westerweel has been made possible by a fellowship of the Royal Netherlands Academy of Arts and Sciences.

References

Adrian, R. J. (1984). Scattering particle characteristics and their effect on pulsed laser measurements of fluid flow: speckle velocimetry vs. particle image velocimetry. *Appl. Opt. 23*, 1690–1691.

Adrian, R. J. (1991). Particle-imaging techniques for experimental fluid mechanics. *Ann. Rev. Fluid Mech. 23*, 261–304.

Alexander, B. F. and K. C. Ng (1991). Elimination of systematic error in subpixel accuracy centroid estimation. *Opt. Engr. 30*, 1320–1331.

Goodman, J. W. (1968). *Introduction to Fourier Optics.* New York: McGraw-Hill.

Keane, R. D. and R. J. Adrian (1992). Theory of cross-correlation analysis of PIV images. *Appl. Sci. Res. 49*, 191–215.

Oppenheim, A. V., A. S. Willsky, and I. T. Young (1983). *Signals and Systems.* Englewood Cliffs, NJ: Prentice-Hall.

Prasad, A. K., R. J. Adrian, C. C. Landreth, and P. W. Offutt (1992). Effect of resolution on the speed and accuracy of particle image velocimetry interrogation. *Exp. Fluids 13*, 105–116.

Wernet, M. and A. Pline (1993). Particle displacement tracking technique and Cramer-Rao lower bound error in centroid estimates from CCD imagery. *Exp. Fluids 15*, 295–307.

Westerweel, J. (1993). *Digital Particle Image Velocimetry.* Ph.d. thesis, Delft University of Technology, The Netherlands.

Westerweel, J., D. Dabiri, and M. Gharib (1997). The effect of a discrete window offset on the accuracy of cross-correlation analysis of digital PIV recordings. *Exp. Fluids 23*, 20–28.

Willert, C. E. (1996). The fully digital evaluation of photographic PIV recordings. *Appl. Sci. Res. 56*, 79.

Willert, C. E. and M. Gharib (1991). Digital particle image velocimetry. *Exp. Fluids 10*, 181–193.

EFFECT OF VARIABLE LIQUID PROPERTIES ON THE FLOW STRUCTURE WITHIN SHEAR-DRIVEN WALL FILMS

A. Elsäßer, W. Samenfink, J. Ebner, K. Dullenkopf, S. Wittig

Lehrstuhl und Institut für Thermische Strömungsmaschinen,
Universität Karlsruhe (TH), D-76128 Karlsruhe, Germany

ABSTRACT

Liquid wall films driven by air flow occur in fuel preparation processes of advanced prefilming gas turbine combustor nozzles or in intake manifolds of SI-engines. There is a need to develop new and more accurate models to describe the heat transfer from the wall to the film. To obtain data necessary for the modeling a new measurement device in combination with an enhanced data processing technique has been developed. The device combines two novel measurement systems. It consists of a film structure measurement system and a specially adapted LDV-System with a miniaturized probe volume. This combination allows simultaneous measurements of film thickness and flow velocity within the film. For the first time detailed information of the internal flow structure are provided under consideration of the effect of variable liquid properties on the film hydrodynamics.

1. INTRODUCTION

Shear-driven liquid wall films play an important role in the fuel preparation process of advanced prefilming gas turbine combustors and intake manifolds of SI-engines (Roßkamp et al. (1997), Rottenkolber et al. (1998)). Advanced two-phase flow CFD-codes have been proven as a valuable tool in design and optimization of these components. Nevertheless, there is still a strong need to develop new and more accurate models for the fluid motion as well as for the heat transfer from the wall to the film. These advanced models have to consider the waviness and the internal flow structure of the wall film. However, for a more realistic simulation of the film flow detailed and accurate experimental data is crucial for an improved physical understanding as well as for the verification of fundamental assumptions used in the numerical code. The major problem governing the experimental investigation of shear-driven liquid films is the very small mean film height $\overline{h}_F$. It is only $100 - 150\ \mu m$ for technical relevant film flows. Conventional probe techniques to determine the internal flow structure for such films are not applicable.
Due to the multitude difficulties in the experimental access there is a lack of information about the internal hydrodynamics of shear-driven liquid films. To solve these problems, a new measurement and data processing technique was developed. The two main components of this novel measurement technique had been presented at the Lisbon Conference 1996 (Wittig et al. (1996) and Samenfink et al. (1996)). It consists of a laser-based film structure measurement system and a novel LDV-System with a miniaturized probe volume. Their key feature is that they allow simultaneous measurements of the film thickness and the flow velocities within the film. This provides detailed information of the internal flow structure and allows for the first time to consider the effect of variable liquid proporties on the flow structure and the film transport mechanisms respectively.

2. MEASUREMENT TECHNIQUES

To achieve the above mentioned comprehensive insight in the physics of liquid transport phenomena, detailed information of the instantaneous film height, wave shape and velocity profiles within the film are required. To perform the measurements a special test facility for film flow investigations was designed and built. Commercial measurement systems do not provide the capability necessary for these investigations. Therefore, the development of a new suitable equipment was necessary. The general working principles of these instruments will briefly be explained in the following sections. A more detailed description

can be found in the papers of Wittig et al. (1996) and Samenfink et al. (1996) mentioned already.

2.1 Test Rig for Film Flow Investigations

The basic item of the test rig used for the experiments was a transparent duct made of acrylic glass as shown in **Figure 1**. It has a rectangular cross section ($30 \times 196\ mm$) and a length of $1000\ mm$. To establish the air flow in the duct it is connected with the suction side of a blower. The air flow (left

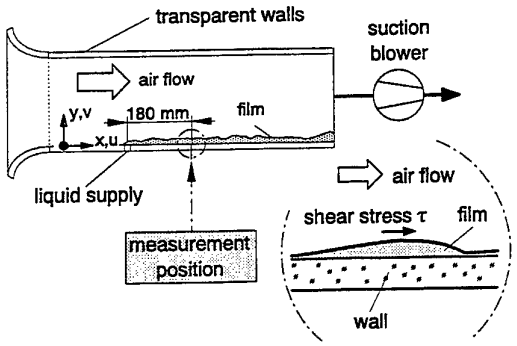


Figure 1: Test section

to right) generates a shear stress τ at the film surface causing the liquid to move downstream. The fluid was supplied by a row of small holes through the channel floor thus forming a continuous wavy film at the bottom wall. For the LDV measurements presented here the film fluid was seeded with starch particles. Free stream velocity and wall film conditions including temperature, pressure and volume flux were controlled continuously.

2.2 Film Thickness and Film Structure

In numerous studies different electrical and optical approaches had been applied by various authors to determine film thickness (capacitive or inductive sensors as well as electrical resistance probes were used). However, the spatial resolution of these methods was generally limited by the sensor dimensions (about 3 to 5 mm in diameter), so individual waves usually could not be detected. Alternative methods based on the analysis of a flourescent dye added to the film or the absorption of light passing a dyed liquid layer have major drawbacks especially in evaporating films. The dyes added usually have different evaporating properties and therefore concentrate in the remaining liquid layer leading to wrong results. During various studies of prefilming atomizers at the Institut für Thermische Strömungsmaschinen at the University of Karlsruhe (ITS), different measurement techniques had been studied and a comprehensive overview was given by Himmelsbach (1992). An improved approach avoiding the above mentioned problems in the exact determination of film thickness was presented by Samenfink et al. in 1996. An advanced technique based on optical absorption without dyes was described, applicable in water, water/glycerine mixtures or alcohols. It uses the effect of absorption in the wavelength range of the near infrared.

The main principle of the system is schematically drawn in **Figure 2**. A laser beam of the intensity

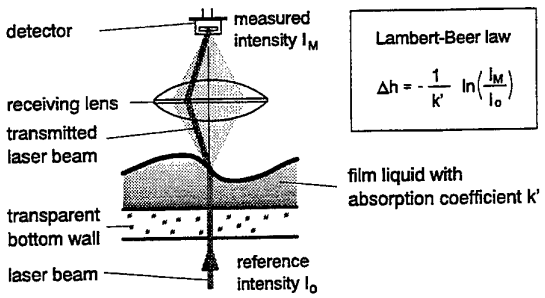


Figure 2: Light absorption in the liquid film

I_0 passes the liquid sheet from the bottom wall. Depending on the tickness of the sheet and the absorption coefficient k' the intensity I_0 is reduced to the value I_M according to the Lambert-Beer law (see **Figure 2**). In the technical relevant thickness range of $h_F \leq 1\ mm$ a value of $k' \approx 1\ mm^{-1}$ is necessary to achieve a sufficient reduction. In the presented system a wavelength of $\lambda = 1480\ nm$ is used for water and water/glycerine measurements (water: $k' = 3.14\ mm^{-1}$). For example a water layer thickness of only 1 mm leads to an intensity reduction of more than 95%. With a large size receiving lens above the film the remaining intensity is focussed on the detector to determine the intensity I_M.

In order to enhance the accuracy of the film thickness measurements intensity losses through reflections at the film surface or optical components (e.g. fiber coupling) were compensated by superposing a second laser beam. The correction beam with a wavelength of $\lambda = 830\ nm$ was therefore not absorbed by the film liquids used in the tests. The intensity losses was exclusively reduced by effects not depending on the film thickness, so this information was used to correct the intensity I_M of the wavelength absorbed in the film. By means of this technique the intensity absorption though the liquid film could be determined with an excellent level of accuracy.

However, this measurement technique do not give direct information on the spatial surface structure, but the film thickness as a function of time. In general shear-driven fuel films occuring in technical applications show a three-dimensional wave pattern on the

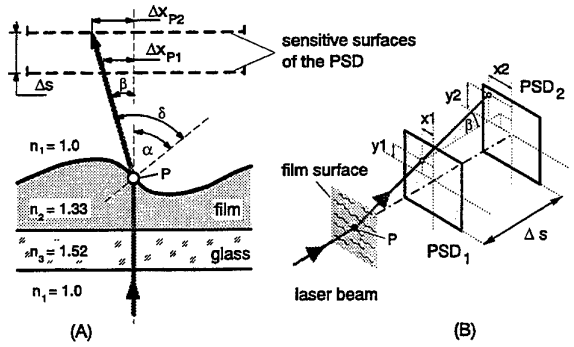


Figure 3: Beam deflection at the film waves and principle of surface angle measurement

surface. These waves determine the internal flow in the film. Therefore, it is necessary to record the surface structure and the film thickness simultaneously. The surface structure is represented by the wave angle α. It can be calculated from the deflection of the transmitted laser beam as shown in **Figure 3**. After the beam passed the bottom wall and the liquid film it enters the air space with an angle δ at the phase boundary. This is caused by the surface angle and the change in the index of refraction $n_2 \rightarrow n_1$. If the angle β can be determined experimentally, α can be calculated by means of the Snellius law and some trigonometric theorems.

$$\begin{aligned} \alpha &= \arcsin\left(\frac{n_1}{n_2}\sin\delta\right) \\ \beta &= \delta - \alpha \\ \alpha &= \arctan\left(\frac{\sin\beta}{n_2/n_1 - \cos\beta}\right) \end{aligned} \qquad (1)$$

However, the main problem remaining is that a simple setup can only detect the displacement Δx with respect to the optical axis. As a consequence the major source of errors is the variation in the height of point P on the film surface. This effect is caused by the wavy film and is directly affecting the beam displacement Δx. Therefore, a more sophisticated technique to determine the correct exit angle δ had to be applied.

As demonstated in **Figure 3A** and **Eqn. 2** two independent position sensitive detectors (PSD) separated by the known distance Δs are necessary. Because the wavy surfaces of the films under investigation were generally three-dimensional, beam deflection occurs in cross stream direction also. The determination of the exit angle β is therefore based on a two-dimensional measurement to detect the components βx and βy in main and cross stream direction respectively. In the design used for the later describes measurements the detector consists of a complex system of beam splitters and PSD devices, as described in detail by Samenfink et al. (1996).

$$\delta = \arctan\left(\frac{\sqrt{(x_2 - x_1)^2 + (y_2 - y_1)^2}}{\Delta s}\right) \qquad (2)$$

For the exact assignment of the velocity data inside the film derived by the LDV system (as described in the following chapter) to the position within the wave, the temporal thickness traces had to be transferred to spatial co-ordinates. The precise spatial reconstruction of the film surface structure was possible by combining the simultaneous film thickness and surface angle data. Calculating the derivative of the time-dependent film thickness the variation of film thickness $\dot{h}_F(t)$ as a function of time is obtained. The function $\dot{h}_F(t)$ can be splitted into a time dependent term and a spatial dependent term

$$\dot{h}_F(t) = \frac{dh_F}{dt} = \frac{dh_F}{dx} \cdot \frac{dx}{dt} \qquad (3)$$

The spatial term represents the surface angle variation and can be directly expressed as a function of the measured wave angle $\alpha_F(t) = dh_F/dx$.
Assuming that the mean transport velocity of the wave $\overline{u}_W = dx/dt$ is constant, $\overline{u}_W$ can be determined by the deviation of the temporal film thickness and the corresponding surface angle measurements. It allows to express the film thickness as a function of the main flow coordinate x with high spatial resolution. The calculated surface structure represents the shape of the waves passing the probe volume with a high level of accuracy.

2.3 Film Velocity Profile Determination

Due to the lack of commercially available systems for the measurement of velocity profiles in thin, wavy liquid films a novel LDV system had to be developed, especially adapted to the required conditions. The crucial feature was an excellent resolution in film height direction coupled with the possibility of avoiding photomultiplier overload through reflections at the persistent moving film surface.

2.3.1 Transmitting Optics

As basic system for the transmitter a two-component fiber optic LDV system was used, looking vertically up through the transparent bottom wall of the test section (see **Figure 4**). In this way excellent optical access to the film flow was achieved. In order to reduce the length of the probe volume a beam expander and a short focal length ($f = 80\ mm$) was utilized. They reduce the transmitter probe volume size to a length of $\Delta y_F \simeq 260\ \mu m$ and a diameter of $\Delta x_F \simeq \Delta z_F \simeq 25\ \mu m$ at the $1/e^2$ intensity point

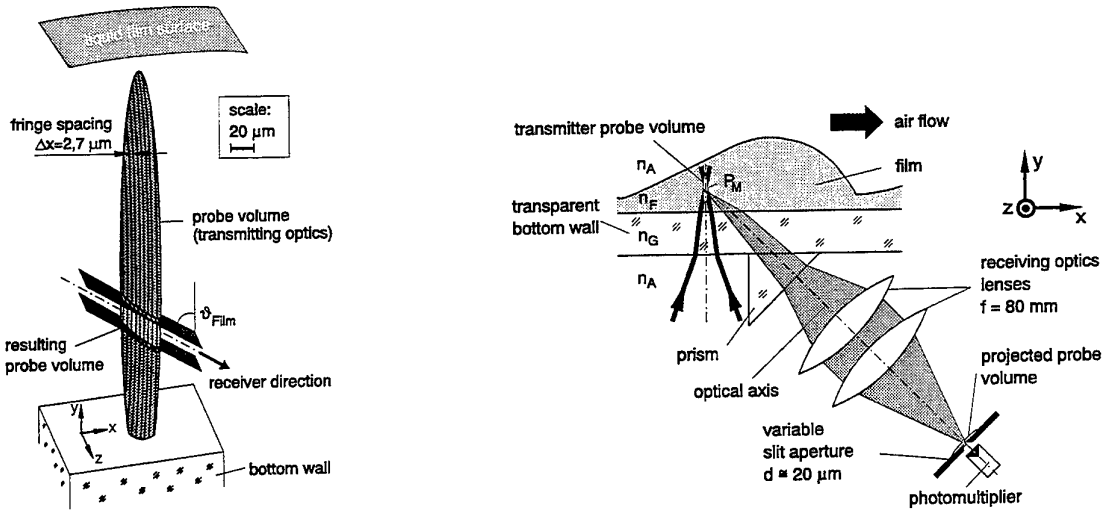


Figure 4: LDV-System with probe volume size reduction

as shown in **Figure 4**. However, the size Δy_F is still one order of magnitude larger than the desired spatial resolution of about $25 - 30\ \mu m$ in film height direction. Therefore, the probe volume length has to be reduced further by the receiver design and orientation.

2.3.2 Receiving Optics

As previously pointed out a 180° backscattering set up would not lead to the needed reduction in the probe volume size and furthermore the reflections at the film surface would cause serious problems considering the signal to noise ratio in a wide range of surface angles. To solve these problems the detector was shifted to an off-axis angle with respect to optical axis of the transmitter, thus cutting a narrow section of the probe volume as shown in **Figure 4**. Simultaneously, this off-axis angle helps to solve the reflection problem at the air/liquid interface. An angle of 45° to the optical axis was chosen, because our previous investigations had shown that reflections in this range occurs relatively seldom for conditions used in the tests. To collect data only in a well defined section of the probe volume in the y-axis direction, a slit aperture was positioned in front of the color splitter in the receiver. The optical signals were detected by a two-component photomultiplier setup in combination with counter processors and a self developed software for data aquisition and analysis.

To reduce astigmatism due to the off-axis angle a prism was fixed perpendicular to the optical axis in order to obtain equal refraction conditions for the scattered light. Different angles of incidence appear only at the boundary between glass and liquid. However, this interface had a small variation in the index of refraction and the optical pathes in the film to the probe volume were very short due to the small film thickness. By means of a prism a minimal abberation could be achieved.

As mentioned earlier the problem of strong reflections at the moving film surface seriously disturbing the measurements had to be solved. The problem and its solution built in the LDV receiving optics is outlined in **Figure 5**. Because the photomultiplier

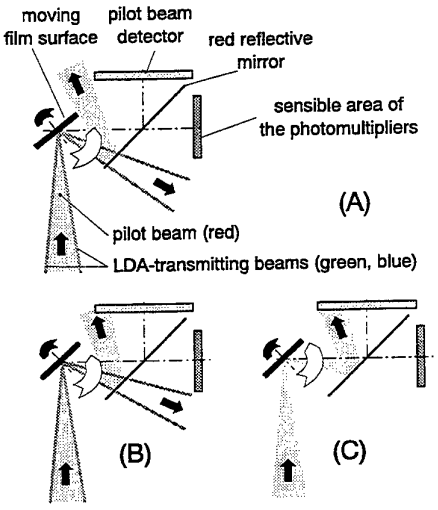


Figure 5: Working principle of photomultiplier protection by an additional pilot beam

tubes had to be protected from the intense light directly reflected at the liquid/air interface to avoid overload and errorneous Doppler bursts, a Bragg-cell was implemented to switch off the laser beams for reflecting conditions. To detect reliably reflecting conditions an additional c_W-Laser (pilot laser) with

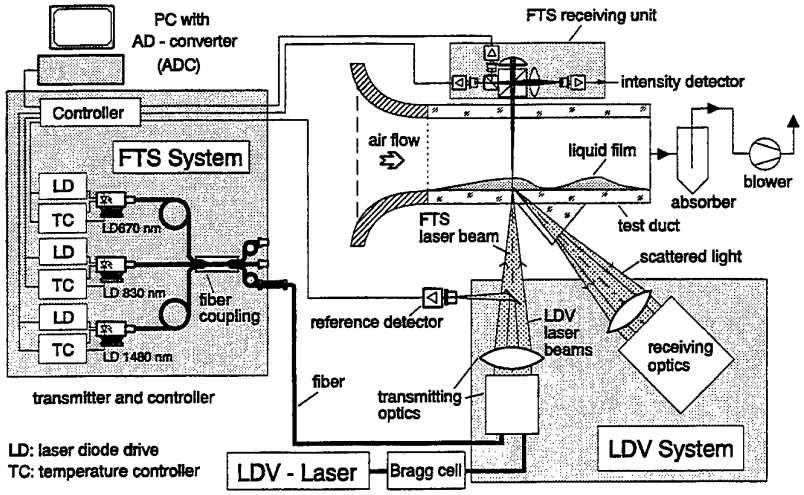


Figure 6: Simultaneous measurements of film velocity and film structure

($\lambda_{Pilot} = 673\ nm$) was coupled into the receiver fiber of the transmitter probe (**Figure 5A**), thus forming a focus by the front lens, too. To seperate the different wavelength in the receiving optics a red reflective mirror was used, light of shorter wavelength can pass onto the photomultipliers. The time span necessary for the electronic and the Bragg-cell to switch off the main beams was gained by a specific optical arrangement in the receiver. The front lens of the receiver collects scattered light in an angular range of 20° and this complete field is observed by the red light detector. The angular range of the green and the blue photomultipliers is reduced by an aperture to 5°. Therefore, red light is reflected into the pilot beam detector first (cf. **Figure 5B**). The main beams can now be switched off prior to full illumination of the photomultipliers by reflection, as shown in **Figure 5C**. Moving further, the reflected light leaves the pilot detector and the measurement can be continued by switching the main beams back on.

2.4 Simultaneous Film Velocity and Structure Measurements

The possibility of simultaneous velocity and film thickness respectively surface structure measurements would provide a major step in the understanding the internal transport mechanisms of shear-driven films. Combining the two instruments to perform time resolved measurements created a valuable tool with high spatial and temporal resolution.

The final layout of the complete optical system is demonstrated in **Fig. 6**. The system was mounted on a high precision 3D-traversing device. An independant spatial movement of the receiving optics relative to the transmitting optics was necessary to scan the height profile. For this a second extremely accurate 2D-traverse unit was applied with a step size of 0.5 μm. By using the same transmitting optics for the LDV and the film thickness measurement system an identical focus location for both devices was guaranteed. This is an important characteristic in the light of measurement accuracy accounting the small wave dimensions.

The electronic coupling, triggering, and control was done under computer control. Film structure information was stored for the passage time of long waves pre and after each LDV event. With this variable length of the time span (depending on the boundary conditions) the recording of the whole wave structure is ensured. Data processing and analysis was done offline after the measurements as described in the sections 3.2 and 3.3.

2.5 Mean Shear Stress Measurement

A crucial parameter for each analytical or experimental study of liquid films on surfaces is the driving shear stress at the liquid/gas interface. To determine the corresponding shear stress values at the measurement location the air velocity profiles in the duct above the film were measured. This is done by a

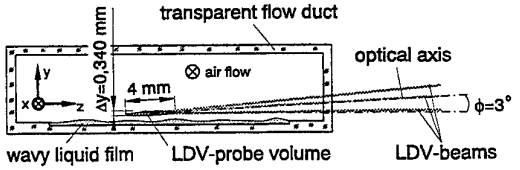


Figure 7: Air flow measurements above the film

standard LDV-system through the transparent side walls. For the measurements the air flow was seeded

with 1 μm water droplets from a ultrasonic atomizer. The air treats the wavy film surface as an additional roughness influencing strongly the flow profile close to the prefilmed wall. The resulting shear stress could be qualified by matching the air flow data to the linear range of the logarithmic law of the wall (Roßkamp, Willmann and Wittig (1997)).

3. DATA PROCESSING

3.1 Film Flow Characteristics

The result of a typical tmporal record from the optical film thickness measurement system is shown in **Figure 8** together with some characteristic parameters of wavy film flow. An individual wave is characterized by a steep gradient at the front (left side) and a moderate gradient at the wave back facing the air flow. The film height between the waves

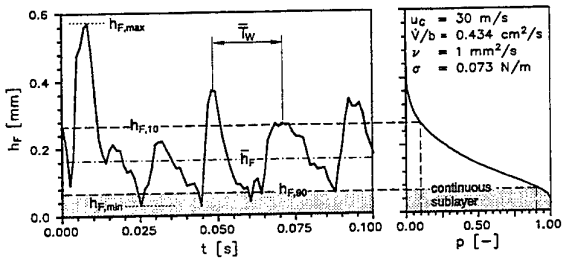


Figure 8: Characteristics of a wavy film flow

does not fall below a typical value. Generally a thin sublayer is continuously present, in this case a minimum thickness of $h_{F,min} \approx 0.040\ mm$. The diagram on the right of **Figure 8** shows the calculated temporal possibility of film liquid existing at a certain height h_F. Close to the wall a continuous sublayer exists leading to a probability $p = 1$ for $h_F \leq h_{F,min}$. As expected, the probability decreases constantly by moving higher inthe film because only a few very large waves are reaching up to this height.

In order to characterize the stochastic nature of the film thickness distribution some statistical parameters are given in the diagram. One is the time mean film thickness $\overline{h}_F$, average from measured data with constant sampling rate. From the probability function two other quantities can be derived. The thickness of the continuous liquid sublayer is described by $h_{F,90}$, a thickness which is exceeded for 90% of the measured time span. The corresponding value $h_{F,10}$ is characteristic for the height of the waves and is exceeded for only 10% of the time. Together with the mean wave velocity $\overline{u}_W$, described in section 2.2, a typical wave length can be derived from $\overline{\lambda} = \overline{u}_W \overline{T}_W$.

3.2 Characterization of Typical Waves

To reach a comprehensive and correct insight to the flow phenomena in shear- driven liquid films preprocessing of the measured data with the film velocity analyzer and the film structure analyzer is necessary. The individual LDV-measurements at a certain distance to the wall are stochastically distributed in waves of different height, length, and shape, because LDV data could only be taken if a particle passes the probe volume. To link the LDV results to its position inside representative wave types a differentiation and classification of wave class was necessary occuring at different flow conditions.

The conditional averaging procedure is based on a selection of typical waves from the data of wave structure analysis, according to each flow condition. In order to get reliable statistical values about the hydrodynamics of liquid films an extensive set of information from the simultaneous measurements was processed as demonstrated in the following section. As an example the pure water film data already presented in **Figure 8** was used.

In a first step the measured thickness traces were examined visually or by computer aided analysis to find and select a frequent appearing wave form. A sample of typical wave forms for this water film is shown in **Figure 9**, where the chosen basic form is marked with the thick black line. In this case it was a large main wave of 0.430 mm maximum height and a short wave back. However, each wave have distinct indi-

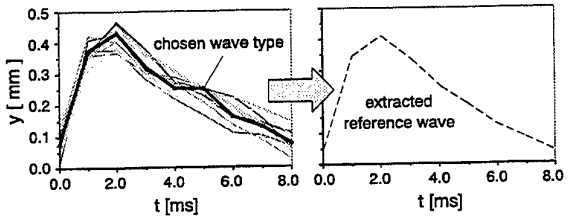


Figure 9: Representative wave determination

vidual characteristics with humps, peaks, and dents. These items disturbed the allocation of the selected wave shape to the measured waves containing the velocity data. Therefore, a reliable smoothing technique had to be developed.

In the second step some wave structures were selected from the stored data sets which were similar to the basic ones. The comparison was done utilizing the method of the 'least square fit'. Particulary due to the varying individual wave shape different weighting factors along the wave length had to be applied. The wave front had a large factor, the back of the main wave a moderate value, and the remaining part a small one. With this procedure the major shape characteristics were preserved. This can be

seen on the left side of **Figure 9** where some of the selected waves are plotted with the one chosen as basic wave form in the first iteration. Finally the extracted reference wave is plotted on the right as the result of averaging. Using the reference wave instead of the initial basic one, the assignment rate of the wave form to the measured film structures could be improved significantly in a second iteration.

3.3 Velocity Data Allocation

The extracted reference wave was then used to allocate the velocity data location inside the waves of similar surface structures (see **Figure 10**). By shifting the reference wave over all the measured film structure elements centered around the LDV-measurement locations (position 1 to position 10 in **Figure 10**) the position of maximum similarity was searched. The actual wave shape was accepted if

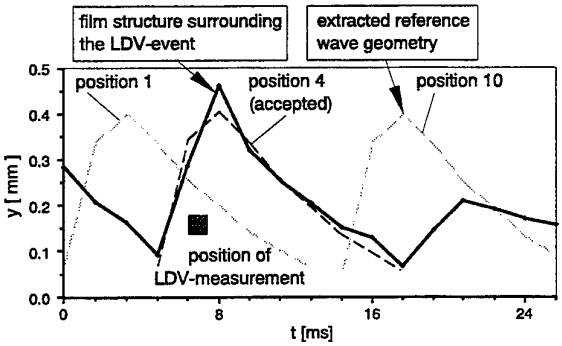


Figure 10: LDV data allocation

the similarity level was high enough. For the examination same procedure and weighting factors as described in the previous section was used.
The processed velocity value was then assigned to a position in a two dimensional table of discrete positions inside the reference wave form. Considering the numerous variations in wave shape, several thousand data sets had to be acquired and checked for a reliable statistic of the velocity distribution.
Figure 11 shows an exemplary result of the evaluated velocity distribution for a typical chosen wave structure. Due to the conversion from a time dependent abscissa to spatial co-ordinates the wave movement is from left to right, so the steep wave front is now located on the right side. At each location inside the wave the mean velocities in main flow direction are indicated. An impression of the velocity deviations is given by the dotted lines around the mean values indicating the $\overline{u} \pm RMS$ range. Due to the averaging process, the deviations result from velocity fluctuations as well as from slightly different flow structure of the individual waves.

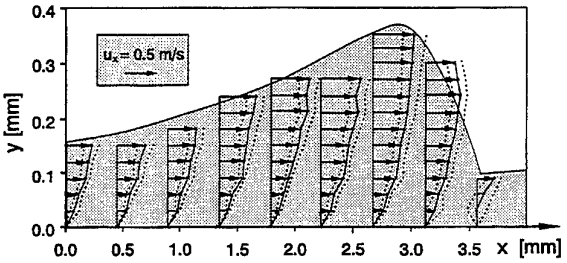


Figure 11: Mean velocity profiles in the wave

For pure water films the profiles in the wave center and at the wave back showed no significant differences. Particulary the velocity gradients near the wall are very similar, so the conclusion can be drawn that the wall shear stress τ_W is similar all over this region (cf. section 4.2). However, at the wave front the mean velocity u_x decreases to zero and the deviation is centered around zero. A detailed analysis shows, that at the wave front many LDV-measurements had negative u_x velocities up to a height of about $h_{F,90}$. This leads to the conclusion that a rolling mechanism is responsible for the liquid transport in the wave, as indicated in **Figure 12**. The fluid bulk is driven by shear forces at the

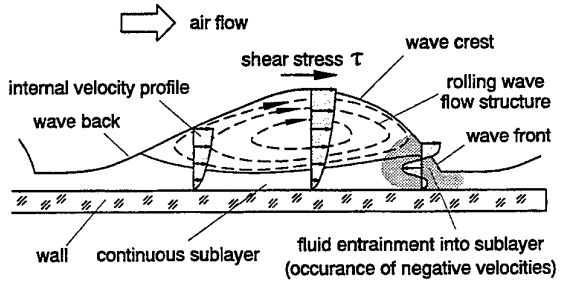


Figure 12: Flow structure of rolling waves

film surface and penetrates the continuous sublayer in the wave front region. This effect forces compensation flows which are oriented opposite to the main flow direction.

4. FILM HYDRODYNAMICS UNDER VARIOUS LIQUID PROPERTIES

Even from simple visualization experiments it is well known, that film transport is influenced significantly by boundary conditions like shear stress and liquid flux. The influence of these parameters to the internal film flow characteristics had been discussed previously by Elsäßer et al. (1997). However, the properties of the liquid particulary the viscosity have significant influence on the resulting film hydrodynamics, too. The capability of the measurement and data processing systems allowed for the first time

a comprehensive and detailed investigation of film charactersitics with different liquid properties. The results of this study are given in the following.

4.1 Wave Hydrodynamics

As demonstrated in **Figure 13** a variation in the kinematic viscositiy ν of the liquid leads to a significant change in film surface structure. The wavy sur-

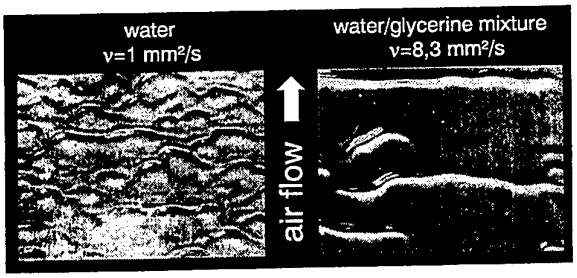


Figure 13: Surface structure visualization

face on films with low viscosity is three-dimensional in character. The single wave trains are sickle-shaped and relatively short in cross flow direction. At higher viscosity the waves becomes more linear with a smooth surface in the spacing in between.
To vary the liquid properties in the tests water and water/glycerine mixtures had been used. By means of water/glycerine mixtures the viscosity could be varied in a wide range ($\nu = 1$, 2.2 and 8.3 mm^2/s) but the surface tension was kept almost identical.
The effect of an increase in kinematc viscosity on the structure of the film surface is demonstrated in **Figure 14** showing the plots of typical temporal thickness traces. The films with the different viscosities are under the influence of identical air velocity $u_G = 30\ m/s$ and mass flux $\dot{V}/b = 0.434\ cm^2/s$, whereby the mass flux is normalized with the film width. The film surface of pure water ($\nu = 1\ mm^2/s$) shows an ensemble of waves with various size and length. Smaller subwaves occur in the spacings between the larger main waves. With increasing viscosity the surface becomes more regular and the subwaves disappear. A decreasing number of large main waves of growing maximum height dominate the film structure. Additionally, the wave front and the wave back gets steeper. However, exact statements about the length of the waves are not possible in this time dependent plot because of the different wave travelling velocities $\overline{u}_W$.
The mechamism of rolling waves travelling on top of a thin but always present sublayer is responsible for the major fraction of the liquid transport in shear-driven films. Recent investigations (Elsäßer et al. (1997)) indicated, that approximately 70% of the liquid mass is transported in the waves of pure wa-

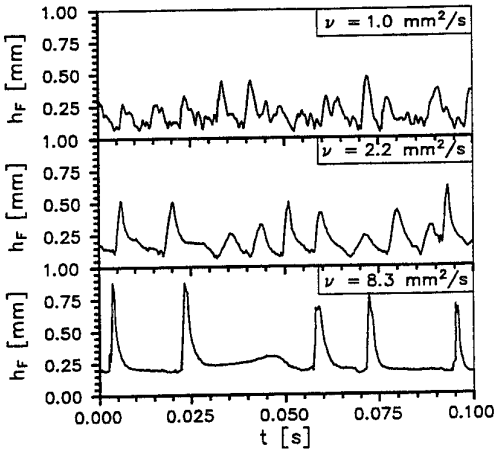


Figure 14: Time dependent film thickness

ter films. This clearly shows the importance of a detailed investigation of the wave hydrodynamics under different liquid properties. The individual wave characteristics for the three cases becomes more clear by comparing the extracted reference waves. Their

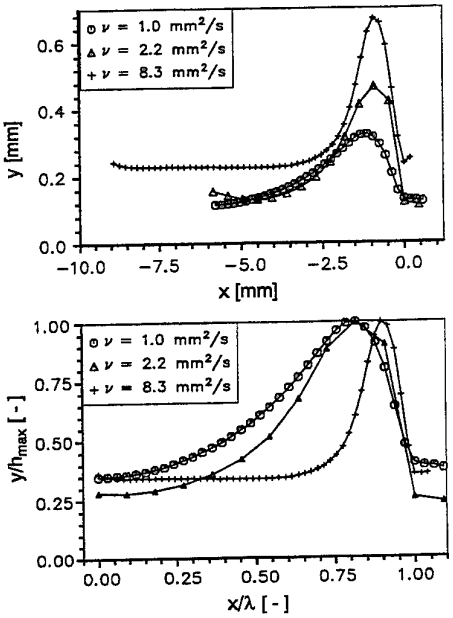


Figure 15: Reference waves for certain fluids

shape represent the structure of a typical average wave under the specific liquid parameters (**Figure 15**). The maximum wave height was about $1.1 \cdot h_{F,10}$ for the boundary conditions mentioned before. The dimensions of the different structures can be discussed easier transforming the temporal to a spatial x-axes by means of $\overline{u}_W$ and $\overline{T}_W$.
Figure 15 demonstrates that the wave length and particulary the height of the wave tips increase with

viscosity. Also the wave back seems to thicken. Furthermore, from the non-dimensionized plot $y/h_{F,max}$ versus x/λ can be seen, that the proportion of the wave crest region significantly decreases with growing viscosity compared to the mean wavelength $\overline{\lambda}$.
For a more detailed analysis of the internal flow field the distributions of the u_x velocity components are given as contour plots in **Figure 16**. The grey scale indicates the level of mean velocity for each position in the wave giving a good survey about the characteristic of the flow field. In the water film with

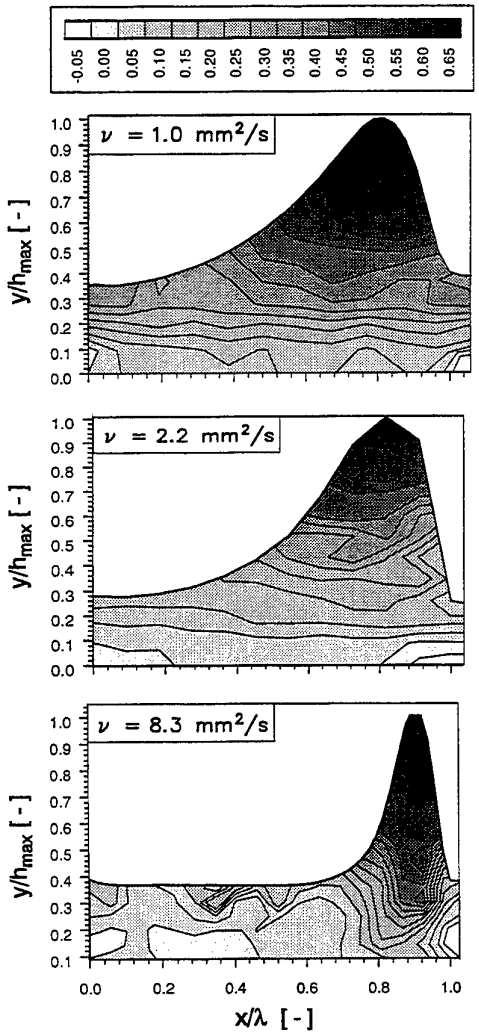


Figure 16: Velocity distributions within the waves

$\nu = 1\ mm^2/s$ the isolines of the velocity are almost parallel to the bottom wall. This indicates for the film height from the bottom to the wave tip a nearly uniforme velocity gradient over the wave length. In pure water films the internal velocity profiles differs only with absolute height, but not in the overall shape as also could be seen in **Figure 11** already. A similar behavior can be observed in films with increased viscosity ($\nu = 2.2\ mm^2/s$), but smaller velocities near the wall. A deviation from this uniform distribution only occurs at the wave fronts where high momentum fluid from the rolling waves entrains the sublayer. This can be observed at the wave back ($x/\lambda \leq 0.1$) also, where interaction with the following wave takes place.
In contrast to these evenly distributed velocities the high viscosity fluid ($\nu = 8.3\ mm^2/s$) shows steeper gradients in the region below the wave crest compared to the long back of the wave. In the wave back mean velocities decrease to nearly $u_x = 0\ m/s$ even to a height of 0.200 mm. This effect leads to a negiglible liquid transport in the gap between the waves, so the transport of fluid takes place mainly inside the wave crests.
With respect to modelling approaches the fact that almost the whole mass is transported in the waves has to be taken into account to get a realistic simulation. Additionally not only the mass transport characteristic is influenced but also the heat transfer perpendicular to the film depends on the internal mixing caused by the different wave shapes and frequencies. Taking into account these results a new and more realistic models could be developed by Roßkamp, Elsäßer et al. (1998) that leads to an enhancement of the Nusselt number up to factor of nearly 3.5 compared to a film with smooth surface.

4.2 Shear Stress Distribution

The before mentioned transport mechanisms influence the modeling of shear-driven liquid films for numerical flow calculation significantly. Due to the steeper velocity gradient in the wave crest region the wall shear stress (calculated by the gradients at the wall from $\tau_W = \nu \cdot \Delta u/\Delta y$) increases markable. τ_W represents the forces from the air flow driving the film. It comprises the Newtonian shear forces from roughness effects to the air flow as well as pressure drag components due to the shape of the wave crest. By means of the results from the simultaneous measurements of film structure and velocity the shear stress distribution along the surface of a typical wave could be determined with a high level of high accuracy.
In **Figure 17** these values are compared with the time mean shear stress $\overline{\tau}$ derived from the velocity profile measurement in the air flow (section 2.5). For a film formed of a fluid with low viscosity the agreement is excellent eccept for the wave front region. There shear stress changes the direction due to the locally negative velocity near the wall. In the other region wall shear stress is uniform due to the homogenious velocity distribution. As already indicated in

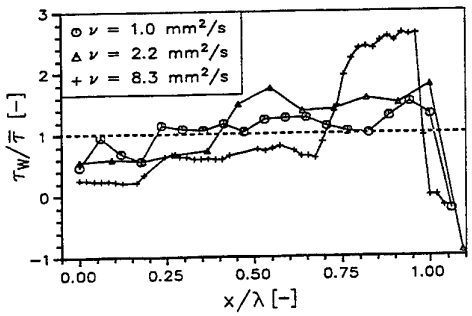


Figure 17: Wall shear stress versus wave length

Figure 16 the fluid with the high viscosity shows a significant increase of τ_W in the wave crest. This can lead to a strong misjudgement of the mass transport if $\overline{\tau}$ is used for film flow simulations, also resulting in errorneous film thickness and film roughness prediction. However, our investigation has clearly shown that for low viscosity fluids up to $\nu \leq 2\ mm^2/s$ the simplification of constant mean shear stress is valid and can be used in predictions of global film transport. If ν exceeds $2\ mm^2/s$ improved model has to be applied, taking into account the strong variation of $\overline{\tau}$ as a function of the wave length.

5. CONCLUSIONS

To improve the knowledge about the transport mechanisms in wavy shear-driven liquid films, important in many technical applications, a novel LDV system was designed and presented in the paper. It allows accurate velocity profile measurements from the wall up to the wave tips in thin wavy films. The instrument was combined with an optical film thickness measurement system to determine the structure of the wavy film flow accurately. An extensive data processing procedure was developed to allocate the measured film velocity data to wave forms with typical shape and size under the actual flow conditions.

With this comprehension set of information it was possible to calculate internal wave quantities with a high level of accuracy, for example the effective shear stress distribution over the wave length. This enabled a more detailed insight in the flow hydrodynamics of the liquid film at various properties. The comprehensive results give fresh stimulus to improve the film transport and heat transfer modelling significantly due to the better understanding of the internal film flow mechanisms.

ACKNOWLEDGEMENTS

Special thanks to our students Jens Läuger for assistance in the experimental part of this work and Stephan Hentz for his excellent contribution in preparing the analysis software.

REFERENCES

[1] Elsäßer, A., Samenfink, W., Ebner, J., Dullenkopf, K. and Wittig, S.: Dynamics of Shear-driven Liquid Films. In: Proceedings of the 7th International Conference on Laser Anemometrie - Advances and Applications, Karlsruhe, Germany, September 8 – 11, 1997.

[2] Himmelsbach, J.: Zweiphasenströmungen mit schubspannungsgetriebenen welligen Flüssigkeitsfilmen in turbulenter Heißluftströmung - Meßtechnische Erfassung und numerische Beschreibung. Dissertation, Institut für Thermische Strömungsmaschinen, Universität Karlsruhe (T.H.), 1992.

[3] Roßkamp, H., Elsäßer, A., Samenfink, W., Meisl, J., Willmann, M. and Wittig, S.: An Enhanced Model for Predicting the Heat Transfer to Wavy Shear-driven Liquid Wall Films. In: 3^{rd} International Conference on Multiphase Flow, June 8 – 12, 1998, Lyon, France, 1998.

[4] Roßkamp, H., Willmann, W. and Wittig, S.: Computation of Two-Phase Flows in Low-NO_x Combustor Premix Ducts Utilizing Fuel Film Evaporation. ASME-Paper 97-GT-226, 1997.

[5] Roßkamp, H., Willmann, W. and Wittig, S.: Heat up and Evaporation of Shear Driven Liquid Wall Films in Hot Turbulent Air Flow. In: Proceedings of the 2^{nd} International Symposion on Turbulence, Heat and Mass Transfer, June 9 – 12, 1997, Delft, Netherlands, 1997.

[6] Rottenkolber, G., Dullenkopf, K. and Wittig, S.: Visualization and PIV-Measurements inside the Intake Port of an IC-Engine. In: Proceedings of the Ninth International Symposium on Applications of Laser Techniques to Fluid Mechanics, Lisbon, Portugal, 1998.

[7] Samenfink, W., Elsäßer, A., Wittig, S. and Dullenkopf, K.: Internal Transport Mechanisms of Shear-driven Liquid Films. In: Proceedings of the Eighth International Symposium on Applications of Laser Techniques to Fluid Mechanics, Lisbon, Portugal, 1996.

[8] Wittig, S., Elsäßer, A., Samenfink, W., Ebner, J. and Dullenkopf, K.: Velocity Profiles in Shear-driven Liquid Films: LDV-Measurements. In: Proceedings of the Eighth International Symposium on Applications of Laser Techniques to Fluid Mechanics, Lisbon, Portugal, 1996.

SESSION 2

WAKES

A STUDY OF THE NEAR-WAKE REGION OF A CIRCULAR CYLINDER

R.Elavarasan, L.Djenidi and R.A.Antonia

Department of Mechanical Engineering
University of Newcastle, Newcastle -2308, Australia

ABSTRACT

The near-wake region of a cylinder is investigated experimentally using laser Doppler velocimetry (LDV) and flow visualization. The Reynolds numbers (R_d) based on the cylinder diameter D and free stream velocity U_1 are 1000 and 2000. The region of investigation is 0.5<x<4D in the streamwise direction. Present experiment provided a useful data base to validate numerical codes. The streamwise vortical structures in the near-wake region are also investigated in the Reynolds number range 160-1000. The mean spacing between these structures decrease faster in the region 160< R_d <400 and nearly constant (of the order of cylinder diameter) in the range R_d >400.

1. INTRODUCTION

The flow behind a bluff body has received significant attention primarily in view of the engineering application. The circular cylinder has been the most widely selected geometry and has been studied over a wide Reynolds number (R_d= U_1 d/ν, U_1 is the freestream velocity, d, diameter of the cylinder and ν is the kinematic viscosity of the fluid) range. While much information has been gathered from theoretical, experimental and numerical studies (see for example the review of Williamson, 1996), of the flow, the physics of the flow especially in the near-wake region of the cylinder is not clearly understood.

There have been many experimental investigations in the region x/d>10, over a wide Reynolds number range. Very good understanding of the flow exists for this region. The flow remains laminar up to R_d =150 (Bloor, 1964 and Roshko, 1954) and transition occurs around R_d=180. The Reynolds number where transition occurs can be inferred from the discontinuities in the Reynolds-Strouhal number relation. With R_d in the range 180-260, vortex loops evolve into pairs of counter-rotating streamwise vortices in the near-wake region. This is followed by transition to fine scale structures as the R_d increases (Williamson, 1996). Extensive flow visualizations in the near-wake established the existence of two and three-dimensional structures in the Reynolds number range 180-4000 (Wei and Smith, 1986, Williamson, 1988 and Lin et al., 1996).

At low Reynolds numbers (R_d <300), flow visualizations allow a clear insight into flow patterns. However as the Reynolds number exceeds about 600, it is quite difficult to distinguish the structures clearly. Hence it is not possible to use the results from flow visualization in order understand the flow dynamics in the near wake region at higher Reynolds numbers. Even at small Reynolds numbers, the physical characteristics and dynamical properties of the structures in the near-wake are not clearly understood because of the lack of experimental data in the near-wake region. Accurate velocity measurements with conventional measuring techniques such as hot wires and hot films are difficult because of low or negative velocities. Even with optical techniques such as LDV and PIV, experimental data in this region are very rare. To our knowledge, the only measurement in the region x/d=3-10 was carried out by Ong and Wallace (1996) using hot wire anemometer. Numerical experiments seem capable of providing the necessary information in this region (Beaudan and Moin, 1994). However, to validate the numerical codes it is almost essential to compare the results with experimental observation. To this purpose LDV is used to measure the velocity field

in the region x/d<4 at two Reynolds numbers (1000 and 2000, corresponding to freestream velocities of 20cm/s and 40cm/s and a cylinder diameter d= of 5mm).

2. EXPERIMENTAL SET UP

The experiments are carried out in a closed circuit constant-head vertical water tunnel. The vertical 2m high working section (250mm square cross section) is made of 20mm thick clear perspex. A 410mm long hollow circular cylinder of 5mm diameter is inserted in the test section at a distance of 700mm from the exit of the tunnel contraction (Figure. 1). The freestream turbulence intensity is about 1%, and the pressure gradient is negligible ($U_1\ d\ U_1/dx$ = $5.5x10^{-4}$ ms^{-2} for U_1=0.2m/s). X, Y and Z are the streamwise, lateral and spanwise co-ordinates respectively.

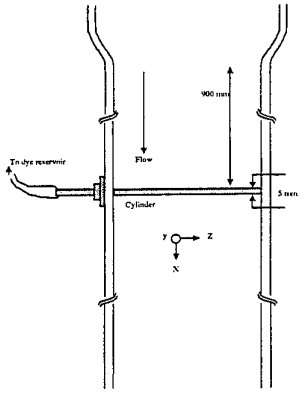


Figure 1. Experimental arrangements.

A one component fiber optic LDV system (Dantec, 4W Ar-ion) is used for measuring the streamwise component of velocity. The dimension of the measuring volume is (0.044 x 0.044 x 0.04mm). Enhanced Burst Spectrum (BSA) is used for processing the Doppler signals. At each location, 50,000 samples are collected. The flow is seeded with iriodin silver particles (about 5m in size) to improve the data rate. In the recirculation region the data rate is about 0.5kHz whereas it is about 2-3kHz for x/d>2. Standard Dantec software (BURSTware) is used to process the signal from the photo multipliers.

3. RESULTS:

The measurements were carried out at various x/d locations across the wake ranging from 0.5 to 4 and along the centerline. Figures 2a and b show the distribution of streamwise component of velocity U_c and the rms u_c' along the centerline, normalized with the freestream velocity U_1.

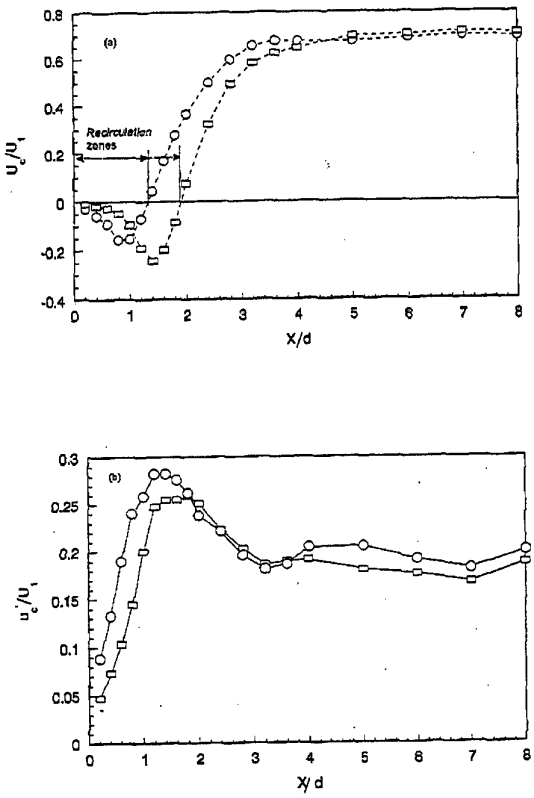


Figure 2. Center line distribution of mean and rms longitudinal velocities. a) U. b) u'.
O R_d =1000, □ R_d =2000.

Close to the cylinder in the recirculation region, the velocity is nearly zero but it quickly becomes negative as x increases reaching a minimum at x/d=1 and 1.5 for R_d =1000 and 2000 respectively. There is a subsequent increase beyond this minimum. The velocity rising steadily and reaching zero at x/d 1.4 and 2 for R_d =1000 and 2000 respectively. The length of the recirculation region can approximately be identified

with the distance from the origin to the point where the velocity first becomes zero after the minimum is reached. The extents of these zones are indicated in figures 2a and b. Beyond x/d>4, U_c / U_1 reaches a value of 0.6 for both R_d=1000 and 2000.

The mean velocity profiles across the wake at various x/d locations are shown in figures 3a and b for R_d=1000 and 2000respectively.

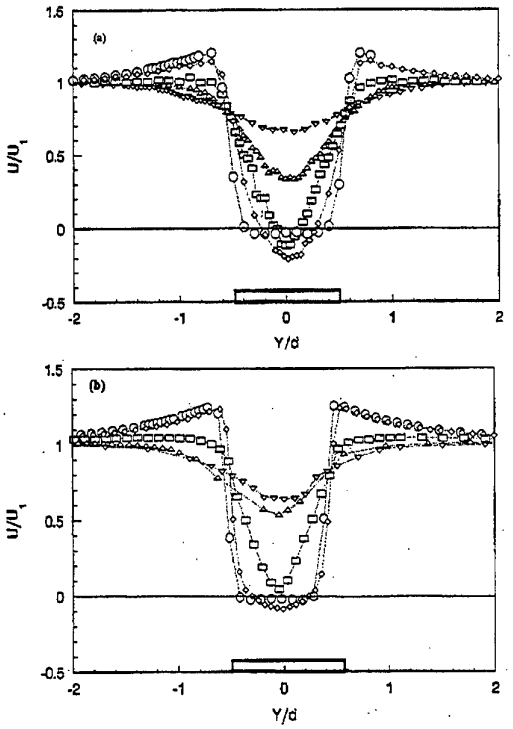


Figure. 3. Mean velocity distribution at various x/d locations. (a) R_d =1000 (b) R_d =2000. O- (x/d)=0.5, ◊ =1, ♣=2, Δ=3, ∇=4.

All profiles show very good symmetry along the centerline. The profiles close to the cylinder in the region x/d<2 and for y/d>0.5, the velocity first gradually increases before slowly decreasing towards the freestream value. This indicate the presence of a strong shear layer in the vicinity of the cylinder. The plots exhibit some of the trends which can be observed in the far-wake region, e.g. the maximum mean velocity deficit decreases as x increases. In the rms profile (Figures 4a and b), the twin peaks identify the region of high shear. The peak value occurs at the edge of the recirculation zone (x/d=2). The variation of $(u_c')_{max}$ reflects the variation of U_c along the centerline. In the recirculation zone, except at the edges, the rms value remains low compared to its value downstream.

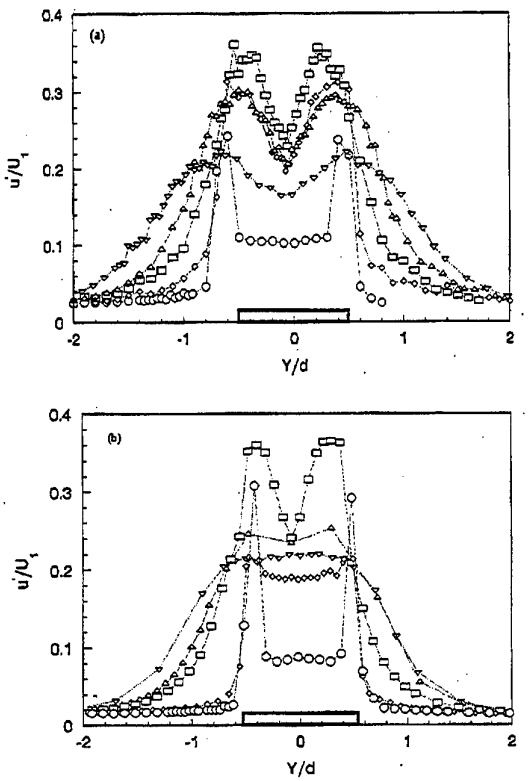


Figure. 4 Distribution of longitudinal rms velocity at various x/d locations. (a) R_d =1000 (b) R_d =2000 Symbols are as in figure 3.

Measurements were also made along the spanwise direction at x/d=0.5 for 150<R_d <1000. Previous Flow visualizations confirmed the presence of two and three-dimensional structures in the transition region range of R_d=150-300. In the present experiment, the spanwise distribution of the mean velocity reflects the presence of these structures. Figure 5a and b show distributions of mean and rms velocity at R_d =180. The distributions are inclined to the Z-axis because of the oblique vortex shedding from the cylinder. The other important feature to be noticed from the plots is the sharp variation exhibited by these mean profiles. This implies the presence of vortices occurring periodically

at almost the same location.

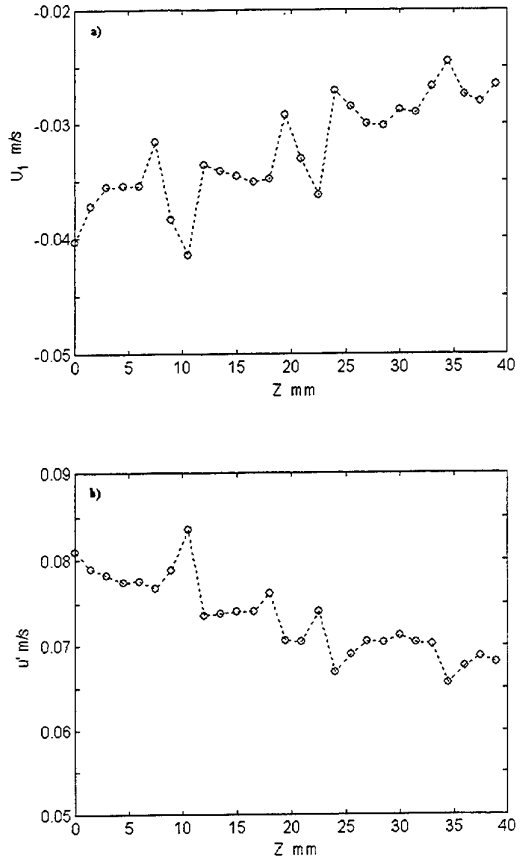


Figure. 5 Mean and rms velocity distributions along spanwise direction at x/d=0.5. R_d = 180. (a) U (b) u'

Previously Mansy et al. (1993) used a scanning laser anemometer to measure these structures at x/d=2 and suggested that these structures have no preferred spanwise location. However, the mean velocity measurements in the present experiments indicate that the streamwise structures must have a preferred location. The spacing between vortex pairs can be calculated approximately by measuring the distance between sharp changes. Figure 6 shows the dependence on R_d of the spacing between vortex pairs (Zs) normalized by the cylinder diameter. It is evident from the figure that, for 150< R_d <400, the spacing decreases faster as the Reynolds number increases compared with the region R_d >400 In the region 400<R_d <1000, the spacing varies at a much slower rate and its magnitude is nearly equal to the cylinder diameter. This observation is in agreement with that, based of flow visualization, of Bays-Muchmore and Ahmed (1993). They concluded that the mean spacing of the streamwise vortex pairs remains constant at approximately one cylinder diameter for 300< R_d <21000.

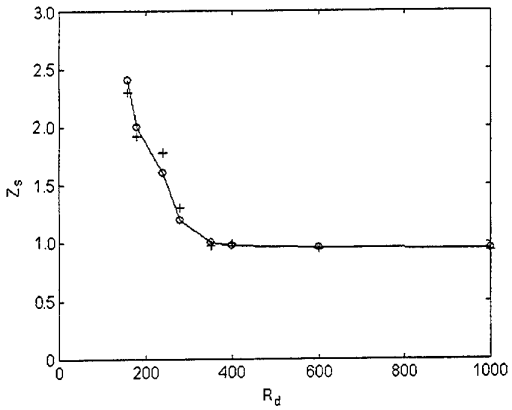


Figure. 6 Variation of mean spacing between streamwise structures with R_d.

+ - LDV , O- Flow visualization

Flow visualizations were also carried out in the region x/d<1. A laser sensitive dye emerged from a slit (0.25mm wide and 100mm long) which was carefully machined along the surface of the cylinder. The cylinder is positioned such that the slit is at the forward stagnation point of the cylinder. The open end of the cylinder is connected to a dye reservoir and a thin laser sheet is used to visualize the flow. Figures 7a-d show instantaneous views of the flow along the x-z plane (spanwise orientation) at various Reynolds numbers in the range 160 to 280. Streamwise vortex pairs can be seen in the form of cells in these figures. The mean spacing between these cells is calculated by ensemble averaging over 300 frames. The values inferred from the visualizations match closely those indicated by LDV measurements (Figure. 6).

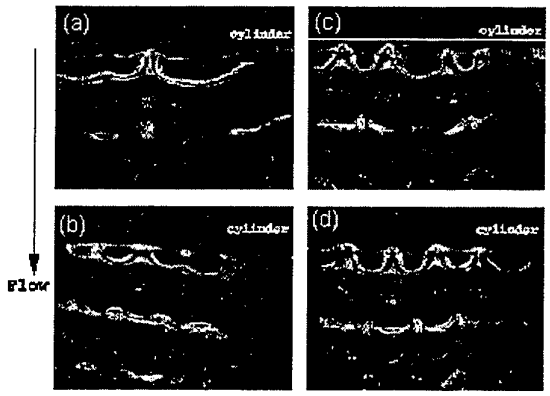


Figure. 7 Spanwise views showing the cell structures. The flow is from top to bottom.

(a) R_d=160 (b) R_d=180

(c) R_d=240 (d) R_d=280

4. CONCLUSION

The velocity field in the near-wake region of a circular cylinder has been accurately measured using LDV. As there are not many experimental data available in the range $0.5<x/d<4$, the present experiment should provide a useful data base for *inter alia,* the validation of numerical codes. The present measurement also provided some quantitative information about the structures that are observed in the near-wake region. Both LDV and flow visualizations indicate that the mean spacing between these structures decrease much faster in the transition region. In the region $400<R_d<1000$, the spacing did not change much and was nearly equal to the cylinder diameter, d.

The authors acknowledge the support of the Australian Research Council.

REFERENCE

Bays-Muchmore, B. and Ahmed, A. (1993) On Streamwise Vortices in Turbulent Wakes of Cylinders. *Phy. Fluids,* **A5 (2)**, 387-392.

Beaudan, P and Moin, P (1994) Numerical Experiments on the Flow Past a Circular Cylinder at Sub-critical Reynolds Number. ***Technical Report - TF-62***, Stanford University, Thermal Sciences Division, Department of Mechanical Engineering.

Bloor, M.S. (1964). The Transition to Turbulence in the Wakes of A Circular Cylinder. *J. Fluid Mech.*, **19**, 290-304.

Lin, J.C., Vorobieff, P. and Rockwell, D. (1996). Space-Time Imaging of a Turbulent Near-Wake by High-Image-Density Particle Image Cinematography. *Phys. Fluids*, **8 (2)**, 555-564.

Mansy, H, Yang, P.M, and Williams, D.R. (1994). Quantitative Measurements of Three Dimensional Structures in the Wake of Circular Cylinder. *J. Fluid Mech.*, **270**, 277- 296.

Ong, L and Wallace, J (1996) The Velocity Field of the Turbulent Very Near Wake of A Circular Cylinder. *Expts. in Fluids*, **20**, 441-453.

Roshko, A. (1954) On the Development of Turbulent wakes from Vortex Streets. **NACA** *Report* 1191.

Wei, T. and Smith, C.R. (1986). Secondary Vortices in the Wake of Circular Cylinders. *J. Fluid Mech.*, **169**, 513-533.

Williamson, C.H.K. (1988). The Existence of Two Stages in the Transition to Three-Dimensionality of A Cylinder wake. *Phys. Fluids*, **31**, 3165.

Williamson, C.H.K (1996). Vortex Dynamics in the Cylinder Wake. *Ann.Rev. Fluid Mech.*, **28,** 477-539.

LDV measurements in the near wake behind an egg-profiled cylinder close to a stationary and a moving wall

M. S. Kim and D. Geropp

Institut für Fluid- und Thermodynamik
Fachbereich Maschinentechnik, Universität-GH-Siegen
D-57068 Siegen, Germany

ABSTRACT

An experimental study of the near wake behind a egg-profiled cylinder model close to a wall has been performed using LDV measuring techniques. The measurements were carried out under different measuring conditions - 3 wall distances (h/D=0.2, 0.5, 1.0), 2 wall types (stationary and moving wall) and 3 Reynolds numbers (Re_D=2.2 x10^4, 5.5 x10^4, 8.5 x10^4). A moving belt rig is used for the simulation of the relative motion between the model and the wall. The time averaged velocity measurements show that the dead water becomes longer when the wall distance decreases. For a clearance of h/D=0.2, a moving wall increases the length of the dead water by more than twice as much. However, the moving wall has no apparent influence on the length of the dead water for a clearance ratio of h/D=1.0. The analysis of measured turbulence shows that Reynolds stresses increase simultaneously with an increase in wall distance. For the case of h/D=0.2 the maximal transversal component of the normal Reynolds stress is much smaller than that for the case of h/D=1.0. A moving wall only has a significant influence on the transversal component of the Reynolds stress for a clearance of h/D=0.2. The influence is smaller in the case of h/D=1.0.

1. INTRODUCTION

When a bluff body moves close to a wall, the wall will have an influence on the flow close to the body. When the fluid on the body separates and a large dead water region develops, the separated flow also changes due to the wall effect. A typical example is the flow around a motor car. In this case the road is the moving wall. The relative motion of the body to the ground is usually neglected in experimental investigations. This results in a - sometimes considerable - deviation between the simulated flow and the real flow, which occurs especially beneath the body and in the dead water. For an understanding of the wall influence on the structure of the near wake behind a bluff body, the so called dead water, a systematic experimental investigation is needed. In previous years, near wake flows behind some bluff bodies (Kim and Geropp (1996) for circular cylinder, Kim and Geropp (1997a) for half ellipse, Geropp and Odenthal for a 2D car model(1996)) close to a wall were measured at our Institute.

This study investigates the effect of the wall distance as well as the type of wall (stationary, moving wall) on the flow behind a egg-profiled model (see figure 3). The experimental results contribute to a better understanding of the flow and can be used as a basis for modeling the dead water and turbulence, for example Geropp and Kim (1996) .

2. EXPERIMENTAL DETAILS

2.1 Wind Tunnel and Moving Belt Rig

The experiments were carried out at our institute in a wind tunnel with an open test section and a nozzle dimension of 1m x 1m. For the simulation of the relative motion between the model and the wall a self-contained moving belt rig is used

The moving belt rig measures 1.73 m x 1 m and is installed through the floor of the working section. At the front of the rig, the gap between the wind tunnel floor and the plane allows the wind tunnel boundary layer to be expelled under the moving belt. Boundary layer suction equipment is installed at the beginning of the front side of the belt. The suction equipment ensures

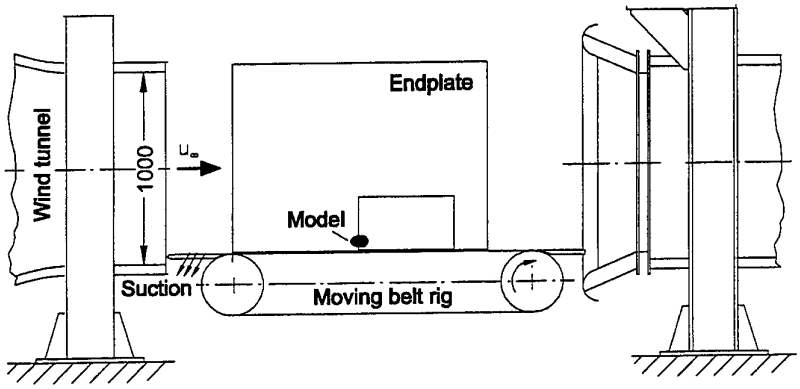


Fig. 1 Schematic of working section with moving belt rig

that no new boundary layer develops. The belt is driven by an internally mounted rear motor at speeds which are synchronous with the wind tunnel wind velocity. Fig. 1 shows the schematic of the working section with a moving belt plane. Some detailed information about the use of a moving belt technique can be found in Kim and Geropp (1997a)

2.2 Laser Doppler Velocimeter

The velocity and turbulence distributions in the near wake region were measured with a two-component LDV. Figure 2 shows the schematic of the LDV.

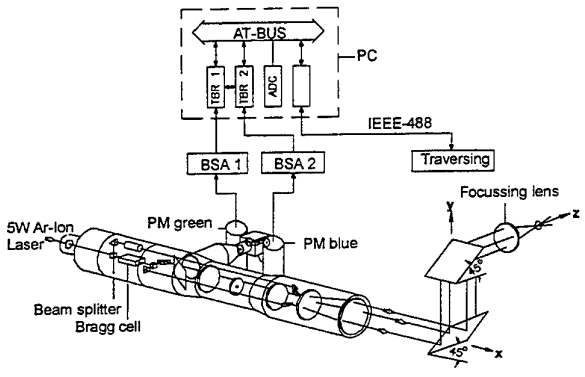


Fig. 2 Laser Doppler Velocimeter

A 5W Ar-Ion laser served as a source. The blue-green source beam is split into two beams from which one is lead through a Bragg cell and finally to a second beam splitter which separates the blue and green components of the original beam. All beams are reflected onto the front lens by two 45° tilted mirrors. The beams are then focused by the lens at a distance of 600 mm. A H_2O-Glycerine mixture in the ratio of 10:1 is dispersed in particle form –approximately 0,8 - 1,5 µm in diameter- into the suction inlet of the wind tunnel. The light which is reflected by the particles is transformed by two Photo Multipliers into electrical signals which are then processed by two Burst Spectrum Analyzers (BSA).

2.3 Model and Measuring Conditions

A egg-profiled cylinder model with a height of D=65 mm, a length of 98 mm (L=1.5xD) and a width of 670 mm (W/D=10.3) was used as test model. Figure 3 shows the model geometry and some definitions of length scale.

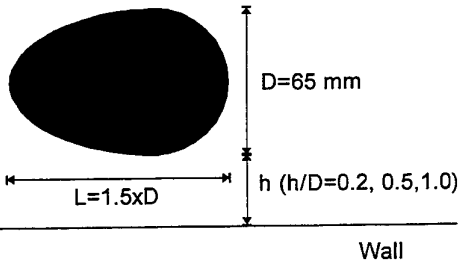


Fig. 3 egg-profiled cylinder model

In order to guarantee a two dimensional flow, two plates were placed at both ends of the model. The velocity and turbulence distributions in the dead water region were measured with a two-component LDV. The relative motion of the model to wall was simulated by a moving belt. The wall distance was adjusted to h/D=0.2; 0.5; 1.0. The velocity at the nozzle was varied from u_∞ = 5 m/s to 20 m/s. This corresponds to a Reynolds number Re_D=2.2 x10^4.- 8.5 x 10^4, which is based on the model height D.

3. RESULT AND DISCUSSION

3.1 Time Averaged Velocity Measurements

Figure 4, 5 and 6 show some exemplary results for the time averaged velocity measurements in the dead water region behind the model. A strong recirculating flow can be observed and is characterized by two contra-rotating vortices. The dissimilar dimensions of the contra-rotating vortices are a direct result of the wall effect. The time averaged velocity measurements in Figure 4 (h/D=1.0) and Figure 5 (h/D=0.2) show that the dead water becomes longer when the wall distance decreases. Figure 5 and Figure 6 compare the flow in the dead water region in the case of a stationary and a moving wall. The wall distance is h/D=0.2 and the Reynolds number Re_D=5.5x10^4. A moving wall increases the dead water. The length of the dead water amounts to L_d/D=3.8xD for a moving wall. In the case of stationary wall the length is L_d/D=1.8xD. The dead water for the case of a moving wall is 110 % longer than that of the stationary wall. Figure 5 and Figure 6 show that the dead water is pulled towards the wall when it is moving. Measurements of other models show the same tendency.

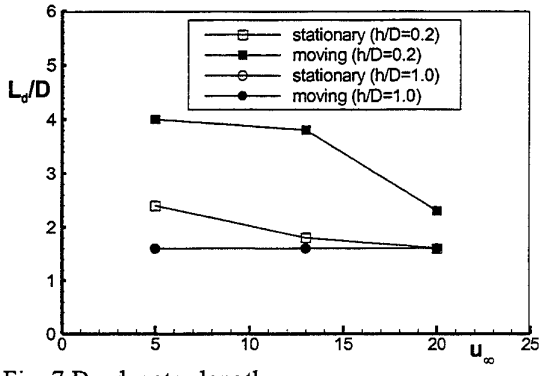


Fig. 7 Dead water length

Fig 7 shows the influence of the wall distance and the wall type (stationary, moving wall) on the length of dead water. A strong influence on the length of dead water can be observed for a clearance of h/D=0.2 which is dependant on the wall type and Reynolds number. The length of dead water for the case of h/D=0.2 decrease with increasing Reynolds number. For the case of h/D=1.0 dead water has a constant value of L_d/D=1.6. Figure 8, 9 and 10 compare the transversal component of the time averaged velocities $\bar{v}/u_\infty$. The maximum positive and negative values for a h/D=1.0 clearance are similar where as for a clearance of h/D=0.2 the maximum negative value on the top side is of a higher magnitude than that of the under side. The maximum negative value for h/d=1.0 has twice the magnitude of that for h/D=0.2. A more asymmetric distribution is observed when the moving wall is used. Figure 11, 12 and 13 show the distributions of the normalized vorticity, which has the definition

$$\omega_0 = \frac{D}{u_\infty}\omega = \frac{D}{u_\infty}\left(\frac{d\bar{u}}{dy} - \frac{d\bar{v}}{dx}\right).$$

The extreme values lies as expected on the free shear layer. The line with the value ω_0=0 lies on the symmetry plane for the case of h/D=1.0 but the zero line for h/D=0.2 shifted towards to the wall. For the case of moving wall a more asymmetric distribution can be observed.

3.2 Reynolds Stress Distributions

The characteristic distributions of the measured Reynolds stresses are plotted in figure 4 for the case of a moving wall. The wall distance is h/D=0.2 and the Reynolds number Re_D=5.5 x10^4. The longitudinal Reynolds normal stress component $\overline{u'^2}/u_\infty^2$ increases along the free shear layer and reaches a maximum shortly behind the middle of the dead water. A slightly asymmetrical structure can be observed and the maximum at the upper side has a higher value than that at the lower side. The results for the transversal Reynolds stress component $\overline{v'^2}/u_\infty^2$ shows that the vertical position of its maximum is not on the axis of symmetry but it is above the position of the free stagnation point. The distribution of the shear stress $\overline{u'v'}/u_\infty^2$ shows a similar behavior like $\overline{u'^2}/u_\infty^2$. If the wall distance increases, the

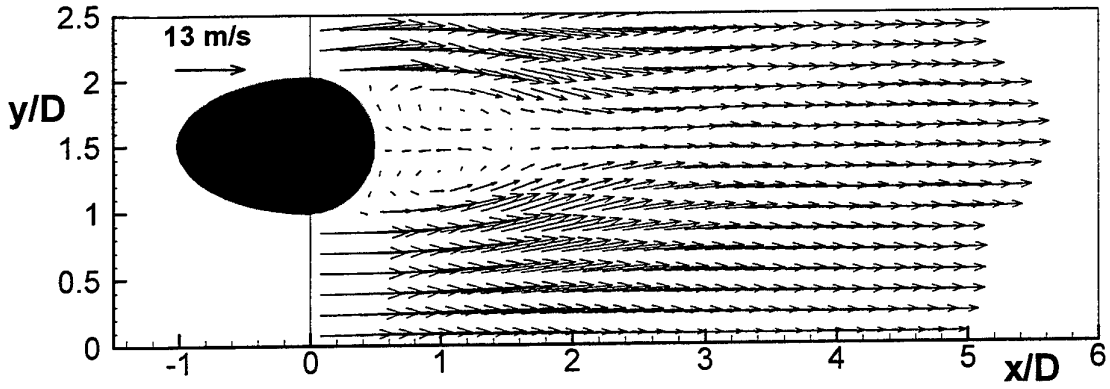


Fig. 3 Time averaged velocity vector in near wake behind an egg-profiled cylinder model
$Re_D = 5.5 \cdot 10^4$, h/D=1.0, stationary wall

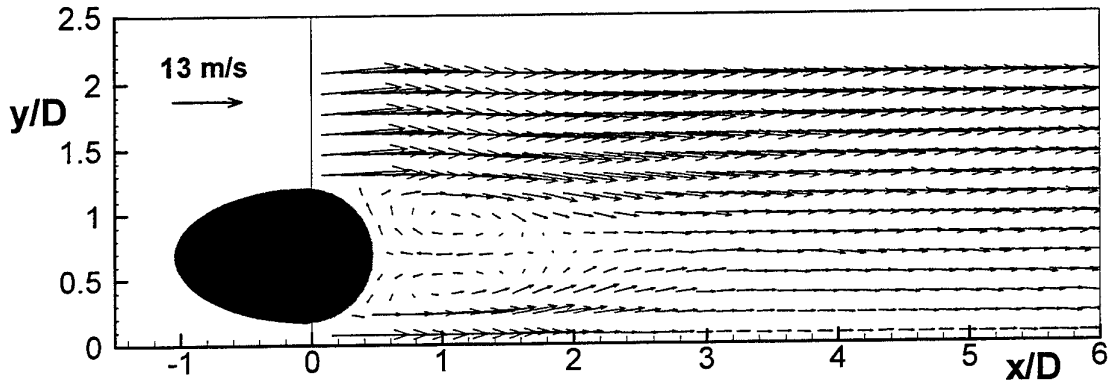


Fig. 4 Time averaged velocity vector in near wake behind an egg-profiled cylinder model
$Re_D = 5.5 \cdot 10^4$, h/D=0.2, stationary wall

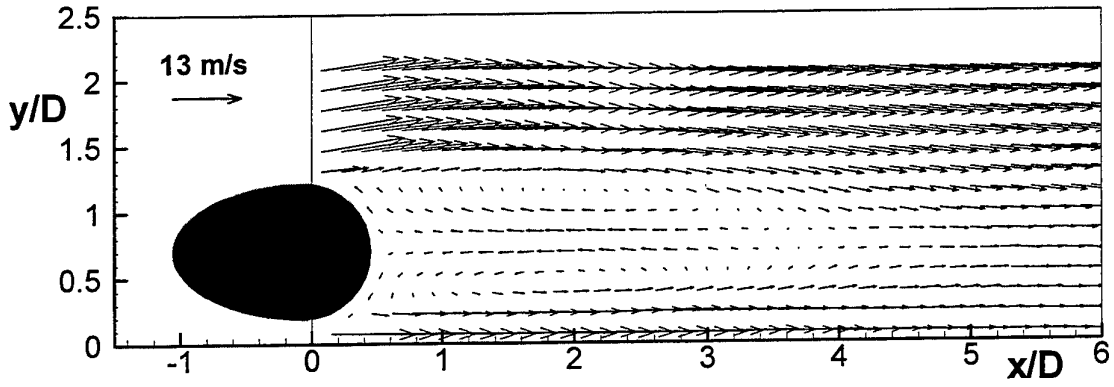


Fig. 5 Time averaged velocity vector in near wake behind an egg-profiled cylinder model
$Re_D = 5.5 \cdot 10^4$, h/D = 0.2, moving wall

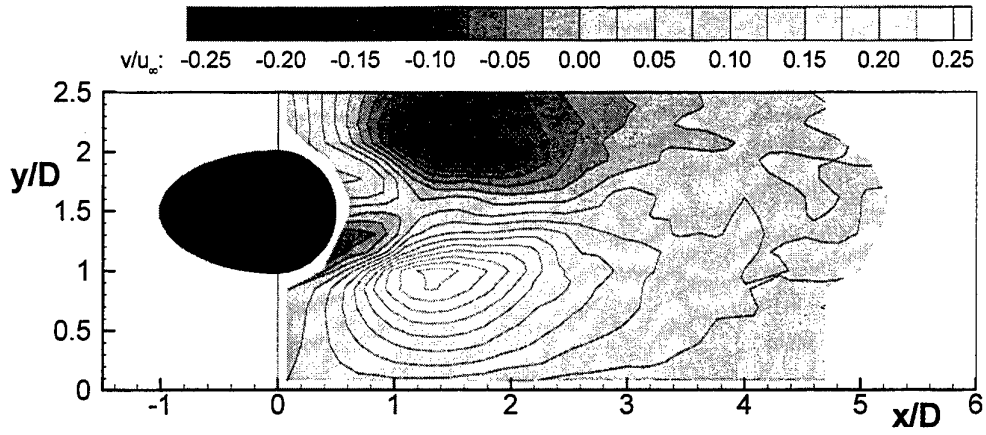


Fig. 8 Normalized time averaged tansversal velocity in near wake behind an egg-profiled cylinder model: $Re_D = 5.5 \cdot 10^4$, h/D = 1.0, stationary wall

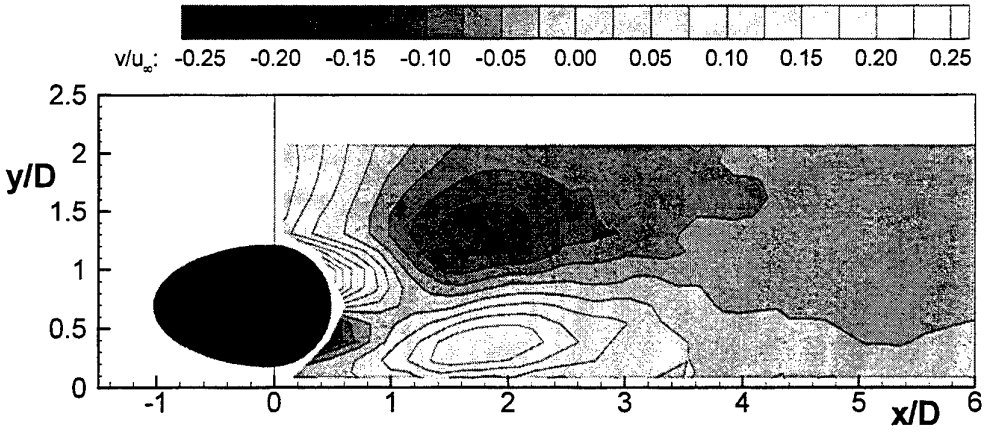


Fig. 9 Normalized time averaged tansversal velocity in near wake behind an egg-profiled cylinder model: $Re_D = 5.5 \cdot 10^4$, h/D = 0.2, stationary wall

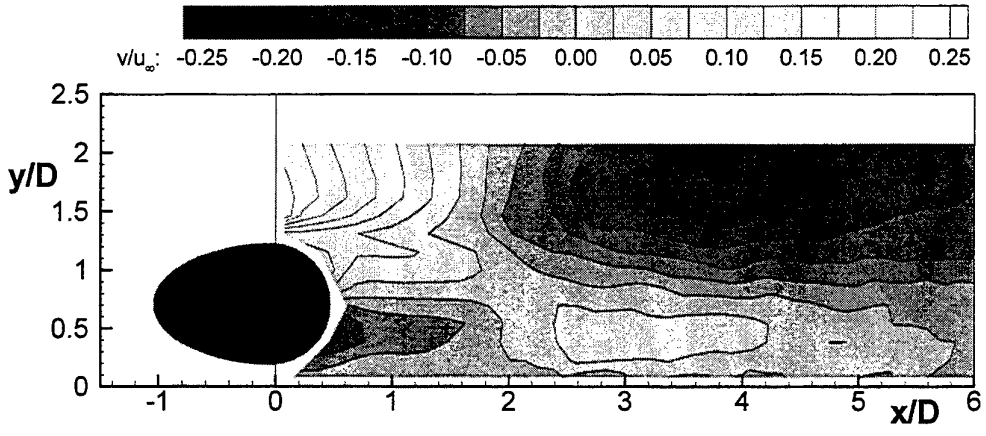


Fig. 10 Normalized time averaged tansversal velocity in near wake behind an egg-profiled cylinder model: $Re_D = 5.5 \cdot 10^4$, h/D = 0.2, moving wall

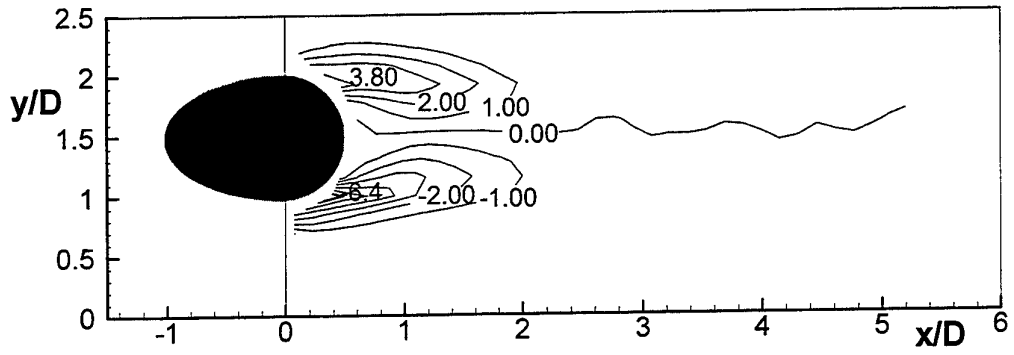


Fig. 11 Normalized time averaged vorticity in near wake behind an egg-profiled cylinder model: $Re_D = 5.5 \cdot 10^4, h/D = 1.0$, stationary wall

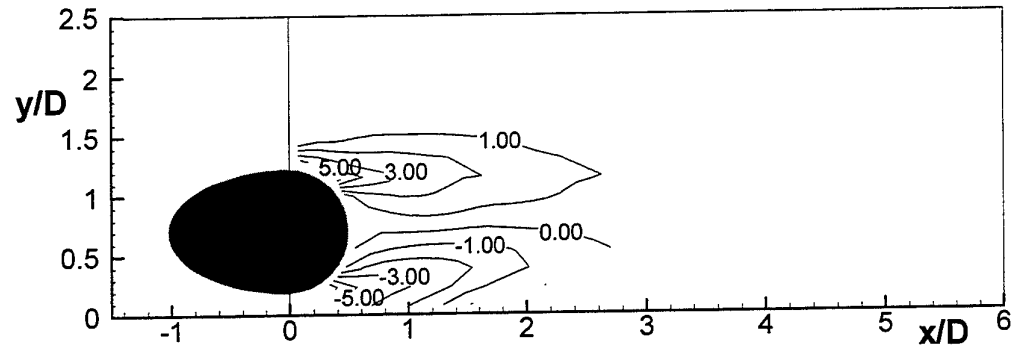


Fig. 12 Normalized time averaged vorticity in near wake behind an egg-profiled cylinder model: $Re_D = 5.5 \cdot 10^4, h/D = 1.0$, stationary wall

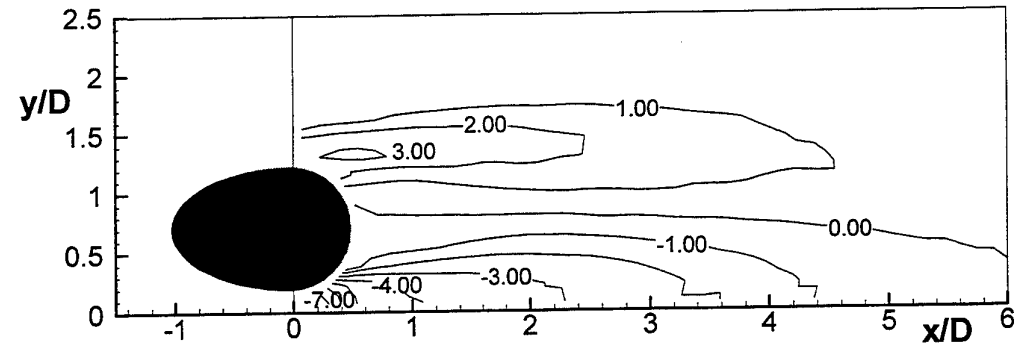


Fig. 13 Normalized time averaged vorticity in near wake behind an egg-profiled cylinder model: $Re_D = 5.5 \cdot 10^4, h/D = 1.0$, stationary wall

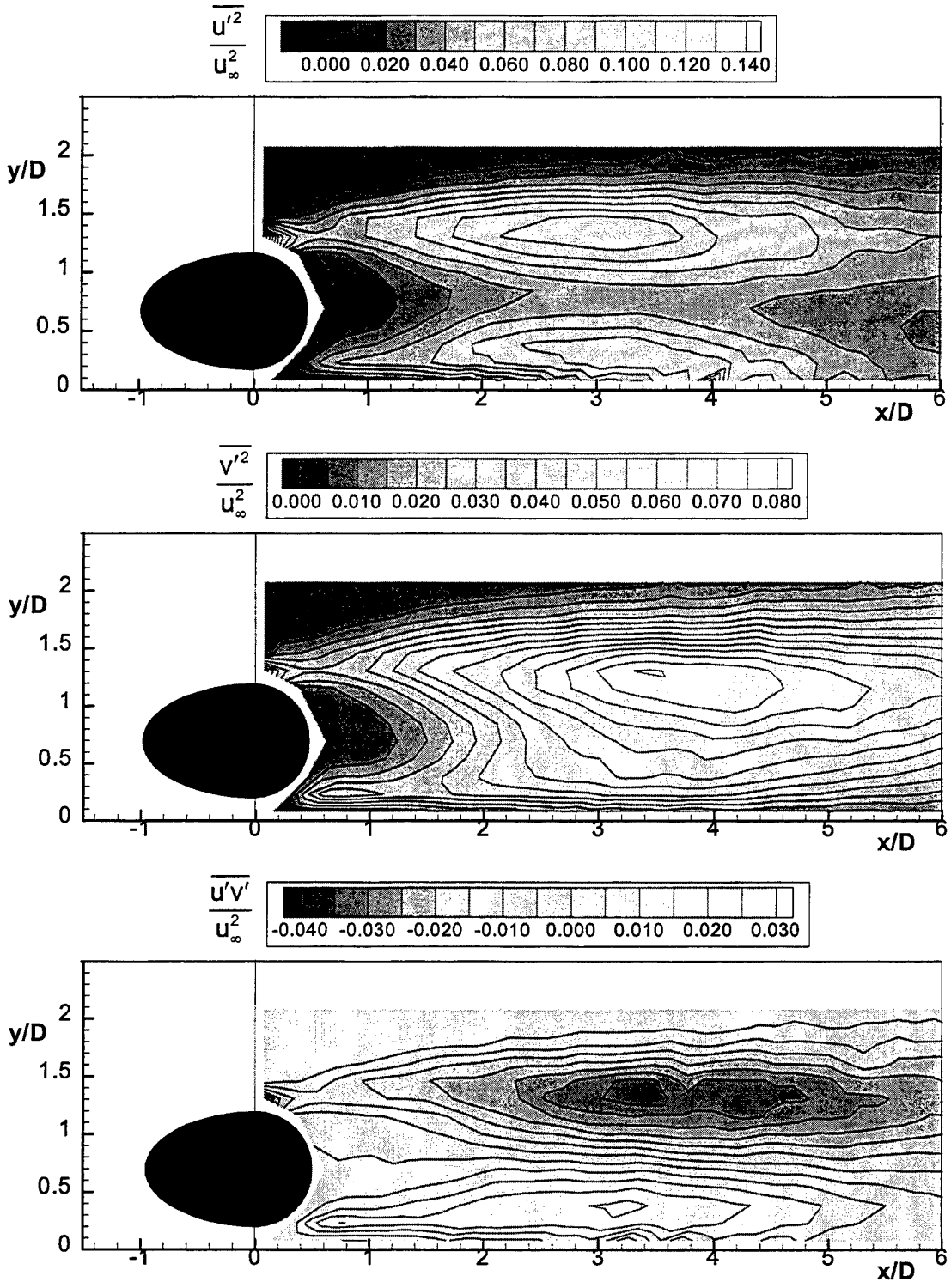


Fig. 14 Turbulence structure in near wake behind an egg-profiled cylinder model
$Re_D = 5.5 \cdot 10^4$, h/D = 0.2, moving wall

h/D	$\left(\overline{u'^2}/u_\infty^2\right)_{max}$		$\left(\overline{v'^2}/u_\infty^2\right)_{max}$		$\left(\overline{u'v'}/u_\infty^2\right)_{min/max}$	
	Stationary wall	Moving wall	Stationary wall	Moving wall	Stationary wall	Moving wall
0.2	0.120	0.125	0.086	0.063	-0.043 – 0.032	-0.043 – 0.032
1.0	0.147	0.168	0.188	0.167	-0.044 – 0.058	-0.044 – 0.058

Table 1 Extreme Reynolds stresses behind an egg-profiled cylinder model

maximal values of the Reynolds stresses increase as well. Table 1 lists the extreme values for the wall distance h/D=1.0 and h/D=0.2. For the case of h/D=0.2 the maximal transversal component of the normal Reynolds stress is smaller than that for the case of h/D=1.0. The moving wall has a larger influence on the transversal component of the Reynolds stress for the case of h/D=0.2. The distributions of Reynolds shear stress show that the extreme values on the top side $\left(\overline{u'v'}/u_\infty^2\right)_{min}$ do not change with a change in wall distance. The extreme values $\left(\overline{u'v'}/u_\infty^2\right)_{max}$ on the under side will be smaller if the wall distance decreases. The influence the moving wall has on the Reynolds normal stresses is most apparent for a clearance of h/D=0.2 and least apparent for a clearance of h/D=1.0.

4. CONCLUSION

This investigation shows that the wall has a strong influence on the flow around the body. The velocity as well as the Reynolds stress distributions are significantly affected. A comparison of the experimental results for a moving and a stationary wall show strong deviations in the dead water region. Therefore, the relative motion of the body with respect to a wall has to be simulated with the use of appropriate experimental equipment (for example a moving belt).

REFERENCES

Geropp, D. & Kim, M.S. 1995, Zonenmethode zur Berechnung ebener Körperumströmungen mit Totwasser und Bodeneinfluß, Archive of Applied Mechanics vol. 65, pp. 270-278

Kim, M.S. & Geropp, D. 1996, LDA-Untersuchungen des Nachlaufes hinter einem wandnahen Kreiszylinders, Proc. 5. Fachtagung Lasermethoden in der Strömungsmeßtechnik, Berlin, pp. 15.1-15.7

Geropp, D. & Odenthal, H.-J. 1996, Laser-Doppler-Messungen im Rezirkulationsgebiet eines ebenen Körpers mit Bodensimulation, Zeitschrift Flugwissenschaften und Weltraumforschung vol. 20, pp. 145-150

Kim, M.S. & Geropp, D. 1997a, Experimental Investigation of the ground effect on the flow around some two-dimensional bluff bodies with moving-belt technique, Proc. 2nd European & African Conference on Wind Engineering, Genova, vol. 2, pp. 791-798

Kim, M.S. & Geropp, D. 1997b, LDV-Measurements in the near wake behind a half ellipse close to a stationary and a moving wall, Proc. 7th International Conference on 'Laser Anemometry - Advances and Applications'. Karlsruhe, pp. 527-534

LDA MEASUREMENTS AND VISUALIZATION OF THE SUPERSONIC FLOW AROUND A LONGITUDINAL CYLINDER WITH DIFFERENT SURFACE ROUGHNESSES

F. Leopold, E. Augenstein, S. Damp, F. Christnacher, E. Bacher

French-German Research Institute of Saint-Louis (ISL)
5 rue du Général Cassagnou, 68301 SAINT LOUIS, France

ABSTRACT

The wake flow of a longitudinal circular cylinder with different surface roughnesses (smooth, riblets, sandpaper) is examined at supersonic speed in order to understand and predict the mechanisms occurring in the turbulent wake. A continuous laser illumination associated with a holographic filter and a high performance CCD camera with different times of exposure allows us to show the unsteady character of this flow. The velocities in the near wake are measured with a conventional laser Doppler anemometer in forward scattering mode. However, the influence of the different surface roughnesses can be found in particular in the viscous sublayer. Therefore, a miniaturized laser Doppler anemometer system with a high spatial resolution has been developed and placed inside the wind tunnel model. For the prediction of the coherent structures in the wake flow a numerical simulation is absolutely necessary. However, the parameters of the different numerical models have to be adjusted especially for the boundary layer flow with the experimental results.

1. MOTIVATION

In the late sixties biologists found that the skin of fast swimming sharks is structured. With the coming-up of the oil crisis a strong interest in drag reduction technology arose. One of the projects was to influence the structure of the boundary layer in the same manner as was observed in the case of the shark's skin. A good overview of this research project is given by Walsh (1990). In spite of nearly 30 years of riblet research, there are, up to now, only a few reports in literature concerning riblets at supersonic regime, such as Robinson (1988) Gaudet (1989), and Coustols & Cousteix (1994). The aim of this work is to determine the influence of riblets or of a rough surface on a supersonic wake flow, especially on the behaviour of the vortices.

Vortex shedding behind blunt bodies appears at supercritical Reynolds numbers in many flow regimes. Von Kàrmàn studied these structures at low velocities and was able to predict their frequencies. Nevertheless, the shedding of vortices from blunt bodies appears not only at low Mach numbers, as shown by Gold (1963), Jaeggy et al. (1972), Seiler et al. (1988), Althaus (1989), Nießen (1994), to mention only a few ones. The introduction of the concept of absolutely and convectively unstable wave propagation was made in the study of plasma instabilities by Briggs (1964) and Bers (1975). In recent years this concept has also been applied to many aerodynamical investigations, for example to boundary layers by Mack (1984). Huerre & Monkewitz (1985), Koch (1986), Monkewitz (1988), Brevdo (1988), Hannemann & Oertel (1989), Triantafyllou et al. (1989), to mention only a few names, found out that the shedding of the coherent structures from the blunt bodies is related to an absolutely unstable region in the near wake.

In this paper the wake flow of a longitudinal cylinder with three different surfaces (smooth, riblets and sandpaper) is examined at supersonic speed. In order to distinguish the different surfaces, a nondimensionalized height h^+ is introduced:

$$h^+ = h \cdot \frac{\sqrt{\frac{\tau_w}{\rho}}}{\upsilon}, \qquad (1)$$

where τ_w denotes the wall shear stress, ν the kinematic viscosity and ρ the density at the wall. The different values for the surfaces considered in this paper can be found in table 1.

Surface type	Height h^+
smooth	0.1
riblets	23
sand paper (rough)	140

Table 1: Nondimensionalized height h^+ for the three different surfaces

Due to the high costs of wind tunnel testing a numerical simulation is established in order to understand and predict these vortices. However, the parameters of the different turbulence models have to be adjusted especially for the boundary-layer flow over the cylinder with different surface roughnesses. Therefore, three different flow measurement techniques - two laser Doppler anemometers and a flow visualization method - are applied in order to get the necessary information for the validation of the numerical simulations.

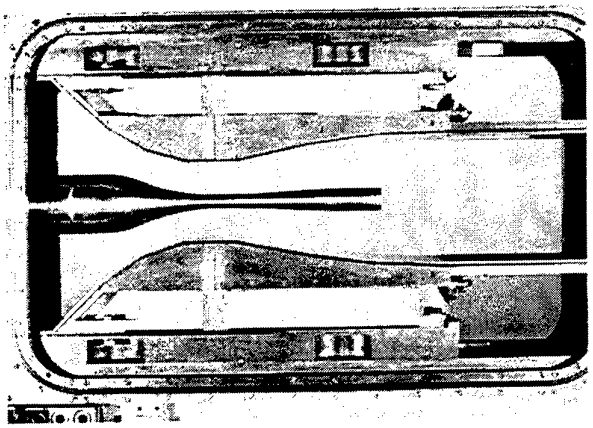
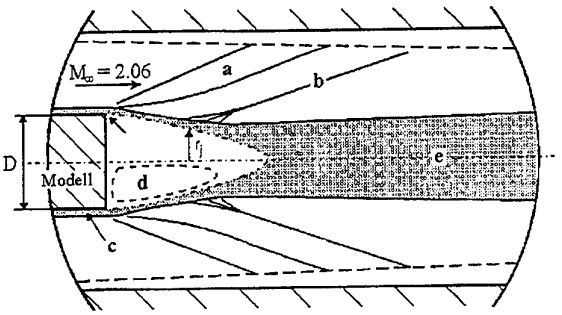


Figure 1: Sting-mounted model in the Laval nozzle for Mach 2.06

2. EXPERIMENTAL SET-UP

All measurements are carried out in the blow-down wind tunnel of ISL at a Mach number of 2.06. The Reynolds number based on the diameter of the cylinder (40 mm) is $1.9 \cdot 10^6$. The flow around a sting-mounted model (fig. 1) is considered. The model is fixed in the settling chamber in order to suppress shocks which would be provoked by attaching the body in the supersonic part of the wind tunnel. The flow configuration is indicated in fig. 2, following Gaviglio et al. (1977). The initial boundary layer is fully turbulent, leaves the model at the edge, is accelerated through the expansion fan towards the axis of symmetry, then develops as a mixing layer which is subjected to recompression with the shock wave, and finally is transformed into the turbulent wake. The mixing layer encloses the recirculation zone, which is at the origin of the coherent structures, shedding from the model.



a: expansion fan, b: recompression shock, c: turbulent boundary layer, d: recirculation zone, e: wake

Figure 2: Schematic illustration of the wake flow

3. FLOW VISUALIZATION USING HOLOGRAPHIC FILTERS

An aerodynamic flow is from an optical point of view a phase object. For its visualization, it is necessary to transform it into an amplitude object. A lot of methods such as shadowgraph and schlieren systems are based on this transformation. A holographic filter, in the filtering plane, can also be applied for the visualization of the index gradients. This filter, which was initially developed for the edge enhancement in optical image processing (Christnacher 1993), allows to visualize the index gradients in all the plane directions. The principle of the optical system is described in figure 3. In a 4-f system, the g(x, y) function in the output plane is equal to the convolution between the f(x, y) function in the input plane and the impulse response of the h(x, y) filter. To visualize the gradients in f(x, y), the impulse response of the filter has to accomplish the following equation:

$$\left|g(x,y)\right| = \left|f(x,y) \cdot h(x,y)\right| = \left|\vec{\text{grad}}\, f(x,y)\right|. \qquad (2)$$

So, in order to obtain this function, the filter must have the following impulse response:

$$h(x,y) = \frac{\partial}{\partial x} + i\,\frac{\partial}{\partial y}. \qquad (3)$$

For the optical implementation of this function, several holographic gratings are superposed on the same photosensitive plate. The final image is the vectorial addition of each diffracted image by the different gratings. Supposing that small density gradients in the flow form the phase object $f = e^{i\varphi(x,y)}$, the vectorial addition of all the images will represent the gradients of the input image

$$I = \frac{144\,\pi^2 d^2}{\lambda^2}\left(\frac{\partial\varphi^2}{\partial x} + \frac{\partial\varphi^2}{\partial y}\right), \qquad (4)$$

as shown by Leopold & Christnacher (1997).

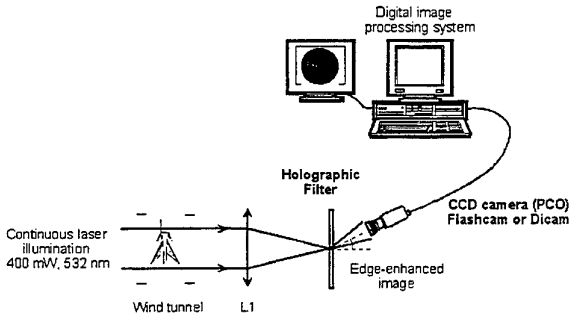
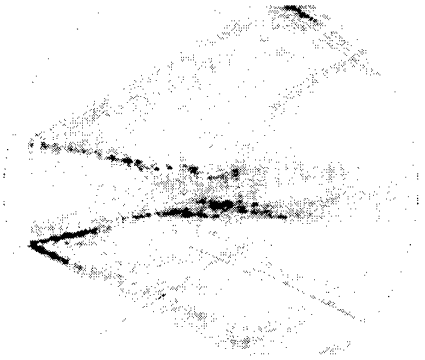
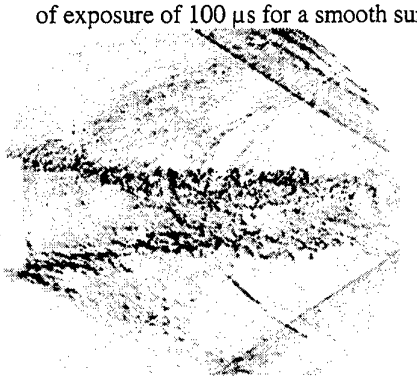


Figure 3: Optical set-up for flow visualization

Figure 3 describes the optical set-up of the flow visualization. The light source is a continuous laser with 400 mW at 532 nm. The beam is extended to the desired field size (15 cm in diameter). After passing the test section, the light is focalized by the lens L1 on the holographic filter. Further on, the image is digitalized by a single-shot camera. Due to the continuous laser illumination, the time of exposure can be chosen with the high-speed camera. Two types of camera are used. The FlashCam camera from PCO allows to realize times of exposure in the range from 1 µs to 40 ms at video rate. The DiCam camera from PCO is an intensified version which allows to realize smaller times of exposure from 5 ns to 1 ms at 8 Hz. These delays correspond to a normal laser pulse. The DiCam camera is used to show the rapid phenomena of the flow, where even the turbulent structures are "frozen". A dynamic sequence can also be recorded on a video tape.


Figure 4: Visualization of the wake flow at the time of exposure of 100 µs for a smooth surface


Figure 5: Visualization of the wake flow at the time of exposure of 5 ns for a rough surface

The image in figure 4 with a time of exposure of 100 µs represents the quasi-steady aspect of the flow. The image at 5 ns (fig. 5) shows the unsteady phenomena such as the coherent structures and the turbulence. The unsteady phenomena are registered in a video sequence and can be quantified after the numerization of the images.

4. MEASUREMENT OF THE VELOCITIES

4.1. Velocities in the near wake

The principle of laser anemometer is to create an intersection of two laser beams with coherent light. Thus a system of bright and dark plane interference fringes is formed parallel to the bisecting plane of the two incident beams. The light scattered by the particles passing through this intersection varies periodically. This frequency is proportional to the velocity of the particles and inversely proportional to the distance between two fringes. Our laser Doppler anemometer is a four-beam set-up which uses two colours of a 10 W argon laser. The green colour can be found at 514.5 nm and the blue one at 488 nm.

The initial blue-green beam is divided by a Bragg cell into four beams, two of each colour. One beam of each colour is shifted to 40 MHz to ensure the displacement of the fringes in order to get access to the velocity inside the recirculation zone. Then the beams are focused on the measuring point. The measuring point can be displaced in all three dimensions. But only the velocities in one symmetrical plane are measured. The scattered light is collected in the forward scattering mode by a convergent optical set-up which focuses the image of the measuring point on the front part of an optical fibre. The scattered light is then divided into its two components. Then these two light beams reach two photomultipliers, the output signals of which are treated by a TSI IFA 750 digital signal processor. For all measurements, the flow is seeded with DEHS particles introduced in the stagnation chamber, just in front of the convergent part of the nozzle. To get a higher density of particles in the recirculation zone, some DEHS are added at the base of the cylinder.

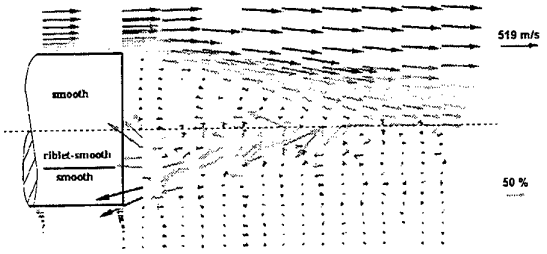


Figure 6: Comparison of the velocities between a surface with riblets and a smooth surface

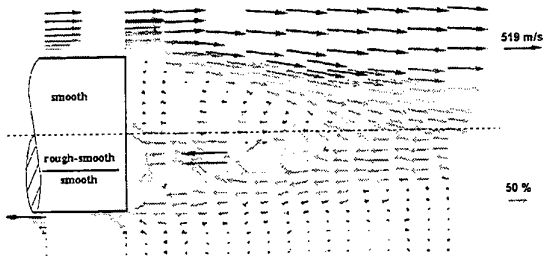


Figure 7: Comparison of the velocities between a rough and a smooth surfaces

The upper halves of figure 6 and 7 show the velocities in the recirculation zone for a cylinder with a smooth surface. The lower parts of these figures indicate the deviations of the local velocity vectors for a surface with riblets (fig 6) and a rough surface (7) as compared with the velocities of a smooth surface. It can be clearly shown that the velocities in the recirculation zone for a cylinder with a rough surface or a surface with riblets are higher than for a smooth one. In particular, the diameter of the wake increases for a rough surface.

4.2. Boundary layer measurement with the Miniature LDA (MLDA)

In research, LDA measurement is the most accurate non-intrusive possibility to measure flow velocities. Four essential points have to be taken into account with LDA boundary layer measurement: dimensions of the measurement volume, its proportions as well as its position and displacement. These points have to be seen under the constraints of the experiment. For our actual experiment these constraints are defined by:

- optical access limited on two sides of the wind tunnel;
- windows about 50 cm by 50 cm;
- distances between the outer side of the windows and the test body of about 25 cm;
- requested spatial resolution of the measurement volume in all dimensions better than 25 µm;
- required spatial accuracy of the position of the measurement volume better than 10 µm;
- due to the vibrations of the installation during blow down, the displacement of the wall is more important than the desired precision;
- diameter of the body under test < 40 mm;
- restricted access through the sting;
- measurement with transonic or supersonic flow speed.

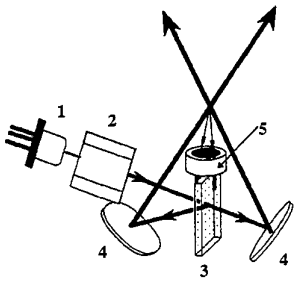


Figure 8: Structure of the optic electronic head of the boundary layer MLDA

The construction of a classical LDA system with the requested properties, especially the small measuring volume, is no problem in principle. Difficulties arise from the fact that the installation vibrates with amplitudes much more important than the demanded spatial accuracy. For measurements near the wall solutions are already presented for this problem. It has been solved by the optical measurement of the displacement between the

measuring volume and the body under test. But due to our working in the transonic or supersonic range, the light beams will be essentially disturbed by air density gradients

Therefore the solution we selected is to build the LDA system into the body under test. No fibre probe with acceptable dimensions and properties is available on the market anyway. In order to fulfil the requested dimensions of the measurement volume and the limiting body diameter, an adapted design is necessary. The principle of this construction can be seen in figure 8.

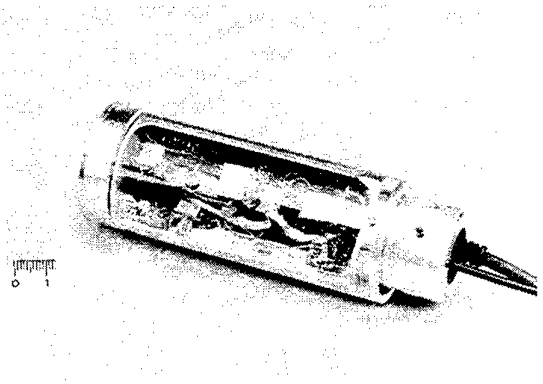


Figure 9: Photography of the boundary layer MLDA with spindle feed, built into the body under test

The beam of the laser diode (1) is collimated (2) and separated by a half-mirror plate (3). The adjustment of the two mirrors (4) defines the crossing point of the two laser beams which determines the measurement volume. Its diameter is defined by the focal length of the collimator lens (2). The length of the measurement volume depends on the beam diameter and crossing angle. To reduce this length, a high crossing angle of about 80 degrees is realized. The backscattered light is directly detected by the detector (5), which is an Avalanche Photo Diode (APD). In the classical arrangement, a receiving lens collects the light onto the detector. This causes problems with the actual system due to very restricted place in system depth. Using directly the detector in an elevated position, the realized detecting angle is comparable to the classical arrangement. This is due to the short distance between measurement volume and detector. The disadvantage of not having a spatial filtering must be accepted. This system is also described by Damp (1995).

The data of the realized system are:

- spatial dimensions: 10 mm · 15 mm · 30 mm;
- measurement distance: 5 mm;
- measurement volume: about 25 µm, spherical;
- fringe distance: about 0.8 µm;
- signal band width (detector and amplifier): 120 MHz.

This optic electronic head of the LDA system has to be traversed to scan the boundary layer. There are no traversing systems available with the required specifications; in general, they fail due to the restricted space. Therefore, we developed two systems at ISL: 1) by using a piezo bimorph stripe element (presented by Damp (1996)); 2) by using a step motor driven spindle feed (see figure 9).
Using the piezo bimorph stripe element has the advantage of high resolution but the stroke is limited to 2 mm and depends on the effective load. Therefore, calibration or on-line distance measurement is necessary. Furthermore, the system has to be carefully damped against mechanical oscillations. The step motor driven spindle feed was realized with 5 mm stroke and 10 µm resolution. This is a more robust solution and therefore, the preferred one. An advantage of the step motor feed is that the measurement or calibration of the displacement is not necessary. Nevertheless, the on-line distance measurement of the traversing would be a verification. But such a measurement system has not been found up to now, respecting the constraints (micrometer resolution, millimeter stroke, 1 cm^3 space consumption).

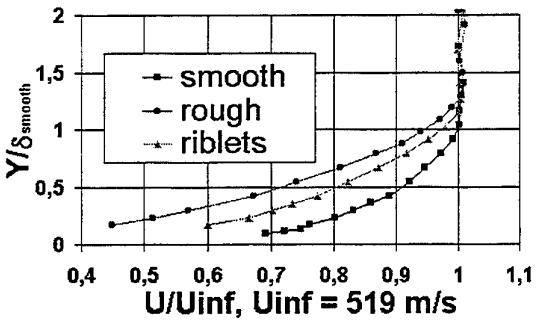


Figure 10: Measured velocity profiles of the boundary layer for different surface roughnesses

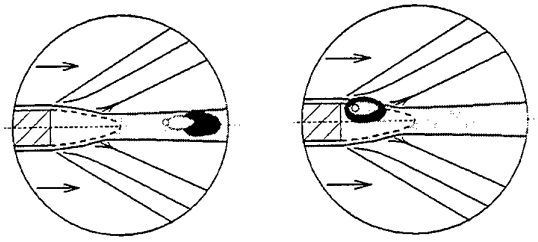
Placing the optic electronic head and the traversing system into the body under test shows the space for the control electronics. A well-established microcontroller design allows the autonomous and/or remote control of the laser diode power, APD supply voltage, amplification gain and, additionally, the control of the stepper motor of the traversing system. Further system parameters and temperatures are

available. This communication is performed by a standard terminal. Figure 9 shows the whole boundary layer LDA measurement system built into the body under test.

Figure 10 shows the measured velocity profiles of the incoming boundary layer flow for the three different surfaces. As expected, the boundary layer thickness for the rough surface is bigger than for the smooth surface. Unfortunately the riblets used here with the nondimensionalized height of 23 are a little too big (Coustols & Cousteix 1994) and we have not found, as shown in figure 10, a significant reduction of the drag coefficient. Nevertheless, the aim of this work is not to study the drag reduction, but to examine the influence of these riblets on the wake flow.

5. NUMERICAL SIMULATION OF THE NEAR WAKE

In order to get a better insight into the origins of the unsteady flow phenomena, three different numerical methods are used in order to predict the wake flow. The simulation of the quasi-steady flow is based on the solution in an axisymmetric coordinate system of the time-dependent Navier-Stokes equations written in conservative form for a compressible ideal gas. The approach used here is the finite volume technique coupled with the upwind flux splitting scheme, which consists in splitting the flux vector into convective and pressure terms and treating them according to their physical aspects in different manners. For the time discretisation a four-step Runge Kutta scheme is applied.



convectively unstable absolutely unstable

Figure 11: Different types of instability

The stability characteristics of the flow can be determined by investigating its impulse response to small perturbations superimposed on the quasi-steady solution. As shown by Leopold (1993), we can distinguish between absolutely unstable and convectively unstable regions due to their different behaviours towards these small perturbations (fig. 11). A region is called absolutely unstable if there are disturbance waves travelling upstream and downstream as well as one wave which remains on the location of its generation and which is amplified in time. In this case, the whole flow field is influenced by one small perturbation. Such a region is the origin of coherent structures. On the other hand, disturbances in a convectively unstable region are carried away with the flow from their generation point and after a sufficiently long time no effect of the perturbation can be remarked. From a mathematical point of view the investigation of the large time behaviour of those small perturbations corresponds to a boundary value problem based on a Fourier-Laplace transformation, supposing the flow to be locally parallel.

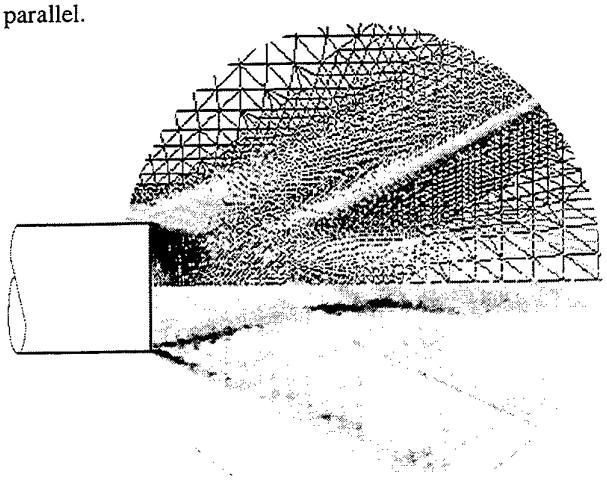


Figure 12: Comparison between the simulated density distribution for a smooth surface and the flow visualization at the time of exposure of 100 μs

Finally the effects of the small-scale turbulence are simulated in terms of the eddy viscosity coefficient using the Baldwin & Lomax (1978) algebraic model or the more sophisticated two-equation model $k\tau$.

6. COMPARISON BETWEEN SIMULATION AND VISUALIZATION

The comparison between the numerical simulation (fig. 12) and the flow visualization with a long time of exposure (100 μs) shows a good agreement for the location of the expansion fan, the mixing layer and the recompression shock.

In figure 13 the measured values for the Reynolds stress tensor are compared to those simulated with the Baldwin-Lomax model following

the approach proposed by Stock & Haase (1984). Then the parameters of the turbulence model for the incoming boundary layer can be adjusted with the LDA measurements. Due to this treatment the simulated and measured velocities in the recirculation zone correspond very well (fig. 14).

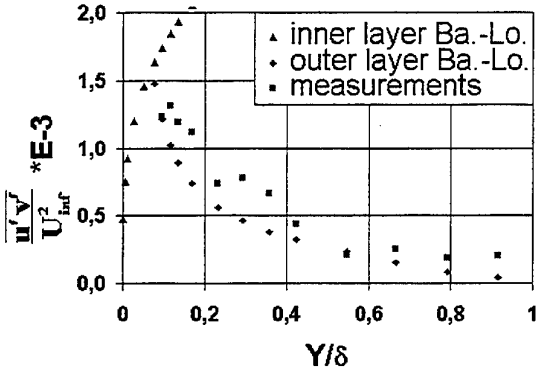


Figure 13: Comparison between the simulated distribution of the Reynolds shear stress with a Baldwin-Lomax model and the measured values

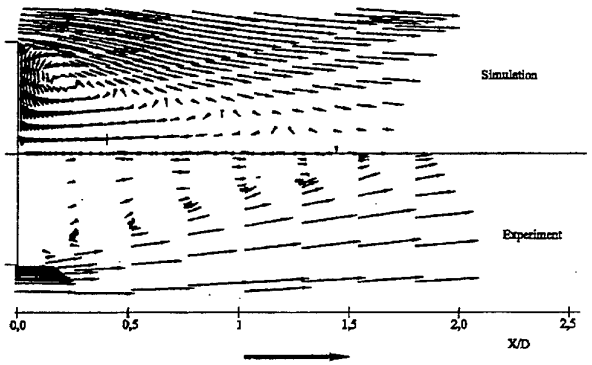


Figure 14: Comparison between simulated and measured velocities

The calculated neutral curves (fig. 15) for the superimposed disturbances clearly indicate the existence of an absolutely unstable region in the recirculation zone (the perturbations have negative propagation velocities which means that they travel upstream). The increasing of the surface roughness is directly related to higher velocities in the recirculation zone, to bigger vortices and therefore, to a larger diameter of the far wake. The length scale of these vortices can be directly compared to the characteristic lengths of the shedding vortices visualized with the method using the holographic filters at a time of exposure of 5 ns (fig. 5).

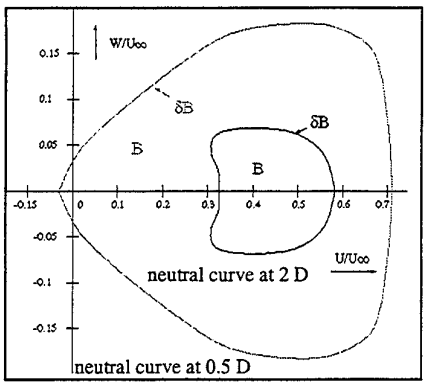


Figure 15: Neutral curves at the positions 0.5 D and 2 D behind the base of the cylinder

7. CONCLUSIONS

A continuous laser illumination associated with a holographic filter and a high-performance CCD camera with different times of exposure allows to show the unsteady character of wake flow. The different surface roughnesses have an important influence on the form of the wake, the velocity distribution and therefore, on the shedding vortices. Due to the different laser Doppler techniques the parameters in the numerical simulations have been validated for several examples. In future, we would like to find the best surface configuration due to these numerical simulation techniques.

ACKNOWLEDGEMENTS

The authors wish to express their sincere thanks to Christophe Demeautis for his assistance for the LDA measurements and to Laurent Gross for his help throughout this work.

REFERENCES

Althaus, W., 1989, Gestörte kompressible Plattennachläufe, Dissertation, RWTH Aachen.

Baldwin, B. S. & Lomax, H., 1978, Thin Layer Approximation and Algebraic Model for Separated Turbulent Flows, AIAA-78-257.

Bers, A., 1975. Linear Waves and Instabilities. Physique des Plasmas, eds. De Witt, C. & Peyraud, J., Gordon and Breach, New York

Brevdo, L. 1988, A Study of Absolute and Convective Instabilities with an Application to the Eady Model, Geophys. Astrophys. Fluid Dynamics, vol. 40.

Briggs, R. J. 1964, Electron - Stream Interactions in Plasmas, Cambridge, MA, M.I.T. Press.

Christnacher, F. 1993, Etude de l'adaptation d'un système optique de reconnaissance de formes à un environnement sévère. ISL R 107/93.

Coustols, E. & Cousteix, E. 1994, Performances of riblets in the supersonic regime, AIAA J., vol. 32, No. 2

Damp, S. 1995, Use of the modified Miniature-LDA in high spatial resolution application; ICIASF'95 Record, Int. Congress on Instrumentation in Aerospace Simulation Facilities; IEEE Catalogue Number 95CH3482-7.

Damp, S. 1996, Einsatz eines modifizierten Miniatur-LDAs zur hochaufgelösten Grenzschichtmessung; GALA'96, 5. Fachtagung: Lasermethoden in der Strömungsmeßtechnik; Verlag Shaker, Aachen, Germany; ISBN 3-8265-1713-X.

Gaudet, L. 1989, Properties of riblets at supersonic speed, Appl. Scie. Research, vol. 46, pp. 245-254.

Gaviglio, J., Dussauge, J.P., Debieve, J.F. & Favre, A. 1977, Behaviour of a turbulent flow, strongly out of equilibrium, at supersonic speeds, Physics of Fluids, vol. 20, No. 10, pp. 179-192.

Gold, H. 1963, Stability of Laminar Wakes, Ph.D. Thesis, California Institute of Technology, Pasadena.

Hannemann, K. & Oertel, H. Jr. 1989, Numerical Simulation of the absolutely and convectively unstable wake, J. Fluid. Mech., vol.199, pp. 55 - 88.

Huerre, P. & Monkewitz, P. A. 1985, Absolute and convective instabilities in free shear layers, J. Fluid Mech., vol. 159, pp. 151-156.

Jaeggy, B.C., Albe F. & Koch, B. 1972, Etude expérimentale de la transition du sillage d'un cône émoussé en vol hypersonique. ISL R 12/72.

Koch, W. 1986, Direct Resonances in Orr - Sommerfeld Problems, Acta Mechanica, vol. 58, pp. 11 - 29.

Leopold, F. 1993, Simulation und stabilitätstheoretische Untersuchungen zum kompressiblen Nachlauf eines längsangeströmten Kreiszylinders. ZLR-Forschungsbericht 93-05.

Leopold, F. & Christnacher F. 1997, Etude des phénomènes d'instabilité dans un sillage supersonique, 7e Colloque Nat. de Visualisation et de Traitement d'Images en Mécanique des Fluides, Saint-Louis.

Mack, L. M. 1984, Boundary Layer Stability Theory, Special Course on Stability and Transition of Laminar Flow, AGARD-R-709.

Monkewitz, P. A. 1988, A note on vortex shedding from axisymmetric bluff bodies, J. Fluid. Mech., vol. 192, pp. 561-575.

Nießen, R. 1994, Speckle-optische Messungen räumlicher Strukturen in einer turbulenten, kompressiblen Nachlaufströmung. ISL R 101/94.

Robinson, S.K. 1988, Effects of Riblets on Turbulence in a Supersonic Boundary Layer, AIAA-86-2628

Seiler, F., Srulijes, J. & George, A. 1988, Wirbel und Druckwellen an Platten, Zylindern und Tragflügelprofilen. ISL R 102/88.

Stock, H.W. & Haase, W. 1987, The Determination of Turbulent Length Scales in Algebraic Turbulence Models for Attached and Slightly Separated Flows Using Navier-Stokes Methods, AIAA-87-1302.

Triantafyllou, G.S., Kupfer, K. & Bers, A., 1989, Absolute Instabilities and Self-Sustained Oscillations in the Wakes of Circular Cylinders, Physical Review Letters, vol. 59, pp. 1914 - 1917.

Walsh, 1990, Riblets, in Viscous Drag Reduction, ed. Bushnell, D. American Institute of Aeronautics and Astronautics, pp. 203-261.

LASER DOPPLER VELOCIMETRY (LDV) AND PARTICLE IMAGE VELOCIMETRY (PIV) MEASUREMENTS OF THE TIME DEPENDENT FLOW BEHIND A CIRCULAR CYLINDER AND COMPARISON WITH RESULTS OBTAINED BY NUMERICAL SIMULATION

Oliver Stenzel and Christoph Lund

Department of Fluid Mechanics, Faculty of Mechanical Engineering
University of the Federal Armed Forces Hamburg, D–22039 Hamburg, Germany

1. INTRODUCTION

The laminar flow of an incompressible newtonian fluid around a circular cylinder is well known and described in literature as *Kármán vortex street*. For its extensive investigations in the past this flow is frequently used as a test case for numerical simulation. In spite of that there still seem to be missing direct comparisons of the time dependent development of the velocity components between experiment and simulation. Until now to our knowledge just comparisons for the mean values have been reported. In this work results for the time dependent flow obtained with LDV and PIV are reported and compared to results of a numerical simulation. The qualitative and quantitative correspondences and differences are presented and discussed.

2. EXPERIMENTAL SET-UP

Figure 1 on the following page shows the side view and the partial top view of the set-up. The dotted area comprising the cylinder and its wake—where vortex shedding is expected—represents the region of interest both for experiment and numerical simulation. Details are shown in figure 2 on the next page with (ξ,ψ) defining a dimensionless coordinate system in which the cylinder diameter is used as a reference length. The region of interest is 352 mm in length, 65.6 mm in height and 328 mm in depth. The cylinder has a diameter of 16 mm and extents over the whole channel depth with 328 mm in length. The measurements are conducted at half channel depth where the flow is taken to be nearly two-dimensional[1].

The fluid (water) is pumped into the reservoir by a centrifugal pump. The flow rate is adjusted to its desired value by an electronically controllable valve and measured simultaneously. The water level in the reservoir is kept constant, thus ensuring an also constant pressure gradient along the channel.

For the LDV measurements a two component backward scattering system (DANTEC) is used. The measuring volume is traversed within a plane in the middle of the channel that is orientated normally to the cylinder axis. The location of the measuring points can be seen in figure 2 on the following page. The tracers used are titanium-oxid particles with a mean diameter of 5 µm.

For the PIV measurements a system (Optical Flow Systems Ltd.) is used that mainly consists of a double oscillator Nd:YAG laser, a cross-correlation CCD-camera with a 1 K by 1 K sensor and a PC equipped with 512 MB RAM in order to record sufficiently long time series of the flow. The area recorded by the CCD-camera is described by a square with its lower left corner at $(\xi = 2.1, \psi = 0.1)$ and its upper right corner at $(\xi = 6.0, \psi = 4.0)$. For better light scattering efficiency the tracers used are silver-coated hollow glass-spheres with a mean diameter of 10 µm.

We define a Reynolds number that characterizes the stationary flow in the middle plane as

$$\mathrm{Re} = \frac{u_\mathrm{m} D \rho}{\mu} \tag{1}$$

with the average horizontal velocity u_m, the newtonian dynamic viscosity μ, the fluid density ρ and the cylinder diameter D. The value of u_m is determined by integrating the inflow velocity profile ($\xi = -2$) over the channel height thus giving a Reynolds number of 100.

Further the Strouhal number Sr and the dimensionless time $\tilde{t}$

$$\mathrm{Sr} = \frac{Df}{u_\mathrm{m}} \quad , \quad \tilde{t} = \frac{t\mu}{\rho D^2} \tag{2}$$

with the separation frequency f of the vortices are used. Thus the dimensionless time computes to $\tilde{t} = t/256$ s. All velocities are made dimensionless with u_m.

[1] The geometrical ratios of this two-dimensional problem are taken from [3].

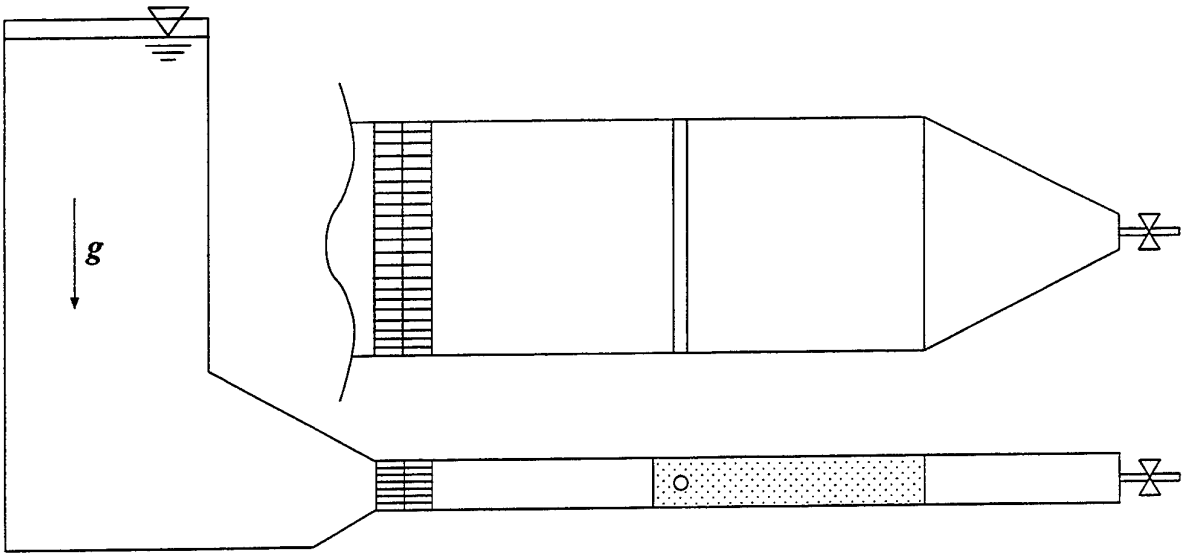


Figure 1: Sketch of the set-up (side view and partial top view)

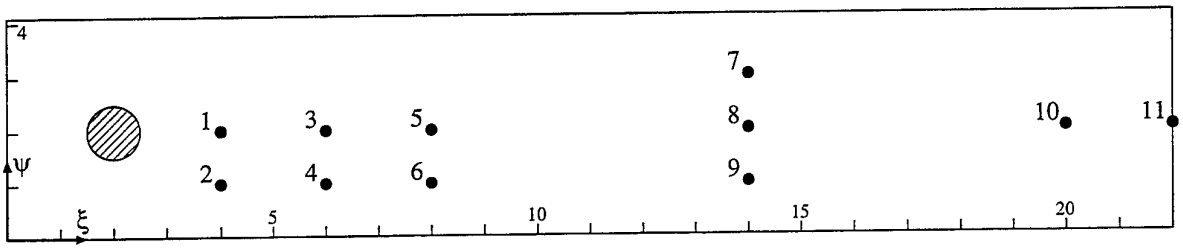


Figure 2: Geometry of the channel and location of the measuring points

Ideally the inflow is fully developed, time independent and of parabolic shape across the channel height. As one can see in figure 3 on the next page the inflow is not of parabolic shape and shows a small vertical component ($\approx 2\%$ of u_m). The reason for the non-parabolic shape obviously is that the length of the inlet is too short to allow the flow to fully develop. The vertical component that results from the 90° change in direction of the flow from the reservoir to the channel is limited to an acceptable value by a flow unifier at the beginning of the inlet. Nevertheless this inflow profile is used for the numerical simulation so that direct comparison is possible.

3. Numerical Simulation

The aim of the simulation is to compute the velocity in the mid-plane area shown in figure 2, where the flow is assumed to be two-dimensional. Using a primitive-variable formulation with cartesian velocity $\mathbf{v}(u,v)$ and pressure p, the simulation is based on the equation of motion for an incompressible isothermal fluid

$$\rho \left(\frac{\partial \mathbf{v}}{\partial t} + \mathbf{L} \cdot \mathbf{v} \right) = -\text{grad}\, p + \text{div}\, \mathbf{T} + \mathbf{f} \qquad (3)$$

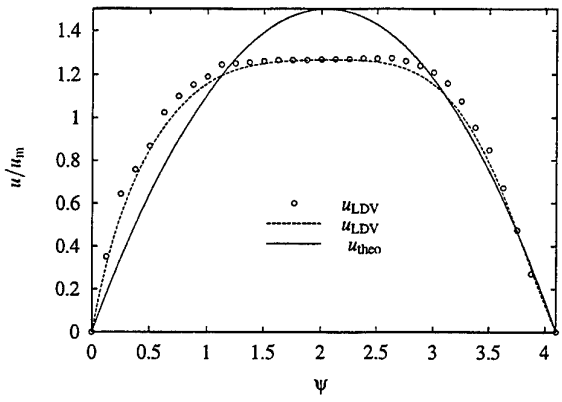
and the continuity equation

$$\text{div}\, \mathbf{v} = 0. \qquad (4)$$

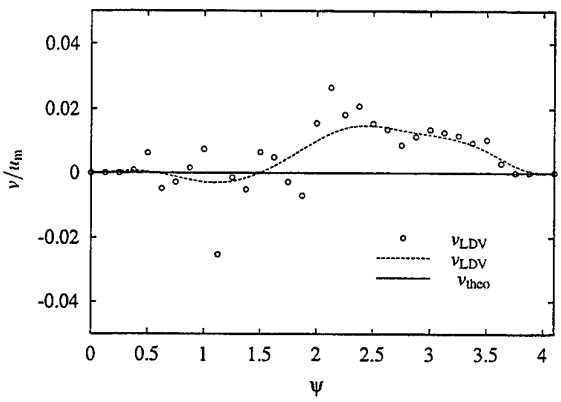
Here t represents the time, ρ the fluid density, $\mathbf{L}$ the tensor of the velocity gradient grad $\mathbf{v}$ and $\mathbf{f}$ the body force per unit volume. In the case of a newtonian fluid the extra-stress tensor $\mathbf{T}$ is connected with the strain rate tensor $\mathbf{D} = \frac{1}{2} (\mathbf{L} + \mathbf{L}^T)$ by $\mathbf{T} = 2\,\mu\,\mathbf{D}$. These equations are supplemented with the initial condition of a fluid at rest, a no-slip boundary condition for all walls and a suitable outflow condition. The inlet velocity is assumed to be of type

$$\mathbf{v}(y,t) = \mathbf{v}_s(y)\ f(t) \qquad (5)$$

where index s refers to the stationary velocity of figure 3 as measured with the LDV equipment. The process function $f(t)$ allows a continuous change in inlet velocity from



(a) Horizontal component



(b) Vertical component

Figure 3: Inflow velocity profile at $\xi = -2$

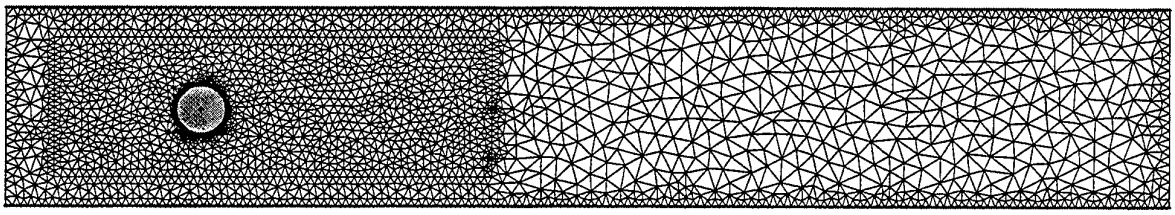


Figure 4: Finite-element mesh with 28 500 unknowns

0 to $\mathbf{v}_s$ and roughly approximates the quasi-linear curve as seen with LDV at $\xi = -2, \psi = 2$ in figure 10. Different functions $f(t)$ will result in a different fluid structure only during the start-up, but not after the vortex shedding has started and the inlet velocity remains unchanged.

The simulation uses a standard Galerkin finite-element method based on the isoparametric triangular Taylor-Hood element with piecewise quadratic shape functions for the velocity and piecewise linear ones for the pressure. The unstructured mesh used to discretize both the entrance and the mid-plane area of figure 2 is shown in figure 4. It extends from $-2 \leq \xi \leq 22$ and $0 \leq \psi \leq 4.1$ and has approximately 28 500 unknowns. The spatial discretization leads to a semi-discrete coupled system of nonlinear ordinary equations. Applying an implicit second-order time discretization this system is transformed into an algebraic nonlinear system which then has to be solved at all timelevels. The timestep size is automatically selected using a local error estimation based on two similar integrations of different timesteps. At the beginning a strong increase in the timestep length is seen; later, with the vortex street fully developed, a periodic change of then small steps.

As an example for the flow computed by the simulation, figure 5 shows several streaklines during vortex shedding. The greyscales refer to different positions where tracer particles of zero mass have been added into the flow. Besides the calculation of the velocity and pressure field, the simulation is also able to compute not easily measurable data, like drag and lift forces on the cylinder as a function of time. Using such data the simulation has been further verified by computing the benchmark-flow described in [3] within the geometry of figure 2. As shown in [2], a very good agreement has been found.

4. Results

4.1 Quasistationary Flow

In the following results of PIV, LDV and simulation for two measuring points (3 and 4) are reviewed.

In general, experiments and numerical simulation agree well with respect to both qualitative and quantitative behaviour. The shape of the osciallations are given likewise with all methods (see figures 6, 7 and 8). Even striking fine structures of the vertical velocity like in figure 9 are found in both experiments and simulation. The marks in the figures represent measured particles (LDV), results of cross-correlating successive image pairs (PIV) and timesteps (simulation). The Strouhal number is be-

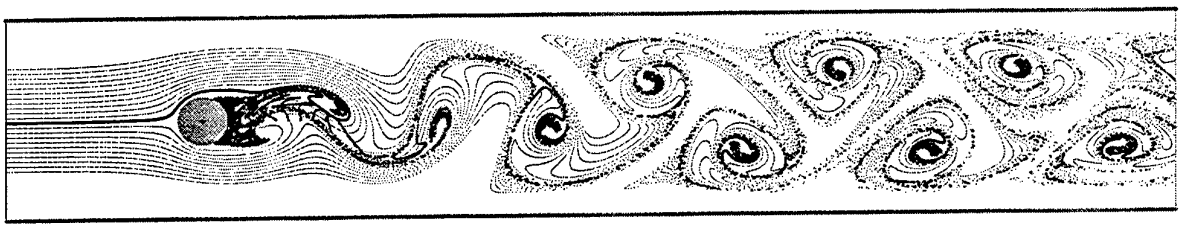


Figure 5: Streaklines during vortex shedding

tween 0.271 (PIV) and 0.281 (LDV) in the experiments and computed to be 0.283 in the simulation.

Further on, PIV is used to gain experimental data of the time dependent velocities within a plane normally orientated to the cylinder axis. It is not possible to get similar velocity maps of flows like the instationary vortex street with LDV because as a point measurement technique LDV can only be used to record velocities at a single point over time. In these experiments PIV image pairs are taken with a frequency of 1.3 Hz. The frequency can be increased up to 10 Hz so that even faster changing flows can be observed with PIV.

Figures 12 and 13 show the contour plot of the absolute velocity and streamlines of the flow. Every second PIV image pair and the corresponding result of the simulation are presented ($\Delta\tilde{t} = 6 \cdot 10^{-3}$). The unusual means of streamlines for instationary flows is chosen in order to visualize the positions of the vortices. The 20 grayscales for the dimensionless absolute velocity represent 0 with white and 2.0 with dark gray. One can find very good agreement in the position of the vortices and the form of the streamlines.

Figures 14 and 15 show a detailed view around measuring point 1 for the same times as in figures 12 and 13. One can observe a vortex core moving from the upper left corner down to the lower right corner. Again very good agreement between experiment and simulation is shown.

4.2 Instationary Flow

In addition to the fully developed *Kármán vortex street* with stationary inflow experiments of the start-up of the flow have been conducted. Figure 10 shows (points: measured with LDV, line: approximation for simulation) how the inflow is started from rest to its maximum value. Figure 11 shows the development of the vortices at point 4. The form of the curve from $\tilde{t} = 0$ to $\tilde{t} = 0.4$ is the same for LDV and simulation. The vortices in the experiment start $\Delta\tilde{t} = 0.05$ earlier to develop. That may be caused by small disturbances in the set-up.

5. Conclusions

The PIV and LDV measurements make available experimental information on the time dependent development of the velocities in the *Kármán vortex street* for a whole cross-section and at discrete points for comparison with numerical simulations. In spite of the three dimensionality and the wall influences[2] excellent agreement between experiments and two dimensional simulation can be found.

The results of the PIV measurements prove that it is possible to extend the application of PIV away from statistical evaluation of turbulent flows towards to the recording of instationary flows that cannot be triggered to external events—like it is possible in turbo machinery—and therefore cannot be recorded by LDV.

References

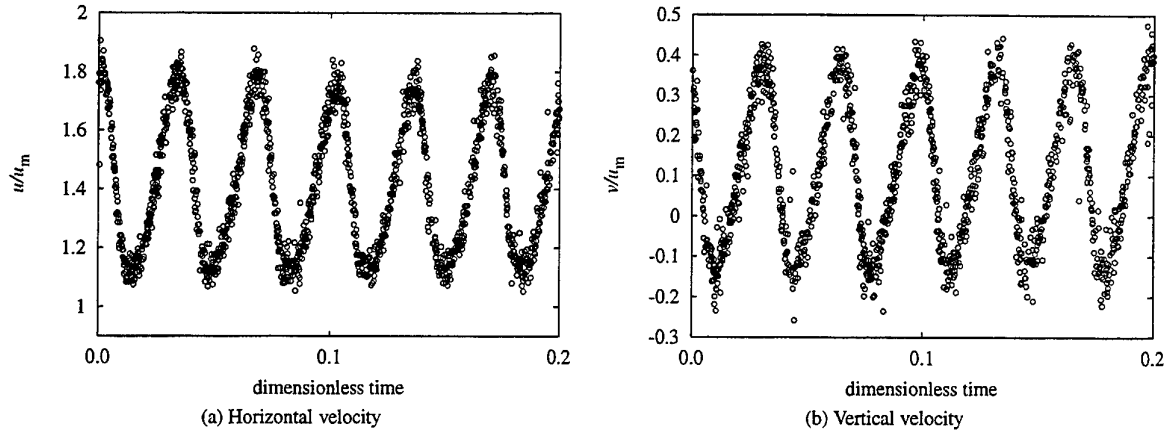
[1] Eisenlohr, H. und H. Eckelmann. *Vortex splitting and its consequences in the vortex street wake of cylinders at low Reynolds number.* Physics of Fluids A **1** (2) (February 1990): 189–192.

[2] Lund, C. *Ein Verfahren zur numerischen Simulation instationärer Strömungen mit nichtlinear-viskosen Fließeigenschaften.* VDI-Fortschrittberichte, Reihe 7, in preparation (1998).

[3] Turek, S. und M. Schäfer. *Benchmark computations of laminar flow around cylinder.* E. H. Hirschel (Ed.), *Flow Simulation with High-Performance Computers II*, Vol. 52 of *Notes on Numerical Fluid Mechanics*. Vieweg, 1996: 547–566. (support of F. Durst, E. Krause, R. Rannacher).

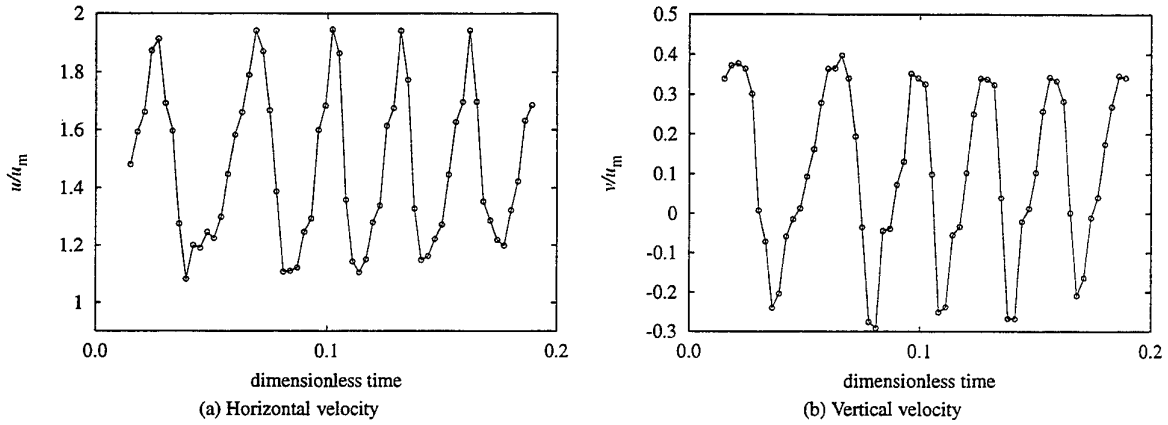
[4] Williamson, C. H. K. *Oblique and parallel modes of vortex shedding in the wake of a circular cylinder at low Reynolds numbers.* Journal of Fluid Mechanics **206** (1989): 579–627.

[2] See [4] and [1] for the sensitiveness of the *Kármán vortex street* against three dimensional effects.



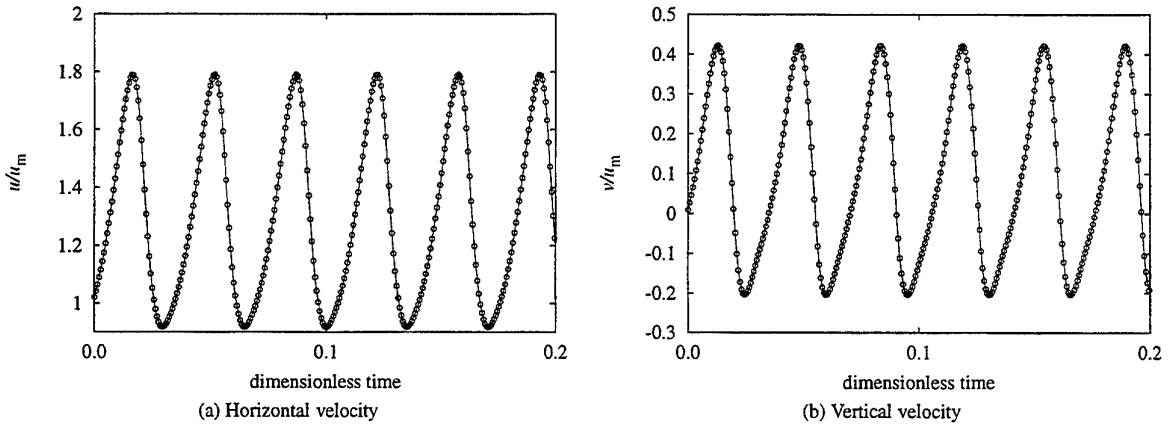
(a) Horizontal velocity (b) Vertical velocity

Figure 6: Results of LDV at point 4



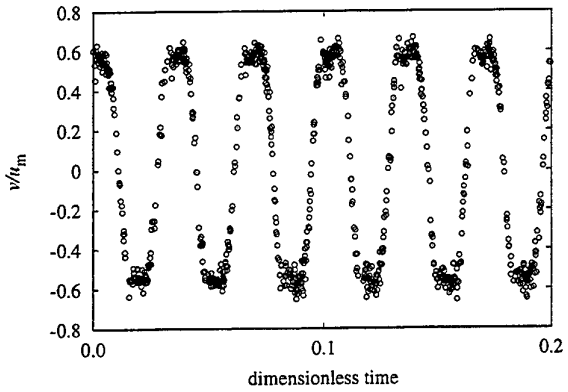
(a) Horizontal velocity (b) Vertical velocity

Figure 7: Results of PIV at point 4

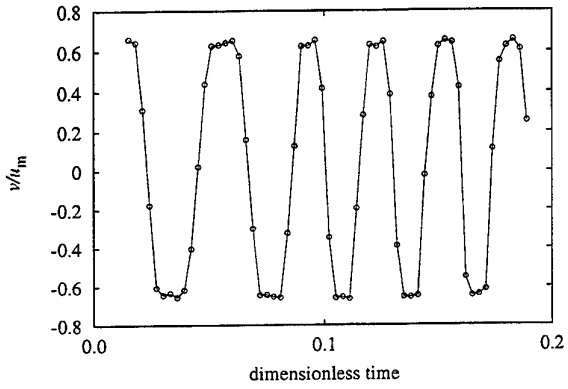


(a) Horizontal velocity (b) Vertical velocity

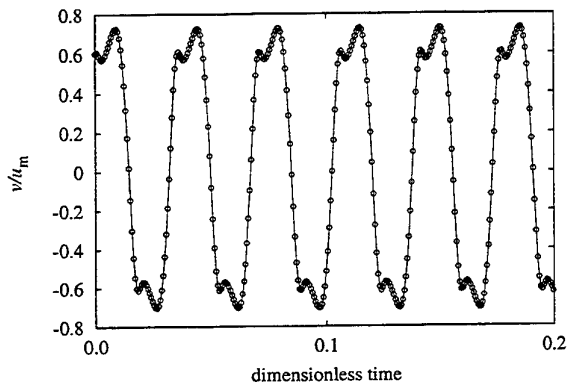
Figure 8: Results of simulation at point 4



(a) Results of LDV



(b) Results of PIV



(c) Results of simulation

Figure 9: Vertical velocity at point 3

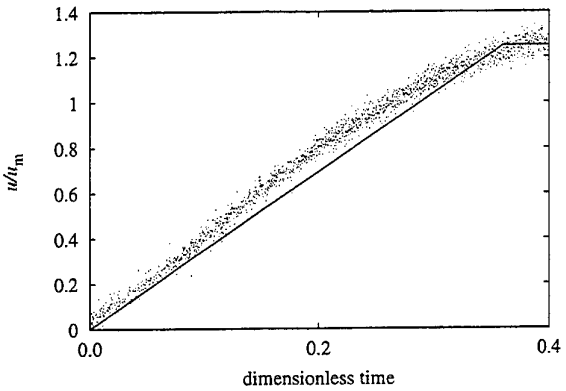
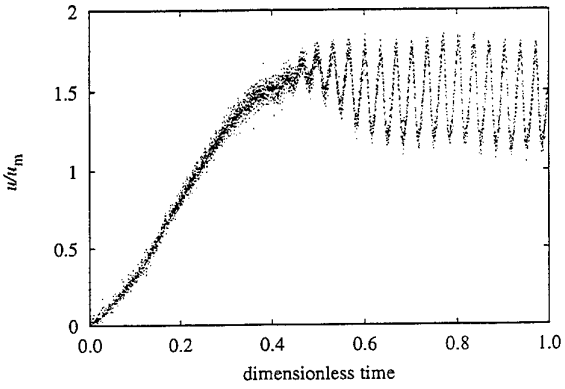
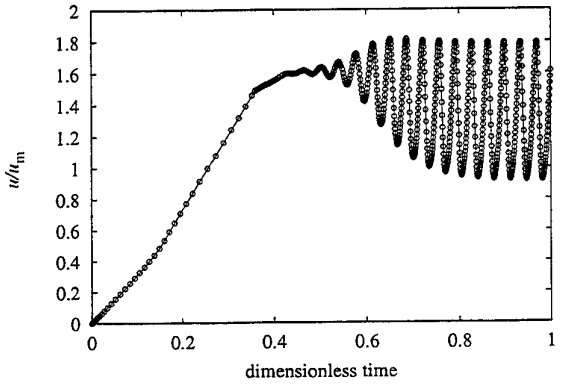


Figure 10: Start-up of the inflow at $\xi = -2, \psi = 2$



(a) Results of LDV



(b) Results of simulation

Figure 11: Horizontal velocity at point 4 during start-up

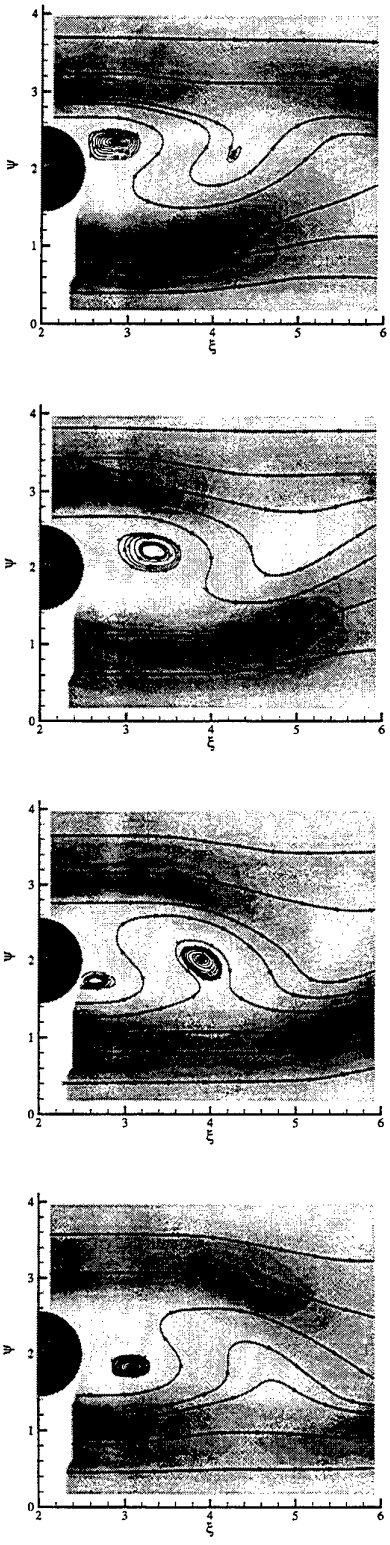


Figure 12: Contour plot of absolute velocity and streamlines—PIV

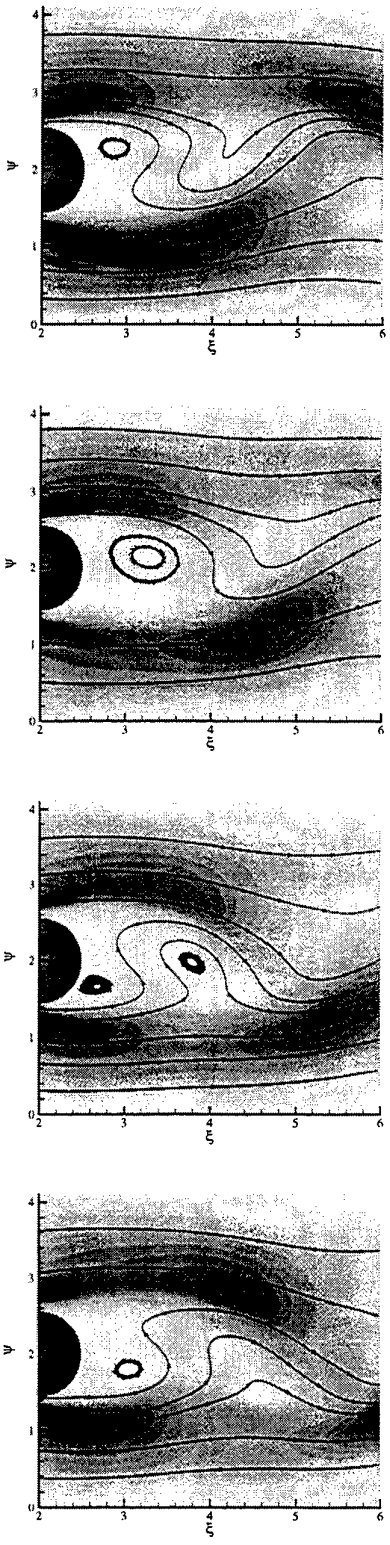


Figure 13: Contour plot of absolute velocity and streamlines—simulation

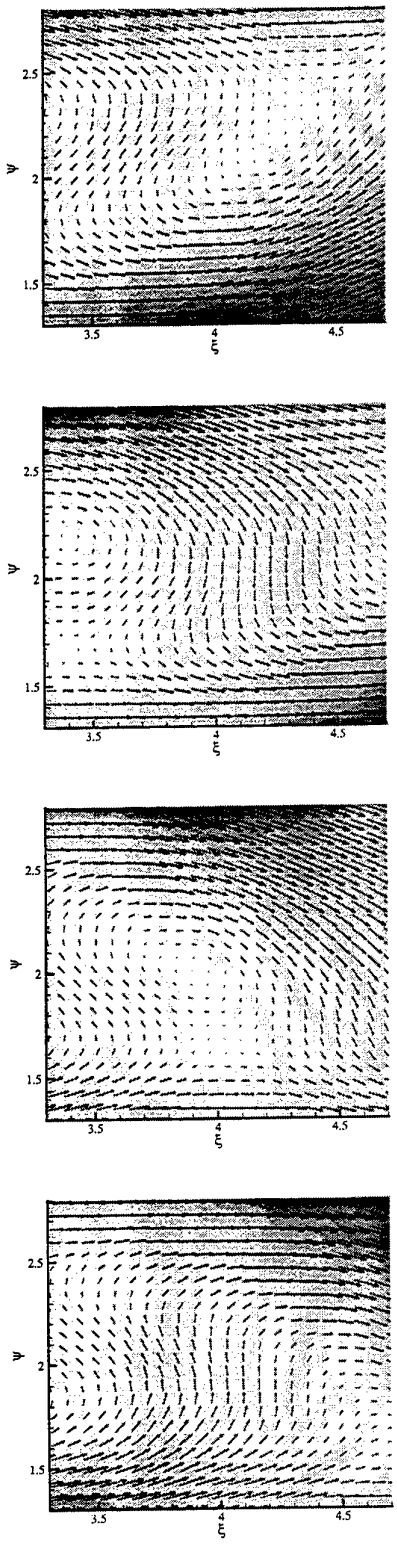


Figure 14: Contour plot of absolute velocity and velocity vectors—PIV

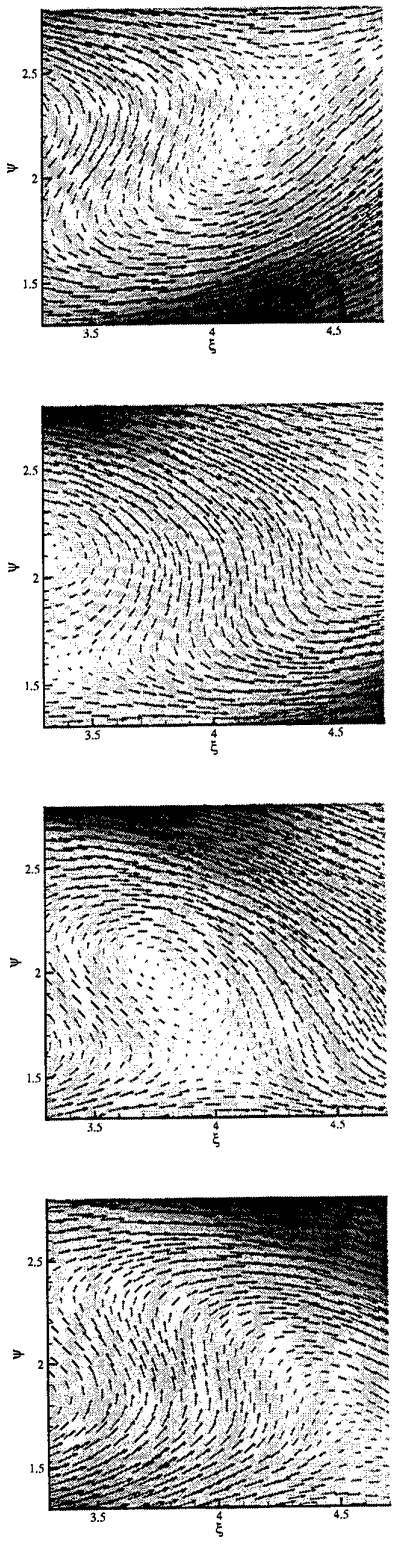


Figure 15: Contour plot of absolute velocity and velocity vectors—simulation

THE STRUCTURE OF SUBSONIC AIR WAKES AT HIGH REYNOLDS NUMBER

Félix Barreras°, Antonio Lozano*, Alexander J. Yates*, César Dopazo°

° *Centro Politécnico Superior de Ingenieros, Area de Mecánica de Fluidos*
Universidad de Zaragoza, Maria de Luna, 3, 50015-Zaragoza, Spain
* *LITEC/CSIC, Maria de Luna, 3, 50015-Zaragoza, Spain*

ABSTRACT

An experimental study has been performed to study the structure of an air wake behind a plate at high Reynolds numbers. To generate the wake, two high speed air streams have been blown past the two sides of a contoured plate with an end width of 1.1 mm. The resulting Reynolds number, based on the plate thickness, has ranged from 1964 to 5892, well in the region of turbulent wake. The air flow field has been visualized with Planar Laser-Induced Fluorescence. Acetone vapor seeded in the air streams has been used as fluorescent tracer. Images have been acquired with a CCD camera slicing the flow both longitudinal and transversally, to analyze the three dimensional structure of the wake. Both the streamwise wavelength, typical for the Von Kármán vortex street, and the spanwise wavelength due to the secondary instability have been measured and their scaling with the plate thickness has been confirmed.

1. INTRODUCTION

Wake flows are common in a large variety of practical applications in aerodynamics and hydrodynamics, e.g., in pumps, fans and turbine blades; aircraft and airfoil wings and even in the human body. For this reason, this type of flows has been extensively studied, analytically, numerically and experimentally.

To explain the transition phenomena in plane wakes, linear stability analysis has been applied among others by Sato & Kuriki (1961), Matingly & Criminale (1972) and Papageorgiou & Smith (1989). A comprehensive list of references can be found in the review of Oertel (1990). The three dimensional Foquet stability analysis of the wake of a cylinder carried out by Barkley & Henderson (1996) shows that there are two critical spanwise wavelengths depending on the critical Reynolds number. The non-linear theory developed by Papageorgiou & Smith (1988) based on asymptotic solutions has been used to study the long-wavelength. Vortex dynamics methods (Meiburg & Lasheras, 1988), and direct numerical simulation (Grinstein et al., 1991, Maekawa et al., 1992) have also been used to improve the understanding of these flows.

From an experimental point of view, Hollingdale reports in 1940 the first set of systematic observations in the wake of a flat plate taking pictures in a water tank. In 1954, Roshko establishes the Reynolds number range, 150÷300, for the transition between stable and irregular vortex shedding in the wake of a circular cylinder and introduces the concept of coherent structures. Later, using hot-wire anemometers, Sato & Kuriki measure in the wake behind different types of thin plates showing the existence of three zones (linear, non-linear and three-dimensional) before reaching the fully turbulent region.

Concentrating in flow visualization experiments to study the three-dimensional wake development, in 1957 Hama bleeds dye through a cylinder surface in a water channel to see the onset of the three dimensional waves on the two dimensional Von Kármán vortex street . In most water experiments either dyes or light scatterers such as aluminum flakes (Williamson, 1996) or hydrogen bubbles (Matingly & Criminale, 1972)) are used to visualize the wake. Information from single planes can be obtained by line seeding (Meiburg & Lasheras), or slicing the flow with light sheets, usually emitted from a laser. Often in this latter case, fluorescent dyes are used (Meiburg & Lasheras and Williamson). The experiments described in Meiburg & Lasheras were conducted in a water channel and the wake was spatially perturbed indentating and corrugating the plate.

In the case of air flows shadowgraph or Schlieren techniques have often been used for wakes with temperature or density gradients. To resolve single planes, light scattering from small particles, e.g. smoke (Corke et al. 1977, Cimbala et al. 1988, Williamson, 1996) or droplets has been the most common solution.

In this paper acetone vapor has been used as a fluorescent molecular tracer to visualize the wake behind the splitter plate region at the exit of a two dimensional nozzle without perturbation. To our knowledge, this is the first time that planar laser induced fluorescence has been applied to visualize an air wake. The short lifetime of the acetone fluorescence (less than 4 ns) ensures a high temporal resolution. Furthermore, the use of a molecular tracer eliminates potential problems of particles lagging the flow. Additionally, as the Schmidt number is close to 1, the presence of the tracer does not alter the mixing of the air streams and information from the smallest vortical structures can be directly inferred from the concentration images due to the equivalence between scalar and velocity scales.

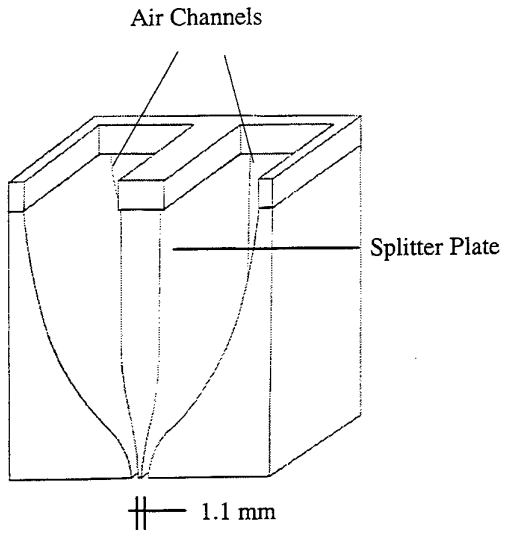


Fig. 1 Schematic of the plate assembly.

2. DESCRIPTION OF THE EXPERIMENT

The wake object of this study forms behind a contoured plate with an end width of 1.1 mm. A schematic of the experimental assembly is depicted in Fig. 1. The air channels located at both sides of the plate have been contoured fitting a 6^{th} order polynomial in order to produce parallel streams at the exit. Both channels have a contraction ratio of 15:1 and an exit width of 3.45 mm. Channels and plate have final straight sections with a length 15 mm. The span of the plate is 80 mm, yielding an aspect ratio of 73.

The air impelled by a 1.1 kW fan flows through a vertical wind tunnel (see Fig. 2) which includes two honeycombs and a wire mesh screen to smooth the turbulence level of the flow and a convergent section (section III) with an area contraction ratio of 6.7:1. The wind tunnel exit section is connected to the plate assembly through another convergent section (IV) with an area contraction ratio of 3.8:1 to adapt the circular section of the tunnel to the rectangular one of the plate head. The total length to exit diameter ratio of the convergent sections is $l/D_e = 15$. The air velocity is varied by regulating the frequency supplied to the fan.

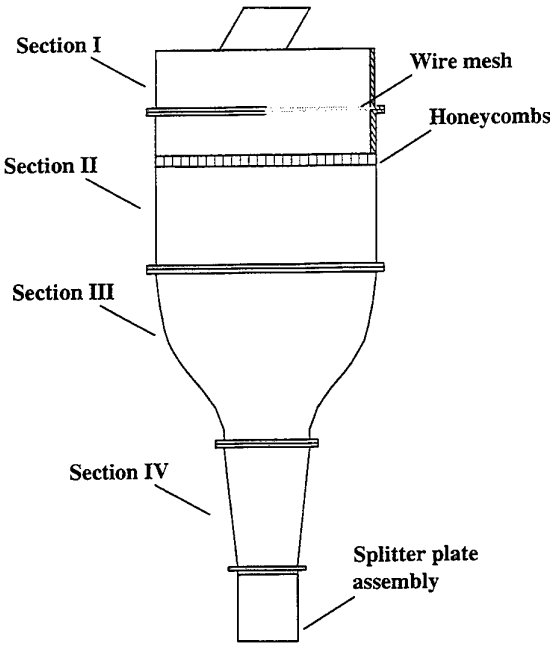


Fig. 2 Wind tunnel and plate head.

Special care has been taken to avoid external vibrations that could force the wake. For this reason, the fan used to blow the air flow was

installed out of the room and connected to the tunnel inlet thorough a flexible hose. The wind tunnel was mounted on a rigid steel supported on rubber wheels.

To visualize the flow structure, Planar Laser-Induced Fluorescence has been used, seeding the air streams with acetone vapor. The acetone has been introduced by spraying a small amount of liquid upstream of the settling chamber (section I of Fig. 2). To excite the acetone, a double cavity Quantel YG781C-10 pulsed Nd:YAG laser has been used, quadrupling the frequency of its emission to obtain 80 mJ pulses at 266 nm with a pulse duration of 6 ns. The laser has been formed into a sheet 4 cm high and 500 μm thick. After excitation, acetone fluoresces in the blue (peak at 435 nm), with an emission efficiency of 0.2% and a lifetime of 4 ns, which enables high temporal resolution imaging without the need of gated cameras (Lozano et al. (1992)). Fluorescence images have been acquired with a Princeton Instruments CCD camera with a 50 mm F1.2 Nikon lens. Data sets have been recorded for two different fields of view, 1.3x1.7 cm and 2.4x3.1 cm. The CCD array has an effective imaging area of 288x384 pixels, which has resulted in resolutions of 45 and 82 μm per pixels respectively.

The air flow velocities have ranged between 25 and 75 m/s corresponding to Reynolds numbers based on the slit thickness of 1964 and 5892 respectively.

3. EXPERIMENTAL RESULTS

3.1 Two dimensional wake

In order to visualize the wake, the left air stream was seeded with a higher acetone vapor concentration . To study the two dimensional structure, the laser beam was formed into a sheet parallel to the xy-plane of the plate, slicing the flow longitudinally. An example of these images is depicted in Fig. 3 for an air velocity of 25 m/s (Re_h = 1,964). The classical vortex street of the two-dimensional wake is clearly visible, together with the external mixing layers formed between the air streams and the quiescent ambient air. A sequence of images for increasing Re_h (2750; 4321 and 5893) can be seen in Fig. 4.

With the resolution of these images (82 mm/pix), the first structure just at the plate end

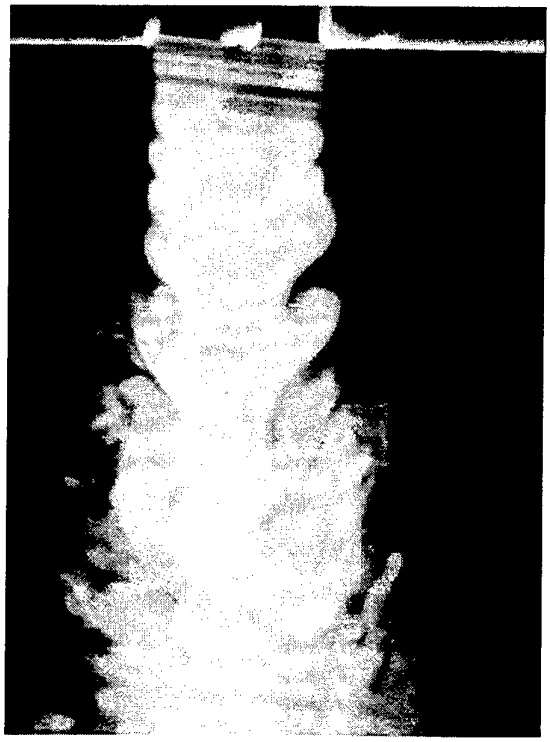


Fig. 3 Fluorescence image of the wake and external mixing layers structures. Air exit velocity 30 m/s (Re_h = 1964).

cannot be seen in detail, and it is difficult to directly measure the two-dimensional wavelength λ_x. For this reason, another set of images with higher spatial resolution (45 μm/pix.) has also been acquired. An example is shown in Fig. 5. Table 1 shows the resulting measurements of the two-dimensional wavelength obtained from the images, adimensionalized with the plate thickness. When the conditions are met for the wake to be far away from the transition region, the wavelength becomes independent of the Reynolds number. It can be noticed, however, how the distance from the plate end to the formation of the first vortical structure is reduced as the Reynolds number increases, varying from 1.51 mm at Re_h = 1964 to 0.48 mm for Re_h = 5893.

3.2 Three dimensional wake

To study the three dimensional structure, the flow was illuminated with the laser sheet parallel to the xz-plane. Figure 6 depicts three of these images for the same Re_h numbers as those in Fig. 4. The transverse wavelength measured directly,

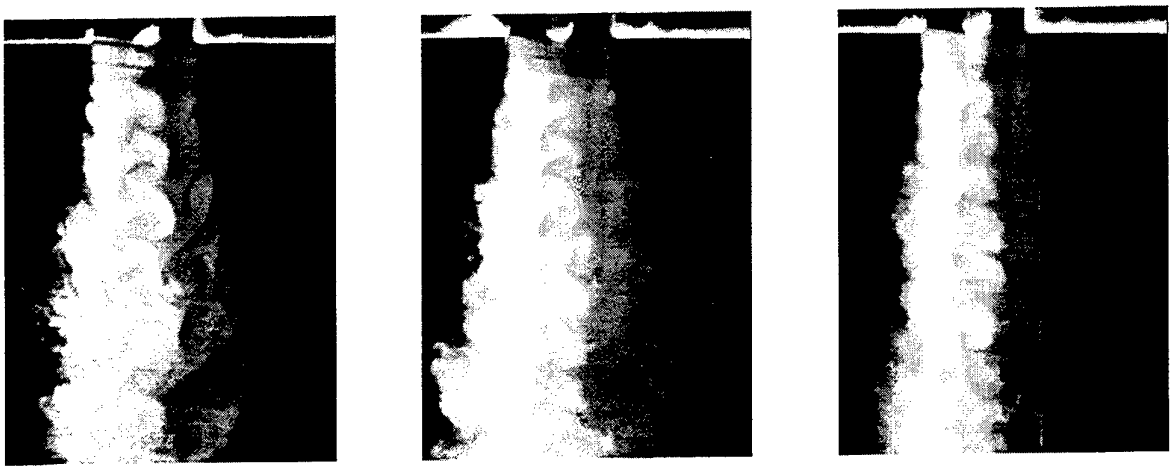


Fig. 4 Images of the plane wake increasing the air velocity. **a)** $Re_h = 2750$; **b)** $Re_h = 4321$ and **c)** $Re_h = 5893$

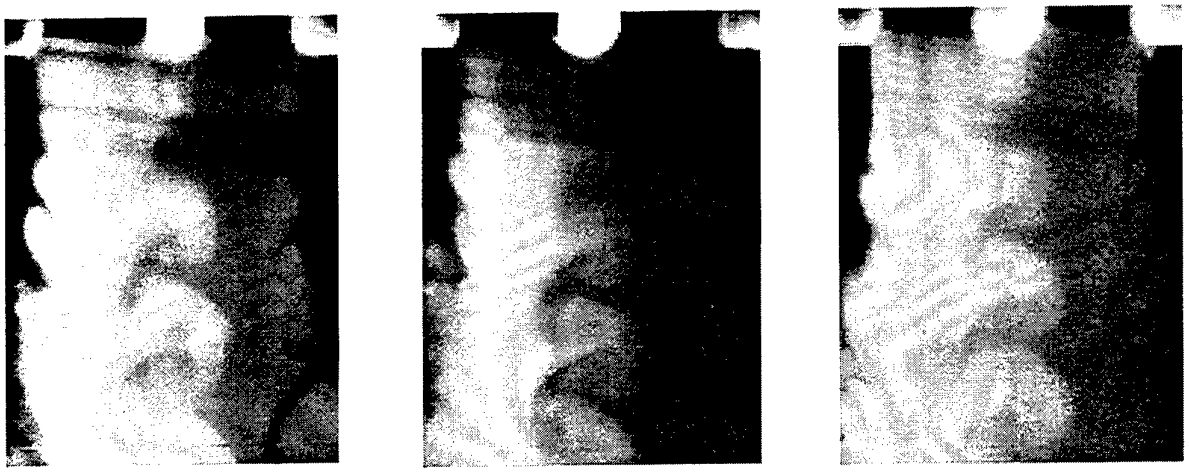


Fig. 5 Similar images as those depicted in Fig. 4 but with an spatial resolution of 45 μm/pix

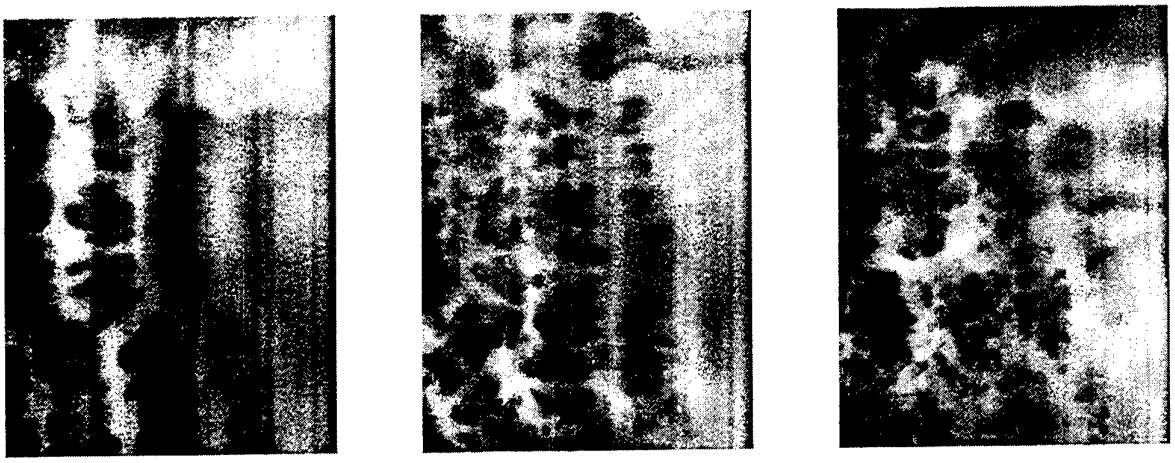


Fig. 6 Transverse sections for same Re_h numbers as those in Figs. 4 and 5. Flow from right to left.

U_a (m/s)	Re_h	λ_x/h	λ_z/h	λ_z/λ_x
25	1964	3.35	1.50	0.45
35	2750	3.25	1.45	0.46
45	3536	3.13	1.48	0.47
55	4321	3.21	1.30	0.40
65	5107	3.17	1.20	0.38
75	5893	3.05	1.17	0.38

Table 1 Two- and three- dimensionless wavelength and its ratio for the different experimental air velocities (and Reynolds numbers).

also adimensionalized dividing by the plate thickness, is showed in table 1. This wavelength is also independent from the Reynolds number for the range in this work, in agreement with the results reported by Williamson.

These images clearly confirm that the flow is well inside the three-dimensional wake region, far from the region of transition of the two modes of instabilities reported in the literature (e.g. regions A and B in Williamson, or modes 1 and 2 in Lasheras).

Conclusions analogous to those extracted from the images of longitudinal sections (Fig.s 4 and 5) can also be obtained from these central-plane sections, both in relation to the length of the longitudinal waves, λ_x, that in this pictures are displayed as the almost vertical white lines, and to the position for the first vortical structure, that in this case is the bright section in the right part of the images. Note also that the "grid" created by the interaction of the spanwise vortices from the Karman street of wavelength λ_x with the streamwise vortices that generate the spanwise wave of wavelength λ_z is not as regular as that described by Williamson (1996) for the transition region in the wake past a cylinder, at lower Reynolds numbers. Observe finally, that the ratio between the spanwise and streamwise wavelengths λ_z/λ_x calculated in table 1 is approximately 2/5, in disagreement with other values reported in the literature and used in numerical simulations, e.g. 2/3 in Meiburg & Lasheras (1988) and 5/3 in Grinstein et.al. (1991).

4. DISCUSSION

A sketch of the model of the wake behind a flat plate resulting from the analysis of the images obtained in this study can be seen in Fig. 7. The letter "S" marks a saddle point. The development of two vortex lines of opposite sign displaced from the wake central plane characteristic of the three-dimensional wake region can clearly be seen, for example in Fig. 5 a). This behavior is similar to that of wakes past streamlined bodies, as cylinder or airfoils. This model for the evolution of the two-dimensional Von Kármán vortex street directly from the near wake region is in disagreement with the one proposed in Sato & Kurike (1961). There, this evolution is analyzed from the transverse displacement of one single row of vortices that

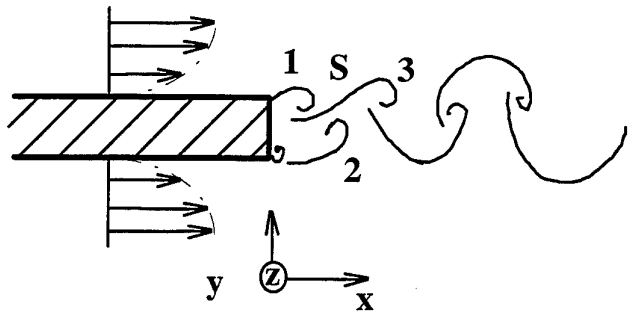


Fig. 7 Sketch of the model of the wake behind a flat plate. "S" marks a saddle point.

originally lies along the wake center-plane. On the other hand, the model described here is in good agreement with the numerical results of *Grinstein et.al.* (1991) for a plane wake behind a flat plate and the linear spatial stability analysis of Matingly & Criminale (1972)

For the lower Re_h analyzed (see Fig. 3), the wake vortical structures disappear before reaching the end of the image field of view. It has to be taken into account that these wakes are formed by interaction of plane unconfined jets that are themselves decelerating. At the higher Reynolds numbers, the structures remain for all the image field.

The observed non-homogeneity of the mesh created by interaction of the streamwise small scale structure with the bigger spanwise ones (see Fig. 6) may be attributable to the presence of intermittent dislocations naturally occurring across the full span of the plate similar to those observed by Prassad & Williamson (1997) for the cylinder wake at certain Reynolds numbers.

Along this paper, several comparisons have been made between the wake behind a flat plate and the one past a circular cylinder, because there are more experimental results reported for the latter. As a direct equivalence between these two cases could be inaccurate, a correspondence between Reynolds numbers in one and the other is proposed, following the analysis performed by Sato & Kuriki. To do that, the drag on a cylinder and a plate in a uniform, parallel flow with zero angle of attack are compared, as a measurement of the energy taken out of the flow that cause the velocity defect. The drags of these two bodies are expressed by

$$D_{part} = 1.328\, b\sqrt{\mu\ \rho\, l\, U^3}$$

$$D_{cyl} = \frac{\pi}{4} C_D\ \rho\, U^2\, d_{cyl}\, b$$

where b is the width of both plate and cylinder, l is the flat plate length over which the boundary layer develops and d_{cyl} is the cylinder diameter.

Considering the width of the plate and the cylinder to be equal, and equating $D_{plat} = D_{cyl}$ the following relation is obtained

$$\frac{l}{d_{cyl}} = 0.591\, C_D \sqrt{\frac{U\, l}{\nu}}$$

U_a (m/s)	Re_h	d_{cyl} (mm)	Re_d
25	1964	0.25	446
35	2750	0.21	525
55	4321	0.17	668
75	5892	0.14	771

Table 2 Equivalence between the cylinder and flat plate wake.

and hence an equivalent Reynolds number for the cylinder wake can be obtained. Results from this equivalence are summarized in Table 2 for the Reynolds numbers in this experiments. Re_h and Re_d are the Reynolds number for the plate and cylinder wakes respectively and d_{cyl} is the equivalent cylinder diameter. The equivalent Re_d also corresponds to the three dimensional region for cylinder wakes.

5 CONCLUSIONS

Planar laser induced fluorescence of acetone vapor has been used to visualize an air wake behind a contoured plate. Among other advantages, this technique doesn't integrate along the line of sight, has an excellent temporal resolution and ensures a flow Schmidt Number close to 1.

The ratio of the spanwise to streamwise wavelength λ_z/λ_x measured directly from the images has given a value of 2/5. For the Reynolds numbers in these experiments, the development of the three-dimensionality of the wake takes place in the near field region and not as consequence of a transversal displacement of one row of vortices generating two lines as proposed by Sato & Kuriki.

The presence of intermittent dislocations naturally occurring in all the span of the wake is proposed as the cause for the irregularities observed in the grid pattern formed by interaction of the streamwise and spanwise vortices an that may be due to the high Re_h number in these experiments.

An equivalence criterion to compare plate and cylinder wakes, based on the drag force over both bodies, showed that the images obtained correspond to the three-dimensional region, far from the two transitions modes for cylinder wakes that occur for a Reynolds number range between 190 and 260.

ACKNOWLEDGMENTS

This project has been partially supported by the Comisión Interministerial de Ciencia y Tecnología and the Dirección General de Estudios Superiores of the Spanish Government under contracts AMB96-0427-C03-01 and PB96-0739-C03-03. AJY has been supported by a European Comission fellowship in the program of Human Capital and Mobility.

REFERENCES

Barkley, D., Henderson, R.D. 1996 Three-dimensional Floquet Stability Analysis of the Wake of a Circular Cylinder. J. Fluid Mech. **322**, 215-241.

Corke, T., Koga, D., Drubka, R., Nagib, H. 1977 A New Technique for Introducing Controlled Sheets of Streaklines in a Wind Tunnel. *IEEE Publication* **77-**CH 1251-8 AES.

Grinstein, F.F., Hussain, F., Boris, J.P. 1991 Dynamics and Topoplogy of Coherent Structure in a Plane Wake. Advances in Turbulence 3. Springer-Verlag Berlin, pp 34-40.

Hama, F.R. 1957 Three dimensional Vortex Pattern behind a circular cylinder. J. Areonaut. Sci. **24**, 156.

Kopp, G.A., Kawall, G., Keffer, J.F. 1995 The Evolution of the Coherent Structures in a Uniformly Distorted plane Turbulent Wake. J. Fluid Mech. **291**, 299-322.

Lozano, A., Yip, B., Hanson, R.K. 1992 Acetone: a Tracer for Concentration Measurements in Gaseous Flows by Planar Laser-Induced Fluorescence. Exp. Fluids. **13**, (6), 369-376.

Maekawa, H., Mansour, N.N., Buell, J. C. 1992 Instability Mode Interaction in a Spatially Developing Plane Wake. J. Fluid Mech. **235**, 223-254.

Mansy, H., Pan-Mei, Y., Williams, D.R. 1994 Quantitative Measurements of the Three dimensional Structure in the Wake of a Circular Cylinder. J. Fluid Mech. **270**, 277-296.

Mattingly, G.E., Criminale, W.O. 1972 The Stability of an Incompressible Two-dimensional Wake. J. Fluid Mech. **51**, part2, 233-272.

Oertel, Jr., H. 1990 Wakes Behind Blunt Bodies. Ann. Rev. Fluid Mech. **22**, 539-64.

Papageorgiu, D.T., Smith F.T. 1988 Nonlinear Instability of the wake behind a flat plate placed parallel to a uniform stream. Proc. R. Soc. Lond. A **419**, 1-28.

Papageorgiu, D.T., Smith F.T. 1989 Linear Instability of the wake behind a flat plate placed parallel to a uniform stream. J. Fluid Mech. **190**, 265-298.

Prasad, A., Williamson, C.H.K. 1997 Three dimensional effects on turbulent bluff body wake at moderated Reynolds numbers. J. Fluid Mech. **343**, 235-266

Roshko, A. 1954 On the Development of Turbulent Wakes from Vortex Streets. *NACA Rep.* 1191, 1-23.

Sato, H., Kuriki, K. 1961 The Mechanism of Transition in the Wake of a Thin Flat Plate Placed Parallel to a Uniform Flow. J. Fluid Mech. **11**, 321-352.

Williamson, C.H.K. 1996 Three Dimensional Wakw Transition. *J. Fluid Mech.* **328**, 345-407.

CHARACTERISATION OF A BLUFF BODY WAKE USING LDV AND PIV TECHNIQUES

Ö. Karatekin, F.Y. Wang, J-M. Charbonnier

von Kármán Institute for Fluid Dynamics, Chaussèe de Waterloo 72
B-1640 Rhode-St-Genèse, Belgium

ABSTRACT

Steady and unsteady near-wake characteristics of a sphere-cone bluff body in incompressible flow were investigated experimentally in the 10^4 Reynolds number range and their salient features discussed. Three-dimensional time averaged measurements were made with LDV while the unsteady flow features were examined with PIV. Comparison of mean velocity and statistical turbulence quantities obtained by the two techniques indicated that PIV results, comprised of two orders of magnitude less sampling points, are in good agreement with the mean flow field revealed by LDV but less so for the quantities related to second moments. This suggests that although the number of PIV images were deemed sufficient to duplicate the mean flow according to the usual variance based statistical criteria, additional samplings are required to ensure a better quantification of higher moment turbulence quantities.

1. INTRODUCTION

The investigation of bluff body wakes has been the subject of many studies (Bearman P.W. 1997, Williamson C.H.K. 1997, Oertel H. 1990). With the advent of Particle Image Velocimetry (PIV) the unsteady nature of the flow field can be captured in a whole field. However the temporal and spatial resolutions of PIV are often limited for a detailed statistical analysis at high velocities. On the other hand, point measurements with Laser Doppler Velocimetry (LDV) can provide detailed statistical information as large amount of data can be collected without placing heavy demand on computer storage space. However the flow field revealed by LDV can be misleading in periodic wakes due to the presence of large scale motion which should be considered separately from the background turbulence. In such case, Grosjean et. a. [1997] proposed to combine LDV and PIV for turbulence measurements in unsteady flows, for the two sets of data would complement each other in providing an enhanced understanding of the flow field.

The capture of large scale coherent structures is crucial for the proper modelling and understanding of bluff body wakes as they are mainly responsible for the energy transport phenomenon. The use of hot-wire or LDV with conditional or phase-averaging sampling techniques have been applied in past. These studies have been recently replaced by PIV technique which provides instantaneous velocity field from which the structures can be directly identified (Lourenco et. a. 1997). However, the application of PIV technique to obtain time dependent motion of coherent structures at high velocities is not straightforward due to the limited data acquisition frequency available from the typical system. Double cavity YAG lasers which are often employed for PIV measurements can achieve sampling frequencies on the order of 10-15 Hz. which are not sufficient for a time dependent analysis of bluff body wakes of reasonable Reynolds number values in wind tunnels. For example, the wake of a cylinder with a typical Strouhal number of St=0.2, a length scale D=0.03 m and a free-stream velocity Uo=20m/s already yields a vortex shedding frequency of 133 Hz in a $Re=4.5x10^4$ flow which is one order of magnitude higher than the capability of YAG lasers. The utilisation of special lasers such as Eximer with a pulse repetition rate up to several hundred Hz or high speed cameras in combination with a continuous laser are some of the very costly alternatives. For the second alternative mentioned, the need for a very powerful and continuous illumination source presents an additional problem.

In the present study the model geometry is a sphere-cone combination representing a planetary entry capsule. Capsule designs are based on a blunt heat shield to resist the high aerothermodynamic loads

during the early hypersonic phase of the planetary entry. This design is however prone to severe aerodynamic instabilities at lower altitudes which could lead to the lost of vehicle in the worst situation. The origin of these instabilities is believed to be due to the unsteady wake which results in an amplification of small angular disturbances around the position (Baillion 1995).

In the schematic of the model presented in figure 1, the origin of the co-ordinate system is situated at the nose of the model. For all the measurements, the model was supported by a 3 mm diameter cantilever rod from the tunnel side wall.

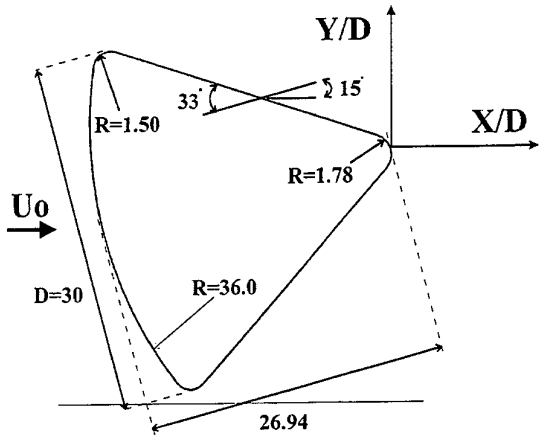


Figure 1. The model drawing (dimensions in mm)

2. LDV MEASUREMENTS

2.1. Set-up

The complete three-dimensional wake flows were mapped by using a TSI™ two component backward scattering LDV system. The fiber optical probe of LDV system was mounted on a three axis programmable traversing system. The doppler frequency information is extracted from the scattered light by IFA 750 Digital Burst correlator and analysed by the commercial data analysis software FIND.

LDV measurements were conducted in the VKI L7 low speed wind tunnel at a Reynolds number of 4.5×10^4 and a blockage ratio of 2.7%. The flow was seeded by vaporising fog oil droplets which produce seeding particles on the order of 1μm in diameter. The typical uncertainty in the measured velocity is less than one percent (Wang et a. 1998).

2.2. Results

Three-dimensional time averaged flow field was obtained by successive measurements of velocity profiles in two orthogonal, namely X-Y and Z-Y planes. The measurements were performed in only one half of the flow field (Z>0) due to flow symmetry. Spatial resolutions in the Y and Z directions were 2 mm while the spatial resolution in the X direction was ranged from 3 to 9 mm.

During the measurements, the LDV system was set to collect either 2048 samples per measurement location or as many data points as possible within a 90 seconds window, depending on the condition first reached. In the latter scenario, a minimum of 800 data points was collected at each measured location. The corresponding three-dimensional flow fields are presented in the following sections.

Average flow field in the symmetry plane. The velocity profiles normalised by the free-stream velocity (U_o) in the symmetry plane are presented in figure 2. The measurements in the symmetry plane where the average in-plane velocity is zero, provided certain characteristic features of the flow field and furnished a reference data set for the comparison with PIV measurements. The flow separated from the shoulder of the model's spherical part creates two large counter rotating vortices in the downstream of the model. The wake closure takes place at approximately X/D=1.2 downstream of the origin.

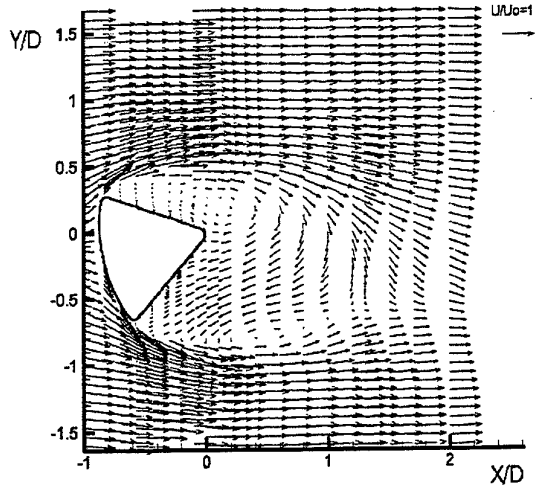


Figure 2. Time averaged velocity vectors in the symmetry plane (Z/D=0)

Velocity field. Three-dimensional volumetric data are plotted for $0.2<X/D<2.0$, $-1.13<Y/D<0.8$ and $0.0<Z/D<0.93$ and shown in figures 3 to 9 where the streamwise axis has been exaggerated for clarity. The streamtrace feature of the commercial software Tecplot™ was used to visualise the velocity data. It is important to note that these streamtraces were constructed from the two-dimensional velocity field in

the selected planes and do not represent the streamlines in general.

The surfaces of constant axial velocity normalised by the free-stream velocity are presented in figure 3. The recirculation zone represented by negative velocity contours is shown to occupy a larger spatial extent in the lower side of the model.

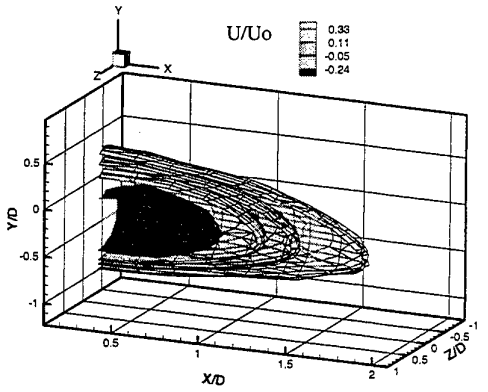


Figure 3. Axial velocity contours

Some important features of three-dimensional mean flow field can be observed in figure 4 where the streamtraces in four measurement planes are shown (i.e. Y/D=0, X/D=2, Z/D=0.93 and Z/D=0). The streamtraces in the symmetry and Y/D=0 planes illustrate the recirculation area confined behind the body. The plane Z/D=0.93 representing the outer limit of the measurement volume is outside of the recirculation region as suggested by the streamtraces being parallel to streamwise axis. A large scale clock-wise swirling structure is present in the exit plane (i.e. X/D=2), revealing out-plane flow motion from the Z/D=0.93 plane.

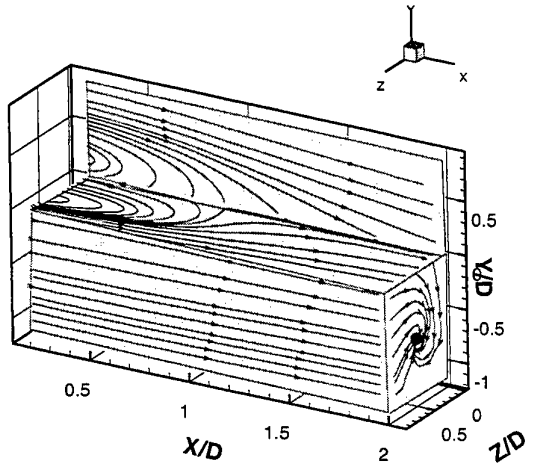


Figure 4. Three-dimensional streamtrace representation of flow field

Streamtraces in the symmetry plane and two cross planes, (i.e. inlet and outlet planes) are drawn in figure 5. The centre of the clock-wise swirl situated at Y/D≈0 in the inlet plane is moved to Y/D≈-0.6 and further away from the symmetry plane (Z/D=0.) in the outlet plane.

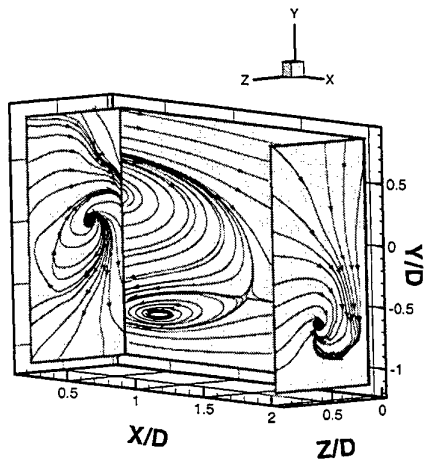


Figure 5. Streamtraces in the symmetry and cross flow planes

Vorticity. The components of vorticity defined by equation 1 were constructed from the measured velocity data by applying the central difference scheme.

$$\vec{\omega} = \vec{\nabla} x \vec{V} = \vec{\omega}_x + \vec{\omega}_y + \vec{\omega}_z \qquad (1)$$

where:

$$\omega_x = \left(\frac{\partial w}{\partial y} - \frac{\partial v}{\partial z}\right), \omega_y = \left(\frac{\partial u}{\partial z} - \frac{\partial w}{\partial x}\right), \omega_z = \left(\frac{\partial v}{\partial x} - \frac{\partial u}{\partial y}\right)$$

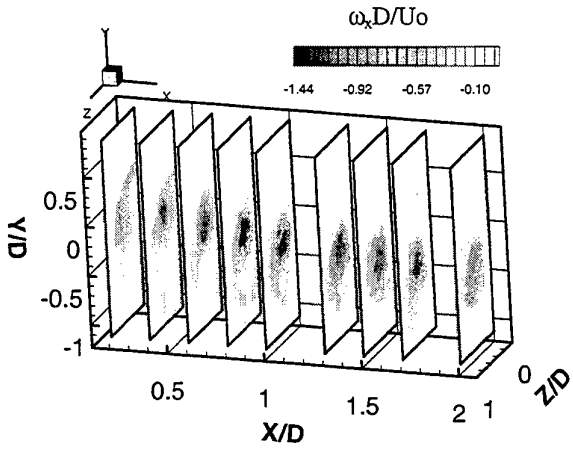


Figure 6. Non-dimensional streamwise vorticity contours

The iso-streamwise vorticity contours, ω_x, at various downstream locations are plotted in figure 6. The location of the maximum streamwise vorticity gradually moves downward, passing through the neighbourhood of wake closure point location where its magnitude is maximum. The existence of streamwise vorticity, its trajectory and distribution were reflective of positive lift force generated by the model at this angle of attack (Wang et. a. 1998).

The measurement volume and its mirror image are shown together in figure 7 where the contours of the total vorticity magnitude are presented in six successive cross planes. The maximum vorticity is concentrated close to the boundaries of the recirculating region while the total vorticity magnitude decreases rapidly outside of the recirculation area where ω_x remains as the significant component of the vorticity.

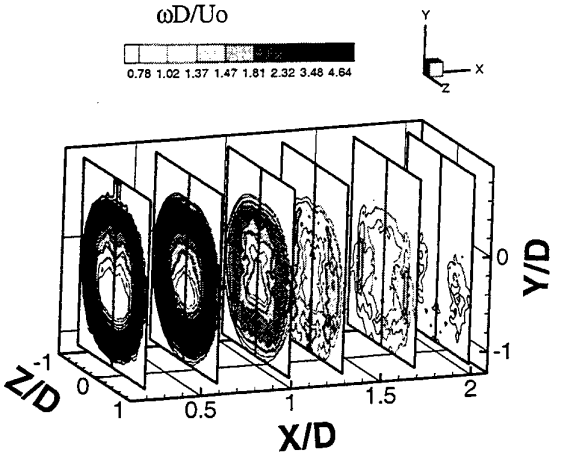


Figure 7. Non-dimensional total vorticity contours

Turbulence intensities. Figure 8 represents the turbulence intensity contours calculated according to equation 2 superimposed on the streamtraces. The location of the maximum turbulence intensity follows that of the shear layer, reaching as high as 30% in the vicinity of wake closure point where all the fluids impinged upon each other and abruptly diverted subsequently.

$$I = \frac{\sqrt{1/3\ (\overline{u'^2} + \overline{v'^2} + \overline{w'^2})}}{U_\infty} \qquad (2)$$

The turbulence intensity contours presented in successive cross planes (Figure 9.) confirm the location of the highest turbulence intensity levels in the lower shear layer in the symmetry plane. The maximum intensity occupies an area much larger in the neighbourhood of wake closure point than the other cross planes. The close examination of the data revealed a strong anti-isotropy in the near wake.

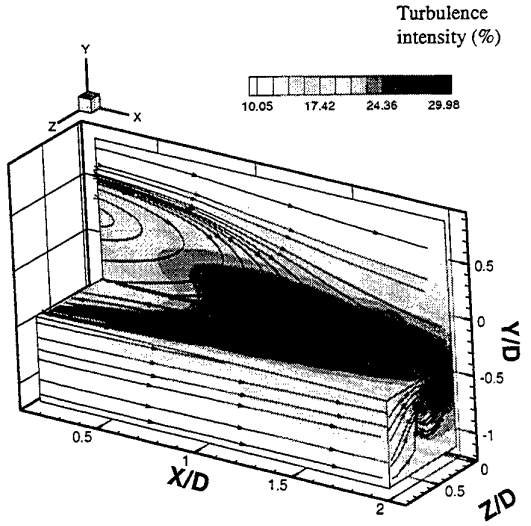


Figure 8. Three dimensional representation of turbulence intensity

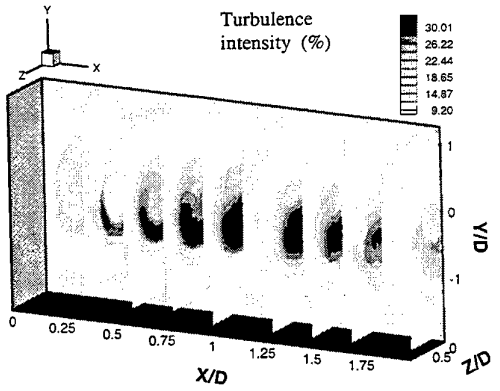


Figure 9. Turbulence intensity in cross planes

3. PIV MEASUREMENTS

3.1 Set-up

The measurements were conducted in the VKI-L7+ tunnel at a Reynolds number of 3.2×10^4 with a blockage ratio of 0.7. A Neodymium YAG laser double pulsing at 10 Hz. was used to illuminate the flow field which was seeded by the same method as for LDV investigation. The images were recorded with a TSI™ cross correlation CCD camera having 640x480 pixels resolution and stored in a personal computer. A TSI™ synchronizer was used to control the timing of the laser and the camera. This measurement set-up allows the acquisition of 6 instantaneous velocity fields at 0.1

seconds apart. For the calculation of statistical quantities, this acquisition procedure will be repeated until the desired number of samples is obtained.

The images were treated with a cross correlation scheme developed at VKI (Scarano 1998). The programme optimises the displacement of the second exposure interrogation area to compensate for the loss-of-pairs due to the in-plane motion with an iterative procedure. The processing of the acquired images uses a Gaussian three-point-fit for the sub-pixel interpolation peak determination. Successive cross correlation steps with window refinement are applied and the final interrogation area is 24x24 pixels which yields a spatial resolution of 1.8x1.8 mm (i.e. 0.06Dx0.06D). For the images processed, the percentage of non-validated vectors was below 5%. The uncertainty in these measurements was mainly due to the errors in calculating the displacement within a given interrogation area which was 0.1 pixel, yielding an uncertainty of 3.7% in free-stream velocity.

3.2 Instantaneous PIV Images

At high Reynolds numbers the near wake of a bluff body is characterized by two types of quasi-periodic shedding of vorticity. The high frequency mode is a small scale instability associated with the rolling up of shear layers which manifests itself in elliptical vortex rings. The low frequency mode is connected with the alternating motion of the shear layers which causes a "fish tail" flapping of the wake. Downstream of the rear stagnation point, large scale vortical structures are created by the mutual interactions between the shear layers. The non-dimensional frequency of this movement was reported to be St=0.16, whereas the high mode frequency is one order of magnitude higher, namely St≈2.1 (Karatekin 1998).

Instantaneous PIV images allow the observation of large and small scale modes concurrently. In figure 10, the small regions of high ω_z concentration correspond to high mode instabilities, while the directions of velocity vectors in the exit plane demonstrate the flapping motion of the wake.

It is not possible with the current set-up to track the temporal evolution of flow structures since the maximum data acquisition of the set-up is limited to 10 Hz. whereas the low mode instability at St=0.16 corresponds to a frequency of 80 Hz. To obtain such time resolved data, while maintaining reasonably high Reynolds numbers, water tunnel experiments present an interesting alternative to conventional wind tunnels, since for the same Reynolds and Strouhal numbers the characteristic frequency can be significantly reduced.

The dye flow visualisations performed in VKI water tunnel at $Re_D \approx 2000$ provide quantitative time dependent information of vortex rings associated with the high mode instability. Although the Reynolds number is one order of magnitude smaller than for the wind tunnel tests, the flow field features expected to be comparable due to the separation location fixed at the shoulders between the spherical and conical parts, as well as attributed to the fact that bluff body wakes between $1.2x10^3<Re<10^5$ are considered to exhibit similar characteristics (Williamson 1997). This regime of Reynolds number is called shear layer transition in which the free shear layers become unstable due to Kelvin-Helmholtz instabilities.

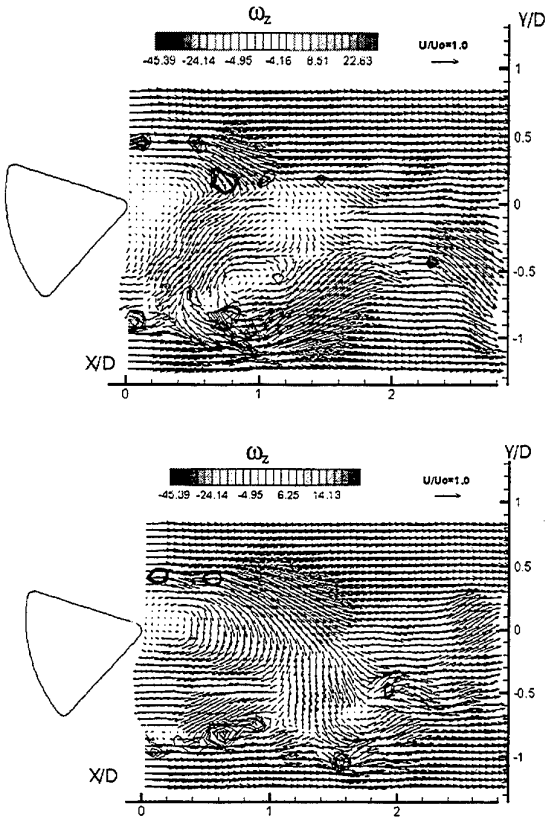
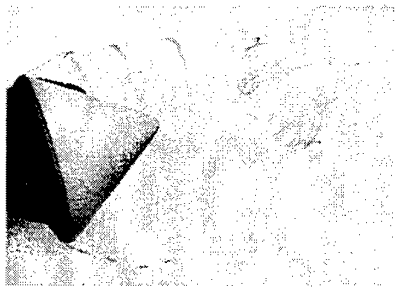


Figure 10. Instantaneous PIV images


Figure 11. Water tunnel visualisations

The dye released from the stagnation point spreads uniformly on the spherical face of the model and separates as free shear layers at the sharp cone-

sphere junction. The roll-up of the free shear layers creates vortex rings which lose their elliptical shapes and destroyed rapidly because of azimuthally nonuniform as well as self and mutual inductions. The vorticity contours superimposed on the instantaneous PIV pictures in figure 10. correspond to the cross section of the vortex rings observed in the water tunnel. The high vorticity regions are situated in the lower and upper shear layers, in the upstream of the rear saddle point which is consistent with the water flow visualisations.

3.3 Statistical Analysis of Data Sampling

Although the preliminary interest of PIV in the current investigation is the observation of unsteady flow motion, it also allows the calculation of statistical quantities. For PIV experiments, the number of samples, N, usually is much smaller compared to LDV investigation due to its severe demand on computer storage. Therefore it is important to assess the minimum number of samples necessary to obtain reasonable averaged flow quantities.

The ideal statistical values for a random signal are defined for stationary data over an infinite time span. There will therefore always be errors in the calculated statistical values of a real signal sampled over a finite time. The estimated error of the average of a series $x(t)$ may be obtained from the following rule (Olivari et. a. 1994):

$$\varepsilon = \sqrt{\frac{\overline{x'^2}}{\bar{x}^2}\frac{1}{N}} \qquad (3)$$

where $\overline{x'^2}$ is variance and $\bar{x}$ is mean value of the signal.

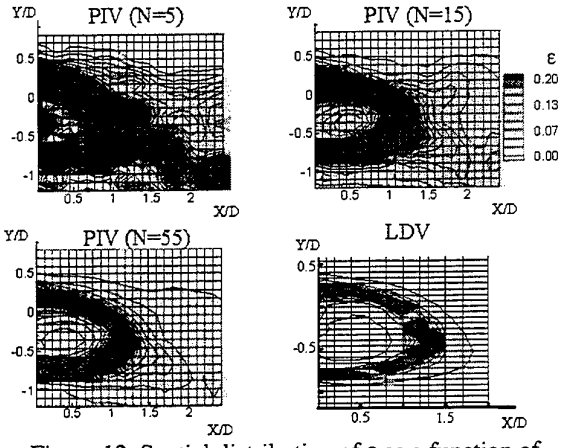


Figure 12. Spatial distribution of ε as a function of sampling number

The mean value and variance were calculated for axial velocity at each measurement node for PIV and LDV data. The associated error, ε, is presented in figure 12. The exact number of samples per node in the LDV data is varied in the range of $800<N<2048$ according to the sampling criterion chosen by the measurement system (section 3.1). The estimated error associated with LDV measurements is therefore calculated by using the lowest sampling size, i.e., N=800.

As the number of samples increases, the calculated mean approaches the true value. Since the error varies with the square root of 1/N, the calculated error is therefore more significant for small values of N. For N>15, maximum values of ε are found to concentrate in a small area around the recirculation zone and change slowly with increasing N. Although in section 2 the flow behind the model is shown to be highly turbulent, this error analysis suggests that for N>15, it is possible to obtain reasonable averaged flow quantities.

4. PIV AND LDV FLOW FIELDS COMPARISON

4.1 Interpolation

In order to perform a node-by-node comparison, the LDV and PIV experiments should ideally employ the same measurement mesh. This is however not the case. Therefore PIV data were interpolated into a grid matching that used by the LDV measurements. Average and root mean square values of u and v velocities were interpolated successively in X/D and Y/D directions by the natural cubic spline method to a final 16x10 grid. The interpolation did not alter the original flow field as presented in figures 13 (a),(b).

4.2 Comparison of Critical Point Locations

The comparison of topologically critical locations, i.e. vortex centres and saddle points based on the streamtraces presented in figures 13(b),(c) indicates no significant change for the upper and lower vortex centres. However the wake closure point revealed by PIV data is situated approximately 0.15D upstream. The exact cause of this discrepancy was not examined.

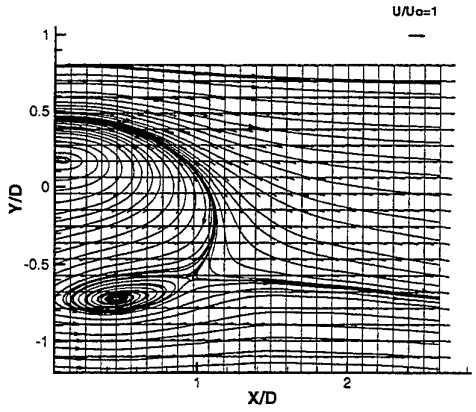
4.3 Comparison of Profiles

Normalized axial velocity profiles, U/Uo as well as velocity fluctuations, U_{rms}, and Reynolds shear stress profiles are calculated according to the equation (4).

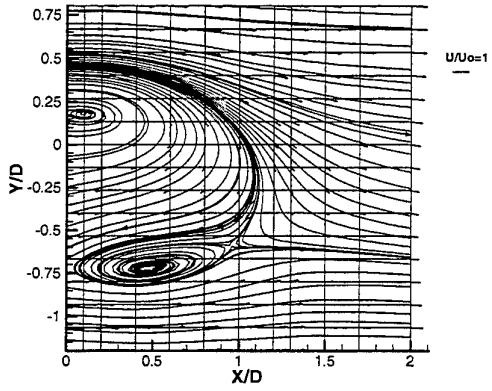
$$\text{Reynold shear stress} = \frac{\overline{u'v'}}{U_o^2},\ U_{rms} = \sqrt{\frac{\overline{u'^2}}{U_o^2}} \qquad (4)$$

These profiles are plotted in figures 14 to 16 at four locations downstream of the model. The first three profiles are in the recirculation area, with the third being in the vicinity of wake closure location. The last

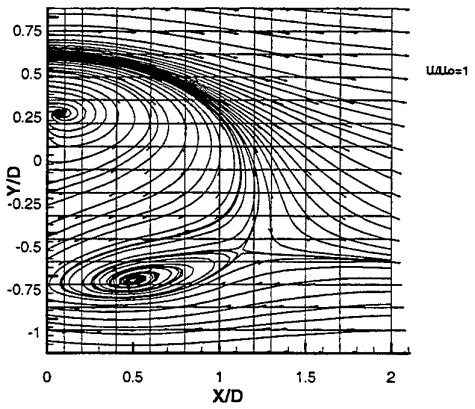
profile is located two body diameters downstream of the origin.



(a)



(b)



(c)

Figure 13. Streamtraces of original PIV (a) interpolated PIV (b) and LDV data (c)

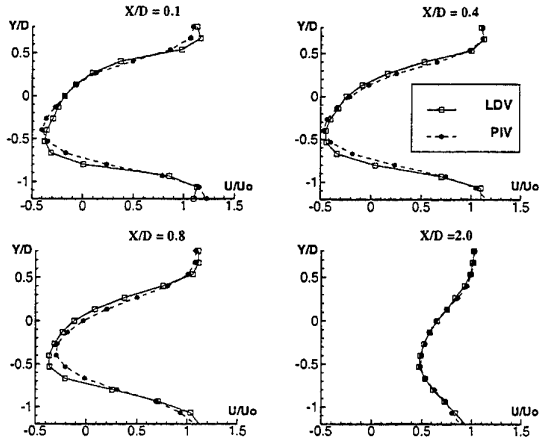


Figure 14. Comparison of velocity profiles

Figure 14. shows that the agreement between the averaged axial velocity profiles, U/Uo, obtained by LDV and PIV is very good confirming the error analysis made in section 3.3. As mentioned in the previous section, only a small difference is observed at X/D=0.8 close to the wake closure location.

While the mean flow depends on the first moment of the data, the variance and correlation are of the second moment quantities. Therefore PIV data obtained by 55 samples is expected to differ more significantly from LDV results for Reynolds stress profiles. Normalized root mean square of axial velocity and Reynolds shear stress profiles are plotted in figures 15 and 16 according to equation (4).

Although the shape of the profiles is in good agreement, PIV results consistently under-estimate the magnitude of U_{rms} up to 20%. Outside of the recirculation region the agreement is better for Y/D>0. Reynolds shear stress profiles show better agreement however PIV data again underestimate the shear stress levels in lower shear layer compared to LDV measurements.

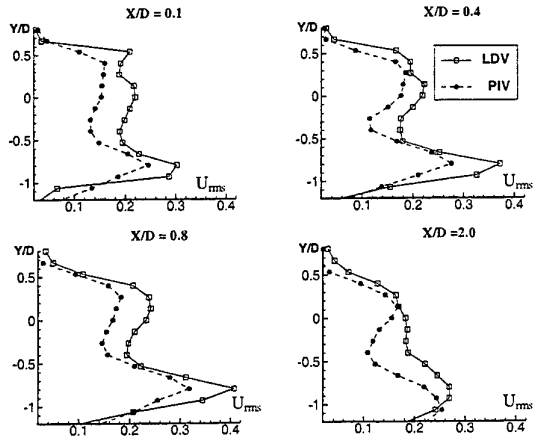


Figure 15. Comparison of normalized U_{rms} profiles

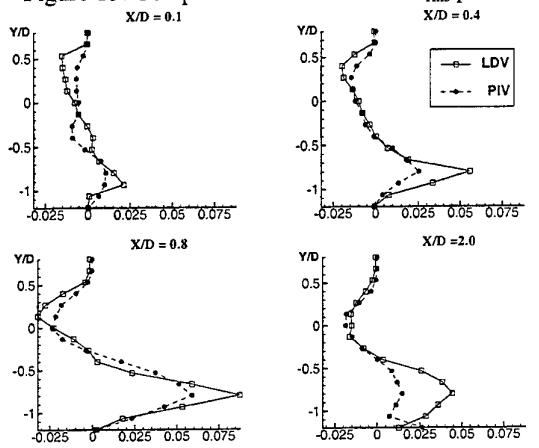


Figure 16. Comparison of normalized Reynolds shear stress profiles

5. CONCLUDING REMARKS

LDV and PIV techniques were used complimentarily to map out the three-dimensional unsteady flow field. Time averaged measurements obtained by LDV showed that for the configuration examined, turbulence intensity and vorticity have their maxima located in the lower region of the recirculation area and in the vicinity of wake closure point. Spatial evolution of total vorticity illustrates that the streamwise vorticity is the only predominant component beyond the wake closure point.

PIV measurements were performed in the symmetry plane to explore the unsteady nature of the near wake which allowed the observation of a low frequency motion downstream of the wake closure point as well as a high frequency motion created by the shear layer instabilities. Comparison of non-dimensional mean velocity profiles obtained by two measurement methods in two similar wind tunnels indicates a very good agreement. However comparison of second order statistical quantities such as U_{rms} or Reynolds shear stress are less favorable indicating that for PIV measurements, additional samples are required to ensure a better quantification of turbulence quantities.

REFERENCES

Baillion M. 1995, Blunt Bodies Aerodynamic Derivatives, in Capsule Aerothermodynamics, AGARD/VKI Special Course on Capsule Aerodynamics, von Karman Institute for Fluid Dynamics, Belgium.

Bearmann P.W. 1997, Near Wake Flows Behind Two- and Three-Dimensional Bluff Bodies, Journal of Wind Engineering and Industrial Aerodynamics, vol. 69-71, pp. 33-54.

Grosjean N., Graftieaux L., Michard M., Hübner W., Tropea C. & Volkert J. 1997, Combining LDA and PIV for Turbulence Measurements in Unsteady Swirling Flows, Meas. Sci. Technol., vol. 8, pp.1523-1532.

Karatekin Ö., Wang F.Y., & Charbonnier J-M. 1998, Visualisition of a Unsteady Wake, 8th International Symposium on Flow Visualization, Sorrento.

Lourenco L., Subramanian S. & Ding Z. 1997, Time Series Velocity field Reconstruction From PIV Data, Meas. Sci., Technol., vol. 8, pp.1533-1538.

Oertel H. 1990, Wakes Behind Blunt Bodies, Annual Review of Fluid Mechanics, vol. 22, pp. 539-64.

Olivari D. 1994, Signal Processing, in Measurement Techniques in Fluid Dynamics, pp. 301-66, von Karman Institute for Fluid Dynamics, Belgium.

Scarano F. & Riethmuller M.L. 1998, Turbulence Analysis on the BFS with Iterative Multigrid PIV Image Processing, Proc. 9th International Symposium on Applications of Laser Techniques to Fluid Mechanics, Lisbon Portugal.

Wang F. Y., Karatekin Ö. & Charbonnier J-M. 1998, An Experimental Study of the Flow Field Around an Apollo Capsule at Low Speed, AIAA-98-03193, 36th Aerospace Sciences Meeting and Exhibit, Reno, USA.

Williamson C.H.K. 1997, Advances in Our Understanding of Vortex Dynamics in Bluff Body Wakes, Journal of Wind Engineering and Industrial Aerodynamics, vol. 69-71, pp. 3-32.

ACKNOWLEGMENTS

The support from ESA's GSTP Programme - Micro-Aerodynamics of Complex External and Internal Configurations is acknowledged with appreciation. The Scientific and Technical Research Council of Turkey for the first author and the NSF-NATO Postdoctoral Fellowship Program in Science and Engineering (Grant Number DGE-9633933) for the second author are likewise gratefully acknowledged.

LIF MEASUREMENTS IN A TURBULENT FAR-WAKE

H. Rehab, L. Djenidi and R. A. Antonia

Department of Mechanical Engineering
Newcastle University, NSW, AUSTRALIA

ABSTRACT

The mixing characteristics of a high Schmidt number passive scalar in the turbulent far-wake of a cylinder are studied. It is shown that the flow is still well organized up to Re=1000 and at x/d=200. As the Reynolds number increases, the concentration probability density functions (pdfs) loose their bimodality and the mixing quality is improved. The concentration fluctuation pdfs are strongly non-gaussian and the concentration fluctuation derivatives imply a strong local anisotropy of the scalar field.

1. INTRODUCTION

The non-intrusive LIF (Laser Induced Fluorescence) flow visualisation technique is a powerful experimental tool to study the structure and dynamics of turbulent flows. In particular, this technique is used to extract quantitative information about the concentration field of a scalar injected in the flow. This is very useful for studing large scale and small scale mixing properties. Most of the experiments to date in a turbulent far-wake have used temperature (rather than dye) as a passive scalar e.g Freymuth and Uberoi (1971), LaRue and Libby (1974), Sreenivasan (1981), Antonia and Browne (1986), Mi (1997). One of the important issues is the isotropy of the scalar field. Antonia and Browne (1986) concluded that the temperature dissipation is not isotropic. Using Taylor hypothesis, the authors measured a value of the ratio $<(\partial\theta/\partial y)^2/(\partial\theta/\partial x)^2>$ where θ is the temperature fluctuation, approximatly equal to 1.8 at the wake centreline. This ratio increases towards the edge of the wake. The normalized temperature fluctuation probability density functions (pdfs) reported by LaRue and Libby (1974) and Mi (1997), are nearly gaussian for the far-wake of a heated cylinder. The pdfs measured by Sreenivasan (1981), are nearly gaussian in the intermediate wake (x/d≈43).

The large difference between the dye diffusivity (Sc=ν/D≈2000, ν and D are respectively the fluid kinematic viscosity and the scalar diffusivity) and the temperature diffusivity (Prandtl number Pr=ν/k≈0.7, k is the scalar conductivity) should affect the mixing caracteristics and therefore be reflected in the shape of the scalar pdf. In this paper, quantitative LIF measurements in the far-wake (x/d=200) of a cylinder are reported. Instantaneous and fluctuating concentration pdfs for two values of the Reynolds number are presented. The fluctuation concentration gradients pdfs have been measured at the resolution scale fixed by the experiment and the isotropy of the scalar field is explored.

2. EXPERIMENTAL SETUP AND METHODS

The measurements are carried out in a constant-head closed-circuit vertical water tunnel. The 2m long square (250*250 mm) test section is made of perspex. A circular cylinder (diameter d=4.6mm and aspect ratio of 40) is inserted in the working section with both ends supported on the opposite walls of the test section (Figure 1a). The Reynolds number based on the free stream velocity, U_0, and the cylinder diameter, d, varies from Re=500 to Re=1000. The plan LIF technique is adopted to measure the local instantaneous concentration of a dye (fluorescein: excitation wavelength ≈ 488nm) in the wake flow. The LIF technique is essentially based on the capacity of a dye to react by fluorescence when excited by a laser sheet. The methodology consists in calibrating the fluorescence intensity emitted (wavelength ≈ 514nm) by the dye in the measuring region with the dye local instantaneous concentration in the flow. The flow

visualisation images are recorded with a CCD camera (spatial resolution of 681*582 pixels), onto video tape, then digitized through a video card (50Hz and a resolution of 768*576 pixels) with 256 grey levels. Once the relation between the grey levels (proportionnal to the dye fluorescence intensity) and the dye concentration is established, we can determine the concentration field in the flow. The pictures are captured with an 'ImagePC' frame-grabber and analysed using the matrix space 'Matlab'.

The flow is seeded with fluorescein dye through a slit (less than 0.5 mm thick) machined along the full cylinder length, at the forward stagnation point of the cylinder (Figure 1b). The dye is injected continuously using a small pump at well known flow rates to avoid flow perturbations. Particular care is paid to the measurement of dye concentrations, which are of the order of 10^{-6} mole/liter.

The uniformity of the dye injection is a critical aspect of the LIF technique. This problem is especially difficult in a wake-type flow since the dye cannot be injected directly in the flow (unlike a jet for example). In order to prevent dye injection non-uniformities along the cylinder length, a second cylinder (external diameter = 2.7mm) with 10 equally spaced holes (0.5mm diameter) along its length is placed coaxially within the principal cylinder (Figure 1b). The dye is then injected through the inner cylinder till the gap space between the two coaxial cylinders is filled with dye, allowing a uniform dye line along the external cylinder slit.
An argon-ion laser (4W of maximum power intensity) is used as a light source. The laser beam is focalised using a large focal (750mm) converging lens before reflecting onto a cylindrical mirror. This reflexion causes the expansion of the laser beam into a plane illuminating light sheet.The thickness of sheet and the uniformity of the light along it are central to the technique. The former fixes the spatial resolution of the images and has to be as thin as the smallest scale associated with the scalar fluctuation. The laser sheet is approximately 250μm thick. This thickness has been measured using the laser sheet trace on a photographic black and white paper which has the property of a very low light expander. The paper is subsequently placed under a microscope thus enabling the thickness to be determined precisely. In order to minimize the light attenuation due to the absorption phenomenon by the dye, weak dye concentrations (10^{-6}m/l) and high laser power intensity are used (2W).

2.1 Spatio-temporal resolution

For the far-wake, the pixel scale corresponds to a real scale of 80μm. However, the spatial resolution of the pictures is limited by the laser sheet thickness ($\eta_R \approx 250$ μm) which is approximatly two Kolmogorov length scale η_k. We estimated that $\eta_k \approx 1.58\ (x/d)^{1/2}\ Re^{-3/4} \approx 578$μm for Re =1000 and x/d = 200. The smallest scalar scale (or Batchelor scale) $\eta_B = \eta_k Sc^{-1/2}$ for the fluorescein (Sc≈2000) is thus not resolved. In the same flow conditions, the time scale based on η_k and the free stream velocity is approximately equal to 2.6ms and is of the same order as the pixel illumination time (1/500 s).

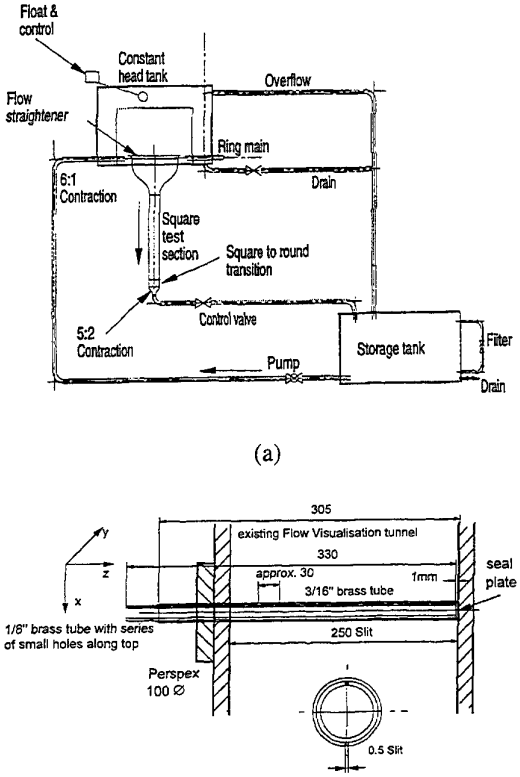


Fig. 1 Sketch of the experimental facility. (a), recirculating water tunnel, (b), Dye injection system.

3. RESULTS

3.1 Topology of the scalar field

Figure 2 shows two typical instantaneous views of the scalar field at x/d=200 at two values of the Reynolds number (Re=500 and 1000). For Re=500, Figure 2a shows that the topology of the flow is still well organized, and coherent structures resulting from the decay of the initial Karman vortices persist, in good agreement with the visualisations of Antonia et al. (1987) at Re=430 and x/d=240. At Re=1000, the organized motion is less clear and less identifiable. Papailiou and Lykoudis (1974) as well as Wlezien (1981), confirmed the existence of a large scale structure in the far-wake at large

Reynolds numbers. These large structures are organized into thin diffusive layers transporting the dye. The layers are associated with three-dimentional strong stretching rates reponsible for the scalar reduction scale process till diffusive scales. This situation is to be compared with the near wake scalar field, where the large scale stretching dominates the mixing process. These pictures show moreover that the unmixed pure fluid represents the most important fraction of the image volume even at the wake centreline. The pdfs of the concentration values calculated for these two pictures are shown in Figure 3. For Re=500, the pdf has one peak corresponding to the weak concentration. At Re=1000, the pdf is bimodal, the first peak corresponding to weak concentrations as for Re=500, and the second peak to intermediate values of C (~$0.4C_0$). The scalar field becomes more homogeneous as Re increases.

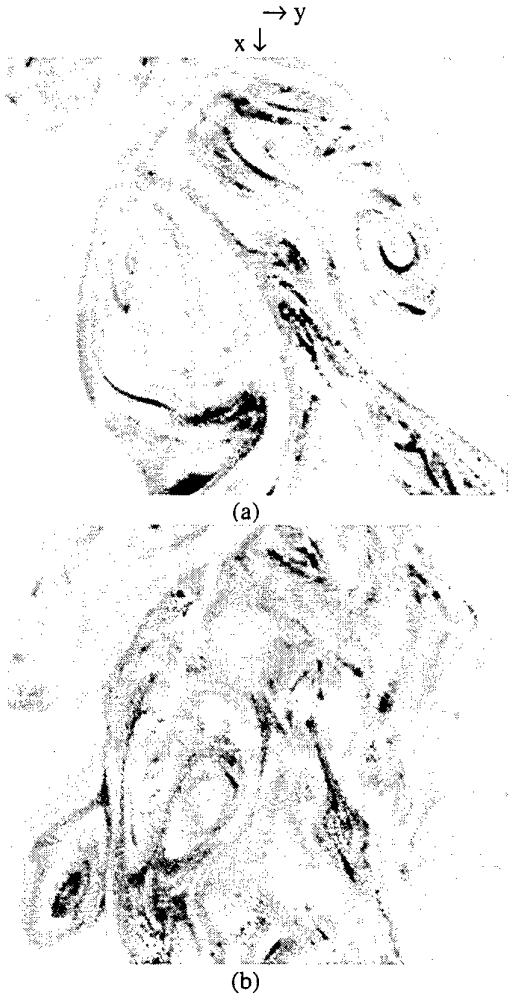


Fig. 2 Instantaneous pictures of the flow at x/d=200. (a), Re=500, (b), Re=1000. The gray regions represent fluorescein dye.

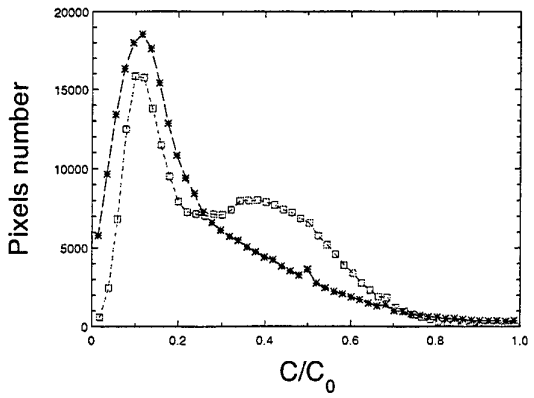


Fig. 3 Concentration probability density functions for: (✱), Re=500 and (□), Re=1000. These pdfs correspond to the concentration values in pictures of Figure 2.

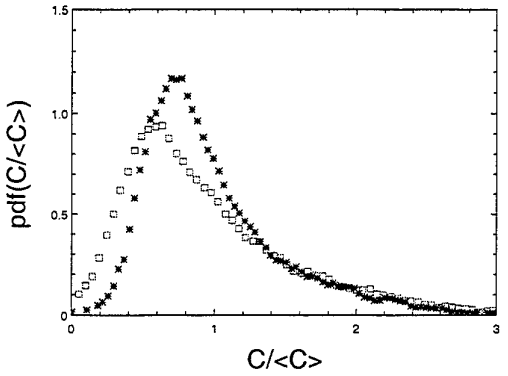


Fig. 4 Normalized centreline concentration probability density functions at x/d=200 for: (✱), Re=500 and (□), Re=1000.<C> is the local mean concentration.

3.2 Instantaneous and fluctuation concentration pdfs

The centreline concentration pdfs of the instantaneous concentration C for the two values of the Reynolds number and at x/d=200 are shown in Figure 4. In both cases, the scalar concentration loses its initial bimodal structure (0 or C_0) and has no memory of the maximal initial concentration C_0. The most propable value of C decreases from 0.75<C> for Re≈500 to 0.5<C> for Re≈1000, <C> is the local mean concentration. This is an indication that the maximal concentration persists further downstream for Re≈500 and homogeneisation of the scalar is more efficient as the Reynolds number increases.

The centreline pdf of the concentration fluctuations C', normalized by the rms concentration Crms, are shown in Figure 5. These

pdfs are simply normalized histograms of C'/Crms caculated over 3000 instantaneous images. First, the pdf shapes are strongly non-gaussien for the two values of Re. The pdfs of temperature fluctuations at a comparable Reynolds numbers (Mi (1997) Re≈1200 and Sreenivasan (1981) Re≈1160) are gaussian downstream of x/d≈43. The difference reflects mainly the effect of the Schmidt number.

The very low diffusivity of the fluorescein (Sc≈2000) compared to the temperature (Pr≈0.7), induces a very slow scalar uniformisation process in the flow. When the Reynolds number is increased (from 500 to 1000), it is observed that the values of C'/Crms are much more distributed indicating that the hirarchy of the scalar scales is extended, as for the velocity field. There is a tendency towards gaussianity of the concentration fluctuations as the Reynolds number and the downstream distance are increased. The dissymetry in the shapes of the pdfs of C' is also an indication of an intermediate scalar mixing state.

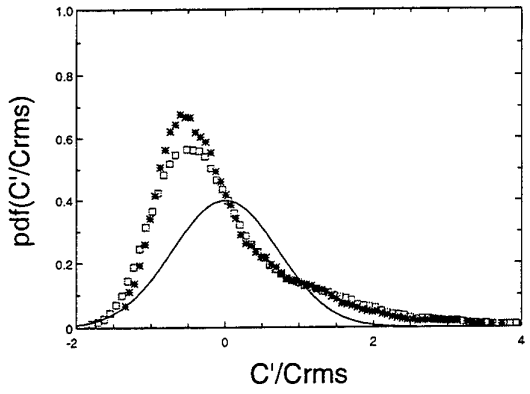


Fig. 5 Normalized fluctuations concentration pdfs at x/d=200 and for: (✱), Re=500 and (□), Re=1000. The continuous line correpond to the gaussien distribution.

3.3 Fluctuation concentration gradients and dissipation

The centreline pdfs of gradients with respect to the x and y directions, of the concentration fluctuation are presented in Figure 6. These gradients are calculated at the resolution scale fixed by the experimental conditions i.e. about two Kolmogorov scales. The fluctuation concentration differences are estimated at the image pixel scale. Note that Taylor's hypothesis is not used. They are normalized by the local concentration rms and the scalar resolution scale. The two pdfs are almost symmetrical with a maximum at zero. The skewness is equal to 0.03 for the y derivative and 0.001 for the x derivative. The symmetry of the gradients pdfs is also found in the results of Dahm et al. (1996) in the far field of a turbulent round jet. However the values of x and y derivatives are different. At the wake centreline, the y-derivative is larger (~ 1.5 times) than the x-derivative indicating a strong anisotropy of the scalar field. This result is in agreement with that of Antonia and Browne (1986) for the temperature derivatives.

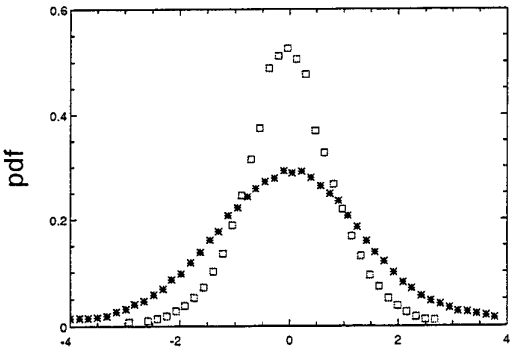


Fig. 6 Normalized fluctuations concentration gradients at x/d=200 and Re=1000. (✱), ($\partial C'/\partial y$) (η_R/Crms) and (□),($\partial C'/\partial x$) (η_R/Crms) where η_R is the resolution scale.

4. CONCLUSIONS

The concentration field of a high Schmidt number scalar in the far turbulent cylinder wake is investigated. The existence of a large scale coherent structure is confirmed up to Re=1000 and x/d=200. The concentration pdfs show that as the Reynolds number is increased the medium is more homogenous. The non-gaussian concentration fluctuations pdfs are an indication of the intermediate scalar mixing state. An asymptotic approach to a gaussian shape is expected at larger distances downstream and at larger values of the Reynolds number. The x and y derivatives of C' imply a fairly strong anisotropy of the small scale scalar field.

REFERENCES

Antonia, R. A. & Browne, L. W. B. 1986 , Anisotropy of the temperature dissipation in a turbulent wake, J. Fluid., Mech. , vol. 163, 393-403.

Antonia, R. A., Browne, L. W. B., Bisset, D. K. & Fulachier, L. 1987, A description of the organized motion in the turbulent far wake of a cylinder at low Reynolds number, J. Fluid. Mech. , vol. 184, 423-444.

Dahm, W. J. A., Su, L. U. & Tacina, K. M. 1996, Four-dimensional measurements of vector fields in

turbulent flows, Paper AIAA , 27th AIAA Dynamics Conference, New Orleans.

Freymuth, P. & Uberoi, M. S. 1971, Structure of temperature fluctuations in the turbulent wake behind a heated cylinder, Phys. Fluids, vol. 14, 2574-2580.

LaRue, J. C. & Libby, P. A. 1974, Temperature fluctuations in the plane turbulent wake, Phys. Fluids, vol. 17, No.11, 1956-1967.

Mi, J. 1997, Private communication.

Papailiou, D. D. & Lykoudis, P. S. 1974, Turbulent vortex streets and the entrainment mechanism of the turbulent wake, J. Fluid. Mech. , vol. 62, 11-31.

Sreenivasan, K. R. 1981, Evolution of the centerline probability density function of temperature in a plane turbulent wake, Phys. Fluids, vol. 24, 1232-1234.

Wlezien, R. W. 1981, The evolution of the low-wavenumber structure in a turbulent wake, Ph.D. thesis, Illinois Institute of Technology.

SESSION 3

Combustion I

THREE-DIMENSIONAL LDA MEASUREMENTS IN A TURBULENT PRECESSING JET FLAME

G.M.Schneider*, G.J.Nathan*, R.E.Luxton*, N. Syred+

* Department of Mechanical Engineering, University of Adelaide, Adelaide, SA 5005 (Australia)
+Division of Mechanical Engineering and Energy Studies, University of Wales, Cardiff CF2 1YF, Wales (UK)

ABSTRACT

The three dimensional velocity field in a turbulent precessing jet diffusion flame is investigated. In the present case the precessing jet flame is generated by mechanically rotating a round jet of propane inclined at 45° relative to the axis of rotation. Three dimensional laser Doppler anemometry enables insight into the fully turbulent, three dimensional velocity field of a precessing jet flame to be gained for the first time, which improves understanding of the NO_X reduction and increased fuel efficiency measured in industrial precessing jet gas burners. Velocity data in the diffusion flame, time-averaged and phase-averaged at the frequency of precession, is presented here. The conditional phase-averaging technique enables velocity contours and vectors to be obtained which reveal flow patterns and structures within the flame. Time-averaging of the velocity data shows that these structures are significant in that they generate a reverse flow (recirculation) region between the exiting fuel jet and its spinning axis. It is suggested that this recirculation assists in stabilising the flame in the high velocity and high shear region near to the nozzle exit. The recirculation in the velocity and high shear region is also found to cause a rapid decay of the mean velocity. The characteristics of the velocity field of a precessing jet flame found here are compared with previous investigations of non-reacting flows with the same initial conditions and with investigations of other turbulent jets.

1. INTRODUCTION

The precessing jet (PJ) has been the subject of detailed investigations at the University of Adelaide, Australia, since 1985. The precessing jet phenomenon is generated naturally by a fluid mechanical instability that follows an orifice plate or a nozzle with a large abrupt axisymmetric expansion into a short chamber. It occurs over a wide range of flow conditions (Nathan and Luxton 1991, Nathan and Luxton 1992, Nathan *et al.* 1992). The time dependent asymmetric reattachment of the jet-like flow within the nozzle is modified by placing a lip at the exit of the short cavity. The exiting jet is deflected, leaving the cavity at an angle from the axis of between 30° and 60°, and the entire flow precesses about the axis of the cavity. This configuration is referred to as the "fluid mechanical" precessing jet nozzle.

The fluid mechanical precessing jet nozzle has been patented and is being commercialised as the "GYRO-THERM" gas burner. It has been retrofitted to a range of large scale rotary kilns in various industries both within and outside Australia (Manias and Nathan 1993). Suction pyrometry measurements in a 2MW laboratory furnace have shown that the maximum time-averaged flame temperature of the PJ flame is typically 150°C lower than that of a comparable swirl burner, which is consistent with a reduction of NO_X emission by about 50%, while maintaining low CO emissions (Nathan *et al.* 1992). In the industrial kilns NO_X emissions are typically reduced by 30-60%, and specific fuel consumption is reduced by 3-10%. Thus the precessing jet flow has potential to contribute significantly to more efficient and cleaner industrial processes (Manias and Nathan 1993 and 1994).

To gain insight into the fundamental effect of precession on the mixing and combustion processes which result from jet precession, a "deterministic" or "mechanical" nozzle has been developed (see Experimental Technique and Fig.1). The mechanical nozzle produces a jet with known and well defined initial conditions (diameter d_e,

deflection angle α_e, frequency of precession f_p, velocity u_e etc.) so that the flow can be compared with conventional jets. In addition, it allows easy conditional phase-averaging of the data and enables the Reynolds number at the origin, $Re=u_e d_e/\nu$ to be decoupled from the Strouhal number of precession, $St_p=f_p d_e/u_e$.

Previously reported measurements in precessing jet flows have revealed the following features of the flow:

- the mixing from the fluid mechanical nozzle is dominated by turbulent structures of a scale which is many times the nozzle dimensions (Nathan and Luxton 1992);
- the entrainment rate of the fluid mechanical PJ nozzle in the first five exit diameters (Nathan and Luxton 1992) is approximately five times greater than that of a simple turbulent jet (Ricou and Spalding 1961);
- the initial spread of both the mechanical and fluid mechanical precessing jets is significantly greater than that of either simple jets or swirled jets (Nathan and Luxton 1991).

For the mechanical nozzle:

- in a high Strouhal number regime ($St_p>5x10^{-3}$) the phase-averaged Reynolds stresses throughout the first four exit diameters of the flow field are an order of magnitude larger than those in a simple jet (Schneider 1996, Schneider *et al.* 1997b);
- conditional measurements of velocity and pressure contours have revealed a low pressure zone between the jet and the spinning axis (Schneider *et al.* 1993).

In the present paper a three dimensional laser Doppler anemometer (LDA) system is used to measure simultaneously all three velocity components in the diffusion flame. In their investigation of a turbulent precessing jet, Schneider (1996) and Schneider *et al.* (1997b) used a 3-dimensional LDA system and phase-averaging techniques to obtain structural information. Similar techniques are applied here in the precessing jet flame.

2. EXPERIMENTAL TECHNIQUE

2.1 The Mechanical Nozzle

The significant parameters in a precessing jet flow are the exit angle, exit velocity, frequency of precession, eccentricity of the jet exit and the exit diameter of the jet. The mechanical nozzle (Fig.1) provides means by which to define precisely and to vary each of these parameters independently. The exit of the jet is centred on the spinning axis. When the nozzle is not rotating ($f_p=0$) the cold flow of the emergent jet exhibits all the well established characteristics of a symmetric turbulent jet. The exit diameter and the exit angle relative to the spinning axis of the nozzle can be changed by means of interchangeable nozzle tips.

The results presented in this paper all relate to an exit diameter $d_e=10$mm, an exit angle $\alpha_e=45°$, a mean exit velocity of $u_e=20$m/s and a frequency of $f_p=29.4$Hz. This corresponds to a Reynolds number Re=24,700 and a precessional Strouhal number $St_p=14.7x10^{-3}$. The mean exit velocity is measured by a pitot probe in the cold flow of the fuel jet with an accuracy ±2%. A 300W variable frequency electric motor, connected to a speed control unit, allows the frequency of precession to be controlled within <±1%.

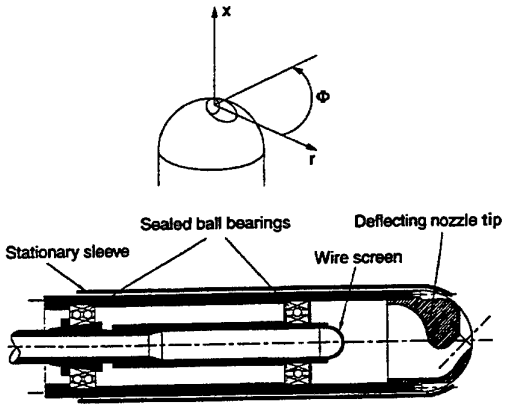


Fig.1: Mechanical Nozzle and coordinate system

2.2 Laser Doppler Anemometer System

Phase-averaged, three dimensional velocity measurements were conducted at the University of Wales, Cardiff. A schematic of the experimental arrangement is shown in Fig.2. The LDA system is a DANTEC three-component backscatter system using a COHERENT Inova 70 series 5 W Argon-Ion laser.

Optics: To remove directional ambiguity, all three colours were frequency shifted by Bragg cells. After the colour separation and beam splitting, the six beams are optically coupled into two fibre optic probe heads. The two heads are set

at 90° to each other and arranged so that the six beams are crossed at 600mm away from the heads. With this arrangement, direct measurements of each of the three velocity components are possible. The tangential, axial and the radial velocities in the present experiments were measured using wavelengths of 514.5nm, 488.0nm, and 476.5nm respectively. The lengths of the control volumes for each of the beams, calculated from the 600mm focal length of the lenses, the beam diameter, the wavelength and the incidence angle are: for the green beam dr=4.9mm; for the blue beam dr=4.6mm; and for the violet beam dΦ=4.5mm. The diameter of each of the control volumes is about 0.16mm.

Signal Processing and Data Acquisition: The signals from the three beams were sent to separate Burst Spectrum Analysers and the resulting frequencies were stored on the PC with their associated arrival times. In addition to the velocity signals, a fourth trigger signal, to reference the angular position Φ of the spinning nozzle, was collected simultaneously. The data was then phase-averaged relative to that reference signal, which identifies Φ_0 (Φ=tangential direction at the exit plane), over multiple cycles of precession with a chosen resolution of 360 parts for each cycle (1° segments). A total number of 14,000 samples were recorded on each of the channels, allowing more than 35 cycles of the precessing jet to be recorded and phase-averaged for each radial position. The software used for the averaging was developed by the University of Wales specifically for the present experiments.

Seeding: To maintain a high data rate, the region around the jet was seeded with Titanium dioxide. A purpose built seeder was used to introduce the sub-4μm particles into the propane flow. These particles have very good scattering characteristics and are expected to have negligible influence on the flow field.

Traversing: The optical heads were mounted on an automatic DANTEC traverse system which locates accurately to within ±0.05mm. The beams were traversed radially (along the green and blue beams) from the nozzle axis, r=0mm, to r=100mm in 10mm steps, thus collecting 11 radial positions for each plane. Six r-Φ planes at the distances x/d_e=2,4,6,8,10 and 12 were measured.

2.3 Discussion of Errors:

The most significant error in the LDA technique used here is the inability to resolve large velocity gradients accurately. This is due to the length of the control volume and limited radial (10mm traversing steps) and angular (1° ≈ 2mm at r_{max} =100mm) resolution, resulting in broadening of the mean velocity. In the present case, for the tangential and axial velocity (green and blue beam) the control volumes (length of 4.9mm and 4.6mm) and the traversing are oriented along a radial line. This leads to inaccuracies of the gradients du_Φ/dr and du_x/dr, whereas the gradients $du_x/d\Phi$ and $du_r/d\Phi$ are resolved with an much higher accuracy due to the angular resolution of 1° and the diameter of the control volume of 0.16mm.

The control volume of the violet beam measuring the radial velocity component lies in the tangential direction. This leads to errors in the gradients du_r/dr and $du_r/d\Phi$. The traversing steps determine the error in radial direction, compared with a small width of the control volume. In the tangential direction the length of the control volume of 4.5mm defines the resolution which is larger than the 1° angular resolution.

It was not possible to estimate the errors in the components du_Φ/dr , du_x/dr, du_r/dr and $du_r/d\Phi$ a priori, since the velocity gradients in a precessing jet were not known. Based on measurements for a comparable simple turbulent jet (Komori and Ueda 1985), the limitations of spatial resolution would be insignificant (<±0.4%). Based on the maximum gradients determined in the present measurements of the precessing jet, the errors are in the order of 2%.

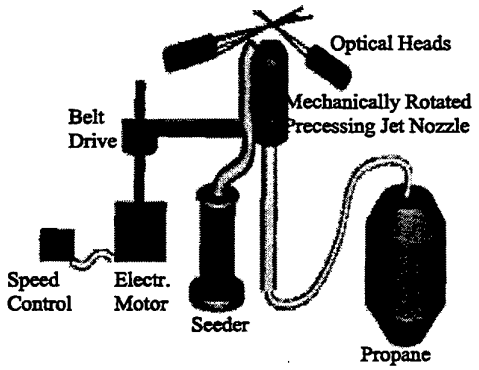


Fig. 2 : The Apparatus

The velocity bias (McLaughlin and Tiederman 1973) due to seeding the surrounding fluid only, was measured by comparing the present results with cold-flow investigations, where the precessing

jet and the surrounding fluid was seeding uniformly (Schneider *et al.* 1997b). This comparison shows that close to the nozzle, at $x/d_e=2$, the bias is approximately 10%. At $x/d_e>2$ the velocity bias is reduced to insignificant levels by ensuring that the surrounding fluid was uniformly seeded with a high particle density, following (Edwards 1981), and a controlled processor was used as shown by Winter *et al.* (1991).

Other potential sources of bias in LDA systems have been eliminated or found to be insignificant here. The fringe bias or angle bias was reduced to a minimum by applying a frequency shift of 40 MHz (Durst *et al.* 1993). The clock-induced error (Bremhorst 1993), produced by the frequency shift of 40 MHz was corrected following (Graham *et al.* 1989). Particle lag effects can be neglected when using particles of Titanium dioxide with a typical diameter $d_p < 4\mu m$ and a density ratio relative to propane of $\sigma = 2{,}300$. Calculating the frequency response (Melling and Whitelaw 1975, Durst *et al.* 1981) of the particles yields approximately 1 kHz, which is larger than the maximum turbulence frequency measured in the jet. From the dimensions of the control volume, the velocity of the flow and the number of bursts per second, a density of the scattering particles of $N=1.8\cdot10^{10}$ particles/m^3 can be calculated. This concentration is sufficient to resolve velocity fluctuations in excess of 100kHz which is about two orders of magnitude higher than the fluctuation frequency in the turbulent jet so that the particle arrival rate is adequate (Durst *et al.* 1981). The in the present case the statistical error in a randomly sampled data set, calculated by Winter *et al.* (1991) and Bremhorst (1993), is negligible.

3. RESULTS

3.1 The Precessing Jet Propane Flame

A long exposure photograph of the flame is shown in Fig 3. The image was taken with a standard SLR camera with an 8s exposure and the aperture set to f11. The experimental conditions are the same as for the LDA measurements. Figure 3 shows that the flame can be divided in two distinct regions: the blue base of the flame ($x/d_e<6$) and the bright yellow region in the far field ($x/d_e\geq6$).

3.2 Phase-Averaged Axial Velocity

Contours of the phase-averaged axial velocity in the precessing jet flame, measured with the LDA system, are shown in Fig 4. The colour scale of the contours is adjusted individually for each figure to show the highest velocity in red and the lowest in blue, so that colours should not be used to compare different figures. For all data the exit Reynolds number is Re=24,700 and the Strouhal number of precession is $St_p=14.7x10^{-3}$.
The two regions of the flame identified in Fig.3 are associated with distinct characteristics in the velocity field.

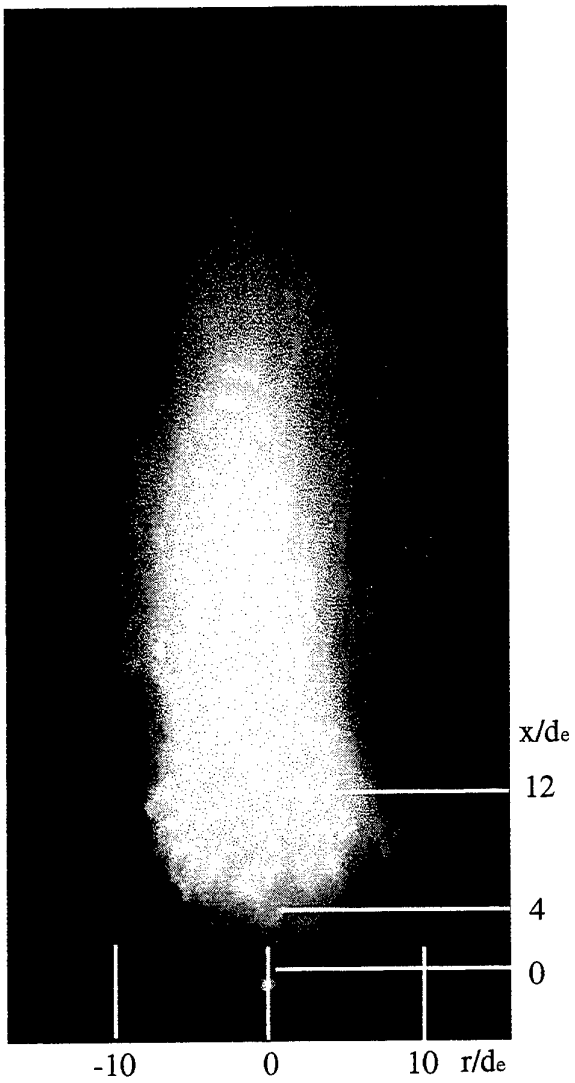


Fig. 3: Image of the precessing jet flame (long exposure); $0\leq x/d_e\leq4$ is described as region I, $4<x/d_e\leq12$ is described as region II; range of measurements: $-10\leq r/d_e\leq10$ and $0\leq x/d_e\leq12$; (Re=24,700, $St_p=14.7\cdot10^{-3}$)

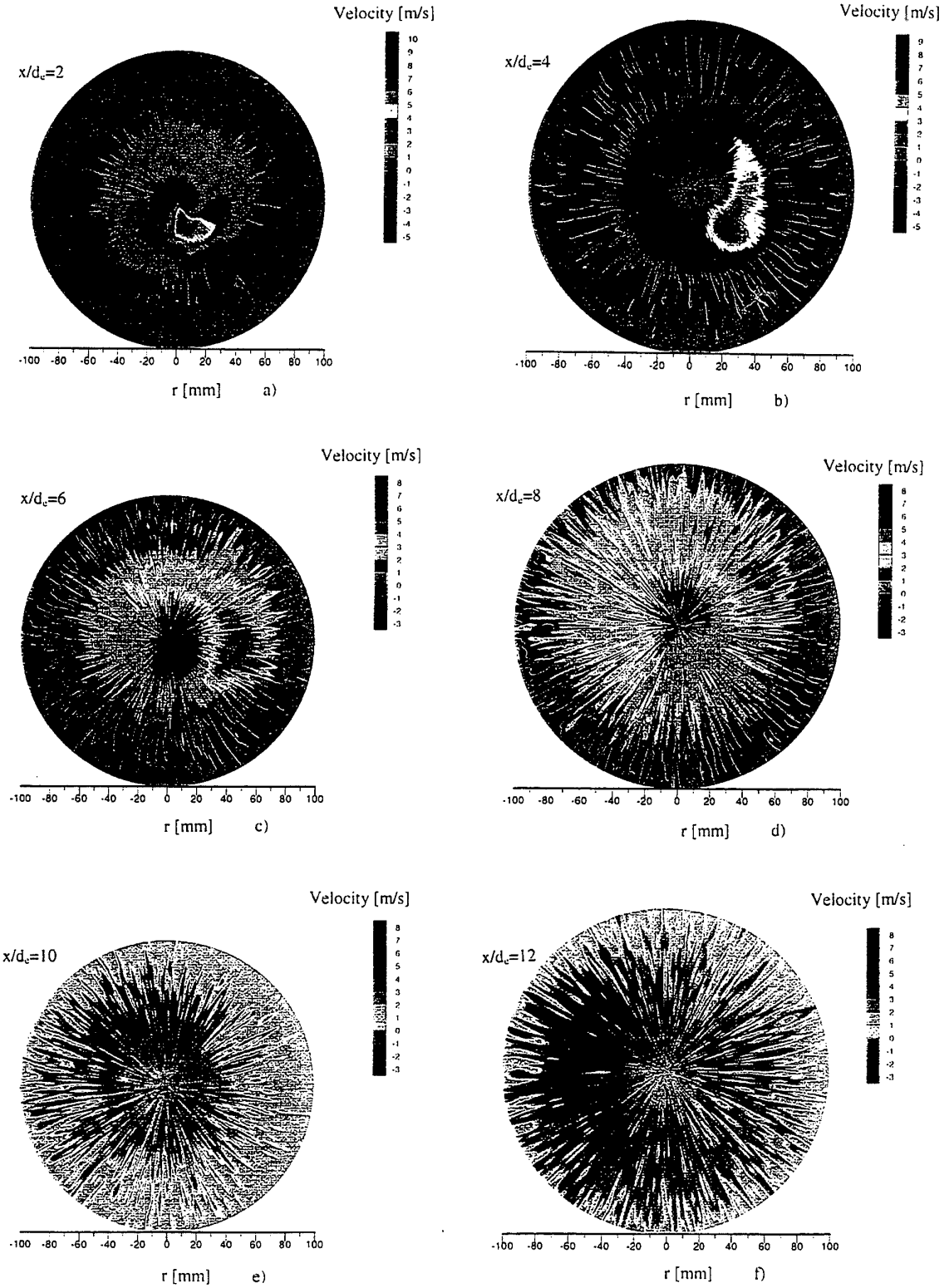


Fig. 4: Phase-averaged axial velocity contours

In **region I**, close to the exit at $x/d_e=2$, Fig.4a, the u_x component of the jet has an elliptically shaped core region, as may be anticipated given the initial inclination of 45°. Two distinct regions of phase-averaged reverse flow exist. One is located between the jet and the spinning axis in which the maximum measured velocity is $u_x=-5.3$m/s at $x/d_e=2$ (Fig 4a) and $u_x=-1.5$m/s at $x/d_e=4$ (Fig.4b). The other phase-averaged recirculation zone is located on the outer edge of the precessing jet in which velocities range between $-1\text{m/s}\leq u_x\leq -1.6\text{m/s}$. The presence of the recirculation corresponds with the high velocity and high shear region associated with the base of the precessing jet. Schneider (1996) and Schneider *et al.* (1997a) has measured high Reynolds stresses in the region $2\leq x/d_e\leq 6$ for a non-reacting precessing jet flow. The visual appearance of the flame in this region at the flame base (up to $x/d_e<6$) is consistent with highly sheared reactions. The maximum total velocity in the core of the jet is measured to be 17.3m/s. This is an order of magnitude larger than the maximum instantaneous flame propagation speed, which Muniz and Mungal (1997) have shown to be less than 3 times the laminar flame speed, which for propane is approximately 0.4m/s. This suggests that stabilisation in the region up to $x/d_e<6$ may occur around the recirculation region, or in the regions of high shear where much lower velocities exist at a given instant. The end of the potential core of the phase-averaged precessing jet flow, where the maximum velocity in the jet is less than the exit velocity of $u_e=20$m/s, occurs at approximately $x/d_e\approx 1.8$.

In **region II** (Fig.3), the flame at $x/d_e=6$ and 8, Figs 4c and 4d, shows that the phase-averaged reverse flow zone between the jet and its spinning axis (central recirculation) is not present in either of these axial positions. Also the phase-averaged reverse flow on the outside of the spinning jet no longer exists. The deformation of the emerging jet increases with the downstream distance, so that the jet is highly skewed at $x/d_e=6$. By $x/d_e=8$ the "wake" or "tail" extends around most of the circumference. In the contours from $x/d_e=10$ and 12 (Figs 4e and 4f) there is no clear phase-averaged structure in the flow at the frequency of precession and the flow field is almost axisymmetric. The radial extent of the jet remains approximately constant from $x/d_e=8$ to $x/d_e=12$. The Reynolds stresses, measured in the non-reacting precessing jet flow in the region II ($6\leq x/d_e\leq 12$) are significantly lower when compared to region I or to a simple axial jet (Schneider 1996, Schneider *et al.* 1997a).

3.3 Time-Averaged Velocity Components

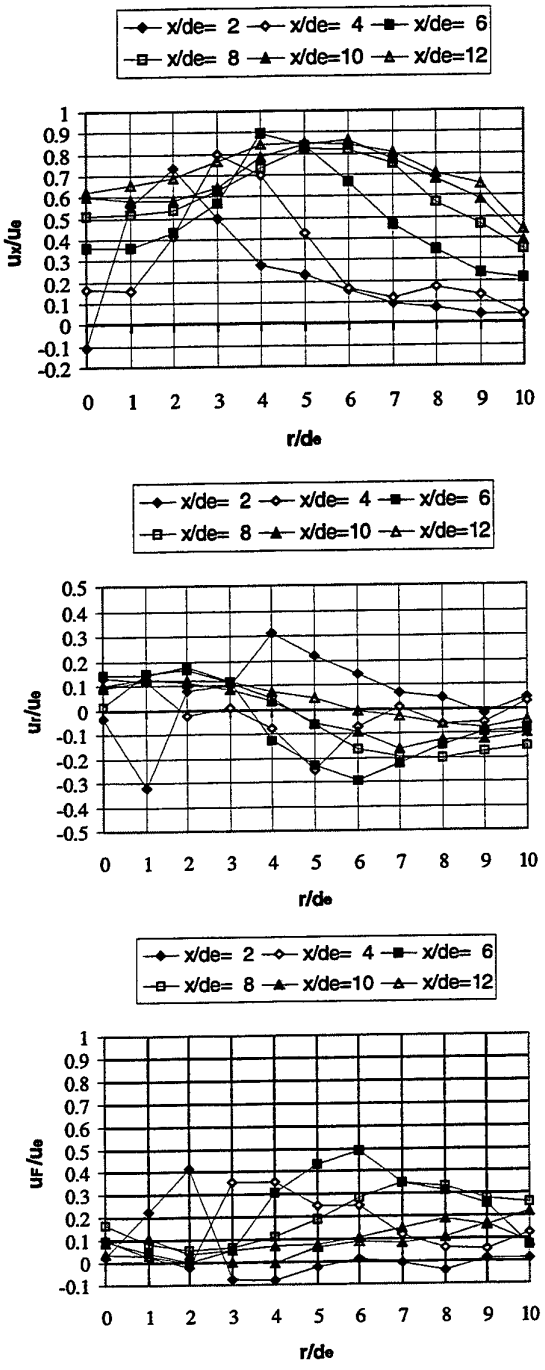


Fig. 5: Time-averaged velocity components: axial, radial and tangential (Re=24,700, $St_p=14.7\cdot 10^{-3}$)

In Fig 5 the time-averaged velocity components are shown. Figure 5a shows that the central recirculation zone also exists at $x/d_e=2$ in the time-averaged flow.

The jet precesses around the recirculation zone. It is interesting to note that the velocity contours become more uniform with increasing axial distance, but again that the radial extent of the flow does not increase significantly from $x/d_e=8$ to $x/d_e=12$.

Figure 5b shows that for $8 \leq x/d_e \leq 12$ the positive radial velocity is very small. Closer to the axis of rotation the negative radial components indicate a net inflow - apparently into the recirculation zone. The tangential velocity component (Fig 5c) is only significant in the initial region of the jet. After six nozzle diameters the overall tangential component is negligible.

Whether or not organised motion exists in this region at a frequency lower than that of the precession has not been resolved by the present measurements. However Newbold *et al.* (1997) have shown that large buoyant motions dominate unconfined flames beyond this region. While both the phase-averaged and time-averaged radial and tangential velocity vectors show inflow in the upstream region of the flow, pressumably induced by the low pressure field between the jet and its spinning axis (Schneider 1996, Schneider *et al.* 1993), these components become insignificant in the region $x/d_e > 8$.

4. CONCLUSIONS

Phase-averaged and time-averaged measurements of the velocity components within the stabilisation region of an unconfined precessing jet flame have revealed organised large-scale motion and flame characteristics. Two distinctive flame regions have been identified:

The first region (x/d_e =2-4) is characterised by a blue flame, indicating high shear stresses at the base of the flame. This is consistent with cold flow measurements of Schneider (1996) and Schneider *et al* (1997a), that showed markedly increased Reynolds stresses in the near field of the precessing jet. Associated with the increased shear at the near burner zone (x/d_e =2-4) an overall increase in the decay of the jet velocity is observed. A comparison of the maximum axial component of the velocity (in the precessing jet and) in the precessing flame and an axial turbulent jet shows that (the precessing jet and) the precessing jet flame decay typically twice as fast in the first 4 diameters. In this high velocity and high shear region a recirculation is apparent. The fuel jet spirals out from the nozzle around a recirculating flow zone and it is suggested that the flame is stabilised on or around this reverse flow region (Muniz and Mungal 1997). However the rapid decay in mean velocity may also be significant. The dimensions of the central recirculation are approximately two nozzle diameters in width (r-direction) and 4 nozzle diameters in height (x-direction). This entire flow precesses within the region $x/d_e<6$. Associated with the reverse flow region between the fuel jet and its spinning axis, the phase-averaged stream lines of the jet are observed to curve both radially towards the nozzle axis, and tangentially in the direction opposite from that of precession. Meanwhile flow is drawn in toward the recirculation zone from the region not occupied by the jet.

The second flame region ($x/d_e>4$) is characterised by a bright yellow flame, consistent with longer residence times in the reaction zones and reduced shear stresses. This finding is consistent with previous measurements in the far field of precessing jet flames (Newbold *et al.* 1997) and cold flow measurements in PJ flows (Schneider 1996, Schneider *et al.* 1997a). The mean velocity profiles at $x/d_e>4$ become more uniform. The small shear stresses in this flame region result in a markedly reduced centreline velocity decay when compared to a simple turbulent jet.

REFERENCES

Bremhorst, K. 1993, Accuracy of Laser Doppler Anemometry, Workshop on Laser Diagnostics in Fluid Mechanics and Combustion, DSTO Melbourne, Australia, pp 1.1-1.8.

Durst, F., Jovanovic, J. & Sender, J. 1993, Detailed measurements of the near wall region of turbulent pipe flow, FED v146, Data validation for CFD Codes, ASME, vol.146, pp 79-87.

Durst, F., Melling, A. & Whitelaw, J.H. 1981, Principles and Practice of Laser Doppler Anemometry (2nd ed), Academic Press, London.

Edwards, R.W. 1981, A new look at particle statistics in laser anemometry measurements, Journal of Fluid Mechanics, vol.105, pp 317-325.

Graham, L.J.W., Winter, A.R., Bremhorst, K. & Daniel, B.C. 1989, Clock-induced bias errors in laser Doppler counter processors, Journal of Physics E: Sci.Instrum., vol.22, pp 394-397.

Komori, S. & Ueda, H. 1985, The large-scale coherent structure in the intermittent region of the self-preserving round free jet, Journal of Fluid Mechanics, vol.152, pp 337-359.

Manias, C.G. & Nathan, G.J., 1993, The precessing jet gas burner – a low NO_X burner providing process efficiency and product quality, Journal of World Cement.

Manias, C.G. & Nathan, G.J. 1994, Low NO_X clinker production, Journal of World Cement.

McLaughlin, D.K. & Tiederman, W.G. 1973, Biasing correction for individual realization of laser anemometer measurements in turbulent flows, Physics of Fluids, vol.16, pp 2082-2088.

Melling, A. & Whitelaw, J.H. 1975, Optical and Flow aspects of particles, Proc.of the LDA-Symposium, The Accuracy of Flow Measurements by Laser Doppler Methods, Copenhagen, Denmark, pp 382-402.

Muniz, L. & Mungal, M.G. 1997, Instantaneous Flame Stabilization Velocities in Lifted Jet Diffusion Flames, Combustion and Flame, vol.111, pp 16-31.

Nathan, G.J. 1988, The Enhanced Mixing Burner, PhD thesis, University of Adelaide, Australia.

Nathan, G.J. & Luxton, R.E. 1992, The flow field within an axi-symmetric nozzle utilising a large abrupt expansion, Recent Advances in Experimental Fluid Mechanics (ed. ZhuangFG) Beijing: International Academic Publishers, pp 527—532.

Nathan, G.J., Luxton, R.E., *Transport Phenomena in Heat & Mass Transfer* (ed. Reizes J A) Amsterdam: Elsevier Science Publishers, 1992, 2:1297—1307.

Nathan, G.J., Luxton, R.E. & Smart, J.P 1992, Reduced NO_X Emissions and Enhanced Large Scale Turbulence from a Precessing Jet Burner, Twenty-Fourth Symposium (International) on Combustion, The Combustion Institute, Sydney, Australia.

Nathan, G.J., Turns, S.R. & Bandaru, R.V. 1996, The influence on NO_X Emissions and Radiation from Turbulent Flames, Combustion Science and Technology, vol.122, pp 211-230.

Newbold, G.J.R., Nathan, G.J. & Luxton, R.E. 1997, Large-Scale Dynamics of an Unconfined Precessing Jet Flame, Combustion Science and Technology, vol.126(1-6), pp 53-78.

Ricou, F.P. & Spalding, D.B. 1961, Measurements of entrainment by axisymmetrical turbulent jets, Journal of Fluid Mechanics, vol.11, pp 21-32.

Schneider,G.M., Vidakovic,S.S., Hooper,J.D., Musgrove,A.R., Nathan,G.J. & Luxton,R.E. 1993, Theoretical and Experimental Pressure Field Evaluation Downstream of a Mechanical Precessing Jet, Fourth Australasian Heat and Mass Transfer Conference, Brisbane, Australia, pp 43-1 – 43-6.

Schneider,G.M. 1996, Structures and Turbulence Characteristics in a Precessing Jet Flow, PhD thesis, Department of Mechanical Engineering, University of Adelaide, Australia.

Schneider,G.M., Hooper, J.D., Musgrove, A.R, Nathan, G.J. & Luxton, R.E. 1997a, Velocity and Reynolds stresses in a Precessing Jet, Experiments in Fluids, vol.22, pp 489-495.

Schneider, G.M., Froud, D., Syred, N., Nathan, G.J. & Luxton, R.E 1997b.,Velocity Measurements in a Precessing Jet Flow Using a Three Dimensional LDA System, Experiments in Fluids, vol.23, pp 89-98.

Winter, A.R., Graham, L.J.W. & Bremhorst, K. 1991, Velocity bias Associated with laser Doppler Anemometer Controlled Processors, Journal of Fluids in Engineering, Trans, ASME, vol.113, pp 250-255.

Wygnanski, I., Fiedler, H. 1969, Some measurements in the self-preserving jet, Journal of Fluid Mechanics, vol.38, pp 577-612.

Quantitative Characterisation of the Precessing Vortex Core and the Vortex Breakdown Phenomena using Particle Image Velocimetry

W. Fick, A. J. Griffiths, G. Schoepf and T. O`Doherty

University of Wales, Cardiff
Division of Mechanical Engineering & Energy Studies
PO Box 685, Cardiff CF2 3TA, GB

1 ABSTRACT

The use of Laser Doppler Anemometry (LDA) phase averaging techniques is limited when dealing with highly turbulent, three dimensional swirling flows. Fine structures in the flow may not be detected and the interpretation of combustion principles governing the rotating flame incomplete. Therefore, isothermal Particle Image Velocimetry (PIV) measurements in the exhaust region of a model swirl burner were carried out at various positions downstream of the burner exit and for two cross sections of the flow.

This work identifies the complex flow structures quantitatively in terms of vector and contour plots and highlights the application of PIV to transient flows. Conclusions are drawn to improved mixing effects due to the Precessing Vortex Core (PVC) and its associated structures in the swirling flame to enhance the reduction of emissions and the capability of burning low calorific value gases.

Furthermore, to correlate the various downstream positions the acquisition of PIV data has been triggered to match the phase of the PVC. This technique allowed phase averaged plots to be derived by overlaying instantaneous plots. Good agreement with previous LDA measurements was also found. The main objective was to quantify the interaction of the flow region dominated by the PVC and the breakdown region, where no definite centre of the PVC was found. Instead, severe vortex shedding took place and primary, secondary and tertiary eddy centres were identified.

The understanding of the complex vortex breakdown region is important for the proposed coupling effect between this region and the Reverse Flow Zone (RFZ) and that between the initiation of the PVC inside the burner body. This could also be part of the explanation for the oscillating effects beyond the actual flame/PVC region as a pulsating behaviour was previously found in swirl burner/furnace systems under combustion conditions.

2 INTRODUCTION

The efficient combustion of low calorific value gas and poor quality fuels is a problem which has been addressed in the past by Syred and Beer (1974), Syred et al. (1977), Syred and Dahmen (1978), Claypole and Syred (1984), Chomiak et al. (1989) and Syred et al. (1997b) with systems including various types of cyclone combustors and in particular swirl burner/furnace combinations.

The fluid dynamics of swirl burners, especially where combustion is concerned, is one of the most complex subjects in fundamental engineering science. The flow in swirl burners, swirl generators and many similar devices can be considered wholly axi-symmetric until the onset of the so-called vortex breakdown (Syred and Beer, 1971). At this point the central part of the vortex changes drastically and is followed by a pattern of phenomena, i.e. a recirculation zone appearing as an ovoid shaped bubble of fluid that remains in the flow at a point just above the burner exit (Syred and Beer, 1972).

The Precessing Vortex Core (PVC), represented by the point of zero velocity in the tangential flow, does not remain on the central axis as experimental work has revealed. A new precessional centre of the vortex was formed, displaced from the central axis of the burner and precesses about the geometric centre in a regular manner. This occurs as the flow becomes unstable soon after the swirl generated central recirculation zone forms (Syred and Beer, 1972). The frequency of precession remains constant for a single case and is determined by the flow conditions and the geometry of the burner. The entire flowfield was no longer axi-symmetric due to three dimensional time dependent instabilities (Gupta et al., 1984).

The physical appearance of the PVC in swirling flames reduces the flame length and generates a high emissivity flame (Syred and Beer, 1973). The PVC creates large pressure variations within the flame, such that to stabilise the flame, a closed loop feed back system is established (O`Doherty et al., 1992). This feedback manifests itself as a Reverse Flow Zone (RFZ) within the structure of the flame. It is this RFZ that stabilises the flame and allows the mixing and re-mixing of the reactants, such that efficient combustion takes place. It has also been noticed that the PVC is present many burner exit diameters downstream of the exhaust region (Yazdabadi et al., 1994a,b).

The flow patterns produced within and past the exhaust of a 100 kW model swirl burner have been investigated experimentally under piloted premixed combustion conditions

by Froud et al. (1995). The PVC dominated the flow and mixing patterns. Its associated cyclical flow was used to trigger a 3 component laser anemometry system. Successive cycles were overlaid and phase averaged to give a three dimensional picture of the rotating flow fields. A description of the flow was thus obtained in terms of phase averaged tangential, axial and radial velocities in tangential/ radial and axial/ radial planes using LDA techniques. Phase averaged temperature characterisation of the flow by Fick et al. (1996c) under identical experimental conditions showed that the resulting calibrated temperature maps show comparable patterns to the LDA velocity measurements and some basic structures associated with the PVC were identified.

The results confirmed previous work by Syred et al. (1994) using the same burner operated isothermally and showed that the centre of the vortex flow was displaced from the central axis of the burner, creating the PVC phenomena as the vortex centre precesses around the central axis of symmetry. As a consequence, the Reverse Flow Zone (RFZ) was also displaced. The RFZ partially lagged behind the PVC by up to 180° acting as a feedback mechanism for the PVC phenomena. Due to the displaced vortex centre, flow between the PVC centre and the wall was squeezed. Thus, due to angular momentum flux consideration, it produced a considerable increase in tangential velocity and gave the characteristic PVC signal. The displaced RFZ was both rotating through a region of forward flow whilst also being of an intermittent nature, giving rise to the excellent flame stabilisation and mixing characteristics of these types of burners.

Fick et al. (1997c, 1998a) discussed the system aerodynamics due to the PVC, and in particular the influence of coherent structures on the flame stabilisation process, temperature, power, excess air levels, mode of fuel entry and emissions (NO_X and CO). In particular it was shown that very low calorific value gases, down to 0.17 MJ/m^3 could be efficiently burnt when small quantities of piloting or support fuel are introduced axially on the centre line. Although very low NO_X emission levels could be achieved with premixed gas consumption, some penalty accrued in terms of CO emission levels, typically of order 150 ppm, as opposed to 50 ppm with non premixed combustion or for a calorific value > 1 MJ/ m^3.

To gain more insight into the highly turbulent nature of the three dimensional swirling flame and to further investigate the fluid mechanics determining the combustion processes involved, Particle Tracking Velocimetry (PTV) images have been and correlated with phase averaged LDA velocity contour maps (Fick et al., 1996a). The results showed very good agreement and the fundamental phenomena determining the complex flow were identified. Previous work by Fick et al. (1996b) correlated flow visualisation techniques, in particular high speed photography, to the results obtained using phase averaged analysis. An additional vortex in the rotating flame was found. The effect of this vortex on the combustion process was advantageous and correlated very well with the main vortices previously found (Fick et al., 1997a).

3 APPARATUS, EXPERIMENTAL CONDITIONS AND TECHNIQUES

3.1 Test Rig

Figure 1 shows a schematic of a 100 kW model swirl burner/ furnace system. The burner is a quarter scaled model of a 2 MW industrial scaled swirl burner/ furnace system with a burner exit diameter (De) of 75 mm and a furnace diameter of 150 mm. The furnace was removed to allow complete access for flow measurements. The combustion air, which can be premixed with fuel, is supplied via two 75 mm diameter tangential inlets. Gas can also be supplied in the non premixed condition, where the fuel is fed through a central pipe situated at the bottom end of the burner. The tangential inlets were also reduced in cross sectional area, therefore allowing the geometric swirl number to be increased. The geometric swirl number could be varied from 0.8 to 4. To prevent blowback of the flame front from the exhaust to the premixed gas inlets, the exhaust was extended back into the swirl chamber.

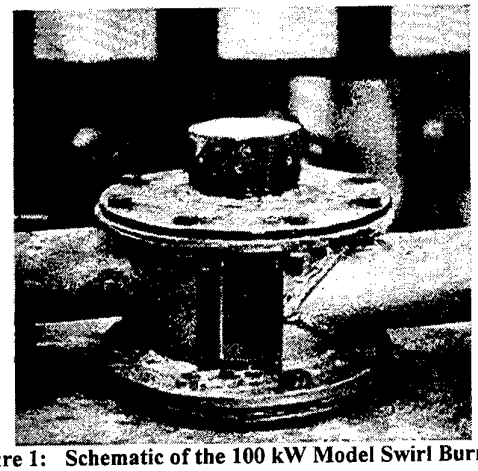


Figure 1: Schematic of the 100 kW Model Swirl Burner/ Furnace System

3.2 Co-ordinate System

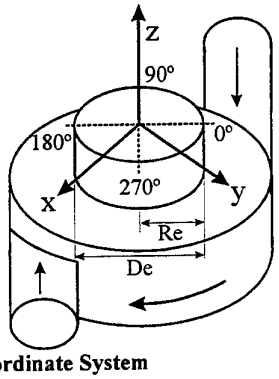


Figure 2: Co-ordinate System

A co-ordinate system, based on the burner exhaust, highlighted in Figure 2, was used: r = radial co-ordinate (r=0 is the geometrical centre of the exhaust), x = co-ordinate (x=0 is the geometrical centre of the exhaust), y = co-ordinate (y=0 is the geometrical centre of the exhaust) and z = axial distance from the burner exhaust (z=0 is at the burner rim, (+) downstream, (-) upstream).

3.3 Laser Doppler Anemometry (LDA) System

The velocity measurements were carried out using a 3D Dantec fibre optic LDA system operating in back scatter mode (Dantec, 1983). The laser was a Coherent Innova 70 Series 5W Argon-Ion laser operating in the 457-528 nm wavelength band. The analysis derived its measurement protocol from engine analysis work using the time pulse generated from a pressure transducer to trigger the LDA system (Yazdabadi et al., 1994a, Froud et al., 1995).

3.4 Particle Image Velocimetry (PIV) System

A Dantec real time processing PIV system was used. The light source used was a Spectron SL456G Nd:YAG pulsed laser, which provided 350 mJ laser pulses of 8 ns duration, based upon the green 532 nm wavelength, with a maximum repetition rate of 66.65 ms. Since the high peak powers of the Spectron laser was too high for transmission via modern fibre optics, a special light guiding arm was used. This arm comprises of a sequence of flexible mirrored joints which deflect the incoming beam from one mirror to the next, irrespective of the orientation of the joint. The pulsing beams are contained within hollow tubes which form the arm and culminates in a lens assembly designed to produce a focused pulsed laser sheet.

A Dantec PIV 700 CCD double image camera (pixel array 768×480) was used to correlate the scattered light from both the first and second pulses of the light sheet. A Dantec PIV Processor 2000, comprising correlator units, input buffers and a synchronisation unit, provided dedicated vector processing and subsequent vector maps of the flow field real time. Specially designed input buffer allowed the simultaneously reading in of an image from the CCD camera, store the image in memory and divide the image into interrogation areas (McCluskey, 1995).

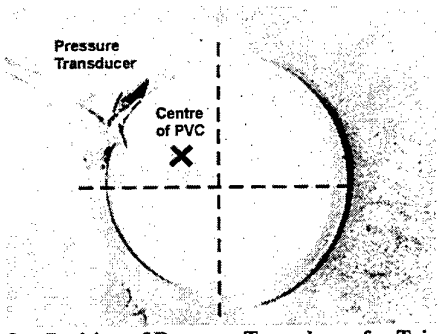


Figure 3: Position of Pressure Transducer for Triggered PIV Measurements

All the major hardware functions were software controlled in the software application package Dantec FlowManager (Dantec, 1996a,b). This package was also used for analysing and processing the cross correlated PIV results. A series of validation methods was then carried out to evaluate the results, i.e. peak-, range-, moving average- and filter-validation techniques and calculation of vorticity and streamlines (Fick et al., 1997a) or tangential, axial and radial velocity components (Fick, 1998b) can be derived.

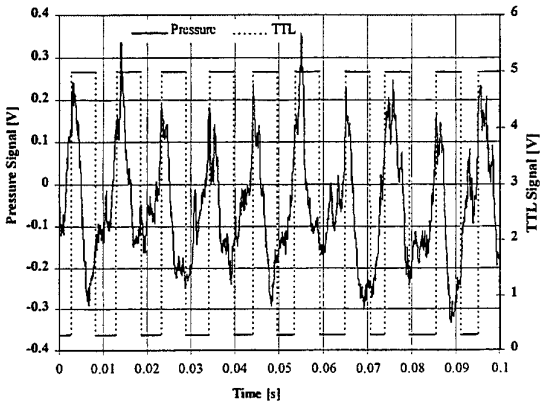


Figure 4: External Triggering System for Phased PIV Measurements

Two modes were used to acquire PIV data:

- Instantaneous PIV plots were obtained in plan view with the PVC captured in a random angular position.
- Phase averaged PIV plots were derived in plan/side view by averaging 8 individually triggered PIV plots. Cyclic fluctuation from a pressure transducer located at the burner rim at 155°, as shown in Figure 3, was converted into a TTL (Transistor to Transistor Logic) signal to monitor and trigger the acquisition of PIV data, as highlighted in Figure 4, hence to capture the flow in a known angular position relative to the PVC (Fick, 1998b). By triggering on the rising or the falling slope of the pressure transducer signal (Figure 4) two angular side view cross sections were evaluated: 155°-335° and 65°-245°, i.e. in- and 90° to the plane of the PVC respectively.

4 RESULTS AND DISCUSSION

Phase averaged LDA has revealed the highly complex flow structures (Fick et al., 1996a). The phase averaged mean rotating tangential velocity contours, shown in Figure 5, characterise the position of the PVC as lying between the large crescent of high tangential velocity and a small negative tangential region. The zero velocity contour marks the centre of the vortex. The phase averaged axial velocity contours, shown in Figure 6, coincide with the crescent shaped region of high tangential velocity and suggest that the flow regimes occurred due to the displacement of the vortex core from the

axis of symmetry and associated precess motion (Fick et al., 1997a). Phase averaged temperature measurements revealed similar structure in terms of rotating temperature fields (Fick et al., 1996c). This technique has also been applied to an industrial scaled swirl burner (Syred et al., 1997a). Both results obtained from LDA analysis and numerical simulation (Lucca-Negro and O'Doherty, 1996) of the three dimensional time dependent velocity components show good qualitative and quantitative agreement.

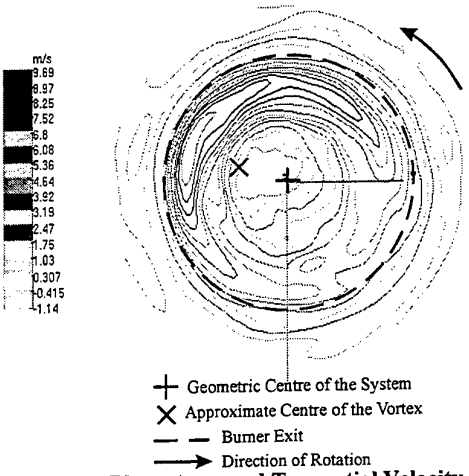


Figure 5: Phase Averaged Tangential Velocity Contour Plot at z/De=0.5, R_e=41,190

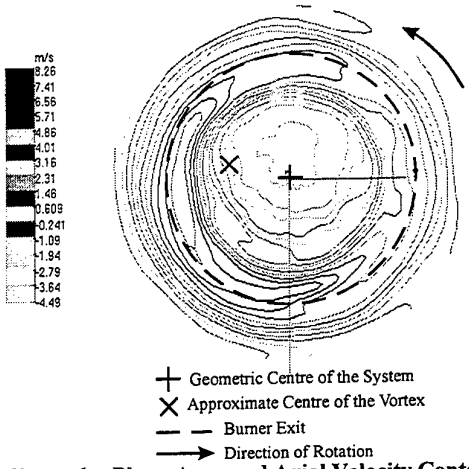


Figure 6: Phase Averaged Axial Velocity Contour Plot at z/De=0.5, R_e=41,190

Figure 7 shows the instantaneous plan view PIV vector plot at z/De=0; a single PVC can be clearly identified. The vortex is located 11 mm away from the geometric centre and corresponds well to a single vortical structure found by Volkert et al. (1996) during the spin-down of rotating cylinder. Further downstream at z/De=0.5 a PVC can be identified at x=73 mm and y=43 mm and clearly shown in Figure 8. The centre of PVC however is closer to the geometric centre of the system at z/De=0 than at z/De=0.5. This is because the PVC is not only twisted and bent against the direction of the flow, but also spiral in shape. Lucca-Negro and O'Doherty (1996) found this feature with isothermal 3D CFD modelling in a full scale industrial sized swirl burner/furnace system.

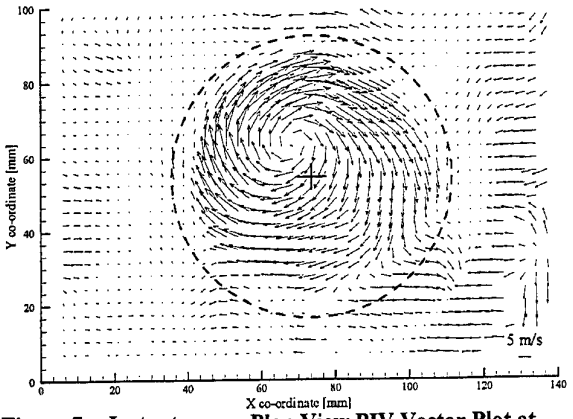


Figure 7: Instantaneous Plan View PIV Vector Plot at z/De=0, R_e=41,190

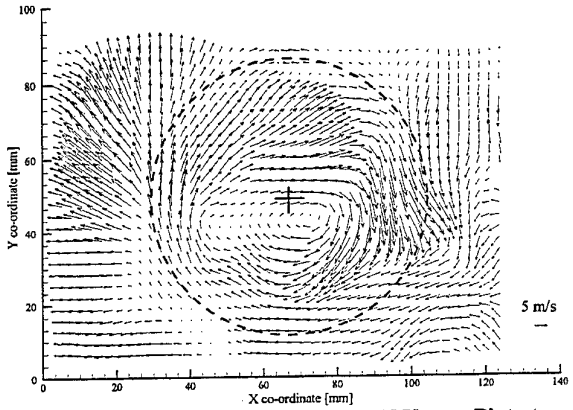


Figure 8: Instantaneous Plan View PIV Vector Plot at z/De=0.5, R_e=41,190

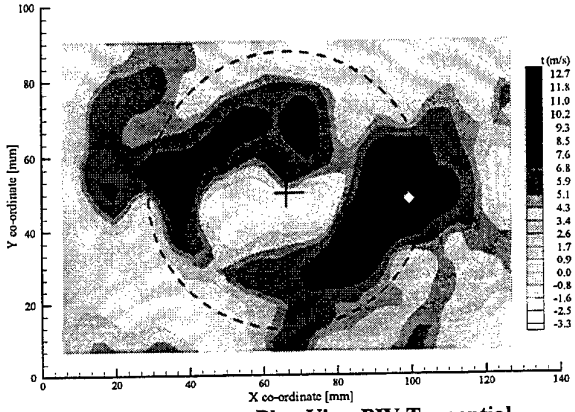


Figure 9: Instantaneous Plan View PIV Tangential Velocity Contour Plot at z/De=0.5, R_e=41,190

Figure 9 reveals a crescent shaped sector of high positive tangential velocities (up to 12.7 m/s). It is positioned at 340°, extends over 130° at r/Re=0.7 and is 20 mm wide. Opposite this region a second crescent shaped region of high tangential

velocities is located (up to 10 m/s). This is where second eddy centre is clearly identified (x=50 mm and y=43 mm, Figure 8). An oval shaped RFZ forms from the precessional centre of the PVC towards the geometrical centre of the system. The centre of the PVC is located between the RFZ and the starting point of the region of the very high tangential velocities for a clockwise rotation.

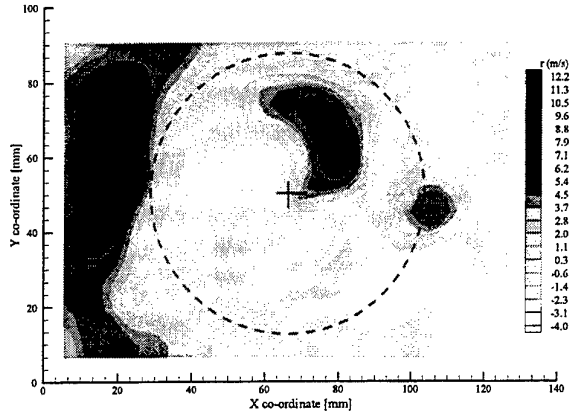


Figure 10: Instantaneous Plan View PIV Radial Velocity Contour Plot at z/De=0.5, R_e=41,190

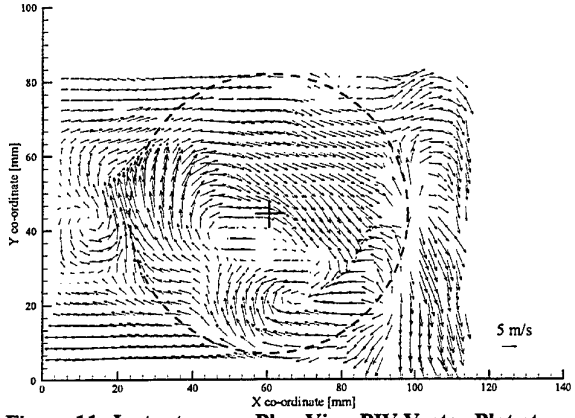


Figure 11: Instantaneous Plan View PIV Vector Plot at z/De=1, R_e=41,190

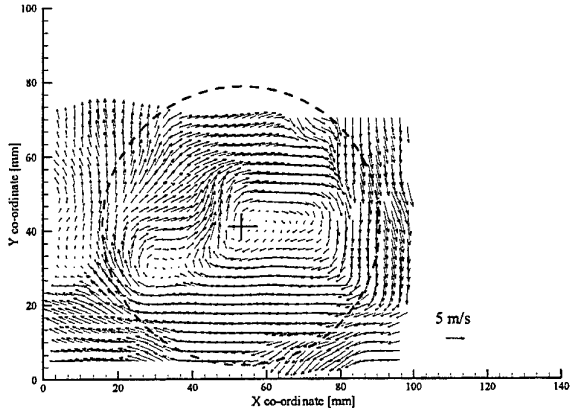


Figure 12: Instantaneous Plan View PIV Vector Plot at z/De=1.5, R_e=41,190

Furthermore, the centre of the PVC is enclosed between a crescent shaped area of positive radial velocities (2 to 9 m/s) and an area of negative radial velocity (0 to -3 m/s). The area of positive radial velocity is located behind the centre of the PVC, whereas negative radial velocities are ahead of the PVC as indicated in Figure 10. The radial velocity contours are more even within the dashed area of the burner exit and peaks to about 12 m/s outside this region (Figure 10).

At z/De=1, Figure 11, a primary vortex centre, most likely the PVC, can be identified at x=47 mm and y=40 mm. The flow around the PVC is heavily distorted and several other eddy centres around the PVC start to develop. In particular, at x=67 mm and y=23 mm a secondary eddy centre with very similar feature to the primary one co-exists. At z/De=1.5, as indicated in Figure 12, the PVC has virtually dissipated. Although vortex/eddy centres were found at x=50 mm and y=40 mm as well as x=30 mm and y=30 mm, no primary or dominant vortex centre could be determined.

It is worth summarising that further downstream from the burner exit (greater than z/De=0.5) the flow field becomes more irregular and eddy shedding can be noticed. The distance from the centres of the additional eddies to the geometric centre of the system varies both at the same height when several instantaneous plots, taken randomly, are compared further with the distance downstream of the burner exit. There is no continuous trend of an increase of the precessional centre of the PVC with increasing height indicating the spiral shape of the PVC.

A series of instantaneous vector plots have been produced in the manner previously described in order to map the orbital path of the PVC. Figure 13 to Figure 15 show the centre of rotation of the PVC (C1) for various Reynolds numbers. Although the basic characteristics of the PVC produced from the LDA data has been validated (Syred et al., 1994 and Froud et al., 1995), the assumption of a circular path was incorrect the further away from the swirl burner exhaust. Variation in Reynolds number (flow rate), as shown in Figure 13 to Figure 15 also reveal that the PVC centres are not found further away from the geometric centre nor that secondary tertiary eddy centres necessarily appear. In fact, no relationship between the position of vortex- and eddy centres (C1, C2 and C3) and Reynolds number was established.

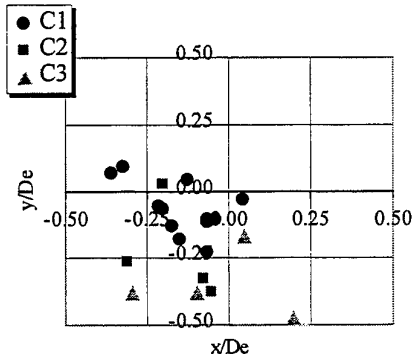


Figure 13: Vortex/Eddy Centres at z/De=0.5, R_e=25,190

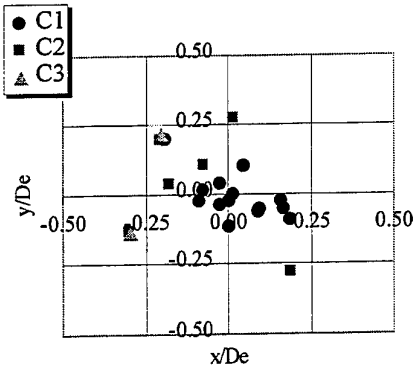


Figure 14: Vortex/Eddy Centres at z/De=0.5, R_e=41,190

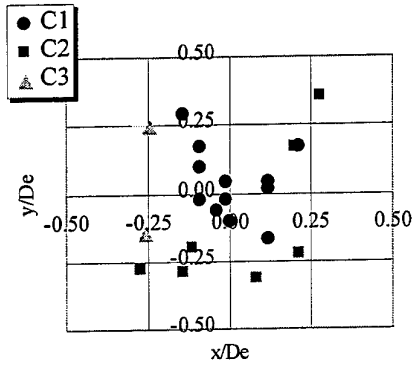


Figure 15: Vortex/Eddy Centres at z/De=0.5, R_e=58,290

The effect of vortex shedding was not only discovered in the tangential/radial direction, but also appears in the axial/radial direction. However, the effect of phase averaging is somewhat noticeable in Figure 16 and Figure 17. The average of eight instantaneous plots is smooth and the overall flow patterns were very steady. The centre of the PVC has already passed the cross section by about 20° in the 155°-335° cross section for z/De=0, when the images were acquired (see Figure 3).

The velocity profile shown in Figure 16 is reasonably symmetric. It can be assumed from Figure 16 that the vortex structure starts to break down at about z=110mm. This is the height where a substantial central RFZ starts to develop. Strong positive axial flow, concentrated at the burner rim where the pressure transducer was situated (Figure 16), indicates the presence of the PVC in this region. However, towards the geometric centre of the system a large and longitudinal eddy causes axial flow reversal. A weaker eddy geometrically opposite the PVC enhances this effect. Numerous weaker eddy structures in the axial/ radial direction are also found past the breakdown of the PVC at z=100mm (z/De=1.25) to z=120mm (z/De=1.5).

In the 65°-245° cross section, Figure 17, the flow is strongly asymmetric. A large eddy opposite the high positive axial velocity region at y=30mm and z=40mm and two smaller eddies in between can be identified. As in the 155°-335° cross section the onset of the RFZ, which signalises the breakdown of the PVC (Syred and Beer, 1972), is at about z=110mm. Once past the breakdown region, the flow is, unlike previously assumed, not symmetric. Although velocity magnitudes have dropped substantially, weaker eddy structures still dominate the flow.

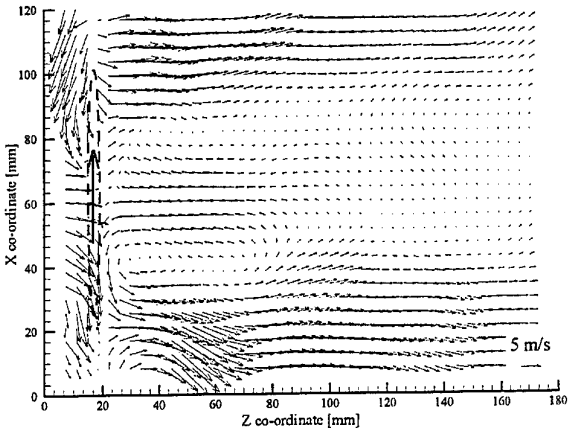


Figure 16: Phase Averaged Side View PIV Vector Plot at the 155°-335° Cross Section, R_e=41,190

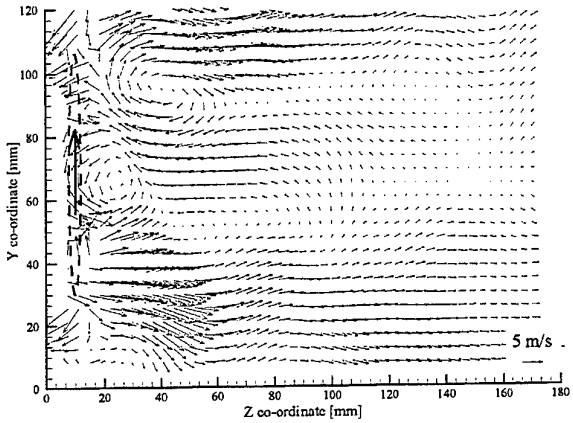


Figure 17: Phase Averaged Side View PIV Vector Plot at the 65°-245° Cross Section, R_e=41,190

The effect of phase averaging on the PIV plots in the tangential/radial plane is more drastic than in the axial/radial plane. When compared to the instantaneous vector plot in Figure 8, the phase averaged vector plot in Figure 18 is somewhat smoother. It can be seen that no secondary or tertiary vortex centres can be identified. However, good quantitative agreement between the phase averaged tangential LDA velocity contours in Figure 5 and the phase averaged tangential PIV velocity contours in Figure 19 is found. Tangential velocities range from –1 m/s to 9 m/s in Figure 5 and Figure 19, but the position of the crescent shaped area of high tangential velocity is found outside the burner exhaust in Figure 19, whereas it was identified inside the burner exhaust in Figure 5. This is due to the fact that by averaging triggered or phased PIV data, more detail of the flow can be preserved. The instantaneous tangential velocity contours in Figure 9 show that the crescent shaped area of high tangential velocity can also be found closer to the geometric centre of the system.

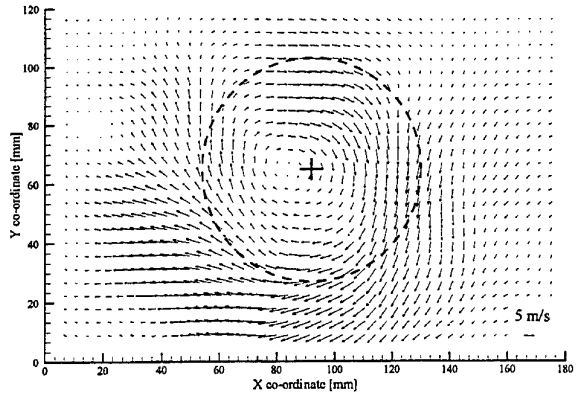


Figure 18: Phase Averaged Plan View PIV Vector Plot at z/De=0.5, R_e=41190

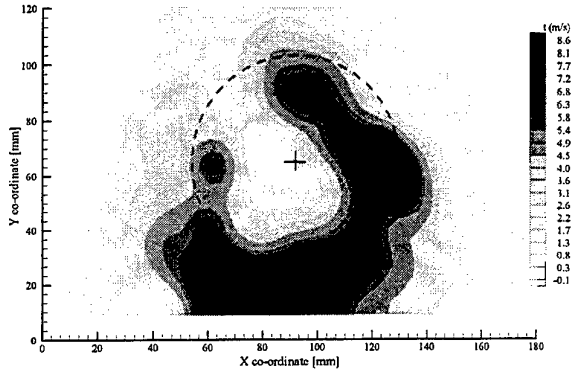


Figure 19: Phase Averaged Plan View PIV Tangential Velocity Contour Plot at z/De=0.5, R_e=41190

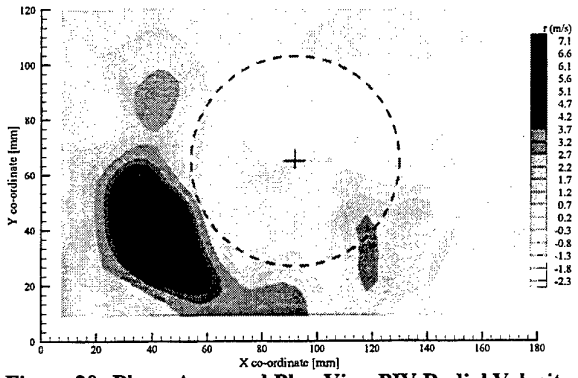


Figure 20: Phase Averaged Plan View PIV Radial Velocity Contour Plot at z/De=0.5, R_e=41190

When compared to the plan view, PIV plots in the tangential/radial plane, the side view PIV plots in the axial/ radial plane reveal a different form of asymmetry. In the tangential/radial direction, as highlighted in Figure 18 to Figure 20, the flow patterns in the 65°-245° cross section are reasonably symmetric. The opposite is the case for the axial/radial plane in the 65°-245° cross section (Figure 17). In the 155°-335° cross section the velocity profile in the tangential/radial plane, Figure 18 to Figure 20, is asymmetric, but the corresponding profile in the axial/radial direction (Figure 16) is reasonably symmetric. This leads to the conclusion that the asymmetric high negative axial reverse flow region associated with the PVC lags the asymmetric high negative tangential reverse flow region by about 90°, as can be seen in comparison of Figure 5 and Figure 6. Furthermore, this lag determines the shape of all eddy structures in the flow. As a result they are, like the RFZ associated with the PVC, truly three dimensional and interact in the tangential/ radial as well as the axial/ radial direction.

5 CONCLUSIONS

The results presented emphasise the importance of instantaneous whole flow field measurement techniques to identify highly complex three dimensional flow structures. The use of phase averaged LDA is limited when a flow, as in this case, is not consistent. As indicated previously by Fick et al. (1996b), it was found in this work, that the PVC did not appear as a coherent and continuous structure, but continuously changes shape and appearance, even during a single cycle, i.e. a single rotation.

The instantaneous and quantitative PIV results further reveal that the flow within the sphere of activity of the PVC is much more complex than evaluated by previous work. The classic flow pattern of a crescent shaped area of high positive tangential/axial velocity with a corresponding kidney shaped area of high negative tangential/ axial velocity is only valid at the burner exit. Further downstream, earlier than previously assumed, severe eddy shedding takes place and asymmetric flow patterns still dominate past the vortex breakdown.

The occurrence of instabilities past the vortex breakdown aided the combustion of low calorific value gases (Fick et al., 1998a). Chao et al. (1991) showed that a PVC and a downstream azimuthal instability, e.g. at the furnace exit contraction, co-exist; this was confirmed by Fick (1998b). Combustion seems to excite these instabilities to an extent that a pulsating Helmholtz type combustor could evolve (Froud et al., 1996 and Dawson et al., 1998). This is most probably due to the geometric shape of the furnace- and furnace exit confinement and in conjunction with asymmetric flow in the axial/ radial direction. Hence further instabilities establish, especially when the transition between swirling flow (with the PVC) and pulsating flow is very narrow and independent on the Reynolds number with the pressure amplitude dependent on the fuel entry mode (Fick et al., 1997b).

6 REFERENCES AND BIBLIOGRAPHY

Chao Y. C., Leu J. H., Hung Y. F. and Lin C. K., 1991, *Downstream Boundary Effects on the Spectral Characteristics of a Swirling Flowfield,* Experiments in Fluids, Vol. 10, pp. 341-348

Chomiak J., Longwell J. P. and Sarofim A. F., 1989, *Combustion of Low Calorific Value Gases; Problems and Prospects,* Prog. Energy Combust. Sci. 1989, Massachusetts Inst of Technology, Cambridge, MA, USA, Vol. 15, pp. 109-129

Claypole T. C. and Syred N., 1984, *Optimisation of a Swirl Burner/ Furnace System for Low Calorific Value Fuels,* Energy

Conservation in Industry, Proceedings of the International Seminar. Volume 1: Combustion and Heat Recovery, Duesseldorf, West Germany, 13-15 Feb 1984, VDI Verlag, Duesseldorf, West Germany, Vol. 1, pp. 316-324

Dantec, 1983, *Laser Doppler Anemometry (LDA),* Published by Dantec Measurement Technology, Dantec Electronics Ltd., Denmark

Dantec, 1996a, *FlowMap Installation & User Guide,* Published by Dantec Measurement Technology, Dantec Electronics Ltd., Denmark

Dantec, 1996b, *The Dantec FlowMap System for Whole Field Flow Measurements,* Published by Dantec Measurement Technology, Dantec Electronics Ltd., Denmark

Dawson J. R., Beale A. J., O'Doherty T. and Syred N., 1998, *Phase Locked Velocity Measurements in an Excited Transient Pressure Field,,* 9th International Symposium on Applications of Laser Techniques to Fluid Mechanics, Lisbon, Portugal, Vol. 1, 3.5

Fick W., Griffiths A. J., O'Doherty T. and Syred N., 1996a, *PIV Measurements in a Highly Turbulent Swirling Flame,* Joint Meeting of the Portuguese, British, Spanish and Swedish Section of the Combustion Institute, Madeira, Portugal, 11.3

Fick W., Griffiths A. J. and O`Doherty T., 1996b, *Visualisation of Coherent Structures in a Highly Turbulent Swirling Flame,* 8th International Symposium on Applications of Laser Techniques to Fluid Mechanics, Lisbon, Portugal, Vol. 1, 10.4

Fick W., Syred N., Griffiths A. J. and O`Doherty T., 1996c, *Phase Averaged Temperature Characterisation in Swirl Burners,* IMechE, Part A, Vol. 210, pp. 383-395

Fick W., Griffiths A. J. and O`Doherty T., 1997a, *Visualisation of the Precessing Vortex Core in an Unconfined Swirling Flow,* Optical Diagnostics in Engineering, http://www.ode-web.demon.co.uk, Vol. 2, Part 1

Fick W., Beale A. J., O`Doherty T., Griffiths A. J. and Syred N., 1997b, *Studies of Resonant Coupling in Swirl Burner/ Furnace Systems,* The Institute of Energy's Third International Conference on Combustion & Emissions Control, Bath, pp. 229-238

Fick W., Syred N., O`Doherty T. and Griffiths A. J., 1997c, *Optimising the Combustion of Low Calorific Value Gases by Utilising Transient Flow Phenomena in Swirl Burners,* Fourth International Conference on Technologies and Combustion for a Clean Environment, Lisbon, Portugal, Session 6, 6.2

Fick W., Syred N., Klinge T., Griffiths A. J. and O`Doherty T., 1998a, *Clean and Efficient Combustion of Simulated Low Calorific Value Gases in Swirl Burner /Furnace Systems,* The Institute of Energy, Vol. 71, pp. 12-20

Fick W., 1998b, *Characterisation and Effects of the Precessing Vortex Core in Swirl Burners,* PhD Thesis, University of Wales, Cardiff

Froud D. Y., O`Doherty T. and Syred N., 1995, *Phase Averaging of the Precessing Vortex Core in a Swirl Burner under Piloted and Premixed Conditions,* Combustion and Flame, Elsevier Science Inc, New York, NY, USA, Vol. 100, pp. 407-412

Froud D. Y., Beale A. J., O`Doherty T. and Syred N., 1996, *Studies of Helmholtz Resonance in a Swirl Burner/ Furnace System,* 26th International Symposium on Combustion, Naples

Gupta A. K., Lilley D. G. and Syred N., 1984, *Swirl Flows,* Abacus Press, Turnbridge Wells

Lucca-Negro O. L. and O`Doherty T., 1996, *Prediction of the Precessing Vortex Core,* The 6th International Symposium on Flow Modelling and Turbulent Measurements, Tallahassee, USA

McCluskey D. R., 1995, *Obtaining High Resolution PIV Vector Maps in Real-Time,* International Workshop on PIV, Fukui, Japan

O`Doherty T., Biffin M. and Syred N., 1992, *The Use of Tangential Offtakes for Energy Savings in Process Industry,* Proc. Instn Mech Engrs, Part E, Vol. 206, pp. 99-109

Syred N. and Beer J. M., 1971, *Attenuating the Precession of Vortex Cores during Combustion in a Swirler,* Gas Waerme International, Bd. 20, Nr. 12

Syred N. and Beer J. M., 1972, *The Damping of Precessing Vortex Cores by Combustion in Swirl Generators,* Astronautica Acta, Vol. 17, p. 783-801

Syred N. and Beer J. M., 1973, *The Effect of Combustion upon Precessing Vortex Cores Generated by Swirl Combustors,* Proc. 14th International Symposium on Combustion, The Combustion Institute, Pittsburg, USA, p. 537

Syred N. and Beer J. M., 1974, *Combustion in Swirling Flows: a Review,* Combustion and Flame, Elsevier Science Inc, New York, NY, USA, Vol. 23, pp. 143-201

Syred N., Dahmen K. R., Styles A.C. and Najim S. A., 1977, *A Review of Combustion Problems associated with Low Calorific Value Gases,* Journal of Institute of Fuel, Vol. 50, pp. 195-207

Syred N. and Dahman, K. R., 1978, *Effect of High Levels of Confinement upon the Aerodynamics of Swirl Burners,* Journal of Energy, Vol. 2, pp. 8-15

Syred N., O`Doherty T. and Froud D. Y., 1994, *The Interaction of the Precessing Vortex Core and Reverse Flow Zone in the Exhaust of a Swirl Burner,* Proc. Instn Mech Engrs, Part A, Vol. 208, pp. 27-36

Syred N., Fick W., O'Doherty T. and Griffiths A. J., 1997a, *The Effect of the Precessing Vortex Core on Combustion in a Swirl Burner,* Combustion Science and Technology, Vol. 125, pp. 139-157

Syred N., Griffiths A. J. and Fick W., 1997b, *A Review of Incineration and Related Work at Cardiff,* First International Symposium on Incineration & Flue Gas Treatment Technologies, IChemE, Combustion, Sheffield University, GB, Session 1, Keynote Paper

Volkert J., Tropea C., Domann R. and Huebner W., 1996, *Combined Application of PIV and LDA to Swirling Flows under Compression,* 8th International Symposium on Applications of Laser Techniques to Fluid Mechanics, Lisbon, Portugal, Vol. 1, 19.1

Yazdabadi P. A., Griffiths A. J. and Syred N., 1994a, *Velocity Components of a Highly Complex Flow Pattern Generated by a Precessing Vortex Core,* Experiments in Fluids, Vol. 17, pp. 84-95

Yazdabadi P. A., Griffiths A. J. and Syred N., 1994b, *Investigations into the Precessing Vortex Core Phenomenon in Cyclone Dust Separators,* Proc. Instn Mech Engrs, Part E, Vol. 208, pp. 147-154

On the extension of a Laser-Doppler Anemometer to the analysis of oscillating flames

by

E.C. Fernandes and M.V. Heitor

Instituto Superior Técnico
Mechanical Engineering Department
Av. Rovisco Pais, 1096 Lisboa Codex
Portugal

E-mail: edgar@termcomb.ist.utl.pt
mheitor@termcomb.ist.utl.pt

ABSTRACT

Optical and probe techniques are used for the analysis of the coupling mechanisms between pressure, velocity and heat release fluctuations typical of pulsed flames, through the combination of laser velocimetry, digitally-compensated thermocouples, chemiluminiscent emissions of free radicals in the flames, and the pressure oscillations is the upstream flows. The results quantify the periodic nature of the mixing process and characterise the momentum and heat flux fluctuations along a cycle of oscillation.

INTRODUCTION

Pulsating flows has been the subject of many investigations covering a wide range of situations, such as: acoustics (Herzog et al, 1996), heart valves (Hirt et al, 1996), in-cylinder combustion chambers (e.g. Liou and Santavicca, 1985, Witze et al, 1984), unstable shear layers (Hussain and Zaman, 1980), pulsed flames (e.g. Lovett and Turns, 1993), pulse combustors (Keller et al, 1987) and afterburners (Heitor et al, 1984, Gutmark et al, 1991 and Sivasegaram and Whitelaw, 1985. Different diagnostic techniques have been used, depending on the purpose of the investigation and on the nature of the flow. For example, the quantification of heat release in pulsed flames has been made through PLIF of OH and CH concentrations (e.g. Gutmark et al, 1989). The velocity field has been measured with hot-wire anemometry in isothermal flows (e.g. Hussain and Zaman, 1980 and Kya and Sasaki, 1985), and with laser anemometry in oscillating flows (Dec et al, 1991). Temperature measurements have been reported with TLAF technique (Dec and Keller, 1990) and with fine bare-wire thermocouples (e.g. Ishino et al, 1996). High speed Schlieren cinematography has also been used in some cases (e.g. Keller et al, 1982 and Ganji and Sawyer, 1989) to record the structure of the reacting flowfield, together with phase average digital photography as a non-expensive visualization technique (Chao et al, 1991). In contrast with the use of those techniques to "steady" flows, their application to unsteady flows requires the knowledge of time and, at least, a variable that can be used as a reference start-flag. In general, the post processing of data is based on the ensemble-average over a moving-window within the period of oscillation (e.g. Tierderman et al 1988).

This paper analyzes the extension of a conventional laser anemometer to the simultaneous measurements of velocity, pressure and temperature and heat release. Measurements were carried out in a bluff-body stabilized flame, under natural acoustic resonance and temporal synchronization was achieved using acoustic pressure fluctuations as a reference signal. The results quantify the periodic nature of the mixing process and characterize the momentum and heat flux fluctuations along a cycle of oscillations. Comparatively to other systems reported in literature for the simultaneous measurement of velocity and temperature fluctuation in reacting flows (e.g. Ferrão and Heitor, 1997) the system analyzed here includes the temporal synchronization of the measurable variables and a novel software that runs on a external microprocessor hosted by the PC.

EXPERIMENTAL METHOD AND PROCEDURES

Flow Configuration

The apparatus consists of a cylindrical duct of stainless steel with a variable length, a diameter of 186mm, which was placed on the top of a cubic plenum of $3m^3$, figure 1. The tube was designed to work with two acoustically opened ends with a length varying from .25mm to 3m in steps of .25mm, allowing the fundamental resonance frequency to range between 50Hz and 1kHz. The burner holder can be moved continuously inside the duct, in order to search for the optimum driving location for heat addition (e.g. Fernandes and Heitor, 1996), and several flame stabilisers can be assembled on the top of it. However, for most of the results described here, the pipe length was kept constant and equal to 0.52m and the flame holder was positioned 10mm downstream of the pipe exit. The resulting flame is open to the atmosphere, but offers the advantage of easy access to the techniques described below.

The primary air was injected with a velocity of 3.4 m/s (Re = 20000) through the plenum, where it was seeded with powdered aluminium oxide (nominal diameter below 1.0μm before agglomeration) making use of a purpose-built cyclone generator. The burner consists of a conical bluff-body with a base diameter of Ø = 103 mm and heigth=250 mm. The pre-mixture is injected through a slot of .5 mm around the border of the base, as shown in figure 2, with an equivalence ratio ϕ =6 and a velocity of 15m/s.

Experimental techniques

Figure 1 shows schematically the various experimental techniques used throughout this work. The radiated sound intensity from the flame was measured with a free-field condenser microphone (B&K 4130) and with a pre-amplifier (B&K 2130) with a flat response over a frequency band of 20Hz to 10kHz. The pressure fluctuations along the duct were measured with a semi-infinite probe with a flat response up to 1kHz.

The light emitted from the flame was used as a signature of the rate of change of heat release (Keller and Saito, 1987) in terms of the chemiluminiscence emission due to the radiative decay of electronically excited radicals existing in the reaction zone, such as <OH*>, <CH*> and <C_2*> (Gaydon and Wolfhard, 1979). The light from the flame was monitored from the <C2*> emissions, by collecting light along a cylindrical line-of-sight of 2mm in diameter, with a 20mm lens diameter with a focal distance of 50mm. The radiation emission was then guided through a fiber optic cable to the entrance slit of photomultiplier (EMI-9658 A), interfaced with an interference filter for 514.5nm with a bandwidth of 4nm. Uncertainties in the ensemble average measurements of light emission are estimated to be less than 2% (Yanta and Smith, 1978) due to a relatively high number of points used for calculating mean quantities, in the order of 3000/phase. Due to the integrated nature of the results along a line-of-sight, a mathematical procedure was implemented based on the Abel's transformation (Tourin, 1968) to obtain the radial profile of radical emission coefficients (e.g. Beyler and Gouldin 1981). The magnitude of the error associated with the Abel's transformation depend on the type of derivative and integral methods implemented, but are less than 5%, according to calculations performed by Correia et al (1997).

Time-resolved velocity information was obtained with a laser-Doppler velocimeter, which comprised an Argon-Ion laser operated at a wavelength of 514.5 nm and a power of around 1W. A fiber optic (DANTEC) was used to guide the beam to an optical unit arranged with a two beam system with sensitivity to the flow direction provided by light-frequency shifting from a Bragg cell at 40MHz, a 310 mm focal length transmission lens, and forward-scattered light collected by a 310 mm focal length lens at a magnification of 1.0. The half-angle between the beams was 5.53° and the calculated dimensions of the measuring volume at the e^{-2} intensity locations were 2.3 and 0.219 mm. The output of the photomultiplier was mixed with a signal derived from the driving frequency of the Bragg cell and the resulting signal processed by a commercial frequency counter (DANTEC

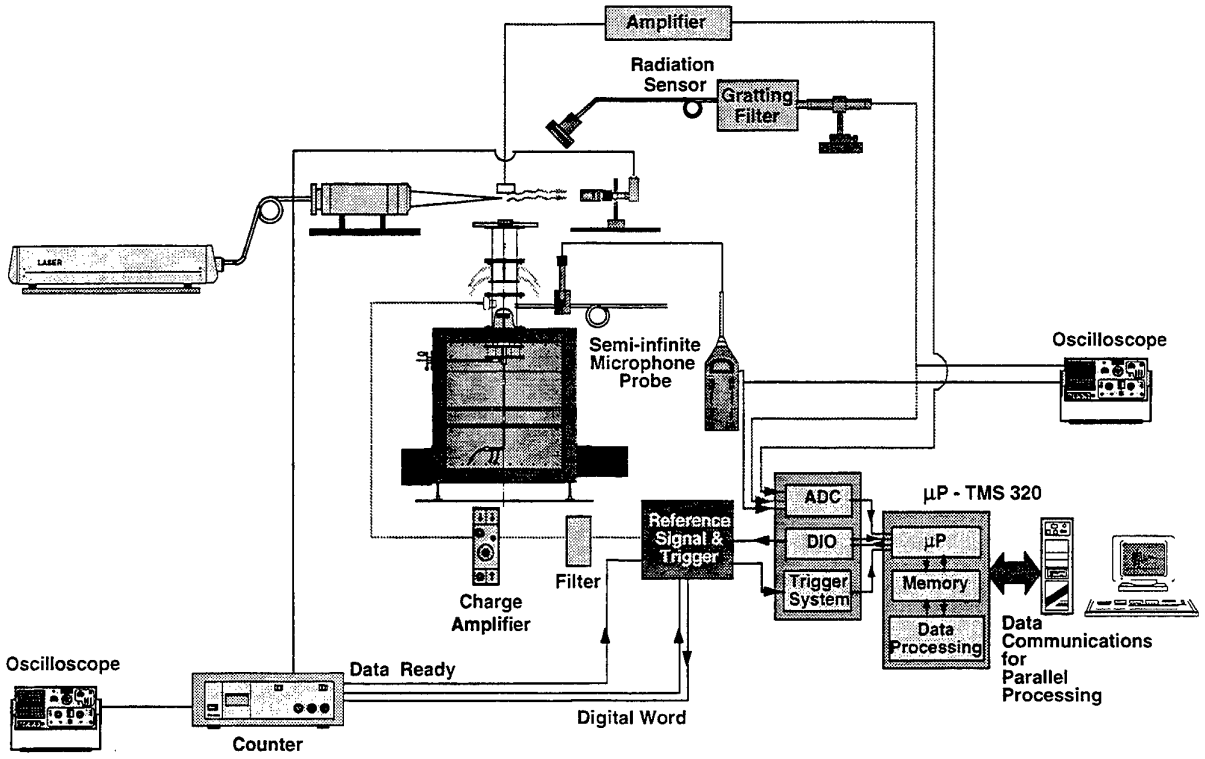


Fig. 1. Schematic drawing of experimental apparatus with identification of the instrumentation used.

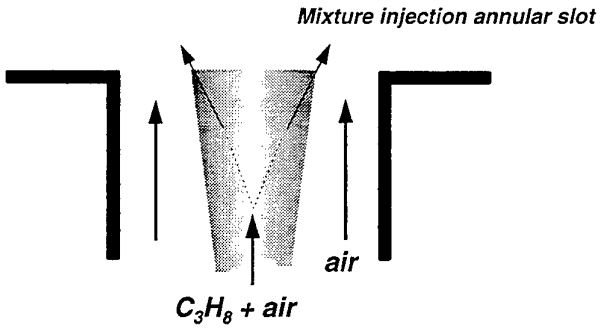


Fig. 2. Schematic diagram of flame holder.

55296) interfaced with a 16-bit DSP board. Measurements were obtained with the laser beams in the horizontal and vertical planes and by traversing the control volume along the horizontal and vertical directions to allow the determination of the axial, U, and radial, V, time-resolved velocities, respectively.

Although various weighting methods have been proposed to correct for velocity bias effects (e.g. Durst et al, 1981), no corrections were applied to the measurements reported here. The systematic errors that could have arisen were minimised by using high data acquisition rates in relation to the fundamental velocity fluctuation rate, as suggested for example by Erdman and Tropea (1981). This could be easily achieved because the rate of naturally occurring particles was sufficiently high for the flow conditions considered here. Spectral analysis of LDV signals was carried out by resample the time series after a linear interpolation with minimum interval time given by the mean data rate.

Temperature measurements were obtained making use of digitally compensated fine-wires

thermocouples, with 38um in diameter, made of Pt/Pt-13%Rh. The related errors are quantified elsewhere (see for example Ferrão and Heitor, 1997) and shown not to be higher than 60K for the time averaged values at the maximum temperature obtained in open flame, and up to 15% for the variance of the temperature fluctuations.

The paragraphs above described the different experimental techniques used throughout this work. We now describe briefly the procedures used to acquire the various signals simultaneously. The Doppler frequency and both scalars, namely pressure and temperature, where acquired simultaneously and post-processed making use of a microprocessor, Texas Instruments-TMSC320C40. The scalars where digitised with a sample-and-hold analog converter at a rate of 40kHz/channel and stored in a circular memory buffer. The acquisition starts only when the pressure signal is going from positive-to-negative, which is given by a pressure reference detector. The buffer access, to collect data simultaneously with the occurrence of a burst, was made through an active pointer, sensitive to velocity data ready signals. The complete system can go up to 12.5kHz of data ready signals, the delay of the board to the data ready signal is less than 100ns and the window resolution between velocity and scalars is less than 1/40kHz. The thermocouple output signal was digitally compensated (e.g Ferrão and Heitor 1992, Durão et al ,1992) from they thermal inertia, following the procedure outlined by Heitor et al (1985). The largest random error incurred in the values of temperature-velocity correlation, as higher as 15%, are due to the spatial separation of the measurements locations of the temperature and velocity because of the thermocouple junction must lie outside the measuring control volume of the laser anemometer.

The complete measuring system was mounted in a three-dimensional traversing unit, allowing an accuracy of the measuring control volume within ±0.25mm.

Data analysis

Important sources of errors that may arise when measurements are taken in periodic flows include *"cycle-to-cycle" variations*, *temporal-gradient bias* and *phase bias*. The former is typically associated with flows inside in-cylinder combustion engines, due to intake and exhaust process. To quantify this type of uncertainty, the method of data acquisition and processing should include a FFT analysis to separate the periodic from the non-periodic component (Dimopoulos et al, 1996). The *temporal-gradient bias* arises when phase-locked ensemble-averaging methods are employed, over a finite time window, to signals with large temporal gradients. The phase bias problem was addressed, for example, by Hussain and Zaman (1980) and consists essentially in a "jitter" effect, i.e. phase variations that generates virtual fluctuations. In the case reported here, this problem may arise through the pressure fluctuations, since this variable is used as a reference signal and is not strictly constant, therefore contaminates the velocity and temperature signals. In the work presented here, these errors were quantified and shown not to affect the results.

Time resolved measurements of velocity, temperature, pressure and reaction rate data obtained under periodic oscillations were statistically analysed following the decomposition proposed by Hussain and Reynolds (1970), for a generic variable γ:

$$\gamma(t) = \bar{\gamma} + \tilde{\gamma}(t) + \gamma'(t)$$

where $\gamma(t)$ is the instantaneous value, U_med is the long time average mean, U_til is the statistical contribution of the organized wave, and $\gamma'(t)$ is the instantaneous value of turbulent fluctuations. An ensemble average over a large number of cycles yields (Hussain and Reynolds ,1970 and Tierderman et al 1988):

$$<\gamma>(t) = \bar{\gamma} + \tilde{\gamma}(t)$$

$$<\sqrt{\gamma'^2}>(t_i) \equiv <\gamma_{rms}> = \sqrt{\frac{(\gamma'(t_i) - <\gamma>(t_i))^2}{n-1}}$$

The ensemble average, or phase average, is then the average at any point in space, of the values of U(t) that are realised at a particular phase interval in the cycle of the periodic oscillations. The phase interval was chosen to be 18°, to minimise the influences of the phase averaging window size on the determination of turbulence quantities in unsteady turbulent flows, as discussed by Zhang et al (1997).

RESULTS AND DISCUSSION

Figure 3 shows a photographic image of "pulsed" and "steady" flames, which were obtained by a small change of less than 0.5% in the equivalence

ratio of ø=6. The evolution from steady to unsteady regime is accompanied by a sharp increase in the sound pressure levels, from around 80 dB (steady flame), to values in excess of 110 dB. For the unsteady condition, the spectrum of the pressure fluctuations in any location of the pipe wall is associated with the excitation of a predominant frequency at 275 Hz, which is associated with a longitudinal standing half-wave. This cyclic process is, according to the Rayleigh criterium, sustained by the temporal and spatial phase relationship that exists between flame energy release and pressure oscillations. The question that does arises when turbulent flames are the main source of energy is due to the presence of a velocity turbulent flowfield, which will be considered below.

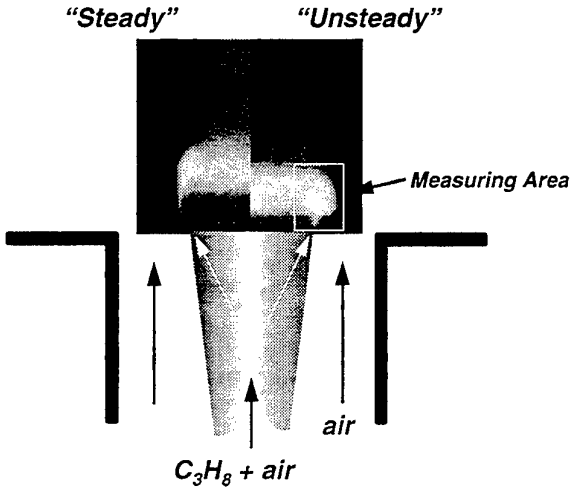


Figure 3 - Photographic image of a "steady" and pulsed flames, together with the identification of the measuring area and the schematic of the flame holder

The analysis consider "rough" combustion conditions for $\emptyset_i$ = 6, U_{jet} =15m/s and U_{plenum} =3.4m/s, corresponding to an overall equivalence ratio at the pipe exit of $\emptyset_T$ =0.1. All data obtained under oscillating conditions were acquired using the instantaneous pressure signal as a temporal reference. The instantaneous pressure fluctuations correspond to signals measured at middle of the pipe, where the amplitude of the pressure fluctuations is maximum.

Figure 4 shows signatures of chemical reaction, obtained after Abel's transformations, for the pulsed flame, as a time sequence for one period of oscillation, together with a schematic draw of the burner with their relative mean velocities. The results show that the large scale structure typical of resonance conditions, which develops along the reacting shear layer surrounding the flow field, exhibits a periodic evolution in time. Generically, the reaction zone can be divided in two main regions, namely the inner flame, for r/R<1.1, which is aligned with the mixture injection slot and the outer flame, for r/R>1.15,which appears to be periodically ignited.

The analysis shows that the inner flame structure is similar to a bluff-body stabilised flame (see for example Ferrão and Heitor, 1997) and works as a flame ignitor of the outer flame, (see image #6 of figure 4). After ignition, the outer flame moves radially outwards, up to r/R=1.3, as the signature of <C2*> emission increase in strength. Subsequently, the reaction zone moves vertically upwards towards the stagnation point, with an estimated velocity of 8 m/s. To improve understanding of this process, the influence of such periodic reacting structure in the velocity and temperature field is analysed below along a radial profile at z/R=0.6.

A main question that arises in the detailed analysis of the present periodic flame is if pressure fluctuation signal emitted by the naturally pulsed flame, is suitable to be used as a reference signal for velocity measurements. This is because frequency variations can affect the velocity signal, creating a virtual turbulent fluctuation that is known to be a function of acquisition time. Figure 5 reproduce time resolved measurements of pressure and velocity for two different acquisition periods (respectively 40 and80 ms) which affect the spreading of points at the end of the signal. While

pressure signal is only used as an absolute reference signal, the spread of data points can have a significant influence on the associated

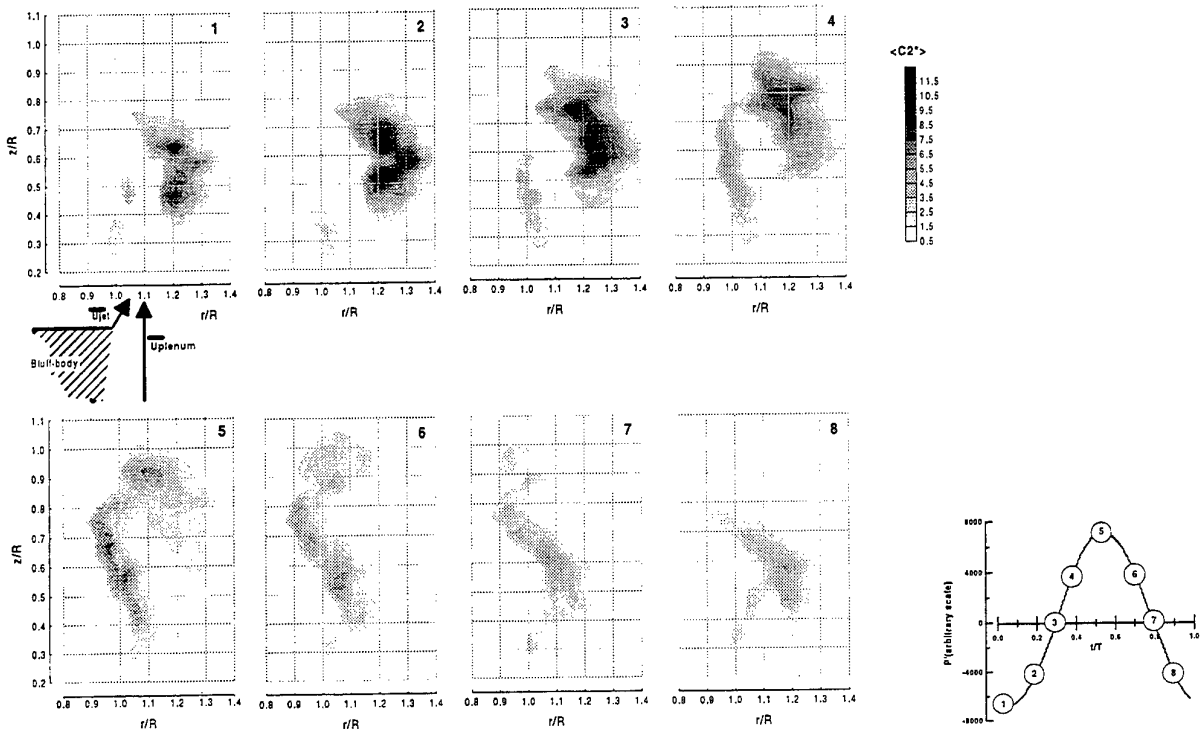


Figure 4 - Time-resolved spatial distribution of phase average <C_2>*

velocity, affecting in this case the velocity rms, as shown in figure 6a. The analysis shows that the influence of frequency uncertainties on the accuracy of the acquired data can be minimized if the acquisition time limit is kept smaller than 40ms. Due to time constraints associated with the acquisition process, see figure 6b, here a value of 40ms was chosen to allow a statistically independent sample of, at least, 10240 data points.

Figure 7 presents the temporal evolution of <U,V>, <Urms>, >Vrms>, <C2*>, <T> ,<Trms> and velocity-temperature correlation, for the region 0.9<r/R<1.5. The ensemble-average velocity vectors (where 8m/s was subtracted from the axial velocity component due to the vortex motion), and the <Urms> and <Vrms> are presented in figure 7a, 7b and 7c, respectively. The velocity vectors are not constant in time and identify the passage of a vortex t/T=0.4 and r/R=1.2 through the presence of a temporal saddle point. This is consistent with the results of figure 7b and 7c, in that the vortex core is associated with maximums of <Urms> and <Vrms>. On the other hand, and at least for this axial station, it seems that the vortex core is free of reaction since it is shown that reaction "starts" at the inner part of the flame, close to r/R=0.9 and at t/T=0.5, and evolves to the location r/R=1.3 where the radical emission of <C2*> reaches maximum values for t/T=0.25. The instantaneous ensemble average temperature profiles, figure 7e, show a rather complex nature, in that they suggest two typical high temperature regions, for r/R<1.04 and at r/R=1.2. Both maxima temperature is of about 1800K while the lowest temperature measured is of the order of 800K. The rms of temperature fluctuations, figure 7f, shows values in the range of 200K to 500K, in a way which is consistent with the findings of figure 7e in the sense that the maximum temperature fluctuations, at each time instant, occurs close to the regions where the instantaneous mean temperature exhibit a higher radial gradient. In addition, if <C2*> map is superimposed on the mean temperature map, it is found that the instantaneous distribution of heat release from the flame is located in zones

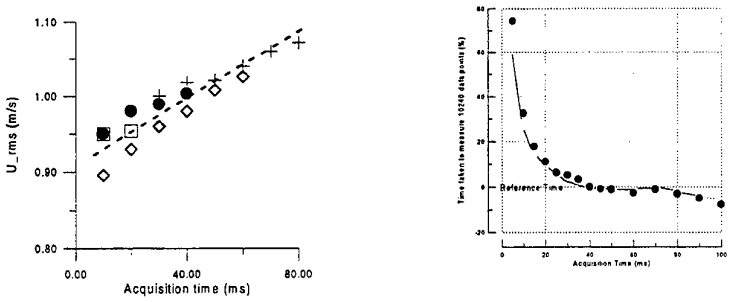


Figure 6 – The influence of acquisition period on
a) Velocity r.m.s of axial component
b) Time taken to measure 10240 data points

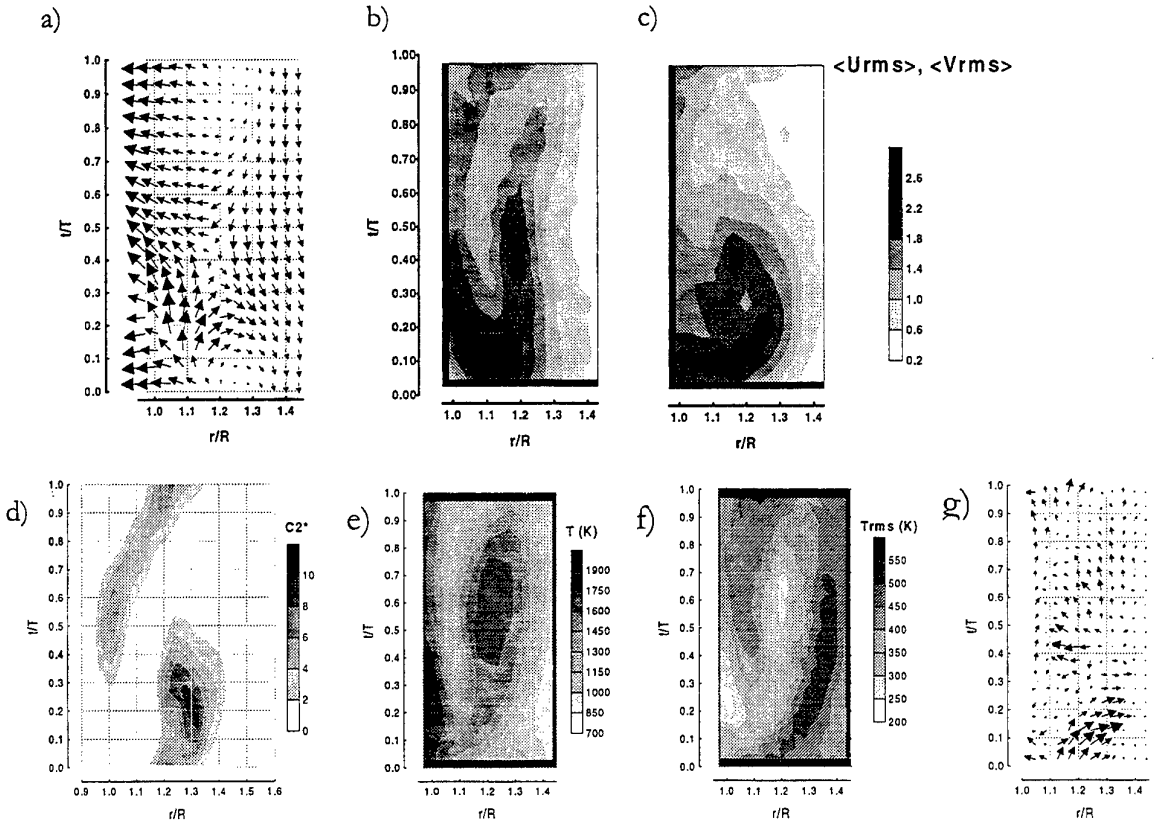


Figure 7 - Temporal evolution of temperature characteristics and velocity-temperature correlation at z/R=0.58

a) Phase average <C2>*
b) Phase average temperature <T>
c) Phase average r.m.s. of temperature fluctuations <Trms>
d) Phase average <u't'>,<v't'> correlation
e) Phase average velocity vectors
f) Phase average rms of axial velocity component
g) Phase average rms of radial velocity component

of large radial gradient of mean temperature, which coincides with the regions where temperature fluctuations are large. The vectors of turbulent heat flux, figure 7g, are high in these regions and normal to the instantaneous flame front, although they exhibit a direction along the isotherms in the vicinity of the flame stabilise, as well as further downstream. This vectors represent the exchange rate of reactants responsible for the phenomenon

of flame stabilisation and the presents results quantify for the first time there temporal evolution along a cycle of flame oscillations. Previous results in the literature for steady state recirculating flames (e.g. Fernandes et al, 1994, Hardalupas et al, 1996, Duarte et al, 1997) have shown the occurrence of zones of non- and counter-gradient diffusion of heat which has been explained in terms of interaction between gradients of mean pressure and density fluctuations. The present results provide new evidence of this interaction in oscillating flames, which is associated with periodic fluctuations in flame curvature. In general, the results quantify the periodic ignition of large-scale reaction zones, which drive the combustion-induced oscillations reported in this paper.

SUMMARY

The experimental analysis of a naturally-pulsed premixed turbulent flame is reported making use of optical and probe diagnostics and including the time-resolved correlation of velocity, temperature, pressure and light emission signals. The results were obtained in the flame stabilised in a wake of bluff-body located on a velocity acoustic antinode, and show that the instantaneous flame structure, based on the analysis of electronically-excited decay of C2 radicals, is composed by two, inner and outer, main regions. The inner flame, behaves as a typical bluff-body stabilised flame, although the influence of a strong unsteady flowfield results in appreciable spatial and temporal deformations. The inner flame acts as a periodic ignitor source of the second reactive structure present, which is considered here as an outer flame. This outer flame front emerges radially at an axial location of about 0.6R, followed by a vertical movement towards the rear stagnation point. This process is accompanied by large fluctuations in the axial and radial velocity components of the flow, with the two flame regions separated by the zone of maximum axial velocity. The time-resolved analysis show that both ensemble average flame fronts occupy successively regions where temperature exhibit high radial gradients, and large temperature fluctuations. In general the results quantify the time resolved process of turbulent mixing along a full pressure cycle in a pulsed flame and suggest that the cycle-resolved nature of the momentum flux may be represented, at least qualitatively, by gradient hypothesis. On the other hand, the nature of the cycle-resolved (i.e. phase averaging) turbulent heat flux shows zones of either gradient and non-gradient characteristics, which appears to be influenced by the temporal evolution of the streamline curvature along a cycle of flame oscillations.

REFERENCES

Beyler, C.L. and Gouldin, F.C. (1981) "Flame Structure in a Swirl Stabilized Combustor Inferred by Radiant Emission Measurements", 8th Symp. (Intl) on Combustion, The Combustion Institute, pp.1011-1019

Charon, O. and Jouvad, D. (1993) "Pulsated O_2/fuel flame as a new technique for low NO_x emission", Combust. Sci. and Tech., 93, pp.211-222

Chao, Y.C., Jeng, M.S. and Han, J.M. (1991) " Visualization of Image Processing of an Acoustically Excited Jet Flow", Experiments in Fluids, 12, 29-40

Correia, D.P., Caldeira-Pires, A., Ferrão, P. And Heitor M.V. (1997) " A Temperature Tomographic Sensor for Combustion Analysis", 17th ICIASF,Pacific Grove, CA USA, September 28-October 2, 1997

Dec, J.E. and Keller, J.A. (1990), "Time Resolved Gas Temperature in the Oscillating Turbulent Flow of a Pulse Combustor Tail Pipe", Comb. And Flame, 80, pp.358-370

Dec, J.E., Keller, J.O. and Hongo, I. (1991) " Time-Resolved Velocities and Turbulence in the Oscillating Flow of a Pulse Combustor Tail Pipe", Comb. and Flame, 83, pp.271-292

Dimopoulos, P., Boulouchos, K. and Valentino,G. (1996) " Turbulent Flow Field Characteristics in a Reciprocating Engine: Appropriate cut-off Frequencies for Cycle-Resolved Turbulence, an analysis of Co-incident 3-D LDV Data Based on Combustion-Related Dimensional Arguments", 8th Intl. Symp. On Appl. Of Laser Techniques to Fluid Mechanics, July, 8th-11th, Lisbon Portugal

Duarte, D., Ferrão,P and Heitor, M.V. (1997) " Turbulent statistics and scalr transport in highly-sheared premixed flames", Proc. 11th Turbulent Shear Flows Symposium, Grenoble, 8-10 September

Durão, D.F.G., Fernandes, E.C., Heitor, M.V., Moreira, A.L.N. and Simões, J.P (1992) LDA Measurements of Velocity and Turbulent Transport Processes in an 150kW Baffle-Stabilized Swirling Flame", 6th Intl. Symp. On Appl. Of Laser Techniques to Fluid Mechanics, July, 20th-23rd, Lisbon Portugal

Durst, F., Melling, A. and Whitelaw, J.H. (1981). "Principles and Practice of laser-Doppler Anemometry", Academic Press.

Eisinger, F.L. (1991) " Combustion air flow induced furnace vibration in an oil-fired utility boiler- a ese study" IMechE 1991, C416/095.

Erdman, J.C. and Tropea, C.D. (1981). "Turbulence-induced Statistical in Laser Anemometers". Proc. 7th Biennal Symp. on Turbulence, Rolla, Missouri.

Fernandes, E.C., Ferrão,P., Heitor,M.V. and Moreira A.L.M (1994) "Velocity temperature correlation in recirculating flames with and without swril",Experimental Thermal and Fluid Science, 9, pp.241-249

Fernandes, E.C. and Heitor, M.V. (1996) "Unsteady flames and the Rayleigh criteria", in Unsteady Combustion, eds. Culick, F., Heitor, M.V. and Withelaw, J.H., Nato ASI Series, Series E: Applied Sciences- Vol. 306 ., Kluwer Academic Publishers, pp. 1-16

Ferrão, P. And Heitor, M.V. (1992) " Simultaneous Measurements of Velocity and Scalar Characteristics for the Analysis of Turbulent Heat Transfer in Recirculating Flames, 6th Intl. Symp. On Appl. Of Laser Techniques to Fluid Mechanics, July, 20th-23rd, Lisbon Portugal

Ferrão, P. And Heitor, M.V. (1997) "Probe and Optical Diagnostics for Scalr Measurements in Premixed Flames", Experiments in Fluids, to appear

Ganji, A.R. and Sawyer,R.F. (1980) " Experimental Study of the Flowfield of a Two-Dimensional Premixed Turbulent Flame", AIAA Journal, Vol.18,no.7

Gaydon, A.G. and Wolfhard, H.G. (1979) Flames- their structure radiation and temperature, Ed. Chapman and Hall, Fourth Edition, London

Gutmark, E., Parr, T.P., Parr-Hanson, D.M. and Schadow, K.C. (1990) "Stabilisation of a premixed flame by shear flow excitation", Combust. Sci. and Tech., 73 , pp. 521-535

Gutmark, E., Parr, T.P., Hanson-Parr, D.M. and Schadow, K.C. (1989) " On the Role of Large and Small-Scale Structures in Combustion Control", Combust. Sci. and Tech., 66, pp.107-126

Gutmark, E., Schadow, K.C., Sivasegaram, S, and Whitelaw, J.H. (1991) " Interaction Between Fluid-Dynamic and Acoustic Instabilities in Combusting Flows Within Ducts", Combust. Sci. and Tech., vol.79, pp. 161-166

Hardalupas, Y., Tagawa, M. and Taylor, A.M.K.P (1996) " Characteristics of counter-gradient heat transfer in a non premixed swirling flame". In: Developments in Laser Techniques and Applications to Fluid Mechanics, ed. Durst et al, Springer-Verlag, pp. 159-184

Heitor, M.V., Taylor, A.M.K.P. and Whitelaw, J.H. (1984) "Influence of confinement on combustion instabilities of premixed flames stabilised on axisymmetric baffles", Combust. and Flame, 57, pp. 109-121

Herzog, P., Valière, J.C., Valeau, V, and Tournois, G. (1996) " Acoustic Velocity Measurements by means of Laser Doppler Velocimetry", 8th Intl. Symp. On Appl. Of Laser Techniques to Fluid Mechanics, July, 8th-11th, Lisbon Portugal

Hirt,F., Eisele, K., Zhang, Z. and Jud,E. (1996) " Pulsatile Flow Behaviour near Cardiac Prostheses Application and Limitation of Laser and MRI Techniques", 8th Intl. Symp. On Appl. Of Laser Techniques to Fluid Mechanics, July, 8th-11th, Lisbon Portugal

Hussain, A.K.M.F. and Reynolds, W.C. (1970) "The Mechanics of an Organized Wave in Turbulent Shear Flow", J.Fluid Mech., vol.41, part2, pp.241-258

Hussain, A.K.M.F. and Zaman, K.B.M.Q. (1980) " Vortex Pairing in a Circular jet Under Controlled Excitation. Part 2. Coherent Structure Dynamics", J. Fluid Mech., vol.101, pp.493-544

Ishino, Y., Kojima, T., Oiwa, N. and Yamaguchi, S. (1996) " Acoustic Excitation of Diffusion Flames with Coherent Structure in a Plane Shear Layer", JSME International Journal, series B, Vol.39, no.1

Keller, J.J. (1995) "Thermoacoustic oscillations in combustion chambers of gas turbines", AIAA Journal, 33, No.12, December 1995.

Keller, J.O. and Saito, .K. (1987) "Measurements of the combusting flow in a pulse combustor", Combust.Sci. and Tech., 53, pp. 137-163

Keller, J.O., Vaneveld, L., Korschelt, D., Hubbard, G.L., Ghoniem, A.F., Daily, J.W. and Oppenheim, A.K. (1982) " Mechanism of Instabilities in Turbulent Combustion Leading to Flashback", AIAA Journal, vol. 20, no.2

Kiya, M. and Sasaky, K. (1985) " Structure of Large-Scale Vortices and Unsteady Reverse Flow in the Reattaching Zone of a Turbulent Separation Bubble", J. Fluid Mech., vol. 154, pp.463-491

Liou, T-M. and Santavicca, D.A. (1985) " Cycle Resolved LDV Measurements in a Motored IC Engine", Transactions of the ASME, Vol.107, pp232

Lovett, J. A. and Turns, S. (1993) "The structure of pulsed turbulent nonpremixed jet flames", Combust. Sci. Tech, 94, pp. 193-217

Sivasegaram, S. and Whitelaw, J.H. (1987) " Oscillations in Confined Disk-Stabilized Flames", Comb. and Flame, 66, pp.121-129

Tierderman, W.G., Privette, R.M. and Philipds, W.M. (1988), "Cycle-To-Cycle Variation Effects On Turbulent Shear Stress Measurements In Pulsatile Flows" Experiments in Fluids, 6, pp.265-272

Tourin, R.H. (1966) Spectroscopic Gas Temperature Measurement Elsevier Publishing Company

Witze, P.O. (1984) " Conditionally-Sampled Velocity and Turbulence Measurements in a Spark Ignition Engine", Combust. Sci. and Tech., vol.36,pp. 301-317

Yanta, W.J. and Smith, R.A. (1978) "Measurements of Turbulent Transport Properties with a Laser Doppler velocimeter", 11th Aerospace Science Meeting, AIAA paper 73-169, Washington, USA

Zhang, Z. Eisele, K. And Hirt, F. (1997) "The Influence of Phase-Averaging Window Size on the Determination of Turbulence Quantities in Unsteady Turbulent Flows", Experiments in Fluids, 22, pp.265-267.

LIQUID FUELLED FLAMES WITH IMPOSED AIR OSCILLATIONS

Y. Hardalupas, A. Selbach & J. H. Whitelaw

Mechanical Engineering Department, Imperial College of Science Technology and Medicine
Exhibition Road, London SW7 2BX, UK

ABSTRACT

The secondary air flow of a swirl stabilised burner was oscillated at a frequency of 350 Hz for swirl numbers of 0.66, 0.7 and 0.81. Time dependent phase-Doppler velocimetry quantified the spray and the air flow and chemiluminescence of the CH radicals the shape and area of kerosene fuelled flames. The results suggest that the imposed oscillations shed a series of vortex rings at the burner exit with the oscillation frequency, increasing mixing and distorting the reaction zone, and potentially reducing the NO_x emissions. The flame lifted off for a critical amplitude, which increased with swirl number, due to the translation of the recirculation zone at a downstream position leading to increased stretch rate, evaluated from the temporal variation of the flame area, and local extinction in the near burner region.

1. INTRODUCTION

The investigation follows from previous considerations of the stability of steady liquid fuelled flames by Hardalupas et al. (1990, 1994a and b) and gaseous flames with imposed oscillations by Bhidayasiri et al. (1997), which revealed details of the variations of velocity, temperature and droplet size, including the contribution of recirculating small droplets of fuel in disk- and swirl-stabilised flames. Previous examination of the addition of fluctuating energy to the air supply of burners include that of Keller & Hongo (1990), who suggested reductions in NO_x in pulsed combustors and described a possible mechanism, the experiments of Haile et al. (1996) which showed that acoustic excitation led to increased mixing and Delabroy et al. (1996) who linked the interaction of a vortex and a flame to increased strain rate, leading to NO_x reduction. However, the understanding of the processes involved is limited and cannot provide design guidelines for imposed oscillations to the air flow to burners for reduced NO_x emissions with stable and efficient combustion. In addition, information on the interaction of imposed oscillations on the air supply and air swirl in swirl stabilised burners is not available.

The purpose of this study is to understand the way imposed oscillations on the air supply to a swirl stabilised burner influences the air flow, spray and flame characteristics and discuss the potential impact of imposed oscillations on flame stability, combustion efficiency and emissions. It presents visualisation of the effects of imposed oscillations on the shape of kerosene-fuelled flames and of their reaction regions, quantifies the mean stretch rates and focuses for the inert flow on the amplitude of the imposed oscillation in terms of velocity fluctuations at the exit of the burner and within the spray. The arrangement of the burner and the measurement methods are described in the following section and the results are described in the third section. The fourth section provides a summary of the more important conclusions.

2. EXPERIMENTAL ARRANGEMENT

The burner of figure 1 provided swirl with an air flow-rate through the annulus of 0.03 m^3/s resulting in a bulk velocity of 17 m/s and a potential heat release of 22.6 kW. Kerosene was delivered by a coaxial air-assist atomiser located on the axis with liquid and atomising air flow-rates of 7.7×10^{-7} m^3/s and 1.8×10^{-4} m^3/s respectively, so that droplet velocities ranged from 3 to 20 m/s and their arithmetic mean diameters from 20 to 70 μm with the

radial distance from the axis. Three swirl numbers of the air flow of 0.66, 0.7 and 0.81 were considered, which resulted in lifted flames with the lower values. The overall equivalence ratio was constant at 0.25 and its local value at the exit of the atomiser was 38. Oscillations were imposed on the air flow by two acoustic drivers (figure 1), with a power of 38 W, except for the swirl number 0.66, where the power was reduced to 9 W to maintain stability, since higher power led to blow-off. The oscillation frequency was 350 Hz, which corresponded to a Helmholtz resonance at the exit of the burner and the resulting higher amplitude led to larger effect on the flame shape than frequencies at 200 and 920 Hz, for which the amplitude was low. This was confirmed by tests at frequency of 460 Hz, corresponding to second resonance, which led to a similar effect on flame shape as for 350 Hz.

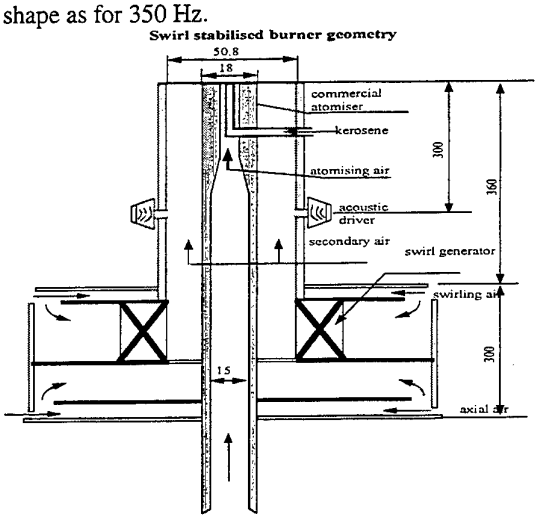


Figure 1 : The swirl stabilised burner geometry.

The velocities within the spray and the air flow at the exit plane of the burner were quantified with an isothermal flow of water with the same flow-rates and similar droplet characteristics, an oscillation power of 38 W and swirl numbers of 0.66 and 0.81. A phase-Doppler velocimeter measured velocities and droplet diameters and comprised transmission optics based on a rotating grating, and receiving optics with three photodetectors. The light refracted from droplets was observed at a forward angle of 30° on the bisector plane of the two laser beams, was focused on a 100 μm slit and passed through a mask with three evenly spaced rectangular apertures before reaching the photodetectors. The optical geometry of table 1 allowed measurement of droplet diameters up to 165 μm and droplet velocities were recorded in 30 size intervals of 5.5 μm. Results are presented for ranges centred at 13.8 and 46.8 μm with statistical uncertainties of less than 2 and 5% in mean and rms values respectively, based on average sample size of 1000. The counter processor was gated at the maximum and minimum velocities in the 2.9 ms oscillation cycle with data acquisition time of 0.5 ms.

Table 1: Phase-Doppler velocimeter

Transmitting optics		
Laser : 1 Watt Ar-ion laser		
Operating power	0.4	W
Wavelength	514.5	nm
Beam intersection angle	3.2	deg.
Fringe spacing	9.23	μm
Number of fringes	14	
Frequency shift	6	MHz
Receiving optics		
Focal length of collimating lens	310	mm
Equivalent aperture at collimating lens: dimension of rectangular aperture 1, 2 and 3	53.3 × 10.6	mm
separation between aperture 1 and 2	13.3	mm
separation between aperture 1 and 3	26.6	mm
Spatial filter slit width	100	μm
Observed spatial slit width	387.5	μm
Phase angle-to-diameter conversion factor for channel 1 and 3	0.468	μm/deg

The air velocities in the exit plane of the burner were quantified in terms of aluminium oxide particles with a nominal diameter of approximately 1.0 μm at six times within each oscillation cycle, within 0.5 ms windows overlapping by 0.02 ms.

The reaction zone was visualised in terms of chemiluminescence of CH radicals at a wavelength of 430 nm and with a lifetime of less than 0.1 ms. The detection of chemiluminescence was achieved by installing an optical filter (centre frequency 429 nm, bandwidth 8.2 nm, peak transmission 45%) in front of an eight-bit black and white intensified CCD camera (Proxitronic HF 1). The images had a resolution of 580 × 770 pixels and the chemiluminescence intensity of each pixel was resolved on a scale from 0 to 255, with spatial resolution of 0.31 mm per pixel after considering the magnification of the lens. The CCD camera was connected to a PC with a frame grabber card (Data-Translation DT-3152) and an exposure time of 0.5 ms. The oscillations imposed with a period of 2.9 ms (350 Hz) and the images of the CH radicals in the oscillating flames were obtained by gating the camera 45° after the velocity maximum and minimum.

Figure 2a shows that a typical flame spectrum within a range of wavelengths from 200 to 900 nm was dominated by the continuum of soot emissions with two distinct peaks corresponding to

emissions of C_2 and CH radicals at 516 and 430 nm respectively. The continuum of the soot emissions is equal to the theoretical emissions of a blackbody at the temperature of the soot, Solomon & Best (1991), so that the soot emission at 430 nm was estimated by linear interpolation between those measured at 420 nm and 442 nm and subtracted from the total intensity measured at 430 nm, figure 2b, to separate the emission due to the CH radicals.

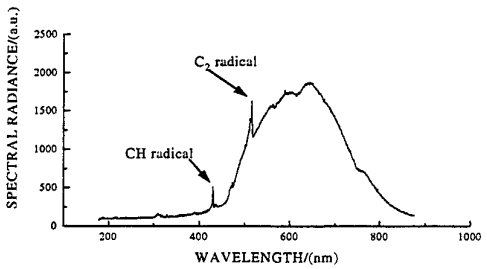


Figure 2a : Flame spectrum for swirl number 0.81

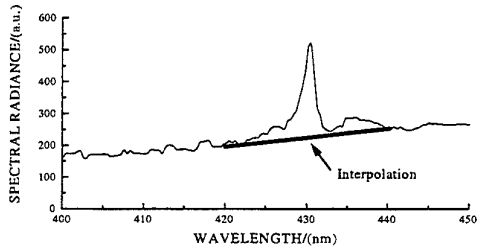


Figure 2b : Interpolation of soot emissions

The mean grey levels were obtained from the images by extracting the intensity at every tenth pixel in the vertical and horizontal directions from 200 pictures and averaging at each position. Spatial variations in the averaged intensity smaller than 3.1 mm were due to interpolation. The contribution of soot was subtracted and the CH concentration is presented as contour plots, normalised by the maximum intensity, and graded linearly from black, corresponding to a low value of CH-radical concentration, to white, corresponding to a high value, on a grey scale divided into twenty equally sized steps of 0.05.

3. RESULTS

The results are presented in two sections. The first describes the velocity characteristics of the isothermal air flow in the exit plane of the burner and the droplet characteristics downstream of the burner exit without and with imposed oscillations. The second section describes the changes of the position and shape of the reaction zones due to imposed oscillations.

3.1 Velocity Characteristics

The axial velocities of the air flow corresponded to swirl numbers of 0.66 and 0.81 and the gated measurements with oscillations confirmed a sinusoidal variation with 350 Hz frequency. Those of figure 3 comprise mean and rms values in the absence of oscillations, the ensemble-averages of maximum and minimum velocities within oscillation cycles, and time-averaged velocities independent of the period of the oscillation cycle. Without oscillations the velocities decreased towards the axis for both swirl numbers, consistent with the findings of Ribeiro and Whitelaw (1980) and Liu et al. (1989) in their near fully-developed annular flows. With imposed oscillations, the time-averaged velocities had a similar trend with the highest swirl number and a more uniform profile with the lowest swirl number. The rms of time-averaged velocity fluctuations was increased by up to 100% with oscillations, as expected, due to the bimodal probability function of velocity at the burner exit and, therefore, did not indicate increased levels of turbulence. This is confirmed by the similarity of the ensemble-averaged rms of the velocity fluctuations without and with oscillations (figure 3). This suggests that the flow turbulence at the burner exit was not responsible for the observed effects on the flow downstream of the burner exit and on the flame.

The ensemble-averaged mean axial velocity profiles of figure 3a & c were integrated with radial distance to quantify the variation of the volume flow-rate during the cycle of the imposed oscillations. The results showed that the volume flow-rate fluctuated with the oscillation frequency and an amplitude of around 1.42×10^{-2} m^3/s between the minimum and maximum velocity in the cycle for the swirl number of 0.81, which was around 50% of the total air flow-rate to the burner. This remained unchanged with the reduction of the swirl number to 0.7 and reduced by around 15 % for swirl number of 0.66. The observed influence of the swirl number on the amplitude is possibly limited to values of swirl numbers below 0.7, which corresponds to the value required for the generation of a recirculation zone at the exit of swirling coaxial jets (Wall 1987). Decrease of the input power at the acoustic drivers from 38 to 9 W for the swirl of 0.66 resulted in 68 % lower amplitude.

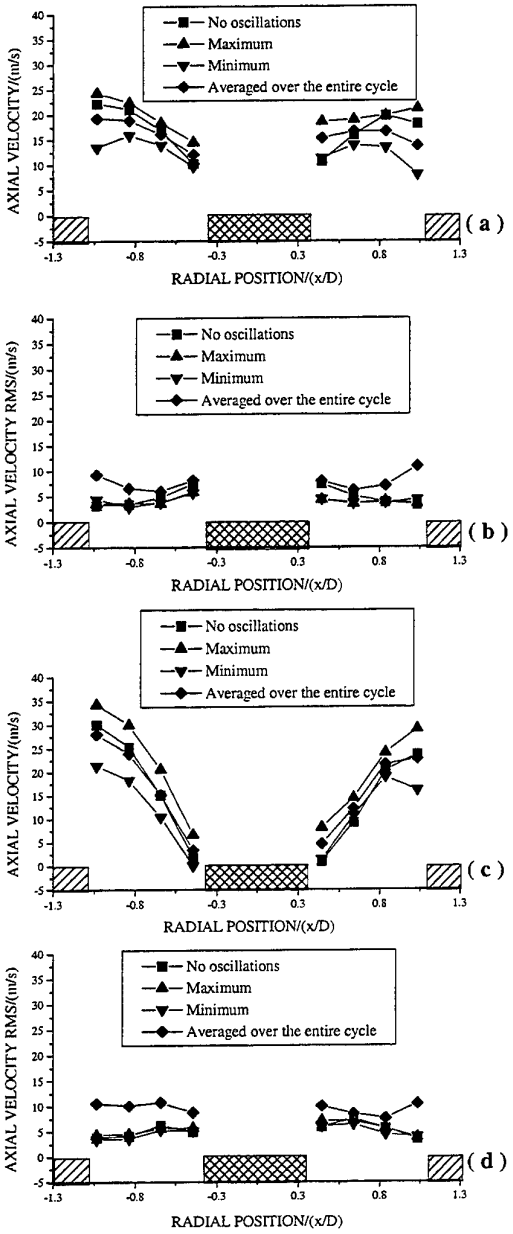


Figure 3 : Velocity profiles for swirl numbers of 0.66 (**a**) and 0.81 (**c**) and rms profiles for swirl numbers of 0.66 (**b**) and 0.81 (**d**) at the exit of the burner

The amplitude of the air flow-rate fluctuation during the cycle quantifies reliably the amplitude of the oscillation and takes into account the enhancement due to resonance, which is not possible either in terms of the input power to the acoustic driver or the rms of the time-averaged velocity at the burner exit. The former method depends on the characteristics of the acoustic driver, even for different units of the same model, and cannot take into account resonances. The latter method did not represent any physical quantity which can compare levels of oscillations at different burners and operating conditions.

The droplet velocities measured in the plane 40 mm downstream of the exit, near the lower boundary of the recirculation zone for the flow without imposed oscillations, correspond to droplet sizes of 13.6 and 46.8 μm with their response times of 0.6 and 6.6 ms. It is expected that the smaller droplets followed the mean and turbulent flow time scales of around 3 and 0.9 ms respectively, assuming that the characteristic length scale and velocity were the burner exit diameter, D, and the length scale of the energy containing eddies, D/10, and the area-averaged air flow velocity at the burner exit and the rms of the velocity fluctuations respectively for the mean and the turbulent flow. The small droplets could also follow the imposed oscillations with period 2.9 ms. The larger droplets could not respond to the characteristics of the flow and indicate the motion of most of the liquid fuel. Figure 4 shows that, without oscillations, the smaller droplets had negative velocities around the axis and the larger droplets did not. Thus, the air flow recirculated in a substantial region around the axis and larger droplets tended to travel through the recirculation region with near-ballistic trajectories. The two swirl numbers gave rise to similar axial velocities with a tendency for increased swirl to spread the recirculation region with small increase in the maximum negative velocities. Imposed oscillations and the larger swirl number led to averaged velocities, which were close to those of the non-oscillated flows (figure 4c & d). The difference of the axial velocity of the small droplets between the minimum and maximum point in the cycle is small within the recirculation zone and increased at the outer edge of the flow to around 4 m/s. Therefore, the imposed oscillations mainly influenced the outer part of the air flow downstream of the burner exit. With the smaller swirl number (figure 4a & b), the averaged velocities of both droplet sizes increased, the recirculation zone shifted downstream and differences between minimum and maximum of the cycle were negligible. The flow characteristics of figure 4b, for the low swirl number and imposed oscillations, led to flame extinction, probably caused by the downstream shift of the recirculation zone, which increased the local stretch rate above a critical value for extinction.

The findings of the velocity characteristics of the air flow help to understand the flow structure with imposed oscillations. The sinusoidal oscillation of the volume air flow-rate at the burner annulus, the presence of the velocity difference between the

minimum and the maximum in the cycle at the outer region of the flow and the shifting of the recirculation zone downstream of the burner exit for low swirl number are consistent with the shedding of vortex rings from the burner exit with frequency of

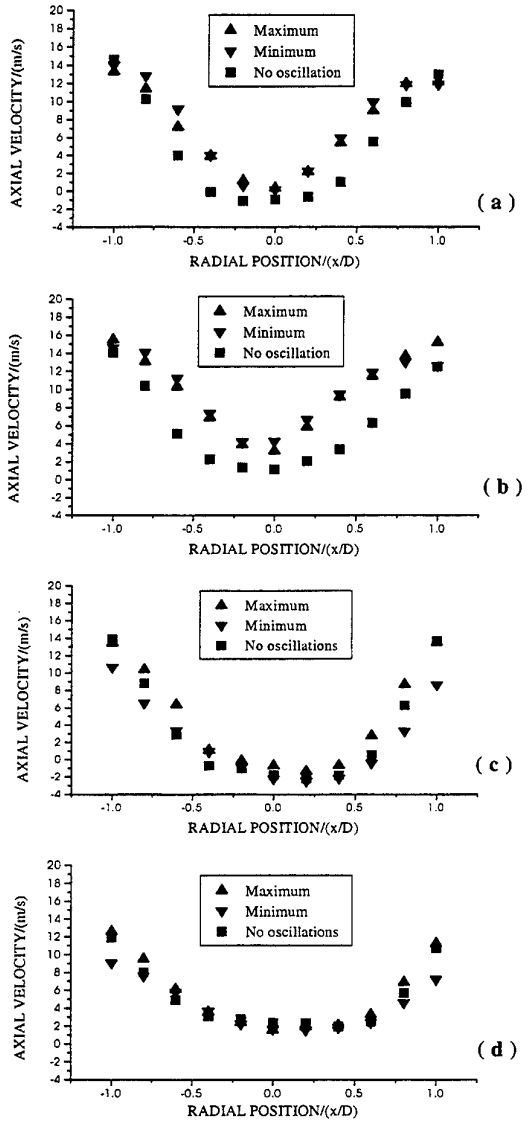


Figure 4 : Velocity profiles for the swirl number of 0.66 and size range centred at 13.8 (**a**) and 46.8 μm (**b**) and for the swirl number of 0.81 and size range centred at 13.8 (**c**) and 46.8 μm (**d**) at an axial distance to the exit of 40 mm

the imposed oscillations, similar to starting vortices in jet flows, in agreement with Maxworthy, 1972 and Weigand & Gharib, 1997. These remained at the outer part of the flow downstream of the burner exit, where velocity fluctuations were observed during the cycle and induced a flow field close to the burner axis with direction away from the burner exit, which could become strong enough to overcome the inverse flow of the recirculation zone generated by the swirling motion, and this occurred for low swirl number with imposed oscillations. The presence of vortex rings at the burner exit is consistent with the velocity measurements and will be further discussed below in association with the flame shape.

3.2 Visualisation of the Reaction Zone

Figure 5 shows CH chemiluminescence concentrations in the near burner region of flames with and without imposed oscillations and with swirl numbers of 0.66, 0.7 and 0.81. The results with imposed oscillations correspond to the time of 45° after the maximum velocity of the cycle. In the absence of imposed oscillations, the boundaries of the time-averaged images are smooth, since the random disturbances caused by turbulence were removed by averaging over 200 images, and the small scale disturbances are associated with the spatial resolution of the images. The flow field in the near burner region was dominated by the recirculation zone with the small droplets reversing their direction and evaporating to provide fuel vapour at the base of the flame. Reaction occurred in the shear layer of the secondary air stream where the fuel vapour mixed with the air stream, as in diffusion flames.

High CH emissions corresponding to the reaction zone are present in the shear layer for all swirl numbers with less intense emission close to the axis of symmetry, figure 5, where a fuel rich region is present and reaction is limited. The lower boundary of the reaction zone was some 35 mm above the burner exit with the swirl number of 0.66, figure 5a, and, although imposed oscillations (9W) led to higher CH concentrations close to the axis, the lower boundary remained at the same position but the flame was shortened, figure 5b. The amplitude of the imposed oscillation for 9W power input was 15% of the total air flow-rate to the burner and represents the maximum amplitude before flame extinction. The velocity results suggest that the shift of the recirculation zone downstream combined with the increased velocity of the large droplets for higher amplitude of oscillation, was responsible for flame extinction. With the swirl number of 0.7, the lower boundary of the reaction zone was 25 mm from the burner, figure 5c, and the flame could be stabilised with imposed oscillations of power input of 38W, corresponding to oscillation amplitude of 50% of the total air flow-rate. However, the flame was lifted at an increased distance of 40 mm, figure 5d, and the

length of the flame considerably shortened. The shortening of the flames, figures 5b & d, was probably associated with the large droplets escaping the reaction zone, which did not allow them to evaporate. The total flame area, determined by the area of the normalised intensity contours of figure 5 for values higher than 0.82, for the low swirl numbers 0.66 and 0.7 increased with imposed oscillations, suggesting locally higher reaction rate. However, the reaction zone was located at a larger distance from the burner exit due to increased lift-off and with short flame length resulting in short residence times for the large droplets to evaporate and burn completely.

For swirl number of 0.81, the flame was attached to the burner exit and imposed oscillations with amplitude 50% of the total air flow-rate did not lift-off the flame (figure 5e & f). This is consistent with the negative velocities of smaller droplets and the wide recirculation zone of the air flow on the previous figure, which did not change with imposed oscillations (figure 4c & d), and, therefore, the flame remained attached to the burner. However, further increase of the amplitude of the oscillations led to flame lift-off and extinction, which was similar to observations for lower swirl numbers. Therefore, there is a critical value of the amplitude of the imposed oscillations for each swirl number, which led to flame lift-off and extinction and, since the amplitude of the oscillations should be large to increase mixing and potentially reduce NO_x emissions, the imposed oscillations should be applied to burners operating at high swirl numbers.

The contours of flames with imposed oscillations had large scale wrinkles, which were not evident by visual observation, and the attached flame with the highest swirl number had a reaction zone with two axi-symmetric wrinkles which were convected downstream from the burner exit. The shape of the wrinkles suggests that they were caused by a sequence of vortex rings shed at the burner exit with the frequency of the oscillation and with initial length scale of the order of the annular width, in agreement with the velocity measurements, as observed in the flames of Delabroy et al. (1996).

Chemiluminescence contours were also observed as a function of time within the oscillation period of 2.9 ms (not presented here) and comparison of the downstream position of wrinkles at two times within the cycle suggested a velocity in direction of the main flow of 15.5 m/s which was lower than the bulk velocity at the exit of the burner, 17 m/s. This is expected since the vortex ring caused the wrinkles on the flame and entrained gases, which will lead to reduction of their propagation velocity according to the conservation of momentum and this suggests that 10% of the initial flow-rate of the vortex was entrained within one cycle. Thus, the vortex rings increased mixing in the near burner region, leading to an increase of the time dependent stretch rate. The increased stretch rate can give rise to local extinction and a lifted flame and, in turn, to reduction of thermal NO_x by quenching, Drake and Blint (1989). Therefore, the increased mixing and stretch rate combined with an attached flame for high swirl numbers could lead to lower NO_x emissions.

The mean stretch rates due to imposed oscillations were calculated by estimating the area of the reaction zone in the near burner region at two observation times during the cycle corresponding to 45° after the maximum and minimum of the sinusoidal velocity fluctuation at the burner exit. Thus, the term $[A^{-1}\ dA/dt]$ is proportional to the propagation velocity normal to the reaction zone over the radius of curvature and the velocity gradient of the flow normal to the reaction zone, Bradley et al. (1992), so that the stretch rates with the swirl numbers of 0.7 and 0.81 were 700 and 250 s^{-1} respectively, around three times higher for the lifted flame. Therefore, flame lift-off occurred due to local extinction by the increased stretch rate.

It is interesting to consider the differences between the gas flames of Milosavljevic (1993) and Bhidayasiri et al. (1997) and those of the present investigation. The first two authors observed that imposed oscillations stabilised lifted flames and are in contrast to the increase in flame lift-off determined with the present liquid-spray fuelling system. Thus, the smaller droplets required to stabilise the flame were downstream of the burner exit for the two lower swirl numbers and oscillations could not modify the ballistic trajectory of the droplets associated with most of the liquid fuel. Bhidayasiri also found a small reduction in NO_x emissions, and similar reductions will be more difficult to determine in the present open flame in which it is more difficult to ensure complete combustion within a well defined region. However, the current study provided understanding on the influence of imposed oscillations on the flame and flow structure. It is anticipated that in a confined flame, the vortex rings will entrain surrounding hot combustion gases and mix them with fuel vapour and air and droplets to enhance evaporation, improve combustion efficiency and reduce NO_x emissions.

4. SUMMARY - CONCLUSIONS

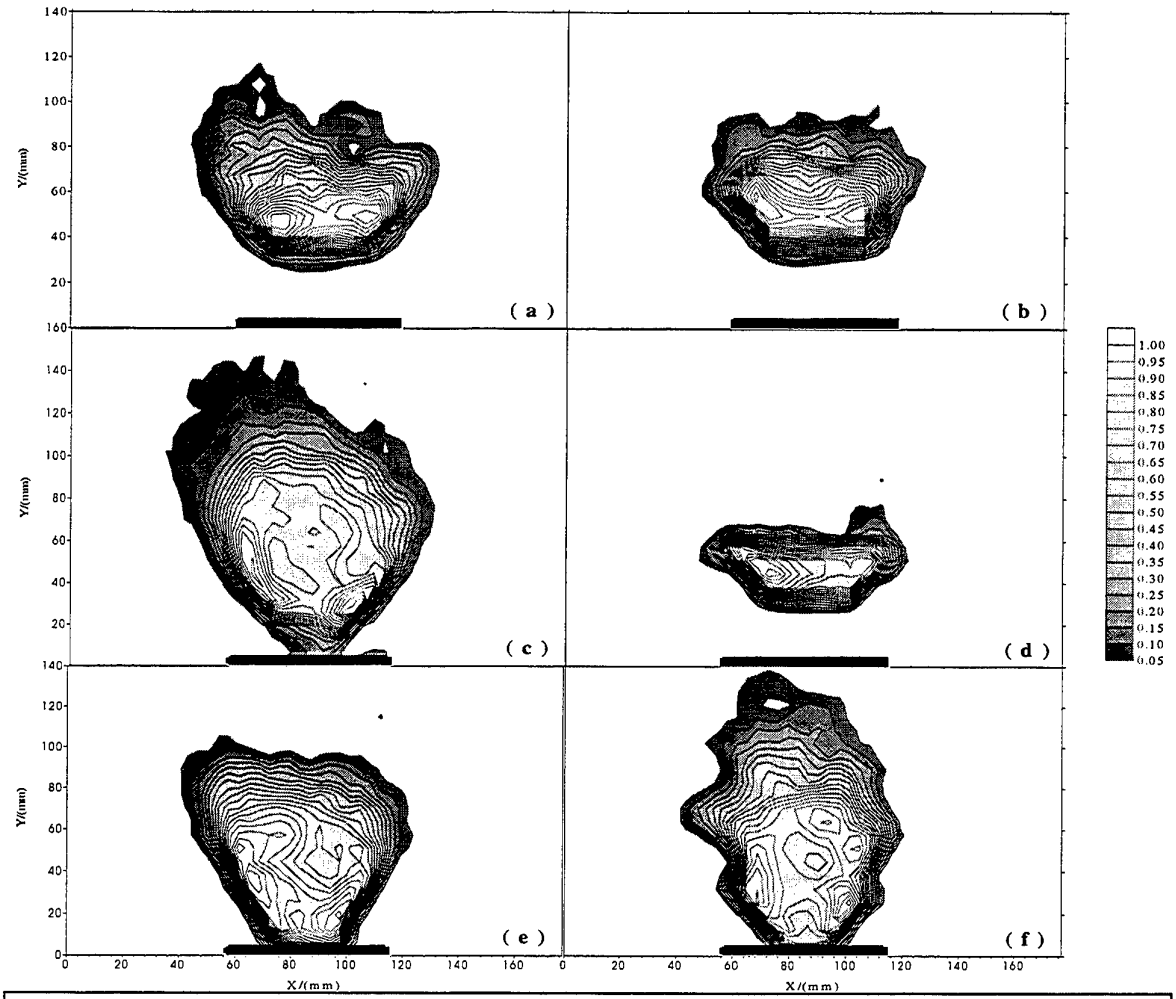


Figure 5 : Distributions of the CH radical concentration of the flame for swirl numbers of 0.66 (**a**), 0.7 (**c**) and 0.81 (**e**) without imposed oscillations and with imposed oscillations for flames with swirl numbers of 0.66 (**b**), 0.7 (**d**) and 0.81 (**f**) an exposure time of 0.5 ms averaged over 200 images, normalised by the maximum values

Oscillations were imposed on the secondary air flow of a swirl-stabilised burner and the air flow, the droplets within the isothermal spray and the kerosene-fuelled flames were examined for swirl numbers of 0.66, 0.7 and 0.81, overall equivalence ratio of 0.25 and frequency of 350 Hz, which had the largest effect within a range from 200 Hz to 920 Hz. A method to visualise quantitatively the reaction zone in liquid fuelled flames, based on the detection of the chemiluminescence from CH radicals emitted at wavelength of 430 nm was also developed. The more important results are summarised below.

1. The acoustic excitation caused the formation of a sequence of vortex rings at the burner exit with dimensions close to the burner annulus, propagating at the outer region and in the direction of the main flow with the frequency of the imposed oscillation, increasing mixing between incoming air and surrounding gases, leading to increased stretch rates and potential reduction of NO_x emissions. Increase of the amplitude of the oscillations above critical values, which increased with swirl number, led to flame lift-off and extinction. Therefore, imposed oscillations should be used to burners with high swirl numbers to achieve high combustion efficiency and potentially lower NO_x emissions.

2. Ensemble-averaged measurements of the isothermal spray showed that flame lift-off occurred when the oscillation caused a transformation of the recirculating zone to a downstream position. Two competing mechanisms were identified, the first, the swirling flow leading to a reverse flow region and,

the second, the induced flow on the burner axis away from the exit by the vortex rings. When the latter mechanism dominated, the recirculation zone shifted downstream and the stretch rate increased, leading to local extinction and flame lifted off.

3. Ensemble-averaged measurements of the rms of air velocity fluctuations in the cycle at the burner exit showed that air flow turbulence remained unchanged. Therefore, increased mixing occurred due to interaction between the vortex rings and the flow downstream of the burner exit.

4. Ensemble-averaged measurements of the air flow at the burner exit quantified the amplitude of imposed oscillations, in terms of the magnitude of the temporal fluctuation of the air flow-rate to the burner normalised by the total air flow-rate. This quantity allows comparisons between different burners and operating conditions, in the presence of resonance.

ACKNOWLEDGEMENTS

The authors gratefully acknowledge support from the EPSRC, Grant G/K 97097 and US Navy Contract N68171-97-C-9009. Y. Hardalupas was supported by an EPSRC Advanced Fellowship.

REFERENCES

Bhidayasiri, R., Sivasegaram, S. & Whitelaw, J.H. 1997, The Effect of Flow Boundary Conditions on the Stability of Quarl-Stabilised Flames, Combust. Sci. and Tech., vol. 123, pp. 185-205.

Bradley, D., Lau, A.K.C. & Lawes, M. 1992, Flame Stretch Rate as a Determinant of Turbulent Burning Velocity, Phil. Trans. R. Soc. Lond., vol. A 338, pp. 359-387.

Delabroy, O., Haile, E., Lacas, F. & Candel, S. 1996, Controlled Pulsed Combustion for NO_x Reduction in Domestic Oil Burners, Proc. 1st European Conf. on small burner Technology, Zurich, vol. 1, pp. 55-64.

Drake, M.C. & Blint, R.J. 1989, Thermal NO_x in Stretched Laminar Opposed Flow Diffusion Flames with $CO/H_2/N_2$ Fuel, Combust. Flame, vol. 76, pp. 151-167.

Haile, E., Delabroy, O., Lacas, F., Veynante, D. & Candel, S. 1996, Structure of Acoustically Forced Turbulent Spray Flame, Proc. 26th Symp. (Int) on Combustion, pp. 1663-1670.

Hardalupas, Y., Liu, C.H. & Whitelaw, J.H. 1994b, Experiments with Disk Stabilised Kerosene-Fuelled Flames, Combust. Sci. and Tech., vol. 97, pp. 157-191.

Hardalupas, Y., Taylor, A.M.K.P. & Whitelaw, J.H. 1990, Velocity and Size Characteristics of Liquid Fuelled Flames Stabilised by Swirl Burners, Proc. Roy. Soc. Lond., vol. A 428, pp. 129-155.

Hardalupas, Y., Taylor, A.M.K.P. & Whitelaw, J.H. 1994a, Mass Flux Fraction and Concentration of Liquid Fuel in a Swirl-Stabilised Flame, Int. J. of Multiphase Flow, vol. 20, pp. 233-259.

Keller, J.O. & Hongo, I. 1990, Pulse Combustion: The Mechanism of NO_x Production, Combust. Flame, vol. 80, pp. 219-237.

Liu, C.H., Nouri, J.M. & Whitelaw, J.H. 1989, Particle Velocities in a Swirling, Confined Flow, Combust. Sci. and Tech., vol. 68, pp. 131-145.

Maxworthy, T. 1972, The Structure and Stability of Vortex Rings, J. Fluid Mech., vol. 51, pp. 15-32.

Milosavljevic, V.D. 1993, Natural Gas, Kerosene and Pulverised Fuel Fired Swirl Burners, Ph.D. thesis, University of London.

Ribeiro, M.M. & Whitelaw, J.H. 1980, Coaxial Jets with and without Swirl, J. Fluid Mech., vol. 96, pp. 769-795.

Solomon, P.R. & Best, P.E. 1991, Fourier Transform Infrared Emission/Transmission Spectroscopy in Flames, in Combustion Measurements, ed. Norman Chigier, pp. 385-444, Hemisphere Publishing Corporation.

Wall, T.F., 1987, The Combustion of Coal as Pulverized Fuel through Swirl Burners, in Principles of Combustion Engineering for Boilers, ed. Lawn C.J., pp. 197-335, Academic Press, London.

Weigand, A. & Gharib, M. 1997, On the Evolution of Laminar Vortex Rings, Experiments in Fluids, vol. 22, pp. 447-457.

PHASE LOCKED MEASUREMENTS IN AN EXCITED TRANSIENT PRESSURE FIELD

J.R. Dawson, A.J. Beale, T. O'Doherty and N. Syred

University of Cardiff
Department of Mechanical Engineering and Energy Studies
PO Box 685, The Parade, Cardiff, U.K.

ABSTRACT

Phase averaged Laser Doppler Anemometry (LDA) techniques have proven to be a powerful experimental method for obtaining quantitative insight into periodic fluid dynamic phenomena, particularly fluid dynamic instability. The field of combustion is no exception.

This work describes the excitation of a combustion driven oscillation in a common swirl burner furnace system in terms of a periodic pressure and velocity field. Two dimensional Phase Locked LDA measurements have been obtained describing the velocity regime over a typical cycle with respect to fluctuating pressure. The results show that over the pressure cycle the velocity field changes accordingly, resulting in bulk inflow and outflow of products and reactants. The tangential velocity results show no evidence of Rankine vortex phenomena whilst the axial velocity results show only minor similarities to the expected high swirl case and flowfield phenomena associated with vortex breakdown.

Finally an investigation into the timing of the heat release with respect to the pressure cycle has also been undertaken with the results supporting Rayleigh criterion.

1. INTRODUCTION

Swirling flows are widely used to stabilise high intensity flames and burn a wide variety of fuels in many industrial applications including gas turbines and industrial furnaces. Previous work has shown that the associate fluid dynamics of swirl generating devices at high swirl depart from axisymmetric behaviour and encounter various forms of vortex breakdown (Sarpkaya, 1971) (Syred and Beer, 1971, 1972.)(Fick et al.1998) leading to large eddy shedding and/or transverse instabilities such as the Precessing Vortex Core (PVC). Furthermore if certain geometrical conditions are met, the system can be susceptible to acoustic instability resulting in a stable combustion driven oscillation.

The PVC phenomenon has been shown by to precess around the burner axis in the low frequency band of 30–200Hz and has also been shown to be a function of flowrate, equivalence ratio and swirl number. Its presence consequently creates a cyclic gradient in the velocity, temperature and pressure fields of the burner. Furthermore it has been suggested by Markstein (1964), Putnam (1976) and Syred et al. (1973) that the PVC and other mechanisms that are responsible for large axial radial eddy shedding may be responsible for the excitation of acoustically driven oscillations.

An extensive amount of research has been undertaken in the field of combustion driven oscillations under various guises including unsteady combustion, vibratory flame movement Kaskan (1951), Behrens (1951), Markstein (1964), oscillatory combustion Roginskii (1961), and pulsating combustion, Keller et al. (1990) and Keller et al. (1994a,b). Oran and Gardner (1985) provide an excellent overview and classification of combustion driven oscillations. Overall, these studies have yielded a vast amount of characteristic data for various different combustion systems, yet a minimum amount of data in terms of system aerodynamics is available. Results have indicated that the mechanisms involved in pulsating combustion lead to increased heat transfer, lower combustion temperatures due to shorter residence times, high turbulence and mixing rates resulting in lower emissions, particularly NOx. Outside the scope of pulsating combustion the excitation and sustainment of combustion driven oscillations has been generally considered detrimental as the occurrence of large pressure fluctuations with frequencies matching the acoustical modes of the system can lead to structural damage, accelerated burning and flame blowout (Markstein, 1964) (Ellis et al. 1951). Recently however, interest in utilising pulsations to reduce emissions in swirl burner and gas turbine systems has been undertaken by Casentini et al.(1997) and Bhidayasiri et al. (1997). Casentini et al. (1997) found that by pulsating the air supply line via a rotor disc at high frequencies (400-480Hz), a reduction of NO up to 21% was achieved. It was also noted that in the low frequency band, 30-60Hz, the effects of the oscillation were insignificant. It must be noted that since the mechanism of oscillation is artificially imposed and therefore does not provide any further understanding into the underlying phenomena of naturally occurring chemical-acoustic

interaction and their effects, be they beneficial or detrimental, on the combustion process.

When a conventional swirl burner fires into a furnace and exhausts through a straight pipe, a Helmholtz resonance has been shown to be excited creating a stable, complex combustion driven oscillation by Syred et al. (1973) and Froud et al. (1996). The oscillation has been shown to be a function of equivalence ratio, swirl number by Froud (1995) and results in a transient but periodic pressure field of high amplitude and low frequency, dramatically altering the systems aerodynamics when compared those reported by Froud. (1995), Syred et al. (1997). Furthermore, the fluctuating pressure and velocity field is coupled with the combustion process such that a periodic heat release occurs coinciding with the systems peak pressure, therefore reinforcing and sustaining the oscillation. The behaviour of the system when driven tends to borrow many of the fundamental characteristics of Helmholtz type pulse combustors in particular:

1.) A transient fluctuation of dynamic pressure and velocity resulting in bulk inflow and outflow of reactants and products.
2.) An associated periodic heat release which acts to reinforce the pressure wave and sustains the oscillation.
3.) Sensitivity to mode of fuel injection and throughput, i.e. correct phasing of the combustion process with the velocity and pressure field (Dawson et al., 1998).

This paper presents and analyses the excitation of a Helmholtz oscillation in terms of the phase relationship between the pressure field, velocity field and periodic heat release in a common swirl burner/furnace system. Phase averaged Laser Doppler Anemometry (LDA) techniques and cycle resolved CH measurements were used to obtain velocity and heat release data.

1. EXPERIMENTAL APPARATUS AND PROCEDURES

2.1 Test Rig

All experiments were performed on a 100kW swirl burner furnace system under combustion conditions with an extraction pipe as shown schematically in figure 1. The burner section consists of two diametrically opposed tangential inlets with replaceable inserts facilitating a change of geometrical swirl number from 0.8 to 4 if required. Combustion air is supplied solely through these tangential inlets via a conventional blower with the volumetric flowrate regulated through the use of rotameters. The fuel inlets are configured in such a way as to allow premixed piloted or a combination of the two. The fuel used was natural gas supplied by the mains. To prevent flashback of the flame front the exhaust was extended back into the swirl chamber. All dimensions are provided in figure 1.

1.2 Operating Conditions

The operating conditions of the combustor were as follows:

1.) Volumetric flowrate of air, Q_{air}=1400l/min
2.) Volumetric flowrate of gas, Q_{ga}=120lmin (60l/min premixed and 60l/min piloted)
3.) Geometrical swirl number, Sg=2.61
4.) Frequency of oscillation, f=35Hz

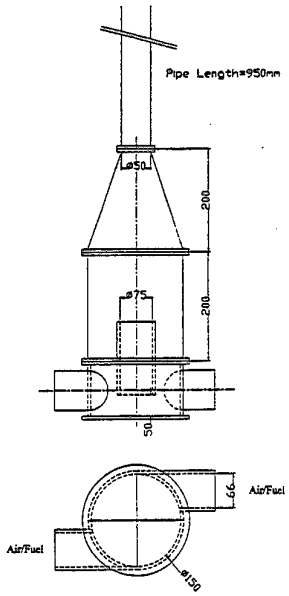


Figure 1: Schematic of Swirl Burner System

1.3 Phase Averaged LDA Procedure

The velocity measurements were obtained using a 2D Dantec fibre optic laser system with Coherent Innova 70 series Argon-ion laser source with an output power of up to 5W. The probe was mounted on a programmable traverse for accuracy. The wavelengths of the two beams, green and blue, were 514.5nm and 488nm respectively.

The measurement plane started 10mm above the burner exit continuing in 15mm increments in the vertical plane until optically restricted by the combustion chamber. Measurements taken in the horizontal plane were taken over the full 75mm radius in 5mm increments.

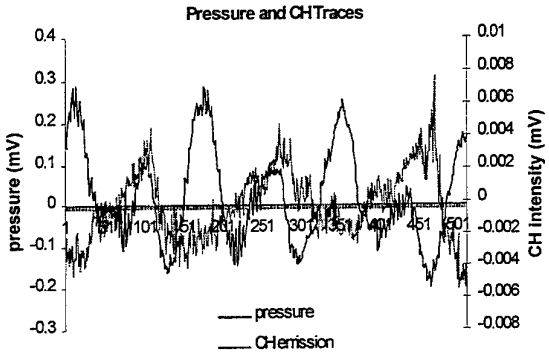


Figure 2: Pressure and CH emission traces

In order to provide insight into the periodic behaviour of the velocity field phase averaged LDA techniques were utilized. A water cooled pressure transducer was mounted to the combustion chamber to monitor the pressure fluctuations and provide a trigger to the LDA system. The

pressure trace characteristic of the geometry employed is shown in figure 2. By outputting the pressure signal into an oscilloscope, a 0-5V TTL trigger signal (a square wave pulse train) could be sent to the Burst Spectrum Analyser (BSA) during the data acquisition period. The BSA in return recorded a sync signal for every positive maximum gradient of the pressure cycle. This split the velocity data into cycles (separated by the sync signals) and enabled a program written in Quick Basic to average them over the selected time steps. The results were then imported into a data visualization package obtaining contour plots for ease of analysis. The original results were divided into 24 time steps, corresponding to 24 phase angles α, however only selected results are presented here.

1.4 Cycle Resolved CH Measurements

A Bandpass filter sensitive to the frequency band of CH emission, 430nm, was inserted into a standard DANTEC forward scatter receiving optic with a focal length of 700mm to prevent overheating. This, in combination with a DISA high voltage unit (which phase shifted the output by 90°) used to power up the receiving optics provided an output spectrum of CH. The spectrum signal was inputted into a PL 202 FFT analyser alongside the pressure signal as shown in figure 2. This enabled CH and pressure data to be obtained in such a manner that the CH fluctuation could be correlated with respect to the pressure cycle. The CH emission trace was acquired via a traverse to ensure the same interrogation area as it LDA counterpart. However CH measurements were obtained for a 5mm increment along the chamber length (z-axis), as opposed to 15mm increments for the LDA measurements, with increments in the radial plane the same as before. The results were then processed via a spreadsheet so that all the CH data could be synchronized with the pressure cycle. These results were then imported into a data visualization package to obtain contour plots.

2. RESULTS AND DISCUSSION

2.1 Phase Locked Velocity Results

The 2D phase locked LDA results are shown in figures 3-6. All the velocity results are presented using the following conventions:

1.) the 0mm point along the x-axis corresponds to the geometrical centre of the burner
2.) the 0mm point on the z-axis corresponds to the start of the measurement plane i.e. 10mm above the burner exit

The axial velocity results for α=0°and 90° is shown in figure 3a. The velocity field sees a strong annular jet located around the rim of the burner exit (x=38mm) and surrounding a Central Recirculation Zone, CRZ from x=0-20mm. This recirculation zone extends the entire height of the measurement plane before starting to lift up and out of the burner towards the taper section when α=90°. As the CRZ lifts out of the burner, an increase in reverse flow over the radial area is evident the top of the measurement plane. This is evidence that products are flowing from the exhaust section into the chamber. As the pressure reaches its peak between α=0° and 45° and starts to decay between α=45° and 90°, it is evident from figure 3a that the flowfield remains relatively uniform over the first quarter of the cycle.

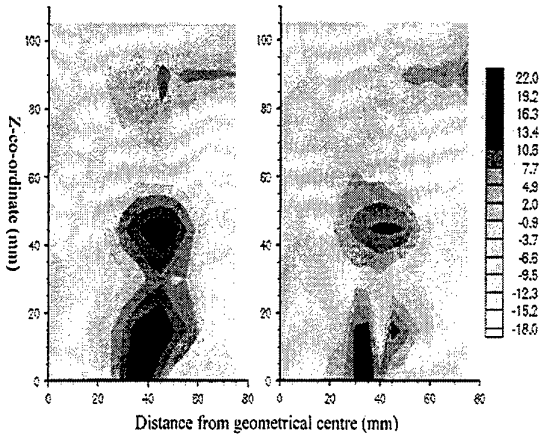


Figure 3a:Axial Velocity Contour Plots for α=0° and α=90° Respectively

The presence of a large reverse flow region, similar in size to the CRZ, is located near the periphery starting at x=60mm. The tangential velocity contour plots for α=0°and 90° is shown in figure 4a. It is instantly noticed that the tangential flowfield shows no evidence of Rankine vortex development, are of irregular form and bears no resemblance to the results found by Froud et al.(1996).

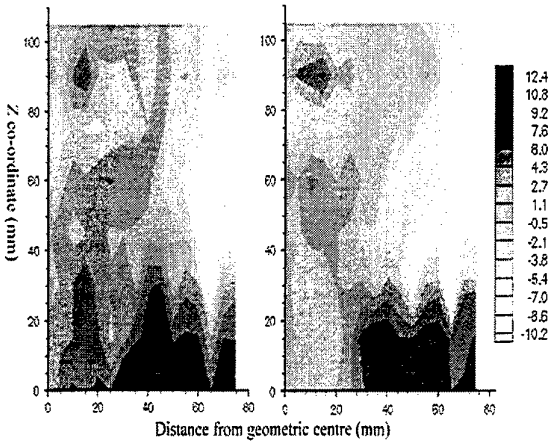


Figure 4a:Tangential Velocity Contour Plots for α=0° and α=90° Respectively

Both α=0° and 90° contour plots are similar in overall structure with peak velocities in the range of 7-10m/s evenly spread to 30mm above the burner exit (z=20mm) and covering virtually the entire radial area. At α=0°, this peak velocity region becomes shifted 20mm away from the geometrical centre. The tangential velocity around the geometrical centre has now lowered to between 0 and 2m/s. It is interesting to note that this occurs alongside the lifting of the CRZ out of the burner exit as shown in figure 3a.

Along the periphery and sitting on top of the peak tangential velocity region is an annulus of negative tangential velocity starting at x=50mm and z=30mm.

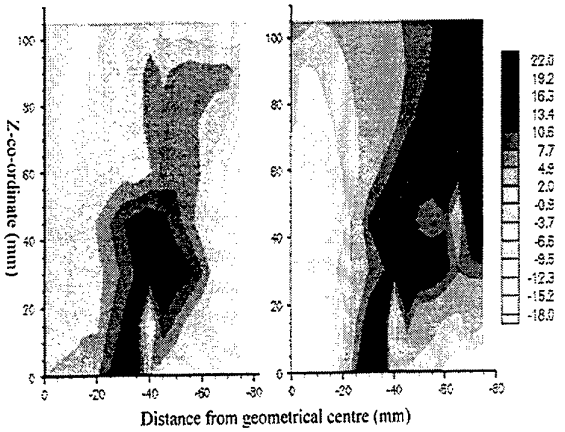


Figure 3b:Axial Velocity Contour Plots for α=180° and α=270° Respectively

roughly similar in size to that shown in figure 3a. Furthermore, it is interesting to note that the peak tangential velocities are approximately half the magnitude of their axial flowfield counterparts indicating that the velocity field is predominantly influenced by the oscillation. The preservation of swirl above the burner exit appears to be very poor, contrary to that found by Froud et al. (1996).

As the pressure drops, changes to the axial and tangential velocity fields become more pronounced. Figure 3b shows the axial velocity contours for α=180° and 270° with figure 4b showing their tangential counterparts. This change in chamber pressure allows the annular jet located around the burner exit to rapidly expand and accelerate towards the periphery reaching a peak axial velocity of 10-13m/s when α=180°. At this point in the cycle traces of the CRZ are noted but substantially diminished, restricted to the geometric centre and lifted from the burner. Evidence of reverse flow at the wall is still evident but also significantly diminished in magnitude and restricted to occupying a thin annular area along the periphery by the rapidly growing annular jet of forward flow. When α=270° the annular jet reaches peak axial velocity, is fully expanded and accelerates along the periphery at 20m/s into the taper section to the exhaust. For the first time in the cycle forward flow occupies the entire chamber downstream. The CRZ is also fully re-established and is re-attached within the burner exit also reaching its maximum velocity albeit negative.

The re-attachment and substantial increase in negative velocity of the CRZ can be attributed to the large shear associated with the flow reversal. The reverse flow previously found at the periphery has now reduced to a corner recirculation zone as found by Froud et al.(1996), and typically found by nozzle effects of confined swirling flows by Scharrer and Lilley (1984) and Lilley (1985). The tangential velocity field also changes significantly when α=180° and 270°. When α=180° the peak tangential velocity starts to spread downstream virtually eliminating the area of negative tangential velocity at the periphery. The flowfield has also started to become more evened out over the entire chamber. The transition to α=270° shows the tangential velocity field almost uniformly blanketing the

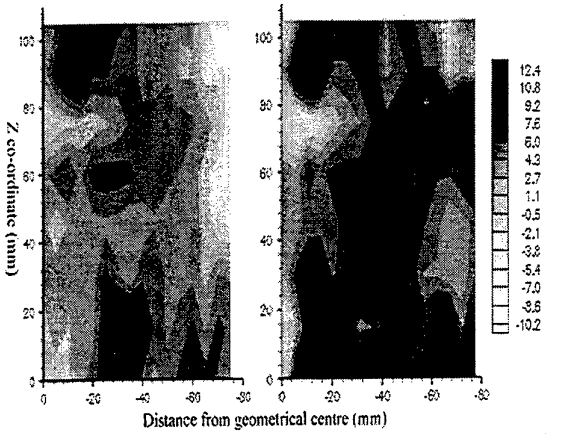


Figure 4b:Tangential Velocity Contour Plots for α=180° and α=270° Respectively

entire chamber with constant velocity again showing no distinct vortex structure.

2.2 Cycle Resolved CH Emission Results

The results in figure5a-d show eight phase angles α to characterise the cycle, corresponding to 45° increments in phase angle. As before the contour plots are presented in the same fashion. It is important to note that this technique provides a relative measurement and therefore is not calibrated to quantify the emission in terms of actual intensity. However, interest in the investigation was solely based on detecting the presence of a periodic heat release and its timing with respect to the pressure cycle in order to qualify Rayleigh criterion. To summarize briefly, according to Rayleigh criterion (Lord Rayleigh 1878) the timing of the heat release in acoustically driven combustion oscillations should coincide with the systems peak pressure to reinforce and sustain the oscillation. The results in figure 5a show the build up of CH corresponding to the beginning of the pressure cycle. When α=0°, it is evident that there is a build up of CH indicating that the reaction has already started as the pressure rises. The intensity of the reaction substantially increases to the α=45° mark where the CH release almost covers the whole chamber area. As the cycle progresses to the α=90° mark, as depicted in figure 5b, a gradual decrease in CH intensity is noticed indicating that the reaction has reached maximum intensity in and around the peak part of the pressure cycle. Hence the excitation and sustainment of the oscillation via Rayleigh criterion appears feasible. When α=135° the reaction appears to be slowing with high CH intensity traces located only at ½ radius and about 40mm above the burner exit. The phase angles of α=180°, 225° and 270° shown in figures 5c and 5d show the minimum reaction intensity as represented by the predominant light gray shades and white. Between α=225° and α=270° there does not appear to be any reaction showing that the flame is restricted below the burner exit. This occurs in situ with the lowest part of the pressure cycle and the peak velocity condition. At this time the large exhausting flow has

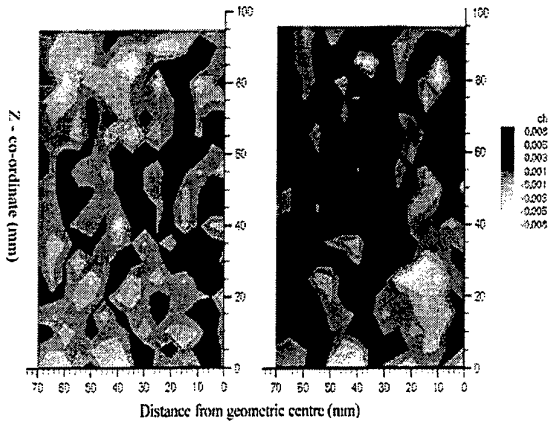


Figure 5a:Contour Plots of CH Emission for α=0° and α=45° Respectively

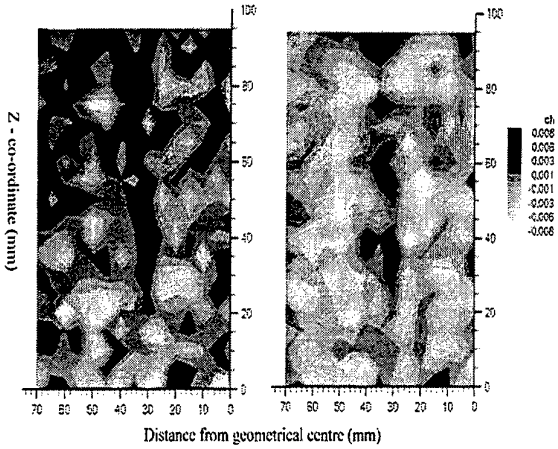


Figure 5b:Contour Plots of CH Emission for α=90° and α=135° Respectively

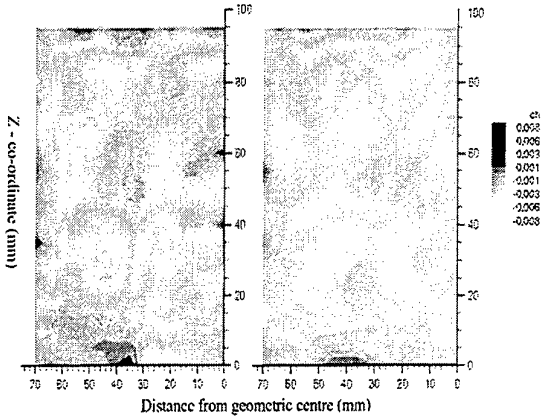


Figure 5c:Contour Plots of CH Emission for α=180° and α=225° Respectively

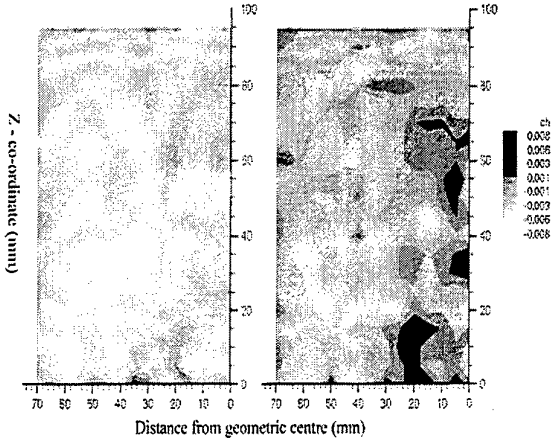


Figure 5d:Contour Plots of CH Emission for α=270° and α=315° Respectively

entrained most of the gases in the combustion chamber resulting in the suppression of the flame below the burner exit (and possibly extinction) and hence the minimum CH condition. It is also noticed that this occurs during the harmonic portion of the pressure trace as shown in figure 2. As the pressure starts to increase from its mimimum towards its maximum, evidence of reaction becomes evident along the geometrical centre. This is due to the slowing of the velocity field allowing the combustible mixture to enter the characteristic reaction zone of the burner. The relationship between the pressure cycle, velocity field and the timing of the heat release shows that this system is highly comparable to the operation cycle associated with Helmholtz pulse combustors.

2.3 Discussion

When considering the velocity results it is first noticed that the both the axial and tangential velocity fields undergo significant changes in form over the pressure cycle. In both measurements planes the pressure cycle syncronises the occurrence of the peak velocity situation in both measurement planes, in other words, there is no phase lag between the peak axial and tangential velocities as both reach their peak values during the same phase of the pressure cycle. Previous work by Froud (1995) has shown that when the PVC is present, depending on its location in the cycle, a phase shift occurs between the tangential and axial velocity fields. This suggests that the PVC phenomenon is either destoyed or absent under the excited conditions for this configuration. Further work will verify whether this occurs for other geometry changes and geometrical swirl number.

Furthermore, with reference to the tangential velocity results, it is clear that there is no coherent vortex structure or preservation of swirl above the burner exit at any time in the cycle. Also, the magnitude of velocity is half that of its axial counterpart. This, very possibly, shifts the expected swirl induced flame stabilisation duties to that of the oscillation and its associated flowfield presented in this work. This is an important result as previous work for a similar geometry by Froud et al. (1996) has shown that a stable Rankine vortex structure is kept throughout the oscillation with the axial velocities never exceeding their tangential counterparts. This implies that downstream swirl is well preserved and hence swirl induced flame stabilisation

effects still partially if not wholly intact. Based on these findings, further work aims to differentiate and classify the effect of geometry on the mechanism of oscillation and the mechanism of flame stabilisation associated with these changes.

Finally, the CH emission results show that Rayleigh criterion is satisfied as the peak heat release occurs in phase with the peak pressure. Previous work by Dawson et al.(1998) has shown that for the configuration of Froud et al.(1996) the timing of the peak heat release does not coincide with the peak pressure and suggested that this is due to the possibility of a different flame stablilisation process.

3 CONCLUSIONS

The excitation of a combustion driven oscillation via Rayleigh criterion has been shown to occur in a common swirl burner furnace configuration under compatible geometry. An investigation into the phase relationship between the velocity regime, transient but periodic pressure field and the timing of a periodic heat release has been performed showing many similarities to Helmholtz type pulse combustors. The two dimensional phase locked LDA results have shown that the velocity field is strongly coupled to the fluctuating pressure field regulating the injection of reactants into the burner and backflow of products from the exhaust section. The timing of the heat release appears to be strongly linked with the coupled velocity and pressure field as well as the mechanism of flame stabilisation.

4 REFERENCES

Bhidayasiri R. Sivasegaram S. and Whitelaw J.H.,1997, *Control of Combustion and NOx Emissions in Open and Ducted Flames*, 4th International Conference of Technologies and Combustion for a Clean Environment, Vol.2, pp.17-25.

Behrens H., *Flame Instabilites and Combustion Mechanism*, Proc. 4th International Symposium on Combustion, The Combustion Institute, Pittsburgh, USA, pp.538-545

Casentini F., Hermann D., Vortmeyer D. and Gleis S., 1997, *NO- and CO- Reduction by Pulsating the Air Flow on a Swirl Spray Burner*, 4th International Conference of Technologies and Combustion for a Clean Environment, Vol.2, pp.17-25.

Dawson J.R., Beale A.J, O'Doherty and Syred N., 1998, *Studies of Combustion Driven Oscillations in a Swirl Burner*, Proceedings of the 50th Anniversary Members Meeting of the IFRF, Vol.2 pI-6-1

Ellis H., Odgers I, Stosick A.J., Van De Verg N. and Wick R.S., *Experimental Investigation of Combustion Instability in Rocket Motors*, Proc. 4th International Symposium on Combustion, The Combustion Institute, Pittsburgh, USA, pp.880-885

Fick W., Griffiths A.J., Schoepf G. and O'Doherty T .,1998, *Quantitative Characterisation of the Precessing Vortex Core and the Vortex Breakdown Phenomena using Particle Image Velicometry*, 9th International Symposium on Applications of Laser Techniques to Fluid Mechanics, Lisbon, Portugal, Vol. 1, 3.2

Froud D.,1995, PhD Thesis, University of Wales, Cardiff

Froud D., Beale A.J., O'Doherty T. and Syred N.,1996, *Studies of Helmholtz Resonance in a Swirl Burner/Furnace System*, 26th International Symposium on Combustion, The Combustion Institute, Pittsburgh, USA, p3355

Kaskan E.W., *An Investigation into Vibrating Flames*, Proc. 4th International Symposium on Combustion, The Combustion Institute, Pittsburgh, USA, p.658

Keller J.O., Bramlette T.T. amd Westbrook C.K., 1990, *Pulse Combustion: The Quantification of Characteristic Times*, Combustion and Flame, 79:151-161

Keller J.O., Barr P.K. and Gemmen R.S., 1994, *Premixed Combustion in a Periodic Flowfield. Part I: Experimental Investigation*, Combustion and Flame, 99:29-42

Keller J.O., Barr P.K. and Gemmen R.S., 1994, *Premixed Combustion in a Periodic Flowfield. Part II: The Importance of Flame Extinction by Fluid Dynamic Strain*, Combustion and Flame, 99:43-52

Lilley D.G., 1986, *Swirling Flows in Typical Combustor Geometries*, Journal of Propulsion, Vol.2, pp. 64-72

Markstein G.H., 1964, *Non – Steady Flame Propogation*, Permagon Press, Heading Hill Hall, Oxford

Oran E.S. and Gardner J.H, 1985, *Chemical –Acoustic Interactions in Combustion Systems*, Prog. Energ. Combust. Sci., 11:253-276

Putnam, A.A., *Combustion Noise in Industrial Burners*, Noise Control Engineering, Vol.7, No.1, pp24-34

Rayleigh J.W.S., 1878, *The Explanation of Certain Acoustical Phenomena*, Nature 18,319

Roginskii O.G., 1961, *Oscillatory Combustion*, Transl. IN Soviet Physics – Acoustics, 7:107

Sarpkaya T., 1971, *On Stationary and Travelling Vortex Breakdowns*, Journal of Fluid Mechanics, vol.45, pp545-559

Scharrer G.L. and Lilley D.G., *Five–Hole Pitot Probe Measurements of Swirl, Confinement and Nozzle Effects on Confined Turbulent Flow*, AIAA paper 84-1705

Syred N and Beer J.M., 1971, *Attenuating the Precession of Vortex Cores during Combustion in a Swirler*, Gas Waerme International, Bd. 20, Nr.12

Syred N and Beer J.M., 1972, *The Damping of Precessing Vortex Cores by Combustion in Swirl Generators*, Astronautica Acta, Vol.17, pp783-801

Syred N and Beer J.M, 1973, *The Effect of Combustion upon Precessing Vortex Cores Generated by Swirl Combustors*, Proc. 14th International Symposium on Combustion, The Combustion Institute, Pittsburgh, USA, p537

Syred N., Fick W., O'Doherty T. and Griffiths A.J., 1997, *The Effect of the Precessing Vortex Core on Combustion in a Swirl Burner*, Combustion Science and Technology, Vol.125, pp.139-157

MEASUREMENT OF UNSTEADY COMBUSTION IN A SIMPLE COMBUSTOR CONFIGURATION

S. Dawson & J.A. Fitzpatrick

Department of Mechanical Engineering,
Trinity College, Dublin 2, Ireland

ABSTRACT

This paper describes results from the simultaneous measurement of fluctuating velocity and surface wall pressure during unsteady combustion in a model dump combustor. It is shown that the signals are highly correlated at both the resonant quarter wave frequency of the combustion chamber and at harmonics of the fundamental frequency. The trends in relative phase as a function of downstream position and inlet velocity are also investigated. The implication of the trends in phase are discussed and a possible driving mechanism for the instability is outlined.

1. INTRODUCTION

The drive towards 'lean burn' operating conditions for dry low emission combustion systems has resulted in an increased incidence of thermoacoustic oscillations, with the subsequent pressure fluctuations often leading to problems of flame extinction and structural vibration. The instabilities arise from unsteady heat release in the system which couples with pressure fluctuations in the combustion chamber, usually at a frequency associated with a longitudinal or bulk acoustic mode of the combustion system. In contrast to the high frequency transverse acoustic modes which traditionally arise in rocket motors, the low frequency longitudinal oscillations are difficult to suppress with traditional control techniques. Therefore, there has been renewed research effort in recent years to improve our understanding of the driving mechanisms behind the instabilities in order to develop more effective modelling and control strategies.

The phase relationships between the various fluctuating parameters in a combustion system have long been known to be of critical importance in the generation of combustion oscillations. Rayleigh (1896) noted that the generation of thermoacoustic oscillations in a duct was dependent on the relative phase between the heat transfer and the pressure oscillations, with the acoustic oscillation being amplified when the heat release and pressure waves were in phase and the oscillation being damped when they were out of phase. Investigations such as that carried out by Lang and Vortmeyer (1987), who monitored the pressure and light emission (which is directly proportional to heat release) in a laboratory combustor, have confirmed the applicability of the criterion to combustion.

The Rayleigh criterion indicates that the main mechanism by which energy may be transferred to the acoustic field is through unsteady heat input at a suitable phase relative to the pressure oscillation. Therefore, considerable effort has been directed towards the identification of the source of the unsteady heat release in various combustor configurations. Particular attention has been focussed on coherent structures in the flow as the driving mechanism for combustion instabilities, as discussed by Schadow and Gutmark (1992). Investigations such as that of Poinsot et al. (1987) have identified large scale coherent structures in the flow in a number of different combustor geometries. Schadow et al. (1989) suggest the burning of vortices as they convect downstream as a probable source of unsteady heat release.

While flow visualisation has shown that unsteady heat release is related to coherent structures in the flow for a number of geometric configurations, there is a lack of quantitative information regarding the dynamic interactions between the various parameters involved in unsteady combustion. In order to clarify these interactions, a detailed investigation of the oscillatory characteristics of a combusting flow in a very simple burner configuration has been carried out. Simultaneous measurements of fluctuating velocity, acoustic pressure, heat release and temperature in the combustion chamber have been

obtained for a range of inlet velocities and equivalence ratios. This paper describes the results from the simultaneous measurement of fluctuating velocity and wall pressure in the combustion chamber. The spectral characteristics of the parameters and their interactions are discussed. The variation in relative phase as a function of the operating conditions is also investigated, and a possible mechanism for the driving of the combustion instability is outlined.

2. EXPERIMENTAL SET-UP

A simple, small-scale, two dimensional model of a premixed dump combustor was used for the investigation. A schematic of the arrangement is shown in Figure 1. The dump combustor geometry was chosen for the study since this type of combustor has been shown to exhibit unsteady combustion over a wide range of operating conditions, as demonstrated by, for example, Sivasegaram and Whitelaw (1987). The combustion chamber was formed from 44mm x 44mm steel box section with 3mm wall thickness. The overall downstream length was 1.175m, with the open downstream end exhausting to atmosphere. The inlet plane (dump) was formed by two rearward facing steps with an expansion ratio at the dump plane of 1:8.8. The high blockage ratio at the steps ensured that acoustic resonances were uninfluenced by upstream geometry and that acoustic frequencies corresponded to a ¼ wave in the downstream duct, with a pressure antinode at the acoustically closed upstream end (at the dump plane) and a pressure node at the acoustically open downstream end (at the exhaust).

Butane was supplied from a pressurised gas cylinder with variable pressure regulator. A compressed air line, again with variable pressure regulator, provided a constant air supply. Both lines had simple gate valves to individually control the flowrates of gas and air and the flowrates were individually metered using variable area flowmeters. The butane and air was mixed a short distance upstream of the rearward facing steps in a conical expansion arrangement.

Fluctuating wall pressure was measured using a Bruel and Kjaer (type 4170) probe microphone which was water cooled. The cooling system had a semi-infinite end condition in order to minimise the distortion effects on the pressure wave. Access to the combustion chamber was provided by suitably drilled and tapped holes in the combustor wall. The probe microphone with cooling system was calibrated against a ½" microphone in an acoustic impedance rig in order to quantify the distortion effects introduced into the measured wall pressure signal.

Fluctuating velocities in the combustion chamber were measured by a single component laser Doppler anemometry system, using a TSI 32mW HeNe laser in forward scatter mode. Optical access to the combustion chamber was provided by two circular sapphire windows, 12.5mm in diameter. TiO_2 was used as seeding particles. The particles were nominally 0.25μm in diameter before agglomeration.

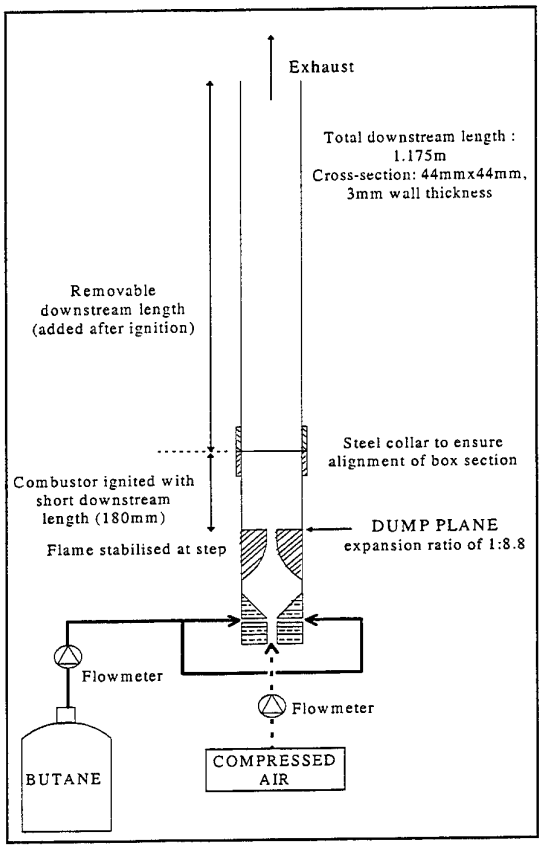


Fig.1 : Schematic of Experimental Configuration

3. DATA ACQUISITION & PROCESSING

The LDA receiving optics were connected to a TSI 1980b counter processor which was interfaced to a Pentium type PC. The LDA velocity data was acquired in the usual way from the counter of validated data and time between data points. The microphone was sampled by an A to D board (Amplicon PC-30PGL), which was interfaced to the

same Pentium type PC. LDA data points were used to trigger the A to D acquisition and both signals were reconstructed using linear interpolation at time intervals equivalent to 100kHz to give an equispaced time series. The data was then low pass filtered using an 8 pole Chebyshev filter and resampled at 1kHz with spectra computed up to 500Hz. Details of the acquisition and signal reconstruction techniques are given by Scholten et al. (1996).

Autospectra of the velocity and pressure are used to show the periodic nature of the fluctuations, while their interactions are quantified by means of coherence functions (frequency domain normalised cross covariance) and phase. The signal processing to yield auto and cross spectra was implemented using spectral analysis software written in MATLAB. Relative phases were subsequently corrected for the bias effects introduced by the microphone cooling system. Wall pressure autospectra were also corrected for the effect of the microphone cooling system.

The mean data rate was 500-600Hz for all tests. Since autospectra and coherences were computed up to 500Hz, the low pass filter effect as detailed by Adrian and Yao (1987) would be expected to be very significant. Therefore, a low pass filter correction was included in the data processing. The main objective from the phase measurements was to investigate the variation in relative phase at the quarter wave frequency. This frequency ranged from 120Hz-150Hz depending on the operating conditions. Therefore, the mean sample rate was of the order of 4 times the frequency to be resolved in all cases, and the relatively low data rate should not significantly affect the investigation into the phase relationships at the quarter wave frequency.

4. RESULTS

An equivalence ratio of 0.9 was found to correspond to the generation of a very strong pressure oscillation at the quarter wave resonant frequency of the combustion chamber for a range of inlet velocities, with harmonics of the fundamental frequency also clearly visible in the freefield pressure spectra. This investigation focussed on results at this equivalence ratio, since coupling between the various fluctuating parameters was expected to be very strong under these operating conditions. Three different inlet velocities, u_{inlet} (the cold flow velocity at the step expansion), were selected for the study - namely, 5.1m/s, 10.2m/s and 12.7m/s. In all cases, the behaviour for u_{inlet} = 12.7m/s was found to correspond closely to that at 10.2m/s. Therefore, in this paper, only plots corresponding to inlet velocities of 5.1m/s and 10.2m/s will be shown.

Wall pressure was measured 220mm downstream from the dump plane. Fluctuating velocity was measured in the mainstream flow direction, with the LDA measuring volume positioned at the midpoint of the combustor cross-section. Measurements were made at positions 25mm, 50mm, 75mm and 100mm downstream from the step expansion.

4.1 Wall Pressure Autospectra

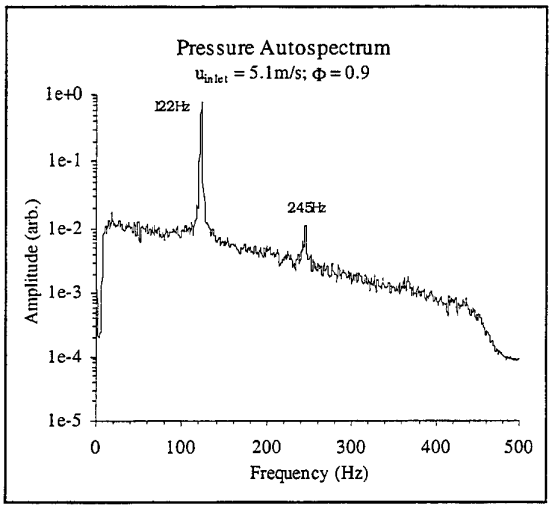


Figure 2(a) : Pressure Autospectrum, u_{inlet} = 5.1m/s

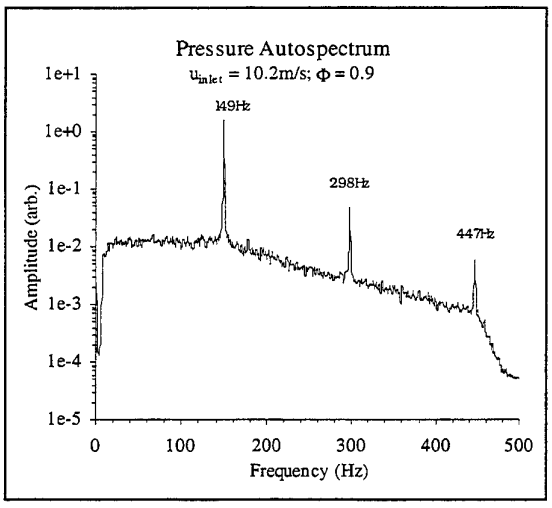


Figure 2(b) : Pressure Autospectrum, u_{inlet} = 10.2m/s

Figures 2(a) & (b) show typical wall pressure autospectra for inlet velocities of 5.1m/s and 10.2m/s. Both plots display similar trends, with a very high amplitude peak at the acoustic resonant frequency. Harmonics of the fundamental acoustic resonant frequency are also apparent in both plots.

Of particular interest is the fact that both even and odd harmonics appear in the autospectra (see Figure 2(b)). From linear acoustic theory, only duct resonances corresponding to a frequency:

$$f = \frac{n\,\bar{c}}{4\,L} \qquad (1)$$

(where L is the length of the duct, $\bar{c}$ is the speed of sound and n=1,3,5,7 etc.) are expected to be amplified in the current experimental configuration, since the step expansion acts as an acoustically closed upstream boundary condition and the exhaust acts as an acoustically open downstream end. The presence of both odd and even harmonics in the pressure autospectra is a strong indication of the non-linear nature of the combustion instability.

4.2 Velocity Autospectra

Figures 3(a) & (b) show typical velocity autospectra for inlet velocities of 5.1m/s and 10.2m/s. Velocity was measured 50mm downstream from the dump plane. As with the pressure autospectra, a peak at the quarter wave resonant frequency is visible in both plots, with the first harmonic of the fundamental frequency also clear in Figure 3(b).

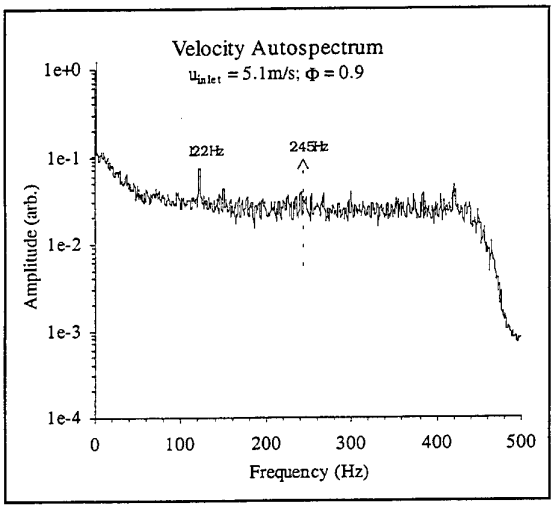


Figure 3(a) : Velocity Autospectrum, u_{inlet} = 5.1m/s

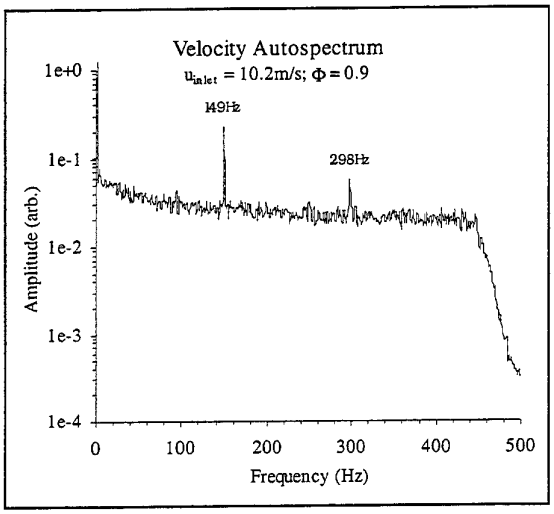


Figure 3(b) : Velocity Autospectrum, u_{inlet} = 10.2m/s

The amplitude of the quarter wave resonant peak for u_{inlet} = 5.1m/s is much lower than that observed at the higher inlet velocities, with the peak only just discernible above background fluctuations. The same observations were made for all four measurement positions downstream. The lower amplitude peaks indicate a weak periodicity in the velocity fluctuations, suggesting weaker coupling between velocity and pressure fluctuations. This may explain why peak to peak freefield pressure oscillations at this inlet velocity were found to be much lower than at the higher velocities, with the generated acoustic oscillation creating a lower pressure 'buzzing' sound which was much more tolerable than the acoustic resonances generated at higher velocities.

A number of investigations have stressed the importance of coupling between hydrodynamic instabilities in the flow and the acoustic frequencies. Jets usually exhibit a number of hydrodynamic instability frequencies as demonstrated by Schadow et al. (1989), the lowest of which is termed the preferred mode frequency. According to Poinsot et al. (1987), the Strouhal number (defined in terms of the jet velocity and the jet width at the nozzle) corresponding to this mode is expected to be approximately 0.25. For the inlet velocities investigated in this study, the preferred mode of oscillation would therefore be expected in the range of 250-640Hz. Since the observed frequencies of the fundamental acoustic mode are at least half that expected for preferred mode oscillation, it would appear that the process in the current experimental configuration is essentially an acoustically driven process, with vortex shedding being forced at the quarter wave frequency.

However, the system is known to be highly non-linear, leading to the possibility of a sub-harmonic response. Therefore, it is possible that vortex shedding at the preferred mode frequency acts as an initial trigger for the combustion oscillations. Provided that a sub-harmonic of the hydrodynamic preferred mode frequency is close to the ¼ wave frequency of the combustion chamber, the vortex shedding may trigger a perturbation in the pressure at the acoustic frequency of the system. The presence of strong pressure oscillations may, in turn, result in vortex merging to form larger vortices at a lower frequency, as was observed by Schadow et al. (1989), thus feeding more energy into the instability at the ¼ wave frequency.

4.3 Coherence

Typical coherences between velocity and wall pressure for inlet velocities of 5.1m/s and 10.2m/s are shown in Figures 4(a) & (b). In both plots, a sharp peak in the coherence levels is visible at the quarter wave resonant frequency. Clear peaks in the coherence plots at the first harmonic are also visible, even for an inlet velocity of 5.1m/s when no corresponding peak in the velocity autospectrum was observed. A peak at the second harmonic for an inlet velocity of 10.2m/s is also clear; again, no corresponding peak in the velocity spectrum was discernible. Away from the resonant frequency and its harmonics, the coherence is practically zero, indicating that the signals are completely uncorrelated at these frequencies.

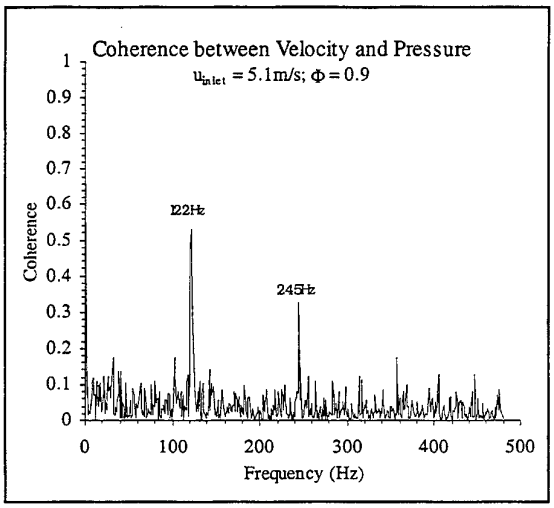


Figure 4(a) : Coherence between velocity and pressure, u_{inlet} = 5.1m/s

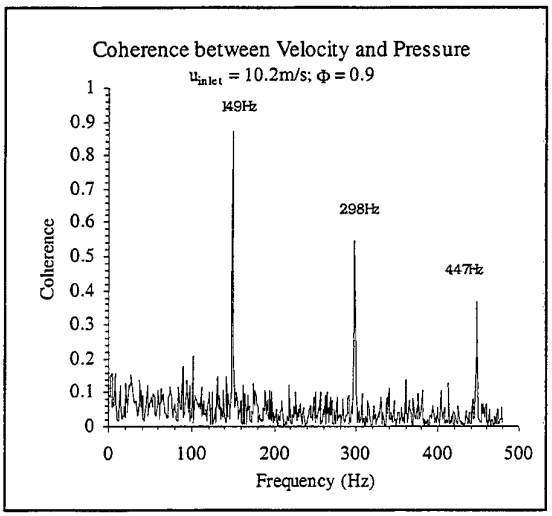


Figure 4(b) : Coherence between velocity and pressure, u_{inlet} = 10.2m/s

The fact that the signals are so coherent at the resonant frequency and its harmonics indicates that the signals are very strongly coupled. This is as would be expected from the Rayleigh criterion, which states that it is the unsteady heat release (which is related to the coherent structures in the flow) which drives the pressure oscillation. The coherence estimate for the lowest inlet velocity is much lower than that for the higher velocities. Again, this behaviour was observed for all four downstream measurement positions. The lower coherence values support the suggestion that the coupling between the fluctuating velocity and pressure is weaker for this operating conditions.

4.4 Phase

Typical phase plots for the two different inlet velocities are shown in Figures 5(a) & (b). From the plots, the phase appears to be completely random. When interpreting the relative phase, it is necessary to refer to the coherence plots again. For most frequencies, the coherence is practically zero. This indicates that the signals are completely uncorrelated and so values of phase at these frequencies are meaningless. However, at the resonant quarter wave frequency and its harmonics, the coherence is very high, indicating that the phase at these frequencies is valid. Thus, the coherence plots may be used as a validation tool, in order to select the frequencies at which the phase between the two signals is meaningful.

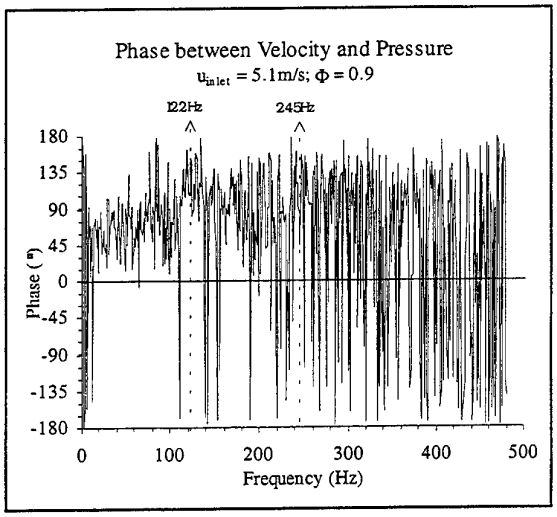


Figure 5(a) : Phase between velocity and pressure, u_{inlet} = 5.1m/s

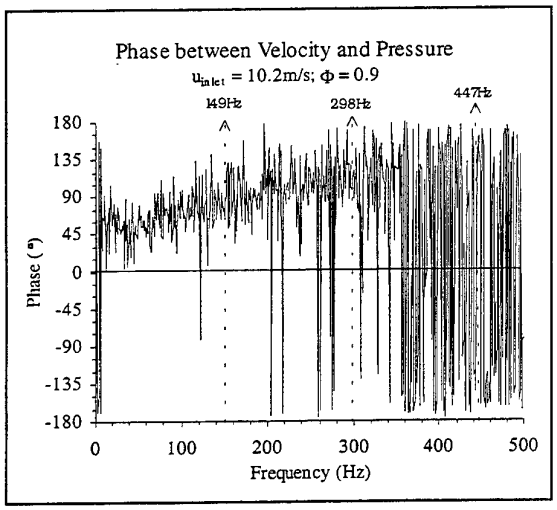


Figure 5(a) : Phase between velocity and pressure, u_{inlet} = 10.2m/s

In order to determine an empirical flame model, Bloxsidge et al. (1988) performed a number of forcing experiments investigating the phase relationships between various fluctuating parameters. The flame was operated under stable conditions and the response of the flame to imposed sinusoidal variations in inlet mass flow was monitored. It was found that the phase between the pressure fluctuations at the flameholder and the heat release rate varied linearly along the duct for each forcing frequency, with the slope of the phase with respect to downstream position increasing linearly with increasing frequency. It was concluded that fluctuations in heat release rate propagated along the duct with the same constant velocity, $\bar{U}$, for all imposed frequencies. Combining these results, the fractional change in heat release at any axial downstream position ($q'/\bar{q}$) was expressed in terms of the fractional change at the flameholder ($q'_G/\bar{q}_G$):

$$\frac{q'}{\bar{q}} = \frac{q'_G}{\bar{q}_G} e^{-i\omega\tau} \qquad (2)$$

where τ is a time lag, equal to

$$\tau = \frac{l}{\bar{U}} \qquad (3)$$

The results implied that the phase between heat release at any axial position and either heat release or pressure at the flameholder was directly proportional to the Strouhal number (St), where

$$St = \frac{f\,l}{\bar{U}} \qquad (4)$$

(f is the resonant frequency and l is the distance downstream from the flameholder). Figure 6 shows the relative phase between temperature and wall pressure in the current experimental configuration, plotted as a function of Strouhal number. From the plot, it can be seen that very similar behaviour to that observed by Bloxsidge exists in the current experimental configuration, with a linear relationship between the relative phase and the Strouhal number.

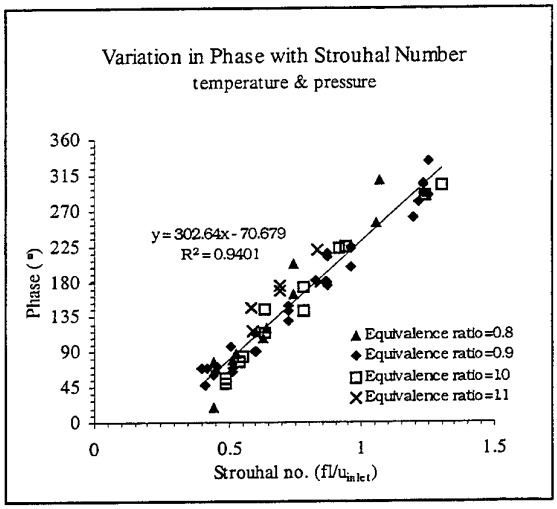


Figure 6 : Phase between temperature and pressure

In order to determine whether a similar relationship exists for the relative phase between velocity and wall pressure, a series of tests were carried out for inlet velocities of 5.1m/s, 10.2m/s and 12.7m/s, with the fluctuating velocity measured at

four different positions downstream from the dump plane (25mm, 50mm, 75mm and 100mm).

Figure 7 shows the resulting trend in phase as a function of Strouhal number. From the plot, the phase relationship between fluctuating velocity and wall pressure is in marked contrast to that between temperature and pressure, exhibiting two distinct regimes. For very low Strouhal numbers (corresponding to positions only a short distance downstream from the dump plane), the phase increases linearly with Strouhal number, as observed with the temperature/pressure measurements. A line with slope equal to that of the temperature/pressure data in Figure 6 has been included in the plot, and is shown by the dotted line in region 1 (Figure 7). The trends in the data in this region appear to mirror reasonably well the trends which were observed in the temperature/pressure data. For higher Strouhal numbers, the phase adopts a practically constant value of approximately 90° (region 2).

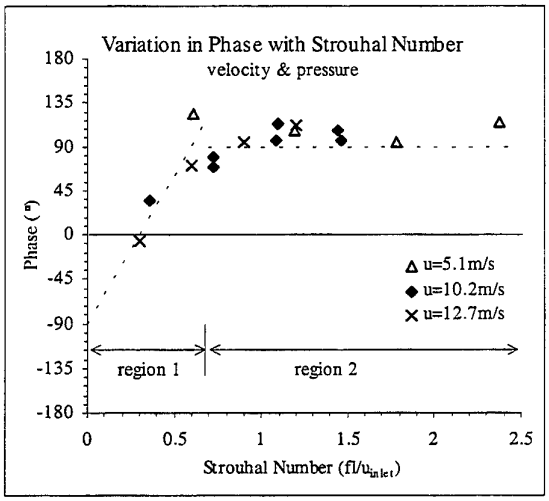


Figure 7 : Phase between velocity and pressure

The two regimes suggest a possible scenario for the generation of thermoacoustic oscillations. In the initial region, the velocity fluctuations resulting from vortex shedding convect downstream at a mean velocity close to the cold flow jet inlet velocity. At the transition point between the two regions, the vortices break down into fine scale turbulence, possibly due to impingement on the walls. The sudden increase in fine scale mixing results in periodic heat release which is convected downstream. Further downstream, the velocity fluctuations are dominated by the high amplitude pressure oscillations.

While the phase relationship between the temperature and pressure fluctuations was found to be linearly proportional to the Strouhal number for the range of downstream positions investigated in this study, it is possible that further downstream the pressure field will dominate the phase of the temperature fluctuations as was observed with the velocity fluctuations. Such a trend was observed by Langhorne (1988) in a model afterburner, with convecting behaviour extending only a short distance downstream from the flameholder. A second type of behaviour, termed 'concurrent' behaviour, was found to exist further downstream, with the phase of the C_2 radical emission (heat release) assuming an almost constant value close to that of the pressure.

5. CONCLUSIONS

The spectral characteristics and interactions between fluctuating velocity and wall pressure in a simple dump combustor have been investigated. Velocity autospectra show periodic fluctuations at the quarter wave resonance and its harmonics for all measurement positions. The peaks in the autospectra for the lowest inlet velocity appeared to be much weaker than those observed at higher flowrates, suggesting weaker coupling between velocity and pressure fluctuations. The coherences showed strong peaks at the resonant frequencies - again, the coherences for the lowest inlet velocity were much lower than for the other settings, suggesting a weaker coupling.

The frequencies of the peaks lie outside the envelope of frequencies expected for a hydrodynamic instability, and it is concluded that the resonance is essentially acoustically driven. However, since the system is non-linear, it is possible that vortex shedding at the preferred mode frequency acts as an initial trigger for the combustion instability, resulting in a sub-harmonic response of the pressure oscillation at the ¼ wave resonant frequency.

The trends in relative phase as a function of downstream position and inlet velocity have also been investigated. Two distinct forms of behaviour were observed. The first, corresponding to short distances downstream from the dump plane, indicates velocity fluctuations which are convected downstream. In the second regime, the phase of the velocity remains practically constant, indicating that the unsteady characteristics of the velocity field are completely dominated by the pressure oscillations in this region.

6. REFERENCES

Adrian, R.J. & Yao, C.S. 1987, Power Spectra of Fluid Velocities Measured by Laser Doppler Velocimetry, Experiments in Fluids, vol. 5, pp. 17-28.

Bloxsidge, G.J., Dowling, A.P. & Langhorne, P.J. 1988, Reheat Buzz : an Acoustically Coupled Combustion Instability. Part 2. Theory, J. Fluid Mech., vol. 193, pp. 445-473.

Lang, W. & Vortmeyer, D. 1987, Cross-correlation of Sound Pressure and Heat Release Rate for Oscillating Flames with Several Frequencies Excited, Combust. Sci. Tech., vol. 54, pp. 399-406.

Langhorne, P.J. 1988, Reheat Buzz : an Acoustically Coupled Instability. Part 1. Experiment, J. Fluid Mech., vol. 193, pp. 417-443.

Poinsot, T.J., Trouvé, A.C., Veynante, D.P., Candel, S.M. & Esposito, E.J. 1987, Vortex-Driven Acoustically Coupled Combustion Instabilities, J. Fluid Mech., vol. 177, pp. 265-292.

Rayleigh, J.W.S. 1896, The Theory of Sound, volume 2, p. 226, MacMillan & Co., London.

Schadow, K.C., Gutmark, E., Parr, T.P., Parr, D.M., Wilson, K.J. & Crump. J.E. 1989, Large-Scale Coherent Structures as Drivers of Combustion Instability, Combust. Sci. and Tech., vol. 64, pp. 167-186.

Schadow, K.C. & Gutmark, E. 1992, Combustion Instability Related to Vortex Shedding in Dump Combustors and their Passive Control, Prog. Energy Combust. Sci., vol. 18, pp. 117-132.

Scholten, J., Dawson, S. & Fitzpatrick J.A. 1996, Minimising Errors for Cross Spectral Analysis using Laser Doppler Anemometry Measurements, Proc. 8th Int. Symp. on Applications of Laser Techniques to Fluid Mechanics, Lisbon, pp. 36.5.1 - 36.5.7.

Sivasegaram, S. & Whitelaw, J.H. 1987, Oscillations in Axisymmetric Dump Combustors, Combust. Sci. Tech., vol. 52, pp. 413-426.

SESSION 4

VORTICES

Experimental study by white light laser tomoscopy and P.I.V. of the interaction of a vortex ring with a flat wall.

P. Dupont, O. Werquin, S. Le Mironet, M. Stanislas

Ecole Centrale de Lille - Laboratoire de Mécanique de Lille (L.M.L URA 1441)

Boulevard Paul Langevin 59 655 Villeneuve d'Ascq

Email : stanislas@ec-lille.fr

ABSTRACT

The interaction of a vortex ring impinging normally on a flat fixed wall is studied. Laser tomoscopy with a white light laser and Particle Image Velocimetry (P.I.V.) are applied using a direct acquisition of the video signal at 25 images/s. This allows to study the phenomenon as a function of time.

1. INTRODUCTION :

Eddies of the order of 100 wall units have been put to evidence in the near wall region of a turbulent boundary layer (Falco 1980). They have been identified as playing an important role in the transfer and production of turbulent energy. The flow in that region being quite intricate, it is interesting to isolate simpler mechanics, so as to better understand these phenomena. This approach has been proposed by Falco (1980-1982) for the interaction between a vortex ring and a Stokes Layer. The interaction of a vortex ring with a fixed wall has also been the subject of several studies both theoretical and experimental (Walker et al 1987, Chu C.C. et al 1995, Shariff et al 1994). They have shown a strong departure from the inviscid theory. The ring always rebounds on the wall, generating in most cases a secondary and even a tertiary vortex. This secondary vortex interacts strongly with the main one and depending on the Reynolds number, can bring it to instability and destruction. Presently, most experimental studies have been done by visualization only. The aim of the present work is to provide some quantitative results with the help of Particle Image Velocimetry. Moreover, color light sheet visualization is used in order to try to get more insight in the way the vortex interacts with the wall.

2. EXPERIMENTAL SET-UP

The tests were performed with the set-up presented in figure 1. The vortex generator is similar to the one used by Chu et al (1993). It works by gravity. An electrovalve allows to output a small volume of fluid from a reservoir through a rigid cylindrical tube of inside diameter D_H = 30 mm. This vortex generator is placed vertically in a water tank fully made of good quality glass. A glass plate is placed horizontal at 10 cm from the bottom of the tank. The opening time of the electrovalve, the height of the reservoir and the distance between the vortex generator outlet and the flat plate are adjustable.

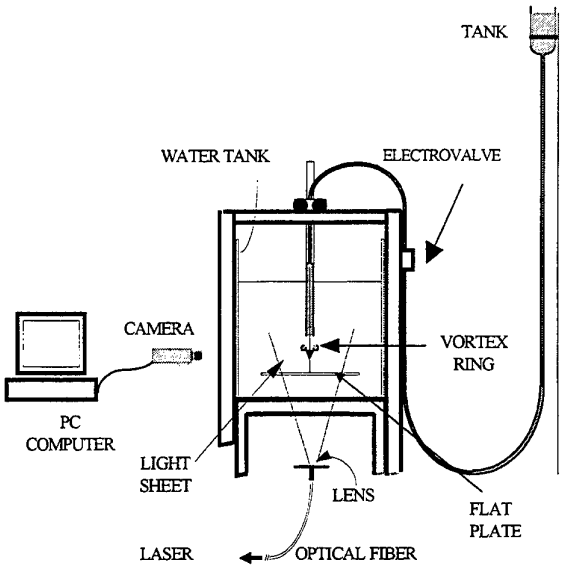


Figure 1 : Experimental set-up

First an Argon-Krypton white light laser has been used for tomoscopy. Sequences of images were recorded both with a Nikon FM 12 photographic camera and with a Panasonic WV-CL350 color video camera. Two different dyes were used : fluoresceine at 2% in the vortex generator and a red food dye on the plate. The field of view was 68*89 mm^2.

In a second step, a pulsed Yag Laser, with an energy of 2*140 mJ and a repetition rate of 12.5 Hz was

used to record P.I.V. images. The light sheet was 1*80 mm^2. Due to the high power of the laser, no seeding was needed. The light scattered by the very fine particles in the water was enough to record good P.I.V images. For the recording, a Pulnix TM6-AS was used in conjunction with a PC micro computer and a Miro frame grabber. This camera provides 760*570 pixels full frame images. The field of view at the scale of flow was 54.7*41 mm^2. Sequences up to 20 s of cross correlation records were registered at the rate of 25 im/s. For this purpose, Miro DC20 compression was used to store the data at the video rate on a disk. The time interval between the two laser pulses was typically 0.04 s. An electronic was developed to synchronize the laser with the camera. The images were analysed by cross correlation, with 32*32 windows, with 50% overlapping and a gaussian peak fitting algorithm.

3 RESULTS.

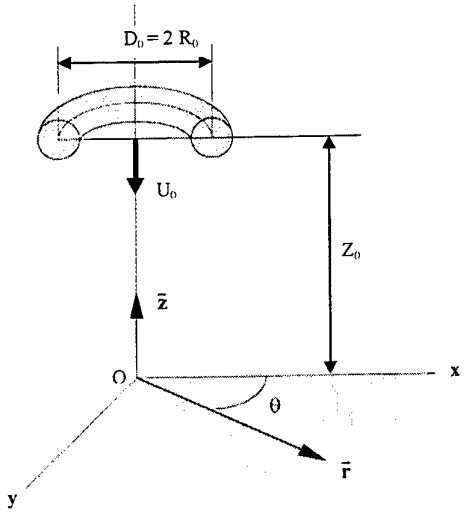


Figure 2 : Reference frame

The reference frame is presented in figure 2. The origin is at the intersection of the tube axis and the surface of the plate. For the interaction, the characteristics of the vortex ring are defined at $Z_0 = 3\ R_0$ were R_0 is the radius of the fully developed ring. It was also checked that $Z_M - Z_0 \geq 2.5\ D_M$, were Z_M is the height of the orifice of the tube. At this distance, the ring is fully developed. D_0 and U_0 are respectively the diameter and translation velocity of the ring at Z_0. The corresponding Reynolds number is $R_{e0} = U_0 D_0 / \nu$. The maximum vorticity measured in the core of the vortex at this altitude is ω_{0max}. To give an order of magnitude at R_{eo} = 705, D_o = 39.11 mm, and U_o = 16.42 mm/s.

All the experimental results are made non dimensional with U_0 and D_0, except the time which is non dimensionalized with U_0 and R_0 in agreement with Chu et al (1995) :

$$t^+ = t \cdot \frac{U_0}{R_0}$$

3-1 Mains characteristics of the fully developed ring

Figure 3 gives a tomoscopic image of the vortex ring at Z_0 for R_{e0}= 630. The ring is visualized by seeding only the reservoir fluid. The symmetry has been verified and only half of the ring is recorded to enhance the resolution.

Figure 4 presents a PIV record of the same vortex at the same location. As can be seen the seeding is quite homogeneous and the ring cannot be detected in the image.

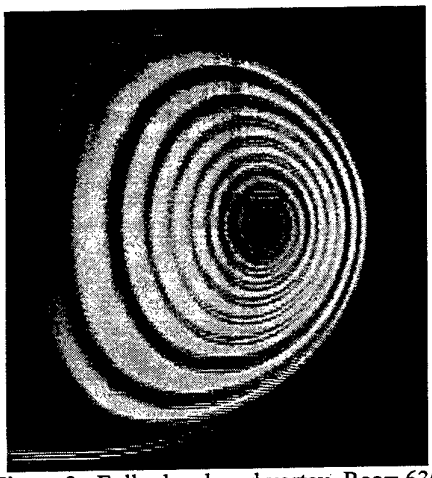


Figure 3 : Fully developed vortex, Reo= 630

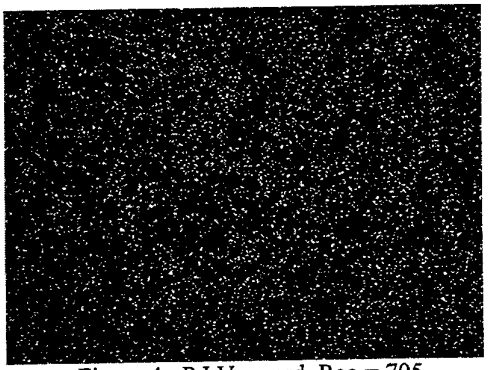


Figure 4 : P.I.V record, Reo = 705

Figure 5 present the velocity map of the ring at Z_0. Figure 6 gives the corresponding vorticity map ω/ω_{omax}. These maps have been obtained by averaging 30 realizations in order to reduce the effect of random errors. Two kinds of errors affect the computation of ω : the truncation error which decreases if h is reduced and the uncertainty on the velocity which is of order 1/h and increases when h diminished. Solutions have been proposed by Lourenco (1996) to increase the accuracy on ω. Here, the vorticity is computed with a centered finite difference scheme with a truncation error of order h^3. The vorticity map in figure 6 compares quite favourably to the one obtained by Shariff et al (1994) by DNS at a Reynolds number $R_{e0} = 2100$. This is confirmed by Figure 7 which presents two vorticity profiles in the radial and vertical direction passing through the center of the vortex. The experimental results are again compared to the DNS by Shariff et al (1994) and show a very good agreement. This indicates a good choice of the scaling parameters.

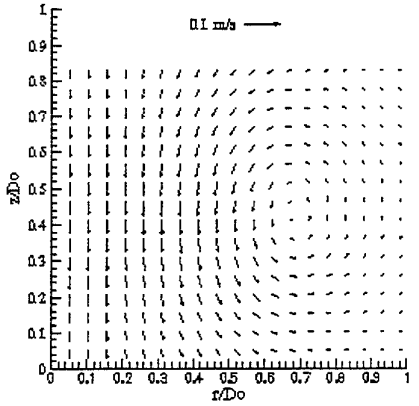


Figure 5 : Reo = 705, velocity map at Zo, averaged on 30 records

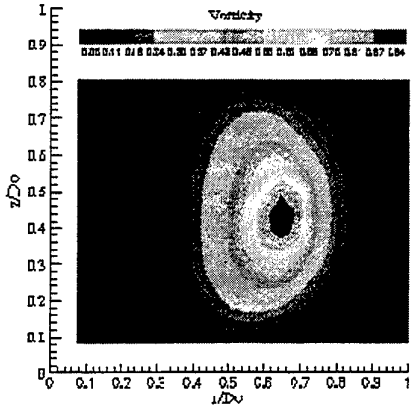


Figure 6 : Reo = 705, vorticity map at Zo, Averaged on 30 records

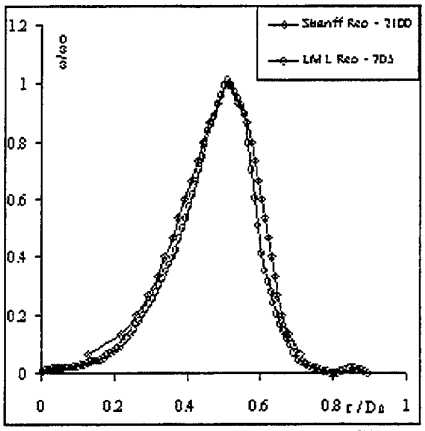


Figure 7 a: Radial vorticity profile Compared to Shariff et al

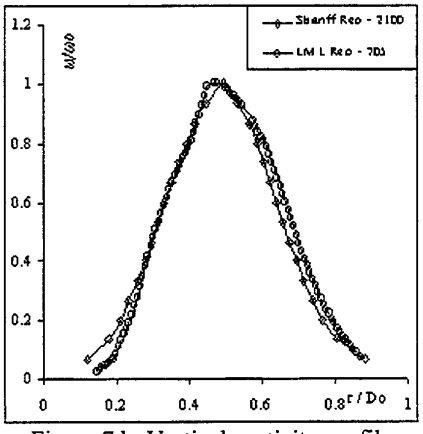


Figure 7 b: Vertical vorticity profile Compared Shariff et al

3-2 Vortex ring wall interaction :

A typical sequence of tomoscopy obtained with the white light laser and with two dyes is presented in figure 10 for Reo = 530. These are photographic images, which clearly show the entrainement of the wall fluid by the main vortex and the formation of secondary vortices. A video film is also available and is presented at the conference.

When the vortex approaches the wall, a separation of the near wall fluid occurs by entrainment. A secondary vortex is formed which is counter rotating as compared to the initial one. This secondary vortex is entrained around the main one and interacts strongly with it. At the end of the sequence a third vortex, also counter rotating starts to form. The laminar entrainement of near wall fluid is made clearly visible by the use of the two colors.

These images can be easily analyzed to trace the center of the vortex ring. A comparison with the results of Walker et al 1987 have been performed and is presented in figure 9. As can be seen, if the general behaviour is quite comparable, there is a discrepancy of about 5% in the position of the extremum which corresponds to the emission of the second vortex. This can be attributed to a size effect (determination on D_0): Walker experiments were carried out by global visualizations, using an extended white light source. This can explain the fact that the estimation of D_0 was less precise in their case. Chu et al (1995) locate this point at 1.83 by laser tomoscopy at R_{e0} = 830 which is much nearer to the present results.

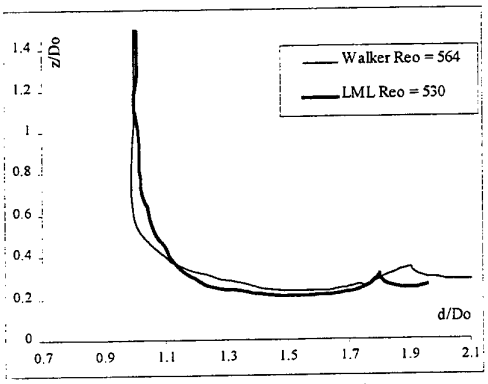


Figure 9 : Trajectory of vortex ring center

Figure 11a presents the PIV velocity fields at Reo = 707. The bottom of each figure corresponds to the wall. Each velocity field has been averaged on 20 realizations. Figures 11b presents the corresponding vorticity maps. The velocity maps clearly shows the primary vortex, while the secondary vortices are more visible on the vorticity maps. Their intensity is about 24 % of ω_0 for the second vortex and 18% for the third one. These maps agree quite well with the numerical simulation of Chu et al (1995), which is presented for Reo = 714 in figure 4 of the reference.

4 CONCLUSION :

An experiment has been built in order to study the interaction of a vortex ring with a flat wall by both PIV and tomoscopy. The results obtained show that tomoscopy is a good way to visualize this phenomenon and that it allows to locate the center of the vortex more precisely than global vizualization. The use of a white light laser offers the opportunity to seed different regions of the flow with dyes of different colors. This is helpful for the physical understanding of the flow. The PIV results agree quite well with DNS by Shariff et al (1994) for the free vortex and shows that the characteristic parameters chosen are well suited. The trajectory of the main vortex center is in good agreement with the results of Walker et al (1987) and Chu et al (1995). The vorticity of the main vortex is given as a function of time and the vorticity of the second and third vortices is estimated experimentally for one value of the Reynolds number.

REFERENCES :

Chu C.C, Wang C,. Hsiet C, 1993, An experimental investigation of vortex motions near surfaces. Phys. Fluids A 5.

Chu C.C., Wang C., Chang C., 1995, A vortex ring impinging on a solid surface-Vortex structure and surface force, Phys. Fluids 7 June

Didden N. , 1979, On the formation of vortex rings: rolling-up and production of circulation. Journal of Applied Mathematics and Physics (ZAMP), vol. 30, pp. 101-116.

Falco R.E., 1980 , The production of turbulence near a wall . AIAA, Pap. N°80-1356.

Falco. R. E,. 1982, A synthesis and model of turbulence structure in the wall region. Physics of Isothermal Flows, pp.43-55.

Lourenco. L. M.,1996: Post processing techniques in particle image velocimetrie. VKI LS 1996-03, pp.88-92.

Orlandi P., Verzicco R., 1993 : Vortex rings impincting on walls : axisymmetric and three-dimensionnal simulations. J. Fluid Mech., Vol. 256, pp. 615-646.

Shariff. K., Orlandi. P. et Verzicco. R., 1994: A numerical study of three-dimensionnal vortex ring instabilities: viscous corrections and early nonlinear stage. J. Fluid Mech., Vol. 279, pp.351-375.

Walker J.D.A, Smith C.R Cerra, A.W. and Doligalski T.L, 1987, The impact of a vortex ring on a wall., J. Fluid Mech., vol. 181, pp. 99-140.

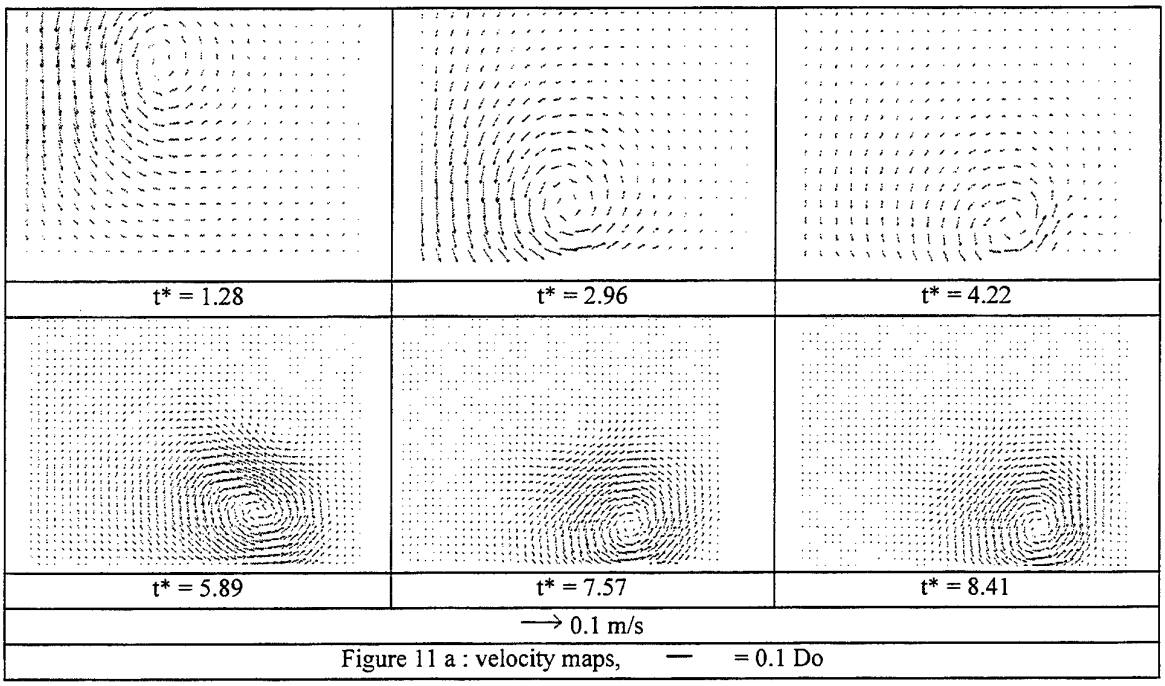


Figure 11 a : velocity maps, — = 0.1 Do

THE APPLICATION OF LASER DIAGNOSTICS TO CYCLONIC FLOW WITH VORTEX PRECESSION

A.J. Hoekstra, A.T. Israël, J.J. Derksen and H.E.A. van den Akker

Kramers Laboratorium voor Fysische Technologie
J.M. Burgers Center for Fluid Mechanics
Delft University of Technology
Prins Bernhardlaan 6, 2628 BW Delft, The Netherlands

ABSTRACT

The core region of the flow field in a gas cyclone separator is dominated by a coherent, low frequency oscillation known as the precessing vortex core (PVC). Due to its spatial character, the PVC hampers the interpretation of velocity data obtained with LDA. To properly evaluate numerical predictions, a correction procedure is needed to separate turbulent and pseudo-turbulent fluctuations. Both PIV and quantitative visualization have been applied to obtain information on the spatial distribution of the PVC and its effect on the flow field. It is shown that a large part of the measured velocity fluctuations in the vortex core can be attributed to the periodic motion of the vortex core and should be considered as pseudo-turbulence.

1. INTRODUCTION

A prominent industrial application of strongly swirling flow is the gas cyclone separator. Although of a geometrically relative simplicity, a cyclone suffers from complex flow features, such as axial flow reversal and strong anisotropy of the Reynolds stresses. These complex features are mainly due to the strong coupling of the tangential velocity component and radial pressure gradient. Generally, only second-moment closure turbulence models are capable of capturing these flow characteristics.

An additional flow phenomenon related to strongly swirling flows is known as the precessing vortex core (PVC), which has already been observed by Smith (1962) and Chanaud (1965) in laboratory scale cyclones. Both authors experimentally observed a time-dependent periodic motion, with a frequency proportional to the flow rate through the device. Until now, the nature of this phenomenon is poorly understood. Chanaud (1965) suggested that vortex precession be closely related to vortex breakdown flows. Garg and Leibovich (1979) applied spectral analysis of LDA measurement data to describe the occurrence of vortex breakdown in a swirling flow. They obtained reasonably good agreement between measured dominant frequencies and predictions by use of a linear inviscid stability analysis.

The presence of a precessing vortex core in a gas cyclone affects the mean and fluctuating velocities as measured by one-point experimental techniques such as Laser-Doppler Anemometry (LDA). Numerical predictions based on the Reynolds averaged Navier-Stokes (RANS) equations and second moment closure do not resolve the precessing vortex core. For the purpose of validating such simulations by means of experimental LDA data, the effect of the PVC on the measured gas flow field in cyclones needs to be estimated. Basically, there is need for a procedure to separate turbulent and pseudo-turbulent fluctuations, which can be attributed to vortex precession. As will become clear in section 3, in particular the vortex core region is affected by the motion of the PVC.

2. THE EFFECT OF VORTEX PRECESSION

In general, two different approaches can be distinguished for considering the effect of the PVC on LDA measurements of the strongly swirling mean flow field. The first approach starts from the observation that the LDA coordinate system is fixed to the cyclone wall rather than to the rotating vortex core center. Hence, the axi-asymmetric motion of the vortex core induces a time-dependent variation of the mean velocity in the LDA measurement volume.

This phenomenon can be compared with the motion of the impeller in a stirred tank reactor. Because the impeller motion is externally triggered,

phase resolved measurements are capable of capturing turbulent quantities without a contribution of pseudo-turbulent fluctuations (see Derksen *et al.* 1998). This is more complicated for the precessing motion of the vortex, which is internally driven, and can have spatial irregularity.

Yazdabadi *et al.* (1994) obtained a clearly sinusoidal PVC signal by use of a hot wire probe as a triggering device to obtain phase-resolved measurements of the swirling flow field in the exhaust pipe of a cyclone. A comparable technique was applied by Liem & Van Den Akker (1992) and Fokke *et al.* (1994) for the velocity field in a hydrocyclone, where the extrema in the axial velocity profile are corrected by use of a filtering procedure on the LDA time series. A more advanced filtering technique, known as adaptive noise canceling, was applied by Hoekstra *et al.* (1998a) for estimating the periodical component in the LDA time series iteratively. All these correction procedures are used to determine phase resolved *mean* velocity profiles, but it appears that they are hardly capable of accurately separating the turbulent and pseudo-turbulent *fluctuations*.

A second approach that aims to correct RMS profiles for vortex core precession was proposed by Volkert *et al.* (1996). They describe the spatial character of the PVC in a rapid compression machine by use of a 2-dimensional probability density function (PDF) of the vortex center. This PDF was obtained by measuring a series of instantaneous flow fields by use of Particle Image Velocimetry (PIV). Two different approaches for obtaining the PDF from PIV data were described in Grosjean *et al.* (1997). Although the mean velocity field in a gas cyclone significantly differs from that studied by Volkert *et al.* (1996), it will be shown that their methodology can be applied to cyclonic flows as well.

The work presented in this paper is part of an ongoing project on the experimental and numerical investigation of high-efficiency gas cyclones with low solids loading. The established centrifugal field and the turbulence level largely determine the collection efficiency of these devices. Hence, a correct estimation of the mean and turbulent velocities, without the contribution of the PVC, is needed. The effect of the PVC on the flow field is studied in a simple laboratory scale vortex chamber. First, the effect of the PVC on the flow field is described analytically to illustrate its effect on measured quantities. Measurement results on the flow field, which are obtained by LDA and PIV, will be presented together with a quantitative visualization of the vortex core motion. Finally, the paper will end with a discussion and with concluding remarks.

3. A PRECESSING VORTEX CORE MODEL

The vortex flow in cyclones is usually described in terms of a core region, which is dominated by a forced vortex near the centerline and an annular flow region with a free-vortex type of swirl distribution. This is also known as a combined vortex that can be analytically described by Burgers' vortex:

$$W(r) = \frac{\Omega}{r}\left[1 - e^{-\beta r^2}\right] \qquad (1)$$

where Ω is the swirl level and β is related to the size, r_c , of the vortical core; $r_c = 1.12 / \beta^{1/2}$. By use of this expression it is possible to describe the effect of the PVC on the flow field with a simple model for its motion.

Assume the PVC can be defined as a rotational motion of the vortex core center about the axis of symmetry with a constant angular frequency, ω, and a constant radius, r*, which is smaller than the vortex core radius r_c. The swirl distribution is defined by Burgers' vortex, and is a function of the distance from the origin of the PVC, r'. The position of the LDA measurement volume is defined by vector **r**, such that **r'** = **r** - **r***. In figure 1, a graphical representation of the PVC model is given. The measurement volume is positioned along the *x*-axis; hence, the measured velocity component, W_{meas}, is perpendicular to this axis. This implies that only part of the velocity according to the Burgers' vortex, W, is measured depending on the angle α between the two vectors.

The measured velocity component, W_{meas}, can now be expressed as a function of the circular motion of the PVC:

$$W_{meas}(r,t) = \left[\frac{r - r^* \cos(\omega t)}{r'}\right] W(r') \qquad (2)$$

In figure 2, the effect of the PVC according to this model is illustrated for an arbritary Burgers' vortex. The size of the vortex core is 0.2R, where R is the radius of the cyclone, and the PVC is assumed to move in a circular orbit with radius r* = 0.05R. By taking the PVC into account, the maximum tangential velocity is slightly reduced and there is a small increase of the vortex core. The magnitude of both effects is related to the size of the vortex core and to the amplitude of the PVC.

The model also illustrates the contribution of the PVC to the signal variance, which can not be attributed to turbulence. The RMS level is high in the vortex core and decays towards the wall.

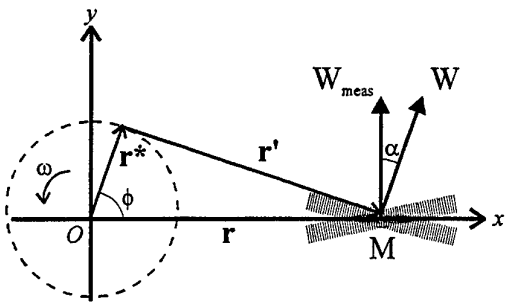


Fig. 1 Graphical representation of the PVC and its effect on the measured velocity component

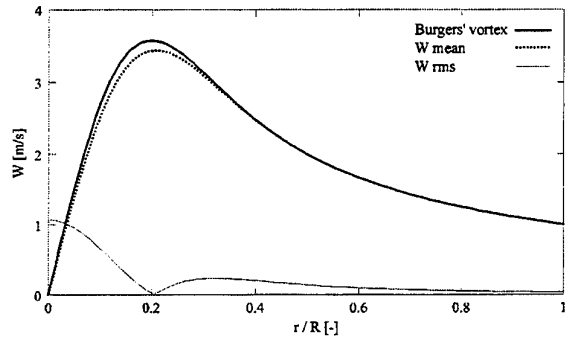


Fig. 2 Application of Burgers' vortex with $\Omega = 1.0$ and $\beta = 31.4$ to PVC model

Note that at r = R the RMS is not equal to zero, because no wall effects are taken into account. A remarkable minimum in the RMS level exists on the edge of the vortex core. It appears that the contribution of the PVC to the RMS level depends on the distance between the LDA measurement volume and the rotating center of the vortex; the local gradient of the mean velocity distribution plays a role, too.

The effect of the vortex core precession on the measured velocity component in the measurement volume is illustrated in figure 3 for three different positions of the measurement volume along the *x*-axis. The effect has been plotted versus the phase $\phi = \omega t$ of the PVC. The vortex precession results in a periodical signal of the measured velocity component at each position, although the amplitude varies. The signal in the vortex core region has a phase lag of π rad with respect to the signal in the free-vortex region. This phase lag should be taken into account when determining phase-resolved mean velocity profiles (see Hoekstra *et al.* 1998a).

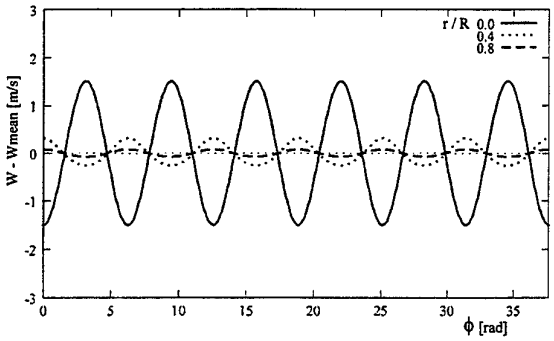


Fig. 3 Fluctuating velocity signal for three radial positions of the LDA measurement volume according to the PVC model for six revolutions of the PVC origin

The velocity signal at position r / R = 0 shows that the amplitude of the signal corresponds to W(r = r*). This implies that the radius of the PVC can be estimated from the signal amplitude A_W at r = 0 and the angular velocity of the solid body rotation:

$$r^* \approx A_{W(r=0)} \Big/ \left(\frac{\partial W}{\partial r} \right)_{r=0} \qquad (3)$$

From actual LDA time series, the amplitude of the signal may hardly be obtained, because of the presence of turbulent fluctuations and owing to the structure of the LDA signal itself, which consists of non-equidistant samples. Furthermore, the PVC was assumed to exhibit a circular motion with constant radius; this still has to be verified experimentally.

4. EXPERIMENTAL ANALYSIS

4.1. Experimental Set-up

Experiments were carried out in a laboratory scale gas cyclone or vortex chamber of 100 mm diameter. The vortex flow was generated by a tangential inlet at a flow rate of 16.3 m^3/h. The perspex model had a flat bottom plate to facilitate visual observation. The air was exhausted to the atmosphere through an exit pipe or vortex finder 50 mm in diameter. The swirling flow in a cyclone can be characterized by the Reynolds number, *Re*, and a swirl parameter, *S*, which is some measure of the ratio of angular to axial momentum. For cyclonic flows, *Re* is usually defined by the inlet velocity and the inlet width, while *S* is a geometric swirl number, defined by Gupta *et al.* (1984):

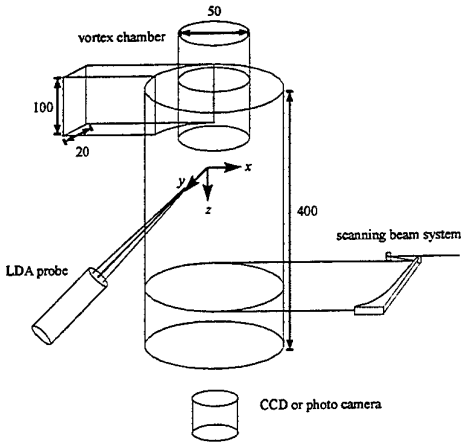


Fig. 4 Experimental set-up of vortex chamber

$$S = \frac{\pi R_c R_e}{A_{in}} \qquad (4)$$

where R_c and R_e are the cyclone and exit pipe radius, respectively, and A_{in} is the area of the tangential inlet. For the geometry studied, $Re = 3\ 10^3$ and $S = 2.4$. A schematic representation of the experimental set-up and the measurement stations is given in figure 4.

4.2. LDA Measurements

A two-component Laser-Doppler anemometer was used to measure the tangential and axial velocity components. The LDA was operated in backscatter mode, and signal processing was performed by use of a Doppler burst correlator of TSI (IFA 750). The laser beams were focused with a 250 mm lens to obtain a measurement volume of approx. 0.78 mm in length and 0.078 mm in width. Due to the cyclone wall thickness of 5.0 mm, the two measurement volumes did not exactly coincide at all radial positions. Measurement results presented here were corrected for the optical distortion due to the perspex wall.

Seeding particles were provided by a pressured air atomizer to obtain water/glycerol droplets of approx. 2 μm diameter. Because of the separation characteristics of a cyclone, very few seeding droplets were present in the vortex core region. The data rates obtained varied from 300 Hz in the outer vortex region to just a few Hz near the centerline.

Velocity profiles were measured along the cyclone radius at four axial measurement stations. These stations were located in the separation section

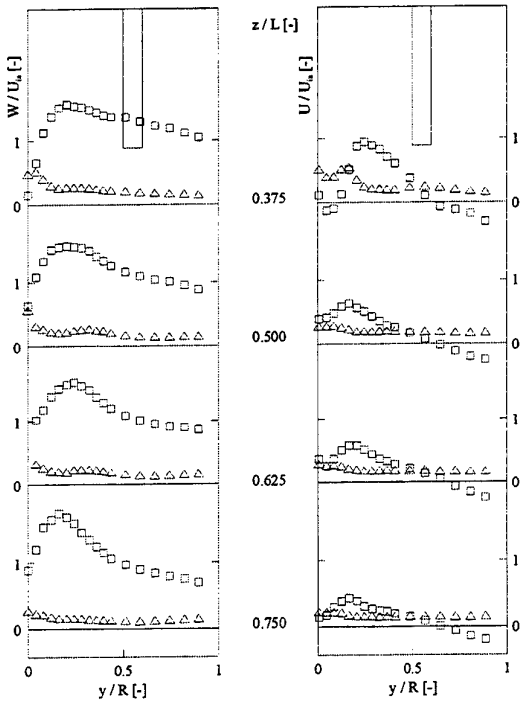


Fig. 5 Tangential (left) and axial (right) mean velocity (□) and RMS (Δ) profiles at measurement stations z/L = 0.375, 0.500, 0.625 and 0.75. All profiles are normalized by the inlet velocity

between the vortex finder and the flat bottom plate. The mean velocity and RMS profiles for the tangential and axial velocity component are presented in figure 5. All statistics were derived from 10^3–10^4 data points per channel, depending on the radial position.

The tangential velocity profiles largely exhibit the well-known Burgers' type of distribution. There is an axial downflow near the wall and an annular upflow region near the center of the cyclone. Close to the vortex finder the vortex core is a region of axial velocity deficit and even reverse flow (also observed by Fokke *et al.* (1994) in a hydrocyclone). The maximum axial velocity corresponds to the position of the edge of the core region (see also Escudier *et al.* 1984). At all levels a small axi-asymmetry of the velocity profile can be noticed.

For both components the RMS level is almost constant along the radius, but increases in the vortex core region and the near wall region. In the vortex core, part of the RMS level can be attributed to the precessing motion of the vortex core, as discussed in section 3.

The presence of a precessing vortex core is revealed by a frequency analysis of the LDA time series. Normalized power spectral estimates of the

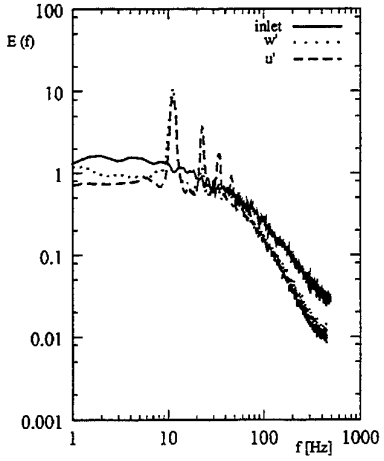


Fig. 6 Power spectral estimates at the inlet section and of the tangential and axial velocity fluctuations at y / R = 0.50 and measurement station z / L = 0.375.

tangential and axial velocity fluctuations are presented in figure 6. Spectral estimates were obtained by a FFT of the time series that were re-sampled at the mean data rate (800 Hz) using linear interpolation. The time series consisted of approx. 10^5 data points for each channel. Both channels show a distinct low-frequency peak at 11 Hz, which can be attributed to the PVC, together with some harmonic components (also observed by Garg & Leibovich 1979). The PVC is driven internally, as proven by the absence of low-frequency oscillations in the inlet flow.

4.3. PIV Measurements

Because of its spatial character, the motion of the PVC could be quantitatively captured, at least in principle, by applying a whole-field technique such as Particle Image Velocimetry (PIV). Although the spatial and temporal resolution of most PIV set-ups is insufficient for the statistical description of the *turbulent* flow variables, the large-scale motion of the PVC could be described in terms of a spatial-correlation map (see Grosjean *et al.* 1997).

The consistent effect of the PVC on the flow field in a radial plane of the vortex chamber was investigated by use of a PIV system. Illumination of the seeding particles was obtained by applying a scanning beam system (Gray *et al.* 1991), which consisted of a 4 W Ar^+ laser, a beam splitter to separate two beams of equal intensity, a rotating polygon mirror, and a parabolic mirror to effect a linear displacement of the laser beam through the measurement volume. The seeding consisted of water/glycerol droplets with fluorescine to improve

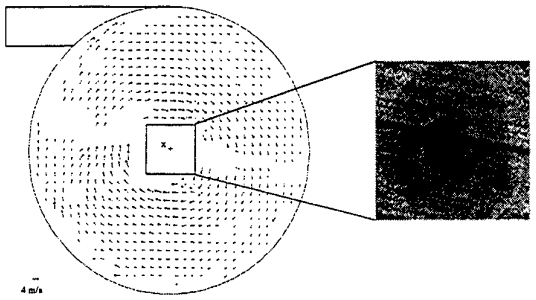


Fig. 7 Vector field at radial plane z / L = 0.75 obtained with PIV. The geometric center is given by (+) and the approximate position of the vortex core by (x). In the vortex core few particles are present.

light scattering. The laser beams were swept through the radial plane at z / L = 0.75 with a temporal separation of 0.21 ms. The doubly exposed images were registered by a conventional photocamera, and digitized to 2240x2240 pixels. The size of the interrogation areas was varied between 64x64 and 128x128 pixels, and processed by use of the autocorrelation function. A vector field obtained with this procedure is shown in figure 7. Due to reflections at the wall, it was not possible to compute good vectors at all radial positions. Near the geometric center, the images were blurred due to low concentrations of seeding droplets.

Estimating the vortex core origin by interpolating the vector field was done by Grosjean *et al.* (1997). In our tests, however, the virtual absence of droplets in the vortex core makes it possible to track the vortex core motion directly by registration of the dark area depicted in figure 7. The current set-up for the PIV experiment, where the flow field is projected on photographic film, proved to be unpractical for the purpose of accurately estimating the effect of the PVC on the flow field.

4.4. Visualization Of The Vortex Core

The vortex core motion was registered by use of a CCD camera with a spatial resolution of 256^2 pixels at an image acquisition rate of 40 Hz. As spectral analysis pointed out, the PVC moves at approx. 11 cycles per second; this implies that the sample rate obeys the Nyquist criterion for resolving the fluctuations. The total number of samples obtained was 1,200. The PVC was visualized by sweeping an Ar^+ laser beam through the measurement plane, at an axial station of z / L = 0.75, at high frequency (typically 3 KHz) to obtain a pseudo-sheet of light. The data were processed by image processing

software. The gray-value pictures were thresholded to separate background and object information. The objects were converted to binary images, and of each object the center of mass was determined with a spatial accuracy of 0.13 mm/px and stored.

The spatial distribution of the vortex core center obtained with the procedure described above, showed, that the PVC is not rotating at constant radial distance of the cyclone's axis, as was assumed in section 3. Rather, a probability density function is needed to describe the spatial path of the core center. This approach has been developed by Volkert *et al.* (1996) and will be applied to the experimental data presented here.

The projection of the vortex center on the *x*- and *y*-axis (see figure 8) can satisfactorily be described by two independent Gaussian probability density functions, $p_x(x)$ and $p_y(y)$, to form the following joint probability density function:

$$p(x,y)=\frac{1}{2\pi\sigma_x\sigma_y}e^{-\frac{1}{2}\left[\frac{x^2}{\sigma_x^2}+\frac{y^2}{\sigma_y^2}\right]} \qquad (5)$$

where $p(x,y)=p_x(x)p_y(y)$. The standard deviation σ_x and σ_y of this 2D PDF are to be determined from the experimental data and were estimated as 1.2 mm and 0.91 mm, respectively. Evidently, the mean position of the vortex core origin does not coincide with the axis of symmetry of the cyclone. This effect has also been observed by Escudier *et al.* (1980) for strongly swirling pipe flow. The mean vortex position was estimated from Gaussian fits as $\mu_x = -0.92$ mm and $\mu_y = -0.75$ mm, respectively.

The probability function for the radius of the vortex core center with respect to the time-averaged core position, p(r*), can be described by a Rayleigh distribution. If the variances of the two independent PDF's for x and y are equal, $\sigma_x^2=\sigma_y^2=\sigma^2$, the most probable value of the Rayleigh distribution is equal to σ. This means that $r^* = \sigma$ could be interpreted as the amplitude of the PVC.

The methodology due to Volkert *et al.* (1996) of accounting for the effect of the PVC on the signal variance, at a certain position of the LDA measurement volume, incorporates the same starting points as the PVC model described in section 3. The probability function of Eq. 5 can be applied directly to describe the motion of the velocity gradient in the bulk of the cyclone. With a suitable description of the mean velocity field around the measurement point, the PDF can be used to 'sample' this field. The measured variance of the fluctuating tangential

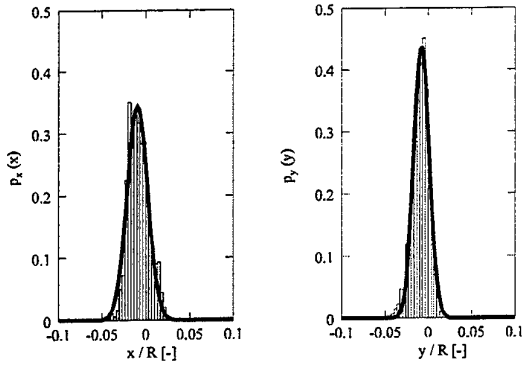


Fig. 8 Measured probability density function along *x*- and *y*-axis with respect to the geometric center. Both distributions are approximated by use of a Gaussian fit according to Eq. 5

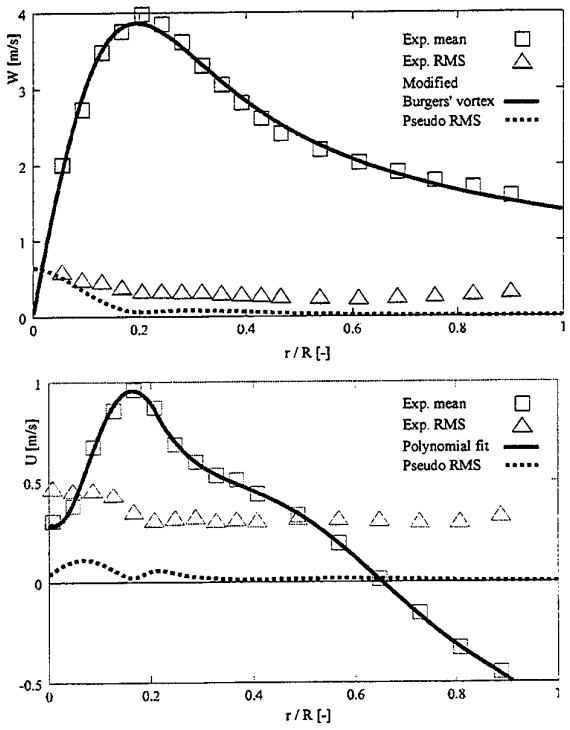


Fig. 9 Application of PDF method on measured tangential and axial velocity profiles (at z / L = 0.75)

velocity component due to the vortex precession can then be evaluated by integration of the velocity fluctuation and its distribution about the measurement point. For more details on the computation, see Volkert *et al.* (1996). To apply the PDF method on the measured tangential velocity profile, an analytical expression is needed.

For cyclonic flows, the free-vortex region can be described by $W \propto r^{-0.8}$; this implies that the Burgers' vortex (Eq. 1) needs to be modified (Gupta *et al.* 1984). In figure 9, the measured tangential velocity distribution and the modified Burgers' vortex are presented. Because of the small axi-asymmetry, the measured velocity profile has been re-normalized. The PDF has been moved to the geometrical origin, and a linear decay function has been applied to take wall effects into account (Grosjean *et al.* 1997). The PDF method demonstrates that a considerable part of the RMS in the vortex core can be considered as pseudo-turbulent fluctuations.

The vortex precession also affects the axial RMS profile. In figure 9 the estimated RMS owing to precession for the axial velocity is presented as well. The same PDF of Eq. 5 was used, but the mean axial velocity is assumed to be equal to the velocity component projected on the *z*-axis. The measured mean axial velocity profile was approximated by use of two 5th order polynomial fit functions. For the axial velocity component, the PDF method also shows that part of the RMS in the vortex core is due to the vortex precession.

5. DISCUSSION

The experimental results obtained with the laser techniques presented here, unequivocally show the presence of a precessing vortex core in cyclonic flow, and its effect on the measured velocity field. The PDF method of Volkert *et al.* (1996) appears to give a good estimate of the contribution of the PVC on the measured RMS level, at least for the tangential velocity component. In figure 10, the measured and corrected RMS data points for the tangential velocity are depicted and compared with a numerical prediction. The numerical result was obtained with the standard Reynolds stress transport model (RSTM) on an axisymmetric computational domain (for details on the numerical work see Hoekstra *et al.* 1998b). The corrected data points were obtained by subtracting the measured variance and the estimated variance owing to precession. Although the simulated RMS can not be considered as a reference, the tangential RMS data correspond better with the data after correction than before. For the axial RMS profile (not presented here), the correction appears to be rather limited, whereas also for this velocity component, the simulation shows a constant RMS level in the core region.

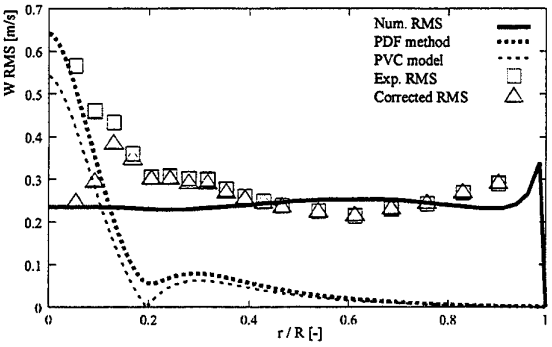


Fig. 10 The measured RMS profile for the tangential velocity component and the corrected profile by use of the PDF method. A considerable reduction of the RMS in the vortex core can be noticed.

This could be due to the fact, that the assumed PDF is not appropriate for the axial velocity measurements. Chanaud (1965) observed the PVC as a rotating *spiral* vortex, which implies that also the measured axial velocity is a projected component.

A disadvantage of the PDF method is the demand for experimental data on the vortex core center distribution (by use of PIV or visualization). Also, a decay function needs to be applied to account for wall effects, which at the moment lacks a sound physical basis.

A way to correct RMS profiles *a posteriori* without additional information on the PVC distribution was mentioned in section 3. Estimating the approximate amplitude of the PVC by use of Eq. 3 and applying the PVC model, a rough estimate of the contribution of the PVC to the RMS level can be determined. In figure 10 the RMS level that results from applying the PVC model with an amplitude $r^* = \sigma$ (section 3.4), is also given. The RMS profile obtained with this procedure only slightly deviates from the PDF method result.

As was mentioned by Grosjean *et al.* (1997), the PDF method gives a rather simplified representation of the effect of the vortex precession on the flow field. The RMS profile for the tangential velocity profile shows that especially the region where the forced and free-type of vortices are connected, the correction is rather limited. This can be attributed to the assumption that the mean velocity profile is not affected by the PVC phase. In Hoekstra *et al.* (1998a), it is shown that the actual maximum tangential velocity varies with PVC position due to wall effects. In this respect, only PIV measurements are able to resolve the whole flow field as a function of the PVC phase.

6. CONCLUDING REMARKS

Cyclonic flow in a vortex chamber exhibits a low-frequency oscillation known as the precessing vortex core (PVC). By applying a simple model for its motion, it was shown that the PVC has a large effect on the RMS profile of the measured tangential as well as axial velocity component. The PDF of the vortex core origin has been obtained by visualization, and is used in the method of Volkert *et al.* (1996) to estimate the signal variance, which results from the core motion. Although the method is a simplified representation of the PVC behavior, up to 50 % of the local RMS can be attributed to the PVC and should be considered pseudo-turbulence. This is important to notice if LDA measurements on cyclonic flow are used to validate numerical predictions.

ACKNOWLEDGEMENTS

The authors gratefully acknowledge the support of the Netherlands Foundation for Chemical Research (SON) and the financial aid from the Netherlands Foundation for Scientific Research (NWO) and Van Tongeren kennemer BV. Thanks are also due to Dr. J. Westerweel for making the PIV-software available.

REFERENCES

Chanaud, R.C. 1965, Observations of oscillatory motion in certain swirling flows, J. Fluid Mech., vol. 21, pp. 111-127.

Derksen, J.J., Doelman, M.S. & Van Den Akker, H.E.A. 1998, Phase-resolved three-dimensional LDA measurements in the impeller region of a turbulently stirred tank, Proc. 9th Int. Symp. on Applications of Laser Techniques to Fluid Mechanics, Lisbon, vol. 1, pp. 14.5.

Escudier, M.P., Bornstein, J. & Zehnder, N. 1980, Observations and LDA measurements of confined turbulent vortex flow, J. Fluid Mech., vol. 98, pp. 49-63.

Fokke, M.G.D., Liem, T.L., Derksen J.J. & Van Den Akker, H.E.A. 1994, LDA and LIF experiments on the quasi-periodic and complex flow in a cyclone, Proc. 7th Int. Symp. on Applications of Laser Techniques to Fluid Mechanics, Lisbon, vol. 1, pp. 16.4.

Garg, A.K. & Leibovich, S. 1979, Spectral characteristics of vortex breakdown flow fields, Phys. Fluids, vol. 22 (11), pp. 2053-2064.

Gray, C., Greated, C.A., McCluskey, D.R. & Easson, W.J. 1991, An analysis of the scanning beam PIV illumination system, Meas. Sci. Technol., vol. 2, pp. 717-724.

Grosjean, N., Graftieaux, L., Michard, M., Hübner, W., Tropea, C. & Volkert, J. 1997, Combining LDA and PIV for turbulence measurements in unsteady swirling flows, Meas. Sci. Technol., vol. 8, pp. 1523-1532.

Gupta, A.K., Lilley, D.G. & Syred, N. 1984, *Swirl flows*, pp. 297, Abacus Press, Cambridge.

Hoekstra, A.J., Van Vliet, E., Derksen J.J. & Van Den Akker, H.E.A. 1998a, Vortex core precession in a gas cyclone, in Advances in Turbulence VII, ed. U. Frisch, pp. 289-293, Kluwer Academic Publishers, Dordrecht.

Hoekstra, A.J., Derksen, J.J. & Van Den Akker, H.E.A. 1998b, The effect of geometry on the flow field in a gas cyclone separator, submitted to Chem. Eng. Sci.

Liem, T.L. & Van Den Akker, H.E.A. 1992, LDV measurements of the turbulent flow in gas cyclones, 13th Symposium on Turbulence, Rolla (Missouri), pp. B.12.

Smith, J.L. 1962, An experimental study on the vortex in the cyclone separator, Trans. ASME (J. Basic Engr), vol. 84, pp. 602-608.

Volkert, J., Tropea, C., Domann, R. & Hübner, W. 1996, Combined application of PIV and LDA to swirling flows under compression, Proc. 8th Int. Symp. on Applications of Laser Techniques to Fluid Mechanics, Lisbon, vol. 2, pp. 19.1.

Yazdabadi, P.A., Griffiths, A.J. & Syred, N. 1994, Characterization of the PVC phenomena in the exhaust of a cyclone dust separator, Exp. Fluids, vol. 17, pp. 84-95.

ON THE ADVANTAGES AND PITFALLS OF STATISTICAL PIV ANALYSIS IN THE MEASUREMENT OF CONFINED VORTEX BREAKDOWN

J.M.M. Sousa[1] and C. Freek[2]

[1] Instituto Superior Técnico/Technical University of Lisbon, Mechanical Engineering Department, Av. Rovisco Pais, P-1096 Lisboa Codex, Portugal

[2] Volkswagen AG, Research and Development, EZMM-1785, D-38436 Wolfsburg, Germany

ABSTRACT

The objective of this work is twofold. Firstly, the difficulties associated with the measurement of velocities in steady confined vortex breakdown using a digital implementation of PIV are discussed. Secondly, aiming to use the measured velocity field in the computation of the out-of-plane component of vorticity, statistical averaging over a series of images is proposed as an alternative to usual filtering procedures. In the present case, the former strategy yields velocity measurements accurate enough to reproduce both the features and the magnitudes of vorticity fields obtained by numerical simulation. However, some care must be taken in the selection of interrogation parameters and differentiation schemes.

1. INTRODUCTION

In the last few years, various developments in Particle Image Velocimetry (PIV) have been bestowing incontestable impetus on the quantitative analysis of complex flows. The unique features of this technique have found conspicuous usefulness in the investigation of the structure of vortical flows. The study of vortex-pair interaction by Willert (1992) using a digital implementation of PIV, and the examination of the three-dimensional structure of vortex breakdown by Brücker and Althaus (1992) combining PIV with volume scanning, substantiate the above assertions thoroughly. However, an accurate quantitative description of vortical flow characteristics may, under certain circumstances, be hampered by limitations intrinsic to this technique. Particle density, dynamic range, interrogation window size, over-sampling, spatial filtering or smoothing, interpolation procedures and specific facets of a particular PIV implementation (see, e.g., Pierce and Delisi, 1995) are factors, which in conjunction with the flow characteristics (strong gradients, turbulence, ...), must be carefully thought about. Otherwise, key quantities in the characterization of vortical flows, such as vorticity maxima, or as fundamental as the velocity field surrounding the vortex, may be significantly misrepresented by PIV flow maps.

PIV measurements of vortex breakdown confined to a cylindrical container have been carried out, e.g., by Westergaard *et al* (1993), with the aim of portraying the oscillating behavior of vortical structures in unsteady regimes. In the present investigation, a conical driver was employed to generate the swirling flow, instead of the classical flat rotor used by the aforementioned authors. The main idea behind this variant was that, from the topological point of view, the tip of the rotating cone would provide a well-defined nodal point for a central streamline impinging upon the rotor wall. At moderate values of the Reynolds number, vortex breakdown inside the closed container can be maintained laminar and steady. As a result, clean flow conditions displaying complex vortical motion and high velocity gradients can be made available. It would be expected that the flow confinement and the mixing provided by a global recirculation would facilitate the generation of high seeding densities exhibiting a considerable degree of homogeneity. This would therefore allow the minimization of bias effects in despite of the presence of stringent tracer displacement gradients. However, the stagnant flow regions characteristic of vortex breakdown make the generation of optimum seeding conditions difficult and the associated out-of-plane motion diminishes the signal-to-noise ratio significantly. These and other sources of uncertainty originate the occurrence of jitter in measured velocity vectors, as discussed, e.g., by Willert (1992), Westerweel (1993) and Raffel et

al (1998). Spatial filtering employing a smoothing kernel is a common procedure for the elimination of jitter, yet leading to a reduction of spatial wavelength range. For the present flow case, an effective alternative to the aforementioned post-processing of velocity vectors was the application of statistical averaging by the use of a series of images. Section 2 provides a description of the test case and the presentation of results concerning velocity field measurements in a meridional plane of the closed container. A comprehensive discussion of the various types of uncertainties affecting these results is also carried out in this section. The calculation of vorticity fields is performed in Section 3, along with an investigation on the effects of interrogation parameters and nature of differentiation scheme. Finally, the most prominent conclusions of the present work are listed in Section 4.

2. VELOCITY FIELD MEASUREMENTS

Results have been obtained for the flow geometry depicted in Figure 1, at a Reynolds number $Re = \Omega R^2/\nu = 2200$ and for a gap-ratio $H/R = 2$. This regime was experimentally investigated in detail by Durão et al (1996), in a study embracing flow visualization and Laser Doppler Velocimetry (LDV). These authors have shown that the regime under investigation was characterized by the presence of an axisymmetric bubble, formed in the symmetry axis as a manifestation of vortex breakdown.

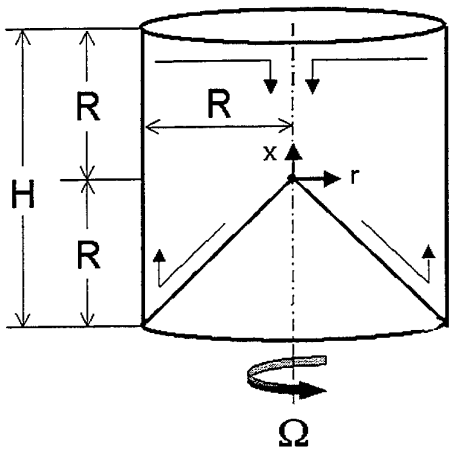


Fig. 1 Schematics of the closed container

As the flow is generated by the rotation of a cone (rotor) in the bottom of the cylindrical container, the dominant velocity component arising in a meridional plane is usually the azimuthal component. Thus, the main obstacle to an efficient application of PIV to this flow lies in its strong three-dimensionality. Such large amount of motion normal to the light sheet leads to a very significant out-of-plane loss of particle pairs, which ultimately originates an important decrease in correlation peak detectability. At least three methods (no panacea) have been suggested for the minimization of the above-mentioned effects (see, e.g., Raffel et al, 1998). The present work combined both the reduction of laser pulse delay (Δt = 3 - 4 ms) and the thickening of the light sheet (l = 2 mm). A circular offset of the light sheet could also have been implemented at the expense of the system's simplicity. However, the efficacy of the foregoing procedure is rather questionable in this case due to large variations in the magnitude of the out-of-plane flow component. It must be mentioned that the value of Δt was also limited by exigent requirements in dynamic range, as a result of the broad range of velocities encountered in flows exhibiting vortex breakdown. Additionally, the thickness of the light sheet had to be optimized taking into account that a reduction in illumination intensity brings up an increase in noise.

Wide variations in the velocity field translate into a large variability in particle image shift. Thus, higher velocities occurring around vortex breakdown structures and near walls are particularly vulnerable to random and bias errors due to in-plane loss of particle pairs, mainly resulting in increased noise and under-estimation of displacement values by the PIV system, respectively. In order to minimize these effects, discrete offset of interrogation windows was applied (Westerweel et al, 1997). This procedure was found to be determinant for the accurate measurement of the velocity field in this kind of flow. However, it cannot be regarded as a total cure in flows characterized by sharp velocity gradients (such as the present one), since the corresponding displacement gradient over the interrogation window will produce in-plane loss of pairs even when (mean) offset is used. As a result, it is rather straightforward to conclude that smaller interrogation areas (IA) should be preferred in the presence of large gradients. For this reason, two different values of IA were employed when comparing the current PIV results against other techniques. This subject will be addressed again later in the paper.

The digital implementation of PIV proposed by Freek et al (1997) was employed to collect a total of N = 300 images, which were used in the computation of ensemble-averaged vectors. A comparison of results for a profile of axial velocity, u, crossing the axis at x/R = 0.6 (i.e., through the breakdown bubble) is shown in Figures 2a and 2b, respectively for 50% and 75% image area overlap (IAO) with IA = 32x32. It must be

emphasized that the flow is laminar and steady. Nevertheless, it can be observed that, as a consequence of the various uncertainties discussed above, the profiles obtained from single images (N = 1) clearly deviate from those computed by statistical averaging (N >> 1). Further, larger discrepancies can be found in the case of IAO = 75%.

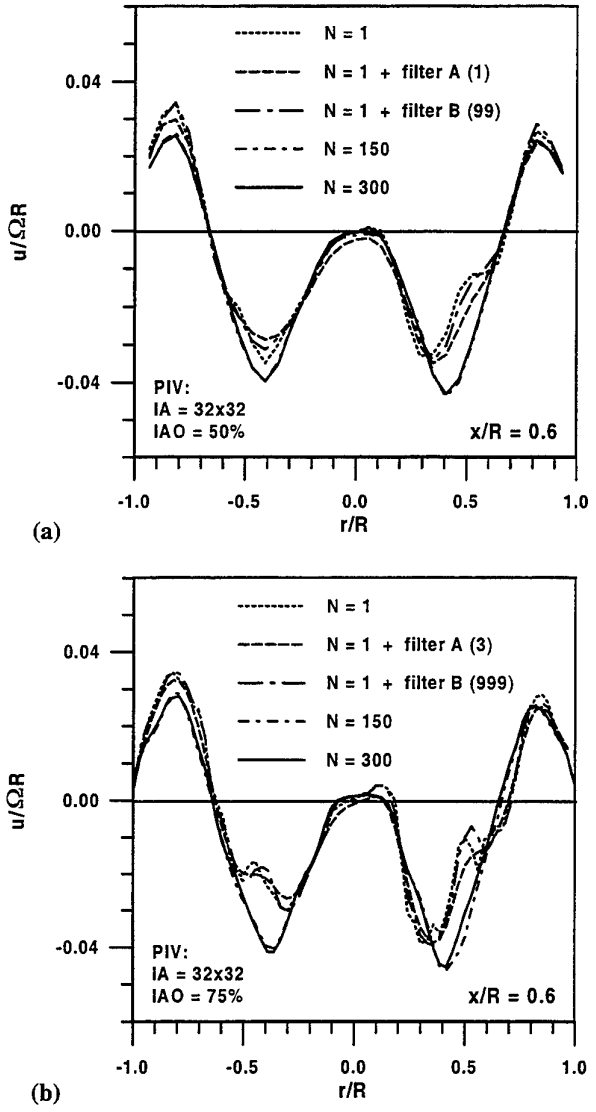


Fig. 2 Effects of filtering and statistical averaging in a u-velocity profile: (a) IAO = 50%; (b) IAO = 75%

Filtering can be used to smooth out the irregularities in the profiles. The figure also shows the results yielded by the application of two filters: A - moving average (3x3); B – filter (5x5) proposed by Nogueira et al (1997). The number of filter passes is indicated in between parenthesis in Figures 2a and 2b. Obviously, the simple application of filtering cannot produce the correct results. Additionally, it can be seen that filter A, though providing a very strong damping of noise, may depreciate the results severely. The profiles for IAO = 50% do not clearly show the reversed flow region in the vicinity of the axis (r/R = 0). However, after one pass of filter A, the flow does not even display the occurrence of stagnation. Finally, one may observe that small differences were found between the profiles computed with N = 150 and N = 300. Still, the results for IAO = 75% exhibited higher sensitivity to the number of samples used in the averaging process.

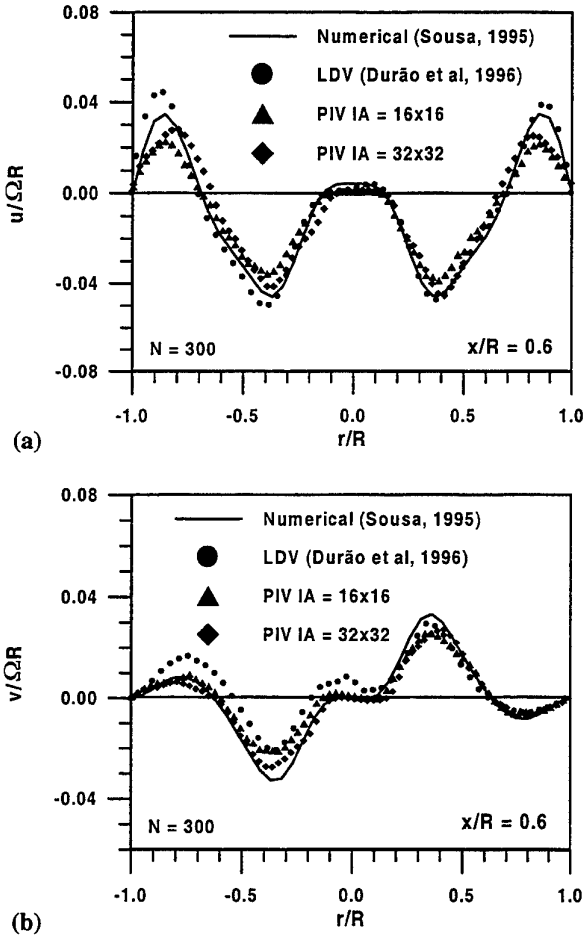


Fig. 3 Comparison of velocity profiles obtained by numerical simulation, LDV and PIV: (a) u; (b) v

A direct comparison of the results against the three-dimensional numerical simulations performed by Sousa (1995) and the LDV measurements reported by Durão et al (1996) is portrayed in Figures 3a and 3b, respectively for axial, u, and radial, v, velocity components. From now on, all the results respect to N = 300. The interrogation of the images was carried

out using *IA* = 32x32 and *IA* = 16x16, with the aim of assessing the effect of displacement gradients for distinct values of *IA*, as discussed before. The same spacing between velocity vectors was set in both cases, thus leading to *IAO* = 75% in the larger window and *IAO* = 50% in the smaller one. Taking the numerical solution as the basic reference, it can be stated that the vortex breakdown bubble was fully captured by the PIV measurements employing *IA* = 32x32. The use of a smaller *IA* yielded an under-estimation of peak velocity values. An explanation can be found by noting that a sufficiently high particle image density could not be guaranteed everywhere during the measurements, due to the accumulation of seeding particles in stagnant flow areas. Hence, the use of the larger *IA* is recommended. However, one may still note that, in despite of a larger under-estimation, the locations of the maxima in *u*-velocity obtained with *IA* = 16x16 for the sidewall boundary layer are in better agreement with those indicated by numerical simulations and LDV.

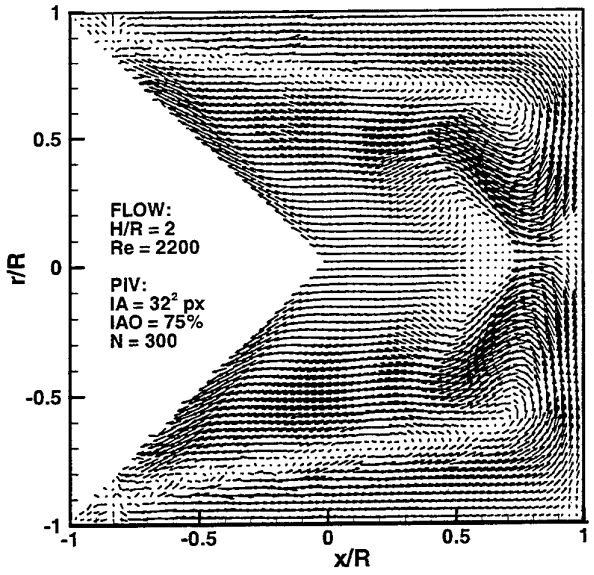


Fig. 4 Velocity vectors in a meridional plane obtained with PIV, using *IA* = 32x32, *IAO* = 75% and *N* = 300

Figure 4 illustrates a more complete view of the flow field in a meridional plane mapped by PIV, employing statistical analysis. The figure shows that the breakdown bubble was not the only flow feature anatomized by the system. In fact, the formation of the Eckman layer over the surface of the rotor and the wavy pattern in the high-speed flow encircling the breakdown structure (and its "wake"), predicted by numerical simulations as well, can clearly be identified in Figure 4. Erroneous vectors appear in the left corners essentially as a consequence of exceeding the dynamic range of the system in these areas. Velocity values over twenty times larger than the maxima encountered in the bulk of the velocity field, and too fast changes in flow direction (i.e., very large curvatures), were in the origin of this problem. Furthermore, it can be observed that the maximum magnitudes of out-of-plane velocity component are also reached at these locations. Irrespectively, the above-mentioned areas are of minor interest for the investigation of vortex breakdown.

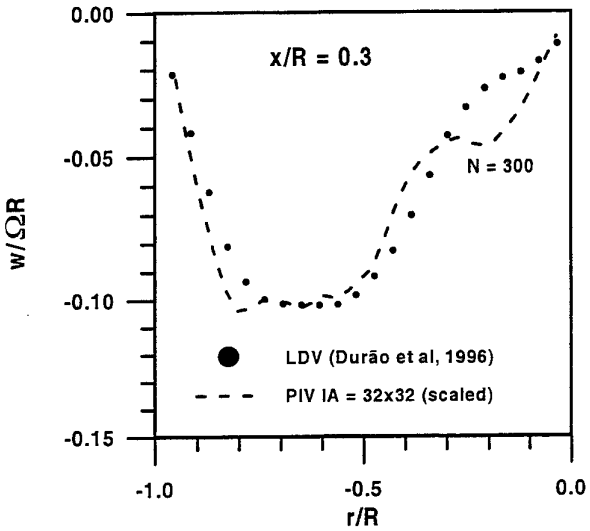


Fig. 5 Estimated profile of out-of-plane velocity component

The flow in the vector map of Figure 4 is very closely axisymmetric, which is in accordance with the findings of Sousa (1995) and Durão et al (1996). However, preliminary measurements indicated a non-axisymmetric nature. A more careful inspection of the results proved that the departure from axisymmetry was due to a non-negligible contribution of the out-of-plane velocity component, *w*, to the radial counterpart, *v*. This fact was an obvious consequence of the necessary thickening of the light sheet discussed a few paragraphs before. As the flow regime under study is known to be steady and axisymmetric, a solution was found in the acquisition of images for both senses of rotation of the rotor. Naturally, if instantaneous views of the flow field are desired, the thickness of the light sheet must be necessarily reduced. Nevertheless, the "contamination" of the radial component by the azimuthal component suggested a strategy for the measurement of the latter velocity without changing the arrangement of the PIV

system. The w-velocity can be extracted from the data by subtracting out the "true" mean flow to a set of images acquired for constant sense of rotation. It must be mentioned that such procedure requires a very careful alignment of the light sheet in order to avoid erroneous results. Figure 5 shows the outcome of this strategy for a profile located at x/R = 0.3. The aforementioned profile (dashed line) was scaled to the LDV data also shown in the figure. Satisfactory agreement was obtained with the reference measurements.

As a general conclusion, it can be asserted that the statistical analysis constitutes an adequate option for the measurement of confined vortex breakdown. The level of accuracy attained in the current results of velocity field generates legitimate expectations for a successful estimation of vorticity as well. This subject will be addressed in the next section. Finally, it can be added that a procedure similar to the one advocated here has been followed by Vogt et al (1996) in the quantification of the velocity field associated with a wing tip vortex in air. This is not surprising, as the aforementioned flow presents many similarities with present, namely dominant flow motion normal to the light sheet.

3. VORTICITY FIELD ESTIMATES

The estimation of a vorticity field based on velocity measurements requires the application of differential operators. Finite differences are an expedite way of estimating derivatives using the (pointwise) measurements of a PIV map. The procedure is easy to implement, further allowing the control of associated errors. However, the proposed task may also be accomplished by making use of two-dimensional signal processing tools. In the present work, four finite difference schemes (see, e.g., Raffel et al, 1998), a (3X3) differentiation filter (Nogueira et al, 1997) and an alternative procedure employing Stokes' theorem, have been utilized to estimate the out-of-plane vorticity field in a meridional plane of the container. Some of the results, portrayed in terms of contour maps of vorticity, are shown in Figures 6b to 6e. The reference solution, shown in Figure 6a, was derived from the numerical calculations performed by Sousa (1995). The second-order accuracy provided by the aforementioned numerical simulations was used as a criterion to select the maps for a direct comparison of results. Consistently, only the schemes insuring second-order "accuracy" in the estimation of the derivatives were represented in the figure (schemes

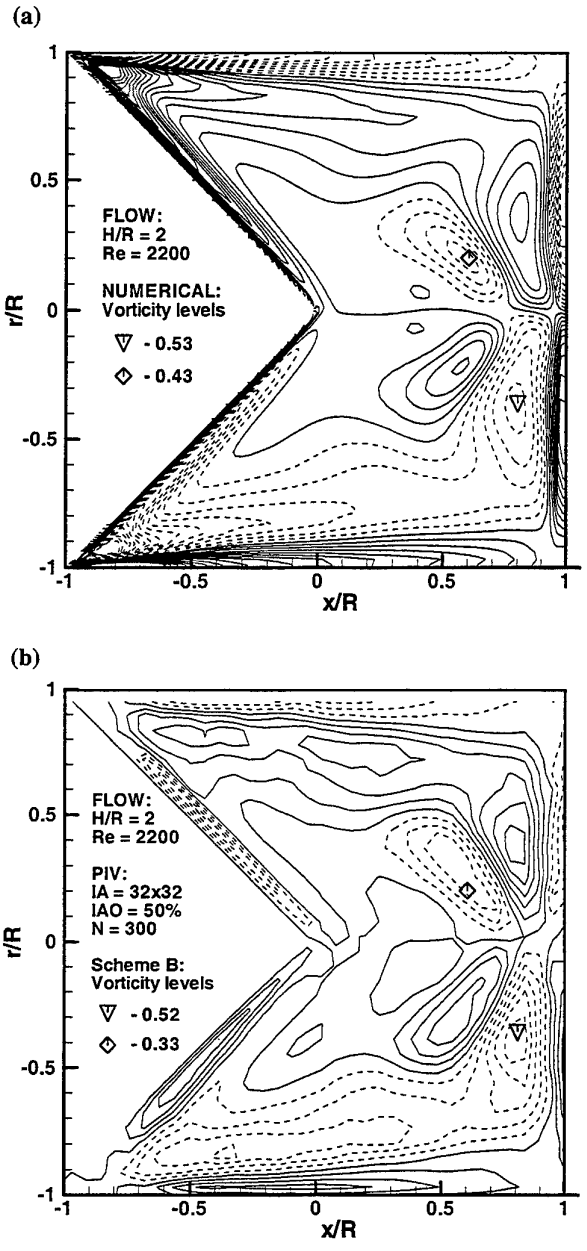
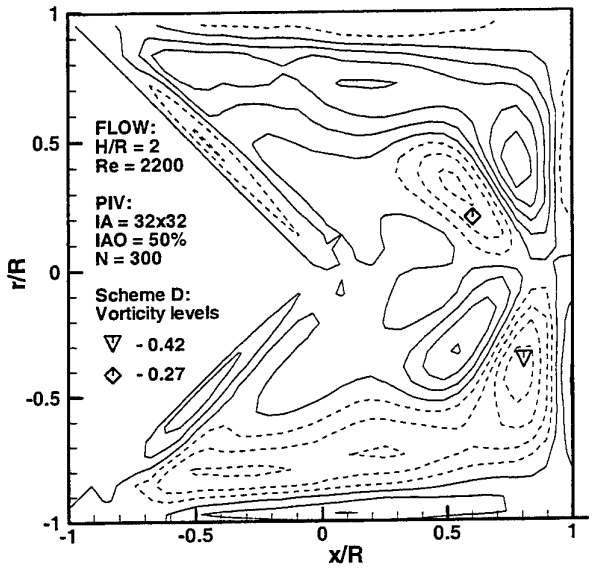


Fig. 6 See next page for caption

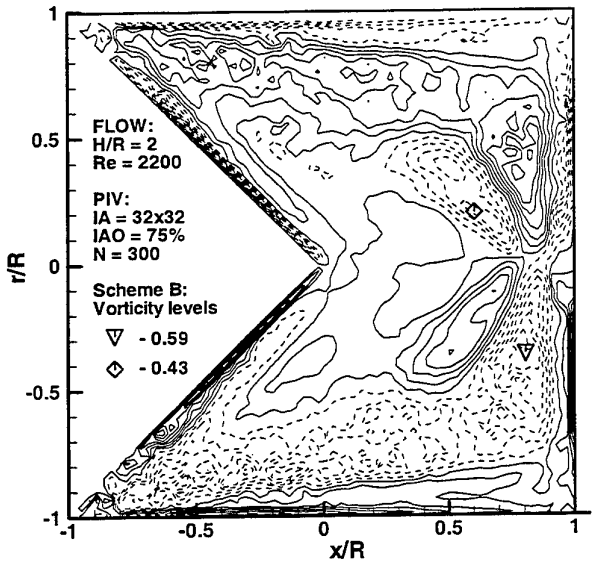
Scheme	Description [3]	$IA = 32^2$ $IAO = 75\%$		$IA = 32^2$ $IAO = 50\%$		$IA = 16^2$ $IAO = 50\%$	
A [1]	Forward diff. (1^{st})	-0.62	-0.45	-0.51	-0.31	-0.43	-0.39
B [1]	Central diff. (2^{nd})	-0.59	-0.43	-0.52	-0.33	-0.43	-0.39
C [1]	Richard. extrapol. (3^{rd})	-0.61	-0.45	-0.56	-0.35	-0.43	-0.41
D [1]	Least squares (2^{nd})	-0.55	-0.38	-0.42	-0.27	-0.42	-0.35
E [2]	2D (3x3) filter (1^{st})	-0.59	-0.41	-0.51	-0.31	-0.42	-0.38
F [1]	Stokes' theorem	-0.59	-0.40	-0.50	-0.31	-0.42	-0.37

[1] Raffel et al (1998); [2] Nogueira et al (1997); [3] Order of "accuracy" from Taylor series expansion

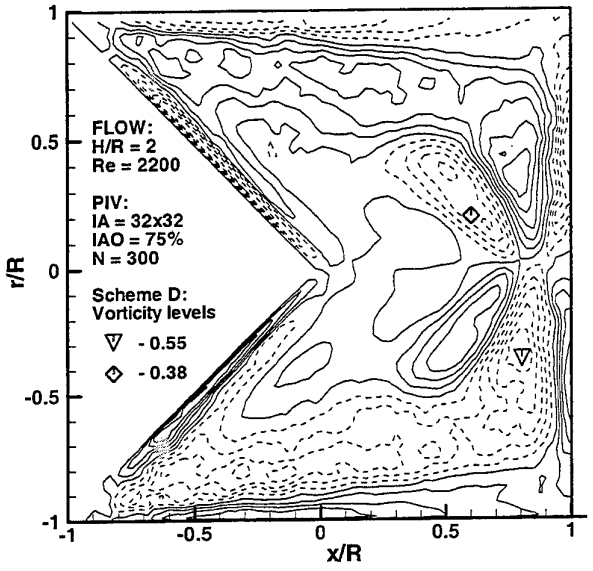
Table 1 Comparison of pointwise vorticity levels in vortices, at x/R = 0.80, r/R = -0.35 (left column), and at x/R = 0.60, r/R = 0.20 (right column), using the various schemes with variable IA and IAO



(c)



(d)



(e)

Fig. 6 (concl.) Contour maps of vorticity in a meridional plane: (a) numerical solution; (b) PIV estimates using scheme B with IAO = 50%; (c) idem using scheme D with IAO = 50%; (d) idem using scheme B with IAO = 75%; (e) idem using scheme D with IAO = 75%

B and D; see also Table 1). It must be mentioned that the effect of over-sampling is also illustrated in the foregoing plots, where Figures 6b and 6c concern IAO = 50%, and Figures 6d and 6e regard IAO = 75%. Vorticity levels were monitored at two different locations very close to local extremes in the computational map. As it might be expected by the results presented in the previous section, the use of the smaller IAO mainly leads to the under-estimation of peak vorticity magnitudes. However, when a value of IAO = 75% is set, the amount of noise in the estimates increases significantly. For a laminar flow, the contour

lines should be smooth, so the irregularities seen in Figures 6d and 6e must have an artificial origin. The doubling of the vorticity uncertainty, resulting from halving the spacing (see Raffel et al, 1998), coupled with the correlation of the data used in the formulas, are the sources of the aforementioned problem. An additional consequence of the increased noise level obtained with $IAO = 75\%$ is the abnormal formation of double-peaked vorticity contours around the breakdown bubble. It can be seen that scheme D allows a minimization of noise effects. However, this is achieved at the expense of smoothing physically meaningful vorticity peaks as well.

Table 1 display a more systematic comparison of estimated vorticity levels at monitor points, which also includes the study of *IA* size effects. The contours obtained for $IA = 16x16$ with $IAO = 50\%$ (not shown) were also quite irregular. This seems to indicate that the influence of grid spacing in the increase of uncertainty was dominant. Although it naturally depends on the differentiation scheme, the use of a larger interrogation window (same *IAO*) may be expected to yield smoothed vorticity estimates. This was true for the monitor point located in the vicinity of the breakdown. However, the results for the monitor point placed near the stationary endwall, exhibited the opposite tendency. An answer for such unexpected behavior can be formulated referring to the findings of Pierce and Delisi (1995). In their investigation, these authors have shown that the measurement of vortical structures using larger values of *IA* in digital PIV may, in some cases, produce augmented values of vorticity maxima. The algorithms commonly used in the determination of the particle displacement (based on the correlation function) are not robust enough to deal with strongly skewed distributions. As a consequence, larger windows may show highly steep jumps in velocity where moderate gradients exist.

Overall, it can be said that the use of $IAO = 75\%$ should only be considered when increased spatial resolution is required (present case). Furthermore, the application of central differencing appears to be a reasonable compromise between minimum noise and minimum smoothing.

4. CONCLUSIONS

Digital particle image velocimetry has been used for the measurement of the velocity field associated with confined vortex breakdown, in a meridional plane of a closed container. The various difficulties encountered in the course of the investigation have been discussed and a few remedies have been suggested, namely a statistical analysis. This allowed obtaining accurate profiles of axial and radial velocity components.

Estimates of the vorticity field have also been procured, employing several differentiation schemes. The effects of interrogation window size and over-sampling have been discussed as well. In the present case, four times over-sampled velocity fields have yielded vorticity levels acceptably close to correct ones, while twice over-sampled data caused the under-estimation of peak values. However, higher "accuracy" was obtained at the expense of reliability.

REFERENCES

Brücker, C. & Althaus, W. 1992, Study of Vortex Breakdown by Particle Tracking Velocimetry (PTV) – Part 1: Bubble-Type Vortex Breakdown, Exp. Fluids, vol. 13, pp. 339-349.

Durão, D.F.G., Pereira, J.C.F. & Sousa, J.M.M. 1996, LDV Measurements of Confined Vortex Breakdown Generated by a Rotating Cone, in Developments in Laser Techniques and Applications to Fluid Mechanics, eds. R.J. Adrian et al, pp. 34-44, Springer-Verlag.

Freek, C., Sousa, J.M.M., Hentschel, W. & Merzkirch, W. 1997, Digital Image Compression PIV: a Tool for IC-Engine Research, Proc. 7th Int. Conf. on Laser Anemometry Advances and Applications, Karlsruhe, pp. 455-464.

Nogueira, J.I., Lecuona, A., Rodriguez, P.A. & Ruiz-Rivas, U. 1997, On the Design of Some PIV Postprocessing Filters, Proc. 7th Int. Conf. on Laser Anemometry Advances and Applications, Karlsruhe, pp. 483-490.

Pierce, W.F. & Delisi, D.P. 1995, Effect of Interrogation Window Size on the Measurement of Vortical Flows with Digital Particle Image Velocimetry, in Flow Visualization VII, ed. J. Crowder, pp. 728-732, Begell House.

Raffel, M., Willert, C.E. & Kompenhans, J. 1998, Particle Image Velocimetry: a Practical Guide, Springer-Verlag.

Sousa, J.M.M. 1995, Experimental and Numerical Investigation of Fluid Flow Instability and Transition. doctoral thesis, Instituto Superior Técnico, Technical University of Lisbon (in portuguese).

Vogt, A., Baumann, P., M. Gharib & Kompenhams, J. 1996, Investigations of a Wing Tip Vortex in Air by Means of DPIV, 19th Advanced Measurement and Ground Testing Technology Conf., New Orleans, AIAA Paper.

Westergaard, C.H., Buchhave, P. & Sorensen, J.N. 1993, PIV Measurements of Turbulent and Chaotic Structures in a Rotating Flow Using an Optical Correlator, in Laser Techniques and Applications in Fluid Mechanics, eds. R.J. Adrian et al, pp. 243-256, Springer-Verlag.

Westerweel, J. 1993, Digital Particle Image Velocimetry: Theory and Application, doctoral thesis, Delft University of Technology, the Netherlands.

Westerweel J., Dabiri, D. & Gharib, M. 1997, The Effect of a Discrete Window Offset on the Accuracy of Cross-Correlation Analysis of PIV Recordings, Exp. Fluids, vol. 23, pp. 20-28.

Willert, C.E. 1992, The Interaction of Modulated Vortex Pairs with a Free Surface, Ph.D. thesis, University of California, San Diego.

ANALYSIS OF ORDERLINESS IN HIGHER INSTABILITIES TOWARD THE OCCURRENCE OF CHAOS IN A TAYLOR-COUETTE FLOW SYSTEM

N. OHMURA, K. MATSUMOTO, T. AOKI and K. KATAOKA

Department of Chemical Science and Engineering,
Kobe University
Rokkodai-cho, Nada-ku, Kobe 657, Japan

ABSTRACT

The purpose of the experimental work is to elucidate the mechanism for the occurrence of chaos in a Taylor-Couette flow system. The attention was focused on the higher instability region from the doubly-periodic to the weakly-turbulent wavy vortex flow. In order to take note of the effect of hysteresis, the inner cylinder rotation was accelerated at a constant rate from rest until a specified Reynolds number was reached. The test section with the radius ratio of 0.625 had an annular gap width of 22.5 mm and an aspect ratio of 4. A fiberoptic laser-Doppler velocimeter was employed to observe a time-dependent, peripheral component of velocity at the central region of vortex cells. At the same time, time-dependent peripheral component of velocity gradients on the wall of the stationary outer cylinder were measured in the neighborhood of one of the outflow cell boudaries with a hot-film shear sensor embedded flush with the inside cylindrical surface. Four vortex cells were always formed regardless of the acceleration rate of the inner cylinder rotation tested in the start-up operation, but the axial wavelength of the two central vortices was shorter than that of the remaining two end vortices. The amplitudes of the fluctuations of velocity and velocity-gradient varied irregularly whereas the first fundamental frequency was maintained in proportion to the inner cylinder rotation as long as the azimuthally-traveling waves existed. It has been concluded that chaos occurs firstly at the inflow cell boundaries as a result of instability in the viscous interaction of end vortices with the fixed bottom and top surfaces and that the chaotic turbulence is propagated along the secondary flow streamlines toward the central vortices and penetrated very slowly toward the center of vortex cells.

1. INTRODUCTION

The Taylor-Couette flow system consisting of two concentric circular cylinders with the inner one rotating experiences several dynamical transitions occurring stepwisely in between laminar and turbulent flow regimes as the Reynolds number is gradually raised: (1) laminar circular Couette flow (LCF), (2) laminar cellular vortex flow (LCVF), (3) singly-periodic wavy vortex flow (SPWVF), (4) doubly-periodic wavy vortex flow (DPWVF), (5) weakly-turbulent wavy vortex flow (WTWVF), and (6) fully-turbulent vortex flow (FTVF) (for a detailed review, see DiPrima and Swinney, 1981 and Kataoka, 1986). There appears the effect of hysteresis in the bifurcation process, depending upon how to reach a steady rotation of the inner cylinder (Ohmura et al. 1995). The aspect ratio of the annular space is also a very sensitive parameter in the formation of a train of vortices (Benjamin, 1978 a & b, Ohmura et al. 1995). In order to investigate the route until chaos appears, particular attention has been focused on the higher instability regions from the doubly-periodic to the weakly-turbulent wavy vortex flow. It is necessary to observe time-dependent vortex flow structures in the central region of vortex cells as well as in the near-wall region. Any probe for velocity measurement should not be inserted into the flow region of the annular space owing to the fact that an undesirable wake flow occurring behind the probe comes round back to it due to the main circulating flow. A fiberoptic laser-Doppler velocimeter was employed to observe time-dependent, peripheral component of velocities at the central region of vortex cells. Time-dependent near-wall velocity gradients were measured with a hot-film shear sensor embedded flush with the inside surface of the outer cylinder. The Reynolds number is defined based on the annular gap width d, the radius R_i and the angular velocity Ω of the inner cylinder:

$$Re = R_i \Omega \, d/\nu$$

2. EXPERIMENT

As shown in Figure 1, the experimental equipment consisted of a transparent outer cylinder of acrylic resin (ID = 120 mm) and a stainless steel inner cylinder (OD = 75 mm), giving an annular gap width d of 22.5 mm and an effective height of 406 mm. The annular space was divided into three portions with two partition discs (2 mm thick). The central portion (test section) with the vertical height H = 90.0 mm had an aspect ratio Γ = H/d = 4 so as to contain 4 vortex cells in normal flow conditions. An aqueous solution of glycerin was used as the working fluid. According to the linearized instability theory (DiPrima & Swinney, 1981), the radius ratio $\eta = R_i/R_o = 0.625$ gives the critical Reynolds number Re/Rec = 75.8 for the transition from LCF to LCVF.

Figure 2 shows the location of a hot-film shear sensor and the positions of observation due to a fiberoptic laser-Doppler velocimeter. The shear sensor was located approximately at the height of the outflow cell boundary of the lowest vortex in touch with the bottom surface. The velocity measurement with the LDV was made along the vertical centerline of the annular gap.

In order to take note of the effect of hysteresis, an acceleration rate of the inner cylinder rotation was controlled to be constant by a computer until a specified Reynolds number was reached. Figure 3 shows schematically the two rates of angular acceleration tested in the start-up operation: case I (0.017 s^{-2}) and case II (0.065 s^{-2}). The observation was made under the steady state operation with no axial flow after a sufficiently large time had passed.

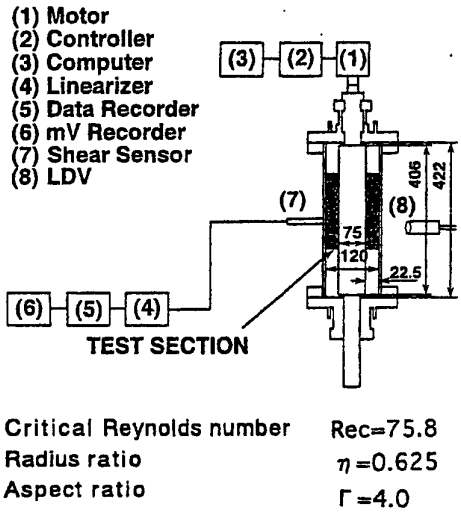


Fig.1 Schematic picture of experimental setup. Dimensions given are in mm.

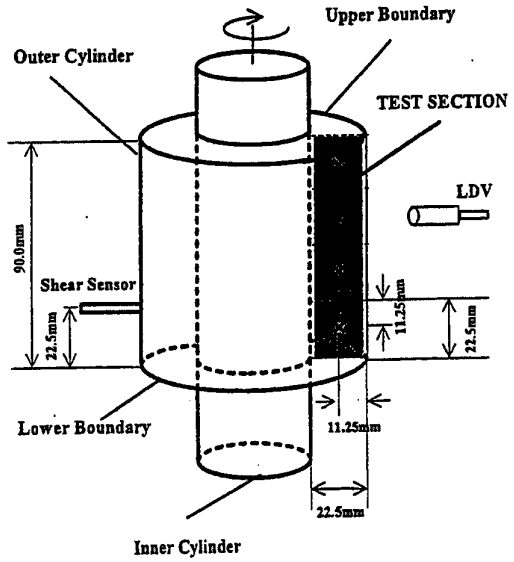


Fig.2 Test section and measuring position.

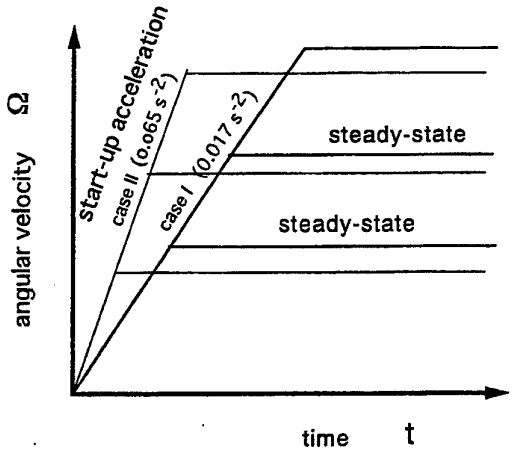


Fig.3 History of acceleration of inner cylinder rotation until reaching a steady state.

3. RESULTS AND DISCUSSION

Two rates of angular acceleration were tested: case I (0.017 s^{-2}) and case II(0.065 s^{-2}). However four vortex cells were always formed in the annular space, regardless of the acceleration rate tested in the start-up operation. It has been found that the two central vortices should be distinguished from the remaining two vortices with respect to the vortex structure. The two vortices being in touch

with the top and bottom end surfaces were named "end vortices". The four vortices were numbered as No.1 through 4 from bottom to top. Figure 4 shows the axial distribution of radial component Vr of velocirty measured along the vertical centerline of the annular space (case I). It can be seen from the figure that the two central vortices were shorter in the axial wavelength (vortex height) than the remaining two end vortices:

Dimensionless axial wavelength

$\lambda/d \fallingdotseq 0.83$ (No.2 & 3 vortices)

$\lambda/d \fallingdotseq 1.11$ (No.1 & 4 vortices).

Figures 5-1 and 5-2 show time-traces and their spectra of the fluctuations of near-wall velocity gradient detected in the neighborhood of the outflow cell boundary between the No.1 and 2 vortices by means of the hot-film shear sensor. Regarding Figure 5-1, the upper two spectra indicate doubly-periodicity of DPWVF structure. The third spectrum indicates definitely the generation of chaotic disturbance at Re/Rec = 22.99 in spite of the persistent quasiperiodic wavy structures. The lowest pair of diagrams for Re/Rec = 25.20 indicate the persistent superposition of wavy motion upon the aperiodic turbulent oscillations. It can be seen from the two figures that there is not a significant difference in spectral structure between the two acceleration rates tested in the start-up operation, i.e. between case I and case II.

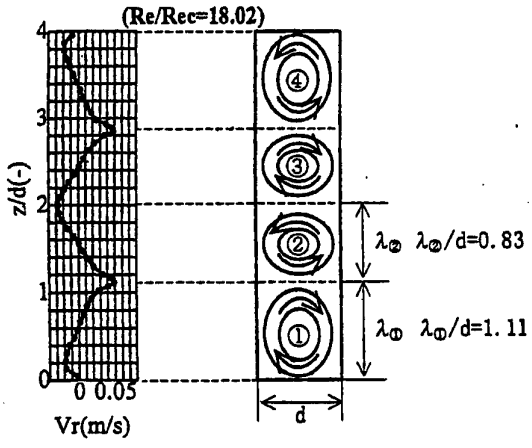


Fig.4 Axial variation of radial component of velocity measured on the centerline of annular gap and the estimated vortex height (axial wavelength): ① end vortex, ② central vortex

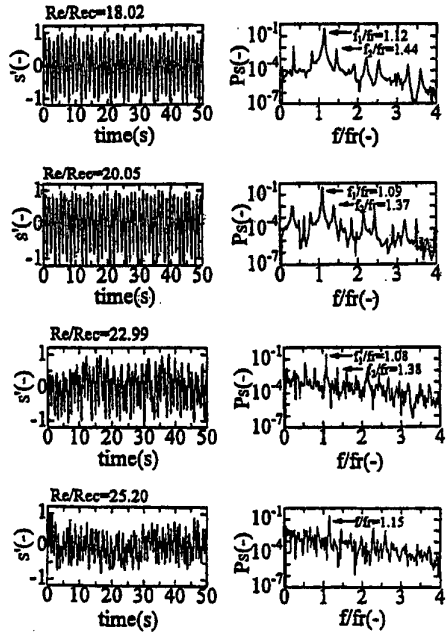


Fig.5-1 Time-traces of local near-wall velocity gradient fluctuations observed in the neighborhood of the outflow cell boundary and their power spectra (case I).

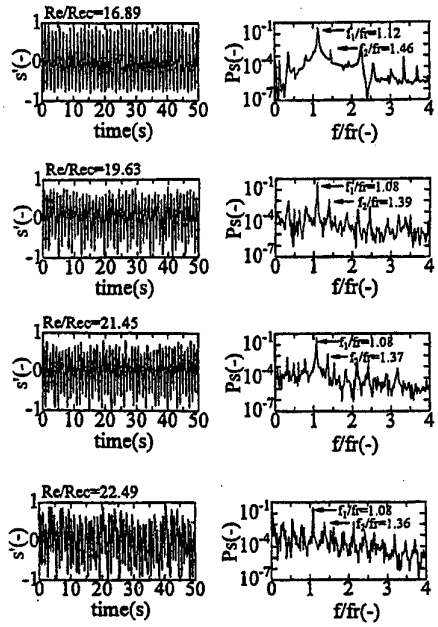


Fig.5-2 Time-traces of local near-wall velocity gradient fluctuations observed in the neighborhood of the outflow cell boundary and their power spectra (case II).

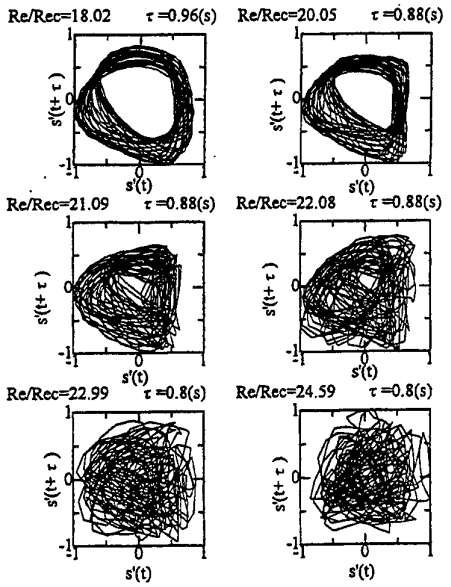


Fig.6-1 Phase space portraits constructed by applying the Taken's embedding method to time-series of local near-wall velocity gradient signals (case I).

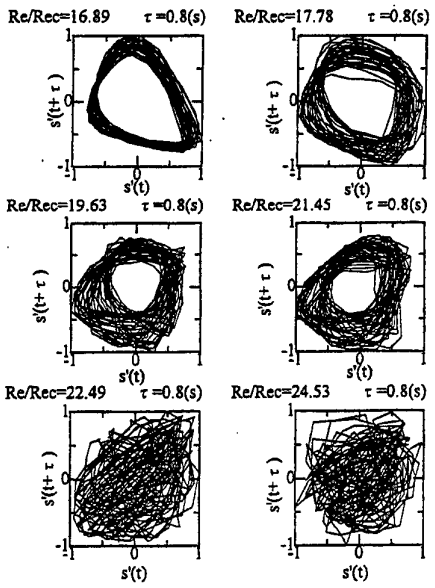


Fig.6-2 Phase space portraits constructed by applying the Taken's embedding method to time-series of local near-wall velocity gradient signals (case II).

Figures 6-1 and 6-2 show phase space portraits constructed by embedding time-series of dimensionless near-wall velocity gradient fluctuations s'(t) into two-dimensional space as $\{s'(t), s'(t+\tau)\}$, where τ is a time delay (Packard et al. 1980, Takens 1981). Regarding Figure 5-1, until the Reynolds number reaches Re/Rec = 21.09 from 18.02, the attractors keep a shape of two-dimensional torus implying doubly-periodicity of DPWVF. When the Reynolds number goes beyond Re/Rec = 22.08, the two-dimensional torus begins to get out of shape with all the orbits wrinkled. This can be interpreted as the generation of chaotic turbulence at the inflow cell boundaries of the two end vortices. As can be seen from those two figures, there is not a significant difference in variation of topological shape of attractor with the Reynolds number between case I and case II.

Figures 7 and 8 show time-traces and their spectra of circumferential component of velocity fluctuations measured at the centers of No.1 & 2 vortices by means of the LDV. The dimensionless first fundamental frequencies f_1/fr were kept equal regardless of the vortex number as well as the Reynolds number. However in the doubly-periodic wavy vortex flow regime, the second fundamental frequency f_{22} of the central vortex (No.2) was lower than the first fundamental frequency f_{12} whereas the second fundamental frequency f_{21} of the end vortex (No.1) was higher than the first fundamental frequency f_{11}. These dimensionless first and second fundamental frequencies of the end vortex are in agreement with those of Figure 5.

It can be seen from the figures that there is an arithmetic relation between f_{21} and f_{22} :

$$f_{11} + f_{22} = f_{21} \quad \text{and} \quad f_{11} = f_{12} \qquad (1)$$

The quasiperiodic wavy structure in the central region of cellular vortices tends to be persistently maintained even when Re goes beyond 23. These pieces of evidence suggest that the generation of chaos occurs due to instability in the shear stresses at both the fixed ends, but that the chaotic disturbance is not penetrated very fast toward the vortex centers.

In addition to the Fourier analysis, a wavelet transform analysis (Walker et al. 1997) was utilized not only to discern the occurrence of chaos but also to extract the characteristic structure of chaotic turbulence.

The wavelet transformation of continuous signal *f(t)* is defined as

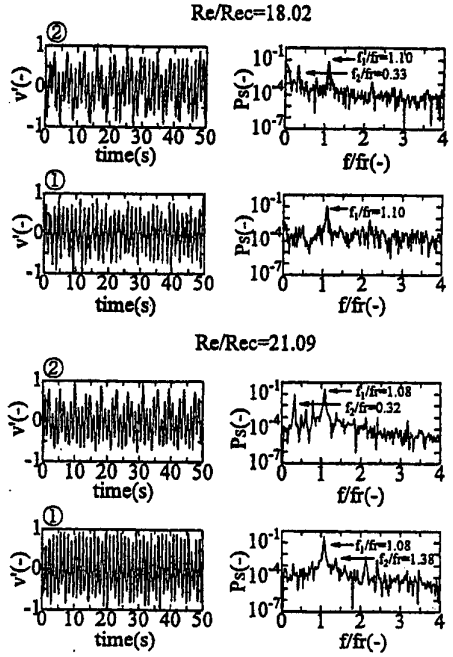


Fig.7 Time-traces of peripheral component of velocity fluctuations observed at the center of vortex cell and their power spectra (case I): ① end vortex, ② central vortex

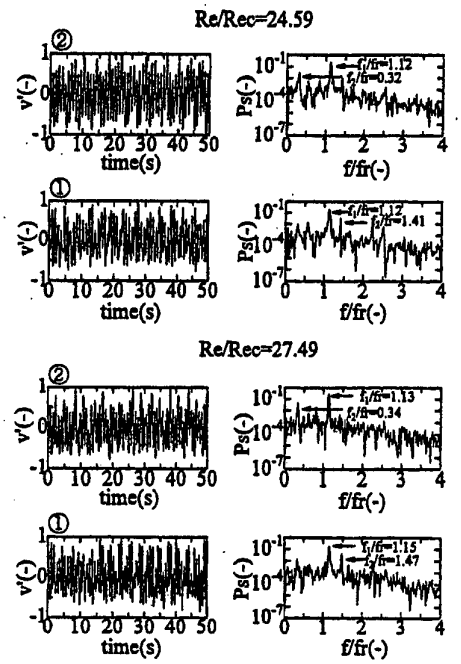


Fig.8 Time-traces of peripheral component of velocity fluctuations observed at the center of vortex cells and their power spectra (case I): ① end vortex, ② central vortex

$$C(\tau, a) = \frac{1}{\sqrt{a}} \int_{-\infty}^{+\infty} g\left(\frac{t-\tau}{a}\right) f(t)\, dt \qquad (2)$$

where $g(t)$ is the wavelet mother function, a is a time-scale parameter for dilatation, and τ is a time-shift parameter.

The signals of the LDV and the hot-film shear sensor were analyzed by calculating Continuous Wavelet Transforms (CWTs). A Mexican-hat wavelet was used as the wavelet mother function.

Mexican hat function

$$g(t) = (1 - t^2) \exp\left(\frac{-|t|^2}{2}\right) \qquad (3)$$

The actual calculation was made in Fourier space using FFT:

$$C(\omega, a) = \sqrt{a}\; G^*(a\omega)\, F(\omega) \qquad (4)$$

where * denotes a complex conjugate. The CWT was obtained as the inverse transform of C(ω, a).

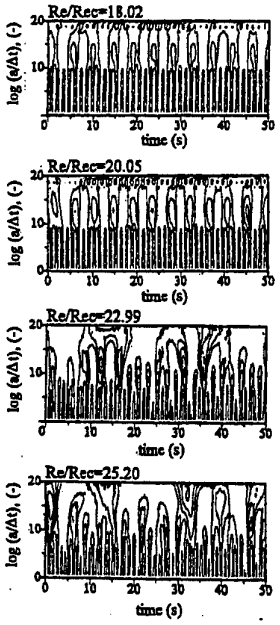


Fig.9 Equi-correlation contour lines of Mexican-hat wavelet transforms obtained from the near-wall velocity gradient signal (case I).

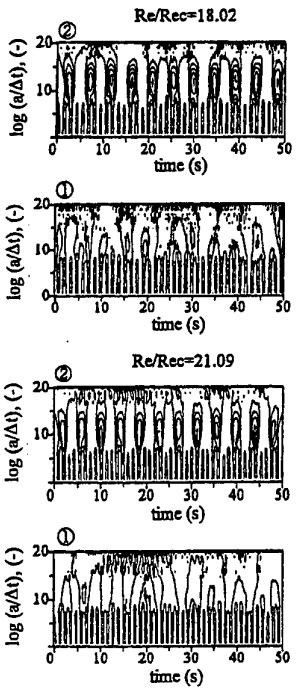


Fig.10 Equi-correlation contour lines of Mexican-hat wavelet transforms obtained from peripheral velocity fluctuations at the center of vortex cells (case I): ① end vortex, ② central vortex

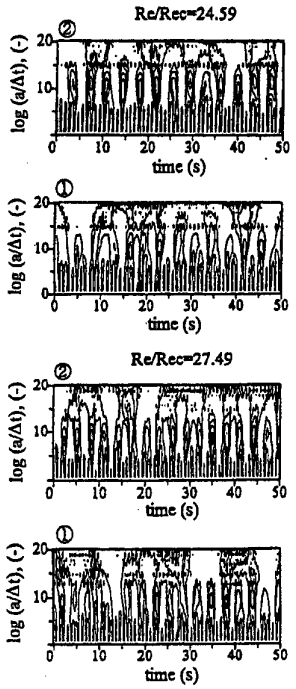


Fig.11 Equi-correlation contour lines of Mexican-hat wavelet transforms obtained from peripheral velocity fluctuations at the center of vortex cells (case I): ① end vortex, ② central vortex

Figures 9 through 11 show equi-correlation contour lines of CWT. As can be seen from CWT diagram of Re/Rec = 18.02, in the regime of SPWVF, the point indicating maximal correlation appears regularly on the CWT diagram with a constant time-period at a constant height (time-scale) of the vertical axis, i.e. at log (a/Δt) = 5. Those figures suggest that the instability leading to the generation of chaos appears in the end vortices earlier than in the central vortices.

In order to examine the occurrence of chaotic turbulence, a comparison was made on the diagrams of CWT between the near-wall region and the central region of cellular vortices. The CWTs of the velocity-gradient signals obtained at Re/Rec = 22.99 indicate clearly the generation of chaotic turbulence around the first fundamental component. On the other hand, the CWTs of the velocity signals obtained at Re/Rec = 24.59 show the persistent existence of regularly periodical first fundamental component.

Two kinds of standard deviations as an index of irregularity were calculated respectively from the sequential data of time-scale on the vertical axis and time-interval on the horizontal axis at which every maximal correlation coefficient $C(\tau, a)_{max}$ relating to the first fundamentals appears on the CWT diagram. The definition of these standard deviations can be expressed as

$$\sigma_a = \sqrt{\sum_{i=1}^{N} \{\left(log\ (a/\Delta t)\right)_i - \overline{log\ (a/\Delta t)}\}^2/N} \qquad (5)$$

$$\sigma_T = \sqrt{\sum_{i=1}^{N} \{T_i - \overline{T}\}^2/N} \qquad (6)$$

The variation of those standard deviations with the Reynolds number is shown in Figures 12 & 13. Comparing between the near-wall and the central flow regions, it has been found that the dynamical transition to the occurrence of chaos is sharper in the near-wall region than in the central region of vortex cells.

Fig.12 indicates that the time-scale standard deviation shows a sharp jump at Re/Rec = 22 but the time-interval standard deviation does not.

This implies that the amplitudes of velocity and velocity-gradient signals vary irregularly while the dimensionless first fundamental frequency is kept

constant. It can be considered that the instability of amplitude is characteristic of steadily rotating flow systems with the periodicity of time period. It can be seen from Fig.13 that the time-scale standard deviation obtained at the center of vortices shows a dull jump around Re/Rec = 24. The belated transition to chaotic turbulent flow implies the slow propagation of chaotic turbulence toward the center of vortices.

4. CONCLUSION

The following conclusions can be deduced:
(1) chaos occurs firstly in amplitude of velocity fluctuations as a result of instability in the viscous interaction of the inflow cell boundaries of the two end vortices with the fixed bottom and top surfaces
(2) the chaotic turbulence is propagated slowly along the secondary flow streamlines of the cell boudaries toward the central vortices.
(3) the chaotic turbulence is penetrated very slowly inward across the secondary flow streamlines toward the center of vortices.
(4) chaos does not appear directly in time-period of velocity fluctuations in this kind of steadily rotating flow systems until the flow becomes fully-turbulent.

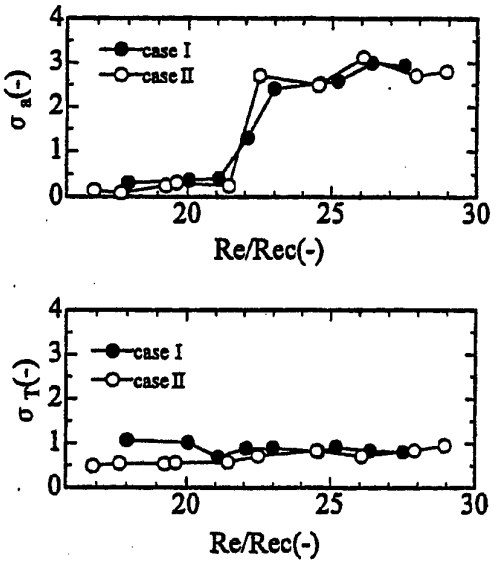


Fig.12 Standard deviations of time-scale and time-interval calculated from maximal points of wavelet transform correlation of the near-wall velocity-gradient signals.

5. ACKNOWLEDGEMENT

The authors wish to thank Mr. T. Yoshimura for his experimental support. This work was supported by Grant-in-Aids for Scientific Research (B)(2) (09450287) from the Ministry of Education, Science, Sports and Culture of Japan.

6. NOMENCLATURE

- a : time-scale parameter for dilatation of wavelet mother function
- d : annular gap width of test section
- f : frequency, Hz
- fr : frequency (revolution number) of inner cylinder rotation, 1/s
- f(t) : continuous signal to be analyzed by wavelet analysis
- g(t) : wavelet mother function
- H : vertical height of test section
- Ps : normalized power distribution function, dimensionless
- R_i, R_o : inner and outer cylinder radii, m
- Re : Reynolds number based on inner cylinder rotation

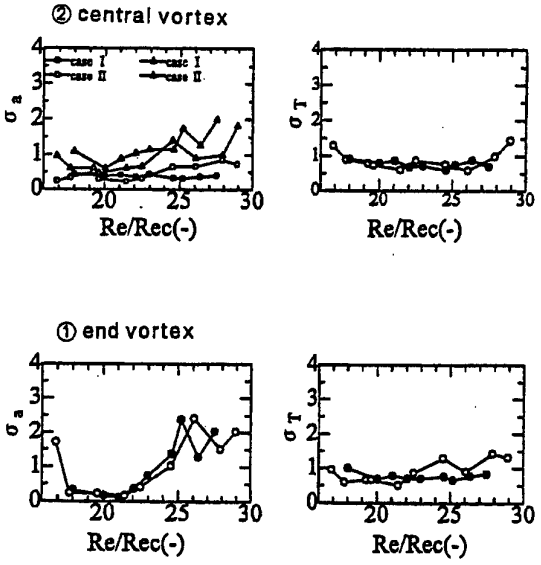


Fig.13 Standard deviations of time-scale and time-interval calculated from maximal points of wavelet transform correlation of peripheral velocity signal observed at the center of vortex cells.

s' : fluctuations of near-wall velocity gradient, dimensionless

T : time-interval at which the maximal point of f_1-component appear s on CWT diagram, s

t : time, s

v' : fluctuations of peripheral component of velocity, dimensionless

Vr : radial component of velocity, m/s

z : axial coordinate along cylinder axis

Greek letters

Γ : aspect ratio (=H/d)

η : radius ratio ($= R_i/R_o$)

λ : axial wavelength (vertical height of vortex), m

ν : kinematic viscosity, m^2/s

σ_a : time-scale standard deviation

σ_T : time-interval standard deviation

τ : time delay for phase space analysis or time-shift parameter for wavelet transformation, s

Ω : angular velocity of inner cylinder, 1/s

ω : angular frequency of Fourier transformation

Overline

$\overline{\quad}$: average

7. REFERENCE

Benjamin, T.B. 1978a, Bifurcation Phenomenain Steady Flows of a Viscous Liquid. I. Theory, Proc. Roy. Soc. London, Vol.A359, pp.1-26.

Benjamin, T.B. 1978b, Bifurcation Phenomenain Steady Flows of a Viscous Liquid. II. Experiments, Proc. Roy. Soc. London, Vol.A359, pp.27-43.

DiPrima, R.C. & Swinney, H.L. 1981, Instabilities and Transition in Flow between Concentric Rotating Cylinders, in Hydrodynamic Instabilities and Transition to Turbulence, ed. H.L. Swinney & J.P. Gollub, Chap.6, pp.139-180, Springer-Verlag, Berlin.

Kataoka, K. 1986, Taylor Vortices and Instabilities in Circular Couette Flows, in Encyclopedia of Fluid Mechanics, ed. N.P. Cheremisinoff, Vol.1, Chap.9, pp.236-274, Gulf Pub., Houston.

Ohmura, N., Kataoka, K., Mizumoto, T., Nakata, M. & Matsumoto, K. 1995, Effect of Vortex Cell Structure on Bifurcation Properties in a Taylor Vortex Flow System, J. Chem. Eng. Japan, Vol.28, pp.758-764.

Packard, N.H., Crutchfield, J.P., Farmer, J.D. & Shaw, R.S. 1980, Geometry from a Time Series, Phys. Rev. Lett., Vol.45, pp.712-716.

Takens, F. 1981, Detecting Strange Attractors in Turbulence, in Dynamical Systems and Turbulence, ed. D.A. Rand & L.S. Young, Lecture Notes in Mathematics, Vol.989, pp.366-381, Springer-Verag, Heidelberg.

Walker, S.H., Gordeyev, S.V. & Thomas, F.O. 1997, A Wavelet Transform Analysis Applied to Unsteady Aspects of Supersonic Jet Screech Resonance, Experiments in Fluids, Vol.22, pp.229-238.

LDV-MEASUREMENTS ON BAROCLINIC WAVES

Bernd Sitte and Christoph Egbers
ZARM, University of Bremen, 28359 Bremen, F.R.G.

ABSTRACT

We report on laboratory experiments of baroclinic instabilities in the rotating annulus cooled from within. The flow undergoes different transitions from the laminar basic state through various stages of instability to an irregular state. Flow visualization studies and LDV-measurements of the radial velocity component were carried out. From the raw LDV-data, time series at fixed points in the rotating annulus were calculated. These time series at different positions in the rotating annulus are analysed with classical linear tools like autocorrelation functions and fourier spectra.

1 THE ROTATING ANNULUS EXPERIMENT

Rotating annulus experiments (Hide & Mason, 1975) have been carried out primarily to obtain laboratory simulations of the large-scale circulation of the atmosphere and recently for vortices (Marcus, 1988), such as Jupiter's Red Spot. The flow in the rotating annulus cooled from within can be characterized by the following control parameters: The geometry can be described by the radius-ratio $\eta = R_1 / R_2$ and the aspect ratio $\Gamma = H/d$, where R_1 and R_2 are the inner and outer radii, H is the height and d is the gap width of the annulus.
In this case R_1 = 45 mm, R_2 = 95 mm, η = 0.47, H = 220 mm, , d = 50 mm, Γ = 4.4.

Furthermore, the Taylor number $Ta = \frac{4 \cdot \Omega^2 \cdot d^5}{\nu^2 \cdot H}$ and the Rossby number $Ro = \frac{g \cdot H \cdot \Delta\rho}{\overline{\rho} \cdot \Omega^2 \cdot d^2}$ are coming into account, where Ω is the angular velocity, ν is the kinematic viscosity and ρ is the density. The Taylor number describes the rotational influence while the Rossby number comprises the influence of density gradient due to temperature differences and the influence of rotation. In Figure 1 the experimental setup of the rotating annulus is illustrated. The inner cylinder can be cooled and the outer one can be heated by external temperature baths. The temperature difference between inner and outer cylinders is controlled by temperature sensors installed just below the surfaces of inner and outer cylinders. The fluid motion on the free surface of the cylinders is visualized by aluminium flakes suspended in the working fluid, which is in this case water. For the experimental investigations on the rotating annulus we use the same LDV-measuring technique as described in previous work of our group (Egbers & Rath, 1996). The analyzing methods for time series analysis are described in more detail in the work of Wulf et al. (1997). As the time scales of baroclinic waves are of the order of 10^3 seconds, automatisation of the experiment is necessary to make long observation times possible. Therefore all components of the setup are controlled by a main computer.

2 RESULTS OF TIME SERIES ANALYSIS OF ROSSBY WAVES

To detect the dynamic behaviour of the occuring Rossby waves in the rotating annulus using linear signal processing techniques the most common and very usefull way is to analyse the time series of a representative velocity component, which is in the rotating annulus experiment the radial one, and to construct the power spectra and the autocorrelation function. The spectrum gives a measure of the amount of power in a given frequency band over a selected frequency range. The autocorrelation function for a periodic signal for example is itself periodic and can often give a less confusing representation of the data than the power spectrum. It therefore provides a useful complementary representation of the data. Irregularity in the time series give rise to a decay in

the autocorrelation function and the rate of decay gives a measure of the degree of irregularity. The extraction of quantitative estimates from the autocorrelation function can be problematical and it is usually used as a complement to the power spectrum.

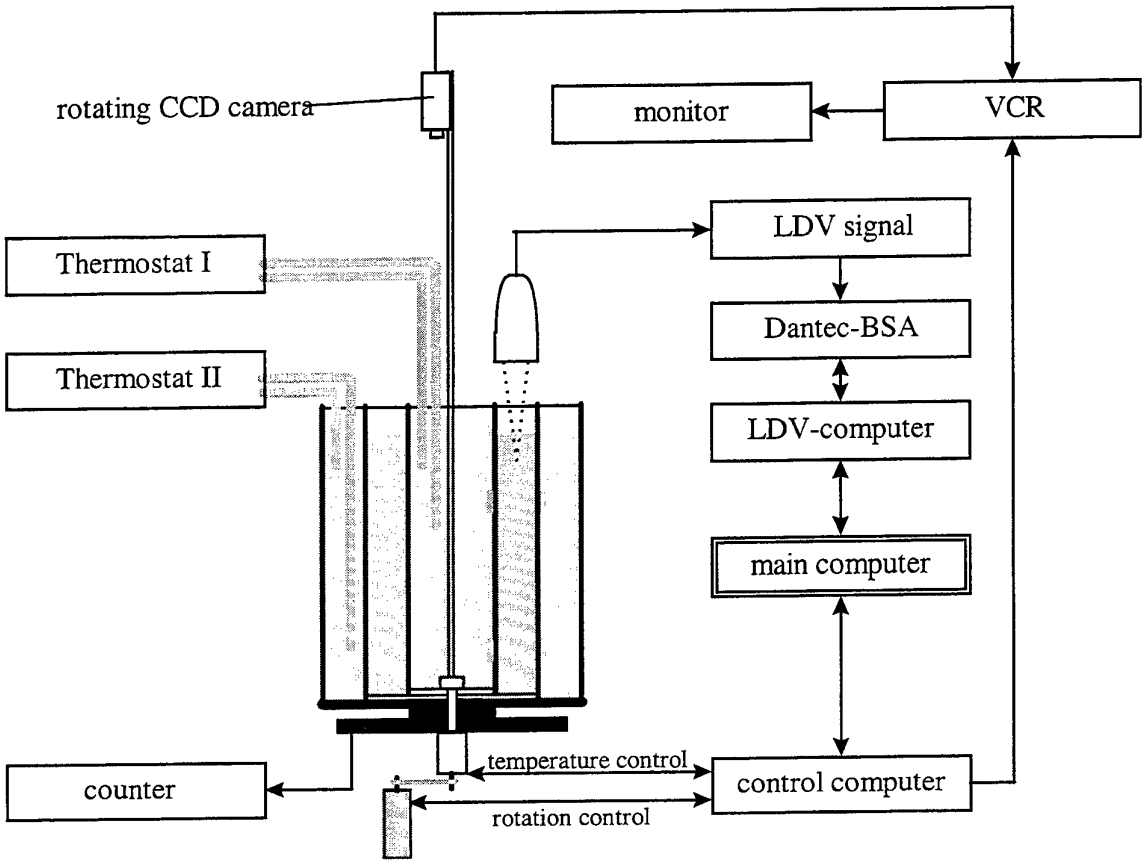


Figure 1: Experimental setup

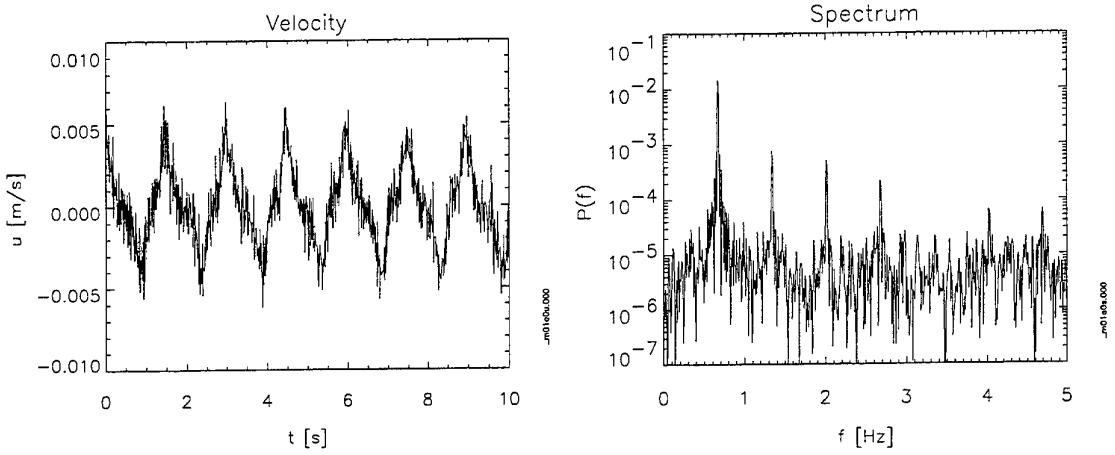


Figure 2: Time series of the radial velocity and power spectrum of the raw data for a m = 4 baroclinic wave, Ta = $6.69 \cdot 10^6$, Ro = 0.61, rotation frequency $f_{rot} = 0.171$

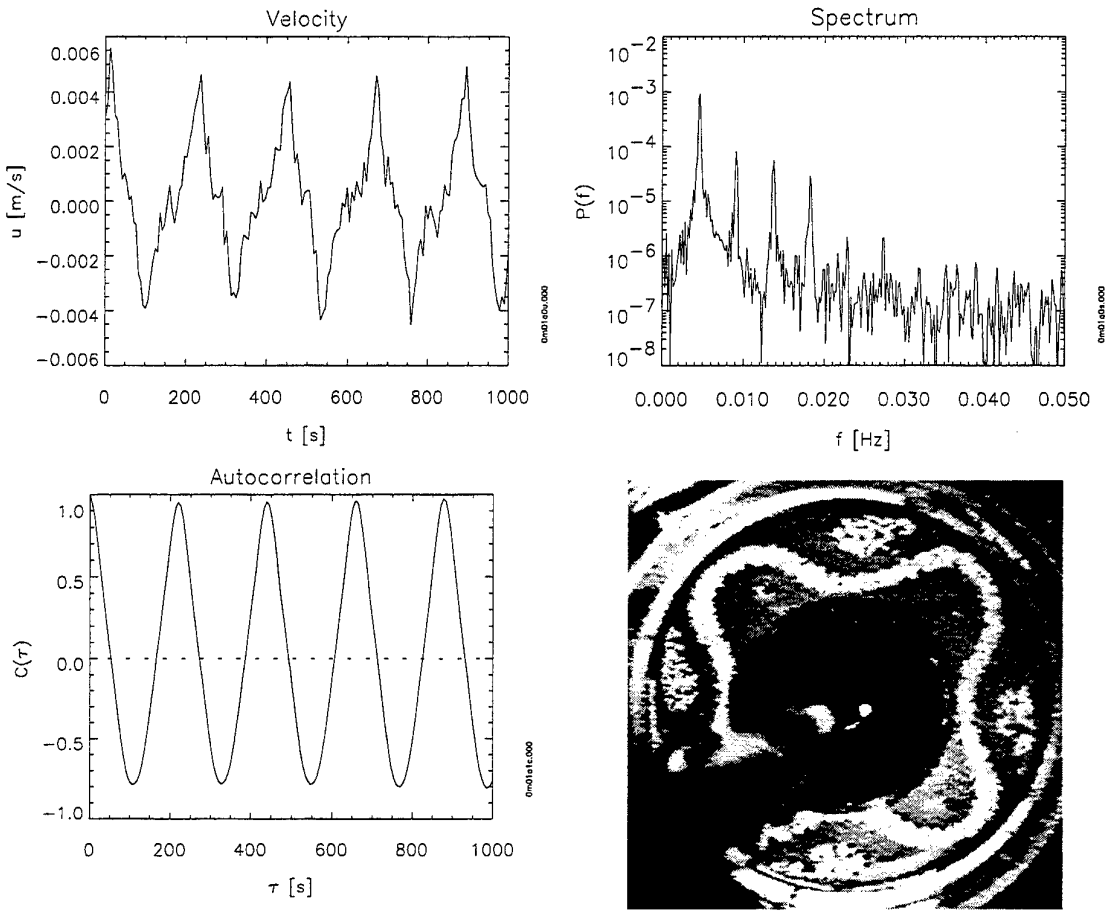


Figure 3: Time series at a fixed point, extracted from the raw data of figure 2, its power spectrum, autocorrelation function and a photograph, Ta = $6.69 \cdot 10^6$, Ro = 0.61, rotation frequency f_{rot} = 0.171

The LDV measurement system is not co-rotating with the cylinder. Therefore, the raw data represent a time series taken on a circle in the rotating annulus. It is not possible to analyse the dynamic behaviour of rossby waves directly from this series. However, one can determine the dominant modes of the waves from its power spectrum. To analyse the full dynamic motion of the wave, however, one needs to investigate a time series at a fixed point in the rotating annulus. But this information is embedded in the LDV-data. If the rotation rate is known, a series at a fixed point can be calculated out of the raw data using only the data points at the beginning of a new period cycle.

A window of the time series and the power spectrum of the raw LDV-data for a baroclinic wave are shown in figure 2, at a rotation frequency of 0.171 Hz. It is a m = 4 mode, shown by the main peak in the power spectrum at 0.43 Hz.

The time series at a fixed point in the rotating annulus, shown in figure 3, is extracted from the raw data shown in figure 2. One should note the change of the time and frequency scales. From this data the drift rate of the wave can be determined directly.

Only a small fraction of the original data is used to calculate the time series in figure 3, so it is possible to extract various independent time series at different points in the cylinder. This is an advantage, if non linear methods are applied.

The method demonstrated above is limited in two ways. First, by the rotation frequency, because $\Delta t = 1/f_{rot}$ is the minimum time step between two points in the time series. Therefore $f_{rot}/2$ is the upper limit of frequency detection. However, the time scales of the baroclinic waves are large compared to $1/f_{rot}$ in this case, so the detectable frequency domain is sufficient. Second, the rotation frequency has to be known very precisely. A small error results in a large distortion of

the calculated time series. A counter registers 1500 pulses per rotation cycle and allows to determine the mean rotation frequency f_{rot} over a long time with nearly arbitrary precision. But small variations of f_{rot} during the measurement will broaden the frequency peaks in the power spectrum



m = 2, Ω = 0.63 1/s m = 3, Ω = 0.73 1/s m = 4, Ω = 0.84 1/s m = 5, Ω = 0.99 1/s

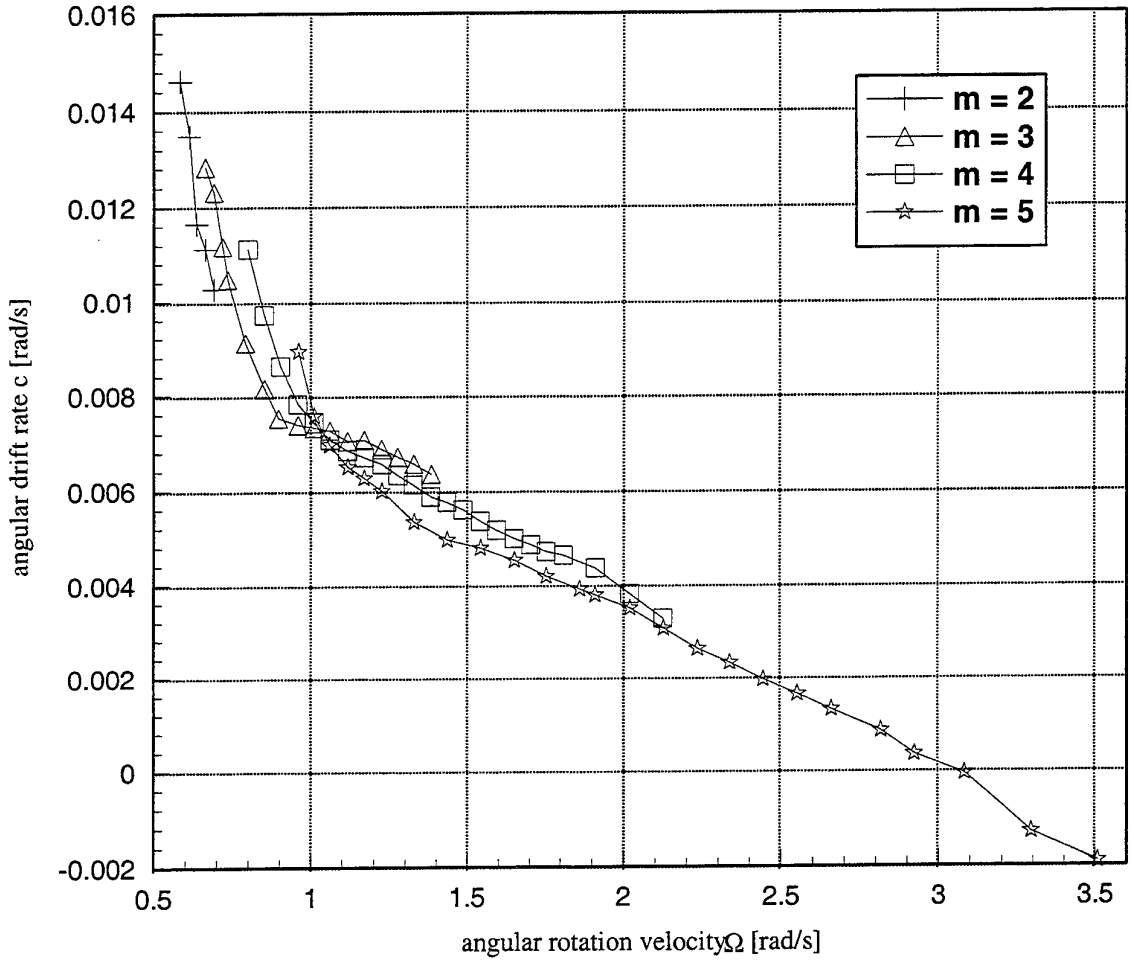


Figure 4: Angular drift rates c of steady waves for different wave numbers, pictures of typical waves for each wavenumber

In this experimental setup the variation is limited to $f_{rot} \pm 0.05\%$. Nevertheless, the effect is not neglectable. The frequency peaks in figure 3 are broadened compared to the power spectrum of figure 2. However, the data quality is good enough to apply nonlinear methods.

In the near future, the correlation dimension and the Lyapunov exponents at characteristic points in the Ro-Ta-parameter space will be determined (Read et al., 1992, Früh & Read, 1997, Fechtmann et al. 1996)).

3 DRIFT SPEED OF BAROCLINIC WAVES

Aside from the LDV analysis, visual investigations were carried out to determine the drift rates c of the steady waves for different modes m (figure 4).

All the data points were taken at a constant temperature difference with the inner wall 3.8 Kelvin cooler than the outer wall. At Ro = 2.1, $Ta = 1.9 \cdot 10^6$, $\Omega = 0.6$ rad/s the transition from the laminar basic flow to the steady m = 2 waves takes place. At Ro = 0.06, $Ta = 7 \cdot 10^7$, $\Omega = 3.5$ rad/s the m=5 mode shows strong irregularities, this is the transition into geostrophic turbulence. These results do agree qualitivly with former results from W.W. Fowlis, R. Hide, 1965.

The drift rate decreases with increasing angular rotation velocity Ω, at the onset of irregular behaviour it changes sign. At low rotation rates, waves with higher wavenumber are faster than waves of lower mode. At Ro = 0.68, $Ta = 6.2 \cdot 10^6$, $\Omega = 1.05 \pm 0.02$ the dispersion changes its sign, at higher rotation rates the waves with higher modes are the slower ones.

LITERATURE

Egbers, C. & Rath, H.J 1996, Developments in Laser Techniques and Applications to Fluid Mechanics, eds. R.J. Adrian, D.F.G. Durao, F. Durst, M.V. Heitor, M. Maeda, J.H. Whitelaw, pp. 45-66, Springer

Fechtmann, C., Wulf, P., Egbers, C. & Rath, H.J. 1996, LDA-Messungen zum chaotischen Verhalten der Strömung im konzentrischen Kugelspalt, Lasermethoden in der Strömungsmeßtechnik, 5. Fachtagung der GALA, 11.-13. Sept. Berlin, vol. V, pp 17.1

Fowlis, W.W., Hide, R. 1965, Thermal convection in a rotating annulus of liquid: Effect of viscosity on the transition between axisymmetric and non-axisymmetric flow regimes, J. Atmos. Dci., 22, pp. 541-558

Früh, W.-G., Read, P. L. 1997, Wave interactions and the transition to chaos of baroclinic waves in a thermally driven rotating annulus, Phil. Trans. R. Soc. Lond. A 355, pp. 101-153

Hide, R. and Mason, P.J. 1975, Sloping convection in a rotating fluid. Adv. Phys. 24, pp. 47-100

Marcus, P.S. 1988: Numerical simulation of Jupitor´s Great Red Spot, Nature 338, pp 693-696

Read, P.L., Bell, M.J., Johnson, D.W., Small, R.M. 1992, Quasi-periodic and chaotic flow regimes in a thermally driven, rotating fluid annulus, J. Fluid Mech., vol. 238, pp. 599-632

Wulf, P., Egbers, C. and Rath, H.J. 1997, Routes to chaos in wide gap spherical Couette flow, Phys. of Fluids, submitted

SESSION 5

Manufacturer's Technical Presentations

SESSION 6

PIV OPTICS

Multilayer PIV Technique with High Power Pulse Laser Diodes

M.Abe[1], N.Yoshida[2], K.Hishida[1] and M.Maeda[1]

1. Department of System Design Engineering,
   Keio University, Hiyoshi, Kohoku-ku, Yokohama, Japan
2. ONO SOKKI CO.LTD., Hakusan, Midori-ku, Yokohama, 226, Japan.

Abstract.

The objective of the present study was to develop and test a multilayer particle image system featureing pulsed laser diodes such that the acquired vector fields would nearly be simultaneous.

We obtained instantaneous and cinematographic two-dimensional velocity fields over multiple layer domains with hardware compactness and at low cost by using laser diodes and conventional CCD cameras. The laser diode emits light in the near-infrared (808nm), and the CCD camera is based on the progressive scan NTSC (640 × 480 pixels, 60Hz) system.

The multilayer PIV system was established by synchronizing laser emission timing and controlling both the synchronous signals and the electrical shutter of CCD cameras. Upon evaluation of the spatial correlation distributions in the "depth" direction the expected three-dimensionality of flow fields were observed.

1. Introduction

The acquisition of getting three-dimensional information in flow fields is quite important in order to construct models for numerical simulations and to comprehend three-dimensional phenomenons. The two-dimensional approach, namely classical particle image velocimetry (PIV[1)]), has and is already put into practical use, but there is a difficulty to extend this to three-dimensional flows. Thus further development of measurement devices for three-dimensional flow fields are on going research topics[2),3)].

One method, holographic particle image velocimetry[4)] can indeed obtain instantaneous high resolution and volumetric velocity fields. The stereoscopic system can also obtain three-component velocity in a planer domain[5),6)], while the scanning laser sheet PIV[7)] can obtain three-dimensional velocity field in a shallow volumetric domain by high speed camera and scanning optics within a small time-wise interval.

Although the volumetric approach of three-dimensional measurement provides a entire velocity field, data processors are heavily loaded to calculate vectors, to storage them, and to extract and analyze the information in the flow field. Difficulties also exist in adapting conventional two-dimensional velocimetry to high speed imaging devices, high power illumination, and special optics. On the other hand a multilayer system provides a temporal two-dimensional velocity fields over a multiple layer domain which is not restricted by depth of focus and arrangement of measurement layers.

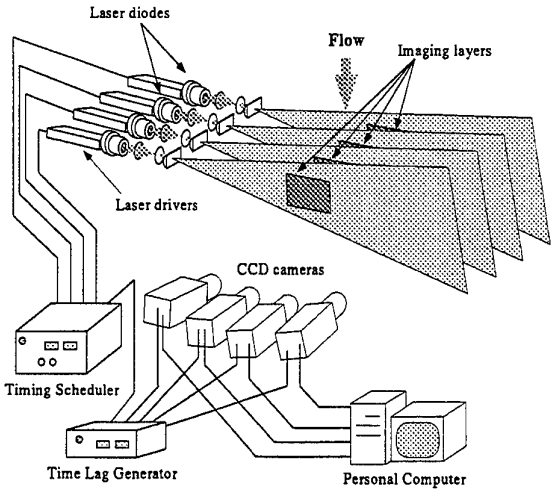


Figure 1 A basic concept of multilayer PIV

The image acquisition when fluid dynamically regarded as simultaneous them provides instantaneous velocity fields in a multilayer domain. By limiting the pulse interval and the duration of the laser diodes, the instantaneous three-dimensional structure observation becomes available. In general, to calculate a spatial correlation, a pair of measurement devices which minimally has the same specification might be required. The multilayer system satisfies this requirement, and with the distributions of spatial correlations into the depth direction available, information three-dimensional structure of flow fields can be investigated.

Further, the application of a laser diode driven in a pulse mode provides flexible controllability in terms of illumination intervals and compactness in the design so that extension to sophisticated multiple layer system in conceivable. The pulse control for illumination provides acquisition of particle image in each individual layer.

2. Instrumentation

Figure 1 depicts the basic conceptual outline of a multilayer PIV system. The CCD cameras are each focused imaging layer, and independently capture an image in each layer by using a time-wise shifted synchronous signal and electrical shutter. A block diagram for controlling the laser sheet and image capturing is shown in Figure 2.

Synchronous signals (V-sync and H-sync) which are slightly time-wise shifted are generated by the synchronizer and given to each CCD camera. A scheduler for laser illumination receives a strobe signal from the synchronizer and scheduled (for timing and duration) emission signals are sent to laser diodes. The electrical shutter duration of each CCD camera is regulated in advance. For each pair of camera and laser, the timing of laser emission and the exposure of CCDs are synchronized, so that the exposure of each image pair is entirely separated.

The capturing and illumination timing are shown in Figure 3, the image of each layer is captured with a short time lag depending on illumination pulse duration, and the adjustment of time lag is based on the synchronous signal.

Thus with a standard CCD camera, by controlling the synchronous signal of each camera and providing exposure duration in advance, a $800\mu s$ or shorter time lag is achieved while independent images are caputured over a multilayer domain. (The time lag depends on lighting duration; the synchronizer can generate a minimum 100ns time lag.)

In this system, the intervals between image pairs are fixed at 16.7ms, because a CCD camera working at standard video rate requires a certain interval to transfer an image from the internal resister to video output line, during which time the closing of electrical exposure is inhibited. By closing of electrical exposure we mean that there is a sweeping out of electrical charges of the CCD to the output line. Hence the charge coupled devices have to transfer their charge to an internal register immediately after closing the electrically shuttered exposure. This limitation of the CCD prevents a flexible shuttering sequence. When there is a high speed phenomenon in the flow field necessitating a illumination intarval for a pair of particle images, a flexible shuttered camera such as a CMD (which allows random access to charge devices without sweep out of charged data) camera may be appropriate.

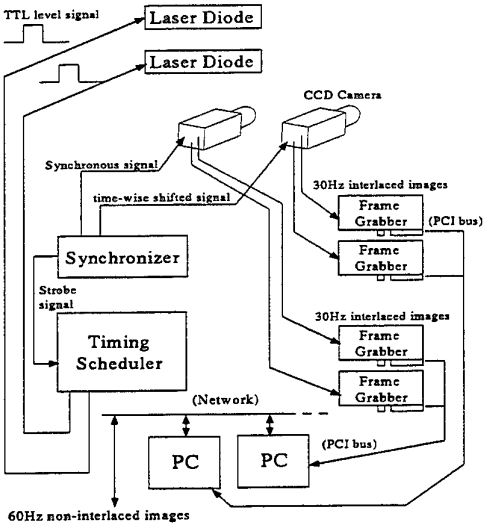


Figure 2 Block diagram of multilayer system

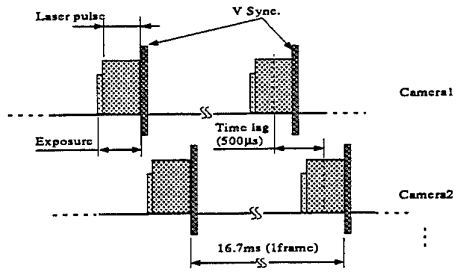


Figure 3 Timing chart

The CCD camera employed was a NTSC progressive scan camera (SONY XC-7500). Though it is a conventional analog camera, by providing a dual output line with a standard NTSC signal, it can provide 60 Hz of information with 640 × 480 pixels resolution. In a dual-output line type CCD camera which has 60Hz time resolution, each line transfers 30Hz interlaced frames which are timewise shifted data (detail shown in Figure 4).

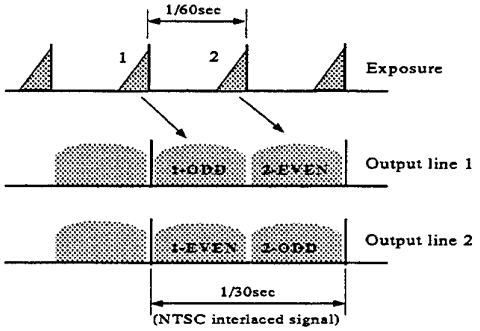


Figure 4 Sequence of dual output line camera

The computer (see Figure 1 and 2) receives digitized images through a pair of standard analog frame grabber boards (DataTranslation DT-3155). A PCI (Peripheral Computer Interface) bus equipped PC provides sufficient transfer rate to capture images in real time, and the frame grabber is able to transfer them directly to the system memory (without analog storage and no external private storage). Two frame grabbers are driven simultaneously and acquire pairs of frames, and received images are transformed into 60Hz non-interlace images by an acquisition software.

The light source for illumination is a near-infrared laser diode which is designed as a pulse laser diode device intended for distance determination on automobiles. It has a wave length of 808nm, and maximum power of 3W (in terms of chopped CW laser) when it works in short pulse mode of 1μs duration and 10% duty ratio at room temperature. The power supply to the laser diode is operated a transistor circuitry. It provides a large electric current to the diode during the input signal when the level is high. Although its repetition rate is sufficient for PIV illumination, the total energy supply is small. If it work in the CW mode, the output power is only several hundreds mW and insufficient. Accordingly, 0.3-0.8ms pulse duration was adopted. Although it is not recommended by the manufacturer, the diode can provide not only 2.5W power, but at over 60Hz repetition rate (at duty ratio 0.2-1%) by using a heat sink.

A laser diode can work in both a CW or pulse mode in spite of its specifications. The maximum output energy depends on the product of electric current, the duration of pulse and the repetition rate. The output energy of a laser diode designed for CW mode is restricted in maximum electric current, and in general, it is lower than pulse mode diode. A pulse mode laser diode is able to withstand a against large electric current (i.e. strong emission), and its maximum output energy depends on duty ratio, which is defined as ratio of repetition frequency to emission duration time. However it can not emit light for long duration time with while maintaining high output power because of heat production. Thus in using a pulse diode laser for long duration time, cooling is necessary. An increase in diode temperature induces both reduction of output power, making its wavelength longer, and shortening the life span of the diode (generally, a 10K increase of temperature results in a 50 percent reduction in the diode's life span). Sufficient cooling allows both high power output and high duty ratio operation.

In consideration CCD sensitivity, a visible wavelength laser is preferable. Unfortunately a typical visible (600-700nm) CW laser diode has only several tens mW, and a high power type near-infrared laser diode can emit several W of power when it is driven in the pulse mode. The sensitivity of standard a CCD camera in the near-infrared is extended to about 900 nm when the IR cut filter is removed, and theillumination wavelength at 808 nm is observed. The low sensitivity of CCD in infrared is compensated by using a low f number camera lens which has a $f0.85$ maximum and used at $f2.8$ or lower.

3. Experiments

3.1. Experimental setup

A dual-layer system was constructed and evaluatedfor further improvement further to a multilayer system for flow in the wake region behind a circular cylinder (shown in Figure 5). Polystyrene particles, 3-30μm in diameter, were seeded into water. The average velocity was 0.02 m/s, and the cylinder was 13 mm in diameter; the Reynolds number was set at about 260. In the wake of the cylinder, a large vortex is generated.

The light sheets optics and laser diodes were set opposite each other but in parallel to obtain depth direction variations of the vector fields. (As

diodes do not emit light simultaneously, they are not broken by re-absorption of photon.) The distance between the light sheets was varied by a precise manipulator mounted on one side of the laser and optics. The thickness of the light sheet was 1mm.

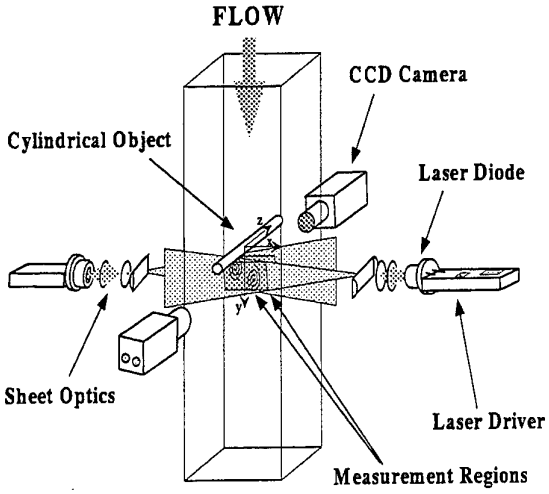


Figure 5 Experimental setup

3.2. Image processing

The image analysis to determine the velocity vector fields on each image plane was performed by the hierarchical approach[8),9)] based on a cross-correlation technique[10)]. A three processing pass strategy was adopted, and processing during the first pass procedure was performed by using a reduced resolution image (320×240 pixels) for processing speed. The hierarchical technique produces not only a high resolution vector field but also higher processing speed. In processing into multilayer images, a faster processing speed compared with classical cross-correlation technique in a single planar domain was achieved.

False vectors were validated by comparing adjacent vectors[11),12),13)], and interpolated by averaging neighboring valid vectors. In the first and second pass, vectors were corrected by iterating a correction process and using a lower threshold for validation. In the last pass the validation and the correction are performed together, and a sub-pixel analysis by fitting adjacent correlation coefficient to a Gaussian distribution was performed.

3.3. Results and discussions

A typical example of instantaneous velocity fields behind a circular cylinder in two parallel planer domains are shown in Figure 6. Distance between each layer was 1mm; what is, arrangement in which the overlapped light sheet region just disappeared. The averaged velocity over the image field was subtracted to observe the vortices. Two-dimensionality was observed in near two section.

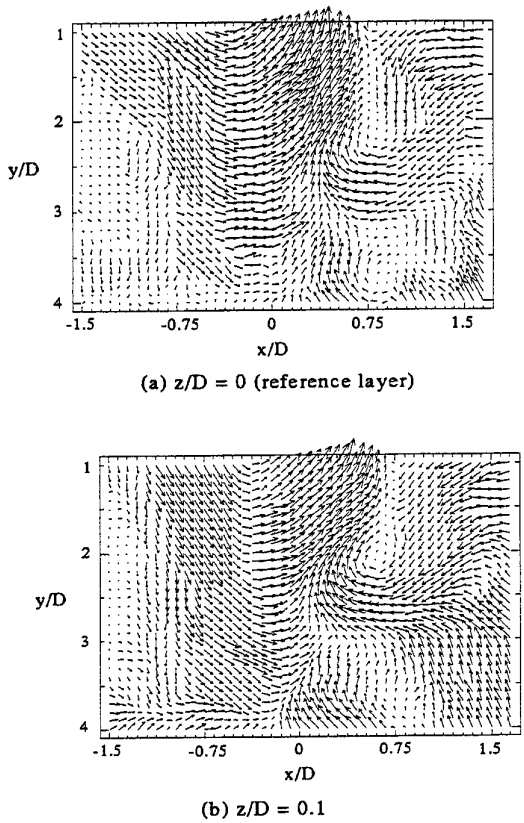


Figure 6 Instantaneous velocity fields in near layers

Figure 7 shows a time series of vector fields in the two layer domain where the distance between each layer was 3mm, and display intervals was 0.1s (vector map, inpractice was obtained at 60Hz). There was no significant change in the flow field up to 0.4s, thus the time lag between each layer image at 800μs is negligibl small and the acquisition of each layer is regarded as simultaneous. And a similar characteristics of vortices and the two-dimensionality behind a circular cylinder was observed, though it was not exactly equal. Changes in the flow field into the depth direction were clearly observed in the lower reaches of the stream, which was also observed in mean velocity profile (Figure 8) based on 120 vector maps (2 seconds).

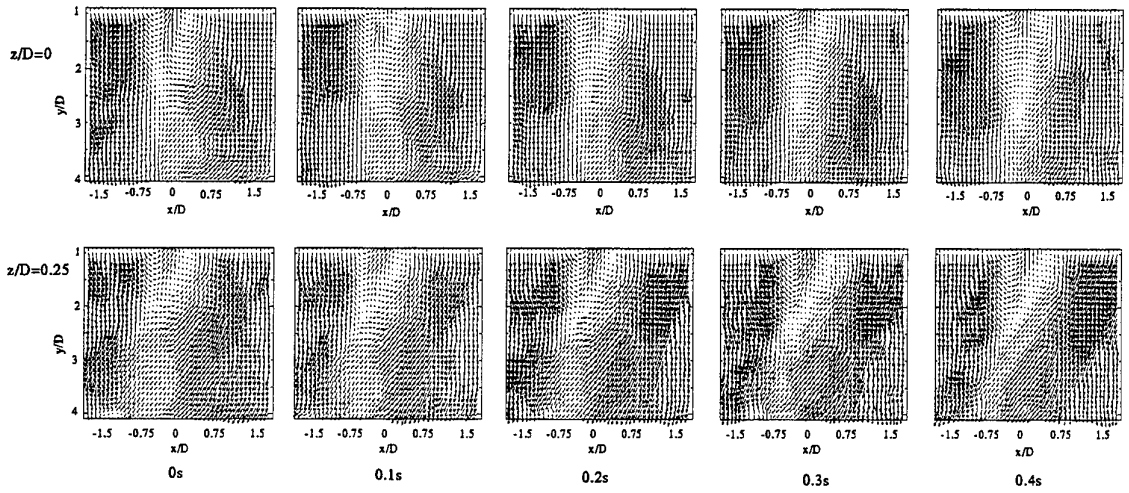
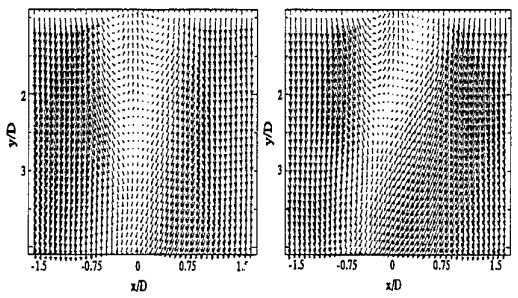


Figure 7 Time series of instantaneous velocity fields in dual-plane domain



$z/D = 0$ $z/D = 0.25$

Figure 8 Mean velocity profiles

In general, to calculate the spatial correlation, two or more measurement devices which have the same specifications are required. The multilayer system satisfies this condition, and correlations distribution of velocity fluctuations in each layer were calculated to observe either two-dimensionality or three-dimensional variations of vortex filaments in the depth direction. A correlation coefficient $R(x, y)$ for x direction fluctuation is defined by the following equation.

$$R(x,y) = \frac{\overline{u_1{}' u_2{}'}}{\sqrt{\overline{u_1{}'^2}}\sqrt{\overline{u_2{}'^2}}} \qquad (1)$$

Here $u_1{}'$ is the velocity fluctuation in the reference plane, and $u_2{}'$ is in the depth-wise shifted plane. The correlation in the y direction is determined in the same way.

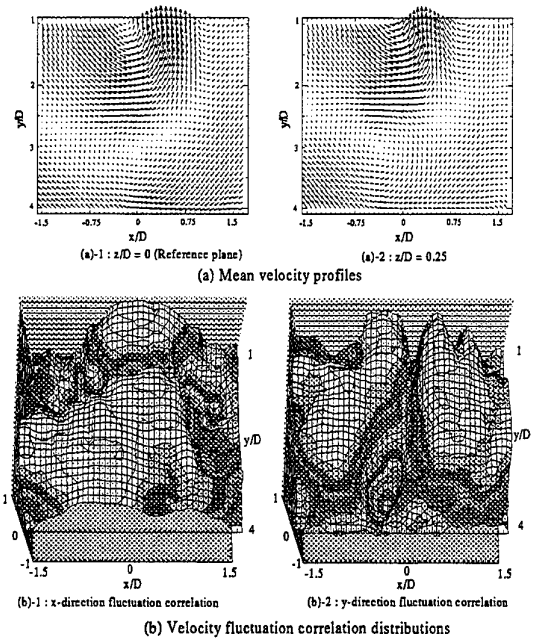


Figure 9 Correlation distributions of velocity fluctuation

The calculated correlation coefficient distribution and the velocity over the entire field in each plane for which the averaged velocity in whole field was subtracted are given in Figure 9. The term for averaging and calculating correlations was 2s, based on 120 vector maps. A left wise drifted vortex into the depth direction was observed in Figure 9-(a). This is considered to be caused by the three-dimensional mutual action be-

tween vortex filaments. In the lower region of the stream, two-dimensionality was attenuated by three-dimensional action.

As for the correlation of fluctuation in the x direction, high correlations are observed at near the vortex region. This is considered to be the vortex motion influence into the depth direction. However, the correlations in the y direction take on negative values at the vortex. This means that a negative fluctuation is generated in the reference plane when a positive one occurs in the other plane. The change in sign is caused by a drift of the vortex, the velocity reverses in the direction from the vortex center. Therefore, the x direction drift of the vortex is detected as a negative correlation of the y direction fluctuations.

4. Conclusions

A multilayer PIV system based on a pair of laser diodes and standard CCD cameras has been developed. The dual-layer system was constructed and applied to flow in the wake region behind a circular cylinder at low Reynolds number. Simultaneous acquisition of particle images in multi-layer domain was achieved so that a condition to obtain the velocity fluctuation correlation distribution was satisfied and was calculated by the constructed system.

In addition to the feasibility of a laser diode as a light source for PIV was shown. The laser diode operated in pulse mode provides the enough output power to illuminate a particle image subsequently captured by a standard CCD camera, and flexible scheduling was achieved. The compactness of the system and low cost for filed illumination provides flexibility in terms of the measurement section and further extension to sophisticated multiple layered system.

Acknowledgment

This work was supported by a Grant-in-Aid of the Japanese Ministry of Education, Science and Culture (grant No.10555062).

References

1) Adrian R J, 1991, Particle-imaging techniques for experimental fluid mechanics., *Ann, Rev. Fluid Mech.*, 23, pp261-304.

2) Klaus D Hinch, 1995, Three-dimensional particle velocimetry, *Meas.Sci.Technol.*, vol.6, pp742-753.

3) Barnhart D H, Adrian R J, Papen G C, 1994, Phase-conjugate holographic system for high resolution particle image velocimetry, *Appl. Optics*, 33(30), pp.7159-7170.

4) I Grant, 1997, Particle image velocimetry: a review, *Proc. Instn. Mech. Engrs.*, vol.211 part C, pp.55-76.

5) Prasad A K, Adrian R J, 1993, Stereoscopic particle image velocimetry applied to liquid flows, *Exp.Fluids*, vol.15, pp49-60.

6) Liu Z C, Adrian R J, Meinhard C D, Lai W, 1996, Structure of a turbulent boundary layer using a stereoscopic large format video-PIV, *Developments in Laser Tech. and Fluid Mech.*, II.8, pp259-273.

7) Ch Brücker, 1997, 3D scanning PIV applied to an air flow in a motored engine using digital high-speed video, *Meas.Sci.Technol.*, vol.8, pp1480-1492.

8) Roesgen T & Totaro R, 1995, Two-dimensional on-line particle image velocimetry, *Exp. Fluids*, vol.19, pp.188-93

9) Christian Willert, 1997, Stereoscopic digital particle image velocimetry for application in wind tunnel flows, *Meas. Sci. Technol.*,vol.8,pp.1465-1479

10) Kobayashi K,Sakakibara J, Hishida K, and Maeda M, 1991, Time-Series Measurements of Turbulent Flow field Using Image Processing System , Experimental and Numerical Flow Visualization, *ASME FED*, Vol.128, pp.155-162.

11) Raffel M & Leitl B and Kompenhans J, 1992, Data validation for particle image velocimetry, *6th Int. Symp. on Appl. of LaserTechniques to Fluid Mechanics*(Lisbon,July 20-23)

12) J Nogueira & A Lecuona and P A Rodriuez, 1997, Data validation, false vectors correction and derived magnitudes calculation on PIV data, *Meas. Sci. Technol.*,vol.8,pp.1493-1501

13) Sakakibara J, Hishida K & Maeda M, 1993,Measurement of Thermally Stratified Pipe Flow using Image-processing Techniques ,*Experiments in Fluids* , No.16, pp. 82-96.

GAS FLOW VISUALIZATION BY LASER DIODE LIGHT SHEET IMAGING

B. Nath, W. Löber, W. Baetz* and W. Holzapfel*

Elster Produktion GmbH, Steinernstraße 19-21, D-55252 Mainz-Kastel, Germany
*Institute of Measurement and Automation, University of Kassel,
Mönchebergstr. 7, D-34109 Kassel, Germany

ABSTRACT

This article describes how flow tests can be carried out by employing the use of a simple, modularly extendable laser light sheet unit which does not include any high-power lasers, only customary monomode laser diodes. Since the luminous power of monomode laser diodes does not yet reach the output power of high-power gas lasers, which are typically used, a highly sensitive video camera with a sensitivity of approx. 0.1 lux is applied to record the images. By means of a frame grabber board, the video signals of the camera are subsequently transferred to a Pentium-based PC for digital post-processing. Following the separation of the video frames, the subtraction of dark-field images and the spreading of gray-scale values lead to a considerable improvement of the resulting images.

Using application examples of the field of gas flow measurement and control, it is then shown how this technology can be utilized in order to create convincing light sheet images which require a comparatively low amount of work.

1. INTRODUCTION

The laser light sheet technique is a method which makes it possible to represent flow patterns in gas measuring and controlling units, Ebinger (1993), Karagoz (1993). For that purpose, a light sheet is generated illuminating a flow field that can be examined in a thin plane layer (thickness: approx. 0.7 mm). Within this layer, i.e. the so-called light sheet, the flow conditions can then be observed using the tracer streaks of scattering particles. The particles are added by means of an aerosol generator.

However, the disadvantage of this method consists in the fact that high luminous intensities are needed in order to visualize gas flows. Such luminous intensities are usually provided by high-power gas lasers (e.g. Argon lasers) in the visible range. This technology requires a lot of devices and is very expensive. In addition, introducing the high luminous intensities into the test specimens often causes problems.

Therefore this article presents a laser light sheet unit, which does not use any high-power gas lasers, but instead uses customary monomode laser diodes. Finally, this article presents the application of laser light sheets to gas flow imaging.

2. LASER LIGHT SHEET UNIT

On account of the progress made in semiconductor technology, it is possible to manufacture compact laser diodes which directly convert the injection current into visible radiation while simultaneously ensuring high efficiency.

In order to generate a light sheet it is necessary to spread the usually collimated radiation of the laser across one plane. If the cross-section of the beam is sufficiently small, this can be accomplished by means of a simple cylindrical lens. However, a laser generally does not have a constant intensity distribution across the cross-section of the beam. The TEM_{00} mode (fundamental transverse mode of the laser source) is characterized by a Gaussian intensity distribution which leads to a very inhomogeneous illumination of the light sheet. In particular, high laser outputs may cause an overexposure in the center and/or an underexposure in the peripheral areas which cannot be compensated for by the dy-

namic range of the recording system. For this reason, a simple, modularly extendable light sheet unit has been developed which does not use any high-power gas lasers or solid-state lasers, but instead uses customary monomode laser diodes.

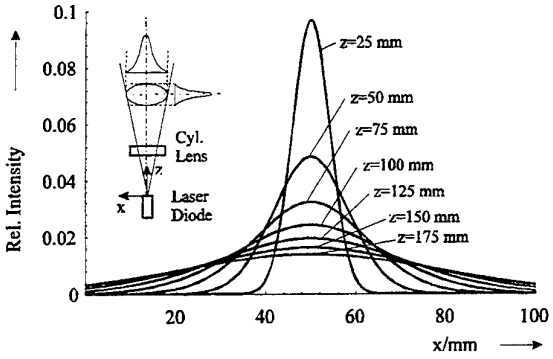


Figure 1: Intensity distribution of a single laser diode (TEM_{00} mode) when the light is diffracted to form a light sheet (x-axis) for various distances from the laser-active area (z-axis).

Contrary to a gas or solid-state laser, the radiation characteristic of a monomode laser diode does not show a collimated output beam with a circular cross-section. Due to the small dimensions of the exit window of the laser-active area (typically 1 x 3 µm), solid-state lasers have a very divergent radiation field – caused by diffraction effects – with the cross-section being approximately elliptic (cf. Figure 1), and the semi-axes parallel and normal to the semiconductor junction. The differing divergence angles normal and parallel to the semiconductor junction result from the rectangular cross-section of the laser-active zone, Yariv (1989). Since the dimensions of the emitting zone are very small, a monomode laser diode is approximately equal to a point source of light. Therefore, a single cylindrical lens is sufficient to collimate the laser radiation in one plane. To ensure that the resulting light span is as thin as possible, the smaller divergence angle in the y-z plane, parallel to the semiconductor junction, is collimated with the cylindrical lens. The divergence angle normal to it determines the spread of the light span.

The intensity distribution of a monomode laser diode is approximately equal to a Gaussian distribution in the far-field region parallel to the semi-axes of the radiation ellipse. Due to the parallel arrangement of several laser diodes, the Gaussian intensity profiles overlap more and more, when the distance z is increased, and ensure an almost constant illumination with small variations of intensity across a wide range (cf. Figure 2). Hence, it is possible to achieve a more uniform illumination than would have been possible with a single laser source (cf. Figure 1). In case of a single radiation source with a Gaussian intensity profile, either specific lens systems, Dantec (1995), must be used, or the usable radiation cross-section must be limited to achieve a more uniform illumination in a light sheet.

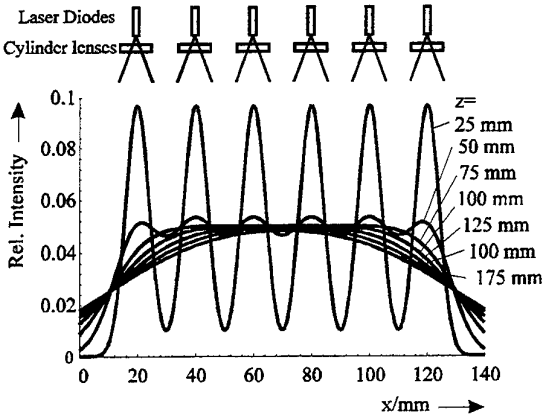


Figure 2: Intensity distribution of a light sheet produced by six parallel laser diodes with a spacing of $\Delta x = 20$ mm and a divergence angle of 22° (FWHM: full width at half maximum) for various distances z from the active areas.

To produce the light, the laser light sheet unit which has been developed (cf. Figure 3) uses two separate modules with three laser diodes each that emit visible radiation at a wavelength of λ=690 nm.

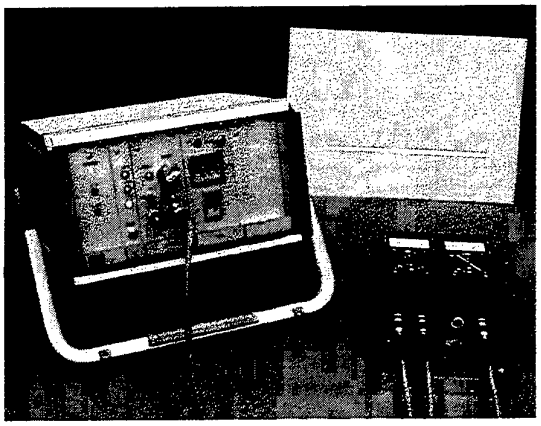


Figure 3: Laser diode light sheet unit equipped with two laser diode modules and a power supply module; operation in continuous-wave mode.

The optical output power of the modules is stabilized and altogether amounts to approx. 0.3 W. The radiation of each laser diode is collimated with a cylinder lens in the plane of the laser-active zone – thus ensuring that a light sheet is created which has a thickness of approx. d = 0.7 mm. Due to the parallel arrangement of the laser diodes, the radiation light spans overlap and form a resulting light sheet with almost constant intensity. The useful illuminated range of the light sheet – with both modules arranged in parallel – amounts to about 100 x 100 mm² with a working distance of 60 - 160 mm (cf. Figure 4).

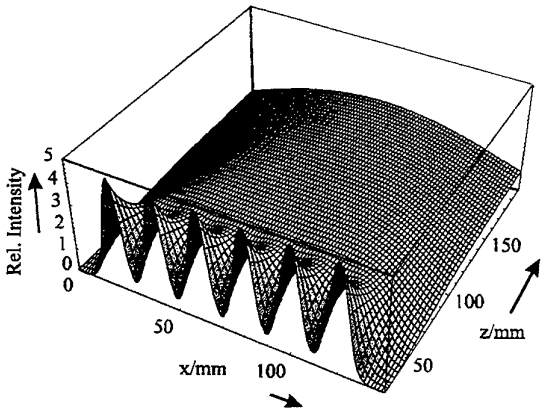


Figure 4: Intensity distribution of a laser diode light sheet produced by six parallel laser diodes with a divergence angle of 22° each and an output power each of P = 50 mW at λ = 690 nm.

The modular configuration allows an increased flexibility with respect to the arrangement of the radiation sources, and ensures that the intensity and dimensions of the light sheet can be adapted to the respective requirements of the measuring task. The control unit of the light sheet allows both a continuous-wave (cw) operation and a pulse operation with pulse lengths ranging from 100 µs to 999 s.

3. TEST SETUP

Figure 5 shows the test setup to record flow images by means of laser light sheets. The test specimen shown is equipped with optical inputs. A circular cylinder, with the flow streaming normally to its axis, is within the reach of the inspection window for the camera. The laser light sheet enters the gas flow channel through the optical inputs on the top and bottom of the test specimen. The light sheet plane is orientated parallel to the flow, and perpendicular to the axis of the test specimen.

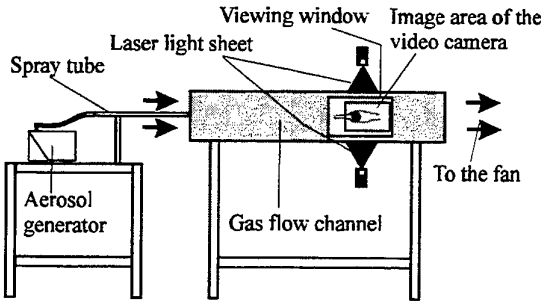


Figure 5: Schematic diagram of the test setup.

A vacuum pump generates the flow through the test setup. The flow is adjusted to a constant volume flow using a Venturi tube operated under critical conditions. To visualize the air flow, an aerosol generator is used to add DEHS (diethyl sebacate) particles with a size of 0.2-1 µm. When these particles pass through the light sheet, together with the flow, they scatter the laser light and are therefore visible. Within the light sheet, an image of the flow pattern appears that is recorded by a video camera through the inspection window. In order to compensate the lower light output of the laser diodes – compared with high-power lasers – as much as possible, a highly sensitive video camera with a sensitivity of approx. 0.1 lux is used to record the images. The analog output signal of the camera is digitized by a frame grabber board installed in a PC and then stored. Eventually the PC can be used for a digital post-processing of the images.

4. IMAGE PROCESSING

In order to provide an optimal presentation of the information contents of the recorded flow images, various digital image-processing techniques are used.

First of all, a digital separation of the frames into fields is carried out. This is required because the video camera operates with the interlaced field technique in accordance with the European CCIR standard. The frame which has been digitized by the frame grabber board consists of two consecutive fields with a time offset of Δt = 20 ms. While one field contains the image information of all even lines at a given time, the other field contains the informa-

tion of the odd lines at the same time plus $\Delta t = 20$ ms. With respect to the example where a non-stationary flow against a cylinder is recorded, this time offset results in a local offset in Figure 6. The size of this local offset is dependent on the flow rate.



Figure 6: Raw flow image recorded by means of the field technique.

By means of the digital separation of the interlaced frames into fields, any frame digitized by the frame grabber board is split into two fields which have only half the height. Thus the image contents gives the impression of being highly compressed. This effect is compensated for by spacing the lines of the resulting image until a blank line emerges between two adjacent lines. The gray levels of the pixels of these blank lines are generated by a linear interpolation of the gray levels of the pixels above and below.

Another important result of the digital separation into fields is the seeming duplication of the sampling frequency of the recording system. Any events which are presented blurred within a frame can now be observed through two consecutive fields. Figure 7 and Figure 8 show the fields created by the odd and even lines as a result of the separation into fields indicated in Figure 6.



Figure 7: Field created from odd lines.



Figure 8: Field created from even lines.

In order to eliminate reflections or extraneous light in the flow images, the separation into fields is followed by the subtraction of dark-field images. For that purpose, a dark-field image is recorded with the camera being unchanged and the laser light switched off. By subtracting the dark-field image from the flow image, only the contents of the image which is caused by the influence of the laser light remains.

Since the original image, in general, consists of only a restricted range of gray levels, finally a spread of the gray levels is carried out to fully utilize the existing pixel depth of 8 bits. For that purpose, the smallest gray level and the highest gray level of the existing gray levels are taken from the histogram. This restricted range is now homogeneously spread across the entire range of possible gray values. Due to the increased resolution of gray values, minor differences between gray levels are now better visible.

5. FLOW TESTS

To show the versatile application of laser light sheets, some examples taken from the field of gas metering will be examined. Additional examples are given for further review by Nath (1998).

5.1 Vortex Meter

Multiple flow analyses have been performed on a vortex meter. Figure 9 shows the formation of the Karman vortex street downstream of a cylindrical bluff body at a Reynolds' number of $Re = 400$. The recorded video sequences distinctly show the uniform shedding of the vortices.

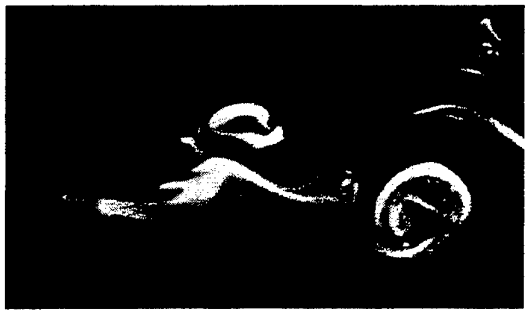


Figure 9: Karman vortex street downstream of a bluff body. Aperture f=1/1,4; exposure time=1/1000 s.

The flow image presented in Figure 9 is also confirmed by the result of a CFD[1] calculation[2] (Computational Fluid Dynamics). Figure 10 shows the pressure downstream of the cylinder with the flow streaming transversally against it. The bright colors correspond to the low pressure values and the dark colors to the high ones. The geometry as well as the limiting conditions, were identical for both the simulation and the test.

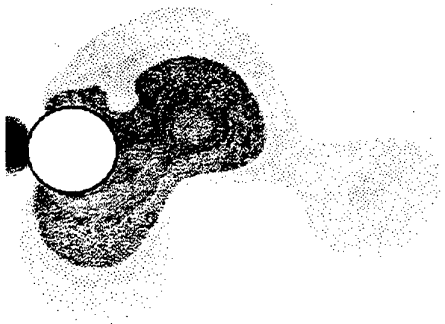


Figure 10: Karman vortex street downstream of a bluff body.

The Figures 9 and 10 clearly show the consistency of the vortex distances which are characteristic of this flow along the main flow direction.

[1] Fluent V4.2, Fluent Inc., Centerra Resource Park, 10, Cavendish Court, Lebanon, NH 03766, U.S.A.

[2] All CFD calculations have been carried out in cooperation with RUHRGAS AG, TAZN, by Dr. A. Hilgenstock and S. J. Kolpatzik. All Persons involved are highly qualified specialists who were very committed to this task.

5.2 Ultrasonic Flow Meter

The ultrasonic flow meter (cf. Figure 11) uses a non-contact acoustical technique that is state of the art in gas measurement technology. Unlike conventional measuring methods, ultrasonic flow measurement does not require any mechanically moving parts or inserts interfering with the cross-section of the flow. Instead, the flow is sampled by ultrasonic signals without any contact. That way, the measuring device has a particularly low flow resistance and generates only a very small pressure drop.

The ultrasonic flow meter ELSTER USM 80 operates with two measuring paths, according to the procedure, measuring the difference of travel times. To accomplish this, two pairs of piezo-ceramic ultrasonic transducers are installed under the angle φ in the flow channel diagonally with respect to the flow; these transducers serve as acoustical transmission links.

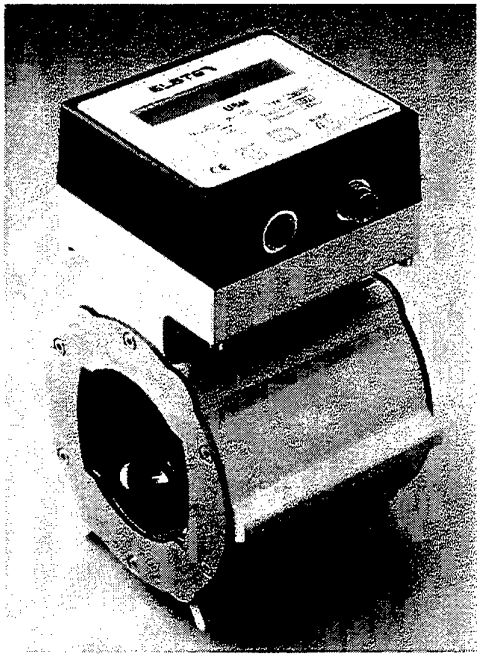


Figure 11: Ultrasonic flow meter ELSTER USM 80.

Using the laser light sheet procedure, it is now possible to determine the ideal installation position of the ultrasonic transducer in order to ensure an optimal flow.

Figure 12 shows the modified housing of an ultrasonic flow meter.

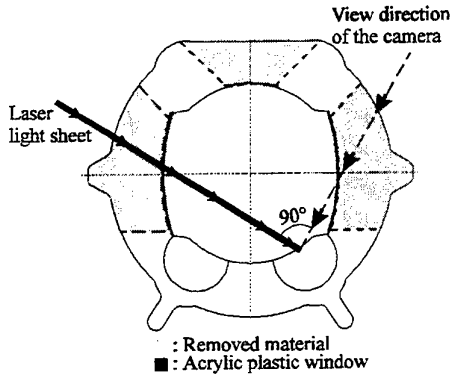


Figure 12: Cut-away view of the ultrasonic flow meter housing with the laser sheet and camera angle displayed

To gain optical access, openings are milled into the housing. The openings are then sealed with acrylic plastic windows to prevent gas from escaping. The laser light sheet is then inserted into the sound path of the transducer. To avoid image distortion of the recorded flow images, the camera is mounted perpendicular to the laser light sheet.

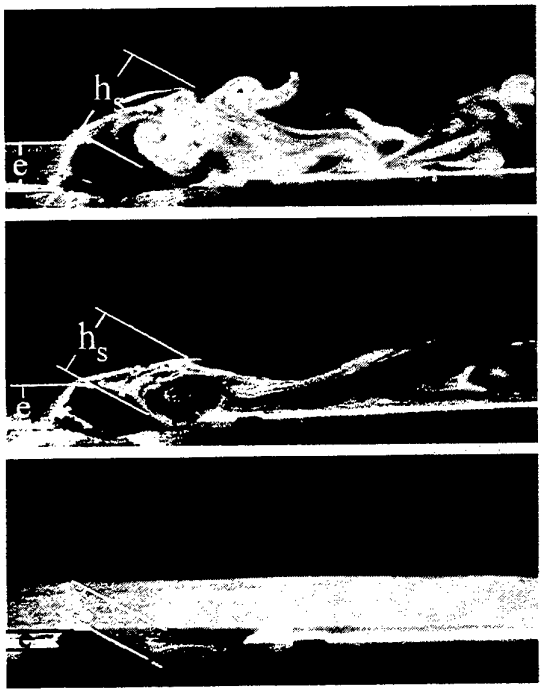


Figure 13: Effect of a piezo-ceramic transducer of an ultrasonic flow meter which projects into the flow within the pipe. Aperture f=1/1,4; exposure time=1/1000 s.

All flow images taken from the ultrasonic flow meter have been recorded at a flow rate of u=1 m/s. The upper image of Figure 13 shows the flow – in the direction of the flow – on an ultrasonic transducer which projects into the flow by e=8 mm. The generation of vortices on the top edge of the ultrasonic transducer are clearly visible. The separating vortices are carried away by the flow and interfere with the sound path of the ultrasonic transducer along a length of h_s=17 mm.

The central image of Figure 13 shows how the disturbed length h_s can be reduced to h_s=9 mm by chamfering the outside edge of the piezo-ceramic transducer. This measure also reduces the generation of vortices downstream of the ultrasonic transducer. By moving back the chamfered ultrasonic transducers to the height e=3 mm, the length of the disturbance can be reduced once more by more than 50% to h_s=4 mm. The generation of vortices on the chamfered edge can be prevented in this installation position as can be seen in Figure 14.

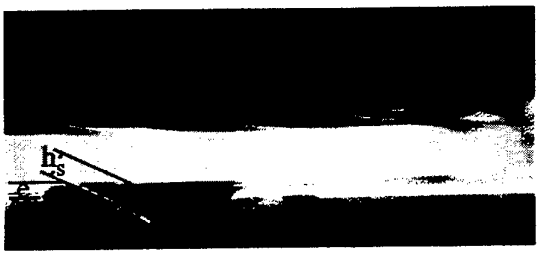


Figure 14: Flow image of a piezo-ceramic transducer of an ultrasonic flow meter which projects into the flow. Aperture f=1/1,4; exposure time=1/2000 s.

This figure shows the same installation position of the ultrasonic transducer as in Figure 13 (bottom), however at a flow rate which is approximately five times as high (u=5 m/s).

Since the variant shown at the bottom of Figure 13 caused the least disturbances, it was used for the ultrasonic flow meter.

Supplementary analyses using a laser doppler anemometer (LDA) have confirmed the results of the recorded flow images (cf. Figure 13). The velocities of the gas flow is shown in Figure 15.

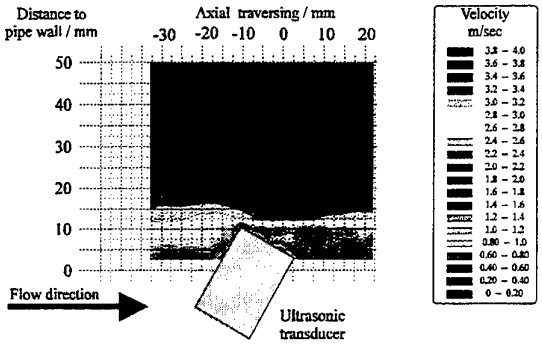


Figure 15: LDA results of the velocities around an ultrasonic transducer which projects into the flow.

Before the ultrasonic transducer there is no distorted flow profile. The gas stream then passes over the transducer surface. Just after the transducer, multiple swirls are generated reducing the flow velocity. The LDA measurement clearly shows the turbulence of the flow in the region surrounding the transducer (Fig. 16).

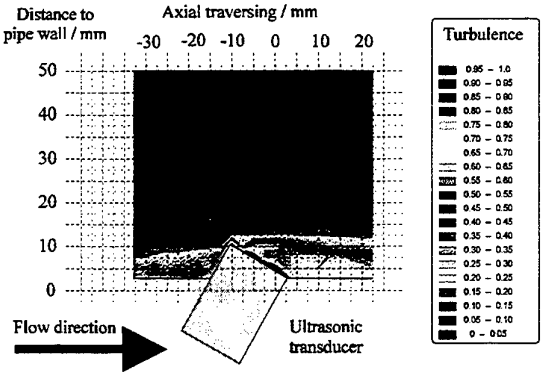


Figure 16: LDA results of the turbulence around an ultrasonic transducer which projects into the flow.

The degree of turbulence is low in front of the transducer. However, it is increased in those areas characterized by a significant generation of vortices in the flow downstream of the ultrasonic transducer.

6. SUMMARY

The tests have shown that commercially available monomode laser diodes can be used in order to build a simple and inexpensive laser light sheet unit which, due to its compact size, allows a good optical access. In connection with the higher packing density of parallel laser diodes, extended light sheets can be set up with a high and homogeneous intensity. Additionally, although the high output power of laser diodes have not yet been reached for the visual spectral region, it can be expected, considering the progress of semiconductor laser technology, that this will be possible in the not so distant future.

Using commercially available CCD video cameras, it is now possible to compensate for the low luminous intensity without any problems. In connection with a digital post-processing of the flow by means of a PC, an optimal evaluation can be ensured.

The application examples which have been provided show that the laser light sheet technique, implementing the use of laser diodes, is an important tool for the development of gas meters and pressure regulators.

7 REFERENCES

Dantec 1995, Illumination Systems, Dantec Measurement Technology A/S, Publication No. 195-105-04, Skovelunde, Denmark

Ebinger, G. et al. 1993, Anwendung des Laserlichtschnitt-Verfahrens zur qualitativen Untersuchung der Durchströmung von Kreiselpumpen, Lasermethoden in der Strömungsmeßtechnik, 2. Fachtagung, Braunschweig, Paper 37

Karagoz, I. 1993, Experimental Investigation of Periodic Flow in Branching Pipes, Flow Measurement and Instrumentation, vol. 4, no. 3, pp. 163-169

Nath, B., Dietrich, H., Baetz, W., Holzapfel, W. 1998, Application of Laser Diodes to Gas Flow Diagnosis, Int. Workshop on 'Flow Diagnosis Techniques', St. Petersburg, Russia

Yariv, A. 1989, Quantum Electronics, 3rd ed., John Wiley & Sons, New York, p. 255

FIBRE OPTIC BEAM DELIVERY OF HIGH PEAK POWER, SHORT PULSE LASER LIGHT FOR PIV

Duncan P Hand, Jonathan D Entwistle*, Darren P Wiles, Andreas Kuhn, Julian D C Jones, Clive A Greated*

Department of Physics, Heriot-Watt University, Riccarton
Edinburgh EH14 4AS U.K.

*Department of Physics and Astronomy, The University of Edinburgh,
Edinburgh EH9 3JZ U.K.

ABSTRACT

We report the use of diffractive optical elements to couple Q-switched Nd:YAG laser beams into optical fibres for PIV beam delivery. For single fibre delivery systems, we have increased the maximum pulse energy density that can be transmitted by a factor of 5 - 10 in comparison with the best that could be achieved using conventional optics. We also applied the DOE to our previously-developed bundle delivery system, comprising nineteen 200 μm core diameter fibres as before. On testing, over 1000 pulses with energies of 30 mJ were successfully transmitted, with no indication of damage. This allows fibre delivery to become a practical option for many air flow PIV applications, as demonstrated here with measurements of flow in a square duct.

1. INTRODUCTION

The objective of the work described in this paper was to deliver light from a Q-switched Nd:YAG laser through a fibre optic with a beam quality suitable for PIV measurements, providing a significantly higher pulse power density than previously demonstrated. The increase in power density without damage was achieved by conditioning the beam with a Diffractive Optical Element (DOE) diffuser before coupling it into the fibre to reduce self-focusing of the beam within the fibre.

Optical fibres are used to deliver laser beams for a wide range of measurement techniques in fluid mechanics. They have distinct advantages over conventional (bulk optic) beam delivery systems, in that they allow measurements to be made in hazardous environments, e.g. combusting flows, limited-access situations, and measurements which require the measurement volume to be traversed. The fibre forms a flexible remote probe, which is easy to align with the measurement volume. In particular, fibre beam delivery is now well-established for single point Laser Doppler anemometry (LDA) measurements, where light from a continuous wave (cw) laser source is delivered to the measurement region. Fibres have also been applied to PIV, but have been primarily limited to low velocity measurements, where a cw laser may also be used and the light sheet formed by scanning optics, as demonstrated by Gray *et al* (1991).

Many PIV measurements require, however, short pulses (~ few nanoseconds) of laser light to measure high velocity flows, Kopenhams & Hocker (1988). Pulse energies of a few of tens of mJ are typically required in order to provide sufficient signal at the camera, when scattering from small particles (~ μm). This means that peak powers can be of the order of 2 MW. Unfortunately, when using conventional optics to couple the light into a fibre small enough to give adequate beam quality, the ensuing high peak power densities result in the fibre being irreversibly damaged. In previous work reported by Anderson *et al* (1995), we investigated this damage, which we found to be highly dependent both on the diameter of the fibre, and on the way that light is coupled into it. We were able to transmit Q-switched Nd:YAG laser pulses at 532 nm with energies of up to about 5 mJ through step-index fused silica fibres with a core diameter of about 400 μm. The use of such large core fibres results in a substantial reduction in delivered beam quality leading to undesirably thick light sheets of limited depth.

In subsequent work, we developed the technique of using fibre bundles for beam delivery, where a circular input array of fibres was transposed to a linear array at the output to deliver pulse energies of 5 - 7 mJ with a reduced fibre core diameter of 200 μm. This system was used for making measurements in combusting flows, described by Anderson *et al* (1996a).

In this paper we describe a new fibre coupling system which uses a diffractive optical element (DOE) diffuser to reduce controllably the beam quality of the laser light before it is coupled into the fibre. This matches the beam to the fibre, in that it increases the number of fibre modes excited, thus reducing the effect of self-focusing within the fibre and hence increasing the damage threshold. With a single fibre, the damage threshold is increased by a factor

of 5 - 10. We have also applied this launch arrangement to the fibre bundle arrangement previously developed, and we were able to transmit pulses of 30 mJ using 200 μm core diameter fibres with no apparent damage.

In this paper we describe the new fibre coupling arrangement, and give details of experimental measurements both with single fibres and with a fibre bundle similar to that previously developed. We also describe the application of this fibre bundle to PIV measurements of air flow in a square duct at velocities of up to 12 ms^{-1}, where it has the advantage of being easy to align and traverse through the measurement volume, so that a number of 'slices' can be taken through the flow. Example results from this application are presented.

2. BACKGROUND

The 'quality' of a laser beam is often defined in terms of how tightly it can be focused. For any laser beam, the product of the laser beam waist (focal spot-size) and focus cone angle (essentially the inverse of the *f-number* which is being used) is a constant, described by the following equation :

$$w_0 \alpha_0 = M^2 \left(\frac{\lambda}{\pi} \right)$$

where w_0 is the beam waist radius (focal spot radius), α_0 is the focus cone half angle measured in the far field and M^2 is a factor which represents and is inversely proportional to the beam quality (for a fundamental Gaussian beam, $M^2 = 1$). The concept is also shown in figure 1.

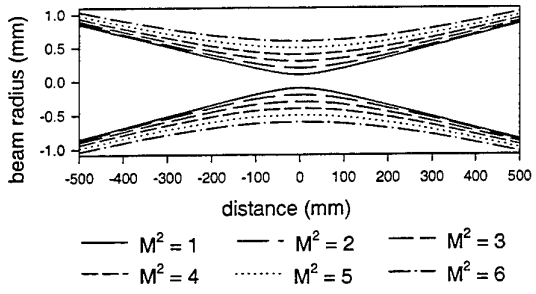


Figure 1 : Variation of focal spot-size with beam quality for a constant cone half-angle (1.7 mrad)

The dimensions of the light sheet required for PIV are application-specific, but typically demand a thickness of less than 2 - 3 mm, and lengths and widths of the order of 100 mm. This means that an M^2 value of less than ~ 50 is required. If fibre delivery is to be used, we are therefore limited to a maximum fibre diameter of ~ 200 μm, with an output divergence half-angle of ~ 100 mrad, as described by Anderson *et al* (1996a).

It has been widely reported, for example by Muller *et al* (1988), Richou & Pellat-Finet (1996) and Setchell *et al* (1990), that coupling nanosecond laser pulses into fibres of such diameters results in catastrophic damage at peak intensities orders of magnitude lower than in blocks of fused silica samples, nominally the same material as the fibre core. This damage normally occurs inside the fibre, a few mm from the end-face. The threshold is highly dependent on launch conditions, and the best results can be achieved if the beam is focused to give a cone half-angle of ~ 100 mrad, about 50 % of the fibre acceptance angle. Nd:YAG lasers of the type typically used for PIV have high beam quality (e.g., $M^2 < 5$), so that when the beam is focused with a 100 mrad cone angle, a beam waist of radius only a few μm is produced. It is important to ensure that this waist is *in front* of the fibre, such that the beam has expanded to the core diameter of (e.g. 200 μm) by time it reaches the entrance face. Even in this optimal arrangement, experiments indicate damage when pulse energies of greater than 1 - 2 mJ are used with this core diameter. Using a smaller cone angle, and bigger focal spot-size, does not help; in fact the damage threshold is further reduced. A larger fibre (1000 μm core diameter) does allow more pulse energy to be transmitted, but then the output beam quality is generally insufficient for the application.

On investigating the reasons for this particular damage process with optical fibres, it became clear that it is the high beam quality of the laser light which is effectively responsible. This high beam quality means that relatively few modes in the fibre are excited, and so the focal point in front of the fibre can be effectively 're-imaged' a few mm inside, as shown in figure 2. 'Re-imaging' results in high optical intensity, and so self-focusing can occur, leading to damage. 'Re-imaging' can be avoided by exciting more modes within the fibre. This requires the laser beam quality to be reduced to match the fibre beam quality; the ideal would be to condition the laser beam to produce a beam waist at the entrance face of the fibre of the same radius as that of the fibre, and with a divergence angle equal to the acceptance angle of the fibre. Such a beam transformation cannot be achieved with normal imaging optics, as it requires a reduction in beam quality by an order of magnitude.

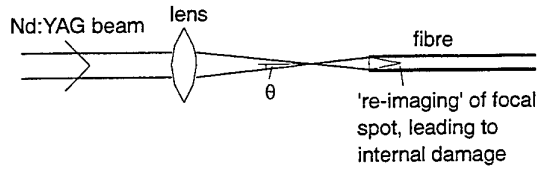


Figure 2 : Conventional Q-switched laser-to-fibre coupling arrangement

One way to achieve beam quality reduction is to modify the laser resonator in some way. However, this is not a viable option with the frequency-doubled Nd:YAG lasers used in PIV. Frequency-doubling is required to give a wavelength suitable for detection with a CCD camera, but is a non-linear process requiring very high peak intensities, and so demands a good beam quality for high efficiency. We therefore devised an alternative approach, where we applied a relatively novel type of optical element, a DOE diffuser, to reduce controllably beam quality.

3. EXPERIMENT AND RESULTS

3.1 DOE Characterisation

A conventional diffuser is a transparent optical material containing microscopic homogeneities that scatter light so that a collimated beam is instead dispersed over a range of angles. However, the angular distribution produced cannot be controlled accurately. In contrast, the DOE diffuser has a surface relief in the form of a periodic pattern that diffracts light over a closely controlled range of angles; the DOE is essentially a computer-generated hologram.

The beam quality after a DOE diffuser may be described by the simple equation :

$$M^2 = \frac{\pi w \alpha_{DOE}}{\lambda}$$

where w is the beam radius incident on the diffuser and α_{DOE} is the half-angle of the diffuser.

The combination of beam radius and DOE diffuser angle are therefore chosen to give the required M^2 value to match the fibre or bundle of fibres. After the diffuser, the beam is then allowed to expand to a suitable diameter before being focused down for coupling into the fibre, as shown in figure 3. The DOEs which were used in these experiments are off-the-shelf items made of fused silica, which have been designed for 633 nm. They still work well at 532 nm, but their diffraction efficiency is somewhat reduced to about 90 %. This means that ~ 10 % of the light is undiffracted, and so still has a high beam quality. Fortunately, the undiffracted light forms a focus a few mm before the diffracted focal point, and so will be focused in front of the fibre, rather than at the surface or inside it, as shown in figure 3. Example intensity cross-sections of the focused spot which is produced at the fibre input face are shown in figure 4. Figure 4 (a) shows the focused spot produced with a 0.5° DOE, whilst the spot produced with a 2° DOE is shown in figure 4 (b).

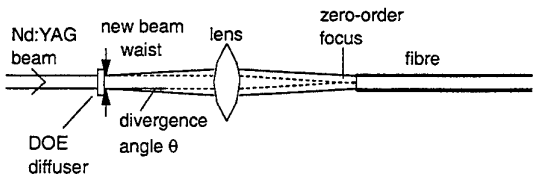


Figure 3 : Optical arrangement for conditioning the laser light and coupling it into the optical fibre

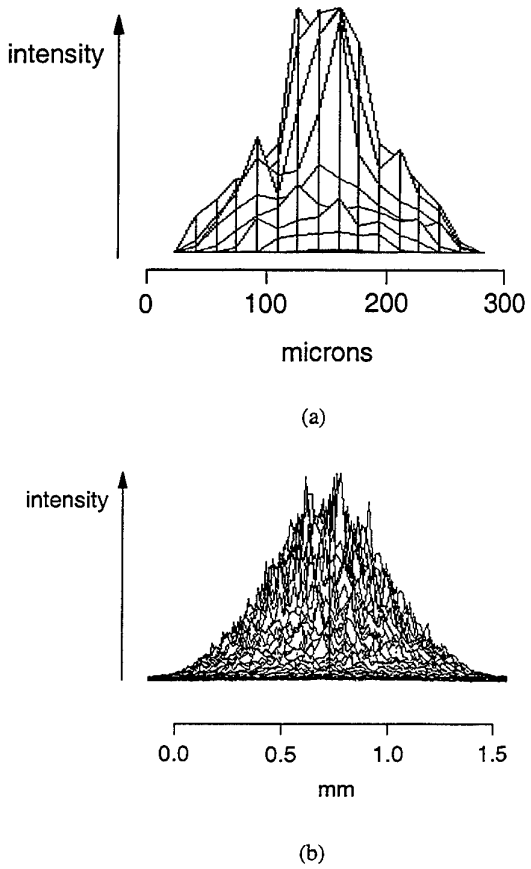


Figure 4 : Typical focused beam intensity profiles with (a) 0.5° DOE and (b) 2° DOE

3.2 Single 200 μm Diameter Fibre Delivery System

The system was initially tested with a single step-index optical fibre, 5 m long, with core and cladding diameters of 200 and 220 μm and an acceptance half-angle of 220 mrad. A fibre cleaving tool was used to prepare the end-faces. The experimental arrangement was as shown in figure 5. A DOE diffuser with a half-angle of 0.5° was used, giving a focal spot-size diameter of 200 μm at the fibre end-face, for a cone half-angle of 100 mrad, actually somewhat less than the acceptance half-angle of the fibre of about 220 mrad. The laser was operated at full power, and neutral density filters were used to reduce the pulse energy. The transmission efficiency was measured to be 50 %. A significant cause of loss is Fresnel reflection at the uncoated surfaces of the DOE, the launching lenses and the input face of the fibre. The remainder of the loss is caused by scattering by the DOE outside the acceptance angle of the fibre.

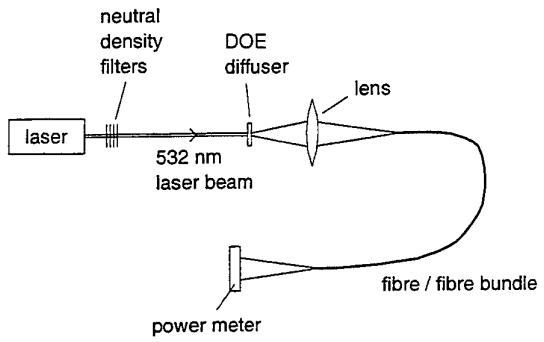


Figure 5 : Experimental arrangement to measure pulse energy transmission through single fibre or fibre bundle

The pulse energy was increased in small steps by selectively removing filters. The laser was operated to give 8 ns pulses at a repetition rate of 10 pulses s^{-1}. At energies below 10 mJ, measured at the fibre output, several thousand pulses were transmitted at each increment without damage. At a nominal output pulse energy of 10 mJ, over 900 pulses were transmitted through the fibre before a 'crack' was heard, following which the fibre input end-face was found to be damaged. The laser pulse energy shows considerable pulse-to-pulse variation. Therefore it is likely that a single high energy pulse caused the damage, rather than the damage mechanism being cumulative. The fibre is easily repaired, however, by simply re-cleaving the input end.

3.3 Fibre Bundle

A fibre bundle similar to the one previously developed by Anderson *et al* (1996b) was constructed and tested. This is shown schematically in figure 6. It consists of 19 fibres, each with core and cladding diameters of 200 and 220 μm respectively, of the same type as was used in the experiments of section 3.2. These fibres are formed into a circular array with an overall diameter of 1.1 mm at the input, and held mechanically with a tapered glass tube. No glue can be used at this point since it would damage with the high laser intensity. A fibre cleaving tool is used to prepare the end-face of each fibre before mounting them in this tube. At the output end, the fibres are held in a linear array using an epoxy resin. This array is then mounted inside a stainless steel tube of 10 mm outer diameter, and polished to give flat fibre end-faces. Most of the fibre cable is protected with a flexible spiral metal conduit, giving a robust remote probe, although the section close to the input end is protected by less robust PVC tubing, to allow the input end to be repaired if laser damage does occur.

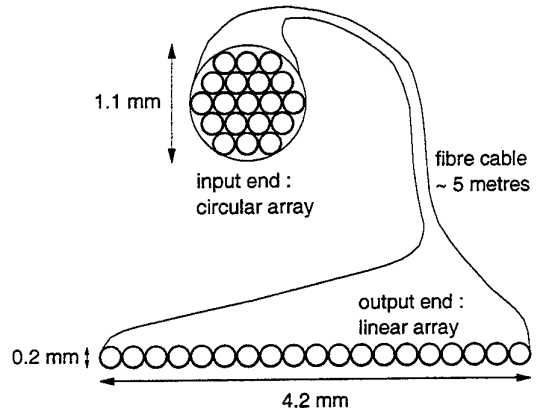


Figure 6 : Schematic diagram of fibre optic bundle

The experimental arrangement shown in figure 5 was also used to test the pulse energy which could be transmitted by the bundle. A DOE diffuser with a half-angle of 2° was used, giving a focal spot-size of 1.1 mm at the fibre end-face, for a cone half-angle of 100 mrad. The laser was operated at full power (giving 100 mJ), and neutral density filters were used to reduce the pulse energy. The transmission efficiency was measured to be 30 %. The transmission energy of the bundle is inevitably less than that of the single fibre, because light falling on the cladding or the interstices between the fibres at the input face is lost. The pulse energy was increased in small steps by selectively removing filters. For the maximum pulse energy available from the laser, 30 mJ was transmitted through the fibre. Over 1000 pulses were transmitted at this energy without any sign of damage.

The divergence half-angle of the beam at the output end of the fibre remained similar to that at the input, of about 100 mrad, substantially less than the numerical aperture of the fibre (about 220 mrad). Thus, having conditioned the light at the input to have a divergence angle somewhat less than the acceptance angle of the fibre improves the beam quality, although presumably at the expense of maximum pulse energy. Light from the various modes at the output of the fibre interferes in the far field to give a speckle pattern. However, the local variations in intensity were less than about 10%, and were not therefore expected to cause problematic inhomogeneities in the light sheet.

4. EXAMPLE APPLICATION - FLOW IN A SQUARE DUCT

To evaluate the performance of the fibre delivery system, a light sheet was formed using a double-pulsed Nd:YAG laser transmitted through the fibre bundle and was used for Digital Particle Image Velocimetry (DPIV) measurements of a fully-developed isothermal turbulent air flow in a square duct of 52 mm square cross-section. The experiment was part of a larger study whose objective is to determine mean primary and second order turbulence

statistics of the flow (such as Reynolds and normal stresses, power spectra and vorticity) and to demonstrate the ability of DPIV to resolve sub-pixel motions.

4.1 Light Sheet Formation

Optical arrangements for light-sheet formation from a delivery fibre bundle have been discussed by us previously, Anderson *et al* (1996a). The light sheet was formed by conditioning the output from the linear array of fibres using a single cylindrical lens with a focal length of 40 mm, adjusted to form a light sheet with a thickness of 1.0 mm at its centre, and a maximum thickness of 2.0 mm over the entire 52 mm depth of the measurement region.

The effect of the special launching conditions is that optical power is divided uniformly over the angular range of 0 to 100 mrad measured from the axis of the fibre at its output. Consequently, the power density across the width and through the thickness of the sheet is more uniform than can be achieved by direct beam delivery of the near-gaussian profile of the Nd:YAG laser. However, the higher beam quality of the direct beam delivery (where no optical fibre is used) allows a thinner light sheet of thickness < 0.6 mm to be produced.

4.2 Experimental Details

The fibre bundle output end, complete with the cylindrical lens to form the light sheet, was mounted on a translation stage in order that the light sheet could be controllably traversed across the duct as shown in figure 7. A Kodak ES1.0 CCD camera imaged this light sheet, and a Coreco f64 frame grabber card, synchronised with the double pulse from the laser, was used to grab sequential images of the sheet, with a time between pulses set at 40 μs. A separate video frame is stored for each element of the pulse-pair. The pulse-pairs and their recording are repeated at a rate of 10 Hz.

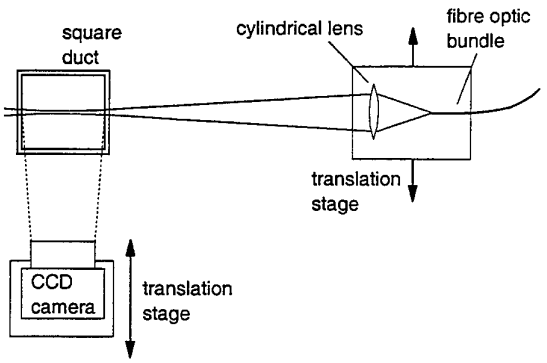


Figure 7 : Plan-view of experimental arrangement : application of fibre bundle to measure flow in a square duct

The duct was operated at a Reynolds number of 2.8×10^4 (based on bulk or average stream-wise velocity), with an air temperature of 28°C. The air flow was seeded using 1 - 2 μm corn oil droplets that were produced by passing Nitrogen at 7 psi through an atomiser. Such particles have often been used for their ability to act as reliable air tracers for PIV measurements in turbulent flows.

Each recorded frame consists of singly-exposed seeding particles. Cross-correlation is used to determine average particle displacements, scaled to yield velocity. Cross-correlation is preferred to autocorrelation of image pairs on a single frame as the dynamic range is increased, and there are fewer random correlations between particle images. In addition, cross-correlation avoids velocity sign ambiguity, especially important in turbulent flows.

In order to improve the accuracy of the derived turbulence statistics, 120 double images were sequentially grabbed at a frequency of 10 Hz to provide 120 independent vector maps for processing.

Before analysis, each image is first cropped and then normalised. Cropping excludes reflections and glare from the walls bounding the flow. Normalisation is used because the two frames in each pair have unavoidably different exposure times. This provides mainly a cosmetic improvement, but one that is helpful to the operator in checking image quality.

Analysis consists of selecting a sub-region of the image (known as interrogation area) and spatially correlating it with its cross-image at the same location by Fourier transformation. The result in the (spatial) correlation plane is a peak whose position relative to the centre of the plane represents the average displacement between particles within the interrogation area. In order to obtain sub-pixel displacements, gaussian peak fitting curves are applied.

Thus each pair of images is analysed with a 32×32 (pixel) interrogation area with a 50% overlap. The diameter of the duct scans 980 pixels, so the cropped region contains 976 x 976 pixels. Thus, each vector map contains 60×60 vectors (3600 in total) of which a quarter are independent measurements.

4.3 Example Results

A series of images were taken at the same distance from the duct inlet (2.7 m) at the mid-wall bisector of the duct. The calculated flow vectors are shown in figure 8. These all have roughly similar magnitude (although the vectors towards the edges of the duct are slightly smaller), and all point in the same direction. However, it is the smaller, fluctuating component which is of interest in this application. This can be is obtained by subtracting the mean for each position across the duct, with the result shown in figure 9.

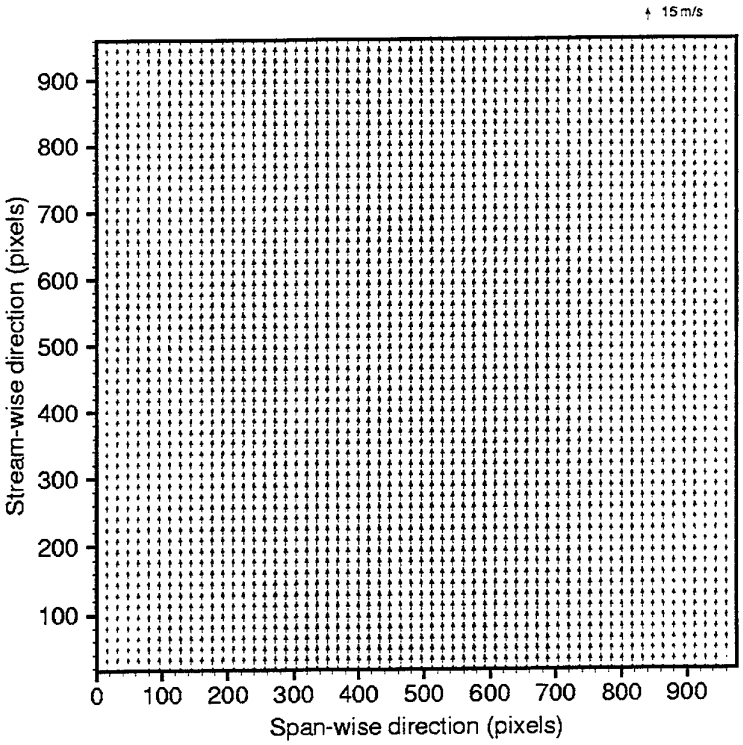


Figure 8 : Calculated flow vectors across duct

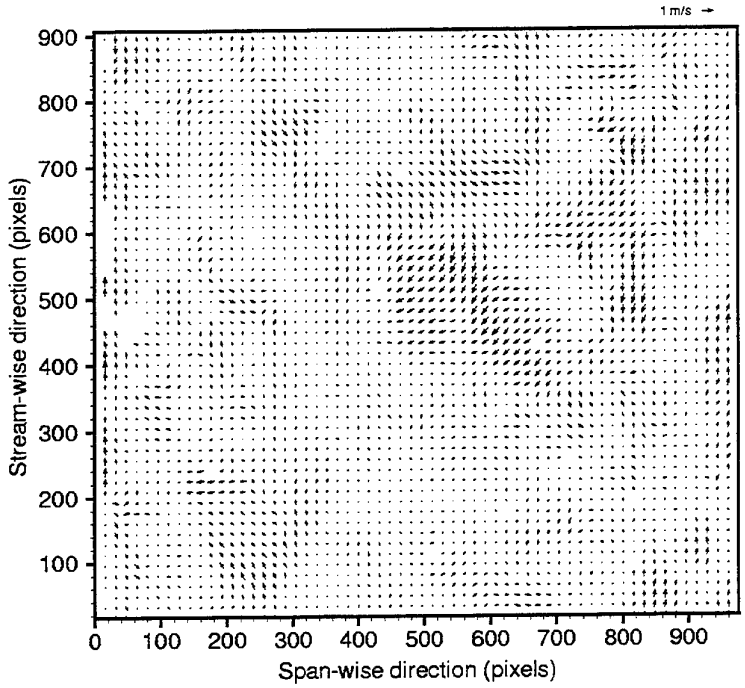


Figure 9 : Fluctuating components of flow vectors across duct

5. DISCUSSION AND CONCLUSIONS

The light sheet produced for our demonstration application had a thickness which varied from 1 to 2 mm over a distance of 60 mm. Whilst this was sufficient in this case, other applications require either a thinner or longer light sheet, thus demanding higher beam quality. To achieve this, it would be necessary to use smaller diameter optical fibres to construct a wider, but thinner bundle. It is not realistic to reduce the core diameter below about 100 μm with current construction techniques, but this would give a factor of 2 increase in beam quality, which would allow the light sheet to be either half the thickness or twice the length.

For some applications, it would also be possible to perform PIV measurements with a single fibre for delivery. 10 mJ delivered through a 200 μm fibre gives sufficient energy for some applications, particularly with larger particle sizes. This provides a very low-cost probe, which is easy to implement, and even to repair, should the front face be accidentally damaged.

Moving to smaller single fibres becomes more difficult, because the reduction in beam quality required to match the laser to the fibre is much smaller, which is harder to achieve with a DOE. It is important to illuminate sufficient periods of the DOE for it to work properly. As the beam size is reduced to give a smaller beam quality reduction, the output consists of a smaller number of larger speckles.

The DOEs themselves have the advantage of being relatively cheap (~ $300 US), off-the-shelf components, which can easily withstand the required pulse energy. They are, however, designed for 633 nm, but it would certainly be possible to manufacture them specifically for another wavelength e.g. 532 nm, which would improve their efficiency.

In conclusion, the use of DOE diffusers to condition a laser beam allows substantially higher energy laser pulses to be fibre-guided without damage. It is hence possible to produce fibre beam delivery systems which are suitable for high speed PIV measurements.

ACKNOWLEDGEMENTS

This research was partially supported by the Engineering and Physical Sciences Research Council, UK.

REFERENCES

Anderson, D.J., Greated, C.A., Jones, J.D.C., Nimmo, G. & Wiseall, S. 1996a Fibre optic PIV studies in an industrial combustor, Proc. Eighth International Symposium on Applications of Laser Techniques to Fluid Mechanics, Lisbon, pp. 18.4.1-8

Anderson, D.J., Jones, J.D.C., Easson, W.J. & Greated, C.A. 1996b 'Fibre-Optic-Bundle Delivery System for High Peak Power Laser PIV Illumination' Rev Sci Inst., vol. 7 pp. 2675-2679

Anderson, D.A., Morgan, R.D., McCluskey, D.R., Jones, J.D.C., Easson, W.J. & Greated, C.A. 1995 Optical fibre delivery system for pulsed laser PIV illumination Meas Sci Technol., vol. 6, pp. 809 - 814

Gray, C., Greated, C.A., McCluskey, D.R. and Easson, W.J. 1991 An analysis of the scanning beam PIV illumination system Meas. Sci. Technol., vol. 2, pp. 717-724.

Kompenhans, J. & Hocker, R. 1988 Application of PIV to high speed flows von Karmen Institute Lecture ser. 1988-06.

Muller, G., Kar, H., Dorschel, K., Ringelhan, H. 1988 Transmission of short pulsed high power UV laser radiation through fibres depending on pulse length, intensity and long term behaviour Proc. Optical Fibers in Medicine III, SPIE Proc 906 pp. 231-235

Richou, B. & Pellat-Finet, P. 1996 Delivery of Nd:YAG laser pulses by large optical fiber : dependence of the laser intensity profile on threshold of energy transmission Proc. High-Power Lasers : Applications and Emerging Applications, Micropolis, France, SPIE Proc 2789 pp. 186-194

Setchell, R.E., Meeks, K.D., Trott, W.M., Klingsporn, P., Berry, D.M. 1990 High-power transmission through step-index, multimode fibers Proc 22nd Boulder Annual Damage Symposium on Laser-Induced Damage in Optical Materials, Boulder, USA, SPIE Proc 1441 pp. 61-70

DIAGNOSTIC TECHNIQUES FOR MICROFLUIDICS RESEARCH

C. D. Meinhart*, S. T. Wereley*, J. G. Santiago and R. J. Adrian*****

*Department of Mechanical and Environmental Engineering
University of California, Santa Barbara, CA 93106

**Beckman Institute for Advanced Science and Technology
***Department of Theoretical and Applied Mechanics
University of Illinois, Urbana, IL 61801

ABSTRACT

This paper examines various techniques that have been developed to measure flow fields in microfluidic devices with micron-scale spatial resolution. These techniques include Scalar Image Velocimetry (SIV), Laser Doppler Velocimetry (LDV), and Particle Image Velocimetry (PIV). Advantages and disadvantages of each technique are presented.

PIV results of flow through a 30 μm thick × 300 μm wide microchannel are presented. These velocity measurements have spatial resolutions of 5.0 μm × 1.3 μm × 1.5 μm. Using 50% overlap, the velocity vector spacing is 680 nm in the spanwise direction of the microchannel.

1. INTRODUCTION

There are several areas in science and engineering where it is important to determine the flow field at the micron scale. Industrial applications of microfabricated fluidic devices are present in the computer, automotive, aerospace, and biomedical industries.

In the aerospace industry, micron-scale supersonic nozzles may play an important role in the development of small-scale aircraft and spacecraft. Figure 1 is an SEM of a supersonic nozzle being developed at MIT. The throat of this nozzle measures approximately 35 μm. The width of the nozzle is 500 μm. These nozzles are being designed for JPL/NASA to be used as microthrusters on micro-satellites, and for AFOSR / DARPA as flow control devices for palm-size micro-aircraft (Bayt et al., 1997).

In the computer industry, inkjet printers account for 65% of the computer printer market (Kamisuki, 1998). Inkjets basically consist of an array of nozzles with exit orifices on the order of tens of microns in diameter. During expulsion, ink is forced out of a micro-reservoir by either a mechanical actuator or by a heating element that boils a small volume of ink. This process can be repeated at a rate of up to several kHz. The industry is focused on making inkjets smaller, thereby increasing printing resolution and increasing repetition rate. Designing inkjets is often too complicated to rely entirely on CFD analysis.

The biomedical industry is currently developing and using microfabricated fluid mechanic devices for patient diagnosis, patient monitoring, and drug delivery. Many of these processes involve chemical reactions and the transport of macromolecules cells through sub-millimeter channels. The details of the fluid motion through these small channels, coupled with nonlinear interactions between macromolecules, cells, and the surface-dominated physics of the

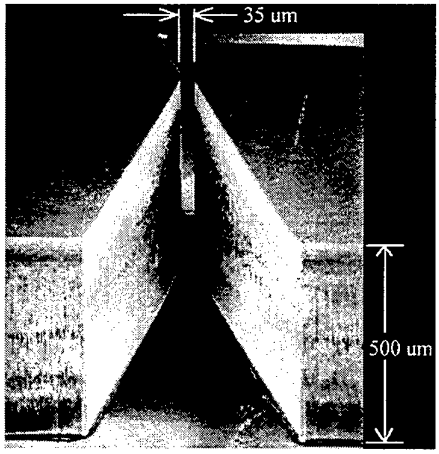


Fig. 1 Scanning Electron Micrograph of a microfabricated supersonic nozzle (courtesy, Robert Bayt and Kenny Breuer, MIT).

channels create very complicated phenomena, which can be difficult to simulate numerically.

The I-STAT device (Affymetrix, Inc.) is the first microfabricated fluidic device that has been widely used in the medical community for blood analysis. All the chemical analysis is performed inside a disposable microfluidic device at the point-of-care, providing doctors with immediate blood-work results without sending the samples to a lab. Since the test sections are completely disposable, the potential for cross contamination is eliminated.

Other examples of microfluidic devices for biomedical research include micro-scale flow cytometers for cancer cell detection (Krulevitch, 1997), micro-machined electrophoretic channels for DNA fractionation, and polymerase chain reaction (PCR) chambers for DNA amplification(Northrup et al., 1995).

Mixing of two fluids, or distributing of chemical species and macromolecules in microchannels is a major challenge facing microfluidics researchers. The low-Reynolds numbers present in microfluidics research precludes turbulence as a possible mechanism to enhance mixing. In many situations, pure molecular diffusion is too slow to achieve adequate mixing. Therefore researchers are developing devices which promote chaotic advection to enhance mixing. Obviously excellent diagnostic techniques are required to determine the presence of chaotic advection.

There has been a wide range of diagnostic techniques developed for microfluidics research. Some of these techniques have been designed to obtain the highest spatial resolution and velocity resolution possible, while other techniques have been designed for application in non-ideal situations where optical access is limited (Lanzillotto et al., 1996), or in the presence of highly scattering media (Chen et al., 1997).

2. SCALAR IMAGE VELOCIMETRY (SIV)

Scalar image velocimetry (SIV) refers to the determination of velocity-vector fields by recording images of a passive scalar quantity, and inverting the transport equation for a passive scalar

$$\frac{\partial c}{\partial t} + (\boldsymbol{u} \cdot \nabla) c = D \nabla^2 c \,. \qquad (1)$$

Here, c is the concentration of the passive scalar, and D is the coefficient of molecular diffusion. Dahm et al. (1992) originally developed Scalar Image Velocimetry (SIV) for measurement of turbulent jets. Successful measurements of velocity depend on having sufficient spatial variations in the passive-scalar field and relatively high Schmidt numbers.

Since SIV uses molecular tracers to follow the flow, it has several advantages at the micro scale over techniques such as PIV or LDV, which use discrete flow-tracing particles. The large surface-to-volume ratios characteristic of microfluidic devices increase the probability of discrete flow-tracing particles depositing on the surface of the device or clogging the device. In addition, molecular tracers follow the flow more faithfully than discrete particles in electrokinetically driven flows (Paul et al., 1997). Typically, molecular tracers have much higher diffusion coefficients than discrete particles. The higher diffusion coefficient can significant lower the spatial resolution and velocity resolution of the measurements.

Paul et al. (1997) analyzed the motion of an uncaged fluorescent dye, using SIV to estimate velocity fields for pressure- and electrokinetically driven flows in 75 μm diameter capillary tubes. A 20 μm × 500 μm sheet of light from a λ = 355 nm frequency-tripled Nd:YAG laser was used to uncage a 20 μm thick cross-sectional plane of dye in the capillary tube.

Only the uncaged dye is excited when the test section is illuminated with a shuttered beam from a continuous wave Nd:YVO_4 laser. The excited fluorescent dye is imaged using a 10x, NA = 0.3 objective lens onto a CCD camera at two known time exposures. The velocity field is then inferred from the motion of the passive scalar. We approximate the spatial resolution of this experiment to be on the order of 100 μm × 20 μm × 20 μm.

Molecular Tagging Velocimetry (MTV) is a related technique that may have applications to microfluidics research. In this technique, flow-tracing molecules phosphoresce after being excited by a grid of UV light. Two CCD cameras image the phosphorescent grid lines with a short time delay between the two images. Local velocity vectors are estimated by correlating the grid lines between the two images Koochesfahani et al. (1996). In order to achieve spatial resolutions on the order of one micron, the molecules would have to be excited with grid lines which are about 500 nm thick (in the illumination plane). While it is possible to focus UV light down to about 500 nm using diffraction-limited low *f-number* optics, it is impractical to generate a grid of several lines that are 500 nm in width over an

appreciable length. In principle, MTV could be used for micro-fluidics research, with obtainable spatial resolutions on the order on tens of microns.

Optical Flow refers to a class of velocimetry algorithms originally developed by the machine vision community to determine the motion of rigid objects. The technique can be extended to fluid flows by assuming the effect of molecular diffusion is negligible, and requiring that the velocity field is sufficiently smooth. Assuming that the image intensity of a passive scalar is proportional to the concentration of the scalar, one can form the constraint equation for optical flow

$$\frac{\partial I}{\partial t} + (\boldsymbol{u} \cdot \nabla) I = 0, \qquad (2)$$

where I is the image intensity when projected back into the flow field. Combining the above constraint with the smoothness criterion that $\|\nabla \boldsymbol{u}\|$ is small, yields the equation for determining optical flow. It is customary to solve optical flow by minimizing the integral

$$\iint_R \left[\lambda \left(\frac{DI}{Dt} \right)^2 + \|\nabla \boldsymbol{u}\|^2 \right] d^2\boldsymbol{x}, \qquad (3)$$

where R is the region of interest, and λ is a parameter that specifies the importance of the constraint compared to the smoothness criteria.

Since the velocity field is computed from temporal and spatial derivatives of the image field, the accuracy and reliability of the velocity measurements is strongly influenced by noise in the image field. This technique imposes a smoothness criterion on the velocity field, which effectively low-pass filters the data, and can lower the spatial resolution of the velocity measurements (Wildes et al., 1997).

Lanzillotto, Leu, Amabile & Wildes (1996) applied optical-flow algorithms to infer velocity fields from 500–1000 μm diameter micro-tubes. This technique indirectly images 1-20 μm diameter x-ray-scattering emulsion droplets in a liquid flow. A synchrotron is used to generate high-intensity x-rays that scatter off the emulsion droplets onto a phosphorous screen. A CCD camera imaging the phosphorous screen detects variations in the scattered x-ray field. Lanzillotto et al. (1996) report a mean velocity field, measured in an 840 μm diameter tube, with a velocity-vector spacing of about 40 microns and axial bulk velocities of 7–14 μm/s. The primary advantage of x-ray imaging technique is that one can obtain structural information about the flow field, without having optical access.

Hitt, Lowe & Newcomer (1996) applied the optical flow algorithm to *in vivo* blood flow in microvascular networks, with diameters ~ 100 μm. The algorithm spectrally decomposes sub-images into discrete spatial frequencies, by correlating the different spatial frequencies to obtain to obtain flow field information. The advantage of this technique is that it does not require discrete particle images to obtain reliable velocity information. Hitt et al. (1995) obtained *in vivo* images of blood cells flowing through a microvascular network using a 20x water immersion lens. We estimate the spatial resolution of this technique to be on the order of 20 μm in all directions.

3. LASER DOPPLER VELOCIMETRY (LDV)

Laser Doppler Velocimetry (LDV) has been a standard technique in fluid mechanics over the past 25 years. In the case of a dual-beam LDV system, the volume of the intersection of the two laser beams defines the measurement volume. The measurement volumes of standard LDV systems have characteristic dimensions on the order of a few millimeters.

Turbulence researchers recognize the importance of obtaining spatial resolutions that are high enough to resolve small-scale turbulent motions. Compton & Eaton (1996) used short focal length optics to obtain a measurement volume of 35 μm × 66 μm. The short-focal-length optics allowed them to obtain measurements as close as 0.1 mm from the wall, which resolves the $Re_\theta = 1400$ boundary layer down to $y^* = 3$.

Using very short focal length lenses, Tieu, Machenzie, & Li (1995) built a dual-beam solid-state LDA system that has a measurement volume of approximately 5 μm × 10 μm. The length of the probe volume is determine by

$$l = \frac{8 f^2 \lambda}{D d \pi}, \qquad (4)$$

where f is the focal length of the lens, λ is the wavelength of light, D is the beam diameter, and d is the beam spacing. For a given wavelength of light, a small probe volume can be achieved by using a short focal length f, and a large beam diameter D, and a large beam spacing d. Tieu et al. (1995) used $f = 12$

mm, D = 3.3 mm, d = 10 mm, and λ = 685 nm, to obtain a probe length of l = 10 μm.

Clearly, a micron-scale probe volume is desirable for microfluidic measurements. However, it introduces significant constraints on the system, which can limit its overall performance. The probability of a scattering particle entering the volume decreases with the probe volume. Since the uncertainty in determining the Doppler frequency depends on the number of fringes in the probe volume, N_{fr}, it is desirable to have a large number of fringes. A micron-scale probe volume significantly limits the number of fringes, and subsequently limits the accuracy of the velocity measurements.

Tieu et al. (1995) applied their micro LDV system to measure the flow through a 175 μm thick channel. The resulting time-averaged measurements compare well to the parabolic velocity profile, except within 18 μm of the wall, where the measurements fail.

Optical Doppler Tomography (ODT) has been developed to measure micron-scale flows embedded in a highly scattering medium. In the medical community, the ability to measure *in vivo* blood flow under the skin allows doctors to determine the location and depth of burns (Chen et al., 1997). ODT combines single-beam Doppler velocimetry, with heterodyne mixing from a low-coherence Michelson interferometer. The lateral spatial resolution of the probe volume is determined by the diffraction spot size. The Michelson interferometer is used to limit the effective longitudinal length of the measurement volume to that of the coherence length of the laser. The ODT system developed by Chen et al. (1997) has a lateral and longitudinal spatial resolution of 5 μm and 15 μm, respectively.

The system was applied to measure flow through a 580 μm diameter conduit. Here, 1.7 μm diameter particles were used to follow the flow.

Advancements in microfabrication technology will facilitate the development of new generations of self-contained solid-state LDV systems with micron-scale probe volumes. These systems will likely serve an important role in diagnosis and monitoring of microfluidic systems (Gharib, 1998).

4. PARTICLE IMAGE VELOCIMETRY (PIV)

Particle Image Velocimetry (PIV) can be used to obtain high-resolution 2-D velocity fields. Urushihara, Meinhart & Adrian (1993) used Particle Image Velocimetry (PIV) to make velocity measurements in turbulent flows with spatial resolutions of up to 280 μm × 220 μm × 200 μm. This high spatial resolution was obtained using conventional interrogation and data processing algorithms (Meinhart et al., 1993). Keane, Adrian & Zhang (1995) developed *super-resolution PIV* and applied it to Urushihara's data to achieve spatial resolutions of approximately 50 μm × 50 μm × 200 μm. The super-resolution PIV algorithm consists of two parts: First, standard-resolution velocity fields are obtained from the image data using standard correlation algorithms. Second, super-resolution velocity fields are obtained by tracking individual particles, using the information from the standard-resolution measurements as a guide.

The spatial resolution of a PIV system is limited by many factors such as particle size, particle seeding density, and image quality. Ultimately, PIV techniques are limited by the diffraction-limited resolution of the optical recording system. Diffraction-limited resolution can be increased by decreasing the *f-number* of the optical system, where the *f-number* is the ratio of the focal length, f, to the aperture diameter of the optical system, D. As *f-number* is decreased, geometric aberrations are increased. Most optical systems have an optimal *f-number*, where resolution-limits resulting from geometric aberrations are balanced by resolution-limits resulting from diffraction. Microscopic objectives have extremely high resolving powers, because they operate with very low *f-numbers*, and they are corrected to be distortion free. Microscope lenses are characterized by their numerical aperture, NA = $n \sin\theta$, where n is the index of refraction of the imaging medium, and θ is the half angle of the light collecting aperture. Oil-immersion objective lenses are available commercially with a NA = 1.4 and a magnification, M = 100. The diameter of the diffraction-limited point spread function, d_s, when projected onto the CCD camera is given by

$$d_s = 2.44M\frac{\lambda}{2NA}, \qquad (5)$$

where M is the geometric magnification of the objective lens. Using image recording light with a wavelength, λ = 560 nm, the diffraction-limited point spread function is d_s ~ 488 nm. Therefore, even an infinitesimally small particle will appear to have a 488 nm diameter, when projected back into the fluid. Assuming that the ratio of the particle-image diameter to the pixel width, (d_τ / d_{pix}) is about three, the centroid of the particle image can be located to

within 1/10th of the particle-image diameter (Prasad et al., 1992). When projected back into the fluid, the particle appears to be 488 nm in diameter, implying that its position can be determined to within 48 nm (i.e. 1/10th of the apparent particle-image diameter). Since we know *a priori* the shape of the particle, and since we are over-sampling the particle image by a factor of three, we can determine the particle's position to within ~ λ/12 (i.e. 48 nm ~ 560 nm / 12).

Santiago et al. (1998) developed a PIV system which is capable of measuring instantaneously 1000 velocity vectors with a spatial resolution of 6.9 × 6.9 × 1.5 microns. The system uses an epi-fluorescent microscope and an intensified CCD camera to record 300 nm diameter polystyrene flow-tracing particles. The particles are illuminated using a continuous Hg-arc lamp. The continuous Hg-arc lamp is chosen for situations that require low levels of illumination light (e.g. flows containing living biological specimens) and where the velocity is sufficiently small so that the particle motion can be frozen by the CCD camera's electronic shutter. The velocity-vector field shown in Figure 2 contains over 900 velocity vectors, with a spatial resolution of 6.9 × 6.9 × 1.5 μm for each vector (Santiago, et al. 1998).

Figure 3 is a schematic of a micro PIV system developed by Chiu, 1998). The system utilizes a pulsed Nd:YAG laser to illuminate fluorescent particles and a cooled frame-transfer camera to record particle images. The pulsed Nd:YAG laser can

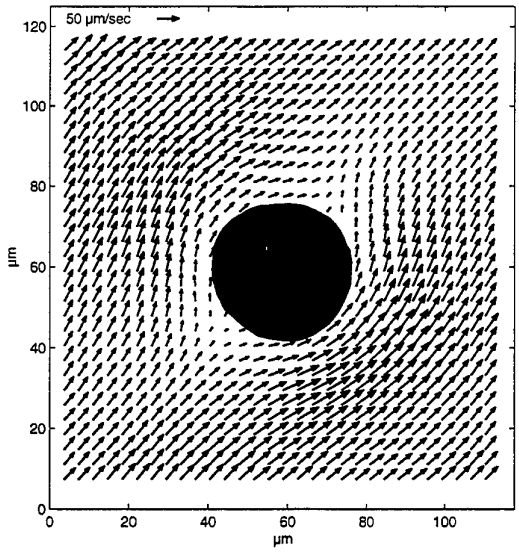


Fig. 2. Micro PIV velocity vector map of a Hele-Shaw flow. The vector field contains over 900 velocity vectors, each measured with a spatial resolution of 6.9 × 6.9 × 1.5 μm. (Reproduced with permission from Santiago et al., 1998.)

be used in situations where low levels of light are not critical, and must be used in situations where the velocity is large enough that only a pulsed light source can freeze the particles motion.

Chiu (1998) applied micro PIV to measure the flow field in a 30 μm high × 300 μm wide rectangular channel, with a flow rate of 50 μl/hr. The flow is imaged by a 60x, NA = 1.4, oil-immersion lens. The 200 nm diameter polystyrene flow-tracing particles were chosen small enough so that they faithfully followed the flow and were 150 times smaller than the smallest channel dimension. The particles were chosen large enough so that errors due to Brownian motion were not significant (Santiago, 1998). Chiu (1998) obtained reliable data with an interrogation spot size (Window 1) of 5.0 μm × 1.3 μm × 1.5 μm. By overlapping the interrogation spot size by 50%, he obtained a velocity-vector spacing of 680 nm in the wall normal position. Figure 4 compares the velocity profile obtained by ensemble averaging the resulting velocity-vector fields to the analytical solution for Stoke's flow in a rectangular duct. The results show excellent agreement between PIV data and the analytical solution (Chiu, 1998).
The first interrogation window was 44 pixels in the streamwise direction and 12 pixels in the spanwise direction, while the second interrogation region was 48 pixels × 16 pixels, respectively. The spanwise dimension of the interrogation region was reduced as much as possible to resolve the shear near the wall of the channel while the streamwise dimension of the interrogation region was elongated so that enough particle images were present to obtain reliable velocity information.
Twenty pairs of single exposure particle-image fields

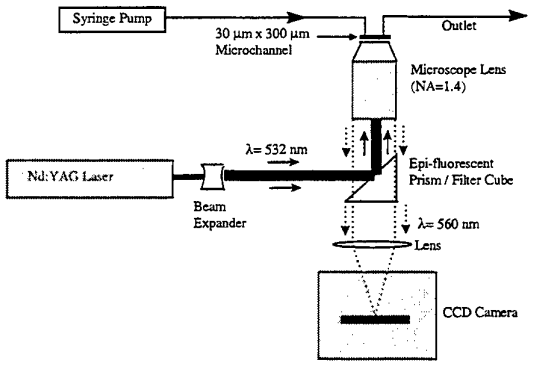


Fig. 3 Schematic of a micro PIV system. A pulsed Nd:YAG laser is used to illuminate fluorescent 200 nm dia. Flow-tracing particles, and a cooled CCD camera is used to record the particle images (Chiu, 1998).

Fig 4. Ensemble-averaged velocity profile measured in a 30• m×300• m channel. The symbols represent ensemble-averaged PIV data, and the line is the analytical solution of Stoke's equation for a rectangular channel. The velocity resolution is approximately 5• m×1.3• m×1.5 • m. With 50% overlap, the spacing between velocity vectors is 680 nm in the spanwise direction.

are cross-correlated at each interrogation spot. The ten correlation functions at each interrogation spot are then ensemble averaged to produce an ensemble-averaged correlation function. The signal peak detected in the ensemble-averaged correlation function is an estimate of the ensemble-averaged velocity vector at that position in space. Furthermore, the ensemble-averaged correlation function has much higher signal-to-noise than an instantaneous correlation function. This allows one to obtain reliable velocity measurements with much higher spatial resolution than is possible using traditional correlation algorithms.

In addition to using ensemble-averaged correlation functions to calculate velocity, the velocity vectors are calculated using a second-order accurate adaptive shifting technique recently developed in our lab, denoted as Central Difference Interrogation (CDI), see Wereley et al. (1998). The adaptive shifting combined with the different sized interrogation windows reduces velocity bias error.

5. DISCUSSION

In order to compare the spatial resolution of different diagnostic techniques, it is important to have a consistent definition spatial resolution that can be extended to all techniques. We define the spatial resolution of an instrument as the volume in physical space that is averaged to obtain a specific measurement. Similarly, we define the temporal resolution of an instrument as the duration of time that is averaged to obtain a specific measurement. Clearly, using the above definition, many aspects of a measuring technique must be considered before one can estimate spatial resolution. For example, the spatial resolution of a specific technique cannot be better than the size of flow-tracing particle used to make the measurement. Technically, the dimension of the averaging volume must be at least several particle diameters large, because the motion of the fluid surrounding the particle affects the motion of the particle. Therefore, the averaging volume of a 1 μm diameter particle is at least several microns in length, in each direction. With this in mind, one must choose particles that are significantly smaller than the smallest length scale that one is trying to resolve.

Further spatial averaging of the flow field may occur during data processing. For example, in PIV, the size of the interrogation spot can limit spatial resolution, and the distance a particle travels between successive exposures can limit spatial resolution.

It is common throughout the PIV research community to assume that the spatial averaging of the correlation is the size of the smallest interrogation window. This is correct in the limit of zero offset between interrogation windows, as is the case for autocorrelation. However, this is not correct in the case of cross correlation where the window offset can become a significant fraction of the window size.

The spatial average resulting from a 2-D correlation may be defined more accurately as the size of the smallest correlation window plus the relative offset between the two windows (assuming that the offset between the windows closely approximates the measured displacement). It is common practice to choose Window 1 as the smaller of the two windows. However, in the case where flow-tracing particles do not diffuse appreciably between successive exposures, one can choose Window 2 to be the smaller of the two windows

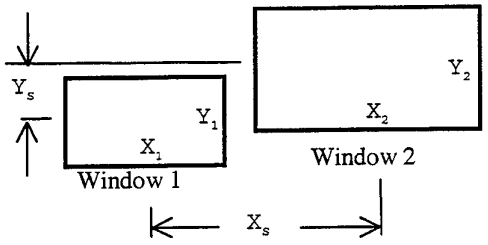


Fig. 5 Layout of a general correlation block for PIV. Window 1 is cross correlated into Window 2.

without loss of generality (Westerweel, 1997). In micro PIV, one often uses sub-micron particles, which can diffuse due to Brownian motion. In this case entropy of the particle image pattern increases, and it is important to choose Window 1 to be smaller than Window 2.

In addition to the effects of spatial correlation, imposing a smoothness constraint on the flow field (as is the case for *optical flow*), or spatially low-pass filtering the velocity data further reduces spatial resolution.

Table 1 compares the spatial resolution of several diagnostic techniques, while Figure 6 shows the range of length scales obtained by various PIV techniques.

Table 1. Comparison of the spatial resolution of several diagnostic techniques for microfluidics.

Technique	**Author**	**Flow Tracer**	**Spatial Resolution** (μm)	**Velocity Range**	**Observation**
LDA	Tieu et al. (1995)	_____	5 × 5 × 10	_____	4 – 8 Fringes limits velocity resolution
Optical Doppler Tomography (ODT)	Chen et al. (1997)	1.7 μm Polystyrene Beads	5 × 15	> 100 μm/s	Can image through highly scattering media
Optical Flow using Video Microscopy	Hitt et al. (1996)	5 μm Blood Cells	20 × 20 × 20	_____	*In vivo* study of blood flow
Optical Flow using X-ray imaging	Lanzillotto et al. (1996)	1 – 20 μm Emulsion Droplets	~ 20 - 40	_____	Can image without optical access
Uncaged-fluorescent dyes	Paul et al. (1997)	Molecular dye	100 × 20 × 20	_____	Velocity resolution is limited by molecular diffusion
Particle Streak Velocimetry	Brody et al. (1996)	0.9 μm Polystyrene Beads	~ 10	10 – 100 μm/s	Particle Streak Velocimetry
Particle Image Velocimetry (PIV)	Urushihara et al. (1993)	1 μm oil droplets	280 × 280 × 200	_____	Turbulent flows
Super-resolution PIV	Keane et al. (1995)	1 μm oil droplets	50 × 50 × 200	_____	Particle Tracking Velocimetry
Micro PIV	Santiago et al. (1998)	300 nm polystyrene particles	6.9 × 6.9 × 1.5	10 – 100 μm/s	Hele-Shaw Flow
Micro PIV	Chiu (1998)	200 nm polystyrene particles	5.0 × 1.3 × 1.5	10 μm/s – 300 m/s	Microchannel Flow

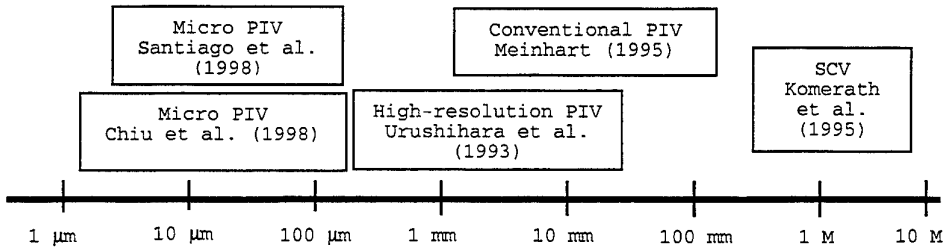


Fig. 6 Range of length scales obtained by various types of PIV techniques.

6. CONCLUSIONS

A significant number of researchers have developed diagnostic techniques for microfluidics. A large number of these techniques can obtain spatial resolutions on the order of, say, 10 μm. All the techniques presented here are restricted to liquid flows.

Micro PIV has been used to obtain spatial resolutions of 5.0 μm × 1.3 μm × 1.5 μm in a 30 μm thick × 300 μm wide microchannel (Chiu, 1998). Using 50% overlap, the velocity-vector spacing in the spanwise direction is 680 nm. The PIV data agrees well with the analytical solution for Stoke's flow in a rectangular channel.

ACKNOWLEDGEMENT

This work is supported at UCSB by a grant from AFOSR/DARPA number F49620-97-1-0515 under the direction of Dr. Mark Glauser, by JPL/NASA under the direction of Dr. Bill Tang, and by the College of Engineering at UCSB. The Beckman Institute for Advanced Science and Technology and a Ford Foundation Post-Doctoral Fellowship support this work at the University of Illinois.

REFERENCES

Adrian, R. J. 1983. Laser Velocimetry. Chapter in *Fluid Mechanics Measurements*, (ed. Goldstein, R. J), Taylor&Francis Publishing, Washington, DC, pp. 155-244.

Bayt, R. L., Ayon, A. A., Breuer, K. S. 1997. A performance evealuation of MEMS-bases micronozzles. *AIAA Paper 97-3169, 33rd AIAA/ASME/SAE/ASEE Joint Propulsion Conference & Exhibit*, July 7-9, Seattle, WA.

Breuer, K. 1996. Personal Communication.

Brody J.P.; Yager P.; Goldstein R.E.; Austin R.H. 1996. Biotechnology at low Reynolds numbers. *Biophys J.*, **Vol. 71**, pp. 3430-3441

Chen Z; Milner T.E.; Dave D. & Nelson J.S. 1997. Optical Doppler tomographic imaging of fluid flow velocity in highly scattering media. *Optics Letters*, **Vol. 22**: pp. 64-66.

Chiu, R. 1998. Master's Thesis, University of California – Santa Barbara, In preparation.

Compton, D. A. & Eaton, J. K. 1996. A high-resolution laser Doppler anemometer for three-dimensional turbulent boundary layers. *Exp. Fluids*, **Vol. 22**, pp. 111-117.

Dahm, W.J.A.; Su, L.K.; Southerland, K.B. 1992. A scalar imaging velocimetry technique for fully resolved four-dimensional vector velocity field measurements in turbulent flows. *Physics of Fluids A (Fluid Dynamics)*, **Vol. 4**, No. 10, pp. 2191 – 2206.

Gharib, M. 1998. Personal Communication.

Hitt, D. L., Lowe, M. L., Tincher, J. R., Watters, J. M. 1996. A new method for blood velocimetry in the microcirculation. *Microcirculation*, **Vol. 3** No. 3, pp. 259-263.

Hitt, D. L., Lowe, M. L., Newcomer, R. 1995. Application of optical flow techniques to flow velocimetry. *Phys. Fluids.*, **Vol. 7**, No. 1, pp. 6–8.

Kamisuki, S., Hagata, T., Tezuka, C., Nose, Y., Fujii, M., Atobe, M. 1998. A low power, small, electrostatically-driven commercial inkjet head. *Proceedings of MEMS'98.*

Keane, R. D., Adrian, R. J. & Zhang, Y. 1995. Super-resolution particle imaging velocimetry. *Meas. Sci. Tech.* **Vol. 6**, pp. 754-768.

Koochesfahani, M.M., Cohn, R. K., Gendrich, C. P., and Nocera, D. G. 1996. Molecular tagging diagnostics for the study of kinematics and mixing in liquid phase flows. *Proceedings in the Eighth International Symposium on Applications of Laser Techniques to Fluid Mechanics*, Lisbon, Portugal, July 8-11.

Komerath, N. M., Fawcett, P. A., Funk, R. B., Reddy, U. C. 1995. Large-area velocity measurement in low-speed flows. *ICIASF'95 Record. International Congress on Instrumentation in Aerospace Simulation Facilities*, Wright-Patterson AFB, OH, USA, 18-21 July.

Krulevitch, P. 1997. Personal Communication.

Lanzillotto, A. M., Leu, T. S., Amabile, M., Wildes, R. and Dunsmuir, J. 1996. Applications of x-ray micro-imaging, visualization and motion analysis techniques to fluidic microsystems. *Proceedings from Solid-state sensors and actuators workshop*, Hilton Head, SC, June 13-16.

Meinhart, C. D, Prasad, A. K. and Adrian, R. J. 1993. A parallel digital processor for particle image velocimetry. *Measurement Science Technology*, **Vol. 4**, pp. 619-626.

Meinhart, C. D. & R. J. Adrian 1995. On the existence of uniform momentum zones in a turbulent boundary layer. *Physics of Fluids*, **Vol. 7** No.4, pp. 694-696.

Northup, M. A., Hills, R. F., Landre, R., Lehew, H. D., Watson, R. A. 1995 A MEMS-based DNA analysis system, *Transducers'95, Eigth International Conference on Solid State Sensors and Actuators*, Stockholm, Sweden, June, pp. 764-767.

Paul, P. H., Garguilo, M. G., Rakestraw, D. J. 1997. Imaging of pressure- and electrokinetically-driven flows through open capillaries. Submitted to *Anal. Chem.*

Tieu, A. K., Mackenzie, M. R., Li, E. B. 1995. Measurements in microscopic flow with a solid-state LDA. *Exp. Fluid*, **Vol. 19**, pp. 293 – 294.

Urushihara, T., Meinhart, C. D. & Adrian, R. J. 1993. Investigation of the logarithmic layer in pipe flow using particle image velocimetry. In *Near-Wall Turbulent Flows*, R. So, et al. (Eds.), New York: Elsevier, pp. 433-46.

Wereley, S. T., Santiago, J. G., Meinhart, C. D., Adrian, R. J. 1998 Velocimetry for MEMS Applications. In *Proceedings of ASME.*

DESIGN AND CALIBRATION OF A STEREOSCOPIC PIV SYSTEM

Daniel C. Bjorkquist

TSI Incorporated
Fluid Mechanics Instrument Division
500 Cardigan Road
St. Paul Minnesota USA 55164

ABSTRACT

PIV is now a well established method for making two-dimensional velocity measurements in a fluid. Measuring the out-of-plane velocity component is of interest for many applications. Stereoscopic PIV, using two cameras viewing the flow from two perspectives, is one technique for measuring all three velocity components in a fluid plane. Two components of velocity nominally perpendicular to the camera optical axis are measured from each camera viewpoint. The pair of two-dimensional velocity vectors for a point in the flow are then combined to yield a three-dimensional velocity vector. By combining the vector fields from the two cameras, the three-dimensional velocity field for the plane in the fluid is measured.

Three optical configurations i.e. Angular Offset, Lens Offset, and Scheimpflüg were considered for the stereoscopic PIV camera. The Scheimpflüg arrangement was selected as the best choice for imaging the laser light sheet, with high image intensity, and a large angle between the cameras, that allows for measurements of air and water flow fields.

Since the Scheimpflüg optical configuration introduces perspective distortion to the left and right images, a procedure to calibrate and correct of the affects of distortion was essential for the design. A calibration function is used to map locations from the fluid to the left and right images. The derivatives of the calibration function are used as the calibration coefficients in converting from image displacement to fluid displacement.

The Scheimpflüg stereoscopic camera system was tested using solid body translation measurements. The measurement results showed an absolute calibration error of -0.28%, -0.18%, and -0.26% in the X, Y and Z directions respectively. The measurement variation was found to depend on the translation direction. The standard deviations for the X and Y measurements ranged from 1.9 μm to 7.8 μm for 1 mm translations. The Z measurement standard deviations ranged from 4.4 μm to 14.9 μm for 1 mm translations.

1. STEREOSCOPIC CAMERA CONFIGURATIONS

The stereoscopic PIV system is required to make measurements similar to standard two-dimensional PIV measurements with the addition of measuring the out-of-plane velocity component. A depth of field larger than the laser light sheet thickness is required. In some two-dimensional PIV experiments the lens aperture must be reduced in order for the depth of field to be large enough so that the entire light sheet thickness is in focus, therefore having the plane of best focus coinciding with the laser light sheet is desirable. Three basic stereoscopic camera configurations were considered: Angular Offset; Lens Offset; and Scheimpflüg. Four selection criteria were used to pick the best optical configuration:

1) The particle images across the camera field of view must be in good focus. This means that the light sheet must be within the camera depth of field.

2) The on-axis velocity measurement accuracy increases with the angle between the camera optical axes, so the ability to work at large camera angles is desired.

3) High intensity images are desired, hence, the system must work at large lens apertures (low f/#).

4) The stereoscopic system needs to be able to measure air flows and water flows through an air-water interface.

The three basic camera configurations are described below and evaluated in view of the above criteria.

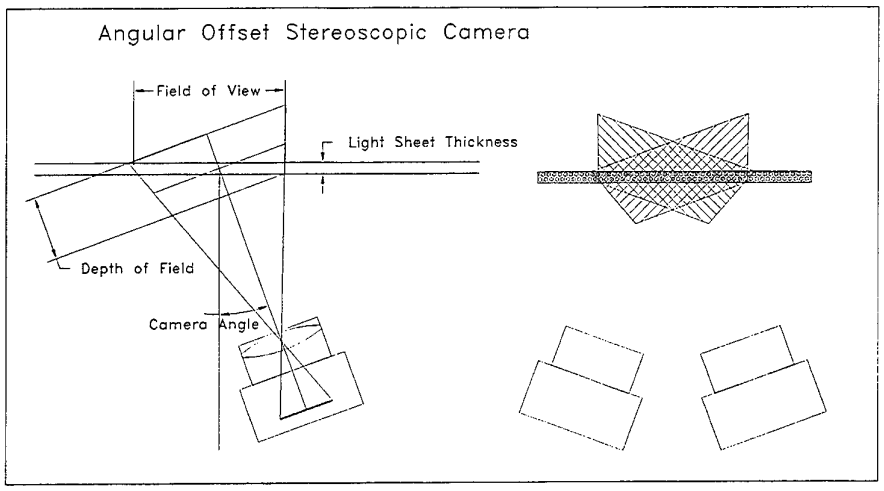


Figure 1 Angular Offset Stereoscopic Camera.

1.1 Angular Offset Stereoscopic Camera

The angular offset stereoscopic camera configuration is the most natural design to record a scene from two perspectives. This design uses two cameras with the lens axis perpendicular to the image sensor axis, i.e. the standard camera configuration. The main problem with this configuration is that the plane of best focus is parallel to the image sensor, not in the plane of the laser light sheet. In order to have the entire field of view in focus a large depth of field is required as shown in Figure 1. The left diagram shows the required depth of field for an angular offset camera to have the light sheet in focus across the field of view. The right diagram shows a stereoscopic angular offset camera pair and the required depth of fields for the two cameras. The depth of field can be increased by decreasing the lens aperture setting, but the decreasing of the lens aperture lowers the image intensity. As the camera optical axis angle increases the required depth of field increases. The requirement for a large depth of field makes the angular offset stereoscopic camera useful mostly in experiments with sufficient laser power to allow the camera to operate with a small lens aperture, in experiments with small magnification factors where the depth of field is naturally large enough to keep the particle images in focus, and in experiments where a small angle between the cameras is acceptable.

1.2 Lens Offset Stereoscopic Camera

With lens offset stereoscopic cameras the laser light sheet, camera lens principal plane, and image sensor are all parallel as shown in Figure 2. The camera optical axis angle is set by translating the lens in the X direction relative to the image sensor. Because of this parallel geometry the ratio of image

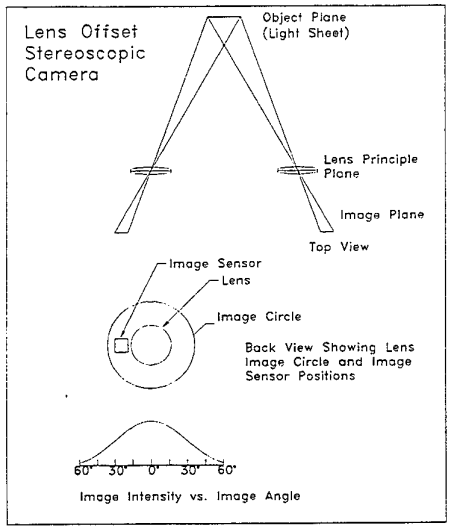


Figure 2 Lens Offset Stereoscopic Camera. The Figure shows the stereoscopic lens offset arrangement and the image sensor position within the image circle produced by the lens. The curve shows the image intensity as a function of image angle.

distance to object distance, i.e. the magnification, across the image is constant. Theoretically this arrangement introduces no image distortion. A prototype of a lens offset stereoscopic camera was built by the author. Some of the problems with this configuration were revealed in the testing of this prototype. In order to get good measurement accuracy for the out-of-plane velocity component a large angle between the cameras is desired. To achieve this, the camera image sensor was moved close to the outer edge of the image circle. Lenses with large image circles and high image quality (Rodenstock APO-Rodagon-N 1:4 f=80 mm) were used. This lens was designed to be used with 6 cm x 7 cm format film, but was used with a 9 mm x 9 mm CCD image sensor positioned just inside the image design area. The image quality is best on the lens axis and decreases towards the edges of the image. Since only the outer edge of the image area is being used, the lens aberrations become apparent in the particle images.

A second problem with using only the outside edge of the image circle is that the image intensity is highest at the center of the image and decreases with the angle from the optical axis by a factor of $\cos^4\theta$, where θ is the angle between the lens axis the point in the image. (Smith 1990). The image intensity is: 100% on the lens axis; 87% at 15 degrees; 56% at 30 degrees; and 25% at 45 degrees as shown in Figure 2. This drop off in image brightness away from the lens axis is noticeable in PIV images at typical camera angles, and makes setting the exposure for a good image across the field of view difficult.

The light sheet, lens principal plane, and image plane are parallel in air. However, these three planes are not parallel in water flow experiments, where the flow is imaged through an air-water interface. The change in index of refraction rotates the image plane. The image sensor must be rotated into this plane of best focus to achieve the good image quality across the field of view (Prasad 1993).

1.3 Scheimpflüg Stereoscopic Camera

The Scheimpflüg principal is used to record images with the image sensor in the plane of best focus when the object plane is not parallel to the lens principal plane. By tilting the image sensor plane and the lens principal plane to the Scheimpflüg condition the plane best focus is adjusted to overlap the light sheet. The Scheimpflüg condition (Horenstein 1977) is satisfied when the object plane, image plane and lens principal plane intersect at a common point as shown in Figure 3. This can be done by mounting the camera body with an angular offset, as in the angular offset stereoscopic camera configuration and then tilting the lens to bring the system into the Scheimpflüg condition. The correct

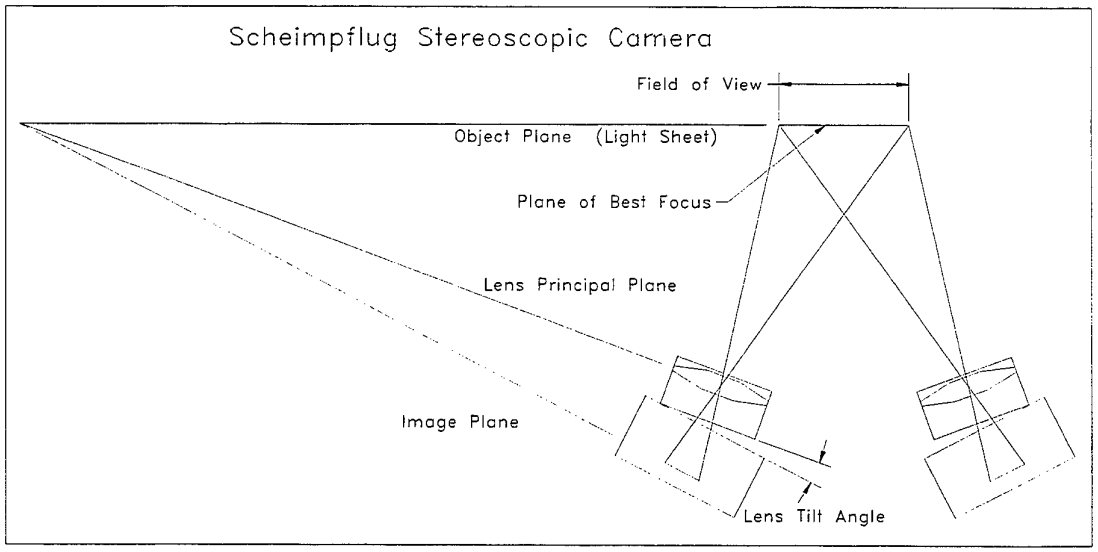


Figure 3 Scheimpflüg Camera Configuration. The Scheimpflüg condition requires the object plane, image plane and lens principal plane to intersect at a common point.

focus and tilt angles are achieved when all of the particles within the camera field of view are in good focus. The Scheimpflüg condition can also be used with a lens offset configuration, as described in the water flow experiment by Prasad (1993) by tilting the image plane.

The Scheimpflüg arrangement allows one to keep the plane of best focus in the plane of the light sheet for both air and water flows while having the camera view the light sheet from an off-axis angle. This allows the lens aperture to be operated with the same aperture settings as two-dimensional PIV. It also has the image sensor near the lens optical axis so that the image intensity is similar to the angular offset camera system.

The Scheimpflüg camera arrangement introduces perspective distortion to the images causing a rectangle in the light sheet plane to be imaged as a trapezoid on the image sensor as shown in Figure 4. In order to use the images recorded with the cameras in the Scheimpflüg condition the velocity vectors must be transformed to convert them from a distorted image space to fluid space.

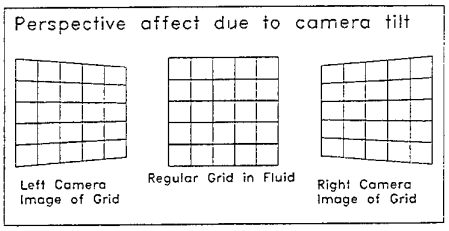


Figure 4 Image perspective in Scheimpflüg images.

2. CALIBRATION

To measure and correct the perspective distortion introduced by the camera optical configuration, and any other image distortions in the system, a calibration procedure is used. The calibration uses a rectangular grid of dots mounted on a traverse system. The calibration grid defines the coordinate system so it is important that the grid be carefully aligned with the light sheet. The calibration grid is also selected to fill the camera field of view as much as possible. If too much border area is left between the edge of the calibration grid and the image edge, then large errors might result in mapping points outside the calibration grid area in highly distorted images.

The calibration grid target is first aligned with the center of the light sheet and centered on the camera system optical axis. A laser diode beam is projected on the camera system optical axis marks the Z axis, aiding in alignment. The target is then traversed to the back of the measurement volume, typically half the light sheet thickness. Images of the target from the two cameras are captured and saved. The target is then traversed forward in several steps with left and right images saved at each position. The number of calibration grid planes used can vary with the experiment. The maximum calibration equation Z order is one less than the number of Z planes used in calibration.

The calibration grid images are analyzed and the centroid of each calibration marker stored in a target file. The locations of the marker points in the fluid are also stored in target files. The set of calibration point locations in the fluid and the set of measured marker centroids are used to compute up to 5^{th} order calibration polynomial equations for each camera. Using high order polynomials allows other image distortions such as those caused by lens aberrations and distortions of access windows to also be corrected in the calibration (Soloff 1997). A set of mapping functions are generated from the calibration polynomial equations.

The derivatives of the mapping functions represent the gradient of particle image displacement to fluid displacement (Soloff 1997). These gradients are the amount of particle image displacement, in pixels, in the x or y direction that is caused by a 1 mm particle motion in the X, Y or Z direction in the fluid. The six gradients for the left camera are shown in Figure 5 for the calibration described in the solid body measurement experiment. The gradients for the right image are similar, but not shown here. The dx_{left}/dX_{fluid} graph shows that a particle with a 1 mm displacement in the fluid will have an x image displacement of 14.25 pixels at the left edge of the vector field and 13.30 pixels on the right edge of the vector field. Table 1 lists the image displacements for a 1 mm motion for one point in the center of the measurement area. Each point in the fluid has a unique set of displacement calibration factors.

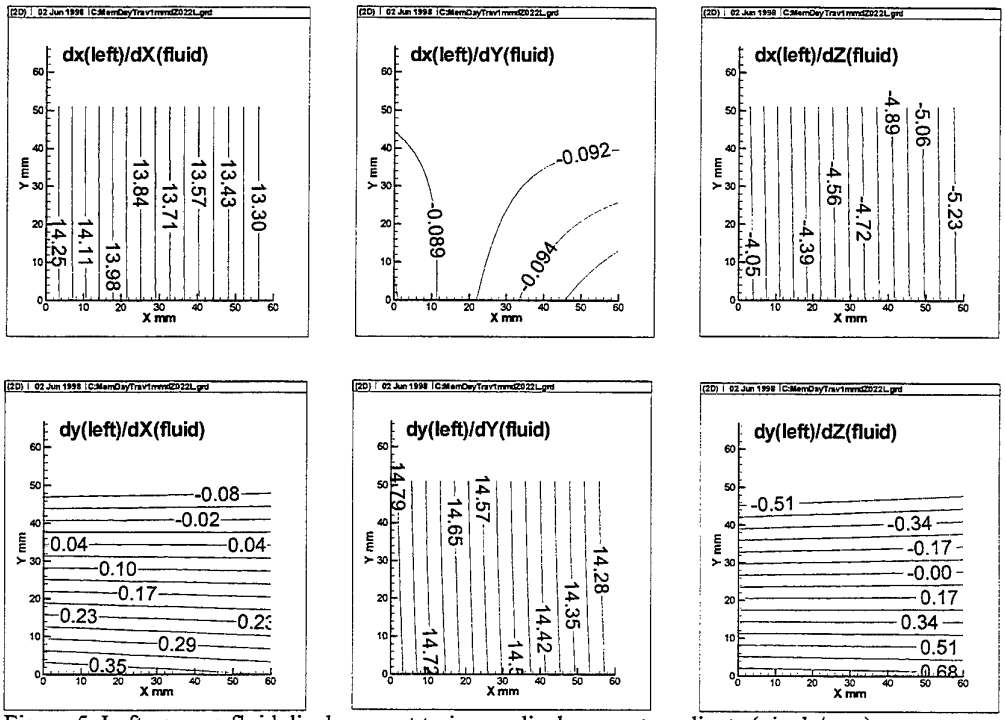


Figure 5 Left camera fluid displacement to image displacement gradients (pixels/mm)

The mapping functions from the cameras to the fluid are also computed. The camera to fluid mapping is used to view the camera field of view and two-dimensional vector locations in the fluid. It is helpful for setting up the system when the image overlap area and vector locations from the left and right images are displayed in the fluid (Z = 0) plane.

The calibration process removes requirements that the cameras be aligned with sub-pixel accuracy. Even when the cameras are perfectly aligned, with the center pixel from the two cameras imaging the same point in the fluid, the image perspective causes the rest of the pixels from the two cameras not to image the exact same location in the fluid.

Table 1 Image Displacements for 1 mm Particle Movement in the Fluid at Center of the Vector Field

Particle movement in fluid	x image displacement pixels	y image displacement pixels
1 mm X	13.77	0.15
1 mm Y	-0.09	14.53
1 mm Z	-4.63	0.11

3. VECTOR FIELD PROCESSING

As the first step towards determination of the three-dimensional vector fields, the left and right images are processed using TSI Insight NT software. The vector nodes are a rectangular grid in the image, with the displacements measured in pixels.

Vector validation, and/or smoothing is done on each of the two-dimensional vector fields. If there is a hole in one of the two-dimensional vector fields then an associated hole in the three-dimensional vector field will also exist.

To locate the velocity vectors in fluid space a three-dimensional vector grid is created to define the locations where the three-dimensional velocity is desired. The three-dimensional velocity vectors are computed only in areas where the left and right vectors fields can be interpolated. The camera to fluid mapping functions are used to find the vector grid overlap area in the fluid. This is done by mapping each edge vector node from the left and right vector fields into the fluid Z = 0 plane and finding the four edges of the vector overlap area in the fluid. A three-dimensional vector grid is then set up using this overlap area.

Generally it is desirable to have the three-dimensional velocity vectors in the fluid on a rectangular grid. To get the velocity on the rectangular grid in the fluid the vector grid points are mapped from the fluid to left and right camera pixel locations. A bi-linear interpolation of the vector field at this image location gives the particle image displacement in the image coordinate system. Mapping and interpolating the vector fields provides the particle image displacement in pixels from the left (dx_{left}, dy_{left}), and right (dx_{right}, dy_{right}) camera perspectives for each vector grid point in the fluid.

The three-dimensional displacement vector is found by solving a set of 4 equations in 3 unknowns. The particle image displacements (dx_{left}, dy_{left}, dx_{right}, dy_{right}) are computed by interpolating the left and right vector fields. The twelve derivatives (image displacement to fluid displacement gradients) are obtained from the calibration as shown in Figure 5, and Table 1. The three displacements in the fluid (dX_{fluid}, dY_{fluid}, dZ_{fluid}) are the unknowns to be solved for. This set of linear equations shown in Table 2 is solved using a least squares method to determine the displacement in the fluid (dX_{fluid}, dY_{fluid}, dZ_{fluid}).

Table 2 Equations for Resolving the Three-Dimensional Displacement in the Fluid.

$$dx_{left} = dX_{fluid}(\delta x_{left}/\delta X_{fluid}) + dY_{fluid}(\delta x_{left}/\delta Y_{fluid}) + dZ_{fluid}(\delta x_{left}/\delta Z_{fluid})$$

$$dy_{left} = dX_{fluid}(\delta y_{left}/\delta X_{fluid}) + dY_{fluid}(\delta y_{left}/\delta Y_{fluid}) + dZ_{fluid}(\delta y_{left}/\delta Z_{fluid})$$

$$dx_{right} = dX_{fluid}(\delta x_{right}/\delta X_{fluid}) + dY_{fluid}(\delta x_{right}/\delta Y_{fluid}) + dZ_{fluid}(\delta x_{right}/\delta Z_{fluid})$$

$$dy_{right} = dX_{fluid}(\delta y_{right}/\delta X_{fluid}) + dY_{fluid}(\delta y_{right}/\delta Y_{fluid}) + dZ_{fluid}(\delta y_{right}/\delta Z_{fluid})$$

4. SOLID BODY MEASUREMENTS

4.1 Experimental Setup

To test the performance and accuracy of the stereoscopic PIV design an experiment of solid body translations was performed. The experiential setup is shown in Figure 6.

Two TSI PIVCAM 10-30 cameras were mounted with camera body angles of ±18.5°. Nikon Micro Nikkor lenses, with 60 mm focal length were attached to Scheimpflüg lens mounts and set at f/8. The field of view was about 72 mm x 70 mm. The

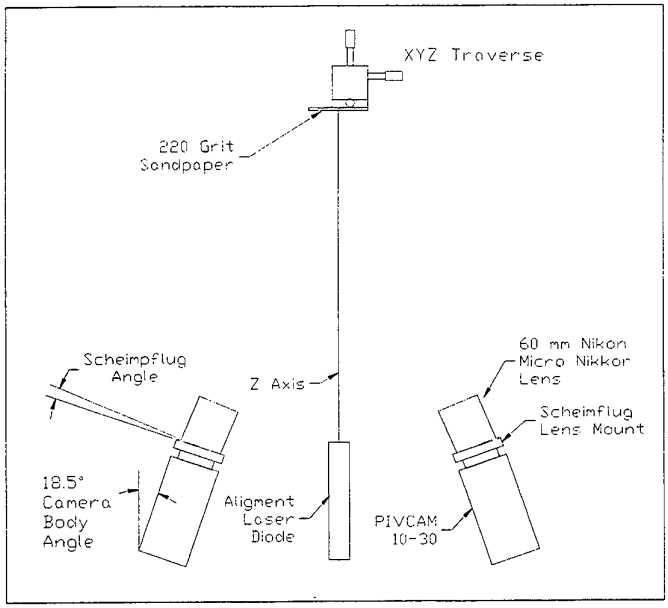


Figure 6 Diagram of Scheimpflüg Stereoscopic Camera System

Scheimpflüg mount tilt angle was adjusted for maximum image sharpness across the field of view. The calibration target was chromed glass with a grid of 13 x 11, 200 μm diameter holes on 5 mm centers. The target was backlit with the 200 μm holes acting as light sources. The calibration marker images averaged 6.8 pixels in diameter. Nine Z-axis locations with 0.5 mm spacing were used in the calibration. Using this 13 x 11 x 9 grid of points, a set of third order calibration equations were computed for each axis.

The accuracy of the fluid to camera mapping function can be estimated by using the calibration equations to convert the calibration grid points from the fluid to the images, and then compared with the mapped location to the measured image locations. Table 3 shows the errors of mapping the calibration marker locations to the left and right images.

Table 3 Calibration Grid Point Mapping Errors at Z=0 Plane

	RMS Error (pixels)	Max Error Absolute Value (pixels)
Left Camera x	0.019	0.049
Left Camera y	0.020	0.039
Right Camera x	0.033	0.048
Right Camera y	0.024	0.057

The solid body measurements involved moving a piece of sandpaper in three directions. A piece of 220 grit sandpaper was glued to a flat surface and attached to a Newport 460A XYZ traverse with micrometer actuators. The sandpaper was used to simulate high density seed particles in a PIV experiment. The traverse was stationary each time an image was acquired and constant (not pulsed) halogen light was used for illumination. The sandpaper images processed very well, so that no vector validation was required to remove spurious vectors.

The sandpaper was traversed 1.000 mm to the right ten times, with an image captured at each position. The sandpaper was then traversed 1.000 mm up ten times. For Z translation the target was moved back and forth between Z = -0.500 and +0.500 ten times. The 1 mm increment was selected to give image displacements of approximately one quarter the interrogation spot size. The images were processed with TSI Insight NT software using two-frame crosscorrelation with a 64 x 64 pixel interrogation spot and 50% overlap, giving vector fields of 30 x 30 vectors.

4.2 Results of the Experiment

A three-dimensional vector grid was created with 25 x 20 vectors covering the two-dimensional vector field overlap area of 62.5 mm x 59.5 mm. The vector fields from the ten translations of 1.000 mm in each direction were combined to produce the statistics shown in table 4.

Table 4 Mean and Standard Deviation of Solid Body Measurements.

Traverse	Mean (mm)	Standard Deviation (mm)
1 mm X Traverse		
measured dx	0.9972	0.0078
measured dy	-0.0170	0.0019
measured dz	-0.0177	0.0149
1 mm Y Traverse		
measured dx	0.0163	0.0014
measured dy	0.9982	0.0048
measured dz	0.0087	0.0044
1 mm Z Traverse		
measured dx	0.0096	0.0077
measured dy	0.0035	0.0074
measured dz	0.9974	0.0096

The absolute calibration errors are -0.28%, -0.18% and -0.26% in the X, Y and Z directions respectively. The error in the average X, Y and Z displacement measurements is a system error. This includes the PIV displacement measurement errors in the image pixels, bi-linear interpolation errors, the calibration errors, calibration target grid spacing errors and traversing distance errors. Further work is necessary to investigate which of these factors is causing the calibration errors.

The measurement variations are a function of the direction of motion. The dx standard deviation was low for the Y translation, and the dy standard deviation was low for the X translation. The dx and dy standard deviations ranged from 1.9 μm to 7.8 μm. The dz standard deviation ranged from 4.4 μm to 14.9 μm.

The residuals from the solution of the 4 equations in 3 unknowns listed in table 2 show how close the dX_{fluid}, dY_{fluid}, dZ_{fluid}, solution is fits the equations. The residuals are found by comparing the measured

image displacements (dx_{left}, dy_{left}, dx_{right}, dy_{left}) to the values computed by inserting the solution (dX_{fluid}, dY_{fluid}, dZ_{fluid}) into the 4 equations. The RMS residuals are shown in table 5, and the maximum residuals are shown in table 6.

Table 5 RMS Vector Solution Residuals

Trans. Dir.	dx_{left} (pixels)	dy_{left} (pixels)	dx_{right} (pixels)	dy_{right} (pixels)
X	0.002	0.089	0.001	0.089
Y	0.002	0.123	0.002	0.123
Z	0.001	0.057	0.001	0.057

Table 6 Maximum Absolute Value Vector Solution Residuals

Trans. Dir.	dx_{left} (pixels)	dy_{left} (pixels)	dx_{right} (pixels)	dy_{right} (pixels)
X	0.006	0.191	0.005	0.197
Y	0.006	0.220	0.006	0.222
Z	0.006	0.229	0.003	0.228

The dx residuals are much smaller than the dy residuals. This is due to the weak influence of the motion in the X and Z directions on the image y displacements, and the weak influence of motion in the Y direction on the image x displacement. If the gradients dx/dY, dz/dY, and dy/dX were zero, system of equations in Table 2 would become two systems of equations. The two dx equations with the unknowns dX_{fluid} and dZ_{fluid} and the two dy equations in the unknown dY_{fluid}. A close solution for dX_{fluid} and dZ_{fluid} can be found. The solution for dY_{fluid} is the average of the y image displacements divided by the dy/dY gradients ($dy_{left}/(dy_{left}/dY_{fluid})$ and $dy_{right}/(dy_{right}/dY_{fluid})$). The dy residual is a measurement of how close the left and right y displacement measurements are. The maximum residual table 6 shows that the worst error was 0.229 pixels for this experiment.

CONCLUSION

The design and calibration of stereoscopic PIV system was described. Three stereoscopic PIV camera configurations were examined: Angular Offset; Lens Offset; and Scheimpflüg. The Scheimpflüg camera was selected as the best choice for stereoscopic PIV because of its ability to align the plane of best image focus with the laser light sheet, and its ability to work at low f/#'s and large camera angles.

The Scheimpflüg lens tilt does add perspective to the images, which causes rectangular objects to be imaged as trapezoids. To correct this image perspective a calibration process of imaging a grid of markers is used. The calibration marker locations in the fluid and measured image marker locations are used to create a set of fluid to camera mapping polynomial equations. The derivatives of the mapping equations are used as calibration coefficients to convert the pair of two-dimensional vectors from the left and right camera images into a three-dimensional velocity vector.

A solid surface was translated in the X, Y and Z directions to produce known object displacements. The displacements were measured with the stereoscopic PIV system. Absolute measurement errors were found to be -.28%, -0.18% and -0.26% in the X, Y and Z directions respectively, in this experiment. The standard deviations of the dX and dY measurements ranged from 1.9 μm to 7.8 μm for 1 mm object displacements. The dZ measurement standard deviation was found to be from 4.4 μm to 14.9 μm for 1 mm object displacements.

REFERENCES

Horenstein Henry, 1997 Beyond Basic Photography Little Brown & Company (Canada) Limited ISBN 0-316-37312-5

Prasad, A. K. and Adrian, R. J. 1993 Stereoscopic particle image velocimetry applied to liquid flows, Experiments in Fluids 15, 49-60 (1993)

Soloff S. M, Adrian, R. J., Liu, Z-C, 1997 Distortion compensation for generalized stereoscopic particle image velocimetry, Measurement Science and Technology December 1997 Vol. 8 Number 12 pages 1441-1454

Smith, Warren J. 1990 Modern Optical Engineering The Design of Optical Systems Second Edition McGraw-Hill Inc. ISBN 0-07-059174-1 pages 144-145

SESSION 7

SPRAYS IN ENGINES

LDA-BASED MEASUREMENTS OF INSTANTANEOUS AND INTEGRATED FLOW RATES IN HIGH PRESSURE GASOLINE INJECTION SYSTEM

Murad Ismailov[1], Tsuneaki Ishima[1], Tomio Obokata[1],
Masayoshi Tsukagoshi[2] and Kazumitsu Kobayashi[2]

[1]Department of Mechanical System Engineering
Gunma University, 1-5-1 Tenjin, Kiryu, 376-8515 Japan
[2] Unisia Jecs Co., 1671-1 Kasukawa, Isesaki, 372-0023 Japan

ABSTRACT

Two time-dependent flows, upstream and downstream a gasoline swirl injector are studied. Instantaneous centerline velocity time series are measured in injection pipe flow by using LDA meter and the series of instantaneous and integrated flow rates and pressure gradient are reconstructed. PDA measurements are employed to the analysis of instantaneous patterns of droplets velocity-size and number density into fuel spray. All measurements are performed at similar temporal resolution close to a few dozes of μs.

Results indicate that flows are well correlated to time-phases. Opening or closing of the injector valve affects both flows as a delta shock-oscillation that afterwards causes spray formation. Laser-based techniques allow verifying the instantaneous injection and spraying characteristics for optimizing gasoline direct injection engines.

1. INTRODUCTION

Phenomena of sprays are extensively aimed at numerous investigations including new theoretical concept by Edwards (1997), application in combustion by Hiroyasu (1985) as well as CFD models by Liu and Reitz (1995) and many others. However, new verification data are expected to improve the models particularly to reveal the transformation from liquid jet to spray. They can be fulfilled through an advanced knowledge of initial and transient conditions in a gasoline injection system (GIS).

To obtain this information, one needs to couple both oscillating flows, upstream and downstream the injector generating a cyclic pressure wave propagation in the fuel transport pipeline and causing time-varying spray dynamics. Flow rate time series can be very accurately measured in injection system by LDA-based meter since Durst et al. (1996). This method permits the achievement of temporal resolution up to 1/1000 of an injection period. On another hand, instantaneous patterns of the spray flow are visualized by using a high-speed CCD-based camera with a resolution close to few μs. Similar timing can be provided by implemented planar scattering techniques Sankar et al. (1997).

By using convenient laser-based instruments newly developed commercial injection systems may be completely examined for the improvement and control of fuel injection and its deposition. Motivated by this idea the authors are considering to apply different non-intrusive techniques and introducing in-situ injection system diagnostics upon instantaneous characteristics. Flow rate and pressure gradient series upstream the injector and fuel droplets velocity-size and number density series downstream the injector are selected as the basic verification values to be measured.

A swirl injector is widely adopted in gasoline direct injection (GDI) engine, Iwamoto et al. (1997), due to short penetration. However, injection instability and fuel deposition at engine speed over 2400 rev/min are indicated by Harada et al. (1997). Because of this a novel swirl injector of Unisia Jecs Co. is selected for the experiments and normal heptane is used as a fuel model.

2. EXPERIMENTS

2.1. Test Injection System

Configuration of the test high-pressure gasoline injection system is sketched in the bottom part of Fig. 1. It consists of a fuel tank, a low-pressure pump and a high-pressure pump limited at 7.0 MPa. The injector installed into the frame of a 2D traversal stand is dealt with the pump system. For introducing LDA measurements a special test section is built up. A quartz pipe with a length of 300 mm and an inner diameter of 3.5 mm is arranged on-line with inflow and outflow section units. The outflow unit is used for installation of the injector. Motor-synchronized controller provides variable sets of injection frequency and duration with encoding resolution of 720 bin/cycle.

Fig. 2 depicts the mean mass flow rate versus injection pressure measured in steady and oscillatory pipe flows at frequency $f = 46$ and 22 Hz and injection duration $\tau = 1, 2, 4$ ms by using mass-balance. The most interesting aspect is framed by the "measured zone" applicable to GDI engines.

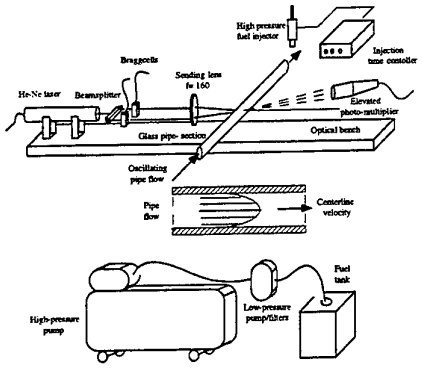


Fig. 1 Test injection system and LDA flow rate meter

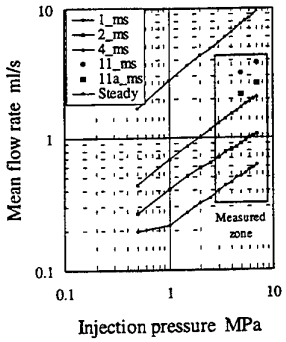


Fig. 2. Flow rate at steady flow and various τ

2.2. Measurements of Instantaneous Flow Rate

LDA flow rate measurements are developed by Durst et al. (1996) and applied for low injection pressure up to 0.6 MPa by Ismailov et. al. (1997). Presently the method is specified for high-pressure gasoline injection system. Transitional Reynolds number $Re_\delta < 700$ limits an application of the method as discussed by Hanjalic et al. (1993). For capillary n-heptane pipe flow at a frequency ranged from 22 to 46 Hz, estimated laminar mean velocity is as low as 4.8 m/s.

The main units of newly developed LDA-meter are framed in the top part of Fig. 1. They are based on a rail-bench and the sending axis is directed normally to the pipeline. A beam emitted from a 16 mW He-Ne laser passes through a beam splitter. The output beams shifted at 1.6662 MHz are intersected in the control measurement volume (CMV) with a length of 485 μm, a diameter of 46 μm and a fringe space of 2.41 μm. The clearance between moving parts of the high-pressure pump is limited to micrometer, therefore non-seeded n-heptane is used. Scattered light is collected on a 100 μm pinhole of a photo-multiplier with an off-axis angle of 30°.

The output signal is connected to a counter and using interface board, the processed data are transferred to a PC. The data rates are varied in the range from 0.4 to 1.2 kHz. An encoder signal is also fed into the interface via a time/angle connector in order to sort the data within one injection period. More than 3000 cycles are measured to completely monitor a centerline velocity series. Mean flow rates z measurements. Comparison of correlated data is illustrated in Fig. 3. Maximum disagreement between LDA and mass balance data is +4/-10 % because of the vibration of pipe connected to the pump of the injection system.

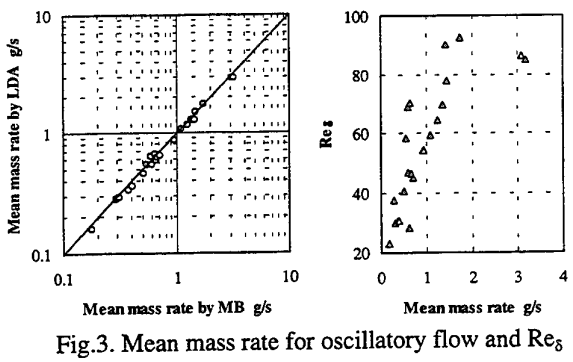


Fig.3. Mean mass rate for oscillatory flow and Re_δ

2.3. PDA Measurements in Spray Flow

An Aerometrics' PDA system is applied on 2D planar measurements into spray flow. A core space within a radius of 10 mm is measured with a radial traversing at 1 mm. The rest radial flow is stepped by 4 mm until measuring volume reaches a spray edge. The axial traverse grid is changed from 1mm, within 5 mm away from the injector nozzle, to 5 mm, while the axial position is settled between 5 and 55 mm away from the nozzle, and to 20 mm, in an axial range of 55 to 95 mm. The data rate is varied from 5 to 18 kHz.

The raw data were sorted in angular phases and IJK-order matrix was constructed. To analyze instantaneous spray patterns, three basic values as axial velocity, Sauter mean diameter and normalized particle number are represented in the matrix. To compute the last value, two measured parameters, a validated samples number N_s and a measurement time T_{run} are processed. The ratio N_s / T_{run} indicates a measurement data rate f_{data}. The product of f_{data} and cyclic period T is a validated number expected in the injection period. Dividing it by encoded phase number N_{phase} one can get a probable number of particles $N_{prob} = f_{data} T_{run} / N_{phase}$. An actual droplets number N_{part} is obtained and used in a rate N_{part} / N_{prob}. That permits processing of whole spray flow at variable data rate.

3. RESULTS

3.1. Pipe Flow Transitions in Gasoline Injection System

For illustration of the method capabilities, typical pipe flow dynamics within a cyclic period represented here and later by angular phase $\alpha = [0°, 360°]$, the time series of centerline velocity $U_o(t)$, flow rate $\dot{V}(t)$, time-integrated mass $m(t)$ and pressure gradient $dp/dz(t)$ obtained for particular injection set of $p = 5$ MPa, $f = 22$ Hz and $\tau = 4$ ms are jointly incorporated in Fig. 4. To illustrate the dynamic flow field, in Fig. 5 numerous velocity profiles are reconstructed for different transient phases A, AB, B, C, D and E as depicted in Fig. 4.

At the point A with phase $\alpha = 73°$ in Fig. 4, the injector valve is set open and the active injection start. Since initial transition as phase AB at $\alpha = 74°$, the velocity field is a flat-flow seen in Fig.5. In the pressure gradient series of Fig. 4 one can observe a negative shock-oscillation while the opening of valve. A time t_{wave} is needed to propagate sound pressure waves along doubled pipe length, being 3.2 ms in measurements. Therefore injection duration set $t > t_{wave}$ causes a full development of transient pressure oscillation. This is shown in the series of Fig. 4 through out serial transitions from B, $\alpha = 82°$, to C, $\alpha = 98°$, and finally to D, $\alpha = 107°$. At D, the valve is reversibly driven to be closed and flow is suddenly dampened.

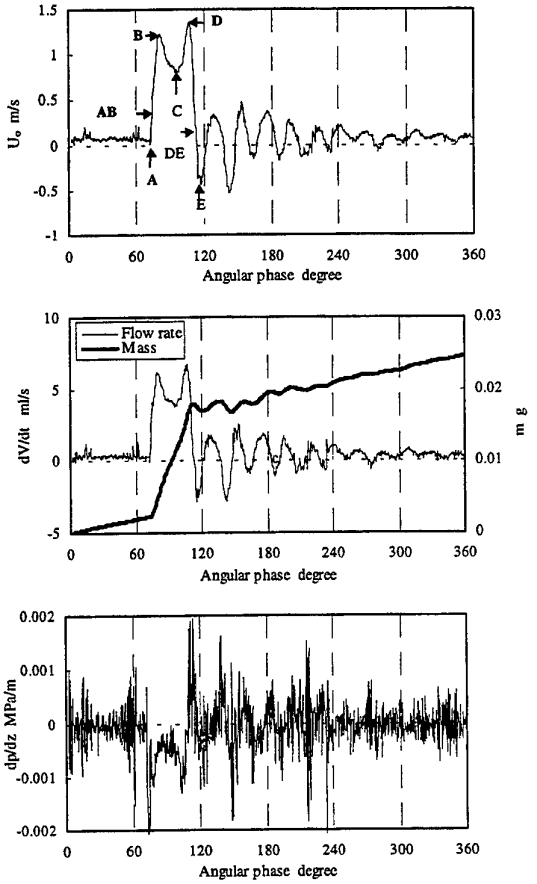


Fig. 4. Centerline velocity U_o, flow rate dV/dt, integrated mass m and pressure gradient dp/dz, at $p = 5$ MPa, $f = 22$ Hz, $\tau = 4$ ms

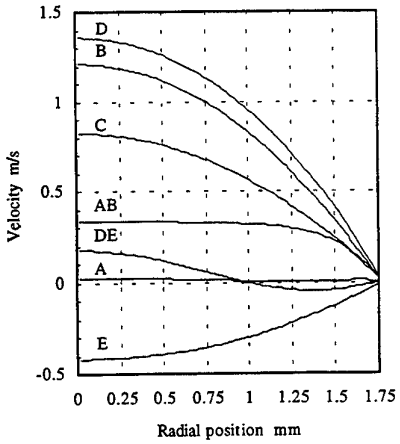


Fig. 5. Velocity field in pipe correspondent to the phases A, AB, B, C, D, DE and E depicted in Fig. 4.

Those results in a transition from D to DE, $\alpha = 113°$, and to E, $\alpha = 118°$ depicted in Fig. 4. As seen from Fig. 5, the velocity field becomes partially reversed at phase DE and completely reversed at phase E whereas pressure gradient reflected to a positive shock-oscillation indicated in Fig. 4 decelerating the flow. Because of the reversed flow, a local flow rate becomes negative. It is fundamental that temporal behavior of pressure gradient causes dynamics of flow field, instantaneous and integrated flow rate depicted in Fig. 4 and 5. The transitional shock-oscillations deal with the time-phases when the injector valve is opening and closing, points A and D respectively. They affect the temporal derivative and change its sign in all dynamic series including integrated fuel mass $m(t)$. The oscillation intensities respect to injection system configuration, fuel viscosity and injection timing set.

In automotive engines delivery of the fuel mass is controlled by engine speed, level of high pressure and cyclic timing set of injection. To obtain a diagram on the fuel mass rates, the data, obtained under variable p = 4, 5, 6 and 7 MPa, τ = 1, 2 and 4 ms and f = 22 and 46 Hz are processed for various temporal injection phases. Influence of injection pressure on instantaneous flow rate is illustrated in Fig. 6. Comparison of the series shows excellent similarity to the well-phased and gradually shifted transitions. Total injection cycle completed in a few dozes of a millisecond and the pipe injection dynamics becomes totally transient. For inner pipe radius R = 1.75 mm and viscosity ν of n-heptane, the ratio of injection duration τ = 4 ms to viscous pipe flow time-constant $T_\nu = R^2 \nu / 4 = 1.26$ s, $\tau / T_\nu = 0.0032$ is too low. This means that injection flow is completely transient.

The well-adjusted phasing is proven by the flow rate series measured at variable injection duration τ = 1, 2 and 4 ms under certain pressure p = 5 MPa depicted in Fig. 7. Start-injection transitions developed from point A to point O are absolutely repeatable irrespective of t.

Delta-type transitions A-to-O are similar to AB evolution discussed early in Fig. 5. Zigzag oscillation settled at the point O delays to point A on the angular shift $\delta\alpha$ = 3° to 5° or about 125 to 150 μs.

3.2. Integrated Injection Fuel Mass

Since the middle of sixties the Bosch (1964) indicator has been used in automotive engineering to measure injection pattern. Aiming at the employment of LDA flow rate meter in the injection systems the integrated mass series are considered as the basic factor to be analyzed for in-situ flow rate measurements. As an example, the series of integrated fuel mass $m(t)$ obtained for τ = 1, 2, 4, 11 ms under p = 5 MPa and f = 22 Hz are depicted in Fig. 8.

The injection period consists of two stages, i.e. two different average temporal derivatives or mass rates, high and low intensive. First, while the injector valve is opened at $\alpha = 75°$, the injected mass m_{op}-series are only gradually shifted versus τ. This means that mass rate dm_{op}/dt depends only on the injection duration, τ. Second, before and after the active injection, is a passive injection while injector valve is closed. This injected mass m_{cl} comes in flow from deposed volumes of the injector. The mass rate dm_{cl}/dt is also varied versus τ.

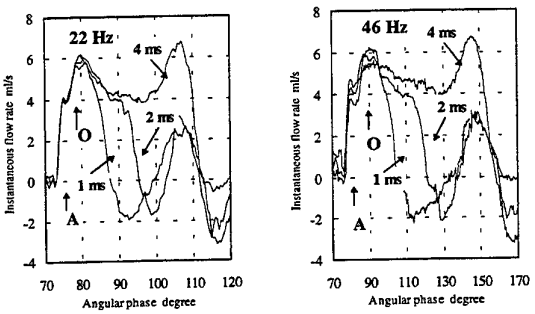


Fig. 7. Flow rate under p = 5 MPa

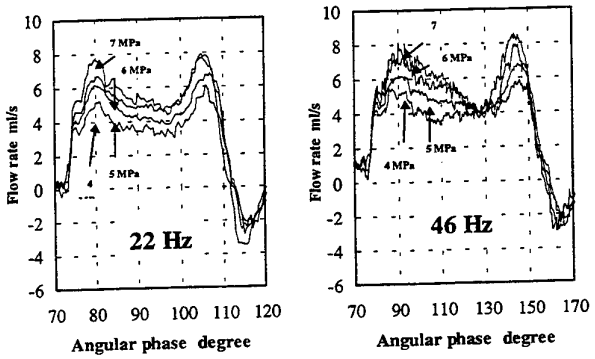


Fig. 6. Flow rates under p = 4, 5, 6, 7 MPa for τ = 4 ms

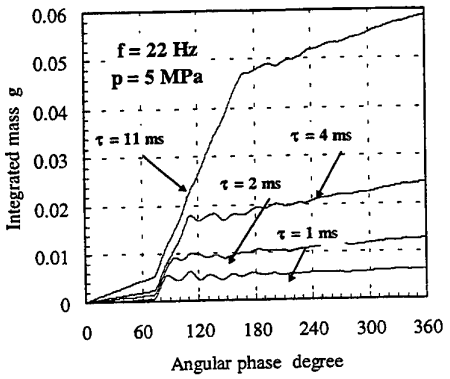


Fig. 8. Integrated masses

In general, both m_{op} and m_{cl} masses are dependent on the injection time rate τ_{op}/T and pressure p. Integral of m_{op} and m_{cl} is total fuel mass injected per cycle. In fact, the active injection time τ_{op} under opened valve is longer than the injection duration set τ driven by the timing controller, $\tau_{op}=\chi\tau$ where $\chi > 1.0$. The passive fuel mass m_{cl} deals with the dead spaces inside of the injector construction used for operational movement of the valve.

Analysis of all data obtained at variable injection sets results in a well-correlated linear relationship between injected masses m_{op} and m_{cl} and active injection time rate τ_{op}/T. This relationship can be expressed by a fitting correlation $m_{op} = \gamma_{op}(\tau_{op}/T)$ and $m_{cl} = \gamma_{cl}(\tau_{op}/T)$ respectively to active and passive masses where γ_{op} = 0.1757 and γ_{cl} = 0.0282 [g] are the mass rate factors induced by presently examined injector respectively. These γ–factors can be obtained only upon the base of integrated instantaneous flow rate series.

The mass rate dm_{op}/dt is sensibly dependent on pressure p. As shown in Fig. 9 for high injection pressures, $p > 4$ MPa, applicable to GDI engines, this relationship is well-governed by a logarithmic law $dm_{op}/dt = ln(p/p_o)^{1.478}$ where p_o = 1.56 MPa.

3.3. Instantaneous Spray Patterns

Core-jet (CJ) and quasi umbrella (QU) fractions superpose investigated spray flow structure is sketched as shown Fig. 10.

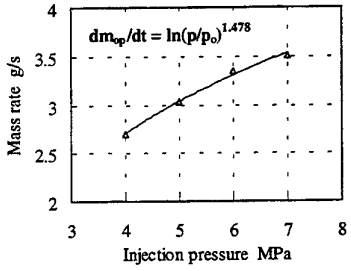


Fig. 9. Mass rate versus injection pressure, $\tau = 4$

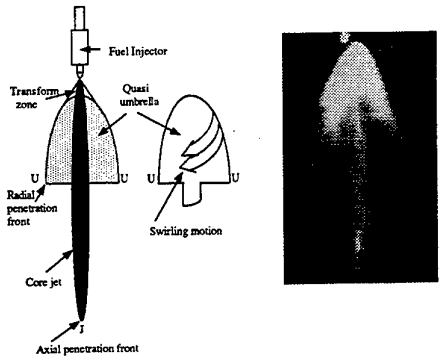


Fig.10. Developed spray structure

Dynamic evolution of these fractions is dependent on p and τ. To reconstruct instantaneous spray flow patterns the time series of axial velocity U_{ax}, Sauter mean diameter D_{32} and normalized particle number N_{part}/N_{prob} are processed for each measurement point. As an example, the time series of U_{ax}, D_{32} and N_{part}/N_{prob} processed at a point (z = 5, r = 5) for τ = 1 ms and p = 5 MPa are plotted in Fig. 11.

The common behavior of spray flow is reflected in the flow dynamics developed upstream the injector as indicated early by the results of flow rate measurements and spray flow visualization. The maximum peak in U_{ax}-series relates to the phase when the valve is driven to be closed, but active injection is continued. After active injection, numerous points/peaks in all series indicate a post-injection spraying. The most intensive effect can be seen in D_{32} and N_{part}/N_{prob} -series.

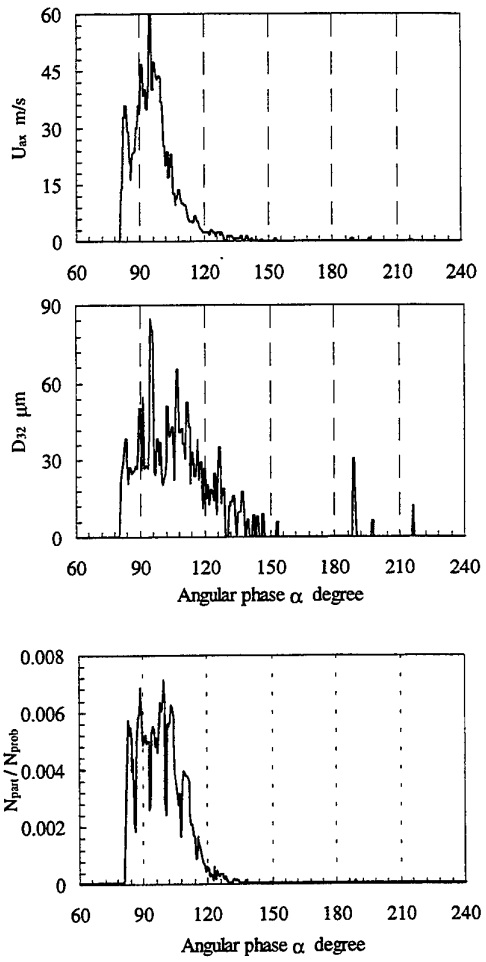


Fig. 11. Sampled series of U_{ax}, D_{32} and N_{part}/N_{prob}

For illustration of the spray dynamics in a planar in-axis section, such as can be observed by using a visualization technique, with the same time series of U_{ax}, D_{32} and N_{part}/N_{prob} at f = 46 Hz and τ = 1 ms, are sampled in Fig. 12. Here, four time phases are selected to represent temporal dynamics, from a start-injection phase $\alpha = 75.0^{\circ}$ (t= 4.521 ms) to a final active injection phase $\alpha = 97.5^{\circ}$ (t= 5.877 ms).

The axial velocity time–series U_{ax} indicate that the starting injection, $\alpha = 75.0^{\circ}$, CJ-fraction goes down with high velocity seen as the vertically tracing passes. The next phase, $\alpha = 82.7^{\circ}$, reveals a jet breakup at z = 5 mm and initial development of CJ and QU fractions in spray. After full development of the spray structure, $\alpha = 90.0^{\circ}$, CJ and QU become separated. As discussed, active injection time τ_{op} is longer than injection duration set τ = 1 ms ($\delta\alpha = 16.6^{\circ}$). At the phase $\alpha = 97.5^{\circ}$, the spray flow is still developing, and at a middle axial range z = 30 to 60 mm, the spray structure is intensively mixing because of a bulkily developed vortex.

Series of Sauter mean diameter D_{32} show that, downstream of axial position z > 40 mm, a number of small droplet size domains (D_{32} < 15 μm) are always remaining in the spray flow. At the start phase $\alpha = 75.0^{\circ}$, a spray part attached to the nozzle is a large droplet size domain. D_{32} is varied from 50 μm in the core to 20 μm on its crown. Development of CJ and QU substructures can be seen at $\alpha = 82.5^{\circ}$ as two domains at the nozzle with a split angle. After separation, α= 90.0 degree, large size particles move down as far as z = 40 mm while the QU fraction becomes thicker and substrate. The last phase, $\alpha = 97.5^{\circ}$, shows that the vortexes structure downstream provide domains of large-size particles.

To consider the optimal combustion process it is important to get exact experimental information about temporal distributions of fuel droplet size and their number density to compute mass fluxes. In the present investigation the normalized particles number N_{part}/N_{prob} is obtained. As can be seen from Fig. 12, the droplet density in the spray is remarkably stratified. Three specified areas indicate a high droplet concentration: near the nozzle (NN), conical edge (CE) of QU fraction at (z = - 25, r = 22) and long vortex edge (VE) located between two points at (z = -95, r = 54) and (z = -55, r = 46). The high pressure and temperature ambient conditions of the combustion can suppress a high number density in the last VE-area as well as a change of particle size and number density in NN and CE areas.

A high density close to the nozzle was observed at the phase α= 75.0°. Afterwards, α= 82.5°, the high-density area is detached from the nozzle. This concords with a common problem of the PDA-technique, because the measurement data rate are low in the liquid jet.

The third phase, $\alpha = 90.0^{\circ}$, illustrates distribution of droplet number in both CJ and QU substructures. At the end of active injection, $\alpha = 97.5^{\circ}$, a high-density domain is located at the nozzle and simultaneously the droplet number is concentrated within QU conical edge and fuel mass flows from QU to CJ.

4. CONCLUSIONS

The present investigation is aimed at the providing complex diagnostics for high-pressure gasoline injection system by employing measurements of instantaneous characteristics of two flows, upstream and downstream the high pressure gasoline injector, with high temporal resolution of a few tens of μs. The results show that gasoline injection sytemm can be well examined by introducing a combination of the laser-based measurements. Accurate data, obtained by using LDA flow rate meter, are available to present initial and transient behavior of the injected fuel flow. It provides a basic information that can be numerically modeled and experimentally verified into the ejected spray flow.

In a framework of industrial employment of this technique the authors are considering on the follows:

1. Developed LDA technique for instantaneous flow rate measurements allows accurately indicating basic transient injection characteristics that directly deal with the fuel injector itself through γ – type factors as well as gasoline injector system supplied to the injector. That permits provision of in-situ flow rate diagnostics of advanced gasoline injector systems, competitively with the Bosch indicator (1964). The LDA flow rate metering technique can be also applied in other engineering fields where accurate dozing of the fluid multi-phase contaminates plays important role in a treatment or operation process.
2. An instantaneous flow rate indicator installing on a high-pressure line of gasoline injection system will be realized by employing proposed LDA-based one as well as a differential pressure sensor.
3. The present PDA-based technique can be competitively used in combination with convenience, Obokata et. al. (1996), and novel, Sankar et. al. (1997), non-intrusive measurements of sprays, for the verification of fuel spray quality and its temporal characterization. This technique makes it available to compute fuel mass fluxes for optimal combustion due to well-reconstructed instantaneous patterns of droplet velocity-size and particle number density. Exceptional PDA-measurements are considered for axial zone of 1 mm close to the injector exit nozzle.

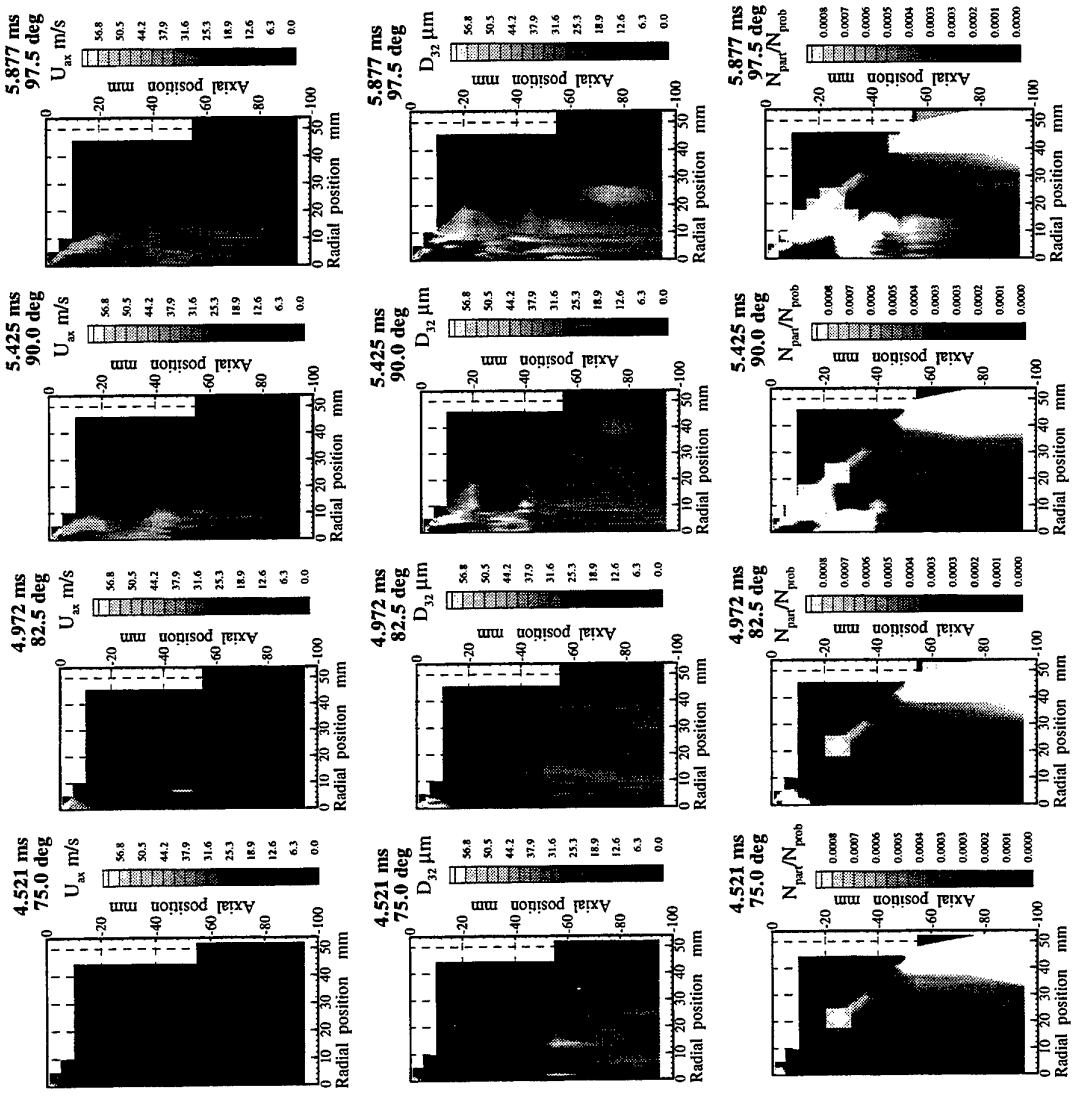


Fig. 12. Instantaneous planar series of U_{ax}, D_{32} and N_{part}/N_{prob} within active injection τ_{op}

ACKNOWLEDGEMENTS

The Alexander von Humboldt Stiftung and the Japanese Society for Promotion of Science supported the first author during present research and development work. The assistance of Unisia Jecs Co. is kindly acknowledged.

REFERENCES

Bosch, W. 1964, Der Einsprtizgesetz-Indikator, ein neues Messgeraet zur direkten Bestimmung des Einspritzgesetzes von Einzeleinsrpritzungen, Motortechnische Zeitschrift, 25. Jahrg, Heft 7, pp. 268-282

Durst, F,, Ismailov, M., Trimis, D., 1996 Measurements of instantaneous flow rates in periodically operating injection systems, J. Experiments in Fluids, 20, 178-188

Edwards, C., 1997, The point-particle/continuum-field theory of spray flows, Proc. ICLASS-'97, Seoul, Korea, pp. 673-681

Hanjalic, K., Jakirlic, S., Hadzic, I., 1993, Computations of oscillations turbulent flows at transitional Re-numbers, Turb Shear Flows 9, Selected Papers, Springer Verlag, pp. 323-342

Harada, J., Tomita, T., Mizuno, H., Mashiki, Z., Ito, Y., 1997, Development of direct injection gasoline engine, SAE Technical Paper Series 970540

Hiroyasu, H., 1985, Diesel engine combustion and its modeling, Proc.COMODIA-85, Tokyo, Japan, pp.53-75

Ismailov, M., Ishima, T., Obokata, T., Tsukagoshi, M., Kobayashi, K., 1997, Control of Transient Injection and Fast Spray Dynamics, Proc. ICLASS-'97, Seoul, Korea, pp. 1015-1022

Iwamoto, Y., Noma, K., Nakayama, O., Yamauchi, T., Ando, H., 1997, Development of gasoline direct injection engine, SAE Technical Paper Series 970541

Liu, Z., Reitz, R.D., 1995, Modeling fuel spray impingement and heat transfer between spray and wall in direct injection diesel engines, Numer. Heat Transfer: Part A: 515-529

Obokata, T., Long, W., Ishima, T., 1996, PDA and LDA measurements of large angle hollow cone spray proposed for hot-premixed combustion type diesel engine, SAE Technical Paper Series 960772

Sankar, S.V., Maher, K.E., Robart, D.M., Bachalo, W.D., 1997, Spray characterization using a planar droplet sizing technique, Proc. ICLASS-'97, Seoul, Korea, pp. 649-656

CHARACTERISTICS OF SPRAYS FROM GASOLINE INJECTORS

C. Brehm, M. Posylkin and J. H. Whitelaw

Thermofluids Section, Department of Mechanical Engineering
Imperial College of Science, Technology and Medicine, London SW7 2BX, England

ABSTRACT

Droplet velocities and diameters of sprays from gasoline injectors, with and without air-assist, were measured in atmospheric air at an axial distance of 51 mm downstream of injector nozzles. A corresponding photographic investigation examined the sprays close to the nozzles and quantified the distance at which the liquid was fully atomised. Conventional double-cone sprays were characterised by two maxima of droplet density, velocity and size at the centre of each of the two cones, with mean velocities of about 20 m/s and spatially averaged Sauter mean diameters of the order of 100 μm. With air-assist, the droplet diameter decreased to around 50 μm with the maximum pressure difference of 700 mbar, but large droplets were still present. At the same time, the distance at which atomisation appeared complete was reduced from about 30 mm to less than 10 mm from the nozzle and the angle between the two cones collapsed to form a single spray with a velocity maximum of about 27 m/s.

1. INTRODUCTION

The effects of spray characteristics from gasoline injectors on engine performance have been investigated and it can be conjectured from the results of Chappuis et al (1997), Vannobel et al (1994) and Posylkin et al (1994) that fuel droplets will not affect engine performance when injection occurs with the valves closed, provided the liquid fuel is allowed to remain in the port for sufficient time to evaporate from hot metallic surfaces. With injection with the valves open, however, the effects of the spray characteristics are ambiguous and not yet fully understood. The results of Brown and Ladomatos (1991) and Almkvist et al (1995) showed that evaporation and film formation are less likely with injection with the valves open and suggested that the droplet characteristics and targeting of the incident spray upstream of the inlet valve are important. Fulcher et al (1995) showed that the smaller droplet diameters of an air-assisted injector led to improved engine performance and to reduced unburned hydrocarbons, while Brehm et al (1996) concluded that improvements may be related more to the orientation of the spray than to the droplet size.

Although investigations of breakup of liquid jets and droplets date to the beginning of this century, the physical processes involved in spray atomisation are still not completely understood. Recent investigations included those of Arcoumanis et al (1996) and Engelbert et al (1995), with the later showing that turbulent flow in airblast atomisers led to the formation of wave-like structures in the liquid near the injector nozzle and to the subsequent breakup of clusters of liquid, which disintegrated to determine the stable droplet size in the downstream spray.

The present investigation is concerned with the characterisation of sprays from port fuel injectors and follows that of Brehm et al (1996) in which the influence of four injector types on the performance of a four-valve engine was examined under steady and transient operating conditions. Experiments were performed with two conventional and two vacuum-driven air-assisted injectors and examined the sprays in the far-field and near-nozzle regions. The measurements were performed by phase-Doppler anemometry (PDA) on the centreline of the sprays and at different horizontal planes downstream of the exit flow of the nozzles. Additional information was obtained from photographs, which depicted the spray at different stages of injection and allowed the

determination of the atomisation length, the distance from the nozzle where the spray was fully atomised. The near-field photographic images examined the structure of the spray from a conventional injector in terms of wavelength, amplitude, jet angle, breakup length and shape of the ligaments produced during the disintegration process. In order to increase the range of flow conditions and to study the influence of aerodynamic forces on jet disintegration, the injection pressure of the liquid was varied from 1 to 5 bar. The experimental arrangement and instrumentation are described in the next section followed by results and summary conclusions.

2. EXPERIMENTAL ARRANGEMENT

The experiments were carried out with two conventional and two vacuum-driven air-assisted injectors, referred to as injectors I-1 to I-4, each mounted on a bench and arranged to spray into a tank from which the accumulated liquid was collected and the fuel vapour removed to the exhaust system by a suction fan. The commercial, unleaded gasoline was injected at a frequency of 3 Hz to allow ready dilution of the fuel vapour in the exhaust system, and with an injection duration of 7 ms which was characteristic of part load engine conditions. The injection pressure was 3 bar, except for the near-nozzle investigation where the pressure regulator of the commercial fuel rail was replaced by a valve in the return line of the excess liquid to allow ready variation of the pressure. Since the spray was injected into atmospheric air, the air-assisted injectors were supplied with pressurised air with the same range of pressure differences as those in the engine at corresponding loads.

The phase-Doppler anemometer was similar to that used by Posylkin et al (1994) and based on that described by Hardalupas et al (1989). It was operated with an Argon-Ion laser tuned to the green wavelength of 514.5 nm, with the laser beam transmitted by an optical fibre to the transmitting unit of the anemometer. The signals from the photomultipliers were processed by a custom-built counter, interfaced to a microcomputer to obtain simultaneously the velocity and size of droplets as a function of time. The maximum frequency of the Doppler signal was around 4 MHz, leading to random uncertainties of velocity of up to 0.1 m/s and of size up to 2 μm which stemmed from the resolution of the 500 MHz internal clock of the phase-Doppler counter. The combination of transmitting and receiving optics during the measurements resulted in a nominal measurement size range up to 360 μm. The characteristics of the phase-Doppler anemometer are summarised in table 1.

Transmitting optics	
Ar^+ wavelength	514.5 nm
operated at	400 mW
Focal length of imaging lens	600 mm
Beam diameter at e^{-2} intensity	1.25 mm
Frequency shift by rotating grating	2.174 MHz
Beam separation	4 mm
Half angle of beams intersection	0.645 °
Number of fringes	9
Frequency to velocity conversion factor	0.12 MHz/ms^{-1}
Receiving optics	
Focal length of collimating lens	310 mm
Separation betw. apertures 1 and 2	13.3 mm
Separation betw. apertures 1 and 3	26.7 mm
Phase to diameter conversion factor	1.040 μm/deg

Table 1: Characteristics of the phase-Doppler anemometer

The optical components for transmission and collection were mounted on a supporting bench, separate from the injector and the fuel rail, in order to simplify traversing the sprays. Measurements of velocity and size were based on at least 1000 samples, resulting in statistical uncertainties of less than 5% in the ensembled mean, 15% in the rms of the velocity signal and 5% in the cumulative size distribution based on the number of droplets (Tate 1982).

The photographic study made use of a conventional 35 mm still-camera (Nikon F-801s) equipped with a high-magnification zoom-lens (Nikon AF Micro Nikkor 55mm) and a 2× teleconverter (Teleplus MC7) mounted between the camera and the lens. Photographs were taken at two distances from the injector and in a darkened environment, with open shutter and a sparklight (Palflash) illuminating the spray for a period of about 20 μs. The sparklight was synchronised with the injector pulse so that the flash occurred with required time delay after the start of injection, and allowed the spray shapes to be frozen at different states of their development.

3. RESULTS AND DISCUSSION

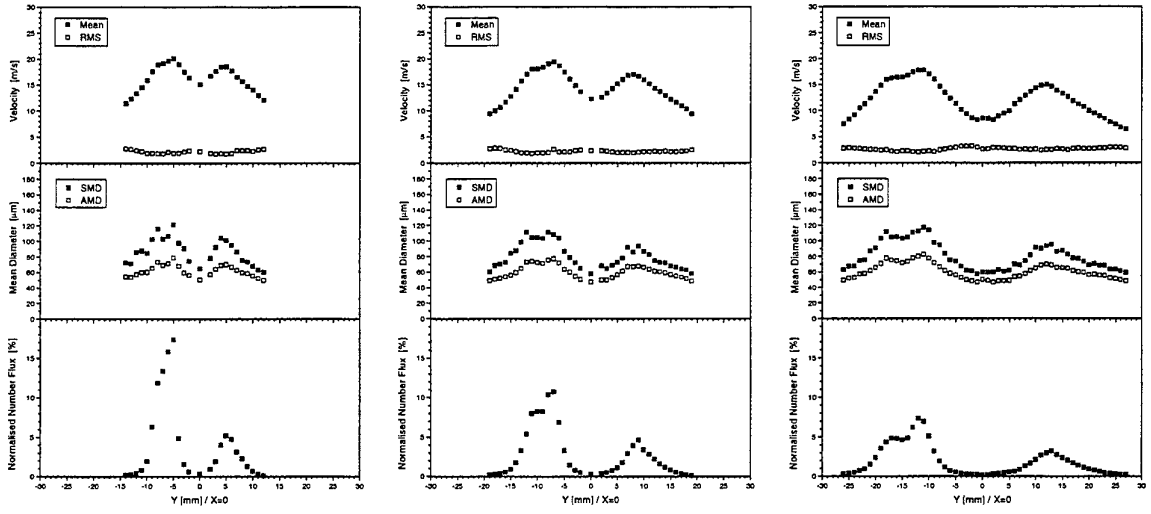
The PDA measurements in the far field of the sprays were obtained in a horizontal plane 51 mm downstream the nozzles, except with the conventional injector I-1 where additional measurements were

carried out at 30 mm and 80 mm. In the case of the air-assisted injectors, pressure differences, Δp, of 0, 0.3, 0.5 and 0.7 bar were selected to simulate the range of manifold depressions from full load to idle. For the photographic examination of the jet close to the nozzle injector I-1 was operated with five injection pressures of the gasoline, from 1 to 5 bar.

The first of the following two subsections corresponds to the investigation of the far field of the spray and is subdivided into two parts which correspond to the unassisted and the air-assisted injectors. First the results of the PDA measurements obtained with the conventional double-jet injector I-1 are shown for the three axial planes followed by the presentation of the corresponding photographs of the sprays at two different stages of injection. In the second part, centreline profiles of the air-assisted double-jet injector I-3 are presented for four pressure differences to examine the influence of the added air on droplet velocity, size and number flux distributions, as well as on the spray angle and the breakup length. The second subsection presents the results of the photographic investigation in the near-nozzle region of the spray from injector I-1 for injection pressures of 1, 3 and 5 bar.

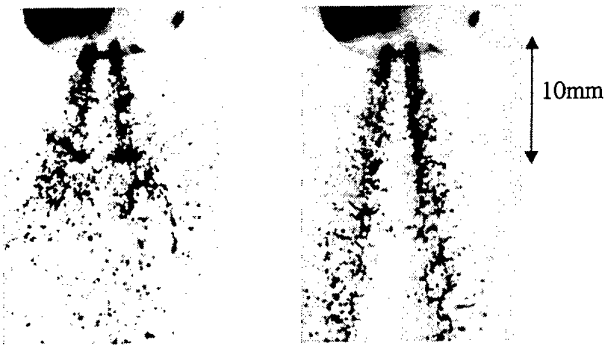
3.1 Spray characteristics in the far field downstream the injector nozzle

Unassisted injectors. Figure 1 presents the distributions of droplet velocity, size and number flux along the centreline of the double cone spray of injector I-1, at the three horizontal planes. The two peaks of droplet flux coincide with those of velocity and size, with an angle of 20 degrees between the jets and maximum droplet velocities decreasing slightly from about 20 m/s close to the nozzle to 17.7 m/s at a position 80 mm downstream due to increasing loss of kinetic energy. The Sauter Mean Diameter (SMD) of the droplets ranged from about 60 μm at the edges of the spray to maximum values of about 120 μm at the peaks and is similar for all measured planes. This suggests that secondary breakup of the droplets did not occur, possibly because the aerodynamic forces induced by the slip between the droplets and the air were not sufficient to overcome the surface tension of the droplets, and that effects of evaporation over a distance of 50 mm, corresponding to a time of flight of about 2.5 ms, were negligible in the atmospheric air and temperature of about 20°C. The Weber number, the ratio of the aerodynamic and the surface tension



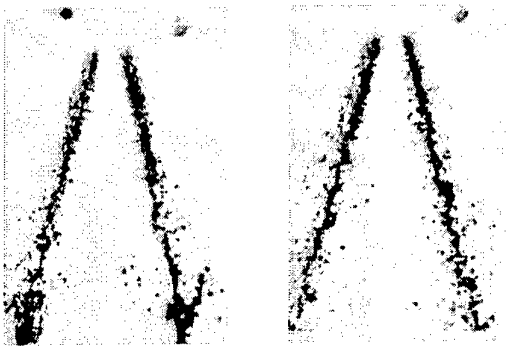
(a) z = 30 mm (b) z = 51 mm (c) z = 80 mm

Figure 1: Centreline profiles of injector I-1 at three horizontal planes downstream of the nozzle



(a) t = 2.5 ms (b) t = 4 ms

Figure 2: Spray photographs of injector I-1 at the initial and stationary phase of injection



(a) t = 2.5 ms (b) t = 4 ms

Figure 3: Spray photographs of injector I-2 at the initial and stationary phase of injection

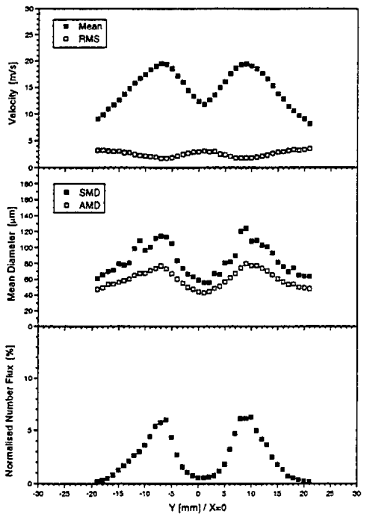
forces, was well below the critical value of 13, which confirms the observation that further breakup of droplets is unlikely to have occurred (Lefebvre 1989).

With the spray of the double-jet injector I-2, investigated previously by Posylkin (1996), droplet velocities similar to that of injector I-1 were observed but the size of the droplets was larger, with spatially averaged SMD of about 130 μm compared to 100 μm at 80 mm. Since the observations of injector I-1 suggested that the droplet sizes in the downstream regions were determined by the size of the ligaments during the primary breakup, the larger droplets from injector I-2 imply less disintegration than from injector I-1.

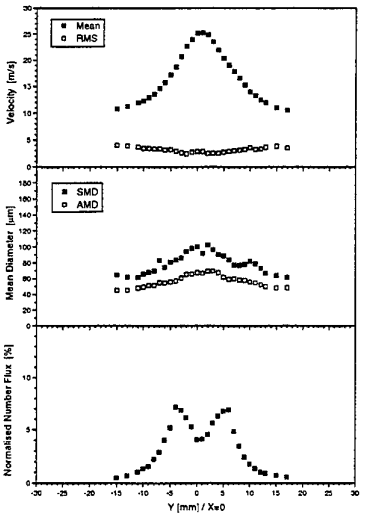
The photographs of figure 2 and 3 corroborate the findings of phase-Doppler anemometry described in the previous paragraphs. Figure 2(a) shows that the spray of injector I-1 had two ring-shaped jets with fast-growing axisymmetric oscillations on the surface during the initial phase of injection and these led to early breakup, whereas injector I-2, fig 3(a), produced two thin and almost straight liquid jets with breakup further downstream. During the stationary phase, fig. 2(b), the spray of the first injector was almost fully atomised at 30 mm from the nozzle, in contrast to that of fig. 3(b), which retained two liquid jets before disintegrating into droplets, some 60 mm from the nozzle. Both injectors gave rise to average droplet diameters smaller than the nozzle diameters, suggesting that disintegration occurred in the second wind-induced breakup regime of Reitz' model (Lefebvre 1989), where the relative motion of the jet and the air caused unstable growth of short-wavelength waves on the jet surface, opposed by the surface tension of the liquid. The differences in the atomisation length and droplet sizes of the two sprays are probably due to the different design of the plate below the needle, such as diameter and angle of the four holes, since each injector nozzle was designed for a particular engine in terms of the spray angle and the quantity of injected fuel. In subsection 3.2 the spray of injector I-1 is examined near the nozzle in greater detail.

Air-assisted injectors. Figure 4 presents characteristics of the spray from injector I-3 with four pressure differences of the added air. It is obvious from fig. 4(a) that the injector produced a spray pattern similar to that of the unassisted double-jet injector I-1 when no air was added and that increase in the air flow caused the angle between the two spray cones to decrease from about 18 to 7 degrees, leading to a nearly single-cone spray as shown in fig 4(b)-(d). The mean droplet velocity increased with added air from 20 m/s to about 28 m/s in the centre of the spray and atomisation was enhanced, resulting in some 30 % reduction in the spatially averaged SMD from about 100 μm to 70 μm. The corresponding photographs revealed that the spray was similar to that of injector I-1 at high load and without assisting air, which is not surprising since the sprays had similar distributions. With increase in pressure difference and consequently in the flow of atomising air, the number of visible droplets decreased but droplets up to about 350 μm in diameter were still present, even with maximum airflow. Without added air, most of the liquid was atomised some 30 mm from the nozzle and this distance decreased with air-assist to less than 10 mm with the highest air flow.

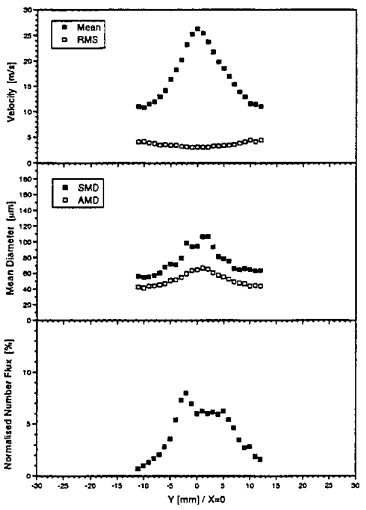
A different pattern was observed with the second air-assisted injector, I-4, since this spray emerged with a constant spray angle of 24 degrees, because of a division barrel below the hole plate



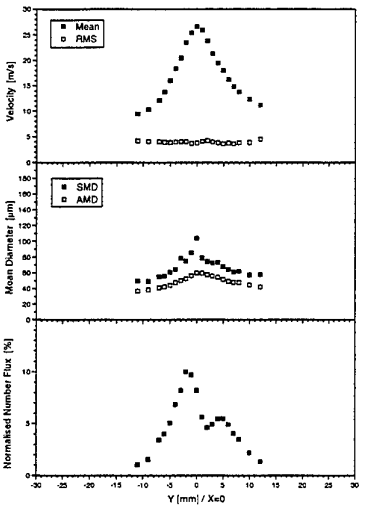
(a) Without additional air



(b) $\Delta p = 0.3$ bar



(c) $\Delta p = 0.5$ bar



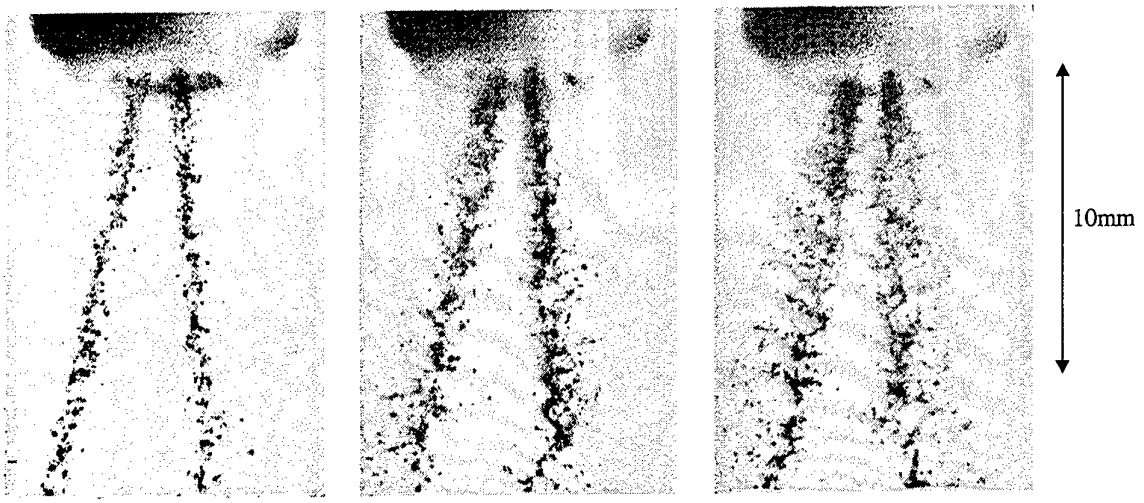
(d) $\Delta p = 0.7$ bar

Figure 4: Centreline profiles of injector I-3 at a horizontal plane 51 mm downstream of the nozzle

which prevented the collapse of the angle between the two spray cones with increase in the air flow. The peaks of the droplet sizes were not so well defined and the droplets became bigger at the edges of the spray, probably due to impingement of liquid on the division barrel in the centre of the nozzle and subsequent breakup and deflection of larger ligaments towards the outer regions. The average droplet sizes were some 50 % smaller than that of injector I-3, with spatially averaged SMD decreasing from 75 µm to 38µm with increase in pressure difference; the droplet velocity decreased from 17 to 14 m/s and the atomisation length from 30 to less than 10 mm and similar to that of injector I-3.

3.2 Spray characteristics near the injector nozzle

A sequence of photographs of the spray from injector I-1 is presented in fig. 5(a)-(c) with injection pressures from 1 to 5 bar. With low injection



(a) p_i = 1 bar (b) p_i = 3 bar (c) p_i = 5 bar

Figure 5: Spray photographs of the conventional double-jet injector I-1 close to the nozzle for different injection pressures of the liquid

pressure, fig. 5(a) shows axisymmetric dilational waves with sequences of thinner and thicker regions of liquid which broke up into clusters some 12 mm downstream of the nozzle with subsequent disintegration to droplets. The amplitude of the waves was of order 0.4 mm and almost no droplets were stripped from the jet surface. This indicates that the aerodynamic shear forces between the moving liquid and the surrounding quiescent air were small so that surface tension dominated and sustained the narrow and compact shape of the jets.

The jet velocity increased with injection pressure and so did the amplitude of the waves which also grew with distance from the nozzle until droplets and ligaments were stripped from the surfaces as shown in fig. 5(b). Further increase in injection pressure produced the "fishbone"-like pattern of fig. 5(c) with thin and elongated ligaments and resulted in smaller droplets, proportional to the thickness of the ligaments. The angle between the tangents of the wave crests increased linearly with injection pressure so that smaller droplets were associated with a wider angle.

The frequency of the dilational waves was derived from the measured wavelength and the velocity at the nozzle exit and increased linearly with injection pressure from about 4 to 18 kHz which was mainly due to the increase in velocity but also due to a decrease in the wavelength. The corresponding breakup frequency of the jets, which is a measure of the appearance of liquid clusters during a given period, could not been obtained from the still photographs as this required sequences of successive shots, but probably increased in a similar way since observations of Engelbert et al (1995) with an airblast atomiser indicate that the frequency of the waves was well correlated with the breakup frequency and about twice that for low values of the slip velocity.

The photographs also provided information of the breakup length of the jet, that is the distance between the nozzle and the location at which the liquid core of the jets broke into ligaments. With increase in injection pressure; the breakup length decreased from 12 to 9 mm, though variations of up to ±3 mm around the mean value were observed. Generally, an increase in jet velocity increased the breakup length and the shear between the moving liquid and the surrounding quiescent air so that disintegration of liquid and subsequent breakup was promoted.

4. SUMMARY AND CONCLUSIONS

Droplet velocities and sizes were measured by phase-Doppler anemometry in the sprays downstream of gasoline injectors and complemented by visualisation of the sprays. The main findings can be summarised as follows:

1. The unassisted injectors I-1 and I-2 produced double cone sprays with two maxima of droplet flux, which coincided with those of velocity and diameter. The spatially averaged Sauter mean diameters were about 100 μm and 130 μm and depended on the design of the hole-plate of the injector nozzle. Droplet diameters were similar in the planes 30, 51 and 80 mm below the injector nozzle, which suggests that the slip velocity between droplets and air was too low for further atomisation and that evaporation effects were negligible.
2. With unassisted injection, the breakup of the liquid into droplets was completed after about 30 and 60 mm with injectors I-1 and I-2, respectively. With air-assisted injection, the breakup was completed about 10 mm downstream of the nozzle, with disintegration of the liquid jets beginning almost immediately after leaving the nozzle at pressure differences larger than 500 mbar.
3. The angle between the two spray cones of the air-assisted injector I-3 decreased from 18 degrees to 7 degrees with increase in the air flow when coalescence occurred; with a dividing barrel to prevent coalescence, injector I-4, a constant angle of 24 degrees was maintained.
4. Atomisation was improved by increase in air pressure difference, leading to a reduction of average droplet sizes from about 75 to 40 μm for the injector with a division barrel and 100 to 70 μm for that without, though droplets of up to 350 μm in diameter were observed.
5. The liquid jet in the near nozzle region had a periodic structure with axisymmetric dilational waves which generated sequences of thinner and thicker regions of the jet. The amplitudes of the waves grew with distance from the nozzle and led to the breakup of the liquid into clusters with subsequent disintegration to droplets. Increase in injection pressure induced a higher slip velocity between the liquid and the surrounding air and increased the frequency of the waves and the jet angle but had only a small effect on the breakup length.

ACKNOWLEDGEMENTS

The research was funded in part by the European Commission in the framework of the Non Nuclear Energy Programme of Joule III.

REFERENCES

Almkvist, G., Denbrat, I., Josefsson, G. and Magnusson, I. (1995) Measurements of fuel film thickness in the inlet port of an SI engine by laser induced fluorescence. SAE Paper 952483.

Arcoumanis, C., Whitelaw, D.S. and Whitelaw, J.H. (1996) Breakup of droplets of newtonian and non-newtonian fluids. Atomization and Sprays, vol. 6, pp. 245-256.

Brehm, C., Carabateas, N., Cousyn, B., Mangano, R., Neveu, F., Posylkin, M. and Whitelaw, J.H. (1996) Evaluation of the influence of injector type in a four-valve engine. SAE Paper 961998.

Brown, C.N. and Ladomatos, N. (1991) The effects of mixture preparation and trapped residuals on the performance of a spark-ignition engine with air-shrouded port injectors, at low load and low speed. Proc. IMechE, vol. 205, pp. 17-30.

Chappuis, S., Cousyn, B., Posylkin, M., Vannobel, F. and Whitelaw, J.H. (1997) Velocity and drop-size distributions in a four-valve production engine. Exp. in Fluids, vol. 22, pp. 336-344.

Engelbert, C., Hardalupas, Y. and Whitelaw, J.H. (1995) Breakup phenomena in coaxial airblast atomizers. Proc. Roy. Soc. Lond., series A vol. 451, pp. 189-229.

Fulcher, S.K., Gajdeczko, B.F., Felton, P.G. and Bracco, F.V. (1995) The effects of fuel atomisation, vaporisation and mixing on the cold start UHC emissions with a contemporary SI engine with intake manifold injection. SAE Paper 952482.

Hardalupas, Y., Taylor, A.M.K.P. and Whitelaw, J.H. (1989) Velocity and particle flux characteristics of turbulent particle-laden jets. Proc. Roy. Soc. London, series A vol. 426, pp. 31-78.

Lefebvre, A.H. (1989) Atomization and Sprays, Hemisphere Publishing Corporation, New York.

Posylkin, M. (1996) Mixture preparation in spark-ignition engines, Ph.D. thesis, Imperial College of Science, Technology and Medicine, London.

Posylkin, M., Taylor, A.M.K.P. and Whitelaw, J.H. (1994) Manifold injection and the origin of dropets at the exit of a valve. Applications of Laser Techniques to Fluid Mechanics, vol. 7, pp. 132-146.

Tate, R.W. (1982) Some problems associated with the accurate representation of droplet size distributions. Proc. 2nd Int'l Conf. on Liquid Atomisation and Spray Systems (ICLASS, Madison), pp. 341-351.

Vannobel, F., Robart, D., Dementhon, J.B. and Whitelaw, J.H. (1994) Velocity and size distributions of fuel droplets in the cylinder of a two-valve production spark-ignition engine. Proc. 3rd Int'l Symposium on Diagnostics and Modelling of Combustion in Internal Combustion Engines (COMODIA-94, Yokohama), pp. 373-378.

COMPARISON OF DIFFERENT DROP SIZING TECHNIQUES ON DIRECT INJECTION GASOLINE SPRAYS

Jean-François LE COZ
Techniques of Energy Application Department
Institut Français du Pétrole, Rueil-Malmaison, France

ABSTRACT

The use of different drop sizing techniques on direct injection gasoline sprays for automotive applications is discussed. The injectors used are swirl injectors with a command nozzle. Two commercial Phase-Doppler systems are tested and compared. One of them gives more satisfying results, but both are hindered by the high droplet concentration. Practically no droplet can be measured in the main part of the spray. A commercial laser-diffraction device is also tested. Measurements remain possible in the whole spray, even with less than 10% transmission. Special tests without evaporation confirm that the results are quite relevant when compared to size estimates obtained by integration of light absorption visualisations.

INTRODUCTION

Direct-injection gasoline engines have the potential to improve fuel economy when used under heterogeneous mixture for part-load operation [1]. The injector is a key device for such engines. The quality of the spray is essential to realise good fuel mixture preparation, that is little droplet/wall interaction and rapid evaporation of the mixture [2]. Matching the spray shape to the engine geometry is important for controlling the location and the concentration gradient of the rich zone where ignition occurs with the help of a spark-plug. These requirements make necessary to analyse the spray characteristics which influence the mixture precisely, in particular the droplet size. The goal of this paper is not to compare different sizing techniques very precisely as in [3] but to compare the practical use of different instruments available on the market in the field of gasoline direct injection sprays.

EXPERIMENTAL APPARATUS

Injection cell and injectors

An injection cell with 4 windows is used, which allows complete optical access and which withstands internal pressure up to 1 MPa. Industrial injectors are tested, which include internal swirl chambers, and a nozzle which opens and closes the orifice under the action of an electromagnetic coil [4, 5]. Injection is pulsed, and the injection duration fixes the injected amount for each injection pulse. Generally, unleaded gasoline is used as a fuel. Gasoline pressures are relatively high between 2 MPa and 8 MPa. The gas in the cell is nitrogen at ambient temperature (300 K) under pressures from 0.1 to 0.45 MPa to reproduce the densities found in an engine combustion chamber at the time of injection.

Light absorption is used to visualise the spray shape. A stroboscope illuminates a ground plate behind the spray and a video camera records the images (Figure 1). Images shown in this paper are mean images of 20 injection pulses, normalised by a mean reference image taken without the spray.

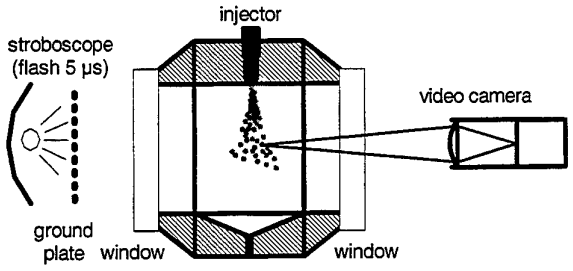


Figure 1 : Injection cell with imaging set-up

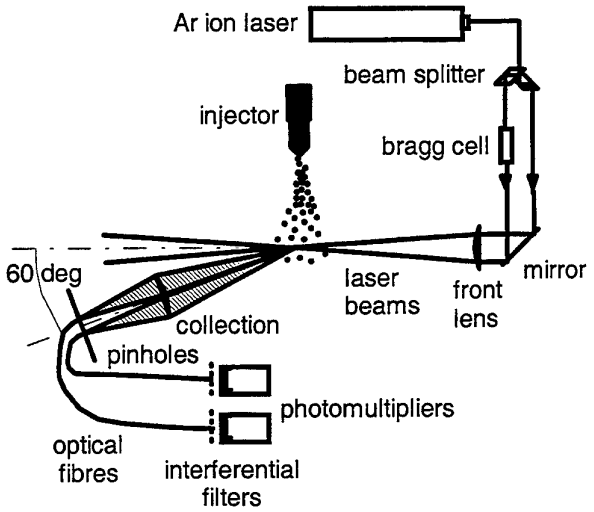


Figure 2 : Phase-Doppler set-up

Phase-Doppler drop sizing

A sketch of the Phase-Doppler arrangement is shown in Figure 2. The emission part is composed of an Ar-ion laser and TSI single-component optics. The scattered light is collected by the TSI APV receiver module. This module is formed by two half-lenses which are symmetrical with respect to the plane orthogonal to the beams. The off-axis angle is fixed to 60 degrees, in order to limit the effective probe volume length.

The optical parameters are given in Table 1. The fringe spacing, the probe volume diameter and the maximum diameter measurable are the result of a trade-off between different factors as described hereafter. The maximum Doppler frequency after down-mixing is limited to 20 MHz in the TSI IFA processor and 50 m/s can be reached in the spray. The very maximum droplet diameter expected in the spray is 100 microns. A small beam expansion ratio (1.66) is chosen to reduce the beam waist to 150 microns. This allows to reduce the probe volume and minimise the probability to have more than 1 droplet at the same time inside. The beam waist remains much larger than the maximum droplet diameter to avoid trajectory effects in the gaussian profile beam. In order to be able to measure higher velocities, the fringe spacing could have been increased. One way was to diminish the beam separation to 13 mm. But then the number of fringes would be only 20. The other way was to increase the emission focal length, and this would lead to a thicker beam waist. Moreover the fringes projected in front of the detectors would also be enlarged, which increases the maximum measurable diameter and decreases the droplet size accuracy. These are the reasons of the chosen optical settings.

laser wavelength	514 nm
beam expansion	1.66
beam diameter	1 mm * 1.66
beam separation	22 mm* 1.66
emission focal length	300 mm
beam waist (probe volume diameter)	~160 microns
fringe spacing	4.23 microns
receiver focal length (back and front)	310 mm
slit width	200 microns
off-axis angle	60 degrees
receiver lens diameter	70.1 mm
receiver aperture height	15 mm
refractive index	1.39
polarisation	orthogonal
maximum measurable diameter	135 microns

Table 1 : Optical settings

The outputs of the receiver module are two optical fibres, which are connected either to the TSI PMs module or to that from Aerometrics. The signal processors are the TSI IFA 750 and the Aerometrics RSA 3000. The TSI system runs with only two detectors. The RSA was configured for only two detectors, instead of three in the standard receiver from Aerometrics. This means than the phase difference is measured once in the two processors.

Diffraction drop sizing

A commercial system from Malvern/Insitec, Spraytec RTS 5001 is used. The receiving focal length is 200 mm. The droplet size range is 1 to 400 microns. This is a too wide range for our application. Because the spray could not be very close to the receiver, the focal length needed to be high enough in order to make the maximum working distance equal to 300 mm. The laser beam diameter is 10 mm. This means that a large part of the spray is integrated. Time-resolved data are given with a sampling period of 0.4 ms.

COMPARISON OF PHASE-DOPPLER SYSTEMS

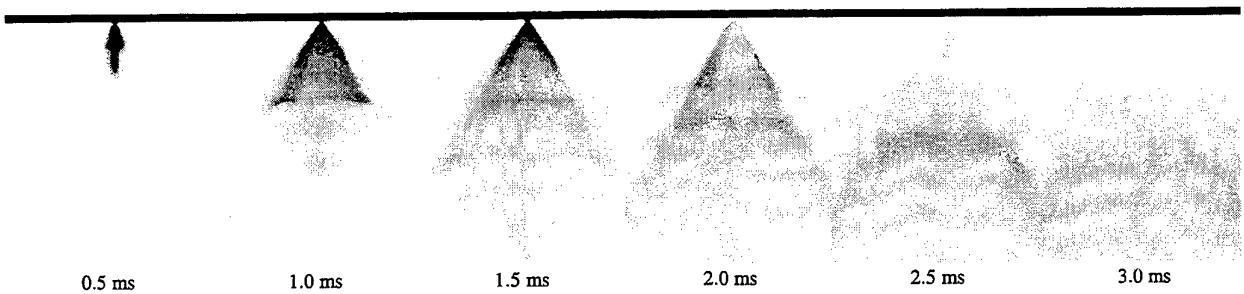
We compare the measurements made by the two systems with the same conditions, for different gasoline and air pressures (Table 2). The measurement point is located 45 mm from the nozzle, and 10 mm or 15 mm from the spray axis. A thorough comparison is done in two conditions (2.5 MPa gasoline pressure, 0.12 and 0.5 MPa air pressures).

Typical images of the spray development in conditions close to these particular ones are given in Figure 3. In 0.12 MPa air, the spray is a hollow cone close to the injector. This cone tends to be filled farther downstream. The spray is not very dense, because light absorption is moderate. In 5 MPa, the spray becomes narrower and darker. Stronger air entrainment from the sides is responsible for contracting the spray and much higher droplet concentrations are found.

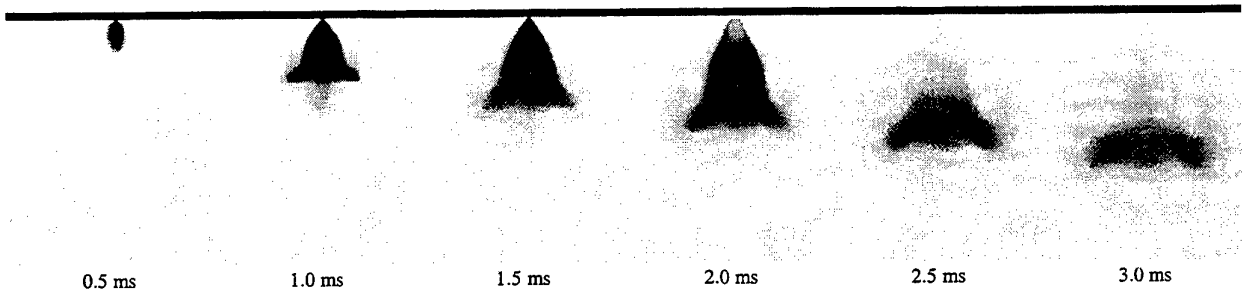
We present scatter plots with all individual droplets measured : velocity versus time, diameter versus time and velocity versus diameter from the left to the right.

At 0.12 MPa air pressure, the TSI system fails in following the main injection (Figure 4). The major part of the validated droplets are in the tail of the spray, where droplet concentration has dropped. The diameter data reveal some negative phases, visible just below the maximum measurable diameter (135 microns).

With the Aerometrics system the first velocity peak up to 25 m/s is displayed (Figure 5). We can remark that the spray penetration is about 20 m/s according to the images. Practically no bad data are seen among the



gasoline pressure 2.5 MPa, air pressure 0.12 MPa, injection duration 1.5 ms



gasoline pressure 2.5 MPa, air pressure 0.45 MPa, injection duration 1.5 ms
scale : images are 45 mm high, times given after beginning of command pulse

Figure 3 : Light absorption images showing typical spray developments

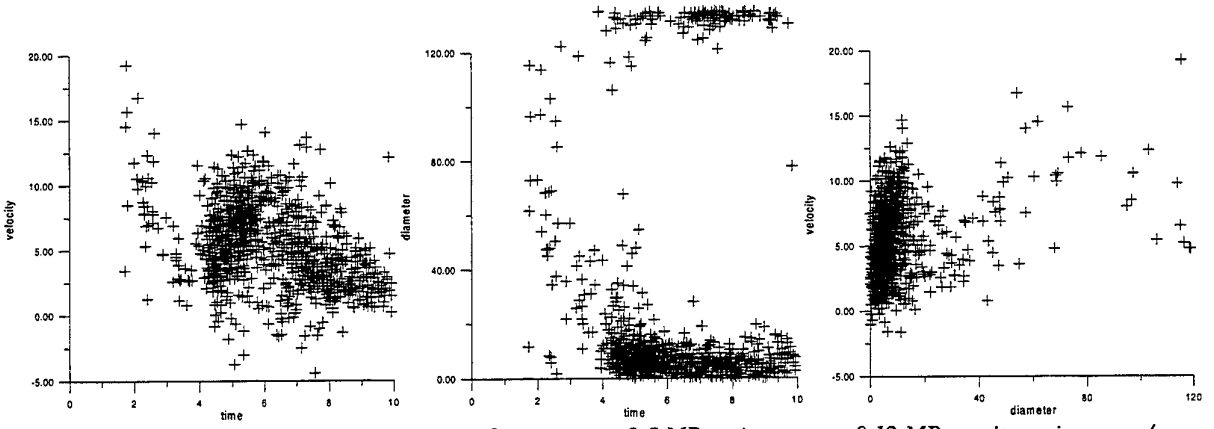


Figure 4 : Results with the TSI system - gasoline pressure 2.5 MPa, air pressure 0.12 MPa, units : microns, m/s, ms

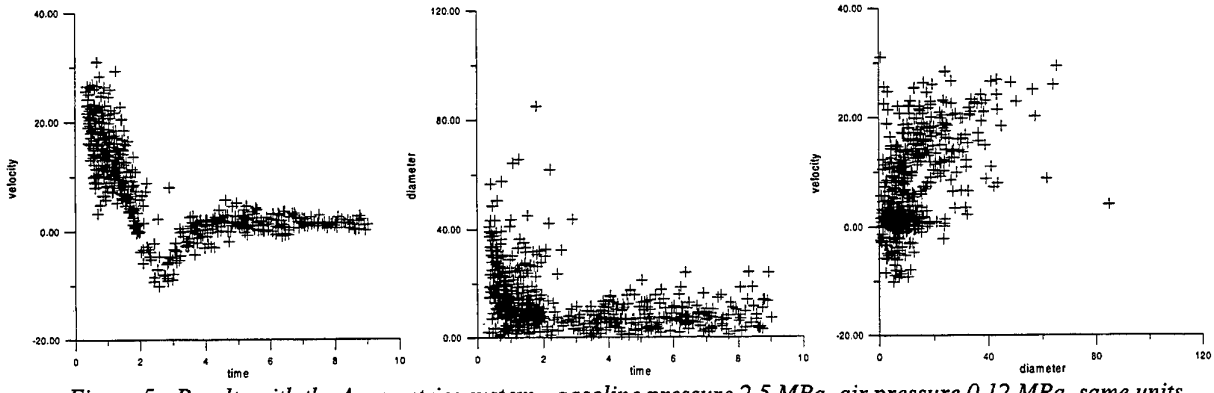


Figure 5 : Results with the Aerometrics system - gasoline pressure 2.5 MPa, air pressure 0.12 MPa, same units

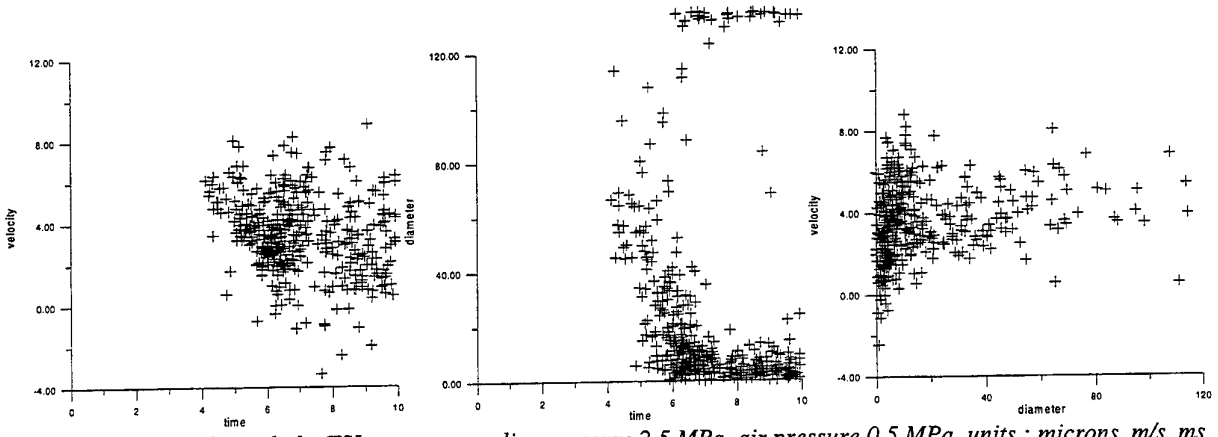


Figure 6 : Results with the TSI system - gasoline pressure 2.5 MPa, air pressure 0.5 MPa, units : microns, m/s, ms

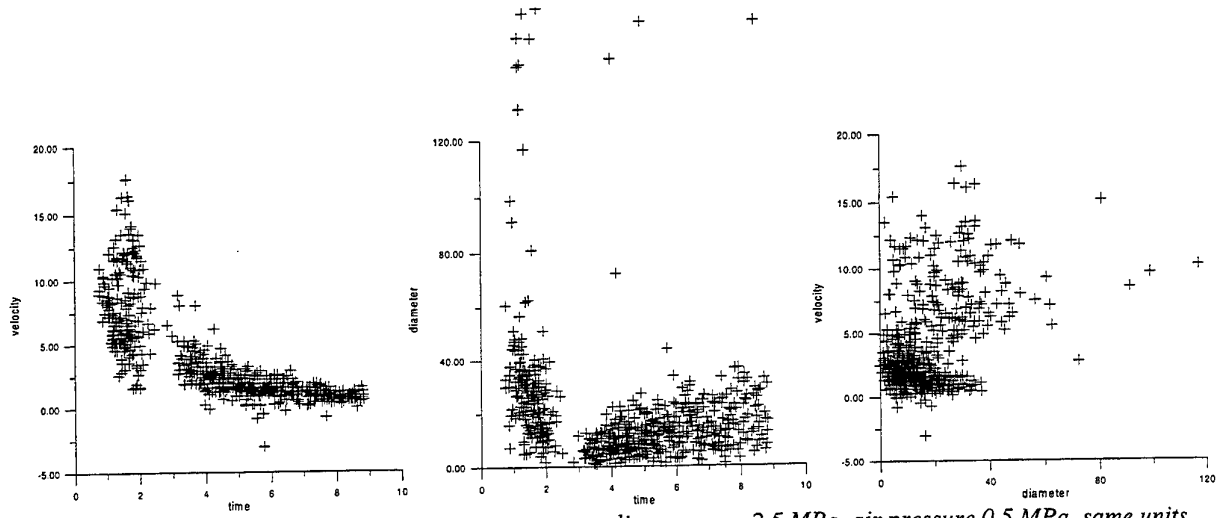


Figure 7 : Results with the Aerometrics system - gasoline pressure 2.5 MPa, air pressure 0.5 MPa, same units

gasoline pressure (MPa)	air pressure (MPa)	distance from axis (mm)	with the TSI IFA system		with the Aerometrics RSA system	
			D_{10} (microns)	D_{30} (microns)	D_{10} (microns)	D_{30} (microns)
2.5	0.12	10	10	27	12	20
5.0	0.12	10	20	40	12	17
2.5	0.25	15	11	28	16	24
5.0	0.25	15	35	63	16	23
2.5	0.5	15	18	38	18	27
5.0	0.5	15	25	51	16	26

Table 2 : Statistical results measured with the Phase-Doppler systems

diameters. The measurement points may not be exactly the same for the two instruments, which could explain that higher negative velocities (coming from the recirculation) seen in Figure 5 with respect to Figure 4.

At 0.5 MPa air pressure, the TSI system fails again more (Figure 6). The time where measurements begins is delayed, so that only the slow tail (droplet velocity below 8 m/s) is caught. The relative concentration of droplets larger than 40 microns is highly increased compared to 0.12 MPa air pressure. This observation seems not physical. The Aerometrics system is still able to measure in the whole spray, but it begins to fail also. The data acquisition rate goes to zero in the main part of the spray (Figure 7). Both measurement systems are placed in a difficult situation, mainly because of too high droplet concentration levels. They react in different manners to

this. It is difficult to say which system gives the more accurate results because no reference measurements are available in dense sprays. However an interesting feature is observed in the tail of the spray with the Aerometrics system : the diameter increases notably with time (Figure 7), whereas it remains constant with the TSI one. This is a typical phenomenon of all high pressure cases (not shown here). A physical explanation can be found for this : smaller droplets quicker vanishing when evaporation is strong.

The arithmetic and volume mean diameters are compared in Table 2. It is clearly shown that the results measured by the TSI system are difficult to interpret. For example, an increase in gasoline pressure should not result in a strong increase of the mean diameter. This is mainly due to evident wrong diameter measurements.

DROPLET CONCENTRATION ESTIMATES

Knowing the amount of liquid injected by one injection pulse, it is possible to estimate the droplet concentration as a function of assumed volume mean diameter. We will consider a typical injected quantity of 20 mm^3 with 1.5 ms command duration, and a total spray volume equivalent to a sphere of diameter 20 mm. We estimate the mean number of droplets contained inside the Phase-Doppler probe volume that is 200 micron long and 160 micron thick. The results of these very simple calculations are given in Table 3.

assumed mean volume diameter (microns)	number of droplets	mean droplet concentration (/mm^3)	number of droplets in the probe volume
10	38.2 E6	9125	37
20	4.77 E6	1139	4.6
40	0.597 E6	142	0.57

Table 3 : Droplet concentrations estimates

The main problem for Phase-Doppler drop sizing in automotive injector sprays appears clearly to be a too high droplet concentration, leading to multiple droplets inside the probe volume. Other consequences are the absorption and the distortion of the emission laser beams which hinders the formation of a good quality probe volume. Even if evaporation eliminates the smallest ones, the concentration remains too high for correct particle measurement and even more for particle counting or flux measurement. It is virtually impossible to characterise this type of gasoline spray by a technique that basically detects particles one by one.

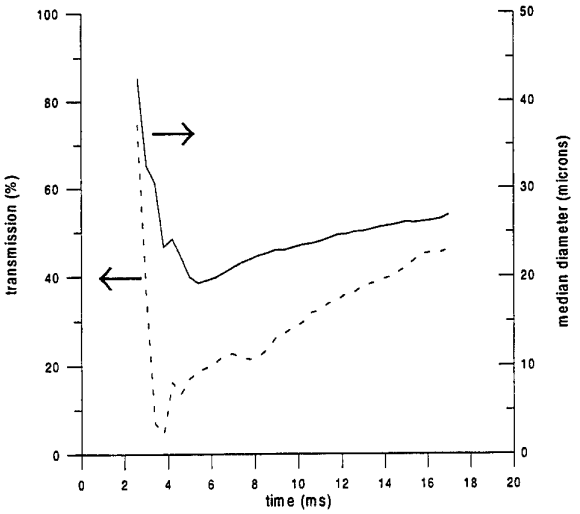


Figure 8 : Results with the Malvern system - gasoline fuel pressure 5 MPa, air pressure 0.12 MPa

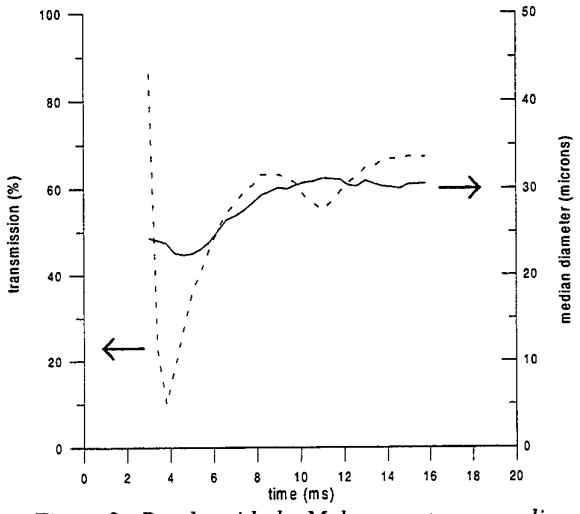


Figure 9 : Results with the Malvern system - gasoline fuel pressure 5 MPa, air pressure 0.3 MPa

RESULTS WITH DIFFRACTION SYSTEM

Gasoline tests

A similar gasoline injector for direct injection is tested under different gasoline and air pressures. Typical curves of transmission coefficient and median volume diameter versus time are shown in Figures 8 and 9, with 5 MPa gasoline pressure. The first injection phase is formed by the largest droplets found in the spray. There is effectively poor atomisation when the flow inside the injector is not established during opening. Then, during the main injection phase, the mean diameter decreases notably and levels off around 20 microns while transmission falls quickly. After the end of injection, the mean diameter increases very slowly. This feature is more pronounced with high pressures (Figure 9 and other cases not

displayed here). In the meantime, transmission regularly increases because the spray expands and moves out of the laser beam.

The minimum mean diameters measured in all test conditions are listed in Table 4.

gasoline pressure (MPa)	air pressure (MPa)	mean diameter (microns)
2	0.12	30
5	0.12	20
8	0.12	20
5	0.3	23
8	0.3	22

Table 4 : Mean diameters measured by diffraction with gasoline

Changing the gasoline pressure from 5 to 8 MPa does not decrease the mean diameter substantially, and increasing the air pressure makes it grow a little. We remark that this last trend was observed with the Phase-Doppler system from Aerometrics.

Dodecane tests

We suspect evaporation for being responsible for eliminating smallest droplets with high gasoline pressures so that it could mask an initial better atomisation. Therefore, tests were conducted with dodecane which does not evaporate very much (boiling point 216°C). The results (Table 5) show that with this fuel much smaller droplets are observed when increasing fuel injection pressure, and again larger ones when increasing the air pressure. The latter effect is less pronounced. Furthermore, as shown by an example in Figure 10, the mean diameter is constant after injection, and transmission is very low, unlike gasoline tests. This confirms that evaporation has significant effects on mean drop diameters with gasoline.

dodecane pressure (MPa)	air pressure (MPa)	mean diameter (microns)
2	0.12	37
5	0.12	25
8	0.12	17
2	0.3	40
5	0.3	27
8	0.3	22
2	0.45	40
5	0.45	32
8	0.45	27

Table 5 : Mean diameters measured by diffraction with dodecane

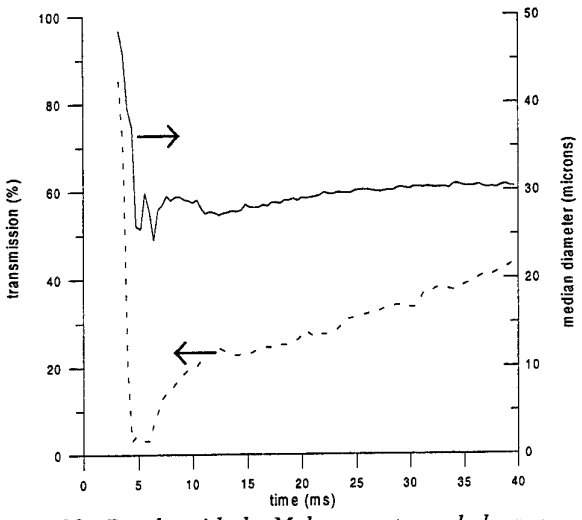


Figure 10 : Results with the Malvern system - dodecane fuel pressure 5 MPa, air pressure 0.3 MPa

Cross-check by light absorption

Light absorption images of the same type as in Figure 3 were taken with dodecane, that is with negligible evaporation. Assuming that no multiple light diffusion occurs, and that the diameter distribution is uniform in the spray, it is possible apply the light extinction equation. As the liquid quantity is known to be the injected quantity without evaporation, which can be measured separately, the Sauter mean diameter can be calculated by integrating the whole spray image. The following formula is found :

$$d_{32} = \frac{3QS}{2V}\frac{V_{liquid}}{\int_S \frac{-Log(I/I_0)}{l} dS}$$ where Q is the scattering coefficient, S the spray projected surface, V the spray volume, V_{liquid} the liquid volume, I/I_0 the light transmission, l the path length through the spray.

Only relative mean diameters are presented in Table 6 below, the reference case being : 2 MPa and 0.12 MPa for gasoline and air pressures respectively. Data from diffraction are taken at the time with minimum transmission. Those from absorption at 1 and 1.5 ms after the beginning of the injection command pulse.

Values from absorption at 1.5 ms are always higher than at 1 ms. This could come from overestimating the liquid volume in the spray, showing that evaporation still occurs. For this reason the values at 1 ms are more reliable. The absorption technique integrates all the spray, and at smaller times after the beginning of injection. Nevertheless the same trends are noticed with absorption and diffraction techniques. The mean diameter increases slightly with air pressure, which is not usual for common pressure swirl atomisers [6].

dodecane pressure (MPa)	air pressure (MPa)	diffraction relative mean diameter (microns)	absorption relative mean diameter at : 1 ms ; 1.5 ms (microns)	
2	0.12	1.	1.	1.07
5	0.12	0.54	0.53	0.58
8	0.12	0.4	0.36	0.45
2	0.3	1.08	1.13	1.22
2	0.45	1.13	1.1	1.41

Table 6 : Comparison between diffraction and global absorption techniques

CONCLUSIONS

The application of phase-Doppler to direct injection gasoline sprays is limited because of too high droplet concentrations. In high pressure conditions, the measurement volume contains several droplets simultaneously. With the two systems tested, the data acquisition rate falls down to nearly zero in the middle of the sprays, and a bias towards the large droplets is observed. In some conditions, wrong droplet diameters can be measured with a high probability.

The system based on diffraction is more easily operated and works correctly even in dense sprays with light transmission of several percent. The results show physical trends that are cross-checked by light absorption images in conditions with weak evaporation.

REFERENCES

[1] Iwamoto Y. et al., "Development of Gasoline Direct Injection Engines", SAE 970541, 1997.

[2] Preussner C. and Kampmann S., "Benzin-Direkteinspritzung, eine neue Herausforderung für künftige Motorsteuerungssysteme", MTZ Motortechnische Zeitung 58 (Oktober 1997), 10.

[3] Dodge L.G., Rhodes D.J., and Reitz R.D., "Drop-size Measurement Techniques for Sprays : Comparison of Malvern Laser-diffraction and Aerometrics Phase/Doppler", Applied Optics, Vol. 26, 11, 1 June 1987

[4] Croissant K. and Kendlbacher C., "Requirements for the Engine Management System of Gasoline Direct Injection Engines", Congress "Direkteinspritzung im Ottomotor", Essen, Germany, March 1997.

[5] Ren W.M., Shen J., and Nally J.F., "Geometrical EffectsFlow Characteristics of a Gasoline High Pressure Swirl Injector", SAE 971641, 1997.

[6] Lefebvre A.H., Atomisation and Sprays, Taylor & Francis editors.

CHARACTERISATION OF A DIESEL SPRAY HEAD BY DIFFERENT LASER BASED TECHNIQUES

L. Araneo°, A. Coghe°, G.E. Cossali°°

° Politecnico di Milano-Milano-Italy
°° Università di Bergamo-Dalmine-Italy

ABSTRACT

The injection of a Diesel Spray into the combustion chamber produces an unsteady two phases flow. The leading edge of the spray (sometimes referred as "spray head") and the gas motion inside and outside of it is a matter of some interest in defining the entrainment and mixing characteristics of the unsteady spray. In the present paper the characteristics of the head of a non evaporating Diesel spray injected into quiescent gas at different densities (1.18kg/m^3÷40 kg/m^3, at room temperature) were analysed by different laser based techniques (Laser beam extinction, 2-D visualisation, LDV, PIV). The use of different techniques allowed to gather complementary information about the dynamics of the spray head and that of the surrounding air. Quantitative image analysis allowed to evaluate tip penetration as a function of gas density and to estimate the dimension of the spray head and the mass of the gas trapped inside the spray. Measurements of tip penetration with different techniques allowed to compare their accuracy.

1. INTRODUCTION

When a non evaporating Diesel Spray is injected into a confined, quiescent gas, an unsteady air flow is generated by droplet-gas interaction. This mechanism is closely related to spray penetration and mixture formation and clearly depends on the gas density and injection conditions, which in turns control droplet size and velocity distributions. Some analogies with the motion of an unsteady gas jet were evidenced (Andriani et al (1996)), but the underlying mechanism for momentum exchange between the injected and the receiving fluid in two phase flows is quite different from that pertaining to single phase flows, and simple qualitative analogies may not be enough to explain quantitative results. Diesel spray penetration has been investigated by many authors and correlations of the experimental data were deduced using analogies with gas jets (Dent (1971)). Differences about the dependence of the results on ambient gas density (Hay and Jones (1972), Naber and Sieber (1996)) is probably related to the critical influence of the transient injection conditions and the width of the density regimes investigated, but it may also be due to the dependence of the results on the measuring technique. A common method to measure spray penetration is by visualisation (through high speed film or CCD cameras) and the results are expected to be dependent on the sensitivity of the system and the threshold level used. The specific objectives of the reported experiments were to investigate the effects of gas density on the development of the spray head and to explore in detail the structure of the transient spray region by comparing two injection modes, and the use of different measuring techniques allowed to compare their capability and accuracy when applied to Diesel sprays. Spray penetration and tip velocity were measured by three techniques: Laser extinction, laser sheet visualisation (LSV) and laser Doppler velocimetry (LDV). Image analysis, LDV and particle image velocimetry (PIV) were used to obtain quantitative estimate of the entrainment process.

2. EXPERIMENTAL SET-UP

The experiments were carried out in a constant volume cylindrical chamber (206 mm internal

diameter) with four 100 mm diameter optical windows to allow optical access to the spray. The gas inside the chamber was pressurised (while keeping the temperature at room conditions) in order to obtain different gas densities and some experiments were conducted by using SF_6 as ambient gas to reach higher densities with relatively low gas pressures: gas density spanned between 1,18 kg/m^3 and 40 kg/m^3. The injection system comprised a high pressure injection pump driven by a variable speed electric motor, a high pressure pipe connecting the injection pump to the injector (a Bosch single hole injector, 0.25 mm nozzle diameter), an electronically controlled by-pass system upstream the injector to run the system in single injection mode when required. Ordinary Diesel oil (ρ=830 kg/m^3) was used throughout all the experiments. The injection pressure was monitored by a pressure transducer positioned at 60 mm from the injector inlet; injection pressure history was very reproducible (Gerla et al. (1996)) and cycle-to-cycle injection pump speed variation was about ±0.5%. The average injected fuel mass delivered during a single injection was measured (in a wide range of injection conditions) by weighting the injected fuel collected over many injections. Throughout the paper, the origin of the time axis is defined as the time at which the spray actually exits the nozzle, which is different from the time at which the measured injection pressure reaches the value of 21.4 MPa (the opening pressure under steady conditions), due to the distance of the pressure transducer from the nozzle exit. Further details on the experimental set-up were already reported (Cossali et al. (1991), Gerla et al. (1996), Araneo et al. (1997))
The average nozzle discharge coefficient, defined as the ratio between the actual injected mass and the nominal injected mass calculated from the injection pressure data, the nozzle diameter, and the injection duration (measured by laser beam extinction), was used to calculate the injected mass flow rate from the pressure curve. The injector was mounted on the top of the chamber and aligned with the chamber axis; the tip protruded less than 4 mm from the top wall.

3. MEASUREMENT TECHNIQUES

In order to gather information about the behaviour of the spray head, different complementary laser based techniques were used and, whenever possible, a comparison of their capabilities is presented

3.1 Laser Beam Extinction

This quite simple technique yields information about spray turbidity with high time resolution and it is quite convenient for measuring tip penetration: an Ar+ Laser beam operated at low power was sent through the spray and then imaged onto a photodiode; the output is proportional to the collected light intensity which gives information about the spray turbidity along the beam path.

3.2 Visualisation

An Ar+ laser beam was spread into a sheet by a combination of spherical and cylindrical lenses and sent through the spray axis to produce a 2-D image of the injected spray; a CCD camera (Flashcam PCO) with 1 μs time resolution captured the image. Image pre-processing comprised background noise subtraction and spray contours enhancement.
The accuracy of the set-up in estimating relative position was evaluated to be of the order of 0.3 mm which was considered sufficient for the present purposes. This technique gives information about tip penetration, spray angles, spray structure.

3.3 Laser Doppler Velocimetry (LDV)

A Laser Doppler Velocimeter was used to measure the gas flow field around the spray , the dual beam LDV system (DANTEC) comprised a 5W (nominal power) Ar+ laser and a conventional fibre optic LDV transmitting unit with a 40 MHz Bragg cell for frequency shifting and directional sensitivity and a front lens of 310 mm focal length. Backscattering configuration was used for gas velocity measurements: the diameter of the geometrical control volume was 0.1 mm and its length was 1 mm. A Dantec PDA processor, with 1 μs time resolution, was used for data acquisition.
Small size (less than 5μm) droplets left behind by previous injections were used as tracing particles. Data were collected over many subsequent injections and radial and axial velocity components were measured (not simultaneously) in a region around the spray cone (3mm ≤ r ≤ 13mm, 2.5mm ≤z ≤ 50mm). The acquisition was triggered by the reaching of the opening pressure (21.4 MPa) and performed over a 6 ms time window for each injection, a period larger than the injection duration. Due to the delay between the reaching of the opening pressure and the beginning of the injection (depending on the injection conditions) the time scale used to present LDV

results will be indicated by ATS (After Trigger Signal) to distinguish it from the time measured from the actual beginning of injection (ASI=After Start of Injection).

3.4 Particle Image Velocimetry (PIV)

Particle Image Velocimetry was used to obtain the gas velocity field on a single injection, to be compared to LDV data which instead give a velocity field averaged over many injections. The PIV system comprised: two separated YAG laser (Quanta System) 532 nm wavelength, working at 10 Hz (pulse energy 0.2 J, pulse duration 10 ns); a flexible high power light guide with a lens system to expand the laser beam; a Dantec 80C42 Double Image 700 CCD camera type 4, 484x768 pixels, allowing cross-correlation and unambiguous velocity direction measurements; a Dantec PIV processor for real time image elaboration; a PC to collect images and perform data processing.
The Diesel pump was tuned at the same frequency of the laser (10 Hz = 600 rpm) and, due to an internal delay of the camera of approximately 52 ms (longer than the injection duration), the acquisition on each injection was triggered by the beginning of the previous one with the necessary delay. Unfortunately, cycle-to-cycle variation of the injection pump speed (±0.5%) produced an uncertainty in timing of about 0.5 ms which is comparable to injection duration (1÷2 ms); however, thanks to the tip penetration measurements performed by the other techniques, the injection delay could be calculated from the PIV images with an accuracy of 0.03 ms

4. RESULTS AND DISCUSSION

4.1 Spray Tip Penetration

Experimental data on spray tip penetration are widely used to compare prediction given by numerical codes; however measurements of tip penetration may apparently depend also on the particular definition of "spray tip". Indeed, the tip arrival at a given location may be detected in different ways, for example as the first drop arriving at that location, or the first "cluster of drops", or again by the detection of a certain concentration of fuel vapour, and so on. The use of different techniques may help to avoid misunderstanding in defining tip penetration; in the present investigation three different techniques were used to measure tip penetration, namely: 2-D visualisation, Laser beam extinction and LDV and a comparison of the results is discussed.

Tab. 1 Experimental Conditions

Gas	Code	Pressure MPa	Temp K	ρ kg/m^3	Injection Pressure
air	A	0.101	301	1,17	LP, HP
air	B	0.200	301	2,31	LP, HP
air	C	0.400	301	4,62	LP, HP
air	D	0.600	301	6,93	LP, HP
SF_6	E	1.18	301	7,00	LP, HP
SF_6	F	1.98	301	12,00	LP, HP
SF_6	G	3.25	301	20,00	LP, HP
SF_6	H	4.77	301	30,00	LP, HP
SF_6	K	6.24	301	40,00	LP, HP

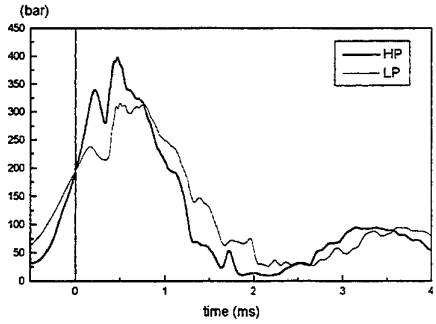


Fig. 1 Injection pressure curves for the two sets of experiments reported in Table 1

In order to investigate the effect of gas density on penetration, measurements were performed under different gas conditions reported in Table 1, and using different gases (namely air and SF_6) to obtain high densities with relatively low pressures. Although the speed of sound was lower in SF_6 the spray tip was always found to move at subsonic velocities.

The injection pressure curve is expected to influence the tip penetration, in particular the pressure time derivative at the beginning of the injection may effect the penetration rate and for this reason two different injection pressure curves (LP

and HP, shown in fig. 1) with different pressure time derivative were used, the fuel load was: 12.2 mg/inj. for LP and 10.6 mg/inj. for HP. It must be reminded that only the injection pressure at the very beginning of the injection can influence tip penetration in the spray near field.

Laser Beam Obscuration technique was used to detects the spray tip at different distances from the nozzle (Z=0÷47.5mm).

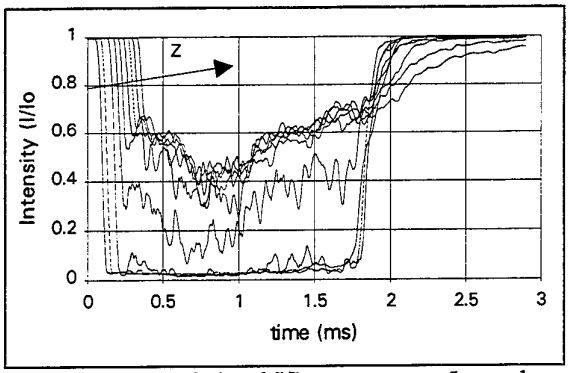


Fig. 2 - Attenuated signal I/I_0: average on 5 samples at z= 0, 2.5, 7.5, 12.5, 17.5, 22.5, 27.5, 32.5, 37.5 mm; Case A.

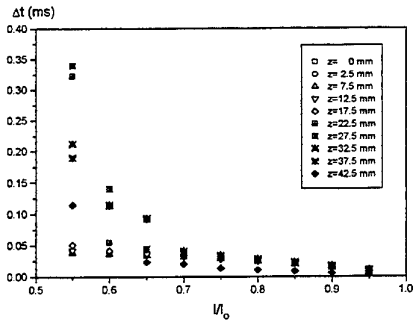


Fig. 3 – Dependence of the time delay in tip arrival measurements by laser beam obscuration ($\Delta t = t_{I/Io} - t_{0.99}$) on attenuation threshold I/I_0; Case A.

Figure 2 shows the attenuation I/I_o (I_o is the undisturbed laser beam intensity) versus time at different locations downstream the nozzle.

The tip arrival time depends on the threshold intensity chosen to evaluate it, and figure 3 shows the difference $\Delta t = t_{th} - t_{0.99}$ (t_{th} is the arrival time detected by using a defined threshold value I/I0) plotted vs. the threshold value.

Decreasing the threshold Δt increases but in a way independent of the nozzle distance Z, except for lower values of the threshold, under which, due to the dilution of the spray at large Z, the measurement become unreliable; it should be noticed that, due to the independence of Δt on Z, the tip velocity measured by Laser Beam Obscuration is independent of the threshold limit.

Images of the injected spray obtained by 2-D visualisation at different times ASI were processed to measure the tip position; again the definition of the tip position depends on the chosen threshold of the gray level (for black and white pictures). The image analysis was performed by subtracting the background, obtained by a picture taken without spray, and evaluating the farthest distance from the nozzle tip at which a given gray level was found. Changing the threshold level from the lowest to 45% of the maximum gray level the tip position changes by an average value of 4 pixels corresponding to 0.3 mm; with values of the maximum spray tip velocity of 150 m/s, this is equivalent to a time uncertainty on tip arrival of 2 μs.

Tip arrival at a given location on the spray axis can also be detected by the first drop crossing the LDV measuring volume; thus, measurements of tip penetration were also performed by positioning the measurement volume along the spray axis at various distances from the nozzle.

The distribution of the drop arrival times at the measurement locations shows, at all the locations downstream the nozzle, a well defined peak at times that compare quite well with the tip arrival time $t_{0.95}$ as defined by the obscuration technique and a quantitative comparison gives average differences of the order of 2 μs (comparable to the time resolution of the instrument). This technique is time consuming because requires a large number of injections, typically 200 for each point, to have the necessary amount of data for statistical analysis, and obviously gives an ensemble average tip arrival time, but it has the advantage of giving well resolved arrival times nearly independent of set-up parameters.

The accuracy of the three techniques in measuring tip penetration is then comparable, the dependence on the threshold level of the obscuration technique results may produce, in the present case, a bias on tip penetration (but not on tip velocity) of about 7 μs every 10% variation of the attenuation threshold; data from 2-D visualization are less reliable at increasing distances from the nozzle due to the tip spreading and LDV definition of tip arrival is threshold independent but time consuming.

Many attempts to model spray tip penetration can be found in the literature and a review of the suggested penetration laws can be found in Dent (1971) , Hay

and Jones (1972), whereas an interesting analysis of the existing models and a presentation of a new one can be found in Naber and Sieber (1996). A characteristic pointed out by the majority of the researchers is the difference between the "near field" and the "far field" behaviour; while it is commonly accepted the validity of the square-root law (i.e. $z_t \div t^{0.5}$) for tip penetration in the far field region, less agreement can be found about the behaviour into the near field region. Moreover, it is difficult to find an agreement in defining the boundary between near and far field. The effect of gas density on tip penetration was studied by many authors (see again Dent (1971) and Naber and Sieber (1996) for a review). From a physical point of view and considering the existing models, an increase of the ambient gas density is expected to decrease the length of the near field region; moreover, tip velocity is also expected to decrease increasing gas density (that increases the drag acting on the drops belonging to the spray head). The raw data obtained by 2-D visualisation are shown in figure 4.

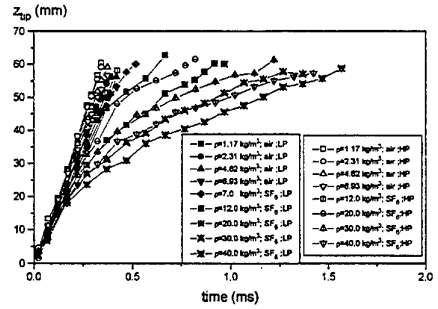


Fig. 4 Tip penetration vs time for all the conditions reported in Table n.1

To take into account the expected effects of gas density a law of the type:

$$(\rho/\rho_o)^{\alpha}\, v = f[(\rho/\rho_o)^{\beta} z] \qquad (1)$$

is proposed (ρ= gas density, ρ_o= fuel density, v = instantaneous tip velocity) where α and β are positive numbers. The results obtained by an optimisation of α and β on both sets of data (relative at different injection pressure curves) are presented in figure 5, where it is evidenced the influence of the injection pressure and the suitability of the proposed law which collapses rather well all the data points together.

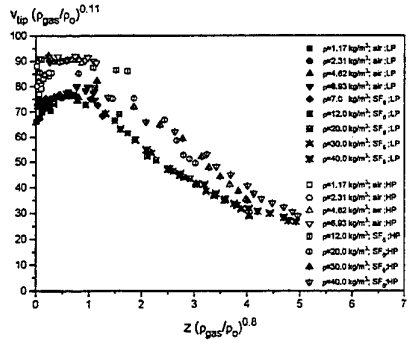


Fig. 5 Tip velocity vs position both *corrected* by density ratio (for all the conditions of Table 1); ρ_{gas}= gas density, ρ_o =fuel density.

The law (1) can be obtained by a similar relation between tip position and time:

$$\eta = (\rho/\rho_o)^{\beta} z = g\,[(\rho/\rho_o)^{\beta-\alpha} t] \qquad (2)$$

The experimental results are plotted in figure 6, the log-log plot evidences the different penetration rates in the near field (η<2) and in the far field (η>2).

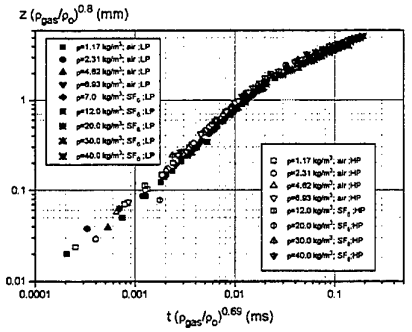


Fig. 6 Tip penetration vs time both *corrected* by density ratio (for all the conditions of Table 1);

4.2 Spray Head Structure

The gas flow field around the spray was measured by LDV for three conditions (namely: LP, ρ=1.18kg/m^3, ρ=7.0 kg/m^3, and ρ=20 kg/m^3), gas radial and axial velocities were measured (not simultaneously) outside the spray region for: r<13 mm and : 2.5mm <z<42.5 mm, over a time interval of 6 ms, large enough to cover the whole injection period. Figure 7 shows the radial velocity versus distance from the nozzle (measured at 10 mm from the spray axis), for different times ASI.

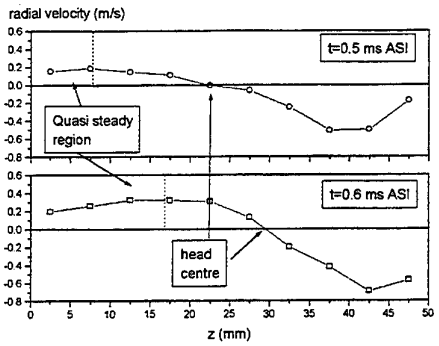


Fig. 7 Radial velocity vs distance from nozzle.

From the profile it is possible to define two different regions: *a)* the region where the velocity is positive (i.e. directed toward the spray axis) and only slightly dependent on z, that may be called *entrainment region*, representing the quasi-steady part of the spray; *b)* the region where the radial velocity changes sign, representing the *spray head* region. It is possible to evaluate at any time the location where radial velocity changes sign, and the boundary between spray head and entrainment region (by the position where the radial velocity reaches the relative maximum) and the results are plotted, together with tip position, vs time in figure 8, where the above defined density corrections of time and space are performed.

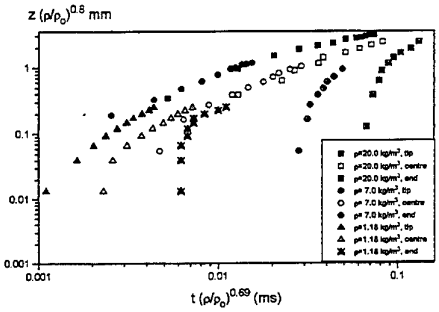


Fig. 8 Tip penetration, head centre position and location of the head-cone boundary vs time for three different gas densities: ρ= 1.18 kg/m3, ρ=7 kg/m3, ρ=20 kg/m^3.

It appears from the figure that the suggested density corrections do not hold for the position of the trailing edge of the spray head, whereas it is still applicable to the position of the head "centre".

4.3 Entrainment Characteristics

From the 2-D images analysis it was also possible to derive the total spray volume as a function of time. The image was first binarysed (by using a given threshold); then it was cut along the spray axis and only the half on the illuminated side was used, it was in fact observed that light extinction by the dense spray caused an apparent asymmetry. The "centre of mass" of the half image was calculated and by Gouldin theorem it was possible to calculate the volume of the solid obtained by rotating the half image about the spray axis. The mass of the gas contained into the spray was estimated by multiplying the volume (diminished by the injected fuel volume which however was almost neglectful) by the gas density. Figure 9 shows the spray mass versus time for different gas density.

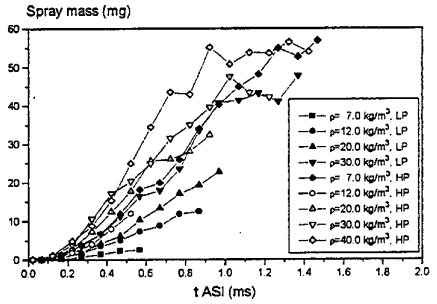


Fig. 9 Mass of gas trapped inside the spray vs time, for different injection conditions (LP,HP) and gas densities.

By introducing the time $\tau = t\,(\rho/\rho_o)^{\gamma}$ it is possible to collapse the curves as in figure 10 and an optimisation of γ yielded the value: γ=0.45 showing that the gas mass contained inside the spray increases with gas density, but the spray volume decreases (like $\rho_{gas}^{-0.55}$) and the fuel is then concentrated in a smaller volume.

To get information about the dynamics of the spray head, LDV and PIV measurements of the surroundig gas velocity were performed. The gas velocity vector fields obtained by PIV and LDV are presented for comparison in figure 11 where the instantaneous flow field (PIV) and the average flow field (LDV) are shown for t=0.4 ms ASI.

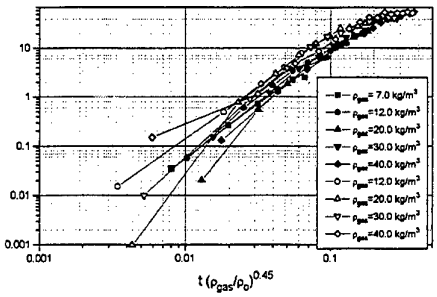


Fig. 10. Mass of gas trapped inside the spray vs time corrected by gas densities, for different injection conditions (LP,HP).

The characteristic flow structure is well evidenced by both techniques. From a qualitative analysis of the flow field, the spray head appears to be on one hand a region of high mixing between the injected fuel drops and the air coming from the main body but, on the other hand, it is a quite compact structure that pushes the ambient gas apart producing low (or no) direct mixing with the surroundings. This peculiar structure may be significant when analysed in the engine contest: a diesel spray injected into the cylinder needs a strong cross flow (swirl, squish) to break the head and distribute the fuel uniformly, and when a spray is injected into a small combustion chamber it may not have enough time before wall impingement to diffuse into the gas charge due to the compactness of the head, then the impact with the wall may remain the only possibility for enhancing mixing.

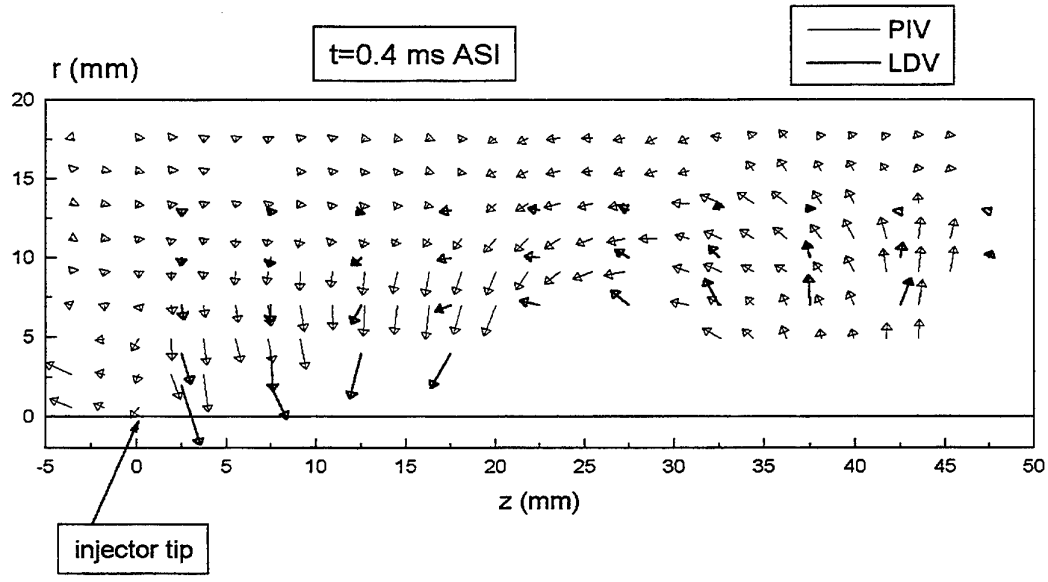


Fig. 11. Mass of gas trapped inside the spray vs time corrected by gas densities, for different injection conditions (LP,HP).

Undoubtedly, the compactness of the spray head may be diminished by a highly turbulent flow, the effect of high turbulence level on such compactness are unknown and they may change the behaviour of the structure. The structure of the gas flow fields measured by the two techniques shows a good agreement, and it is noteworthy the fact that PIV allowed to get results about the flow field closer to the spray region. However it should be noticed that the absence of LDV measurements close to the spray region is due to an excess of caution in avoiding contamination of gas velocity measurements by spray drop velocity data. PIV evidences better the peculiar recirculation flow around the spray head: the gas is first pushed apart by the spray head front, then recirculated along the head side and finally entrained into the following spray cone. Quantitative comparison between single shot PIV and mean LDV

velocity fields it is somehow difficult because, due to cycle-to-cycle variation, the instantaneous flow field (PIV) is necessarily different from the average one (LDV). However, during the quasi-steady period it is reasonable to expect a better agreement between the two kind of fields, thus a quantitative comparison of the PIV and LDV measured velocity fields was performed on data collected during the main injection period. The magnitude and direction of the PIV vectors were averaged around the points were LDV measurements were available. The angle defined by the vectors show differences lower than 20° for more than 90% of the vectors, and for these vectors the velocity magnitude of the PIV data is usually smaller (on the average: 35% smaller) then the magnitude of the LDV vectors. This last difference may in part be explained by observing that PIV is more sensitive to the biggest droplets which due to their inertia may not follow properly the acceleration produced by the entrainment. The difficulty in estimating the accuracy of PIV velocity measurement is increased by the considerable amount of data elaboration which must be performed to get *reasonable* flow fields (data filtering etc.). However, the comparison seems to confirm an acceptable degree of accuracy, the uncertainty being compensated by the information about spatial correlation of the velocity flow field and the high time resolution. Although the present results hold only for non evaporative sprays and should not be extrapolated to engine conditions, it is reasonable to expect that some of the peculiarities pointed out here may be found under such conditions.

CONCLUSIONS

The reported research led to the following conclusions:

- The techniques used for tip penetration measurements (namely: laser beam extinction, laser sheet visualisation and LDV) show a comparable accuracy; the dependence on the threshold level of the extinction technique results may produce, in the present case, a bias on tip penetration (but not on tip velocity) of about 7 μs every 10% variation of the attenuation threshold; data from 2-D visualisation become less reliable at increasing distances from the nozzle due to the tip spreading, LDV definition of tip arrival is the most reliable and threshold independent but it is more time consuming.
- Tip penetration depends on the injection pressure increase in the very first part of the injection. The effect of increasing gas density (studied in a large range of conditions: 1.18÷ 40 kg/m^3) is to decrease the tip velocity and to decrease the near field length.
- LDV and PIV measurements of the gas flow field around the spray head show an acceptable qualitative agreement; quantitative comparison shows differences which may be due to many reasons like the fact that instantaneous (PIV) and ensemble averaged (LDV) field are compared; a systematic underestimation of the velocity magnitude by PIV can also be explained by the fact that PIV is more sensitive to the largest drops (floating in the gas) that may not follow properly the gas flow.

ACKNOWLEDGEMENTS

The experimental work was done at TEMPE-CNR laboratories (previously CNPM-CNR). The authors would like to thank Mr G. Brunello for the valuable cooperation and Dr. G. Ragosta (Fluxoptica -Dantec) for the loan of the PIV equipment.

REFERENCES

Araneo, L., Coghe, A., Cossali, G. E., 1997 Experimental Analysis of Structure and Characteristics of a Diesel Spray Head Vortex, 3th Annual Conference on Liquid Atomization and Spray System, Firenze-Italy .

Cossali, G. E., Brunello, G., Coghe, A., 1991 LDV Characterisation of Air Entrainment in Transient Diesel Sprays, SAE paper No. 910178.

Gerla, A., Brunello, G., Cossali, G. E., Coghe, A., 1996 Effect of Gas density and temperature on Air Entrainment in a Transient Diesel spray, SAE paper No. 960862.

Dent J.C., 1971, A basis for the Comparison of various Experimental Methods for Studying Spray penetration, Transaction of the SAE Vol. 80, pp 1881-1884.

Naber J.D., Sieber D.L, 1996, Effects of gas Density and Vaporization on Penetration and Dispersion of Diesel Sprays; SAE paper n.960034

Andriani R., Coghe A., Cossali G.E., (1996), Near Field Entrainment in Unsteady Gas Jets and Diesel Sprays: a Comparative Study. Twenty-sixth Symp (Int.) on Combustion, The Combustion Institute, pp 2549-2556.

Hay N., Jones J.L., (1972) Comparison of the various Correlations for Spray Penetration. SAE paper n. 720776

APPLICATION OF TWO-COMPONENT PHASE DOPPLER ANEMOMETRY TO THE STUDY OF TRANSIENT DIESEL SPRAY IMPINGEMENT

H. G. Chalé-Góngora and M. Brun

Ecole Centrale de Lyon
Laboratoire de Mécanique des Fluides et d'Acoustique - UMR CNRS 5509
36, avenue Guy de Collongue, B.P. 163, 69131 Ecully Cedex, France

ABSTRACT

The wall flow formed after the impingement of a transient Diesel spray on a flat plate is analysed using a two-component Phase Doppler Anemometer (PDA). Temporal mean values are used as a first approach to investigate the global effects of two experimental parameters: the characteristics of the incoming flow, determined by the nozzle-to-plate distance, H, and the plate temperature, T_p. Then, a special ensemble averaging technique for filtering PDA data is employed in order to obtain the temporal evolution of the wall flow under an "engine-like" configuration.

1. INTRODUCTION

The concern of achieving a more efficient combustion in Diesel engines through the optimisation of the atomisation and mixture formation processes has oriented the development of fuel injection systems towards high injection pressures. In small direct injection engines, the improved spray penetration may lead to spray impingement on the combustion chamber walls provoking very complex spray/wall interactions. Since these interactions have a great influence on the mixture formation process through droplet dispersion and evaporation, they also affect the combustion efficiency and, thus, the pollution emissions of Diesel engines.

The study of Diesel spray impingement involves certain difficulties associated with the transient nature of the flow and the presence of two phases, liquid droplets and gas, which interact in many different ways as the spray develops. Besides a strong polydispersion, the spray presents a very high density so that isolated droplet impacts are practically impossible to observe. Therefore, the fundamental mechanisms of transient spray impingement have been approached through the study of single droplet impingement by several authors (see, for example, Labeish, 1994, and Mundo et al., 1995).

In the same way, the wall/jet interactions of steady turbulent impinging jets have been studied by many authors. Landreth and Adrian (1990) describe the wall flow formed by impinging turbulent jets as a complex pattern of primary vortices, originated in the incoming jet shear layer, and secondary vortices induced by the flow of the primary vortices over the wall. As the boundary layer thickness increases, mean radial velocities decrease and, at a certain distance from the impingement point, they reach a similarity profile. The secondary vortices form near separation points in the boundary layer and break away from the wall flow into the outer flow, as pointed out by Didden and Ho (1985). This organised movement improves the mixing of passive scalars, such as temperature and mass concentration (Özdemir and Whitelaw, 1992). In the free jet region, the results obtained for steady impinging jets may be correlated to those of unsteady impinging jets during a certain time of the injection period. But after the impact, the wall flow is sensibly retarded and air entrainment is more important due to the presence of a large wall vortex (Tanabe and Sato, 1990).

Information on the wall flow formed after the impingement of a transient two-phase jet is relatively limited since not many authors have treated this phenomenon. Studies on Diesel spray impingement have reported interesting results on size and velocity distributions of droplets (Katsura et al., 1989, Coghe and Cossali, 1992), effect on air entrainment (Cossali et al., 1993) and heat transfer characteristics (Arcoumanis and Chang, 1994). However, a better understanding of the structure and development of the wall flow, as well as more detailed data in the near wall region are still needed.

In previous works, the authors have presented the alterations produced by a flat wall on the spray structure (Chalé et al., 1997), and have presented some characteristics of the mean wall flow under different

experimental conditions (Chalé and Brun, 1998). Certain results of these works are briefly developed in this investigation. The main objective of this paper is to present a detailed analysis of the temporal evolution of the wall flow formed after the impingement of a transient Diesel spray on a flat surface.

2. EXPERIMENTAL FACILITY

The experimental facility, further detailed in our previous works, is shown on Figure 1. It consists mainly of a conventional fuel injection system equipped with a Bosch distributor pump and a traversing mechanism allowing tri-dimensional positioning of the spray with respect to the measurement volume. A single-hole Diesel injector with nozzle hole diameter $d = 0.2$ mm and length $l = 1$ mm was fed by one of the pressure lines of the injection pump. Fuel was injected into a quiescent environment at atmospheric pressure and temperature. The impingement angle was 90°, while the needle opening pressure and injection frequency were 190 bar and 13.9 Hz, respectively, which produced an injection duration of 2 ms. The temperature control unit of the heating aluminium plate ensured a uniform temperature over the whole plate surface with a good precision (±1°C).

A control unit commanded the number of cycles to be studied and worked as a delaying system which controlled the start and duration of data acquisition through a TTL pulse at the burst detector inhibitor (BDI) entry of the signal processor. The unit also provided an encoder signal based on the needle lift sensor signal which was used to synchronise data acquisition through many cycles.

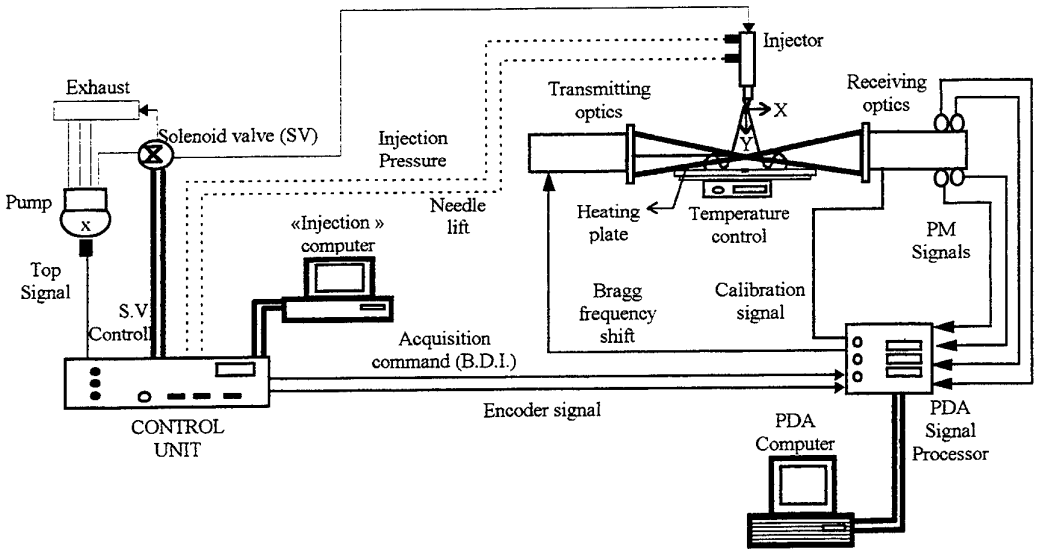


Fig. 1 Schematic diagram of the experimental facility.

3. MEASUREMENT TECHNIQUE

A two-component Phase Doppler Anemometer with very good spatial and temporal resolution was used for the simultaneous measurement of the diameter and two perpendicular velocity components of the droplets. The system comprised an Argon-ion laser (2 W nominal power in multiline mode), a transmitting optics equipped with a Bragg cell producing a 40 MHz frequency shift, a receiving optics incorporating 4 photomultiplier tubes, a 58N50 enhanced signal processor (Dantec Electronics) and a microcomputer.

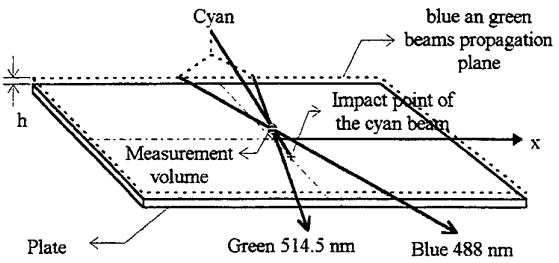
A most interesting aspect of our experimental configuration was the definition of the optical setup chosen for this study (Table 1) which allowed measurements up to 0.2 mm from the plate surface. The laser beams were oriented in such a way that the green (514.5 nm) and blue (488 nm) beams propagated parallel to the plate surface. The third beam (cyan) hit the surface right after intersecting the other two to form the measurement volume. So, both fringe planes were rotated 45° to the X and Y laboratory coordinate system (Figure 2a). The beam separation used in these experiments made the third beam hit the plate at a distance far enough to allow the visualisation of the whole measurement volume through the eye-piece of the receiving optics but, also, to avoid laser beam reflections by the liquid film formed after the spray

impinged on the plate. The overall configuration of the PDA system (*i.e.* optics, electronics and software setup) was defined in order to produce velocity and size measurement ranges adequate for our flow, while diminishing the effects of laser beam reflections on the measured quantities, at the same time.

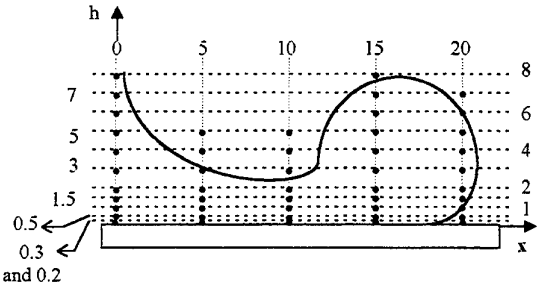
Table 1. Optical setup parameters

	Ux	Uy
Fringe spacing (μm)	5.3227	4.8861
Number of fringes	15	16
Wavelength (nm)	514.5	488
Beam diameter (mm)	1.35	1.35
Beam separation (mm)	30	31
Probe vol. dimensions		
length (mm)	1.6824	1.5443
diameter (mm)	0.0814	0.0772
Velocity range (m/s)	-53 to 186	-49 to 179
Phase factors (degree/μm)		
${}_1\Phi_2$	4.7156	
${}_2\Phi_3$	2.3267	
Lens focal length		
transmitting (mm)	310	
receiving (mm)	310	
Scattering angle	70°	
Frequency shift (MHz)	40	
Max. size range (μm)	112	
Max. concentration ($1/cm^3$)	$5x10^6$	
Fuel/air refractive index	1.46/1	

In addition, the receiving optics was inclined 25° from the horizontal plane so that the light cone from the measurement volume was not truncated. In this way, certain optical setup parameters were defined in a slightly different way. The polarization orientation of the transmitter, originally parallel to the fringes, was now 45° relative to the fringe plane. The rotation angle of the fringes was 20° relative to the scattering plane while the polarizer in the receiving optics was set parallel, that is at 0°, to match the transmitting optics polarization. Finally, the choice of the scattering angle (about 70° in forward scatter) was made following Pitcher et al. (1990) in order to reduce measurement errors due to possible refractive index changes of the droplets. Besides ensuring a linear phase/dropsize theoretical relationship, *i.e.* one dominant scattering mechanism in the scattered light intensity distribution, this scattering angle also provided quite acceptable data acquisition rates.



(a) Orientation of the laser beams



(b) Measurement locations (in mm)

Fig. 2 Experimental details in the wall zone

The wall flow was only investigated on one radial plane, since previous studies showed that the spray was nearly symmetrical. Our PDA measurements were thus made at five radial positions 5 mm apart, starting at the centreline up to 20 mm. At each radial position, the measurement volume was traversed perpendicularly to the plate surface starting at 0.2 mm in one step of 0.1 mm, one step of 0.2 mm, two steps of 0.5 mm and in subsequent steps of 1 mm until the observed spray envelope (Figure 2b). An ensemble of 2000 to 5000 data were collected at each measurement location.

4. TIME RESOLVED ANALYSIS ALGORITHM

Following the Reynolds decomposition, the local instantaneous velocity for an unsteady turbulent flow can be written as:

$$u(t,i) = U(t,i) + u'(t,i) \qquad (1)$$

where the value $U(t,i)$ represents the mean evolution of the velocity $u(t,i)$ during cycle i, and $u'(t,i)$ the turbulent fluctuation of velocity about this average. Because of random modifications of conditions in engine flows, the mean value $U(t,i)$ may differ from one cycle to another. This leads to a different decomposition of the instantaneous velocity into three components: ensemble averaged mean velocity,

turbulent fluctuation and cycle-to-cycle variation of the mean velocity (Heywood, 1988):

$$u(t,i) = \langle U(t) \rangle + u'(t,i) + \hat{u}(t,i) \qquad (2)$$

with

$$\langle U(t) \rangle = \frac{1}{N_c} \sum_{i=1}^{N_c} u(t,i) \qquad (3)$$

$$\hat{u}(t,i) = U(t,i) - \langle U(t) \rangle \qquad (4)$$

where Nc is the number of cycles. Note that the ensemble averaged velocity of Equation (3) depends only on time, since cyclic variation has been averaged out. If these variations can be neglected, the ensemble averaged turbulence intensity is provided by the root mean square of the velocity fluctuations, u_{RMS}, calculated around the ensemble averaged mean velocity:

$$u_{RMS}(t) = \sqrt{\frac{\sum_{i=1}^{N_c} \left[u(t,i) - \langle U(t) \rangle \right]^2}{N_c}} \qquad (5)$$

In our case, the injection bench used for our experiments showed minimum variations in injection pressure and needle lift histories, so that we might suppose that cycle-to-cycle variations are minimised. However, it is hazardous to assume that the unsteady spray itself presents null cyclic variations of mean and turbulent velocities, so one must bear in mind that the calculated value of u_{RMS} includes all fluctuations around the ensemble averaged mean velocity.

The problem now is to reconstruct the temporal evolution of velocity from a database presenting a different resolution in time and space. In studies of flows in engines, the ensemble averaged mean velocity is usually calculated by low pass numerical filtering and then it is discretized at regular intervals of time, Δt (Socoliuc and Brun, 1996). The mean velocity is then calculated as the arithmetical mean of the Nv values contained inside a moving window of width L_F, and symmetrically distributed around time t, which corresponds to the centre of the window. The width of the moving window represents in fact the cut-off frequency, f_c, separating the high frequency phenomena (turbulent fluctuations) from the low frequency phenomena (mean values); f_c is given by the spectral response of the numerical filter:

$$f_c = \frac{1}{L_F} = \frac{6N}{L_F^*} \qquad (6)$$

where the width of the moving window is expressed in seconds (L_F) or in crankshaft angle degrees (L_F^*), °CA, and N is the rotation speed expressed in rpm. The choice of the cut-off frequency should be made taking into account the characteristic scales of the physical phenomenon under study. Nevertheless, in practice, this choice is somewhat arbitrary and is a matter of debate (Fansler and French, 1988).

As we mentioned above, the temporal resolution of our data files varies with the measurement location but it also varies through the injection period. This is partly due to the randomness of the acquisitions made by PDA and partly to the nature of the flow. Also, we must note that the transient Diesel spray has an injection duration of the order of 2 ms, or 10°CA under our experimental conditions, compared to a complete cycle (720°CA). For such reasons, the use of constant width and time intervals of the moving window, like those used for other engine flows, is inappropriate for all of the measurement points investigated as well as for the whole of injection cycle.

To overcome this difficulty, we have conceived a special data treatment based on a cut-off frequency which is directly related to the instantaneous data rate. This filtering helps us avoid the overestimation of the turbulent fluctuation intensities, which occurs specially during steep gradients of the instantaneous velocity, and it reconstructs the evolution of the mean velocity in a correct way. The width of the moving window, as well as the time step used for the calculations, were thus defined according to a fixed number of successive raw data, rather than to a fixed time interval.

After several calculations, we found that the best compromise consisted of an initial smoothening over five successive raw data followed by a filtering with a moving window of a width equivalent to 20 raw data. Finally, a time interval equivalent to 1 raw data was employed as calculation step in order to maximise the sensitivity of our treatment, albeit a significant increase of calculation time.

5. RESULTS

5.1 Parametric analysis of the temporal mean value

First, our results are presented as temporal mean values in order to compare them with studies of steady jets found in literature, although this procedure might not be quite adequate for a highly unsteady pulsed flow like ours, as we have stated before. Also, attention must be made when treating velocity and turbulence information as in single-phase flows since our measurements stem from a flow consisting of a liquid and a gaseous phase. We must then keep in mind that our measurements characterise only the behaviour of the dispersed phase.

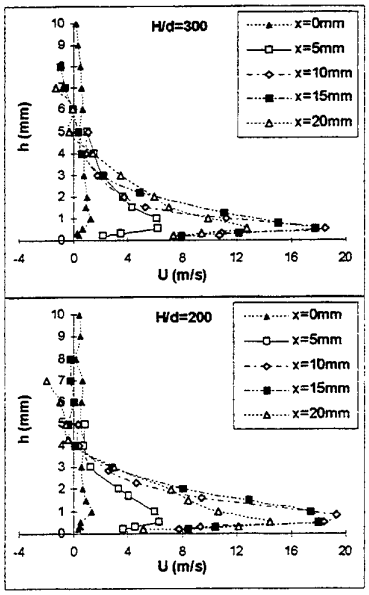


Fig. 3 Mean radial velocity profiles as a function of radial position, x, for two different nozzle-to-plate distances; Tp = 20°C; h is the distance from the plate.

As shown by the results on Figure 3, the mean radial velocity profiles of the wall spray are quite similar to those of steady turbulent wall jets (Özdemir and Whitelaw, 1992) although our spray develops in a different way. Mean radial velocity grows with increasing radial distance reaching a maximum between x = 10mm x = 15mm and then decays, as reported by Landreth and Adrian (1990) for a submerged round turbulent water jet. However, in our case, mean radial (tangential) velocity profiles do not reach a similarity profile, and vertical flow reversals, indicated by negative values of the mean axial (normal) velocity, appear at significantly upstream positions compared to steady ilmpinging jets.

Influence of the nozzle-to-plate distance. When the nozzle-to-plate distance decreases, three main effects are observed:

(1) First, the value of the maximum mean tangential velocity increases. This maximum velocity takes place close to the plate surface; together with the results on mean diameter, this observation confirms that the wall spray momentum is concentrated in the near wall region as pointed out by Arcoumanis and Chang (1994).

It is interesting to note here that estimations of the boundary layer thickness, based on the half velocity thickness, $h_{0.5}$, of the maximum velocity, indicate that the boundary layer stays attached to the wall surface even at large radial distances and that its thickness remains constant as the spray spreads on the wall.

(2) Second, vertical flow reversals occur at positions closer to the impingement point, as illustrated by Figure 4. In studies on steady turbulent impinging jets (Landreth and Adrian, 1990, Didden and Ho, 1985), this flow reversals have been interpreted as the onset of separation of the boundary layer. Our previous observations indicate that, in the present case, this upward flow is related to the high intermittence of the flow, which introduces important disturbances in the near wall region.

(3) Finally, the mean diameter of the droplets increases slightly.

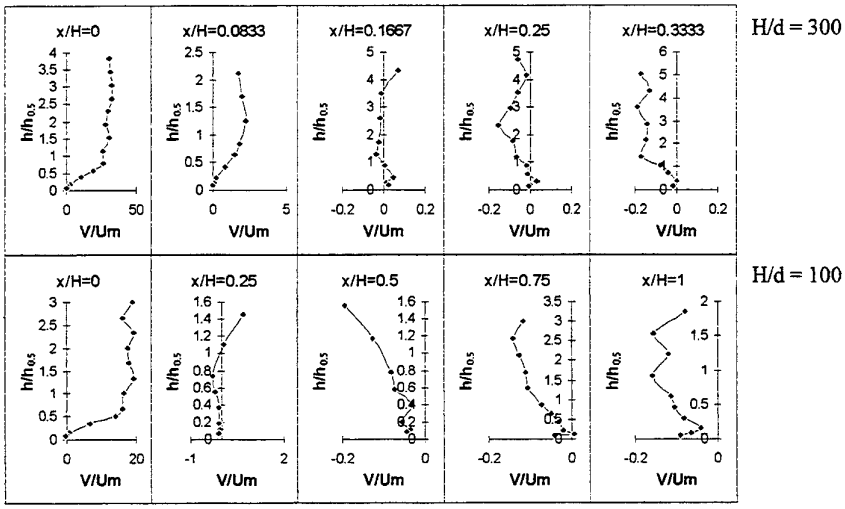


Fig. 4 Development of normalised mean axial velocity profiles for two nozzle-to-plate distances; Um is the maximum mean radial velocity at each radial position; $h_{0.5}$ is the half velocity thickness corresponding to $Um/2$; Tp = 20°C.

Influence of the plate temperature. On the other hand, as the plate temperature rises, the behaviour of the wall spray is strongly modified and velocity profiles become more irregular. More details of this results are given in Chalé and Brun (1998). An increase of the plate temperature produces the following effects:
(1) The maximum mean tangential velocity occurs farther from the plate surface and its value decreases. This indicates that the thermal effects add up to the viscous effects to form a thicker layer, provoking a stronger deceleration of the flow.
(2) Vertical flow reversals appear at a shorter radial distance from the impingement point and this upward flow is more intense for the highest plate temperatures.
(3) Also, the overall Sauter mean diameter (Figure 5) of the droplets in the wall flow decreases, in agreement with the observations of Özdemir (1991).

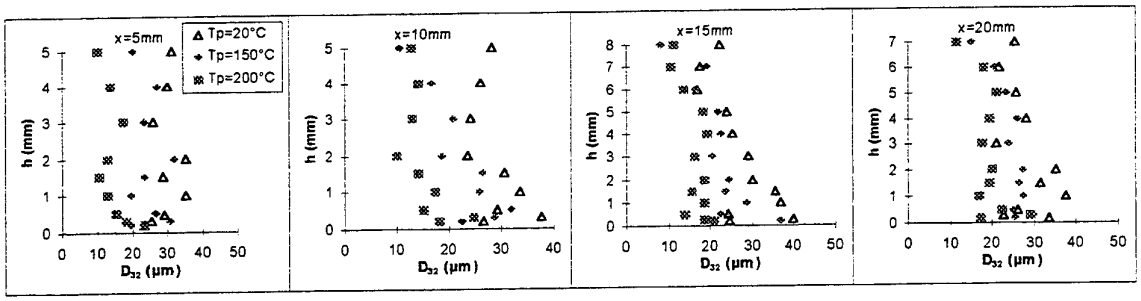


Fig. 5 Development of the Sauter mean diameter profiles, D_{32}, for different plate temperatures; $H/d = 100$.

5.2 Time resolved analysis

The temporal analysis of the wall flow was performed for one nozzle-to-plate distance, $H/d = 100$, combined with different plate temperatures. This experimental setup was chosen in order to approach an "engine-like" configuration.

In the near wall zone of the *development region*, $x = 5$ mm, the tangential velocity of the droplets at room temperature presents an initial maximum value, then it drops down steeply and finally it decreases slowly during the final part of the cycle. Both velocity and diameter profiles in this region exhibit similar trends to those of the approaching free spray. In the outer region above this zone, $h < 1$ mm, velocities are lower and decrease rapidly to nearly zero (Figure 6).

Further downstream (Figure 7), in the *main wall-jet region*, the radial velocity in the outer region passes alternatively from positive to negative values, and so does the normal velocity. This oscillatory behaviour, also observed in all the measurement points located beyond the main wall-jet region and far from the plate surface, suggests that a vortex-like structure is passing through the measurement volume.

At the largest distances from the impingement point, the *wall vortex region*, the radial velocity also exhibits an oscillating pattern (Figure 8). These oscillations are observed in the normal velocity (not shown in this paper) even at the closest positions to the plate surface, which would mean that the vortex structure is able to affect the whole flowfield across the entire cross-section

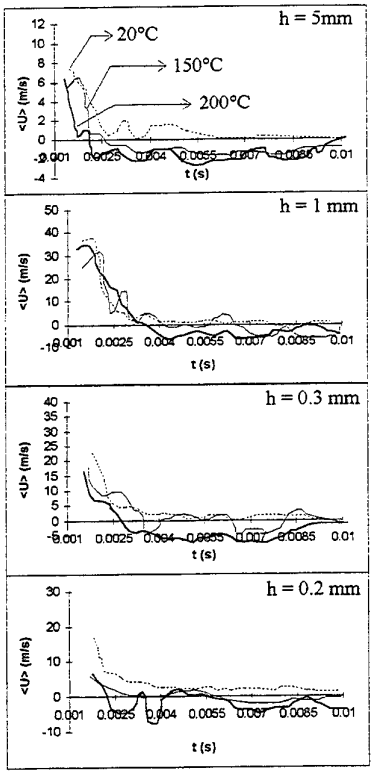


Fig. 6 Temporal evolution of the mean radial velocity in the development region at different wall temperatures; $H/d = 100$.

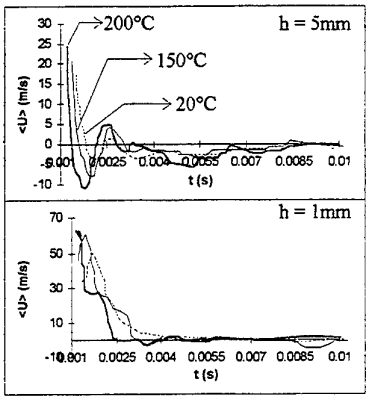


Fig. 7 Temporal evolution of the mean radial velocity in the main wall jet region at different wall temperatures; $H/d = 100$.

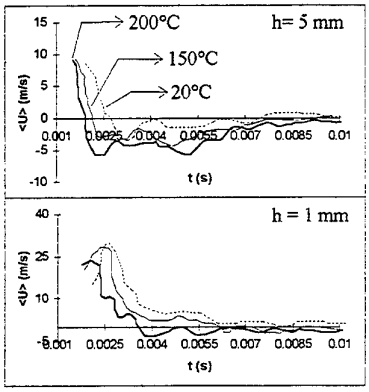


Fig. 8 Temporal evolution of the mean radial velocity in the wall vortex region at different wall temperatures; $H/d = 100$.

Figure 7 shows that, in the main wall jet region, the tangential velocity of the droplets at the spray arrival is bigger for the higher plate temperatures; but after the passage of the wall-jet front, its value is generally lower than for the unheated plate. An increase in the amplitude of the oscillations of the droplets velocities with the plate temperature is also observed.

The temporal evolution of the Sauter mean diameter is shown in Figure 9. In the case of the heated plate, at the arrival of the spray, the mean diameter in the near wall region remains nearly unchanged as the spray passes from $x = 5$ mm to $x = 10$ mm contrary to the trend observed for the unheated plate. However, in the main wall jet region after the passage of the wall-jet front, droplet sizes are larger for the heated plate. Finally, the turbulent fluctuations of velocity increase with wall temperature, specially at the spray front, after which these profiles follow the same trends for the heated and the unheated plate (Figure 10).

It seems then that increasing the plate temperature provokes a faster penetration of the wall-jet front. This implies higher relative velocities between air and droplets which could promote droplet break-up in the jet front, as suggested by Arcoumanis and Chang (1994). In addition, the results of normal velocities for the heated plate suggest that a stronger head vortex with a more pronounced effect at larger radial positions is formed.

The higher fluctuating velocities for high plate temperature may then be explained by the contribution of the air turbulence due to an enhanced air entrainment. The stronger vortex can also increase the probability of droplet coalescence by entraining more small droplets, which might explain the apparition of some bigger droplets jus after the spray arrival.

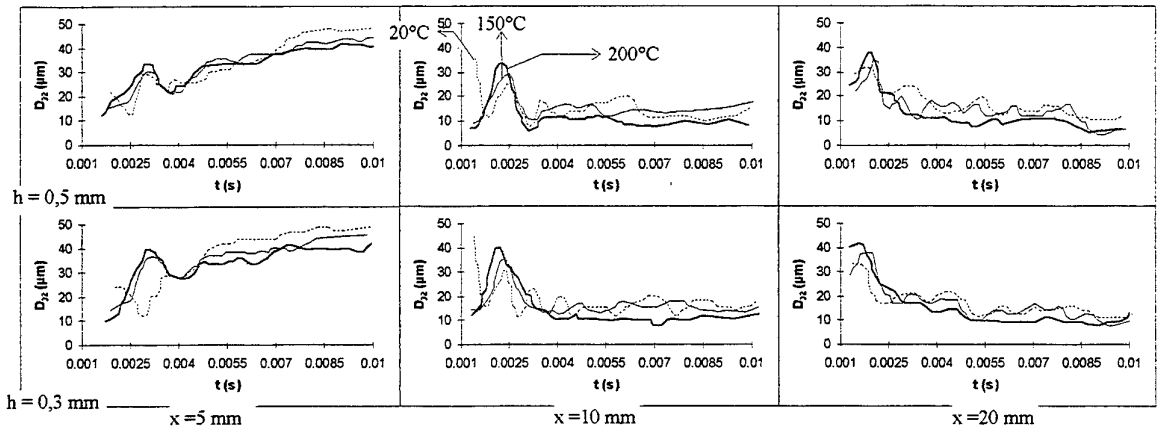


Fig. 9 Temporal evolution of Sauter mean diameter of the wall spray at different wall temperatures; $H/d = 100$.

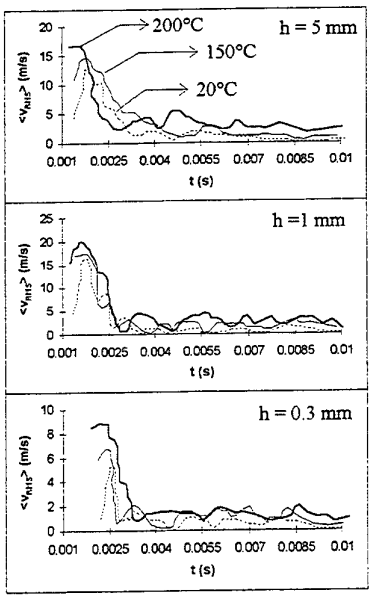


Fig. 10 Temporal evolution of the turbulent fluctuation of the normal velocity in the development region at different wall temperatures; $H/d = 100$.

6. CONCLUSIONS.

Phase Doppler Anemometry has been applied for the characterisation of the wall flow formed after the impingement of a transient Diesel spray. An adequate setup of the technique has allowed measurements in the near wall zone. A special data treatment has been used to reconstruct the temporal evolution of the wall flow characteristics.

Our results have brought to light the behaviour of the characteristic regions of the wall spray. Noticeably, the temporal evolution of velocities in the external zones of the wall flow confirms the presence of a vortical structure, which is appears between the *main wall jet* region and the so-called *vortex region*. That is, in a region where the droplets are strongly decelerated. The wall vortex plays in its turn a key role in the evolution of the droplet field over the wall. Finally, the wall temperature has a considerable influence in the mean droplet diameters and velocities most probably by affecting the characteristics of the continuous phase.

AKNOWLEDGEMENTS

H.G. Chalé was supported during his resarch work by the Consejo Nacional de Ciencia y Tecnología (CONACYT), Mexico.

REFERENCES

Chalé H.G., Georjon T. & Brun M., 1997, Flow Characteristics of Impinging Transient Diesel Sprays Using Phase Doppler Anemometry, Proc. ASME FED Summer Meeting, Vancouver, FEDSM97-3324.

Chalé Góngora, H.G. & Brun, M., A Study on Diesel Spray Impingement Dynamics Using Phase Doppler Anemometry and Video Imaging, 1998, 14th. Annual Conf. on Liquid Atomization and Spray Systems, Manchester.

Didden, N. & Ho, C.M., 1985, Unsteady Separation of an Impinging Jet, J.Fluid Mech., vol. 160, pp. 235-256.

Fansler, T.D., & French, D.T., 1988, Cycle-Resolved Laser-Velocimetry Measurements in a Reentrant-Bowl-in-Piston Engine, SAE Paper 880377.

Labeish, V.G., 1994, Thermodynamic Study of a Drop Impact against a Heated Surface, Exp.Thermal and Fluid Science, vol. 8, pp.181-194.

Landreth, C.C. & Adrian, R.J., 1990, Impingement of a Low Reynolds Number Turbulent Circular Jet onto a Flat Plate at Normal Incidence, Exp. in Fluids, vol. 9, pp. 74-84.

Mundo, CHR., Sommerfeld, M. & Tropea C., 1995, Droplet-Wall Collisions: Experimental Studies of the Deformation and Breakup Process, Int.J. Multiphase Flow, vol. 21-2, pp. 151-173.

Özdemir, I.B., 1991, Impingement of Single and Two-Phase Jets on Unheated and Heated Plates, Ph.D. thesis, Imperial College, London.

Pitcher, G., Wigley, G. & Saffman, M., 1990, Sensitivity of Dropsize Measurements by Phase Doppler Anemometry to Refractive Index Changes in Combusting Fuel Sprays, Proc.5th.Int.Symp. on Appl. of Laser Techniques to Fluid Mechanics, Lisbon, 14.4.

Rask, R.B., 1981, Comparison of Window Smoothed-Ensemble and Cycle-by-Cycle Data Reduction Techniques for Laser Doppler Anemometer Measurements of in-Cylinder Velocity, SAE Paper 840375.

Socoliuc, M. & Brun, M., 1996, A Study on the Speed Dependence of the Intake Flow of a Motored Four-Stroke Engine Using Laser-Doppler Velocimetry, Proc.8th.Int.Symp. on Appl. of Laser Techniques to Fluid Mechanics, Lisbon, 22.5.

Tanabe, H. & Sato, G.T., 1990, Experimental Study on Unsteady Wall Impinging Jet, SAE Paper 900605.

DIESEL SPRAY WALL IMPINGEMENT CHARACTERISATION BY MEANS OF P.D.A. AND HIGH SPEED VISUALISATION

J.M. Desantes, J Arrègle, J. V. Pastor
CMT. Departamento de Máquinas y Motores Térmicos
Universidad Politécnica de Valencia, Spain

U. González
Instituto Mexicano del Petróleo, Mexico

ABSTRACT

The paper presents experimental results of Diesel spray impingement and an analysis of the behaviour of the wall spray. The process is characterised in high pressure Diesel spray injected against a high density gas, at room temperature and impinging against flat surfaces. The micro and macroscopic spray behaviour is characterised using phase Doppler anemometry and high speed visualisation.

INTRODUCTION

The application of high pressure injection systems to high speed low displacement D.I. Diesel engines increases the quantity of fuel that reaches and interacts with the combustion chamber walls. This phenomenon has a significant effect on the processes of air entrainment and evaporation, and determines the development of the combustion process. For these reasons, the study and comprehension of the spray wall impingement has increased in recent years.

The study of Diesel wall spray presents some difficulties, for the theoretical and experimental analysis, due to the strongly transient behaviour of the injection process and the inaccessibility to the combustion chamber. The process is highly space- and time-dependent in terms of drop velocity and size as well as regarding the spray macroscopic behaviour.

The objective of the work reported in this paper is the improvement of the knowledge about Diesel wall spray behaviour through an experimental study of high pressure Diesel sprays injected against a high density gas, at room temperature. In order to simplify the problem and facilitate the interpretation of the results, the piston wall has been simulated by a flat surface. A set of tests with different incidence angles allow to obtain information on the behaviour of a Diesel spray before, during and after impingement, which can be easily generalised.

The micro and macroscopic spray behaviour is characterised using phase Doppler anemometry and high speed visualisation.

BACKGROUND

Different authors have studied the development of Diesel wall sprays by means of different experimental techniques such as laser Doppler velocimetry (LDV) and Phase Doppler anemometry (PDA) [5] [6] [12] [17], light extinction methods [9], photographic techniques, shadowgraphy and tomography [14] [18], in-cylinder endoscopy [24], high speed camera visualisation [1] [2], simulation with gas sprays [10] [15] [16] [22] and other experimental techniques such as hot wire anemometry [16]. Main results from these studies are summarised below.

SPRAY STRUCTURE - Regarding the aspect of the spray contour several authors agree in the existence of a peculiar narrow zone in the wall spray area in the proximity of the impingement point. Later on, the spray spreads leading to an increase of the wall spray thickness in the frontal region [9] [14]. This increase is associated to the existence of a vortex in the peripheral region of the wall spray, region where most of the air entrainment occurs and, as a consequence, spray thickness increases [17]. The existence of this vortex and its motion was detected by means of tomographic techniques [14] and LDV [12]. Different researchers remark the existence of similar structures in gaseous sprays [10].

MACROSCOPIC BEHAVIOUR - For straight impingement (90°) the temporal evolution of the wall spray radius R_w and thickness h_w after impingement

has been described as a function of injection conditions and ambient air [17]:

$$R_w = 3.87\Delta P^{0.89}\rho_a^{-0.24}\left(t-t_w\right)^{0.48}$$

$$h_w = 1.23\Delta P^{0.52}\rho_a^{0.048}\left(t-t_w\right)^{0.35}$$

Wall spray penetration represented by the temporal evolution of R_w has a dependence of time and air density very similar to that of a free spray [3] [13]. On the contrary, thickness h_w seems to be independent of the gas density.

In studies carried out in transient gaseous sprays for similar geometric conditions [10], it was found that spray penetration for free sprays depends on $\Delta P^{0.25}\ t^{0.5}$. Later on, for impingement onto a flat surface perpendicular to the spray axis, spray penetration is proportional to $(t-t_w)^{0.5}$ and independent on the distance between the nozzle and the surface. Several authors remark that this distance has not a significant influence on the subsequent development of the wall jet [19].

In the case of oblique impingement, the behaviour of the wall spray is asymmetric. Nevertheless, penetration in every direction remains proportional to $(t-t_w)^{0.5}$ as in the case of a gaseous spray under similar conditions [21]. The behaviour of the spray after the oblique impact can be analysed with the analogy of an oblique collision of a liquid spray against an obstacle. Taylor studied this case [23] considering that the spray changes into a sheet that flows on the wall. This problem has analytic solution for the two-dimensional case. However, mass and momentum conservation equations for the case of oblique impingement of a cylindrical spray have not analytic solution capable of describing the spray thickness after impingement as a function of the direction. By virtue of this, Naber and Reitz [19] proposed an empirical solution of this thickness as a function of the incident angle and the exit direction considered.

MICROSCOPIC BEHAVIOUR - Available information regarding microscopic behaviour of the spray after impingement is contradictory. Some authors [9],[17] mention a weak effect of the spray impingement on droplets size for test conditions similar to those of the engine. However, other studies [14] show higher Sauter Mean Diameters for impinging sprays than for the equivalent free sprays. Likewise, higher diameters were found for straight impingement than for the oblique case. In other studies [12], the temporal evolution of the drop size was found to be independent of the radial distance to the impact point.

EXPERIMENTAL FACILITIES

HIGH DENSITY GAS INJECTION RIG – The rig used in this work was developed trying to achieve three main objectives: i) to reproduce the same air density of the engine at the end of compression, ii) to allow the observation and optical access compatible with PDA measurements, and iii) to permit the use of standard Diesel injection systems. Among the different gases available, SF_6 was chosen because of its high molecular weight and its viscosity, very similar to that of the air. At room temperature, SF_6 allows experiments at a density of 30 kg/m^3 with a relatively low pressure of less than 0.5 MPa. In addition, SF_6 is an inert gas, avoiding corrosive effects on the rig, and its optical properties are very similar to those of air. Details about the high density gas injection rig are given in references [4] and [7].

IMAGE ACQUISITION SYSTEM -For the acquisition of spray images, a conventional photographic camera with Macro objective and 60 mm lens has been used with films of sensitivity ISO 100/21. The camera is manually operated and the exposure time is fixed by an EG&G Microflash device allowing 0.5 μs light pulses. The flash is located in front of the camera and a set of light diffusers ensures homogeneous illumination.

PHASE DOPPLER ANEMOMETRY - The emitting optics of the PDA system includes a 4 W water-cooled Ar+ Laser source. transmitting optics is a TSI LDV probe while collecting optics and electronics are those of a standard Dantec 1-component system. PDA measurements were performed without temporal gating. The 1×cycle signal given by the injection pump bench was used as a trigger for the system. The PDA optics was mounted vertically on an X-Y-Z table that permits measurements at any point in the spray.

SIMPLE IMPINGEMENT MODEL

In order to detect the principal parameters controlling Diesel spray penetration after impingement against a flat wall, different simplifying hypotheses are considered. The problem is then analysed by mean of dimensional analysis. This type of raising provides good results in the case of free sprays. [8].

The spray tip penetration S for a free spray is a function of the momentum flux through the injector $\dot{M} = \rho_0 u_0^2 \frac{\pi}{4} d_0^2$, the ambient density ρ_a and the

time t spent since the start of injection. Applying the Buckingham π theorem the following relationship is obtained:

$$S\alpha\left(\frac{\rho_0}{\rho_a}\right)^{\frac{1}{4}} u_0^{\frac{1}{2}} d_0^{\frac{1}{2}} t^{\frac{1}{2}} \quad \text{(Eq.1)}$$

The same reasoning in applied to the case of a wall spray with origin on the impingement point. The first step is to determine the initial conditions regarding momentum flux just after impingement. It is assumed that the spray density does not change and that there is no mass exchange between liquid and gas phases. The flux is considered as not-rotational and potential, which implies that liquid velocity before and after impingement has the same modulus.

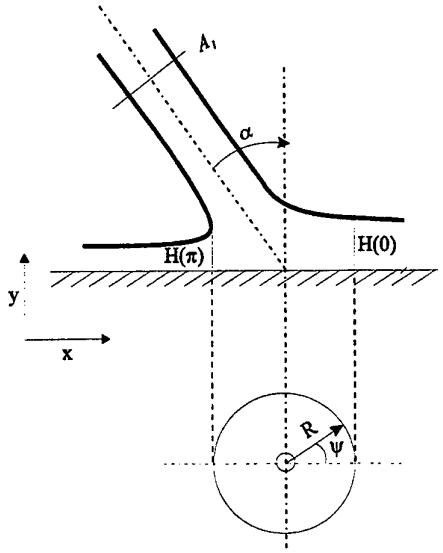


Figure 1 - Analysis of momentum conservation during impingement.

Continuity equation:

$$A_1 = 2\int_0^{2\pi} R\,H(\psi)\,d(\psi) \quad \text{(Eq.2)}$$

Momentum conservation equation along X axis:

$$A_1 \operatorname{sen}\alpha = 2\int_0^{\pi} R\,H(\psi)\cos(\psi)\,d(\psi) \quad \text{(Eq.3)}$$

The consideration of mass and momentum conservation is not enough to describe the radial distribution of the wall spray thickness H(ψ). To solve this problem in more complex models, Naber y Reitz [19] proposed the following empirical equation:

$$H(\psi) = H(\pi)e^{\beta\left(1-\frac{\psi}{\pi}\right)} \quad \text{(Eq.4)}$$

where β is a function of the impingement angle α and can be obtained from the continuity and momentum conservation equations. Combining (Eq.4) with (Eq.2) and (Eq.3) the following expression is obtained:

$$\sin\alpha = \left(\frac{e^{\beta}+1}{e^{\beta}-1}\right)\frac{1}{1+\left(\frac{\pi}{\beta^2}\right)} \quad \text{(Eq.5)}$$

Per analogy with the case of a free spray, an equation is obtained which allows the estimation of the impingement print shape and its temporal evolution as a function of the incidence angle (given by parameter β), the considered direction ψ and the fuel/air density ratio [11].

$$S(\psi,t) = K\,e^{-\beta\frac{\psi}{\pi}}\left(1+a\cdot\left(\frac{\rho_0}{\rho_a}\right)^{1/2}\right)^{\frac{1}{4}}(t-t_w)^{\frac{1}{2}} \quad \text{(Eq. 6)}$$

Parameter K takes into account the momentum of the incident spray, which is mainly a function of the injection conditions and the distance between the nozzle and the surface. Parameter a is an experimental fitting parameter which corresponds to the ratio between velocity and fuel concentration on the free spray axis (a=1 for Sc=1).

PENETRATION IN THE FORWARD DIRECTION

One of the principal aspects of the wall spray macroscopic behaviour is the penetration law, which reflects the fuel/air mixing intensity. Figure 2 shows an example of the temporal evolution of the wall spray profile with an incidence angle of 60 degrees.

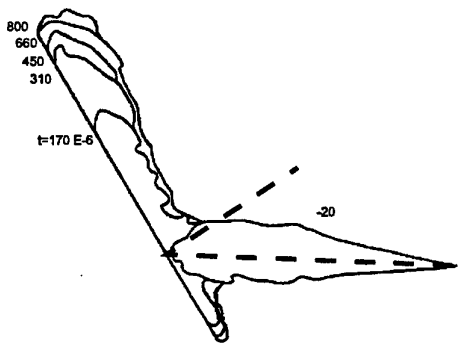


Figure 2 - Example of the temporal evolution of the wall spray boundary.

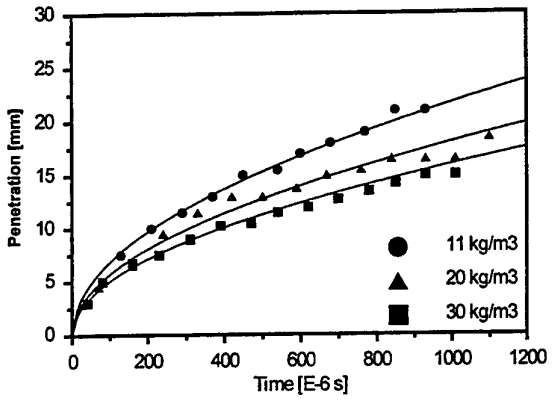


Figure 3 - Wall spray penetration in the principal direction- Incidence angle: 90°.

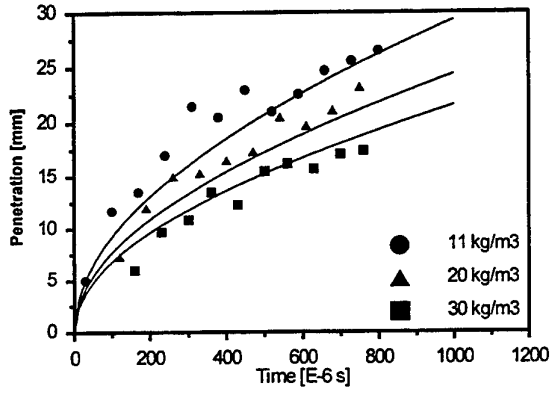


Figure 4 - Wall spray penetration in the principal direction- Incidence angle: 60°.

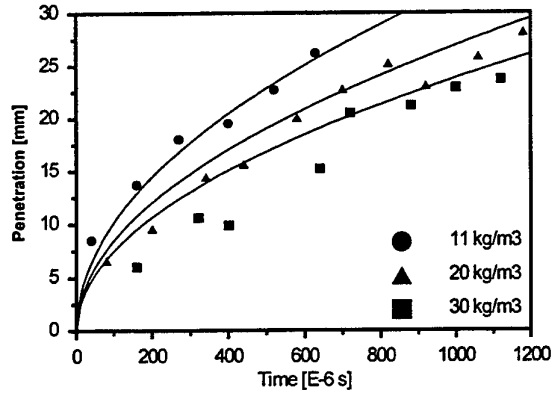


Figure 5 - Wall spray penetration in the principal direction- Incidence angle: 45°.

On the basis of these contours, a spray penetration law is obtained from the impingement point in the main direction defined by the projection of the free spray axis on the obstacle (Figures 3, 4 and 5). The experimental results obtained for three values of gas density are compared with the theoretical penetration curves fitted from equation (Eq.6).

The mentioned theoretical expression predicts accurately the effect of the impingement angle on spray penetration on the forward direction ψ=o and acceptably the influence of gas density also.

RADIAL DISTRIBUTION OF SPRAY PENETRATION

By means of visualisation of the spray print on a transparent obstacle information of temporal evolution of the radial penetration of the spray in any direction ψ is obtained. Symbols in figures 6 and 7 represent the position of the wall spray limits at four different instants after impact for incidence angles of 45° and 60° respectively. Solid lines correspond to the fitted results given by equation (Eq.6).

Predictions of this simple model match satisfactorily the experimental results in most directions ψ for all the operation conditions tested. However, in the back direction ψ = 180° predicted penetration in not so accurate. The difference is due to the interference of the peripheral zone of the free spray that in this region (ψ = 180°) impacts on the surface before the spray axis does.

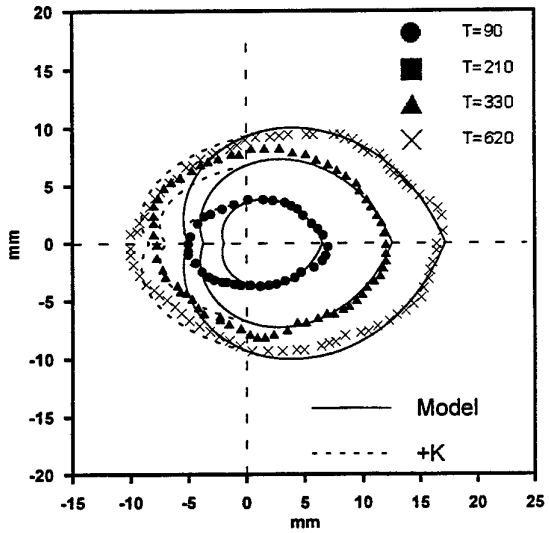


Figure 6.- Evolution of the spray contour – Incidence angle: 45°, gas density: 30 Kg/m^3.

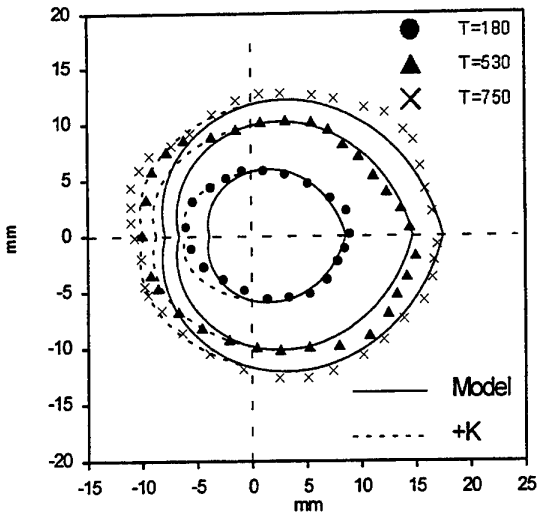


Figure 7.- Evolution of the spray contour – Incidence angle: 60°, gas density: 30 Kg/m^3.

To take into account this effect, which depends on the cone angle of the free spray, a correction term is introduced in the predicted penetration. Is labelled as +K and is represented by a dashed line in figures 6 and 7.

SPRAY VOLUME

Influence of impingement upon air entrainment rate is of vital importance for Diesel combustion and it is reflected on the spray volume evolution.

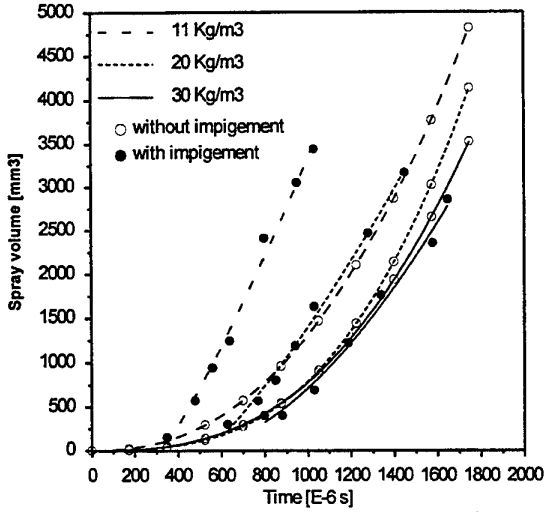


Figure 8.- Effect of impingement on spray volume.

This volume depends directly on the penetration laws previously analysed but also on the evolution of the wall jet thickness.

The analysis of the spray limits (Figure 1) shows that thickness increases with time to the power of 0.4-0.5. But, contrarily to penetration, this thickness seems independent of gas density variations. These results are quite similar to those available in the literature [17].

Figure 8 shows, for an incidence angle of 90° and different gas densities, the experimental temporal evolution of the wall spray volume compared to the volume of the same spray without any obstacle [3].

It can be seen that the influence of impingement upon air entrainment, compared to the free spray case, does depend on gas density. Whilst for densities of 11 and 20 Kg/m^3 impingement increases the volume of the spray, for 30 Kg/m^3 spray volume is practically the same with and without impingement.

MICROSCOPIC BEHAVIOUR

Measurements of droplets velocity and size by means of PDA have been performed on three planes parallel to the surface and on 8 axes at 45° each other. Particularly interesting results are given by the measurements just after impingement. On the one hand, these measurements allow characterisation of the initial conditions in terms of droplets velocity and diameter for the spray that will become a wall jet. On the other hand, measurements show the influence of the impact on droplets atomisation and coalescence.

Figures 9-a to 11-b show the evolution of mean velocity and Sauter Mean Diameter as a function of time, for three measurement points 3 mm downstream the impact point on planes parallel to the 45° surface at distances of 0.5, 1.5 and 3 mm, and for three different gas densities. The results obtained at any instant along the injection process are grouped into three zones: spray leading edge, central zone and spray trailing edge.

As in the case of free sprays [3] [20], the unsteady character of Diesel injection has an important influence upon atomisation and coalescence. SMD increases for measurement points far from the spray tip. In the case of a gas density of 30 kg/m^3, SMD changes from 20 μm to 45-50 μm for the point closest to the surface and from 20 μm to 28 μm for the farthest point.

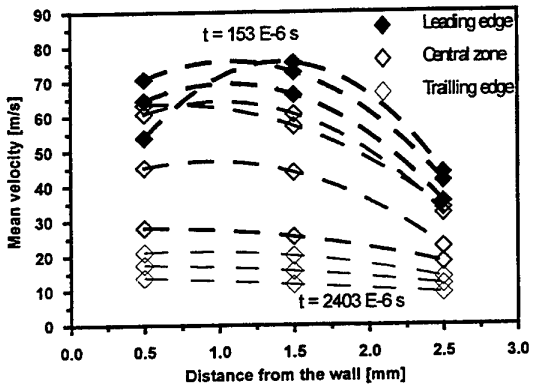


Figure 9-a – Mean velocity - ρ = 11 kg/m^3.

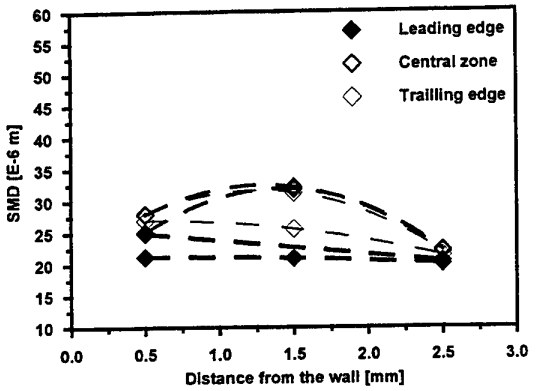


Figure 9-b – Sauter Mean Diameter - ρ = 11 kg/m^3.

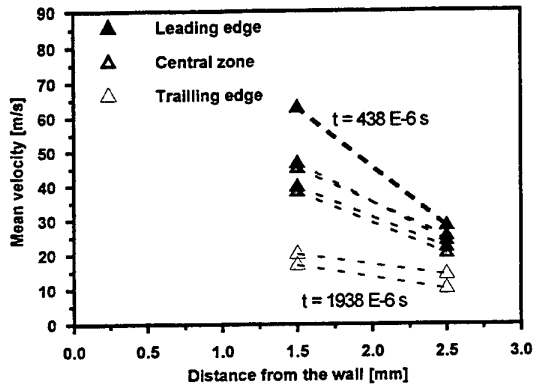


Figure 10-a – Mean velocity - ρ = 20 kg/m^3.

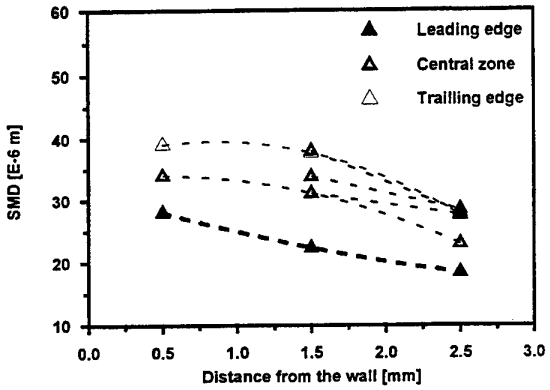


Figure 10-b – Sauter Mean Diameter - ρ = 20 kg/m^3.

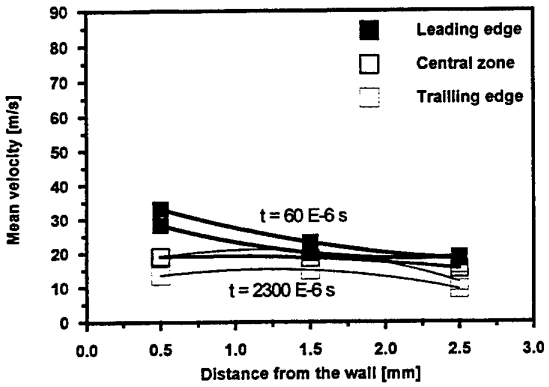


Figure 11-a - Mean velocity - ρ = 30 kg/m^3.

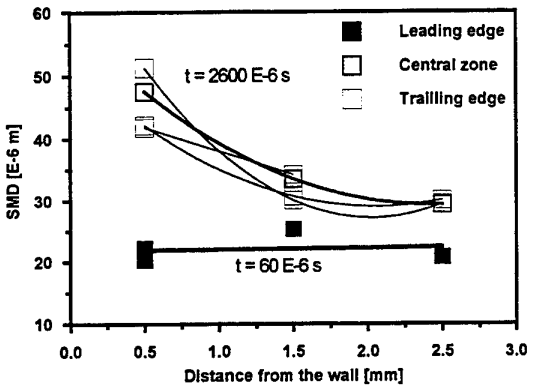


Figure 11-b - Sauter Mean Diameter - ρ = 30 kg/m^3.

The different behaviour as a function of distance to the obstacle is probably due to the appearance of a gradient of fuel concentration. As a consequence of the presence of a physical object, the droplet concentration must be higher in the area close to the wall than in the free face of the wall jet. As in the free spray case, the relatively high velocities observed for densities of 11 and 20 kg/m^3 provoke that coalescence were still not dominant with regard to atomisation and the differences of SMD between the leading edge, central zone and trailing edge are small.

The comparison of SMD measured for the wall spray at 30 kg/m^3 and for the equivalent free spray show that impingement seems to have no influence on the leading zone of the spray. On the contrary, SMD on the trailing edge changes from 30-35 μm before impingement to 45-50 μm after it. This is due to an increase in fuel concentration as a consequence of the confinement of the spray on the obstacle surface. This phenomenon is not negligible, as the fuel spred on the surface should represent an important mass amount.

Spray wall impingement seems to have not any direct significant effect on droplets size. However, the local increase of fuel concentration caused by the presence of the obstacle increases coalescence in the central zone of the spray and specially in the trailing edge. This effect is more evident for a density of 30 kg/m^3 than for the lower densities; the spray velocity at the measurement point is higher as coalescence predominates on atomisation.

The results shown above correspond to the fraction of wall jet placed on the principal axis of symmetry. Although for an obstacle at 45°, this fraction is surely the most important in terms of fuel mass, the contribution of the rest of the spray is not negligible. Figure 31 shows SMD averaged along the whole injection, adimensionalised with SMD on the principal axis of symmetry and at the same distance from the impact point.

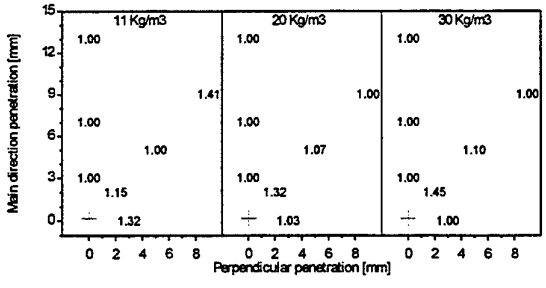


Figure 12 - Distribution of averaged adimensionalised SMD for the wall jet.

As in the free spray case, SMD is the resultant of an equilibrium between coalescence et atomisation relatively constant, despite the important differences in velocities and concentrations.

CONCLUSION

The experimental characterisation performed on the behaviour of Diesel sprays impinging against flat surfaces has allowed to obtain information easily generalised about two fundamental aspects:

- Wall jet penetration and spray volume evolution
- Droplets size evolution

This information has two main applications:

- The development and validation of a simple model to describe accurately the macroscopic behaviour of the spray. It has been embodied into a phenomenological model of Diesel sprays to help in the design of combustion chambers and in the analysis of the combustion process in the engine.
- The description of the influence of impingement upon droplets size and the subsequent evolution of atomisation and coalescence processes in the wall jet, which constitutes an important data base to feed and validate 3D modelling of Diesel Sprays.

AKNOWLEDGEMENT

The authors acknowledge that part of this research has been performed under the contract JOU2-CT93-0330 in the frame of the JOULE 2 European programme and wish to thank PSA Peugeot-Citroën for supporting the experimental work.

REFERENCES

[1] Al- Rub, M.A., Farrell, P.V., Senda, J., "Near Wall Interaction in Spray Impingement.", SAE Paper 960863, 1996.

[2] Allocca, L.,Corcione, F.E., Goloni, S., Papetti, F., "Assessment of Wall Heat Transfer Model for an Impinging Diesel Spray.", ASME, 1993.

[3] Arrègle, J., "Diesel sprays structure and internal dynamics analysis."(in Spanish), SPUPV, ISBN 84-7721-610-X, 1998.

[4] Bradshaw, P. Love, E.M., "The Normal Impingement of a Circular Air Jet on a Flat Surface.", Aeronautical Research Council, London, 1961.

[5] Brunello, G., Coghe, A., Cossali, G.E., Gamma, F., "LDA Analysis of Spray - Wall Interaction.", Sixth Annual Conference of ILASS- Europe on Liquid Atomization and Spray Systems. Pisa, Italy, 1990.

[6] Brunello, G.,Callera, S., Coghe, A., Cossali, G.E., Gamma, F., "LDV and PDA Analysis of Spray-Wall Interaction.", Conference Proceedings of ICLASS91, Gaithersburg, Maryland, 1991.

[7] Coghe A., Cossali, G.E., "Phase Doppler Characterization of a Diesel Spray Injected into a High Density Gas under Vaporization Regimes.", VII International Symposium of Application of Laser Technology to Fluid Mechanics, Lisbon, 1994.

[8] Correas D., "Theoretical and experimental study of isothermal Diesel free sprays", (in Spanish), PhD Thesis, UPV, 1998.

[9] Fujimoto, H., Senda, J., Nagae, M., Hashimoto, A., "Characteristics of a Diesel Fuel Spray Impinging in a Flat Wall.", International Symposium COMODIA 90, 1990.

[10] Fujimoto, H.,Hyun, G., Nogami, M., Hirakawa, K., Asai, T., Senda, Jiro., "Characteristics of Free and impinging Gas Jets by Means of Image Processing", SAE Paper 970045, 1997.

[11] González, U., "Influence of wall impigement on the characteristics of a D.I. Diesel spray" (in Spanish), PhD Thesis, UPV, 1998.

[12] Guerrassi, N., Champoussin, J.C., "Experimental Study and Modeling of Diesel Spray / Wall Impingement.", SAE Paper 960864, 1996.

[13] Hiroyasu, H., Arai, M. , "Fuel Spray Penetration and Spray Angle in Diesel Engines." Trans. JSAE, Vol.21, 1980.

[14] Hiroyasu, H., Nishida, K., Min, J.C., Arai, M., Yoshida, H., "Computed Tomographic Study of internal Structure of a Diesel Spray Impinging on a Flat Wall." International Symposium COMODIA 90, 1990.

[15] Hyun, G.,Nogami, M., Senda, J., Fujimoto, H., "Study on unsteady gas jet- Comparison of experimental results with numerical analysis by discrete vortex method.", JSAE9635638, 1996.

[16] Iida, N., Hirawo, K., Sato G., "Experimental Study of Transient Gas Jet Impinging on a Wall.", SAE Paper 900479, 1990.

[17] Katsura, N., Saito, M., Senda, J., Fujimoto, H., "Characteristics of a Diesel Spray Impinging on a Flat Wall.", SAE Paper 890264, 1989.

[18] Matsui, Y., Sugihara, K., "Sources of Hydrocarbon Emissions from a Small Direct Injection Diesel Engine.", JSAE, 1986.

[19] Naber, J.D., Reitz, R.D., "Modeling Engine Spray/Wall Impingement.", SAE Paper 880107, 1988.

[20] Payri, F., Desantes, J.M., Arrègle, J., "Characterization of D.I. Diesel sprays in High density conditions.", SAE Paper 960774, 1996.

[21] Rajaratnam, N., "Turbulet Jets", Elsevier Scientific Publishing Company, Amsterdam, ISBN 0-444-41372-3, 1976.

[22] Su, W., Xie, H., Lin, R., Shi,S., "Experimental Study on the Effects of Spray Impingement and Structure on Spray Mixing Rate by Gas Simulation.", SAE Paper 960775, 1996.

[23] Taylor, G.I., "Oblique Impact of a Jet on a Plane Surface." Phil. Trans Roy Soc. (Lond) A, Vol.260, 1966.

[24] Werlberger, P.,Cartellieri, W.P., "Fuel Injection and Combustion Phenomena in a High Speed DI Diesel Engine Observed by Means of Endoscopic High Speed Photography." SAE Paper 870097, 1997.

VARIABLES DEFINITION

a, K	empirical constants
d_0	nozzle diameter [m]
H	wall spray thickness [m]
$\dot{M}$	momentum flux [m^2 kg / s^2]
ΔP	injection drop pressure [Pa]
S	penetration [m]
SMD	Sauter Mean Diameter [m]
t	time [s]
t_w	impact time [s]
u_0	nozzle exit velocity [m/s]
α	Incident angle [rad]
β	function of the incidence angle
ρ_a	air density [kg/m^3]
ρ_0	fuel density [kg/m^3]
ψ	radial direction [rad]

SESSION 8

COMPLEX FLOWS 1

LASER VELOCIMETRY MEASUREMENTS IN A CYCLONE SEPARATOR

M.J. Fisher and R.D. Flack

Department of Mechanical, Aerospace and Nuclear Engineering
University of Virginia, Charlottesville, VA 22903-2442 USA

ABSTRACT

A laser velocimeter was used to measure the three-dimensional flow field at seven planes in a Plexiglas cyclone separator using water as the working fluid. Two different inlet flow conditions were studied. Results showed tangential velocity profiles that exhibited the characteristics of forced and free vortex flow. The axial velocity profiles showed that backflows were present in the studied device. Typical tangential velocity magnitudes were between 4.6 m/s and 11.5 m/s. Typical axial velocity magnitudes were between 0.8 m/s and –4.0 m/s. The peak tangential velocity increased as the distance from the inlet was increased. The magnitudes of the axial velocities also increased with increased distance from the separator inlet.

1. INTRODUCTION

Cyclone separators are widely used in industrial applications to separate particles or fluids from a transport fluid. The cyclone separator is a relatively simple device that has no moving parts. The separating action in this device is a result of the swirling flow that produces a centrifugal force on the fluid and particles moving through it. This centrifugal force causes the most dense fluid or particles to move to the outside wall of the separator, while the less dense material moves to the center of the separator. The swirling flow is produced by the inlet flow that enters tangent to the radius of the separator, and is forced to follow the inside wall of the device. The separated materials then exit the device through different outlets. The cyclone separator used in this study is employed in industrial applications to remove contaminants such as waxes, polystyrene foam, polyethylene, hot melt adhesives and other floatable material from pulp sludge for paper processing.

The flow passage in a cyclone separator is typically cylindrical in shape at the inlet region and commonly a conical section is used near the exit region. An air core typically forms along the centerline of the separator; thus the device employs two working fluids. The device has one inlet, and two outlet passages called the underflow (accepts) and overflow (rejects). The inlet is aligned tangent to the radius of the separator, and along the inside surface of the wall. Different outlet configurations are used. For the current effort the overflow exits the separator through a "vortex finder" which is positioned along the axis of symmetry of the flow passage in the region opposite the inlet, and the underflow exits radially outward from a position on the peripheral wall in the region opposite the inlet.

The tangential velocity component of the flow has the highest magnitudes, and thus is the most dominant component of velocity. The axial velocity component has magnitudes smaller than the tangential velocity, and is the second most dominant component. The radial velocity component has very small magnitudes, and is of very little practical importance.

1.1 Previous Cyclone Separator Studies

Bradley (1965) cataloged a significant amount of the early work dealing with the operation, design and performance of hydrocyclones (cyclone separator using water as the transport fluid), and gave a review of the early experimental efforts to determine the flow velocities in hydrocyclones. The following discussion contains a short synopsis of a portion of these studies and other more recent efforts.

The first hydrocyclone patent was granted in the United States in 1891. A number of researchers have since studied the hydrocyclone employing both analytical and experimental techniques. Some of the earliest measurements of tangential velocities inside a hydrocyclone used probes, paddles or vanes mounted on a freely rotating spindle, which was placed inside the air core. Measurements using this technique were first reported by Fontein and Dijksman (1952). Similar measurements were taken later by Lilge et al. (1957-1958). Siato and Ito (1951) used a variation of the above method by

attaching small spheres to a rotating spindle using thin threads. This device was placed into the flow of a transparent test section, while a stroboscope was used to measure the rotational speed of the spheres. This method improved the measurement quality, but the threads crossed velocity gradients, and thus measurement error was still present.

The faults of these methods led to the use of other measurement techniques, which have produced the most useful and accepted data. Kelsall (1952) used a stroboscope with a rotating microscope objective lens to determine the velocities of aluminum flakes that seeded the flow in a transparent test section. This method was used to determine the tangential and axial velocity components, and the radial velocities were calculated using continuity considerations. Similarly, photographic techniques were employed by Ohashi and Maeda (1958). This technique used a stroboscope, which flashed at precisely controlled time intervals to determine the velocity of the seed particles.

More recently Dabir (1983) used laser velocimetry to determine the tangential and axial velocities in a hydrocyclone operating with no air core. The radial velocities in this study were also calculated using continuity considerations. Hsieh and Rajamani (1991) also used laser velocimetry to determine the tangential and axial velocity components in a hydrocyclone operating with an air core. Although this study included the effects of the air core, the radial velocities were again calculated, and not directly measured.

1.2 Research Objectives

The geometry used in this study significantly differs from those used in the above mentioned studies. A lack of precise knowledge of the actual flow field in this particular industrial cyclone separator makes theoretical modeling and thus optimizing the design of this device very difficult. Detailed experimental velocity fields can be used to identify the presence of backflows, or other important flow characteristics, which are directly related to the geometry of this device, and effect its performance. Thus, the goal of this research is to measure the internal flow field in a centrifugal separator using laser velocimetry to gain a physical understanding of the operation of this device and to aid in the improvement of theoretical modeling. The long-term result of these improved theoretical models will be the ability to optimize separator geometries to increase separating efficiency and reduce power consumption.

The research consisted of measurement of the three-dimensional velocity profiles at seven planes within one particular Plexiglas cyclone separator. In each of these planes, the velocities were measured from the air core to the separator wall. For this paper, typical results for two significantly different inlet flow rates are reported. These tests were all run at one reject rate.

Pulp sludge, the actual working fluid, consists of approximately 1% paper pulp and 99% water. It is not adequately transparent to employ laser velocimetry. Thus, water was chosen as the working fluid in this study. Pulp sludge is, however, a non-Newtonian fluid, while water is a Newtonian fluid. Thus, this research serves as an initial step towards the eventual measurement of the flow of a clear non-Newtonian fluid representing the pulp sludge in a cyclone separator.

The research reported herein gives a significant set of data which qualitatively documents the complex internal flow phenomena and which can be used to validate and develop better computational models of the cyclone separator internal flow field.

2. EXPERIMENTAL FACILITY

2.1 Cyclone Separator and Support Rig

The test specimen used for this study was a Plexiglas full-scale model of an industrial cyclone cleaner. This model is illustrated in figure 1. The working fluid used in this study was tap water, which contains naturally present particles. These particles provided sufficient flow seeding, and therefore no additional seeding was required.

The Plexiglas cyclone separator test specimen was connected in a hydraulic flow loop. The inlet flow for the separator was produced by two 0.75 kW centrifugal pumps in a series configuration. Water was pumped from a 2000 liter reservoir, which was used to damp out flow fluctuations. Gate valves were placed in the inlet and accepts lines to adjust the inlet flow rate and accepts flow rate. Orifice flow meters were used to measure the flow rates in the inlet and accepts lines. Flexible hose was placed in the inlet and

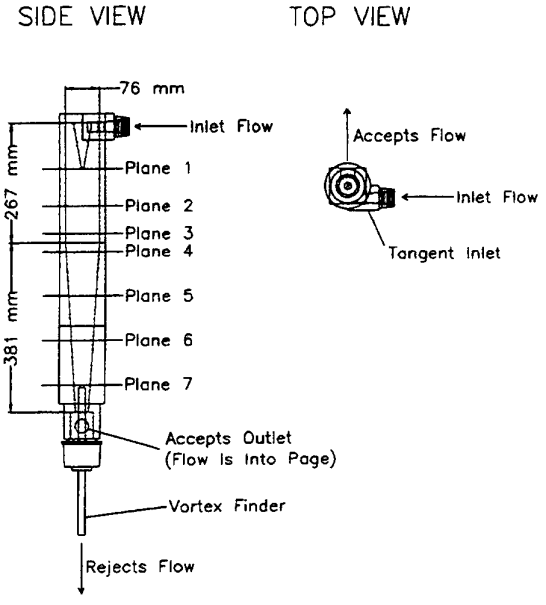


Figure 1: Plexiglas Cyclone Separator

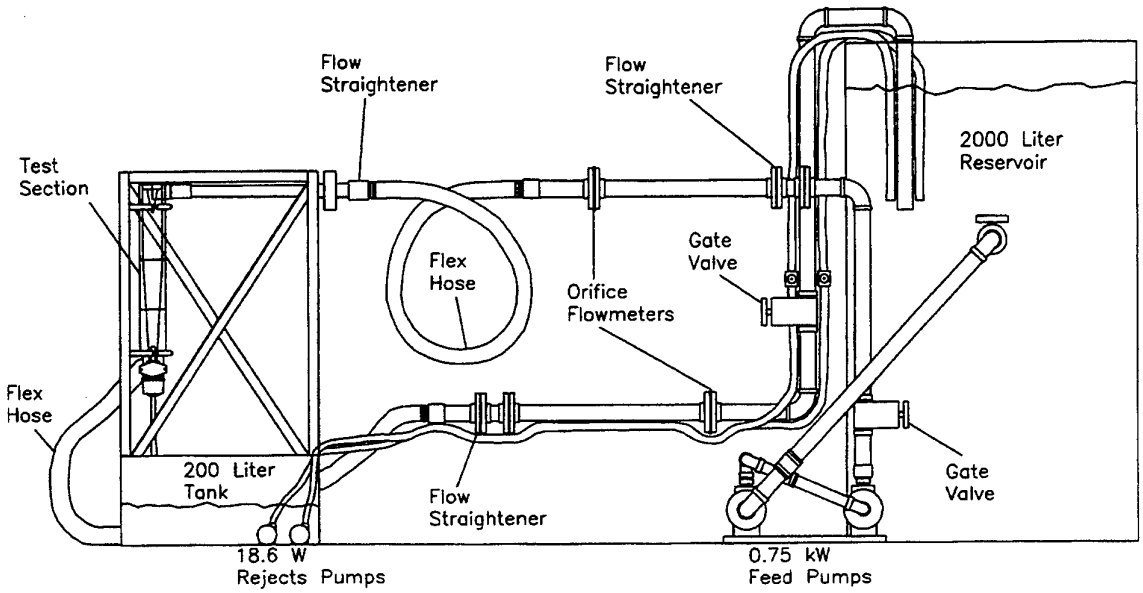


Figure 2: Hydraulic Flow Loop

accepts lines to allow the test specimen to be rotated to access various measurement areas. The test specimen's inlet and outlet were connected to sections of straight pipe. The straight pipe on the inlet was preceded by a flow straightener. The rejects flow exited the separator through the vortex finder, and was discharged to the atmosphere through a short section of hose. This flow was collected into a 200 liter tank and was pumped into the 2000 liter reservoir by two submersible 18.6 W pumps. Figure 2 shows the above described flow loop.

2.2 Laser Velocimeter System

The measurement system used for this research was a commercially available three-dimensional backscatter laser Doppler velocimeter. The emission source used with this laser velocimeter was a continuous wave, 500 mW, Argon-Ion laser. The laser velocimeter system incorporated fiber optic cables, which were used to connect the measurement probes to the transmitting optics. The measurement probes were mounted on a software controlled three-dimensional traverse. Figure 3 displays the laser velocimeter system.

3. MEASUREMENT METHODOLOGY

3.1 Measurement Difficulties

The formation of the air core at the typical operating conditions of this system presented significant problems related to the measurement method used. The air core produced an interface between the water and the air. This boundary was unsteady and caused significant reflection when irradiated by the beams. The light reflected by this surface entered the receiving optics, and greatly degraded the Doppler burst signals. This phenomenon was present whenever measurements were made along the test fixture's axis of symmetry, and made it difficult to take measurements in these positions. This problem was overcome by moving the beams off the test section's axis of symmetry, and avoiding contact with the air core.

The reflection problem was resolved by moving the beams off the axis of symmetry. However, this caused significant refraction problems. Because the surfaces of the test section were cylindrical and conical in shape, the pair of beams bent non-symmetrically when they crossed the air/Plexiglas and Plexiglas/water interfaces of the separator. This bending took place in all three dimensions due to the three-dimensional shape of the test fixture. This non-symmetric bending of the beams at the inside and outside surfaces of the test section made it difficult to predict critical measurement parameters, namely the probe volume position, the separation angle of the beams, and the direction of the measured velocity. Figure 4 is 2-dimensional ray tracing that graphically illustrates the bending of a pair of beams as they pass through the top portion of the test fixture. The arrow at the probe volume in figure 4 represents the direction of the measured velocity. The use of more than one set of beams to measure two or more velocities concurrently was not possible

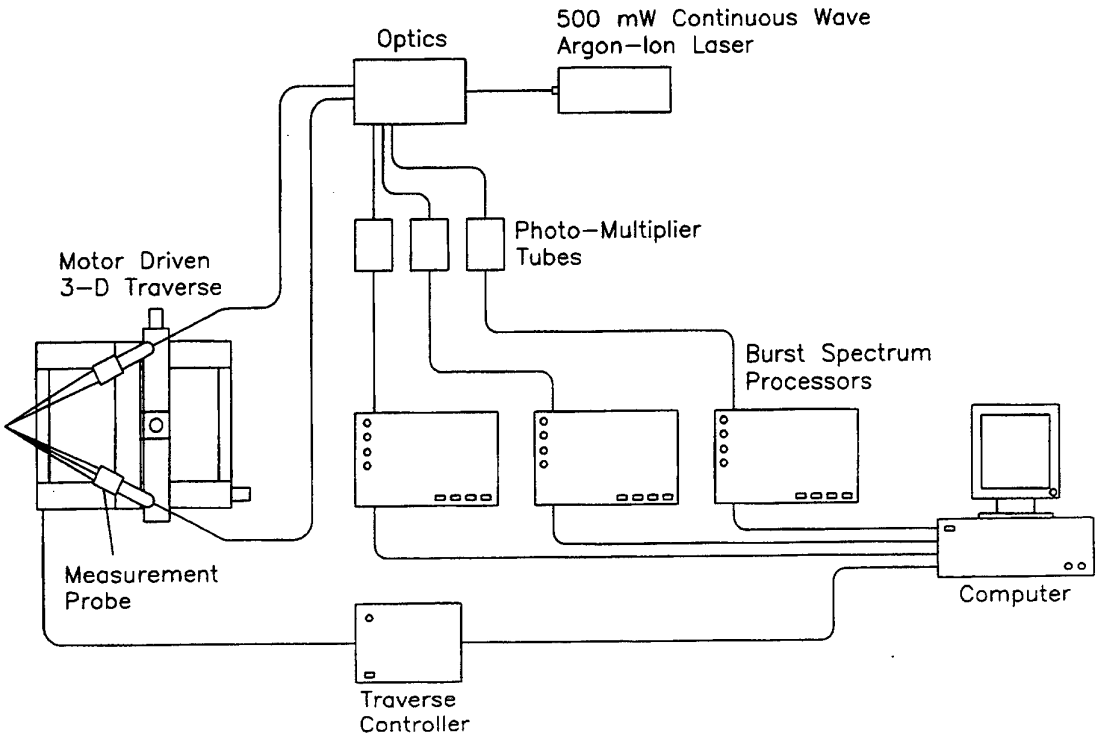


Figure 3: Laser Velocimeter System

because the non-symmetric bending would cause the probe volumes produced by each set of beams not to coincide.

3.2 Analytical Laser Beam Refraction Model

Because of the non-symmetric bending phenomena, an analytical model of the laser beams passing through the test section was developed. This model utilized Snell's law to mathematically determine each beam's path through the test specimen and flow passage. Using this information, the critical measurement parameters discussed above were calculated, and the measurement of off-axis positions was permissible.

3.3 Velocity Determination

The determination of the three-dimensional velocity profile in the specimen required that three separate and unique measurements be made in the flow at the desired position. These measurements did not represent purely tangential, axial or radial velocities because of the refraction effects discussed above. Instead, the measurements represented the combination of these three velocities in a set

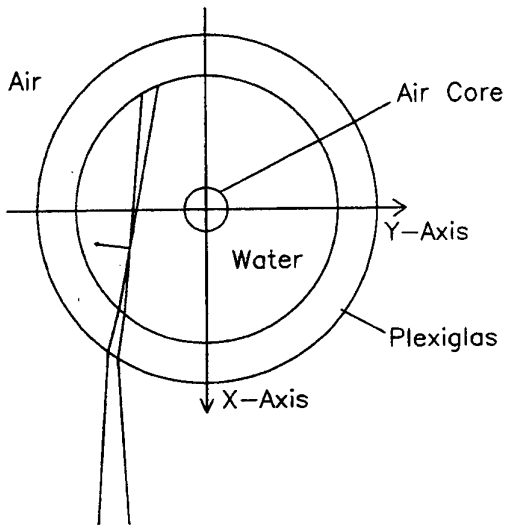


Figure 4: Ray Tracing of Beams in the Test Fixture

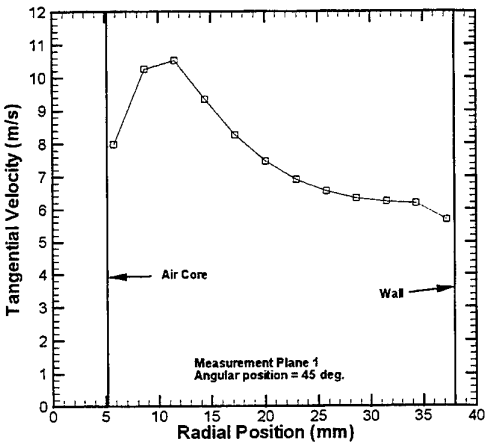


Figure 5: Tangential Velocity Profile for Plane 1 with Flow Condition #1

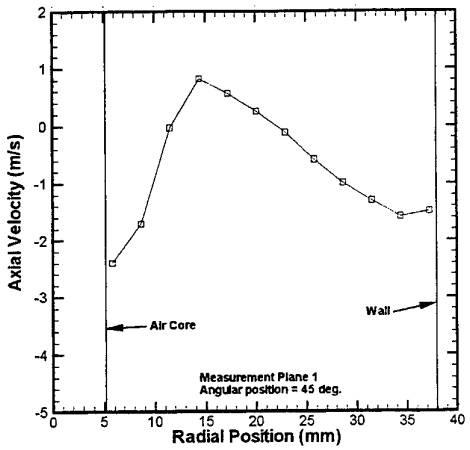


Figure 6: Axial Velocity Profile for Plane 1 with Flow Condition #1

of non-orthogonal but distinct measurements. These three measurement magnitudes and directions were then used with the properties of vector projections to determine the three-dimensional velocity in a Cartesian coordinate system. These Cartesian velocity components were then resolved into the tangential, radial and axial velocity components.

4. RESULTS AND DISCUSSION

Measurements were made at seven planes in the test specimen, and with two different flow conditions (flow condition #1: inlet flow = 3.2 l/s, reject rate = 10%; flow condition #2: inlet flow = 2.5 l/s, reject rate = 10%). Figure 1 shows the position of the measurement planes. In each plane measurements were taken at a constant angular position of 45°, and were spaced at equal radial increments. The axial velocity profile was integrated for each of the cases presented below to determine the axial flow rate at the given plane. These integrated flow rates were compared to the measured flow rates from the inlet orifice flow meter. In each case, the percent difference between the flow rates was less than 6%.

4.1 Plane 1, Flow condition #1

The tangential, axial and radial velocity profiles for plane 1 at flow condition #1 are shown in figures 5, 6 and 7 respectively. The tangential velocity profile exhibits the characteristics of a forced vortex at the region near the air core, and those of a free vortex in the outer portion. The peak tangential velocity shown is 10.5 m/s. The axial velocity profile shows high downward velocities in the region near the air core. The bulk axial flow is in the downward direction, however, a flow reversal exists near the center of the profile. The radial velocity profile shows that this velocity component

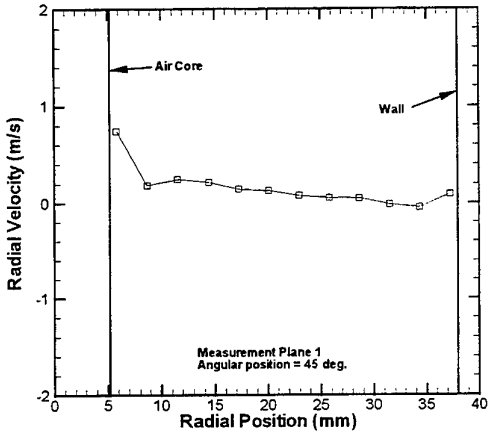


Figure 7: Radial Velocity Profile for Plane 1 with Flow Condition #1

has magnitudes that are near zero over the complete profile. The mean of the absolute values of the radial velocities is only 2 % of the mean of the tangential velocities for this case. This indicates that the tangential velocity is the more dominant velocity component.

4.2 Plane 5, Flow Condition #1

Figures 8 and 9 show the tangential and axial velocity profiles from plane 5 with flow condition #1. These plots show trends similar to the previously discussed tangential and axial velocity profiles. In this plane, the peak tangential velocity is 11.0 m/s. The tangential velocity gradient in the free vortex region, for this plane, increased by a small amount

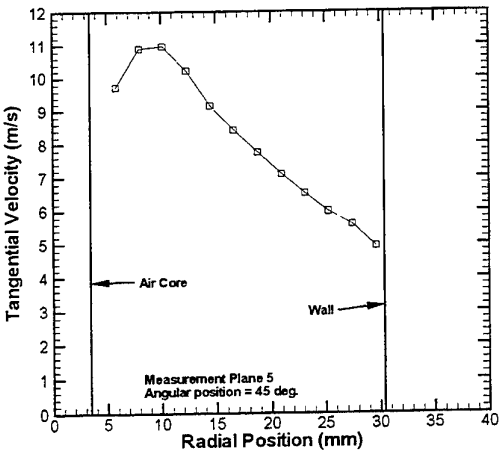


Figure 8: Tangential Velocity Profile for Plane 5 with Flow Condition #1

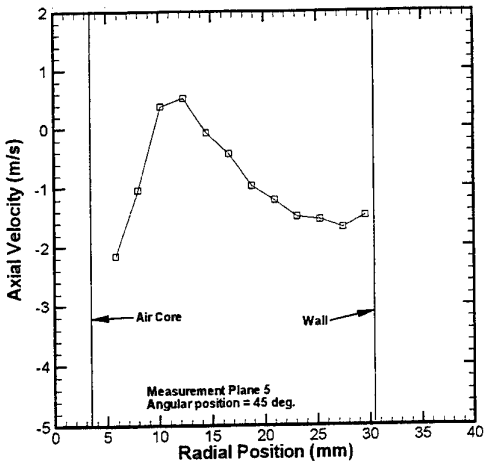


Figure 9: Axial Velocity Profile for Plane 5 with Flow Condition #1

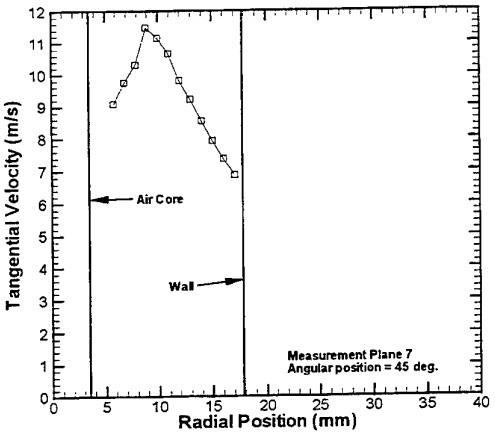


Figure 10: Tangential Velocity Profile for Plane 7 with Flow Condition #1

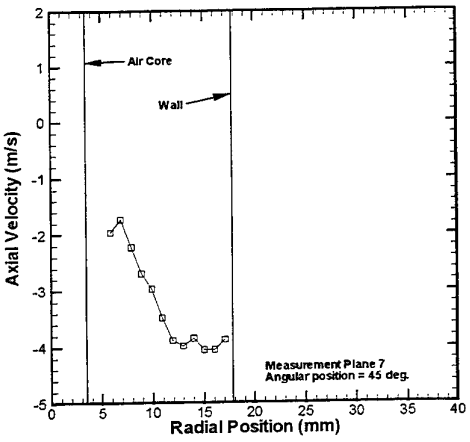


Figure 11: Axial Velocity Profile for Plane 7 with Flow Condition #1

from plane 1. The flow reversal that was present in the center of the axial velocity profile in plane 1 still exists in plane 5, and the magnitudes of the axial velocities in planes 1 and 5 are very comparable.

4.3 Plane 7, Flow Condition #1

The tangential and axial velocity profiles from plane 7 with flow condition #1 are shown in figures 10 and 11. The flow passage in this plane has a much smaller area than the previous planes, and therefore significant differences in the velocity profiles exist. The tangential velocity in this plane has a maximum value of 11.5 m/s. The tangential velocity gradient in this plane is much larger than in the previously discussed planes. The axial velocity profile in this plane does not exhibit a backflow region, and the magnitudes of this profile are significantly larger than those in planes 1 and 5.

4.4 Plane 1, Flow Condition #2

Figure 12 shows the tangential velocity profile in plane 1 with flow condition #2. This plot exhibits the same trends as the tangential velocity profile in plane 1, with flow condition #1. The velocity gradients of these profiles are also very

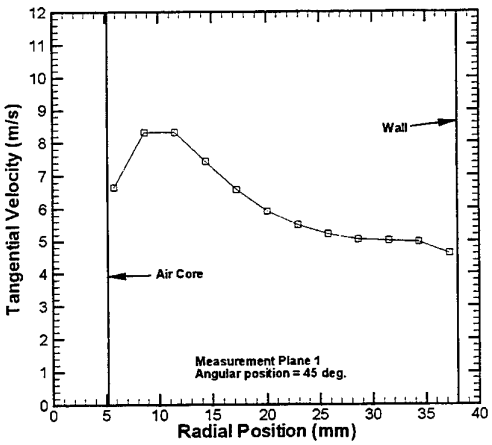


Figure 12: Tangential Velocity Profile for Plane 1 with Flow Condition #2

similar. The maximum tangential velocity at this plane is 8.3 m/s. This value is 21% lower than the maximum tangential velocity from plane 1 with flow condition #1. This velocity decrease agrees well with the decrease in inlet flow rate of 20%.

5. SUMMARY AND CONCLUSIONS

The three-dimensional flow field at seven planes in a hydrocyclone was determined at two different operating conditions. These flow fields were compared, and the important conclusions from these comparisons are:

- At each measurement plane, the measured tangential velocity profile exhibits the characteristics of a forced vortex at the region near the air core, and those of a free vortex in the outer portion of the flow.
- The tangential velocity is the most dominant velocity component in the studied hydrocyclone.
- The peak tangential velocity increases as the distance from the inlet region increases.
- The ratio of peak tangential velocities for different flow rates is approximately equal to the ratio of the coinciding flow rates.
- Backflows exist in the axial velocity profile in the areas near the cyclone's inlet region, but are not present in areas opposite the inlet.
- The radial velocity is the least dominant velocity component in the tested hydrocyclone.
- The flow rates calculated by integrating the axial velocity profiles agreed within 6% of the directly measured flow rates, which indicated sufficient measurement accuracy.

6. ACKNOWLDEGMENTS

This research was supported in part by the Technical Association of the Pulp and Paper Industry and the Black Clawson Company. The authors would also like to thank John Egan for his expertise and suggestions.

7. REFERENCES

Bradley, D. 1965, The Hydrocyclone, pp. 27-30, Pergamon Press, New York.

Dabir, D. 1983, Mean Velocity Measurements in a 3 Inch Hydrocyclone Using Laser Doppler Anemometry, Ph.D. Thesis, Dept. of Chem. Eng., Michigan State University.

Fontein, F.J. and Dijksman, C. 1952, Inst. Mining & Met. Symposium on Recent Developments in Mineral Dressing, p. 229.

Hsieh, K. T. and Rajamani, R. K. 1991, Mathematical Model of the Hydrocyclone Based on Physics of Fluid Flow, AIChE Journal, vol. 37, pp. 735-746.

Kelsall, D.F. 1952, A Study of the Motion of Solid Particles in a Hydraulic Cyclone, Transaction Institute of Chemical Engineering, vol. 30, No. 2, pp. 87-108.

Lilge, E.O., Fregren, T.E. and Purdy, G.R. 1957-1958, Apparent Viscosities of Heavy Media and the Driessen Cone, Trans. Inst. Min. & Metall., Lond., vol. 67, pp. 229-249.

Ohashi, H. and Maeda, S. 1958, Motion of Water in a Hydraulic Cyclone, Chem. Engng., Japan, vol. 22, p. 200.

Saito, N. and Ito, K. 1951, On the Velocity Distribution in a Simple Vortex, Geophys. Mag., Tokyo, vol. 22, p. 283.

Investigation of Internal Flows by Means of the Stereoscopic PIV Method

J. Schabacker, A. Bölcs
Laboratoire de Thermique appliquée et de Turbomachines (LTT)
Swiss Federal Institute of Technology
1015 Lausanne, Switzerland

ABSTRACT

The setup of a stereoscopic PIV system for the study of the flow characteristics in a model of an internal gas turbine coolant passage is presented. The PIV system consists of two Kodak ES1.0 cameras arranged using the stereoscopic angular displacement method. The data acquisition rate of the system is high and thus allows for the investigation of the flow in complex geometries where many measurement planes are required to obtain a comprehensive understanding of the flow phenomena. From the statistical distribution of the instantaneous velocity components, the mean velocity field and the turbulence quantities of the flow are calculated.

NOMENCLATURE

x	Cartesian coordinate in axial duct direction
y	Cartesian coordinate in cross duct direction
z	Cartesian coordinate in horizontal duct direction
U	Mean velocity component in x-direction
V	Mean velocity component in y-direction
W	Mean velocity component in z-direction
u'	Fluctuating velocity component in x-direction
v'	Fluctuating velocity component y-direction
w'	Fluctuating velocity component in z-direction
u'v',u'w'	Cartesian components of turbulent shear stress
U_b	Bulk mean-velocity
D_h	Hydraulic diameter D_h=D
M	Magnification of PIV images
d	grid wire diameter
Tu	Turbulence level
Φ	Flow variable
N_G	Number of groups

1. INTRODUCTION

In the present study, the particle-image-velocimetry (PIV) method was employed for the investigation of the flow field in a model of a stationary two-pass coolant passage. PIV was chosen for such a study because of its high data acquisition rate and the good spatial resolution of the measured flow fields. A sketch of a typical passage arrangement is shown in Figure 1. The straight sections of these coolant passages are connected by 180° bends. To enhance heat transfer, the walls are roughened by ribs or pin fins that lead to very complex flow conditions in the passage.

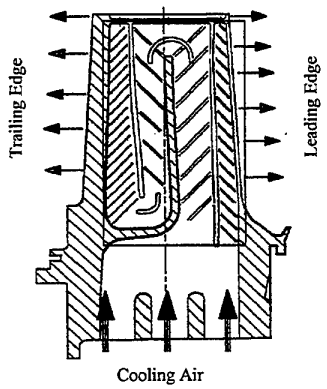


Figure 1 Internal coolant passage in a turbine blade

The measurement of this highly three-dimensional flow in the passage with a single-camera PIV system could contain substantial errors because the out-of-plane motion of a particles perpendicular to the light sheet plane produces a systematic measurement error that increases with increasing distance from the optical axis, e.g., Lourenco (1988). In principle, an error correction for the in-plane components is feasible if the out-of-plane component of the flow is known. However, Schabacker and Bölcs (1996) applied the correction to single-camera 3D PIV velocity measurements and showed that the effect of the out-of-plane motion can not be corrected completely, although the correction does improve the measurement accuracy.

This measurement error can be avoided by using a stereoscopic PIV setup. A comprehensive analysis of the translation method and an application to rotating disc flow has been given by Prasad and Adrian (1993). Westerweel and Nieuwstadt (1991) have reported performance tests on three-dimensional velocity measurements with an angular digital two-camera stereoscopic PIV system.

For the present investigation, a stereoscopic digital

PIV system that employs the angular displacement method and commercially available devices was assembled. No modifications to the cameras were made. The small amount of defocusing of the images towards the edges was found to have a minor influence and was tolerated. This system is capable of measuring simultaneously all three velocity components. Subsequently, an ensemble average of the velocity data in identical spatial windows is calculated leading to the mean and fluctuating velocity field.

2. TEST FACILITY

A sketch of the test section is shown in Figure 2. For the PIV experiments, air was chosen as the working medium. A Polytec L2F-A-1000 Aerosol Generator generates 1-3 μm oil droplets that are injected upstream of the settling chamber to guarantee a homogeneous seeding density in the test section.

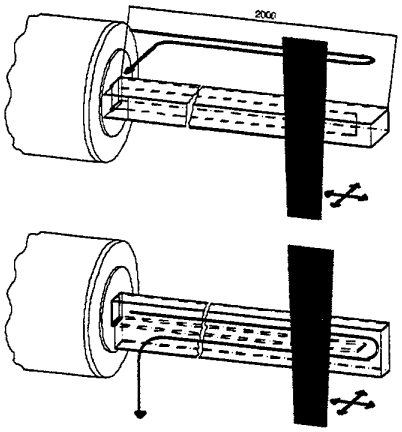


Figure 2 Sketch of the internal coolant test facility

The test rig is equipped with a model of a two-pass cooling passage of a gas turbine blade. The flow path in the downstream and upstream leg has a cross-section of 100x100 mm^2 with a corresponding hydraulic diameter D_h=100 mm and a length of $19D_h$. The test section is made of 5-mm thick glass to obtain good optical properties for the PIV experiment.

The total section including the section entrance can be turned 90° around the streamwise-axis without changing the flow conditions in the duct. This allows an easy optical access to the positions of interest for the PIV measurements.

3. THE PIV SYSTEM

A Quantel TwinsB Nd-Yag double oscillator pulsed laser provides light pulses having a maximum energy of 320 mJ at a wavelength of 532 nm. The time delay between a pair of pulses can be adjusted from 1μs to 1s with a pulse duration of 5 ns. A plano-concave lens (-30 mm focal length) combined with two plano-cylindrical lenses (76.2 and 300 mm focal length) transform the beam into a thin vertical light sheet. The complete system including laser, light sheet optics and camera is mounted on a traversing system shown in Figure 3 that allows precise positioning.

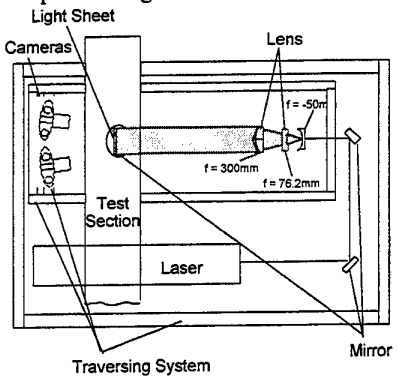


Figure 3 PIV setup

A sketch of the digital PIV system is shown in Figure 4. The system consists of two independent Kodak ES1.0 cameras each having its own PC. The ES1.0 has a CCD interline transfer sensor, which has a pixels array of 1008(H) by 1018(V) pixels. Each pixel measures nine microns square with a 60% fill factor using a microlens. The camera outputs 8-bit digital images with 256 gray levels. For PIV applications, the camera is used in a special double exposure frame triggering mode. This mode allows the capture of two images separated by a delay ranging from 2 μs to 66 ms. Nikkor 55mm micro lenses are mounted on the cameras. For a typical recording situation, the cameras are placed with an oblique angle of 5° at a distance of 0.7m from the light sheet plane. The time delay between a pair of pulses is set to 50μs.

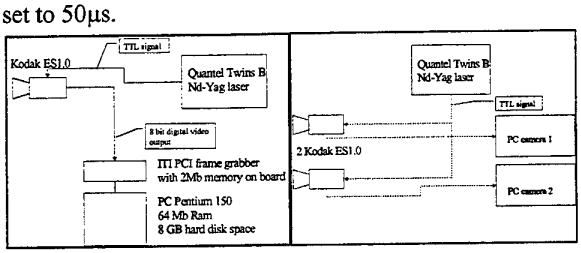


Figure 4 Digital PIV system

The PIV image acquisition starts with a signal from the laser. Two images are captured in rapid succession. This is accomplished by capturing the first image in the photo diode array, transferring this image to the CCD array and then capturing a second image in the photo diode array. The first image is transferred from the CCD to the frame grabber while the second image is being captured by the photo diode array. The second image is then transferred into the CCD array and subsequently onto the frame grabber's second image buffer. The frame grabber is an Imaging Technology PCI frame grabber with 2 MB memory onboard. The PC's are equipped

with 64 MB RAM and 8 GB hard disk space. During the PIV measurement series, 50 images are written in real time into the PC's RAM memory. Subsequently, the acquisition is stopped and the images are saved on the hard disk.

3.1 Data Reduction

The PIV recordings from the right and left camera are interrogated independently with the PIV software package VISIFLOW from AEA Technology. For the images, a cross-correlation analysis method is used with an interrogation window size of 64 by 64 pixels and 50% overlap between the interrogation windows. Each recording results in a 30 by 30 vector field of the instantaneous velocity. Usually the data contains a small number of spurious vectors (<2%). The vector field is therefore validated with predefined thresholds for the vector continuity and velocity magnitude. Vectors that do not fall within the thresholds are removed and the remaining gaps are filled by a weighted average of surrounding vectors.

From the processed vector fields, the instantaneous three-dimensional velocity fields are reconstructed. Note that the stereoscopic measurements provide the third velocity component, but even if the out-of-plane component is not required, stereoscopic recording increases the measurement accuracy because it corrects the in-plane velocity for the effects of perspective.

For angular PIV systems, where both cameras observe the light sheet from the same side, the corresponding interrogation positions for the two images in the plane of the light sheet do not match in general. Therefore, a calibration of the camera system is performed that also corrects for the distortion of the images in the lenses and the glass walls of the passage. A precision grid inserted into the field of view was used by others to find the matching points into the two images. In the present study, however, this is troublesome, since it requires opening the test section frequently. An alternative non-intrusive calibration technique was developed using the fact that both cameras record an identical particle pattern. For low particle densities, individual particles could be identified in corresponding images from the right and left camera and be used for the calibration of the camera arrangement. However, for typical particle densities in PIV images, it is difficult to find identical particles in both images. Therefore, groups of particles are correlated instead of tracking individual particles. Thus, a displacement field is processed from two corresponding images as shown in Figure 5.

The displacement vectors are arranged on a regular grid that is identical to the grid of the processed velocity vectors from the two cameras. In a subsequent step, the instantaneous three-dimensional velocity field can be reconstructed from the parallax (the apparent difference in the recorded displacements between the right and left image) between the images. For this, the velocity fields from the right and left camera are interpolated on an identical grid according to the allocation specification found from the calibration. For the interpolation, a linear algorithm is applied to the measurements.

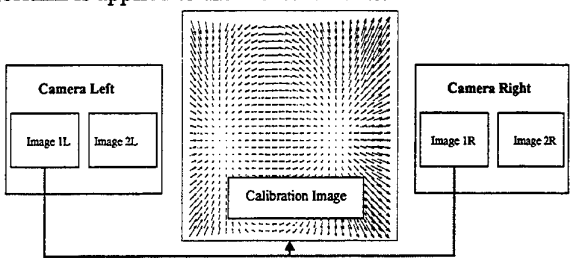


Figure 5 Calibration of the stereoscopic PIV system

For most industrial applications, the engineers are interested not only in the instantaneous flow but also more importantly in the mean velocity field and the turbulence quantities of the flow.

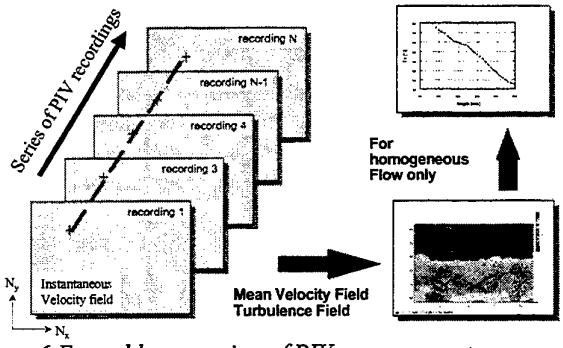


Figure 6 Ensemble averaging of PIV measurements

In order to obtain PIV measurements in this form, the statistical distribution of the velocity components is calculated in identical spatial windows in a series of instantaneous PIV measurements as illustrated in Figure 6. From these statistical distributions, the ensemble average and the statistical central moments are calculated which yield the desired mean velocity field and Reynolds stresses of the flow.

3.2 Measurement Procedure

The stereoscopic PIV method yields the 3D-velocity field within a plane of light in the flow. In order to study the 3D characteristics of the flow in a measurement volume, the volume is scanned with the light sheet as shown in Figure 7. Subsequently, for steady flow condition the 3D mean velocity field can be reconstructed from these measurements.

In the upstream and downstream leg of the passage, the measurement planes are oriented parallel to the mean flow direction. For a typical experiment, the flow in nine horizontal planes is measured, then the test section is turned and the measurements are repeated. This yields a regular grid of 9 x 9 measurement planes. In order to

give a better impression of the flow, the 9 x 9 grid is interpolated into a 30 x 30 grid. For the interpolation, an inverse distance algorithm is used. From this grid, the flow in planes that are not directly accessible by the measurements can be extracted. Due to the interpolation of the velocity data, errors can occur. This is in particular the case towards the edges of the domain. Note that these interpolated vector fields therefore should only be regarded as a qualitative representation of the velocity field. Nevertheless, they can provide a good qualitative understanding of the flow in planes that are not directly accessible.

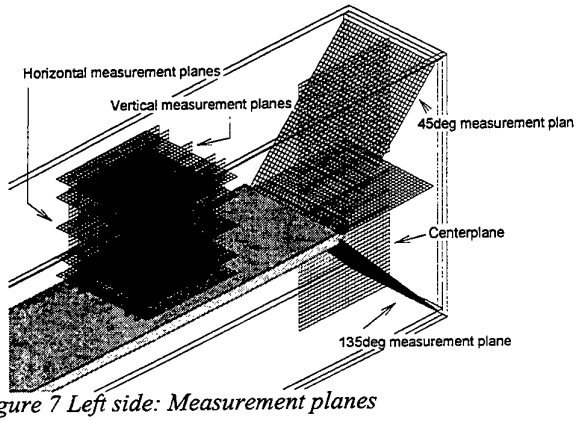


Figure 7 Left side: Measurement planes

In the bend region, measurements are carried out in planes parallel to the test section wall and in planes that are aligned perpendicular to the streamwise flow direction.

4. TURBULENCE GRID

The setup of a new measurement method requires a validation of the results in known flow conditions in order to apply the measurement system to the intended task.

In order to simulate the type of flow conditions found in turbomachinery, PIV measurements downstream of a turbulence grid were carried out. The grid was placed normal to the mean flow direction of the incoming flow. The grid had a wire diameter *d* of 0.9 mm and a mesh length (distance between grid wires) of 5 mm.

Preliminary measurements were carried out with a single-camera DPIV system in two measurement planes that were located directly downstream of a vertical grid wire and halfway between two grid wires. A sample size of 1500 images was taken to ensure a small statistical uncertainty. The contour maps of the streamwise turbulence and transverse turbulence downstream of the grid are shown in Figure 8. The flow is strongly inhomogeneous near the grid. This is due to the initially isolated wakes that develop downstream of the grid bars. With increasing distance from the grid, the wakes grow in size and eventually coalesce into a homogeneous turbulent flow. Roach 1986, stated that the flow can be considered to be homogeneous by ten mesh lengths downstream of the grid. This agrees well with the PIV measurements, where the grid influence is visible up to a distance of about x/d=60 being approximately 11 mesh lengths.

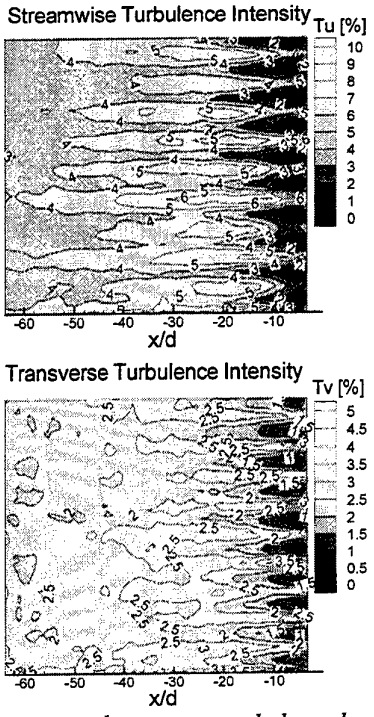


Figure 8 Streamwise and transverse turbulence level downstream of the turbulence grid (single-camera PIV measurements)

Subsequently, the turbulence field was averaged along lines of constant distance from the grid in order to smooth out the wire effect. The streamwise turbulence level decay downstream of the grid is shown in Figure 9. In the figure, the results of the measurements in planes behind a grid wire and halfway between the wires are superimposed.

The PIV images were interrogated with 32x32 pixels and 64x64 pixels interrogation window size. Figure 9a reveals that the position of the measurement plane relative to the grid strongly influences the measured turbulence decay, i.e. in the plane directly downstream the grid wire, the turbulence is higher than half-way between the wires. The grid effect diminishes up to a distance of about x/d=20 from the grid.

Roach (1986) gives a correlation for the decay of the streamwise turbulence level behind square mesh arrays of round wires as:

$$Tu = 0.8\left(\frac{x}{d}\right)^{\frac{-5}{7}}.$$

Equation 1 Turbulence decay behind a grid

In Figure 9, the turbulence decay behind the grid according to this correlation is compared with the measurements. A good agreement between measurements and calculated turbulence decay close to the grid is obtained for a 32x32 pixels interrogation window size. However, the small window size increases the uncertainty in the measurement of the instantaneous velocity field and therefore predicts the turbulence level likely too high in regions of low flow turbulence. This is particularly observable in the measurements at x/d>80. In this region, the 32x32 pixels interrogation window cannot predict turbulence intensities below 3.5%.

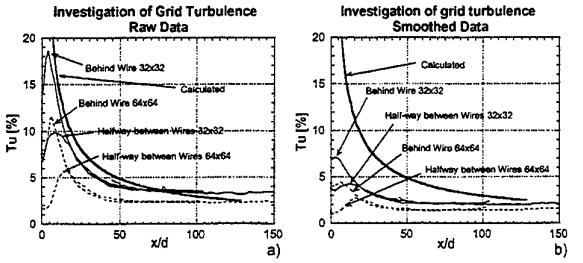


Figure 9 Streamwise turbulence level decay downstream of grid (Single-camera PIV measurements)

The interrogation of the PIV recordings with 64x64 pixels window size yields the overall prediction of lower turbulence levels. This is attributed to the increase of the interrogation window size that leads to a larger measurement volume in the flow. The velocity variations that exist in small distances over the much larger interrogation window are averaged within the corresponding measurement volume in the flow. Thus, the contribution of small-scale eddies to the predicted flow turbulence is smoothed out during the PIV evaluation process.

In order to reduce the noise in the PIV images that arises due to the quantization of the gray level distribution and the sampling process during the recording on the matrix of the CCD chip, digital smoothing of the processed velocity field can be carried out. Figure 9b shows the turbulence level that is predicted from the smoothed data. Again, the PIV images were interrogated with 32x32 pixels and 64x64 pixels window size. For the data smoothing, the default inverse exponential filter of VISIFLOW was used. As expected, the turbulence level decreases as smoothing is applied to the data leading to a very poor prediction near the grid. Further downstream, the turbulence level approaches levels of Tu=2% and Tu=1.5% for a 32x32 pixels and 64x64 pixels interrogation window, respectively. Note that for a 32x32 pixels interrogation window size and subsequent smoothing of the data, smaller turbulence intensities are predicted than for 64x64 pixels interrogation without data smoothing.

Subsequent to the single-camera measurements, stereoscopic PIV measurements were carried out downstream of the turbulence grid. The streamwise turbulence level decay measured by the stereoscopic PIV measurements is shown in Figure 10.

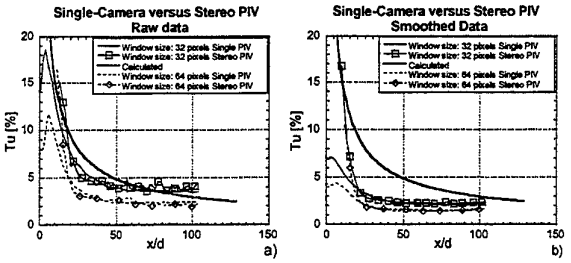


Figure 10 Decay of streamwise turbulence level obtained from single-camera and stereoscopic PIV measurements

For a better comparison, the single-camera PIV measurements are superimposed in the figure. The agreement between the single-camera measurements and the stereoscopic PIV measurements is good. Almost identical turbulence levels are obtained for x/d>20.

Near the grid, the stereoscopic PIV measurements predict higher turbulence and the first valid measurement point is located further downstream of the grid with regard to the single-camera measurements. The discrepancies are attributed to the optical noise in the stereoscopic PIV measurements near the grid. This reveals one major difficulty of the stereoscopic method in comparison to the classical single-camera PIV method: due to the oblique viewing orientation of the two cameras, the stereoscopic PIV method requires larger optical access to the measurement section. This implies that objects located in the view path oblique to the measurement plane that would not have been seen by a single-camera system can hide the measurement plane in the case of stereoscopic measurements. Moreover, the area behind the light sheet plane that is seen from the two cameras is larger and therefore can lead to an increase of the optical noise in the measurements.

The ratio between in-plane fluctuating velocity component u' and out-of-plane fluctuating velocity component w', is presented in Figure 11a. Roach (1987) gives a mean value for the ratio of the fluctuating velocity components (u'^2/w'^2) of 1.25. Thus, the flow behind the grid is not isotropic and the streamwise component u'^2 is larger than its normal counterpart w'^2. From the stereoscopic measurements, one obtains ratios between 0.03 and 0.1 depending on the interrogation window size and the postprocessing of the data. From this, one can conclude that the stereoscopic measurements overpredict the out-of-plane fluctuating velocity. This is attributed to the higher measurement uncertainty of the out-of-plane velocity component. Note that near the grid the ratio decreases due to the influence of optical noise in this region that increases the measurement uncertainty of the out-of-plane velocity component.

As one increases the interrogation window size, the measurement uncertainty of the out-of-plane velocity component decreases yielding a larger ratio of (u'^2/w'^2). However, even with a window size of 64 x 64 pixels and a subsequent smoothing, the ratio does not reach values of 1. It is therefore assumed that for flows with small turbulence levels, the stereoscopic PIV measurements likely overpredict the fluctuating out-of-plane component.

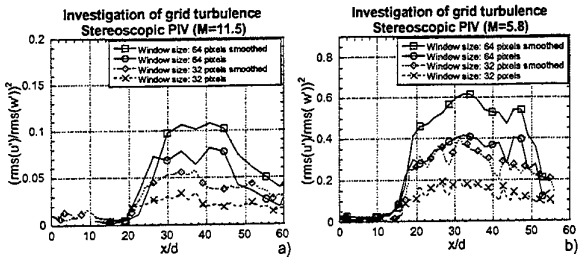


Figure 11 Ratio between in-plane u'^2 and out-of-plane w'^2 components (M is the image magnification)

In order to increase the accuracy of the out-of-plane fluctuating velocity component, the distance between the cameras and the light sheet plane can be reduced. This improves the area ratio between particle image size and CCD matrix pixel size and therefore decreases the sampling and digitalization errors of the imager. A similar improvement could be obtained by using a higher resolution CCD camera, which, however, is currently commercially not available. In Figure 11b, the $(u'/w')^2$ ratios for an image magnification of M=5.8 are shown. The figure reveals the significant improvement of the accuracy of the out-of-plane component for the smaller image magnification. Like the M=11.5 case, the highest ratio is obtained for a 64 pixels windows size with subsequently smoothing of the data. The peak ratio of $(u'/w')^2$ increases from 0.1 for M=11.5 to 0.6 for M=5.8.

To this point, only the ratio between $u^{2'}$ and $w^{2'}$ that was obtained from identical processed images was discussed. However, the single-camera PIV measurements behind the grid, shown in Figure 9, illustrate that the in-plane fluctuating velocity components should be obtained from the raw data base in order to achieve a good prediction of high turbulence levels, i.e. no smoothing of the velocity fields has to be performed. On the other hand, for the stereoscopic grid measurements it was shown that the out-of-plane fluctuating velocity component is better predicted from smoothed velocity data. The best turbulence prediction by the stereoscopic PIV measurements can therefore be expected from the combination of the raw data for the in-plane fluctuating velocity components and the smoothed data for the out-of-plane component. The $(u'/w)^2$ ratios that were obtained from such a hybrid approach are shown in Figure 12.

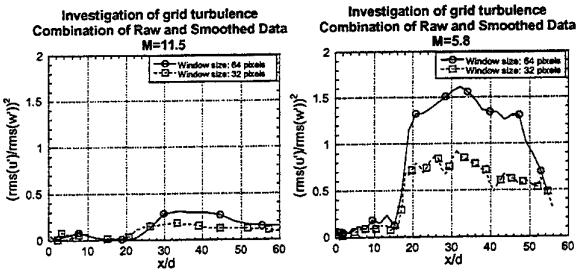


Figure 12 Ratios between the in-plane u'^2 and out-of-plane w'^2 components obtained from a combination of raw and smoothed data (M is the image magnification)

For M=11.5 the ratio increases to 0.3 for 64 pixels windows size. For M=5.8, values of $(u'/w')^2$ larger than 1 are obtained by the measurements. This indicates that sufficient measurement accuracy for the out-of-plane velocity component can be achieved with this image magnification.

Thus, from the previously presented study the following conclusions can be drawn:

- The in-plane mean velocities and fluctuating velocities as well as the out-of-plane mean velocity field should be derived from an evaluation of the images without prior smoothing of the data.
- The out-of-plane fluctuating velocity component should be obtained from an evaluation of the images after smoothing the data in order to decrease the measurement uncertainty of the out-of-plane components.

Consequently, the images have to be interrogated twice. This doubles the interrogation time but also leads to a better accuracy of the results and is therefore strongly recommended for the stereoscopic measurements. For stereoscopic PIV measurements that are evaluated according to the proposed procedure, a good measurement accuracy of the three-dimensional turbulence field can be expected in highly turbulent flow.

5. MEASUREMENT UNCERTAINTY

In order to study the convergence of the PIV statistics and to get an idea about the number of samples that are required to obtain the flow data with certain accuracy, an experimental study was conducted with the stereoscopic PIV system. The PIV measurements were carried out in the bend region of the passage, thus in a highly three-dimensional and turbulent flow region. To assess the measurement uncertainty, the result that was obtained from the statistical investigation of the entire sample size was used as an estimator for the respective flow variable. Subsequently, the same flow variables were recalculated from groups of smaller sample sizes. The fractional error of these sample values was calculated according to:

$$\frac{\Delta\Phi_{i,No.Samples}}{\Phi_{i,Max}} = \frac{\left|\frac{1}{N_G}\sum_{i=1}^{N_G}\left|\Phi_{i,No.Samples}\right| - \left|\Phi_{i,Max}\right|\right|}{\left|\Phi_{i,Max}\right|}$$

Equation 2Definition of fractional error

where $\Phi_{i,Max}$ is the flow variable obtained from the entire sample, and $\Phi_{i,No.Samples}$ and N_G are the flow variable and number of groups that were calculated from smaller sub-samples.

The flow characteristic is shown in Figure 13. The flow in the measurement position is highly three-dimensional. Note that the out-of-plane velocity component W is approximately three-times higher than the corresponding in-plane velocity U. The turbulent character of the flow is revealed in the turbulence level that reaches values between 10% and 30% of the reference velocity U_b.

For this investigation, 400 samples corresponding to 800 cross-correlated PIV images were taken into account for the calculation of the estimators for the flow variables. Subsequently, groups of smaller samples sizes were created and the fractional error associated with these groups was calculated according to Equation 2.

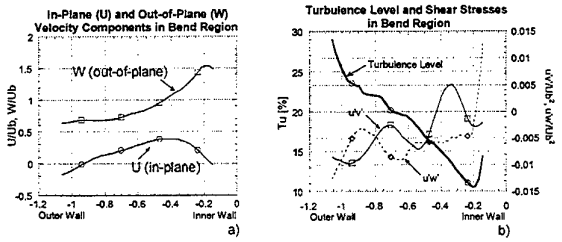


Figure 13 In-plane and out-of-plane velocity components and turbulence quantities

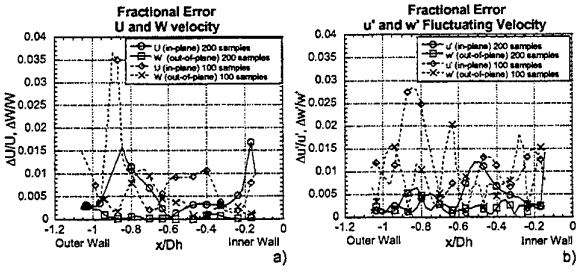


Figure 14 Fractional error in the measurements of the fluctuating velocity components

The fractional error in the measurement of the out-of-plane mean velocity as shown in Figure 14a, is relatively low if one considers the high level of turbulence and the rather low number of 200 samples. For the in-plane U velocity component higher fractional errors occur. This is attributed to the smaller magnitude of the U velocity component in comparison to the W component. Nevertheless, the fractional error for both velocity values remains below 1.5% for a sample size larger than 200 samples. A similar picture is obtained for the fractional error in the measurement of the u' and w' fluctuating velocities and the turbulent kinetic energy of the flow shown in Figure 14b and Figure 15a, respectively. For these quantities, a fractional error below 2% can be expected for a sample size of more than 200 samples.

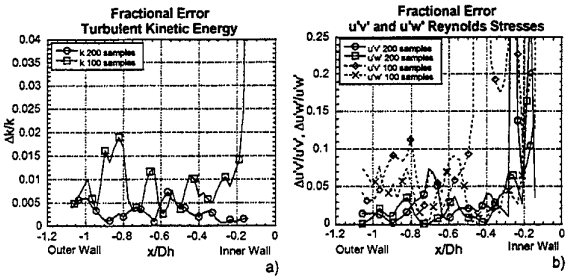


Figure 15 Fractional error in the measurements of the turbulent kinetic energy and shear stresses

The measurement of the Reynolds stresses u'v' and u'w' shown Figure 15b, is associated with a higher fractional error. For these flow variables, a fractional error below 10% can be expected for more than 200 samples in regions where sufficiently high shear stresses occur in Figure 13b.

6. APPLICATION OF THE STEREOSCOPIC PIV SYSTEM

Some examples of measurements conducted in the coolant passages will be presented here in order to demonstrate the performance of the stereoscopic PIV system. In Figure 16(left), the flow in the centerplane of the coolant passage without rib arrangement is presented. The figure was obtained from a superposition of different measurement positions each having a square measuring area of 1 hydraulic diameter. The secondary flow downstream of the bend is shown in Figure 16(right). For this figure horizontal and vertical measurement planes were combined as shown in Figure 7. Figure 17(left) presents the secondary flow field that develops in the bend region of a coolant passage with 90° rib arrangement. The corresponding streamwise (out-of-plane) velocity component is shown in Figure 17(right).

7. CONCLUSIONS

The setup of a stereoscopic PIV system was presented. From the application of this system to the flow behind a grid, conclusions were drawn regarding the interrogation of stereoscopic PIV recordings. The study of the measurement error revealed that already relatively small sample sizes are sufficient to measure the mean velocity component with a reasonable high accuracy. The PIV measurement technique was shown to be capable of obtaining velocity measurements with a high spatial resolution. These measurements are especially useful for

the validation of CFD simulations.

REFERENCES

L.M. Lourenco, 1988, "Some Comments on Particle Image Displacement Velocimetry," Von Karman Institute for Fluid Dynamics, Lecture Series 1988-06

A.K Prasad, R.J Adrian, 1993, "Stereoscopic Particle Image Velocimetry Applied to Liquid Flows," Experiments in Fluids, Vol. 15, pp. 49-60

P.E. Roach 1987
The generation of nearly isotropic turbulence by means of grids
Heat and Fluid Flow, Vol. 8, June

J. Schabacker, A. Bölcs, 1996, "Investigation of Turbulent Flow by Means of the PIV Method," 13th Symposium on Measuring Techniques for Transonic and Supersonic Flows in Cascades and Turbomachines, Zurich, Switzerland, September 5-6

J. Westerweel, F. T. Nieuwstadt, 1991, "Performance Tests on 3-Dimensional Velocity Measurements with a Two-Camera Digital Particle-Image-Velocimeter," Laser Anemometry, Vol. 1, pp. 349–355

ACKNOWLEDGEMENTS

This study was supported by ABB Corporate Research, Ltd., Switzerland.

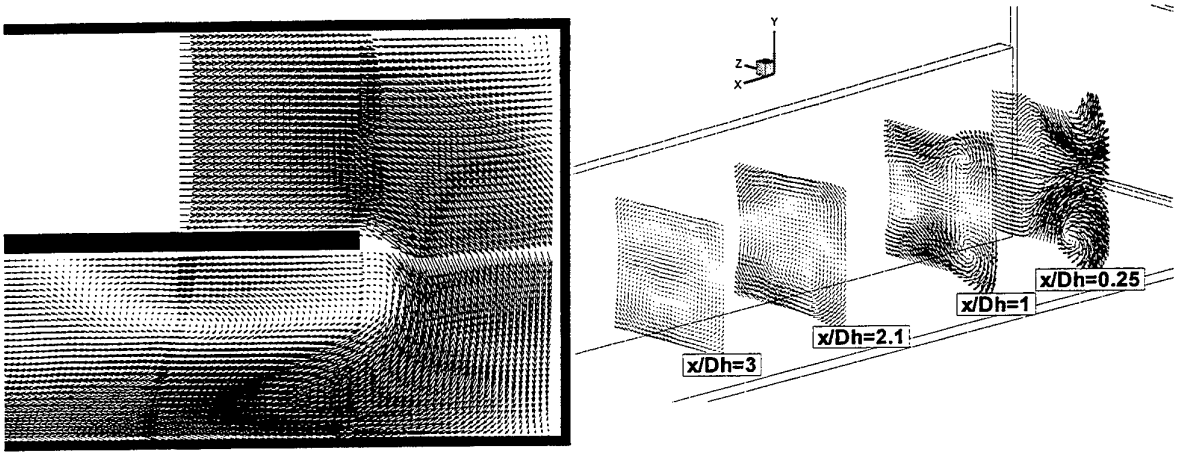


Figure 16 Flow field in the centerplane of the coolant passage (left) and downstream of the bend (right) at a flow Reynolds number of 50.000 (The figure on the right side was obtained from the interpolation of measurement planes as shown in Figure 7)

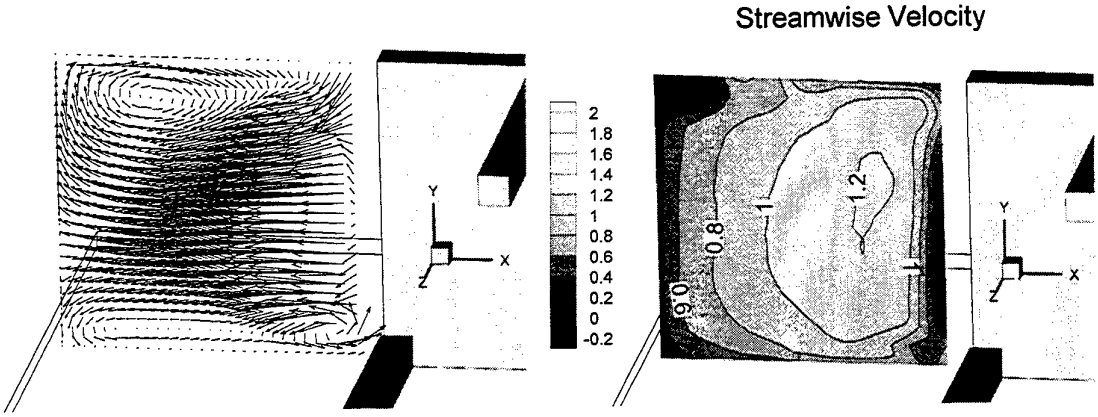


Figure 17 Flow field in the 90° cross-section plane of the coolant passage with 90° rib arrangement at a flow Reynolds number of 50.000. Vector map (left) and streamwise (out-of-plane) velocity component obtained from stereoscopic PIV measurements (right)

EFFECTS OF CENTREBODY ROTATION ON THE LAMINAR FLOW OF A SHEAR-THINNING LIQUID THROUGH AN ECCENTRIC ANNULUS

M P Escudier and I W Gouldson
Department of Engineering; Mechanical Engineering
University of Liverpool, Liverpool, L69 3GH

ABSTRACT

The paper is concerned with fully developed laminar flow through an annulus of an aqueous solution of a mixture of xanthan gum and CMC which is a shear thinning liquid with power-law index – 0.36. For a highly eccentred annulus ($\varepsilon = 0.8$) the effect of rotation is to increase the axial velocity within the narrow gap and increase velocity gradients in the vicinity of the centrebody. Recirculation occurs for eccentricities of both 0.5 and 0.8, and occupies the major part of the annulus in the latter case. The situation is more complex than for a Newtonian fluid because the tangential velocity is coupled with the axial flow.

1. INTRODUCTION

The work discussed here is part of a programme of research, motivated by drilling hydraulics, in which the flow of both Newtonian and non-Newtonian liquids is being investigated in pipes and annuli. The flow of a drilling fluid (mud) in the annulus between the drillpipe and wellbore wall during the drilling of oil and gas wells represents the rare example of a laminar flow with industrial relevance (Ooms and Kampman-Reinhartz (1996)), in this paper therefore we limit attention to laminar flow. In an earlier paper (Escudier and Gouldson (1997)) we presented experimental data for the fully developed laminar flow of a Newtonian liquid in an annulus including the effects of centrebody rotation and eccentricity. A simplifying feature in that situation is that the tangential/radial flow is decoupled from the axial flow, and may be treated separately, though the reverse is not true and the axial flow is influenced by rotation. In contrast, for a non-Newtonian fluid all three components of velocity are coupled. The present results consist of axial and tangential velocity measurements for the fully-developed laminar flow of a non-Newtonian liquid in the same flow geometry as for the Newtonian fluid.

Whilst there is an extensive literature for laminar flow of a Newtonian fluid in annular geometries, for non-Newtonian liquids relatively little work has been reported: Prasanth and Shenoy (1992) and Dostal et al (1993) provide numerical solutions for the helical flow of a power-law fluid through a concentric annulus; Mitsuishi and Aoyagi (1973) considered the flow of a Sutterby fluid through an eccentric annulus; HoTung et al (1993) investigated the effect of polymer additive on the flow in an eccentric annulus in the absence of bulk flow and Bakhtiyarov and Siginer (1995) investigated the behaviour of linear fluidity fluids in a similar situation. Most previous experimental work on the combined effects of eccentricity and rotation for non-Newtonian fluid flow has been concerned with the transport of drilled cuttings (see e.g. Thomas et al (1992)). Theoretical work on the combined problem is limited to the computational study of power-law fluids reported by Lockett (1992).

2. EXPERIMENTAL CONDITIONS

Measurements were carried out for flow through a 5.8 m long pipe consisting of six modules of precision-bore glass tubing (100.4 mm ID) with a stainless steel centrebody (50.8 mm OD), i.e. an annulus with radius ratio $\kappa = 0.506$. The glass tubing was supported on linear bearings which permitted the geometry to be eccentered between $\varepsilon = 0$ and ε near 1. A DC motor and gearbox allowed the centrebody to be rotated at speeds up to 126 rpm, monitored by an optical encoder with a resolution of 0.1 rpm. Bulk flow through the annulus was provided by a progressive cavity Mono pump and monitored by a Fischer and Porter electromagnetic flowmeter. A

Dantec fibreflow LDA system with a measuring volume length (in water) of 0.19 mm was used to measure the radial variation of the axial and tangential velocities. For the most part, velocity profiles were taken in the four orthogonal planes shown in Figure 1 (Sectors A, B, C & D) for an eccentricity of $\varepsilon = 0.8$. The bulk axial flow velocity U was nominally 0.4 m/s whilst the rotational speeds of the centrebody N were 40 rpm and 126 rpm. For comparison, velocity measurements are included for $\varepsilon = 0$, N = 0 and U = 0. In addition, to allow the construction of streamline maps in the absence of bulk flow, measurements were made of the tangential velocity along radii at 30° intervals for $\varepsilon = 0.5$ and 0.8 with N = 40 rpm.

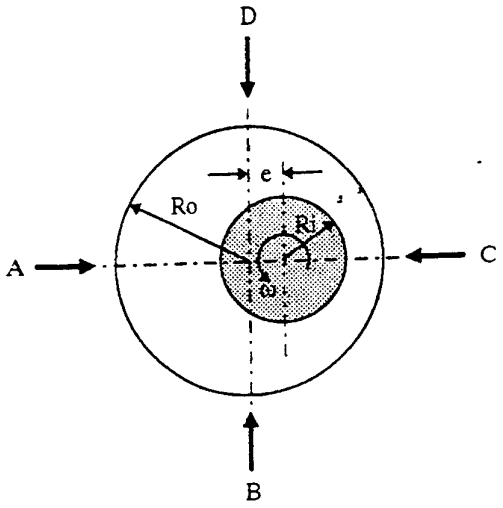


Figure 1 Eccentric geometry and circumferential locations at which velocity profiles were taken

The test fluid was an 0.1%/0.1% w/w blend of xanthan gum (XG) and carboxymethylcellulose (CMC). To allow assessment of the Reynolds and Taylor numbers, viscometric data pertaining to each individual profile were measured using a Bohlin VOR controlled-strain rheometer. As can be seen from the typical data shown in Figure 2, the Cross model provides an accurate representation of the flow curve for the XG/CMC blend

$$\text{i.e. } \frac{\mu-\mu_\infty}{\mu_0-\mu_\infty} = \frac{1}{1+(\lambda\dot{\gamma})^n}$$

with μ_0 = 0.078 Pa.s, μ_∞ = 0.00204 Pa.s, λ = 0.933s and n = 0.524. The viscometric data are also well fitted by a power law i.e. $\mu = C\dot{\gamma}^m$ with m = 0.356 and C = 0.045 Pa.s$^{0.644}$.

The viscosity used to define a Reynolds number for each flow (U ≠ 0) corresponds to a shear stress τ such that the measured pressure drop Δp over a length L is given by

$$\tau = \frac{\Delta p.d}{2L}.$$

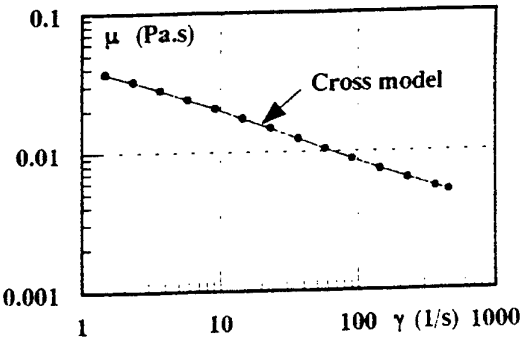


Figure 2 Viscometric data for 0.1% XG/0.1% CMC

For cases with no bulk flow, an effective viscosity has been determined corresponding to a shear rate given by

$$\dot{\gamma} = \frac{2\omega\left(1-\kappa^{\frac{2}{n}}\right)^{-1}}{n}$$

i.e. the shear rate at the inner cylinder for a power-law fluid in a concentric annulus.

3. EXPERIMENTAL RESULTS

The velocity profiles in Figure 3 are for axial flow in both the concentric and eccentric annulus geometries in the absence of rotation. The flattening of the profile for the concentric case corresponds to the usual behaviour for a shear-thinning fluid when compared to the theoretical result for a Newtonian fluid

$$\frac{u}{U} = \frac{2[1-(r/R_O)^2-(1-\kappa^2)\ln(r/R_O)/\ln\kappa]}{(1+\kappa^2)+(1-\kappa^2)/\ln\kappa}$$

consistent with the earlier results of Escudier and Gouldson (1995) and also Nouri and Whitelaw (1993). The numerical calculations of Manglik and Fang (1995) for a Newtonian fluid are used as the basis of comparison for the eccentric case. Although ideally the flow should be symmetrical about A, C, the measurements show a slight discrepancy between sectors B and D. The most significant difference

compared with the calculated profiles of Manglik and Fang (1995) for a Newtonian fluid is the much steeper velocity gradients in the vicinity of the inner cylinder ($y/\delta = 1$) i.e. the profile maxima are skewed towards the inner cylinder. This behaviour is consistent with the reduced viscosity associated with the high shear rate in the vicinity of the highly curved surface of the inner cylinder.

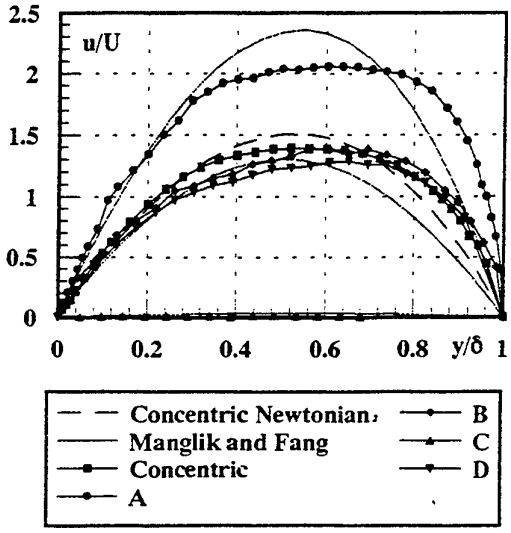


Figure 3 Axial velocity profiles without rotation, Re = 1500, $\varepsilon = 0$ and $\varepsilon = 0.8$. Concentric Newtonian - Manglik and Fang, ■ concentric, ● Profile A, ◆ Profile B, ▲ Profile C, ▼ Profile D

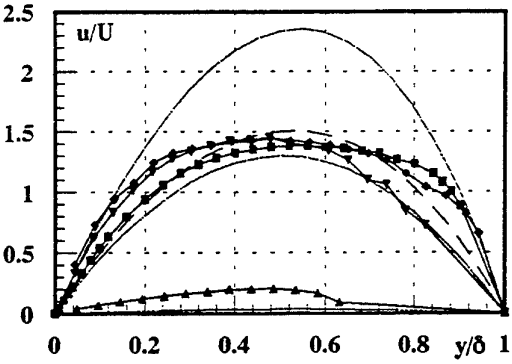


Figure 4 Axial velocity profiles, Ta = 2220 (40 rpm), Re = 1500, $\varepsilon = 0$ and $\varepsilon = 0.8$.

The addition of a rotation speed of 40 rpm (Figure 4) causes the locations of the peak velocities of opposing profiles B and D to shift towards the outer wall but for the magnitudes to remain at values consistent with those without imposed rotation. An increase in rotation speed to 126 rpm (Figure 5) results in a marked increase in velocity in the widening gap (Profile D) with a peak velocity in this quadrant equal to that for the wide gap (Profile A). As with a Newtonian fluid (Escudier and Gouldson, 1997), there is an increase in the velocity in the narrow gap (Profile C) and a reduction in the wide gap velocity (Profile A) as rotation speed is increased. However, for the non-Newtonian liquid the maximum velocity in the narrow gap shows a far greater increase due to rotation than was found for a Newtonian fluid: the data shown in Figure 6 reveal approximately a 50 fold increase between 0 rpm and 126 rpm compared with a 30% increase for a Newtonian fluid. This difference is also attributed to the decreased viscosity associated with the highly sheared flow in the narrow gap. It is apparent that the rate of increase of this maximum velocity decreases as the rotation speed increases, suggesting that at higher rotation speeds the maximum velocity is likely to reach an upper limit.

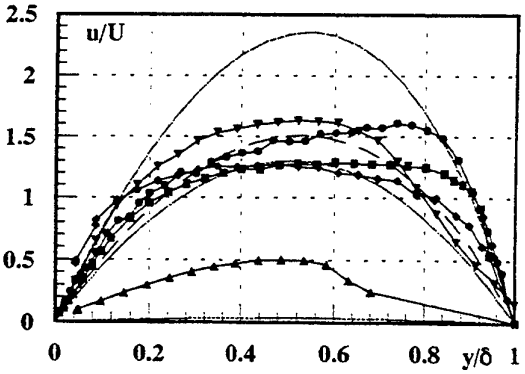


Figure 5 Axial velocity profiles, Ta = 2.5×10^5 (126 rpm), Re = 1210, $\varepsilon = 0$ and Ta = 9.4×10^5 (126 rpm), Re = 1780, $\varepsilon = 0.8$

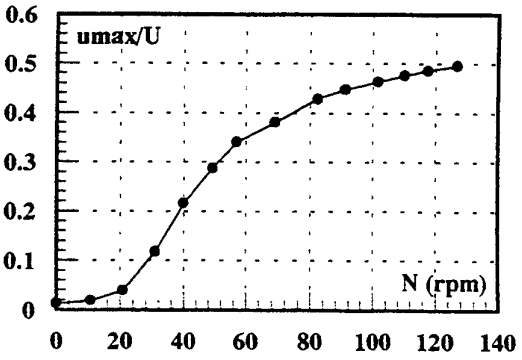


Figure 6 Maximum axial velocity in narrow gap (Profile C), Re = 1400-1660

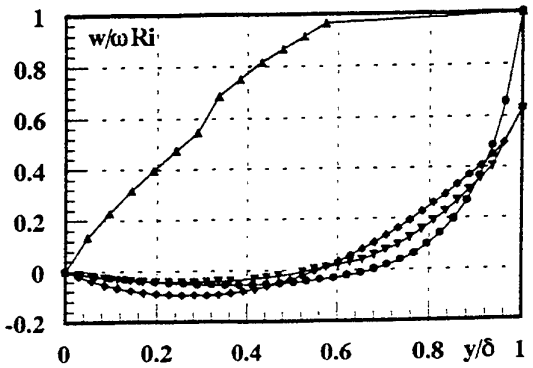


Figure 7 Tangential velocity profiles, Ta = 2220, Re = 0, ε = 0.8

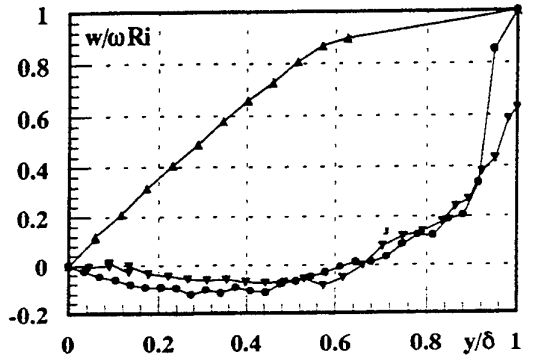


Figure 8 Tangential velocity profiles, Ta = 2220, Re = 1590, ε = 0.8

An imposed bulk flow influences the tangential velocity profiles generated by rotation (Figures 7, 8 and 9) in a number of ways. Both the extent and the magnitude of the recirculation show an increase (Figures 8 and 9) compared with rotational flow alone (Figure 7). In contrast, the velocities in the narrow gap are reduced by the addition of axial flow. The normalised velocities are reduced again by an increase in rotation speed from 40 to 126 rpm (Figure 9). The profile in the narrowing gap (Profile B) shows an increase in velocity but a reduction in the radial size of the region of re-circulation close to the centrebody with the addition of bulk axial flow for both rotation speeds. In the widening gap (Profile D), both the extent of the zone of re-circulation increases and also the magnitude of the velocities show an increase with imposed axial velocity, whilst an increase in rotation speed for the combined flow reduces the re-circulation magnitude.

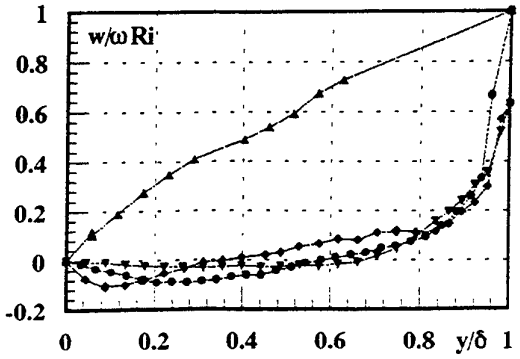


Figure 9 Tangential velocity profiles, Ta = 2.5 x 10^5, Re = 1210, ε = 0 and Ta = 8.9 x 10^5, Re = 1700, ε = 0.8

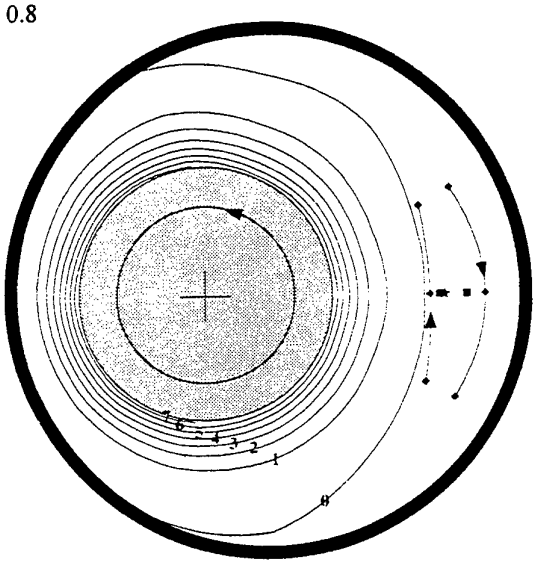


Figure 10 Streamline plots, Ta = 2220, Re = 0, ε = 0.5

Contour	$\Psi/\omega R_I(R_O-R_I)$	Contour	$\Psi/\omega R_I(R_O-R_I)$
0	0	6	0.227
1	0.0387	7	0.265
2	0.0758	◆	-0.00189
3	0.114	■	-0.00379
4	0.152	★	-0.00618
5	0.189		

The normalised stream function contours shown in Figures 10 and 11 are generated from twelve velocity profiles taken at 30° intervals with rotation at 40 rpm and no axial flow for two eccentricities (ε=0.5 and ε=0.8). The stream function is defined to be zero on the outer wall of the annulus. For comparison, the computed streamlines for a Newtonian fluid are shown in Figures 12 and 13. For the computed streamlines the stream function is defined to be zero on the outer wall and one on the surface of the inner cylinder. To make a direct comparison with the results for the non-Newtonian liquid, the values

shown in Figure 12 should be multiplied by 0.296 and those of Figure 13 by 0.130. As for a Newtonian fluid, there is a strong increase in the magnitude of the recirculation when ε is increased from 0.5 to 0.8: a maximum recirculating stream function 2.3% of that of the stream function at the centrebody for ε=0.5 in contrast to 48% for ε=0.8. The recirculation for ε=0.8 occupies about 75% of the annular space leaving only a small region to transport fluid in the direction of rotation.

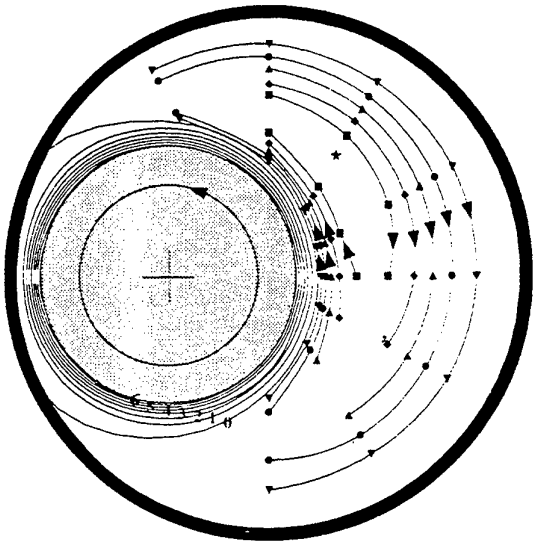


Figure 11 Streamline plots, Ta = 2220, Re = 0, ε = 0.8

Contour	$\Psi/\omega R_I(R_O-R_I)$	Contour	$\Psi/\omega R_I(R_O-R_I)$
0	0	▼	-0.00947
1	0.0189	●	-0.00189
2	0.0379	▲	-0.00284
3	0.0568	◆	-0.0379
4	0.0758	■	-0.0474
5	0.0947	★	-0.0549
6	0.114		

Resistance to flow in the rotation direction created by eccentering the geometry leads to a decrease azimuthal fluid transport (i.e. pumping) as the annulus is eccentered: as seen in Figure 14, the maximum stream function decreases monotonically with eccentricity.

4. CONCLUSIONS

There is a large effect of rotation on the axial velocity profile for the flow of a shear-thinning liquid in an eccentered annular geometry (ε=0.8). The maximum velocity in the smallest gap increases by a factor of 50 at the highest rotation speed, compared

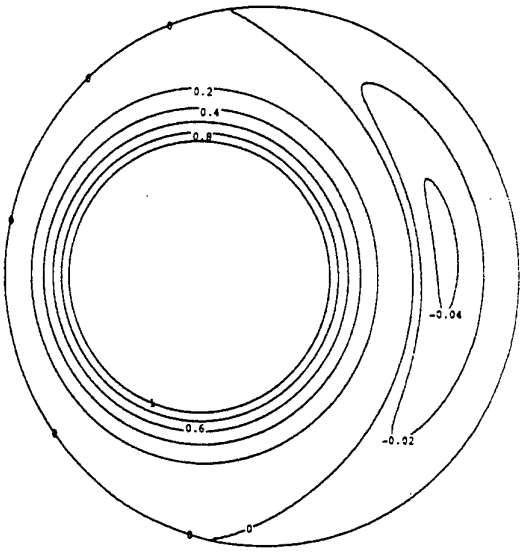


Figure 12 Computed streamlines for Newtonian fluid. Ta = 2220, ε=0.5

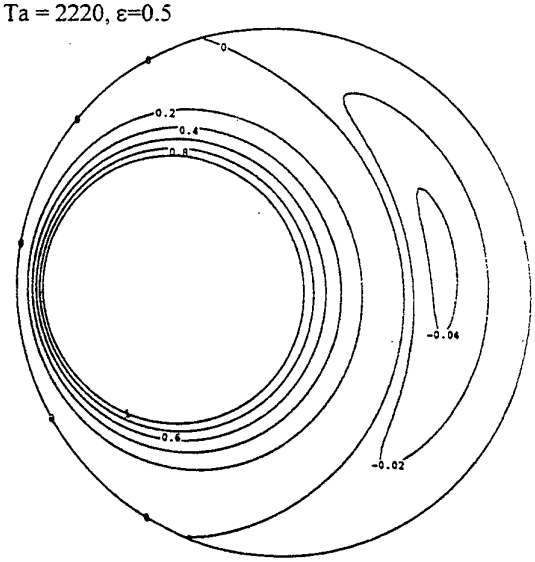


Figure 13 Computed streamlines for Newtonian fluid, Ta = 2220, ε=0.8

with an increase of 30% for a Newtonian fluid subjected to the same rotation speed.

The addition of bulk flow has no effect on the tangential velocity of a Newtonian fluid because it is de-coupled from the axial flow. Due to the shear-thinning nature of the non-Newtonian liquid, the tangential and axial velocity profiles are strongly coupled.

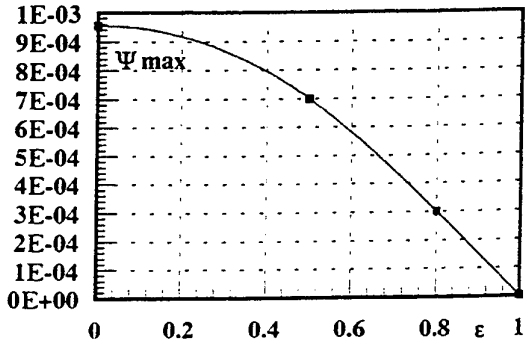


Figure 14 Variation of maximum stream function with eccentricity, Ta = 2220, Re = 0

5. NOMENCLATURE AND DEFINITIONS

d	mean annular gap width R_O-R_I (m)
e	displacement of centrebody axis from outer pipe axis (m)
L	axial length (m)
n	power-law index
R_I	outer radius of centrebody (m)
R_O	inner radius of outer tube (m)
Re	bulk axial Reynolds number $2\rho Ud/\mu_E$
Ta	Taylor number $(\rho\omega/\mu_E)^2 R_I d^3$
u	axial component of velocity (m/s)
u_{MAX}	peak value of u in a given sector of the annulus (m/s)
U	bulk axial velocity (m/s)
w	tangential component of velocity (m/s)
y	distance from inner wall of outer tube (m)
δ	gap width (A, B, C or D) (m)
Δp	pressure drop over a length L (Pa)
ε	eccentricity e/d
κ	radius ratio R_I/R_O
μ_E	effective dynamic viscosity of fluid (Pa.s)
ψ	stream function (m^2/s)
ρ	fluid density (kg/m^3)
ω	angular velocity of centrebody (rad/s)

ACKNOWLEDGEMENTS

The authors gratefully acknowledge the financial support of EPSRC/MTD (research grant GR/F87813) and Shell Research BV. Figures 12 and 13 were prepared by Professor F T Pinho, University of Porto.

REFERENCES

Bakhtiyarov, S. & Siginer, D.A. 1995, Flow of linear fluidity fluids in eccentric annuli. Developments and applications of non-Newtonian flows, ASME FED-231/MD-66, pp 135-140.

Dostal, M., Zitny, R., Sestak, J. & Houska, M. 1993, Helical flow of power-law fluids, AIChE J., Vol. 39, No. 1, pp 189-192.

Escudier, M.P. & Gouldson, I.W. 1995, Concentric annular flow with centrebody rotation of a Newtonian and a shear-thinning liquid, Int. J. Ht and Fluid Flow, Vol. 16, pp 156-162.

Escudier, M.P. & Gouldson, I.W. 1997, Effects of centrebody rotation on laminar flow through an eccentric annulus, Proc. Eighth International Symposium on Applications of Laser Techniques to Fluid Mechanics, Lisbon, Springer Eds R.J. Adrian, D.F.G. Durao, F. Durst, M.V. Heitor, M. Maeda and J.H. Whitelaw.

HoTung, J.N., Kleis, S.J. & VanArsdale, W.E. 1995, The effect of polymer on azimuthal velocity profiles in an eccentric cylinder apparatus, ASME AMD-175, pp 65-70.

Lockett, T.J. 1992, Numerical simulation of inelastic non-Newtonian fluid flows in annuli, PhD Thesis, University of London, Imperial College.

Manglik, R.M. & Fang, P.P. 1995, Effects of eccentricity and thermal boundary conditions on laminar and fully developed flow in annular ducts. Int. J. Ht. and Fluid Flow, Vol. 16, pp 298-306.

Ooms, G. & Kampman-Reinhartz, B.E. 1996, Influence of drillpipe rotation and eccentricity on pressure drop over borehole during drilling, European J. Mechanics B/Fluids, Vol. 15, pp 695-711.

Mitsuishi, N. & Aoyagi, Y. 1973, Non-Newtonian fluid flow in an eccentric annulus, J. ChE Japan, Vol. 6, No. 5, pp 402-408.

Nouri, J.M. & Whitelaw, J.H. 1993, Flow of Newtonian and non-Newtonian fluids in a concentric annulus with rotation of the inner cylinder, ASME Jnl. Fluids Eng., Vol. 116, pp 821-827.

Prasanth, N. & Shenoy, U.V. 1992, Poiseuille flow of a power-law fluid between coaxial cylinders, J.App.Poly.Sci., Vol. 46, pp 1189-1194.

Thomas, R.P., Azar, J.J. & Becker, T.E. 1982, Drillpipe eccentricity effect on drilled cuttings behaviour in vertical wellbores, J.Pet.Tech., pp 1929-1937.

ENERGY LOSSES ON A 90° TEE JUNCTION

R. Maia[1], F. T. Pinho[2], M. F. Proença[1] and A. Schulte[3]

[1] Department of Civil Engineering, Faculdade de Engenharia, Universidade do Porto, Portugal
[2] Department of Mechanical Engineering, Faculdade de Engenharia, Universidade do Porto, Portugal
[3] INEGI- Instituto de Engenharia Mecânica e Gestão Industrial, Portugal

ABSTRACT

The flow in a 90° tee junction with sharp edges is investigated in detail by means of LDA techniques for an inlet Reynolds number of 32 000 and a flow rate ratio of 50%. A strong recirculation zone was found attached to the upstream wall of the branch pipe and the shear layer that formed in the middle of the pipe was responsible for the highest levels of turbulence. No separation was detected in the straight outlet pipe. Mean flow measurements in a similar tee with a rounded edge at the bifurcation showed a shorter, thinner and weaker recirculation bubble, which suggests that a lower loss coefficient will be measured.

1. INTRODUCTION

The flow in pipe network systems is of great engineering importance due to its widespread industrial applications as in fluid transport and heating and its proper design requires the knowledge of pressure losses in pipes, as well as fittings and accessories. As far as pressure losses in straight pipes are concerned there is an established knowledge in the literature, except for cases involving new fluids of non-Newtonian characteristics (Gyr and Bewersdorff, 1995). For pressure losses in fittings and accessories there is also a wide range of information available in the literature (Idel'cik, 1986 and Miller, 1986), but the accuracy of the results is not so high. In fact, (1) most of the data were obtained in the early half of the century, (2) there is lack of data for some flow configurations and (3) the energy loss coefficients not always follow a consistent definition.

One of the more complex accessories is the bifurcation and the present work is aimed at investigating the flow in a 90° tee junction. The first systematic experimental work in this geometry was carried out in Munich by Vogel (1928). Gardel (1957) extended the analysis to include the effects of area ratio and curvature of the junction. Also, Boldy's (1970) work and Ito and Imai's (1973) systematic experimental study on the effect of rounding the junction corner for a 90° tee should be emphasised. Their work is on the basis of the energy loss coefficient values for a tee proposed by the British Hydromechanics Research Association (Miller, 1986). Most of these works are quoted throughout this paper. Although not explicitly referenced, most recent research on bifurcating flows aiming at two-phase fluids as well as biomechanical systems, such as the human and animal circulatory system, must also be referred.

The project of more energy efficient systems requires the optimisation in the design of fluid transport networks and this is the ultimate goal of the present work. In particular, this paper is part of a research project aimed at investigating the effect of geometrical changes on the energetic performance of 90° flow bifurcations operating with both Newtonian and non-Newtonian fluids. The project follows previous work by Maia (1992), who concluded that the traditional pressure field characterisation is no longer enough to improve the design of the pipe accessories, but requires a deeper knowledge of the relationship between flow geometry, pressure field and flow kinematics. In the present contribution, the flow is fully characterised for one flow configuration in a sharp edged tee but some recent results of the mean flow in one rounded-edge tee for the same flow conditions are also included.

The paper is organised as follows: in the next section the rig and instrumentation are described and the experimental uncertainties quoted. Then, the results of pressure measurements for the sharp-edge tee are presented and are followed by a detailed mean and turbulent flow characterisation, where a brief comparison with new data for a rounded-edge tee is

included. A summary of the main findings and of future work closes the paper.

2. TEST RIG AND INSTRUMENTATION

The experiments were carried out in the closed circuit rig schematically shown in Fig. 1. The 90° tee junction was inserted at the intersection of three 2.6 to 2.8 m long pipes of 30 mm internal diameter. The water flow was driven by a volumetric Mohno pump supplied by a tank with constant head regulation by means of an overflow tube. A variable speed controller operated the pump and three inflow/outflow valves enabled to study all possible flow configurations up to a Reynolds number of 32 000 in the main pipe. In this paper, only the configuration of inflow in the straight pipe and 50% out flowrates in the straight and branch pipes will be investigated.

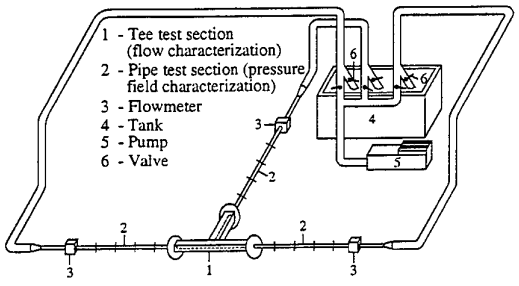


Figure 1- Schematic representation of the experimental set-up.

The flowrate was monitored by three magnetic flowmeters, one in each pipe. The temperature of the water was monitored by means of a PTC100 sensor located in the tank and kept between 15 and 20°C.

The leading pipes and the tee were manufactured of transparent acrylic to allow the use of optical diagnostic tools. The last 30 to 35 diameters approaching the bifurcation and the tee were machined from a block with an external square outer cross section of 50 x 50 mm^2 in order to reduce optical diffraction. The reference tee geometry has sharp-edges whilst the second tee has a rounded edge with a ratio of radius of curvature to pipe diameter of 0.1.

Pressure measurements were performed on seven measuring planes in each of the three 2 m long pipes adjacent to the bifurcation flow field characterisation area (Fig. 1); each pressure section had four pressure taps uniformly distributed around the pipe and was connected to a valve switch board leading to a differential pressure transducer which was interfaced with a computer via an AD converter. The overall uncertainty of the flowrate measurements varied between 2.5% and 0.6% for low and high flowrates, respectively.

Table 1 - Laser-Doppler characteristics

Laser wavelength	820 nm
Laser power	100 mW
Measured half angle of beams in air	3.81°
Size of measuring volume in water (e^{-2} int.)	
minor axis	37 μm
major axis	550 μm
Fringe spacing in air	6.31 μm
Frequency shift	1.0 MHz

The velocity measurements relied on a miniaturised fiber optics laser-Doppler velocimeter from INVENT, model DFLDA, similar to that described by Stieglmeier and Tropea (1992), with a 120 mm front lens mounted onto the 30 mm diameter probe. Scattered light was collected by a photodiode in the forward- and back-scatter modes, depending on optical access; the main characteristics of the anemometer are listed in Table 1. The signal was processed by a TSI 1990C counter interfaced with a computer via a DOSTEK 1400A card, which provided the statistical quantities. The maximum uncertainties in the longitudinal mean and rms velocities at a 95% confidence level are, respectively, of 1.1% and 2.7% in low turbulence regions and of 1.6% and 5.5% in high turbulence regions. The uncertainty of the transverse mean and rms velocity components is 1.3% and 6.0% in low and high turbulence regions, respectively. The curvature of the pipe walls was duly accounted for in both the positioning of the control volume and in the value of the conversion factor.

The velocimeter was mounted on a milling table with movement in the three coordinates and the positional uncertainty was ± 100 μm in all three directions.

3. RESULTS AND DISCUSSION

3.1 Pressure Field Characterisation

According to Fig. 2, which also presents the system of coordinates to be used hereafter, the energy balances applied to each of the two possible flow paths on the investigated horizontal non-symmetrical flow configuration yields

$$\frac{p_3}{\rho g}+\frac{U_3^2}{2g}-\frac{p_1}{\rho g}-\frac{U_1^2}{2g}=\lambda_3\frac{l_3}{d_3}\frac{U_3^2}{2g}+\lambda_1\frac{l_1}{d_1}\frac{U_1^2}{2g}+\frac{\Delta p_{3\text{-}1}}{\rho g} \quad (1)$$

and

$$\frac{p_3}{\rho g}+\frac{U_3^2}{2g}-\frac{p_2}{\rho g}-\frac{U_2^2}{2g}=\lambda_3\frac{l_3}{d_3}\frac{U_3^2}{2g}+\lambda_2\frac{l_2}{d_2}\frac{U_2^2}{2g}+\frac{\Delta p_{3-2}}{\rho g} \quad (2)$$

where l_i, p_i and U_i are the distance from fully developed flow cross sections on pipe i to the point of intersection of the three pipes, the static pressure and the bulk mean velocities on those cross sections, respectively; λ_i and d_i represent Darcy's friction factor and the diameter of pipe i and Δp_{3-1} and Δp_{3-2} are the apparent local pressure losses between the main pipe (3) and the branch (1) and the straight (2) pipes, respectively. Pressure measurements on the fully developed flow regions in each pipe evaluated the friction factor λ_i and the apparent pressure variation due to the tee was determined by application of equations (1) and (2) to the whole set of pressure measurements.

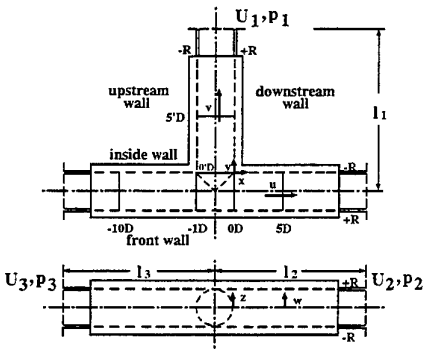


Figure 2- Flow configuration and coordinate system in the tee-junction.

Measurements of the pressure field along the pipes for the sharp-edge tee and the flow configuration in Fig. 2 were carried out for inlet pipe Reynolds numbers in the range $5\,000 \le Re \le 32\,000$ and for the flow rate ratio (Q_1/Q_3) varying from 0 to 1.0. Expressing the local energy losses in terms of the bulk velocity in the main pipe (referred <u> in later sections) the evaluation of the apparent pressure variations Δp_{3-1} and Δp_{3-2} defined above enable the quantification of corresponding local loss coefficients K_{31} and K_{32} which are defined by

$$K_{31} \equiv \frac{\Delta p_{3-1}}{\frac{1}{2}\rho U_3^2} \quad \text{and} \quad K_{32} \equiv \frac{\Delta p_{3-2}}{\frac{1}{2}\rho U_3^2} \quad (3)$$

The variation of loss coefficient K_{31} with the flowrate ratio Q_1/Q_3 for different constant inlet Reynolds number is shown in Fig. 3. The figure includes also information from the literature. Similar presentation of K_{32} would show a better agreement of the same correspondent literature data. To assess the effect of the inlet Reynolds number, the loss coefficient K_{32} is plotted in Figs. 4 for a constant flow rate ratio.

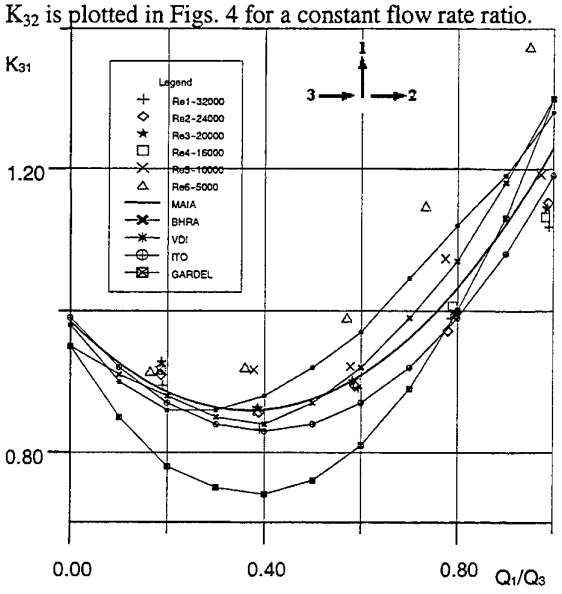


Figure 3- Variation of the local loss coefficient K_{31} in a sharp edge 90° bifurcation as a function of the flow rate ratio for different resultant inlet Reynolds number.

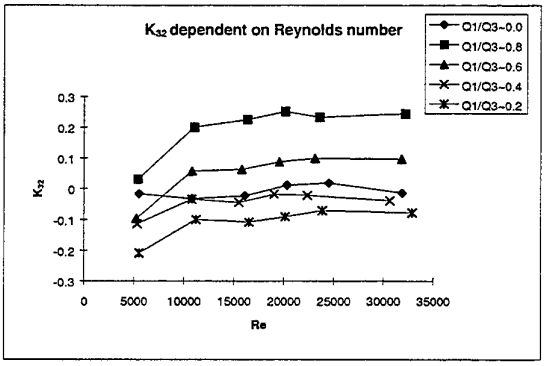


Figure 4- Variation of the local loss coefficient K_{32} (straight flow) in a sharp edge 90° bifurcation with the inlet Reynolds number for a flow rate ratio.

Due to space limitations, both Figs. 3 and 4 refer to different but only one of the two referred loss coefficients. Comparative analysis of all those plots show that the measurements agree well with the literature data at high Reynolds numbers and that the local loss coefficients generically increase (K_{31}) or decrease (K_{32}) as the Reynolds number decreases

towards the transitional regime. The literature data pertains to the high Reynolds number turbulent flow regime, where the local loss coefficient becomes independent of the Reynolds number and this could explain some of the observed discrepancies.

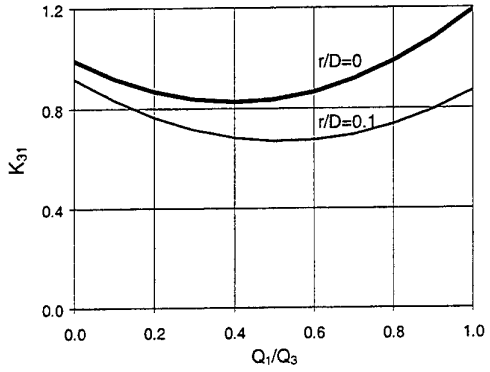


Figure 5- Round-edge effect on local loss coefficient K_{31} (straight flow), according to Ito and Imai (1973).

The pressure field characterisation for the rounded corner geometry (r/D=0.1) has not yet been carried out for this project. Anyway, the correspondent studies presented in the literature permit to foresee that, for the r/D=0.1 round edge, significant effects are expected only in the loss coefficient for the main to side branch, i.e., K_{31}, as can be assessed in Fig. 5. According to Miller (1986) and Ito and Imai (1973), sharp-edged case straight flow coefficient values (K_{32}) can be applied to this case. (r/D=0.1)

3.2 Mean Velocity Field

Fig. 6 presents a vector plot of the x- and y-directions mean velocity components (u and v, respectively) in the horizontal diametral plane for the sharp edge bifurcation. The flow in the inlet pipe becomes fully developed well ahead of the bifurcation; the radial profiles of the axial velocity component and of the normal Reynolds stresses collapse for stations -10D and -5D and compare well with data from the literature, except that the turbulence is slightly higher but this can be accounted for by the Reynolds number effect. The present measurements are for a Reynolds number of 32 000 whereas the data in the literature pertain to higher Reynolds numbers.

The nomenclature used is that in Fig. 2, u and v designate the velocities in the x- and y- directions and we call the readers' attention to the names of the various walls mentioned here, which facilitate the understanding. Note also that u is the longitudinal velocity in the main inlet and outlet pipes whereas v is the transverse velocity. The role of these two velocity components is reversed for the branch pipe. All mean and turbulent velocities have been normalised by the inlet bulk velocity and from now on we always refer to these values. In referring to measuring stations a prime designates the branch pipe, and negative stations are in the inlet pipe (see Fig. 2: 0D and 0'D represent the entrance to the outlet and branch pipes, respectively).

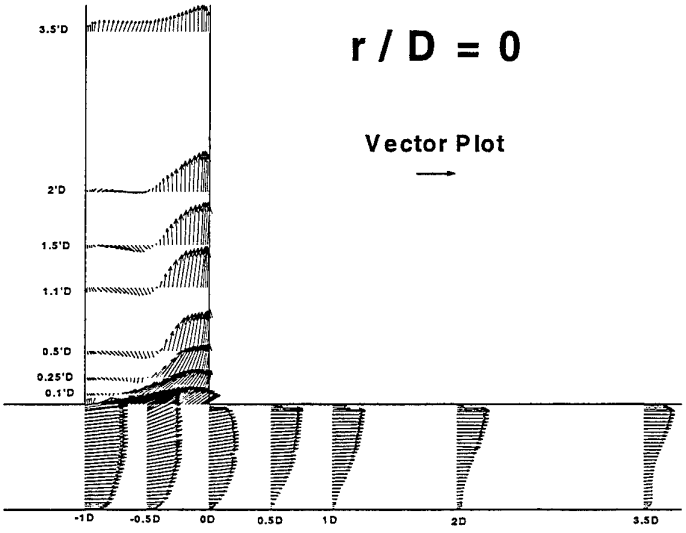


Figure 6- Vector plot of u- and v- mean velocity components in the diametral horizontal plane for the sharp-edge tee bifurcation.

On approaching the beginning of the bifurcation (-1.0D) the flow in the inlet pipe deviates towards the inside wall. In the middle of the bifurcation (-0.5D) the maximum longitudinal velocity has dropped only to about 0.9, indicating that in the first half of the branch pipe the main flow does not deviate significantly towards the side branch. Indeed, the onset of a recirculation zone at the edge of the upstream wall of the branch pipe blocks the passage of fluid which is forced into it only at the downstream half of the cross-section.

The recirculation bubble in the branch pipe is about 2.0D long and, although its maximum width occurs near the entrance, the width remains fairly constant up to about 2.0'D and the maximum longitudinal velocities in the stream occur at 1.5'D. The shape of the bubble at the end of the recirculation is rather strange. At 2.0'D the flow near the upstream wall is already positive but there is still a small negative velocity near the pipe axis. Although this is a turbulent flow, this finding is in agreement with the laminar flow pattern measured by Maia (1992). Close inspection of the vectors inside the recirculating region show also that the flow is moving away from the wall, and continuity requires that an inflow into the wall region must take place. The hint is obvious: we are in the presence of a strong 3D flow with the w velocity component feeding fluid into this region from above and below the diametral plane. This component of the velocity vector has not been measured yet, but these results suggest the need to do it, at least in the branch pipe.

Horizontal transverse velocities in the main and branch pipes are very low everywhere accounting only for flow redevelopment and continuity, the exception being at the entrance of the branch pipe where the flow tends to be aligned at 45° relative to both the x and y axis.

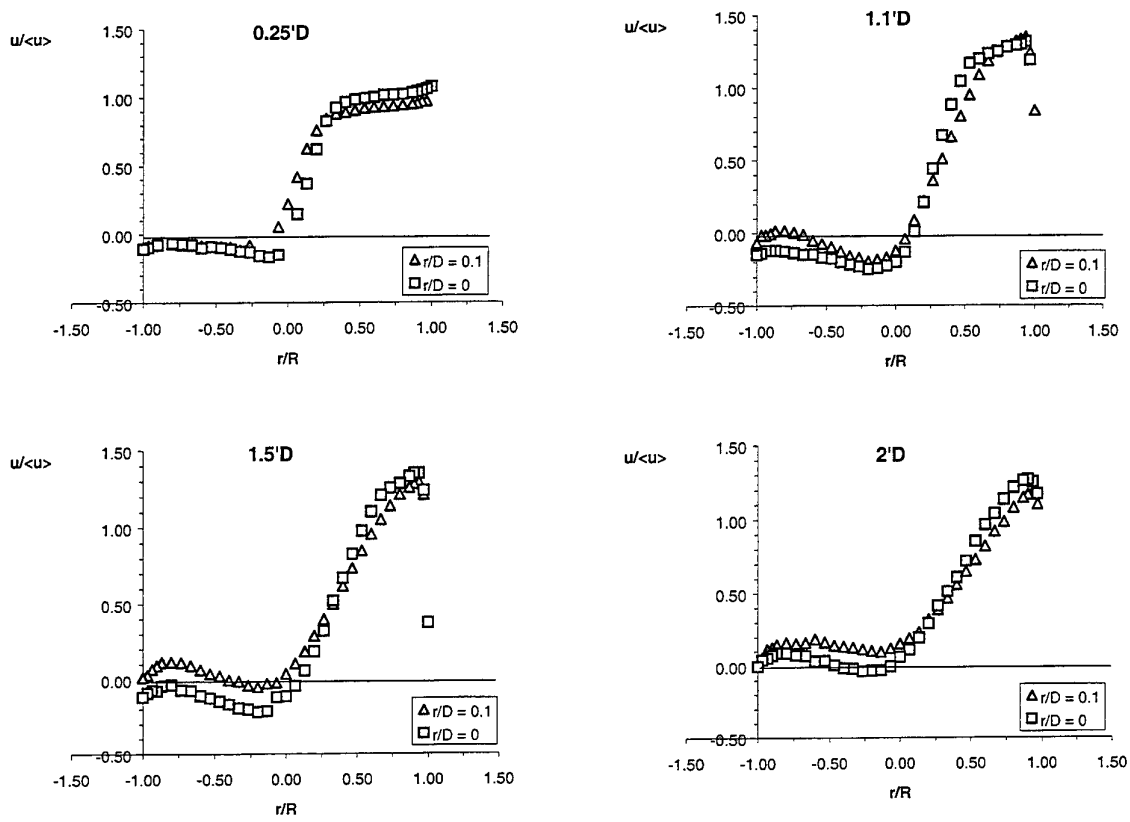


Figure 7- Some horizontal transverse profiles of the longitudinal velocity component in the branch pipe for the sharp and round edged tees.

In the straight outlet pipe the longitudinal velocity profiles are initially skewed towards the inside wall, because of the suction effect of the branch, and then start to redevelop. This is well observed in profiles of the transverse velocity, not shown here, carrying u-momentum from the inside wall region to the vicinity of the outside wall of the main outlet pipe.

It is worth emphasizing that, for this flow rate ratio (50%) there is no flow separation in the main outlet pipe, although we are close to it: an inflection point is clearly identified in the vector profile at 1.0D, near the outside wall. The vertical transverse velocity profiles taken at -0.5D show a second negative velocity region located near the bottom and top walls which we think result from the blockage effect that exists in the passage from the main to the side branch at that location. The intersection of both pipes has an elliptical shape and the main flow into the branch occurs in the middle horizontal diametral section, where cross section areas are larger and thus flow resistance is smaller. The complex 3D flow created at the bifurcation probably generates an adverse pressure gradient near the top and bottom walls which force a small separation.

For the round-edge tee the main flow features remain almost unchanged, with the flow going into the straight pipe not being very affected. Anyhow, comparing the longitudinal velocity profiles of the rounded and sharp edged junctions in the branch pipe (fig. 7) shows that the main effect of the curved edge is to reduce the length, width and strength of the separated flow region. A shorter recirculation bubble in a similar flow situation, but with a different edge curvature, has been observed in the limited experiments of Sierra-Espinosa and Bates (1997) and it suggests that lower energy losses will be measured here for the bifurcated flow.

3.3 Turbulent Velocity Field

Contour plots of the normalised rms of the u and v velocities (u' and v') are presented in Figs. 8 and 9 for the sharp-edge tee, respectively. Measurements of these quantities for the round-edge tee are still under way and therefore are not presented here.

Limitations of space do not allow the presentation of some transverse profiles of u' and v', which would allow an improved understanding of some of the effects. Also, the contour plots are drawn in the horizontal diametral plane, and we are not including here figures describing the variation of the turbulent quantities with the z-direction.

The main turbulent flow features are observed in the bifurcation, the side branch and at the beginning of the outlet straight pipe and they are dominated by the various shear/ boundary layers. Near the inlet of the bifurcation the turbulent flow field has characteristics of a fully developed pipe flow. Then, on entering the bifurcation region there is a shift of the longitudinal mean flow towards the inside wall, with the consequent depletion of fluid and deceleration in the outside wall region of the bifurcation. Flow deceleration contributes positively to turbulence

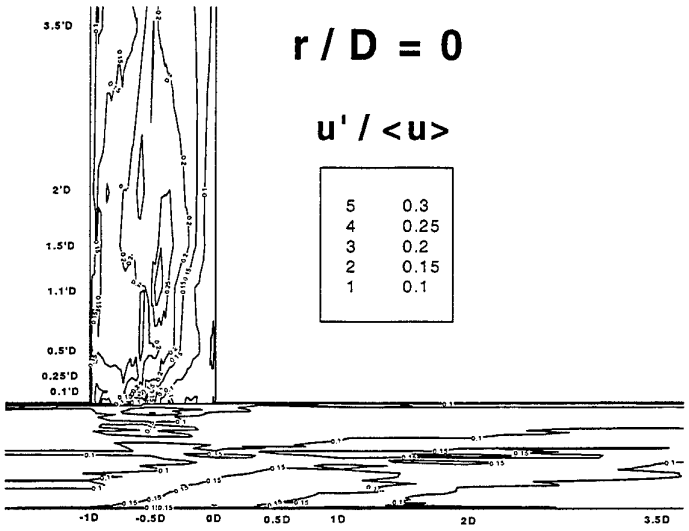


Figure 8 – Contour plots of the normalised turbulence u´/<u> for a sharp-edge tee.

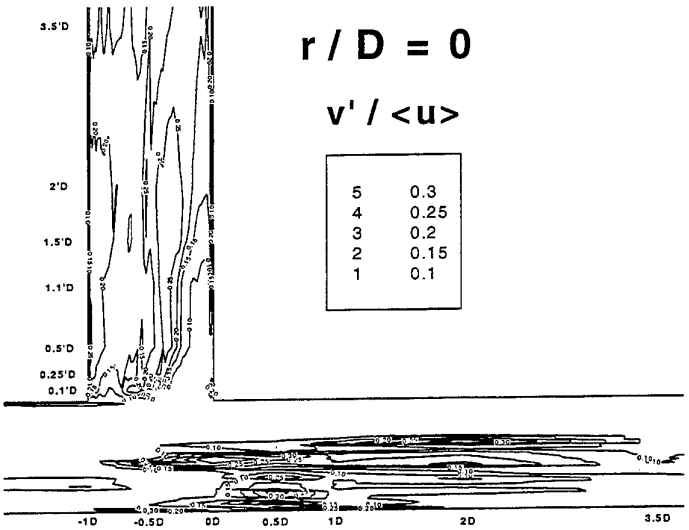


Figure 9 – Contour plots of the normalised turbulence v'/<u> for a sharp-edge tee.

production via a normal rate of strain-normal stress interaction (first term of the right-hand-side of Eq. 4) and hence longitudinal turbulence increases in the outside wall region of the main outlet pipe until about station 1D.

Production of $$\overline{u'^2} = -\overline{u'^2}\frac{\partial U}{\partial x} - \overline{u'v'}\frac{\partial U}{\partial y} - \overline{u'w'}\frac{\partial U}{\partial z} \qquad (4)$$

Simultaneously, on the inside region the wall has given place to the entrance of the branch pipe with the consequence that suddenly the production of u' by Reynolds shear stress has significantly diminished. The mean flow analysis also shows that in this region the local mean U velocity drops suddenly near the centre of the branch pipe and then it remains fairly constant at a low value because, although flow is exiting to the branch pipe the region is also being fed by fluid from the outside wall region. That sudden local flow deceleration near the entrance to the branch pipe can explain the local maximum in u'. Here there are also gradients of the transverse mean velocity but contours of v' do not show any local maximum.

Going into the outlet pipe there is a reversed behaviour. From about 0.5D to 1.0D, along the outside wall region the shear layer becomes fairly weak because the region has been depleted of fluid and so turbulence production by shear velocity gradient and shear Reynolds stress interaction will be small. Since the longitudinal velocity profile is skewed towards the inside wall, u-momentum will now be transferred from the inside towards the outside wall region, ie., there will be acceleration of fluid in the outside wall region and this represents a sink of turbulence. Both effects, plus the initial peak of u' at inlet and consequent higher turbulent diffusion and turbulence redistribution by pressure strain between 0D and 1.0D will contribute to the decrease of u' at the outside wall region, as the fluid flows downstream. Conversely, at the inside wall the fluid will decelerate and the boundary layer has been re-established, both events contributing to increase turbulence.

The recirculation region in the branch pipe creates a very strong shear layer at its edge, in the centre of the pipe. Here, there is an intense production of longitudinal turbulence (now v') which increases until 1.5D, the station where the mean velocity shear gradient is the steepest and the widest. Note also the peak longitudinal turbulence at the upstream wall of the eddy. This maximum is not locally produced, but represents turbulence generated in the shear layer, which is now being convected into the wall region by the reversed flow. The mean flow analysis has shown that the upstream wall region is being fed by fluid from the locations above and below the horizontal diametral plane and we think that this fluid actually comes from the part of the shear layer in those upper and lower regions of the branch pipe having higher turbulence. This argument is reinforced by the fact that axial

turbulence decays if we move along the upstream wall, towards the entrance of the branch pipe.

Vertical traverses of the longitudinal velocity show also production of turbulence by the wall shear layer at the top and bottom walls in the outlet and side branch pipes, but not so much in the bifurcation region because there, the shear layer is very weak.

For the transverse velocity component (v in the main inlet and outlet pipes and u in the branch pipe) the contours are not very different although for a different reason. With the exception of the entrance to the branch pipe, gradients of the transverse mean velocity are always very small in comparison with gradients of the longitudinal mean velocity. This means that direct production of transverse turbulence will be negligible and so it has to be acquired via a different mechanism, the redistributive role of the pressure strain and possibly turbulent diffusion. So, since the transverse turbulence will acquire its energy from the longitudinal turbulence its variations will follow closely those of the latter. This is exactly what is observed except for the local maxima in the contour plots of v' in the centre of the main outlet pipe which are absent from the contour plot of u'. In this region we experienced difficulties to measure in backscatter due to light reflections and excessive noise, and the data is very scattered. Consequently this particular data should be regarded with suspicion until a new measurement is carried out.

In the bifurcation region, the fluid changes direction especially near the entrance of the branch pipe and both the x- and y- components of the velocity vector become equally important, as well as its corresponding mean velocity gradients. In this region the mean gradients of V become non-negligible and the transverse turbulence starts to increase.

Similar measurements need to be performed for the rounded-edge tee and for both geometries measurements for the z-direction velocity component should be carried out in the region of the recirculation zone in the branch pipe. The two complete sets of data should enable us to relate the pressure and velocity data in order to draw final conclusions regarding the design of more efficient bifurcations.

4. CONCLUSIONS

Detailed measurements of the longitudinal and horizontal transverse mean and turbulent velocities have been carried out in a 90° tee junction for an inlet Reynolds number of 32 000 and a flow rate ratio of 0.5. The flow in the branch pipe is three-dimensional and possesses a recirculation region of complex shape and 2.0D long in the horizontal diametral plane. A strong shear layer exists in the middle of the branch pipe, but most certainly it has a U-shape, and in this region production of turbulence is at its maximum. The flow in the outlet straight pipe did not separate.

In spite of the complex 3-D flow the main features of the turbulent flow field could be explained on the basis of the identification of accelerating/deccelerating flow regions and shear/ boundary layers.

Preliminary measurements of the mean flow in a similar tee with a round edge between the main and branch pipes were also presented and showed a shorter, thinner and weaker recirculation bubble, suggesting that lower local loss coefficients will be determined in the pressure measurements that are about to be carried out.

ACKNOWLEDGEMENTS

The authors would like to acknowledge the financial support of JNICT through project PBIC/C/CEG/2440/95. A. Schulte would also like to thank the Leonardo da Vinci programme of the European Union for the scholarship that allowed his stay at INEGI. The authors are listed alphabetically.

REFERENCES

Boldy, A. P. 1970, Performance of Dividing and Combining Tees. BHRA Technical report 1061.

Gardel, A. 1957, Les Pertes de Charge dans les Écoulements au Travers de Branchements en Té. Bulletin Technique de la Suisse Romande, n° 9 and 10.

Gyr, A. and Bewersdorff, H.- W. 1995, Drag Reduction of Turbulent Flows by Additives. Kluwer Academic Publishers, Dordrecht.

Idel'cik, 1986, Handbook of Hydraulic Resistance, Hemisphere Publishing Company, New York.

Ito, H. and Imai, K. 1973, Energy Losses at 90° Pipe Junctions, Journal of the Hydraulics Division, Proceedings of the ASCE, Vol. 99, n° HY9.

Maia, R. 1992, Investigações Numéricas e Experimentais do Efeito das Perdas de Carga Localizadas em Sistemas de Tubagens. Métodos e Técnicas para o Seu Estudo Sistemático. O Caso Particular do Tê a 90°, PhD Thesis, University of Porto.

Miller, D. S. 1986, Internal Flow Systems, BHRA Fluid Engineering, 3rd edition.

Sierra-Espinosa, F. Z. and Bates, C. J. 1997, Prediction and Measurement of a Turbulent Flow in a 90° Pipe Junction, Proc. of the V Encontro Nacional de Mecânica Computacional, Guimarães, Portugal, vol. 2, pp 945-955.

Stieglmeier, M. and Tropea, C. 1992, A Miniaturized, Mobile Laser-Doppler Anemometer, Applied Optics, vol. 31, pp 4096.

VDI (Verin Deutcher Ing.) 1984. Druckverlust, VDI- Warmeatlas, VDI Verlag, Dusseldorf.

3D L.D.V. MEASUREMENTS IN A ROTATING COOLING CHANNEL

by Pierre GICQUEL, Yves SERVOUZE and Bernard TANGUY

Office National d'Etudes et de Recherches Aérospatiales
29, Avenue de la Division Leclerc
BP 72
92322 CHATILLON CEDEX
FRANCE

ABSTRACT :

This work presents an experimental investigation of a flow inside a rotating cooling channel by a 3D Laser Doppler Anemometry measurements, with the objective to study the flow and heat transfer in rotating cavities of cooled blades of gas turbine engines
Measurements were performed first in static mode at 2 Reynolds numbers : 5. 10^3 and 25. 10^3 . After this first static approach, the second step of the study has consisted to analyse the same channel section during rotation.
A specific optical 3D LDV setup based on a commercial system has been developped for this application and, in spite of some difficulties, used succesfully for the first time in this type of complex flows.
The axial velocity (U) profile deformation, resulting from the Coriolis acceleration, appears very clearly like an important result, which is in a good agreement with computational data code. In the transverse sections, the two others velocity components (V, W) show a secondary flow structure with two contrarotating vortices.
The first results obtained during this experimental work demonstrate that, in such a flow, with complex secondary structures, 3D LDV analysis seems to be the most suitable tool, but its implementation on this application was and stay yet a hard challenge.

1. INTRODUCTION

A good knowledge of the heat exchanges occuring in the cooled turbine of an aeronautical turbomachinery must be a great step to have a better understanding of the flow behavior in a rotating channel, in order to be able to predict wall heat transfers by CFD code.
Such studies, concerning the effect of rotation on the flow in a smooth duct, have been conducted at ONERA for many years [1], [2], [3] with the aim to know better the heat exchanges behavior in such a case. Two approaches have been explored : an experimental one for the direct determination of local heat exchange coefficient; a numerical one based on the resolution of the Navier-Stokes equations [4]. Until now only thermal measurements have been performed by the use of thermocouples and optical infrared pyrometer. Experimental data which are collected in those tests reveal a deficiency of 3D velocity results. Some results of 2D measurements have been published by Cheah et al. [5] and more recently by Liou and Chen [6], but not at all information in 3D measurements. This present work was then motivated to use a 3D LDV system to be able to characterize the details of the turbulent flow field.

2. EXPERIMENTAL SETUP

2.1 Experimental rig and test section

The measurements have been realized on a mock-up of the internal ventilation cavity's rotor blade of a turbine high pressure stage.
A general view of the experimental rig is presented on the picture of figure 1. This experimental rig allows thermal and aerodynamic measurements on two different test sections, respectively with the same geometry. The test section is connected to a radial arm and can rotate inside an enclosure (figure 2). The radius of the support is 223 mm and the maximum radius of the test section is 405 mm.

2.2 Test section

Figure 3 shows the test section configuration which has a square cross section (a = 20 mm) with a corresponding hydraulic diameter of D_H = 20 mm. The length of the arm is 8.1 D_H and the thickness of the divider wall is 5 mm. At the turn section, the space between the tip of the divider wall and the channel outer wall is equal to D_H. The upper wall of the model has a glass window giving optical access to the flow inside the channel in both configurations, centrifugal and centripetal. The maximum rotation speed of this test section is less than 1000 rpm for mechanical strength reasons.

The upstream of the centifugal arm is also a square duct with the same area. This duct, which is a part of the support, is connected to a circular vertical duct included in the shaft of the experimental rig. The axis of these ducts are located in two parallel plans separated by 5 mm. Like we are going to see latter, this does not give uniform inlet conditions in the test section.

2.3 3D LDV experimental setup

The Laser Doppler Velocimeter works in back scattered light. A specific development has been done here based on a classical LDV configuration [7]. A diagram of the optical configuration is shown on figure 4.

The emitting side is built with a 5 W argon-ion laser (Spectra 2040E) and a Colorburst (TSI) multicolor beam separator. The three wavelengths (514.5 nm, 488 nm and 476.5 nm) are then connected to the emitting optical head by monomode optical fibers of 4 microns core. Two compact optical heads have been built and fitted with the six monomode optical fibers. On the first one we have connected the two wavelengths 514.5 nm and 488 nm for a 2D emitting optical head. The third component (476.5 nm) is then connected on the second head.

For the receiving side, a commercial optical head (Aerometrics) is used with a multimode optical fiber of 200 microns core. According to the fact that the distance between the test rig and the software control room is more than 20 meters, each fiber (monomode and multimode) is 25 meters long.

Both, emitting and receiving heads are fitted out with 500 mm focus lens and coupled together in a compact and light system. All this optical compact setup is then put on a X, Y, Z orthonormed moving table.

This moving mechanical system is associated with a software piloted with the main DSA computer, in order to move the measurement volume to analyse the maximum points in the test section.

The software acquisition consists of a DSA (Doppler Signal Analyser) connected to a computer which can perform in line or off line data analysis.

The main difficulty was, for the rotating mode, to get signal from seeding particles (here oil droplets) at each passage of the channel, which is here 20 mm large. To solve this crucial problem, one pulse per revolution opens a measurement window upon crossing of the model. The width of this window was 100 µs, less than the channel crossing time, which leads to an average measurement domain of 2 mm in the circumferential dimension.

The flow velocity is measured by adding up a large number of mock-up crossings the measurement volume. The aim was to validate 1000 particles for each point. The seeding system was a type of « Laskin nozzle » used with pure olive oil. These oil particle droplets are injected far upstream of the flow test section. Any measurements were possible to get the real size of the particles in the test section. However, others experiments with this kind of seeding system give submicronic sizes.

For measurements in the sections of the arms, the compact LDV system is orientable with the receiving head in vertical position (Z axis). In this case the component V of the velocity is directly got with green color wavelength and the U and W components are deduced from blue and violet color wavelengths. In the median section of the bend, in order to obtain measurements near the outer side, the 2D emitting heads is pointed in the vertical position. Then, the U and V components are directly got with the blue and green color wavelengths respectively. We must also take in account that in rotating mode the velocity V_1 deduced from channel 1 signal is :

$$V_1 = \Omega \, . \, r \; + / - \; V$$

where Ω is the rotating speed, r the radius position and V the component velocity in the channel. Figure 5 shows the optical configuration of the two emitting heads.

An optical fiber is connected on the central wheel in order to get a pulse signal per revolution. This signal allows to open a time measurement window of 100 µs width. This window, less than the channel crossing time, leads to an average circumferential dimension of 2 mm. By this way we assume that the mean velocity is temporal but also spatial with a measurement volume of 2 mm.

According to the test section dimension, only 25 measurement points were possible for each section.

For each measurement point, the mean velocity is got by a sample of 1000 particles validated.

For the static mode analysis a time of about 1 mn was necessary to get this sample. The main difficulty was found in rotating mode where 15 mn were sometime required to validate 1000 particles.

3. RESULTS AND DISCUSSION

As it was a challenge to use the 3D LDV system on this application in rotation, a first approach has been performed in static mode before working with rotation.
All measurement results are reported in normalized velocity. Nevertheless, the simulate laws show a flow development velocity around 5 m/s with a rotating speed of 1000 rpm which are representative of a real engine.

3.1 Velocity-field in static mode

In static mode, two Reynolds numbers (5 10^3 and 25 10^3) have been performed. Three sections of the outward arm have been prospected (figures 6 and 7). Like a result of the flow development in those sections, the profil of the axial velocity (component U) shows that the flow is fully developed and almost uniform. After the sharp bend in the inward arm, the profile of the axial velocity is greatly modified by the location of the sharp bend upstream. The near wall velocities are higher on the external side of the duct. By this way it is then possible to follow the progressive filling of the velocity deficits along the divider wall.
The secondary velocity vectors (V and W) are shown on the figures 8 and 9, in the three sections of the outward arm. Each section presents a single vortex. The maximum secondary velocity is about 10 to 15 percent of the flow velocity development U_b. This vortex is the result of the upstream supply test section.
In the inward arm, for Reynolds number of 5 10^3 , we have found the classical arrangement with two vortices. In the center of the section, seeding particles are moved from the inner wall to the outer wall. Along the lateral walls the movement is inverted and the maximum secondary velocity in the first section downstream of the bend is about 30 percent of U_b.
For Reynolds number of 25 10^3 , at the first section of the inward arm, measurements close to the lateral walls were difficult or even impossible to get. It was very difficult to get secondary components with clear histograms. Analysis at the other sections give better measurements, but the slight density of measurement points does not allow to show clearly the secondary flow.

3.2 Velocity-field in rotating mode

In this second step of this flow analysis we have tested the two previous Reynolds number : 5 10^3 and 25 10^3 with one Rossby number : 0.33.
For Reynolds number of 5 10^3 we can follow the flow development in three sections, respectively in the centrifugal and centripetal ducts (figure 10).
In the centrifugal duct a progressive deformation of the axial velocity profile with an increase of the U component along the positive pressure side and a deficit along the suction side. In the first section this deficit reaches 20 % of the mass flowrate velocity and increases until 28 % in the last section upstream of the bend where the flow anticipates its crossing in the turn by a deficit of velocity along lateral sides. In this configuration the deficit can reach 80 %.
In the bend, the maximum velocity is close to the divider wall. This is shown like a classical arrangement by CFD codes and the velocity profiles are skewed toward the positive pressure side.
In the centripetal arm, the axial velocity profiles are not uniform. Nevertheless we can see that the behaviour of the flow is quite different of the static mode one. The maxima of velocity is near the divider wall with a slight displacement towards the positive pressure side.
Now, looking at the results in the cross section secondary flow (figure 11), it appears that the behaviour of the flow is deeply different in centrifugal and centripetal arms. In the centrifugal arm two contrarotating vortices settle progressively. After, a single vortex appears in the bend and keeps in the centripetal arm. The maximum secondary velocity is about 10 percent of U_b at the first section and increase up to 17 percent at the end of the centrifugal arm.
The maximum secondary velocity is about 67 % in the bend and decreases in in the centripetal arm from 25 % to 18 %.
In addition and to conclude the campaign, for a Reynolds number of 25 10^3, two Rossby numbers have been performed : 0.033 and 0.066. The only measurements made in the median section (figure 12) show that rotation has no effect (Ro = 0.033) or a slightly effect (Ro = 0.066) on the axial velocity profile. Concerning the cross section secondary flow, for Rossby number of 0.033, the single vortex fills the main part of the duct, except near the internal side. For Rossby number of 0.066, the arrangement of the secondary flow in two contrarotating vortices is more confused but the single vortex has disappeared.

4. MAIN CONCLUSION

The first results obtained during this experimental work demonstrate the validity of a 3D LDV in a such case. They show also a few insufficiencies due to an application deemed difficult.

Without rotation, measurements show a double counter-rotating symmetric vortex downstream of the bend which don't change in all the inward arm. In the outward arm, the flow, which is fully developped, presents a secondary structure composed of a single vortex.

In rotating mode, two Reynolds numbers (5 10^3 and 25 10^3) have been also performed, associated with the Rossby number. The effect of Coriolis force leads to the distortion of axial velocity in the centifugal arm. The near wall velocities are much higher on the pressure side. This effect is less marked when the nondimensional Rossby number decreases.

These measurements confirm also the simulation results on this type of flow got at ONERA with MSD code.

A new experimental investigation is planned before the end of 1998 on the same test section, with turbulence promoters inside the channel, with the aim to study the influence of no smooth channel on the internal flow.

ACKNOWLEDGMENTS

The authors gratefully acknowledge DRET for the financial support of this study under contract N° 94/001 BC 136 sous thème 7.1.7

The authors would like also to thank their colleagues for their help and support in this work, in particular : Mr J. Leloup, Mr P. Nail and Mr R. Pasquier.

REFERENCES:

[1] J. Guidez, M. Izard, P.J. Michard et J. Perucchini, 1989. Study of flow and heat transfer in rotating cavitites European Forum on Propulsion (AAAF/RAeS/DLR). Bath, T.P. ONERA N° 1989-33

[2] J. Guidez, P.J. Michard, D. Dutoya, J. Perucchini, 1989. Etude théorique de l'écoulement dans un canal en rotation. Approche expérimentale par la visualisation de l'écoulement dans un canal courbe. 74-B PEP/AGARD Luxembourg.

[3] Y. Servouze, A. Ristori, 1992. Echanges thermiques dans les canaux de refroidissement des aubes de turbines. 80 th PEP/AGARD Antalya (Turkey).

[4] D. Dutoya, M. Errera, P.J. Michard, A. Ristori, 1991. Présentation d'un code de calcul d'écoulements compressibles 3D dans des canaux et des cavités de forme complexe. PEP/AGARD CFD techniques for propulsion applications, San Diego (USA).

[5] S.C. Cheah, H. Iacovides, D.C. Jackson, H. Ji, B.E. Launder, 1996. LDA investigation of the flow development through rotating U ducts. Transactions of the ASME , Vol 118, pp 590-596.

[6] TM Liou, C.C. Chen, 1997. LDV study of a developing flow through a smooth with a 180 deg. straight-corner turn. International gas turbine and aeroengine congress and exibition, Orlando, Florida, paper 97-GT-283.

[7] J. Labbé, G. Janssens and B. Tanguy, 1991. Design of a 3D Laser Doppler Velocimeter fitted for combustion measurements. 4th International Conference on laser anemometry. Cleveland OH, (USA).

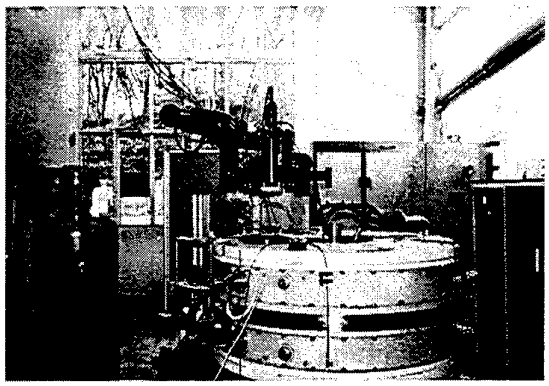


figure 1 : Picture of the test rig

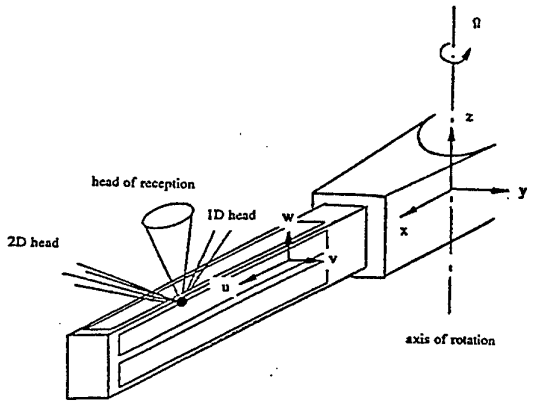


Figure 3: The test section

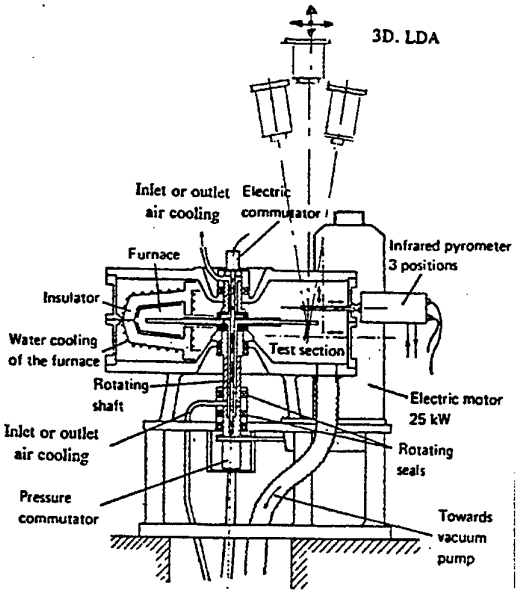


Figure 2 : The test rig

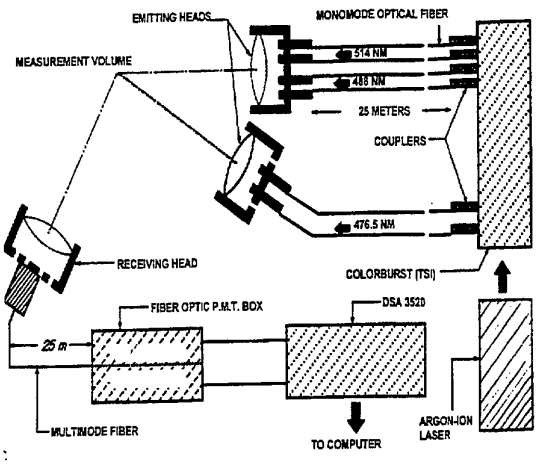
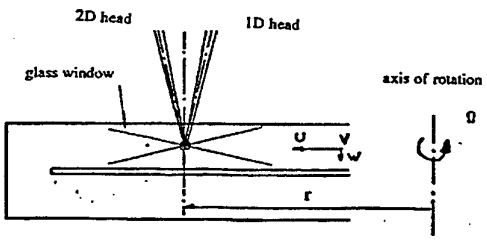
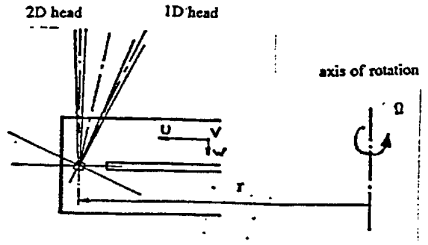


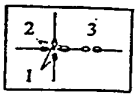
Figure 4 : Diagram of the 3D optical fiber LDV system



a) measurements in the duct



b) measurements in the bend



channel 1 : green

channel 2 : blue

channel 3 : purple

c) marks of the beams on the glass window

Figure 5 : Optical arrangement of the 3D LDV

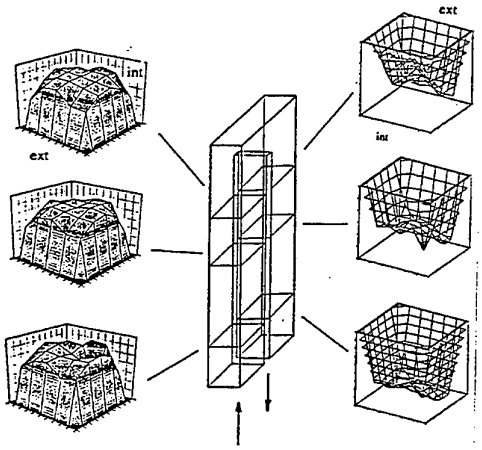


Figure 6 : Flow development in static mode
Re = 5 10^3, Ro = 0

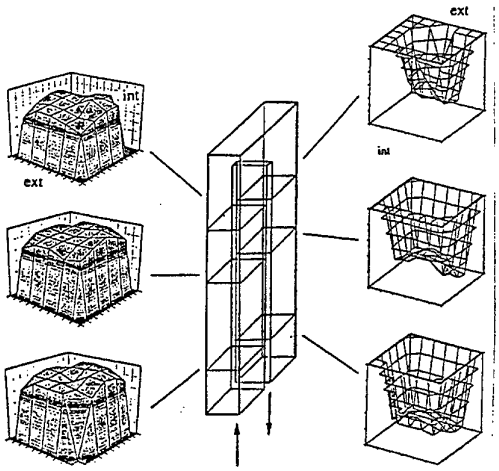


Figure 7 : Flow development in static mode
Re = 25 10^3 , Ro = 0

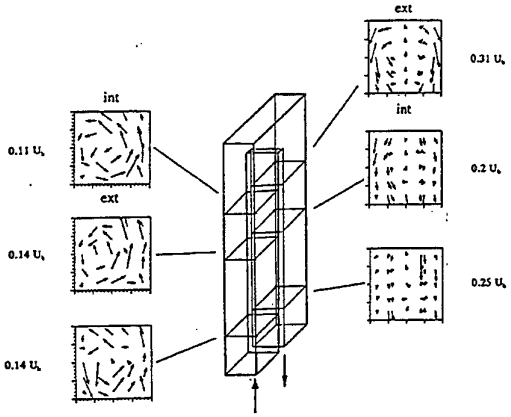


Figure 8 : Cross section secondary flow in static mode
Re = 5 10^3, Ro = 0

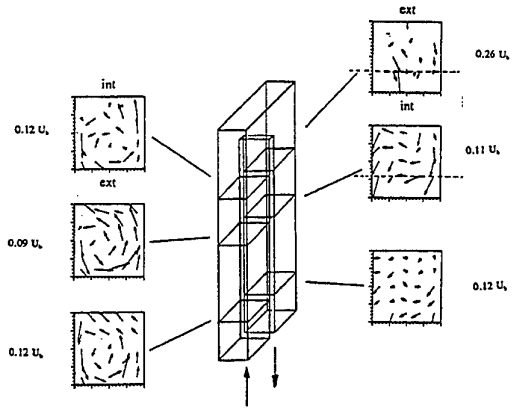


Figure 9 : Cross section secondary flow in static mode
Re = 25 10^3 , Ro = 0

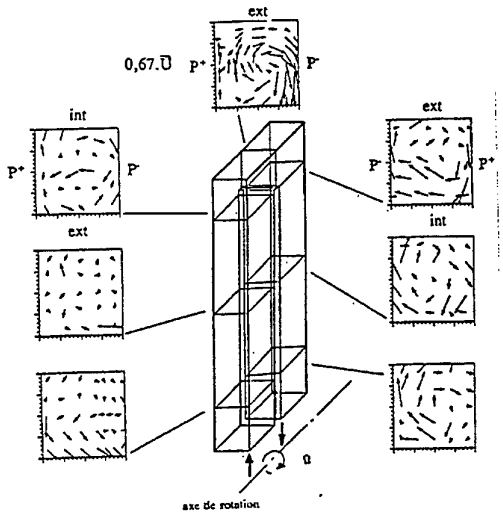


Figure 11 : Cross section secondary flow in rotating mode
Re = 5 10^3, Ro = 0.33

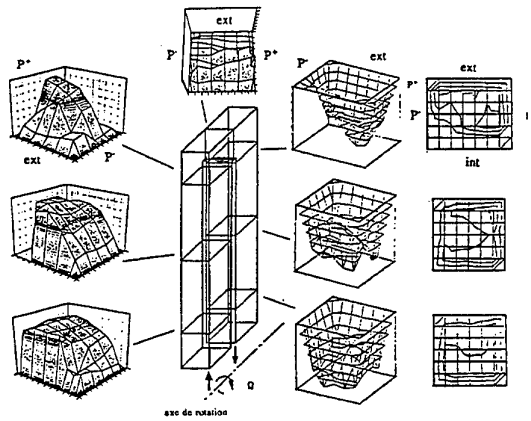


Figure 10 : Flow development in rotating mode
Re = 5 10^3, Ro = 0.33

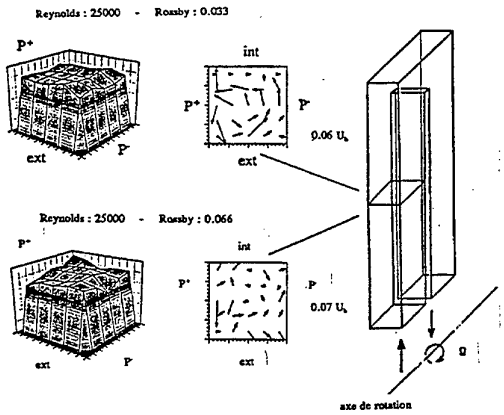


Figure 12 : Flow development and cross section secondary flow in rotating mode
Re = 25 10^3, Ro = 0.033 and 0.066

SESSION 9

Two-Phase Flows
Instrumentation I

REFRACTIVE INDEX MEASUREMENTS WITH PHASE DOPPLER ANEMOMETRY IN THE SIZE RANGE 0.3 TO 20μm

P. Volkholz, A. Melling, and F. Durst

Lehrstuhl für Strömungsmechanik, University of Erlangen-Nürnberg, Cauerstr. 4
91058 Erlangen, Germany

ABSTRACT

Many applications require the non-intrusive measurement of particle size and refractive index in the size range 0.3 to 20μm. Standard phase Doppler anemometers (PDA), however, have a lower size limit of about 5μm and, when extended by a second receiving optics unit (EPDA), can measure the refractive index only of particles larger than about 30μm. This paper first gives an error analysis of the standard EPDA system followed by a description of a planar four detector PDA-system, which allows size and refractive index measurement in the size range 0.3 to 20μm, by using a new signal evaluation method, referred to as the Joint Phase Match Method. The applicability and accuracy of the described PDA-system for small particles is examined using simulations and verification experiments.

1 INTRODUCTION

The non-intrusive measurement of particle size and refractive index of small particles is important in a variety of applications. Examples are the characterization of electro-hydrodynamic and ultrasonic atomizers as well as process control in spray drying. Also, via the refractive index, bubbles can be discriminated from solid particles, which is of importance, for example, in film coating.

Standard phase Doppler anemometer (PDA) and extended phase Doppler anemometer (EPDA) systems, designed for the measurement of particle size and refractive index in the size range up to 120μm or more, are, however, not suited for measuring small particles. Below 30μm, size measurements become increasingly inaccurate due to oscillations in the phase diameter relationship, whereas measuring the refractive index actually becomes impossible. This will be shown with the help of an error analysis of an EPDA-system given in section 2.

The goal in this work, therefore, was to provide a PDA-system that is capable of performing

- size measurements in the range 0.3 to 20μm with a resolution of $\pm 0.25\mu$m, and
- refractive index measurements in the range 1.2 to 1.6 with a resolution of ± 0.005.

2 ACCURACY AND LIMITS OF STANDARD EPDA

The standard EPDA (Extended Phase Doppler Anemometer) in the form discussed here was suggested by Naqwi *et al.* [6] in 1991 and applied by Brenn *et al.* [3] to the refractive index measurement of particles larger than about 30μm.

The EPDA is investigated here in order to estimate its measurement accuracy and the resulting limitations in its applicability. Whereas the measurement accuracy of the EPDA will serve as guideline for what can be reasonably expected of a small particle PDA-system, the limitations with respect to particles smaller than about 30μm will justify the development of a new PDA system.

2.1 Principle of operation

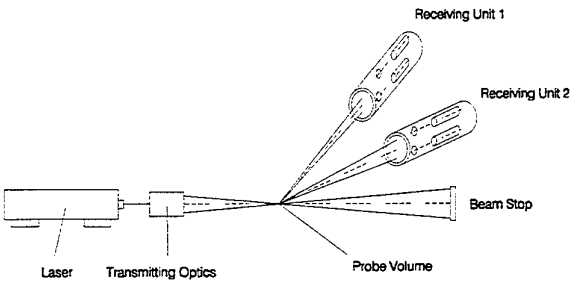


Figure 1: Optical setup of a standard EPDA-system.

Figure 1 schematically shows the setup of a standard EPDA-system, which consists of a standard PDA extended by a second receiving optics unit. The optical

Table 1: Geometrical configuration of of the standard EPDA-system used by Brenn *et al.* [3].

parameter	value	est. error
laser wavelength λ in nm	633	
beam-inters. half-angle α	1.69°	±0.02°
off-axis angle ϕ_1	60°	±0.5°
off-axis angle ϕ_2	30°	± 0.5°
elevation angle ψ	±3.69°	±0.05°
receiving cone half-angle	2.77°	

parameters for the EPDA-system used by Brenn *et al.* [3] are summarized in Table 1. The second receiving unit allows the measurement of two, instead of only one, phase difference value per particle. The relationship between the measured phase difference value Φ_m and the particle size d_p is given by the so-called phase factor F, which, for refracting particles large compared to the wavelength, is given by [1]:

$$F=\frac{4\pi}{\lambda}\left(\sqrt{1+m^2-m\sqrt{f_i+2\sin(\alpha)\sin(\psi_i)}}\right.$$
$$\left.-\sqrt{1+m^2-m\sqrt{f_i-2\sin(\alpha)\sin(\psi_i)}}\right) \quad (1)$$

where $f_i = 2\cdot(1+\cos(\alpha)\cos(\psi_i)\cos(\phi_i))$.
From the two phase difference values

$$\begin{aligned}\Phi_{m_1} &= F_1(m,\lambda,\alpha,\psi_1,\phi_1)\cdot d_p\\ \Phi_{m_2} &= F_2(m,\lambda,\alpha,\psi_2,\phi_2)\cdot d_p\end{aligned} \quad (2)$$

measured per particle, the refractive index can be isolated as a function independent of particle size d_p [3]:

$$m=-\frac{1}{2}\frac{\sqrt{f_2}-A\sqrt{f_1}}{A-1}+\sqrt{\left(\frac{1}{2}\frac{\sqrt{f_2}-A\sqrt{f_1}}{A-1}\right)^2-1} \quad (3)$$

where

$$A=\left(\frac{\Phi_{m_1}\sin(\psi_2)}{\Phi_{m_2}\sin(\psi_1)}\right)^2\frac{f_1}{f_2} \quad (4)$$

2.2 Refractive index measurement accuracy

The accuracy of refractive index measurements is limited by three factors:

1. the accuracy with which the angles α, ψ, and ϕ are known,
2. the accuracy of the phase difference measurement, and
3. the oscillations in the phase factor, i.e. in the phase diameter relationship, as can be seen in Fig. 2.

to 1.)
From experience in the laboratory it is reasonable to quantify the uncertainties as listed in Table 1. In general, such random errors Δl_i of measured quantities l_i

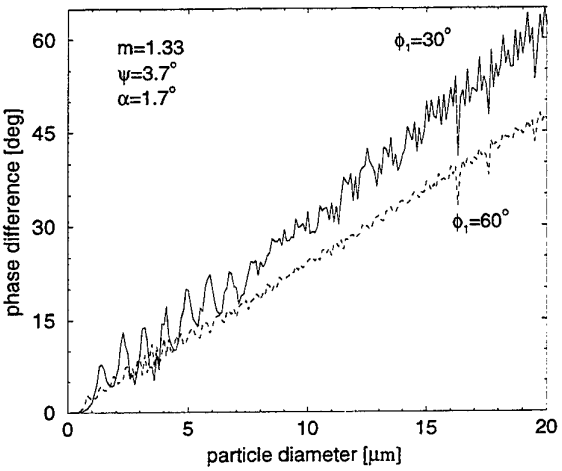


Figure 2: Phase-diameter relationship for a standard PDA-system calculated with Mie-Theory instead of Eq. 1.

lead to a combined error ΔR according to:

$$\Delta R=\sqrt{\sum_i\left(\frac{\partial R}{\partial l_i}\cdot\Delta l_i\right)^2} \quad (5)$$

Applying Eq. 5 to the equation for the refractive index, Eq. 3 leads to a measurement error due to uncertainties in the optical parameters for the setup summarized in Table 1 given by the approximate equation:

$$\Delta_\alpha m \approx 0.142\cdot(m-1.2)^2+0.023 \quad (6)$$

Eq. 6 was obtained by fitting a quadratic curve through a set of calculated $\Delta_\alpha m$ values. For m=1.34, for example, the error due to uncertainties in the optical alignment is $\Delta_\alpha m \approx \pm 0.025$. This value, which is independent of particle size, is rather substantial. For example, it already makes differentiating between water (m=1.336) and ethanol (m=1.362) difficult. The knowledge of the exact optical configuration is therefore absolutely essential.

to 2.)
The refractive index error $\Delta_\Phi m$ due to phase difference measurement errors can be derived in the same way as the error due to uncertainties in the optical parameters. However, the error due to phase difference measurement errors is a function of particle size and refractive index and is approximately given by

$$\Delta_\Phi m \approx \frac{\Delta\Phi}{d_p}\cdot(5.4\cdot(m-1.2)^2+0.5) \quad (7)$$

and is plotted for m=1.34 and $\Delta\Phi=\pm 4°$ as a function of d_p in Fig. 3. Equation 7 was again found by a quadratic fit.

One sees that even at d_p=100μm the refractive index error is already $\Delta_\Phi m=\pm 0.025$. Towards smaller

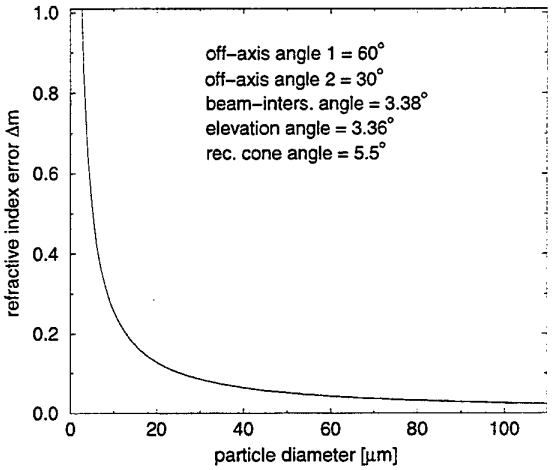


Figure 3: Refractive index error due to phase difference measurement errors as a function of particle size plotted for $\Delta\Phi=\pm 4°$ and a refractive index of m=1.34.

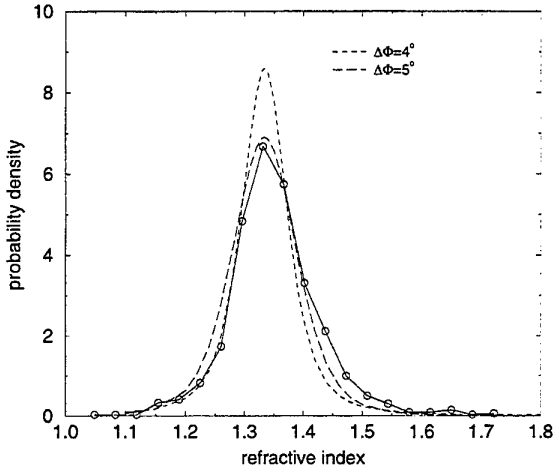


Figure 4: Comparison of refractive index measurement results taken from [3] with the probability density function obtained from error analysis given by Eq. 8.

particles the error becomes very large even though the oscillations in the phase-diameter relationship according to Mie-Theory have not been taken into account.

Figure 4 emphasizes the influence of the phase difference measurement error on the refractive index measurement. The figure shows a comparison of a refractive index measurement performed by Brenn *et al.* [3] in a polydisperse water spray, with a mean diameter of $\bar{d}_p$=51.6μm and a half-width of $\pm$15μm, with the error analysis presented above. Since the error analysis assumes a Gaussian error distribution, the curve in Fig. 4 was obtained according to

$$f_N(m, \Delta m(d_p)) = \frac{\exp\left(-\frac{1}{2}\left(\frac{m-\overline{m}}{\Delta m(d_p)}\right)^2\right)}{\Delta m(d_p)\sqrt{2\pi}} \qquad (8)$$

to 3.)

As was shown in Fig. 3, the refractive index error due to phase measurement errors becomes very large for small particles with the EPDA-method. Due to oscillations in the phase diameter relationship, moreover, this method of using the ratio of two measured phase differences to determine the refractive index does not work for particles smaller than about 30μm. This can be seen in Fig. 5, where the refractive index m is plotted as a function of the particle diameter d_p for the specific EPDA setup described in Table 1. This plot, generated using Mie-scattering calculations, makes clear that the refractive index obtained from a measurement according to Eq. 3 is no longer independent of the particle size for particles $\leq$ 30μm. Hence, neither the diameter nor the refractive index can be measured in this size range with a standard EPDA-system.

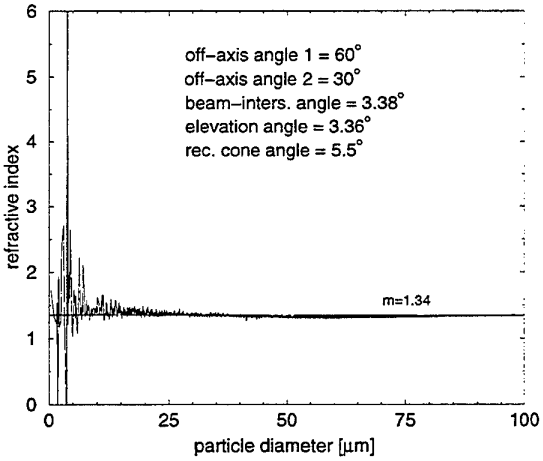


Figure 5: Refractive index obtained from Eq. 3 by calculating the theoretical phase difference values according to Mie–Theory for m=1.34.

2.3 Result

The discussion of the characteristics of a standard EPDA-system presented above can be summarized as follows:

1. Since the refractive index measurement error is of the order $\Delta m \approx \pm 0.025$, it is not possible to measure the refractive index of an individual particle with sufficient accuracy. Only under the assumption that a measured spray consists of only one material is it possible to obtain the correct refractive index by averaging over a sufficiently large number of samples.
2. The limited accuracy with which the optical parameters and the measured phase difference can

be determined limits the refractive index resolution of a standard EPDA-system to about ± 0.005, even when averaging over a large number of samples.

3. As Fig. 3 and 5 show, a refractive index measurement in the size range below 20μm is not possible with a standard EPDA-system. In the following sections, therefore, the development of a small particle PDA-system is described, which allows the measurement of refractive index in this size range with the same accuracy as EPDA for large particles.

3 PDA-SETUP FOR THE SIZE RANGE 0.3 TO 20μm

3.1 Phase diameter relationships in the submicrometer range

As Figure 2 shows, discriminating size classes using a standard PDA is possible down to only about 2μm, since the phase difference value then becomes similar to the measurement error, assuming the usual phase difference measurement error of $\Delta\Phi$=4° to 5°. In order to make size class distinctions in the submicrometer range, a different setup with a very large phase factor is required.

There are basically four ways to increase the phase factor and, hence, the size resolution:

1. increasing the beam-intersection half-angle α,
2. reducing the off-axis angle ϕ,
3. increasing the elevation angle ψ, and
4. reducing the laser wavelength λ.

Increasing the beam-intersection half-angle α [2] is only possible within limits, since doing so reduces the signal visibility and increases the Doppler signal frequency f_D according to:

$$f_D = \frac{1}{\lambda} \cdot v_\perp \cdot \sin(\alpha) \qquad (9)$$

where $v_\perp$ is the perpendicular velocity component.

The next two options mentioned above obviously lead to a setup where the off-axis angle is 0° and the elevation angle very large, e.g. 30° [5]. Phase diameter relationships for such a planar setup with an elevation angle of 30° are shown for several laser wavelengths in Fig. 6. One sees very well that already the reduction of the wavelength from λ=633nm to λ=532nm improves the size resolution in the submicrometer range. However, only when using ultra-violet lasers (λ=257nm) is a size distinction between 0.1 and 0.2μm possible [4].

3.2 The 2π-ambiguity problem

Looking at the phase diameter relationship shown in Fig. 7 for the size range up to 10μm, one sees the major problem with a setup that is optimized for the submicrometer range: the 2π-ambiguity problem. This means that if such a PDA is to be used in an application where the particle sizes vary from submicrometer to several micrometers, the measured phase difference values are no longer unambiguous. This problem can be overcome by evaluating the phase differences measured at three or more detectors, as will be discussed in section 4.

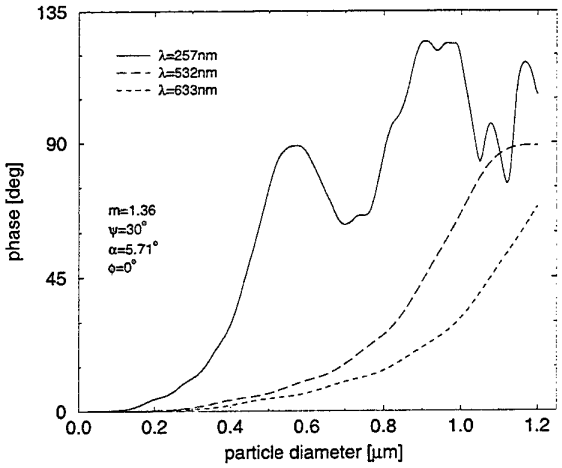


Figure 6: Phase-diameter relationships for a planar setup plotted for several wavelengths (polarization angle=0°).

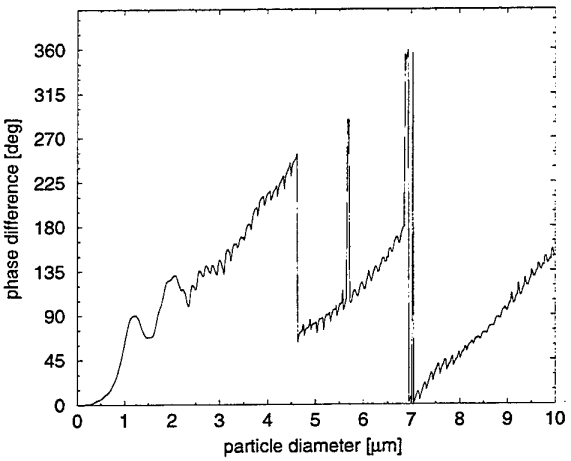


Figure 7: Phase diameter relationship for a planar setup with α=5.71°, ψ=30°, and λ=532nm for the size range up to 10μm to demonstrate the 2π-ambiguity problem.

3.3 Selection criteria for the optical setup

In Fig. 7, the phase diameter relationship was plotted for an elevation angle of 30° relative to a signal from a detector in the forward direction (0°). Obtaining a reference signal from this angle is, however, not recommendable in a planar setup, since, as Fig. 8 makes clear, only slight deviations in the alignment lead to erratic phase difference values for particles larger than about 4μm.

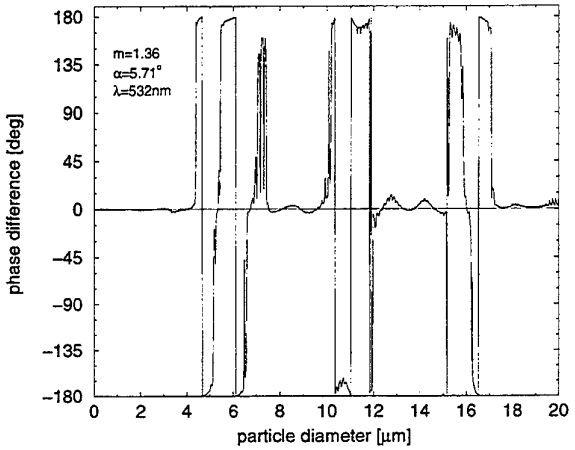


Figure 8: Phase diameter relationship for a planar setup where the detector is located at an elevation angle of 0.1°, calculated for a receiving-cone half-angle of 4.2°. For particles larger than about 4μm the phase diameter relationship shows large erratic oscillations.

For this reason, a detector should not be placed at an elevation angle smaller than about 15°, as investigations described in more detail in [7] have shown.

4 DATA PROCESSING: JOINT PHASE MATCH METHOD

In order to overcome phase difference measurement ambiguities due to

1. the oscillations in the phase diameter relationship, and
2. the 2π-ambiguity problem

more than two detectors are needed. It can be shown that for measuring particle sizes at a known refractive index three detectors suffice, whereas for measuring particle sizes without an *a priori* knowledge of the refractive index four detectors are necessary. With four detectors three independent phase difference values can be measured per particle.

In this method, referred to as the "Joint Phase Match Method", all the possible size-refractive index combinations are searched to identify the combinations that return the measured phase difference values within a certain error margin. This is done by generating a database of phase difference values with Mie-Theory for 40,000 size–refractive index combinations, spanning the size range from 0.1 to 20μm in steps of 0.02μm and the refractive index range from 1.2 to 1.6 in steps of 0.01.

Even when using four detectors, one usually obtains several possible size–refractive index combinations for every measured particle. The reason for this is the oscillations in the phase diameter relationship in combination with the limited phase difference measurement accuracy. This effect can be investigated by looking at the average number of other possible solutions for each d_p-m–combination in the database as a function of the phase difference measurement error[1]. Fig. 9 shows that although the phase–diameter–refractive index sets themselves are not multi-valued, i.e. no multiple solutions for $\Delta\Phi$=0°, a phase difference measurement error of $\Delta\Phi$=4° on average leads to about one other solution per d_p-m–combination. For a phase difference measurement error of $\Delta\Phi$=8°, used for the evaluation of the measurements in section 5, the average number of multiple solutions is already 6. Fig. 9 also makes clear that using more than four detectors reduces the number of multiple solutions; however, it does not remove the problem.

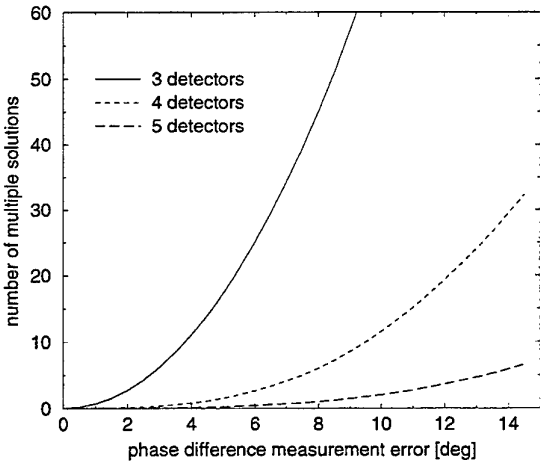


Figure 9: Average number of multiple solutions per d_p-m–combination as a function of the phase difference measurement error $\Delta\Phi$.

The same kind of calculation can also be performed for a fixed refractive index. In this case the average number of multiple solutions is reduced to a negligible amount. This result leads to the possibility of determining the refractive index under the assumption that it is unique. In an actual measurement, the Joint Phase

[1]Multiple solutions at the same refractive index that differ by less than 0.2μm from the d_p-m–combination are not counted.

Match Method first looks for the size–refractive index combinations that correspond to a measured phase difference set. Although several size–refractive index combinations will be found for each measured particle, only the correct refractive index will ideally appear as a solution for every particle. With this refractive index the size distribution can be obtained.

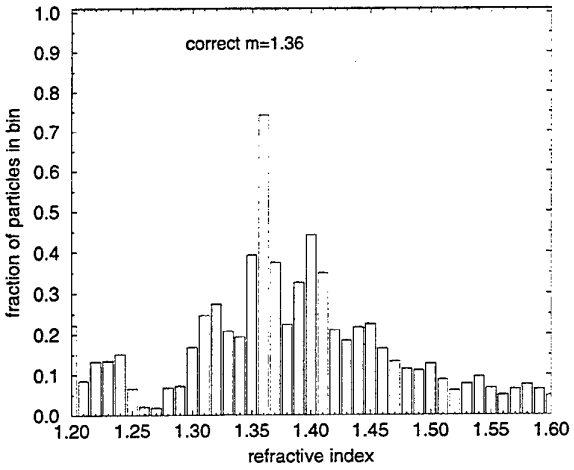


Figure 10: Refractive index of a measurement simulated with small alignment errors and a phase difference measurement error of $\Delta\Phi$=8°, evaluated using the Joint Phase Match Method.

Figure 10 shows a simulated measurement evaluated with the Joint Phase Match Method[2]. Each bin in the diagram shows the fraction of particles for which the corresponding refractive index was a possible solution, i.e. it is **not** a probability density distribution. The correct refractive index is identified by the bin with the largest fraction. In the simulation presented in Fig. 10 over 75% of the evaluated particles have a solution for the correct refractive index of m=1.36. This is less than the expected 100% due to the limited resolution of the look-up database, which leads to particles being overlooked by the evaluation program.

[2]The simulation method using a Gaussian random number generator and Mie-scattering theory is described in [7].

5 VERIFICATION MEASUREMENTS

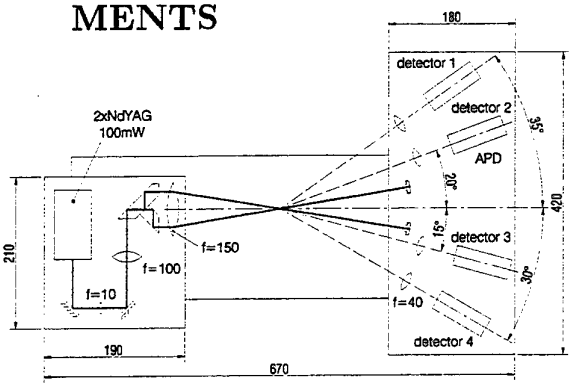


Figure 11: Experimental setup used for size and refractive index measurements for particles smaller than 20μm.

The optical setup used for size and refractive index measurements in the size range 0.3 to 20μm is shown in Fig. 11. The optical parameters are summarized in Table 2.

Table 2: Optical parameters of the implemented PDA-system.

wavelength	532nm
beam-inters. half-angle α	5.71°
off-axis angle ϕ	0°
elevation angle ψ_1	-35°
elevation angle ψ_2	-20°
elevation angle ψ_3	15°
elevation angle ψ_4	30°
receiving-cone half-angle	4.2°
polarization	0°
beam spacing a	30mm
focal length transmitting lens f_T	150mm
fringe spacing Δx	2.7μm
diameter of probe volume b_{MV}	30/65μm
focal length of receiving lens f_R	40mm
distance probe vol. – receiving lens	200mm
magnification of receiving lens	1:4
pinhole diameter	50 μm

Fig. 12 shows the measurement of 200 monodisperse 0.5μm latex particles, which was performed using a probe volume diameter of 30μm. Despite the fact that this measurement was performed in the submicrometer range, the measured refractive index differs only by 0.06 from the correct refractive index of m=1.59. However, since in the submicrometer range the phase difference value is only a weak function of the refractive index, the margin to the other refractive indices is very small and the size distribution is virtually independent of the refractive index with which the evaluation is performed.

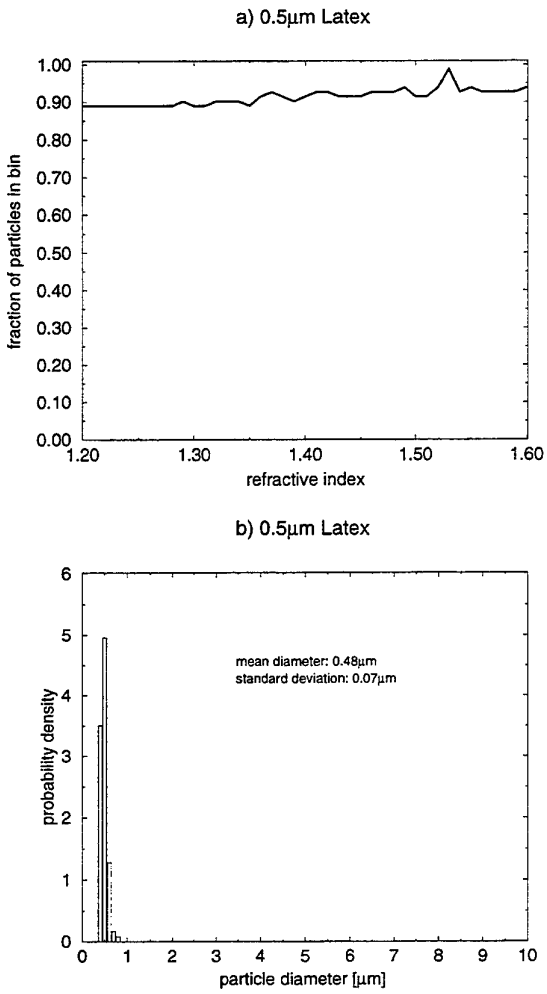


Figure 12: a) measured refractive index and b) size distribution of monodisperse 0.5μm latex particles.

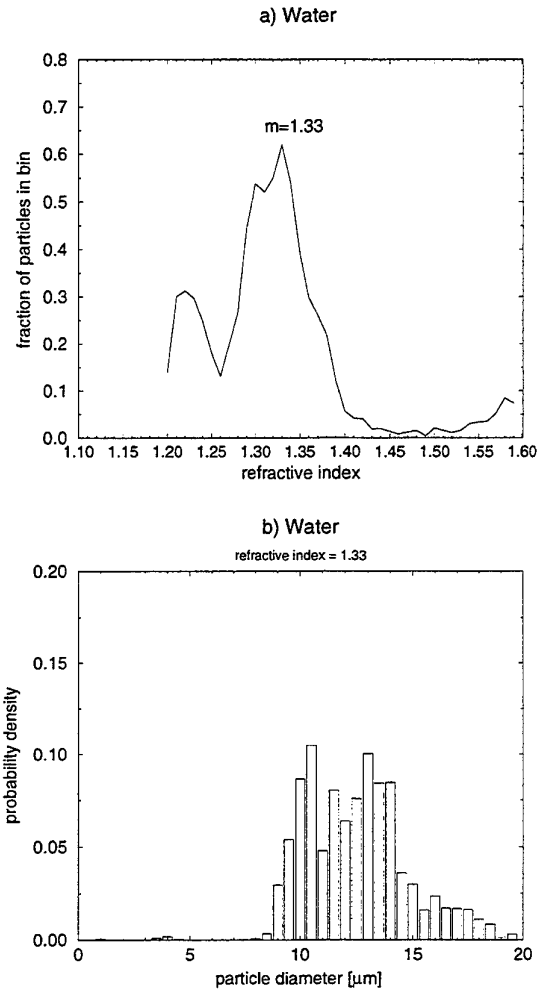


Figure 13: a) measured refractive index and b) size distribution of a water spray.

One, therefore, has to conclude that refractive index measurements are not possible in the submicrometer range.

Figures 13 and 14 show examples of measurements performed on sprays generated by an aerosol generator (nebulizer) and demonstrate the capability of the presented 4-detector PDA-system to measure the refractive index in addition to the size distribution (for more measurements see [7]). The size distributions are not very smooth due to the fact that these measurements were performed using only 5,000 samples. Of these 5,000 samples usually only about 3,500 were evaluated to the correct refractive index, and, of course, only these were used for obtaining the presented size distributions. In order to obtain smooth distributions with a bin size of Δ=0.5μm more than 8,000 samples are necessary. The focus in this work, however, is on measuring the refractive index, and for this a few thousand samples were sufficient.

6 CONCLUSIONS

This paper has taken a detailed look at measuring the refractive index in sprays for particles smaller than 20μm with phase Doppler anemometry.

From the investigations presented in this report, the following main conclusions can be drawn:

1. Standard EPDA-systems are not suitable for the measurement of the refractive index in the size range below 20μm, due to the oscillations in the phase diameter relationships.
2. Even in the size range for which the standard EPDA-system is designed, i.e. up to 120μm, the refractive index measurement error is between

$$\Delta m = \pm 0.025 \quad \text{and} \quad \pm 0.05$$

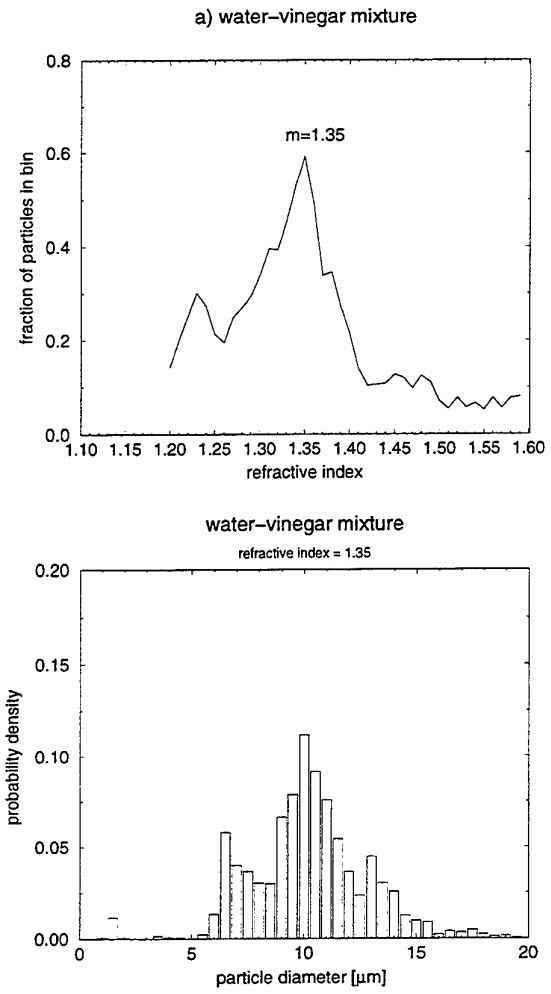


Figure 14: a) measured refractive index and b) size distribution of a spray consisting of a 1:1 water-vinegar mixture (refractive index of vinegar: 1.372).

due to phase difference measurement errors and uncertainties in the optical parameters.

3. The refractive index measurement error Δm is too large to measure the refractive index of individual particles. Only by averaging over a large number of samples can the refractive index of a one-component spray be determined.
4. In order to span the size range from submicrometer up to several micrometers, while at the same time enabling refractive index measurements in one component sprays, a 4-detector planar PDA-setup with large elevation angles is required.
5. Refractive index and corresponding size distribution measurements in the size range 0.3 to 20μm are possible in one-component sprays using a Joint Phase Match Method. The accuracy of the refractive index measurement is about $\Delta m = \pm 0.005$.

The capability of measuring the refractive index in the size range below 20μm is, therefore, no more restricted than for larger particles.

7 ACKNOWLEDGMENTS

The work presented in this paper is part of a research project funded by the Deutsche Forschungsgemeinschaft (grant Du 101/35-1&2).

References

[1] K. Bauckhage. The phase Doppler difference method, a new laser-Doppler technique for simultaneous size and velocity measurements. *Part. Part. Syst. Charact.*, 5:16–22 - 66–71, 1988.

[2] H.-H. Benzon and P. Buchhave. The phase Doppler method applied to very small particles. In *3rd Int. Congress on Optical Particle Sizing*, pages 261 - 267, Yokohama, Japan, 1993.

[3] G. Brenn and F. Durst. Refractive index measurements using the phase-Doppler technique. *Atomization and Sprays*, 5:545 - 567, 1995.

[4] F. Durst, A. Melling, and P. Volkholz. Advantages of UV lasers in laser and phase Doppler anemometry for submicrometer particles. In *Proc. 8th Int. Symp. on Applications of Laser Techniques to Fluid Mechanics*, page 6.3.1, Lisbon, 1996.

[5] A. Naqwi, F. Durst, and G. Kraft. Sizing of submicrometer particles using a phase-Doppler system. *Applied Optics*, 30(33):4903 - 4913, 1991.

[6] A. Naqwi, F. Durst, and X. Liu. Extended phase-Doppler system for characterization of multiphase flows. *Part. Part. Syst. Charact.*, 8:16–22, 1991.

[7] P. Volkholz and A. Melling. Phase-Doppler anemometry for size and refractive index measurement in the particle size range 0.3 to 20μm. Technical Report LSTM 547/E, Lehrstuhl für Strömungsmechanik, University of Erlangen-Nürnberg, Germany, 1997.

VELOCITY, SIZE AND CONCENTRATION IN SUSPENSION MEASUREMENTS OF CYLINDRICAL JETS AND SPHERICAL DROPLETS

F. Onofri, L. Bergounoux, J-L. Firpo, J. Misguish-Ripault

IUSTI, UMR CNRS 6595-Université de Provence
Technopôle de Château-Gombert, 5 rue E. Fermi, Marseille 13008, France
Email : Onofri@iusti.univ-mrs.fr, Fax : (33) 4 91 10 69 69

ABSTRACT

The principle of an optical technique for simultaneous velocity, size and concentration in suspension measurements of spherical droplets and cylindrical jets is proposed. The technique is based on Phase Doppler Anemometry working in a dual burst configuration, i.e.: the probe volume is smaller than the mean droplet size and induces two signals for each detected particle, a refracted and a reflected signal. The particle size and velocity are deduced from the reflected signal which is almost unaffected by internal particles inhomogeneities, whereas the amplitude ratio between the reflected and refracted signals is shown to be useful for the diagnosis of the particle inhomogeneities and more particularly, for the measurement of the particle concentration in a suspension of monodispersed scatters. Numerical simulations based on geometrical optics and a Monte Carlo model, and an experimental test on cylindrical jets of liquid suspensions are used to demonstrate the validity of the proposed technique.

1. INTRODUCTION

Numerous industrial processes use transport powders as liquid suspensions before spraying them for surface coating, drying or combustion applications. Among the most important parameters suitable to control or to further optimize the drying or deposition processes, we find classically the droplet size and velocity distributions and the concentration in suspension of individual flying droplets. Experimentally, an optical technique such as Phase Doppler Anemometry (PDA), which is now a well established particle sizing and velocity technique for studying two-phase flows, seems to be a good candidate to obtain the two first characteristics. Nevertheless, some previous works on the sizing of paint sprays (Domnick et al (1994)) or on food drying processes (Manasse et al. (1993) for instance, have shown undesirable effects of inhomogeneities inside droplet such as a spread in the measured droplets size distributions. Some solutions with severe limitations have been proposed to solve this problem : *i)* the use of collection angles where additional scattering from inhomogeneities is expected to be insignificant, *ii)* the use of near-infrared laser beams to reduce the size parameters of inhomogeneities, *iii)* the use of off-line reconstruction algorithms and calibration experiments, see Manasse et al. (1993, 1994). Note that the simultaneous concentration measurement in homogeneities inside particles was beyond the scope of these contributions, which were focused on size measurement improvements.

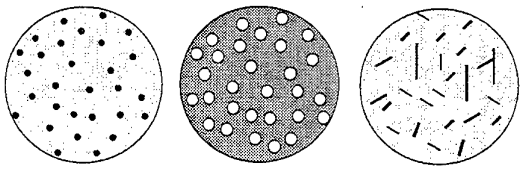


Figure 1 The sizing and concentration measurement in suspension, small inclusions or heterogeneities, of spherical and cylindrical particles is considered here.

The purpose of the present work is to introduce a new approach, based on PDA, for on-line and accurate sizing of optically inhomogeneous spherical and cylindrical particles in addition to the performance of a measurement of the material particles inhomogeneity.
For the sake of convenience, we consider here a special case of optically inhomogeneous material: a liquid suspension of monodispersed spherical particles of known diameter and refractive index. Nevertheless, the principal of the proposed technique could also be applied to the diagnosis of solid particles with solid inclusions as well as liquid droplets with gaseous or liquid inclusions.

2. PRINCIPLE

2.1 The Dual Burst Technique (DBT)

The principle of this new extension of PDA is based on the use of the dual burst operating mode, i.e. the optical probe volume is reduced so as to be smaller than the mean particle size in order to obtain two Doppler signals for each particle detected: a refracted and a reflected signal.

Under such conditions, the real part of the particle refractive index can be deduced from the phase of the reflected signal, the imaginary part, from the amplitude ratio between the two signals, and the particle diameter and velocity, from the phase and Doppler frequency of the reflected signal, see Figure 1. The reader is directed to references from Onofri et al. (1995, 1996a) to obtain a full description of this technique including some experimental applications for material recognition or coalescence studies in two-phase flows.

2.2 Inhomogeneous particles

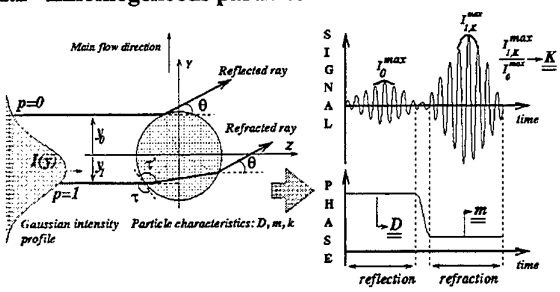


Figure 2 Schematic of the principle of the Dual Burst Technique for simultaneous measurement of the complex refractive index, size and velocity of spherical particles.

In the PDA principle, for homogeneous particles and for a plane wave illumination, one can easily optimize the optical setup parameters to select a dominant scattering mode, see Naqwi et al. (1988). This step is fundamental to obtain a linear phase-diameter relationships and to limit Trajectory Effects (TE), see Sankar et al. (1992), Gréhan et al. (1993). According to Geometrical Optics (GO), the refracted and reflected rays scattered by a particle and which reach the detectors are well defined according, mainly, to the particle refractive index and the detectors location and solid apertures angle.

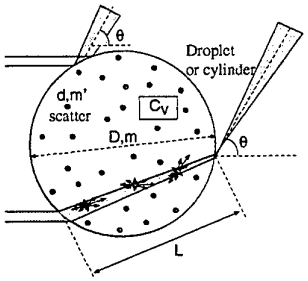


Figure 3 The nominal single refracted rays are attenuated by the scatters present in the liquid suspension.

When particles are no longer homogeneous, additional scattering processes occur inside the particles, and the selection of a dominant scattering mode becomes almost impossible with classical systems. One major feature of the DBT operating mode is that, during the particle trajectory in the probe volume, the different scattering processes are delayed in time due to the successive illumination of the different impact parameters (for a collection angle of 60° and a water droplet of diameter D they are spatially separated by about 0.95D). Thus, due to the small probe volume size, one can expect that phenomenon to produce reflected signals which are almost not "contaminated" by additional internal scattering and the signal phase can be used for accurate size measurements. Conversely, the nominal refracted rays through the particles will be very sensitive to the presence of any inhomogenities inside the particles. The principle of the proposed technique, for the internal concentration in suspension diagnosis, is to attribute the refracted signal amplitude attenuation, compared to the reflected signal, to an apparent extinction phenomenon that can be related to the particle suspension concentration.

3. MODELS

3.1 Geometrical optics with extinction

Beer-Lambert approach

Assuming a low suspension concentration, and thus a single scattering mode, the refracted ray attenuation or apparent extinction, reads for the maximum of the refracted Doppler signal:

$$I_{1,K}^{max} = I_{1,0}^{max} e^{-KL} = I_{1,0}^{max} e^{-NC_{ext}L} = I_{1,0}^{max} e^{-\frac{6C_V}{\pi d^3} C_{ext} L} \quad (1)$$

where $I_{1,0}^{max}$ is the maximum of the refracted signal when the concentration in suspension is equal to zero. K, which corresponds, for absorbing solutions, to an absorption term (related to the refractive index imaginary part, k, as $K=4\pi k/\lambda$). N is the number of scatters in the suspension per volume unit and C_V, corresponds to the volume concentration in scatters. C_{ext} is the scattering cross section of individual scatters in the suspension, with a diameter d, a refractive index m', and for the wavelength λ/m. L is the optical thickness of the particle for rays refracted in the detectors direction, with $L = D.\sin(\tau')$. D is the particle diameter and τ', the angle defined in Figure 2, which depends mainly on the particle refractive index and the detector location ($\theta \approx \phi$ or $\theta \approx \psi$), depending of the PDA geometry considered). The validity of Eq. (1) is limited in two ways: the optical width of the media must be small ($NC_{ext}L<1$) to be in the single scattering mode and the term $I_{1,K}^{max}$ must only be due to refracted rays which have followed a direct path through the particle, without any scattering by the suspension. The first condition limits the refracted ray attenuation to be less than $\approx 37\%$. Thus, as the attenuation depends on both the droplet diameter, the size parameter of the scatters in the suspension and their concentration in the solution, the application range of this equation is expected to be severely limited mainly when large variations in suspension concentration or in the particle size distribution are considered. To satisfy the second

condition, the optical thickness of the suspension must be small and the refracted rays have to be collected in the smallest possible solid angle around the nominal refracted ray scattering direction. Note that this last condition is better satisfied when considering suspensions of small scatters (compared to the laser wavelength) as the diffracted light by these scatters is not so strongly concentrated in the forward direction as for large particles.

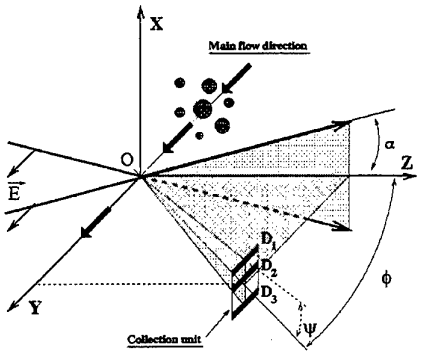


Figure 4 Phase Doppler « Modified Standard » geometry.

Intensity-measuring-based techniques are not usually considered to be very convenient for the diagnosis of local structures in two-phase flows as the light intensity that is collected by the detectors is affected at the same time by the phenomenon under study and a tremendous number of factors, which may vary in a complex way, in time and in space. Thus, under such conditions, the problem is to know whether to attribute the measured signal fluctuations to the phenomenon under study or to some "external" events. In the principle of the DBT, the amplitude of the reflected signal is used as a reference signal to take into account these fluctuations; this signal is somehow used for an on-line intensity calibration, delayed in time by only a few micro seconds depending on the droplet velocity and size. In Eq. (1), the nominal refracted rays intensity, which can not be obtained directly for an inhomogeneous particle, can be calculated from the measurement of the reflected signal. With geometrical optics (GO), one can calculate the relation between these two quantities. For a point detector, if we use Fresnel's amplitude coefficients, ε_1 and ε_2, see Van de Hulst (1957), and include a divergence term to account for the curvature of the particle surface, the interrelation reads:

$$\frac{I_{1,0}^{\max}}{I_0^{\max}} = \frac{\varepsilon_1^2}{\varepsilon_0^2} \frac{\tan(\tau')}{\tan(\tau')-\tan(\tau)} \tag{2}$$

Thus, with Eq. 1, the suspension concentration in scatters inside the particle can be deduced from the following expression:

$$C_V = -\frac{\pi . d^3}{6D\sin(\tau')C_{ext}} \left[\ln\left(\frac{I_{1,K}^{\max}}{I_0^{\max}}\right) + \ln\left(\frac{\varepsilon_1^2}{\varepsilon_0^2} \frac{\tan(\tau')}{\tan(\tau')-\tan(\tau)}\right)\right] \tag{3}$$

Trajectory Effects:

In the so-called "Modified Standard" (MS) or "Planar" PDA geometries (see Xu et al. (1994), Aizu et al. (1993), and Onofri (1995) for a detailed review), trajectory effects (TE) are eliminated for particles moving along the expected main flow direction. When the DBT is used with such geometries, as recommended here, an additional type of TE comes out for the amplitude ratio of the refracted to the reflected signal amplitude: the ratio changes with particle locations perpendicularly to the expected main direction (TE occurs for positions along the OX axis in the case of an MS geometry, see Figure 4). This TE has negligible effects on phase and thus on diameter measurements, but it can have a significant influence on the amplitude ratio between the different scattering processes. It can nevertheless be eliminated in three ways.

Let us consider, for an MS geometry, that the intensity profile in the probe volume, along the (OX) axis, is of the form:

$$I(x) = I(0)\exp\left[-2(x/\omega_0)^2\right] \tag{4}$$

where ω_0 is the beam waist radius (almost equivalent to the probe volume diameter), and I(0) the maximum intensity along the beam axes. If we assume a collection unit with two symmetrical detectors (i=1 and 3, in figure 4), the low pass filtered Doppler signals for refraction and reflection will read:

$$\begin{aligned} I_{1,K}^{(i)}(x) &= g^{(i)} I_{1,K}^{\max}(0)\exp\left[-2\left(x \pm x_1\right)^2/\omega_0^2\right] \\ I_{0,K}^{(i)}(x) &= g^{(i)} I_0^{\max}(0)\exp\left[-2\left(x \pm x_0\right)^2/\omega_0^2\right] \end{aligned} \tag{5}$$

the symbol $\pm$ meaning that the sign should be positive for detector 1 and negative for detector 3. g^i corresponds to the electronic gain of each detector, which is expected to be linear. x_1 and x_0 are the impact parameters defined in Figure 5, with $x_1 = D\cos(\tau_x)$ and $x_0 = D\cos(\psi/2)$, where τ_x is deduced by solving the transcendental equation:

$$\psi = 2\tau_x - 2\cos^{-1}\left[\cos(\tau_x)/m\right] \tag{6}$$

We assume here that the variation of the Fresnel's coefficients with the particle trajectory is negligible as the displacement of the particle in the probe volume is small compared to the distance of the detectors from the probe volume. Let $R^{(i)}$ be the ratio of the refracted burst to the reflected burst maximum for each detector:

$$R^{(i)}(x) = \frac{I_{1,K}^{(i)}(x)}{I_0^{(i)}(x)} \exp\left[-2\left(\left(x \pm x_1\right)^2 - \left(x \pm x_0\right)^2\right)/\omega_0^2\right] \tag{7}$$

We can sum the two ratios to obtain an expression independent from the gain of each detector and from the particle position along the (OX) axis:

$$\frac{\ln(R^{(1)})+\ln(R^{(2)})}{2}=\ln\left[\frac{I_{1,K}^{\max}(0)}{I_0^{\max}(0)}\right]-2\left[\frac{x_1^2-x_0^2}{\omega_0^2}\right] \quad (8)$$

Thus we found for the volume concentration in scatters:

$$C_V=\frac{-\pi.d^3}{6D\sin(\tau')C_{ext}}\left[\frac{\ln(R^{(1)})+\ln(R^{(2)})}{2}+\ln\left(\varepsilon_1^2/\varepsilon_0^2.\frac{\tan(\tau')}{\tan(\tau')-\tan(\tau)}\right)+2\left(\frac{\left[\cos^2(\tau_x)-\cos^2(\psi/2)\right]p^2}{\omega^2}\right)\right] \quad (9)$$

Thus to eliminate TE along the (OX) axis one can use the logarithm of the amplitude ratio of the refracted to the reflected burst from two symmetrical detectors (as they are usually in common PDA system). A second possibility is to use (for the amplitude ratio measurements) a single detector located in the scattering plane ($\psi=0$) as in this case the correction term is equal to zero in Eq. 9. There is no need for a correction of TE provided that the detector aperture along (OX) can be considered as small. The third possibility is to use an elliptical probe volume with a longer axis along (OX) (made with laser sheets, see Onofri 1995). In this case, the correction term in Eq. 9 tends to zero. Then the use of the amplitude ratio from only one detectors is enough.

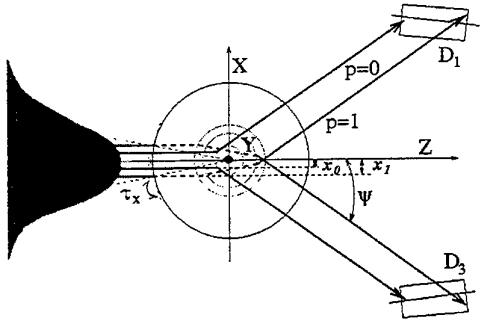


Figure 5 Two symmetrical detectors can be used to eliminate Trajectory effects on the signal intensity ratio when a MS geometry is used.

3.2 Monte Carlo model and multiple scattering

When the particle concentration in scatters increases, multiple scattering may become a dominant phenomenon, the Beer-Lambert approach developed in the previous section is expected to drop. Thus, to take into account this effect, a Monte Carlo approach has been developed.

To describe the suspension, we consider a collection of randomly distributed scatters inside the particle. So the mean free path $\tilde{l}$ for a ray (pencil of radiation in Chandrasekhar's terminology) between two scatters is given by $\tilde{l}=1/NC_{ext}$. Table 1 gives an overview of the evolution of this last parameter with the scatter size. The probability that a ray goes over a distance l inside the suspension without scattering is: $P(l)=1/[\tilde{l}\exp(-l/\tilde{l})]$. The simulation procedure is then divided in four steps:

(1) the phase diagram of the scatters inside the suspension is calculated using the Lorenz-Mie theory with parameters: λ/m, m', d and for a particular polarisation. A look up table of the probability density for an incident "ray" to be scattered in the direction θ is then created.

(2) along the (OY) axis, from –D/2 to D/2, over n_i impact parameters are defined and the paths of the corresponding rays, impinging on the particle, are followed until they go out of the particle, or until they experience n_r internal reflections with the particle-air interface. To calculate the intensity of reflected and refracted rays at the particle interface, Fresnel's coefficients are used for a particular polarisation. When a ray has reached the probability of being scattered by a scatter, the look up table calculated in step 1 is used to find its scattering direction. For each impact parameter over n_p rays are considered, step a) in Figure 6.

(3) a table is created with impact parameters as inputs and the scattering directions, the number of collisions, the path length of each ray as outputs. This table is used to provide afterwards various statistical and integrated quantities. In the present case a rectangular aperture is simulated for the PDA detectors by integrating the intensity of the different rays over the defined solid aperture angles. The beam half angle is also taken into account by adding the collected rays intensity at the two equivalent scattering angles (for the planar geometry: $\psi\pm\alpha$).

(4) to simulate the Gaussian intensity profile in the probe

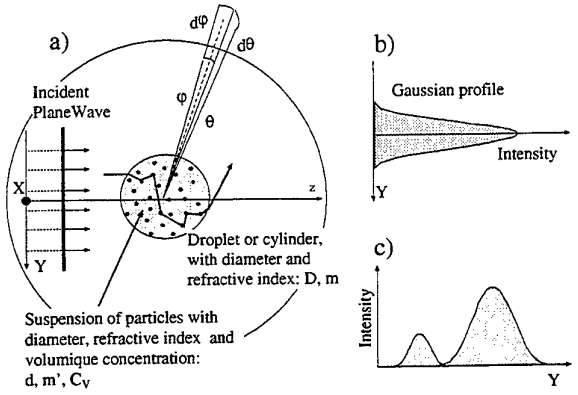


Figure 6 In the Monte Carlo procedure the path of rays from a incident plane wave is followed during the different scattering processes: reflection, single refraction, internal scattering. The spatial distribution of the scattered light is afterwards weighted by a Gaussian to account for the probe volume intensity profile and the droplet trajectory.

volume and a trajectory, the intensity of each ray collected by the detectors is weighted by a sliding Gaussian function, along the (OY), steps b) and c) in Figure 6. Each

signal is then interpolated by a Gaussian interpolating function to find its maximum.

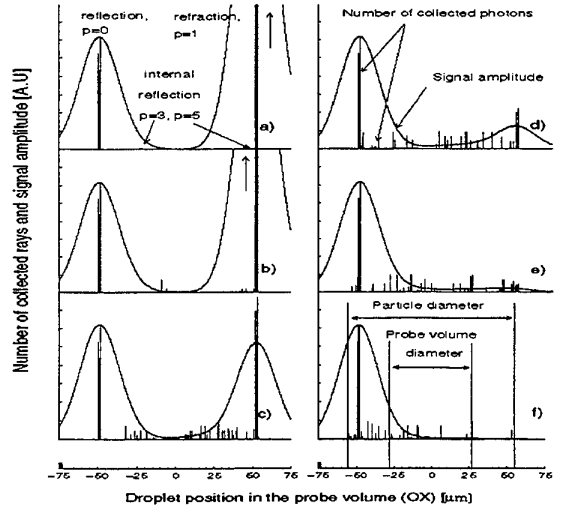


Figure 7 Monte Carlo simulations of low pass filtered PDA signals for a 110 µm diameter cylindrical jet with increasing volume concentration in latex particles with diameter 0.35µm. C_V evolves from a) to f) as 0, 0.0125, 1.25,2.5,5,10 with n_i=3000, n_p=50, n_r= 7.

Figure 7 shows some signals obtained by this procedure. The optical parameters used, detector 2, a 110µm diameter cylindrical jet with different concentration in suspension, are equivalent to those used for the experimental

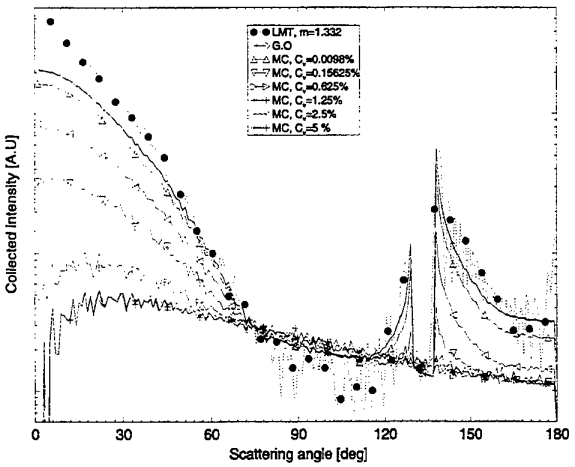


Figure 0 Collected light intensity versus the scattering angle, for a 110 µm liquid jet with increasing concentration in suspension.

test: a planar geometry, see table 2 and the next section. In this figure, the suspension volume concentration in latex particles of diameter 0.35 µm increases from a) to f) as 0, 0.0625, 1.25, 2.5, 5, 10%. The vertical bars correspond to the collected rays before the application of the Gaussian sliding window and the continuous curves to the signals amplitude afterwards. Figure 8 presents the scattered light intensity, by a cylindrical jet with increasing suspension, that is collected by a detector like those defined in table 2. The calculation have been made for a single Gaussian beam illumination (perpendicular to the jet as the scattering plane).

3.3 Experimental setup and procedure

For a precise control of the suspension concentration and for experimental facilities, tests of the proposed technique were carried out on cylindrical jets (one circular cross-section) rather than spherical droplets. Note that it has been shown by Mignon (1997) that phase Doppler Anemometry can be used, without any particular problems, to size cylindrical particles with axes perpendicular to the beam plane. The only modification that have to be done is to use a planar geometry for the optical set up ($\phi = 0, \psi \approx 6$, particles trajectories along (OX)). In our experimental setup, the jet was fixed. In order to simulate a particle velocity, and thus to produce the required two bursts, we used a rotating mirror to shift the probe volume, see Figure 8. The trajectory radius described by the probe volume was sufficiently large to ensure that the particle trajectory deviation was less than 0.05° from the direction perpendicular to the fringes. The raw Doppler signal output from a one component Aerometrics systems (based on a 10mW HeNe laser) were stored on a 8-bits LECROY 9314L digital oscilloscope and read out to a PC for further analysis.

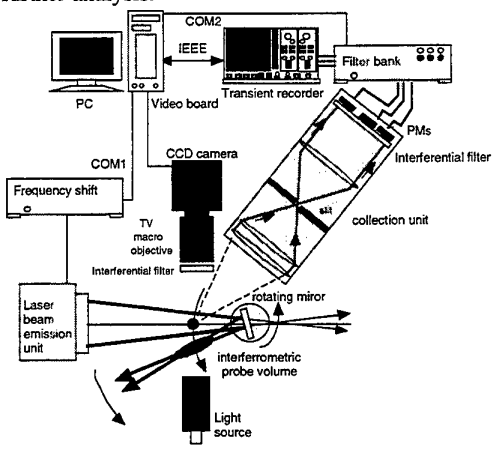


Figure 8 Schematic of the experimental setup

Solutions were made of different water suspensions of spherical polystyrene particles from Bangs laboratories, Inc. Five latex particle sizes were used, *d=0.06, 0.35, 0.61, 1.60, 3.30,* see table 1 for some of the optical characteristics of these particles and the corresponding solutions for 10% volume concentration. Dilutions with distilled and micro-filtered water were used to obtain smaller suspension concentrations. Polystyrene has a refractive index of 1.588 for λ=0.6328µm; under ambient tempera-

ture its relative refractive index to water is of 1.192. Due to the latex density, $\rho=1.050g/ml$, and agglomerating internal forces, solutions were put in a ultrasonic system before to be use. To produce cylindrical jets, the liquid suspensions were ejected from a syringe through a needle with known internal diameters: 110, 170, 220, 370µm, see Figure 9. The length of the needles was about, a hundred times their diameter, which was expected to be enough to obtain a laminar flow at the needle output. The liquid jet diameter and stability was controlled and measured during the experiments by a classical video imaging and acquisition board system.

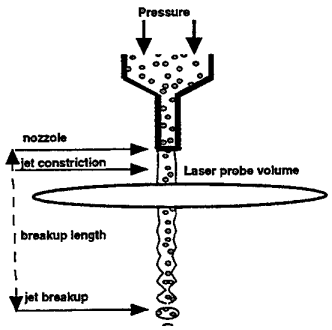


Figure 9 Position of the probe volume along the jet axis

3.4 Experimental results

Figure 10 presents some typical experimental Doppler bursts obtained for a 110 µm jet and increasing suspension concentration, detector 1. In a) the burst from the left part is the reflected one, the other is the refracted one. For all concentrations, the reflected burst amplitude and visibility remain almost constant whereas, at the same time, a strong decay is observed for the refracted bursts.

	Diameter for the latex particles [µm]				
	0.06	**0.35**	**0.61**	**1.6**	**3.3**
N [m^{-3}]	$6.97\ 10^{20}$	$4.26\ 10^{18}$	$7.90\ 10^{17}$	$4.46\ 10^{16}$	$5.09\ 10^{15}$
C_{ext} [m^{-2}]	$2.74\ 10^{-18}$	$3.17\ 10^{-15}$	$3.27\ 10^{-13}$	$7.36\ 10^{-12}$	$1.68\ 10^{-11}$
Q_{ext}	$9.70\ 10^{-4}$	0.0329	1.12	3.66	1.97
$\tilde{l}$ [m]	827	74	3.9	3.1	12
K [m^{-1}]	$1.91\ 10^{3}$	$1.35\ 10^{4}$	$2.85\ 10^{5}$	$3.28\ 10^{5}$	$8.55\ 10^{4}$
k	$9.62\ 10^{-5}$	$6.80\ 10^{-4}$	$1.30\ 10^{-2}$	$1.65\ 10^{-2}$	$4.31\ 10^{-3}$

Table 1 Optical characteristics of the scatters and the suspensions. N, $\tilde{l}$, K and k are calculated for a suspension with a 10 % of scatters in volume. C_{ext} and Q_{ext} ($=4.C_{ext}/\pi d^2$) were computed for the laser wavelength λ/m'.

Laser Wavelength, λ [µm]	0.6328		
Laser Power [mW]	10		
Beam waist diameter [µm]	52		
Half beam angle, α [°]	2.27		
Polarization	perpendicular		
Detectors locations and apertures, N°	*1*	*2*	*3*
Mean elevation angle, ψ [°]	54	55.3	58.2
Off-axis angle, ϕ [°]	0	0	0
Detectors angular width, δψ [°]	0.57		
Detectors angular height, δϕ [°]	0.57		

Table 2 Optical parameters used for the experimental set up and for the numerical simulations.

Figure 11 presents the evolution of the measured amplitude ratio between the refracted and reflected bursts, in logarithm scale, for a 110 µm jet with increasing volume concentration in scatters of five different diameters. In all cases, the curve evolution is first linear up to a concentration which depends on the scatter size: more than 10% for the smallest scatters and 1.25% for the 1.6 µm. This evolution corresponds to an exponential decay of the refracted burst amplitude, in agreement with the law predicted by the GO model assuming a dominant single scattering process for solutions of low optical thickness. The relative evolution of the slopes is also in qualitative agreement with the formal absorption coefficients, K, calculated in table 1. Afterwards, the attenuation efficiency, which may be defined as the local slopes of the amplitude ratio versus the concentration, decrease, it seems from these measurements, that after a transition zone another exponential decay regime is reached.

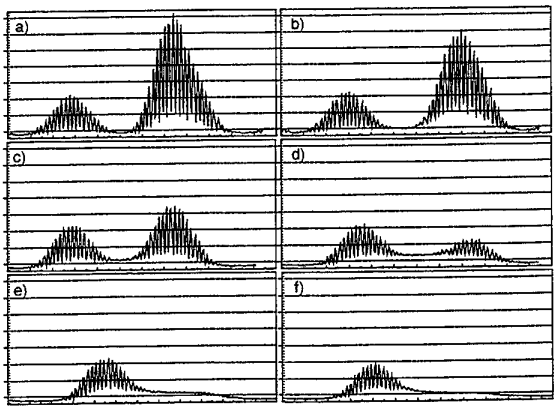


Figure 10 Experimental High pass filtered Doppler signals obtained for a 110 µm liquid jet with increasing suspension concentration : .0049, .31,.75, 1.25, 2.5 and 5%, from left to right and up to down, respectively. The suspension is made of 0.35 µm latex particles in water.

Figure 12, presents a comparison between the measured jet diameter from the refracted and the reflected signals for suspensions of different scatter sizes and concentrations. The corresponding standards deviations from the expected diameter are also plotted. For this particle size, 220 µm, the reflected burst provides size measurements with deviation less than 5% over all concentrations (from 0 to 10% at least) whereas, with the refracted signals, this deviation is limited to concentrations below 0.2%, and the

deviation goes up to 50% for concentrations around only 1%. For higher concentrations it is almost impossible to get reliable size measurements (the phase-shit oscillates "randomly" between 0 and 2π).

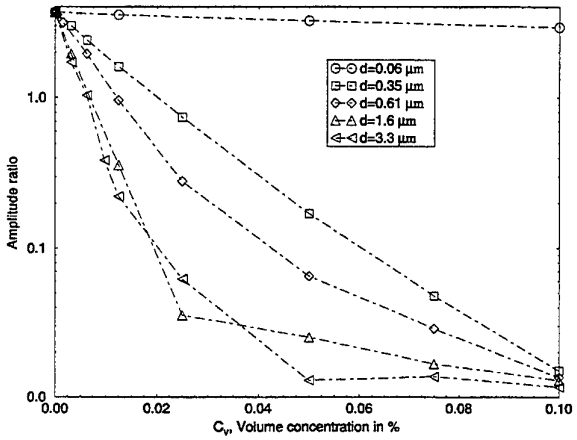


Figure 11 Experimental intensity ratio evolution for a cylindrical jet with increasing concentration in suspension

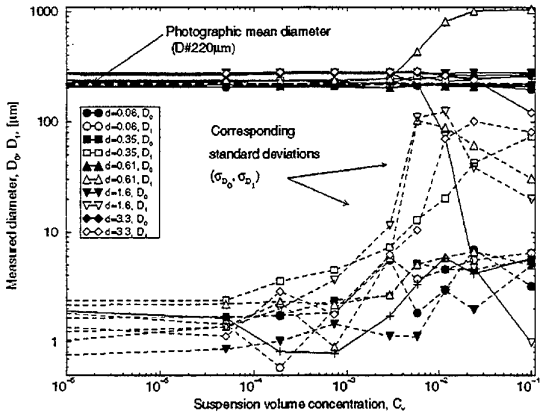


Figure 12 Comparison between size measurements obtain from the reflected and refracted signals

4. DISCUSSIONS

Numerical predictions and experimental results

Figure 13 presents the evolution of the amplitude ratio with the suspension concentration for a 110 µm diameter jet, according to experiments and the two previously exposed models. The qualitative agreement found by comparing Figures 7 and 10, is confirmed here quantitatively, and has been observed for all experiments. The Beer-Lambert approach is valid for suspension with small optical thicknesses, whereas the Monte-Carlo approach is valid over all the concentration variation considered here.

Optical parameters and measurements range

For the experimental setup, the optical parameters were chosen mainly in order to meet the following conditions:

- an optical probe volume with a sharp intensity profile. The reduction of the probe volume diameter leads to a better separation between the two bursts and a reduction of internal scattering effects on the reflected burst. Unfortunately this also leads to a reduction in the particle transit time in the probe volume and thus a decrease in the possibility for accurate phase determination. Thus, a compromise has to be found.

- a nominal amplitude ratio (not too high) and a refracted signal not too sensitive to the particles in homogeneity, in order to extend the measurement dynamics range on the particle diameters and concentration in suspension. These parameters depend strongly on the laser beam polarization; and the collection angle (through the distance L). For water droplets this ratio is close to unity, for a scattering angle around 69° and the perpendicular polarization, see Onofri (1995b). The laser wavelength also plays an important role trough the factor C_{ext}. Note that the use of several wavelengths may be used to obtain an estimation of the scatter sizes, in addition to their concentration, as C_{ext} depends on both these two parameters, provided that the scatter size is of the order of magnitude of the laser wavelength.

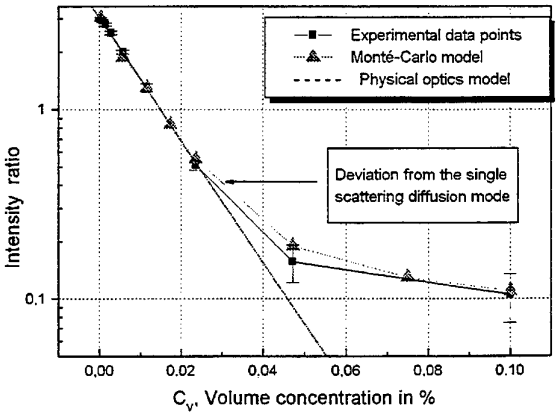


Figure 13 Comparison of numerical predictions and experimental results for a 110 µm jets and 0.35µm latex particles.

In Figure 11, the highest sensitivity to suspension concentration occurs for values below 1 to 5%, or 10% (depending on the scatters). To increase this parameter to small concentrations in scatters, one possibility is to increase the distance L, through the proper choice of the collection angle. Some preliminary simulations, not reported here, have shown that at the rainbow angle position (back scattering location highly sensitive on the particle refractive index), a parallel polarization and for the case considered here, one can expect a sensibility to suspension concentration multiplied by a factor four. The increase in the concentration measurement dynamic range seems to be more difficult to optimize, and will be investigated in a future work.

Signal processing

With a classical PDA setup, Doppler bursts have the following form:

$$S(t) = P_s[1 + V\cos(\omega t + \phi)] \quad (10)$$

where P_s, V, ω, ϕ, are respectively, the signal pedestal, visibility, pulsation, and phase. From all of these terms only P_s can not be clearly attributed to an interference phenomenon. The scatters inside the suspension induce some perturbations on the laser beams coherence and thus on the signal visibility and phase. Thus, the amplitude of high pass filtered Doppler bursts, $S(t) = P_s V\cos(\omega t + \phi)$, which are classically used by PDA hardware for signal processing, may be affected to the particle inhomogeneity in two ways: through the pedestal and through the visibility (which is a very complex parameter). Figure 14, shows the typical evolution of the reflected and refracted burst visibility versus the jet concentration in suspension. The reflected signal visibility is very lightly affected by particle inhomogeneity unlike the refracted one. Consequently, during the experimental tests, the amplitude ratio was calculated from the signal pedestal by using the raw output signals from the PDA system rather than the filtered and logarithm amplified signals. Note that in theory, the amplitude of the high pass filtered signals, $P_s V$, could be used too, but this requires developing more complex models, than those developed here for experimental raw data inversion

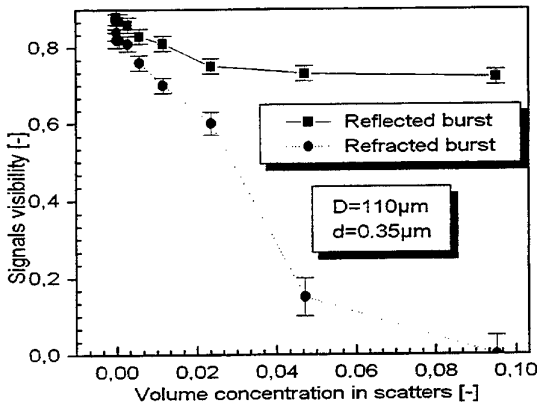


Figure 14 The signal visibility of the refracted signal is highly affected by the particle inhomogenity unlike the reflected burst.

5. CONCLUSION

A method for on-line and accurate sizing of optically inhomogeneous spherical and cylindrical particles in addition to the particles velocity and material non homogeneity has been proposed. Numerical tests based on Geometrical optics and a Monte Carlo approach have shown good agreements with the experimental test performed on cylindrical jets of different concentration in a suspension of small particles.

6. REFERENCES

Aizu Y., Durst F., Gréhan G., Onofri F. and Xu T-H. , A PDA System Without Gaussian Beam Deffects, in 3rd Optical Partical Sizing conference , Yokohama (JAPAN), pages 461-470, 1993.

Bangs labs, Inc. 9025 technology drive, Fishers, IN 46038-2886, USA.

Bergounoux L., Misguish-Ripault J., Firpo J-L, André J., Monte Carlo calculation of backscattered light intensity by suspension : comparison with experimental data , App. Opt, V. 35, pages 1735-1741, 1996.

Domnick J., Lindenthal A., Tropea C., Xu T-H., Application of PDA in paint sprays, Atomization and Sprays, V.4, N.4, 1994.

Hess C.F. and Wood G.P., « The pulse Displacement technique - a single Particle Counter with a size range larger thant 1000:1 », in 3rd Optical Particle Sizing Conference , Yokohama , Japan, pages 475-482, 1993.

Gréhan G., Gouesbet G., Naqwi A.and Durst F., Particle Trajectory Effects in Phase Doppler Systems: Computations and Experiments, Part. Part. Syst. Charact., pages 332-338, V. 10, 1993.

Manasse U., Wriedt T., Bauchhage K., Optimization of PDA parameters for sizing of optically inhomogeneous liquid droplets, in 3rd Optical Particle Sizing Conference , Yokohama, Japan, 1993.

Manasse U., Wriedt T., Bauchhage K., Reconstruction of real size distributions hidden in PDA results obtained from droplets of Inhomogeneous liquids., Part. Part. Syst. Charat., V. 11, 1994.

Mignon H., Anémométrie Phase Doppler et particules non sphériques: cas des cylindres et des ellipsoïde, PhD Thesis, Université de Rouen, France, Jan. 1997.

Onofri F., Gréhan G., Gouesbet G., Xu T-H., Brenn G. and Tropea C., PDA with Dual Burst Technique for Particle Refractive Index Measurements , 7 th Int. Symposium on Applications of Laser Techniques to Fluid Mechanics, Lisbon, July 11-14, 1994.

Onofri F., Mignon H., Gouesbet G., Gréhan G. and Tropea C., Phase Doppler measurements of non spherical particles: cylindrical and multilayered particles , 4th Optical Particle Sizing conference-Partec95, Nurnberg, Germany 21-23 March, 1995a.

Onofri F., Prise en compte de la dimension finie des faisceaux d'éclairage en granulométrie optique: anémométrie phase Doppler- Diagnostics des ecoulements diphasiques , PhD thesis, Université de Rouen, France, Nov. 1995b.

Onofri F., Girasole T., Gréhan G., Gouesbet G., Brenn G., Domnick J., Tropea C. and Xu T-H., Phase-Doppler Anemometry with Dual Burst Technique for Measurement of Refractive Index and Absorption Coefficient simultaneously with Size and Velocity , Part. and Part. Syst. Charact., V 13, pages 112-124, 1996a.

Onofri F., Blondel D., Gréhan G. and Gouesbet G., On the Optical Diagnosis and Sizing of Coated and Multilayered Particles with PDA , Part. and Part. Syst. Charact., V. 13, pages 104-111, 1996b.

Naqwi A. and Durst F., Light scattering Applied to LDA and PDA Measurements, Part1: Theory and Numerical treatments, Part. Part. Syst. Charact., pages 245-258, N.8, 1998.

Rheims J., Dahl H., Wriedt T., Bauckhage K., Sizing coated spheres with Phase Doppler Anemometry, in 4th Optical Particle Sizing Conference-Partec95, Nürnberg, Germany, pages 409-418, 1995.

Van de Hulst H.C., Light Scattering by Small Particles, Dover Publications, Inc. New York, Chapter 12, 1957.

Sankar S.V, Inenaga A. and Bachalo W.D., Trajectory dependent scattering in Phase Doppler interferometry: minimizing and minating sizing error, 6th Int. Symposium on Application7 of laser techniques to fluid mechanics, Lisbon, Portugal, July 20-23, paper 12.2, 1992

Xu T-H. and C. Tropea C., Improving performance of 2D Phase-Doppler Anemometer, Meas. Sci. and Tech., 5, pages 969-975, 1994

Principle Of Statistical Dependence And Its Application To Sizing Of Irregular Particles Using Phase Doppler Technique

Amir Naqwi and Chris Fandrey

TSI Incorporated

P.O. Box 64394, St. Paul, MN 55164

ABSTRACT

A theoretical formulation of statistical dependence to measure complex processes is presented. Application is then made to the measurement of irregular particles with a phase Doppler system. Earlier results had shown that the dynamic size range of a standard system is very limited. Two alternative solutions to this problem are presented and experimentally verified.

1. INTRODUCTION

Diagnostics of complex processes poses a challenge as many influences on the instrument response remain unknown or difficult to model. The principle of statistical dependence allows one to treat these unknown influences as random variables. For this purpose, we may consider a measurement process where several quantities, M_1, M_2, ... M_n are measured. These measurands depend on certain process properties of interest, P_1, P_2, ... P_m. In a typical measurement situation, it would be of interest to determine the probability distribution $P(P_j)$ of a certain combination P_j of the process properties.

We may now consider a hypothetical situation where the combination P_j may be present all the time. Due to unknown influences, the measurands will still show fluctuations, so that a certain set of values for a combination of measurands M_i will be measured with a conditional probability $P(M_i|P_j)$. In a process, where P_j is not present consistently, the probability of measuring M_i as a result of P_j is given as the following joint probability function:

$$P(M_i \cap P_j) = P(M_i|P_j)\,P(P_j)\,. \qquad (1)$$

When integrated over all the possible combinations of P_j, the above relationship takes the form

$$P(M_i) = \int_{P_j} P(M_i|P_j)\,P(P_j)\,dP_j\,, \qquad (2)$$

where the left-hand side is *measurable*. It is the multi-parameter probability distribution of the measured quantities M_i. Various correlations and moments of this distribution function may be expressed as

$$\overline{\prod_i M_i^{k_i}} = \int_{P_j}\left\{\int_{M_i}\left[\prod_i M_i^{k_i}\right]P(M_i|P_j)\,dM_i\right\}P(P_j)\,dP_j \qquad (3)$$

The above equation may be utilized for obtaining useful statistical information about the properties of the complex process under investigation, provided that the term {...} can be modeled in terms of the properties. The following two-step procedure may be used for this purpose.

1. Consider dimensional relations between the process properties and the measurands to select the combinations and the values of k_i.

   For example, the property of interest P_1 may be the volume of certain complex objects and the quantity being measured M_1 may be the shadow area of these objects. In this case, dimensional analysis suggests that the term {...} should be modeled as

$$\int_{M_1} M_1^{3/2} P(M_1|P_1)\, dM_1 = K_1 P_1$$
$$\int_{M_1} M_1^{3} P(M_1|P_1)\, dM_1 = K_2 P_1^2 \qquad (4)$$
$$\int_{M_1} M_1^{9/2} P(M_1|P_1)\, dM_1 = K_3 P_1^3$$

where K_1, K_2 and K_3 are the calibration constants.

2. Experimentally determine the calibration constants.

Two type of experiments are possible, i.e. mono-property and polydisperse property setups. In the first type of experiments, the property values are held fixed and measurand distributions are measured.

In the above example, an object of known volume P_1 could be suspended and spun around to obtain shadow area distributions. Such distributions may be referred to as *mono-property measurand distributions*. In order to determine the calibration constants, Eqs. (4) may be expressed as

$$K_1 = \left[\overline{M_1^{3/2}}\right]_{P_1} \Big/ P_1$$
$$K_2 = \left[\overline{M_1^{3}}\right]_{P_1} \Big/ P_1^2 \quad , \qquad (5)$$
$$K_3 = \left[\overline{M_1^{9/2}}\right]_{P_1} \Big/ P_1^3$$

where $\left[\overline{M_1^{3/2}}\right]_{P_1}, \cdots$ are moments of mono-property measurand distributions.

Besides obtaining the calibration constants, mono-property experiments allow to verify the models based on dimensional analysis, e.g. linearity of the relationship between $\left[\overline{M_1^{3/2}}\right]_{P_1}$ and P_1 can be checked.

Alternatively, model equations (4) may be substituted in Eqs. (3) to obtain calibration correlations in the following form:

$$K_1 = \overline{M_1^{3/2}} \Big/ \overline{P_1}$$
$$K_2 = \overline{M_1^{3}} \Big/ \overline{P_1^2} \quad . \qquad (6)$$
$$K_3 = \overline{M_1^{9/2}} \Big/ \overline{P_1^3}$$

In order to determine the calibration constants, moments of the properties must be known for the calibration experiments.

Once the calibration constants are established, the set of Eqs. (6) can be used to compute the first three moments of the property P_1 based on non-integer moments of the measurand M_1 in any process involving similar complex objects as used for calibration. The generalized formulation of Eq. (3) allows one to measure correlations between various properties (e.g. $\overline{P_1^2 P_2^3}$) using correlations between the measurands.

The above formalism is applied in the present work to sizing of irregular particles using a phase Doppler system. For this purpose, we will consider a single measurand, i.e. phase shift Φ, and a single property, i.e. particle size D.

2. PRINCIPLE OF PHASE DOPPLER TECHNIQUE

The phase Doppler system for sizing and velocimetry of particles is shown in Fig. 1. The output beam of an Argon-Ion laser is transmitted to the beam conditioning optics which is connected to the transmitting probe that focuses pairs of monochromatic beams, such that they cross at the focal point, where interference fringes are produced. As a particle crosses these fringes, it scatters light, which oscillates in time with a frequency that is proportional to the velocity component normal to the fringes. Laser beam pairs of different color are used to measure different components of velocity.

The oscillatory signals collected by the two receivers have the same frequency but are shifted in phase, which is used to measure the particle size. The signal conditioning electronics employ photomultipliers to convert the optical signals into electrical signals.

The output of the electronics is routed to a signal processor, which determines the frequency of the individual signals and phase shift Φ between the phase Doppler signals. The modern processors are capable of transferring the measured data at a high speed to a

computer where a software package reduces the results and displays them in real-time.

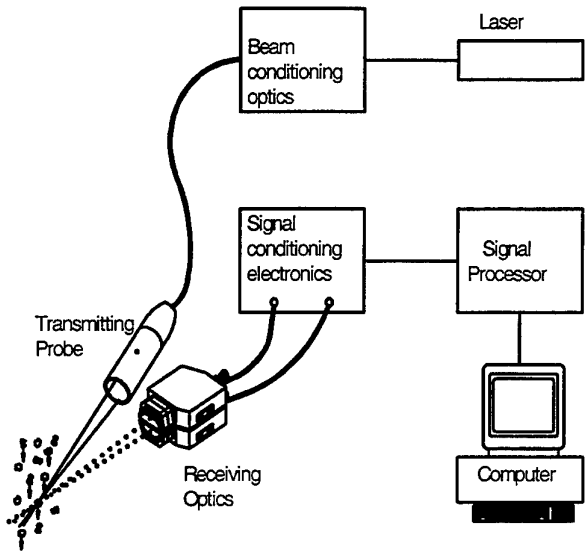


Figure 1: Schematic diagram of a phase Doppler system

3. STATISTICAL DEPENDENCE APPLIED TO THE PHASE DOPPLER MEASUREMENTS

In the case of phase Doppler technique for sizing statistically irregular particles, Eq. (2) may be expressed as

$$P(\Phi) = \int_{D=D_{\min}}^{D_{\max}} q(D,\Phi)p(D)dD\,, \qquad (7)$$

where $P(\Phi)$ is the measured phase distribution and $p(D)$ is the unknown particle size distribution. The conditional probability function $q(D,\Phi)$ is referred to as the monosize phase distribution (MPD) function, see Naqwi [1]. Taking moments of Eq. (7), a simplified form of Eq. (3) is obtained,

$$\overline{\Phi^m} = \int_{D=D_{\min}}^{D_{\max}} \left\{ \int_{\Phi} \Phi^m q(D,\Phi)d\Phi \right\} p(D)dD\,. \qquad (8)$$

The phase shift represents the path length delay of light rays interacting with the particle. These path lengths vary linearly with the particle size in a statistical sense. Also for nearly backscatter collection of signals, the sign of the phase shift does not have any significance (both positive and negative signs occur with equal probability). Hence, Φ is taken as the absolute value of the phase shift. Based on the above dimensional considerations, the following calibration correlations may be proposed:

$$\int_{\Phi} \Phi^m q(D,\Phi)d\Phi = K_m D^m \quad \text{for } m = 1,2,3,\cdots \qquad (9)$$

Substituting the above equations in Eq. (8), the following relations between the moments of particle size and moments of phase shift can be obtained.

$$\overline{D^m} = \overline{\Phi^m}/K_m \quad \text{for } m = 1,2,3,\text{L} \qquad (10)$$

Direct measurements of MPD functions for irregular alumina and corn starch particles are presented by Naqwi and Fandrey [2] by measuring particles within an Aerodynamic Particle Sizer (APS). Figures 2 and 3 show micrographs of alumina and corn starch particles. As can clearly be seen, the alumina particles have a highly nonspherical shape while the corn starch particles are more spherical with a nonhomogeneous internal structure.

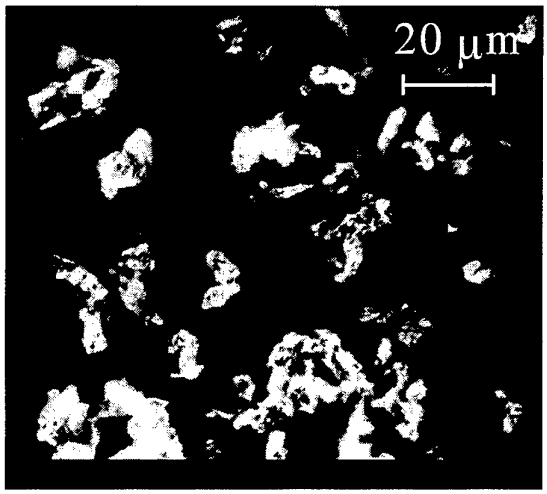


Figure 2: Micrograph of alumina particles

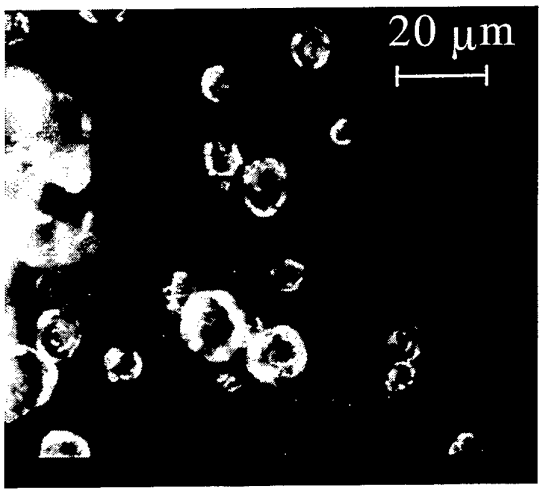


Figure 3: Micrograph of corn starch particles

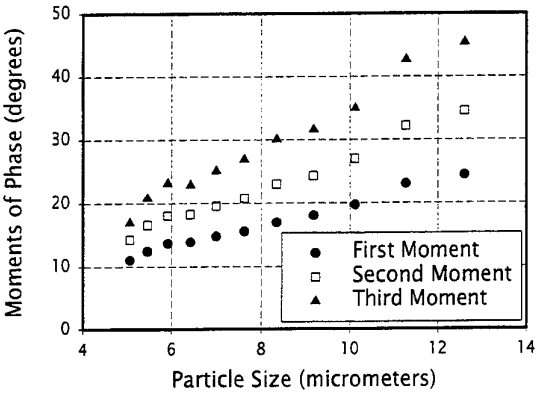


Figure 4: Moments of MPD for alumina particles

Since the APS provided an aerodynamic size for each particle, the phase distributions for individual sizes could be constructed. The fringe spacing was 6.17 μm for these experiments.

The first three moments of these distributions are shown in Figures 4 and 5. The trends clearly show a linear relationship between the first three moments and particle size, as predicted on the basis of dimensional considerations. The corn starch particles also have higher moment values than for the corresponding size of alumina particles. Also, the curves for corn starch become flat for particle size exceeding twice the fringe spacing, as the MPD function fills the entire range of 360° phase shift.

Slopes of the curves in Figs. 4 & 5 represent the calibration constants K_1, K_2 and K_3. Once established experimentally, these constants can be used in Eq. (10) to facilitate conversion of moments of absolute phase shift into the moments of particle size distribution. The first three moments allow for the direct measurement of D_{10}, D_{20} and D_{30}.

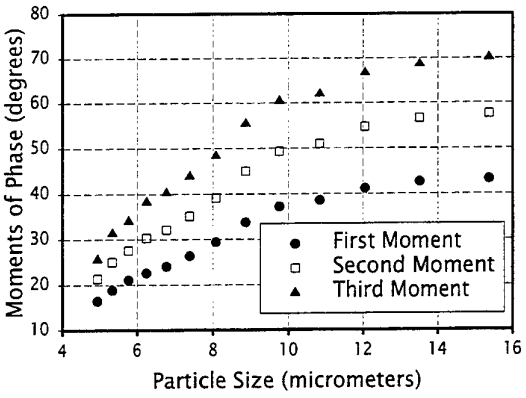


Figure 5: Moments of MPD for corn starch particles

4. DYNAMIC RANGE CONSIDERATIONS

In the calibration data of Figs. 4 and 5, the dynamic range was limited to approximately 3 to 1 [2]. The maximum standard deviation was limited to about 50°, as it corresponds to the phase distribution that fills the

entire 360° range. The minimum achievable standard deviation was about 15 degrees.

This lower limit was caused by measurement uncertainties. The main source of broadening for the measured phase is believed to be the nanosecond jitters in the transfer time of the signals through the photomultipliers. These nanosecond delays may have caused significant phase errors as the in-coming optical signals had a period of around 25 ns due to 40 MHz frequency shifting in the Bragg cell; i.e. 1 ns jitter corresponded to 14° phase error.

Bragg cells are not available for frequencies much smaller than 40 MHz. However, a substantially smaller optical signal frequency can be obtained by using two Bragg cells; i.e. one in each beam. In this configuration a small shift frequency can be realized; e.g. 1 MHz shift frequency can be obtained by operating the two Bragg cells at 40 and 39 MHz. Using this configuration, we expected to reduce the phase error associated with PMT transit time jitter and consequently, decrease the minimum achievable standard deviation and thus increase the dynamic range. Additional calibration experiments were carried out to determine the standard deviation (second moment) of the phase distribution for monosize particles of alumina, using a dual Bragg cell configuration.

Further experiments involved sieving three polydisperse alumina samples into narrow size bins and measuring phase shift data for particles from each sieved bin. As shown in Figure 6 the particle sizes ranged from approximately 6.5 μm to 125 μm. For these experiments the frequency shift was 500 kHz, the optical receiver centroidal spacing was 16.48 mm, and the fringe spacing was 46.3 μm.

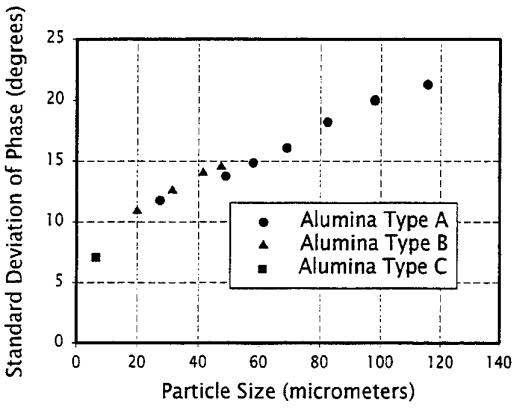


Figure 6: Standard deviation of phase versus size for large Alumina particles

The results show that the minimum standard deviation did indeed decrease to about 7 degrees (with more stringent signal validation, a standard deviation of 4 degrees is possible). Assuming the linear trend continues until a standard deviation of 50 degrees is reached the dynamic range would be approximately 50 to 1.

The second group of calibration experiments — aimed at increasing the dynamic range — were performed with a TSI Aerodynamic Particle Sizer (APS) using similar configuration as used for the data in Figs. 4 & 5. For these experiments the frequency shift was returned to 40 MHz. However, the receiver centroidal spacing took one of two values, 16.48 mm or 46.55 mm. The fringe spacing was reduced to 6.17 μm. It was expected that larger centroidal spacing will be effective for smaller particles and vice versa, so the combination of the two measurements should allow one to cover a large dynamic range.

The results given in Figure 7 show that the receiver spacing has a significant effect on the results. The minimum standard deviation with a detector spacing of 16.48 mm is just under 10 degrees. The slope of the two data sets in Figure 7 is significantly different, which verifies that a three-detector arrangement (two values of centroidal spacing) should help extend the dynamic size range.

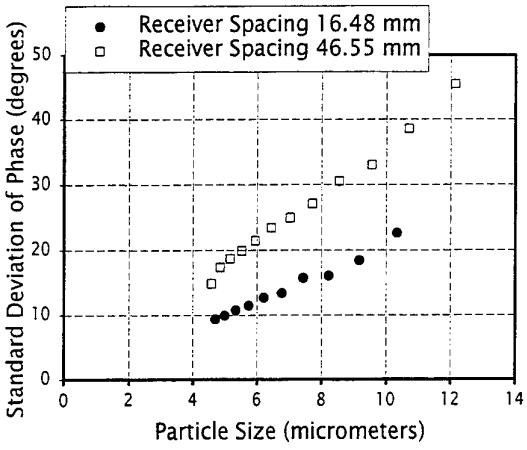


Figure 7: Calibration dependence on receiver spacing

The data in Figs. 6 & 7 suggest two possible options for obtaining a acceptable dynamic range in future work. Firstly, lowering the laser beam frequency shift by using two Bragg cells reduces the minimum standard deviation at small particle sizes, resulting in an increased dynamic range. Secondly, using a three detector system with two different receiver spacings would allow for improved precision over a larger particle size range. The final choice will depend on which option, or combination of options, results in the best overall system performance and the relative cost considerations.

Future work will also be focused on the application of this technique to in-situ field measurements. Initial applications most likely will include measurements in processes such as grinders, mills, or agglomerators. This phase Doppler technique has the advantages of being able to give velocity-resolved size distributions as well as providing data on particles found close to moving mechanical parts such as blades, grinding heads, etc. Eventually it is hoped that this technique will provide a reliable means of making in-situ measurements of irregular particles in both the industrial and research environments.

REFERENCES

[1] A. Naqwi, "Sizing of irregular particles using a phase Doppler system", Particle and Particle System Characterization 13 (1996) 343–349.

[2] A. Naqwi & C. Fandrey, "Phase Doppler measurements of irregular particles and their inversion to velocity-resolved size distributions", Powder Handling and Processing 9 (1997) 45–51.

A HIGH POWER, HIGH RESOLUTION LDA/PDA SYSTEM APPLIED TO DENSE GASOLINE DIRECT INJECTION SPRAYS

G. Wigley[1], G.K. Hargrave[1] and J.Heath[2]

[1]Engineering Faculty, Loughborough University, LE11 3TU, UK
[2]Lotus Engineering, Hethel, Norwich, NR14 8EZ, UK

ABSTRACT

A new generation LDA/PDA transmitter system has been designed and constructed. The heart of the optical system is a new type of Bragg cell. Advances in laser power handling and symmetrical splitting at high Bragg angles of the shifted and unshifted beams have made it possible to construct a simple elegant high power LDA/PDA transmitter. The optical system integrates the Bragg cell with a laser beam expander to offer a variable beam separation with a high beam expansion ratio. It is being applied to characterise the atomization of gasoline by the high pressure automotive fuel injectors as found in Gasoline Direct Injection (GDI) engines. This optical system is seen as a significant contribution to LDA/PDA transmission design not only as a research tool for use in flows of a demanding nature but, due to its opto-mechanical simplicity, flexibility and cost, a valuable asset in the teaching laboratory.

1. INTRODUCTION

The frequency shifter is the weakest link in the whole optical transmission system, Wigley (1987). Bragg cells generally require considerable effort to obtain optimum optical performance as the diffraction efficiency is sensitive to alignment, the diffraction angle is small, dictating that beam steering and aperture components be employed, while the transmitted beam is degraded in its circular cross-section, transverse intensity distribution and polarization. The use of fibre optics, Buchhave and Knuhtsen (1986), corrected for the deficiencies of the transmitted beam quality but thermal blooming in the Bragg cell and coupling to the fibre still limits the use of high laser powers and beam expansion. The alternative to the Bragg cell was the rotating diffraction grating, Oldengarm (1976), although its optical performance was far superior to the Bragg cell the magnitude of the frequency shift and stability, together with diffraction grating's mechanical fragility, limited its general application. In an attempt to improve the optical performance of the Bragg cell and produce a frequency shift of 40 MHz Pitcher and Wigley (1994) used a Bragg cell as both the beam splitter and frequency shifter with a 50/50 laser power split between the unshifted and shifted beams. Recent advances in Bragg cell design and manufacture have now resulted in frequency shift units that share the good points of both the Bragg cell and rotating diffraction grating.

2. LDA/PDA TRANSMITTER SYSTEM

The heart of this optical system is a Bragg cell that uses a tellerium dioxide crystal with an anisotropic acousto-optical interaction to provide 50/50 beam splitting of the input beam symmetrically about the optical axis and a 40 MHz frequency shift between the output beam pair with low power built-in driver electronics, Gooch & Housego (1997). The main advantages of this Bragg cell are:- thermal blooming with high laser powers has been eliminated, the output beams have a true circular cross-section, and the effective Bragg angle has been increased dramatically. However, the Bragg condition is polarization and wavelength dependent and the frequency shifted beam has the polarization direction rotated through 90 degrees.

These advantages have allowed the construction of a simple high power LDA/PDA transmitter system by integrating the Bragg cell with a two lens laser beam expander that offers variable beam separation and high beam expansion ratio. The excellent beam aligning properties of a symmetrical optical design are maintained and beam alignment devices are not necessary.

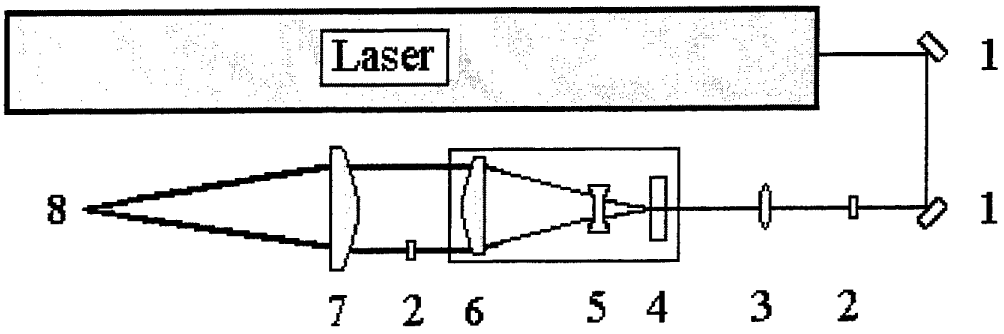


Figure 1 Schematic of Optical Layout

A schematic of the LDA/PDA transmitter system, in one component form, is shown above in Figure 1. Prisms (1) steer the laser beam through a half-waveplate (2) to align the polarization plane of the beam with the Bragg cell. The lens (3) images the laser cavity beam waist into the Bragg cell (4) to ensure a beam waist at the measurement volume. The focal length of this beam waist adjusting lens is determined by the laser beam output diameter and the required measurement volume diameter.

Two beams of equal intensity exit the Bragg cell, symmetrically about the optical axis, with an angular separation of 1.88 degrees. The first order diffracted beam is frequency shifted by +40 MHz and has an orthogonal polarization direction to the zero order beam. The laser beam expander, lenses (5) and (6), expand and collimate these diverging beams to produce a beam separation of up to 50 mm with an expanded beam diameter of 4.4 mm. A second half-waveplate (2) is then required to match the shifted and input beam polarization directions. The Bragg cell and beam expander lenses are integrated into a single opto-mechanical unit 300 mm long.

The beam separation control is a simple translation of the Bragg cell, along the optical axis, followed by a small refocus of lenses (3) and (5) to achieve collimation of the beams. The three element front lens (7) focuses the two beams to form the diffraction limited measurement volume (8).

For two colour operation, 488 nm (blue) and 514 nm (green) wavelengths, the prisms (1) are replaced by Pellin Broca dispersing prisms and the components (2) to (6) have to be duplicated with the second Bragg cell and half waveplate rotated through 90 degrees. The orthogonal blue and green beam pairs would be combined on the optical axis before the front lens (7), Pitcher and Wigley (1994). This is not seen as an unnecessary complication due to the high degree of flexibility offered since the variable beam expanders can be set to:- (a) equalise the beam separation for each wavelength, (b) equalise the dimensions of the two measurement volumes or, (c) create unequal measurement volume diameters with one inside the other.

The specification for the beam diameter at the front lens and the measurement volume dimensions are given in Table 1. These have been calculated using Gaussian beam theory but substituting the equivalent single thin lenses for the complex optical geometry of the beam expander.

The measurement volume dimensions refer to the TEM_{00} Gaussian beam diameter at the $1/e^2$ points. These dimensions are seen as the minimum since use of the inter-cavity aperture actually reduces the output laser beam diameter and will therefore increase beam waist dimensions. It is the specific requirement for this mode that limits the output power of the Argon-Ion laser.

Wavelength	Separation	Diameter	Measurement Volume Dimensions			
Transmitter Lens Focal Length			300 mm		450 mm	
			Diameter	Length	Diameter	Length
514.5 nm	50.0 mm	4.16 mm	0.047 mm	0.57 mm	0.071 mm	1.27 mm
	30.0	2.07	0.095	1.14	0.142	2.56
488.0 nm	50 mm	4.39 mm	0.042 mm	0.51 mm	0.064 mm	1.15 mm
	30	2.19	0.085	1.02	0.128	2.31

Table 1 Specification of Measurement Volume Diameters for the LDA/PDA Transmitter

The Coherent Innova 90-4 in use will maintain TEM_{00} mode at the full current of 45 amps with inter cavity aperture 4 to produce beam powers of up to 0.4 and 0.8 watts per beam in the 488 and 514 nm lines respectively at the front lens.

GASOLINE DIRECT INJECTION SYSTEMS

The current research is the analysis of the atomization of gasoline by high pressure automotive fuel injectors as found in Gasoline Direct Injection (GDI) engines. GDI fuel systems fall into two categories:- low pressure dual fluid (air assisted) injection and high pressure single fluid injection, Hargrave et al (1998). Dual fluid systems employ a sequenced pair of injectors in which fuel is first metered into a pressurised air chamber where it resides for a short delay period before being injected into the combustion chamber via a nozzle, fuel being atomised as a result of the air and fuel flow through the nozzle. Typically, air pressures of 6 to 10 bar are employed, with a charge injection duration of 4 to 7 ms. High pressure single fluid injection systems typically operate at fuel pressures between 50 and 120 bar and rely for atomization upon the high velocities generated as the fuel emerges through a nozzle into the combustion chamber. The fuel injection duration for single fluid systems is in the range 0.5 to 4.5ms. Maximum fuel delivery rates for GDI applications are typically 60 mg/injection. These sprays when compared with conventional gasoline fuel injectors are well atomized, densely laden with droplets and when injected into an environment under atmospheric conditions, as for early injection, have a rapid penetration.

FUEL SPRAY RIG

In this rig the GDI injectors were mounted to spray vertically down through an opening in a large steel plenum, 0.6 m diameter by 1 m high. The plenum was connected to an exhaust blower to establish a low velocity co-flow of air below the injector to capture and draw all the spray into the plenum. The plenum contained two large filter cones, cascaded one above the other, which were filled with foam to catch and allow the injected liquid to be drained after the experiment. The experiments use gasoline as there is sufficient evidence to suggest that there are no inert test fluids that can simulate accurately the atomisation characteristics of this fuel.

The injectors were supported from a gantry incorporating three precision traverses, two horizontal and one vertical to position the spray with respect to the LDA/PDA measurement volume. For the dual fluid GDI injectors the air supply was obtained from regulated 'shop air' while the fuel was supplied by a heavy duty automotive petrol pump. For the single fluid GDI injectors the much higher fuel pressure was supplied by a pneumatic/hydraulic ram system fed by 'shop air'. Both the single and dual fluid GDI injector types were driven by a common control unit. This provided the electronic timing gates for the solenoids governing the air and fuel supplies to the injector and their relative phasing. Its cycle time was derived from a stable function generator. The control unit also provided external trigger pulses for synchronising the data acquisition system for the optical diagnostics and the logging of the injector operating conditions.

EXPERIMENTAL TECHNIQUE

To illustrate the performance of this high power, high resolution LDA/PDA transmitter in characterising sprays measurements are presented in the near nozzle region of a high pressure single fluid GDI injector. The configuration of the transmission system for this application was:- beam separations of 45 and 50 mm with laser powers per beam of 120 and 250 milliwatts for the 488 and 514 nm wavelengths respectively. With the 300 mm final focusing lens this resulted in measurement volume diameters of 49 and 41.5 microns with fringe spacings of 3.44 and 2.94 microns for the 514 and 488 nm wavelength respectively i.e 14 fringes in each measurement volume.

The receiver optical system, a Dantec 57X10, was positioned at a scattering angle of 70 degrees for:- (1) a high spatial resolution as the effective measurement volume length was reduced to 0.1 mm (2) operated at full aperture for best dropsize resolution and (3) an insensitivity of the dropsize/phase relationship to unknown or refractive index changes of the fuel.

The Dantec enhanced 58N50 PDA signal processor was used which, at full bandwidth, allowed an axial velocity measurement range of -34 to 120 m/s a horizontal velocity measurement range of -30 to 103 m/s and a dropsize range of up to 66 microns.

The injector X-Y traverse directions are shown in Figure 2, a plan view schematic of the injector relative to the static LDA/PDA transmitter system, which indicates the positive flow directions for the radial and tangential velocity components at radial locations of R_x and R_y respectively. The Z-axis and axial velocity component were measured positive, vertically down from the nozzle.

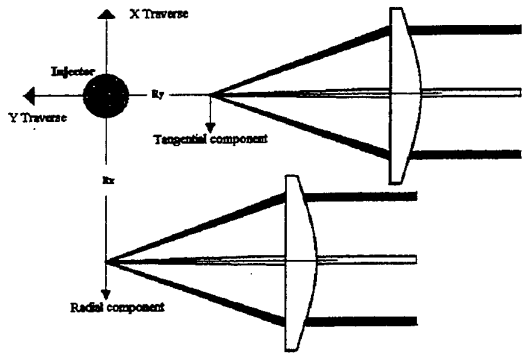


Figure 2 Plan View Schematic of Injector Traverse

Although the PDA system could be configured to measure 2 velocity components (2D) and size its operation was not restricted to this. Examining the performance of the system in 2D only, 1D and size, and 1D only configurations brought a deeper understanding of the spray behaviour. LDA/PDA was not the only optical diagnostic applied in this work, single-shot planar imaging was used to study the spatial structure and growth of the spray as a function of time. The light source for the single-shot imaging was a Continuum SureliteII Nd:YAG laser, frequency doubled to 532nm and providing a pulse duration of 10ns. Digital imaging used a Kodak Megaplus 4.2 CCD camera which provided 1000 by 1000 pixel images at a resolution of 8 bits. The CCD camera was connected to a Matrox IM1280 frame grabber and image processor installed in an IBM 486 computer.

The laser was operated at approximately 15mJ per pulse and with a light sheet height of 150mm. The light sheet travelled in the minus X direction, Figure 1, and the Kodak CCD camera replaced the front lens of the LDA/PDA system. Two methods of imaging were found necessary to faithfully represent the true nature of the spray. Firstly, the vertical light sheet was aligned with the vertical symmetry axis of the spray and secondly, aligned to illuminate a diffuse scattering plate placed behind the injector to back-light the spray. A trigger from the injector control box supplied a delay unit to generate a laser pulse at any time after the opening signal to the fuel supply solenoid.

The injector was operated at 50 Bar fuel pressure with a fuel solenoid opening time of 0.84 ms corresponding to a fuel delivery of 11.0 mg per injection. The injection frequency was set at 10 Hz, to synchronise with the pulse repetition rate of the laser used for the imaging and to remove all droplets from a spray before another commenced.

MEASUREMENTS AND DISCUSSION

The axial measurement locations chosen were:- Z = 1, 3 and 5 mm and then in 5 mm increments down to Z = 50 mm. In the work presented here the main interest is in the first three locations i.e. in the dense, near nozzle region of this hollow cone spray.

A back-lit image of the spray emerging from the nozzle is shown in Figure3. From nozzle to spray tip is 10 mm, the nozzle hole diameter is 0.9 mm and the time was 0.56 ms after the trigger, 0.12 ms after fuel first appears at the nozzle.

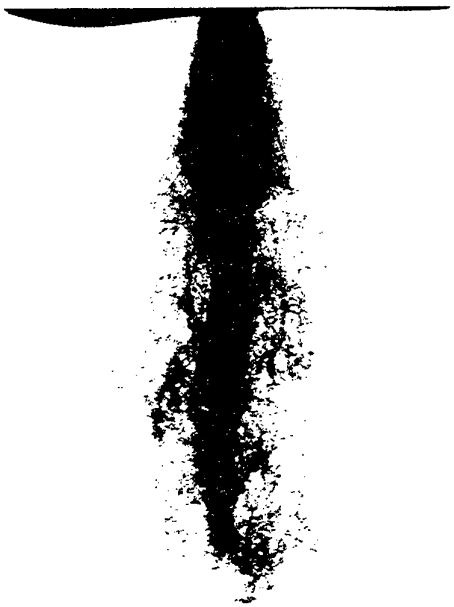


Figure 3 Spray Tip Emerging from Nozzle

Radial scans were made from the nozzle axis to 1.3 mm in steps of 0.1 mm, 2.8 mm in steps of 0.2 mm and 4.5 mm in steps of 0.3 mm at Z = 1, 3 and 5 mm respectively. At each measurement position 20,000 validated data samples were attempted.
The first PDA data to be shown, in Figure 4, are of the discrete sample plots for the axial and radial velocity components and dropsize as a function of time together with their respective mean profiles averaged over 20 micro-second time bins. The time was, as for the imaging, relative to the opening signal to the fuel solenoid. The measurement position was Z = 1 mm and R_x = 0.8 mm.. This position was chosen as it shows initially, between 0.44 and 0.63 ms, the injected fuel moving axially

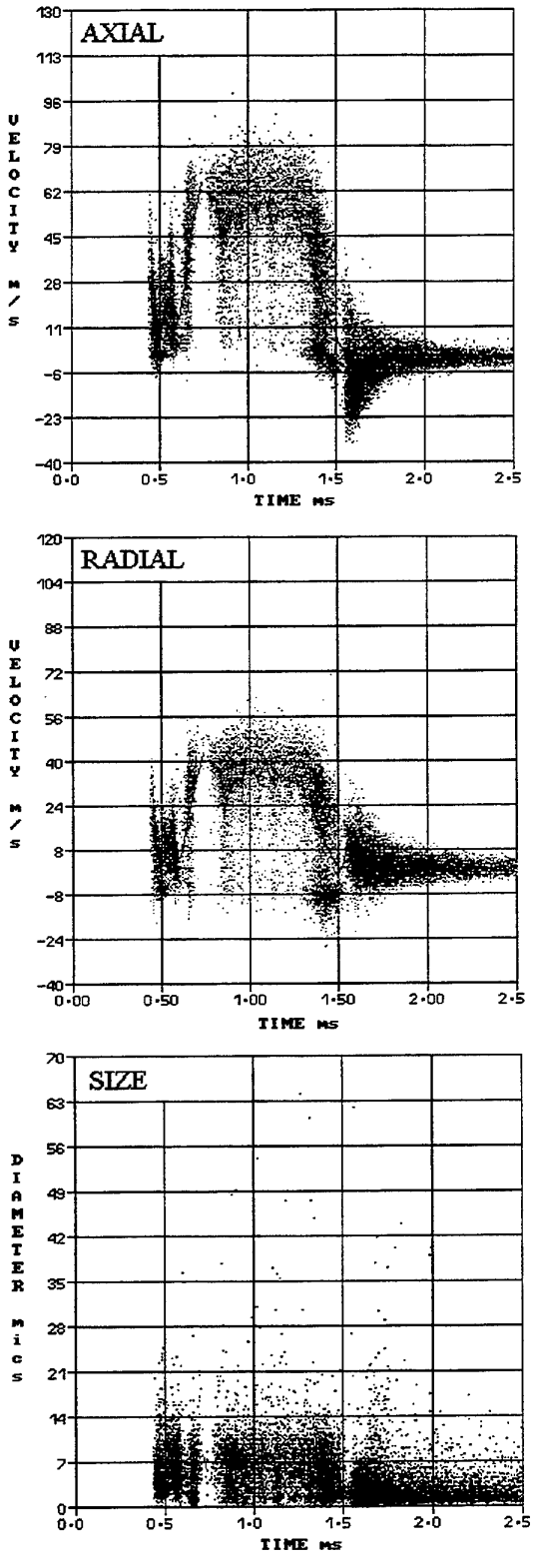


Figure 4 Data Samples with 2D/Size Configuration

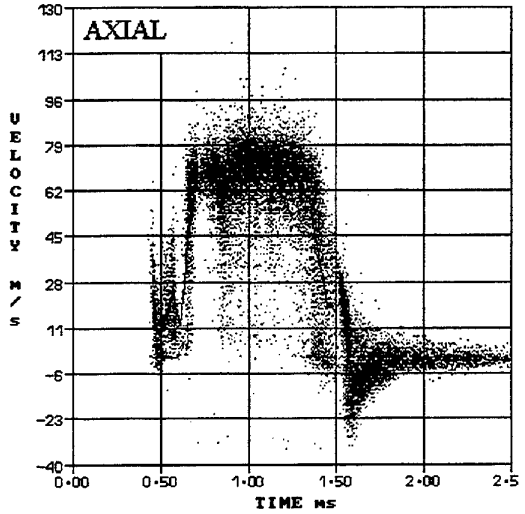
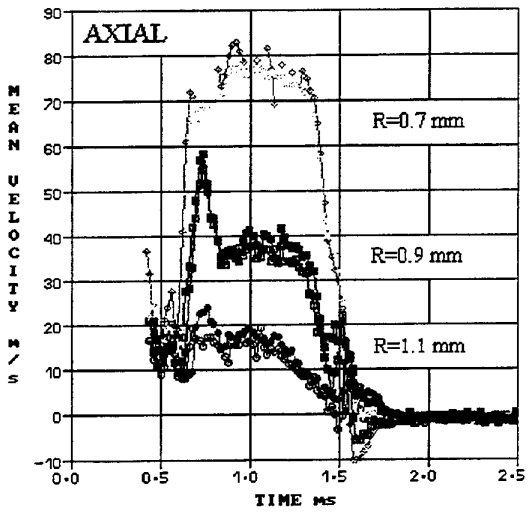


Figure 5 Velocity Samples with 2D Configuration

down from the nozzle as is also seen in Figure 3. After this time the spray cone develops and high axial and radial velocities are measured. The spray cone is held until 1.37 ms after which it collapses. These data show excellent detail of the velocity fluctuations inherent in the complex break-up and atomization processes of the liquid fuel exiting the nozzle. The fact that these fluctuations are visible after the many injections necessary to build up a sufficient number of data samples suggest that these are coherent processes, i.e. the same for each injection, rather than a chaotic process.

The image of the spray in Figure 3 clearly shows that the fuel exists in filament like forms apart from the relatively small droplet diameters detected by the PDA. The measurement scan was therefore repeated but without size, i.e. in 2D-LDA configuration. The axial velocity sample data directly equivalent to that in Figure 4, is shown in Figure 5. Although there are the same number of samples, ~20,000 they were collected in 310 cycles rather than 635, as for the case in Figure 4, but an increase in validated data rate would be expected. However, a major difference is to be seen in the higher mean axial velocity profile for the 2D-LDA measurement. This is due to appreciably more high velocity data samples being collected. The inference that can be drawn from this is that as the LDA is not size and shape dependent then, under these spray conditions, it is providing a better estimate of the local fluid velocity. Applying 1-D LDA decreases the measurement time further and allows more of the dense spray regions to be probed, since the probability of only two beams forming a measurement volume must be higher.



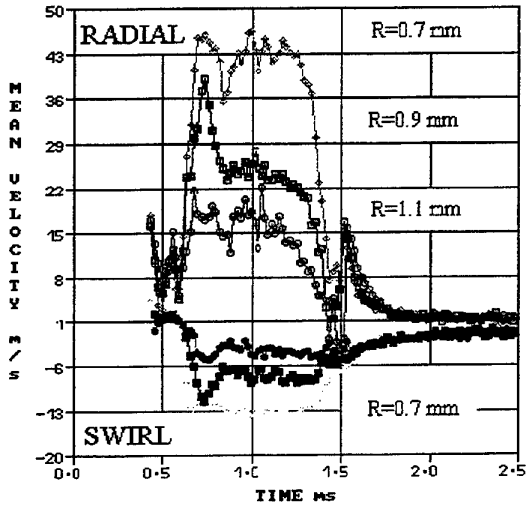
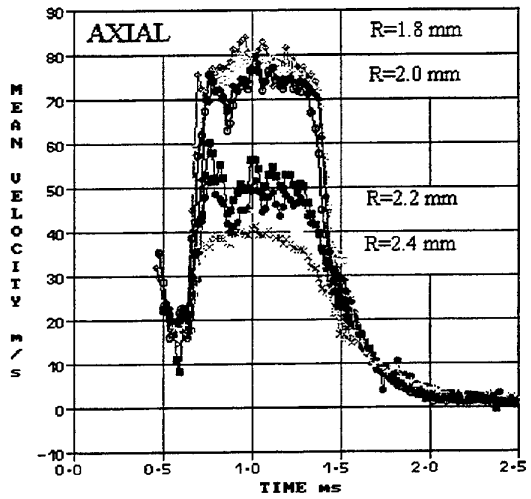


Figure 6 Mean flow profiles at Z = 1 mm

To complete the presentation of data and discussion of the spray at 1 mm below the nozzle the mean profiles of the three components of velocity are shown in Figure 6. In the left hand plot two sets of axial velocity profiles are overlaid. They relate to the measurement scans in the R_x and R_y directions and indicate a high degree of symmetry in the flow field. The position R = 0.7 mm represents the radial location for the maximum in the velocity profiles, not only for the axial flow component, but also for the radial and swirl flow components. The negative swirl component indicates that the fluid leaves the nozzle in anti-clockwise direction. As the hollow cone begins to develop, the sample distribution in Figure 4 exhibits a minimum at 0.71 ms while all three mean velocity profiles indicate maximum values at this time.

The development of the spray cone further downstream can be seen from the three component mean velocity data at Z = 3 mm in Figure 7. The symmetry of the spray on the two measurement axes, as judged by the overlaying of the axial profiles, has been maintained. The spray cone is also increasing in size as the axial velocity gradient between the velocity maxima at R = 1.8 and 2.0 mm is small. The magnitude of the axial and radial velocity components has been sustained as injection proceeds but this is not so for the swirl velocity which decreases rapidly as break-up and atomization of the liquid fuel progresses.



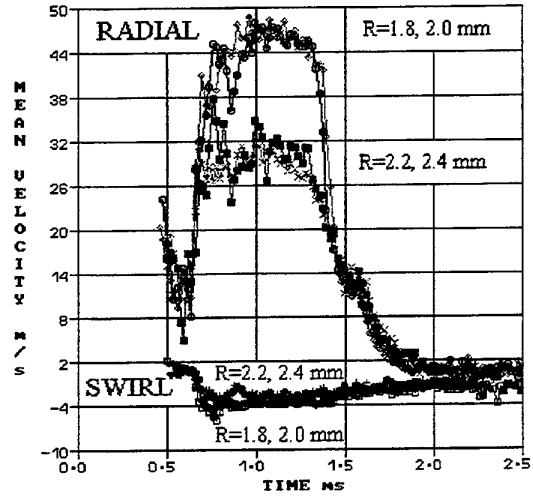
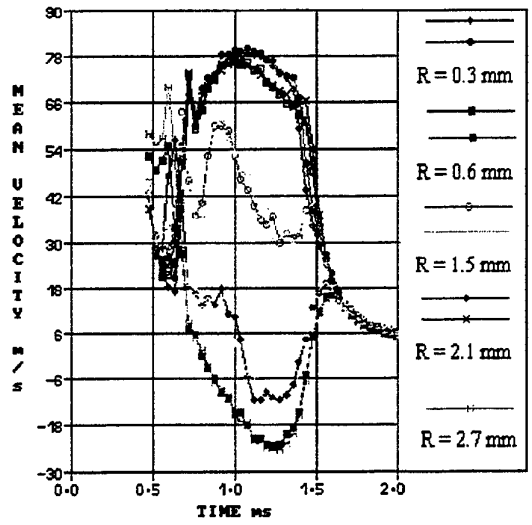


Figure 7 Mean Flow Profiles at Z = 3 mm



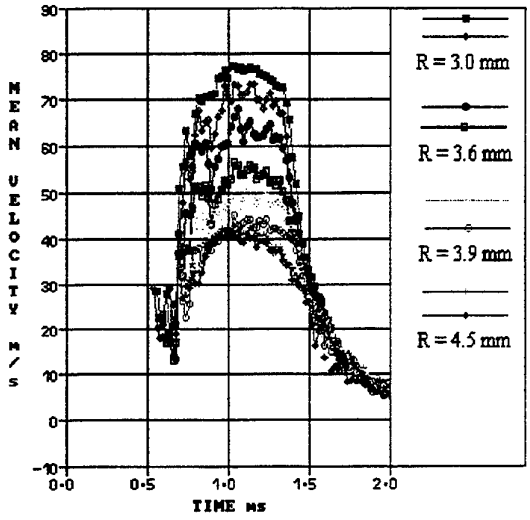


Figure 8 Mean Axial Velocity Profiles at Z = 5 mm

In the measurement plane 5 mm below the nozzle the recirculation zone, inside the hollow cone, is easy to probe with the 2D-PDA configuration but it is still very enlightening to compare this data with that obtained from the 2D-LDA configuration. On the left hand side of Figure 8 a comparison for the two data sets is shown for the mean axial velocity profiles from close to the spray centre, R = 0.3 mm, out to the maximum axial velocity profile, found at Z = 2.7 mm, they are virtually indistinguishable. The 2D-LDA data is the upper marker in the key. However, this is not the case for the mean axial profiles from Z = 3.0 mm and out towards the spray periphery at Z = 3.9 mm. As discussed earlier the 2D-LDA data consistently indicate a significantly higher mean velocity profile, apart from the very edge of the spray at Z = 4.5 mm.

Earlier it was concluded that as LDA is not size and shape dependent then it should provide a better estimate of the local fluid velocity under those conditions when atomization is incomplete. An examination of the spray structure with the laser imaging system was made at the time the axial mean velocity peaks, 1.0 ms,. Two images are presented, the left one, Figure 9, used diffuse back lighting, the right one, Figure 10, side illumination with a laser sheet. With the magnification employed, the image length is 10 mm, the surface of the spray cone, on the left, is only in focus for the region around 3 mm below the nozzle.

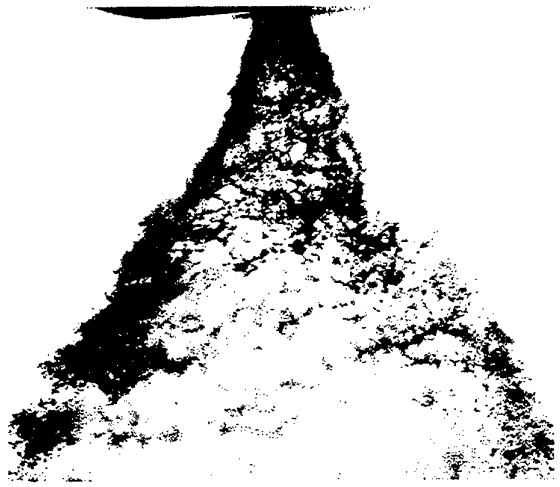


Figure 9 Back Lit Image of Spray - Time 1.0 ms

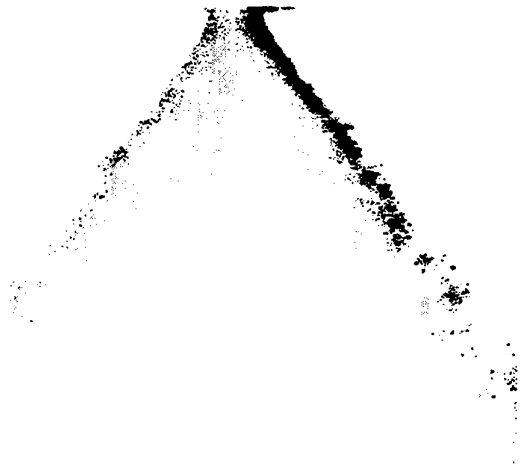


Figure 10 Laser Sheet Image of Spray -Time 1.0 ms

Filaments of fluid, some several millimetre long, are plainly seen twisted around the spray periphery and even persevere downstream below Z = 10 mm.

The laser sheet travels from right to left and the image in Figure 10 can only be in focus on the outer limits of the spray cone. The differences in light scatter from the two sides of the spray cone indicates the high degree of laser light scattering and attenuation of the transmitted light. What resembles a fine cloud of droplets inside the spray cone is purely a result of multiple light scattering occurring, i.e. laser speckle. If only this image was available one would come to the false conclusion that the spray cone contains many small droplets but also a small population of large ones. The laser light sheet highlights only the cross-section of the fluid filaments.

The back-lit image shows that the spray shape is assymmetrical after ~ 3 mm below the nozzle. The 2D-PDA data also shows this lack of symmetry in Figure 11 for the radial profiles of all three mean velocity components and dropsize across the spray

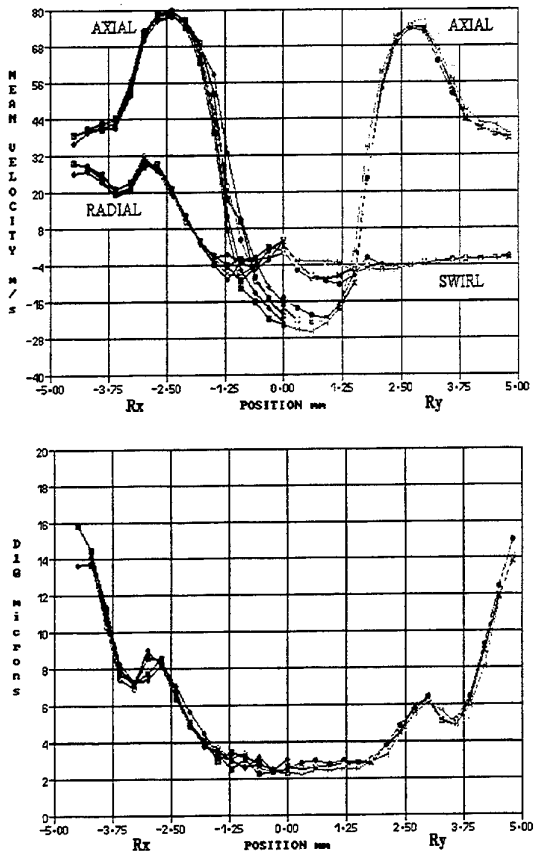


Figure 11 2D-PDA Data Profiles Across the Spray

for radii R_x and R_y for 4 time bin averages centred about the time 1.0 ms.

The most interesting feature of these profiles is in the spray cone shortly after the axial velocity profiles have peaked where an inflexion in the swirl velocity profile correlates with one in the dropsize profile. This identifies the spatial location of the region containing the fluid filaments which as they propagate downstream and break-up will act as a source of large droplets.

CONCLUSIONS

A new generation of LDA/PDA transmitter systems has been designed and constructed. Simultaneous 2D LDA and PDA measurements have been presented to characterise the atomization of gasoline by high pressure automotive fuel injectors In the near nozzle region where atomization was incomplete it was found that the 2D-PDA measurements would underestimated the fluid flow velocity and that laser light sheet imaging could lead to false impressions of the atomization processes

REFERENCES

G. Wigley, 1987, Laser Anemometry Measurement Techniques in Internal Combustion Engines, Second International Conference on Laser Anemometry - Advances and Applications, Strathclyde, Scotland.

Buchhave, P. and Knuhtsen, J., 1984 Fiber-Optic Anemometer Measurements, First International Symposium on Applications of Laser Doppler Anemometry to Fluid Mechanics, Lisbon, Portugal.

Oldengarm, J., 1976, Development of rotating diffraction gratings and their use in laser anemometry, Optics and Laser Technology, Vol. 69.

Gooch and Housego, 1996, A-O Frequency Shifter, FS040-2B, Technical Data Sheet, Ilminster, England.

G. Pitcher and G. Wigley, 1994, Simultaneous Two-Component Velocity and Dropsize Measurements in a Combusting Diesel Spray, Seventh International Symposium on Applications of Laser Techniques to Fluid Mechanics, Lisbon, Portugal.

G. K. Hargrave,. G. Wigley, J. Allen and A. Bacon, 1998, Optical Diagnostics and Direct Injection of Liquid Fuel Sprays, Paper C541/056/98, IMechE Conference Transactions, Optical Methods and Data Processing in Heat and Fluid Flow, London.

A NEW APPROACH TO ELIMINATE THE MEASUREMENT VOLUME EFFECT IN PDA MEASUREMENTS

H. -H. Qiu and C. T. Hsu

Department of Mechanical Engineering
Hong Kong University of Science and Technology
Kowloon, Hong Kong

ABSTRACT

A new model of phase-size correlation was introduced to improve the accuracy of sizing large particles in two-phase flows. This model takes both the refractive and reflective mechanisms into consideration and, hence, the assumption of single scattering mechanism for conventional phase-Doppler anemometry is not unnecessary. As a result, the Gaussain beam defect and slit effect can be eliminated. This method only need to use a three-detector PDA system to determine the phases of Doppler signals scattered from a spherical particle in the measurement volume. The results of simulations by using the Generalized Lorenz Mie Theory (GLMT) with this new method were compared with the results from the simulation based on the conventional method. The results show that the new developed method can greatly reduce the Gaussian beam defect and the slit effect for particle sizing using a PDA system.

INTRODUCTION

Laser Phase-Doppler Anemometry (PDA) is nowadays widely used for velocity measurement and particle sizing in experimental studies of dispersed two-phase flows. The new extensions in dynamic range, signal processing and measuring the particle refractive index have made PDA one of the most versatile and accurate techniques available today. One of most important applications of PDA is to determine the local mass flux and concentration in multiphase flows, especially in sprays. Such measurements are essential when studying droplet evaporation, spray deposition and cooling, etc. To this end, the particle size, velocity and size dependent measurement volume (or cross-sectional area) must be determined accurately. Among the above parameters, the accurate measurement of droplet size is the utmost important since the particle volume depends on the third power of the particle diameter. Because PDA is based on single particle scattering theory, it is often required to decrease the measurement volume size in order to achieve highly accurate results in dense particle conditions. Unfortunately, a simple reduction in the measurement volume size can cause the phenomena in conflict with the assumption of a uniform illumination. Consequently, the result suffers from error for sizing large particles due to the nonlinearity in the phase/diameter relationship because the beam intensity is practically nonuniform (Saffman 1986, Bachalo and Sankar 1988, Sankar et al. 1992, Grehan et al. 1991, Qiu and Sommerfeld 1992, Qiu and Hsu 1995). This nonlinear effect is usually called as Measurement Volume Effect (MVE) or trajectory ambiguity. Recent investigation using an extended Phase-Doppler anemometry has shown that the MVE also has large effect to the refractive index measurement results (Durst et al. 1994). There are numerical tools developed to simulate the Gaussian beam defect by using Geometrical Optics Theory (GOT) and Generalized Lorenz Mie Theory (GLMT) (Grehan et al. 1992). For the effect of the slit image in the measurement volume, previous studies focused on the vignetting effect from receiving optical aperture and slit (or pinhole) to the effective measurement volume size. The experimental studies by Durst et al. (1994) showed that the nonuniform

illumination effect due to image boundary of the spatial slit filter in the receiving optics is even more critical than the Gaussian beam defect. The Fourier Optics Method recently developed by Qiu and Hsu (1996) has been successfully used to simulate the slit effect. Apparently, the Measurement Volume Effect (MVE) consists of the Gaussian beam defect and the slit effect, which greatly hinder the accuracy in particle sizing. Various solutions to minimize the trajectory ambiguity have been proposed for classical geometry (Qiu and Sommerfeld 1992), or more original designs such as the planar geometry (Aizu et al 1993) and spatial frequency geometry (Qiu and Hsu 1995). A promising one is the dual mode geometry which integrates a standard PDA (SPDA) with a Planar PDA (PPDA) (Tropea et al. 1994). One of the important features of PDA in a planar configuration is the temporal separation of the contributions of two scattering mechanisms, reflection and refraction, to the light received by the photodetectors. By using the SPDA/PPDA phase ratio together with the burst-centering technique and the amplitude/size ratio, the scattering mechanism may be validated. This implies the possibility of suppressing measurement errors due to the mixing of the two modes of scattered light, and therefore, makes it possible to perform refractive-index measurements by the comparison of the reflective and the refractive phases. However, all of above methods for the elimination of the measurement volume effect are based on the signal validation scheme. If the phase ratio or amplitude/size ratio is not within the expected tolerance, the measured phase will be invalid. Because the effective measurement volume size or cross-sectional area is strongly dependent on the validation scheme, the methods will reduce the measurement volume size for those particles moving in negative Y position. The cross-sectional area reduction in Y direction is particle size dependent and it also results in the measurement volume asymmetrically to its intensity distribution. To correct this variation the measurement volume needs to be calibrated. Certainly, this kind of correction is still feasible in a simple directional flow, such as sprays. However, in complex two-phase flow conditions, such as in swirling flows, due to arbitrary particle trajectories, the projection of the effective cross-sectional area in each particle size and moving direction will be very complex. The consequence is that the calibration method could be very complicated. Furthermore, as PPDA has relative larger fluctuation in the size-phase relation than SPDA when small particles are encountered, the validation method only based on the SPDA/PPDA phase ratio is not enough to completely eliminate the measurement volume effect especially the slit effect which is also sensitive to the small particles. The main reason for the need of strong validation by using the phase ratio and amplitude/size ratio is only to identify the scattering mechanism. Because only one scattering mechanism was assumed in the conventional scattering model of PDA, any other scattering mechanisms are considered as the error sources for size measurements. If a complete scattering model can be developed by taking both the refraction and reflection into consideration to determine the particle size, no validation between the scattering mechanisms is necessary.

In this study a recently developed scattering model Qiu and Hsu (1995) including both refraction and reflection was used and modified for calculating the particle size-phase relation. One of the advantages of this method is only a conventional three-detector receiving unit can be used. In this model the signal phases from the three detectors are used to calculate the particle size. Because the fringe patterns from the refraction and reflection are different in space and moving direction, it has been found that there is an optimized optical orientation where the particle size can be solved analytically. To demonstrate the capability of the new developed approach, the model was simulated numerically by using both Geometrical Optics Theory (GOT) and Generalized Lorenz Mie Theory (GLMT). Different optical parameters such as the measurement volume size, the focus lengths of the sending and receiving lenses, the size and shape of the receiving aperture, the particle size and its trajectory, and the phase conversion factors are used to analyze the performance of the new developed method.

ANALYTICAL DISCRIPTION

The schematics of a conventional phase-Doppler system is shown in Fig. 1, where the receiving optics consists of a three-detector system is used.

The phase difference ϕ between the three receiving detectors can be determined from the three Doppler signals. If we assume the scattering light as being dominated by refraction, from the geometrical consideration the relation between the phase difference of the outer detectors and the particle size can be described as following:

$$\phi = C_1 \cdot D \qquad (1)$$

where D is the particle diameter.

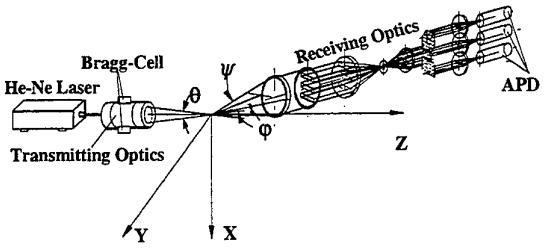


Fig. 1: Optical layout of a phase Doppler anemometry

The phase conversion factor C_1 can be written as (Bauckhage, 1988):

$$C_1 = 4\pi\left\{\sqrt{1+m^2-\sqrt{2}m\sqrt{1+\sin\frac{\theta}{2}\sin\psi+\cos\frac{\theta}{2}\cos\psi\cos\varphi}}\right.$$
$$\left.-\sqrt{1+m^2-\sqrt{2}m\sqrt{1-\sin\frac{\theta}{2}\sin\psi+\cos\frac{\theta}{2}\cos\psi\cos\varphi}}\right\} \quad (2)$$

where m is the particle refractive index and the angles, θ, φ and ψ, are defined in Fig. 1.

Equation (1) is true only when the scattering is dominated by the refractive light. When the particle size is not small in comparison with the laser beam diameter in the measurement volume, the light dominance and then the phase-size relation depend on the particle location. This effect is called *Gaussian beam effect* or *trajectory ambiguity,* as documented by Gréhan et al. (1991), Sankar et al. (1992), Qiu and Sommerfeld (1992), Qiu and Hsu (1995).

The Gaussian beam effect is due to the Gaussian distribution of laser beam intensity in the measurement volume. When the particles pass through the focused beams on different trajectories, it can cause a change in balance between the reflected and refracted rays. If the dominant light occurs sequentially depending on the two scattering mechanisms (refraction and reflection). In either case, the trajectory dependence can lead to significant errors. For example, when the scattering light is dominated by reflection, the phase conversion factor can be written as:

$$C_0 = \frac{4\pi}{\sqrt{2}}\begin{pmatrix}\sqrt{1+\sin\frac{\theta}{2}\sin\psi-\cos\frac{\theta}{2}\cos\psi\cos\varphi}\\ -\sqrt{1-\sin\frac{\theta}{2}\sin\psi-\cos\frac{\theta}{2}\cos\psi\cos\varphi}\end{pmatrix} \quad (3)$$

Because the reflective fringe pattern moves in the opposite direction to that of the refractive pattern, the phase and size relation for the receiving optics is described as:

$$2\pi-\phi=|C_0|\cdot D \quad (4)$$

Therefore, the detection of the wrong scattering component will occur, leading to the misrepresentation of mid-range size particles as being very large. This has a significant effect on size measurements.

COMBINED SCATTERING MODEL

According to the model proposed by Qiu and Hsu (1995), the relationship between the measured signal phase and particle diameter for a conventional PDA system can be described as the following form

$$\phi = 2\arctan\left(\frac{I_1\sin\left(\frac{C_1D}{2}\right)-I_0\sin\left(\frac{C_0D}{2}\right)}{I_1\cos\left(\frac{C_1D}{2}\right)+I_0\cos\left(\frac{C_0D}{2}\right)}\right) \quad (5)$$

where both refractive and reflective rays are taken into consideration.

If the intensities of refractive and reflective rays can be measured experimentally or determined analytically, the phase-size relation can be uniquely quantified by using equation 4. Unfortunately, a method to separately measure the intensities of each rays has not been available yet and, therefore, it is difficult to directly calculate the phase-size relation by using equation 4 for a two-detector system. For a three-detector system, the signal phases for each detector with different elevation angles can be described as

$$\begin{cases}\phi_1 = 2\arctan\left(\dfrac{I1_1\sin\left(\frac{C1_1D}{2}\right)-I1_0\sin\left(\frac{C1_0D}{2}\right)}{I1_1\cos\left(\frac{C1_1D}{2}\right)+I1_0\cos\left(\frac{C1_0D}{2}\right)}\right)\\ \phi_2 = 2\arctan\left(\dfrac{I2_1\sin\left(\frac{C2_1D}{2}\right)-I2_0\sin\left(\frac{C2_0D}{2}\right)}{I2_1\cos\left(\frac{C1_1D}{2}\right)+I2_0\cos\left(\frac{C1_0D}{2}\right)}\right)\end{cases} \quad (6)$$

In the system equation 6, because there are total five unknowns ($I1_1$, $I1_0$, $I2_1$, $I2_0$, and D), it still can not be solved. However, in a standard PDA system, the elevation angles of each detectors are quite small,

therefore, the magnitude of scattering intensities are almost the same for each detectors. In this case, $I1_1 \approx I2_1 = I_1$ and $I1_0 \approx I2_0 = I_0$ can be assumed which have also been proved by GLMT simulations. Hence, only three unknowns have to be determined now. A further simplification is based on the method suggested by Qiu and Hsu (1995) where the magnitude of the phase conversion factors for refractive and reflective rays are used as the key factor for the optimization process. By taking the same magnitude for the phase conversion factors for refractive and reflective rays, i.e., $C1_1 = C1_0 = C_1$ and $C2_1 = C2_0 = C_2$ the equation 6 can be rewritten as

$$\begin{cases} \phi_1 = 2\arctan\left(\dfrac{I_1 - I_0}{I_1 + I_0}\tan\left(\dfrac{C_1 D}{2}\right)\right) \\ \phi_2 = 2\arctan\left(\dfrac{I_1 - I_0}{I_1 + I_0}\tan\left(\dfrac{C_2 D}{2}\right)\right) \end{cases} \quad (7)$$

Hence, the relationship between the measured phases, ϕ_1, ϕ_2 and the particle size, D can be described as

$$\frac{\tan\left(\dfrac{\phi_1}{2}\right)}{\tan\left(\dfrac{\phi_2}{2}\right)} = \frac{\tan\left(\dfrac{C_1 D}{2}\right)}{\tan\left(\dfrac{C_2 D}{2}\right)} \quad (8)$$

Because in equation 8 only D is unknown, the equation can be solved now by using the two measured phases and optical geometry. A further optimization method has been found if $C_1 = 2C_2$ is selected. Finally, the relationship between the particle size and the measured signal phases for the combined model can be given by

$$D = \frac{4}{C_1}\arctan\left(\sqrt{1 - \frac{2\tan\left(\dfrac{\phi_2}{2}\right)}{\tan\left(\dfrac{\phi_1}{2}\right)}}\right) \quad (9)$$

By measuring the signal phases of different detectors, the particle size can be determined.

RESULTS OF SIMULATION

To evaluate the performance of the newly developed model by using Eq. (8), the Generalized Lorenz Mie Theory (GLMT) was adopted to simulate the different particle sizes in comparison with the conventional single scattering mechanism assumption. The simulation was carried out for the system geometry as shown in Fig. 1 with the parameters given in Table 1.

Table 1 Optical parameters

Wavelength (λ)	0.5145	μm
Beam Waist Diameter	100	μm
Transmitting Angle	2.2916	degree
Receiving Elevation Angle 1	3.69	degree
Receiving Elevation Angle 2	1.845	degree
Off-Axis Angle	46	degree
Refractive Index	1.33	

The results of simulation are shown in Fig. 2-4. As shown in Fig. 2, a 30 μm water droplet passing through the measurement volume parallel to the Y-axis at z = 0 μm will yield large phase transition (> 100% in this special case) when the scattering mechanism changed from the reflection to refraction. If the phase is determined by the conventional method, i.e. directly calculated by GLMT, large measurement error may occur. Only very small fluctuation (< 2%) for the phase determination by using the newly developed method and hence the measurement volume effect can be neglected.

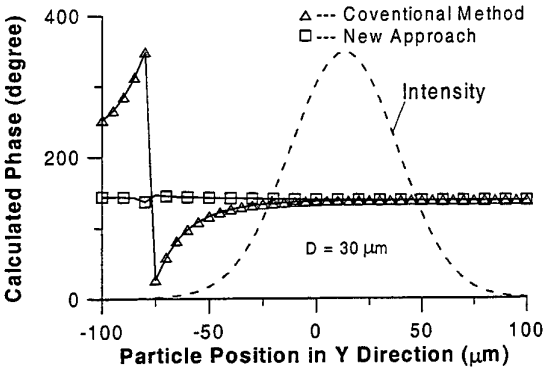


Fig. 2 Comparison of the phase measurement results between the conventional method and new approach ($z = 0\mu m$, $r_0 = 50\ \mu m$)

Fig. 3 and 4 show the similar results for droplets with 50 and 70 μm respectively. Although the scattering changing from the reflection to refraction yields large phase change for the conventional method, the calculated phase using the new approach is almost constant which is proportional to the particle

diameter. Following conclusions can be drawn from the above demonstration. The new developed method can eliminate the measurement volume effect completely even for a conventional three-detector PDA system which is very commonly used in two-phase flow measurements. Because no strong validation scheme is necessary other than the signal-to-noise ratio (SNR), the measurement volume can be accurately determined by the conventional methods and hence high accuracy in the particle mass flux and concentration measurements. By applying this method in the dual mode PDA system, this method can further improve the accuracy for the refractive index measurements.

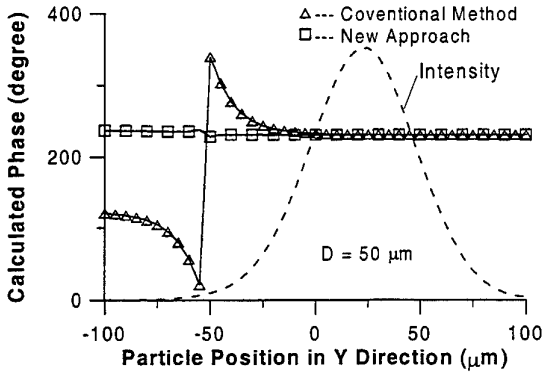


Fig. 3 Comparison of the phase measurement results between the conventional method and new approach ($Z = 0\mu m$, $r_0 = 50\ \mu m$)

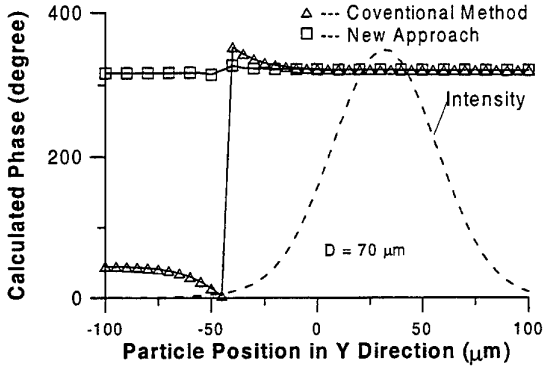


Fig. 4 Comparison of the phase measurement results between the conventional method and new approach ($Z = 0\mu m$, $r_0 = 50\ \mu m$)

CONCLUSION

A new phase-size correlation model is proposed and investigated towards an accurate sizing of large particles. This new system has the same transmitting optics as a conventional three-detector PDA system, but with optimized orientation of receiving units. The key point to this newly developed method is to set $C_1 = C_0$ and $C_1 = 2C_2$. The performance of this new method was simulated by using the GLMT. The results of the simulation show that the new method can effectively eliminate the Gaussian beam effect and slit effect for sizing large particles. The newly developed model is described in equation 8 for describing the phase-size correlation using a geometrical optics method, which is specially suitable for sizing large particles. Therefore, applying this method to a conventional PDA system is expected with no Gaussian beam defect and slit effect. The next step to this work is to perform validation tests experimentally by using this method.

ACKNOWLEDGMENT

This work was supported by the Hong Kong Government and Hong Kong University of Science & Technology under the RGC/ERG Grant No. HKUST 812/96E and G-HK96/97.EG11.

REFERENCE

[1] Aizu Y, Durst F, Gréhan G. Onofri F, Xu T-H: "PDA systems without Gaussian beam defects.", *Proc. 3rd Int. Conf. Optical Particle Sizing*, Yokohama, pp461-470.

[2] Bachalo, W. D. & Sankar, S. V., 1988: "Analysis of the light scattering interferometry for spheres larger than the light wavelength, *Proc. 4th Int. Symposium on Applications of Laser Anemometry to Fluid Mechanics*, Lisbon paper 1.8.

[3] Durst F., Tropea C. and Xu T.-H. 1994: "The Slit Effect in Phase Doppler Anemometry", *2nd. Int. Conf. on Fluid Dynamic Measurement and Its Applications*, Beijing, 38-43.

[4] Grehan G., Gouesbet G., Naqwi A., and Durst F., "Evaluation of Phase Doppler System using Generalized Lorenz-Mie Theory," *Proc. of the Int. Conf. on Multiphase Flows '91-Tsukuba*, 291-294 (1991).

[5] Qiu H. -H. and Hsu C. T. (1995): "Optimization of EPDA Parameters for Accurate Material Recognition in Multiphase Flow", *2nd Int. Conf. on Multiphase Flow* '95-Kyoto, IN1-IN9.

[6] Qiu H. -H. and Hsu C. T. (1995): "A New Spatial Frequency Method For Sizing Large Particles in Laser Anemometry", *ASME Fluids Engineering Summer Meeting and 6th Int. Conf. on Laser Anemometry,* South Carolina, vol. FED 229, 81-88.

[7] Qiu H. -H. and Hsu C. T. (1996): "A Fourier Optics Method for the Simulation of Measurement-Volume-Effect By the Slit Constraint", Proc. of *8th International Symposium on Applications of Laser Techniques to Fluid Mechanics*, Lisbon, pp 12.6.1-12.6.8.

[8] Qiu H.-H., and Sommerfeld M., "The impact of signal processing on the accuracy of phase-Doppler measurements," *Proc. 6th Workshop on Two Phase Flow Predictions*, Erlangen, 167-185 (1992).

[9] Saffman,M. 1986: The use of polarized light for optical particle sizing, *Proc. 3rd Int. Symp. on Applications of Laser Anemometry to Fluid Mechanics*, Lisbon.

[10] Sankar, S. V., Inenaga, A.S., and Bachalo, W. D. 1992: "Trajectory Dependent Scattering in Phase Doppler Interferometer: Minimizing and Eliminating Sizing Errors", *Proc. 6th Int. Symp. on Applications of Laser Anemometry to Fluid Mechanics*, Lisbon.

[11] Tropea C., Xu T.-H., Onofri F., Gréhan G. and Haugen P. 1994: " Dual Mode Phase Doppler Anemometry", *Proc. 7th Int. Symp. on Applications of Laser Techniques to Fluid Mechanics*, Lisbon, pp18.31-18.3.7.

SESSION 10

PIV SIGNAL PROCESSING

Advanced Evaluation Algorithms for Standard and Dual Plane Particle Image Velocimetry

O. Ronneberger, M. Raffel, J. Kompenhans
DLR, Institut für Strömungsmechanik
Bunsenstr. 10, D-37073 Göttingen, Germany

ABSTRACT

The widely-used evaluation algorithms[1] for PIV recordings have some short comings, in that they introduce superfluous statistical and systematical errors. For example, they introduce the so-called "peak-locking" effect. These errors can be significantly reduced by using better algorithms.

The following considerably improved analysis and algorithms will be described and demonstrated on real PIV recordings:

- *Analysis of errors of CCD's and the electric transmission of the video signal.*
- *An FFT-based cross correlation algorithm using completely free-shaped and free-sized interrogation windows which exhibits the same accuracy as an optimally programmed direct correlation.*
- *A Gaussian fit algorithm using different weights for the values in the correlation plane due to the error distribution of correlation coefficients.*

1 INTRODUCTION

The major part of the PIV scientific community (including nearly all commercial PIV software vendors) is using the same evaluation algorithms for PIV recordings namely the cross correlation of two "power of 2" sized rectangular interrogation windows via FFT and the three-point peak fit estimator for sub pixel resolution, see, e.g., Willert and Gharib (1991); Westerweel (1993). These algorithms have the advantage that they are easy and fast to implement, but they introduce superfluous statistical and systematical errors.

Due to the increased requirements at our work on dual plane PIV (Raffel et al., 1995, 1996), where the height of the correlation peak is used to get information about the third component of the velocity, we had to consider all effects, that influence the shape, the height and the statistical and systematical errors of the correlation peak.

2 RECORDING OF THE IMAGES

There are three important effects influencing the shape of a particle image (Fig. 1). The influence of the particle size is negligible in nearly all our applications in air flows (e.g., the diameter of our oil droplets is around $1\mu m$. The geometrical image assuming an ideal camera objective is even smaller. Compared to the resolution of a CCD sensor (1 pixel is about $10\mu m \times 10\mu m$) we can neglect the particle diameter). So the geometrical particle image may be represented by a Dirac delta function.

As no camera objective is ideal, the real particle images on the image plane are distorted due to the limited spatial bandwidth of the camera objective (yielding the so-called Airy pattern) and due to abberations (assumed to have Gaussian character). These two effects are combined in the point spread function of the camera objective. Usually only the effect of the aperture, the Airy pattern (Fourier transform of the circular aperture hole) is taken as the point spread function. In our experiments the effects of the lens abberations were in the same order as the effects of the limited bandwidth. Especially near the borders of the image plane elliptical particle images are encountered frequently. However, if the point spread function does not change on the interrogation area, the light intensity distribution on the image plane can be mathematically described as the convolution of the geometrical

[1] These widely-used algorithms are the recording of the images with CCD cameras, the cross correlation of two "power of 2" sized rectangular interrogation windows via FFT and the three-point peak fit estimator for sub pixel resolution.

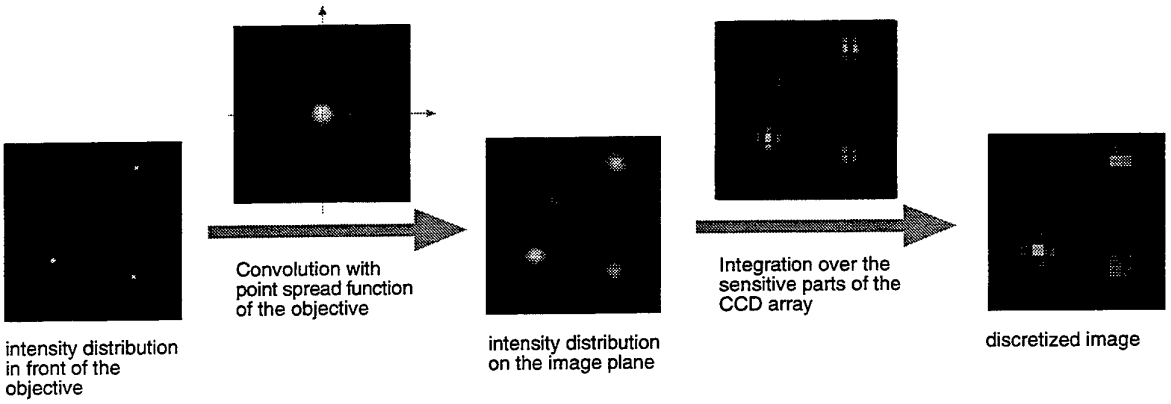


Fig. 1: Effects influencing the intensity distribution of a particle image.

particle images with the point spread function of the camera objective.

The next step is the integration of the light intensity over the sensitive area of each CCD pixel. In the case of a normal CCD sensor, the sensitivity is the same all over the active area of the pixel. Recent CCD sensors have micro lenses to collect more light. Then the sensitivity distribution for each pixel is a more complicated function. The integration over the sensitive area can mathematically be described as the convolution of the light intensity distribution on the image plane with the sensitivity function of the pixel and the sampling of this function at the centre of each pixel (see fig. 1).

After exposure the charges on the CCD are read out, amplified, and sequentially transmitted to the frame grabber as a time dependent voltage. The frame grabber is located in the camera or in the PC. The amplification and transmission may also introduce errors to the signal. Very common errors originate from an impedance mismatch between the amplifier, the transmission line and the frame grabber. A typical transmission error found with a digital camera (the frame grabber is located within the camera) is illustrated in Figure 2.

The image is transmitted as a sequence of horizontal lines, so the aforementioned effects are found only in the x direction. By comparing the joint probability of the values assumed by pixels succeeding in x- and y-direction respectively, one can detect such errors quite easily, since these statistics should be isotropic in a normal PIV recording. A more detailed discussion of these effects and an algorithm to correct such distorted images is described in Ronneberger (1998).

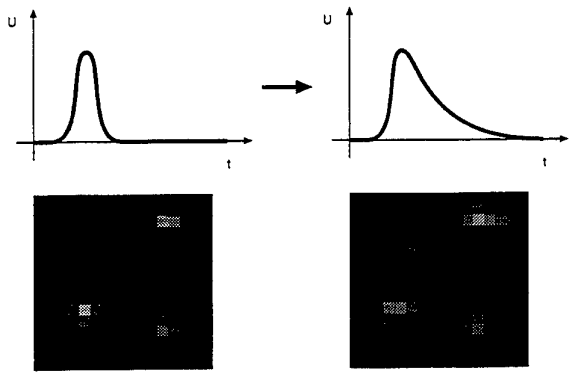


Fig. 2: Errors due to the electrical transmission of the video signal result in horizontal distortions of the image.

3 FFT-BASED FREE SHAPE CROSS CORRELATION

The estimate of the cross correlation is the central point of each PIV evaluation. The most common way to obtain an estimate is to take two equally-sized rectangular parts of the two PIV recordings (Fig. 3 and Fig. 4), and to make use of the FFT.

$$\mathbf{a'} := \mathbf{a} - \bar{\mathbf{a}} \quad (1)$$

$$\mathbf{b'} := \mathbf{b} - \bar{\mathbf{b}} \quad (2)$$

$$\mathbf{R} = \frac{\mathrm{FFT}^{-1}\left(\mathrm{FFT}^{*}(\mathbf{a'}) \cdot \mathrm{FFT}(\mathbf{b'})\right)}{\mathrm{RMS}(\mathbf{a'}) \cdot \mathrm{RMS}(\mathbf{b'})} \quad (3)$$

The use of the standart FFT algorithm limits the possible linear dimensions of the partial images to powers of 2 (e.g., 16, 32, 64, 128, ...)

To understand the result of such an estimate of the correlation, the equivalent direct correlation is illustrated

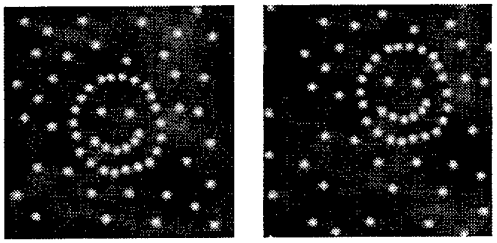


Fig. 3: Example for a pair of PIV recordings: The particle pattern has moved upwards and to the right

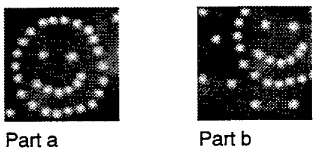


Fig. 4: The simplest estimate of the cross correlation, is based on two equally sized parts of the images. The parts are cut out at the same position in each image.

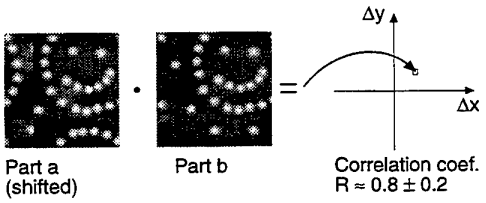


Fig. 5: The simple FFT-based correlation relies on the assumption that the partial images are parts of periodical images. So a shift of the partial image (a) results in the illustrated circular effects (i.e. the pixels leaving the image during the shift are wrapped around).

in Fig. 5 for one displacement $(\Delta x, \Delta y)$.

There are two effects that unnecessarily distort the correlation: Since the second partial image was taken at the same position as the first one, we did not capture all particle images of the shifted particle pattern. This is usually denoted as "in plane loss of pairs". The second effect is a random contribution due to the decorrelation caused by the circular effects (in the illustrated example R varies between 0.6 and 1.0)

One common way to work around this problem is to cut the second partial image in a second pass at the proper position and calculate the cross correlation again. In this case, one obtains the undistorted correlation for at least one displacement. However, the neighbouring values in the correlation plane (which are used for the peak fit) are still distorted in the same way as above. This 2-pass method has some more shortcuts: It still relies on "power of 2" sized windows, and one has to define a rule to decide in the first pass, whether or not a found peak position is correct or represents an outlier.

The optimal accuracy is reached only if one cuts the proper part of the second image for *each* displacement. In this case the mean $(\overline{\mathbf{b}})$ and the RMS value (RMS(**b'**)) depend on the displacement. It seems, that such an algorithm can only be implemented by calculating the correlation in a direct way:

$$R_{kl} = \frac{\sum_{i,j}(a_{ij} - \overline{\mathbf{a}}) \cdot (b_{i+k,j+l} - \overline{\mathbf{b}_{[k,l]}})}{\mathrm{RMS}(\mathbf{a} - \overline{\mathbf{a}}) \cdot \mathrm{RMS}(\mathbf{b}_{[k,l]} - \overline{\mathbf{b}_{[k,l]}})} \qquad (4)$$

where $\mathbf{b}_{[k,l]}$ denotes the partial image **b** cut at position k, l.

However, with some simple mathematical transformations eq. 4 can be evaluated using the FFT. The correlation coefficient of two datasets q and p (with subtracting the mean value) can be rewritten as

$$\sum_{i=1}^{N}(p_i - \overline{p}) \cdot (q_i - \overline{q}) = \sum_{i=1}^{N} p_i q_i - \frac{1}{N}\sum_{i=1}^{N} p_i \sum_{i=1}^{N} q_i. \qquad (5)$$

Therefore, we can postpone the subtraction of the mean value to a later stage of the calculation. Using eq. 5 we can rewrite the numerator of the direct correlation (Eq. 4) as

$$r_{kl} = \sum_{i,j} a_{ij} b_{i+k,j+l} - \frac{1}{NM}\sum_{i,j} a_{ij} \sum_{i,j} b_{i+k,j+l} \qquad (6)$$

where $N \cdot M$ is the number of pixels in the partial image **a** (the denominator will be treated in the same way). To use the FFT, we have to pad zeros around partial image **a** to enlarge it to a "power of 2" size (Fig. 6). To get rid of the rectangular shape of the small window, we describe this cutting and padding procedure by multiplying with a

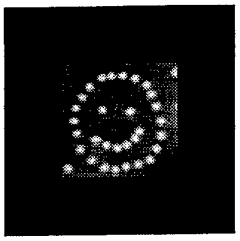


Fig. 6: To use free sized or even free shaped interrogation windows in an FFT-based correlation, the partial image must be padded with zeros to a "power of two" size

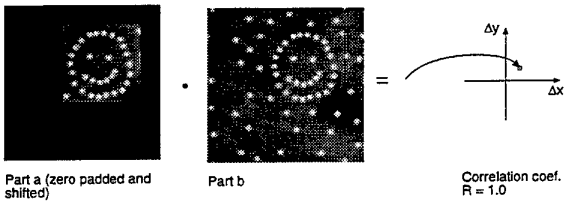


*Fig. 7: The FFT-based free shape correlation combines the advantages of the direct correlation (free-sized and free-shaped windows, high accuracy) and the simple FFT-based correlation (high speed). The Figure shows the equivalent direct correlation for one displacement. Note: The mean and the variance of partial image (b) (used in the normalization of the correlation) must **not** be integrated over the whole partial image. Instead it has to be recalculated for each displacement. In the example shown above, the mean and variance are integrated only over the pixels inside the small rectangle. After a mathematical transformation of the governing equation it is still possible to make use of the FFT to reduce the computing time substantially.*

mask **m**. The numerator of the direct correlation (Eq. 4) then becomes

$$r_{kl} = \sum_{i=1}^{N}\sum_{j=1}^{M} m_{ij}a_{ij}b_{i+k,j+l} - \frac{1}{\sum m_{ij}}\sum_{i=1}^{N}\sum_{j=1}^{M} m_{ij}a_{ij}\sum_{i=1}^{N}\sum_{j=1}^{M} m_{ij}b_{i+k,j+l} \quad (7)$$

With a normalized mask $\sum m_{ij} = 1$ we can now rewrite this equation utilisizing the FFT as

$$\mathbf{r} = \mathrm{FFT}^{-1}\left(\mathrm{FFT}^{*}(\mathbf{ma})\cdot\mathrm{FFT}(\mathbf{b})\right) - \sum \mathbf{ma}\cdot\mathrm{FFT}^{-1}\left(\mathrm{FFT}^{*}(\mathbf{m})\cdot\mathrm{FFT}(\mathbf{b})\right) \quad (8)$$

Where **ma** denotes the element by element multiplication of two images:

$$(\mathbf{ma})_{ij} = m_{ij}\cdot a_{ij} \quad (9)$$

With the definition of a cross correlation operator $\otimes$ as

$$\mathbf{x}\otimes\mathbf{y} := \mathrm{FFT}^{-1}\left(\mathrm{FFT}^{*}(\mathbf{x})\cdot\mathrm{FFT}(\mathbf{y})\right) \quad (10)$$

the completely free shaped cross correlation can be written as

$$\mathbf{R} = \frac{\mathbf{ma}\otimes\mathbf{b} - \sum\mathbf{ma}\cdot\mathbf{m}\otimes\mathbf{b}}{\sqrt{\left(\sum\mathbf{ma}^2 - \left(\sum\mathbf{ma}\right)^2\right)\cdot\left(\mathbf{m}\otimes\mathbf{b}^2 - \left(\mathbf{m}\otimes\mathbf{b}\right)^2\right)}} \quad (11)$$

The effect of such a correlation is illustrated in Fig. 7

In the standart cross correlation one has to compute three Fourier transforms. The FFT-based free shape correlation needs six Fourier transforms (The Fourier transform of the mask can be calculated once before the whole evaluation). So the computing time will only be doubled compared to the "traditional" evaluation. That is much faster than doing a direct correlation as described in Fincham and Spedding (1997). Please note, that this algorithm returns exactly the same result as the direct correlation described there. The only difference is, that it is much faster and more flexible with respect to the shape of the window.

4 THE STATISTICAL ERROR OF CORRELATION COEFFICIENTS

The error of a correlation coefficient depends on its value. It does not follow a normal distribution, which is obvious, because it can assume values only between -1 and 1. Accordingly the values in the correlation plane have to be weighted when the peak fit is performed.

For a correlation coefficient r of two datasets, where the distributions form a binormal or two-dimensional Gaussian distribution around their mean values, one can use *Fisher's z-transformation*, which associates each measured r with a corresponding z,

$$z = \frac{1}{2}\ln\left(\frac{1+r}{1-r}\right) \quad (12)$$

Then, each z is approximately normally distributed with the same standard deviation. Although the grey values in a PIV recording are not really normally distributed, the Fisher transform still performs satisfactorily.

5 PEAK FITTING FOR SUB PIXEL RESOLUTION

To resolve the particle image displacement with sub pixel accuracy, usually a function is fitted to the correlation peak and its surroundings. According to section 2, the shape of the particle image is given by the point spread function of the camera objective convoluted with the sensitivity distribution of one CCD pixel. Assuming a Gaussian point spread function and a rectangular sensitivity distribution, the shape of the correlation peak will be a Gaussian bell convoluted with a 2D triangular function. Until now we have not found an analytical expression for this function. So we use a Gaussian bell, keeping in mind, that especially for very small particle images (diameter around 1 pixel) this assumption might produce some systematical and statistical errors.

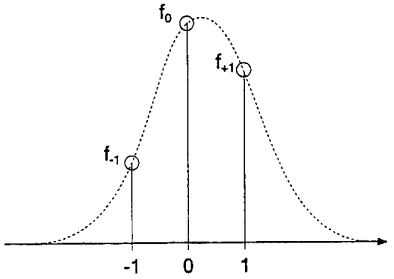


Fig. 8: The most common way to estimate the sub pixel position of the correlation peak is to use two one dimensional "fits" through the highest value and its two neighbours (three-point estimator). *Although it is fast and easy to implement, it is only suitable for a very small range of particle image diameters and produces systematical errors for smaller peak diameters.*

The most common method to fit the Gaussian curve to the correlation data, is to do two one dimensional fits to the highest value and its two neighbours (Fig. 8). A detailed analysis of these *three-point estimators* may be found in Westerweel (1993). Although the technique is fast and easy to implement, it is only suitable for a very small range of particle image diameters and produces systematical errors for smaller peak diameters. Particularly for elliptically shaped peaks (usually found in the corners of a PIV recording due to lens abberations) the two one dimensional fits will not return the correct centre of this peak.

Therefore, we perform a two dimensional Gaussian fit using the Levenberg-Marquardt method from Press et al. (1992). Due to the aforementioned not-normal distribution of the errors of correlation coefficients, the best results would be reached, when fitting a Fisher-transformed Gaussian bell to the Fisher-transformed correlation plane. As the Fisher-transformed Gaussian bell is a very unpractical and complicated function, we use the Fisher transform only to determine the weight for each value and perform a weighted fit (Fig. 9).

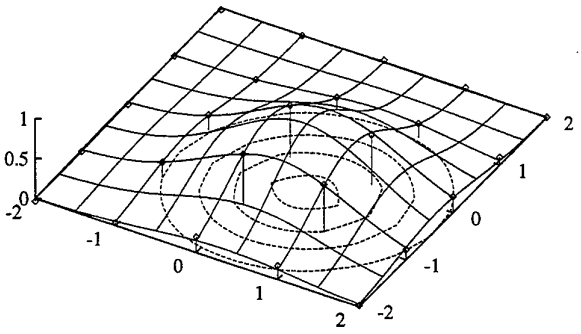


Fig. 9: Iterative Levenberg-Marquardt fit to determine the exact position of the correlation peak: A two dimensional Gaussian curve is fitted to the highest correlation coefficient and its surrounding in the correlation plane. This can handle elliptical peaks properly and the values can be weighted according to the Fisher transform.

For very sharp peaks, all of the tested fitting algorithms tend to return too wide and too low Gaussian bells. With the assumption that all particle images inside the interrogation area have the same shape, due to the point spread function of the camera objective, all random correlation peaks will have the same shape as the main correlation peak, if there are not too big gradients of the particle displacement (Fig. 10).

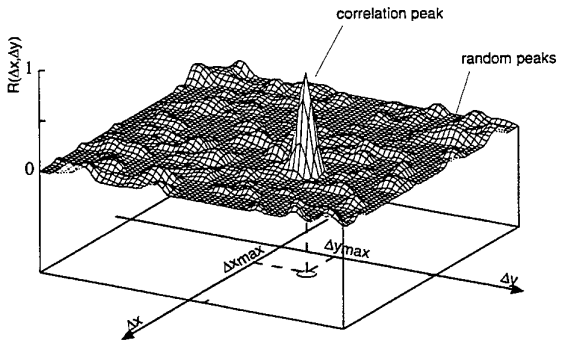


Fig. 10: All random peaks have the same shape as the correlation peak (assuming that all particle images inside the interrogation area had the same shape and that there are no big gradients of the particle displacement). This additional information can be used to achieve a better peak fit.

This additional information about the shape of the correlation peak can be extracted quite easily from the correlation function after eliminating the phase of the Fourier transform (see below). After the shape of the peak has been determined in this way, one can compute a peak fit with fixed shape parameters to determine the position and the height of the correlation peak.

This technique highly improves the quality of the peak fit (especially the determination of the peak height) and is the main key in the evaluation of dual plane recordings in air flows.

To determine the mean shape of all random correlation peaks, the phases in the Fourier transformed correlation function are eliminated by retaining only the magnitude of each spatial frequency component.

$$\mathbf{Q} = \mathrm{FFT}^{-1}\Big(|\mathrm{FFT}(\mathbf{R})| \Big) \qquad (13)$$

As a result of this operation, all random peaks are shifted to position (0,0) and one can perform a peak fit with a known position and height to determine the shape. Please note that this shift only works, if the peak shape is symmetrical and the real parts of the Fourier-transformed peak are positive. This is usually automatically fulfilled for correlation peaks of PIV recordings, because the shape of a particle image does not change from the first to the second recording. This results in a shifted auto correlation for the random peaks.

6 EXPERIMENTAL VERIFICATION OF THE IMPROVEMENTS

To quantify the improvements under real conditions, images with two 1024x1024 pixel CCD-cameras which looked though a beam splitter at the same measurement volume were taken at the same time. The non-moving air in the measurement volume was seeded with 1μm oil droplets and illuminated with an Nd:YAG-laser light sheet. Due to the small differences between the position, angle and magnification of the two cameras, an apparent displacement field results, that contains nearly all possible sub pixel displacements (Fig. 11). To determine the true displacement field, a matrix, describing a rotation, a magnification and a shift was fitted to the measured displacement field.

Prominent "peak-locking" effects are found, when the displacement field of these two images is evaluated by means of the usual three-point Gaussian fit. The RMS difference between this result and the true displacement field is 0.112 pixel. One can separate this error into a systematic error of 0.066 pixel and a statistical error of 0.087 pixel (figure 11).

The errors of the displacement field obtained with the improved techniques are shown in figure 13. The dis-

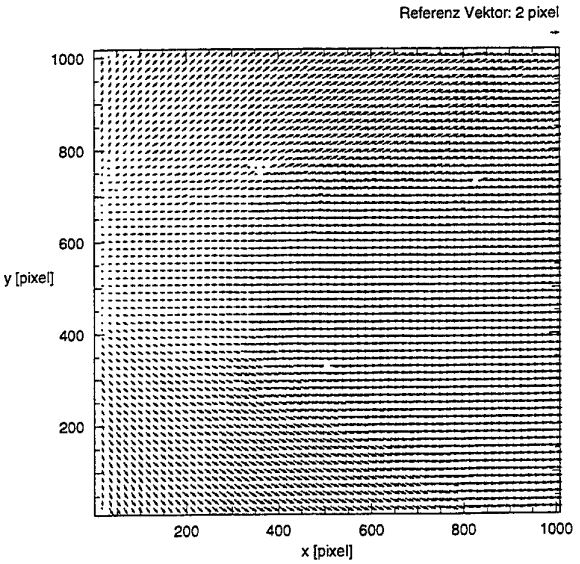


Fig. 11: The two images for this PIV evaluation were taken with two slightly misaligned cameras focused on the same part of non-moving air seeded with 1μm oil droplets.

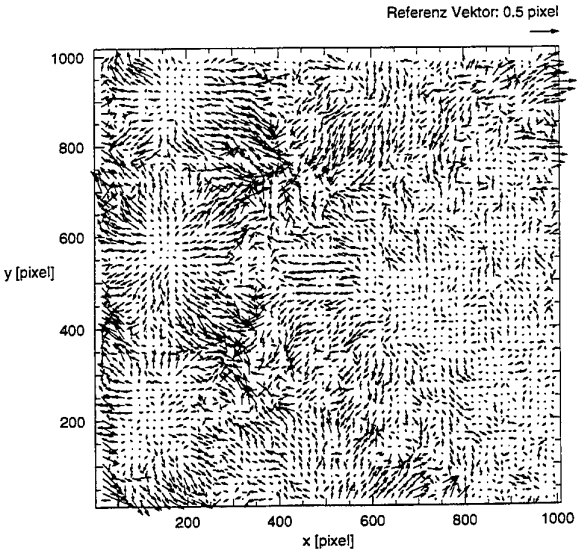


Fig. 12: Difference between the true displacement field and the measured displacement field using a normal 32x32 pixel interrogation window for the cross correlation and the three-point Gaussian fit to obtain the sub pixel position of the peak.

systematic error:	0.066 pixel
statistical error:	0.087 pixel
resulting error:	0.112 pixel

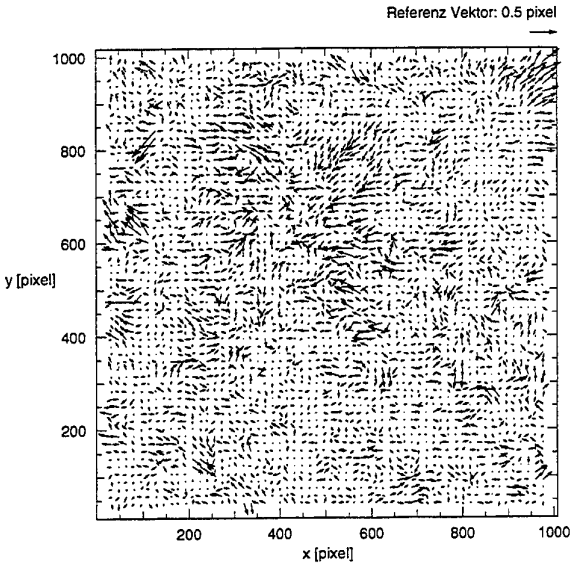


Fig. 13: Difference between the true displacement field and the measured displacement field using the advanced cross correlation with a 32x32 pixel interrogation window for the first and a 64x64 pixel interrogation window for the second image. The Gaussian peak fit was done using 9x9 pixels around the peak and the additional information from the random peaks.

systematic error:	0.0177 pixel
statistical error:	0.070 pixel
resulting error:	0.073 pixel

placements systematic error is reduced by nearly 75% to 0.0177 pixel and the statistical error is reduced by 20% to 0.070 pixel. The systematic and statistical error of the peak height is also reduced by 30% when using these techniques.

7 OTHER APPLICATIONS FOR THE FREE SHAPE CORRELATION

There are a lot of useful applications for the FFT-based free shape correlation. The first (and perhaps most important) advantage is that one can adapt the size of the interrogation window to the fluid dynamics of the experiment.

In regions with big gradients in one direction, e.g., a boundary layer which has big gradients normal to the wall, it can be useful to decrease the window size perpendicular to the wall while increasing it parallel to the wall.

Another application is the evaluation of stereo PIV recordings (using the Scheimpflug criteria) without de-warping the images before the evaluation. De-warping of images can introduce errors to the shape of the particle images and it is very time consuming. It is now possible just to warp the interrogation grid and to warp the interrogation window shape.

In PIV recordings containing objects (e.g., a wing profile) one may now make a local adaption of the interrogation window shape, so that one can measure the boundary layer very close to curved wall of an object (Fig. 14 - 16)

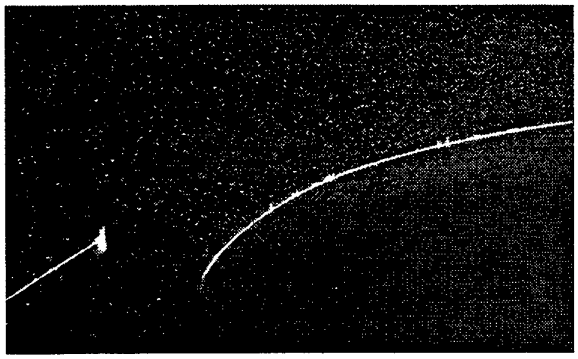


Fig. 14: PIV recording with curved walls and reflections

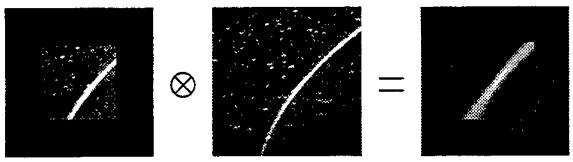


Fig. 15: With a rectangular interrogation window it is not possible to resolve the flow very close to the wing profile. The correlation plane contains no visible peak. (The operator ⊗ denotes here the FFT-based free shape correlation)

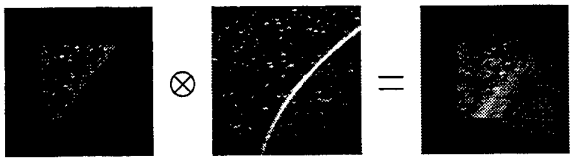


Fig. 16: With a free shaped interrogation window the flow close to the profile can be resolved. There is now a clear peak in the correlation plane near to the center

8 NOMENCLATURE

Two dimensional data arrays like images are represented by bold Roman letters (e.g., **a**). All operations on these arrays are defined element by element, e.g., $\mathbf{c} = \mathbf{a} \cdot \mathbf{b}$ has to be interpreted as $c_{ij} = a_{ij} \cdot b_{ij}$. The other definitions are:

$\bar{\mathbf{a}}$	Mean value of array **a**
RMS(**a**)	Variance of array **a**
FFT(**a**)	Fast Fourier transform of **a**
$\mathrm{FFT}^{-1}(\mathbf{a})$	Reverse FFT
$\mathbf{a} \otimes \mathbf{b}$	simple FFT-based cross correlation of **a** and **b**
R	Array containing the normalized 2D correlation function

REFERENCES

Fincham, A. M. & Spedding, G. R. 1997, Low cost, high resolution DPIV for measurement of turbulent fluid flow. *Experiments in Fluids*, vol 23, pp. 449–462.

Press, W. H. et al. 1992, *Numerical recipes in C: the art of scientific computing – 2nd ed.* Cambridge University Press.

Raffel, M., Derville, A., Willert, C., Ronneberger, O. & Kompenhans, J. 1996, Dual-plane correlation for three-dimensional particle image velocimetry on planar domains. In *8th International Symposium on Applications of Laser Techniques to Fluid Mechanics, Lisbon.*

Raffel, M., Ronneberger, O., Gharib, M. & Kompenhans, J. 1995, Feasibility study of three-dimensional PIV by correlating images of particles within parallel light sheets. *Experiments in Fluids*, vol 19, pp. 69 – 77.

Ronneberger, O. to appear 1998, Messung aller drei Geschwindigkeitskomponenten mit Hilfe der "particle image velocimetry" mittels einer Kamera und zweier paraleller Lichtschnitte. Forschungsbericht, Deutsches Zentrum für Luft- und Raumfahrt.

Westerweel, J. 1993, *Digital particle image velocimetry: theory and application.* Delft University Press.

Willert, C.E. & Gharib, M. 1991, Digital particle image velocimetry. *Experiments in Fluids*, vol 10, pp 181–193.

PARTICLE IMAGE VELOCIMETRY USING AN IMAGE RELAXATION METHOD

Kazuo Ohmi [1] and Dao Hai Lam [2]

[1] Department of Information Systems Engineering
Osaka Sangyo University, Daito, Osaka 574, Japan
[2] Department of Information Science Engineering
Ho Chi Minh City University of Technology, Ho Chi Minh City, Vietnam

ABSTRACT

The relaxation method is applied to PIV measurement of fluid flows using a multiple frame particle tracking algorithm. The benchmark test is conducted on the PIV standard images accessible on the net, as well as bluff body wake images derived from the authors' own experiment. In the course of test measurement, the relaxation method algorithm is improved from the original one of Barnard & Thompson (1980) in order to meet possible loss of particle images between two frames. Through this improvement, the performance of particle tracking using the relaxation method becomes more satisfactory.

1. INTRODUCTION

The key point of the particle tracking PIV system is how the software tracks the movement of a large number of particles from frame to frame with a good accuracy. In this context, there have been generally two widely-used methods based on a careful analysis of centroid coordinates of particles in every image frame. The first one is the binary image cross correlation method (Uemura & Hasegawa (1987)), in which the best frame-to-frame link of particle centers is searched for by using cross correlation templates. The advantage of this method is that it needs basically only two image frames to get reasonable vector maps and that the computing time is quite short if the template shifts are limited to the centroid coordinates of the preselected candidate particles.

The second one is what the present authors would call four-frame in-line tracking method (Kobayashi *et al* (1988)), in which the displacement of particles is pursued over four sequential image frames, while taking into account the geometric consistency of every possible particle paths. The merit of this method is that the tracking is usually free from rotation and/or shear deformation of the examined flow field, which is not the case of the first method. On the contrary, this second method has its own problems concerning density of resultant vectors and computing time.

The relaxation method of the present work has been known as one of the most powerful optical flow algorithms in the field of computer vision and motion capture analysis, though it has been so far quite rarely employed in the PIV measurement of fluid flows. This method shares the merits of the binary image cross correlation method and those of the four-frame in-line tracking method, because the tracking is free from a certain extent of rotation and/or shear deformation of the flow field, in spite that only two image frames are used to map the velocity. Another advantage of the method is that the most probable frame-to-frame link of particles is obtained through iterative calculation of all the particle link probabilities and, in most cases, the results are more satisfactory if compared to other tracking algorithms without iterative calculation. In addition, the method incorporates, as one of the calculated probabilities, the disappearance or occlusion of particle images between frames, which is inevitable in usual fluid experiments.

However, in the original algorithm of this image relaxation method by Barnard & Thompson (1980), as well as in the first application of the method to PIV by Lee & Baek (1995), this probability of particle image loss is defined only implicitly, that is to say, the no link probability is defined as the remainder of all the possible link probabilities at every updating stage. Obviously, this type of definition does not seem suitable for PIV images, in which several percent of particle images are usually lost between frames. Therefore, in the present paper, the relaxation method is further improved from Barnard & Thompson (1980), by introducing a new explicit definition of this no link probability.

The new PIV algorithm is tested on two series of particle motion images in fluid flows. The first one is a 2D wall shear flow taken from the PIV standard images open on the net (http://www.vsj.or.jp/piv/). This set of images are generated artificially based on a CFD result and regarded as a good measure of every PIV algorithm, because everyone knows the correct frame-to-frame link of existing particles. The second sample is a 2D bluff-body wake flow taken from the authors' own fluid experiment. These are purely experimental particle images and, accordingly, do not include any correct data as in the first example. All the measurement results are compared to those of the binary image cross correlation method and then, some discussion is made as to the accuracy of particle tracking.

2. PRINCIPLE OF PARTICLE TRACKING

The basics of the relaxation method consist, as in the case of the binary image cross correlation method, in pursuit of the most probable link of a reference particle in relation to the displacement of neighboring particles. However, in the binary image cross correlation method, the correct link estimate is increased only when the neighboring particles find their partners in the form of completely parallel and equidistant link, whilst in the present relaxation method, the correct link estimate is increased if only the neighboring particles find their partners in the vicinity of the end of parallel and equidistant link. And this increase of correct link estimate may be expressed discretely via simple increment of integral variables, but in many of the previous trials using this relaxation method, non-integral probabilities are introduced between every possible link of the particles, and the increase of correct link estimate is expressed by weighted summation of the link probabilities of the neighboring particles. Among the link probabilities of every particle, the no link probability is also included. In addition, in order to make further difference of probabilities between the correct link and the other links, iterative calculation is carried out in which every particle link probability is updated using the latest link probabilities of the neighboring particles. In this process, the correct link probability is gradually increased close to unity and the other probabilities tend to zero.

All these principles are expressed mathematically as follows. If the particle i in the first frame has a possible link to the particle j in the second frame, their respective coordinates $\boldsymbol{x}_i$ and $\boldsymbol{y}_j$ should satisfy:

$$\left|\boldsymbol{x}_i - \boldsymbol{y}_j\right| < R_s \tag{1}$$

where R_s is the maximum possible displacement of the particles in the first frame. At the same time, within the extent of the first frame, the neighboring particle k of the particle i is defined as those satisfying

$$\left|\boldsymbol{x}_i - \boldsymbol{x}_k\right| < R_n \tag{2}$$

where $\boldsymbol{x}_i$ and $\boldsymbol{x}_k$ are their respective coordinates and R_n the radius of the neighboring region in which are preserved the consistency of particle distribution patterns.

On the other hand, the probability P_{ij} of the particle i in the first frame matching the particle j in the second frame must satisfy

$$\sum_j P_{ij} + P_i^* = 1 \tag{3}$$

where P_i^* is the probability of the particle i having no matching partner in the second frame. In the present work, the initial values of P_{ij} and P_i^* are given by

$$P_{ij}^{(0)} = P_i^{*(0)} = \frac{1}{M+1} \tag{4}$$

where M denotes the number of the possible matching particles in the second frame (referred to as 'possible partners' hereafter). These initial values can be provided in other ways; for instance, one can compute the cross correlation function for each possible partner and normalize it so as to satisfy eq. (4). This kind of presetting is useful indeed for iterative calculation to converge more quickly, but the final results are nearly identical.

In order to update the match probability P_{ij} of the particle i in the first frame with respect to the particle j in the second frame, reference is made to the match probability P_{kl} of the neighboring particle k with respect to its own possible partner l. The updated probability is defined by

$$\widetilde{P}_{ij}^{(n)} = P_{ij}^{(n-1)} \cdot \left(A + B \cdot \sum_{\substack{k \\ l \ni eq.(6)}} \sum_{l} P_{kl}^{(n-1)} \right) \tag{5}$$

where A and B are weight constants (these are fixed here at A=0.3 and B=3.0 according to Barnard & Thompson (1980)) and the double summation is limited to the particle pairs satisfying the following equation,

$$\left|\boldsymbol{d}_{ij} - \boldsymbol{d}_{kl}\right| < R_c \tag{6}$$

in which $\boldsymbol{d}_{ij}$ and $\boldsymbol{d}_{kl}$ are the displacement vector from particle i to j and that from particle k to l respectively and R_c is the radius of the search area within which the neighboring particles are expected to find their possible partners. In the authors' case, R_c is set around 10% of R_s, the radius of the first-level search area.

The updated probability $\widetilde{P}_{ij}^{(n)}$ has to be normalized to meet eq.(3) and the scheme for normalization employed by previous researchers (Barnard & Thompson (1980) in their motion capture analysis and Lee & Baek (1995) in their PIV measurement) is the following.

$$P_{ij}^{(n)} = \frac{\widetilde{P}_{ij}^{(n)}}{\sum_j \widetilde{P}_{ij}^{(n)} + P_i^{*(n-1)}} \tag{7}$$

This normalization uses the no match probability P_i^* from the precedent generation, the reason for which is understandable but the process lacks in consistency.

The update of the no match probability P_i^* using that of the preceding generation is rather difficult, because the fact that the neighboring particles are unable to find their partners does not necessarily reinforce the no match probability of the reference particle. So, for simplicity, this probability is usually updated implicitly in the normalization process, which is as follows,

$$P_i^{*(n)} = \frac{P_i^{*(n-1)}}{\sum_j \widetilde{P}_{ij}^{(n)} + P_i^{*(n-1)}} \tag{8}$$

This means that the no match probability is defined only as the remainder of all the possible match probabilities and, obviously, this does not seem suitable for a PIV algorithm as described in the preceding section.

In the present work, the authors propose an improved type of definition, where the no match probability is updated via an explicit scheme,

$$\widetilde{P}_i^{*(n)} = \sum_{m<C} \frac{D \cdot P_i^{*(n-1)}}{M} \tag{9}$$

where C and D are new empirical constants (C=0.1 and D=5.0 in the present case) and m denotes the ratio of the number of links satisfying eq.(6) with respect to the total number of possible links of all the neighboring particles. According to this new update scheme, eqs.(7) and (8) are redefined respectively as,

$$P_{ij}^{(n)} = \frac{\widetilde{P}_{ij}^{(n)}}{\sum_j \widetilde{P}_{ij}^{(n)} + \widetilde{P}_i^{*(n)}} \tag{7}'$$

$$P_i^{*(n)} = \frac{\widetilde{P}_i^{*(n)}}{\sum_j \widetilde{P}_{ij}^{(n)} + \widetilde{P}_i^{*(n)}} \tag{8}'$$

In the present work, the relaxation method is tested comparatively in both of the two schemes. And in brief, the usual relaxation method uses eqs.(1) to (8), whereas the present improved method employs eqs. (7)', (8)' and (9) instead of eqs.(7) and (8).

3. RESULTS AND COMPARISON

In the present work, the authors are concerned with two series of particle motion images. To both of them are applied three types of particle tracking algorithms, namely binary image cross correlation method, previously proposed relaxation method and the authors' improved relaxation method, the principles of which are explained in the preceding section.

The first test image is that of a 2D wall shear flow near a nozzle, taken from the PIV standard image series (Okamoto *et al* (1997)). This standard image is open on the net (http://www.vsj.or.jp/piv/) and supported by the VSJ-based PIV Standard Project Council. The image set tested here bears a series number '01' and is shown in Figure 1, not as a selected single frame image but as an overlapped image of four sequential frames. However, in the present work, all the particle tracking algorithms are applied to the first two frames only.

The resultant vector maps are illustrated in Figures 2 to 4, which are respectively obtained from algorithms of the binary image cross correlation method, the previous relaxation method and the improved relaxation method. Main input parameters required for these methods are given in Table 1, comparably with the second test image. The table excludes the number of iterations in the relaxation method, which is fixed at 20 through a visual check of chronological results. The reason for this is that the computation of norms for checking convergence requires often as much time as the update of probabilities.

The second test image is that of a 2D bluff-body wake, taken from the authors' own flow visualization experiment (Ohmi (1996)). The vortex wake behind a cylinder is visualized using fine white-colored Nylon-11 particles and a 4W Argon-ion laser light sheet in water. The original images were captured with a NTSC video camera connected to a PC with a 48MB frame grabber.

Although the flow speed of this series of particle images may be slightly too high with respect to the fixed frame rate of the video camera, it is shown in Figure 5 as an overlapped image of four sequential frames. And as is the case of the first test image, all the particle tracking algorithms are applied to the first two frames only.

The resultant vector maps are shown in Figures 6 to 8, corresponding respectively to the results of the binary image cross correlation method, the previous relaxation method and the improved relaxation method. The relevant parameters are given in Table 1 together with those of the first test image. The number of iterations in the relaxation method is also fixed at 20.

It is evident from the PIV standard image case that the results of the relaxation method are more satisfactory than that of the binary image cross correlation method, in the sense that the number of spurious vectors, from a visual observation, is clearly reduced. And comparing the two algorithms of the relaxation method, the results of the improved algorithm are further more satisfactory because the vector map is apparently free from spurious links in any portion of the flow image.

This improvement in measurement accuracy is confirmed by checking the error rate of the resultant vectors Since the home page of the PIV standard image project provides correct velocity data of the relevant flow in the form text files, a direct check of the error rate is possible in principle. As a result, it is indeed confirmed that this error rate is drastically reduced with the introduction of the relaxation method, and that this goes up to a 0.1% level when the improved relaxation method is employed.

Table 1 Major parameters of the two test images

	PIV standard image	Cylinder wake image
Image size	256 x 256 pix	512 x 484 pix
Gray level	8 bit/pix	8 bit/pix
Threshold	128	90
Search area R_s	15 pix	12 pix
Vicinity $R_n^{(*)}$	24 pix	19 pix
Flexibility $R_c^{(**)}$	3 pix	2.5 pix

(*) In the binary image cross correlation method, this should be read as a half of the template size .
(**) Not used in the cross correlation method.

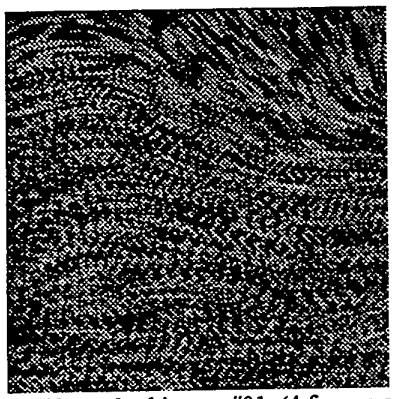


Fig.1 PIV standard image #01 (4 frames overlapped).

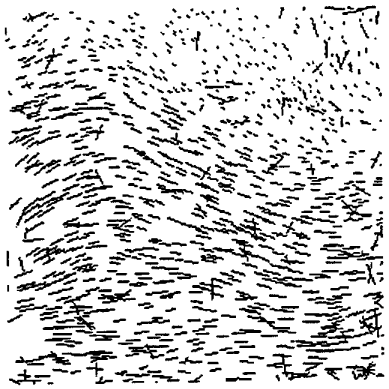


Fig.2 Binary image cross correlation method.

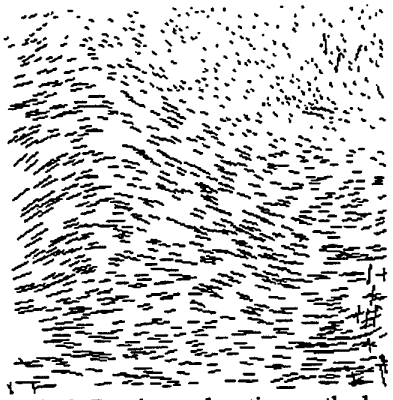


Fig.3 Previous relaxation method.

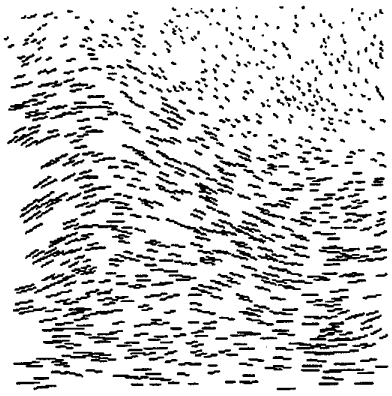


Fig.4 Improved Relaxation method

In the second case of the cylinder wake image, it is again observed that the vector map results are more and more satisfactory when the used algorithm is changed from the binary image cross correlation method to the previous and to improved relaxation method. However, in this case, even the improved relaxation method is not necessarily perfect as is seen from a small number of spurious links in some accelerating shear flow regions. This is mainly because the captured image of the particles in this second sample is slightly elongated in shape, due to comparatively long exposure time of the camera, and in consequence, the number of overlap of particle images is increased to some extent. Needless to say, the exposure time is controllable, but the basic problem here consists rather in localization of the centers of the individual particle images. This point will be studied in the authors' next-coming paper.

4. CONCLUDING REMARKS

It is more and more convinced that the relaxation method in image analysis provides nearly the best particle tracking algorithm in many types of the PIV measurement. In particular, when the improved algorithm is used, the resultant vector maps seem to obtain more accuracy getting to a practical-use level.

Apart from the algorithm performance, the number of parameters required for computation is also an important index (simplicity) of each method. This number is increased only by one (referring to R_C in eq.(6)) in the relaxation method if compared to the binary image cross correlation method. The same thing is probably true ('probably' because the number of required parameters differs depending on the details of the algorithm) with respect to the four-frame in-line tracking method.

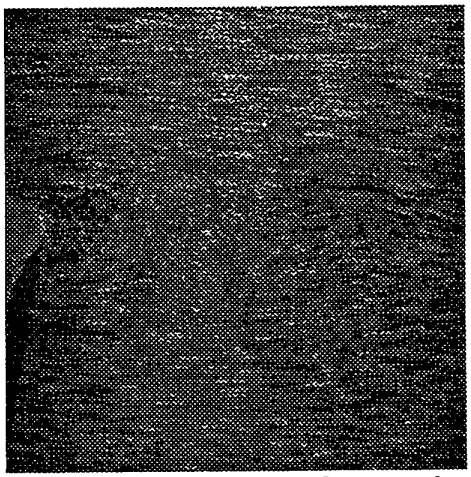


Fig.5 Cylinder wake vortex flow (4 frames overlapped).

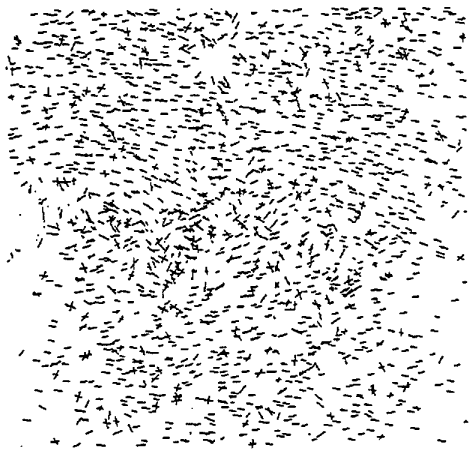


Fig.6 Binary image cross correlation method.



Fig.7 Previous relaxation method.

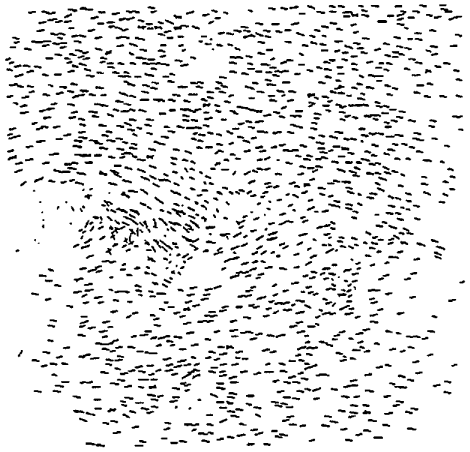


Fig.8 Improved Relaxation method.

In general, the additional parameter R_c can be set around 10 to 15 % of the main search area R_s. So there seems to be no complicity caused by this additional parameter. However, this one is considered as a kind of flexibility parameter, indicating to what extent the rigidity of fluid motion is preserved in a local area. So in some cases, this is a key parameter of the flow in question, probably relating to a certain theoretical model (Taylor's microscale as suggested by Lee & Baek (1995)). Accordingly, it is now necessary to examine into good estimates of this parameter used in the relaxation method.

The computing time is obviously greater than the that of the binary image cross correlation method, but in most cases, less than the four-frame in-line tracking method despite the iterative calculation. The reason for the latter is that the relaxation method does not iterate area search of particles. It must be pointed out that the relaxation method enables two-frame particle tracking as is the case of the binary image cross correlation method. All these observations lead to the conclusion that this relaxation method should be adopted in many PIV systems in the near future and that the algorithm should be further improved in order to meet the growing necessity of exploring turbulent flow phenomena.

ACKNOWLEDGEMENTS

The author thanks to the Institute for Industrial Research of Osaka Sangyo University for their Bunya-betsu Research Grant during the fiscal year 1996. They are also indebted to Suzuki Motors Foundation for their Research Grant-in-Aid of the year 1997. Finally they are especially thankful to Dr. Koji Okamoto of the University of Tokyo for his elaboration of the PIV standard image on the net, without which the present work would have been in more difficulty.

REFERENCES

Barnard,S.T., Thompson,W.B., 1980, Disparity Analysis of Images, IEEE Trans on Pattern Analysis and Machine Intelligence, Vol.2, No.4, pp.333-340.

Kobayashi,T., Saga T., Segawa,S. 1988, An Automatic Velocity Measurement using Image Processing Technique and its Particle Tracking (in Japanese), J. Visualization Society of Japan, Vol.8, No.30, pp.171-174.

Lee,S.J., Baek,S.J., 1995, Two-Frame PIV and its Application to a Turbulent Channel Flow, Proc. PIV-Fukui '95, pp.217-226.

Ohmi,K. 1996, Cross Correlation PIV Measurement Using Different Flow Visualization Method (in Japanese), J. Visualization Society of Japan, Vol.16, Suppl.No.1, pp.219-222.

Okamoto, K., Nishio, S., Saga, T. and Kobayashi, T., 1997, "Standard Images for Particle Imaging Velocimetry", Proc. PIV-Fukui '97, pp.229-236.

Uemura,T., Hasegawa,Y. 1987, A High Speed Image Analysis for Velocity Measurement using Correlation Technique (in Japanese), J. Visualization Society of Japan, Vol.7, Suppl., pp.11-14.

A NEW ALGORITHM FOR THE EVALUATION OF PTV DATA USING POINT MATCHING DISTANCE MEASURES AND DETERMINISTIC ANNEALING

A. Kuzmanovski, M. Stellmacher and K. Obermayer

FR2-1, FB Informatik, Technische Universität 10587 Berlin, Germany

1. ABSTRACT

We describe a new method for the evaluation of single pulse multiple exposure PTV data which allows the joint estimate of several local flow field parameters, among them components describing local translation, rotation and shear. The method operates on particle coordinates, which can be extracted from digital images using the CLEAN algorithm by Schwarz (1978), and is based on an algorithm recently proposed by Gold et al. (1996) for matching problems in stereo vision and statistical pattern recognition. For flows with small velocity gradients our method compares favorable to cross-correlation techniques. When velocity gradients become larger, for example near vortices and in shear flows, the new method leads to strongly improved velocity estimates, and additionally allows an estimate of the strength of the local rotation and shear components. The method can in principle be extended to stereo data, because computational expenses grow linearly with the number of particle coordinates only.

2. INTRODUCTION

Particle image velocimetry is an established and widely used quantitative method for measuring flow fields in experimental fluid mechanics. Most of the current interrogation methods (see, e.g., Adrian (1991)), however, are designed to estimate the local velocity only. In our contribution we describe an approach which allows the additional estimation of local rotation and shear components and which can be extended to the analysis of stereoscopic PIV data in a computationally efficient manner, if necessary.

Our approach is based on algorithms which were developed for matching 2D point sets or graphs by Gold et al. (1996) for problems in stereo vision and pattern recognition. Starting from a cost function for the similarity between two sets of points, the optimal correspondences and the parameters of the transformation are estimated using the principle of maximum entropy and deterministic annealing (Yuille et al. (1994)). The estimation procedure is robust against missing particles and positional noise, and improves on the standard cross-correlation techniques. In the following, the method is explained in the framework of single pulse double exposure PTV data but maximum entropy inference and deterministic annealing can also be used to improve interrogation algorithms for other exposure paradigms.

3. THE INTERROGATION ALGORITHM

Figure 1 schematically shows particles within an interrogation window at two different exposure times. Between the exposures the particles move to new positions following the local flow of the fluid. We assume that the location of the points j between the two frames, $\mathbf{X}_j \rightarrow \mathbf{Y}_j$, can be described by a linear transformation $(\mathbf{t}, \mathbf{A})$, $\mathbf{Y}_j = \mathbf{A}\mathbf{X}_j + \mathbf{t}$, which approximates the projection of the - usually non-linear - local flow onto the plane of the laser sheet. Our goal is to find the corresponding particles in both frames and at the same time estimate the parameters

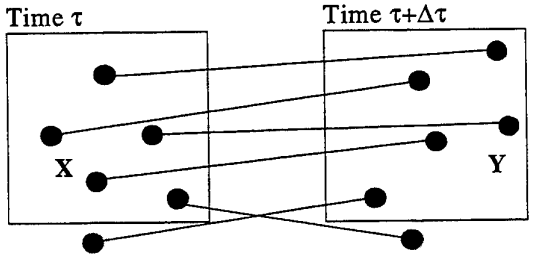


Figure 1: Cartoon of the interrogation window for two subsequent exposures. Black circles denote particles. Lines indicate correspondences. Hashed circles denote "missing dots".

(**t**, **A**) of the transformation. Due to velocity components perpendicular to the laser sheet and due to out of spot noise there may exist a certain number of points which do not have a corresponding partner in the other frame. These missing partners are indicated by the hashed circles outside the frames in Fig. 1. Following Gold et al. (1996) we now define a cost function

$$E(m,\mathbf{t},\mathbf{A})=\sum_{j=1}^{J}\sum_{k=1}^{K} m_{jk}\left\|\mathbf{Y}_j-\mathbf{t}-\mathbf{A}\mathbf{X}_k\right\|^2+$$

$$g(\mathbf{A})+\alpha\sum_{j=1}^{J} m_{j(K+1)}+\alpha\sum_{k=1}^{K} m_{(J+1)k}, \quad (1)$$

where **t** is the translation vector, **A** is the transformation matrix, and m_{ij} are binary assignment variables. Choices for **A** could include rotation and shear, for example

Shear $$\mathbf{A}=\begin{pmatrix}1 & 0\\ a & 1\end{pmatrix},$$

Rotation $$\mathbf{A}=\begin{pmatrix}\cos(\theta) & -\sin(\theta)\\ \sin(\theta) & \cos(\theta)\end{pmatrix}. \quad (2)$$

Let j = 1...J, k = 1...K denote the individual particles in the different frames and their total number, and let j = J+1, k = K+1 denote the "missing partners". Because a particle in the first frame either has exactly one match in the second frame or is matched to its "missing partner", the following constraints hold:

$$\sum_{k=1}^{K} m_{jk}\le 1,\ \sum_{j=1}^{J} m_{jk}\le 1,$$

$$\sum_{j=1}^{J} m_{jk}+m_{(J+1)k}=\sum_{k=1}^{K} m_{jk}+m_{j(K+1)}=1.$$

The second term, g(**A**), on the r.h.s. of eq. (1), is a regularizer for the free parameters of the transformation matrix, and the second and third term on the r.h.s. of eq. (1) is the cost for non-matches. The values of the local flow field parameters and the optimal values of the assignment variables are now given by the global minimum of the cost function (1).

The optimization problem is solved using the principle of maximum entropy and deterministic annealing which leads to the following iterative optimization procedure suggested by Gold et al. (1996):

Initialization

BEGIN Outer Loop

BEGIN Inner Loop

Calculation of the probabilities $\langle m_{jk}\rangle$:

If $j \neq J+1$ and $k \neq K+1$:

$$\langle m_{jk}\rangle=\exp\left(-\beta\left(\left\|\mathbf{X}_j-\mathbf{t}-\mathbf{A}\mathbf{Y}_k\right\|^2\right)\right)$$

else

$$\langle m_{jk}\rangle=\exp(-\beta\alpha)$$

Normalization of the $\langle m_{jk}\rangle$:

$$\langle m_{jk}\rangle=\frac{\langle m_{jk}\rangle}{\sum_{j'=1}^{J+1}\langle m_{j'k}\rangle};\ \langle m_{jk}\rangle=\frac{\langle m_{jk}\rangle}{\sum_{k'=1}^{K+1}\langle m_{jk'}\rangle};$$

Calculate **t** and **A** via $\frac{\partial E}{\partial t_i}=0;\ \frac{\partial E}{\partial a_i}=0$

END Inner Loop

Increase β

END Outer Loop

where the t_i are the components of the translation vector and a_i are the components of the transformation matrix to be determined. This procedure minimizes the cost function (1) in an expectation-maximization fashion (Dempster et al. (1977)). In the first (E-)step the assignment probabilities $\langle m_{jk}\rangle$, are calculated given the old estimates of the flow field parameters. In the second (M-)step, the flow field parameters are reestimated by replacing m_{jk} by $\langle m_{jk}\rangle$ in the cost function and and minimizing it w.r.t. a_i, t_i analytically or via conjugate gradient methods. Annealing in the inverse computational temperature β, finally, leads to the minimum of E.

In the following, parameters were set to α=15.0. Annealing was performed via an exponential schedule, $\beta_{t+1}=\beta_\varepsilon\beta_t$, with $\beta_{Start}=10^{-4}$, $\beta_\varepsilon=1.07$ and $\beta_{max}=10^4$.

4. EXTRACTION OF PARTICLE COORDINATES

In order to extract particle coordinates from real DPIV images, we implemented a modified version of the CLEAN algorithm by Schwarz (1978). During each iteration of this algorithm, the brightest pixel in the image is selected, and a Gaussian blob, centered at the pixel's location, with a predefined width σ and an amplitude given by the gray value of the selected pixel is subtracted from the image. Negative values are set to zero. The algorithm terminates, when all gray values are below a predefined threshold θ. The set of particle coordinates is then given by the set of coordinates of all selected pixels.

5. BENCHMARK RESULTS ON ARTIFICIAL DATA

Figures 2, 3 and 4 show benchmark results obtained for artificial data sets. Coordinates of between 6 and 31 particles were randomly generated to lie within a circular interrogation area of radius 32 pixels (list of particle coordinates for first frame **X**). The list of particle coordinates for the second frame (**Y**) was then generated by (i) applying a transformation (**A**, **t**) to the coordinates of the first frame and (ii) randomly changing the location of a certain percentage ("percentage out-of-plane noise") of points in the second frame, mimicking particle noise due to the velocity components perpendicular to the laser sheet. Pairs of frames were first analysed by the point matching algorithm of section 2 in order to recover particle matches and transformation parameters. Benchmarks were then performed with the cross-correlation method on pixel images which were generated by labelling each particle's location by a small cosine blob of width $\sigma_b = 5$.

1000 pairs of frames were tested for every set of parameters, and the percentage of unsuccessful interrogations (relative error in one of the recovered transformation parameters larger than 5%) was determined.

Figure 2 shows the percentage of unsuccessful interrogations as a function the percent out-of-plane noise for different numbers of points in the

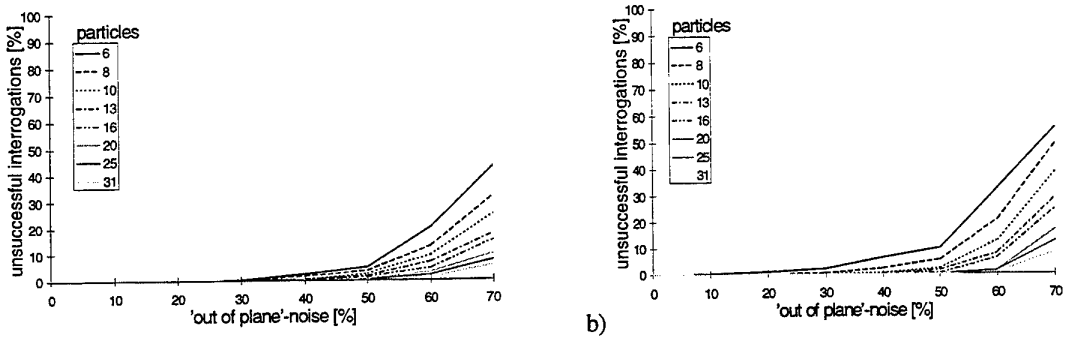


Figure 2: Benchmark results for extracting the translation components out of artificial DPIV-data for point matching (a) and cross-correlation (b) as interrogation methods.

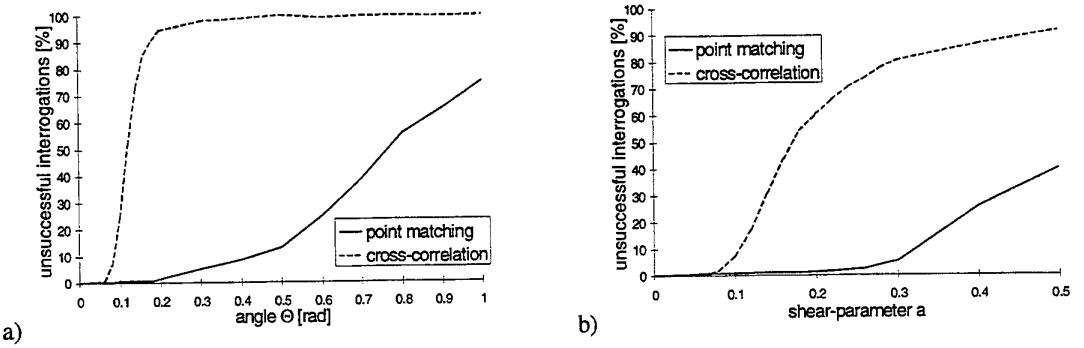


Figure 3: Benchmark results for artificial DPIV-data, which include strong rotation (a) and shear (b) components.

interrogation spot. The transformation was pure translation of 12.8 pixels in random directions. As expected, the errors increase with increasing percent noise and decreasing numbers of particles, however, the average percentage of unsuccessful interrogations remains below 10% for most of the parameter settings, even for 50% noise. Interrogation by point matching (Fig. 2a) performs slightly better than standard cross-correlation (Fig. 2b).

Figure 3 shows the effect of adding rotation (θ from eq. 2, Fig. 3a) and shear components (a from eq. 2, Fig. 3b) to the base translation of 12.8 pixels along the x-axis. Parameters were: σ_b = 5, 15 points per frame, and 25% out-of-spot noise. The point matching algorithm performs very well up to fairly high values for deformation and rotation, i.e. for fairly high values for the local velocity gradient, while the cross-correlation technique breaks down at a value of 0.078 for the rotation angle θ and the shear component a. As expected the breakdown occurs at values for which the positional error introduced by the gradient of the velocity becomes larger than the diameter of the particles (see Keane (1990)).

Figure 4 shows the algorithm's performance for a simulated potential flow around a cylindrical object. Particles were randomly distributed within an array of size 1024*1024 according to an overall density of 0.005 particles / pixel. The translation vector for every particle was then calculated using the equations

$$t_1 = u_\infty \left(1 + R^2 \frac{y^2 - x^2}{r^4} \right) \Delta\tau ,$$

$$t_2 = -2u_\infty R^2 \frac{xy}{r^4} \Delta\tau \qquad (3)$$

for the potential flow, where (x, y) are the 2d spatial coordinates of the cylinder, u_∞=12.0 is the velocity of the laminar flow, $r^2 = x^2 + y^2$, R=300 is the radius of the cylinder and $\Delta\tau$ =0.5 is the "time between exposures". Translation and rotation components were then estimated for interrogation windows of size 64*64 which were centered on the grid points of an 31*31 grid. The average number of particles per interrogation window was 16, 25% out-of-plane noise and positional noise (gaussian noise with deviation of 1.7 pixels). Before cross-correlation techniques were employed, images were again generated by labelling each particle's location by a small cosine blob of width σ_b = 5.

Figures 4a, b and c show the original flow field, the flow field recovered by the point matching algorithm and the flow field recovered by the cross-correlation technique. Point matching achieved an average error of 0.57 pixel per iterrogation window, the cross-correlation technique 0.73.

Computation time per interrogation spot scales quadratically with the number of particles for the point matching algorithm and with Nlog(N) with the number N of pixels within the interrogation spot for the cross-correlation technique. Computation time is equal for the point matching an the cross-correlation techniques for a spot radius of 32 pixels and 8 points /spot. For interrogation windows of 64*64 pixels with 15 particles the point matching algorithm however performs 4 times slower.

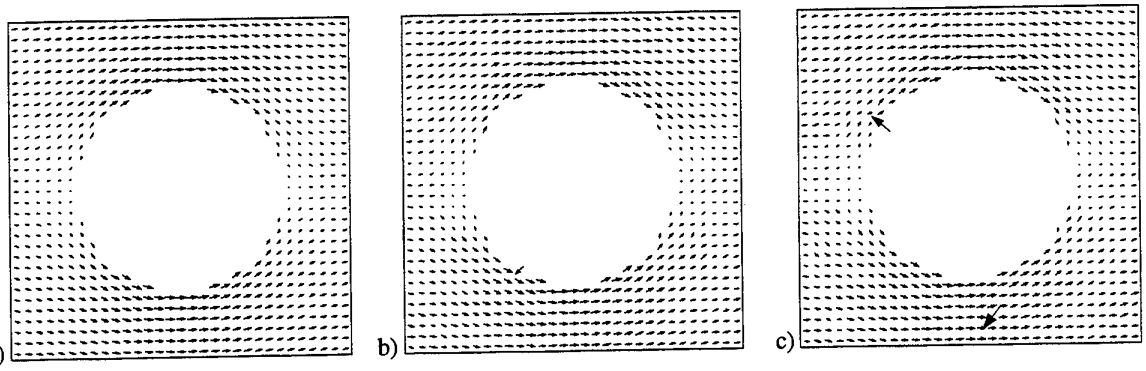


Figure 4: Potential flow: a) original data, b) flow field recovered by point matching, c) flow field recovered by cross-correlation.

6. RESULTS FOR REAL DPIV-DATA

In this section, the point matching algorithm of section 2 and the cross-correlation technique as implemented in the VisiFlow© evaluation software are applied to single pulse double exposure DPIV-data obtained from an artificial heart pump (Berlin heart, courtesy A. Ziemann and K Affeld).

The flow was illuminated with a pulsed light sheet with two Xenon laser lamps, the light interval was 2 ms. Shown is a vortex, which is created by entrance of fluid through the entrance valve (lower left in Fig. 5, not shown). The frame sequence was recorded by a 1024*1024 pixel interlaced video camera (Adimec Mx12).

Parameters were: size of the interrogation spot: 64*64 pixels, the overlap: 50%, average particle density: 15 particles per spot, and average particle diameter: 3 pixels. Cross-correlation was performed directly on the image data (8bit, 1024*1024 pixels). Gaussian peak estimation was used in order to achieve sub pixel accuracy. In order to apply the point matching algorithm, particle coordinates were extracted using the CLEAN algorithm of section 4 with $\sigma = 4.5$ and $\theta = 6$.

Figures 5a, b show the flow fields extracted by the cross-correlation and the CLEAN / particle matching technique, respectively. Note, that the point matching technique leads to an overall smoother and more realistic flow field, in particular close to the vortex in the lower left corner. Figures 6a-c show an

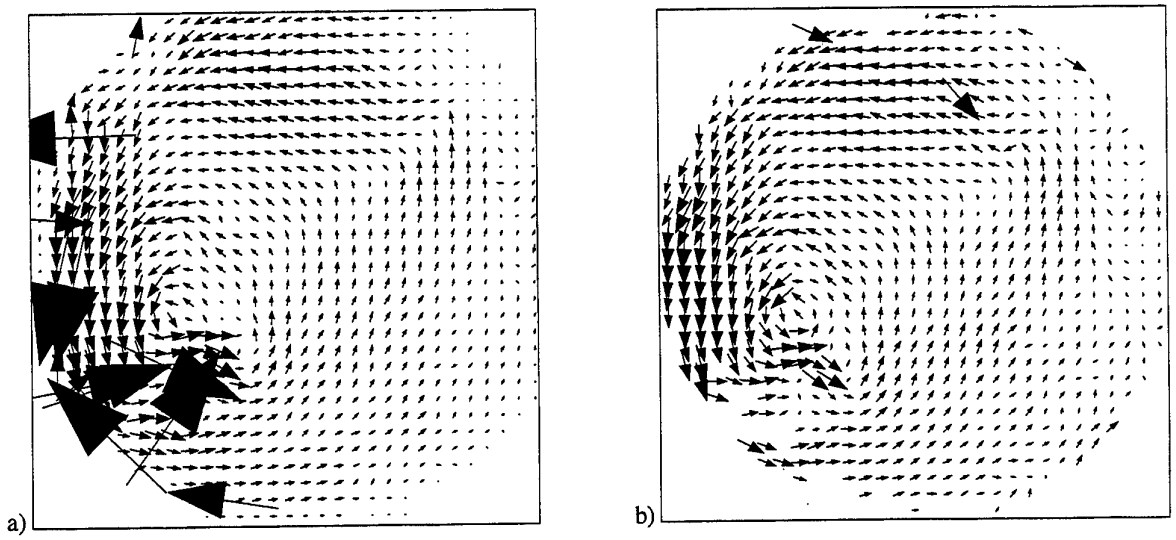


Figure 5: Flow field within an artificial heart pump. a) VisiFlow® result, b) point matching result (translation only).

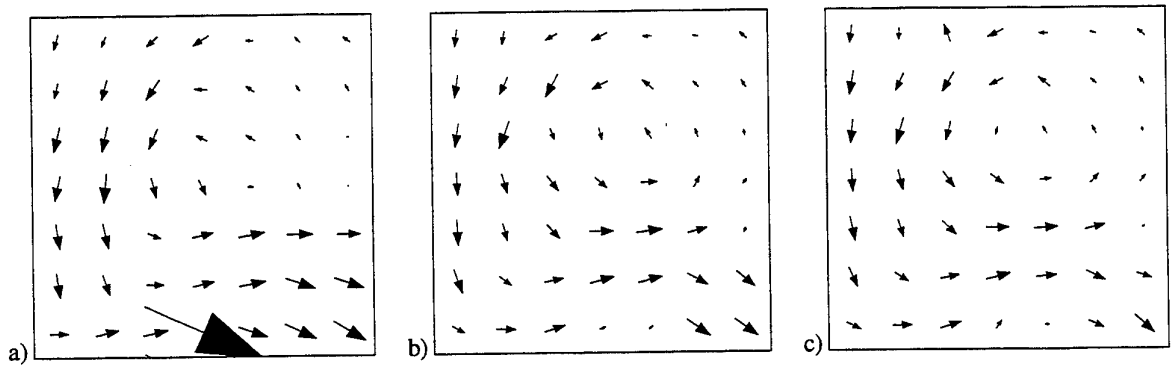


Figure 6: Enlarged section around the vortex region of Fig. 5. a) VisiFlow® result, b) point matching result (translation only), c) point matching result (translation and rotation).

enlarged section around the vortex. Visual inspection shows that the best results are obtained by jointly estimating translation and rotation parameters using point matching (Fig. 6c), followed by point matching estimation of translation only (Fig. 6b).

Computation time for the CLEAN algorithms was 3.6s per approximately 4200 particles, which amounts to 3.64 ms per interrogation spot.

7. DISCUSSION

In our contribution we investigated a new method for the evaluation of PTV data. The algorithm is based on maximum entropy inference and deterministic annealing, hence it shows robust convergence to the global minimum of the particle matching cost function. Even in the presence of noise, good estimates of the flow field parameters as well as the particle correspondences are obtained.

The results of the algorithm can be exploited along two lines. On the one hand, the estimated flow field parameters can be assigned to the center of the interrogation window, which leads to a richer representation of the flow field (in the sense of estimating more parameters than translation). On the other hand, the values of the assignment variables can be used to find the local translation vectors for each pair of particles, which leads to a flow field representation with maximum spatial resolution, but using local velocity only. The algorithm is more powerful than correlation-based methods but it expects particle coordinates rather than image frames as input. In order to fully assess its performance we combined the matching algorithm with the CLEAN procedure for particle detection, and applied it to DPIV data of flow fields in an artificial heart pump. The new method shows an improved performance, in particular in regions of high velocity gradients.

Note that the maximum entropy framework is not specific to the form and parametrization of the individual cost of a particle match in eq. (1). Other individual costs may be used depending on the problem at hand. Therefore it is straightforward to extend the algorithm, for example to 3D PTV either using 3D coordinates and a Quaternion parametrization for the 3D transformation matrix (Walker et al. (1991)) or 4D coordinates (two coordinates in two images) with the parametrization of the individual cost determined by the geometry of the image acquisition system.

ACKNOWLEDGEMENTS

This work was funded by TU Berlin via IFP 11/21.

REFERENCES

Adrian, R.J.,1991, Particle-imaging techniques for experimental fluid mechanics. Ann. Rev. Fluid Mechanics 23, 261-304.

Dempster, A.P., Laird, N.M., Rubin, D.B., 1977, Maximum likelihood from incomplete data via the EM algorithm. J. R. Stat. Soc. Ser. B 39, 1-38.

Gold,S., Rangarajan, R., Mjolsness, R., 1996, Learning with Preknowledge: Clustering with Point and Graph Matching-Distance Measures. Neur. Comp. 8, 787-804.

Keane, R.D., Adrian. R.J., 1990, Optimization of particle image velocimeters. Part I: Double pulsed systems. Meas. Sci. Technol. 1, 1202-1215.

Schwarz, U.J., 1978, Mathematical-statistical description of the iterative beam removing technique (method CLEAN). Astron. Astrophys. 65, 345-356.

Walker, M.W., Shao, L., 1991, Estimating 3-D location parameters using dual number quaternions. CVGIP: Image Understanding. 358-367.

Yuille, A., Kosowsky. J.J., 1994, Statistical physics algorithms that converge. Neur. Comp. 6, 341-356.

AN ADVANCED MQD TRACKING ALGORITHM FOR DPIV

Lichuan Gui, Wolfgang Merzkirch, Ralph Lindken

Lehrstuhl für Strömungslehre, Universität Essen,
D-45117 Essen, Germany

ABSTRACT

The Minimum Quadratic Difference (MQD) method is explained and compared with the PIV correlation-based evaluation using fixed interrogation windows (auto- or cross-correlation). The comparison is performed by studying the evaluation accuracy achieved when applying these methods to pairs of synthetic PIV recordings for which the true displacements are known. The influence of the magnitude of the particle image displacement and evaluation window size on the accuracy are investigated. In all these cases the best results in terms of a statistical error are obtained with the MQD method. The evaluation speed achievable with the MQD method by making use of the FFT is comparable to that common for the widely used auto- or cross-correlation algorithm.

1. INTRODUCTION

A brief description of a method for evaluating particle image velocimetry (PIV) recordings was given by Gui and Merzkirch (1996). This method, named the Minimum Quadratic Difference (MQD) method, is based on a least-square algorithm, and it is in principle a tracking of patterns of particle images. The minimum of the quadratic difference of the gray values in the considered digital patterns is a criterion of the tracking quality. An analysis of the algorithm shows that the quadratic difference includes a correlation function, and the question arises how the MQD method compares with the traditonal PIV evaluation scheme using the correlation function for studying and comparing the contents of fixed interrogation windows, either by auto- or cross-correlation. The present paper aims at giving such comparisons, particularly on the basis of the evaluation accuracy obtainable with these methods.

Among the various PIV evaluation methods correlation-based algorithms play a major role. Correlation-based interrogation schemes and details of the respective procedures were described, discussed, and reviewed, e.g., by Cenedese and Paglialunga (1990), Keane and Adrian (1990), Adrian (1991), Willert and Gharib (1991), Heckmann et al. (1994), Westerweel et al. (1996). A number of different working routines and tools can be used for improving the performance of the method. E.g., it is common to accelerate the evaluation by applying the Fast Fourier Transformation (FFT). When making use of the FFT technique, interrogation windows of arbitrary size (i.e. window side lengths in pixels different from being powers of 2) can be used as shown by Gui and Merzkirch (1998). Alternative methods for increasing the speed of evaluation were reported by Roesgen and Totaro (1995) and Hart (1996). Sub-pixel accuracy in determining velocity vectors is possible and in many cases realized with a three-point Gaussian (exponential) curve fit. The observed dependence of the evaluation accuracy on the magnitude of the particle displacement can be reduced and partly avoided by applying a discrete offset of the interrogation window (Willert 1996; Westerweel et al. 1997).

In the following we shall give a short description of the MQD method. Problems of evaluation accuracy will then be discussed on the basis of synthetic PIV recordings, and thereafter we shall demonstrate how the FFT technique can be used for accelerating the evaluation by the MQD method.

2. MINIMUM QUADRATIC DIFFERENCE (MQD) METHOD

The MQD tracking algorithm, a method for tracking ensembles of particle images in digital particle image velocimetry (DPIV) recordings by making use of a least square technique, has been described by Gui and Merzkirch (1996). Unlike the „traditional" tracking schemes no single particles but ensembles of particle images, that we call here „patterns", can be tracked in PIV recordings with high particle number densities. If two single exposed PIV recordings are taken, an image pattern **G** is selected in the first exposure at an evaluation point (x_0, y_0). The image patterns **G'** at different positions in the second exposure are compared with **G**, and the differences of the gray value distributions between **G** and **G'** are examined. The displacement experienced by the particle images in the considered pattern is determined by searching the minimum of the differences of the gray value distributions. This tracking process is shown in Fig.1.

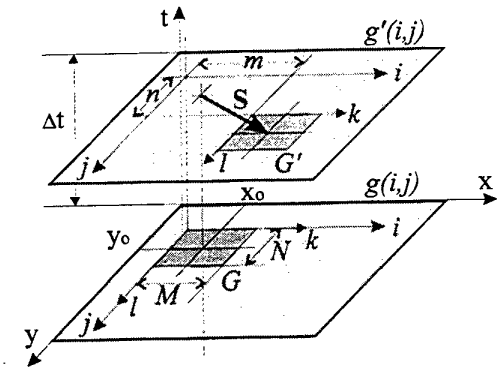


Fig. 1: Tracking ensembles of particle images

G, **G'** are confined areas („patterns") of size M×N pixels and their elements G_{ij}, G'_{ij} can be considered to be matrices

$$\mathbf{G} = \{G_{k,l}\} = \begin{Bmatrix} G_{11} & G_{21} & \cdots & G_{M1} \\ G_{12} & G_{22} & \cdots & G_{M2} \\ \vdots & & & \vdots \\ G_{1N} & G_{2N} & \cdots & G_{MN} \end{Bmatrix}$$

and

$$\mathbf{G}' = \{G'_{k,l}\} = \begin{Bmatrix} G'_{11} & G'_{21} & \cdots & G'_{M1} \\ G'_{12} & G'_{22} & \cdots & G'_{M2} \\ \vdots & & & \vdots \\ G'_{1N} & G'_{2N} & \cdots & G'_{MN} \end{Bmatrix},$$

the degree of similarity of the two matrices can be expressed by the difference

$$|\mathbf{G}-\mathbf{G}'| = \sqrt{\sum_{k=0}^{M-1}\sum_{l=0}^{N-1}\left(G_{k,l}-G'_{k,l}\right)^2} = \sqrt{\sum_{i=0}^{M-1}\sum_{j=0}^{N-1}\left(g(i,j)-g'(i+m,j+n)\right)^2} \quad . \quad (1)$$

g(i,j), g'(i,j) are here the gray values of the pixels (i,j) in the two recordings of particle image fields separated by a time interval Δt. (m,n) is the position of the pattern **G'** relative to **G**. The areas covered by **G** and **G'** are only small fractions of the whole particle image field. According to Eq.(1) the displacement of the tracked pattern (m*,n*) can be found by determining the minimum of the quadratic difference (MQD)

$$D(m,n) = \frac{1}{M\cdot N}\sum_{i=0}^{M-1}\sum_{j=0}^{N-1}\left(g(i,j)-g'(i+m,j+n)\right)^2 \quad (2)$$

in varying the values of m and n.

3. COMPARATIVE STUDY OF THE EVALUATION ACCURACY

The accuracy of the MQD tracking method is investigated here with synthetic PIV recordings. The synthetic PIV recording is constructed by identifying the location, size, and brightness of the particle images in a recording taken from a real PIV experiment (single exposure), that is available in a format of 768×512 pixels. The gray value distribution of each particle image is assumed to have a continuous asymmetric Gaussian (exponential) profile. The image density in the synthetic recording is 10 to 30 particle images in a 64×64 pixels interrogation window, and the particle image diameter is between 3 and 6 pixels; an example is given in Fig.2. The whole pattern of the synthetic images is then displaced in 40 steps. For each step we have a pair of two identical particle image distrbutions but with a known and constant displacement, and these artificial pairs of PIV recordings are then subjected to an evaluation by the different algorithms. The known displacement is chosen to vary between 0 and 20 pixels.

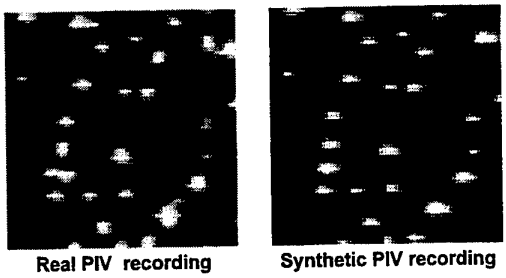


Fig.2: Simulation of the PIV recordings in a 64 × 64 - pixel interrogation

The PIV recordings were evaluated by using both the cross-correlation and the MQD tracking method. Sub-pixel accuracy was achieved by applying a three-point exponential curve fit (Willert and Gharib 1991). Each pair of displaced recordings is evaluated at more than 800 interrogation points. The RMS error in pixels (px) made in these evaluations is shown in Fig.3.

The results in Fig.3 demonstrate that the evaluation errors of the MQD method is a periodical function of the particle image displacement with a period of one pixel, and it is not dependent on the discrete part of the displacement like that of the correlation algorithm. The evaluation error of the MQD method is obviously smaller than that made with the correlation algorithm, except for a very small area around the displacement zero.

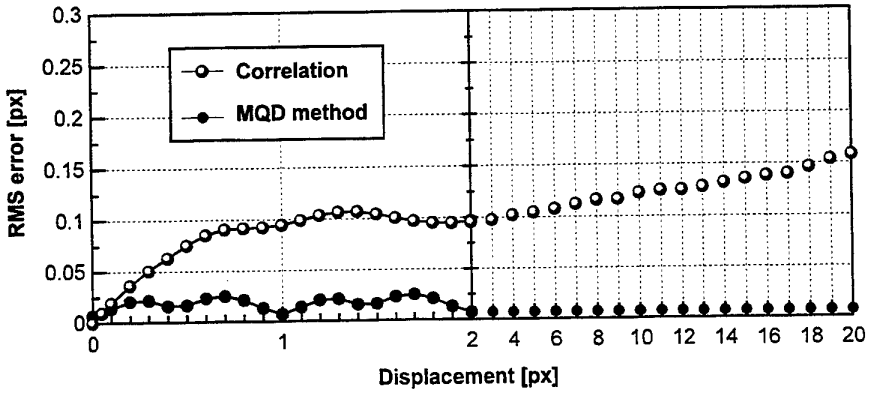


Fig.3: RMS estimation errors of the displacement for a 64 × 64-pixel interrogation window by using correlation algorithm and MQD method

For comparing the accuracy of the correlation method and the MQD method at very small displacements (≤1 pixel) a simple laser speckle experiment was performed. A ground glass plate illuminated by laser light was displaced parallel to the plane of the plate, and recordings were taken with a CCD camera. The displacements were then determined with the two methods, and a comparison of the measured results for 10 chosen values of the displacement is given in Fig. 4. Four different sizes of the interrogation window (correlation) and the „pattern" (MQD), respectively, were used, and the results in Fig.3 clearly show that the result of the evaluation by the correlation method is dependent on the chosen size of the window, while the result obtained with the MQD method is independent of the pattern size. This demonstrates another advantage of the MQD method.

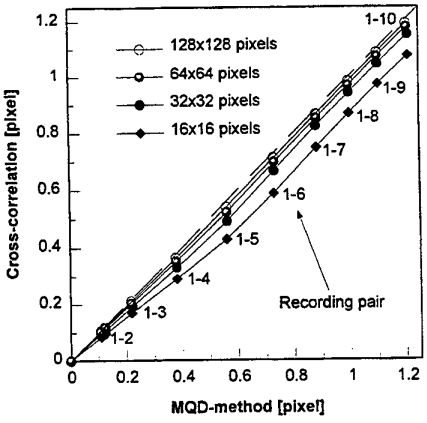


Fig.4: Average displacements of laser speckle images estimated by two algorithms with different interrogation window sizes

4. ACCELERATION OF THE EVALUATION SPEED

An evaluation of PIV recordings by applying the MQD method in its original form (eq.(2)) requires a considerable computer time or capacity. This is similar to the case, when PIV recordings are evaluated by the correlation-based interrogation technique without using the FFT. In order to accelerate the evaluation by the MQD method with the FFT technique, the interrogation function D(m, n) is replaced by an equivalent function D*(m, n), which is defined as

$$D^*(m,n) = M \times N \times D(m,n) - \sum_{i=0}^{M-1}\sum_{j=0}^{N-1} g(i,j)^2$$
$$= Q(m,n) - 2\Phi(m,n) \qquad . (3)$$

here: $$Q(m,n) = \sum_{i=0}^{M-1}\sum_{j=0}^{N-1} g'(i+m, j+n)^2$$

$$\Phi(m,n) = \sum_{i=0}^{M-1}\sum_{j=0}^{N-1} g(i,j)\,g'(i+m, j+n)$$

If $g'(i,j)^2$ has been calculated before the calculation of Q(m,n) needs only addition operations and can be carried out rapidly. The FFT technique can be used to accelerate the calculation of function Φ(m, n) with a padding technique. The procedure consists of the following steps:

1. Defining the periodicity M*, N* for a periodical correlation function Φ*(m, n)

$$\begin{cases} M^* = 2^{\alpha} & \text{if } 2^{\alpha-1} < M + 2\rho \le 2^{\alpha} \\ N^* = 2^{\beta} & \text{if } 2^{\beta-1} < N + 2\rho \le 2^{\beta} \end{cases} \qquad (4)$$

α, β : integers

2. Defining a function $g_1(i, j)$ in the period $[0 \le i < M^*, 0 \le j < N^*]$, see Fig.5a

$$g_1(i,j) = g(i-\rho, j-\rho)$$
if $\rho \le i < M+\rho$ and $\rho \le j < N+\rho$ (5)
$$g_1(i,j) = 0$$
else where

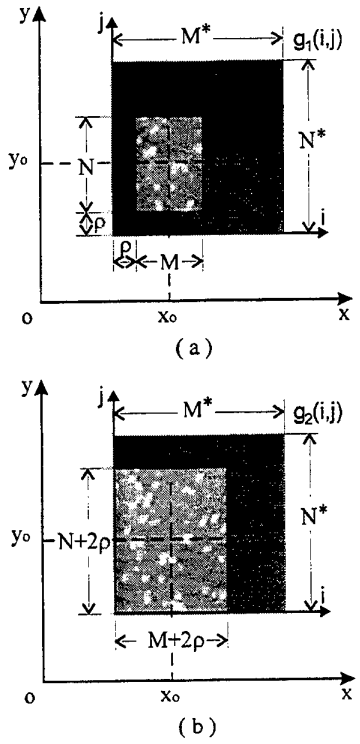


Fig.5: Definition of the correlated functions

3. Defining a function $g_2(i, j)$ in the period $[0 \le i < M^*, 0 \le j < N^*]$, see Fig.5b

$$g_2(i,j) = g'(i-\rho, j-\rho)$$
if $0 \le i < M+2\rho$ and $0 \le j < N+2\rho$ (6)
$$g_2(i,j) = 0$$
else where

4. Defining periodical functions $g_1(i, j)$, $g_2(i, j)$

$$\begin{cases} g_1(i+kM^*, j+lN^*) = g_1(i,j) \\ g_2(i+kM^*, j+lN^*) = g_2(i,j) \end{cases} \qquad (7)$$
$k, l = 0, \pm 1, \pm 2, \pm 3 \cdots$

5. Calculating the correlation function Φ*(m, n) by using the FFT

$$\Phi^*(m,n) = \sum_{i=0}^{M^*-1}\sum_{j=0}^{N^*-1} g_1(i,j) \cdot g_2(i+m, j+n) \qquad (8)$$

ρ is here the tracking radius, which determines the maximal component of the particle image displacement that can be estimated. $\Phi^*(m, n)$ can be proved to be the same as $\Phi(m, n)$ in the area $[-\rho \leq m < \rho, -\rho \leq n < \rho]$. The new evaluation function $D^*(m, n)$ can then be determined with $\Phi(m, n)$ and $Q(m, n)$. The computational speed of this advanced MQD method is demonstrated by test runs on a computer with a CPU of „IBM 6x86 P166+". The results in Fig.6 show that the evaluation with the advanced MQD tracking algorithm can be performed at very high speed as with the correlation algorithm.

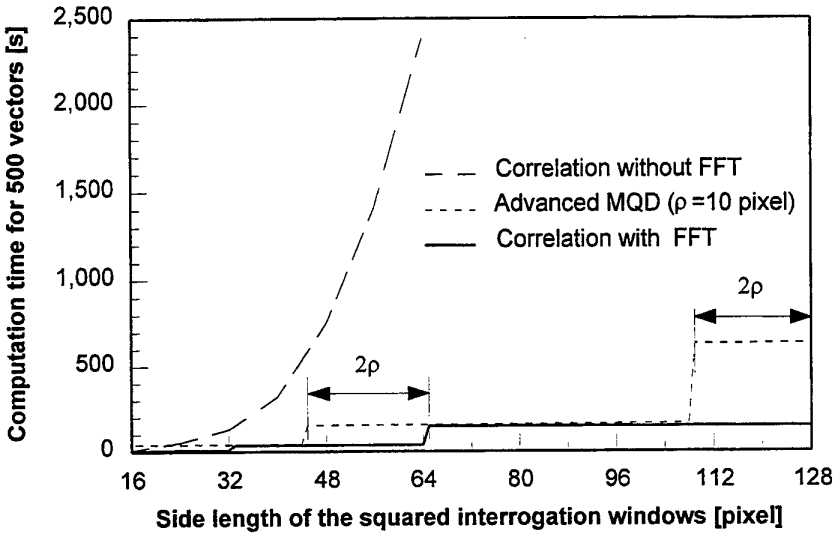


Fig. 6: Computation time for 500 vectors by using different algorithms with different sizes of the interrogation window

5 SUMMARY AND CONCLUSIONS

Our investigations were aimed at comparing a PIV evaluation method described earlier in a short communication (Gui and Merzkirch 1996) with the widely used method in which a correlation function is used for determining the particle image displacements. For this comparison we used synthetic particle image recordings whose distributions of particle images were taken from real experiments. These particle image distributions were displaced numerically so that the true value of the displacement was known, and the pairs of displaced synthetic recordings were then subjected to an evaluation by the two methods considered in these studies.

Our comparison is concered with the accuracy that can be achieved in the evaluation, particularly when the displacement is small ($\leq$ 1 pixel). The error that we determine is a statistical mean from several hundred evaluation positions in the whole recordings. Note that the true displacement value is the same for any of these positions. We investigate the influence of two parameters on the accuracy of the measurement, these parameters being selectable in an experiment or for the evaluation procedure: magnitude of the displacement and evaluation window size. Considerably smaller RMS errors were obtained with the MQD method. This result is explainable by the fact that in the evaluation algorithm of the MQD method a term appears that accounts for a non-uniform distribution of the particle images and for a non-uniformly distributed illumination intensity (see eq.(3) in Gui and Merzkirch 1996), while these effects are not taken into account in the correlation-based method and therefore contribute to the measurement error.

Besides accuracy, evaluation speed is another quality criterion for these algorithms. A fast evaluation requires the application of the FFT technique. The MQD method in its original form (Gui and Merzkirch 1996) does not allow a direct application of FFT. In section 4 we have shown how the MQD method can be modified so that the FFT becomes applicable for

accelerating the evaluation. The evaluation speed decreases with the size of the evaluation window. The computational time for the evaluation increases as a step function of the side length of the evaluation window, the stepwise increase occuring with the MQD method for a window size smaller than with the correlation-based interrogation for which the increase occurs when the side length increases to the next power of 2 (in pixels), see Fig.6. But for wide ranges of the window side lengths the evaluation speeds for the two methods are nearly equal.

ACKNOWLEDGEMENT

L. Gui gratefully acknowledges financial support by Deutscher Akademischer Austauschdienst (DAAD)

REFERENCES

Adrian, R. J. 1991: Particle-Imaging Techniques for Experimental Fluid Mechanics. Annu. Rev. Fluid Mech. 23, 261-304

Cenedese, A.; Paglialungga, A. 1990: Digital direct analysis of a multiexposed photograph in PIV. Exp. Fluids 8, 273-280

Gui, L.; Merzkirch, W. 1996: A method of tracking ensembles of particle images. Exp. Fluids 21, 465-468

Gui, L.; Merzkirch, W. 1998: Generating arbitrarily sized interrogation windows for correlation-based analysis of particle image velocimetry recordings. Exp. Fluids 24, 66-69

Hart, D. P. 1996: Sparse array image correlation. 8th Int. Sym. on Applications of Laser Techniques to Fluid Mechanics, July 8-11, Lisbon, Portugal

Heckmann, W.; Hilgers, S; Merzkirch, W.; Schlüter, T. 1994: Automatic Evaluation of Double-Exposed PIV Records by an Autocorrelation Method. Optical Methods and Data Processing in Heat and Fluid Flow, C485/021, City University, London,UK

Keane, R. D.; Adrian, R. J. 1990: Optimization of particle image velocimeters. Part I: Double pulsed systems, Meas. Sci. Technol. 1, 1202-1215

Roesgen, T.; Totaro, R. 1995: Two-dimensional on-line particle image velocimetry. Exp. Fluids 19, 188-193

Westerweel, J.; Draad, A.; Hoeven, J.; Oord, J. 1996: Measurement of fully-developed turbulent pipe flow with digital particle image velocimetry, Exp. Fluids 20, 165-177

Westerweel, J.; Dabiri, D.; Gharib, M. 1997: The effect of a discrete window offset on the accuracy of cross-correlation analysis of digital PIV recordings, Exp. Fluids 23, 20-28

Willert, C. E.; Gharib, M. 1991: Digital Particle Image Velocimetry. Exp. Fluids 10, 181-193

Willert, C. 1996: The fully digital evaluation of photographic PIV recordings. Appl. Sci. Res. 56, 79-102

SESSION 11

WALL FLOWS

TURBULENT BOUNDARY LAYER INVESTIGATIONS WITH CONVENTIONAL- AND STEREOSCOPIC PARTICLE IMAGE VELOCIMETRY

C.J. Kähler, R.J. Adrian* and C.E. Willert

Deutsches Zentrum für Luft- und Raumfahrt, Institut für Strömungsmechanik, Göttingen, Germany
* Department for Theoretical and Applied Mechanics, University of Illinois, Urbana, Illinois, USA

ABSTRACT

Stereoscopic PIV (SPIV) measurements from an artificially tripped boundary layer flow along a flat plate with zero pressure gradient are presented to demonstrate the power of SPIV in turbulence research. The components of the double correlation tensor of fluctuating velocities are calculated in stream-wise span-wise planes at three vertical locations (y^+=220, 100, 30) to deduce the average dimensions of the dominant flow structures.

Aside from this statistical approach, instantaneous velocity fields are examined in order to retrieve the contribution of the various flow structures to the Reynolds stress and their significance for existing vortex models. The shape, extent and spatial distribution of slightly twisted low-speed streaks is clearly visible and in quantitative agreement with experimental and numerical results. However, the distribution of the out-of-plane motions shows that no pairs of long stream-wise counter-rotating vortices flank the low speed regions. Furthermore, it seems that the outward migration of low momentum fluid is a result of an interaction between high and low speed fluids.

1. INTRODUCTION

The statistical theory of turbulence in form of the Reynolds equation in the boundary layer approximation implies that in wall-bounded flows a strong correlation between the velocity fluctuations parallel to the mean flow and those in wall normal direction is of primary importance for the turbulent transport of mass and momentum. Since vortices with an orientation other than exactly wall-normal will induce such transport, a number of partially contradicting vortical models have been proposed in the past. This idea intends to explain the complex turbulent motion in terms of relatively simple vortical structures interacting with the mean flow. Figure 1 shows two basic vortical models, based on loop-shaped structures.

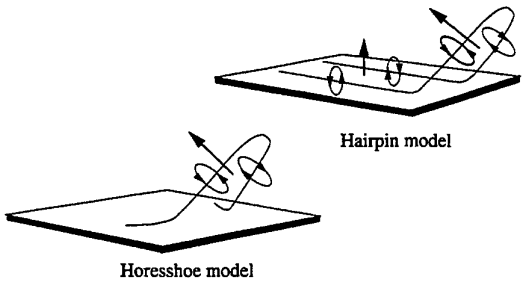


Fig 1. Schematic representation of vortical models based on loop-shaped structures in the near wall region of a turbulent boundary layer. The long arrows indicate the outflow of low-momentum fluid, induced by the vortex line.

Both models explain the outflow of low momentum fluid by means of inclined vortex loops. In the wall-parallel or stream-wise span-wise plane these loops appear as counter rotating vortices with a typical out-of-plane motion between the vortex cores. In order to explain the generation and the outward migration of elongated low-speed streaks, the hairpin model possesses two extended stream-wise vortices. Thus, a frequent occurrence of sufficiently strong stream-wise vortices in SPIV data can provide an indication toward the validity of the proposed models.

In the following we will present velocity correlation measurements from an artificially tripped boundary layer flow along a flat plate with zero pressure gradient. Since this approach reveals only information about the mean characteristics of the flow structures, instantaneous velocity fields will also be examined in order to deduce the contribution of the

various flow structures to the Reynolds stress and their relation to existing vortex models.

2. EXPERIMENTAL SET-UP

2.1 Wind Tunnel

The experiments were performed in an open circuit wind tunnel at the Department of Theoretical and Applied Mechanics at the University of Illinois. This facility, especially designed for boundary layer investigations, is 20 m long, 3.4 m wide and 2.5 m high. A contraction ratio of 10:1 in combination with a series of screens and a honeycomb (to reduce lateral motions) lead to a low turbulence level in the test section (for details see Meinhart, 1994).

The turbulent boundary layer was formed on a 0.91 m wide and 6.09 m long horizontal flat plate which was placed 0.1 m above the floor of the test section. The plate was raised from the tunnel wall to prevent the boundary layer exiting the settling chamber from affecting the measurements on the plate.

The measurements were taken at a free stream velocity of 1.6 m/s. To ensure uniform transition of the boundary layer, a 4.7 mm diameter trip wire was placed 1.5 m downstream of the elliptically-shaped leading edge. This distance allowed the boundary layer to reach an unstable state before the trip. In order to minimize the influence of this artificial disturbance on the flow structures, the measurements were taken 4 m behind the leading edge of the plate (approximately 50 boundary layer thicknesses downstream of the wire). At this location the Reynolds number based on the momentum thickness was $Re_\theta \approx 950$.

A zero pressure gradient boundary layer flow could be achieved using an adjustable upper tunnel wall in conjunction with 23 static pressure ports along the boundary layer plate.

Optical access to the boundary layer was provided from the side by 0.3 m by 0.7 m float glass windows, and from below by 0.6 m wide and 2.7 m long windows embedded in the boundary layer plate and the floor of the test section.

2.2 Measuring Technique

For the illumination of the 1 μm oil droplets, two frequency doubled Nd:YAG lasers (Continuum Lasers YG660B-20) delivering up to 200 mJ during the pulse duration of 8 ns were used. With a lens system the laser beam was formed into a sheet of about 0.6 mm thickness in the test section, corresponding to $\Delta y^+ \approx 3$. The introduction of the light sheet into the test section was achieved by a mirror prism combination as shown in figure 2. The position of the light sheet could be smoothly adjusted by moving the prism in a vertical direction. For the determination of the exact distance of the light sheet from the wall, a square metal block covered with burn paper was placed on the flat plate and illuminated by the light sheet. Using a micrometer, the distance between the base of the metal block and the burn pattern could be measured very accurately.

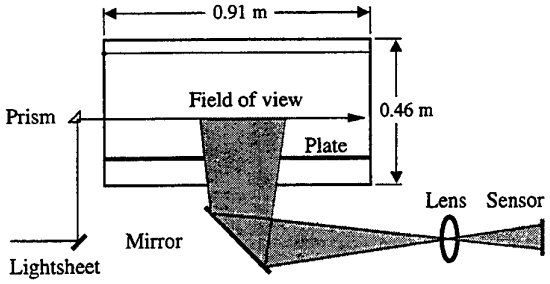


Fig 2. Cross-section of the wind tunnel test section and optical arrangement for SPIV measurements in stream-wise span-wise planes.

For the imaging of the illuminated particles, two Kodak Megaplus 4.2 full frame CCD cameras with 2029 by 2044 pixel resolution CCD sensors were used in a translation imaging configuration (image plane parallel to object plane). The opening angle between these cameras is limited to 25°, due to the strong decrease of the modulation transfer function toward the edge of the field of view.

The 80 mm × 80 mm observation area is imaged with a constant magnification by means of two Nikon EL-Nikkor 302.5 mm F/5.6 enlarging lenses that are optimized for normal operation at large magnification. These lenses are mounted in a reverse direction to provide the appropriate magnification with little aberration, minimal distortion and a large aperture (53.6 mm). The mean particle image diameter given by the optical system is $d_p \approx 3 - 4$ pixel. The cameras and two lenses are mounted on a translation stage so that the adjustments for the measurements in the different planes could be made possible by moving the whole system. The shift could be measured by means of a micrometer

2.3. Image Reconstruction

The translation method for the stereoscopic recording offers the advantage that no de-warping procedure has to be applied, because the magnification is constant over the field of view. But since the interrogation spots from each of a pair of stereoscopic images must correspond to the same

region of flow, the de-warping technique cannot be avoided (especially when the imaging is influenced by a mirror between object plane and the camera, as shown in figure 2).

In order to determine the local misalignment between the two observation areas, the mapping function between the two images and the object plane has to be determined. Therefore a calibration grid usually has to be mounted into the light sheet and recorded by each of the two cameras to find the projection between the images and the physical coordinates. This method of image reconstruction requires the calibration grid to be perfectly aligned within the light sheet. If this is not the case, the image reconstruction will still yield nicely overlapping de-warped images of the calibration grid, yet the position of identical particle images may differ between the views, see Willert (1997). Additionally, interrupting the experiment and entering the test section may lead to different boundary conditions which may affect the imaging.

To avoid these problems, a non-intrusive approach based on the particle image fields was implemented. For this purpose the mean misalignment due to translation, rotation or distortion caused by the mirrors or glass plates between the lenses and light sheet has to be calculated. A simple cross-correlation was calculated between the images of the left and right cameras, using 64 by 64 pixel^2 interrogation windows. The offset between the windows was Δx=157 pixel and Δy=13 pixel respectively (calculated with a 512 by 512 pixel^2 interrogation window). The output of this step is a displacement field which contains information about the local misalignment between the two observation areas. The misalignment vector field between the two camera views can now be changed from a discrete into a continuous representation by means of fitting a non-linear least squares surface to the vector data. The coefficients of this surface can then be used to de-warp the images of <u>one</u> camera view such that it matches the other view.

It is clear that this procedure can be applied to each image pair to guarantee that everything involved in the measurement is unaffected by wind tunnel vibrations, thermal distortions e.g. for the duration of the measurement. This becomes important in noisy environments or for long acquisition times. The only disadvantage is a possible reduction of the observation area due to mechanical misalignment.

For the calculation of the velocity vectors interrogation windows of 64 × 64 pixel^2 were used, corresponding to 2.5 mm^2 in physical space or $\Delta x^+ \approx 12$. The number of obviously incorrect vectors is less than 1% for all y-locations, which clearly shows the reliability of the measurement technique. The average displacement of the particle images is 12 pixel for a light pulse delay of 300 µs which also kept the "peak-locking" effects small (Kähler, 1997).

4. RESULTS

4.1 Double Velocity Correlation in the xz-Planes

In this section the average dimensions of the turbulent flow structures in form of double velocity correlation values and their variation with the distance from the wall will be presented. The investigation of the spatial correlation tensor of the velocity fluctuations is initiated by the stochastic random scale picture introduced by Reynolds. This approach allows quantitative statements about the average dimension of the turbulent flow structures. Several length scales with physical meaning can be derived from correlation functions such as the dissipation function or the integral length scale which plays a dominant role in the transport equations proposed by Rotta (1972).

The following table shows the local mean velocities calculated as a spatial average over all 51 SPIV recordings for a given wall distance y and the location of the observation plane scaled with the boundary thickness δ and u_τ/ν (u_τ is the friction velocity and ν the kinematic viscosity).

u [m/s]	y [mm]	y / δ	y^+
1.55	45	0.60	220
1.31	20	0.26	100
1.04	6	0.08	30

The contours of the following plots are spaced in intervals of 0.1 for the primary correlation, (excluding 0 and 1) and 0.05 for the other. For simplicity the 0.5 correlation is emphasized with a thicker line width. Continuous lines indicate positive correlation whereas dotted lines denote regions with negative correlation values.

In accordance with the early hot wire investigations by Grant (1958) and Tritton (1967) the correlation function depends on the distance from the wall to a large extent. In the outer region of the boundary layer, where the intermittent nature of the flow plays a dominant role, the R_{uu} curve of the correlation tensor shows a slight elliptical shape with a stretching in stream-wise direction (figure 3, upper contour plot). When approaching the wall, the stretching and the regions of negative correlation become more pronounced (lower plot). This indicates that at $y^+ = 30$ the dominant flow structures extend in the mean flow direction beyond the correlation plane ($\Delta x^+ > 400$). The negative correlation in the z-

direction indicates a very large span-wise variation in the stream-wise component of velocity corresponding to a wide range of length scales. R_{ww} exhibits a nearly circular shape for all y-values, only its size decreases slightly (figure 4). The extent of the R_{vv} correlation, which can be not measured using conventional PIV, is very small in the outer and logarithmic region of the boundary layer, but in the buffer layer this correlation exhibits a pronounced correlation in stream-wise direction accompanied by a reduced correlation in span-wise direction (figure 5). The similarity between R_{uu} and R_{vv} indicates some relationship between the dominant structures, but the very long stream-wise extent of R_{uu} compared with R_{vv} and R_{ww} does not seem to be consistent with a simple eddy structure.

For the turbulent mixture the cross-correlation R_{uv} is more important than the normal components of the correlation tensor because these quantities reflect the transport of relatively low-momentum fluid outwards into higher speed regions and the movement of high-momentum fluid toward the wall and into lower speed regions. With intrusive measurement techniques this quantity (and R_{vv}) is difficult to measure due to the small size of the region where a correlation can be measured (the signal from a single probe could be affected by approaching the second probe). The sign of R_{uv} shows that transport of relatively low-momentum fluid outward into higher speed regions ($u' < 0$ and $v' > 0$) and movement of high-momentum fluid toward the wall into lower speed regions ($u' > 0$ and $v' < 0$) are the predominant processes in the near wall region. In addition, the strong elliptical shape implies that the turbulent mixing in the wall-normal direction is related to the low-speed streaks. But obviously only a small part of a streak shows a correlated motion in both stream-wise and wall-normal direction with sufficient strength (lower curve of figure 6).

In quantitative agreement with the studies by Lee et al. (1974) the R_{uw} curve, shown in figure 7, exhibits at $y^+ = 30$ two separated extrema slightly shifted in stream-wise direction. The interpretation suggested for this remarkable observation can be found in the paper of Lee et al. (1974).

Since the flow structures have a history of development while they are transported downstream, the various correlation values will include realizations of a large number of structures at various stages of their life history. Thus, this approach tends to smear out the details of the organized flow pattern. In order to obtain detailed information about the formation and interaction of these moving flow structures, the instantaneous flow fields need to be analyzed in detail.

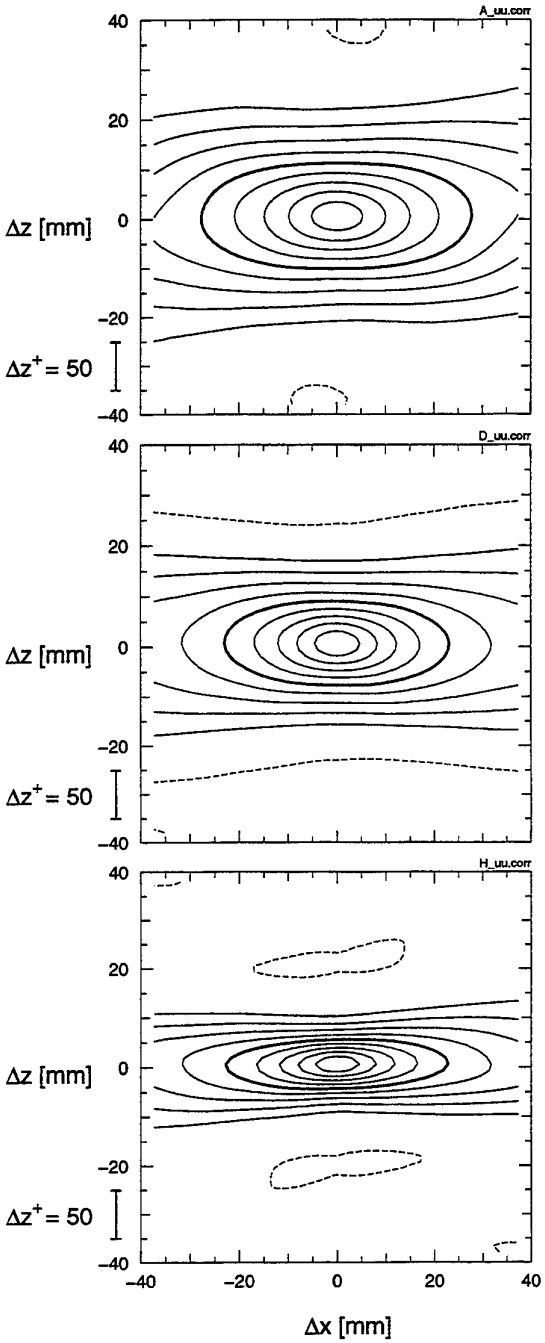


Fig 3. Two-dimensional spatial correlation function R_{uu} of fluctuating stream-wise velocity at $y^+ = 220$, 100, 30 (top to bottom)

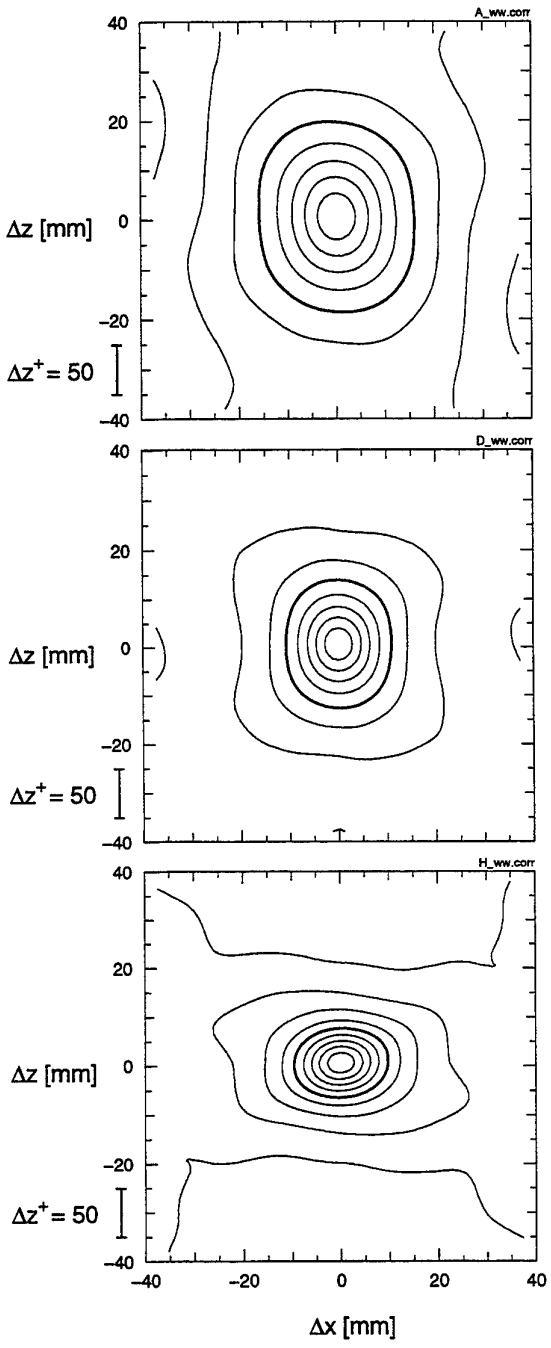


Fig 4. Two-dimensional spatial correlation function R_{ww} of fluctuating span-wise velocity at y^+=220, 100, 30 (top to bottom)

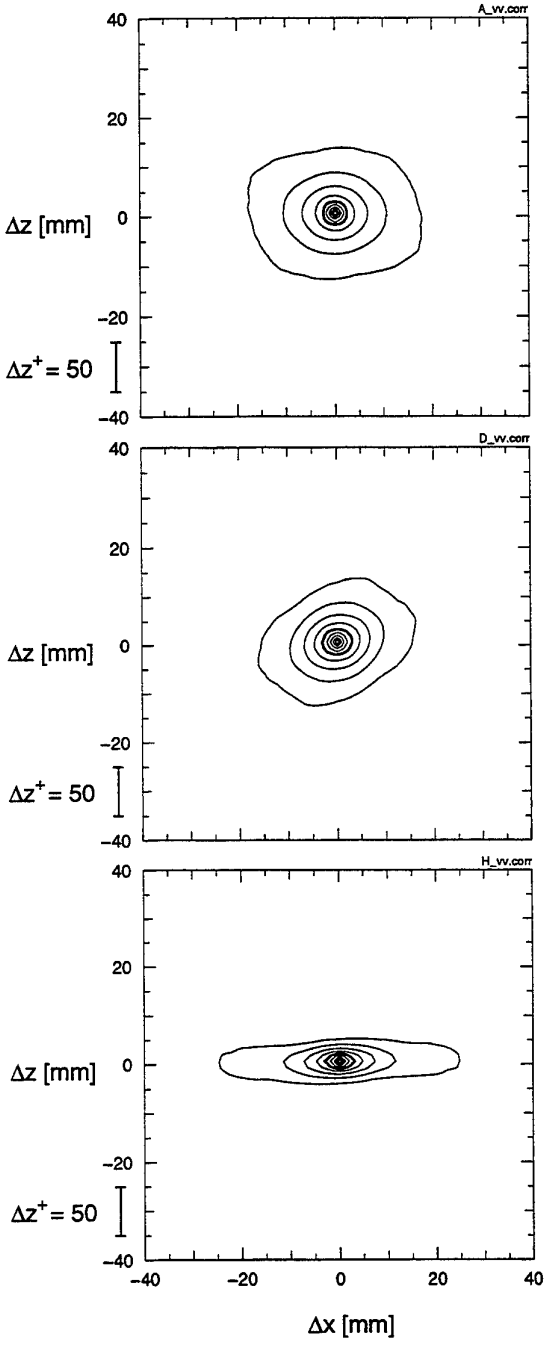


Fig 5. Two-dimensional spatial correlation function R_{vv} of fluctuating wall-normal velocity at y^+=220, 100, 30 (top to bottom)

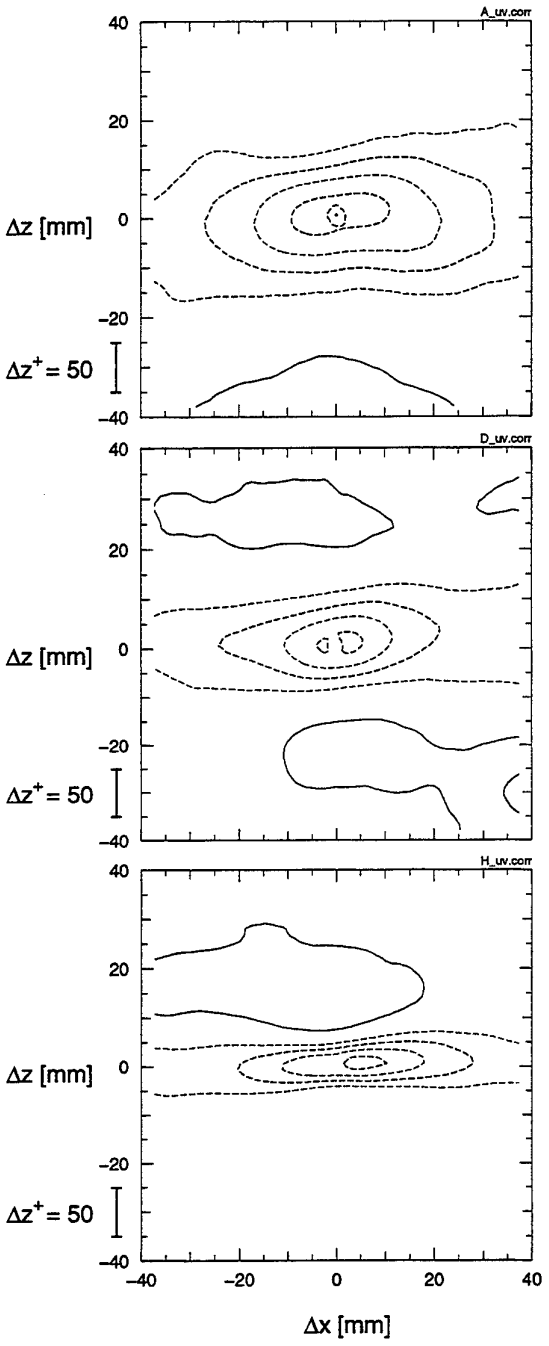


Fig 6. Two-dimensional spatial correlation function R_{uv} of fluctuating stream-wise velocity with wall-normal velocity at $y^+ = 220, 100, 30$ (top to bottom).

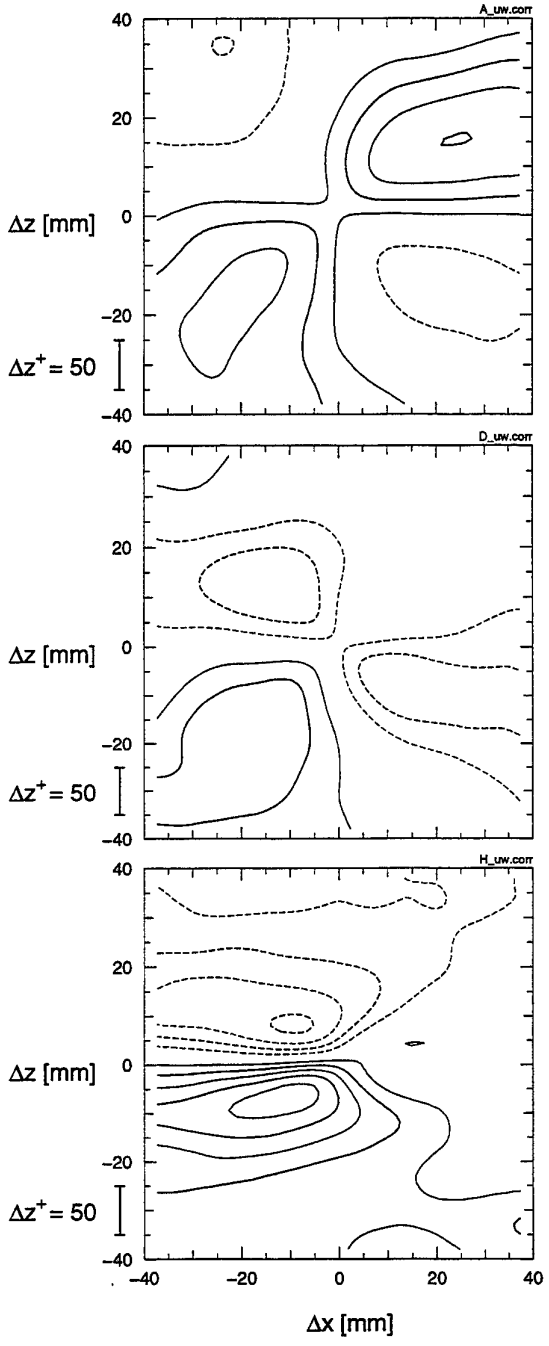


Fig 7. Two-dimensional spatial correlation function R_{uw} of fluctuating stream-wise velocity with span-wise velocity at $y^+ = 220, 100, 30$ (top to bottom).

4.2 Instantaneous Flow Structures in the xz-Planes

Figure 8 shows an instantaneous flow field of the stream-wise span-wise plane measured at y^+=30. This region is of primary importance for the production of turbulence. The local mean velocity of 1.04 m/s has been subtracted to make the fluctuating velocities u' (stream-wise) and w' (span-wise) visible. The mean flow direction is from left to right. Predominant structures are the elongated regions of low-speed fluid convecting with approximately half the local mean velocity. The shape, extent and spatial distribution of these slightly twisted flow regions are in quantitative agreement with experimental and numerical results. High speed regions are usually less elongated and broader than the low speed regions since these regions generally originate at larger y-values, where the correlation functions are less streaky in nature.

Using the information of the out-of-plane motion, the processes of near wall turbulence can be studied in more detail. Kline et al. (1967) found that the u' component of the velocity is low (u' < 0) in the region where the flow moves away from the wall (v' > 0). This agrees with the distribution of the wall-normal component of the velocity in figure 9 (heavy lines denote v' > 0), but the extent of this vertical motion is significantly shorter than the low speed streaks at the same y-value. This is in agreement with the R_{uv} correlation from the previous section and numerical results (Robinson 1991). The distribution of the out-of-plane motions indicates further that no pairs of long stream-wise counter-rotating vortices flank the low speed regions, as proposed by Kim et al. (1971). Otherwise one would expect to detect a sign change in the out-of-plane motion on both sides of the streaks or at least a large v' variation. Therefore, the proposed mechanism of streak-formation by counter rotating vortices seems doubtful. Only the lifting of low speed regions into higher momentum flows is accompanied by two weak stream-wise vortices. This is clear because any local motion away from the wall is associated with a stream-wise vortex pair, but it seems that these vortices are produced locally. So the uplift and the local stream-wise vortices which flank the lifting fluid is probably a result of an interaction between high and low momentum fluids, as proposed by Praturi and Brodkey (1978). The similar stream-wise extent of sweeps and regions of significant outward motion support this conjecture.

Since the ejection phenomenon is directly related to the occurrence of positive Reynolds shear stress, it can be reasonably used to identify this randomly in space and time located phenomenon, Wallace et al (1972).

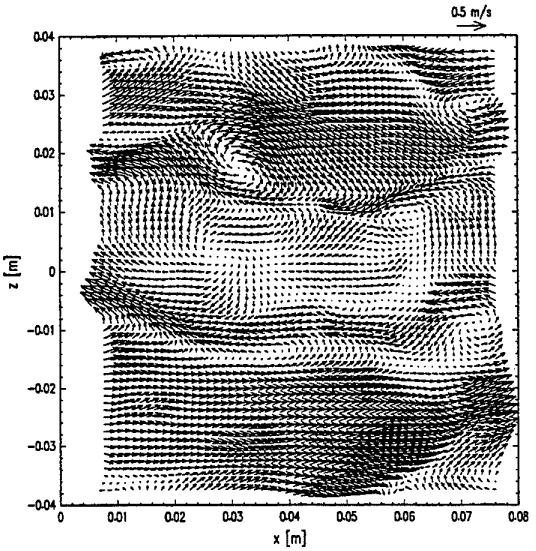


Fig 8. u', w' velocity vectors in an xz-plane at y^+=30.

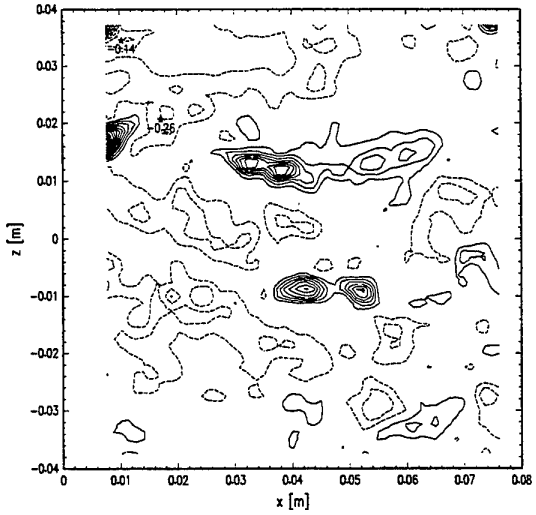


Fig 9. Contours of out-of-plane motion v' in an xz-plane at y^+=30 (dashed lines denote wall-ward motion).

Figure 10 shows the regions of ejection (u' < 0 and v' > 0) and sweeps (u' > 0 and v' < 0) with statistical relevance to the production of turbulence. The dotted lines denote ejections whereas the solid ones denote sweeps. The strong ejections are often associated with high speed fluid coming from the outer part of the boundary layer. But sweeps are not very pronounced due to the fact that the wall-ward momentum is distributed over larger structures. So

high speed regions exhibit most often a direction nearly parallel to the wall or slightly towards the wall at y^+=30, in agreement with the observations by Corino and Brodkey (1969)

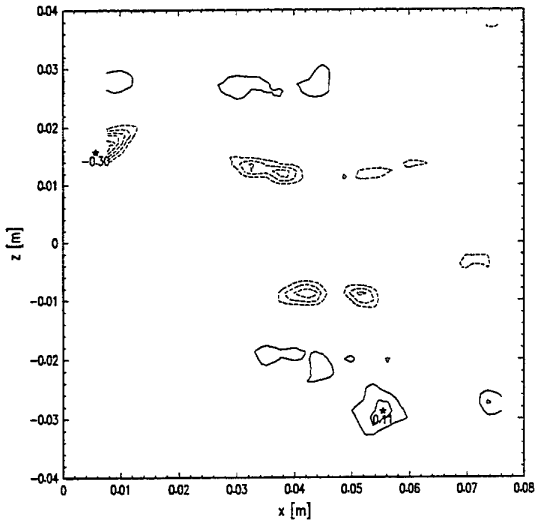


Fig 10. Contours of ejections (dashed lines) and sweeps in an xz-plane at y^+=30.

ACKNOWLEDGEMENTS

The authors would like to thank H-P. Kreplin and H. Eckelmann for the numerous valuable discussions and J. Kompenhans for the initiation of this project.

REFERENCES

Corino, E.R. & Brodkey, R.S. 1969, A visual investigation of the wall region in turbulent flows. J. Fluid Mech., vol 37, pp. 1-30.

Grant, H.L. 1958, The large eddies in turbulent motions. J. Fluid Mech., vol 4, pp. 133-190.

Kähler, C.J. 1997, Ortsaufgelöste Geschwindigkeits-messungen in einer turbulenten Grenzschicht. Deutsches Zentrum für Luft- und Raumfahrt. Research Report DLR-FB 97-32.

Kim, H.T., Kline, S.J. & Reynolds, W.C. 1971, The production of turbulence near a smooth wall in a turbulent boundary layer. J. Fluid Mech., vol 50, pp. 133-160.

Kline, S.J., Reynolds, W.C., Schraub, F.A. & Runstadler, P.W. 1967, The structure of turbulent boundary layers. J. Fluid Mech., vol 30, pp. 741-773.

Lee, M.K., Eckelman, L.D. & Hanratty, T.J. 1974, Identification of turbulent wall eddies through the phase relation of the components of the fluctuating velocity gradient. J. Fluid Mech., vol 66, pp. 17-36.

Meinhart, C.D. 1994, Investigation of turbulent boundary-layer-structure using PIV. PhD thesis, University of Illinois at Urbana-Champaign.

Praturi, A.K. & Brodkey, R.S. 1978, A stereoscopic visual study of coherent structures in turbulent shear flow. J. Fluid Mech., vol 89, pp. 251-272.

Raffel, M., Willert, C. & Kompenhans, J. 1998, Particle Image Velocimetry - A Pracitcal Guide, Springer-Verlag, Berlin.

Robinson, S.K. 1991, The kinematics of turbulent boundary layer structure. NASA Technical Memorandum 103859.

Rotta, C. 1972, Turbulente Strömungen. B.G. Teubner Stuttgart.

Tritton, D.J. 1967, Some new correlation measurements in a turbulent boundary layer. J. Fluid Mech., vol 28, pp. 439-462.

Wallace, J.M., Eckelmann, H. & Brodkey, S. 1972, The wall region in turbulent shear flow. J. Fluid Mech., vol 54, pp. 39-48.

Willert, C.E. 1997, Stereoscopic digital particle image velocimeters for application in wind tunnel flows. Measurement Science and Technology, vol. 8, pp. 1465-1479.

Experimental study of a high Reynolds number turbulent boundary layer using DPIV.

M. STANISLAS, J. CARLIER, J.M. FOUCAUT, P. DUPONT

Ecole Centrale de Lille
LML URA 1441
BP 48
Cité Scientifique
F59651 Villeneuve d'Ascq Cedex
email : stanislas@ec-lille.fr

ABSTRACT

An experiment has been carried out in a specific wind tunnel by means of Digital Particle Image Velocimetry. This wind tunnel was conceived specially for the study of turbulent boundary layers. The Reynolds number, based on momentum thickness, can reach 20 000 and the boundary layer thickness is of the order of 0.3 m. The DPIV measurements have been carried out with a two YAG laser system and a Kodak digital camera which CCD size is 2048 x 3072 pixels. The PIV analysis was done by auto-correlation and by cross-correlation with a window shift. To make a statistical analysis, one hundred velocity fields have been stored and an ensemble averaging has been performed for two Reynolds number : R_θ = 10 000 and 18 500. The velocity profiles obtained have been compared to hot wire profiles. A good agreement is obtained between the two methods. Only the points nearest to the wall differ, due to the window size in PIV. Double spatial correlations have been deduced from the velocity maps. They show interesting features of the flow.

1 INTRODUCTION

Wall turbulence is a very active subject of research, both on the numerical and experimental point of view. Recent progress in DNS (Robinson (1991), Rempfer and Fasel (1994)) have allowed some insight in the near wall organization. But, until quite recently, experimental studies were limited to conditional sampling with hot wire rakes (Blackwelder and Kaplan (1976)) or to visualizations (Kline et al (1967), Falco (1983)) which give only a qualitative indication of the structure of the flow. Moreover, these can be misleading due to the fact that the smoke (or dye) as a passive scalar, does not diffuse the same way as the vorticity. The strong development of PIV in the last few years has opened a wide field for the experimental study of turbulent flows. A first application to near wall turbulence has been performed by Meinhart and Adrian (1995). The aim of the present study is to compare PIV measurements to classical hot wire anemometry in order to validate the method and to allow a detailed study of the flow structure. In their work, Meinhart and Adrian (1995) have carried out measurements with R_θ between 930 and 6845. The boundary layer thickness δ was of the order of 0.08 m. They measured fields up to $h = 1.2\ \delta$ with large format photographic film. In the present study, the field height is of the order of 0.25 δ. Two Reynolds number have been tested : R_θ = 10 000 and 18 500. This completes thus the contribution by Meinhart and Adrian (1995) toward the high Reynolds numbers.

2 EXPERIMENTAL SET-UP

2.1 Test facility

Figure 1 present a front view of the wind tunnel used. It has been conceived specially for the study of turbulent boundary layers. The Reynolds number, based on momentum thickness, can be varied between 7800 and 21000. The boundary layer thickness is of the order of 0.3 m. The test section is 1 x 2 m^2 and 20 m long. The last 5 m are transparent on all sides to allow the use of optical methods. The free stream velocity can reach 10 m/s. The longitudinal pressure gradient is negligible (< 0.07 Pa/m at 10 m/s). The wind tunnel can be used in closed loop with temperature regulation or opened to the outside to allow the use of smoke. In the present study, it was used in the open loop configuration. The wind tunnel is computer controlled by a PC, both for the velocity (± 0.01%) and for the temperature in closed loop (± 0.2 C). The boundary layer under study develops on the lower wall. It is triggered at the entrance of the tunnel by a grid layed on the floor. The origin of coordinates is placed in the middle of the lower wall at the entrance of the tunnel. The x axis is parallel to the wall and to the flow, the y axis is normal to the wall, the reference frame is direct.

Hot wire anemometry was performed in a previous study (Carlier (1996)) with DANTEC probes of boundary layer type. They use 5 microns tungsten wire.

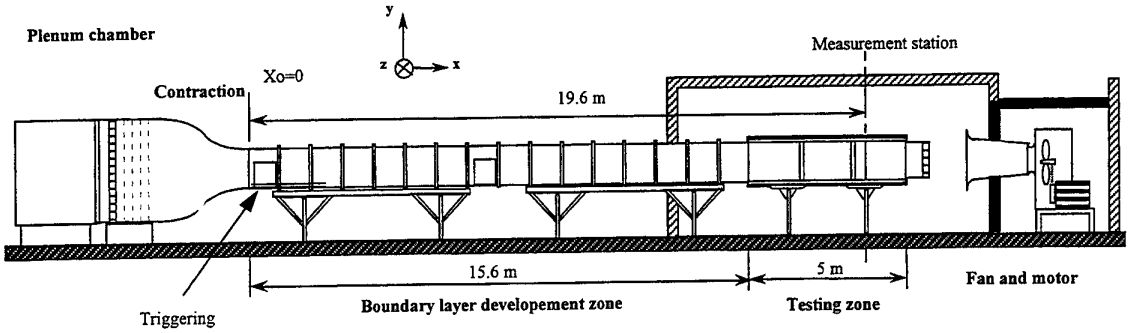


Figure 1 : Front view of the turbulent boundary layer wind tunnel.

A single wire of 1.2 mm in length and uv and uw X-wire probes of 1.4 mm in length were used to obtain the main components of the Reynolds stress tensor. A DISA 55M bridge was used for the measurements. The signal was digitized on 16 bits and stored directly on disk. This allows to compute all the moments up to the fourth order.

2.2 PIV set-up

The PIV experiments were realized in the frame of a recent European project (Stanislas et al (1997)). Figure 2 presents a sketch of the PIV set-up. The laser used was a BMI double cavity YAG laser with a repetition rate of 10 Hz and an energy per pulse of 255 mJ. The light sheet was generated by a cylindrical lens of focal 150 mm and a spherical lens of focal 91 mm. the distance between the two lenses was 65 mm. The laser and optical bench were placed under the wind tunnel. A mirror placed at 45° allowed to introduce the light sheet vertically, parallel to the flow, in the symmetry plane of the wind tunnel. The distance between the spherical lens and the lower wall was 1.5 m, allowing a light sheet of 150 mm x 1 mm in the region of interest.

The seeding was introduced at the inlet of the test section, under the triggering device, approximately 16 m upstream of the region of interest. PEG was used as seeding particles with a diameter of the order of 1 micron. The concentration was adjusted to obtain good quality PIV recording. As far as the outer flow was not seeded, some intermittency was observed in the external part of the boundary layer. This intermittency decreased when the Reynolds number increased.

The recording lens was an AF Micro-Nikkor 1/4D 200 mm f/4 tele/macro lens. For the present tests, the f-stop was fixed at 1/5.6. A Kodak DCS 460 digital camera was used. This fully digital camera has a CCD size of 2048 x 3072 pixels and 18.4 x 27.6 mm^2. The pixel size is 9 x 9 μm^2. The framing rate is 1 image every 12 s. The images are stored on a removable PC-MCIA disk which can contain 40 images. They can also be transferred through a SCSI bus at a rate of 1 im / minute. The camera has been used in the single frame double exposure mode.

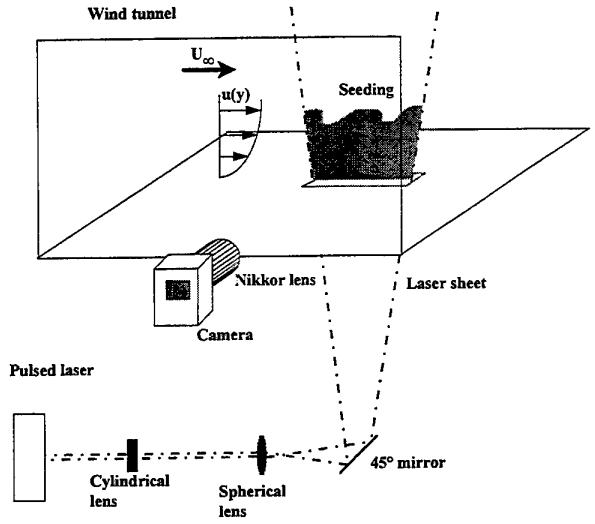


Figure 2 : Sketch of the PIV set-up.

3 RESULTS

Measurements were performed for two values of the external velocity : 5 and 10 m/s. Table 1 summarizes the main characteristics of the flow for these two velocities. With the DCS 460, 110 records were stored for each velocity. The time interval between the two exposures was 200 µs at 5 m/s and 100 µs at 10 m/s.

U (m/s)	Re_θ	δ (mm)	θ (mm)	u_τ (m/s)
5.2	10000	290	29	0.192
10.1	18500	280	28	0.352

Table 1 : Main flow characteristics

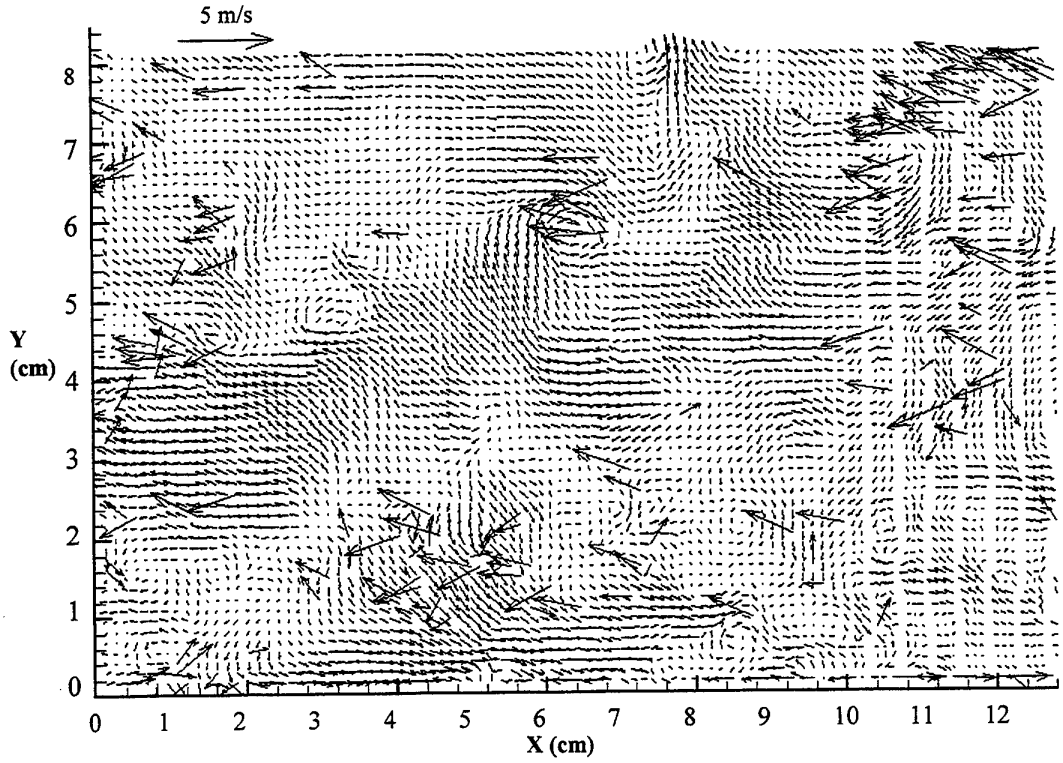


Figure 3 : Raw data obtained with 64 x 64 interrogation windows.

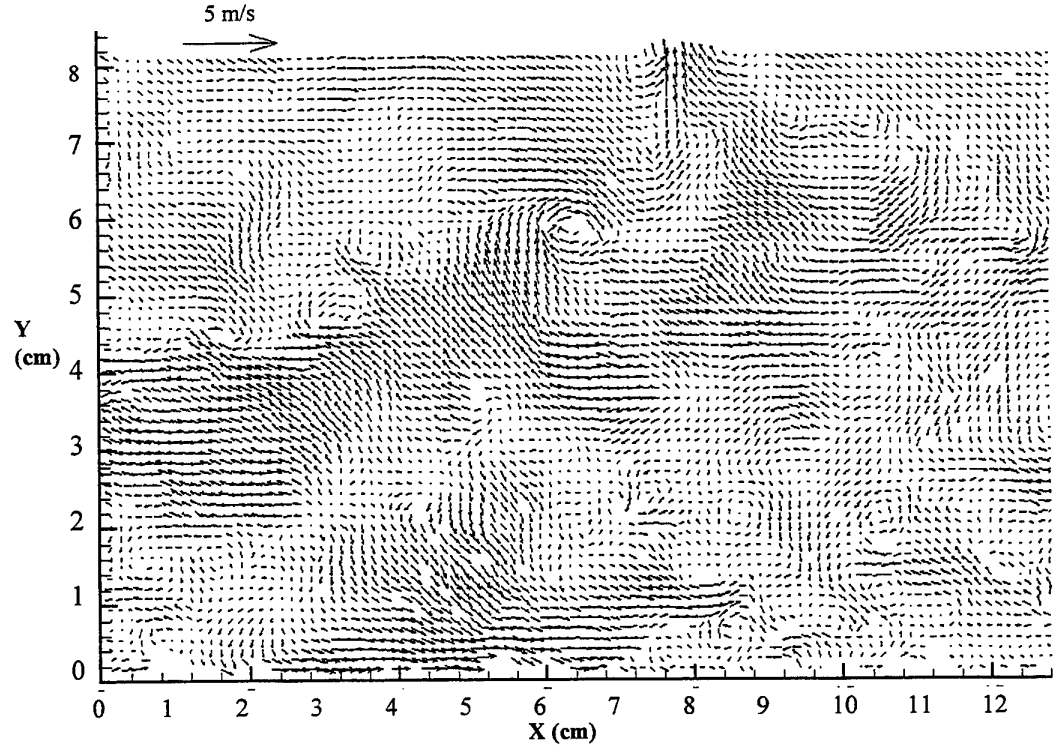


Figure 4 : Filtered velocity field deduced from figure 3.

3.1 Results obtained with digital PIV

All the images recorded were processed with the PIV software developed at IMFL-ONERA (Monnier and Stanislas (1998)). This package uses auto and cross-correlation through FFT and a 2D gaussian peak fitting algorithm. In a first step, the analysis was done by autocorrelation with 64 x 64 windows. This gives 95 x 60 (5700) vectors in each map. The window size is then 2.69 x 2.69 mm2 at the scale of the flow. In a second step, the analysis was performed with 32 x 32 interrogation spots and by cross-correlation with a shift of 16 pixels. This gives 190 x 122 (23 180) vectors in each map. In both cases, a global histogram test was used to remove the evidently false vectors. For 64 x 64 analysis, the bounds were: $3 \leq u \leq 24$ and $-5 \leq v \leq 6$ pixels. Figure 3 gives an example of the raw vector map obtained with the 64 x 64 analysis. The local mean velocity ($\overline{u}(y)$) has been subtracted. The field of view is 80 x 124 mm2. Due to the large number of images, the removal of false vectors, even at the last stage and specially for the 32 x 32 recordings, could not be performed by hand. Thus, taking advantage of the fact that the flow is quasi-parallel (1996), an automatic procedure was applied to each map. This procedure can be separated into two steps, both based on three criteria. The first step consists in searching for the best peak among the three higher peaks detected in the correlogram. This optimization uses a first criterion based on a comparison between the local velocity and a mean velocity averaged along x. The second and third criteria are respectively based on a comparison between the local fluctuation magnitude and direction (obtained after subtraction of the mean velocity) with neighborhood means. The second step consists in replacing the remaining bad vectors by holes using the same criteria. The process is iterative until there is no hole to add to the velocity map.

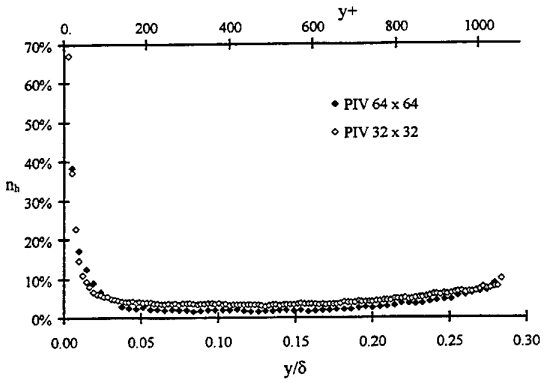


Figure 5 : Number of holes.

Figure 4 gives the filtered velocity map corresponding to the raw one in figure 3. In figure 4, some holes can be observed. Each false vector was removed from the map and no interpolation was performed to replace it. Figure 5 presents the number of holes as a function of the wall distance for Ue = 5 m/s and for the best 100 maps based on the criterion of seeding uniformity. As can be seen, this number is quite low in a major part of the field (2 to 3%). It increases slowly outward, due to the seeding intermittency mentioned above. It increases more drastically near the wall, due to the strong velocity gradient encountered there.

After this cleaning procedure, an ensemble average was computed for each velocity. This was performed taking into account the holes. In order to make comparisons with hot wire anemometry (HWA) results, a second averaging was performed along the x axis, based on the hypothesis that the flow is quasi-parallel.

3.2 Comparison between DPIV and HWA results

As far as the results obtained for both Reynolds numbers lead to quite comparable conclusions, only those corresponding to Ue = 5 m/s will be discussed here. Figure 6 presents the mean velocity profiles in logarithmic coordinates and figure 7 the convergence of the data as a function of the number of records at a sample point in the middle of the field.

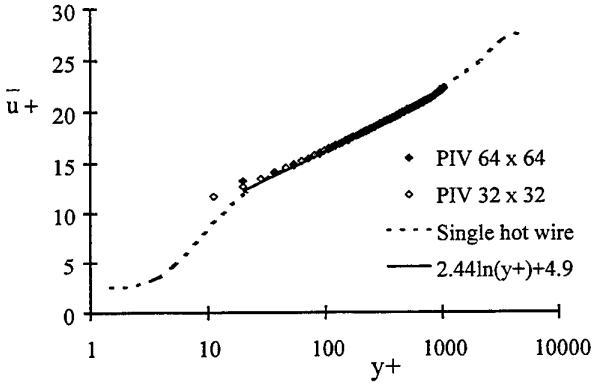


Figure 6 : Mean velocity profiles.

As can be seen, the agreement is quite good between the PIV results with both interrogation windows and with HWA. A difference appears for the first few points near the wall, due to the velocity gradient inside the interrogation window. To give orders of magnitude, the 32 x 32 spot is 17 in wall units, that is 1.35 mm at the scale of the flow. This has to be compared to the size of

the X-wire probes which is of the order of 1.4 mm. The velocity variation in the window corresponding to the point nearest to the wall, deduced from the hot wire measurements, is in this case 1.6 m/s. The mean velocity in the window being also 1.6 m/s. As can be seen, in such a configuration, PIV overestimates the mean velocity of about 42 %. As far as the convergence is concerned (fig. 7), the two analysis present curves which superimpose quasi perfectly. The convergence of the turbulent statistics is driven by two parameters: the number of particle doublets per unit area on the record and the number of records. Consequently, supposing that the analysis is driven to make use of all the information contained in the record, to obtain the best convergence, it is necessary to put the seeding as high as compatible with a good quality record. Then, the only parameter available to enhance convergence is the number of records. In the present case, the convergence is quite good for $\overline{u}$.

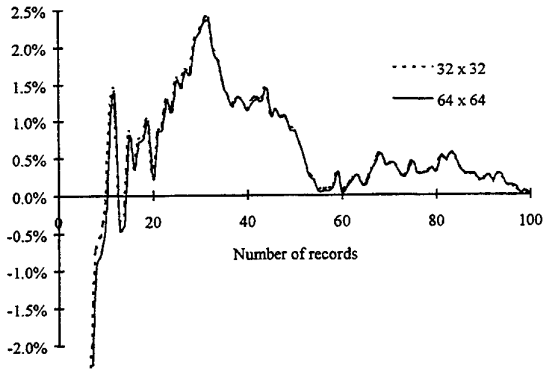


Figure 7 : Convergence of $\overline{u}$.

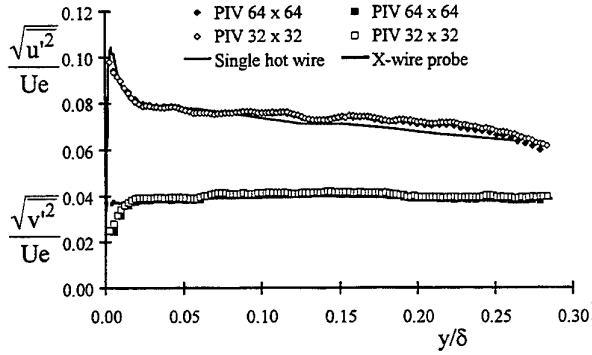


Figure 8 : Turbulence intensity.

Figure 8 presents the two components of the turbulent intensity which are accessible by PIV in the present set-up. They are plotted both in wall variables. As can be seen, the agreement is quite good except near the wall. The $\sqrt{\overline{v'^2}}$ component seems more realistic by PIV than by HWA which is influenced by the near wall. This is confirmed by HWA measurements at lower Reynolds number which gives the same shape of $\sqrt{\overline{v'^2}}$ as the present PIV measurements. The magnitude and position of the $\sqrt{\overline{u'^2}}$ peak are not obtained by both PIV analysis. The convergence of $\sqrt{\overline{u'^2}}$ is presented in figure 9 at a sample point in the middle of the field. It appears smoother than the convergence of $\overline{u}$.

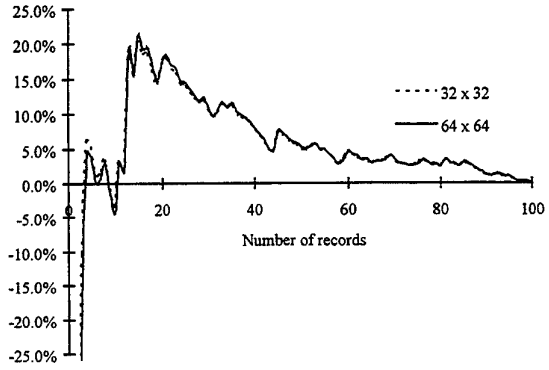


Figure 9 : Convergence of $\sqrt{\overline{u'^2}}$.

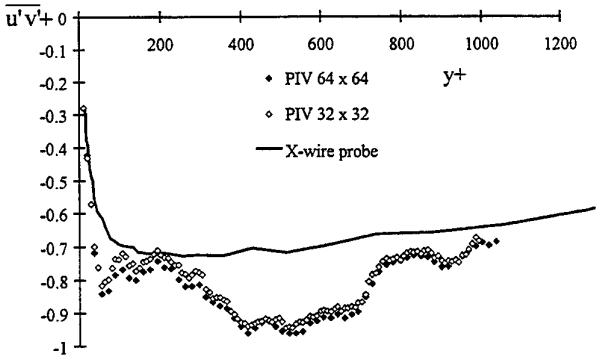


Figure 10 : Turbulence shear stress.

The turbulent shear stress is plotted in wall units in figure 10. Here, a significant disagreement appears between PIV and HWA. In this case, it is known from previous analysis (Carlier (1996)) that $\overline{u'v'}$ is underestimated by HWA in this experiment.

Theoretically, $\overline{u'v'}^{+}$ should be near to 1 in the major part of the inner layer (y+ < 600). In practice, the experimental results obtained by different authors and reported by Balint & al (1991) show that the plateau is quite localized and that there is some dispersion on it's value. In figure 10, apart from the very near wall region (y+ < 50), the main disagreement between the HWA and PIV results is for 200 < y+ < 700. The shape of the PIV results is quite unusual in this region and should be taken with caution. $\overline{u'v'}$ being a quantity sensitive to small errors, the influence of statistical convergence, window size and inhomogeneous seeding in this region has to be looked at in more detail.

The flow conditions studied by Meinhart and Adrian (1995) are recalled in table 2.

	Re_θ	U (m/s)	δ (mm)	θ (mm)	u_τ (m/s)
Case 1	930	1.6	75.7	9.1	0.074
Case 2	2370	3.79	82.8	9.84	0.158
Case 3	6845	10.88	78.03	9.71	0.400

Table 2 : Main flow characteristics of Meinhart and Adrian (1994)

A comparison of the main characteristics of their and the present PIV experiments is summarized in table 3 where d is the size of the interrogation window.

	Number of realizations	d (mm)	d+
Case 1	60	2	9
Case 2a	115	2	20
Case 2b	100	2	14
Case 3	65	2	52
Present 64x64	100	2.7	35
Present 32x32	100	1.35	17

Table 3 : Main characteristics of PIV exp. by Meinhart and Adrian (1995) and present.

Their interrogations were all performed with 128 x 128 pixels windows with an overlapping of 50%. The use of 4 " x 5 " large format photographic film allowed to obtain about 10 000 vectors per record.

As can be seen from table 1 and 2, the lowest Reynolds number in the present experiment is not too far from the highest one of Meinhart and Adrian (1995). The difference is mainly in the physical size of the boundary layer. From table 3, it can be seen that the range of interrogation window size is quite comparable in wall units, while the number of pixels per window is much lower in the present case.

The results of Meinhart and Adrian (1995) show comparable tendency for the mean velocity. The agreement is quite good in the logarithmic and wake region, but some departure from classical laws is observed in the buffer layer where the velocity gradients are large compared to the window size.

Concerning the normal Reynolds stresses both experiments come to comparable conclusion. The agreement is good with classical values of these parameters, but the PIV results are limited by the window size very near to the wall.

As far as the shear stress is concerned, the results of Meinhart and Adrian (1995), although they show a significant amount of dispersion due to convergence, are in better agreement with the literature than the present ones.

3.3 Double spatial correlations

Once validated PIV results represent a huge amount of data on the instantaneous characteristics of the flow. Further analysis is needed to extract information on the structure of the flow. This has been done on a phenomenological point of view by Meinhart and Adrian (1995). A more systematic approach consist in using Proper Orthogonal Decomposition (POD) as proposed by Lumley and like was done by Rempfer and Fasel (1994) on a Direct Numerical Simulation to characterize mathematically the coherent structures containing most of the energy. An intermediate step consists in computing the double spatial correlations out of the PIV velocity maps. Time and space time correlations has been studied in detail in turbulent flows by HWA. Spatial correlations are only accessible by methods like PIV which provide ensembles of instantaneous velocity fields. In the present study, a preliminary test was performed on the 100 maps available. An example of result is given in figure 11 and 12 which show respectively the correlation R11 and R21 at R_θ = 10 000. These are defined by :

$$R11 = \frac{\overline{u'(\vec{x})u'(\vec{x}+d\vec{x})}}{\overline{u'^2(\vec{x})}} \quad \text{and} \quad R21 = \frac{\overline{v'(\vec{x})u'(\vec{x}+d\vec{x})}}{\sqrt{\overline{u'^2(\vec{x})}}\sqrt{\overline{v'^2(\vec{x})}}}$$

where $\vec{x}$ is a fixed position vector and $d\vec{x}$ describes the field.

The fixed point in figures 11 and 12 is at y+ =100 (the field of view is not going down to the wall), which is well in the logarithmic region of the boundary layer. As expected, both correlations present a maximum for dx+ = 0 and dy+ = 0 and decrease monotonically when the moving point goes away. One of the interests is that these correlations can be computed at each point in the field and provide information on characteristic scales of the flow. In the present case, both correlations show a downstream angle to the wall which is of the order of 15° for R11 and 20° for R21, indicating a stronger correlation in that direction. This angle is comparable to that often mentioned in the literature for the backs of the coherent large scale motions (see Robinson (1991)). In the present results, due to the limited size of the PIV windows, the correlation R11 is still high on the border of the field. The fact that this field is of the order of 1000 in x+ indicates that R11 extends significantly further in that direction with a marked asymmetry toward downstream. If both correlations have approximately the same extend in y, R21 has apparently a shorter length in x than R11 and evidences a second principal direction which is at an upstream angle of 45° to the wall. A conditional averaging based on the quadrant method indicates that this last direction is strongly linked to the ejection process (u'<0, v'>0) while the downstream feature is associated with sweeps (u'>0, v'<0). The computation of integral scales along these directions should give an estimation of the characteristic lengths of both phenomenon.

4 CONCLUSION

A PIV experiment has been performed in a turbulent boundary layer using a CCD camera and small "pixel windows". This allows to obtains more than 20 000 velocity vectors in a field of the order of 0.25 δ. The mean values computed out of 100 records and averaged along x agree quite well with hot wire measurements. The influence of the interrogation window size very near to the wall has to be studied in more details. Only the turbulent shear stress has an unusual behaviour. This may be attributed to statistical convergence, PIV accuracy or inhomogeneous seeding and still has to be clarified.

Globally, the agreement with the experiments of Meinhart and Adrian is quite good. In particular, the effect of the velocity gradient on the PIV measurements in the buffer layer is comparable. The RMS values are also in good agreement, apart for $\overline{u'v'}$ which is found at a higher level by Meinhart and Adrian.

The PIV results contain a huge amount of information on the instantaneous characteristics of the flow. Ways have been proposed to reduce this information to characteristic parameters usable for modelling. Proper Orthogonal Decomposition and wavelets analysis are powerful mathematical tools that are very promissing for doing such a reduction. It has been shown here that PIV can also provide statistical entities like the double spatial correlations, which are inaccessible by other measurement methods and which can provide some good insight into the physics of the flow.

This work has been performed under the EUROPIV project. EUROPIV (A cooperative action to apply Particle Image Velocimetry to problems of industrial interest) is a collaboration between LML URA CNRS 1441, DASSAULT AVIATION, DASA, SIREHNA, CIRA, DLR, DRA, FFA, INTA, ISL, NLR, ONERA, VKI and the universities of Delft, Madrid, Oldenburg, Rome, Rouen (CORIA URA CNRS 230), St Etienne (TSI URA CNRS 842), Warwick.

The project is managed by LML URA CNRS 1441 and is funded by the European Union within the Industrial and Materials Technologies Program (Contract N°: BR.PR - CT95- 0118)

REFERENCE

Balint J.L., Wallace J., Vukoslacevic P., 1991 , The velocity and vorticity vector fields of a turbulent boundary layer., J. Fluid Mech., vol 228, pp 53-86.

Blackwelder R.F., Kaplan R.E. , 1976, On the wall structure of the turbulent boundary layer. J. Fluid Mech., vol 76, pp 89-112.

Carlier J., 1996, Caractérisation par anémométrie à fil chauds d'une couche limite turbulente à grand nombre de Reynolds., DEA report, Univ. of Lille.

Falco R.E., 1983, New results, a review and synthesis of the mechanism of turbulence production in boundary layers and its modification.aiaa 1983., J. Fluid Mech., vol , pp 1-16.

Kline S.I., Reynolds W.C., Schraub F.A., Runstadler P.W., 1967, The structure of turbulent boundary layers. » J. Fluid Mech., vol 30, pp 741-773.

Meinhart C. D., Adrian R.J., 1995, Measurement of the zero pressure gradient turbulent boundary layer using Particle Image Velocimetry., AIAA 95-0789.

Monnier J.C., Stanislas M., June 1998, Final report of AD Action Group 19 on Particle Image Velocimetry, GARTEUR report TP099.

Rempfer D., Fasel H.F., 1994, Evolution of three-dimensional coherent structures in a flat plane boundary layer., J. Fluid Mech., vol 260, pp 351-375.

Robinson. S.K., 1991, Coherent motions in the turbulent boundary layer. J. Fluid Mech., vol, pp 601-639.

Stanislas M., Foucaut J.M., Dupont P., Carlier J., 1997, Study of a turbulent boundary layer by high resolution DPIV., Brite Euram Contract N°: BR.PR - CT95- 0118, to appear.

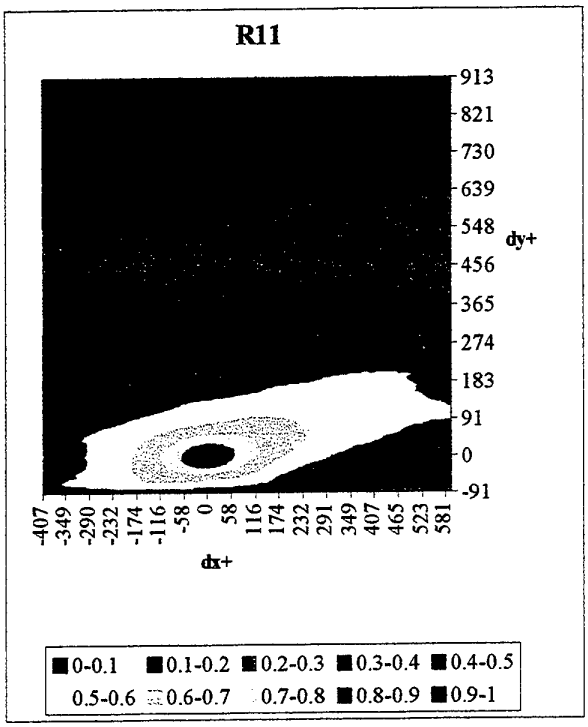


Figure 12 : Spatial correlation R11.

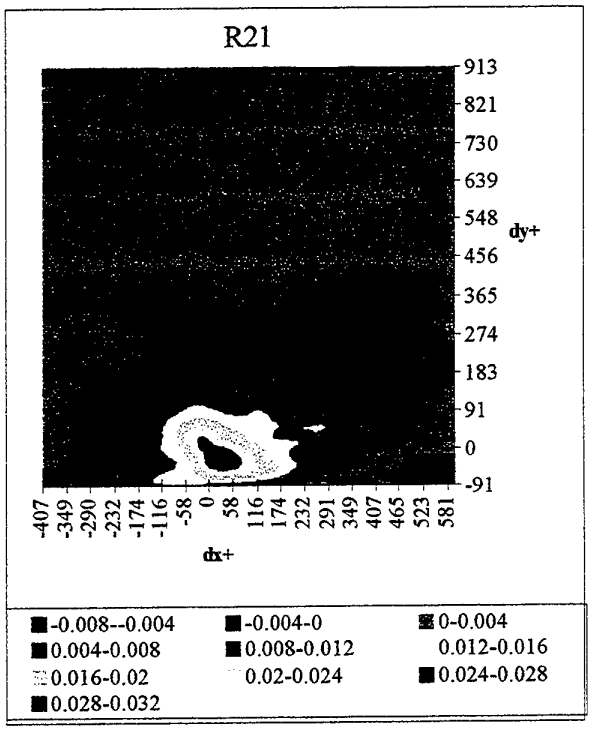


Figure 13 : Spatial correlation R21.

REYNOLDS NUMBER DEPENDENCE OF NEAR WALL TURBULENT STATISTICS IN CHANNEL FLOWS

M. Fischer, F. Durst and J. Jovanović

Lehrstuhl für Strömungsmechanik, University of Erlangen-Nürnberg, Cauerstr. 4
91058 Erlangen, Germany

ABSTRACT

Theoretical coniderations show that the turbulent fluctuations and the dissipation rate are not universal in inner scaling due to an influence of the outer boundary condition and to an additional production term. A quantification of the number dependence from theoretical considerations is not possible at present. A new method for the statistical interpretation of laser-Doppler signals is derived and applied to investigate the wall-limiting behaviour of turbulent quantities. A Reynolds number dependence of turbulent fluctuations for low Reynolds numbers could be quantified experimentally.

1 INTRODUCTION

Fully developed, turbulent channel flows have been discussed extensively in the literature with regard to the mechanisms of wall bounded turbulence. The mean flow properties and the turbulence quantities of the flow close to the wall have often been assumed to be Reynolds number independent when normalized with inner variables. When measurements of mean velocity, RMS-values and higher order moments did not fullfill this 'Law of the Wall', the deviations were attributed to experimental errors inherently present when hot-wire or laser-Doppler anemometry (LDA) measurements were carried out in the near wall region of a wall bounded flow. These errors increase with decreasing distance from the wall and show a strong Reynolds number dependence. For a long time it was felt that there was no way to answer the question of the universality of turbulent fluctuations close to a wall. This belief came to an end when numerical results from DNS became available. These data clearly reveal a Reynolds number dependence close to the wall for the time mean velocity, the RMS-values of turbulence velocity fluctuations, the Reynolds shear stress, etc. To date, no physical explanation has been given for this finding. This paper presents a theoretical approach to the problem and an experimental clarification.

2 THEORETICAL CONSIDERATIONS

Integration and time-averaging of the momentum equation for an incompressible fluid and application to two-dimensional channel flow yields:

$$1 - \frac{y^+}{Re_\tau} = \frac{d\overline{U}^+}{dy^+} - \overline{u^+v^+}, \quad \text{with} \quad Re_\tau = \frac{u_\tau H}{2\nu} \qquad (1)$$

Renewed integration of Eq. (1) results in an expression for the mean velocity that shows a number dependence in the form of two substractive terms, one that can be connected to the pressure drop and the other one due to the Reynolds stress:

$$U^+ = y^+ - \underbrace{\frac{y^{+2}}{2Re_\tau}}_{\text{pressure drop term}} - \underbrace{\int_0^{y^+} \overline{u^+v^+}\,dy'^+}_{\text{Reynolds stress term}} \qquad (2)$$

Using Taylor series expansions for the fluctuation components, one can show that the Reynolds stress is proportional near the wall to the third power of the distance from the wall:

$$\left.\begin{array}{ll} u^+ \approx a_1^+ y^+ & +a_2^+ y^{+2} \\ v^+ \approx & +b_2^+ y^{+2} \\ w^+ \approx c_1^+ y^+ & +c_2^+ y^{+2} \end{array}\right\} \rightarrow \overline{u^+v^+} \approx \overline{a_1^+ b_2^+} y^{+3} \qquad (3)$$

At the wall, by definition, there exists no number dependence. With increasing y^+, first the pressure drop term is expected to dominate the number dependence and later the Reynolds stress term. In the limit of high number, the number influence vanishes, with the consequence that deviations from

the "Law of the Wall" decrease with increasing number.

Changes of streamwise turbulent fluctuations are reflected in the equation of the turbulent kinetic energy $k^+ = \frac{1}{2}\overline{u_i^+ u_i^+}$:

$$0 = +\overline{u^+v^+}\frac{\partial U^+}{\partial y^+} + \frac{\partial \overline{u_i^+ u_i^+ v^+}}{\partial y^+} + \overline{u_i^+ \frac{\partial p^+}{\partial x_i^+}} + \epsilon^+ - \frac{\partial^2 k^+}{\partial y^{+2}}, \tag{4}$$

In the very near wall region, the dissipation rate $\epsilon^+ = \overline{\frac{\partial u_i^+}{\partial x_k^+}\frac{\partial u_i^+}{\partial x_k^+}}$ is balanced by turbulent diffusion. Inserting Eq. (3) into Eq. (4) results in a direct relationship between k and ϵ:

$$\frac{2(k^+)_w}{y^{+2}} = (\epsilon^+)_w \tag{5}$$

Applying the 2-point-correlation technique (Jovanović et al. 1995) and considering the spatial derivations of the product of velocity fluctuations shows finally that the dissipation equation can be subdivided into an inhomogenous and a homogenous part, which are identical at the wall.

$$\epsilon^+ = \overline{\frac{\partial u_i^+}{\partial x_k^+}\frac{\partial u_i^+}{\partial x_k^+}} = \underbrace{\frac{1}{2}\triangle^+ k^+}_{\text{inhomogeneous}} + \underbrace{\epsilon_h^+}_{\text{homogeneous}} \tag{6}$$

The homogeneous part of ϵ can be modelled according to Eq. (7) (see Jovanović et al. 1996) with $Re_\lambda = \frac{\lambda\sqrt{2k}}{\nu}$, λ =Taylor micro scale.

$$0 = \underbrace{2A\frac{\epsilon_h^+ \overline{u^+v^+}}{k^+}\frac{\partial U^+}{\partial y^+} + 20B\frac{k^+}{R_\lambda}S_{12}^+\frac{\partial U^+}{\partial y^+}}_{\text{production term}} \underbrace{\Psi\frac{\epsilon_h^{+2}}{k^+}}_{\text{sink term}}$$
$$+ \underbrace{-\frac{\partial}{\partial y^+}\left[C_\epsilon \frac{k^+}{\epsilon_h^+}\overline{v^{+2}}\frac{\partial \epsilon_h^+}{\partial y^+}\right]}_{\text{transport term}} - \underbrace{\frac{1}{2}\triangle^+ \epsilon_h^+}_{\text{viscous destruction}} \tag{7}$$

Near the wall, besides the viscous destruction, only the additional production term shows a significant number dependence. An analysis of the dynamical equations of the turbulent dissipation rate concludes that the groth of ϵ in the near-wall region and at the wall with increasing number is a consequence of the behaviour of the extra production term in the ϵ equation. This term accounts for the influence of the mean flow deformation on the partition of the dissipation tensor. Owing to the normalization of the deformation tensor with the scales that characterize the two-point correlations at the origin (zero separation in space), the extra production term in the ϵ equation is sensitive to number variations and vanishes at sufficiently high numbers. The resulting trend for ϵ_h^+ is to increase with increasing Reynolds number up to a limiting value.

3 EXPERIMENTAL SETUP

To study low Reynolds number effects on fully developed plane channel flows, a water flow facility was set up that permitted mean velocities of up to 2.5 m/s to be obtained. Figure 1 shows a schematic of the test rig used for the present investigations. To drive the flow at a constant, pre-chosen flow rate, a total head tank was installed with a water head of approximately 6 m. Experimental investigations on how to set up fully developed low Re-number flows were performed in the two- dimensional channel with dimensions $L \times B \times H = 1 \times 0.18 \times 0.01$ m. The channel test section was proceeded by a rectangular contraction (0.15x0.18 m), providing a defined profile at the channel inlet. Upstream of the contraction, honeycomb and grids were installed to improve the flow uniformity.

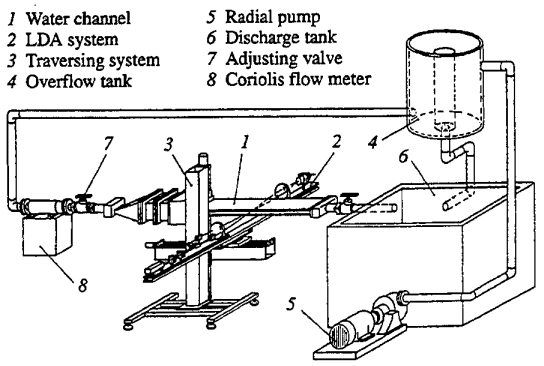


Figure 1: Sketch of channel flow facility showing major parts of the test-rig.

The developing boundary layers were tripped by plates inserted at the entrance of the channel with an optimised height of 0.75 mm, giving a blockage ratio of 15%, as determined by Durst et al. (1998). The measurements reported in this paper were performed 71 channel heights downstream of the channel inlet using laser-Doppler anemometers with measuring control volumes of various sizes. Two different LDA optical systems were employed to ensure the correct measurement of near wall time averaged flow properties. Since the limiting values of the measured flow properties for $y^+ \to 0$ were of interest, reliable measurements for $y^+ \leq 4$ were needed. The parameters of the LDA systems used for this purpose are shown in Table 1. A TSI-

Table 1: Computation of wall-next measuring positions for the different LDA setups and for a few exemplaric numbers. (The measuring volume size is based on the e^{-2} Gaussian intensity cut-off point, b.e.f.: beam expansion factor)

Laser	b.e.f.	R_e	d	d^+	y^+_{min}
HeNe (15 mW)	2.5	3500	80μ	1.7	0.85
HeNe (15 mW)	2.5	10000	80μ	4.3	2.15
HeNe (15 mW)	2.5	21000	80μ	8.0	4.0
Nd-YAG (100mW)	10	10000	30μ	1.7	0.85
Nd-YAG (100mW)	10	21000	30μ	3.3	1.65

1990 counter was employed for measurement of the Doppler frequency. It was operated in the total burst mode with at least 32 cycles per burst being measured. The mean velocity and velocity fluctuations were computed using arrival time averages to correct for velocity bias at the very low data rates.

To allow measurements very close to the wall and to reduce intercepting reflected light, the transmitting and receiving optics were tilted at small angles towards the channel wall. In this way, the measuring control volume could be located with an positioning accuracy of about 5 μm, with the closest location being about half a measuring volume diameter away from the wall. The wall shear stress was determined directly from the near wall mean velocity measurements using the polynomial fit procedure described by Durst et al. (1996).

4 CONTROL VOLUME EFFECTS

Due to the spatial velocity distribution of the mean flow and the spatial distribution of the moments of the turbulent velocity fluctuations, the actual velocity measured for each scattering particle does not correspond to the velocity value at the centre of the measuring control volume but rather to time and volume integrated information. In the following derivations, the ellipsoidal shape of the control volume and the discreteness of particle detection will be taken into account.

The time averaged as well as the fluctuating parts of the velocity may be expanded in Taylor series.

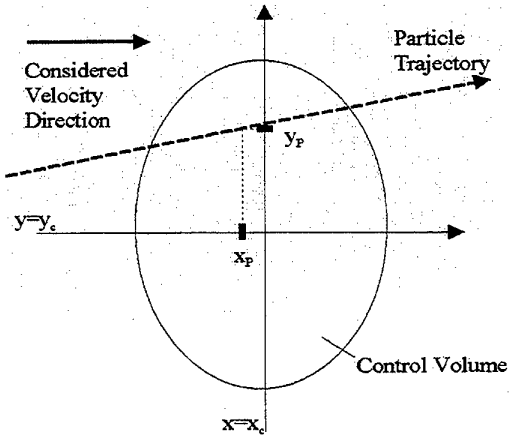


Figure 2: Control volume sketch

$$\underline{U}(t,\underline{x}) = \overline{\underline{U}}(\underline{x}) + \underline{u}(\underline{x},t) \tag{8}$$

$$\overline{\underline{U}}(\underline{x}) = \overline{\underline{U}}(\underline{x}_c) + \sum_{n=1}^{\infty} \frac{1}{n!} \left(\frac{\partial^n \overline{\underline{U}}(\underline{x})}{\partial x_i^n} \right)_{\underline{x}=\underline{x}_c} x_i^n \tag{9}$$

$$\underline{u}(\underline{x},t) = \underline{u}(\underline{x}_c,t) + \sum_{n=1}^{\infty} \frac{1}{n!} \left(\frac{\partial^n \underline{u}(\underline{x},t)}{\partial x_i^n} \right)_{\underline{x}=\underline{x}_c} x_i^n \tag{10}$$

If one now decomposes the instantaneous velocity for one event into mean and fluctuating parts at the position of the particle trace and alternatively in expressions of the whole control volume (that correspond to the information of the measurement), a connection between measured time averaged quantities and those in the center of the control volume arises:

$$\overline{U}(x_c,y,z) + u(x_c,y,z,t) = \overline{U}_{c_v} + u_{c_v}(t) \tag{11}$$

Volume integration results in the following correction equations for mean velocity and turbulent intensity.

$$\overline{U^+}_{c_v} \approx \overline{U^+}(y_c^+) + \frac{1}{8} \left(\frac{d_y^+}{2} \right)^2 \left(\frac{\partial^2 \overline{U^+}}{\partial y^{+2}} \right)_c \tag{12}$$

$$u_{c_v}^{+2} \approx \overline{u^{+2}(\underline{x}_c)} + \frac{1}{8} \left(\frac{d_y^+}{2} \right)^2 \left[2 \left(\frac{\partial \overline{U^+}}{\partial y^+} \right)_c^2 + \left(\frac{\partial^2 \overline{u^{+2}}}{\partial y^{+2}} \right)_c \right] \tag{13}$$

The measured mean velocity is very close to the time averaged value at the centre of the measuring

control volume since the correction depends only on the second derivative of the mean velocity profile (which is very small in the vicinity of the wall). The correction for turbulent intensities consists of a term due to the mean velocity gradient accross the measuring control volume and a term due to the curvature of the RMS-value profile of the longitudinal velocity fluctuations. The sum of both terms enlarges the measured rms-value fluctuations in comparison to the centre value to be measured. Analysis of the wall limiting behaviour of equation (13) shows that the second correction term can contribute up to about 16% of the total correction in Eq. (13). Similar to the above derivations, correction equations can also be derived for higher order moments.

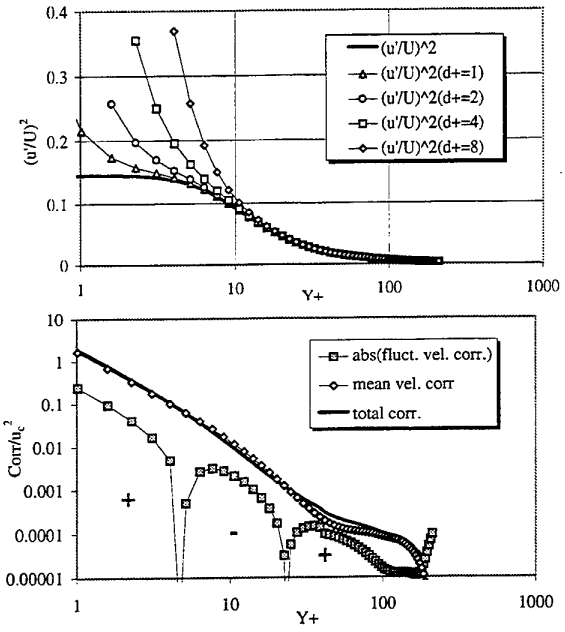


Figure 3: Expected influence on measured tubulence level using DNS-data. and illustration of the contibution of the different terms in eq. (13).

DNS data of Gilbert and Kleiser (1991) ($Re_m = 6,700, Re_\tau = 210.7$) were evaluated in order to simulate, for different control volume sizes, the expected effects of the derived corrections on the mean velocity U, the turbulence level u'/U, the Skewness factor $S = \frac{\overline{u_{c_v}^{+3}(t)}}{(u_{c_v}^{+2}(t))^{3/2}}$, and the Flatness factor $F = \frac{\overline{u_{c_v}^{+4}(t)}}{(u_{c_v}^{+2}(t))^2}$. In Fig. 3 (top) it can be seen that the corrections raise the measured turbulence level of the velocity fluctuations by more than one hundred percent near the wall. Computations were made only for the locations for which the control volume does not contact the wall (i.e. for y^+ values $y^+ > d^+/2$).To illustrate the difference between the two correction terms of Eq. (13) the terms are plotted in Fig. 3 (Bottom) for one size of the control volume ($d^+ = 1$) as an example. It is remarkable that the second correction term decreases the correction in the buffer layer.

The control volume size, d_y, enters the correction terms in Eqs. (12) and (13) as a weighting factor. However, use of the effective optical diameter (computed from the Gaussian light intensity distribution in the volume) for size corrections neglects the fact that each velocity measurement is dependent on the size distribution of scattering particles, on the scattered light detection system, on the LDA signal amplification, and on the discrimination level employed in the signal processing electronics. To obtain the real effective measuring control volume size of a particular LDA system, it is suggested to apply the system to a laminar flow and to measure the mean velocity and variance. Applying Eq. (13) to such measurements yields that the only unknown quantity in this equation is the effective control volume size. Besides a small noise

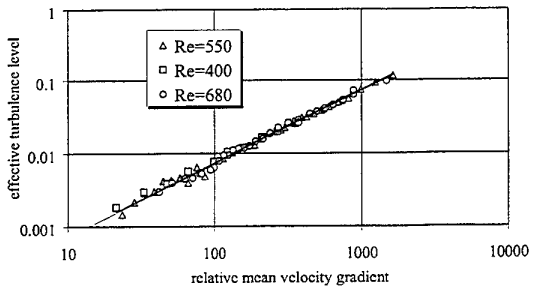


Figure 4: Effective turbulence level plottet against the relative mean velocity gradient

contribution, only the term defined by the mean velocity gradient remains. Thus the measured fluctuations are expected to obey the following expression:

$$\underbrace{\sqrt{\frac{u'^2_{c_v}}{\overline{U}^2} - \frac{u'^2_{noise}}{\overline{U}^2}}}_{\text{effective turbulence level}} = d_y \quad \underbrace{\frac{1}{4\overline{U}}\left(\frac{\partial \overline{U}}{\partial y}\right)_c}_{\text{relative mean gradient}} \tag{14}$$

Analysis of the slope of the curve in Fig. 4 results directly in the effective control volume size. After

the determination of d_y, the same optical and electronical configuration can then be applied to the turbulent boundary layer.

5 EXPERIMENTAL RESULTS

In Fig. 5 the mean velocity distributions for various numbers are shown. A systematic variation in

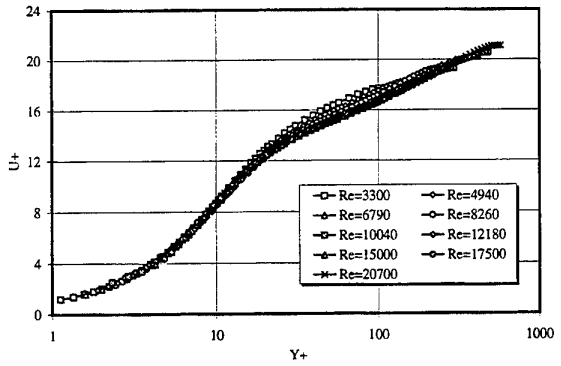


Figure 5: Mean velocity profiles non-dimensionalized on inner variables

the core region of the flow with increasing number can be reported. Of particular interest was the behaviour very close to the wall. Analysis of data from DNS have shown that at the outer edge of the viscous sublayer, the sum of the pressure drop term and the Reynolds stress term are nearly independent of Reynolds number and therefore cannot be resolved experimentally. According to direct numerical simulations of turbulent channel flow, the streamwise velocity component accounts for about 75% of the dissipation rate at the wall (Kim et al., 1987; Antonia et al., 1992): $(\epsilon^+)_w \approx 1.3 \left(\frac{u'^2}{U^{+2}}\right)_w$. Therefore the measurement of streamwise turbulent fluctuations gives an insight into the influence of Reynolds number on $(\epsilon^+)_w$. In Fig. 6 the RMS-values of the uncorrected data are compared with the corrected ones. They reveal the influence of control volume effects on position and intensity of the measured RMS-maximum. Figure 7 shows that a Reynolds number dependence in the viscous sublayer can be seen clearly, leading to increasing wall limiting values with increasing number. For the evaluation of these values, the near wall data in the region $y^+ < 10$ were extrapolated to the wall position. In Fig. 8 the resulting values extracted from the measurements are plotted against number. Comparison between experiment and DNS results reveals the same trend but a remarkable deviation in the absolute values of u'/U at higher Reynolds numbers. The measured turbulent fluc-

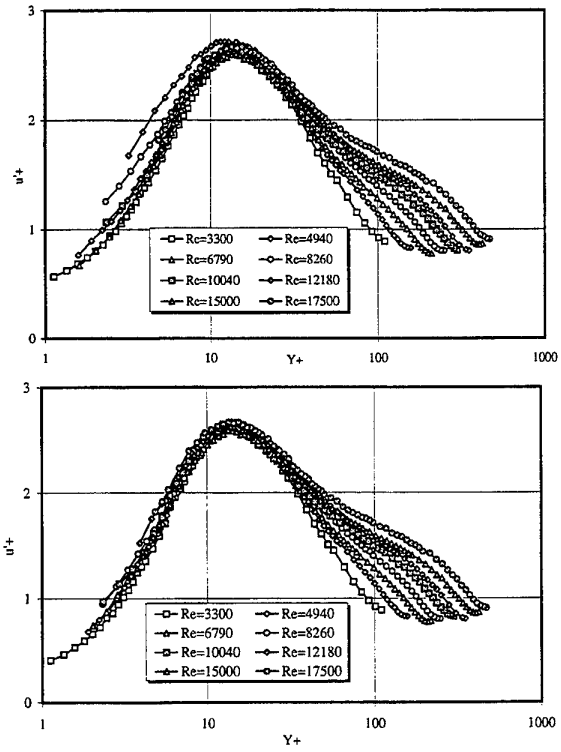


Figure 6: Profiles of the RMS values of turbulent fluctuation measured (top) and corrected (bottom)

tuations can be approximated quite well by an analytical expression that contains a limiting value for very high numbers and and a subtractive part inversely proportional to the number.

$$(u'/U)_w = (u'/U)_{w;Re\to\infty} - A/Re_\tau \qquad (15)$$

Fitting of Eq. (15) yields for the constants: $(u'/U)_{w;Re\to\infty} = 0.40 \pm 0.01$ $A = 7.0 \pm 0.5$. Extrapolating this result, one would expect the number effects to vanish asymptotically above $Re_m \approx 35000$.

6 CONCLUSIONS

Near-wall laser-Doppler measurements were performed in a turbulent channel flow in order to examine the number dependence of time-averaged turbulence quantities in the vincinity of the wall. A new method for the statistical interpretation of LDA-signals was proposed and realized in order to get acurate local flow information in regions of high shear rate. Deviations from the 'Law of the Wall' for the mean velocity down to the inner edge of the buffer layer could be experimentally quantified.

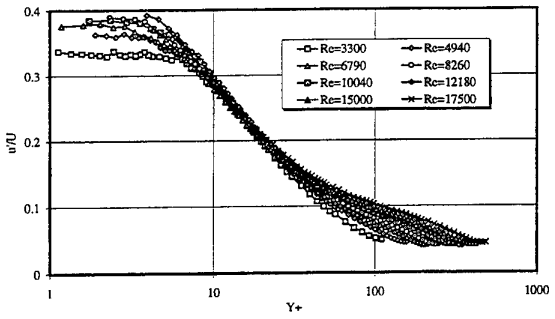


Figure 7: Streamwise turbulent fluctuation normalized with mean velocity

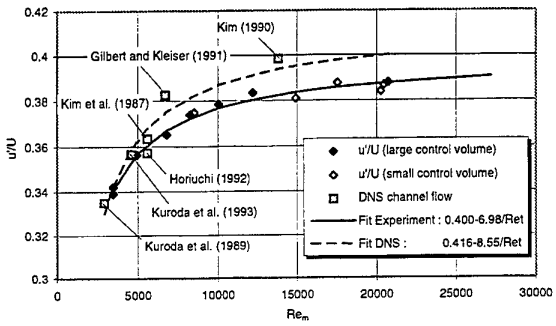


Figure 8: Plot of determined wall limiting values for u'/U. Comparison with DNS-data

The wall limits of fluctuations have been experimentally determined and put into the frame of an analytical treatment. The turbulent fluctuations exhibit a number dependence in the near wall region. The experimental finding have implications for the modelling of low Reynolds number flows.

ACKNOWLEDGEMENTS

This research received financial support through the Deutsche Forschungsgemeinschaft within the project Du 101/49-1.

REFERENCES

Antonia, R.A; Teitel, M.; Kim, J.; Browne, L.W.B., Low-Reynolds number effects in a fully developed channel flow, J. Fluid Mech. 236: 579-605, 1992

Durst, F.; Kikura,H.; Lekakis, I.; Jovanović, J.; Ye, Q.-Y., Wall shear stress determination from near-wall mean velocity data in turbulent pipe and channel flows, Exp. Fluids 67: 257-271, 1996

Durst, F.; Fischer, M.; Jovanović, J.; Kikura, H., Methods to set up and investigate low Reynols number, fully developed turbulent plane channel flows, J. Fluid Eng., in press, 1998

Gilbert, N. and Kleiser, L., Turbulence model testing with the aid of direct numerical simulation results, 8th Symp. on Turbulent Shear Flows, Sept. 9-11, TU Munich, pp. 26.1.1-26.1.6, 1991

Jovanović, J.; Ye, Q.-Y. and Durst, F., Statistical interpretation of the turbulent dissipation rate in wall-bounded flows, J. Fluid Mech. 293: 321-347, 1995

Jovanović, J.; Ye, Q.-Y.; Jakirlić, S. and Durst, F., Turbulence closure for dissipation rate correlations, submitted to J. Fluid Mech., 1996

Kim, J.; Moin, P. and Moser, R., Turbulence statistics in fully developed channel flow at low Reynolds number, J. Fluid Mech. 177: 133-166, 1987

Kim, J., Collaborative Testing of Turbulence Models (Organized by P. Bradshaw), Data Disk No.4., 1990

Kuroda, A.; Kasagi, N. and Hirata, M., A direct numerical simulation of fully developed turbulent channel flow, Int. Symp. on Comput. Fluid Dynamics, Nagoya, pp 1174-1179, 1989

Kuroda, A.; Kasagi, N. and Hirata, M., Direct numerical simulation of the turbulent plane Couette-Poiseulle flows: Effect of mean shear on the near wall turbulence structures, 9th Symp. on Turbulent Shear Flows, Kyoto, Japan, Aug. 16-18, pp. 8.4.1-8.4.6, 1993

LDV ANALYSIS OF TEMPORAL INTERMITTENCY IN PIPE FLOW

E. Nino and C. Serio

Dipartimento di Ingegneria e Fisica dell'Ambiente
Università della Basilicata, Potenza, Italy

ABSTRACT

Transitional pipe flow has been analysed by Laser Doppler Velocimetry. Our main objective was to analyse the correlation structure of the strong temporal intermittency, which characterises the flow close to the transition to turbulence. In doing so the Reynolds number dependence of the covariance function has been studied. The range we have analysed covers the transition to turbulence and moderately developed turbulence (Reynolds number from 1500 to 5000). The correlation structure we have evidenced is generally in agreement with the deterministic, dynamical, interpretation of temporal intermittency, which explains the intermittent behaviour as a result of a saddle node bifurcation. In addition, our analysis has evidenced fluctuations even before the onset of turbulence. The structure of these fluctuations is perfectly autoregressive, which leads us to conclude that the transition to turbulence can be viewed as a transition from linear randomness to (non-linear) homogeneity.

1. INTRODUCTION

Transition to turbulence in pipe flow is still now an important fundamental problem in fluid mechanics (e.g. Darbyshire and Mullin (1995), Tritton (1988) and references therein. From a mathematical point of view, pipe flow is believed to be linearly stable and yet it is observed to be unstable in the laboratory. According to Wygnanski and Champagne (1973, 1975) unstable flow results from instabilities in the inlet region of the pipe where turbulent patches may be generated by sharp entry geometry and/or instability in the boundary layer. Above a critical value of the Reynolds number (Re) these turbulent patches does not decay when they move along the tube so that, at a fixed point in the pipe, we can observe alternatively turbulent and laminar motion. This phenomenon yields a strong temporal intermittency which has been recognised as one of the fundamental mechanism for the transition to turbulence whatever the type of flow may be (e.g. Libchaber (1985), Ruelle (1985), Manneville and Pomeau (1980)). The analysis of the correlation structure of this kind of intermittency is the main objective of this study.

From a theoretical point of view, Manneville and Pomeau (1980) have extensively studied the onset of turbulence through temporal intermittency. Dynamical systems which exhibit temporal intermittency are characterised by a regular motion in phase space, interrupted by randomly distributed bursts of strong chaoticity. According to Manneville and Pomeau (1980) the frequency of turbulent bursts increases as the Reynolds number rises above a critical value, Re_c (for our experiment this critical Re falls in the interval 1800-2100). More precisely the time duration of laminar phases is proportional to some power of $1/(Re-Re_c)$ so that for Re which approaches the critical value, the laminar period diverges and there is no temporal intermittency. Conversely, when Re becomes large, the period of the laminar phases becomes zero and the flow becomes homogeneously turbulent.

A dynamical interpretation of temporal intermittency has been proposed by Ruelle (1985) who explained the presence of strong bursts of intermittency as the result of a saddle node bifurcation. According to this description three

distinct flow regimes may be individuated as a function of Re.

1. For Re< Re_c the fluid motion is regular, i.e. linear, hence, the velocity field admits a perfect autoregressive representation.
2. For Re≈ Re_c the character of the flow should be autoregressive, i.e. regular, for long times, interrupted by bursts of strong chaoticity, hence, the temporal intermittency.
3. For Re> Re_c the fluid motion is chaotic.

This picture may be directly compared to our results.

1. For Re< Re_c (we have extensively examined Re=1500), the flow is characterised by fluctuations whose covariance function is perfectly modelled by a couple of dampened Fourier modes (autoregressive stochastic behaviour) rather than pure Fourier modes as it should be for a limit cycle (autoregressive deterministic behaviour). This autoregressive behaviour mimics $1/f^2$ noise at high frequency. The mechanism, which generates these slight fluctuations in the velocity field, is an incomplete process of re-laminarization as the flow progresses downstream. We stress that the character of the fluctuations is linear.
2. At the onset (we present data for Re=2000 and Re=2500), the character of the velocity fluctuations is autoregressive for long times, interrupted from bursts whose statistical structure is not autoregressive, i.e. non-linear. The statistical structure of these bursts is well represented by a lorenztian-like (algebraic) model. This twofold behaviour is well seen in the covariance function, which crosses over from a small-scale algebraic character to large-scale autoregressive behaviour. The flow lacks spatial homogeneity, the turbulent bursts, indeed, are spatially localised, hence, the phenomenon of temporal intermittency.
3. After the transition, Re> Re_c (we have extensively examined Re=5000), the character of the fluctuations change and the algebraic, non-autoregressive, behaviour becomes dominant for the covariance function. The flow becomes spatially homogeneous.

These results fairly agree with the idea of a saddle node bifurcation, however the presence of linear randomness before the onset, lead us to conclude that the deterministic view is correct in the context of a mean-field theory so that the phenomenon would be better described in the framework of noisy rather than deterministic maps. For this reason, the onset of turbulence in pipe flow could be better described as transition from linear randomness to non-linear homogeneity.

The paper is organised as follows. After presenting the experimental details (section 2), we focus on the correlation structure of the flow for different values of the Reynolds number (section 3). Conclusions are drawn in section 4.

2. EXPERIMENTAL APPARATUS

Our measurements have been made in a water tunnel (Fig. 1). Basically, the hydraulic part is a closed water tunnel comprised of an horizontal cylindrical pipe 6 m long, whose inner and outer diameters are 0.05 and 0.06 m, respectively, and a water tank which provides water to the horizontal pipe by a direct coupling through a smooth plastic tube whose diameter is 1/5 of the diameter of the water tunnel.

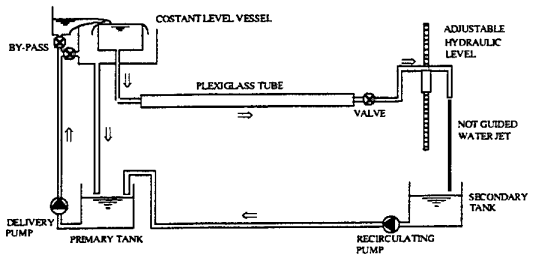


Fig. 1: Constant level water tunnel

This kind of coupling realises a sudden expansion (aspect ratio 5:1) which produces a large disturbance at the inlet so that we expect the development of weakly turbulent flow also at very modest values of the Reynolds number. Note that unlike it might appear from the schematic diagram of Fig. 1, the entry geometry does not involve sharp edges or corners and there are not regions of separated flow. An adjustable hydraulic level (see Fig. 1) allows us to obtain different flow regimes. A secondary hydraulic circuit powered by two pumps provides to send back the water to the tank. The secondary circuit has been specifically realised in such a way to maintain a constant hydrostatic pressure drop between the tank and the inlet side of the water tunnel. The turbulence we observe is the result (i): of disturbances at the inlet and (ii) instability of the boundary layer in the inlet region of the pipe

The LDV system is comprised of an optical part and a data acquisition system. The optical part (see

Figure 2) was developed at our laboratory. Two incident laser beams generated by a single He-Ne Laser obtain the test volume. The two beams are obtained by a rotating diffraction grating. The speed of rotation can be varied in order to produce a frequency shift between the two crossing beams, which, in turn, allows us to be sensitive to the sign of the velocity.

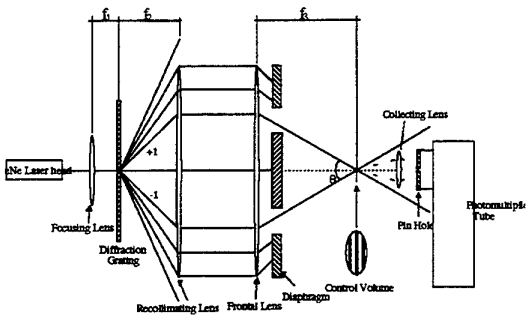


Fig. 2: Optical set - up

The data acquisition system is a TSI digital burst correlator, model IFA-655. The system was operated in such a way to count up the particles passing through the test volume so that, in addition to velocity observations, the time between samples was recorded, too. In this way almost continuous time

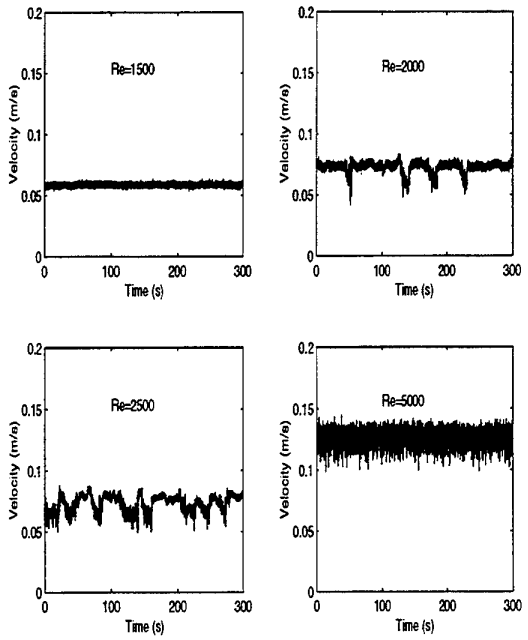


Fig. 3: Velocity time history for different Reynolds number. X/d=100.

records were obtained and proper weight could be given to each sample so that mean velocities and higher order moments could be calculated with little or no bias caused by the particle arrival statistics. No artificial seeding was employed. The nearly continuous series was, then, digitally low pass filtered (re-sampled) in order to have equi-spaced samples. The re-sampling rate is given by $\Delta t=r_o V^{-1}$, where r_o has been set equal to the linear dimension of the LDV test space which, in turn, determines the smallest resolvable scale by our equipment, r_o =1 *mm*. Furthermore, V is the mean value of the velocity time series. The low-pass filtering operation consists simply in computing the average value of the velocity during the time interval Δt

$$v(i\Delta t)=\frac{1}{\Delta t}\sum_{j=1}^{n_i}\Delta t_{ij}u_{ij};\sum_{j=1}^{n_i}\Delta t_{ij}=\Delta t;i=1,\ldots,\frac{T}{\Delta t} \quad (1)$$

where u_{ij} indicates the original velocity time series, Δt_{ij} is the time between two consecutive velocity samples T is the total observational period and, finally, n_i gives the number of velocity samples within each time interval Δt. Because of experimental restrictions, we measured only the component of the velocity in the streamwise direction. Measurements were considered at three different positions along the tube: X/d=20, 60, 100, where X gives the distance from the inlet and d is the inner diameter of the tube. The Reynolds numbers considered in this study are: Re=1500, 2000, 2500, and 5000 respectively. Here the Reynolds number is defined as usual: $Re=Ud/\nu$ with U the mean flow velocity and $\nu=10^{-6}\,m^2s^{-1}$ the kinematics viscosity of water at 20 °C.

3. STATISTICAL CHARACTERIZATION OF THE TRANSITION

Figure 3 shows segments of the velocity time series for the four Reynolds number considered in our analysis. The data shown in Figure 3 were recorded 100 diameters downstream (X/d=100). The transitional, intermittent, character of the flow is quite evident. For Re=1500 an erratic behaviour around a mean value predominates. For Re=2000 the presence of intermittent bursts is striking. The frequency of these bursts greatly increases for Re=2500. The strong temporal intermittency is no longer visible for Re=5000. The statistical characterisation of the transition has been based on

the covariance function of the velocity fluctuations. To begin with we analyse the disturbances which originate close to the inlet region. These disturbances may be viewed as the *driving force* of the velocity fluctuations far away from the inlet.

3.1 Inlet Turbulence, X/d=20

The normalised covariance function for Re=1500 is shown in Figure 4. The shape of the covariance functions do not critically depend on Re, although the macroscale of turbulence does. They are well fitted by the simple algebraic model:

$$R(\tau) = \frac{C(\tau)}{\sigma^2} = \frac{a}{a + \tau^{\alpha}} \qquad (2)$$

where $R(\tau)$ is the autocorrelation or normalised covariance function and $C(\tau)$ is the covariance function; $\tau = t/\Delta t$ is the normalised time lag, Δt being the sampling interval and σ^2 is the variance of the velocity series; a and α are parameters to be determined. The ability of this model to represent the observed covariance function is well evident from Fig. 3. It is interesting to note that beyond the cut-off scale $\tau_o = (a)^{(1/\alpha)}$, $C(\tau) \sim \tau^{\alpha}$, that is the covariance function obeys a scaling law. The best fit values for a and α are $a=112 \pm 2$ and $\alpha=1.540 \pm 0.004$, in the case of Re=1500. For Re=5000, we have $a=30 \pm 1$ and $\alpha=1.588 \pm 0.006$. We see that the scaling exponent agrees fairly well for the two cases, however the cut-off scale is $\tau_o \approx 20$ for Re=1500 and $\tau_o \approx 10$ for Re=5000. It should be noted that the covariance function of the observations tends to zero as τ becomes large, which leads us to conclude that the underlying process is stationary.

3.2 Turbulence Far Away From the Inlet

In this section, we will focus on the correlation structure of the flow far away from the inlet. We will start with the correlation structure before the intermittent transition, then we will be dealing with the case after the transition (i.e. Re=5000). The transitional region will be described in the end, since this case encompasses aspects, which are peculiar to both laminar and turbulent flow. Below a critical Re, which for our experiment falls in the interval 1800-2100, the turbulence generated at the inlet just decays while the flow moves downstream. The observed covariance function for X/d=60 is shown in Figure 5. By comparison with Fig. 4, which shows $R(\tau)$ for X/d=20, it is possible to see the dramatic change in the correlation structure. Not only the covariance function becomes negative, which indicates the presence of an oscillatory component, although dampened, in the velocity time series, the flow develops an incredible long-range correlation: $R(\tau)$ approaches to zero only for $\tau > 1000$. The most general expression for the covariance function of a dampened linear system is:

$$C(\tau) = \sigma^2 \sum_{i=1}^{p} a_i \cos(\beta_i \tau) \exp(-\gamma_i \tau); \quad \sum_{i=1}^{p} a_i = 1 \qquad (3)$$

where p is the number of oscillating mode of the system. Model (3) is, indeed, a composition of dampened waves and for our case it turned out to be that only two terms, were sufficient to give a perfect representation of the observed covariance function, as it is possible to see from Figure 5. The best fit values for the six parameters are here summarised:

$$a_1 = 0.574 \pm 0.006 \qquad a_2 = 0.426 \pm 0.06$$
$$\beta_1 = (26.34 \pm 0.07)\,10^{-4} \qquad \beta_2 = (47.3 \pm 0.1)\,10^{-4}$$
$$\gamma_1 = (15.95 \pm 0.07)\,10^{-4} \qquad \gamma_2 = (20.30 \pm 0.07)\,10^{-4}$$

Relation (3) is the covariance function of a stochastic autoregressive (linear) process whose variance spectrum scales according to $1/f^2$ as the frequency becomes large. For Re=5000 the turbulence begins to grow while the flow progresses downwards. Figure 6 shows the covariance function for X/d=100. It nearly coincides with that for X/d= 60 (not shown in figure for the sake of clearness) which leads us to conclude that the flow tends to become spatially homogeneous. Another important results which confirms that the flow tends towards homogeneity is that the algebraic model (2) fits to the data for any X/d. The parameters of the fit for the case shown in Figure 6 are $a=33 \pm 2$ and $\alpha=1.90 \pm 0.02$.

Finally, we discuss the transition region, which occurs for Re larger than approximately 1800 and lower than approximately 4000. Here, we limit ourselves to discuss the case Re=2500 and X/d=100. This choice is motivated by the fact that the phenomenon of temporal intermittency is very well observed 100 diameters downstream. Figure 6 shows a plot of the covariance function. Its long tail is quite evident, however close to the origin the function has evident crossover behaviour. We think that the covariance function crosses-over from an algebraic behaviour, which characterises the locally disordered

flow (turbulent puffs), to a dampened oscillation which is characteristic of the decaying turbulence. In other words, the flow contains both locally disordered flow whose statistical structure is the same as that which characterises the flow for Re=5000 and decaying turbulence which has a behaviour as that found, e.g., for Re=1500. To check this hypothesis, we consider for the covariance function the model:

$$C(\tau)=\sigma^2\sum_{i=1}^{p}a_i\cos(\beta_i\tau)\exp(-\gamma_i\tau)+a_3\frac{a}{a+\tau^{\alpha}} \quad (4)$$

where $(a_1+a_2+a_3=1)$. The model above is just the composition of a small-scale algebraic decay and large-scale autoregressive behaviour. The best fit is shown in Figure 7 and we see that the agreement is perfect. The value of the parameters is here summarised

$$a_1 = 0.310 \pm 0.002 \qquad a_2 = 0.451 \pm 0.02$$
$$\beta_1 = (8.2 \pm 0.1)10^{-4} \qquad \beta_2 = (2.65 \pm 0.4)10^{-4}$$
$$\gamma_1 = (7.4 \pm 0.09)10^{-4} \qquad \gamma_2 = (15.5 \pm 0.1)10^{-4}$$
$$a = 147 \pm 1 \qquad \alpha = 1.900 \pm 0.006$$

This last result just emphasises that the correlation structure of the turbulent bursts is not autoregressive, so that temporal intermittency by no way can be explained as a spatially localised increase of the level of the linear fluctuations. Thus we have really a regular motion in phase space for long times, interrupted by bursts of strong chaoticity autoregressive dynamics, we have that for Re=5000 the underlying attracting set, if any, is not regular. The flow has a pre-fractal behaviour, which leads us to conclude that the system develops a non-trivial non-linearity. The transition to turbulence in pipe flow can be, then, viewed as a transition from linear randomness to non-linear homogeneous turbulence.

4 SUMMARY AND CONCLUSIONS

In this paper we have analysed the Reynolds number dependence of the covariance function for pipe flow. Observations of the streamwise component of the velocity field have been reported for different locations along the axis of the tube, namely *X/d*=20, 60, 100, where *X* denotes the distance from the inlet and *d* is the inner diameter of the pipe.

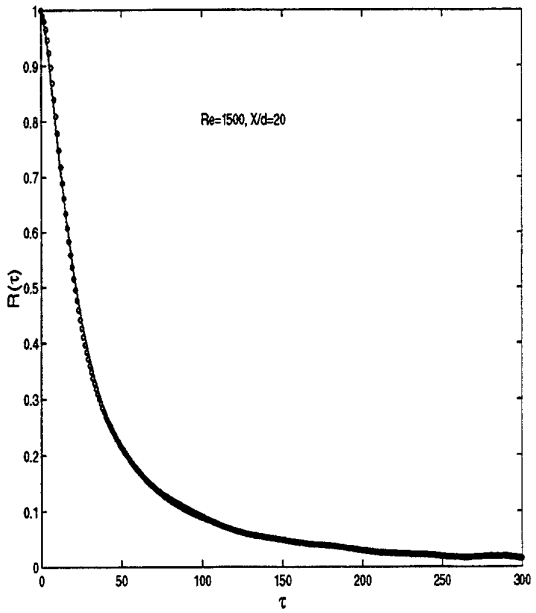


Fig. 4: Observed autocorrelation function (dots) and model fitted to data points (solid line). X/d = 20, Δt=0.02 s. The number of velocity data points is N = 2022759.

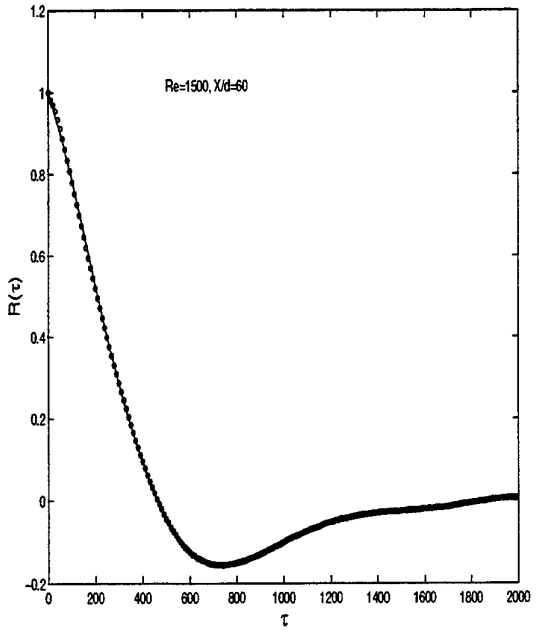


Fig. 5: Observed autocorrelation function (dots) and model fitted to data points (solid line). X/d = 60, Δt=0.018 s. The number of velocity data points is N = 2178856.

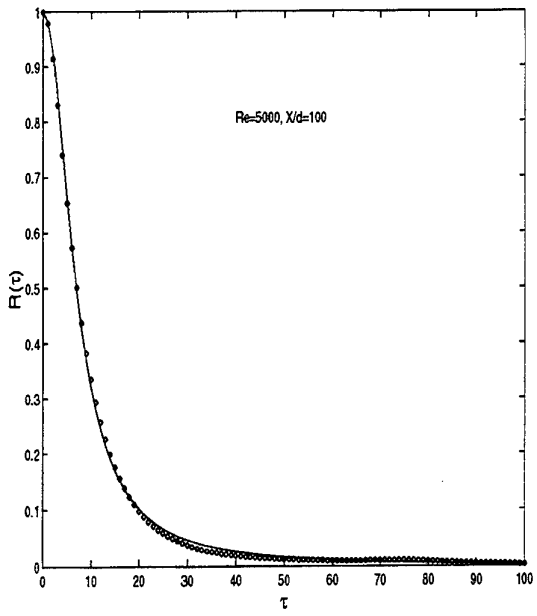


Fig. 6: Observed autocorrelation function (dots) and model fitted to data points (solid line). X/d = 100, Δt=0.078 s. The number of velocity data points is N = 3229227.

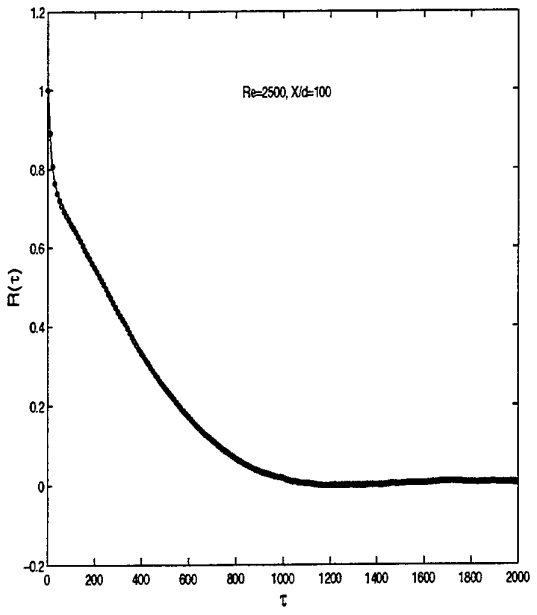


Fig. 7: Observed autocorrelation function (dots) and model fitted to data points (solid line). X/d = 100, Δt=0.014 s. The number of velocity data points is N = 1840492.

The main features of our experimental results can be summarised as follows:

1. Turbulence was induced by using a sharp inlet;
2. For Re < 1800, turbulence did not grow, it was dampened by viscosity and the most interesting characteristics was a very long-range dynamical correlation which yielded $1/f^2$ noise, although as a limiting case of an autoregressive (linear) behaviour.
3. A crossover character of the flow was evident in between Re=2000-3000. In this case the most disordered part of the flow was spatially localised in the pipe which yielded the characteristic phenomenon of temporal intermittency. Both decaying and non-decaying turbulence was easily recognised in the flow.
4. For values of Reynolds number greater than Re=3000 (we have extensively analysed the case Re=5000) the turbulence grew while the flow progressed downstream and tended rapidly towards homogeneity. The covariance function was, then, well described by a Lorentzian-like (algebraic) model, whatever the location along the tube could be. However the exponent of the model changed increasing towards the limiting value of 2.

The correlation structure of developed turbulence was, then, identical to that of the strong bursts present at the onset and was in any case non-autoregressive, which leads us to conclude for chaos. This conclusion is also supported from the behaviour of the covariance function, which, after the transition, exhibits pre-fractal structures. While clarifying the dynamics of the transition to turbulence in pipe flow, our results clearly shows that temporal intermittency implies a crossover from decaying to growing turbulence. The character of the decaying turbulence is linear, whereas spatial homogeneity is the salient feature of growing turbulence so that the phenomenon of temporal intermittency may be interpreted as a transition from linear randomness to non-linear homogeneity. In this respect, our findings seem to be in better agreement with the idea of phase-transition from linear fractality to homogeneity, recently introduced by Bershadskii (1996) in a different context. The flow, then, should crosses-over from a random mono-fractal structure to a multifractal structure. Before transition the mono-fractal structure is, indeed, consistent with the $1/f^2$ noise behaviour we have evidenced for Re=1500. From our preliminary results on the transition, a multifractal behaviour has been evidenced for Re=6000 (e.g. De Tommaso et al

(1996)). This brings us to another important aspect of our analysis. We have found pre-fractal behaviours at very modest value of the Reynolds number. Although limited in size, this form of scale invariance is consistent with the concept of ESS scaling (Benzi et al (1996)). This form of scaling has been directly detected for Re as low as 6000 (e.g. Esposito et al (1996)). The present analysis, then, clearly shows that ESS scaling is not possible below Re≈5000, because below such a critical value of Re the flow is lacking spatial homogeneity.

REFERENCES

Benzi R., Ciliberto S., Tripiccione R., Baudet C., Massaioli F., and Succi R. 1993, Extended Self-Similarity in Turbulent Flows, Phys. Rev. E vol. 48 pp. R29-32.

Benzi R., Biferale L., Ciliberto S., Struglia M. V., Tripicione R. 1996, Generalized Scaling in Fully Developed Turbulence , Physica D , vol. 96 pp. 162-181.

Bershadskii A. 1996, Phase-Transition from Fractality to Homogeneity in a Large-Scale Universe, Phys. Lett. A vol. 222 pp. 375-377.

Darbyshire G. and Mullin T. 1995, Transition to Turbulence in Constant-Mass-Flux Pipe Flow J. Fluid. Mech. Vol. 289 pp. 83-114.

Di Tommaso R. M., Esposito F., Laurenzana R., Nino E., Serio C. 1996, Scale Invariance and Multifractal Structure in Transitional Pipe Flow, Europhys. Lett., vol. 36 pp. 669-674.

Libchaber A. 1985, in Turbulence and Predictability in Geophysical Fluid Dynamics and Climate Dynamics. ed. M. Ghil, R. Benzi and G. Parisi, pp. 17. North-Holland, Amsterdam

Manneville P. and Pomeau Y. 1980, Commun. Math. Phys. Vol. 74 pp. 189-199.

Esposito F., Nino E., Serio C. 1996, Self-Scaling Properties of the Structure Functions at Moderate Reynolds Number, Europhys. Lett. vol 25 pp. 653-658.

Ruelle D. 1985, in Turbulence and Predictability in Geophysical Fluid Dynamics and Climate Dynamics, ed. M. Ghil, R. Benzi and G. Parisi, pp. 3, North-Holland, Amsterdam.

Tritton D. J. 1988, Physical Fluid Dynamics, pp. 1-519, Oxford Science Publishing, Oxford.

Wygnanski I. J. and Champagne F. H. 1973, On Transition in a pipe. Part 1. The Origin of Puffs and Slugs and the Flow in a Turbulent Slug.t J. Fluid. Mech., vol. 59 pp. 281-335.

Wygnanski I. J. and Champagne F. H. 1975, On Transition in a Pipe. Part 2. The Equilibrium Puff, J. Fluid. Mech., vol. 69 pp. 283-304.

STREAMWISE VORTEX PRODUCTION BY AN ARRAY OF INCLINED JETS

X. Zhang* and A. Rona†
Department of Aeronautics and Astronautics
University of Southampton
Southampton SO17 1BJ, England

ABSTRACT

A model test was conducted on longitudinal co-rotating vortices generated by an array of inclined jets in a turbulent flat plate boundary layer. Velocity measurements were performed at a number of jet speeds and at different locations. The study established a database of mean velocity field and turbulent stresses, and provided insight into the flow physics. In particular, it was observed that as the vortices develop downstream, the centre of the vortex moved spanwise in the skew direction of the jet and away from the wall. The streamwise vorticity decreased downstream. Increasing the jet velocity ratio (λ) increased the maximum vorticity almost linearly between $\lambda = 0.5$ and 1.25. The rate of increase slowed down above $\lambda = 1.25$. The characters of the vortex were changed significantly when the jet velocity ratio was increased above unity. When the jet velocity ratio was below unity, the main vortex was deeply embedded inside the boundary layer.

1 INTRODUCTION

This study concerns with the streamwise vortices generated by pitched and skewed wall jets[1] in a turbulent boundary layer devloping on a flat plate. The objectives are: (i) to investigate the vortex generation mechanism of co-rotating air jets, (ii) to provide turbulence data for numerical model and turbulence model validation and (iii) to provide design guidelines of air jet vortex generators.

An air jet issued from an aerodynamics surface into a turbulent flow field will generate streamwise vortices under a wide range of flow conditions. The primary flow parameters include pitch angle, skew angle, velocity ratio, and oncoming flow profile. If a skew angle is introduced, a single vortex will eventually be formed. This observation is supported by both experimental[1, 2] and computational[3] studies. The single vortex is stronger than the contra-rotating vortices otherwise generated by a pitched jet without skew[3]. The convective properties of the vortices in a cross-plane normal to the streamwise direction can be useful in turbulent flow control and have an added advantage of offering potential of active control.

Previous studies on the air jet vortex generators have not provided sufficient information to give a full account of flow physics[2], particularly the velocity and stress field which is vital for theoretical modelling attempts. There were also some confusion on the effects of particular parameters such as the jet exit[4], and velocity ratio. These parameters influence the relative position and strength of the vortex in a turbulent flow, thus the effectiveness of near-wall manipulation of shear stress. All these influence the application of the devices.

The current study forms part of a wide study on the streamwise vortices including computational modelling[3] and wind tunnel model tests[5]. In the past, Laser Doppler Anemometry studies of a single streamwise vortex embedded inside a turbulent boundary layer on a flat plate were performed[6]. The flow represents a basic test case for engineering applications and data validation. In this study, the nearfield evolution of streamwise vortices embedded in a turbulent boundary layer was examined in a wind-tunnel test. Co-rotating vortices were produced by an array of inclined round jets. The control parameter is the jet velocity ratio.

2 EXPERIMENTAL SETUP

The tests were performed in the R.J. Mitchel wind tunnel in the Department of Aeronautics and Astronautics, University of Southampton. The closed circuit low speed tunnel has a working section 3.5m

*Senior Lecturer
†Research Assistant, Now Senior Research Engineer, von Karman Institute, Rhode Saint Genese, Belgium.

wide by 2.6m high. A flat plate boundary layer is developed on a 2.43m long and 10mm thick aluminum plate supported above the tunnel floor. The oncoming freestream velocity U_∞ at the leading edge is 20m/s. The inclined jet nozzle has a diameter D=14mm and is located at 1.13m downstream of the leading edge of the plate. The boundary layer thickness δ_{99} at 100mm upstream of the nozzle exit is approximately 25mm, the displacement thickness 3.02mm and the momentum thickness 2.40mm.

The jets were produced by round nozzles connected with an air supply. The nozzles were skewed and pitched at 45° to the oncoming stream and arranged in a co-rotating fashion. The exit of the nozzle was flush with the flat plate surface. A schematic of the coordinates system for the co-rotating system is shown in Fig. 1. The lateral separation distance between the jets was set at 75mm and a total of eight nozzles were employed. The velocity ratios of the jet, $\lambda = V_j/U_\infty$, were 0.5, 0.75, 1.0, 1.25 and 1.5, where V_j was the jet speed.

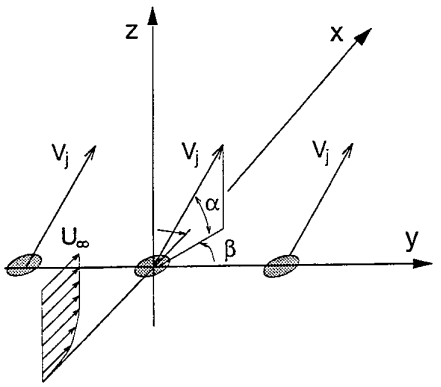


Figure 1: Schematic of measurement coordinates.

Measurements were made on cross-planes at x=5D, 10D, 20D, 30D, and 40D downstream of the jet exit. For each cross-plane section, the number of measurement points ranged from 720 to 792. The smallest distance of the measurement point to the wall was 0.95mm. The mean velocity was measured with a three-component Dantec LDA system. The signals were then analyzed using three DANTEC Burst Spectrum Analyzers. A total of 5000 bursts (instantaneous samples) were collected for each point. The typical coincidence rate was 30%. This gave at least 1500 bursts for the stress analysis. The measured data is presented in the paper in terms of velocity vectors, contours of velocity and streamwise vorticity ($\Omega_x = \partial w/\partial y - \partial v/\partial z$) which has been calculated for each data point on the measurement grid, where u is the streamwise velocity, v spanwise velocity and w transverse velocity. Natural cubic splines were used to obtain the derivatives of w and v with respect to the coordinates y and z. In presenting the data, unless otherwise stated the velocity is normalised by U_∞ and length scales by D.

The LDA beam measurement volume had a cross-section size of 0.326mm. It was concluded that the uncertainty in the x, y, z measurements was ±0.16mm. The uncertainty in the tunnel speed measurement was ±0.25m/s. The uncertainty in the LDA velocity measurement was influenced by the uncertainties in the beam separation, focal length, wavelength and errors in the tunnel speed which determines the Doppler frequency. Following the procedure of Moffat[7] the uncertainty in the velocity measurement was estimated at ±0.31m/s when the freestream value was 20m/s. An analysis was performed on the uncertainties in the turbulent stress measurement, following Benedict and Gould[8]. An example of the results is given in Fig. 2, where 95% uncertainty in the normal stress $\overline{uu}$ measurement is presented. Typical values of the uncertainty are about 12% of the measured value.

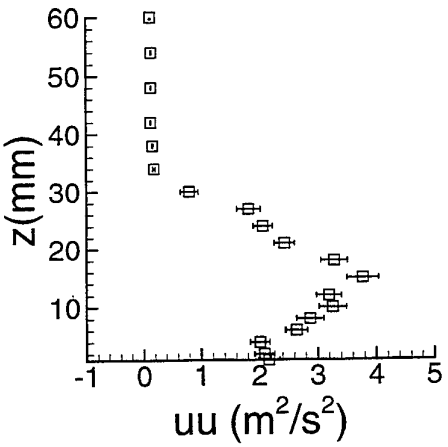


Figure 2: 95% uncertainty in $\overline{uu}$ measurement at x=10D, and y=1.07D; λ = 1.0.

3 RESULTS AND DISCUSSION

A major feature of the current flow is a single streamwise vortex in the cross-plane (y-z plane) downstream of the jet exit. The formation of the single vortex follows an initial flow region immediately downstream of the jet exit where complex flow physics are present. Amongest them are spanwise moments introduced by the skewed jet, production of cross-plane vorticity through the jet-cross flow interaction, turbulent shear stress production, flow entrainment, etc. Apart from the velocity measurements on the cross-sections downstream of the jet exit, measurements were also conducted on a rectangular plane parallel to the solid surface around the jet exit. These measurements serve to highlight the induced flow features while the streamwise vortices are being formed on the cross-plane. Results at $\lambda = 0.5$ and 1.0 are presented in Figs. 3 and 4. Immediately downstream of the jet exit, the flow is characterized by entrainment and regions of flow circulation are observed in the vicinity of the jet exit. On the surface, oil flow suggests that a spiral point is formed downstream of the jet exit (no included). Measurements at z=2.5mm show no recirculation flow region at this height, suggesting the confinement of the recirculation flow region.

The longitudinal vortex could be clearly seen in the velocity vector plots (see later discussion). The changes in the jet velocity ratio will only alter the surface flow pattern quantitatively. Downstream in the immediate vicinity of the jet exit, the velocity vectors indicate that on the downwash side, the flow is quickly turned towards the jet skew direction. This feature reflects both the effect of the spanwise moment introduced by the skewed jet and the forming of the streamwise vortex after the jet exit which induces the secondary spanwise flow. The contours of the flow speed show highly distorted flow outside the jet exit with a high speed core on the downwash side (Figs. 3(b) and 4(b)), which is followed downstream by a low speed area. This area of low speed flow is caused by the induced flow entrainment/turning flow the oncoming turbulent boundary layer flow. The interaction between the jet flow and the induced low speed flow is highlighted by the complex turbulent kinetic energy distribution (Figs. 3(c) and 4(c)). High turbulent kinetic energy level, $(\overline{u}^2+\overline{v}^2+\overline{w}^2)/2$, is observed. The area of high turbulent kinetic energy is localised in the upwash side, close to the jet column. Turbulent kinetic energy production occurs in the shear flow between the jet column moving away from the outlet with a O(1) normal velocity component and the essentially planar slower flow circumventing

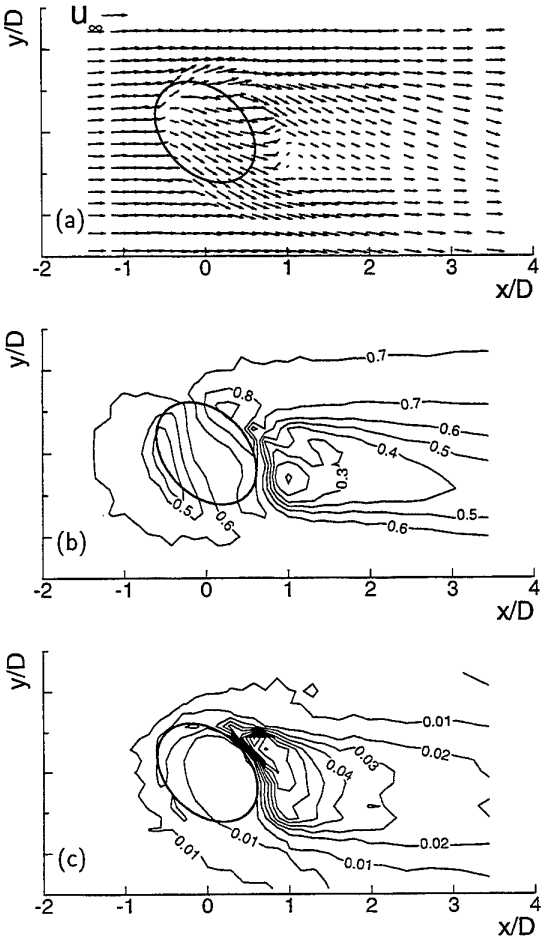


Figure 3: Flow around the jet exit at $\lambda = 0.5$ and z=2.5mm: (a) velocity vectors; (b) speed contours; and (c) turbulent kinetic energy contours.

the jet. There is some analogy with the wake formed downstream of a cylindrical body but the clockwise vorticity in the x-y plane induced by the jet skew gives a unique flow. This is asymmetric, featuring a kinetic energy maximum offset with respect to the y=0 line, as opposed to a symmetric wake.

Major features of the streamwise vortex can be seen in Figs. 5, 6 and 7, where the cross-plane velocity vectors are shown. Measurements confirm that a single vortex is generated by a jet downstream of the jet exit. In Fig. 5, the effect of the jet velocity ratio is shown. Whilest at $\lambda = 0.75$, the streawise vortex is relatively weaker compared with that at $\lambda = 1.25$, its centre is located much closer to the wall. Strong spanwise velocity is produced at $\lambda = 1.25$ by the co-rotating jets. Fig. 6 gives vortex development in

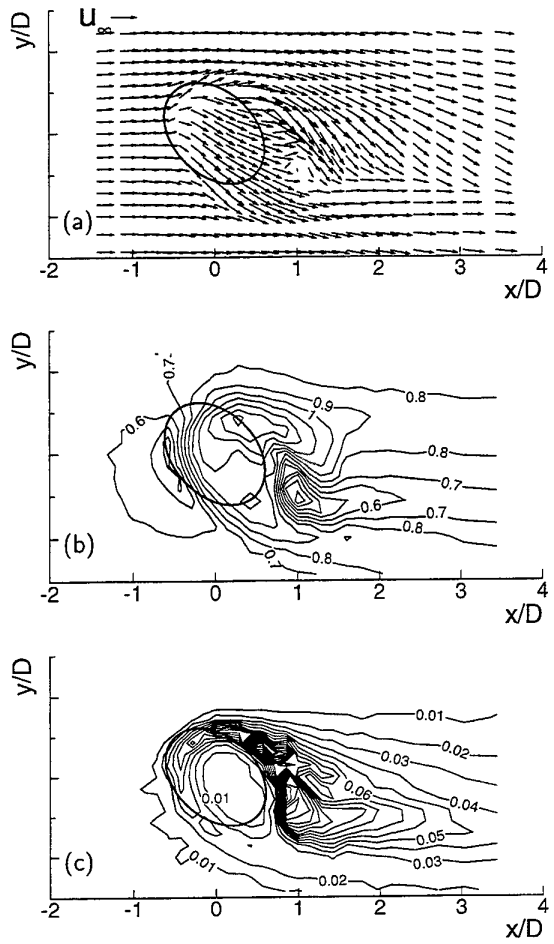


Figure 4: Flow around the jet exit at $\lambda = 0.5$ and z=2.5mm: (a) velocity vectors; (b) speed contours; and (c) turbulent kinetic energy contours.

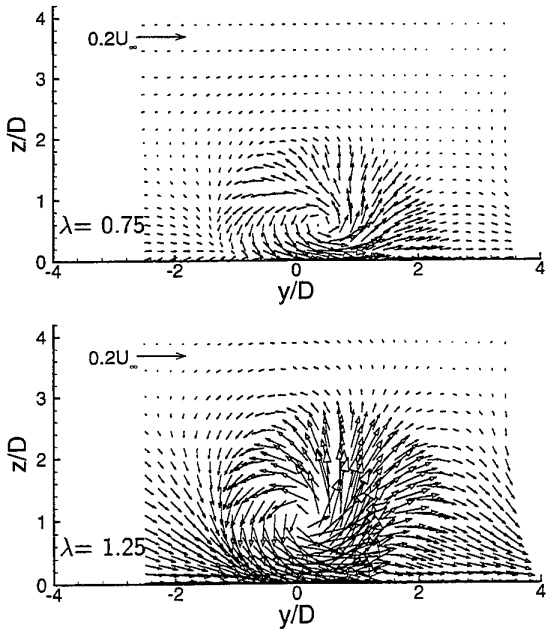


Figure 5: Effect of jet velocity ratio; Cross-plane velocity vectors at x=5D.

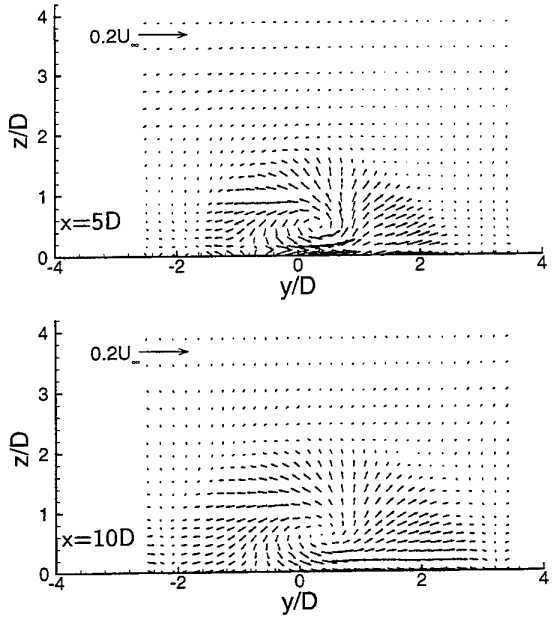


Figure 6: Cross-plane velocity vectors at $\lambda = 0.5$.

the streamwise direction. The vortex is diffused in the turbulent boundary layer and its size increased downstream. Fig. 7 shows the vortex array downstream of the $\lambda = 1.5$ jets, suggesting the current nozzle spacing is adequate for the streamwise vortex development with discrete vortices observed at x=20D.

An earlier single jet study[3] proved the existence of two contra-rotating vortices immediately downstream of a jet exit. However, the two vortices are of different strength and size. The weak one disappears rather quickly, leaving the primary streamwise vortex as seen in Figs. 5, 6 and 7. The array of the inclined jets allow the generation of an array of streamwise vortices trailing downstream. One effect of these vortices is flow convection inside the boundary layer. Fluid flow with high streamwise velocity (mean kinetic energy) is convected to the near-wall

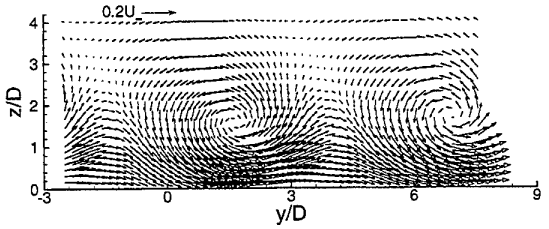


Figure 7: Cross-plane velocity vectors at $\lambda = 1.5$ and x=20D.

region on the downwash side and fluid flow with low streamwise velocity is convected to regions away from the wall.

In Figs. 5, 6, and 7, the flow in the cross-plane is seen to be dominated by a single vortex. However, an area of contra-rotating vorticity still exists on the upwash side of the main vortex. This feature can be observed in Fig. 8. In Fig. 8, an area of induced vorticity (positive value) is located to the upwash side of the main vortex. This feature is observed at all the jet velocity ratios tested. The induced vorticity is at its strongest at the high velocity ratios. Fig. 8 also gives an indication of the size of the main vortex and its location. It can be seen that at the low jet velocity ratios the vortex is located near the wall. This feature highlights an important feature of air jet vortex generator–that a vortex can be created near the control surface though jet velocity ratio changes. From the velocity vectors, it can be seen that the main vortex experiences changes in both size, strength, and position with the jet velocity ratio. The strength of the vortex is described in this study by the maximum streamwise vorticity and circulation level in the cross-plane. The measured vortex parameters are given in Tables 1 and 2, including the maximum vorticity (Ω_m), position of the maximum vorticity (y_m, z_m), vorticity at centre of the vortex (Ω_c), centre of the vortex (y_c, z_c), and circulation level (Γ). The circulation level is defined as

$$\Gamma = \int_y \int_z \Omega_x dy dz$$

In calculating the circulation level, only data with value less than -0.05 are used. This practice helps to eliminate the noise present in the measured data. According to Table 2, the maximum vorticity is always located beneath the centre of the main vortex and is to the upwash side of the centre of vortex.

As the vortex develops downstream of the jet exit, it moves in the spanwise direction and away from the solid wall due to the influence of the wall

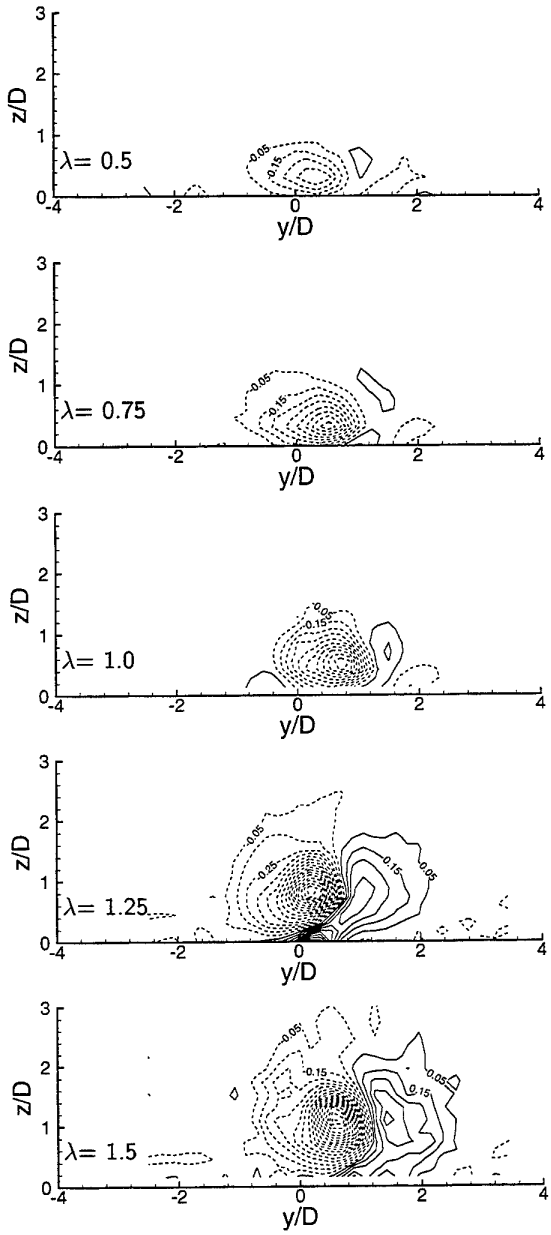


Figure 8: vorticity contours at x=5D.

and the adjacent co-rotating vortices. The reduction in the vortex strength is quite rapid (see Table 1), where a linear reduction with downstream distance is noted. As the jet velocity ratio varies, the characters of the vortex experience changes as well. Table 2 suggests this change of character occurs between $\lambda = 1.0$ and 1.25. When the jet velocity ratio is lower than unity, the main vortex is deeply embedded in-

side the turbulent boundary layer. The centre of the vortex moves in the skew direction of the jet and also away from the wall. When the jet velocity ratio is increased above unity, the spanwise position of the vortex changes, being reduced to $y_c/D = 0.116$ at $\lambda = 1.25$ from $y_c/D = 0.596$ at $\lambda = 1$ and x=5D. In the mean time the movement away from the wall continues. It is obvious that the size of the vortex changes significantly above $\lambda = 1.0$. As the jet velocity ratio increases, the maximum vorticity rises almost linearly between $\lambda = 0.5$ and 1.25. The rate of increase with the jet velocity ratio is slowed down near $\lambda = 1.5$. At velocity ratios above $\lambda = 1.5$, the earlier single jet study[5] suggested that the jet will penetrate the turbulent boundary layer. When this occurs, the strength of the vortex will remain high as in the freestream the effects of the turbulent dissipation and diffusion are reduced compared to that inside the boundary layer. However, the effect of the vortices on the near-wall flow is reduced and their effectiveness in flow control restricted.

Examples of the induced turbulent stress distribution are given in Fig. 9. In Fig. 9, the main shear stress distribution is presented at x=5D for all the jet velocity ratios tested. The measured primary shear stress $-\overline{u'w'}$ does reveal an important feature of the flow, namely the existence of an area of negative $-\overline{u'w'}$ between the center of the vortex and the wall. This area of negative $-\overline{u'w'}$ is located directly beneath a local area of high $-\overline{u'w'}$. The areas of low primary shear stress and high primary shear stress are separated in the transverse direction by the center of the vortex. This feature characterises the flow at $\lambda > 0.5$.

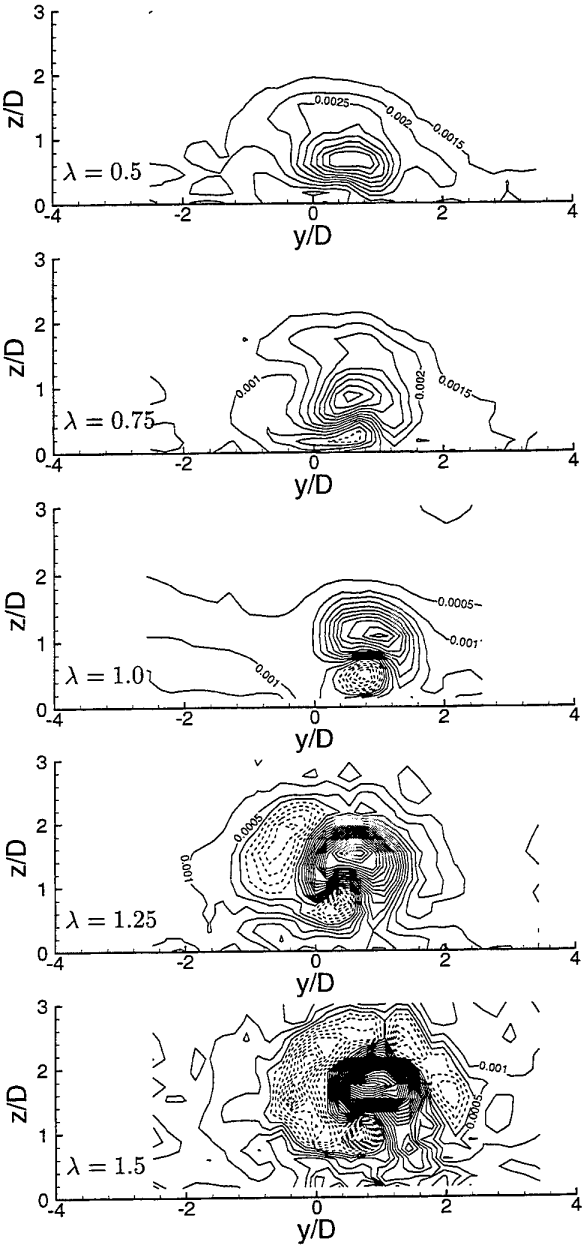


Figure 9: Primary shear stress $(\overline{-uw})$ contours at x=5D.

4 SUMMARY

A model test study has been conducted of longitudinal co-rotating vortices generated by an array of inclined jets in a turbulent flat plate boundary layer. Velocity measurements were performed for a number of jet velocity ratios and at different locations, yielding a database of both mean and turbulent properties. The study also provided insight into the flow physics. In particular, it was observed that:

- A single main vortex follows each skewed jet.
- Immediately after the jet exit, the flow is characterized by induced flow entrainment.
- As the vortices develop downstream, the centre of the vortex moves spanwise in the skew direction of the jet and away from the wall. Increasing the jet velocity ratio increases the maximum vorticity almost linearly between $\lambda = 0.5$ and 1.25. The rate of increase slows down above $\lambda = 1.25$.
- The characters of the vortex change significantly when the jet velocity ratio is increased above unity. When the jet velocity ratio is below unity, the main vortex is deeply embedded

inside the boundary layer. When the jet velocity ratio is increased above the unity, the size and strength of the vortex increase significantly.

ACKNOWLEDGEMENT

The study is supported under EPSRC grant GR/J17722. Aldo Rona's attendance to the meeting was supported by the von Karman Institute through the EU TMR grant ERB 4001 GT 970345.

References

[1] Wallis, R.A, 1956, A preliminary note on a modified type of air-jet for boundary-layer control, ARC, CP-513, London, U.K.

[2] Johnston, J.P. and Nishi, M., 1990, Vortex generator jets–a means for flow separation control, *AIAA J.*, Vol. 28, No. 6, pp. 989–994.

[3] Zhang, X. and Collins, M.W., 1993, Flow and heat transfer in a turbulent boundary layer through skewed and pitched jets, *AIAA J.*, Vol. 31, No. 9, pp. 1590-1599.

[4] Freestone, M.K., 1985, Preliminary tests at low speeds on the vorticity produced by air-jet vortex generators, Research Memo. Aero. 85/01, Dept. of Aeronautics, City University, London, U.K.

[5] Zhang, X. and Collins, M.W., 1997, Nearfield evolution of a longitudinal vortex generated by an inclined jet in a turbulent boundary layer, *ASME Journal of Fluids Engineering*, Vol. 119, pp. 934-939.

[6] Zhang, H.L. and Zhang, X., 1996, An LDA study of longitudinal vortices embedded in a turbulent boundary layer, *The 8th International Symposium on Applications of Laser Techniques to Fluid Mechanics*, Lisbon, Portugal, July 8-11.

[7] Moffat, R.J., 1988, Describing the Uncertainties in Experimental Results, *Experimental Thermal and Fluid Science*, Vol. 1, pp. 3-17.

[8] Benedict, L.H. and Gould, R.D., 1996, Towards better uncertainty estimates for turbulence statistics, *Experiments in Fluids*, **22**(2), pp. 129-136.

Table 1: Circulation variation at $\lambda = 1.0$.

	x=5D	x=10D	x=20D	x=30D
Γ	-0.608	-0.501	-0.385	-0.264

Table 2: Effect of velocity ratio at x=5D.

	$\lambda = 0.5$	0.75	1.0	1.25	1.5
Ω_m	-0.436	-0.824	-1.013	-1.631	-1.514
y_m/D	0.357	0.536	0.714	0.179	0.536
z_m/D	0.307	0.307	0.568	0.879	1.093
Ω_c	-0.323	-0.480	-0.672	-1.202	-1.478
y_c/D	0.290	0.401	0.596	0.116	0.463
z_c/D	0.485	0.584	0.779	1.031	1.248
Γ	-0.210	-0.472	-0.608	-0.216	-0.514

SESSION 12

Two-Phase Flows
Instrumentation II

PIV IN TWO-PHASE FLOWS: SIMULTANEOUS BUBBLE SIZING AND LIQUID VELOCITY MEASUREMENTS

I. Dias and M.L. Riethmuller

von Kármán Institute for Fluid Dynamics, Chaussèe de Waterloo 72
1640-B Rhode-St-Genèse, Belgium

ABSTRACT

A two-phase measurement technique based on the simultaneous sizing of the dispersed phase and PIV measurement of the continuous phase is presented.

The referred technique has been applied to study the formation of bubbles, when air is injected into quiescent water through a single needle.

The efficient application of the PIV technique to measure the liquid velocity field in bubbly flows is based on the use of fluorescent tracers combined with optical filters. Strong optical effects at the air/water interface limit the use of the PIV image for the accurate determination of the bubble contour. Therefore, a supplementary CCD-camera acquires simultaneously the bubble shadow images.

The results show the evolution of the liquid velocity field around a growing bubble during its formation cycle, as well as a comparison between the velocity of motion of the bubble interface and the velocity of the immediate surrounding liquid.

1. INTRODUCTION

The injection of gases into liquids in the form of bubbles is a common industrial operation in the casting of metals and chemical or nuclear reactors. Recently, strong effort has been conducted to develop theoretical and mathematical models able to predict the complex behaviour of bubbly flows. Nevertheless, the details of the interaction between the liquid flow field and the forming bubbles are still not well established. Therefore, detailed experimental data is required to improve the understanding of the physical phenomena involved, as pointed out by Murai and Matsumoto (1995) and Hassan and Canaan (1991).

The present work concerns the experimental investigation of the bubble formation process. Individual bubbles are created when air is injected, at low flow rate, through a single needle into stagnant water. The upward movement of the detached bubbles to the free surface follows an helicoidal path, creating a strong asymmetric wake which might influence the formation of the subsequent bubble.

The first objective of this study is the development of a two-phase visualisation and measurement technique to provide simultaneously the liquid velocity and the size of the forming bubble. The second objective is the application of the referred measurement technique to investigate the importance of the bubble wake effect on the bubble formation process.

PIV is a non-invasive measurement technique yielding quantitative, full-field, instantaneous velocity maps of the flow (Meynart and Lourenço, 1984). Several studies have been reported, where the velocity fields in a bubbly flow system are determined using PIV for the continuous phase and PTV - particle tracking velocimetry - for the dispersed phase [Sridhar *et al* (1991); Liu and Adrian (1993); Philip *et al* (1994); Oakley *et al* (1995); Hilgers *et al* (1995)], or simply PTV for both phases as reported by Hassan *et al* (1993). Recently, Gui & Merzkirch (1996) developed a digital mask technique to separate the phases in a two-phase flow.

Fluorescent seeding of the liquid phase combined with optical filters, allows the discrimination of the particles from the light reflected by the dispersed phase [Hassan *et al* (1993); Philip *et al* (1994); Hilgers *et al* (1995)]. This aspect is important when a large fraction of the PIV image is occupied by reflections from the interface.

The present technique has the advantage of yielding accurate sizing of the dispersed phase structures and high density velocity vectors of the continuous phase, which is particularly important in the analysis of the bubble formation process.

2. EXPERIMENTAL INVESTIGATION

2.1 Set-up

The experimental study of the bubble formation process is performed in the facility represented in Fig. 1. The measurement technique couples the liquid PIV measurement with the sizing of the bubbles using the shadow detection method.

The bubbles are generated by the injection of air into a stagnant water tank, through a needle mounted on its base. This container is constituted by a Plexiglas square base of 97 mm side and 4 mm thickness glass walls of 154 mm height. It is filled with tap water up to a height of 100 mm, and the top is open to the atmosphere. The stainless steel needle has internal and external diameters, respectively of 3 and 4 mm, and 30 mm of length. Constant gas flow rate regime is ensured by the use of a sonic hole at the base of the needle in the air feeding system. Air flow is provided by a 50 l pressurised gas bottle. A needle valve allows a fine control of the flow rate that enters the air reservoir mounted underneath the water tank and connected to the needle. This stainless steel cylindrical reservoir (60 mm diameter and 40 mm height), is equipped with a Validyne transducer monitoring the pressure. The air issued from this reservoir passes through a 25 μm diameter sonic hole, ensuring a constant mean air flow rate entering at the needle base. "Constant gas flow rate" regime is guaranteed when sonic working conditions are attained, i.e. pressure in the reservoir must be at least 1.9 times larger than the pressure at the needle entry; and the pressure in the reservoir is kept constant. During the time duration of one experiment, this last requirement is easily satisfied due to the use of a pressurised gas bottle as feeding system. The absolute pressure in the gas reservoir is 1.92 bar, corresponding to an air flow rate of 0.1485 ml/s and a bubbling frequency around 2 Hz.

The PIV image is obtained illuminating the flow with an Argon-Ion laser, Spectra-Physics model 2016-05S. The laser is working on "single wavelength mode", having as primary output wavelength 514.6 nm and a power of 2 Watt. A system of lenses, pin-holes and a Bragg cell is employed to expand the initial 1 mm circular Gaussian laser beam into a flashing converging light sheet of approximately 1 mm thickness and 2 cm in width, at the camera field of view (FOV). The acousto-optic modulator (Bragg cell) used is from Isomet, model 1201E-1 and the Digital drive, model 221A-2 (series 200), works with a centre frequency of 40 MHz. The laser sheet is aligned with the axis of the needle and the viewing area of the camera is 14x10 mm^2. A system composed by a normal lens is not suitable to visualise such a small observation area. Instead, a microscope Technical 2 from Jenoptik Jena, equipped with a 164 mm lens and an ocular (MF-Meβprojektif K 4:1), yielding a magnification of 1.6 is used and directly connected to the acquisition camera. The bubble obstructs the passage of the light to the opposite side of the laser. As a consequence a significant part of the FOV is in the dark. A circular flat mirror (46 mm diameter), forming an angle of 15° with the tank wall is used to reflect the upper part of the laser sheet. Since it is not blocked by the needle or bubble, it illuminates the dark side of the bubble. The lack of symmetry of the flow surrounding the bubble justifies the need to illuminate both sides of the bubble. A red filter is placed in front of the camera which captures the images of the particles to block the intense green light reflected by the bubbles and allow the passage only of the light emitted by the fluorescent particles. The high pass filter (wavelength) used is opaque below 515 nm. The red filter, microscope and the CCD-camera are aligned and positioned at 90° with the laser sheet and parallel to the viewing area.

The bubble contour images are acquired by another CCD-camera equipped with a 105 mm Nikkor-P photographic lens (aperture 1:2.5) and an extension tube, aligned with another red filter and positioned with an angle of 60° with the side wall of the tank. The red filter is similar to the one used for the PIV camera, because its main objective is also to suppress the strong reflections of the bubble interface. The background illuminating source is a diffused white light (100 Watt) located on the opposite side of the tank, facing the acquisition camera which collects light in forward scattering mode. The image obtained with this camera is the shadow of the bubble. Although the light emitted by the fluorescent particles is not intercepted before reception by the acquisition camera, its intensity is low in comparison with the background white light and it does not reduce the contrast quality of the bubble contour images.

Both CCD-cameras used in this experiment are from i2S France, model IEC 800BC with 756(H)x581(V) pixels of resolution. The PIV camera works in Standard European video CCIR mode (40 ms). Laser flashes duration is equal in both fields of the interlaced image (2.4 ms), and the pulse separation is 16 ms. The bubble contour camera works in shutter mode (integration time of 1 ms), while the background white light is continuous. Fig. 2 shows the timing diagram of the CCD-cameras working modes and respective illumination systems.

The two CCD-cameras and their respective acquisition systems are synchronised in line mode by connecting the video output of the PIV camera (master) to the input of the contour camera (slave). The image acquisition system is composed by a Matrox PIP-1024 acquisition board and controlled by PC-Scope software. This system acquires four frames of 512x512 pixels each. The synchronisation precision is found to be better than 1 ms.

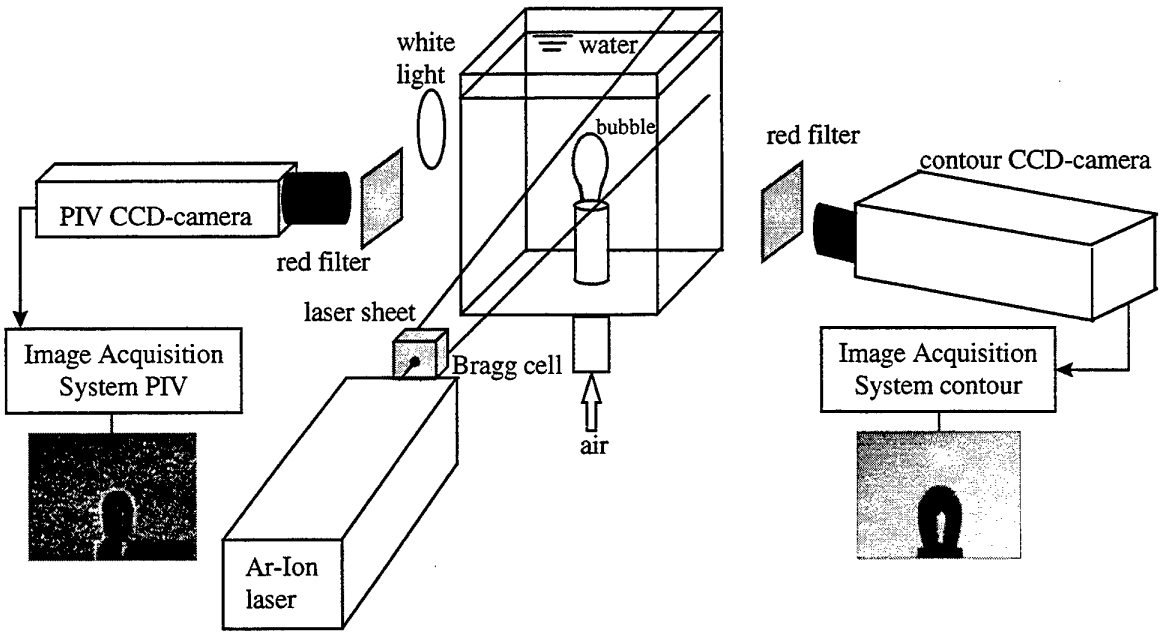


Fig. 1 Schematic representation of the experimental set-up

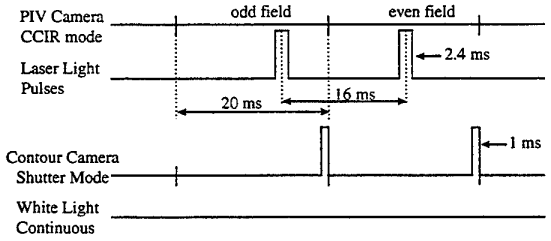


Fig. 2 Timing diagram of the cameras working modes and illumination systems

2.2 Fluorescent Particles

Fluorescent seeding of the liquid phase allows a clear discrimination of the signal emitted by the particles and the intense neutral reflections occurring at the bubble interface.

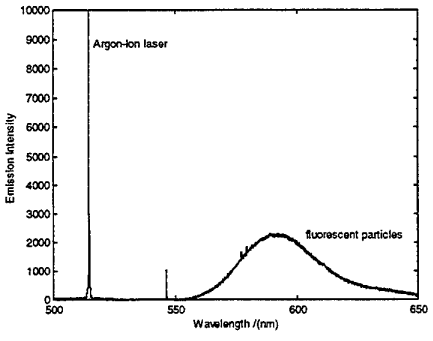


Fig. 3 Emission spectra of the laser (λ=514.6 nm) and fluorescent particles (λ~590 nm)

In the study of the bubble formation process, this aspect is important because the interface reflections occupy a large part of the FOV. The emission spectrum of the incident light, Argon-Ion laser emitting at 514.6 nm (green), and the fluorescence signal emitted by the particles around 590 nm (red) are shown in Fig. 3. The red filter blocks the passage of light below 515 nm.

The neutrally buoyant particles (10 μm) are a light orange vinyl pigment (water soluble), from Lefranc & Bourgeois.

3. DATA PROCESSING

3.1 Shadow Detection Method

The interlaced images of the bubble shadows are separated into the odd and even fields. The contour of the bubble in each of the fields is then determined.

The algorithm developed to determine the bubble interface co-ordinates in an image is a new combination of different basic schemes. This method can be summarised by the following sequence of operations:

1. image gradient determination (G)
2. image gradient histogram equalisation (G*)
3. images subtraction (D)
4. binarization according to an appropriate threshold
5. contour determination.

Given a two-dimensional image function F(x,y), the magnitude of the vector gradient G[F(x,y)] is represented computed as follows:

$$G=\left[\left(\frac{\partial F}{\partial x}\right)^2+\left(\frac{\partial F}{\partial y}\right)^2\right]^{\frac{1}{2}} \quad (1)$$

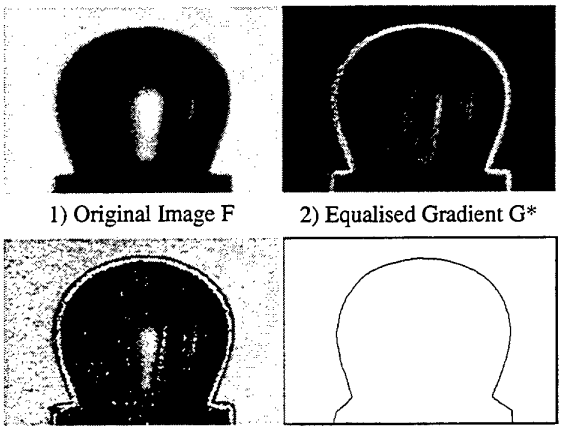
Typically, the histogram of the field gradient has a narrow distribution band. To improve the contrast of the image, its histogram is flattened by performing a linear contrast stretching operation (*i.e.* dark becomes darker and bright becomes brighter).

As proposed by Bow (1992), the subtraction of the equalised image gradient (G*) to the original noisy image (F) is the image difference (D):

$$D=F-G^* \quad (2)$$

which denotes a high pixel level transition at the edges and a low fine noise level. In this case, a single threshold value is suitable for the whole image binarization.

The proposed method has the advantage of eliminating fine noise effect and operates with an almost insensitive threshold level for the binarization. The bubble interface co-ordinates are obtained by detecting line-by-line the left and right transitions of the binarized image. An example of the sequence of operations previously described, starting from the original noisy image until obtaining the bubble contour, is shown in Fig. 4. The uncertainty in the size (equivalent diameter) determination is estimated to be 3%.



1) Original Image F 2) Equalised Gradient G*

3) Difference Image D 4) Contour

Fig. 4 Sequence of operations performed in the shadow image for the bubble contour detection

3.2 Particle Image Velocimetry

The digital PIV images are interrogated using the cross-correlation algorithm WIDIM, developed by Scarano (1997). This procedure performs the displacement of the second exposure interrogation area to compensate for the loss-of-pairs due to the in-plane motion and optimises it with an iterative procedure.

The processing of the acquired images uses a Gaussian three-point-fit for the sub-pixel interpolation peak determination. The original interlaced PIV image of 512x512 pixels is separated into the odd and even fields of 512x256 pixels resolution. The initial window size is 64x64 pixels, one step refinement is performed yielding a final window size of 32x32 pixels. A 75% overlapping factor is used leading to a final grid spacing of 8x8 pixels, and a total number of 1769 vectors. The percentage of non-validated vectors keeps below 5%.

The velocity uncertainty is mainly associated with the uncertainty in determining the particles images displacement, which is less than a tenth of a pixel. The large dynamic range of the present case, leads to an uncertainty of 2.5% within a confidence level of 75%.

4. RESULTS AND DISCUSSION

4.1 Optical Effects

Important optical effects occur at the air/water interface, depriving the 'extraction' of the bubble contour from the PIV image.

A first result concerns this preliminary study, done in order to determine the nature of these optical effects. This test consists in the immersion of a hollow glass bulb (17 mm external diameter and 0.5 mm glass thickness) in the container with stagnant water and fluorescent particles. The bulb and surrounding water are illuminated with a green light sheet and an image is acquired (Fig. 5). A red filter is used to block the green light before reaching the camera. The glass bulb is used to simulate a static bubble, avoiding the complexity of a moving interface.

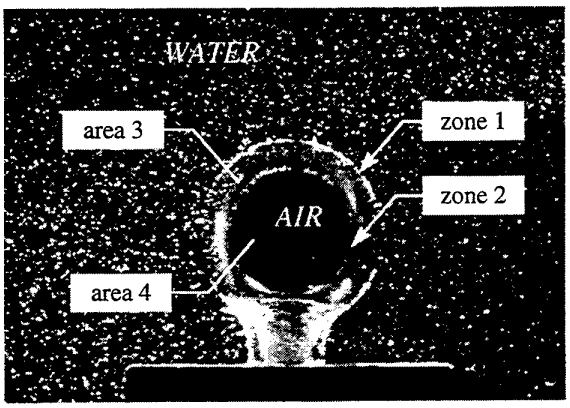
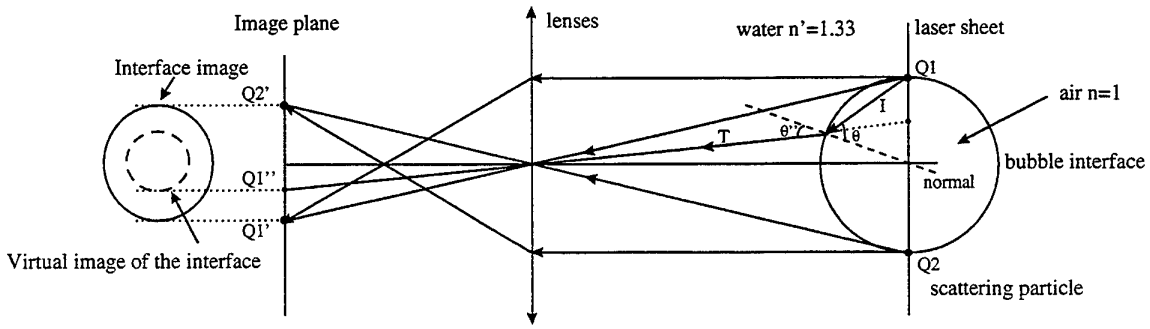


Fig. 5 Image of an hollow glass bulb and surrounding stagnant water with fluorescent particles



I - Incident Ray T - Refracted Ray θ - Angle of Incidence θ'' - Angle of Refraction

Fig. 6 Simplified optical ray tracing diagram of the beams scattered from particles laying on the surface of a spherical bubble.

The external surface of the bulb (zone 1) can be clearly distinguished, because a fine layer of fluorescent particles is sticking on this static surface. A virtual image of the bubble surface (zone 2), that in the camera image plane is seen inside the real surface (zone 1) is yielded as a result of the internal refractions of the image of particles laying on the bubble surface. Area 3 is the region delimited by the real external surface of the bubble (zone 1) and the virtual image of the same surface (zone 2). It is important to understand that it does not correspond to the real thickness of the glass bulb, as it appears six times larger.

A simplified ray tracing model of a spherical air bubble, with a thin layer of fluorescent particles immersed in stagnant water and cross illuminated by a laser sheet, is schematised in Fig. 6. When a light ray excites the surface static particles (Q1 and Q2), the latter emit fluorescent light in all the directions. Following the optical path of one of the light rays inside the bubble (I), when it reaches the air/water interface part of the light is reflected inside the bubble and other part refracts through the water (T). The light ray is travelling from air to water, *i.e.* increasing refractive index, according to Snell's law the ray is deviated towards the normal ($\theta'' < \theta$). In the image plane, this (internal) refraction results in a virtual image of the particle (Q1'' and Q2'') positioned closer to the axis centre than the image of the particles (Q1' and Q2') resulting from the (external) reflections. The "integration" of this effect over all the bubble surface yields as result an internal concentric ring, called the virtual image of the interface, corresponding to the zone 2 in Fig. 5.

In area 3 (Fig. 5), external reflections of the particles in the surrounding liquid can be observed. The intensity of those reflections undergoes a rapid decay with respect to zone 1. The images of the particles in both sides of the interface, between the two phases, within a small region are identical (mirror effect), leading to the erroneous idea that this region (area 3) might correspond to the continuous phase. In the black core of the bulb image (area 4), low intensity image of the particles are still existing but can hardly be seen. The optical effects observed in the hollow bulb, such as the virtual image of the surface and external reflections of the seeding particles are expected also for a bubble interface.

In Fig. 7, an example of a bubble contour image and the corresponding PIV image of the liquid around the bubble can be observed. In the PIV image, the bubble core is identified as the dark central region apparently without particles images (area 4 in the bulb test).

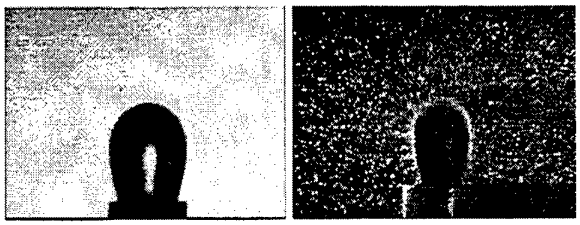


Fig. 7 Original bubble contour image (left) and corresponding PIV image of the surrounding liquid (right)

The co-ordinates of the bubble surface are obtained after processing the bubble image. This information is then superimposed to the corresponding PIV image (Fig. 8). The comparison between the bubble co-ordinates, obtained by the contour image, and the borders of the bubble core in the PIV image reveals an important underestimation of the bubble size given by the PIV image.

Since the interface of a growing bubble is continuously moving, the external surface of the bubble cannot be clearly distinguished in the PIV image as it is possible in the bulb test. Referring to the bulb test, this means that the external limit of area 3 (zone1) cannot be defined in the PIV image. The determination of the bubble interface co-ordinates using the limits of the bubble core region is therefore incorrect. A correction scheme, allowing the determination of the bubble

surface (zone 1) knowing the borders of the bubble core region (zone 2), would yield inaccurate results because the local curvature of a growing bubble and therefore the thickness of the ring (area 2) is continuously changing. This fact emphasises the need for a second synchronised camera to accurately determine the bubble contour.

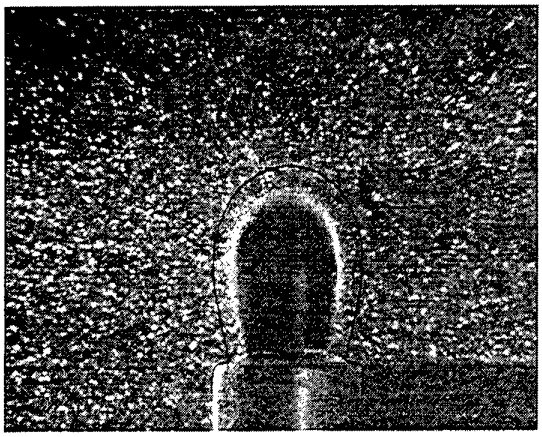


Fig. 8 PIV image superposed by the bubble contour

4.2 Velocity Comparison

The liquid velocity field evolution around a growing and detaching bubble in stagnant water can be observed in Fig. 9. The first field (top left) corresponds to the initial burst out of the air flow from the needle. This stage is one of the fastest of the whole formation cycle. Nevertheless, the magnitude of the vertical component of the surrounding liquid velocity is even higher than the one observed in the region immediately surrounding the bubble. Therefore, the wake of the preceding bubble might have an important suction effect on the formation of the following bubble and cannot, *a priori*, be neglected as made in many theoretical models available [Tan and Harris (1986); Liow and Gray (1988)].

In the necking phase, just prior to detachment from the needle (bottom right field), the wake effect becomes negligible. The bubble lift-off results simultaneously from the upward translation of the bubble and the liquid entrainment at its base.

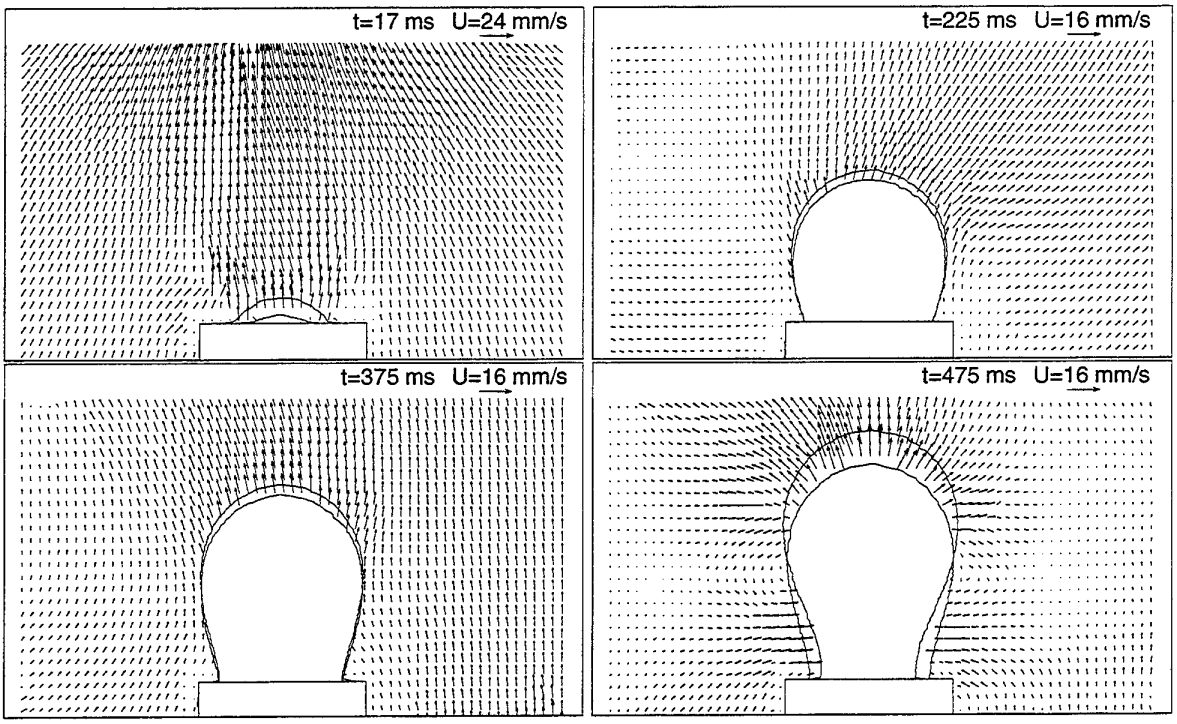


Fig. 9 Liquid velocity field (PIV) and bubble contours (shadow detection method).The two contours shown in each plot are separated in time by 20 ms. Needle external diameter is 4 mm.

The comparison between the liquid velocity profile, measured by means of PIV technique, and the theoretical solution for potential flow surrounding a translating sphere (Batchelor, 1979) can be observed in Fig. 10.

The experimental data presented corresponds to the final phase of bubble growth, as shown in Fig. 9 (bottom right). The velocity profile is extracted from the region above the top of the bubble, where potential flow assumption is valid, at an angle of 90^0 from the top surface of the bubble. In this position, the radial velocity corresponds practically to the streamwise velocity component.

In the necking phase of the bubble, just prior to detachment, the movement of the top of the bubble can be approximated by the upward translation of a sphere, because bubble expansion is negligible. According to the potential flow theory, provided the speed of the water is small enough for it to be regarded as incompressible, the radial velocity V_r in the water is:

$$V_r = \left(\frac{R}{r}\right)^3 V_T \qquad (3)$$

where R is the radius of the sphere, r is the radial distance from the centre of the sphere and V_T is the translation velocity. The input conditions for the determination of the potential flow solution are the equivalent bubble spherical radius R and the translation velocity. These parameters are evaluated from the bubble contour evolution, experimentally obtained with the shadow detection method. The top of the bubble is approximated by a sphere of radius R equal to 1.8 mm and the mean translation velocity is 42.3 mm/s.

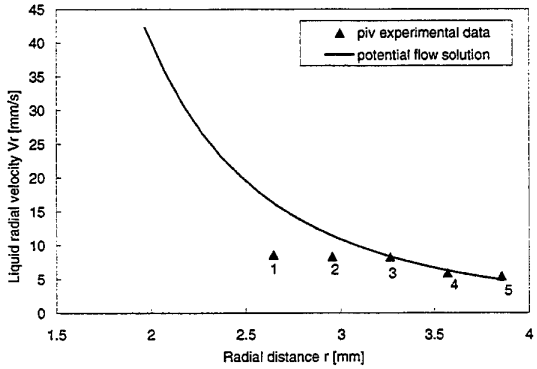


Fig. 10 Comparison of the liquid velocity measured by PIV and potential flow solution

It is assumed that the translation velocity is constant during the time interval (20 ms) between the acquisition of the two consecutive bubble contours. To obtain the PIV measurements, the laser is triggered at two different instants separated by 16 ms. The velocity determined is the velocity of the fluid averaged over this period. However, the theoretical solution is calculated for an instant that is the median between the two laser pulses.

The interpretation of the PIV measurements in the vicinity of the bubble moving interface is schematised in Fig. 11. The numbering of the velocity vectors in Fig. 11 corresponds to the PIV data shown in Fig. 10, where the first position is the closest outside of the second contour of the bubble. The velocity vectors number 1 and 2, are determined over final windows that partially include the gas phase. As mentioned previously, external reflections of the particles can be seen inside the bubble contour having a non determined and erroneous contribution for the evaluated displacement. These vectors cannot be considered as a valid measurement and show a clear underestimation when compared with the potential flow solution. Once the search window is entirely belonging to the liquid phase (vectors 3, 4 and 5), the PIV measurement is valid and is in agreement with the potential flow solution as it can be observed in Fig. 10.

The minimum distance from the air/liquid interface at which PIV measurements can be safely interpreted is half of the final window size. The absolute distance can be reduced using smaller windows, but on the other side the number of particles contributing to the correlation function is also diminished, decreasing the confidence level of the measurement.

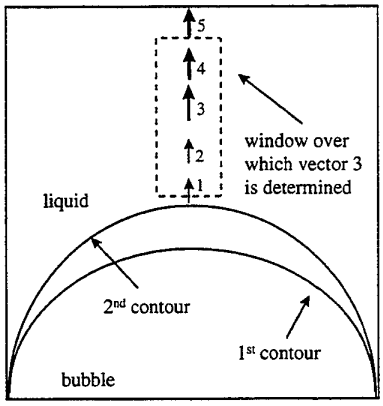


Fig. 11 Schematic representation (not at scale) of the liquid velocity vectors, measured using PIV technique, in the vicinity of a bubble moving interface. Vectors 1 and 2 are non valid measurements.

PIV is a valuable technique to analyze the overall features of the liquid flow around a forming bubble, but these results suggest that one should be careful in interpreting the velocity field in the vicinity of the air/liquid interface. It is therefore suitable to analyze the importance of the wake effect in the formation of the subsequent bubble. However, the

shadow detection method is preferable for the bubble contour and interface velocity determination. These results emphasize the importance of accurately determining the bubble contour, and therefore the need of a second synchronized CCD-camera.

5. CONCLUSIONS

In the present work, a two-phase measurement technique is used to study a bubble formation process. This technique is based on the simultaneous sizing of the bubble and PIV measurements of the surrounding liquid using fluorescent particles. Individual bubbles are formed when air is injected into stagnant water through a single needle. Constant gas flow rate bubbling regime is ensured by using a sonic hole in the air feeding system.

It is shown that the bubble contour co-ordinates cannot be obtained from the PIV image because of the important optical effects which occur at the bubble interface when crossed by a laser light sheet. Therefore, a supplementary CCD-camera is required to acquire the bubble contour images.

The bubble sizing algorithm performs the binarization of the difference image, instead of the original bubble contour image. This method has the advantage of eliminating fine noise effects and of operating with an almost insensitive threshold level for the binarization. The uncertainty in the bubble size and growth velocity determination, using the shadow detection method, is less than 3%.

The suction of the preceding bubble has a non-negligible effect on the formation of the following bubble.

The importance of accurately determining the bubble contour, using a second synchronised CCD-camera, in complement to the PIV measurement is emphasised by the limitations of the PIV technique to measure the flow field in the vicinity of the water/air moving interface.

REFERENCES

Batchelor, G.K. 1979, An introduction to fluid dynamics, pp. 451-479, Cambridge University Press.

Bow, S.T. 1992, Pattern recognition and image processing, pp. 248 - 311, Marcel Dekker Inc.

Gui, L. & Merzkirch, W. 1996, Phase-separation of PIV measurements in two-phase flow by applying a digital mask technique, ERCOFTAC, vol. 30, pp. 45-48.

Hassan, Y.A. & Canaan, R.E. 1991, Full-field bubbly flow velocity measurements using a multiframe particle tracking technique, Exp Fluids, vol. 12, pp. 49-60.

Hassan, Y.A., Philip, O.G., Schmidl, W.D. 1993, Bubble collapse velocity measurements using a particle image velocimetry technique, ASME, FED-172, pp. 85-92.

Hilgers, S., Merzkirch. W., Wagner, T. 1995, PIV measurements in multi-phase flows using CCD- and photo-camera, ASME, FED-209, pp. 151-154.

Liow, J.L. and Gray, N.B. 1988, A model of bubble growth in wetting and non-wetting liquids, Chem. Eng. Sci., vol. 43, pp. 3129-3139.

Liu, Z.C. & Adrian, R.J. 1993, Simultaneous imaging of the velocity fields of two phases, Particulate two phase flow, M.C. Roco ed., Butterworth-Heinemann, Stoneham, M.A

Meynart, R. & Lourenço, L.M. 1984, Laser speckle velocimetry in fluid dynamics applications, Digital Image Processing in Fluid Dynamics Lecture Series, von Karman Institute for Fluid Dynamics, pp. 175-195.

Murai, Y. & Matsumoto, Y. 1995, Three dimensional structure of a bubble plume - measurement of the three dimensional velocity, Flow visualization and image processing of multiphase systems, ASME, FED-209, pp. 187-194.

Oakley, T.R., Loth, E., Adrian, R.J. 1995, Cinematic two-phase PIV for bubbly flows, Flow visualization and image processing of multiphase systems, ASME, FED-209, pp. 123-128.

Philip, O.G., Schmidl, W.D., Hassan, Y.A. 1994, Development of a high speed particle image velocimetry technique using fluorescent tracers to study steam bubble collapse, Nuclear Engineering and Design, vol. 149, pp. 375-385.

Scarano, F. & Riethmuller, M.L. 1997, Iterative multigrid approach in PIV image processing with discrete window offset, submitted to Exp Fluids.

Sridhar, G., Ran, B., Katz, J. 1991, Implementation of particle image velocimetry to multi-phase flow. Cavitation and multiphase flow forum, ASME, FED-109, pp. 205-210.

Tan, R.B. & Harris, I.J. 1986, A model for non-spherical bubble growth at a single orifice, Chem. Eng. Sci., vol. 41, pp. 3175-3182.

ACKNOWLEGMENTS

The partial support of "FUNDAÇÃO PARA A CIÊNCIA E TECNOLOGIA - PORTUGAL", program PRAXIS XXI, who provides a Ph.D. fellowship (BD/5921/95) is gratefully acknowledged.

PIV Application for Spray Characteristic Measurement

Yuji Ikeda, Naoki Yamada, Nobuyuki Kawahara,
Daisuke Shimo and Tsuyoshi Nakajima

Department of Mechanical Engineering
Kobe University
Rokkodai, Nada, Kobe 657 JAPAN

1. INTRODUCTION

Particle Image Velocimeter (PIV) has been applied for various flow field measurements in many applications. This technique can solve problems in which laser Doppler velocimeter (LDV) techniques can hardly measure the instantaneous spatial flow structure because it is a point measurement. But, LDV can measure a time series velocity at high data rate, while recent digital PIV has a limitation in high repetition rate image recording due to laser, camera and other hardware limitations. PIV [Adrian, (1997), Grant, (1994)] has been applied for high resolution measurement [Keane, et al., (1994)], high speed flow [Bauckhage, et al., (1985), Humphreys, et al., (1993)] and high turbulent flow in SI engine [Tanabe, et al., (1995)], and so far. A recent improvement of processing technique and new developments of laser and camera such as cross-correlation camera can allow us to measure significant flow field information with good SN ratio and high spatial resolution. A selection of seeding particle material became less important because of high laser power and fine resolution camera. But, particle response and followability to high speed flow, highly oscillating flow and shear flow still remain as an unsolved problem. Furthermore, the disadvantage is that PIV can not process the flow image well when the particle diameter distribution is wide. A large particle produces strong scattered light intensity and causes a saturation on the photo-sensitive devices. On the other hand, scattered light intensity from small particles are proportional to the square of their diameter [Van de hulst, (1981)], that means the diameter information should be included in the PIV image as its intensity information. But, the light intensity depends also on particle number density. It is very hard to say that the diameter information can be extracted from the light intensity information. Flows of our interest are spray and combusting flows. In order to characterize the mass flux at points PDA is powerful tool to measure, but not good for wide a spatial distribution flow so as to define the flame front and its evaporation speed. Visualization technique can allow us to see the droplet trajectory in a plane but hardly provide information in time series. Especially, in application of PIV for spray characteristics measurement, these features should understood as droplet diameter, number density and velocity. To characterize spray behavior and its dynamics, the applications of phase Doppler technique [Safferman, et al., (1984), Baukhage, et al., (1985), Rudoff, et al., (1987)] have been carried out by many researchers [McDonell, et al., (1986), Edwards, et al., (1988), Akamatsu, et al., (1994), Kawahara, et al., (1995)]. Size-classified techniques [Edwards, et al., (1990), Kawahara, et al., (1996)] have been proposed as a better method to describe spray dynamics and its stokes number effect in practical burners. The velocity vector maps of each size-classes can be implemented and represented in two-dimensional plane. [Ikeda, et al., (1997)] This information can be very useful to evaluate PIV velocity vector maps.

The purpose of the present study is to describe the feasibility of PIV technique in application for practical spray characteristics measurements to resolve the velocity maps of different droplet size ranges. The comparisons of PIV data to size-classified PDA data were investigated in a practical spray burner.

2. EXPERIMENTAL APPARATUS

Figure 1 shows the experimental apparatus and Fig. 2 [Kawahara, et al., (1995)] shows the gun-type burner used in this measurement. A direct observation and laser sheet visualization are shown in Fig. 3. The heavy-oil was pressurized at 0.7 MPa and a hollow cone spray was produced at 60 degree [Kawahara, et al., (1995)]. In a previous study we have measured the detailed spray characteristics both

under isothermal and combustion conditions [Kawahara, et al., (1997)]. The light source was a Nd:YAG laser (double pulsed, 400 mJ per pulse), a cross-correlation camera (KODAK ES1.0) was used as the PIV components. The images were captured by CCD camera and then transferred to the processor (DANTEC FlowMap) and vector calculations was done in the processor and stored in the PC. The laser light duration at each pulse was 8 ns and the droplet movement on the CCD array while this 8 ns duration was ignoble small. The wavelength of the light source is 532 nm (green) and optical interference filter has been used in the reacting flow measurement to remove the strong emission from the flame. The area of interest in this study is 100x100 mm and the spatial resolution is 100 μm.

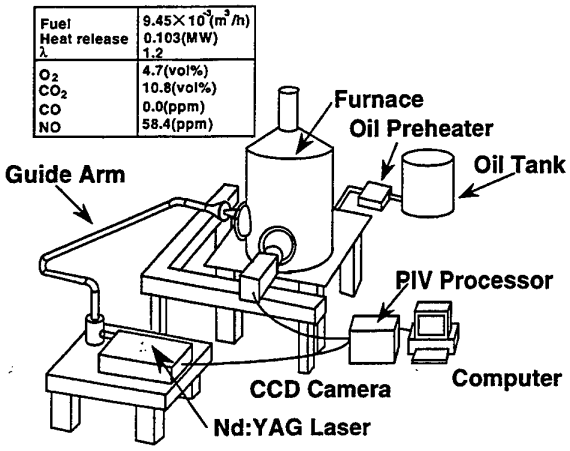


Fig. 1 Experimental apparatus

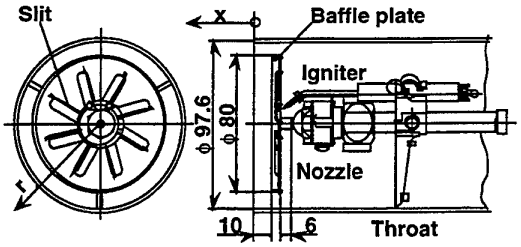


Fig. 2 Gun-type burner

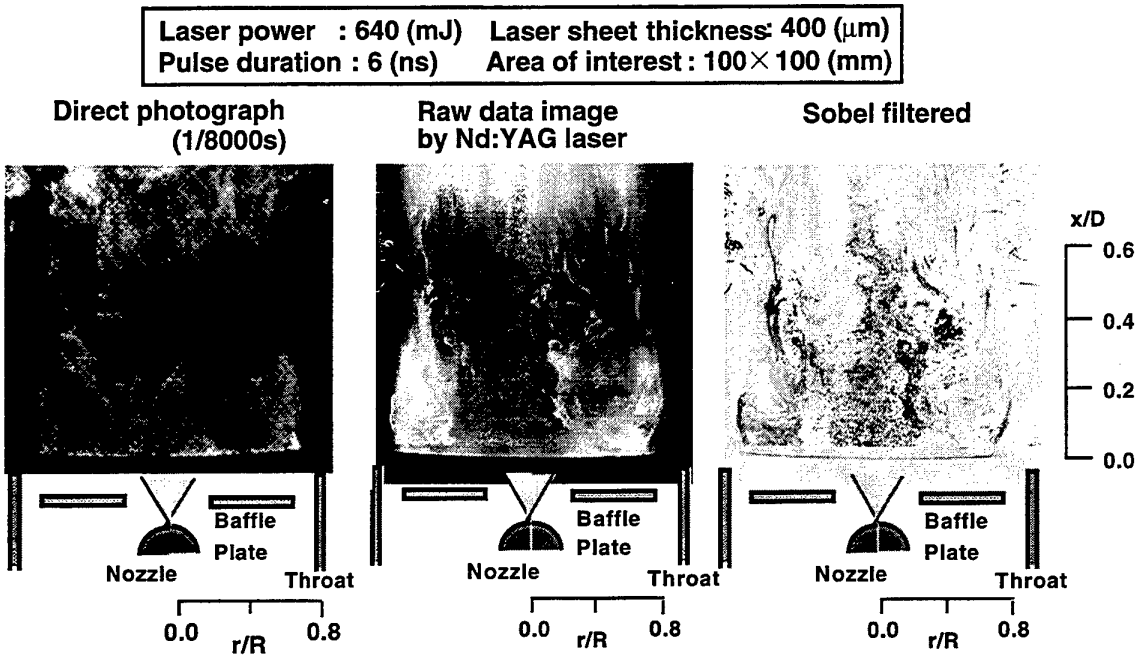


Fig. 3 Spray image

3. RESULTS AND DISCUSSION

3-1. Cold Flow Measurement

Two-dimensional velocity vector in several size-classes were measured in a cold flow by PDA [Kawahara, et al., (1995)]. The results are shown in Fig. 4. It was found that in the recirculating flow region, small fuel droplets could follow properly the turbulent recirculating flow and it is represented by their negative velocity. But large droplets penetrated into the recirculating flow region which was shown by the straight velocity vectors. This result was used to compare to those measured by PIV.

In our previous study, it was found that the recirculating zone was oscillating and the CO/CO_2 time variation were measured directly, that was about 100 Hz [Ikeda, et al (1995)]. This recirculating flows play a role of flame recess to prevent from soot formation and melting. LDV and PDA can show its fluctuating behavior but it was hard to show the spatial structure and its size. Then, PIV measurement were carried out to show the fluctuating behavior of recirculating zone as shown in Fig. 5. Here, an optical set-up and processing parameter were carefully examined. These fluctuating recirculating zone were without spray. Once, spray were injected in this flow, interaction of spray droplet behavior and turbulent shear characteristics were dramatically changed. That what we want to see and characterize.

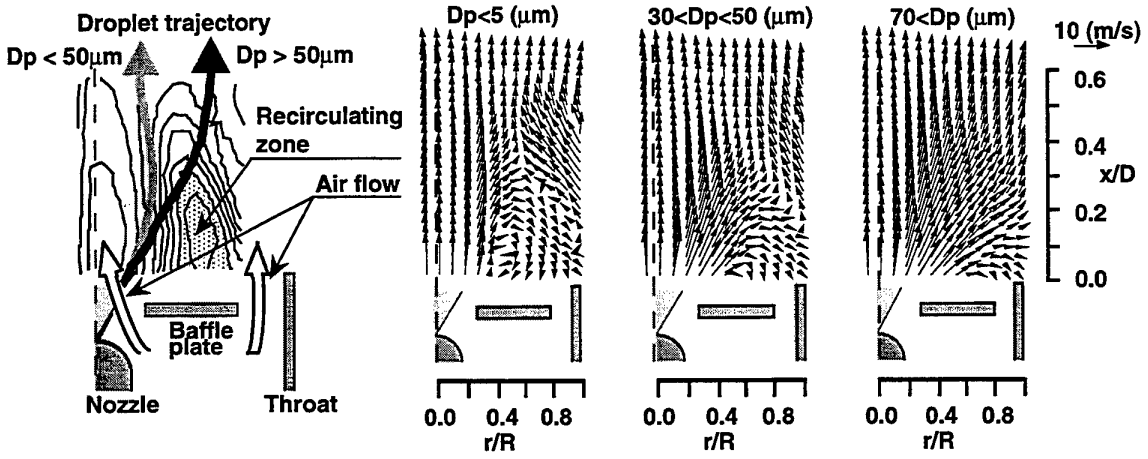


Fig. 4 Velocity vector

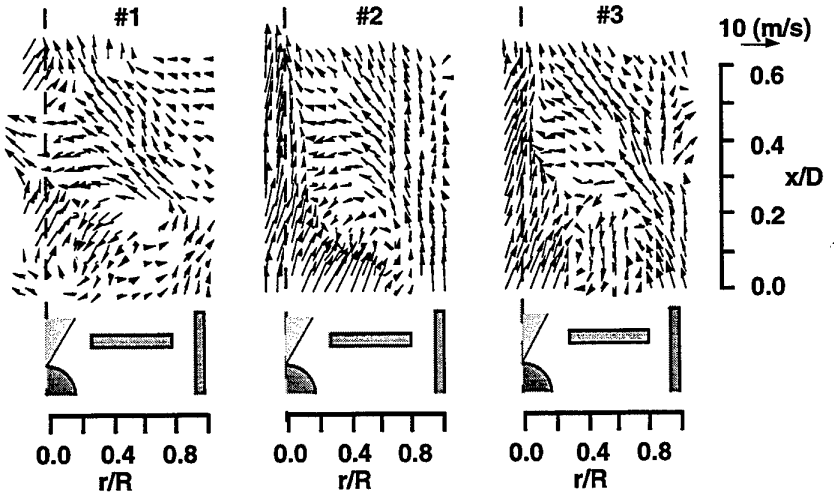


Fig. 5 Instantaneous velocitys vector at different shot

3-2. Parameter optimization

It is well know that PIV is not a perfect tool to measure spray flow because of large droplet distraction . There are many parameters to be considered so as to optimize to total PIV image for practical spray. But, what is the best one? There are no evidence. Here, we implemented the droplet vectors as a reference which was measured by size-classified PDA [Ikeda, et al., (1997)].

First of all, a comparison of auto-correlation and cross-correlation has been examined as shown in Figs. 6 and 7. Figure 6 was an instantaneous vector and the averaged (1000) velocity vectors were shown in Fig. 7. Since this flow has recirculating flow and large droplets penetrate the recirculating zone, it is very different to say which method is better. Based on the velocity profiles in these figures, it was found that the auto-correlation contained much irregular vector. An image shift and several selection of interrogation area have been examined. The cross-correlation image can show the strong droplet penetration which was observed by PDA data [Kawahara, et al., (1995)], while the auto-correlation could not show the droplet dynamics. It is hard to define and quantify the difference of three method, but it is clear that the cross-correlation method was better than that of auto-correlation. From now on, let's discuss with the cross-correlation data only. The laser power was set-up to the maximum, but not over saturation that was 130 mJ per pulse.

As seen in Fig. 8, the recirculating flow vector differed from each other. It was difficult to chose the optimum interrogation area. This value should be considered to cover maximum velocity and velocity gradient. For selecting the better set-up, the velocity profile at x/D=0.13 and 0.34 were examined by changing several set-up.

By comparing these two velocity vectors the strong droplet penetration can be seen by 64x64 pixel as the interrogation area. But, there are few discrepancies in axial and radial velocity profiles. The most important feature was that this PIV could measure the wide velocity range and the negative velocity at the recirculating zone could be measured or not.

Then, let's use 64x64 pixel as the interrogation area. Furthermore, in order to cover the wide velocity range and not loose the large velocity gradient feature. The laser pulse separation was also examined for optimum parameter set-up as shown in Fig.4. Here, we used 64x64 pixel with 20 μs as a good condition. The PIV can provide instantaneous flow structure but not so good to characterize the static parameter. There are many data to be averaged. Here, we examined the number of averaging images from 10, 100, 200, 1000, and 2000. Then, 1000 samples were selected.

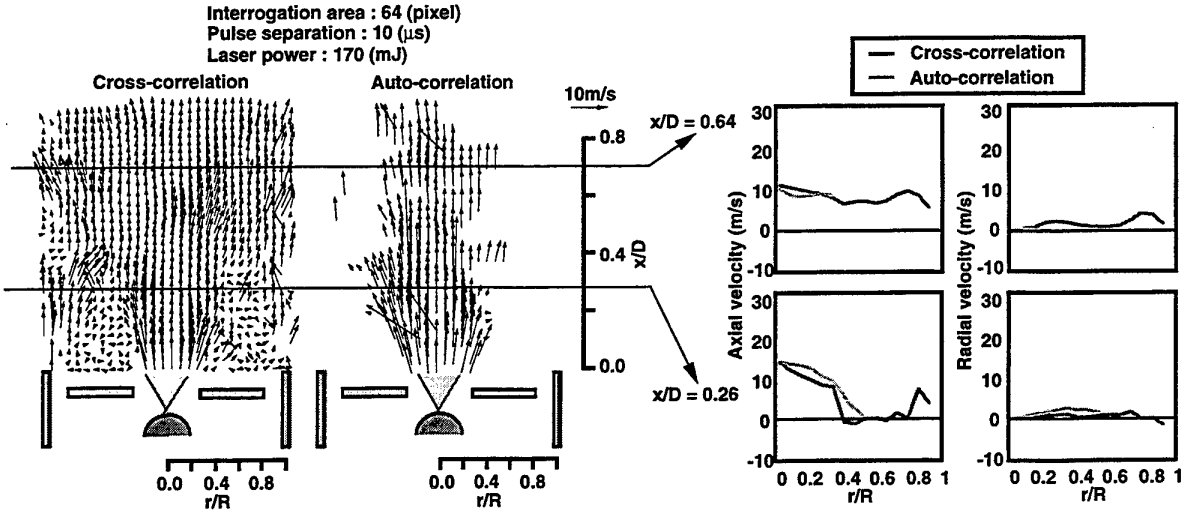


Fig. 6 Comparison of instantenious velocity vectorsmeasured by cross- and auto-correlation

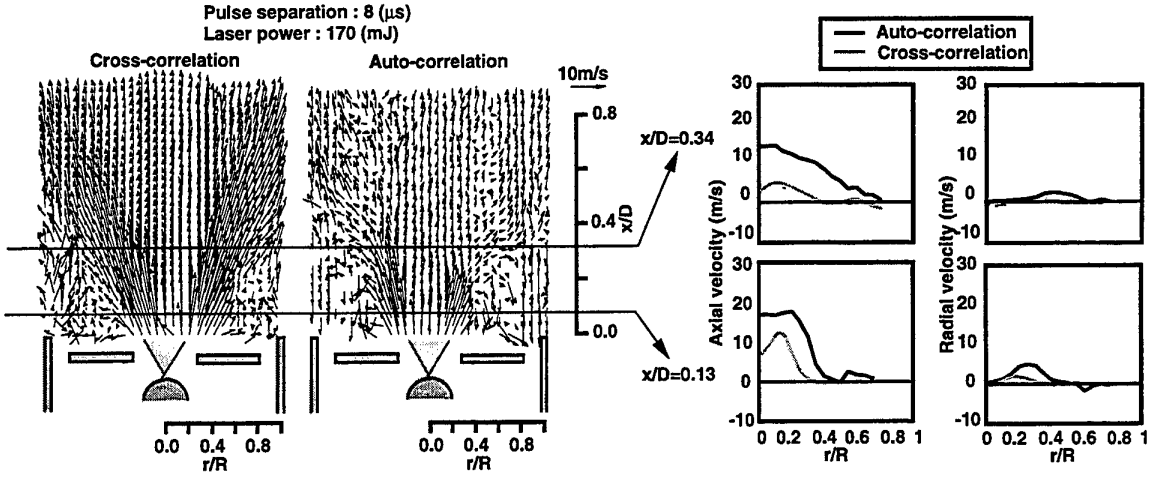


Fig. 7 Comparison of averaged velocity vectors measured by cross-correlation and auto-correlation

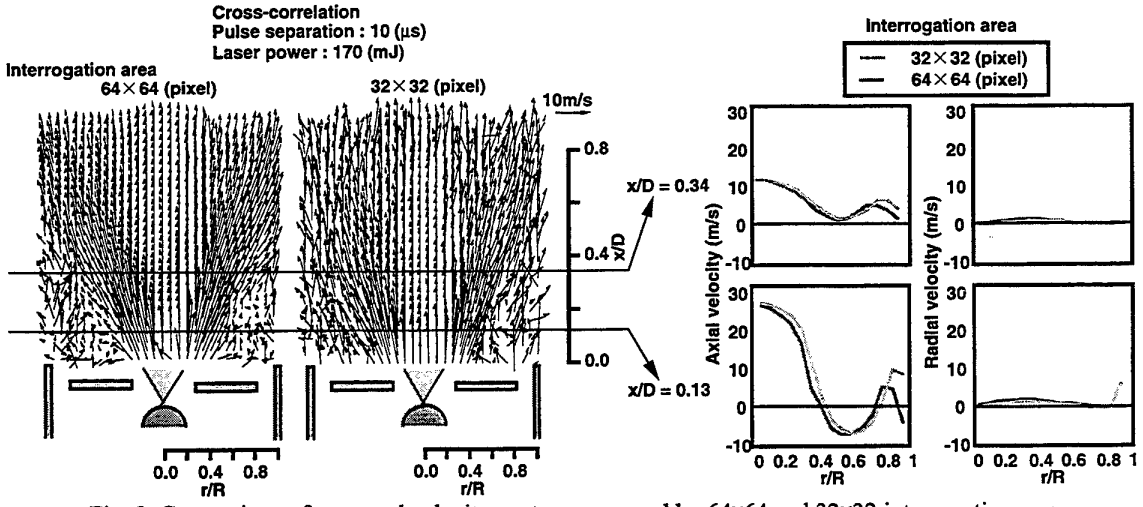


Fig. 8 Comparison of averaged velocity vectors measured by 64x64 and 32x32 interrogation area

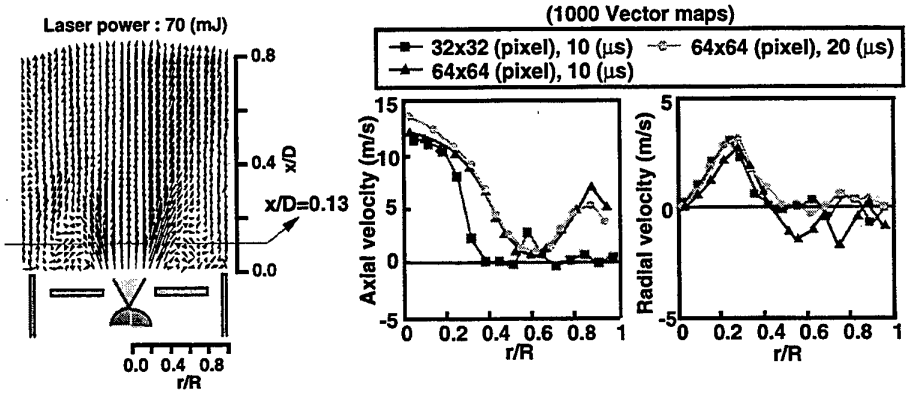


Fig. 9 Parameter optimization by interrogation area and puls separation

3-3. Comparison of PDA and PIV

The SMD velocity profile both in axial and radial were compared to those measured by the optimized PIV as shown Fig. 10. The negative flow in the recirculating zone has negative velocity and the tendency agreed well with PIV. In the axial direction at all locations, it was clearly observed PIV data can agree with the PDA (SMD) data. But, there are some discrepancy in the radial velocity profile. PDA measured 10,000 samples at each point, while PIV measure 1,000 samples. PDA has smaller measurement volume than PIV so that the averaged data should be different from each other. The maximum and minimum velocity of PDA were larger than PIV.

The negative velocity of PDA was larger than PIV. This was because of sample number, volume averaging effect, droplet number density distribution. But the difference of negative velocity were less than 1 m/s. As explained above, the small droplet can follow the recirculating zone so as to show the average velocity peak, while the larger droplet penetrate the recirculating zone. Then, let's see this droplet behavior in detail. The size-classified droplet velocity profiles were plotted and compared to that of PIV in Fig. 11. There are very good agreement between PIV and 20-30 μm vectors.

At the recirculating zone, the axial velocity by PIV was almost zero at r/R=0.6, where the axial velocity of 20-30 μm by PDA was almost the same value of zero. The same thing can be observed at different location at x/D=0.36. It was found that optimized PIV can demonstrate medium size spray behavior in the practical burner.

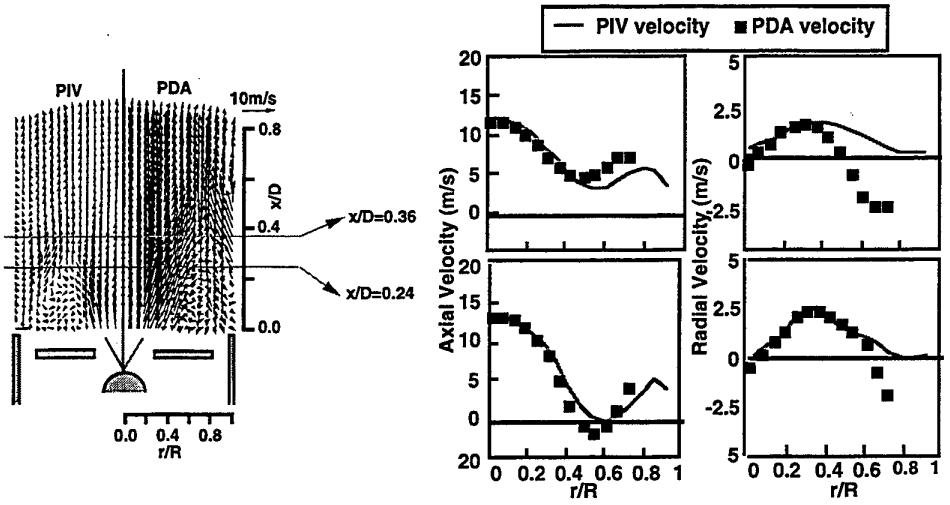


Fig. 10 Comparision of velocity vectors by PIV PDA (SMD)

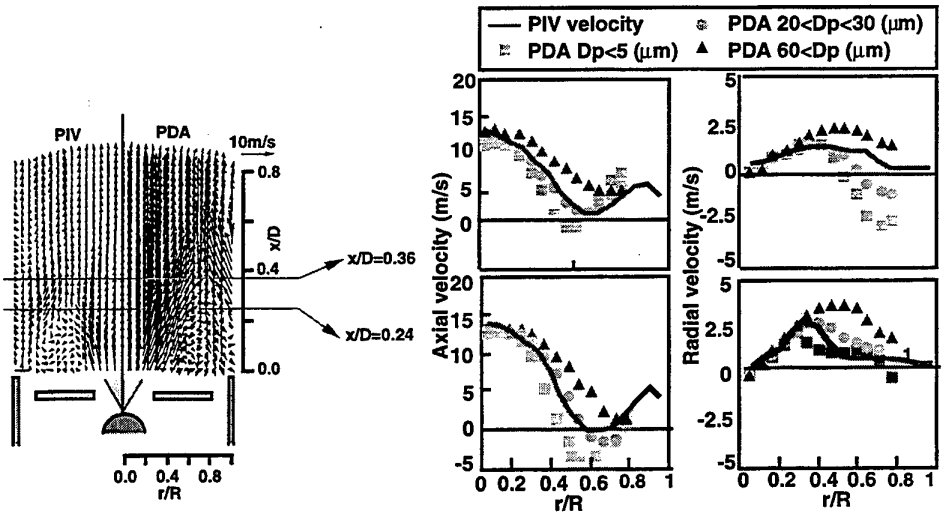


Fig. 11 Evaluation of PIV velocity by size-classified PDA data

4. CONCLUSION

PIV measurements were carried out in the practical burner under isothermal conditions. A size-classified PDA data was used to evaluate the PIV data. The size of recirculating zone can be measured well and good agreement has been achieved in both methods. An optimum set-up PIV can demonstrate the flow dynamics of wide velocity range in the practical spray burner. The SMD velocity vector and size-classified velocity vector were used to evaluate the PIV results. It was found that the PIV velocity agreed well with the droplet velocity of 20-30 μm. The optimum set-up PIV can be a good candidate to understand the spray flow characteristics.

REFERENCE

Adrian, R., J., 1997, Dynamic ranges of velocity and spatial resolution of particle image velocimetry, Measurement Science and Technology, Vol. 8, pp1393-1398.

Akamatsu, F., Nakabe, K., Katsuki, M., Mizutani, Y. and Tabata, T., 1994, Structure of Spark-Ignited

Spherical Flames Propagating in a Droplet Cloud, Application of Laser Technique to Fluid Mechanics 7th Int. Symp., Lisbon, pp.212-223, Springer-Verlag.

Bauckhage, K., 1985, International Conference Laser Anemonetry Advances and Application, Manchester, pp.261-278.

Edwards, C.F., 1988, ASME Paper HTD-vol.104, pp.99-110.

Edwards, C.F., et al., 1990, Measurement of Correlated Droplet Size and Velocity Statics, Size Distribution, and Volume Flux in a Steady Spray Flame, Fifth International Symposium of laser Techniques to Fluid Mechanics, Lisbon.

Grant, I., 1994, Particle Image Velocimetry, SPIE Milestone Series Volume MS 99

Humphreys, W. M., Rallo, R. A., Hunter, W.W., Bartram, S. M. and Blackshire, J. L., 1993, Application of particle image velocimetry to Mach 6 flows, Fifth International Conference on Laser Anemometry: Advances and Applications, SPIE Vol. 2052, Peter J. de Groot; Ed., pp. 519-526

Ikeda, Y., Nakajima, T. and Kurihara, N., 1997, Size-Classified Droplet Dynamics and its Slip Velocity Variation of Air-Assist Injector Spray, SAE International Annual Meeting, SAE Paper No.970632.

Ikeda, Y., Kawahara, N. and Nakajima, T., Flux Measurement of O2, CO2, and NO in Oil Furnace, 1995, Measurement Science and Technology Vol. 6, pp826-832.

Kawahara, N., Ikeda, Y., Nakajima, T. and Kuruhara, N, 1995, Droplet Followability and Slip Velocity Analysis of Evaporating Spray on Gun-type Burner, 4th International Congress on Optical Particle Sizing, Vol.4, pp.593-602.

Kawahara, N., Hirohata, T., Ikeda, Y. and Nakajima, T., 1996, Size-Classified Droplet Dynamics of Combusting Spray in 0.1MW Oil Furnace, 8th Int. Symp. on Application of Laser Measurement on Fluid Mechanics, Lisbon, pp10.5.1-10.5.8.

Kawahara, N., Ikeda, Y. and Nakajima, T., 1997, Droplet Dispersion and Turbulent Structure in a Pressure-Atomized Spray Flame, AIAA Paper 97-0125.

Keane, R.D., Adrian, R.J. and Zhang, Y., 1996, Super-resolution Particle Imaging Velocimetry, Meas. Sci. Technol, vol.6, pp.754-768.

Kompenhans, J. and H^cker, R., 1988, Application of Particle Image Velocimetry to High Speed Flows, Particle Image Displacement Velocimetry, von Karman Institute for Fluid Dynamics, pp.67-84.

McDonell, V.G., et al., 1986, A Comparison of Spatially-Resolved Drop Size and Drop Velocity Measurements in an Isothermal chamber and a Swirl-Stabilized Combustor, 21st Symp. (Int.) on Comb., pp.1961-1971.

Rudoff, R.C., et al., AIAA 25th Aerospace Science Meeting, Nevada, AIAA-87-0062.

Saffman, M., et al., 1984, The 2nd International Symposium on Application of LDA to Fluid Mechanics, Lisbon, pp.8.1.

Tanabe, M., Kataoka, M., Masahiko, F., Noh, Y., In-Cylinder Fuel Distribution, Flow Field, and Combustion Characteristics of a Mixture Injected SI Engine, SAE Transaction, Engine Combustion and Flow Diagnostics, pp.33-49.

Van de hulst, H., C., 1981, Light Scattering by Small Particles, Dover Publications, Inc..

Advanced Measurement Techniques for Injector Validation

W.Scheuerpflug, S.Funke

BMW Rolls-Royce AeroEngines GmbH

SUMMARY:

To investigate the fuel breakup and the eventual mixing characteristics of gas turbine injector configuration a suitable measurement technique was developed. Particle image velocimetry (PIV) as a well known technique to measure non-intrusively was combined with stereoscopy to allow for 3-dimensional acquisition and analysis of the velocity distribution. The determination of the 3-dimensional flow characteristics is a prerequisite to understand and quantify derived flow properties like shear stress, turbulence and mixing behaviour. Ultimately it can help to quantify the mixing properties for fuel injectors in an industrial environment.

KEYWORDS:

3-D-PIV, stereoscopy, correlation analysis, PIV

INTRODUCTION:

The prognosis for the global air traffic requires not only the continued effort to increase the overall efficiency of aero-engines and to reduce unnecessary emissions, but a more comprehensive reduction of all emission products during the flight cycle /1/. In particular the contribution of carbon dioxid at high altitude with respect to global warming and nitrogen oxides to the reduction of the stratospheric ozone layer requires continued effort to improve combustion processes over the complete range of operation. Additionally the spray behaviour at altitude relight conditions is a safety aspect that needs detailed attention.

The fuel dispersion and the subsequent mixing with the surrounding oxygen or with combustion products is not yet fully understood. Most of the missing knowledge is due to the fact that spatially and temporally resolving measurement techniques are not readily available for the hostile environment in a combustion chamber. Tests to determine the injector characteristic thus have to be carried out at ambient conditions at burning and cold conditions alike.

MEASUREMENT TECHNIQUES

Non-intrusiveness is a prerequisite to investigate injector flows. Therefore it is a typical application for laser techniques. Commonly to measure fuel distribution laser light sheet images are used to study the spray angles at different engine conditions qualitatively (figure 1).

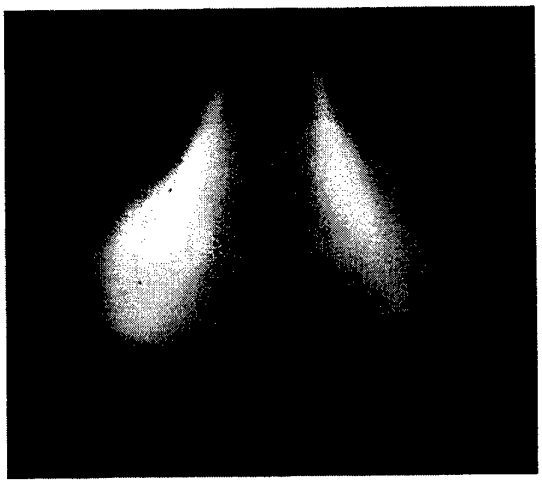


Figure 1: Qualitative laser light sheet of a kerosine spray

This technique can be used quantitatively by temporally modulating the laser beam. This leeds directly to particle image velocimetry technology. During the last decade PIV has evolved as a suitable

method for 2-dimensional flow analysis. To facilitate the acquisition and analysis a light sheet illuminates a well-defined plane (figure 2). The laser light sheet is either pulsed or otherwise being modulated to allow two images being taken from a fluid with tracers during the acquisition of a frame (autocorrelation) or on two subsequent frames (crosscorrelation). From the displacement of individual tracer images and the known time interval between the two pulses the velocity can been calculated with correlation analysis. In conjunction with the measurement of the droplet distribution by laser dispersion techniques (not shown here) the spray can be fully and quickly characterized.

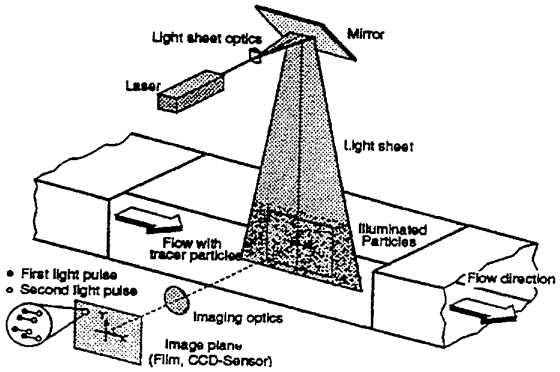


Figure 2: General PIV-setup (from /2/)

3-D-ACQUISITION

Swirl flows and mixing flows with strong turbulence require the simultaneous acquisition of all 3 components of velocity and all it´s 1st. derivatives with good spatial resolution and accuracy. Several attempts have been made to allow the acquisition of the 3rd. component of velocity, most notably with stereoscopic means and with holography. Since the latter one has more stringent requirements with regard to optical environment (vibration, phase relationship) to the rig, it was not considered an option for an industrial application.

Some authors /3/, /4/, /5/ have studied different constellations of stereoscopic devices. For this application an extended („thick") laser light sheet was used like shown in figure 3.

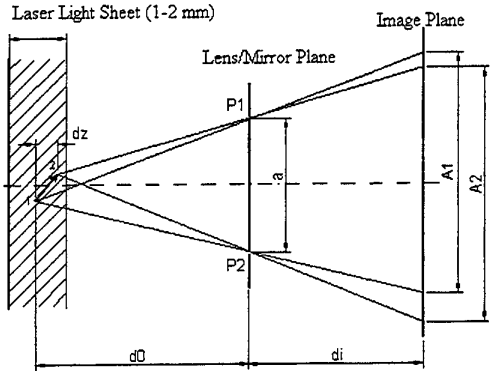


Figure 3: Laser light sheet stereoscopy

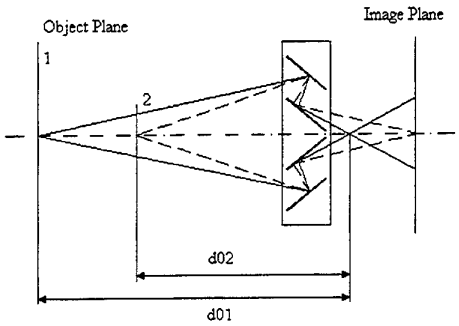


Figure 4: Stereoscopic setup

An industrial mobile application of stereoscopic PIV doesn´t allow for separated cameras as often proposed, since the displacement difference measurements needed for the determination of the 3rd. components is highly dependant on a rigid relationship from one individual pixel to another one. So an „on-chip" solution was favoured. The light sheet had a limited thickness of 1.5 mm to enable particles to stay inside the sheet even during a motion perpendicular to the sheet. The lens system has to allow sharp imaging of all particles inside the sheet.

The CCD camera used has a resolution of 1000 x 1000 pixel. This gives a pixel field of ca. 500 x 1000 pixel for both views. This is clearly much less than photografic films can resolve, but is compensated by the relative ease and reduction of processing time. During test runs individual checks can be performed immediately.

STEREOSCOPIC SETUP AND RESOLUTION CONSIDERATIONS

Rigs used for combustion and fuel diagnosis have a very limited optical access, in this case the distance from the window plane to the nozzle axis was 200 mm. The maximum distance between the outer mirrors was 130 mm . The camera was a DALSA D4 with 1k x 1k with a 50 mm lens system of NIKON and a magnification of M=0.13. The mathematical concept is following /8/. Regarding figure 3 the z-component is given by:

$$dz = \frac{d_0 \cdot dA}{M_{gesamt} \cdot a}. \qquad (1)$$

$$\text{with } dA = A_2 - A_1 \qquad (2)$$

$$v_z = \frac{dz}{dx} \qquad (3)$$

With the distance d_0 and the mirror separation a usually determined by technical restrictions of the rig the pixel size and the lens magnification is of great importance.

3-D-ANALYSIS

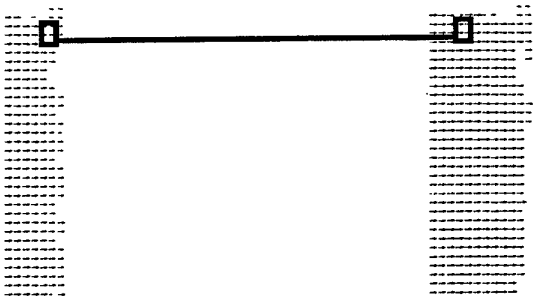


Figure 5: Vector map correlation

The camera acquires the left and the right view of the particular scene. The differences of the x-components of the velocity vectors were calculated according to equation (1) to determine the z-component and the true x-component (fig.5). Therefore the final vector field is reduced to half it´s original size.

DEVELOPMENT STRATEGY

The stereoscopic setup was developed and validated in several steps:

1. a solid perspex model simulating a spray and consisting of particles with a similar mass and diameter was rotated on a turning table to allow repeatable images to be taken. The optical arrangement and the acquisition method was tested and optimized as well as the evaluation algorithm. An error estimation was started.
2. a similar concentration of the same type of particles in water in a cylindrical vessel was rotated by a magnetic swirler to test the system with moving targets.
3. a closed wind tunnel with a fuel injector nozzle was used for air/particle flow. The air was seeded with the same type of particles as during the previous tests. The measurements were taken at low speed (approx. 2m/s).
4. in the sprayer rig a kerosene spray was investigated with 2-D- and 3-D-methods at relight conditions.

Further tests will expand the velocity range toward higher ranges.

AIR FLOW NOZZLE

The aforementioned stereoscopic PIV-setup was used to study a steady state air flow through a LPP (lean premixed prevapourized) nozzle to test flashback properties of the nozzle. Air was forced through a closed system powerd by a fan as shown in figure 6. The nozzle was placed above a window which gave optical access to the flow.

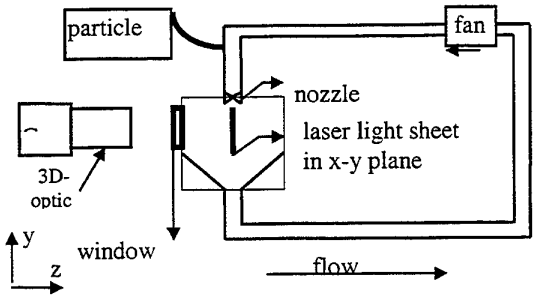


Figure 6: Air flow nozzle test circuit

The results are shown in figure 7. The x- and y-components of the velocity are represented by vector lines, while the z-component is illustrated by the black and white background colour. The structured flow is clearly visible and as expected.

FUEL SPRAY ANALYSIS

In the same way fuel injectors are being tested. A spray measured with 3-D-PIV at altitude relight conditions is shown in figure 8. At this lean operating point the droplet density is sufficient to obtain a sufficient number of vectors. Due to the turbulent environment

CONCLUSIONS

3-dimensional acquisitions of several flow fields were performed non-intrusively. The z-velocity and the corrected y-component was determined by stereoscopy. Results are currently limited to lower flow regimes like at high altitude relight conditions, but can be achieved with more powerful lasers, adjusted pixel sizes and more light transmissive optics. In general 3D-PIV is a versatile tool for a detailed study of flow characteristics relevant for global values like mixing and can contribute to large-scale injector validation in many ways. More effort is required to fully exploit 3d-data.

LITERATURE:

/1/ G.Kappler, R.Moore, J.Hourmouziadis: Hochleistungs-Turbofan-Triebwerk, ein Familien-konzept, Vortrag DGLR Tagung, Bremen 1992

/2/ Particle Image Velocimetry, TSI Seminar on Fluid Flow Instrumentation

/3/ M.P.Arroyo, C.A.Greated: Stereoscopic particle image velocimetry, Meas.Sci.Technology 2 (1991), 1181 - 1186

/4/ R.G.Racca, J.M.Dewey: A method for automatic particle tracking in a three-dimensional flow field, Experiments in Fluids 6, 25 - 32 (1988)

/5/ Imamoto, Ishigaki: Visualisation of velocity distribution by stereo photography,

/6/ I.Kimura, Y.Kohno: Measurements of three-dimensional velocity vectors in a flow based on spatio-temporal image correlation

/7/ W.T.Lai: A new approach in experimental fluid research, published by Th.Dracos: „3-dimensional velocity and vorticity measuring and image analysis techniques", Kluwer Academic Publishers (1996)

/8/ C.Willert: Vector Field Operators, published in: Application of Particle Image Velocimetry, course organized by the University of Oldenburg and DLR, Göttingen (1996)

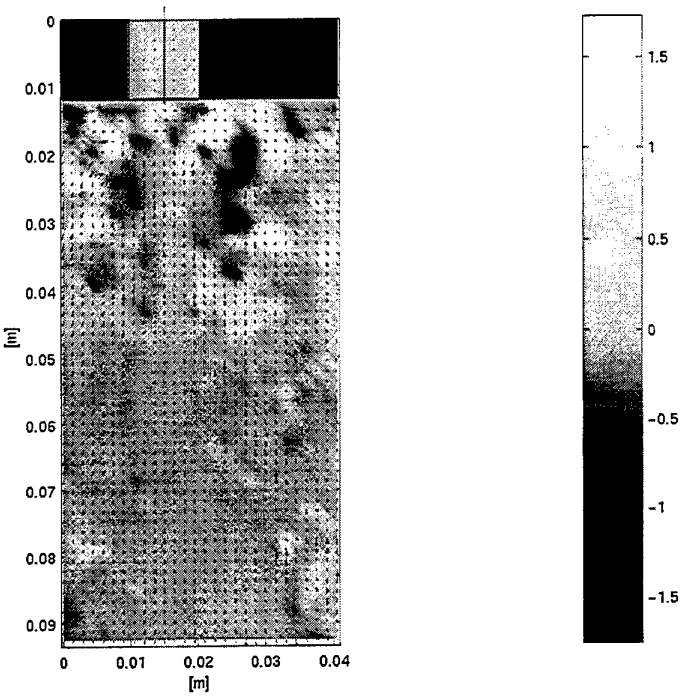


Figure 7: 3-D-Velocity distribution of a LPP nozzle



Figure 8: Stereoscopic image of a fuel spray

Development of a 2 Colour PIV System for In-Cylinder Spark Ignition Engine Flows

D.P.Towers, C.H.Buckberry, M.Reeves.

Applied Optics Laboratory, Rover Group, Gaydon Test Centre, Banbury Road, Warwick, CV35 0RG, England.

ABSTRACT

This paper describes the development of a 2 colour PIV system for the measurement of in-cylinder air flows over a two-dimensional plane. The 2 colour PIV recording, development and interrogation processes are examined particularly with regard to mechanisms which may introduce crosstalk between the 2 colour images which prevents measurements in regions of near zero velocity. A number of filter and camera combinations for use in PIV interrogation are presented with corresponding vector maps for comparison.

The PIV data is recorded through the curved glass cylinder via a corrective optic in a production geometry optical engine. The problems introduced by the engine rig are discussed with respect to the quality of particle images attainable. A number of realisations of the flow field for the same operating conditions are presented to illustrate the typical cycle to cycle variations in bulk flow and turbulence.

1. INTRODUCTION

Automotive engine manufacturers face increasing levels of emissions legislation whilst at the same time market forces require improved vehicle driveability necessitating higher power and torque output. The development and optimisation of the combustion system to meet these demanding requirements is being performed by a combination of fired engine test bed data, experimental data from optical diagnostics, and information from computational fluid dynamic (CFD) codes.

The Rover Group's Applied Optics Laboratory has developed diagnostics for in-cylinder flow fields both for use in the design process and as medium to long term research tools. In both cases instantaneous whole field data is required, i.e. pulse illuminated images, in order to gain an understanding of a flow where the turbulence intensity reaches a similar magnitude to the bulk flow and the bulk flow may vary significantly from cycle to cycle of the engine. Rapid understanding of in-cylinder flows has been obtained using a high speed flow visualisation technique employing a Copper Vapour Laser and high speed video camera recording images at 9000 frames per second. This provides planar images of the temporal evolution of the in-cylinder flow over a number of consecutive cycles for qualitative interpretation. To quantify a plane of the flow field a PIV system has been developed.

The PIV system was developed in order to :

- develop an understanding of the in-cylinder flow field, both quantitatively and qualitatively,
- assess cycle to cycle variations in both bulk flow pattern and turbulence,
- use the quantitative data for correlation with CFD predictions.

The turbulence integral length scales (of ~1mm) combined with the size of the field of 80×80mm necessitates the use of film as a recording media for adequate sampling. Furthermore, the use of image labeled PIV is critical to unambiguously identify the local flow direction in the highly turbulent flow, as well as to increase the dynamic range of the measurements, Adrian (1991). Two colour image labeling was chosen as it is equally applicable to film and CCD methods and the recordings produced give a direct, unambiguous visualisation of the flow field as well as enabling quantitative analysis.

Two colour PIV utilises two laser pulses with well separated wavelengths such that the first and second particle images are recorded in different emulsion layers of a colour film, Goss (1989). This approach retains registration between the first and second pulse images. The film is developed and interrogated using 2 sets of colour filters and a CCD camera with analysis via cross-correlation.

2. PIV IN ENGINES

The first application of PIV to in-cylinder flows was by Reuss et al (1989,1990) who produced quantitative data with a spatial resolution comparable to the turbulent integral length scale, and in the presence of a flame. The optical engines studied gave axial swirl flows in a horizontal plane (parallel to the head gasket) with a (low) 8:1 compression ratio and a non-production, flat topped combustion chamber. Modern 4 valve per cylinder pent-roof combustion chambers generate tumble about an axis parallel to the engine crankshaft. To resolve this flow structure requires imaging 'vertical' planes through the curved cylinder wall. This problem was resolved by Reeves et al (1994) using a corrective lens in a Rover production geometry optical engine. The preceeding works were performed using conventional double pulsed PIV requiring manual identification of flow direction.

Directionally resolved PIV data was obtained by Nino et al (1992,1993) using 2 colour, and by Reuss (1993) using electro-optical image shifting. The papers concentrated on axial swirl based research engines with the images recorded through flat windows. Manual post-processing of the PIV data was still required in these cases.

Within the Rover Group we are interested in the development of PIV for use in production geometry engines operating at compression ratios of up to 11:1 and at speeds up to 2000rpm. We additionally require to image both vertical and horizontal planes to resolve tumble and axial swirl based combustion systems respectively.

2.1 The Rover Optical Engine

The Rover developed optical engine is shown schematically in figure 1. The engine uses a standard production cylinder head and accurately represents production geometry. The engine has an extended piston, the upper part running in a full stroke glass barrel. The upper ring pack is lubricated by the oil based seed particles. The engine can be operated at up to 2000rpm. The piston is slotted around a static 45° inclined mirror giving optical access to the combustion chamber via a piston crown window (for configurations allowing a flat window in the piston). This enables the study of axial swirl with a production cylinder head (compare Reuss (1989,1990) and Nino (1993)).

Vertical planes, for imaging tumble, are examined by introducing the laser light sheet (LLS) via the 45° mirror and piston crown window, or directly via the glass barrel. The image is produced in side scatter through the glass barrel and corrective optic (not shown). Introducing the LLS via the glass barrel is generic in that it can be applied to engines with any piston crown geometry.

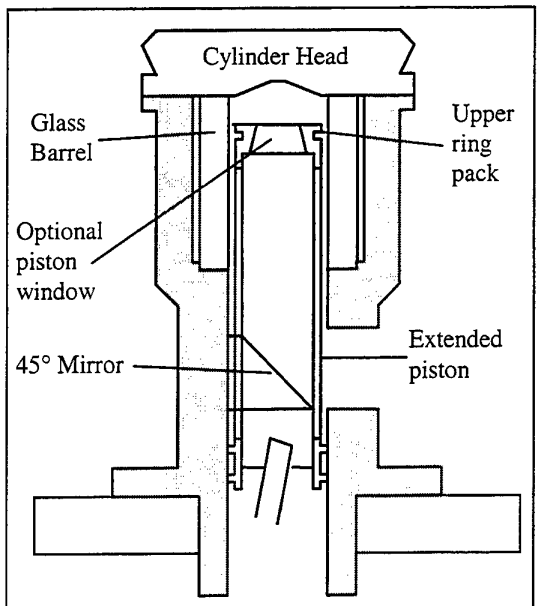


Figure 1 - Schematic diagram of the Rover Optical Engine

This paper reports on PIV data obtained in vertical planes introducing the LLS via the glass barrel along the bore centreline. This limits the image quality of the raw PIV data for the following reasons :

- the LLS reflects and scatters around the cylinder introducing a background speckle pattern (the intensity of the background increases for LLS planes away from the bore centreline),
- the lubricant (seed particles) produces a film on the glass barrel distorting the particle images,
- the corrective optic, following Reeves et al (1994), produces a particle image approximately double the size of a diffraction limited image at the same lens F# thereby requiring ~4 times the incident laser energy for equivalent exposure levels.

3. DESIGN OF A 2 COLOUR PIV SYSTEM

The purpose of image labeled double pulsed PIV is to enable two separate images to be obtained each containing particle images from only one of the laser pulses. With 2 colour PIV recorded on film (as required by in-cylinder flows), there are a number of

stages in the image recording, film development, and image reconstruction process which can cause crosstalk to occur between the two images.

The presence of crosstalk between the two images gives a cross-correlation function with a central peak, i.e. for zero particle displacement, as well as the desired signal peak. When crosstalk is present :

- it is not possible to measure near zero displacements (or velocities),
- the desired signal peak becomes distorted by the central peak for low displacements causing a bias in these measurements (the bias may be low or high depending on the level of crosstalk and whether the first or next highest peak of the correlation function is taken),
- manual and time-consuming post-processing of the correlation data often becomes necessary owing to the errors in the peak location data.

Our requirements from this PIV system are not to obtain exceptionally high accuracy velocity measurements. It is far more important to obtain information on the bulk flow patterns and cycle to cycle repeatability of the flow field. Therefore a low level of crosstalk is permissible as this will normally cause the flow direction to be approximately correct, only the speed will be in error. It is also important for the interrogation of the images to be as automated as possible, both in terms of scanning the photographic transparencies and post-processing the correlation peak location data to obtain optimum continuity in the velocity data from point to point.

3.1 PIV Recording System

Each laser wavelength must lie within the spectral sensitivity curve for a single colour film layer, and the two colours must be in different film layers. Furthermore, the exposure needs to be controlled to give a suitable minimum exposure density whilst being below the saturation level of the emulsion layer, Smallwood (1992). The wavelengths used in these experiments were 532nm and 610nm with recordings on Kodak EPN colour reversal film. If the exposure exceeds the saturation level for the intended film layer then an exposure may be formed in the other film layers causing crosstalk between the images. To predict the experimental parameters which determine the exposure, e.g. LLS dimensions, laser energy requirements, a Mie scattering calculation has been performed for the seed particle size range to be used, Towers (1994). The optimised parameters used in these experiments are given in table 1, and this data has been used to generate the plots of figure 2 of average film exposure against particle size for the two illumination wavelengths. The figure also shows the exposure limits for minimum acceptable image density and saturation for the relevant film layer. It can be seen from the graphs that the majority of particles in the range 1 to 6 microns produce exposures between the minimum satisfactory exposure (density of 1 under the minimum transmission) and the saturation level for both the green and red light sheets. This light scattering model provides a good starting point for setting the recording parameters. Experimental optimisation may also be necessary due to various transmission losses not considered in the model.

Table 1 - Optimised Experimental parameters for 2 Colour PIV Recording.
Magnification : 0.9
Lens F# : 6.8
Wavelengths : Green 532nm, Red 610nm
Polarisation : Green - horizontal, Red - vertical
Pulse Energy : Green 60mJ, Red 90mJ
Light Sheet Height : 100mm
Light Sheet Thickness : Green 0.2mm, Red 0.3mm
Seed Particles : Olive Oil, mean size 2 microns.

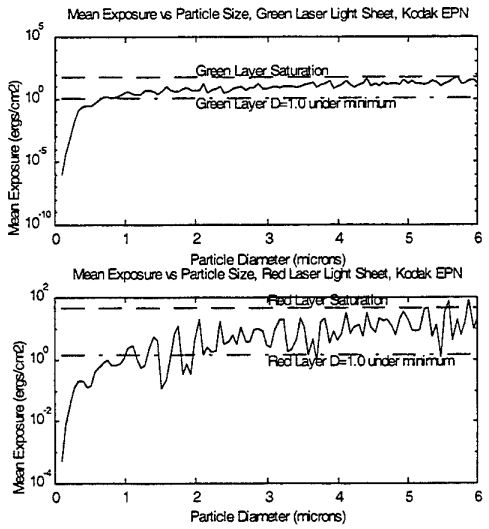


Figure 2 - Graphs of Average Exposure against Seed Particle Size for Green and Red Laser Pulses

The optical system to record the PIV images is shown schematically in figure 3, following Towers and Buckberry (1996). The optics allow separate optimisation of the LLS focus via negative spherical lenses located in both the 532nm and 610nm beams (each on an X-Y-Z translation mount). A common cylindrical lens in both beams gives a common LLS

orientation. The LLS was introduced into the engine through the glass barrel and therefore gave significant levels of flare and background to the PIV images, but allowed the use of non-transparent piston crowns. The images were recorded onto medium format transparency film.

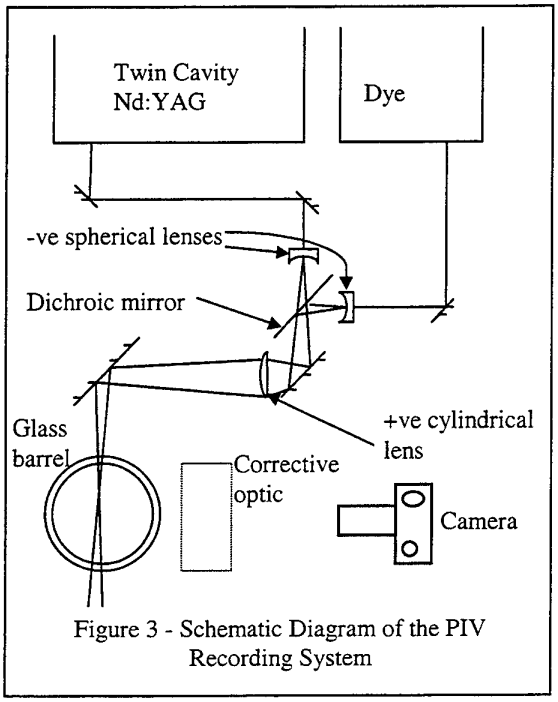


Figure 3 - Schematic Diagram of the PIV Recording System

3.2 PIV Interrogation System

The film development process results in a spectral broadening of the incident laser light. Each exposed film layer will transmit over a broad spectrum approximately equivalent to the width of the spectral sensitivity curve for the particular film layer concerned. The Kodak EPN emulsion (and most colour reversal films) have overlapping green and red spectral sensitivity curves.

A number of systems have been explored for the interrogation of 2 colour PIV images in order to resolve the inherent crosstalk in the developed transparencies. The optical configurations for the systems are shown in figure 4. Each approach is discussed below.

a) System A, see figure 4a). This arrangement utilises two black and white CCD cameras imaging the PIV slide via a red and green interference filter (the filters were at 532nm for the green film layer, 640nm for the red, and both of 10nm FWHM). A common light source and imaging lens are used. The use of a Nikkor imaging lens allows a wider aperture to be used than is available with microscope objectives which is required due to the low light transmission of the interference filters. It was found that the lens needed to be used at full aperture with a 50W lamp in order to obtain visible particle images. The two CCD cameras were pixel matched by cross-correlating the images obtained with a black and white PIV slide over a matrix of 64 by 64 pixel areas. It was possible to registrate the images to <1 pixel error over the central 256×256 pixel region of the 512×512 pixel image.

An example PIV vector map scanned using this system is given in figure 5. No crosstalk was observed between the sets of red and green images, hence the resolution of the small vortices present in the flow field. However, it was found that only the brightest particle images were transmitted by this system giving a maximum of ~3 particle image pairs in each interrogation region. Therefore neighbouring vectors show significant levels of variation as there is little averaging taking place over an interrogation region via the correlation procedure, and there is a significant number of regions with no particle image pairs. Suitable quality particle images were only obtained from approximately the central third of the total PIV image as outside this range the particle image size becomes larger owing to the limitations of the corrective optic. This effect is augmented by the poor light transmission of this system.

This interrogation system has been successfully used in situations where the image background was negligible and where the corrective optic was not necessary.

b) System B, see figure 4a). This is identical to system A except that broadband colour gelatin filters were used for colour separation. This improved the camera registration to better than 0.5 pixels across the whole 512×512 images owing to the reduced filter thickness. The percentage of light transmitted was also improved allowing the Nikkor lens to be stopped down. This gave sufficient depth of field to scan 4 medium format transparencies mounted side by side on the translation stages as an overnight batch operation taking ~12 hours.

A vector map produced with this approach is given in figure 6. A high level of crosstalk was observed making it impossible to measure small velocities. The main bulk flow is identified, and where possible low velocity vectors are selected in order to identify flow direction, the magnitude of the vector being larger than the actual velocity. Up to three quarters of the total transparency width were suitable for analysis.

c) System C, see figure 4b). This approach uses the filters between the lamp and the PIV slide thereby allowing the use of a single black and white CCD camera capturing images sequentially when the green and then red filters are inserted in front of the lamp. The system is similar to that used by Nino et al (1993). A rotary solenoid was employed to switch between the two filters. This approach should give green to red image registration values limited only by chromatic aberrations (≤0.1 pixels), however, the rotary solenoid introduced vibrations giving errors up to 0.3 pixels (this is still an improvement on either system A or B above). The filters selected were a 560nm low pass (Ealing 35-5354) for the green image, and a 665nm long pass (Comar 03 GB 50) for the red. A 50 W lamp was used allowing batch scanning of 4 PIV transparencies as for system B.

Three vector maps produced using this system are given in figure 7. A minimal level of crosstalk was observed between the green and red images after the hot mirror was added to remove most of the infra-red radiation from the lamp. The remaining crosstalk is believed to be due to a combination of residual infra-red radiation and over-exposure of the green and red particles during recording and interrogation. The over-exposure in the interrogation system occurred in the centre of the field and was deliberate in order to obtain sufficiently bright particle images at the horizontal edges of the field of view (compare figure 7 to figures 5, 6). Particle speeds over the range <1 to 11m/s were measurable with unambiguous direction (1 pixel in the digitised particle image field is equivalent to a flow velocity of ~0.5m/s).

d) System D, see figure 4c). This system is proposed to overcome the mechanical movement required in system C and is to be evaluated shortly. Two lamps are used to provide the two colour illumination simultaneously with the images being separated on a 3 chip colour CCD camera. (A colour CCD with white light illumination has been found to give significant crosstalk due to overlapping spectral sensitivity curves for the green and red sensors of the camera). This system is expected to further reduce the image registration error whilst allowing faster scanning of the PIV slide.

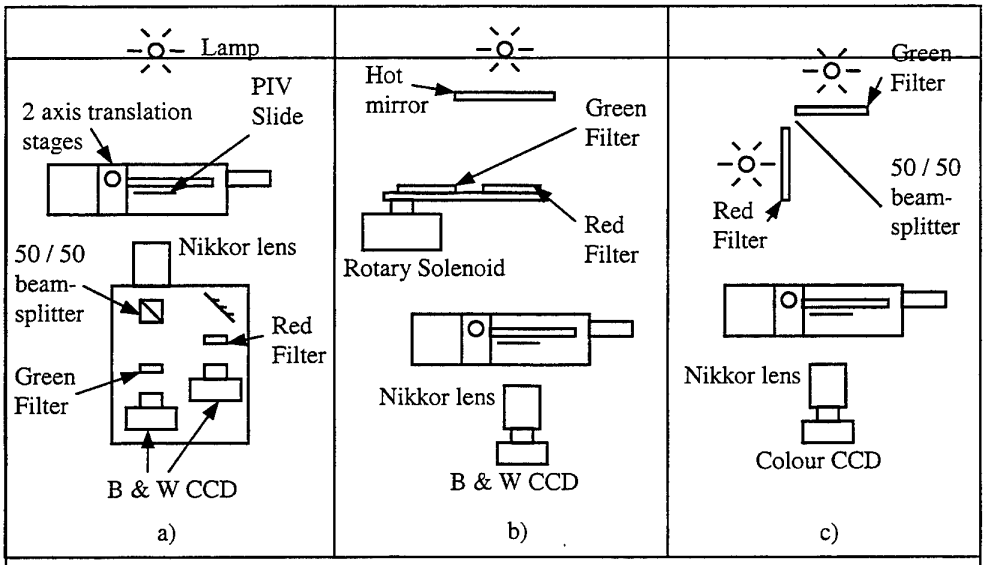


Figure 4 - 2 Colour PIV Interrogation Systems

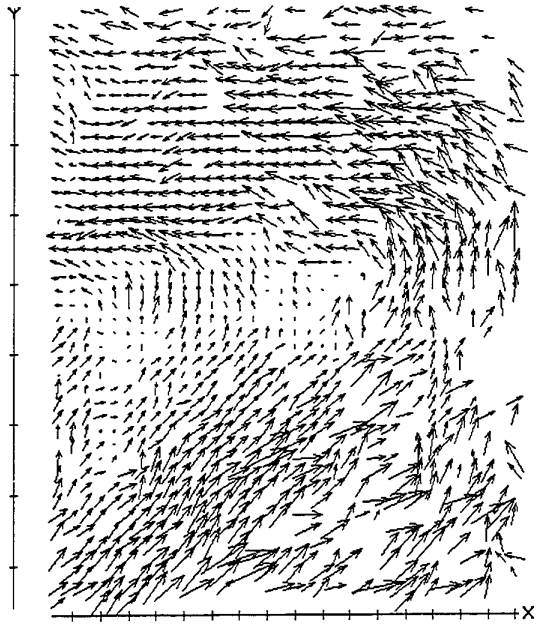


Figure 5 - Vector map produced with Interrogation System A and Interference Filters (figure 4a)

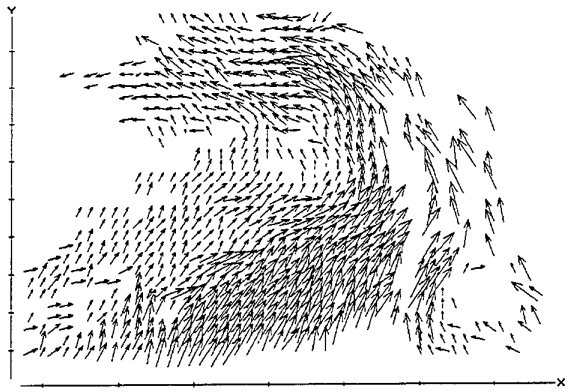


Figure 6 - Vector map produced with Interrogation System B and Broadband Gelatin Filters (figure 4a)

3.3 PIV Analysis and Post-Processing Software

The PIV software suite allows scanning of the image data to hard disk, cross-correlation analysis, peak location via centre of mass calculation for the 5 highest peaks, and post-processing continuity assessment of the vectors. It was found experimentally that the vector maps of figure 7 could be semi automatically post-processed. A few seed vectors (~10) would be selected of high signal to noise and good continuity with their neighbours, normally in areas of the bulk flow. Vectors were automatically added to this map iteratively against speed and direction continuity limits. The resultant vector map then requires further manual post-processing particularly in areas of turbulence. The vector maps of figures 5 and 6 were not of sufficient quality for this process to operate reliably and therefore were optimised manually. No interpolation or smoothing has been applied to any of the vector maps shown.

4. RESULTS

Three vector maps are presented in figure 7 which were interrogated using system C shown in figure 4b). All the vector maps presented, figures 5, 6, 7, are orientated with the inlet valve at the upper right corner, and exhaust valve at the upper left corner. The images show the flow at 90° before top dead centre compression with the engine motored at 1000rpm and a compression ratio of 10:1. The maps show an absence of vectors in approximately vertical lines on the right hand side due to imaging of reflections of the LLS. The exact velocity and distance scales have been removed to preserve confidentiality. Approximately 70% of the vectors in the three maps of figure 7 are from the highest or second highest peak of the correlation function.

The results in figure 7 show the typical cycle to cycle fluctuations which occur in this type of flow field. These data illustrate the problems in classification of the flow field in terms of bulk flow pattern changes superimposed with turbulence of a similar magnitude to the bulk flow. Whilst all the images show a classical anti-clockwise tumble the upper half of the field shows significant cycle to cycle variations as do the vortices outside the main bulk flow. It is also evident from the velocity fluctuations in the main jet flow rising from the piston crown (for example in figure 7a) that there is a significant level of out of plane flow.

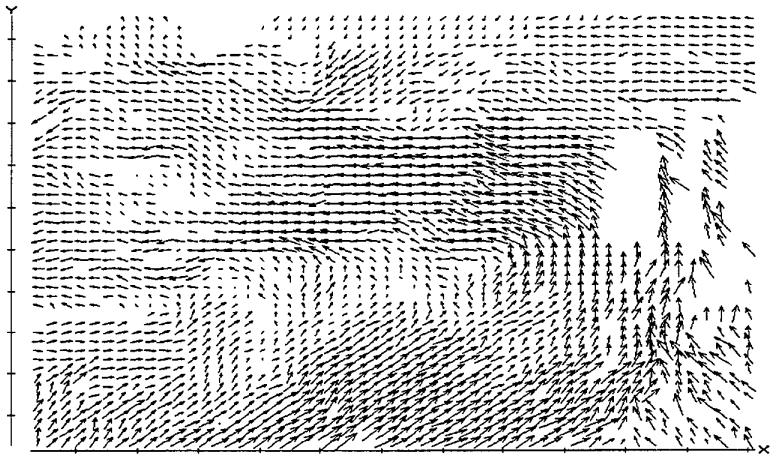


Figure 7a)

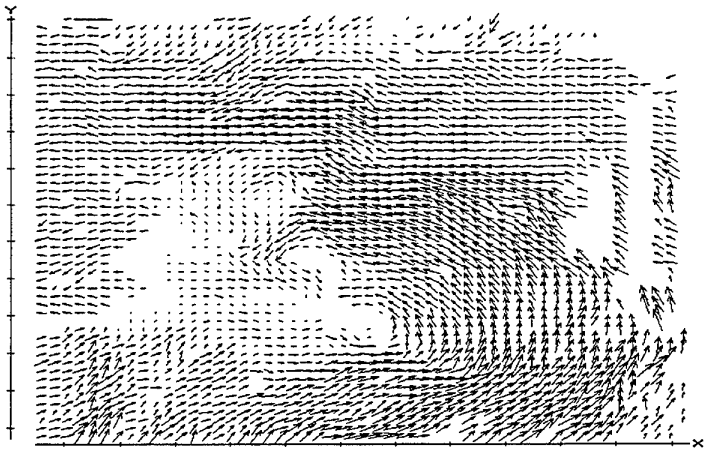


Figure 7b)

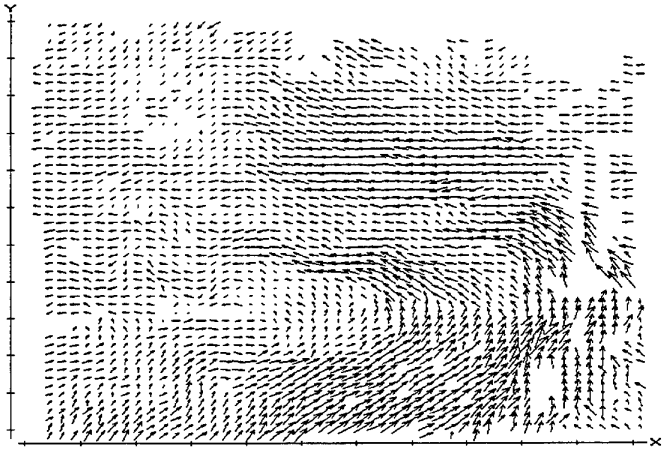


Figure 7c)

Figure 7 - Vector maps produced with Interrogation System C (figure 4b)

5. CONCLUSIONS

This paper has shown that 2 colour PIV may successfully be applied to measure in-cylinder flow fields in a realistic geometry optical engine. To the authors knowledge this is the first time high resolution, directionally resolved PIV data has been obtained through a curved glass cylinder wall using a corrective optic.

The possible sources of crosstalk in 2 colour PIV have been reviewed. A range of filtering schemes have been assessed in order to minimise the level of crosstalk. It has been shown that crosstalk may be fully eliminated by choosing narrow band filters at appropriate wavelengths. The wide range of particle image brightness resulting from the use of the corrective optic system combined with high levels of background scatter and the needs of batch processing have necessitated the use of a less optimal filter arrangement. This has resulted in a measurable velocity range of <1 to 11 m/s with unambiguous flow direction.

ACKNOWLEDGMENTS

The authors gratefully acknowledge the support of the Rover Group in the preparation of this paper. The authors also acknowledge a number of useful discussions with Martin Haste, Colin Garner, Jeremy Coupland, and Neil Halliwell of Loughborough University.

REFERENCES

Adrian R.J., 1991, Particle Imaging Techniques for Experimental Fluid Mechanics, Annual Review of Fluid Mechanics, volume 23, p.261-304.

Goss L.P., Post M.E., Trump D.D., Sarka B., MacArthur C.D., Dunning G.E., 1989, A Novel Technique for Blade to Blade Velocity Measurements in a Turbine Cascade, AIAA, paper 89-2691.

Nino, E., Gajdeczko, B.F., Felton, P.G., 1992, Two-Color Particle Image Velocimetry Applied to a Single Cylinder Two-Stroke Engine, SAE, paper 922309.

Nino, E., Gajdeczko, B.F., Felton, P.G., 1993, Two-Color Particle Image Velocimetry in an Engine with Combustion, SAE, paper 930872.

Reeves, M., Garner, C.P., Dent, J.C., Halliwell, N.A., 1994, Particle Image Velocimetry Measurements of Barrel Swirl in a Production Geometry Optical IC Engine, SAE Congress and Exp. Detroit, paper 940281.

Reuss D.L., Adrian R., Landreth C.C., Fench D.T., Fansler T.D., 1989, Instantaneous Planar Measurements of Velocity and Large-Scale Vorticity and Strain Rate in an Engine Using Particle-Image Velocimetry, SAE paper 890616.

Reuss D.L., Bardsley M., Felton P.G., Landreth C.C., Adrian R., 1990, Velocity, Vorticity and Strain Rate Ahead of a Flame Measured in an Engine using PIV, SAE, paper 900053.

Reuss D.L., 1993, Two-Dimensional particle Image Velocimetry with Electrooptical Image Shifting in an Internal Combustion Engine, SPIE proceedings, volume 2005.

Smallwood G.J., 1992, A Technique for Two-Colour Particle Image Velocimetry, M.Sc. Thesis, Department of Mechanical Engineering, University of Ottawa, Ontario, Canada.

Towers, C.E., 1994, The Application of Two Dimensional Imaging Techniques to Transonic Aerodynamics and Combustion Research, Ph.D. Thesis, Department of Engineering, Warwick University, Coventry, England.

Towers, D.P. & Buckberry, C.H., 1996, Application Of 2-Colour PIV to In-Cylinder Flow Velocity Measurement, Proc. I. Mech. E. conf. Optical Methods and Data Processing in Heat and Fluid Flow, City University, London, UK.

Multi-Intensity-Layer PIV for spray measurement

Naoki Yamada, Yuji Ikeda and Tsuyoshi Nakajima

Department of Mechanical Engineering
Kobe University

ABSTRACT

A new PIV data processing method called Multi-Intensity-Layer PIV was proposed in application for injector spray analysis. By using the principle that the light scattered from small particle is proportional of its diameter squared. The light intensity information was extracted from PIV data. There are two methods: intensity weighted and number density weighted.

The measurement results demonstrate that the different droplet dynamics of different diameter can be described by this Multi-Intensity-Layer PIV, that is, the small droplet follows the vortex shear and high turbulent flow, while the larger droplet penetrate the shear flow.

It was found that this Multi-Intensity-Layer PIV can be a useful tool to describe spatial spray behavior even they have large droplet diameter distribution.

INTRODUCTION

Recent laser measurement techniques for flow analysis have been developing not only in optical equipment such as laser source, camera, optics and fiber, but also in data acquisition hardware / software. These developments can allow us to understand flow structure and its feature in time and space. Laser sheet visualization using high power laser and CCD camera enables us to elucidate flow characteristics in a two-dimensional plane, but turbulent flow characteristics in time evaluation can hardly be measured by these method. However, Laser Doppler technique (LDV) and phase Doppler technique (PDA) can contribute to describe turbulent characteristics and droplet dynamics at very high data rate. These methods have been implemented for practical flows and combustion measurements [Chigier, (1991), Taylor, (1993)] and various feasibility studies have been examined in these decades. Particle Image Velocimeter (PIV) [Raffel, (1998), Grant, (1994)] took over a major role of entire flow velocity measurement from LDV and PDA in terms of instantaneous spatial flow structure imaging, however, there are several limitations in PIV, which can be solved by LDV, that is time series data, turbulent spectrum analysis, small measurement volume, near wall measurement, wide dynamic range. For instance LDV is capable for time-series flow fluctuation measurements, while PIV has to solve the seeding problems which include error sources based on wide particle diameter distribution, non-uniform particle number density, low repetition rate of detected image due to laser and camera. Furthermore, PIV needs interrogation area optimization for its wide dynamic velocity range, non-uniform particle density and so on. In spite of these disadvantages, PIV can be implemented in many different applications [Grant, (1994)] and demonstrate its special feature in whole flow measurements. For understanding of fine turbulent flow structure, a super-resolution PIV has been developed [Keane, (1996)]. By using CW laser and high repetition rate laser (Cu-vapor laser) with high speed camera, time series velocity measurements were examined [Humphreys, (1993)]. But, it is clear that PIV data includes much information of different particle sizes in the same plane and the particle number density is one of the big error source in PIV measurement. However, one can realize -as we did- that the difference in scattered light intensity can be used to show the different droplet dynamics and the accuracy of PIV can be improved regarding spray characteristics measurement.

The flow field illuminated by laser sheet can tell us that there are spatial structures such as large turbulent structure, branch structure, entrainment of the ambient air, and so on. PDA can be useful for acquiring the fuel droplet velocity and its diameter simultaneously at a measurement point but can not get the instantaneous spatial velocity distribution, that means we can not know the details of time-specific spatial phenomenon by PDA. That is why we need to develop the brand-new PIV-based method, as we call 'Multi-Intensity-Layer PIV', which can get instantaneous spatial velocity distributions and its droplet diameter information at the same time.

The purpose of this study is to propose a new data analysis method for PIV which is based on Multi-Intensity-Layer images. The feasibility study of Multi-Intensity-Layer PIV were carried out in a fuel injector measurement [Ikeda, et al., (1995, 1997a, 1997b)], in which small fuel droplets followed

turbulent eddies, while large droplets penetrated straight the recirculating flow region due to its large momentum. The droplet dynamics of different sizes were observed even in a small region. The standard PIV can not describe the difference of droplet dynamics of each size-classes. The developed analysis improved significantly its flow measurement accuracy and multiple images of different droplet dynamics size were examined.

EXPERIMENTAL APPARATUS

The PIV measurement was carried out on an air-assist gasoline injector which has been analyzed by us [Ikeda, et al., (1997a, 1997b)]. The liquid is discharged through a small aperture under high applied pressure (274.4kPa), the pressure energy is converted into kinetic energy (velocity). The specific of this injector is that the fuel is already atomized in the small tube hence the liquid film does not appear at the exit of the injector and the poppet valve open/close timing is accurately controlled by electric signal (TTL). The schematic of used injector [Ikeda, et al., (1995)] and the PIV set-up are shown in Figure 1. The laser was a Nd:YAG (400mJ/pulse) with a cross-correlation camera (1k x 1k) and a commercial PIV software (Dantec FlowManager) has been used [Ikeda, et al., (1998)] and NIH Image [Buch, et al., (1996)] was used for post-processing for distributing the layers.

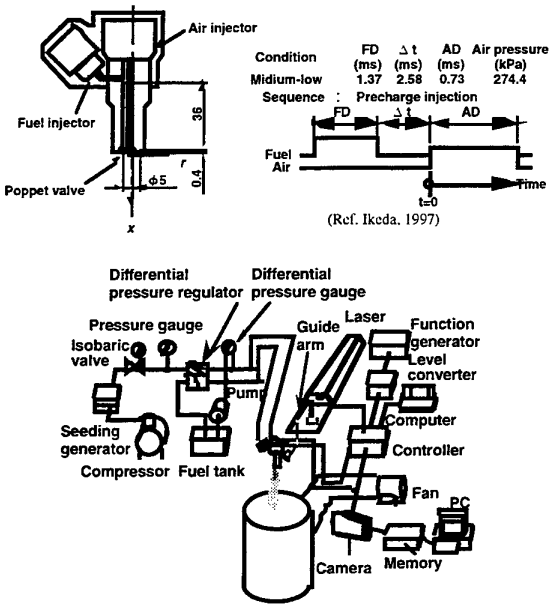


Fig. 1 Experimental appartus and injector Configuration

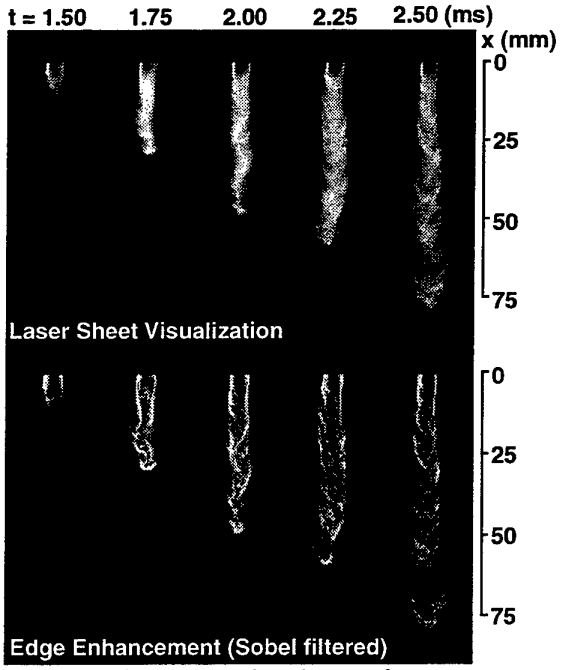


Fig. 2 Laser sheet image of spray

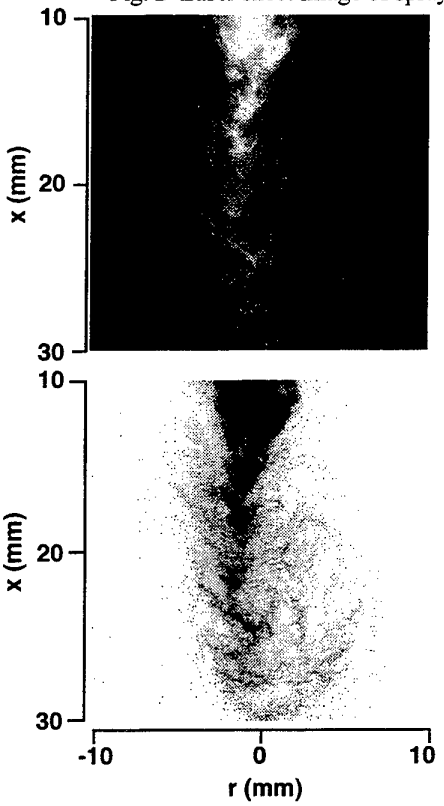


Fig. 3 Spray tip image used for Multi-Intensity-Layer PIV

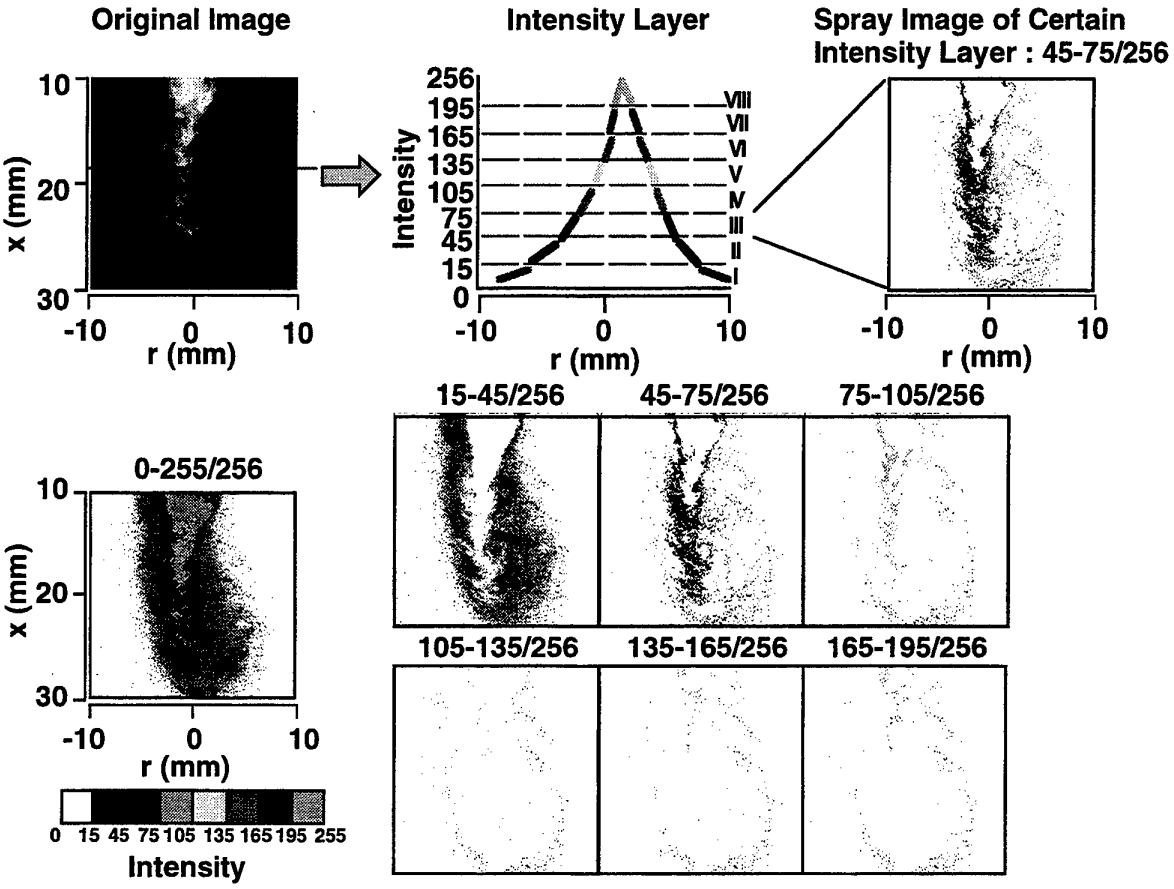


Fig. 4 Concept of Multi-Intensiy-Layer PIV

RESULTS AND DISCUSSION

Spray images

Figure 2 shows a laser sheet visualization image and a fitted images to emphasize the edge [Ikeda, et al., (1997b)]. A spray tip structure contains many eddies and overlapping, not stable. The light intensity at the spray tip and spray shell can be enhanced well by the filtering technique. It is clearly observed that there are branch structures [Nishida, (1992)] which have been also observed in SI and Diesel spray researches [Agates, et al., (1992)]. This branch structure can be understood based on preferential concentration [Fessler, et al., (1995)] and coherent turbulent structure.

We have measured the spray characteristics and the droplet dynamics by PDA [Ikeda, et al., (1995)] and the results showed that it was important to characterize the droplet dynamics using several droplet size classes. Droplets less than 30μm can follow the turbulent flow and droplets over 50μm penetrates and shows straight velocity vectors both in recirculating flow region and at the spray tip [Ikeda, et al., (1997a)]. As it can be seen in the picture, it is clear that the light intensity from the particles are not uniform in areas where different size droplets exist and large number density variation are also yielded. However, the intensity information can tell some features of droplet dynamics. How to extract the feature and characteristics and implement them in PIV data analysis, this is the target of this study. Based on general understandings for the laser illuminated images of fuel sprays, there are droplet diameter information and number density information were included. In this study actual spatial resolution was set up to be 20μm in each pixel. Previous PDA measurement results indicated that droplet less than 30μm could follow to the vortex well, so that this 20μm was selected not to have aggromalation and collision. Furthermore, diameter informations should be acquired from the images based on a principle that says the Mie scattering intensity from a particle is proportional to the squared value of its diameter.

Concept of Multi-intensity-PIV

As explained in the above section, light scattered intensity from a small particle is proportional to its diameter [Van de Hulst, (1981)], the original CCD image contains the particle location and its scattered light intensity. As practical in PIV, we have to take care of not to saturate CCD plane by adjusting laser power and aperture. We propose to utilize its intensity information to demonstrate its diameter information on PIV data.

Flows of our interest are spray combustion and fuel injection as shown in Figs.2 or 3. The flow physics we have to understand are: how small droplet follows to the turbulence, how much entrainment air comes from surroundings into injection fuel, how large droplet penetrates into the strong shear flow region, how the turbulent momentum transfer occurs, how aggromation and separation happen, how droplet evaporate so as to produce combustible gas mixture, and so on. Here, these parameter should be measured: turbulent intensity of each droplet, droplet trajectory, evaporation speed of each droplet, Stokes effect and so on.

In this study, in order to show that the small droplet follows to the vortex and large droplet penetrate the strong shear flow region, we examined eight intensity layers to show eight droplet diameter dynamics.

Figure 4 shows a concept of the Multi-Intensity-Layer PIV. The light scattered intensities were digitized in 8 bit, that is from 0 to 255 levels. At a certain location or plane, the intensity distribution can be obtained easily. Here, we used eight layers as a trial. The right-hand side picture is the spray image of the intensity level 3. After recording the PIV images, these intensity layers are calculated and each pixel is sorted to the intensity level. Data flow charts of conventional and Multi-Intensity-Layer PIV were depicted in Fig. 5. The difference of these two methods is that the images captured by CCD camera were reprocessed by NIH Image in case of Multi-Intensity-Layer PIV.

First analysis method, an intensity weighted method is by averaging all pixel intensity and sorting each interrogation area into a certain intensity level from 1 to 8. Detail information on normalizing each interrogation area was shown in Fig. 6.

Second analysis method is a number density weighted. As shown in Fig. 7, the number density at each intensity layer was calculated at the first stage within each interrogation area. The velocity vector was calculated in each layer. The number density ratio of each layer were multiplied by the velocity vector and the compound velocity vector was obtained by summing eight layer velocity vector.

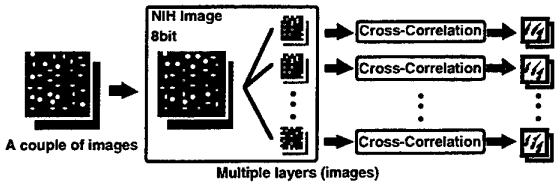


Fig. 5 Flow chart of data processing of Multi-Intensity-Layer PIV

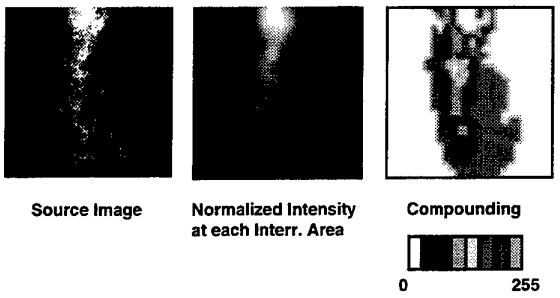


Fig. 6 Intensity weighting of each interrogation area into 8 layers

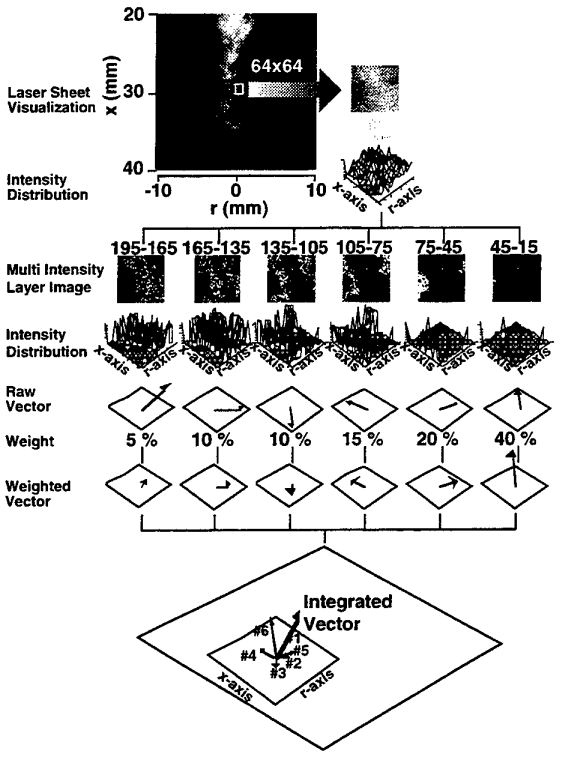


Fig. 7 Data processing of number density weighting

Measured results by Multi-Intensity-Layer PIV

The Multi-Intensity-Layer PIV analysis was examined for the spray characteristics measurement shown in Fig. 3 [Ikeda, et al., (1995)]. The droplet diameter at the spray tip varies from 0 to 30μm which was measured by size-classified PDA [Ikeda, et al., (1997a)].

The scattered light intensities were digitized and sorted in 8 levels. The spray images of these light levels are shown in Fig. 4. Since the light intensity level can be defined in 255 level, the numbers shown above the layered images indicate the applied low and high intensity. The double pulsed laser was used so as to have two consecutive images of each intensity level.

Before considering optimization of laser pulse separation and interrogation area, double pulsed images of each layers were processed to show velocity vector maps as shown in Fig. 8 by comparing them to the conventional PIV velocity map.

The axial velocity distributions at two locations were calculated at different intensity layers as shown in Fig. 9. It is clear that there are large velocity differences between the layers and it is very hard to select reasonable one. How to extract one velocity at each interrogation area is defined as follows: First, average intensity at each interrogation area was calculated and selected its level. The concept of this compounding method can be seen in Fig. 6. For defining the representative intensity at each interrogation areas, the most equivalent layer from the 8 layers was selected at each interrogation area by averaging the intensity in each interrogation area. Then the 'Compounded vector map' was generated by putting the vectors on each interrogation areas from various layers. The selection of level number is the key feature in this analysis. The interrogation area size used in this measurement was 64 x 64 pixel, which corresponds to 1.3 x 1.3 mm in the physical dimensions. After selecting the intensity layer for every interrogation area, the velocity vector was calculated. Calculated axial and radial velocity distributions were compared to those obtained by conventional PIV as shown in Fig. 10. There were several saturation region in conventional PIV data and hence big discrepancies are shown. At x=16.7mm, the axial velocity measured by Multi-Intensity-Layer PIV indicates lower value than those by conventional PIV. This is due to the fact that the velocities tend to be calculated only from the strong light intensity data in the conventional PIV. The same tendency is observed at the lower location. The velocity vectors were measured by size-classified PDA [Ikeda, et al., (1997a), Edwards, et al., (1990)] so that the evaluation can be done very easily. PIV can not identify the droplet velocity of a certain diameter. That is, we can not know the quantitative droplet diameter of each droplets captured on CCD array. This is the limitation. Our objective for layering is not to get the quantitative droplet diameter but for classifying its sizes based on scattered intensity. This is why we applied the layer and not more detailed intensity levels.

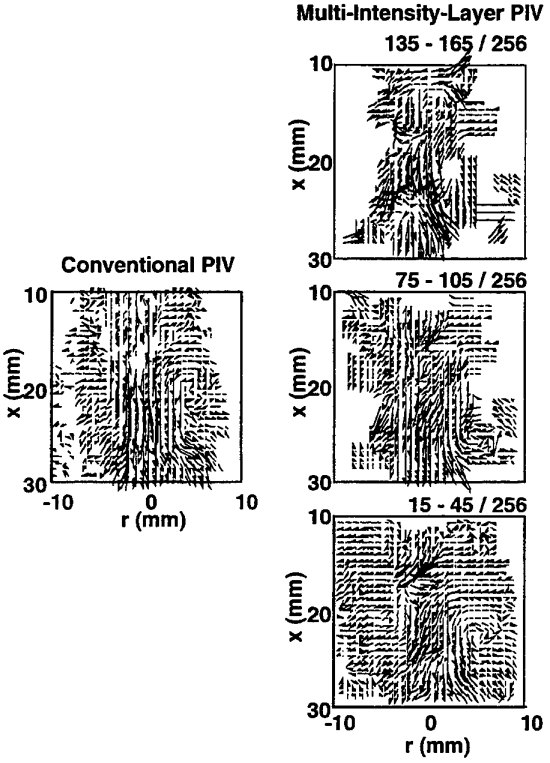


Fig. 8 Comparison of velocity vector map at different intensity layers

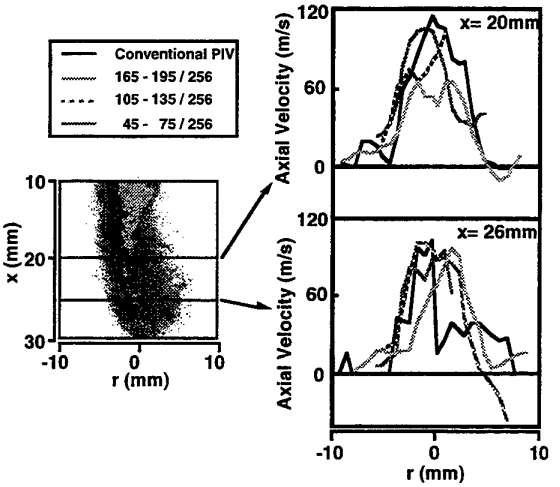


Fig. 9 Axial velocity distribution calculation at different intensity layer

Comparison of standard PIV and Multi-Intensity-Layer PIV

In Multi-Intensity-Layer PIV, it can show the typical droplet dynamics as shown in Fig. 11, that is, small droplet can follow well to the vortex flow but the large droplet penetrate the strong turbulent flow region. The layer of 15-45/256 shows the larger vortex flow than the conventional PIV and the 165-195/256 layer indicates the stronger velocity vector than the conventional PIV.

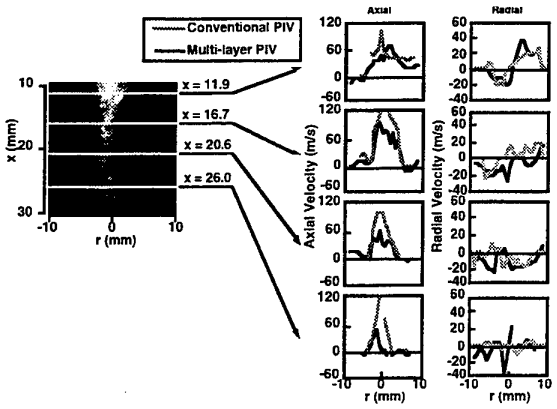


Fig. 10 Comparison of velocity obtained by conventional PIV and Multi-Intensity-layer PIV

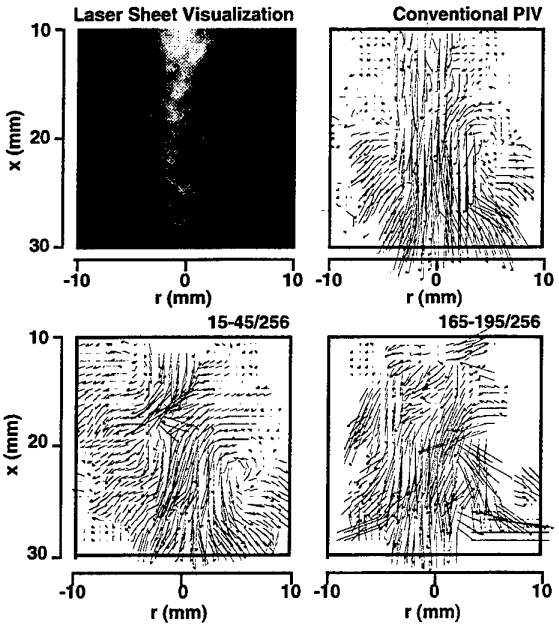


Fig. 11 Instantaneous velocity vector

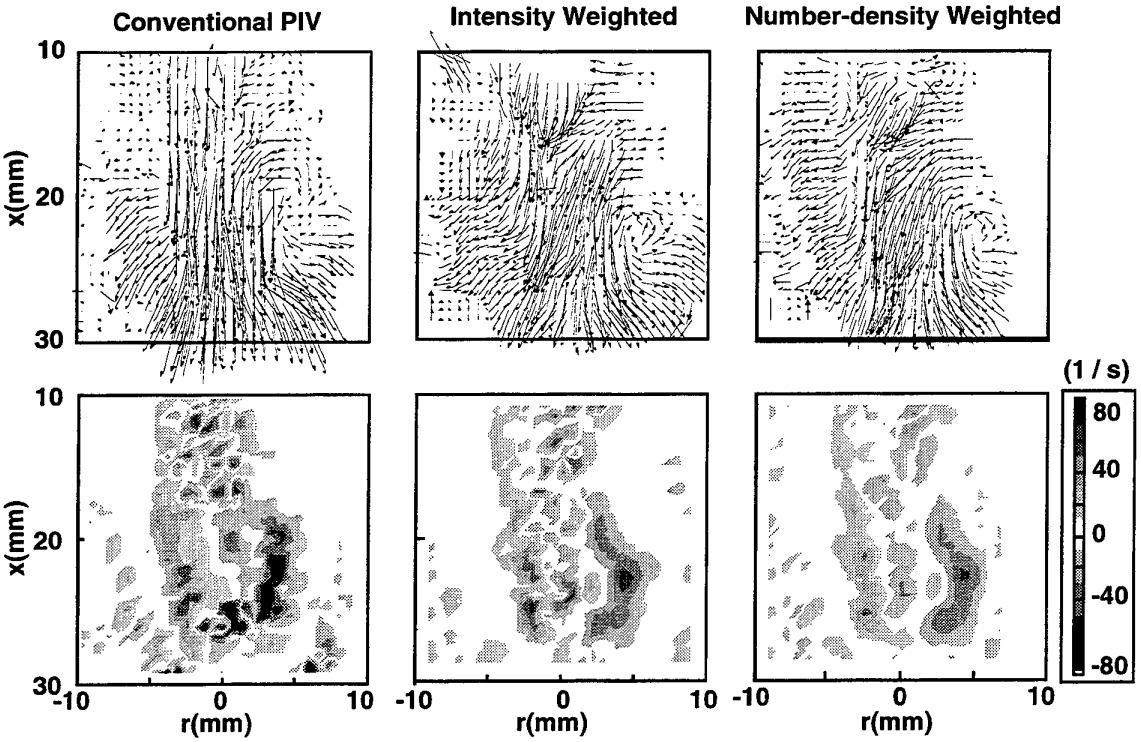


Fig. 12 Velocity vectormaps and those vorticity

It was found that the Multi-Intensity-Layer PIV could demonstrate different droplet size dynamics by using its light scattered intensity information. This technique can contribute very much to understand the spatial turbulent structure of spray and injection flow.

Figure 12 shows the compound velocity vector maps of the different weighted method, intensity weighted and number density weighted. The calculated vorticity were also demonstrated.

The spray tip structure observed in Fig. 3 indicated the branch structure and the interaction of droplet dynamics and turbulent momentum transfer. The vorticity map by Multi-Intensity-Layer PIV described the vortex evolution on the center axis. The red and blue islands generated in turn which described the vortex interaction caused by strong shear and droplet penetration.

These two methods should be chosen for the flow. If the droplet diameter is small and very much disperse, the second one: number density weighted method is better. While the droplet diameter distribution is very wide, the intensity weighted method is much nice.

Comparison of PIV results with PDA

In order to evaluate the PIV data processing, these three PIV show the axial velocity profile in comparison of the measured size-classified data [Ikeda, (1997a)]. PDA measurement were done at very high data rate, and the shown velocity has 2msec duration.

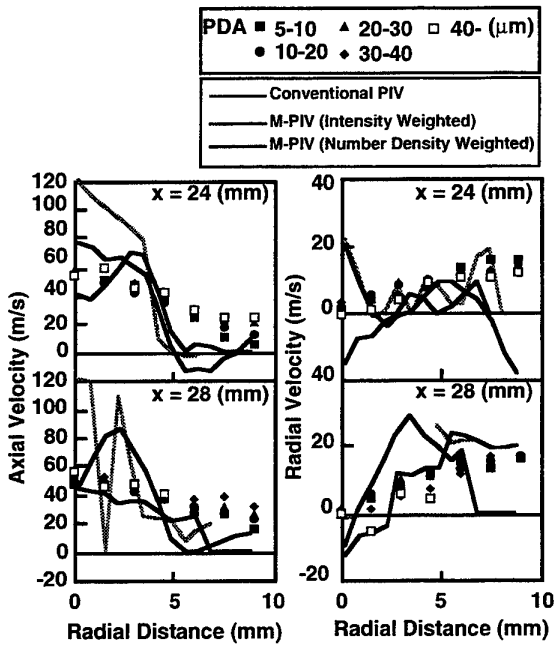


Fig. 13 Data evaluation of three PIV methods by measured PDA data

Three PIV data was instantaneous one.

Near the center axis, the conventional PIV show larger velocity than the other PIV and PDA data. The number density weighted PIV was closer to the measured one, because the spray droplet at this spray tip were very small and disperse well.

It was found that the disadvantage of the conventional PIV were improved by Multi-Intensity-Layer PIV, which happened when the droplet diameter has its distribution. The number density weighted PIV shows its advantages in order to understand flow structure and mixing characteristics at the spray tip.

CONCLUSIONS

A Multi-Intensity-Layer PIV was proposed to solve the conventional PIV disadvantages in application for spray, and succeeded to demonstrate the droplet dynamics of different droplet diameter. The injector measurement was done to show this advantages. Two methods were examined, intensity weighted and number density weighted. It was found that the number density weighted method shows fine vortex dynamics at spray tip.

The Multi-Intensity-Layer PIV can provide better information of vortex rotation and its evolution at the spray tip. Large amount of differences were observed comparing this Multi-Intensity-Layer PIV with the conventional one. That means the Multi-Intensity-Layer PIV can be a very useful tool to characterize different droplet dynamics for fuel injector analysis. But, many critical parameters should be quantified to describe the different diameter droplet behaviors.

REFERENCES

Raffel, M. et al. 1998, Particle Image Velocimetry A Practical Guide, Springer-Verlag.

Measurement Science and Technology, 1997, Vol. 8, No. 12.

A. Agates, et al. 1990, A study on the structure of diesel spray, International Symposium COMODIA 90, pp. 199-204.

Chigier C. 1991, Combustion Measurements, Hemisphere Publishing Corp.

Edwards, C.F., et al. 1990, Measurement of Correlated Droplet Size and Velocity Statics, Size Distribution, and Volume Flux in a Steady Spray Flame, Fifth International Symposium of laser Techniques to Fluid Mechanics, Lisbon.

Grant, I. 1994, Particle Image Velocimetry, SPIE Milestone Series Volume MS 99

Humphreys, W. M., et al. 1993, Application of particle image velocimetry to Mach 6 flows, Fifth International Conference on Laser Anemometry: Advances and Applications, SPIE Vol. 2052, Peter J. de Groot; Ed., pp. 519-526

Van de Hulst, H. C. 1981, Light Scattering by Small Particles, Dover Publications, Inc.

Ikeda, Y., et al. 1995, Spray Formation of Air-assist Injector for Two-Stroke Engines, SAE International Annual Meeting, SAE Paper No.950271.

Ikeda, Y., et al. 1997a, Size-Classified Droplet Dynamics and its Slip Velocity Variation of Air-Assist Injector Spray, SAE International Annual Meeting, SAE Paper No.970632.

Ikeda, Y., et al. 1997b, Cycle-resolved PDA Measurement of Size-classified Spray Structure of Air-Assist Injector, SAE International Annual Meeting, SAE Paper No.970631.

Ikeda, Y., et al. 1998, PIV Application for Spray Characteristics Measurement, 9th Int. Symp. on Application of Laser Measurement on Fluid Mechanics, in printing.

Buch, K. A. et al. 1996, Experimental study of the fine-scale structure of conserved scalar mixing in turbulent shear flows, Journal of Fluid Mechanics. vol. 317, pp. 21-71.

J. R. Fessler, et al. 1995, Particle-turbulence interaction in a backward-facing step flow, Stanford Report, No. MD-70.

Keane, R.D., et al. 1996, Super-resolution Particle Imaging Velocimetry, Meas. Sci. Technol, vol.6, pp.754-768.

Nisida, M. et al. 1992, Observation of high pressure fuel spray with laser light sheet method, SAE Paper, No.920459.

Taylor, A M. K. P. 1993, Instrumentation for Flows with Combustion, Academic press

SESSION 13

PIV DATA PROCESSING

On the accuracy of a DIC-PIV system based on massive sampling

C. FREEK, J.M.F. RAPOSO, J.M.M. SOUSA*, W. HENTSCHEL, W. MERZKIRCH**

Volkswagen AG, Research and Development, Wolfsburg, Germany
*Instituto Superior Técnico, Mechanical Engineering Department, Lisbon, Portugal
** Universität GH Essen, Lehrstuhl für Strömungslehre, Essen, Germany

ABSTRACT

Particle image velocimetry (PIV) has been mainly used to investigate instantaneous velocity fields, whereas the application of this technique to obtain mean flow fields is reported seldom. The cause is the necessary large amount of image data required, which is the main limiting condition. In this communication the technique is used to compute mean velocity quantities including mean velocity, root-mean squares (RMS), Reynolds shear stress and power spectra. The accuracy of the PIV technique is assessed, including the characterisation of the most relevant correction methods with Monte Carlo simulations and measurements in a low Reynolds number open water channel. Typical occurring errors lie in a range of a few percent and are easily overlooked if the measurements are not validated against other techniques. In the current evaluation, no significant differences were found with respect to the Laser-Doppler Anemometry (LDA) results, when comparing mean and RMS velocities. For the mean velocity component, the global differences are below 1% between PIV, LDA and direct numerical simulation data. The profiles presenting the turbulence intensities show very good agreement as well and are in accordance of better than 3%. It is shown that PIV may provide similar accuracy as LDA techniques, if the same number of instantaneous measurements is used to compute statistics.

1. INTRODUCTION

Particle image velocimetry (PIV) is an effective, instantaneous and non-intrusive technique for the measurement of velocity fields in fluid mechanics. Since its introduction as the laser speckle technique in the 1970's, Backer and Fourney (1977), Simpkins and Dudderar (1978), wide applications can be found in many areas of fluid mechanics, Lourenço et al. (1986), Kompenhans and Höcker (1988) and Reuss et al. (1989). An extensive review of the principle, the historical development and the application of diagnostics in flow visualisation were given by Merzkirch (1987) in general and, in particular for PIV, by Adrian (1991) and Hinsch (1993). On the other hand, digital particle image velocimetry (DPIV) is well known for its simplicity and flexibility, Westerweel et al. (1990). The method received more attention when Willert and Gharib (1991) found that the problem of direction ambiguity could be removed by means of the cross-correlation method applied to a pair of successive images. However, storage capacity and evaluation time are strong limitations of conventional DPIV systems.

Particle image velocimetry has been mainly used to characterise the instantaneous features displayed by time-dependent flow phenomena. The use of DPIV techniques to compute mean flow fields is reported very seldom as the amount of image data required is a limiting condition. To measure the mean flow field and the mean fluctuation levels (RMS) with considerable accuracy, several thousands of images are required. It was shown that image compression eases the handling of such an amount of image data and that the MJPEG compression method can be used without any loss of relevant information in the images, Freek et al. (1997). During the development process of such a Digital Image Compression PIV (DIC-PIV) system, several uncertainties in the cross-correlation evaluation scheme were found, which essentially led to the underestimation of the mean velocity when comparing the results with accurate LDA measurements. The aim of this communication is to show the errors, which may occur when employing the cross-correlation function in the computation of flow field statistics from PIV images. Further, we intend to provide a review of some correction methods to yield confident results. In a first step Monte Carlo simulations are carried out to access the evaluation uncertainties due to the different evaluation and correction methods only. In a second step, DIC-PIV measurements are carried out in a water channel to investigate the errors in mean velocity, RMS,

Reynolds shear stress and power spectra. It should be emphasised that typical occurring errors lie in a range of few percent, which is easily overlooked if the measurements are not validated against other techniques.

2. "STANDARD EVALUATION ALGORITHM" IN DIGITAL PIV

The standard digital PIV cross-correlation algorithm evaluates the displacement between the particle images indirectly by correlating two successive images which are illuminated by one light pulse each. Dividing the images into interrogation spots and evaluating the displacement of the particles within the two successive interrogation spots, the velocity map over the entire plane can be found. The interrogation spots from one image at time t and time $t+dt$ are transformed into the Fourier domain by using a two-dimensional FFT algorithm. The cross-correlation function in Fourier space is obtained from the product of the first interrogation spot with the complex conjugate of the second interrogation spot. The result is transformed back to physical space. The correlation between the two interrogation spots results in a large spike. Its displacement from the origin corresponds to the spatial shift of particles between t and $t+dt$ time instants. A peak-finding algorithm, which assumes a Gaussian distribution for the cross-correlation peak, is employed to estimate the centre of the highest peak in the respective control area. The magnitude of the velocity vector is then simply obtained by dividing the shift from the origin by the elapsed time dt. Its direction is immediately obtained from the cross-correlation map.

To better describe the applied correction methods it is necessary to briefly review the analytical description of the interrogation method, given by Adrian (1988) and Adrian (1984). There, it is shown that an estimate of the spatial correlation over a finite area can be expressed as

$$R(\vec{p}) = \int W_1(\vec{x}) I_1(\vec{x}) W_2(\vec{x}+\vec{p}) I_2(\vec{x}+\vec{p}) d\vec{x} \qquad (1)$$

The image intensities are denoted as I_1 and I_2, their window functions as W_1 and W_2 and $\vec{p} = (r,s)$. Applied to an N x N interrogation window, Equation (1) is then computed by

$$R[r,s] = \frac{1}{N^2} \sum_{i=1}^{N} \sum_{j=1}^{N} I_1[i,j] I_2[i+r, j+s] \qquad (2)$$

This spatial correlation can be decomposed into three components,

$$R(\vec{p}) = R_D(\vec{p}) + R_C(\vec{p}) + R_F(\vec{p}) \qquad (3)$$

where $R_C(\vec{p})$ is the mean background correlation , $R_F(\vec{p})$ is the correlation between mean and fluctuating image intensities and $R_D(\vec{p})$ is the correlation between the images fluctuating intensities. The latter is the one which contains the correlation peak used to estimate the displacement.

2.1 PEDESTAL REMOVAL

To improve peak detection and therefore the displacement estimate, the terms $R_C(s)$ and $R_F(s)$ can be eliminated by subtracting the mean image intensity $\bar{I}_1$ and $\bar{I}_2$ from I_1 and I_2 before correlation.

$$\hat{R}[r,s] = \frac{1}{N^2} \sum_{i=1}^{N} \sum_{j=1}^{N} \left(I_1[i,j] - \bar{I}_1\right)\left(I_2[i+r, j+r] - \bar{I}_2\right) \qquad (4)$$

2.2 PEAK HEIGHT NORMALISATION

To further improve the peak detectability a normalisation of $\hat{R}[r,s]$ is usualy employed. By dividing the correlation function by the square-root from the product of the images variances, one may normalise the correlation peak, (Willert 1995), i.e.

$$\hat{R}_n[r,s] = \frac{\sum_{i=1}^{N} \sum_{j=1}^{N} \left(I_1[i,j] - \bar{I}_1\right)\left(I_2[i+r, j+r] - \bar{I}_2\right)}{\sqrt{I_1'^2 I_2'^2}} \qquad (5)$$

2.3 VELOCITY BIAS CORRECTION

So far the we have altered the original spatial correlation from Eq. 3 to

$$\hat{R}_n(\vec{p}) = \hat{R}_D(\vec{p}) \qquad (6)$$

It is however still possible to improve the displacement estimate. Decomposing $\hat{R}_D(\vec{p})$ into a mean and a fluctuating term, as

$$\hat{R}_D(\vec{p}) = \left\langle \hat{R}_D(\vec{p}) \right\rangle + \hat{R}'_D(\vec{p}) \qquad (7)$$

The fluctuating term $R'_D(\vec{p})$ is related with the correlation between individual particles, and accounts

for the measurement noise. The mean term $\left\langle \hat{R}_D(\vec{p}) \right\rangle$ containing the correlation peak can be seen as,

$$\left\langle \hat{R}_D(\vec{p}) \right\rangle \propto R_{\Gamma\Gamma}(\vec{p}-\vec{p}_D)\cdot F_O \cdot F_I \tag{8}$$

where $R_{\Gamma\Gamma}(\vec{p}-\vec{p}_D)$ (which represents the peak) is the spatial self-correlation of the particle pattern $\vec{\Gamma}$ shifted by the particle image displacement $\vec{p}_D$. This term is scaled also by F_O and F_I, both representing loss of correlation. F stands for the out-of-plane loss of particles, which can be experimetally minimized but never eliminated. As for F_I it represents the in-plane loss of correlation which be viewed as due to loss of particle pairs as a result of the identical size of each interrogation window. Generally we have,

$$F_I(\vec{p}) \propto \int W_1(\vec{x}) W_2(\vec{x}+\vec{p}) d\vec{x} \tag{9}$$

But specifically for equally uniform window functions this is,

$$F_I[r,s] = \left(1-\frac{|r|}{N}\right)\cdot\left(1-\frac{|s|}{N}\right) \tag{10}$$

As can be seen, F_I always decreases as a function of the displacement magnitude. Ultimately, the correlation peak $_{\Gamma\Gamma}(\vec{p}-\vec{p}_D)$ is slightly skewed towards the centre of the correlation domain. As this effect is propotional to the width of the correlation peak, it increases with the particle diameter. A way around is the use of uniform interrogation windows with different sizes, leading to a constant F_I, which in turn originates a non-skewed and unbiased correlation peak (Keane and Adrian, 1993). A more convenient correction method is given by Westerweel (1993a,b) which allows the use of equal-sized interrogation windows. The so-called "velocity bias" is then corrected by means of Eqs. (8) and (10), i.e.

$$\hat{R}_n[r,s] = \hat{R}_D[r,s] \ / F_I[r,s] \tag{11}$$

2.4 DISCRETE WINDOW OFFSET

Due to the nature of this technique, a certain amount of the original particles leaves the domain of the second interrogation spot, resulting in a decrease in quality and height of the correlation peak. This may lead to an underestimation of the particle displacement. To increase the signal-to-noise ratio (SNR), an integer-pixel displacement shift of the second interrogation window proportionally to the local velocity gradient was proposed by Westerweel et al. (1995). This technique minimises the loss of particles in the in-plane component and results in a theoretical residual displacement of the correlation peak smaller than 1/2 pixels. The authors show that the SNR, defined as total signal power divided by the total noise power, is dependent on the velocity fluctuation u' and on a constant c for the case without shift, i.e.

$$\frac{S}{N} = \frac{u'^2}{c^2} \tag{12}$$

(Westerweel et al., 1995). For the case of local shift and low turbulence intensity, it was concluded that the SNR can be written as

$$\frac{S}{N} = \frac{1}{4c^2} \tag{13}$$

(Westerweel et al., 1995), and for the case of local shift and high turbulence, it can be written as

$$\frac{S}{N} \approx 3\frac{u'^2}{c^2} \tag{14}$$

(Westerweel et al., 1995). In the low turbulence case, the SNR does not depend any longer on the velocity fluctuation u' and, therefore, the relative measurement error is constant. For the case of the high turbulence intensity the relative measurement error is still dependent on the velocity fluctuations, but the SNR is three times the SNR of the non-local shift case.

The above authors further concluded that the noise reduction is not dependent of the size of the tracer particles, as c can be associated with the particle diameter. This review shows that the window off-set does not necessarily improves the measurement accuracy, which is not the case for the other corrections. However, it should be applied, as it increases the measurement reliability, viz., the number of particles in the interrogation spot.

2.5 INSTABILITY DUE TO PEAK-FIT ESTIMATORS

To accurately estimate the displacement of the correlation peak a sub-pixel estimator can be employed. A discussion regarding the performance and accuracy of different estimators can be found

elsewhere. The most frequently used one is the centroid method and the Gaussian peak-fit (Willert and Gharib, 1991), i.e., respectively

$$\hat{\varepsilon}_C = \frac{R_{+1} - R_{-1}}{R_{-1} + R_0 + R_{+1}} \tag{15}$$

$$\hat{\varepsilon}_G = \frac{\ln R_{-1} - \ln R_{+1}}{2(\ln R_{-1} - 2\ln R_0 + \ln R_{+1})} \tag{16}$$

The sub-pixel displacement is denoted with $\hat{\varepsilon}$ and the correlation values subsequently with R_{-1}, R_0 and R_{+1}. The centroid method is the most stable one, but it performs less accurately and it is strongly biased towards integer values, which leads to the so-called "peak-locking" effect. By the contrary, the Gaussian peak-fit estimator results in a much better approximation of the peak shape, thus leading to higher sub-pixel accuracy and, therefore, to a reduction in "peak-locking". The programming drawback of the Gaussian peak-fit estimator is the necessary use of the logarithmic function, as it is not defined for values smaller or equals zero. Furthermore, care has to be taken if the denominator is very close to zero. As a consequence, it may be necessary to decide, before applying the peak-fit estimator, if the Gaussian peak-fit can be applied or if the centroid method should be used instead. In our algorithm this criteria is adopted to prevent a discontinuous behaviour in the estimation of the sub-pixel displacement and, eventually, instabilities in the PIV evaluation program.

2.6 GRID REFINEMENT

To extend the dynamic range of the PIV evaluation method a grid refinement procedure can be used. This method decreases the size of the interrogation spots after every evaluation of the flow field and the integer-pixel displacement is used to shift the second interrogation window proportionally to local velocity vector. The remarkable advantage of this method is that particle displacements larger than the interrogation size can be resolved and, as a result, the spatial resolution can be increased. Such procedure has been in use since a long-time in numerical calculations. Kemmerich and Rath (1994) made its application to PIV.

3. EXPERIMENTAL ARRANGEMENTS

To assess the system's response to different algorithms under real flow conditions, PIV measurements at a low Reynolds number open water channel were carried out. LDA measurements and DNS computations were used as reference for comparison. In the following subsection, the experimental arrangements used are described.

3.1 ASSESSMENT OF THE DESCRIBED METHODS

To test the performance, reliability and the effect of the above-referred methods in comparison with the so called "standard evaluation algorithm" , Monte Carlo simulations were performed. For this test case, artificial images were generated in steps of 0.1 pixels displacements in x and y (resulting in a 45° vector of displacement), employing particles of 3-pixels in diameter. The particle density was quantified as 4 particles per 8 x 8 pixels interrogation spot. The Bessel-function of the particle imaging pattern was approximated by a Gauss-function. For a more detailed description see Willert (1995). Out-of-plane loss of particles and defocusing were not simulated.

3.2 THE EXPERIMENTAL SET-UP AND THE DIC-PIV SYSTEM

More general investigations can be carried out under real flow conditions. For this purpose, a low Reynolds number open water channel is used, Freek et al. (1997). The water channel consists of a 2.5 m long open duct made of Plexiglas, with a height of 200 mm and a width of 300 mm. The maximum surface velocity is approximately 0.07 m/s for a water depth of 110 mm. The flow at the test area approximates a zero pressure gradient boundary layer characterised by a Reynolds number Re_θ= 770, based on the surface velocity and momentum thickness.

The DIC-PIV system used in this investigation uses an image compression method. The principle and the application of the DIC-PIV system to boundary layer flows as well as to in-cylinder flows was given by Freek et al. (1997). A detailed description of the errors involved on this method was provided by Freek et al. (1998). The flow field is imaged by a Sony XC-750CE CCD camera with 768 x 576 pixels, operating in an interlaced mode. Throughout the prescribed experiments, a 1-Watt Argon-ion laser is used as a light source for the illumination of the selected planes in the flow field. The laser beam passes through a Bragg cell, which controls the pulse separation and pulse width, and it is then coupled into a mono-mode optical fibre. At the end of the optical fibre, the laser beam is expanded by the use of cylindrical and spherical lenses, producing a laser light sheet that has a height of 100 mm and a thickness of 1 mm.

3.3 THE LDA SYSTEM

In order to assess the quality of the results produced by the implemented PIV system, LDA measurements

may be used as reference. A fibre-optical 2D-LDA DANTEC system has been used together with a DANTEC BSA (Burst Spectrum Analyser). See Table 1 for a detailed description of optical and geometrical parameters. A PC was employed to control the BSA and to store the measured data, as well as for automatic control of the probe head by means of a 3-axis translation system. This allowed the scanning of the flow field in the water channel in steps of 0.5 -2 mm.

Laser power fibre out	W	1.3	1.1
Virtual beam waist	mm	1.35	1.35
Wavelength	nm	514.5	488
Focal length	mm	400	400
Beam separation	mm	38	38
Half angle of beam intersection	deg.	2.720	2.720
Major axis of the ellipsoid	mm	4.091	3.880
Minor axis of the ellipsoid	mm	0.194	0.184
Velocity transfer constant	m/s/MHz	5.422	5.143

Table 1 : Optical and geometrical parameters of the LDA system

4. RESULTS AND DISCUSSION

4.1 UNCERTAINTIES

In the present subsection, the various measurement uncertainties are discussed. The result of the cross-correlation, i.e. the displacement of the particles, Δx_{pixel}, is measured in pixel dimension. To convert from pixel dimension to metrical dimension, it is necessary to establish a calibration factor. This is done by photographing a known measure, L_c, and relating it with the number of pixels, N_{pixel}, in the image. As a calibration tool, a ruler was employed in the water channel. Dividing the displacement by the time between the two laser pulses, Δt, finally results in a velocity, v, in meters per second. The velocity of the PIV measurements is given in the following formula:

$$v = \frac{\Delta x_{pixel}}{\Delta t} \frac{L_c}{N_{pixel}} . \qquad 17)$$

An image from the calibration tool was made and, via image processing, it was overlaid with a variable calibration circle, which can be controlled in steps of one pixel. The goal is to equalize the diameter of the circle with the length of the calibration tool. The length of the calibration tool is estimated with an uncertainty of 0.5mm , leading to an uncertainty of 0.5% for 100mm length. In some cases it could not be distinguished whether the radius of the circle should be one pixel bigger or smaller, so we have to account for an uncertainty of 0.4% for two pixels in 500 pixels length. The pulse distance was generated by the electronically synchronisation device with an uncertainty smaller than 0.001% in time, Δt. With a Gaussian reproduction of errors, this would lead to an overall systematic error of less than 0.65% for the calibration uncertainty.

The overall uncertainty of the LDA system (photomultiplier, digitizing, etc.) evaluating a single burst is better than 0.5%, Dörner (1997). The evaluated frequency is transformed into velocity in units of meters per seconds by using the following formula:

$$v_{LDA} = \frac{f_D}{2 \sin \vartheta} \lambda , \qquad 18)$$

where the half-angle ϑ is calculated using the focal length and half beam-spacing:

$$\vartheta = \tan \frac{f_{probe}}{0.5 x_{spacing}} . \qquad (19)$$

The uncertainty in the half-angle can be estimated with a systematic error of less than 0.3%. The wavelength of the laser source can be considered without any systematic and random uncertainty. As a result, systematic and random errors of less than 0.3% and 0.5%, respectively, should be considered.

Additionally, a statistical analysis after Yanta and Smith (1978) can be carried out to estimate the uncertainty of computed mean and RMS values as a function of a given number of samples. For the water channel case, with 70 mm/s mean velocity, a variance of 10 mm/s was computed from 3000 samples. Thus, the error interval is $\varepsilon_{mean} = \pm$ 0.358 mm/s (0.5% of the surface velocity) and for the RMS velocity the interval leads to $\varepsilon_{rms} = \pm$ 0.025 (2.5% of the RMS velocity). The resulting uncertainties are shown in Table 2.

Water channel $\varepsilon_{PIV\,mean}$	%*	1.2
Water channel $\varepsilon_{PIV\,rms}$	%*	2.5
Water channel $\varepsilon_{LDA\,mean}$	%*	0.8
Water channel $\varepsilon_{LDA\,rms}$	%*	3
*Based on the surface velocity of 0.07m/s		

Table 2 : Uncertainties in the measurements

4.2 RESULTS FROM THE MONTE CARLO SIMULATIONS

Figure 1 shows the error in mean pixel displacement, defined as

$$\varepsilon_{mean} = disp._{simulated} - disp._{evaluated} \qquad (20)$$

and Figure 2 shows the value for rms.
The evaluation was carried out with an interrogation area (IA) size of 32 x 32 pixels resulting in 1645 individual vectors. The standard evaluation method leads to an under-estimation of around 0.05 pixels with a variation of ± 0.02 pixels.

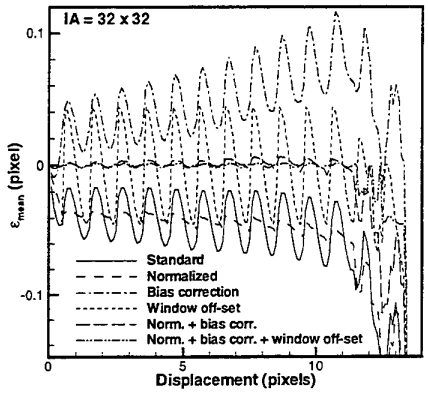


Figure 1: Error in mean displacement.

The curve is characterised by steep slope between 0 and 0.5 pixels displacement and continues with an almost horizontal slope. The function is modulated by a secondary function with an amplitude of 0.04 pixels and a frequency of exactly one pixel. This behaviour is in good agreement with that reported by other authors, e.g. Westerweel (1993).
Using the normalisation method, we see that the modulation disappears, but the error level still remains. If we switch on the velocity bias correction instead of the normalisation, the curve is over-estimating the pixel displacement, but the steep gradient between 0 and 0.5 pixels displacement remains. Once again, the curve continues with a relatively flat gradient, including the modulation phenomena. In the third step, we just apply the window off-set method, which results in the removal of under- or over-estimation of the mean error, but the modulation still remains. The absolute error is slightly smaller but the modulation has now an amplitude of 0.05 pixels. The combination of the standard method and velocity bias correction finally corrects the under-estimation and damps the modulation also. The joint application of all three methods, the normalisation, velocity bias correction and window off-set, leads to almost the same result. Turning to the Figure 2, which shows the error in RMS, we clearly see that standard evaluation, normalisation, velocity bias correction and the combination of normalization and velocity bias correction yield almost in the same result. The single application of window off-set is very effective as it maintains the RMS error level constant, apart from the well-known modulations. The combination of all methods reduces the error to a base level of 0.015 pixels, with a modulation characterised by an amplitude of 0.03 pixels.

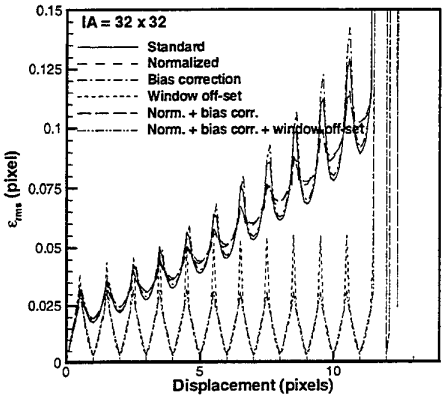


Figure 2: Value of rms displacement.

From the results presented above, we can conclude that the error for a synthetic image is less than 0.01 pixels in mean and below 0.03 pixels in RMS, for a IA of 32 x 32 pixels. It is also interesting to notice that the so-called "peak-locking error" does not exist if the correlation function is normalised and the velocity bias correction is applied.

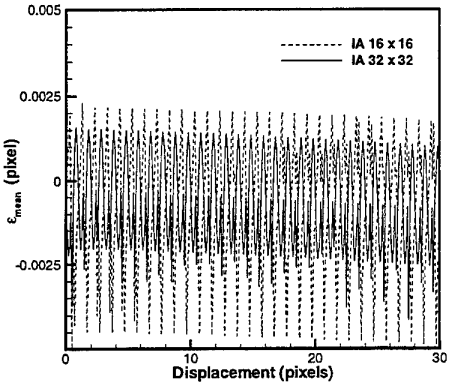


Figure 3: Error in mean displacement for grid refinement.

More important than the error values themselves, are the characteristic curves because in a real application, due to noise and spurious vectors, the error values are larger but the trend lines remain the same.

Figure 3 and 4 show the effect of grid refinement for two different interrogation spot sizes, IA 16 x 16 pixels and IA 32 x 32 pixels. It can be seen that the errors in mean and RMS are the same as in Figure 1 and 2, which proves that this method extends the dynamic range without introducing any noticeable additional error.

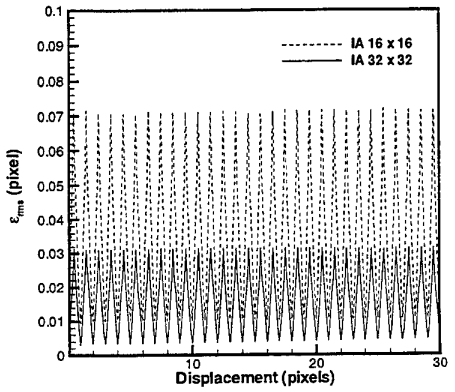


Figure 4: Value of rms displacement for grid refinement.

4.3 RESULTS FROM THE LOW-REYNOLDS NUMBER OPEN WATER CHANNEL

We now turn ourselves to the comparison between LDA, DNS and DIC-PIV, obtained for the water channel experiment.

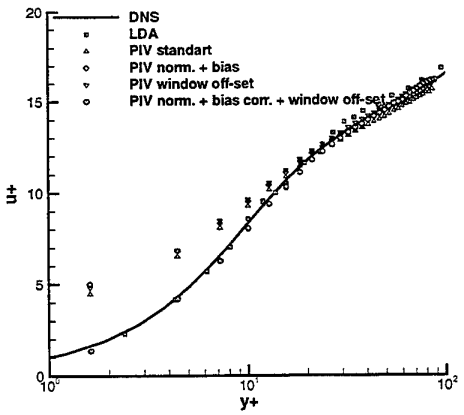


Figure 5: Mean velocity in wall co-ordinates.

It can be seen in Figure 5 that, the standard evaluation method under-estimates the mean value on the low velocity gradient region of the profile, over estimating in the near wall region due to the higher velocity gradient present in this area. Contrary to the Monte Carlo simulations, the window off-set performs better than the normalisation and the bias correction. The step velocity gradient near the channel wall is only reproduced correctly by the combination of all three correction methods.

Figure 6 shows the velocity fluctuation of u'+, v'+ and u'v'+. The DIC-PIV evaluation, containing all three correction methods, reproduces the measurements of u'+ with a negligible error, except for the region y+ < 10. The standard case clearly shows higher velocity fluctuations around 30%. The same conclusion applies to the quantities v'+ and u'v'+. However, the combination of normalization and bias correction results in even slightly higher values. This was expected, as the instantaneous velocity is corrected towards higher values by the combination of those methods.

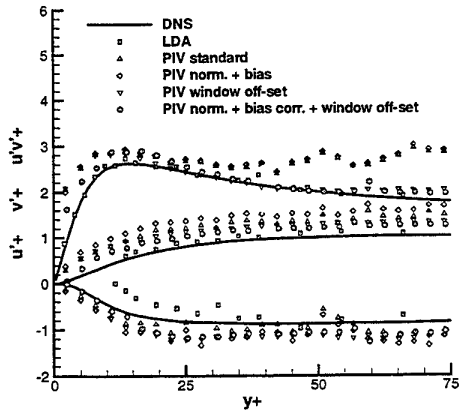


Figure 6: Turbulence intensities in wall co-ordinates.

In order to better analyse and understand the effect of the estimator corrections, a comparison between time series computed using the various methods is depicted in Figure 7, for the U component at y+ = 33. A time series for LDA is also shown in Figure 7, at the same position and employing the same sampling frequency, 25Hz, as in the DIC-PIV signal. This was achieved by resampling the original LDA signal, which was measured with an average sampling frequency of roughly 100 Hz.

The effect of each algorithm is readily apparent from the results. The better correction is the one which produces the largest number of meaningful vectors, i.e., the one reducing the number of spurious measurements.

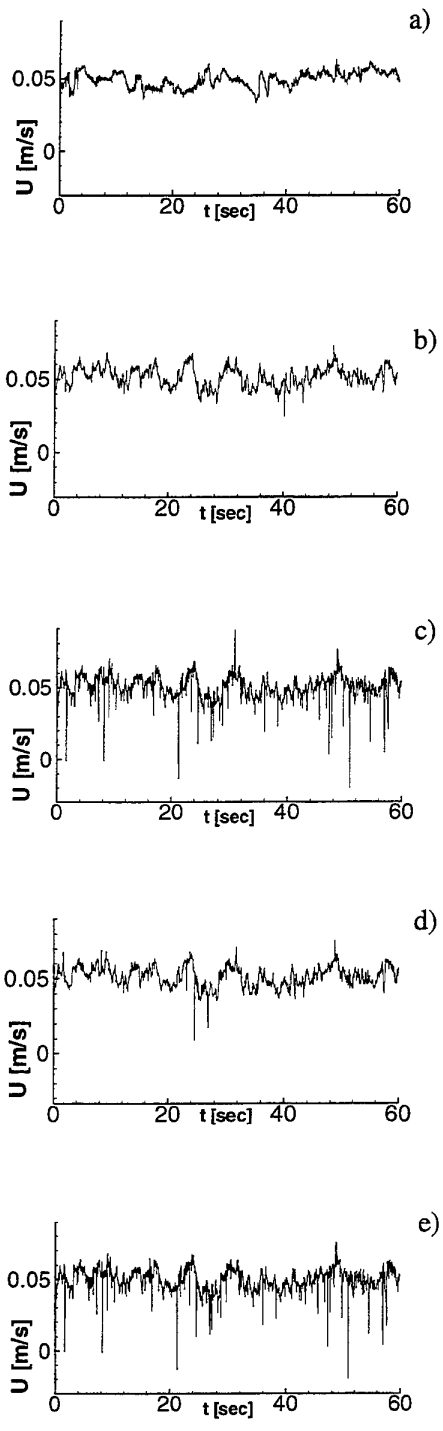


Figure 7:Time series of velocity; a) LDA signal, b) PIV signal with norm., bias corr. and window off-set, c) PIV signal with norm., bias corr., d) PIV signal with window off-set, e) PIV signal with standard method.

These are depicted as large spikes, characterising velocity values that are, in general, lower than the average of all measurements. It is clear that the spikes mostly appear in time series obtained by evaluation methods not including the adaptive shift technique, i.e., cases c) and e). Naturally, the power spectra computed from respective signals reflect the foregoing observations. The amount of spurious measurement values in the signal increases the power at higher frequencies, as a manifestation of noise. This view supports the statement that it is important to apply a normalised correlation function and the need to correct for the velocity bias before estimating the exact location of the correlation peak. Furthermore, it is elementary to use the adaptive window off-set method, as only the combination of all described methods yields adequate measurement accuracy.

This was demonstrated in Monte Carlo simulations and corroborated now in real flow conditions. It is also interesting to note that it was possible to reproduce the –5/3 slope in the power spectrum, which agrees with the expected behaviour of the inertial sub-range, Figure 8.

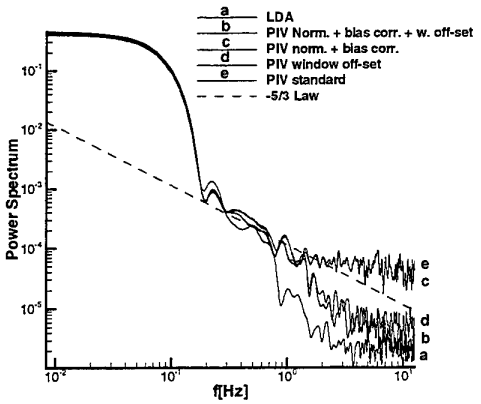


Figure 8: Power spectra.

5. CONCLUSIONS

In this communication the accuracy of a cross-correlation PIV technique was assessed in detail using Monte Carlo simulations. Real flow conditions were investigated as well and validation was provided by LDA measurements in a low-Reynolds number open water channel. Correction methods that must be considered in the evaluation process are reviewed, their characteristics are pointed out by means of Monte Carlo simulations and their effects under real flow conditions are quantified. Furthermore, the reliability of the PIV technique for the measurement of mean velocity fields was demonstrated. From the present investigation one may draw the following conclusions which find application in both ideal and

applied conditions. The local mean intensity of the interrogation area has to be subtracted, as advocated before by Adrian (1988). The velocity bias correction has to be applied before estimating the sub-pixel displacement of the correlation peak, as suggested by Westerweel (1993a). The adaptive window shift, suggested by Westerweel et al. (1995), is fundamental to obtain a correct evaluation of the flow velocity in real flow conditions. It was proved that without incorporating the aforementioned procedures in PIV evaluation schemes may lead to a mean velocity under-estimation of 5% and over-estimation of fluctuation velocities, like RMS, of 30% is obtained. It must be stressed that these errors are incurred even for situations close to ideal conditions of seeding and optical access. Furthermore, it was shown that the present DIC-PIV system which is based on image compression does not introduce additional noticeable errors in mean velocity quantities. The differences among LDA, PIV and DNS lie below 1% for mean velocity and below 3% for RMS and Reynolds shear stress. Good agreement was also observed for a local time series and corresponding power spectrum. This communication shows that a proper implementation of digital PIV including image compression yields negligible errors in various kinds of turbulence statistics.

ACKNOWLEDGEMENTS

The authors grateful acknowledge the help of Dr. M.-A. Beeck for discussions and review of the manuscript. J.M.F. Raposo carried out this work as a part of the TMR programme financed by the European Commission. The author gratefully acknowledges this support.

REFERENCES

Adrian R.J. 1984: Appl. Opt. Vol. 23 pp. 1960

Adrian R.J. 1986: Multi-point optical measurement of simultaneous vectors in unsteady flow - a review. Int. J. Heat and Fluid Flow, pp. 127-145.

Adrian R. J. 1988: Statistical properties of particle image velocimetry measurements in turbulent flow. Laser Anemometry in Fluid Mechanics ed. R. J. Adrian et al. Proceedings of the 4th International Symposium Lisbon, Portugal, pp 115-29.

Adrian R. J. 1991: Particle-imaging techniques for experimental fluids mechanics. Ann. Rev. Fluid Mech., vol. 23, pp. 261-304.

Backer D.B. and Fourney M.E. 1977: Measuring fluid velocities with speckle patterns. Opt. Lett. Vol. 1, pp. 135-137.

Dörner C. 1997: Private communication. Dantec/invent Measurement Technology, Germany.

Freek C., Sousa J.M.M., Hentschel W. and Merzkirch W. 1997 : Digital Image Compression PIV, a Tool for IC-Engine Research" 7th International Conference on Laser Anemometry – Advances and Applications, 8-11 September 1997, Karlsruhe, Germany, pp. 455 - 464..

Freek C., Sousa J.M.M., Hentschel W. and Merzkirch W. 1997: On the accuracy of an MJPEG-based digital image compression PIV-system. Submitted to Exp. Fluids.

Hinsch K.D. 1993 : Particle image velocimetry, in : Speckle Metrology, ed. R.S. Sirohi, pp. 235-323, Marcel Dekker, New York.

Keane R. D. and Adrian R. J. 1993 : Appl. Sci. Res. Vol. 49, pp. 191, Institute of Physics Publishing.

Kemmerich Th. And Rath H.J. 1994 : Multi-level convolution filtering technique for digital laser-specle-velocimetry. Exp. in fluids, Vol. 17, pp. 315-322, Springer Verlag.

Kompenhans J. and Höcker R. 1988: Application of particle image velocimetry to high speed flows. In Particle Image Displacement veloimetry. (Ed.. M. Riethmuller) Rohde-Saint-Genese: von Karman Inst. Fluid Dyn. pp. 67-84.

Lourenco L, Krothapalli A, Riethmuller ML, Buchlin JM (1986): A non-invasive experimental technique for the measurements of unsteady velocity and voracity fields. AGARD-CP-413, pp. 231-239.

Merzkirch W. 1987 : Flow Visualisation, 2nd ed., Academic Press, Orlando.

Reuss D. L., Adrian R. J., Landreth C. C., French D. T. and Fansler T. D. 1989: Instantaneous planar measurements of velocity and large-scale vorticity and strain rate in an engine using particle image velocimetry. SAE Technical Paper Series 890616.

Simpkins and Dudderar T. D. 1978: Laser speckle measurements of transient Bénard convection. J. Fluid Mech., Vol. **89**, pp 665-671.

Spalart P. R. 1988 : Direct simulation of a turbulent boundary layer up to $Re_\theta = 1410$. J. Fluid Mech. **187**, pp. 61-98.

Westerweel J., Dabiri D. and Gharib M. 1995: Noise reduction by discrete image shifting in DPIV. In: J.P. Crowder, Proceedings of the Seventh International Symposium on Flow Visualisation, Begell House, New York, pp. 688-694

Westerweel J., Flor J.B., Nieuwstadt F.T.M. 1990: Measurements of dynamics of coherent flow structures using particle image velocimetry. In: Adrian R.J. et al., editors, Applications of a Laser Technique in Fluid Mechanics, Springer-Verlag, pp. 285-307

Westerweel J. 1993a : Digital Particle Image Velocimetry - Theory and Application, Delft University Press.

Westerweel J. 1993b : Optical diagnostics in fluid and thermal flow. SPIE, Vol. 2005, pp. 624-35.

Willert C.E., Gharib M. 1991: Digital Particle Image Velocimetry. Exp. Fluids 10, pp. 181-193.

Willert C.E. 1996; The Fully Digital Evaluation of Photographic PIV Recordings. Appl. Sci. Res. Vol. 56, pp. 79-102.

Yanta Z. and Smith R. A. 1978: Measurements of turbulent transport properties with a Laser-Doppler velocimeter. AIAA Paper 78-169, 11th Aerospace Science Meeting, Washington.

WAVENUMBER SPECTRUM ESTIMATION FROM IRREGULARLY SPACED DATA: APPLICATION TO PIV DATA PROCESSING

W. Hübner[‡], C. Tropea[†] and J. Volkert[‡]

[†] *Fachgebiet Strömungslehre und Aerodynamik, TU Darmstadt, Petersenstr. 30, 64287 Darmstadt, Germany*
[‡] *Lehrstuhl für Strömungsmechanik, University of Erlangen-Nürnberg, Cauerstr. 4, 91058 Erlangen, Germany*

ABSTRACT

The problem of 2D wavenumber spectrum estimation from randomly sampled data is examined. Two new estimators are proposed, one based on a spatial sample and hold procedure and one based on the projection slice theorem, commonly used in tomography. Each estimator is tested using simulated PTV data. Initial results indicate that these estimators have the potential to extend spectral estimates beyond the convential Nyquist limits imposed when using regularly sampled data.

1. INTRODUCTION

When describing turbulent motions in a statistical sense much of our fundamental theoretical knowledge exists in the form of either spatial correlations or wavenumber spectrum [15]. Examining flows experimentally using point measurement techniques such as Hot Wire Anemometry or Laser Doppler Anemometry, requires therefore a transformation of the obtained velocity time series into spatial information, either through the simultaneous use of multiple probes or through application of the Taylor hypothesis. The first possibility is tedious at best and the second is only applicable for f-type correlations. In this respect Particle Image Velocimetry (PIV) provides a unique opportunity to estimate spatial correlations of velocity fluctuations, even for non-stationary and possibly also for non-homogeneous turbulence fields.

The term PIV is understood here to encompass also Particle Tracking Velocimetry (PTV), the usage being generally chosen according to particle density but in essence residing in the data processing applied. A good overview of current PIV and PTV techniques is given in [7,12], whereby the increased use of 3D PTV is noteworthy. One main distinction between PIV and PTV is the fact that PIV velocity vectors are equally distributed in space, corresponding to a regular pattern of interrogation spots. PTV on the other hand provides a velocity vector for every identifiable tracer particle pair and as such, is a spatially irregular sampling of the velocity field. While most commercial systems offer only a PIV processing, methods do exist which allow, even for high particle densities, an individual particle tracking to be accomplished. The most well known of these is the Super-Resolution PIV presented in [5].

Addressing the problem of wavenumber spectrum estimation from PIV or PTV data has many analogies with frequency spectrum estimation from velocity time series obtained using an LDA. In this analogy the roles of time and space are almost perfect counterparts. In the more familiar case of frequency spectrum estimation, it has long been recognized that the irregular (or near random) sampling of the velocity in time can be both advantageous and disadvantageous. The advantage lies in the principle ability to estimate the spectrum far beyond the average Nyquist frequency, while the disadvantage lies in having to find an estimator suitable for randomly sampled data. This topic has been exhaustively studied in recent years and an appropriate estimator for frequency spectra can be found in [9,11]. The main subject of the present paper is to investigate similar estimators applied to spatially irregular sampled data, to yield wavenumber spectra. Emphasis will be placed on 2D PTV data, although no fundamental exclusion of 3D PTV data can yet be identified.

Returning to the space/time analogy, it can be seen that PIV velocity vectors, which are local spatial averages over one interrogation spot, would correspond to short time averages of LDA data. Such time averaging of LDA data prior to further processing is never performed, as the high time resolution of LDA is sacrificed. Similarly, except for the aes-

thetics of a regular pattern of velocity vectors, there also doesn't appear to be any fundamental advantage of locally averaging the spatial data from a PIV system. Certainly other techniques have been proposed which dispense with this practice altogether and retain the spatial resolution offered by the chosen particle density [13]. One exception is the use of PIV vectors in the pre-estimation procedure of super-resolution PIV, which indeed will constitute its main justification in the present paper.

A final remark concerning the analogy is that stationarity in time will correspond to homogeniety in space and for the following discussion these states will be assumed.

Therefore, the starting point of the present paper is that PTV data is available and that an estimate of wavenumber spectra is to be made from the spatially irregularly sampled data. Much can be learned from previous experience of spectral estimation in time domain before proceeding. One of the first suggestions to deal with the irregular sampling in time, was to perform a direct Fourier transform (DFT) on the data, utilizing the arrival time information in the estimate but with the computational penalty of not being able to apply FFT algorithms [2,3]. This is not a viable approach due to the extremely high variability of the estimate, which was recognized by its authors at the time and since confirmed. Therefore, there is no reason to pursue a 2D DFT as a procedure to apply in the present case.

A more widely used technique is the slot correlation, in which resolution and variability are traded off through the choice of slot (or bin) width in lag time τ [6,14]. This is no doubt a possible route to also obtain a 2D spatial correlation from PTV data. However it has been shown that refined reconstruction methods can achieve a lower estimator variance at high frequencies than the slot correlation [9].

In time series analysis, the slot correlation also displays a bias if the data set mean was poorly estimated or if there was a velocity/sample rate correlation (the origin of statistical velocity bias in LDA data processing). With PTV data there is no reason to believe that there will exist any correlation between particle spatial density and velocity, at least if all the particles are following the flow with no slip. Therefore this is one aspect of time series analysis , which, in the analogy, does not appear in the analysis of spatially distributed velocity information.

Two procedures for wavenumber spectrum estimation from irregularly spaced data will therefore be pursued. The first is a direct extension of the technique given by [9,11] from one dimension (time) to two dimensions (space).

The second technique has its origins in tomography and it involves the application of the projection slice theorem (PST) [8]. The following two sections describe each of these techniques respectively. First results are obtained using simulated data, derived from direct numerical simulations (DNS), for which the wavenumber spectrum was known. The influence of noise has not yet been considered. These results and their discussion are given in the final section.

2. WAVENUMBER ESTIMATION USING A 2D SAMPLE AND HOLD WITH REFINEMENT

To review briefly the approach of [9], the LDA time series data is resampled at regular time intervals $(1/f_r)$ using a sample and hold (S+H) reconstruction. This procedure is illustrated schematically in Fig.1. The velocity data is available from the LDA at the particle arrival times t_i. A reconstruction is obtained by resampling at a frequency f_r, along t using the last valid velocity value.

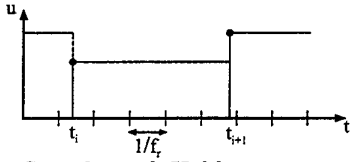


Figure 1: Sample and Hold reconstruction from LDA velocity data.

The expected autocorrelation of the resampled data is derived similar to the procedure given in [1] and is denoted by $R_{uu}^{(r)}(k\Delta\tau_r)$. This function is related to the true autocorrelation function through a linear filter matrix $\mathbf{F}$,

$$R_{uu}^{(r)} = \mathbf{F} R_{uu} \tag{1}$$

which when inverted, yields a non-biased and consistent estimator of the true autocorrelation function

$$\hat{R}_{uu} = \mathbf{F^{-1}} \hat{R}_{uu}^{(r)} \tag{2}$$

The frequency spectrum can be obtained via a Fourier transformation. The only parameter involved in the filter $\mathbf{F}$ is the mean data rate $\dot{n}$ (particles/s). All details of this procedure can be found in [9].

Applying this technique to two spatial dimensions first requires an equivalent spatial sample and hold, which can be envisioned graphically as illustrated in Fig. 2. For a given grid point lying on a regular mesh (ξ_i, ψ_j), a velocity value will be assigned which corresponds to the nearest sample lying in the third quadrant, P_k. (The choice of quadrant is presumably immaterial). Using the next particle in a direction aligned with the mesh, would result not only

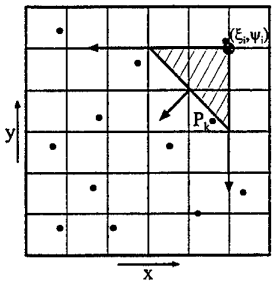


Figure 2: Spatial Sample and Hold

in using particles far removed from the mesh point, but many mesh points would get assigned the same value. Thus the choice of a 45° direction. It should also be remarked, that the value to be assigned may just be a single velocity component or the velocity magnitude, depending on what wavenumber spectrum is to be estimated.

The next step is to estimate the probability that the velocity of a given particle will be used. There are two cases to be considered, as shown graphically in Fig. 3.

Case 1: In this case a particle occurs at (x_1, y_1)

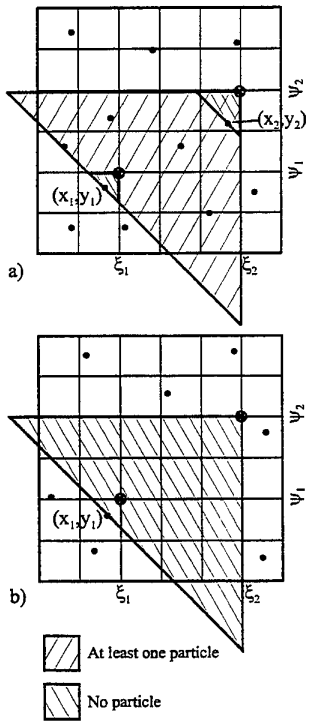


Figure 3: Possible cases for S+H resampling: a) Case 1; b) Case 2.

which is to the lower left of (ξ_1, ψ_1) and no further particle is found in the triangle

$$x = \xi_1 \quad y = \psi_1 \quad y = (x_1 + y_1) - x \qquad (3)$$

Furthermore at least one particle occurs in the triangle

$$x = \xi_2 \quad y = \psi_2 \quad y = (x_1 + y_1) - x \qquad (4)$$

excluding the triangle given in Eq. (3). No further particle is found in the triangle

$$x = \xi_2 \quad y = \psi_2 \quad y = (x_2 + y_2) - x \qquad (5)$$

The probability of this case occurring can be evaluated by assuming the particle distribution follows a Poisson distribution, characterized by a mean data density of $\dot{n}$ particles/area. The probability of finding at least one particle in an area $\Delta\xi\Delta\psi$ is then

$$P(\Delta\xi, \Delta\psi) = 1 - e^{-\dot{n}\Delta\xi\Delta\psi}, \qquad (6)$$

where $\Delta\xi\Delta\psi$ represents the resolution of the resampling grid. The probability for the above case becomes

$$P_1(x_1, y_1, x_2, y_2) = \left(1 - e^{-\dot{n}\Delta\xi\Delta\psi}\right)^2 \cdot e^{-\frac{1}{2}\dot{n}(\xi_1 - x_1 + \psi_1 - y_1)^2} \cdot e^{-\frac{1}{2}\dot{n}(\xi_2 - x_2 + \psi_2 - y_2)^2} \qquad (7)$$

Case 2: In this case a particle is found at a position (x_1, y_1) to the lower left of (ξ_1, ψ_1) and no further particle is found in the triangle (shaded area in Fig. 3b)

$$x = \xi_2 \quad y = \psi_2 \quad y = (x_1 + y_1) - x \qquad (8)$$

The probability for this case occurring is

$$P_2(x_1, y_1) = \left(1 - e^{-\dot{n}\Delta\xi\Delta\psi}\right) \cdot e^{-\frac{1}{2}\dot{n}(\xi_2 - x_1 + \psi_2 - y_1)^2} \qquad (9)$$

These two cases can now be used to relate the measured spatial correlation on the ξ/ψ mesh to the spatial correlation of the particles.

An equation results in the form of Eq. (1), in which the filter matrix $\mathbf{F}$ is now only a function of the particle area density $\dot{n}$. This equation has been derived, however due to its length, it is not shown. Reference is made to [4]. The next step is to find the inverse function $\mathbf{F^{-1}}$. This has not yet been accomplished.

3. WAVENUMBER ESTIMATION USING THE PROJECTION SLICE THEOREM (PST)

The projection slice theorem used in tomography will be used to derive an estimator for wavenumber spectra. The projection slice theorem (PST) is shown pictorially in Fig. 4. Basically it says that the one-dimensional Fourier transform of a projection of the function $f(x, y)$, is a slice of the two-dimensional Fourier transform $F(\omega_x, \omega_y)$ of the original function. The Fourier transform of the projection of the field

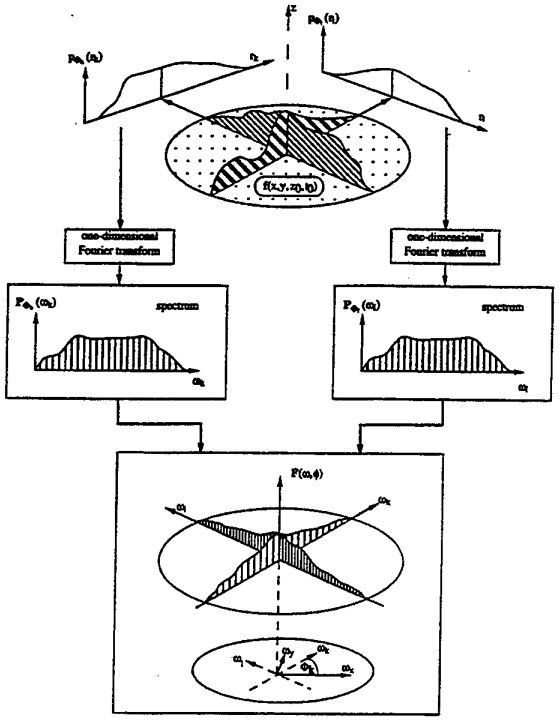


Figure 4: Pictorial representation of the projection slice theorem.

$f(x,y)$ onto the axis r rotated an angle ϕ with respect to x is given by

$$P_\phi(\omega) = \int_{-\infty}^{\infty}\int_{-\infty}^{\infty} f(r,s)\,ds \quad e^{-jr\omega}dr \qquad (10)$$

where the integral over s is the projection. The PST states that

$$P_\phi(\omega) = F(\omega,\phi) = F(\omega_x,\omega_y) \qquad (11)$$

$$\text{for} \quad \omega_x = \omega\cos\phi \qquad (12)$$

$$\omega_y = \omega\sin\phi$$

It can also been extended to apply to the power spectral density. This means that the power spectrum of the projected field is related to the power spectrum of the two-dimensional field through

$$P_\phi^*(\omega)\,P_\phi(\omega) = F^*(\omega_x,\omega_y)\,F(\omega_x,\omega_y) \qquad (13)$$

A further consideration of applying the PST to PTV data leads to the necessity of introducing small slices of width dr to carry out the integration in the s direction, as illustrated in Fig. 5.

Introducing a slice of width dr will obviously be equivalent to a a spatial filter, the question to be investigated is whether dr can be made substantially smaller than a typical PIV interrogation spot, in which case some advantage in resolution can be gained using the PST.

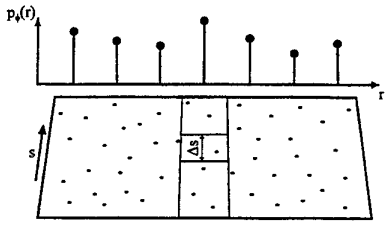


Figure 5: Slice of width dr to integrate in s-direction.

4. APPLICATION TO SIMULATED DATA

The estimation algorithms described in the previous sections have been applied to simulated PTV data. With simulated data the correct wavenumber spectrum is known and thus both the extension and the the variance of the estimator can be evaluated. Furthermore, the data can be noise free, which for the present purpose is advantageous.

Data was generated using homogeneous isotropic turbulence fields computed by direct numerical simulation (DNS) of the Navier Stokes equations. By DNS homogeneous isotropic turbulence fields are computed according to the following procedure.

First, a fluctuating velocity field is generated on an isotropic mesh. Both the integral length scale and the turbulent kinetic energy are introduced by scaling this velocity field with a prescribed spectrum. As usual in DNS, the mesh size implicitly defines the Kolmogorov length scale. The viscosity is then evaluated to satisfy that scale. The computation was performed in a box, using periodic boundary conditions in all directions. To get a turbulence field with higher moment statistical properties, the fluctuating field must freely evolve satisfying the Navier Stokes equations.

A typical input turbulence field is shown in Fig. 6, in which lines of constant velocity are shown. Note that there is no mean flow. This input field is a slice of the DNS data available on a mesh of 256x256 grid points. The autocorrelation of this field is shown in Fig. 7, where the integral length scale is determined to be $I = 0.093$. The total field dimensions are 2.8x2.8 or 30x30 length scales. There were approximately 9 DNS grid points per integral length scale.

Velocity samples were randomly distributed in the field according to a Poisson distribution with density parameter $\dot{n}$. The velocity at any given point was interpolated using weighted mean of the neighboring four DNS grid points. The resolution of the input DNS fields and also the linear interpolation used for assigning velocity values will also limit the validity of the following comparisons, however some first parameter dependencies can still be identified.

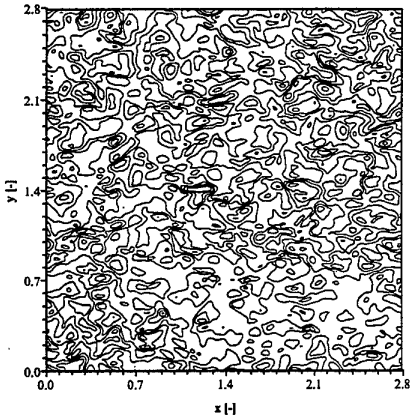


Figure 6: Turbulence field simulated with DNS

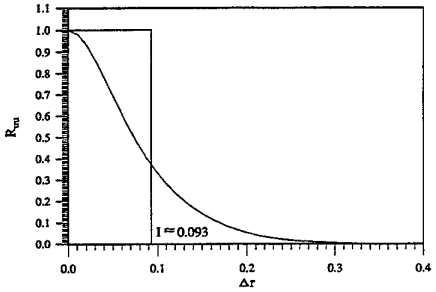


Figure 7: Integral length scale

Sample and Hold Estimate

In Fig. 8 and 9 the dependence of the sample and hold (S+H) spectral estimate, without the refinement given in Eq. (2), on the particle density and the resampling rate is given, respectively. In Fig. 8 a resample mesh of 1024x1024 is used and the particle density is varied between $1/I^2$ and $60/I^2$. The wavenumber spectrum obtained directly from the DNS field is shown for comparison. To simplify the comparison only a slice of the spectrum at 90° is shown for each of the estimates.

The DNS spectrum corresponds to the prescribed spectrum, showing small fluctuations which correspond to its variability, since only one realization has been used. At low particle rates the S+H wavenumber spectrum exhibits a filter like behavior, with a slope of approximately -1.7 and a cut-off at approximately 50. Note, that the wavenumber is defined as $k = 2\pi/\lambda$. The smallest resolvable wavenumber is therefore 2.24 $(2\pi/2.8)$ and the maximum wavenumber is 1149 $\left(\frac{2\pi}{2(2.8/1024)}\right)$. The wavenumber corresponding to the integral length scale is 67 $(2\pi/0.093)$. Clearly the low particle density acts as a filter, through which high wavenumber fluctuations can no longer be resolved. A similar behavior is seen in the time domain, whereby the slope is -2 and the cut-off frequency is given by $\dot{n}/2\pi$ [1]. However in time series analysis, a S+H resampling also leads to so called "step noise", which raises the entire spectrum uniformly across all frequencies. An equivalent to this step noise is not observed in the wavenumber spectrum.

Increasing the particle density improves the estimate, however at a value of 60 P/I^2, an asymptotic distribution is obtained. The asymptotically reached spectrum follows the flow spectrum until about $k = 100$, after which it flattens out. In time series analysis a continual improvement with increasing particle density could be expected. In the present case this is not observed, probably due to the interpolation step necessary in generating the simulation data. The wavenumber spectrum obtained for 60 P/I^2 presumably corresponds to the true spectrum of linearly interpolated data from the DNS data set. In Fig. 9 the influence of the resample rate is investigated. In time series analysis the resample rate does not influence the estimation (Nyquist frequency). Fig. 9 indicates that a higher resample rate in space does however improve the wavenumber spectra estimate.

Estimate from PST

Estimates of the wavenumber spectrum using PST are shown in Fig. 10 for a bin width of $\Delta r = 0.0155$. This leads to a maximum wavenumber of 202 $(\frac{2\pi}{2\Delta r})$. In Fig. 10 the particle density has been varied between 10 and 60 P/I^2. As with the S+H estimate, the spectrum improves with increasing particle density, as can be expected. However at all particle densities the high wavenumber behavior is uniformly flat, indicating that this part of the spectrum corresponds to an interpolation noise present already in the simulation data. At 60 P/I^2 there is on average approximately 1 particle/DNS grid cell.

In Fig. 11 the influence of the bin size Δr on the spectrum is shown. In fact the estimate improves with broader bins. For the narrowest bin of $\Delta r = 0.0039$, there are in average about 80 particles per integration slice at a particle density of 60 P/I^2 and an angle of 0° or 90°. This increases to 330 particles for $\Delta r = 0.0155$.

Fig. 12 shows the influence of the number of slices (N_A) being averaged to estimate the mean spectrum. Note, that for the slice under 90° and the mean over 8 angles the curves are shifted up/down. As expected, the variance of the estimate decreases with increasing the number of angles. Investigating isotropic turbulent fields, this represents an important advantage of the PST procedure compared to the 2D S+H method, since the number of velocity fields to be measured can be reduced.

In Fig. 13 a comparison of the result from both

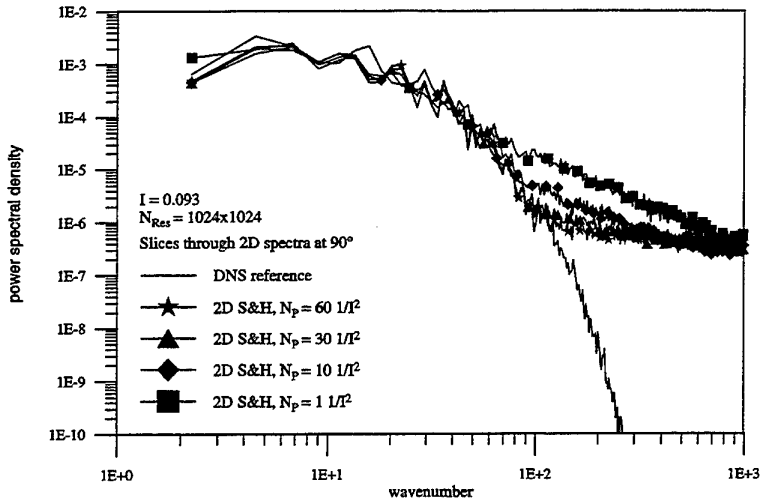


Figure 8: Power spectral density from 2D S&H at different particle densities

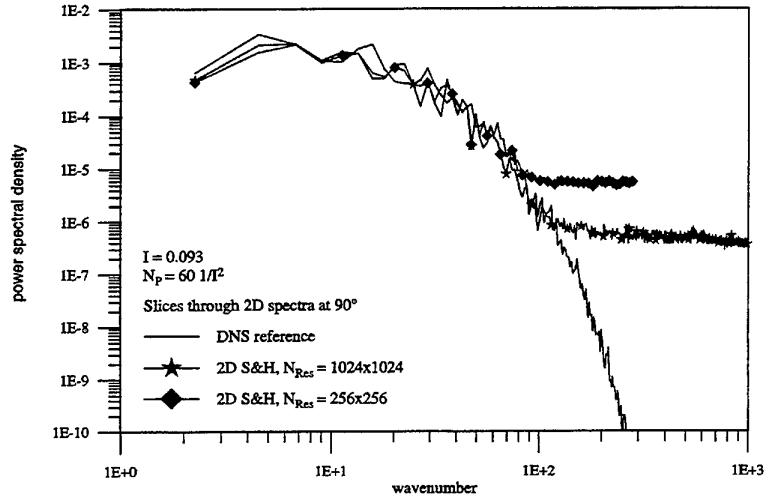


Figure 9: Power spectral density from 2D S&H with different resampling rates

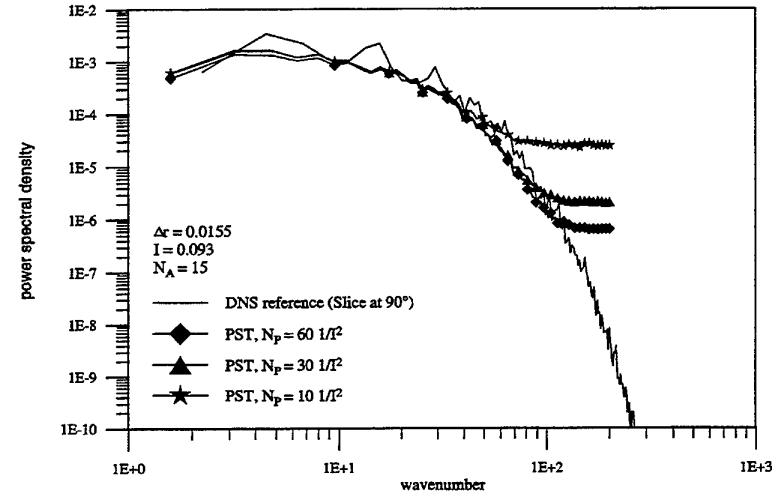


Figure 10: Power spectral density from PST at different particle densities

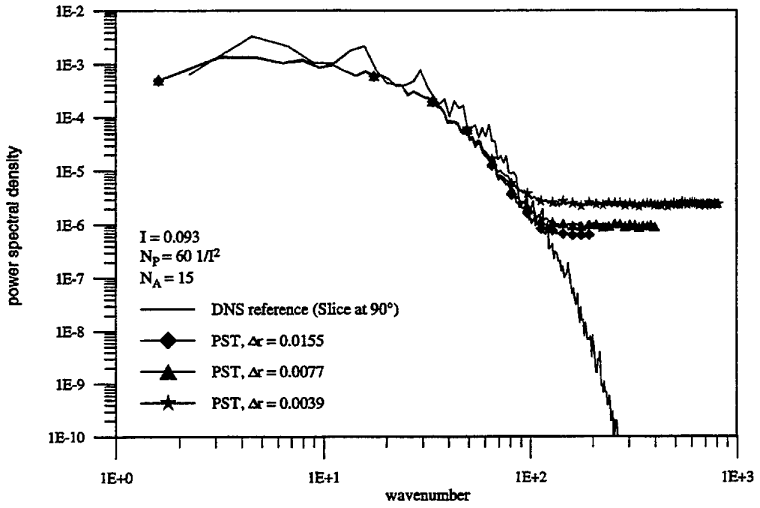


Figure 11: Power spectral density from PST with different sizes of the bins (Δr)

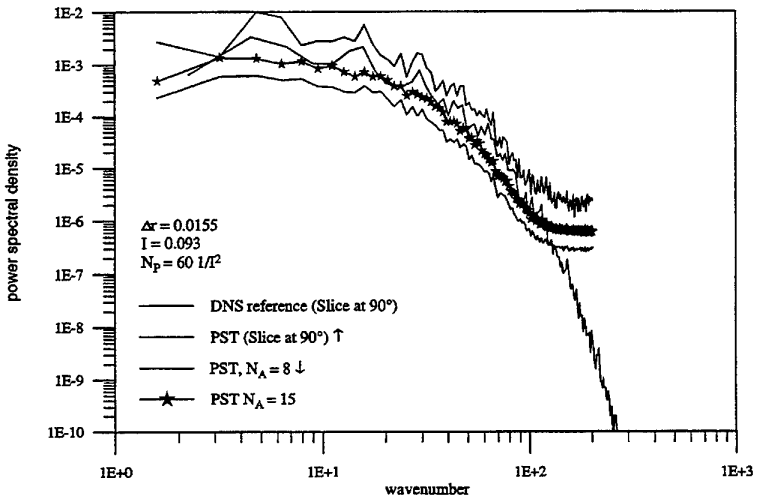


Figure 12: Power spectral density from PST, means over a different number of angles

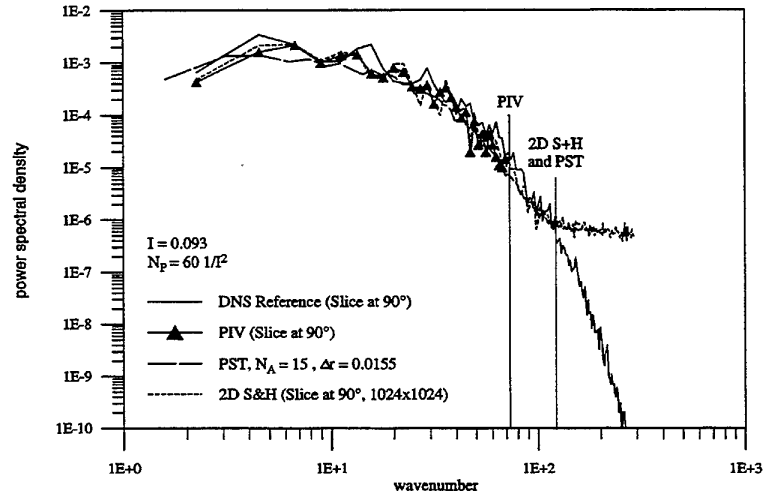


Figure 13: Comparison between the estimated power spectral density from 2D S&H, PST and PIV

the PST and the 2D S+H procedure and an estimate of the PSD as derived from PIV measurements is presented. The chosen number of of interrogation arrays (IA) corresponds to a number of 14 particle pairs per IA. While the maximum resolvable wavenumber according to the PIV resolution is 71, the spectra obtained by the presented estimators both follow the theoretical spectrum until $k = 100$. The main difference between the two proposed estimators for irregularly sampled data is expressed by a smaller variance of the PST results through averaging over several angles.

5. SUMMARY AND OUTLOOK

The present paper is a first presentation of two estimators for wavenumber spectra from PTV data. The first of these estimators, the sample and hold with refinement has not yet been fully formulated since a closed form for the refinement step must still be derived. However a sample and hold procedure for two dimensions could be presented. The procedure for the second estimator, based on the projection slice theorem is complete.

The performance of each of these estimators could not yet systematically evaluated. The main obstacle is the generation of homogeneous isotropic turbulence fields with known spectral content. The technique presently used, taking velocity field data from DNS computation, is rather unsatisfactory because the resolution of the primary data is quite coarse. Much finer grids become very demanding on computational time. Alternative methods of signal simulation must be sought.

A restriction which has not yet been discussed at length is that of homogeniety. In the analogy with time series analysis, that corresponds to statistical stationarity. If a signal is transient in time, a spectrum estimated over a longer period of the signal will be some weighted average of the changing spectral content. Similar averaging can be expected over space with the proposed estimators, if the turbulence field is non-homogeneous. At best, a smaller observation window can be applied and traversed across the field.

Although the present estimators are far from being complete, already other applications can be recognized. For instance wall arrays of hot-film sensors are used to monitor the passage of velocity fluctuations. The minimum spacing between sensors is physically limited, thus also the maximum resolvable wavenumber of disturbances. A random placement of arrays together with one of the above wavenumber estimators may prove to be advantageous in this case.

ACKNOWLEDGEMENTS

The close consultation with Holger Nobach in deriving the spatial S+H scheme is gratefully acknowledged. W. Hübner was supported by the PROCOPE program during his stay at École Centrale de Lyon, where Marc Michard was very helpful in assisting with organizing suitable PIV experiments. Thanks are also due to Henry Pascal for providing the DNS fields used to simulate PTV data and to Lance Benedict for several useful discussions.

REFERENCES

[1] Adrian, R.J. and Yao, C.S. 1987 *Power Spectra of Fluid Velocities Measured by Laser Doppler Velocimetry* Exp. in Fluids **5** 17-28

[2] Gaster, M. and Roberts, J.B. 1977 *The Spectral Analysis of Randomly Sampled Records by a Direct Transform* Proc. R. Soc. Lond. A. 27-58

[3] Gaster, M. and Roberts, J.B. 1975 *Spectral Analysis of Randomly Sampled Signals* J. Inst. Maths. Applics. **15** 195-216

[4] Hübner, W. 1998 *Abschätzung von zweidimensionalen Leistungsdichtespektren aus nicht-äquidistant abgetasteten Skalarfeldern: Anwendung auf Particle Tracking Velocimetry* Diplomarbeit Universität Erlangen-Nürnberg, Germany

[5] Keane, R.D. Adrian, R.J. and Zhang, Y. 1995 *Super Resolution Particle Image Velocimetry* Meas. Sci. Technol. **6** 754-768

[6] Mayo, W.T. Jr. Shay, M.T. and Riter, S. 1974 *Digital Estimation of turbulence power spectra from burst counter LDV data* Proc. of the Second Int. Workshop on Laser Velocimetry, Purdue Univ., West Lafayette, Indiana 16-26

[7] Measurement Science and Technology 1997 Special Issue: Particle Image Velocimetry, vol. **8**, no. 12, 1379-1583

[8] Mersereau, R.M. and Oppenheim, A.V. 1974 *Digital Reconstruction of Multidimensional Signals from their Projections*, Proc. of the IEEE, vol. **62**, no. 10, 1319-1338

[9] Nobach, H. Müller, E. and Tropea, C. 1998 *Efficient Estimation of Power Spectral Density from Laser Doppler Anemometer Data* Exp. Fluids **24** 5/6 499-509

[10] Nobach, H. 1997 *Verarbeitung stochastisch abgetasteter Signale*, Dissertation Universität Rostock, Germany

[11] Nobach, H. Müller, E. and Tropea, C. 1996 *Refined Reconstruction Technique for LDA Data Analysis*, Proc. 8th Int. Symp. of Appl. of Laser Techn. to Fluid Mechanics, Lisabon, Portugal **23.2**

[12] Raffel, M. Willert, C. and Kompenhans, J. 1998 **Particle Image Velocimetry: A Practical Guide** Berlin, Springer

[13] Ruck B. 1995 *A new Laser-Optical Method for Visualization and Real-Time Vectorization of Flow Fields* Proc. 6th Int. Conf. Laser Anemometry, Hilton Heat, South Carolina, FED vol. **229** 179-194

[14] Scott, P.F. 1974 *Random Sampling Theory and its Application to Laser Velocimeter Turbulence Spectral Measurements* Report 74CRD216, General Electric Co, Cooperate Research and Development

[15] Tennekes, H. and Lumley, J.L. 1972 **A First Course in Turbulence**, The MIT Press, Cambridge, Massachusetts

The Elimination of Correlation Errors in PIV Processing

Douglas P. Hart

Massachusetts Institute of Technology
Department of Mechanical Engineering, Room 3-246
Cambridge, MA 02139-4307

ABSTRACT

A non-post-interrogation method of reducing sub-pixel bias errors and eliminating spurious vectors from particle image velocimetry (PIV) results is presented. Unlike methods that rely on the accuracy or similarity of neighboring vectors, errors are eliminated before correlation information is discarded using available spatial and/or temporal data. Anomalies are removed from the data set through direct element-by-element comparison of the correlation tables calculated from adjacent regions. The result is in an error correction method that is highly robust to out-of-boundary particle motion, particle overlap, inter-particle correlations, and electronic and optical imaging noise. Consequently, the sample volume size required to resolve tracer particle displacement can be reduced improving the resolution as well as the accuracy of PIV.

1. INTRODUCTION

Because Particle Image Velocimetry (PIV) is based on the statistical correlation of imaged subregions to determine local flow velocities, it is subject to inherent errors that arise from finite tracer particle numbers, sample volume size, and image resolution. These errors, in extreme cases, are relatively easy to detect as they tend to vary substantially from neighboring vectors in both magnitude and direction. Despite this, correcting these errors is often difficult as present computer algorithms lack the innate pattern recognition ability of humans. Furthermore, such errors need not present themselves in obvious manners. Velocity vectors determined by correlating finite subregions of tracer particle images are often biased to varying degrees by particles entering and exiting the sample volume in the time between exposures, correlations occurring between unmatched particle pairs, particle overlap, non-uniform particle distribution, and variations in image intensity [Keane et. al. 1992; Prasad et. al. 1992; Westerweel et. al. 1993, 1994, 1997; Raffel et. al. 1994; Lourenco et. al. 1995; Fincham et. al. 1997]. Such errors along with errors associated with excessive velocity gradients and the finite sample volume size necessary to image a statistically meaningful number of tracer particles limit accuracy and resolution and thus, limit the usefulness of PIV.

Currently, the most widely used and accepted technique to eliminate correlation errors is to compare vectors with their neighbors to determine if they are in some statistical or physical sense inconsistent. This technique, analyzed in detail by Westerweel (1994), is based on the assumption that vectors resulting from correlation errors are far removed in magnitude and/or direction from their neighboring vectors. It assumes that the resolution of PIV data is high enough and the flow features benign enough that apparent discontinuities in the flow will not present themselves in the data and be eliminated by such a correction algorithm. In addition, an error can only be detected and replaced with an interpolated value using this approach. Even if the region represented by the vector contains sufficient information to determine the local flow velocity, that information is discarded prior to error correction. Thus, the true correlation in that region can not be determined without an attempt at reprocessing. Furthermore, it addresses only the most obvious of correlation errors and does not address the more subtle problems that severely limit sub-pixel accuracy and resolution. Thus while extremely useful, post-interrogation error correction techniques are not ideal.

Presented herein is a robust and computationally efficient method of removing errors from PIV results and resolving vectors from regions where noise in the correlation table obscures tracer particle displacement. This method, based on an element-by-element comparison of the correlation tables taken from adjacent regions, does not rely on the accuracy or similarity of neighboring vectors as does post-interrogation correction techniques. Because of the

effectiveness of this method at eliminating correlation anomalies, the size of interrogation regions can be reduced improving spatial resolution. Furthermore, recursive correlation techniques can be implemented without generating excessive spurious results.

1. CORRELATION ERRORS

PIV images are typically processed by subdivision into a regular grid of overlapping windows that bound regions of similar flow velocity; a velocity vector is then found for each window by autocorrelation or cross-correlation. Autocorrelation and cross-correlation produces a table of correlation values over a range of displacements, and the overall displacement of particles in the window is represented by a peak in this correlation table. Errors occur primarily from insufficient data whether it be a lack of imaged flow tracers or poor image quality, and/or from correlation anomalies generally resulting from unmatched tracer images within the correlated sample volume.

Insufficient Data

As the number of tracer particles within a sample volume increases, the probability of any finite region in close proximity existing with a particle set of similar intensity and pattern decreases. Thus, the probability of obtaining an accurate measure of the displacement of a set of particles using correlation increases as the number of particles increases. Keane and Adrian (1992) demonstrated this by showing that the number of spurious vectors that appear in PIV data drop dramatically as particle numbers within correlated subregions are increased up to an average of about ten particle images per region. Unfortunately, while this, in general is true, there is a limit due to finite intensity and spatial resolution capabilities of current imaging technology. Tracer particle seeding densities can be increased to a level in which the spacing between the particles contains more flow information than the particles themselves. Adding more tracers to a flow with this seeding density decreases the probability of obtaining an accurate correlation rather than increases it. Furthermore, very high seeding densities can alter the characteristics of the flow being measured and make it difficult if not impossible to adequately illuminate and image the tracer particles within a specific region of interest.

An alternative is to increase the size of the sample volume thereby increasing the number of tracer particles in the interrogation region without increasing the seeding density. This, however, results in a decrease in resolution and, as with seeding density, there is an upper limit.

Correlation Anomalies

When the difference between the movement of tracer particles in one region of a sample volume versus another is greater than the radius of a single tracer particle, than increasing the sample volume size results in an increase in correlation anomalies without increasing the peak correlation value [Keane and Adrian, 1992, Hart 1996]. There is, thus, a reduction in the correlated signal-to-noise ratio. This is due to a separation in the correlation peaks of individual particle images that is greater than the width of the correlation of a single particle image against itself. Increasing the sample volume exacerbates the problem as the relative separation in individual particle correlations from one region to another due to gradients in the flow increases as well. It, however, does reduce correlation anomalies associated with particles entering and exiting the sample volume in the time between exposures. As the sample volume is increased, a smaller fraction of particles enter and exit relative to the total number of particles that remain within the sample volume between exposures. Consequently, there is a reduction in correlation anomalies associated with this phenomenon.

In addition to excessive velocity gradients and out-of-boundary particle motion, problems associated with particle image overlap, non-uniform illumination of the sample volume, reflections off surfaces, particle coalescence, non-uniform flow seeding and image discretization all contribute to the number of correlation anomalies. These problems, although generally not as sever as velocity gradient and out-of-boundary effects, contribute to sub-pixel bias errors and are often the cause of spurious vectors.

Several processing methods have been developed that are less prone to these effects than the traditional spectral correlation methods. Okamoto et. al. (1995) developed a least energy correlation method they refer to as the *string method* that is relatively robust to large velocity gradients. Keane and Adrian (1992) and Westerweel, Dabiri and Gharib (1997) demonstrated that sub-pixel bias errors associated with correlation anomalies from particles entering and exiting the sample volume in the time between exposures could be significantly reduced by correlating with an offset interrogation window. This processing technique has the same effect as the shift and multiply technique or the much faster sparse array image correlation technique [Hart 1996]

that does not rely on forced periodicity of data and this method is nearly identical to the sub-correlation technique proposed by Fincham and Spedding (1991) that also relies on offset correlation windows. These processing techniques, although an improvement over standard spectral processing, are still subject to errors from out-of-plane particle movement, variations in image intensity, particle overlap and errors associated with seeding density.

2. CORRELATION ERROR CORRECTION

Both errors resulting from insufficient data and errors caused by correlation anomalies can be eliminated during processing, regardless of the method of correlation, simply by multiplying the correlation table generated during processing by the correlation table generated from one or more adjacent regions (Fig. 1).

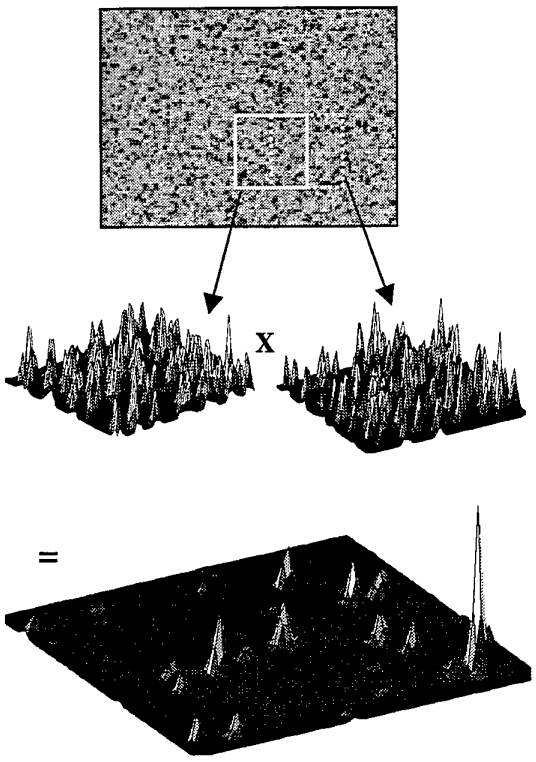


Figure 1. – Elimination of correlation anomalies by multiplying the correlation tables from adjacent regions. Correlation values that do not appear in both tables are eliminated allowing tracer particle displacement to be resolved.

This is effectively a correlation of a correlation. It is not an averaging technique. Any correlated region that does not appear in both correlation tables is eliminated from the resulting table. As the probability of exactly the same anomalies appearing in another region is very small, correlation anomalies, regardless of their source, are eliminated from the data. Furthermore, spurious vectors due to insufficient data are eliminated as any peak in one correlation table that does not exist within the other is eliminated. Even if both correlation tables do not contain the information necessary to resolve the correct correlation peak, combined in this manner, the peak is either easily resolved or it becomes evident that neither table contains sufficient data. (This is often the result of a single particle image within the sample volume in one exposure and multiple images in another – rare in well-seeded flows.) The resulting correlation peak found in the table is weighted to the displacement of the tracer particles within the overlap of the combined regions as information within this region identically effects the correlation values in both correlation tables. Particle displacements in regions outside the overlap influence the calculated displacement but to an extent that depends on the similarity in displacement. Thus, rather than a reduction in resolution, there is an improvement that depends on the size of the overlap and the gradient of the velocity relative to the size of the sample volume.

Under extreme conditions, valid correlations can be eliminated if the displacement of the tracer particles of the combined regions relative to each other is greater than about one particle image diameter (Fig. 2).

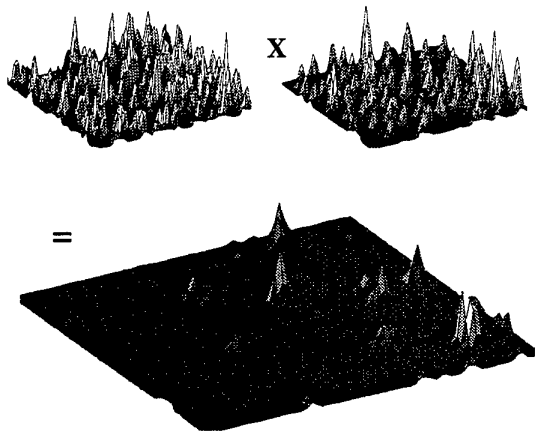


Figure 2. – Illustration of the effect of an excessive velocity gradient on the correlation signal using correlation error

correction. Signal strength is significantly reduced when tables are multiplied from regions where particle displacement differs by more than one particle diameter.

It is therefore, desirable to maintain a relatively high level of overlap between regions. The level of effectiveness of this technique, however, increases as the size of the overlapped region decreases due to a reduction in the level of shared information.

Although an extensive analysis of the optimum overlap has not been conducted, a fifty-percent overlap has been shown to effectively eliminate correlation errors (Fig. 3). As most correlation algorithms currently use a fifty-percent overlap based on Willert and Gharib's analysis (1991), there is virtually no increase in computational requirements to implement this error correction technique. Furthermore, as it requires a simple element by element multiplication between tables, it is generally easier and computationally more efficient to implement than it is to conduct post-interrogation error correction.

Unlike post-interrogation techniques that process data after most of the correlated information is discarded, this error correction technique uses all available correlation information within the interrogation regions to resolve particle displacement before the correlation peak is determined.

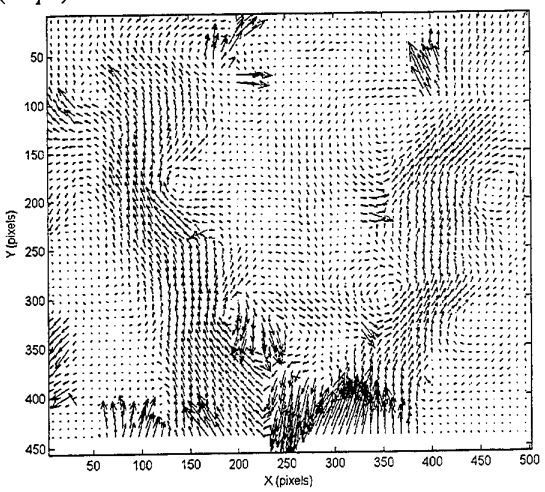
In addition, it does not rely on the accuracy of neighboring correlations to determine errors nor will valid correlations be eliminated if they vary substantially from neighboring regions.

3. PERFORMANCE TEST

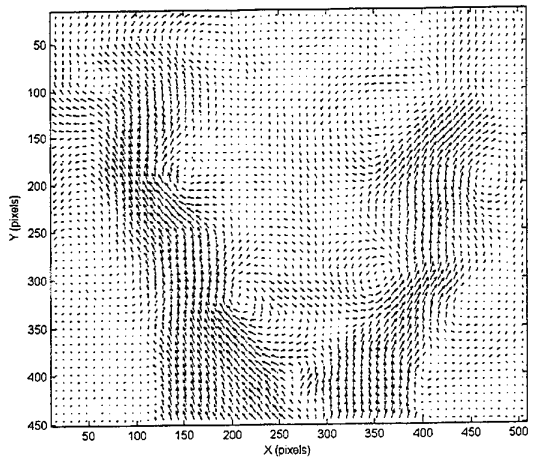
The relative performance of correlation error correction was investigated using Monte Carlo simulations. The effects of large velocity gradients, out-of-boundary motion, and seeding density were studied.

The simulations were conducted using pairs of synthetic generated images with randomly distributed 256 grayscale Gaussian particle images 4 *pixels* in diameter. Correlations were conducted using FFT spectral correlation on 64 *x* 64 *pixel* interrogation regions with 10 particle images per region. Results using correlation error correction were compared with non-spurious results taken from uncorrected data.

Fig. 4 illustrates the effect of translation on bias errors by comparing uncorrected results with results corrected from fifty-percent overlapping regions. Here the standard deviation of the displacement error from one thousand interrogation regions are plotted as a function of imposed particle translational displacement normalized by the interrogation size (64 *px*).



(A)



(B)

Figure 3. *– Elimination of processing errors using correlation error correction. 3(A) represents uncorrected PIV results of a high Reynolds number swirling flow undergoing sudden expansion. 3(B) illustrates the same data processed using correlation error correction. The corrected vectors are true tracer particle displacements and not interpolated values.*

The correlation error corrected results show a twenty-five percent improvement in resolving sub-pixel displacement. Note that the bias error increases linearly with translational displacement. This is consistent with errors conjectured by Adrian (1991) and analyzed in detail by Westerweel, Dabiri, and Gharib (1997). It is, to some extent, the result of fewer matching particle image pairs between

correlated regions. In translational flow, particles are convected out of and into the interrogation region. These convected particles do not have a corresponding image to correlate against. Consequently, an increase in translational flow has a similar effect to a reduction in seeding density, Fig. 5.

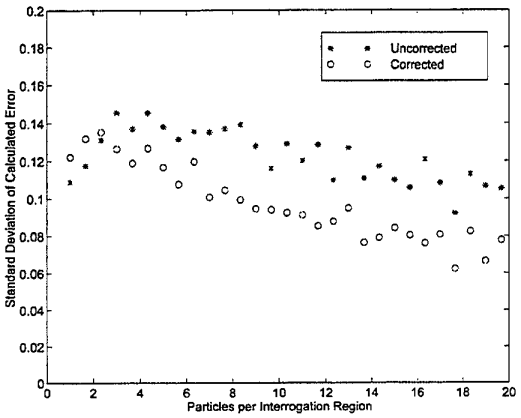


Figure 4. *– Effect of translational displacement on sub-pixel accuracy. Correlation error correction improves sub-pixel accuracy by eliminating anomalies in the correlation table and strengthening the peak correlation signal.*

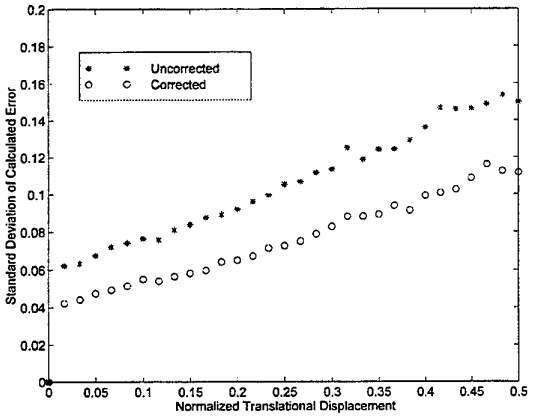


Figure 5. *– Effect of seeding density on sub-pixel accuracy.*

Errors associated with translational motion exist for out-of-plane particle displacement as well. It, however, is particularly limiting to PIV as it restricts measurements to regions of nearly planer flow or restricts the minimum width of the sample volume and thus, restricts spatial resolution.

As shown in Fig. 6, correlation error correction is highly effective at resolving particle displacements from regions with significant out-of-plane flow. Here the percentage of valid vectors is plotted against normalized out-of-plane translational particle displacement. The uncorrected data begins to produce excessive spurious results at fifty-percent displacement. Using fifty-percent overlapped regions, correlation error corrected data produces few spurious results until almost 90% displacement. At 100% displacement, all particles within the interrogation region move out of the region between exposures. Thus, there exists no data to determine flow velocity regardless of the correlation algorithm.

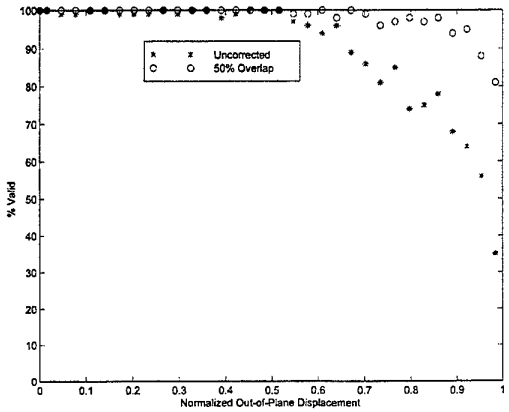


Figure 6. *– Effect of out-of-plane flow on PIV processing. Correlation error correction using fifty-percent overlapped regions significantly improve the ability to resolve particle displacements.*

While correlation error correction is highly effective at reducing errors associated with anomalies in the interrogation region, it is only marginally effective at resolving errors associated with large velocity gradients. Velocity gradients cause one part of an interrogation region to correlate at a different value than another region. It imparts a distortion that most correlation techniques are not able to resolve. When the distortion results in particle displacements greater than about one particle diameter, the relative correlation signal-to-noise ratio decreases significantly.

Fig. 7 shows a plot of the percentage of valid vectors as a function of normalized velocity gradient in the ***ij*** interrogation plane;

$$G_{\nabla} = \frac{m\left|\nabla \bar{v}_{ij}\right| N\Delta t}{d}$$ where N is the interrogation size (64 *px* in this case), m is the image magnification, Δt is the time between exposures, and d is the average imaged particle diameter. As shown, correlation error correction increases the number of valid vectors calculated from regions of high velocity gradients. At this level, however, the probability of

acquiring a valid correlation is unacceptably low and at lower levels, the improvement is marginal.

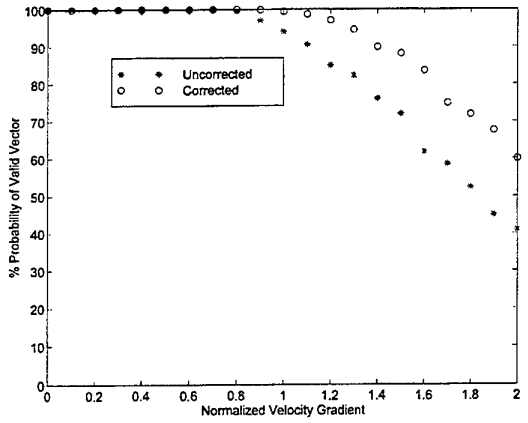


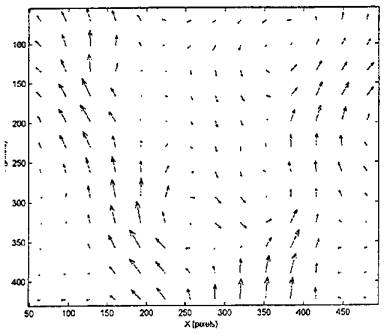
Figure 7. – Effect of velocity gradient on PIV processing. Correlation error correction improves the ability to resolve tracer particle displacements in regions that have high velocity gradients.

4. HIGH ACCURACY/ HIGH RESOLUTION PROCESSING

Because of the robustness of correlation error correction in removing spurious vectors and correlation anomalies, the size of the interrogation region needed to obtain an accurate correlation can be greatly reduced. Furthermore, recursive correlation processing can be used to iteratively arrive at local particle displacement without generating spurious results; a region is correlated, the interrogation window size is then reduced and offset by the previous result before re-correlating with the new window over a reduced region. The result of this correlation process can be quite dramatic as is illustrated in Fig. 8. Here recursive correlation along with correlation error correction is used to iteratively resolve the velocity of a swirling flow undergoing sudden expansion.

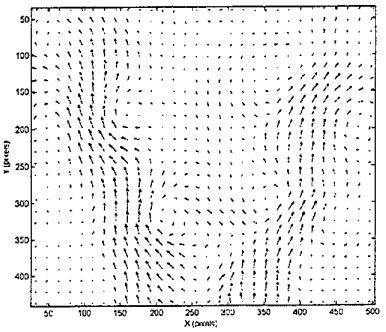
Figure 9 shows the same data resolved to 4x4 *pixel* interrogation regions generating 60,000 vectors each representing a 0.8mm^3 region of the flow. Using sparse array image correlation, results from the entire image are processed in less than one minute (>1,000 vectors/sec) [Hart, 1996]. While it is unlikely that the original image contains tracer particle displacement information to the resolution implied by this plot, it illustrates the possibility of correlating images to the available resolution of the data without generating spurious results.

(A)



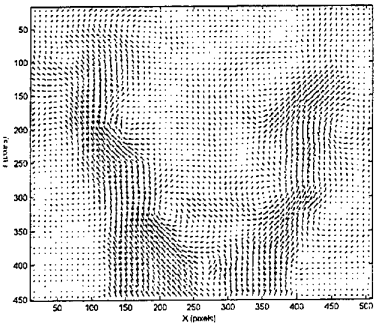
150 vectors (64x64 pixel sub-windows)

(B)



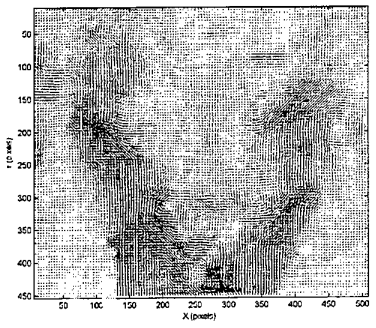
750 vectors (32x32 pixel sub-windows)

(C)



3,350 vectors (16x16 pixel sub-windows)

(D)



15,000 vectors (8x8 pixel sub-windows)

Figure 8. – Recursive processing (A to D) of a PIV image of a high Reynolds number swirling flow undergoing sudden expansion.

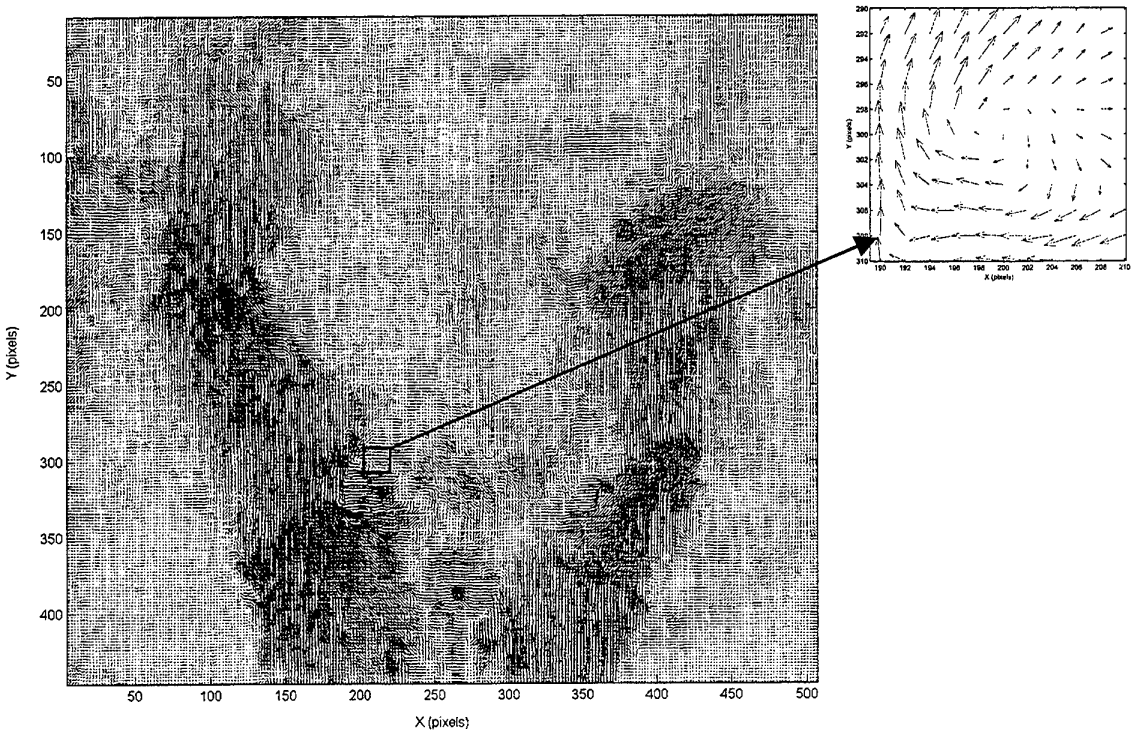


Figure 9. – 60,000 vectors calculated from a 486x512 image of a high Reynolds number swirling flow undergoing sudden expansion using recursive correlation. Each vector on average represents a single tracer particle in the flow and is the result of as many as ten sub-window correlations. These results are processed at a rate of over 1,000 vectors/sec using sparse array image correlation with correlation error correction

5. CONCLUSIONS

Stochastic correlation values can be eliminated during PIV processing by element-by-element multiplication of correlation tables calculated from adjacent regions. This correction method, which is essentially a correlation of a correlation, reduces sub-pixel bias errors and eliminates spurious vectors resulting from unmatched particle pairs, out-of-boundary motion, particle overlap, inter-particle correlations, and electronic and optical imaging noise. Particle displacement information that does not correlate equally in the combined regions is minimized. The resulting calculated displacement is weighted to the adjoining area thereby improving spatial resolution.

Correlation error correction, unlike post-interrogation methods, uses all available correlation information calculated from interrogation regions and does not rely on the accuracy or similarity of neighboring vectors. Consequently, it resolves tracer particle displacement vectors from regions that would otherwise be discarded. Thus, the correction method presented herein reduces bias errors and eliminates spurious vectors while improving spatial resolution and vector yields.

REFERENCES

Adrian, R. J. (1991) "Particle imaging techniques for experimental fluid mechanics." *Annual Review of Fluid Mechanics* Vol. 23, pp. 261-304.

Fincham, A. M.; Spedding, G. R. (1997) "Low Cost, High Resolution DPIV for Measurement of Turbulent Flow," *Experiments in Fluids.*, Vol. 23, pp. 449-462.

Fincham, A. M.; Spedding, G. R.; Blackwelder, R. F. (1991) "Current Constraints of Digital Particle Tracking Techniques in Fluid Flows," *Bull Am Phys Soc.* Vol. 36, 2692.

Hart, D.P., 1996, "Sparse Array Image Correlation," 8th International Symposium on Applications of Laser Techniques to Fluid Mechanics, Lisbon, Portugal.

Keane, R. D.; Adrian, R. J., 1990, "Optimization of Particle Image Velocimeters," *Measurement Science and Technology*, Vol. 2, pp. 1202-1215.

Keane R.D.; Adrian, R.J., 1992, "Theory of cross-correlation of PIV images," Applied Scientific Research, Vol. 49, pp. 191-215.

Landreth, C. C.; Adrian, R. J., 1990, "Measurement and Refinement of Velocity Data Using High Image Density Analysis in Particle Image Velocimetry," Applications of Laser Anemometry to Fluid Mechanics, Springer-Verlag, Berlin, pp. 484-497.

Okamoto, K; Hassan, Y. A.; and Schmidl, W. D., 1995, "New Tracking Algorithm for Particle Image Velocimetry," *Experiments in Fluids*., Vol. 19, pp. 342-347.

Prasad, A.K.; Adrian, R.J.; Landreth, C.C.; Offutt, P.W., 1992, "Effect of Resolution on the Speed and Accuracy of Particle Image Velocimetry Interrogation," Experiments in Fluids, Vol. 13, pp. 105-116.

Raffel, M.; Kompenhans, J., 1994, "Error Analysis for PIV recording Utilizing Image Shifting," Proc. 7th International Symposium on Applications of Laser Techniques to Fluid Mechanics, Lisbon, July, p. 35.5.

Westerweel, J. (1994) "Efficient Detection of Spurious Vectors in Particle Image Velocimetry Data," *Experiments in Fluids*., Vol. 16, pp. 236-247.

Westerweel, J.; Dabiri, D.; Gharib, M., (1997) "The Effect of a Discrete Window Offset on the Accuracy of Cross-Correlation Analysis of Digital PIV Recordings," *Experiments in Fluids*, Vol. 23, pp. 20-28.

Willert, C. E.; Gharib, M. (1991) "Digital Particle Image Velocimetry," *Experiments in Fluids*, Vol. 10, pp. 181-193.

Particle Imaging Velocimetry Standard Images for Transient Three-dimensional Flow

Koji OKAMOTO
Nuclear Engineering Research Laboratory
University of Tokyo
Tokai-mura, Ibaraki 319-11, JAPAN

Shigeru NISHIO
Dept. of Marine System Engineering
University of Osaka Prefecture
Sakai, Osaka 593, JAPAN

Toshio KOBAYASHI, and Tetsuo SAGA
Institute of Industrial Science
University of Tokyo
Roppongi, Tokyo, 106, JAPAN

ABSTRACT

The Particle Imaging Velocimetry (PIV) can measure the whole two-dimensional or three-dimensional flow field simultaneously without disturbing the flow field. Comparing with the traditional measurement technique, the whole field measurement is a great advantages to investigate the flow field. However, there are no standard evaluation tools for investigating these PIV techniques, resulting in the no standard PIV techniques. The current status of the PIV technique is far from the popularization or generalization technique. To popularize the PIV technique for practical use, the PIV standards and the PIV guide tools should be settled.

The Visualization Society of Japan (VSJ) started a project for PIV standardization and popularization in 1996 (PIV-STD). The objectives of the PIV-STD is to popularize the complicated PIV system, and to be a standard tool for the measurement of flow field. The PIV-STD developed the PIV standard images to provide the evaluation tool for the PIV techniques. The new images were based on the the transient three-dimensional motion. The developed PIV standard images are distributed using the Internet, (`http://www.vsj.or.jp/piv`). The developed PIV standard images can be accessed around the world through the Internet. They can be applied for the performance investigation of any PIV techniques.

1 INTRODUCTION

The Particle Imaging Velocimetry (PIV) is a quantitative velocity measurement technique, with visualizing the flow field by small tracer particles and with analyzing the visualized digital images. The PIV can measure the whole two-dimensional or three-dimensional flow field simultaneously without disturbing the flow field. Comparing with the traditional measurement technique, e.g., Laser Doppler Velocimeter and Hot Wire Anemometer, the whole field measurement is a great advantages to investigate the flow field.

Lots of PIV techniques had been developed and applied to various flow fields. The techniques include Cross-correlation technique (e.g., Adrian, 1991), Four-step particle tracking technique (e.g., Kobayashi et al., 1989), and so on. The developers analyzed the effectiveness of their PIV techniques using their own evaluation. There are no standard evaluation tools for investigating these PIV techniques, resulting in the no standard PIV techniques. Therefore, the users should determine the selection of the appropriate PIV technique without any useful information. When the users could get the velocity distribution using some PIV technique, there also were no standard evaluation tools for the measured velocity data. In order to get the accuracy information of there measured data, they have to evaluate the data by their-selves. Also, the PIV system needs lots of know-how, because the PIV system contains many steps, i.e., test section fabrication, visualization, image capture, image analysis, particle tracking, and evaluation of accuracy.

The current status of the PIV technique is far from the popularization or generalization technique. To popularize the PIV technique for practical use, the PIV standards and the PIV guide tools should be settled. With using the PIV standards, any user can easily apply the PIV technique onto their target flow field with the accuracy information.

The Visualization Society of Japan (VSJ) started a

project for PIV standardization and popularization in 1996 (PIV-STD). The objectives of the PIV-STD is to popularize the complicated PIV system, and to be a standard tool for the measurement of flow field. The activities of the PIV-STD is summarized as follows,

- Development of Standard Images for transient 3D PIV
- Analysis using the Standard Experimental Problems
- Development of PIV Database.

The PIV technique is roughly classified into two steps, i.e., Visualization and Image Processing. In this study, the standard for the Image Processing technique for PIV is focused. The Image Processing includes image enhancement, particle detection, particle tracking, image cross correlation, velocity averaging and erroneous evaluation.

Gharib et al. (1995) proposed the PIV standard images for evaluation of the DPIV technique. They distributed the PIV images for the Rankine vortex function and the shear layer function. The images were based on the two-dimensional velocity distribution, without any noise. However, in the actual measurement, the three-dimensional motion and the image noise could not be neglected.

The PIV-STD (Okamoto et al., 1997) developed the PIV standard images with considering the three-dimensional motion. The developed PIV standard images are distributed using the Internet, (`http://www.vsj.or.jp/piv`). We provided the several Standard Images with several parameters. However, the images were based on the stable velocity distributions. Therefore they could not be applied to the evaluation of three-dimensional turbulence measurement.

In this study, the PIV standard images were improved to treat the transient three-dimensional motion. The effectiveness of the 3D standard images was discussed. The standard PIV images were based on the transient three-dimensional flow field. The flow field was illuminated by the laser light sheet or cylindrical laser light. The three-dimensional motion was shown in the images. The images were taken from several different angles. The developed PIV standard images are also distributed using the Internet (`http://www.vsj.or.jp/piv`).

In the above home page of PIV standard images, the correct particle 3D locations and correct velocity distributions were also provided. Because the correct three-dimensional motions were known, the effectiveness and accuracy for the image processing technique could be easily checked. Particle 3D position extraction was one of the problems for 3D stereo PIV. Using the standard images, the extraction algorithm was also checked.

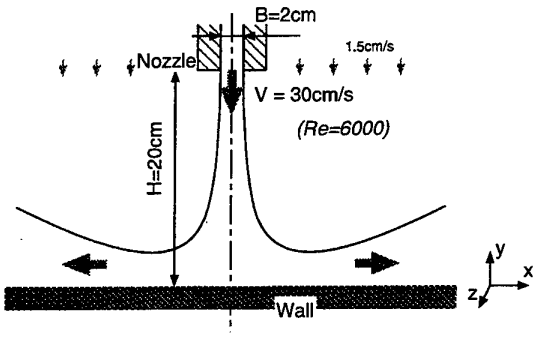


Figure 1: Schematic of the target flow field

2 STANDARD IMAGES

2.1 Requirement of the Standard Images

The objective of the PIV standard images is the evaluation tool for PIV techniques. The requirement of the standard images are as follows.

- Parameters

  In the PIV images, there are lots of configuration parameters, i.e., density of tracer particle, concentration of the particles, velocity, velocity gradient, laser sheet thickness and so on. The PIV images should be designed to be expressed by these parameters.

- Evaluation

  Using the standard images, the velocity field will be reconstructed by the PIV techniques. The information of the flow field should be known, because the comparison between the reconstructed velocity field and the correct velocity field should be carried out to evaluate the effectiveness of the PIV technique.

- Flow field

  The standard images are generated by the computer graphics. The generated images should be close to the actual PIV images. Transient and three-dimensional effects should be taken into account.

  In the three-dimensional measurement, identification of the particle three-dimensional position is one of the most important process. Therefore, camera location, orientation and magnification should be considered. Since the flow fields are inside the vessel usually, the refraction at the vessel wall should also be taking into account.

- Distribution

  The standard images should be easily distributed to the world. Any user can get the images at any time.

2.2 Target Flow Field

In this study, to provide the transient three-dimensional flow filed, the following flow field is taken as the target.

- The three-dimensional flow field with transient three-dimensional velocity vector.
- The tracer particle is micro-sphere with ideal scattering. The size of the particle is large enough to identify the individual particles.

The target flow field should be known for the standard images. The flow field should also have the transient three-dimensional velocity vector. In this study, the velocity vector calculated by the three-dimensional Large Eddy Simulation (LES) code is selected as the target flow field (Tsubokura et al., 1997). The flow filed is the same with the previous two-dimensional standard images (Okamoto et al., 1997). Figure 1 shows the schematic view of target flow field. The two-dimensional plane jet impinges on the wall, with jet Reynolds number, 6000, i.e., turbulent. There are lots of vortexes with various scales. The simulation volume is $53B \times 10B \times 3.9B$ for x, y, z-directions, where B is the nozzle width. The volume is divided into 300 × 100 × 34 meshes with variable mesh size. The flow field is solved with using the LES technique. The transient three-dimensional velocity distributions in certain target volume are extracted from the simulation results with every 15 msec. The particle movement in the image is calculated using the extracted transient three-dimensional velocity vector.

Figure 2 shows the example of the instantaneous in-plane (x−y) velocity distribution of the simulated flow field around the nozzle exit and impinging point. The injected jet impinges on the wall with higher turbulent flow, then the jet flows along the wall. The three-dimensional vortexes are generated and transfered to downstream.

2.3 Computer Graphics

The global coordinate system (x, y, z) is defined as shown in Fig.1. With considering the camera location and orientation vector, the global coordinate has been transformed to the camera coordinate system with a simple linear transformation. Then, the particle projection (X, Y) on the camera is calculated with considering the refraction at the vessel wall. To determine the refracted light path, the light path length between camera focus and particle is set to be minimum. In this study, one or three cameras are used to capture the flow field with the particles.

The image size is fixed to be 256×256 pixel. One pixel has 256 intensity level (8bit). The particle image is generated with writing the particle onto the image. The intensity at the location (X, Y) in the image caused by the scatter from the particle (x_p, y_p, z_p), whose projection is (X_p, Y_p), is expressed as follows,

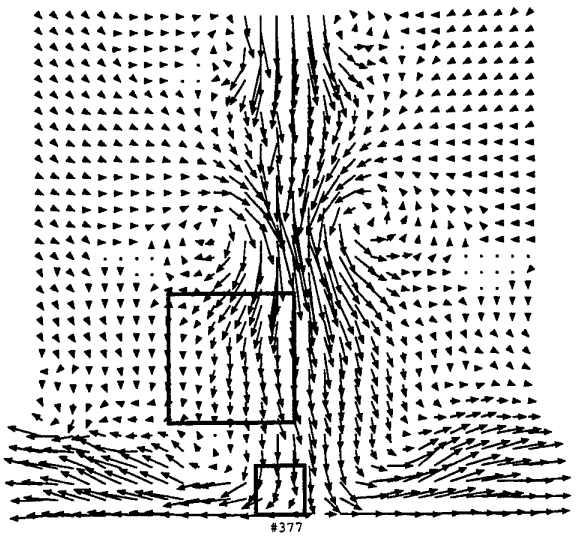


Figure 2: Velocity distribution of the target flow field

$$I(X,Y) = I_0 \exp\left(-\frac{(X-X_p)^2 + (Y-Y_p)^2}{(d_p/2)^2}\right) \quad (1)$$

In order to emulate the laser illumination, the maximum intensity (I_0) is defined with considering the particle location. For example, under the cylindrical light illumination, it is expressed as,

$$I_0 = 240 \exp\left(-\frac{z_p^2 + x_p^2}{\sigma_l^2}\right) \quad (2)$$

where $2\sigma_l$ is the diameter of the cylindrical light.

As an initial condition, the particles are randomly generated in a certain volume. The diameter of the particle is also determined by the random generator with considering the average and standard deviation of the diameter. Then the initial image is generated with using the above equations.

The particle movement is calculated from the LES velocity data with every 15 msec. Since the particle three-dimensional location and the time are known, the three-dimensional velocity at the point and the time is calculated using the linear interpolation of the LES data. The particle location is shifted with considering the velocity, resulting in the new particle locations in the next image. Then the new image at the next time step is generated with using Eqs. (1) and (2). This procedure is repeated for certain repetition time.

In the image generation, with increasing the number of particle, the occlusion of the particles are occurred. In this case, only the higher intensity particle is visualized. Because of the occlusion, the image may have a sudden intensity variation. In order to overcome the sudden variation, the particle image is

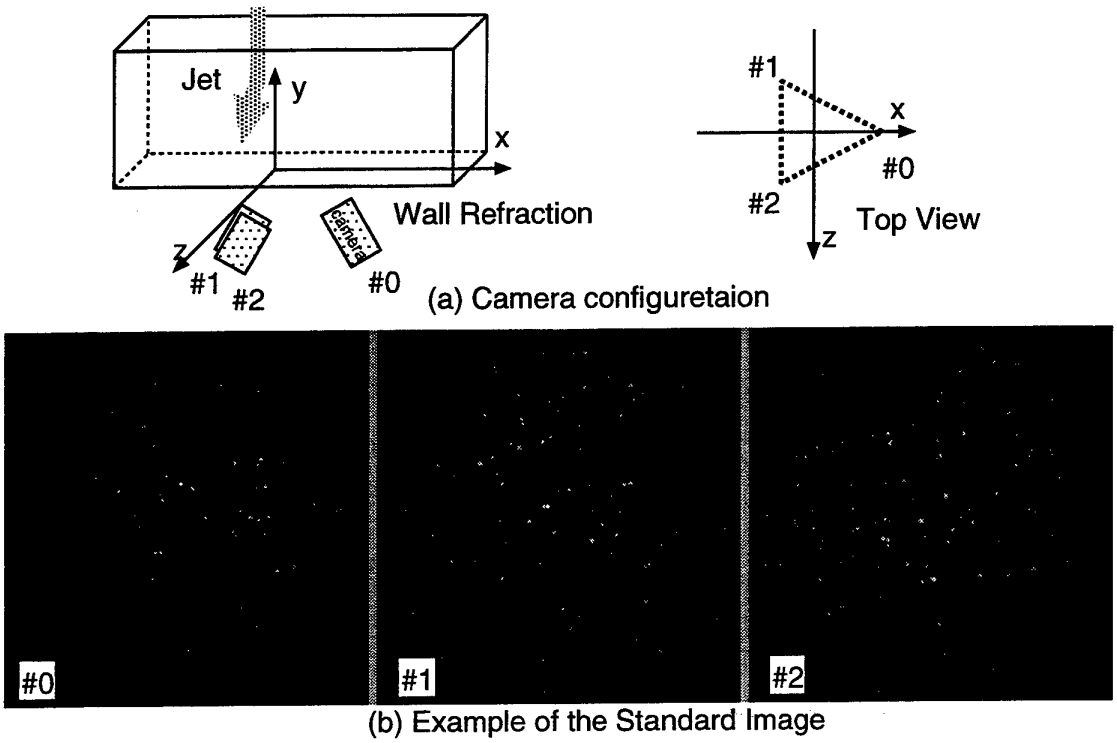


Figure 4: Standard Image #377

initially generated in the larger image, i.e., 512×512 pixel image. Then the averaged value of the neighbor 4 pixel is taken as the intensity of the image (256×256).

2.4 Example of the standard image

The PIV standard images are distributed with using the Internet. The URL of the images is `http://www.vsj.or.jp/piv/`. This address is the same with that of the two-dimensional standard images. The animation of the standard images are also shown. Anybody can download the standard image file through anonymous FTP or HTML.

The distribution of the standard images are easily achieved with using the Internet. Anybody can access the PIV standard images from the world. The animation of the PIV standard images is also helpful to understand the characteristics of the images.

Even in two-dimensional PIV images, there are lots of parameters (Okamoto et al., 1997). In this study, six series of the transient 3D PIV Standard Images are constructed. There are three categories of the images.

2.4.1 Transient Two-dimensional Image

In No.301 and 302, the flow field is illuminated by the two-dimensional laser light sheet. The each series contain the 144 serial images (720ms) with transient three-dimensional flow field. Figure 3 shows the example of the standard image No.301. The downward jet with variable scale vortexes are interacted. The 145 serial images are provided in No.301. Time interval of the particle movement calculation is 0.1msec, while the images are generated every 5msec. Therefore, the 145 images correspond to 720msec. Number of the visible particle in the image is about 4,000, whose average diameter is 5 pixel. The standard deviation of the particle diameter is 2 pixel. The displacement of the particle is 0 to 10 pixel/interval. Three-dimensional motion (out-of-plane) is about 10% of the laser light thickness.

Since the flow field is three-dimensional and transient, the correct vector field is also 3D and transient. The cross-sectional velocity distribution (at $z = 0$) is provided for every time intervals. The transient velocity information are available on the Internet.

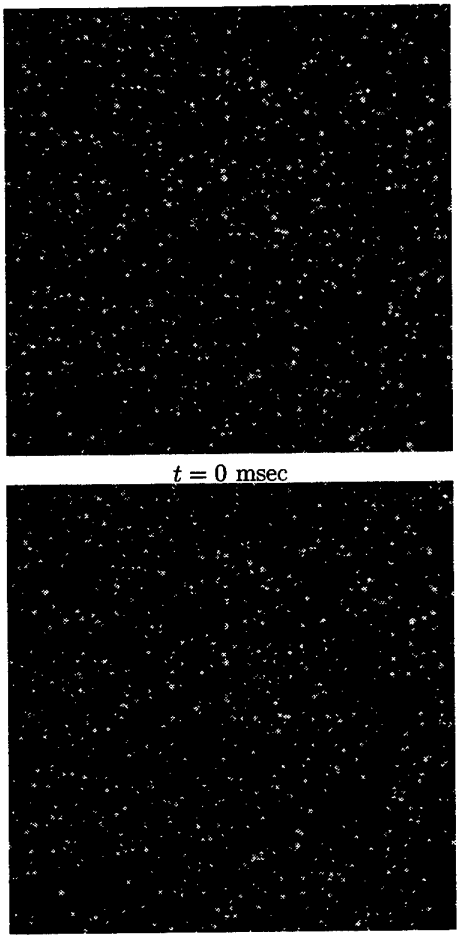
In the three-dimensional standard images, the information of the particle location is important. The correct particle location information is also provided on the home page. At every time step, the particle

3D location and particle centroid in the image are written in the file. Using the particle ID number, the actual particle movements in 3D and/or in the image are known.

2.4.2 Transient Three-dimensional Images with horizontal three cameras

A cylindrical laser light volume illumination is used for No.351 and 352. The each series contain the 144 serial images (720ms) with transient three-dimensional flow field. The flow field is the same with that of No.301.

Three cameras are settled on the horizontal plane. Center camera (#1) is located on the z axis, i.e., perpendicular to $x-y$ plane. The vessel wall is also settled on parallel to the $x-y$ plane. So, camera #1 has small refraction effects. While, left and right cameras (#0,#2) are set with the angle of 30 degree to z axis. Because of the refraction, the particle images are distorted. The refraction index in the water and wall is 1.33



$t = 0$ msec

$t = 5$ msec

Figure 3: Standard Images (#301)

The images with grid point particles are provided to calculate the camera position correctly. Also, the accurate particle three-dimensional position and projection point on the images are also provided as a text file. In order to calculate the particle three-dimensional positions, reconstruction procedure from the three camera images are needed. This standard images are used to calibrate the three-dimensional reconstruction algorithm.

In the standard images, three-dimensional particle position and velocity distributions are also distributed. All of the recorded particles had its own ID number. Since the particle positions are written on the file with the ID, it is very easy to track the actual particle movement. That means, anybody can easily check the accuracy and effectiveness of their 3D PIV algorithm. The transient three-dimensional velocity data at 3D grid point is also helpful to check the algorithm.

2.4.3 Transient Three-dimensional Images with three cameras

No.371 and 377 are illuminated by cylindrical laser light. In No. 371, the camera locations are almost the same with No. 351, however, they have disturbances. This disturbances simulate the uncertainty of the camera setup. The camera has inclined horizontally and vertically.

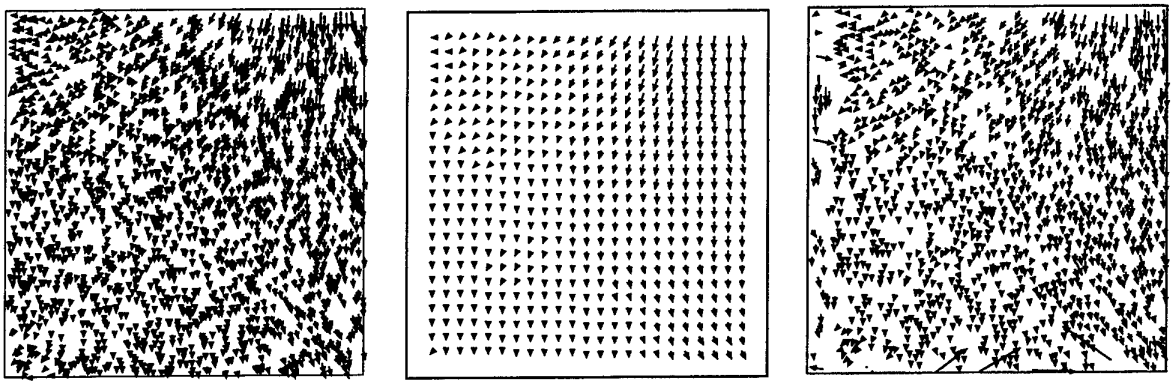
In No. 377, the flow field near the wall impingement is viewed from bottom. The three cameras are settled on the corner of triangle as shown in Fig. 4. The refraction index in the water and wall is 1.33. Because the flow field at the impingiment is highly turbulent, interesting particle motions are visualized. The reconstruction of three-dimensional particle position will be difficult. This image is a challenging problem.

In the current status, the evaluation of the reconstructed velocity from the PIV standard images should be done by the users with comparing the reconstructed data with the correct one. The development of standard evaluation tool will also be important topics.

3 APPLICATION OF STANDARD IMAGES

3.1 Transient Velocity Tracking

To clarify the effectiveness of the transient three-dimensional Standard images, the No. 301 is analyzed, using the two-dimensional cross-correlation technique (e.g., Adrian, 1991) and Spring Model technique (Okamoto et al., 1995). Figure 5 shows the comparison between the correct velocity distribution



Correct Cross-Correlation Spring Model

Figure 5: Reconstructed Vectors

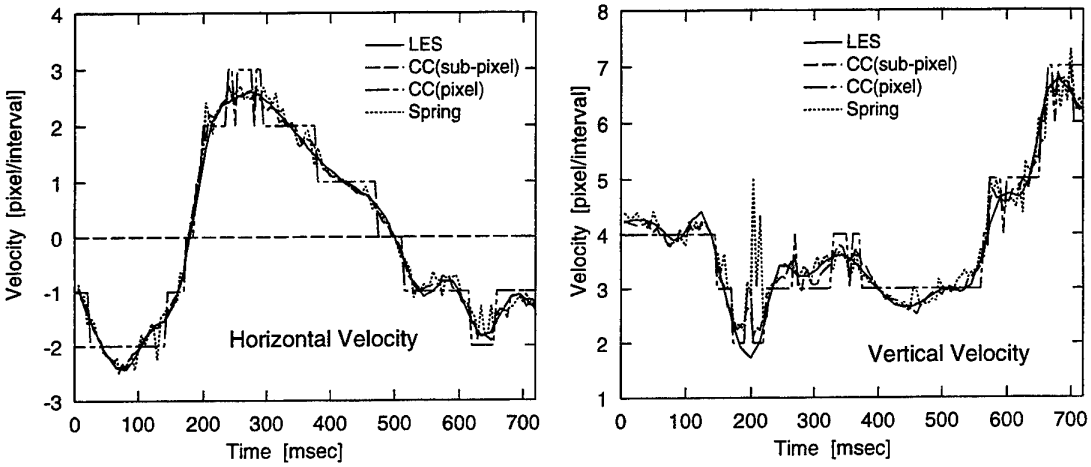


Figure 6: Transient velocity fluctuation at (140,100) of #301

and reconstructed velocity distributions. In the cross-correlation, the interrogation region is 16×16 and the search area is 20×20. The sub-pixel accuracy is achieved with interpolating the cross-correlation function in the 2nd order polynomial. In the spring model technique, the particle centroids are calculated from the image, with using the Laplace filtering and binarization. The maximum number of the particle in one cluster is 18, and search area is ± 10 pixel. For the noise reduction, the neural network algorithm(Kimura et al., 1994) is applied. Since the number of particles in the image is relatively large, the cross-correlation technique gives a better result. Also, the images contain no noise, therefore, there are almost no erroneous vectors. The spring model can track the individual particles with relatively high accuracy.

The standard image has transient information. The tracerability of the transient velocity is checked using the standard image (#301). Figure 6 shows the transient velocity at $(x, y) = (140, 100)$ pixel. The solid line shows the correct velocity data (LES data). The cross-correlation with/without sub-pixel accuracy and spring model results are shown. In the cross-correlation, the velocity can be obtained at the grid point. However, in the spring model, they are obtained at particle location. In this study, the velocity is calculated with averaging the velocity vectors around the grid point (4 pixel radius). Since the particle may not exist around the grid point, the averaged data contain some errors. The sub-pixel cross-correlation can trace the fluctuation correctly. There are high frequency errors in the spring model, because of the lack of vector. In these standard images, the information of the images are large enough to calculate the two-dimensional velocity.

Using the all of the 720 msec data, the average

Table 1: Summary of Averaged Value (pixel/interval)

Technique	$\overline{u}$	$\sqrt{\overline{u'^2}}$	$\overline{v}$	$\sqrt{\overline{v'^2}}$
LES(Correct Answer)	-0.07	1.60	3.78	1.19
CC (with sub-pixel)	-0.04	1.61	3.78	1.14
CC (pixel accuracy)	-0.04	1.63	3.78	1.17
Spring model	-0.03	1.62	3.86	1.10

velocity ($\overline{u}$) and RMS ($\sqrt{\overline{u'^2}}$) are obtained. Table 1 shows the summary of the calculated velocity and RMS. These averaged values agree with the correct value well. The errors caused by the tracking algorithm could be canceled and/or be negligible in the analysis of standard image #301.

The present analysis is the demonstration of PIV-STD for the two-dimensional algorithm. With using the 3DSTD images, the three-dimensional algorithm will be evaluated.

4 CONCLUSIONS

The standard images which aims to establish a evaluation code of PIV were proposed. The standard images have been developed based on the calculated velocity field by means of three-dimensional LES. The transient and three-dimensional motions are taking into account in the standard images. To generate the images, the wall refraction at the vessel surface are considered. The effectiveness of the present standard images are demonstrated with using the cross-correlation and Spring model technique.

REFERENCES

Adrian R. J., 1991, "Particle-imaging techniques for experimental fluid mechanics," Ann. Rev. Fluid Mech., Vol. 23, 261.

Gharib, M. et al., 1995, "Center for Quantitative Visualization," `http://www.cqv.caltech.edu/`

Kimura, I., Kuroe, Y., and Ozawa, M., 1993, "Application of Neural Networks to Quantitative Flow Visualization," J. Flow Visualization and Image Processing, Vol.1, No.4, 261.

Kobayashi,T., Saga,T., Segawa,S., Knada,H,, 1989, "Development of a Real-Time Velocity Measurement System for Two-Dimensional Flow Fields Using a Digital Image Processing Technique", Trans. of JSME, (B), Vol.55, No.509, 107.

Okamoto, K., Hassan Y.A., Schmidl, W.D., 1995, "New Tracking Algorithm for Particle Image Velocimetry", Experiment in Fluids, Vol.19, No.5, 342.

Okamoto, K., Nishio, S., Kobayashi, T. and Saga, T., 1997, "Standard Images for Particle Imaging Velocimetry," Proc. PIV'97-Fukui, Fukui, 229.

Tsubokura, M., Kobayashi, T. and Taniguchi, N., 1997, "Visualization of 3-D structures in a plane impinging jet using Large Eddy Simulation," Proc. FLCOME'97, Vol.2, 875.

MEASUREMENT OF VELOCITY FIELD SPECTRA BY MEANS OF PIV

Luiz M. Lourenco [#], M. Bahadir Alkislar [#] and Rahul Sen [*]

[#] Fluid Mechanics Research Laboratory
FAMU/FSU College of Engineering
Florida State University – Building 114
Tallahassee, FL 32306

[*] Noise Engineering
Boeing Commercial Airplane Group
M.S. 67-ML, P.O. Box 3707
Seattle, WA 98124

ABSTRACT

A Particle Image Velocimeter has been developed for the measurement of field velocity spectra. The velocity spectra are computed via the velocity auto-correlation function, obtained by correlating corresponding velocity fields at variable time delays. The PIV system features a single microcomputer that controls the dual camera (Kodak ES1.0) arrangement, and is capable of acquiring up to 128 image pairs, per camera, at a maximum frame rate of 30 Hz. The system also synchronizes a pair of dual Nd-Yag lasers for the flow illumination. Using this system, field and point-wise spectra have been obtained and compare very well with those obtained by means of Hot Wire Anemometry. The special requirements in the PIV velocity measurement accuracy as well as the system's limitations due to quantization noise are discussed.

1. INTRODUCTION

PIV is a measuring technique capable of providing at different time instants the synoptic velocity field. However, the time resolution is limited to the framing rate of digital cameras used for the image recording, and is typically insufficient to record time sequences in rapidly evolving or turbulent flows. Therefore only time-averaged quantities, such as the mean velocity and Reynolds stresses, can be obtained to characterize the flow unsteadiness. To obtain velocity spectra, PIV is usually supplemented with single point methods, such as Hot-Wire Anemometry or Laser-Doppler Velocimetry.

The objective of this study is to propose and develop a method that makes it possible to obtain field spectra with the PIV technique. The advantage of such an approach stems from the spatial nature of PIV technique. First, the technique provides a global view versus a local view of the distribution of time scales. Second, in addition to time correlation, time-space correlation and cross-spectra can be obtained, a daunting task if one is limited to the use of single point probes.

2. PRINCIPLE

To achieve the aforementioned goal a Particle Image Velocimeter is implemented to measure the flow field spectra of the velocity and the its derivatives, e.g., vorticity. The limitation imposed by the fixed and slow camera image acquisition rate was resolved by using two cameras to synchronously record the same flow region at variable separation times. The temporal auto-correlation function is obtained by measuring the velocity field at time t and at $t+\tau$, where τ can be varied to any delay amount. The correlation is function of the variable lag τ and is obtained by the long time average of the repeated number of individual measurements, defined as:

$$R_X(x,y,\tau) = \frac{1}{N}\sum_{n=0}^{N-1} X_n(x,y,t)\cdot X_n(x,y,t+\tau) \quad (1)$$

In equation 1 X may represent any of one of the flow variables such as u and v (the velocity components), U (the velocity magnitude), or Ω (the vorticity), evaluated by means of PIV. The previous formulation indicates that the correlation function

may be obtained for any point in space where the velocity is measured, and that there are no restrictions imposed by the limited acquisition rate, on the time scale, τ, which can be resolved.

The spectrum of $X(x, y, n\tau)$, S_X is related to the correlation function by means of a Fourier transform.

$$S_X\left(x, y, \frac{2\pi m}{N\tau}\right) = \left(\sum_{n=0}^{N-1} X_n e^{-j(2\pi mn/N)}\right)^2 \qquad (2)$$

Unlike single point techniques, which limit the measurement of spectra to the velocity variable at point in space, this approach is very flexible. Other spectral distributions such as the cross-spectra of the u and v velocity components as well as spectra of velocity derivatives such as vorticity can be easily obtained from the cross-correlation, R_{uv}, and the auto-correlation R_Ω respectively.

3. Experimental Configuration

The principle of measuring field correlation and spectra was put to test in the measurement of a well-documented jet flow. The experiment consisted of the measurement of the velocity and vorticity distribution of a two-dimensional, incompressible, jet issuing from a rectangular nozzle into ambient air. This test flow was chosen because it contains shear layers with large velocity gradients, rolling into large, interacting, vortical structures.

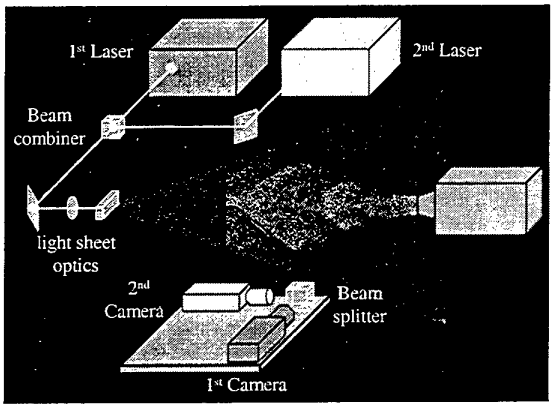


Figure 1: Experimental Set-up.

In this experiment the nozzle width is 10 mm, and has an aspect ratio of 4:1. Measurements are carried out at the mid plane of the jet that contains the minor axis, and extend from the nozzle exit to 6 widths downstream of the exit. The flow Reynolds number based on the jet width and the average mass flow velocity, of 17.1 m/sec, is 11,400. For these conditions the exit velocity profile, has a top-hat shape, and the Strouhal number based on the natural flow instability is 0.95.

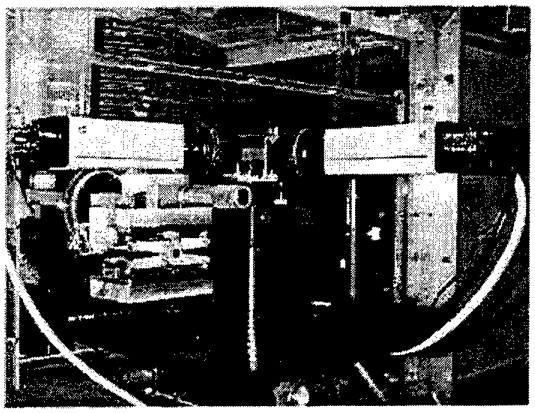


Figure 2. Dual camera system with the beam splitter cube.

To control the delay, τ, two independent PIV systems are incorporated into one setup as shown in figure (1). Two dual, double pulsed, frequency doubled Nd-Yag lasers (Spectra-Physics PIV-400), provide co-planar illumination sheets at time t and $t+\tau$. The time between the double light pulses of each laser sheet is adjusted according to the jet velocity and set at Δt=12 μsec. As shown in figure 1, the beams of the twin laser system, have orthogonal polarizations and are combined by means of a polarizing beam splitter cube. The illumination pulses of each laser are initiated by independent timing signals generated by the Kodak ES1.0 cameras. The cameras operate in the "double exposure mode", and are synchronously triggered with an adjustable delay, τ, between them, at a rate of 15 Hz.

The flow images at time t and $t+\tau$ are split from each other by beam splitter and acquired by the two separate cameras. Image separation using the laser illumination with orthogonal polarizations is feasible because the light scattered by the seed particles retains the polarization of the illuminating beam. This polarization filter is quite practical because it enables acquisitions of images with very small delays, including at τ=0, without any interference.

Figure 2 is shows the image recording set-up that includes the Kodak ES1.0 cameras. Each camera has a resolution of 1000^2 square pixels, with 9 μm on the side.

4. TEST OBJECTIVE AND RESULTS

The main objective in this experiment is to use the PIV configuration described in section 3 to obtain field spectra and determine the natural roll-up frequency of the large-scale vortical structures in the shear layer of the rectangular jet. This result is to be compared with that obtained by spectral analysis of a hot-wire signal. The velocity is computed using a novel mesh-free, second order accurate processing algorithm. This algorithm is designed to improve the accuracy and spatial resolution of conventional cross-correlation schemes. The main cause for the limited spatial resolution in conventional schemes is the finite correlation window size, of the order of 16^2-32^2 pixel. Since the measurement represents an average over the correlation window, it can be weighted towards the areas of the window with higher seeding density and/or reduced velocity. This is especially restricting when the technique is applied to the study of flows with large velocity and/or seeding density gradients, e.g. shear layers.

In this study a novel algorithm is used to achieve velocity data with high spatial resolution. The interrogation regions consist of particle images that have sizes ranging from 3^2 to 4^2 pixels. The displacement between image pairs is found in the usual manner by means of a cross-correlation, and a velocity (displacement) vector is assigned at the mid-distance between image pairs. Therefore, each particle pair contributes to a second order approximation of the velocity. However, unlike the traditional way these velocities are evaluated in an unstructured grid.

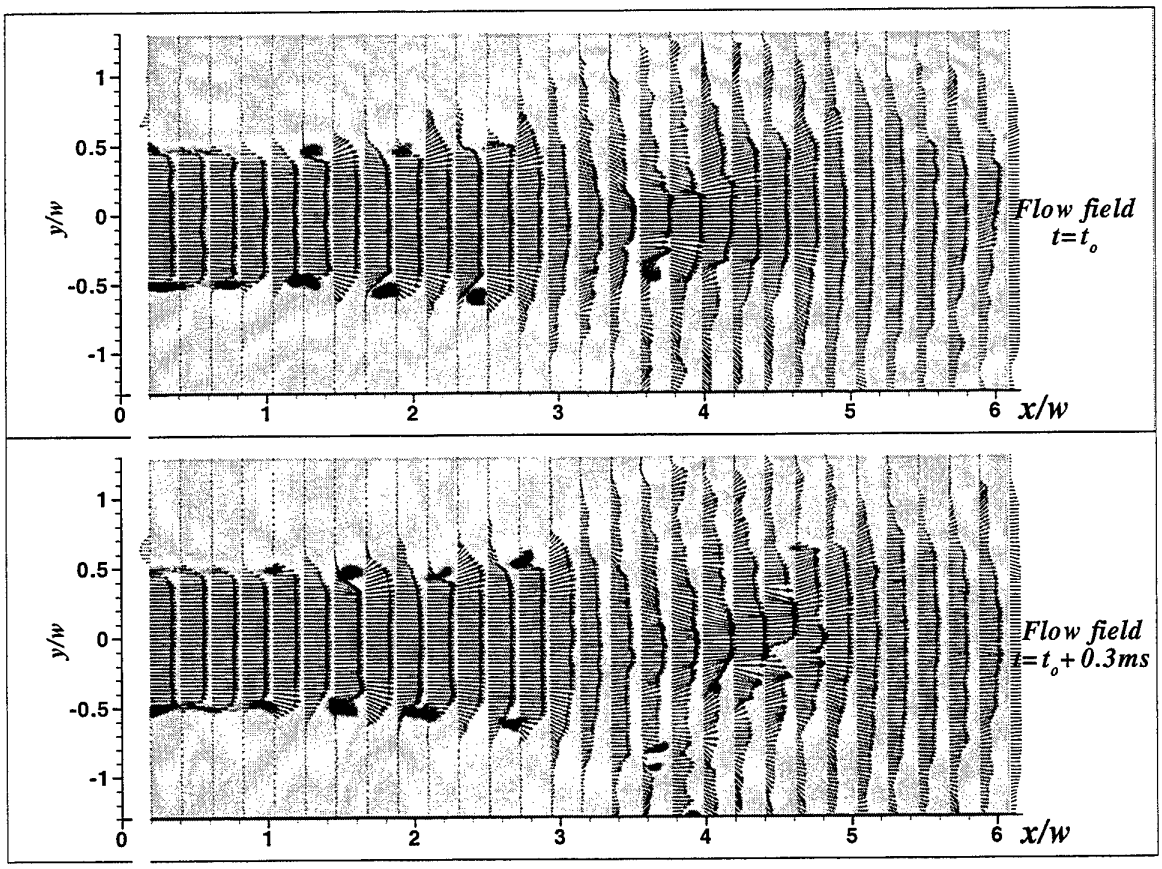


Figure 3. Synoptic velocity and vorticity field at reference time and delay time of τ=0.3 msec. (vector skip of 6 is applied in x-direction).

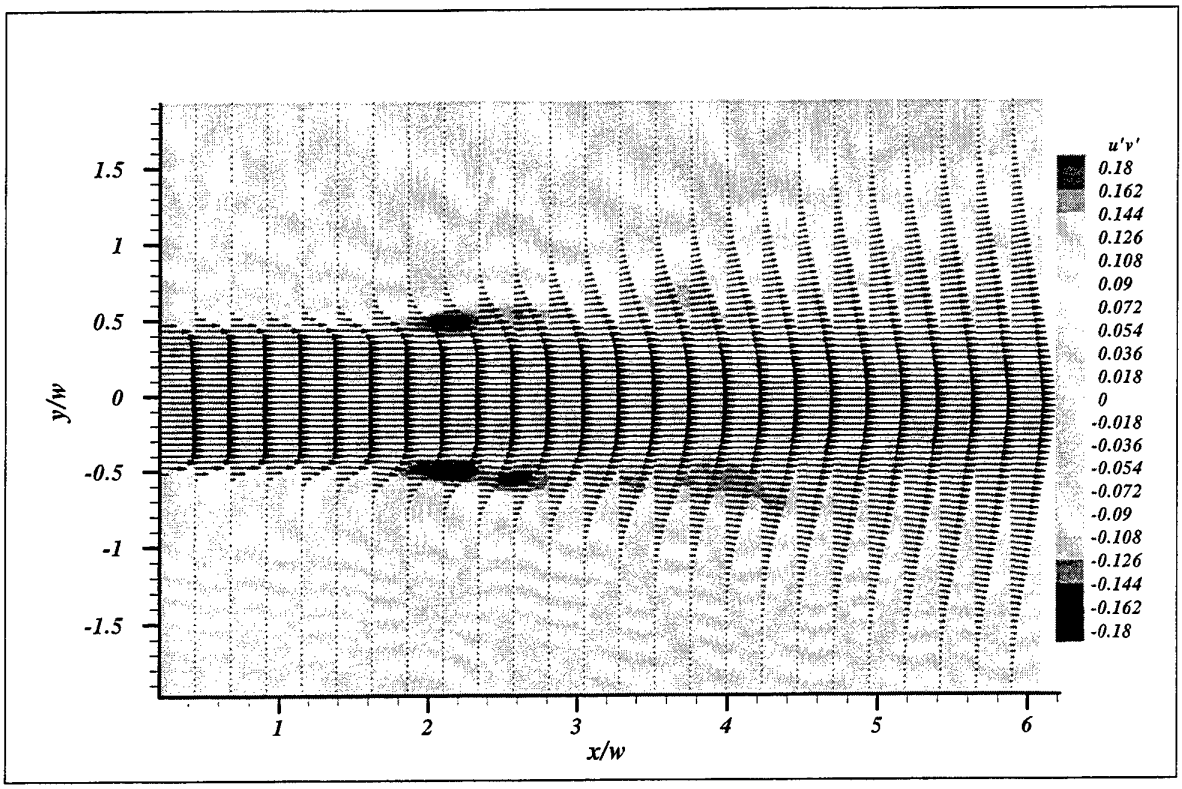


Figure 4: Average velocity and Reynolds stress distribution.

Description of the flow field at any point is given by an analytical function found by a least squares fitting algorithm. In this approach the function that is used is a second order polynomial:

$$\vec{u} = \vec{a}\,x^2 + \vec{b}\,x + \vec{c}\,y^2 + \vec{d}\,y + \vec{e}\,xy + \vec{f} \qquad (3)$$

However, other functional forms could be used, including a Gaussian interpolator.

The marked advantage of this approach is that the field is described at any point with accuracy of second order, including the derivatives that are found by differentiating the previous equation.

$$\frac{\partial \vec{u}}{\partial x} = 2\vec{a}\,x + \vec{b} + \vec{e}\,y$$
$$\frac{\partial \vec{u}}{\partial y} = 2\vec{c}\,y + \vec{d} + \vec{e}\,x \qquad (4)$$

For the purposes of presentation the velocity field is represented with vectors in a regular mesh. The new scheme is very efficient and incorporates a vector validation procedure, making it independent of operator intervention. The time it takes to compute a vector field depends on the computer hardware and it ranges from 1,400 mesh points/sec on a Pentium 200 MHz dual Pro to several thousand on a 500 MHz Alpha based PC.

To achieve the high resolution and accuracy in both the velocity and velocity derivatives necessary for the calculation of spectral data each field consists of 15,000 grid points, covering a 60x20 mm^2 area of the jet.

Figure 3 is a typical example of synoptic fields of velocity and the out-of-plane vorticity component, displayed as color contour, obtained at a reference time t and delayed time instant t+0.3 msec.

As shown in figure 4, conventional averages, such as the mean velocity and Reynolds stress distribution may be obtained from each of the reference and delayed data sets. While these average fields are indicative of the average position and strength of vortices shed in the shear layer, they do convey any information on their characteristic time scale. This information is obtained by means of the correlation function or its spectral counterpart. Since the phenomena we wish to characterize is vorticity controlled, the vorticity is used as the correlation

variable, and the time-correlation of the vorticity field is obtained using equation 1.

To construct the correlation function 13 delays from $\tau = 0$ up to 1.2 msec with equal increments of 0.1 msec are used. For each delay the discrete correlation function is computed from the average of 30 corresponding reference and delayed velocity fields.

Figure 5 is a composite that shows the evolution of the correlation with time for a point in the shear layer (x/w=1.4 and y/w=0.5), as well as the contour plot of the distribution of the correlation function for a fixed x/w=1.4. This figure clearly shows that at that position in the shear layer the vorticity rolls-up with a period of about 0.6 msec.

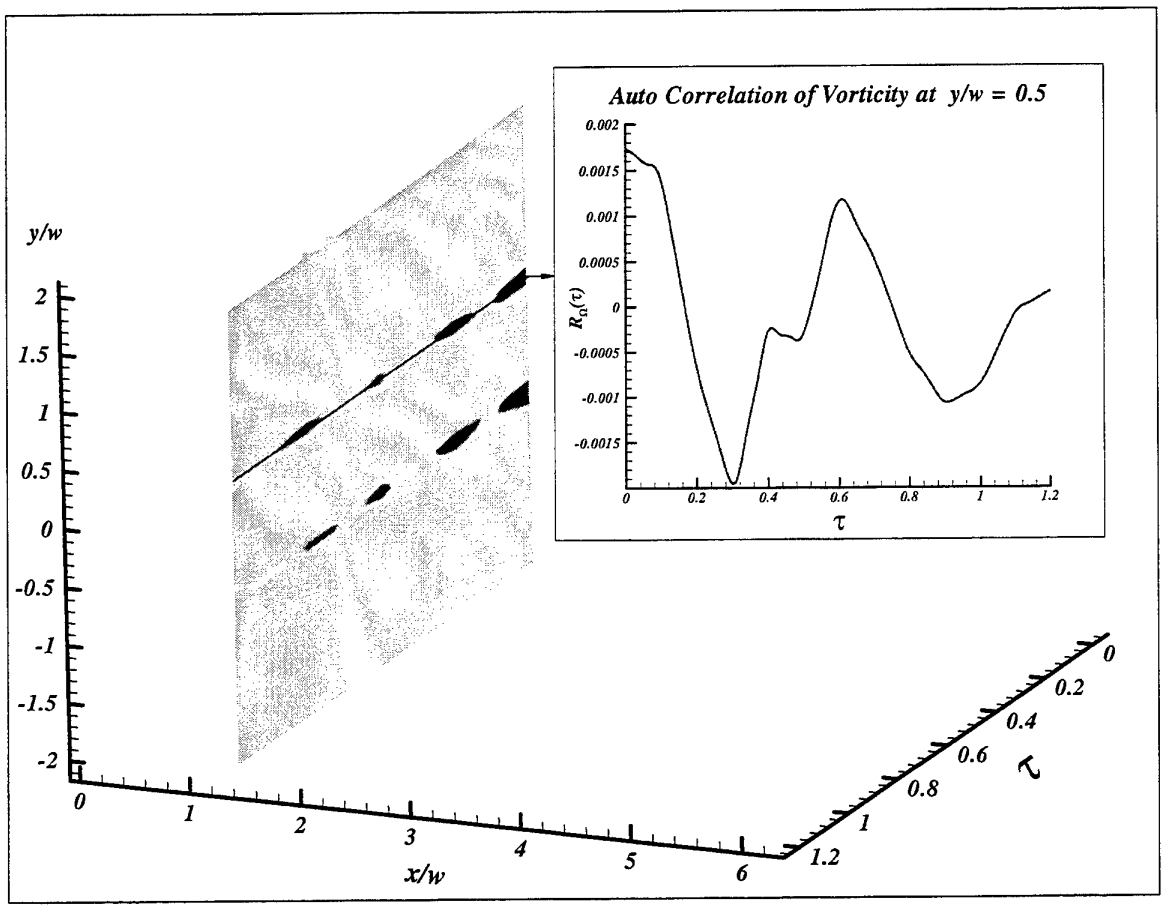


Figure 5: Correlation of vorticity at x/w=1.4, y/w=0.5.

The spectral distribution corresponding to the point located at x/w=1.4 and y/w=0.5 is shown in figure 6. This spectrum, obtained from the correlation of Ω_Z, has a frequency resolution of 100 Hz (bandwidth) corresponding to the incremental delay between the reference and the delayed fields. Furthermore, the plot shows essentially only a single harmonic contribution. The measured frequency corresponds to a shear layer roll-up frequency of about 1543(±100 *Hz*). For the purpose of comparison the shear layer roll-up frequency was measured independently by computing the spectrum of the signal produced by a single hot-wire positioned at the same location. The power spectral density of this hot-wire signal is presented in figure 7, and clearly identifies the roll-up frequency at 1594 *Hz*, well within the frequency resolution limit (±100 *Hz*) of our measurement. Further evidence of the vortical interactions, in the form of pairings is obtained by the analysis of the correlation function further downstream (x/w=1.8). This evidence is in the form of the period doubling (frequency halving) as shown in figure 8.

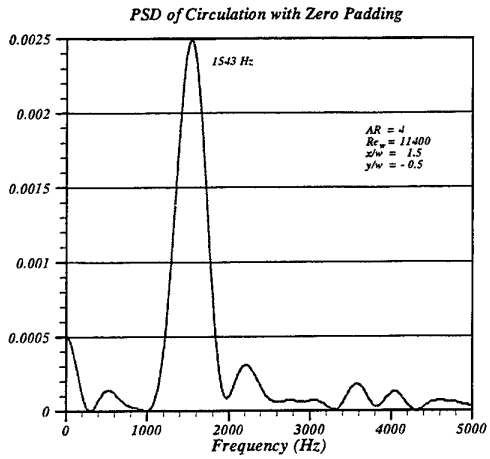


Figure 6: Spectrum of vorticity at x/w=1.4, y/w=0.5.

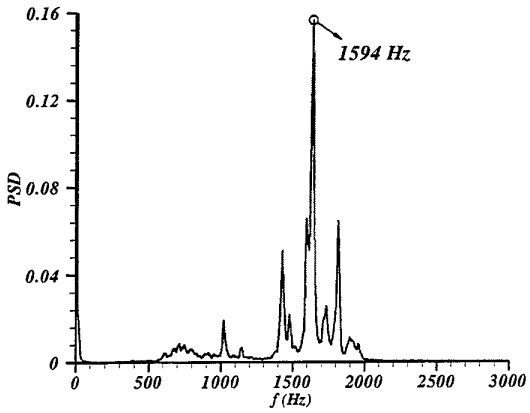


Figure 7. Power Spectral Density function of hot-wire measurement.

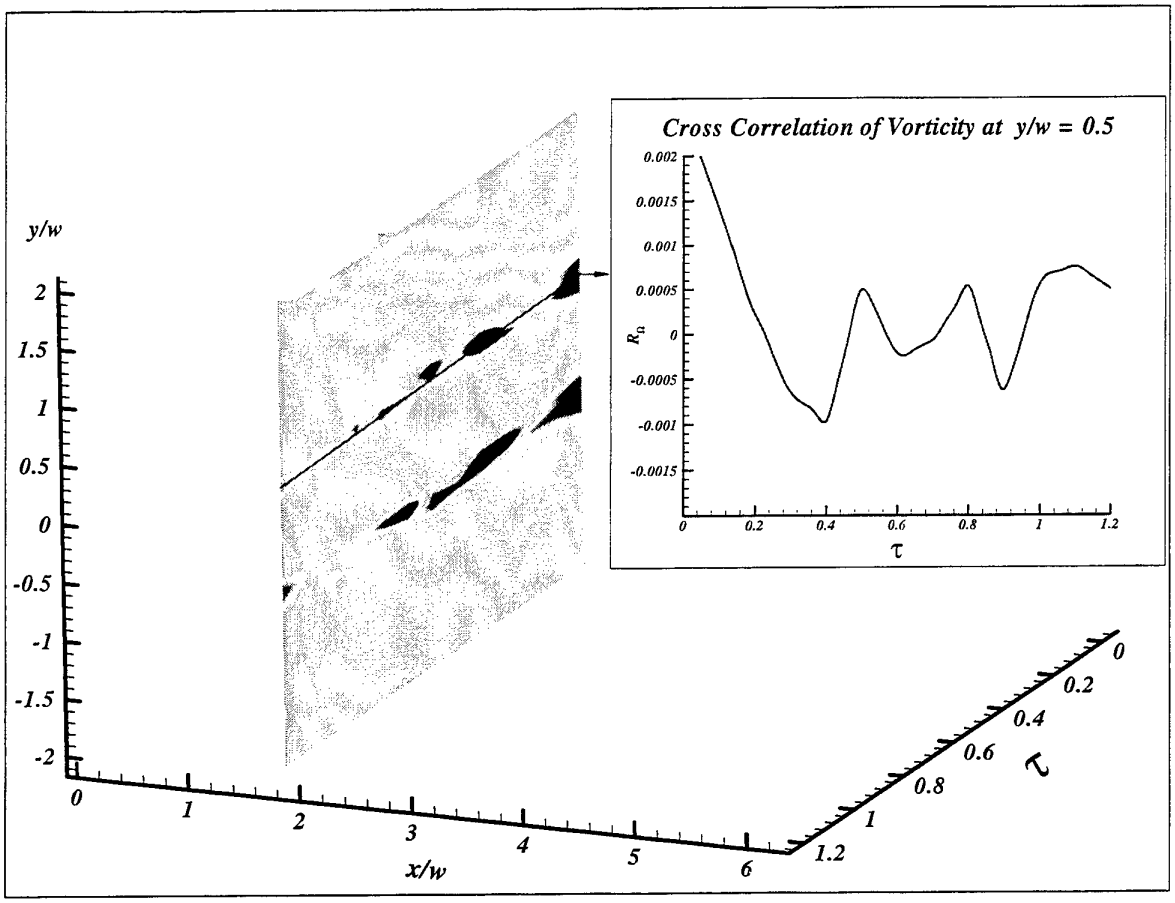


Figure 8. Correlation of vorticity at x/w=1.8, y/w=0.5.

5. CONCLUSIONS

This paper presents the first field velocity correlation (spectra) measurements using the Particle Image Velocimetry technique. This is an important breakthrough in the characterization of unsteady flow because field correlations provide the detailed distributions of temporal and spatial-temporal flow scales. As an example, the technique has been applied to characterize the shear-layer instability of jet flow. The flow time scales obtained with this technique are checked against hot-wire data and compare extremely well.

ACKNOWLEDGEMENTS

This work was supported in part by the Boeing Company and NASA Ames Research Center

REFERENCE

Lourenco, L.. Mesh-free second order accurate scheme for PIV processing. To submitted to Experiments in Fluids.

SESSION 14

MIXERS

DISSIPATION ESTIMATION AROUND A RUSHTON TURBINE USING PARTICLE IMAGE VELOCIMETRY

K.V. Sharp, K.C. Kim*, R.J. Adrian

Department of Theoretical and Applied Mechanics
University of Illinois
Urbana, IL 61801, USA

*School of Mechanical Engineering
Pusan National University
Pusan, Korea

ABSTRACT

Particle Image Velocimetry (PIV) measurements have been acquired in a cylindrical tank stirred by a Rushton turbine. Two datasets were acquired in the r-z plane with magnification 0.26 and 0.56. Phase-averaged velocity fields and mean square gradients were calculated. The mean velocity field averaged over all blade positions is presented. The mean square gradients are used to estimate turbulent dissipation, ε, in the measurement volumes. Two estimates of ε are presented, one based only on $\overline{u_{1,1}^2}$, and the other based on all of the available measured components. Both employ isotropic assumptions. The applicability of the isotropic assumptions is assessed by comparing the magnitudes of the mean square gradients, and the methods of dissipation estimation are compared. The normalized local dissipation, averaged over all blade positions, is calculated versus r/R at the centerline of the blade, and versus z for several values of r/R where R is the radius of the blade.

1. INTRODUCTION

Mixers consisting of a Rushton turbine blade rotating in a cylindrical chamber are common in industry. The mechanisms for mixing in such systems are not well understood, nor are the relationships between mixing mechanisms and dissipation mechanisms. These deficiencies manifest themselves in the form of difficulty in determining the proper relationships for scaling up model results to full scale systems. This study elucidates some of the fundamental structures and characteristics of this flow by performing two-dimensional field measurements in the r-z plane using Particle Image Velocimetry (PIV).

Previous studies using primarily single-point or photographic measurement techniques have provided significant insight into dominant flow structures and characteristics such as the vortices shed from the blade tips. Yianneskis *et al.* (1987) used laser-slit photography and Laser Doppler Velocimetry (LDV) techniques to investigate the mean flow in the tank, the formation of ring vortices in the bulk flow, and the trajectory of the tip vortices. The trajectory and structure of the tip vortices was analyzed by Van't Riet and Smith (1975) using photographic velocity measurements. Stoots and Calabrese (1995) also presented measurements of the mean velocity field using LDV.

Turbulent dissipation in a stirred mixer has been measured by Wu and Patterson (1989), Rao and Brodkey (1972), Cutter (1966), Okamoto *et al.* (1981), and Komasawa *et al.* (1974) among others. Wu and Patterson (1989), using LDV data, calculated ε locally on the basis of the turbulent macroscale and turbulent velocity. Rao and Brodkey (1972) determined the velocity microscale (dissipation length) and mean square velocity from hot-film data. These parameters were then used to estimate turbulent dissipation. Cutter (1966) used an energy balance coupled with photographic velocity data to estimate dissipation. Both Komasawa *et al.* (1974) and Okamoto *et al.* (1981) used energy spectra results to estimate the turbulence microscale, λ. From this, ε was calculated using the isotropic relationship:

$$\varepsilon = 15\nu\overline{u^2}/\lambda^2 .$$

In the current study, direct calculation of mean square gradients in the plane of the flow is available from the 2-D PIV data. The velocity fields can be considered as filtered fields, since the resolution of PIV data is spatially limited and may not resolve the smallest scales of velocity, which are on the order of the Kolmogorov scale. Direct measurement of the mean square gradients in phase-locked velocity fields allows for the calculation of two different dissipation estimates. Both estimates employ isotropic assumptions for the gradient components requiring out-of-plane information.

Using information from two datasets with differing magnifications, and thus velocity spatial resolutions, it is possible to consider the effect of spatial resolution on estimates of dissipation using 2-D PIV data. It is also possible to assess the applicability of the isotropic assumptions since the magnitudes of the mean square gradients can be compared for a given dataset.

2. EXPERIMENTAL SET-UP

The mixer and tank configuration, along with the coordinate system, is shown in Figure 1. A photo of the six blade symmetric Rushton turbine used in this experiment is shown in Figure 2. The turbine diameter (D) is 50.8 mm, and the tank was designed to have a test section diameter, T, equal to $3D$. The tank was filled such that the water depth equaled the tank diameter, and the blade is centered vertically at $T/2$. To best match computational boundary conditions, a non-baffled tank was used for the measurements.

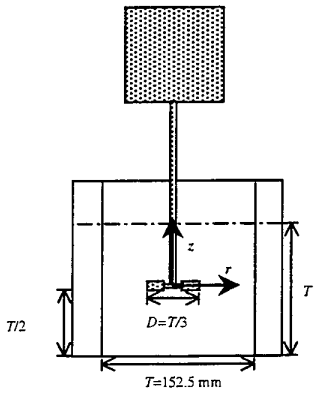


Figure 1: Dimensional relationships between blade diameter, filled tank depth, turbine clearance, and tank diameter.

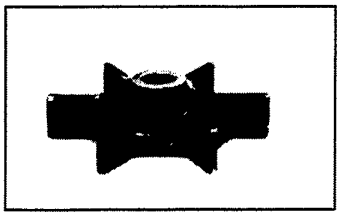


Figure 2: Photo of the Rushton turbine used in this experiment.

All of the measurements were taken with an impeller speed of 100 RPM. A pulsed Nd:Yag laser was used to illuminate the particles, providing a projected lightsheet in the r-z plane of the flow. The camera was mounted such that the 1K by 1K CCD array was parallel to the lightsheet; thus projections of the flowfield velocities in the r-z planes were measured. The full experimental set-up is shown in Figure 3. Using this six-blade symmetric disk turbine, only 60 degrees of phase-locked information was required to define the entire flowfield assuming that the flow around each of the blades is the same. Phase-locked data were acquired in increments of 10 degrees over the total range of 60 degrees. Two hundred images were acquired at each radial blade position.

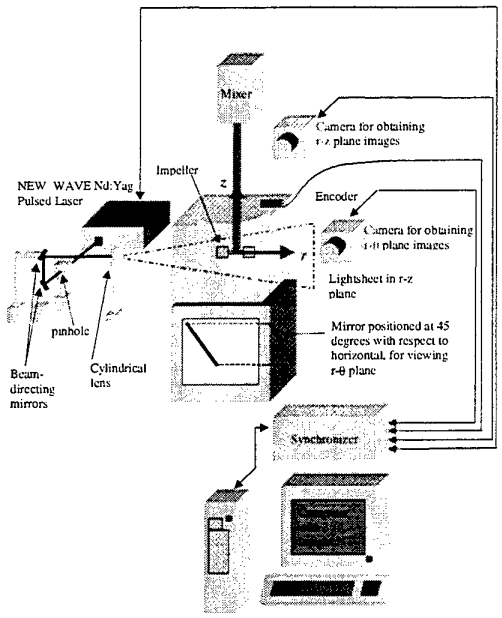


Figure 3: Experimental set-up.

Particle Image Velocimetry (PIV) measurements were taken for two differing fields of view. The

fields of view were 34.4 mm by 34.7 mm and 16.1 mm by 16.2 mm. An appropriate time between pulses was selected for each case, limited at the upper end by the significant out-of-plane particle motion caused by the strong tangential velocity component. Interrogation of the images was performed using a two-frame cross-correlation algorithm in INSIGHT NT Software from TSI, Inc. Thus, 100 velocity fields were obtained from two hundred images at each blade position. The interrogation window size was 24 pixels by 24 pixels in the first field of view and 32 pixels by 32 pixels in the second field of view. This provided velocity spatial resolution of 0.82 mm and 0.51 mm respectively. The magnification for the first case was 0.26, hereafter referred to as Case 1, and 0.56 for the better-resolved case, hereafter referred to as Case 2. Spurious vectors were removed in the region with high out-of-plane velocity component using CLEANVEC (Soloff and Meinhart, 1998).

3. RESULTS

The mean field averaged over all realizations for all blade positions (600 velocity fields) is shown in Figure 4. A one-dimensional plot of radial velocity versus axial position is shown in Figure 5. The axial position, z, is normalized by blade width, W. The radial velocity in this figure is averaged over all blade positions, and the result compared with a velocity profile from Rutherford *et al.* (1996). A sequence of the phase-averaged velocity fields is shown in Figure 6. Each of these velocity fields represents an average over 100 velocity fields. A sequence of typical instantaneous (single realization) velocity fields is shown in Figure 7.

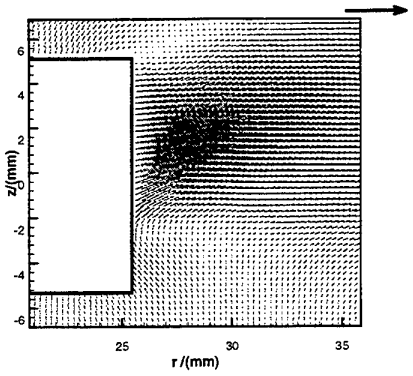


Figure 4: Mean velocity field averaged over all blade positions for Case 2 dataset, including blade outline. The reference vector has magnitude V_{tip}.

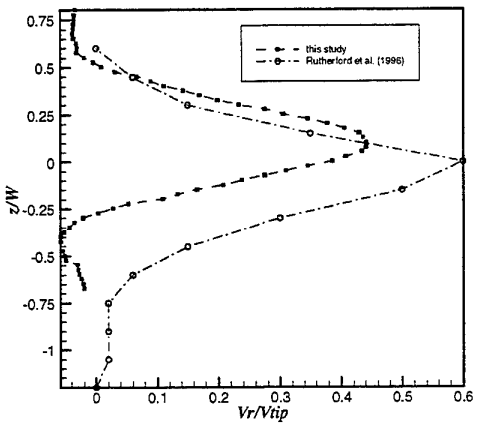


Figure 5: Comparison of mean radial velocity averaged over all blade positions for this study and Rutherford *et al.* (1996).

Direct measurement of turbulent dissipation, ε, requires simultaneous knowledge of velocity gradients in all three directions. In this two-dimensional study, simultaneous velocity gradient information is available for $u_{1,1}$, $u_{1,2}$, $u_{2,1}$, $u_{2,2}$ where the "1" corresponds to the radial direction and "2" corresponds to the axial direction. Knowledge of these four components allows for computation of five terms in the full twelve-term turbulent dissipation equation:

$$\varepsilon = \nu \left\{ \begin{array}{l} 2\left(\overline{u_{1,1}^2} + \overline{u_{2,2}^2} + \overline{u_{3,3}^2}\right) + \\ \overline{u_{1,2}^2} + \overline{u_{2,1}^2} + \overline{u_{1,3}^2} + \\ \overline{u_{3,1}^2} + \overline{u_{2,3}^2} + \overline{u_{3,2}^2} + \\ 2\left(\overline{u_{1,2}u_{2,1}} + \overline{u_{1,3}u_{3,1}} + \overline{u_{2,3}u_{3,2}}\right) \end{array} \right\}.$$

The tangential direction is "3", and no information regarding this velocity component is obtainable using PIV in the r-z plane.

Data acquisition using two magnifications allows for analysis of the effect of velocity scale resolution on the estimation of dissipation from PIV data. Two *estimates* of dissipation are presented. The velocity fields used for these estimates can be considered to be filtered velocity fields, since it is likely that all of the small scales are not accurately resolved. Thus, the estimates of dissipation presented are not intended to replace a full three-dimensional simultaneous measurement of all velocity gradient components, but rather to provide insight into the different methods of estimating dissipation using PIV data.

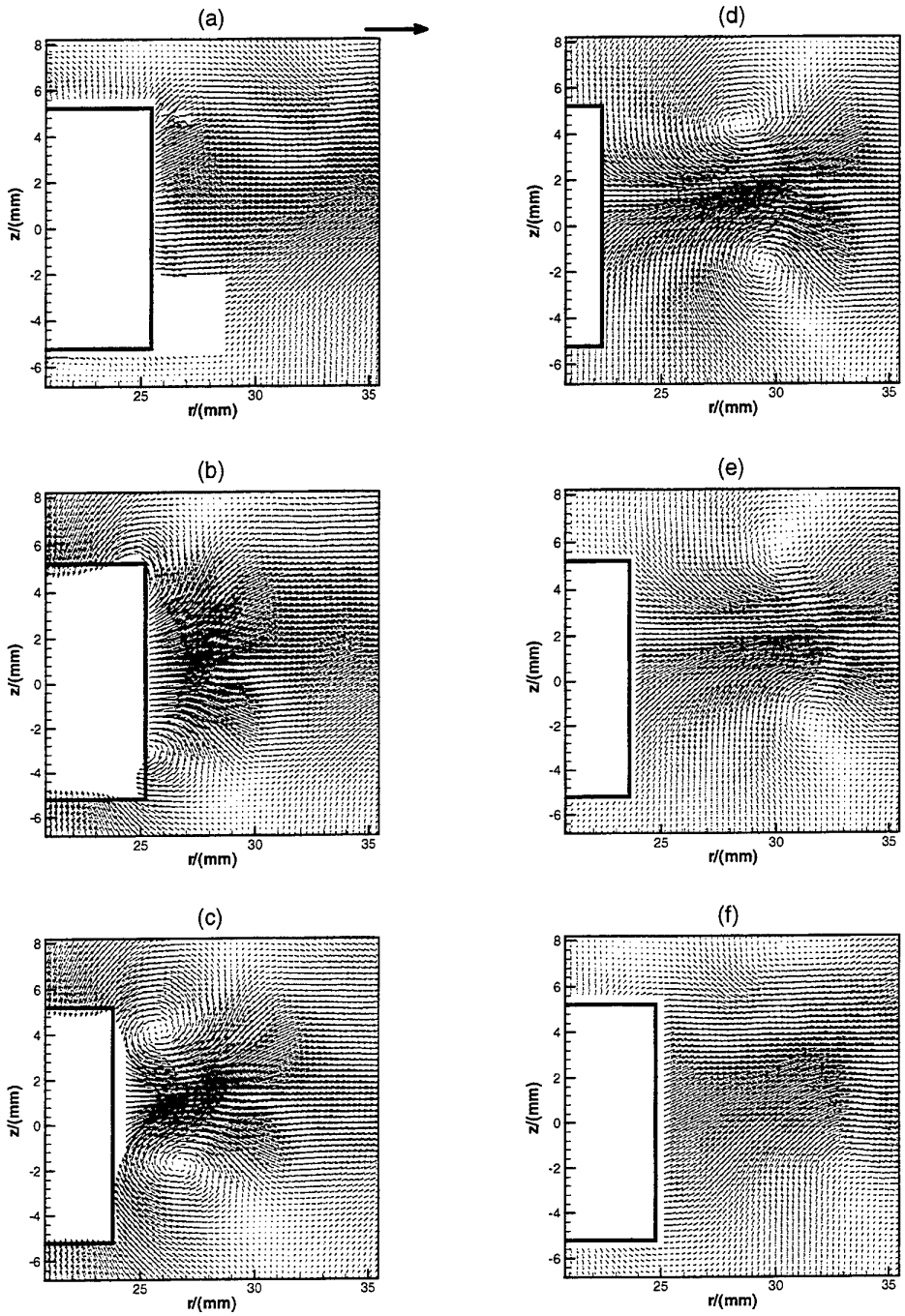


Figure 6: A series of phase-averaged velocity fields for Case 2. The degrees after blade passage are as follows: (a) 0, (b) 10, (c) 20, (d) 30, (e) 40, and (f) 50. The reference vector in frame (a) has magnitude of V_{tip}.

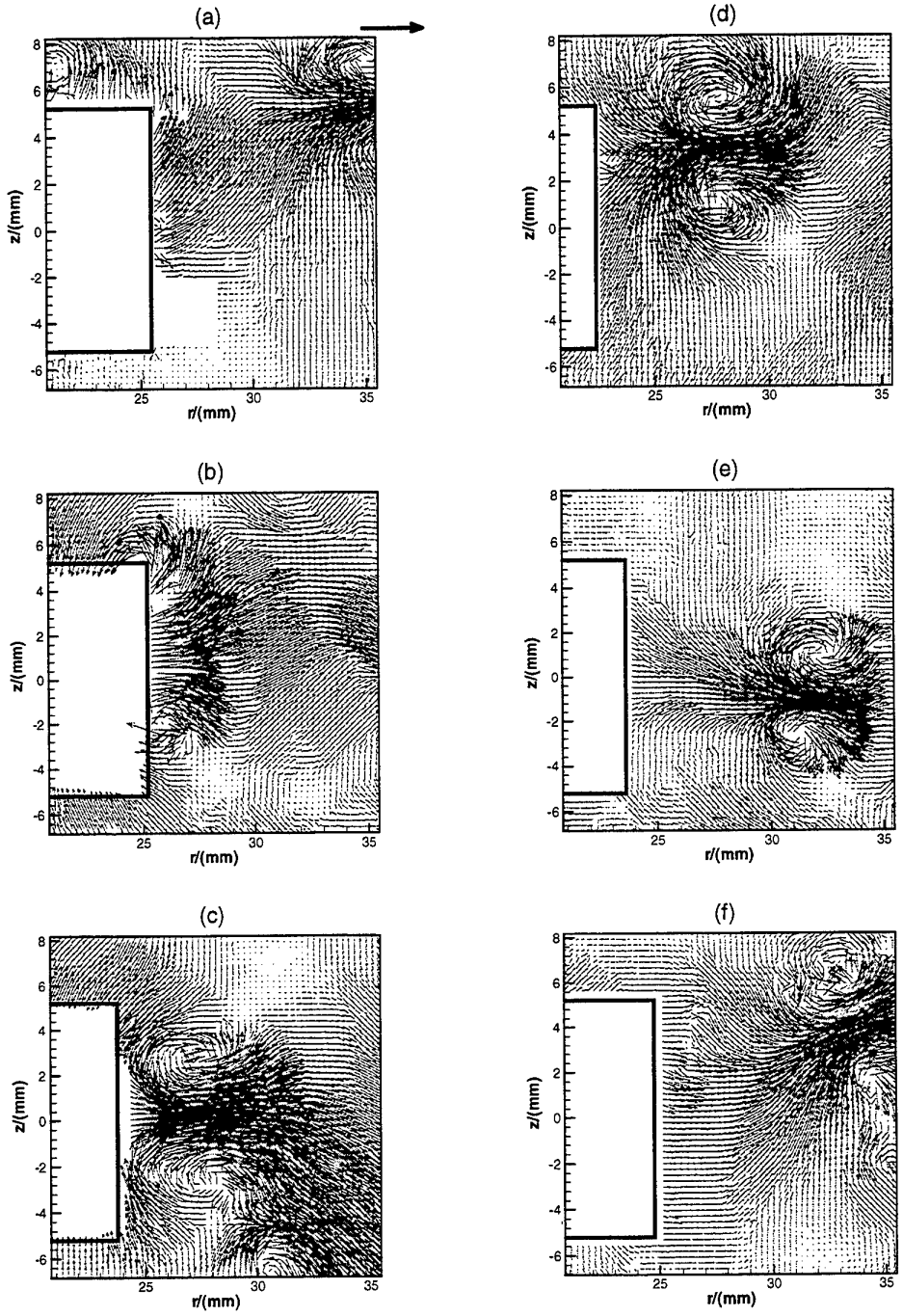


Figure 7: A series of typical instantaneous velocity field for Case 2. The degrees after blade passage are as follows: (a) 0, (b) 10, (c) 20, (d) 30, (e) 40, and (f) 50. The reference vector in frame (a) represents the magnitude of V_{tip}.

For isotropic turbulence,

$$\varepsilon = 15\nu\overline{u_{1,1}^2}.$$

We use this relationship for the first estimate of dissipation, ε_{i15}. It relies only on a single velocity gradient and assumes the values for all other components are statistically isotropic. The second estimate of the turbulent dissipation, ε_{iso}, uses all known components and assumes the unknown values to be statistically isotropic. For this second estimate, the average of $\overline{u_{1,1}^2}$ and $\overline{u_{2,2}^2}$ is used to approximate $\overline{u_{3,3}^2}$. Similarly, the average of $\overline{u_{1,2}^2}$ and $\overline{u_{2,1}^2}$ is used to approximate $\overline{u_{1,3}^2}$, $\overline{u_{3,1}^2}$, $\overline{u_{2,3}^2}$, and $\overline{u_{3,2}^2}$. The averages of the cross terms, $\overline{u_{1,3}u_{3,1}}$ and $\overline{u_{2,3}u_{3,2}}$, are estimated as $-1/2\left(\frac{\overline{u_{1,1}^2}+\overline{u_{2,2}^2}}{2}\right)$. This estimate is thus defined as:

$$\varepsilon_{iso} = \nu\left\{\begin{array}{l} 2\left(\overline{u_{1,1}^2}+\overline{u_{2,2}^2}+\frac{1}{2}\left(\overline{u_{1,1}^2}+\overline{u_{2,2}^2}\right)\right)+ \\ \overline{u_{1,2}^2}+\overline{u_{2,1}^2}+4\left(\frac{1}{2}\left(\overline{u_{1,2}^2}+\overline{u_{2,1}^2}\right)\right)+ \\ 2\left(\overline{u_{1,2}u_{2,1}}\right)-4\left(\frac{1}{2}\left(\frac{1}{2}\left(\overline{u_{1,1}^2}+\overline{u_{2,2}^2}\right)\right)\right) \end{array}\right\}.$$

These methods of calculating the dissipation estimate were used with both of the acquired datasets, Case 1 and Case 2. Table 1 presents area-averages of the dissipation estimates. These estimates are averaged over the same physical area (z =-7.36 mm to z = 8.70 mm and r/R = 1 to r/R = 1.43) in both cases. This physical region was selected since it represents the physical region of measurement for Case 2. Note that this is not an area average over the entire field of view for Case 1.

To assess the applicability of the isotropic estimates on dissipation estimation in a filtered field such as that acquired by PIV, the area-averaged magnitudes of the mean square gradients were computed. Table 2 presents the ratios of mean square gradients used in the isotropic assumptions. If the isotropic assumptions were perfect, all of the values in this table would be equal to 1.

For Case 2, with higher magnification and thus better small scale velocity resolution, the area average dissipation estimates are shown versus estimation method and specified area in Table 3. The region close to the blade is defined as the region between the top and bottom blade edges in z and r/R = 1 to r/R = 1.25.

Table 1: Comparison of area averaged dissipation estimated between Case1 and Case 2. Results from both dissipation estimates, ε_{i15} and ε_{iso}, are shown for the two datasets.

Degrees behind blade passage	Case 1(M = 0.26)		Case 2(M = 0.56)	
	ε_{i15}	ε_{iso}	ε_{i15}	ε_{iso}
0	0.0059	0.0050	0.0134	0.0112
10	0.0066	0.0051	0.0265	0.0190
20	0.0102	0.0079	0.0273	0.0190
30	0.0119	0.0097	0.0346	0.0250
40	0.0095	0.0085	0.0308	0.0237
50	0.0074	0.0063	0.0257	0.0205
overall	0.0086	0.0071	0.0264	0.0197

Table 2: Comparison of the area-averaged ratios of mean square gradients for the Case 2 dataset.

Degrees behind blade passage	$\overline{u_{1,1}^2}/\overline{u_{2,2}^2}$	$\overline{u_{1,2}^2}/\overline{u_{2,1}^2}$	$\overline{u_{1,2}^2}/2\overline{u_{1,1}^2}$	$\overline{u_{2,1}^2}/2\overline{u_{1,1}^2}$	$\overline{u_{1,2}u_{2,1}}/-\frac{1}{2}\overline{u_{1,1}^2}$
0	0.90	1.08	0.78	0.72	0.44
10	1.00	1.24	0.68	0.55	0.21
20	1.24	1.68	0.76	0.45	0.29
30	1.17	1.48	0.74	0.50	0.29
40	1.06	1.32	0.76	0.58	0.32
50	1.06	1.24	0.76	0.62	0.35
overall	1.07	1.34	0.75	0.57	0.32

Table 3: Comparison of the area-averaged dissipation estimates for the near blade region and the entire measurement region.

Degrees behind blade passage	ε_{iso}	ε_{iso} near blade	ε_{i15}	ε_{i15} near blade	$\frac{\varepsilon_{iso}(near\ blade)}{\varepsilon_{iso}(meas\ vol)}$	$\frac{\varepsilon_{i15}(near\ blade)}{\varepsilon_{i15}(meas\ vol)}$
0	0.0112	0.0078	0.0134	0.0109	0.6964	0.8134
10	0.0190	0.0272	0.0265	0.0416	1.4316	1.5698
20	0.0190	0.0330	0.0273	0.0494	1.7368	1.8095
30	0.0250	0.0478	0.0346	0.0649	1.9120	1.8757
40	0.0237	0.0315	0.0308	0.0381	1.3291	1.2370
50	0.0205	0.0161	0.0257	0.0204	0.7854	0.7938
overall	0.0197	0.0272	0.0264	0.0376	1.3152	1.3499

Table 4: Turbulence microscale and turbulence Reynolds number for Case 2.

Region or point	λ/(mm)	Re_λ
Near blade	1.1	55
Whole field of view (Case 2)	1.1	45
Blade centerline and r/R = 1.02	0.9	50

The turbulence microscale (λ) and turbulence Reynolds number (Re_λ) are found using the following relationships:

$$\lambda^2 = \frac{\overline{u_r^2}}{\overline{u_{r,x}^2}}$$

$$Re_\lambda = \frac{\sqrt{\overline{u_r^2}}\,\lambda}{\nu}$$

where u_r is the radial velocity. These quantities, shown in Table 4, are calculated on the average over the previously defined near-blade region, on the average over the entire field of view, and at the specific point r/R = 1.02 on the centerline of the blade.

In this flow, N_{Re} is on the order of 4000, where $N_{Re} = \rho ND^2/\mu$, N = number of revolutions per second and D = blade diameter. The power number, N_p, is defined as $P/\rho N^3 D^5$ where P = the power input to the flow. Using a Reynolds number versus power number curve for the Rushton turbine (Bates *et al.*, 1966, p. 133), the power number is approximately 4.5. Therefore, the power input is calculated to be 0.007 Watts. The LIGHTNIN mixer used in this

experiment was unable to measure power accurately enough to use a direct reading.

The mean turbulent dissipation in the flow is defined as:

$$\bar{\varepsilon} = \frac{P}{\rho V}.$$

The volume of this apparatus is 0.0028 m^3. Thus the mean turbulent dissipation, $\bar{\varepsilon}$, is calculated as 0.0025 m^3/s^2. Using this value, the Kolmogorov scale is estimated as 0.14 mm. Although this estimate has its limits of applicability due to the significant non-isotropic and inhomogeneous structure of the flow, it provides at least an idea of the required resolution of velocity scales. The minimum resolution in this experiment is 0.52 mm, which is four times the Kolmogorov scale. The estimates of dissipation presented in this paper are not meant to provide final values for dissipation in a mixing flow, but instead to evaluate methods of surrogate dissipation calculation and to elucidate trends in dissipation concentrations.

Figure 8 shows a plot of ε^* vs. z for several r/R positions in the flow, where ε^* is the estimated dissipation normalized by the tank-averaged dissipation, $\bar{\varepsilon}$. The results are averaged over all blade positions for Case 2 (higher magnification). Every other datapoint is plotted in this figure and the next. The estimation method used in this data is ε_{iso}, which relies on all the measured components plus estimates for the others. A comparison of the two methods for estimating dissipation is shown along the blade centerline and versus r/R in Figure 9. Again, these estimates of dissipation are averaged over all blade positions, or 600 realizations.

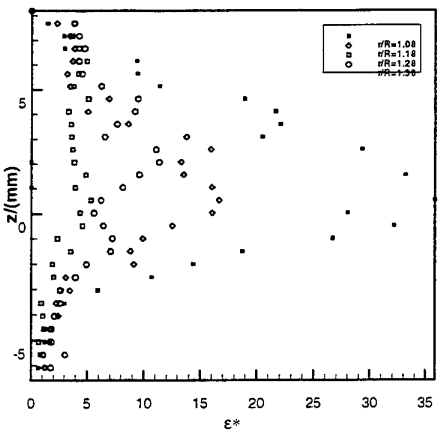


Figure 8: ε^*, averaged over all blade positions, vs. z for varying r/R.

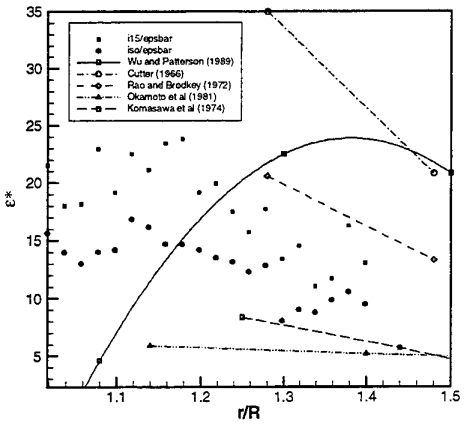


Figure 9: ε^*, averaged over all blade positions, versus r/R at the blade centerline.

4. DISCUSSION:

4.1 Velocity Fields

The general shape of the radial velocity profile versus axial position near the blade is similar in this study and in Rutherford *et al.* (1996). There are some differences in experimental configurations for these studies, namely the distance from the centerline of the disk to the bottom of the tank, the impeller rotation speed, the dimensional size of the impeller and tank, and the existence of baffles. The impeller speed in Rutherford *et al.* (1996) is 200 RPM, twice that used in the current study. The maximum radial velocity in this study appears lower than in Rutherford *et al.* (1996), even when normalized by V_{tip}. The maximum radial velocity is seen above the centerline in the unbaffled tank with the clearance below the disk centerline equal to $T/2$, where T is the diameter of the tank and also the fluid depth. This slight inclination of the mean flow has also been seen in Yianneskis *et al.* (1987) for the same clearance.

The plots of the mean velocity field show well-defined tip vortices in the region close to the blade, as expected. The tip vortices appear to have similar axial convection velocities for the first 20 degrees following blade passage. Thus the phase-averaged fields for 10 and 20 degrees behind blade passage show axial and radial locations of the vortex cores approximately equal to the axial and radial locations of the vortex cores in instantaneous velocity fields. Further behind the blade, the vortices convect both positively and negatively in the axial direction. The instantaneous velocity fields shown in Figure 7 are not sequentially acquired, but rather random

realizations from each blade position. The blank region just outside the lower half of the blade in the 0-degree position represents a region of high laser light reflection from the blade itself and thus a region of poor data acquisition. The mean velocity field averaged over all blade positions shows evidence of a radial jet being pumped in the *r-z* plane by the passage of the blades.

4.2 Dissipation estimates

A comparison of the estimates of dissipation between Case 1 and Case 2 shows that the estimates are consistently higher with the Case 2 data. The lower estimates in Case 1 correspond to the data with lower resolution and it is likely that the mean square gradients are being underestimated.

For Case 2, the better-resolved case, the ratios of mean square gradients are used to assess the applicability of isotropic assumptions to dissipation estimations using PIV data. The ratio of $\overline{u_{1,1}^2}/\overline{u_{2,2}^2}$ is within 25% of 1 for all individual blade positions. Generally, $\overline{u_{1,1}^2}$ is larger than $\overline{u_{2,2}^2}$. The exception to this case is the 0-degree blade position. The mean square levels in the 0-degree case are skewed, however, due to the existence of such a strong reflection from the blade in the CCD images and should not be considered reliable results. In all cases $\overline{u_{1,2}^2}$ and $\overline{u_{2,1}^2}$ are less than $2\overline{u_{1,1}^2}$. The cross term, $\overline{u_{1,2}u_{2,1}}$, is also less than its' corresponding isotropic assumption $-1/2\,\overline{u_{1,1}^2}$. Thus the estimation of dissipation (ε_{i15}) using only multiples of $\overline{u_{1,1}^2}$ is higher than that which employs more of the directly measured components (ε_{iso}), as shown in Table 1.

In Table 3, the average of both dissipation estimates is shown for Case 2 data. The area average of the dissipation estimates is taken over the entire measurement volume, and also over a smaller measurement volume close to the blade, corresponding to $-W < z < W$ and $1 < r/R < 1.25$. This table shows that, in all cases except the 0-degree and 50-degree positions, the area average over the region close to the blade is considerably higher than that over the entire measurement region. The ratio of the area average close to the blade to that in the entire measurement region is highest at blade positions 20 and 30 degrees behind blade passage. This is the plane in which the tip vortices are strongest inside $1 < r/R < 1.25$.

The calculated turbulence microscales are on the order of 1 mm, consistent with those found by Wu and Patterson (1989) and Rao and Brodkey (1972). Using these microscales, the turbulence Reynolds number is also on the order of turbulence Reynolds numbers in previous studies, specifically the study by Wu and Patterson (1989).

Figure 8 shows that ε^* is highest just outside the tip of the blade ($r/R = 1.08$). The maximum value of ε^* occurs near $z = 0$ for all profiles, and generally decreases with axial and radial distance from the blade tip. These results are similar to those of Wu and Patterson (1989), though they found a double-tipped profile shape for r/R of 1.08 and had a much larger range of values for r/R. This double-tipped shape is not evident in Figure 8 at lower r/R, but rather at $r/R = 1.38$. Data at larger r/R values with the current dissipation estimation technique and experimental configuration are required to definitively evaluate the dissipation magnitude trends at higher distances from the blade tip. The maximum value of ε^* found by Wu and Patterson (1989) is approximately 22 near the vertical centerline and with $r/R = 1.29$. These results were for a rotation rate of 200 RPM, twice that in this study. The maximum value of ε^* in this study at $r/R = 1.28$ is 6 near $z = 0$.

Results from this study, Cutter (1966), Rao and Brodkey (1972), Wu and Patterson (1989). Okamoto *et al.* (1981), and Komasawa *et al.* (1974) are compared in Figure 9. The general trend in this study for $1.2 < r/R < 1.4$ is for decreasing ε^* with distance from the blade tip. This trend is also seen for the previous studies between $1.2 < r/R < 1.5$. In the previous studies, for $r/R < 1.28$, Cutter (1966) and Rao and Brodkey (1972) found maximum ε^* as r/R neared 1. To the contrary, Wu and Patterson (1989) found that ε^* decreased as r/R neared 1 to a minimum value near 5. It is worth noting that the range of r/R values available in this study is limited by the field of view, with the maximum r/R value being approximately 1.4. The data available in previous studies for larger r/R aids in discussion of overall trends of dissipation versus position. Considering the results of this and previous studies, it appears that ε^* decreases as the distance from the blade tip increases in the r direction. Also that the dissipation decreases as the distance from the blade increases in the axial direction.

Details aside, the principle conclusions to be drawn from Figure 9 are that there is little agreement between the magnitude of the data, emphasizing the difficulty of measuring dissipation, and that the general level of dissipation in this region is 10-20 times the volume mean dissipation, emphasizing the intense concentrations of dissipation in the near-blade region.

5. CONCLUSIONS

This work describes a method for estimating turbulent dissipation using 2-D PIV data. Although these data do not provide enough information to directly measure all the required velocity gradients, two-dimensional information is provided. Two estimates of dissipation are calculated, one using only one of the velocity gradient components and the other using all known components. The isotropic estimate using only $\overline{u_{1,1}^2}$ gives higher overall values for dissipation than the estimate which relies on all known components and uses isotropic assumptions for the others. A comparison of the mean square gradients shows that the statistically isotropic assumptions are off by up to 40% when averaged over all the blade positions. Although this is a significant amount of variation, the variation may decrease for higher Reynolds numbers. This velocity field may be considered a filtered field since it has limited resolution, and a PIV study with higher resolution could provide further information as to the appropriateness of these assumptions in a mixer flow. Stereo PIV could also be used to provide additional velocity gradient information for assessing the isotropic assumptions.

Even with the limited spatial resolution of velocity, the dissipation estimates calculated in this work are within the range of the dissipation calculations in previous studies. The magnitude of dissipation measurements in the near-blade region varies significantly between the studies discussed. However, the estimate of dissipation in the near-blade region is consistently 10-20 times higher than the volume averaged dissipation, emphasizing the high concentration of dissipation in this region.

REFERENCES

Bates, R.L., Fondy, P.L & Fenic, J.G. 1966, Impeller Characteristics and Power, in Mixing: Theory and Practice, ed. by Uhl, V.W. & Gray, J.B., vol. 1, pp. 111-178, Academic Press, New York

Cutter, L.A. 1966, Flow and Turbulence in a Stirred Tank, A.I.Ch.E.J., vol. 12, pp. 35-45.

Komasawa, I., Kuboi, R. & Otake, T. 1974, Fluid and Particle Motion in Turbulent Dispersion-I: Measurement of Turbulence of Liquid by Continual Pursuit of Tracer Particle Motion, Chem. Eng. Sci., vol. 29, pp. 641-650.

Okamoto, Y., Nishikawa, M. & Hashimoto, K. 1981, Energy Dissipation Rate Distribution in Mixing Vessels and its Effects on Liquid-liquid Dispersion and Solid-liquid Mass Transfer, Int. Chem. Eng., vol. 21, no.1, pp. 88-94.

Rao, M.A. & Brodkey, R.S. 1972, Continuous Flow Stirred Tank Turbulence Parameters in the Impeller Stream, Chem. Eng. Sci., vol. 27, pp. 137-156.

Rutherford, K., Mahmoudi, S.M.S., Lee, K.C. & Yianneskis, M. 1996, The Influence of Rushton Impeller Blade and Disk Thickness on the Mixing Characteristics of Stirred Vessels, Trans. I.Chem.E., vol. 74, part A, pp. 369-378.

Soloff, S., and Meinhart, C. 1998, CleanVec: PIV Vector Validation Software, Private Communication.

Stoots, C.M. & Calabrese, R.V. 1995, Mean Velocity Field Relative to a Rushton Turbine Blade, A.I.Ch.E.J., vol. 41, no.1, pp. 1-11.

Van't Riet, K. & Smith, J.M. 1975, The Trailing Vortex System Produced by Rushton Turbine Agitators, Chem. Eng. Sci., vol. 30, pp. 1093-1105.

Wu, H. & Patterson, G.K. 1989, Laser-Doppler Measurements of Turbulent-Flow Parameters in a Stirred Mixer, Chem. Eng. Sci., vol. 44, no. 10, pp. 2207-2221.

Yianneskis, M., Popiolek, Z. & Whitelaw, J.H. 1987, An Experimental Study of the Steady and Unsteady Flow Characteristics of Stirred Reactors, J. Fluid. Mech., vol. 175, pp. 537-555.

VISUALISATION OF THE TRAILING VORTEX SYSTEM PRODUCED BY A PITCHED BLADE TURBINE USING A REFRACTIVE INDEX MATCHED AUTOMATED LDA-TECHNIQUE

M. Schäfer[*], P. Wächter[*], F. Durst[*], M. Yianneskis[**]

[*] Institute of Fluid Mechanics, Friedrich-Alexander-University of Erlangen-Nürnberg
[**]King's College, London

ABSTRACT

The trailing vortex system near impeller blades has been identified as the major flow mechanism responsible for mixing and dispersion in stirred tank reactors. In the area of the trailing vortices highest values of turbulence occur and the major portion of the total energy introduced to the stirred vessel is dissipated here.

Despite the importance of trailing vortices for the mixing process, little is known about their formation and development within and in the immediate vicinity of the impeller blades. In particular, there is a lack of detailed quantitative information on the characteristics of trailing vortices, for example vorticity, vortex dimension and the distribution of turbulence kinetic energy.

This paper provides detailed information on the flow field produced by a 45° pitched blade turbine and describes a technique to visualise the formation and development of trailing vortices using laser-Doppler-anemometry. The results lead to a better understanding of trailing vortices and provide valuable information to engineers for the optimisation of mixing processes in industry. In addition, the validation of numerical computations with CFD of the flows in stirred tank reactors requires more detailed information on the flow field than is available to date so that the data gained in the present study can significantly support the ongoing developments in CFD.

1 INTRODUCTION

The flow generated in a stirred tank reactor is very complex and extensively three dimensional, especially in the impeller region. The flow conditions near the impeller blades are responsible for the formation of so called trailing vortices. Extensive studies have been carried out in the past to learn more about the characteristics of trailing vortices and their importance for several mixing processes. This is mainly due to the high levels of turbulence and local energy dissipation rates associated with the formation, development and break down of the trailing vortex system. Therefore trailing vortices can be considered as the essential flow mechanism for following mixing applications:

- Gas dispersion
- Liquid dispersion like in emulsion processes
- Solid-liquid systems in which high energy dissipation rates are needed (e.g. dissolution of agglomerates)
- Solid-liquid systems in which high energy dissipation rates must be avoided due to the formation of fine and labile products (e.g. cell damage in fermentation processes)
- chemical reactions which are controlled by micro-mixing phenomena (see for example Fournier *et al.* (1996)).

The trailing vortex system produced by a Rushton turbine is the most extensively studied in the literature. Van't Riet and Smith (1975) used photographic techniques to visualise the formation and development of trailing vortices in a gas dispersion process. They reported that high rates of turbulence exist within the trailing vortices and it was concluded that most of the energy introduced to the stirred tank is dissipated here. In other reported studies measurement techniques like Pitot tubes and hot wire anemometry were also used for the investigation of the flow field produced by a Rushton turbine (see for example Gunkel and Weber (1975)).

The development of the laser-Doppler-velocimetry (LDV)-technique enabled a more reliable quantitative study on flow fields in stirred tank reactors, since (a) LDV provides flow information even in unsteady and highly turbulent flow regions as well as in the recirculation regions in the tank and (b) it is an unobtrusive technique. Therefore the LDV-technique has been widely employed to study the characteristics of the flow in stirred tanks. Also the trailing vortex system generated by a Rushton turbine was focused in more detail (see for example Yianneskis *et al.* (1987), Wu and Patterson (1989a), Stoots and Calabrese (1995)). These investigations provided quantitative information on the velocity components and their turbulent fluctuations within the trailing vortex pair generated at each impeller blade of a Rushton turbine. In addition, it was reported that the periodic nature of the flow in the vicinity of the impeller necessitates angle-resolved LDV-measurements, in which the flow information is assigned to the corresponding angle of the impeller blades. Yianneskis and Whitelaw (1993) have shown that if the LDV-measurements are processed as 360° ensemble-averaged measurements, then the fluctuating quantities contain both periodic and turbulence contributions and this can

lead to an overestimation of apparent turbulence quantities in the impeller stream of a Rushton turbine by up to 400%. Detailed quantitative flow information within the stirrer element between the rotating impeller blades where reported by Schäfer *et al.* (1997), who used a refractive index matching method to gain optical access to the inner part of the impeller, and the results gave details of the exact formation of the trailing vortices behind each stirrer blade.

Pitched blade turbines (PBTs) have been found to be more efficient than other impellers (e.g. Rushton turbine) with respect to liquid phase mixing and solid suspension processes. They are also employed in gas dispersion processes. The trailing vortex system generated by pitched blade turbines was studied by Tatterson et al. (1980) by using flow visualisation techniques. Compared with a Rushton turbine only one trailing vortex is formed behind each blade of a PBT. Ali *et. al* (1981) used a high speed, stereoscopic motion picture technique, to visualise the trailing vortex system in an oil into water dispersion and the trailing vortices have been identified as the major flow mechanism responsible for dispersion. LDV-measurements on the flow field were also reported (see for example Ranade and Joshi (1989), Kresta and Wood (1993), Hockey and Nouri (1996)), but most of these investigations have been concerned with 60° PBT and/or with the mean and fluctuating (r.m.s) velocities in the bulk flow of the vessel or at least outside the impeller swept volume. The only investigations concerned primarily with the trailing vortex structure were the flow visualisation studies of Tatterson and co-workers but the understanding and quantification of the vortex mean flow and turbulence structure is still far from complete.

The main objectives of the present investigation are to provide a better understanding of the generation and formation of the trailing vortex system by a 4/45° pitched blade turbine and to quantify the characteristic flow variables like mean and r.m.s velocities and turbulence kinetic energy within and in the vicinity of the trailing vortices. Another major objective is to provide a comprehensive and detailed experimental data set for the flow field produced by a PBT, which is suitable for the validation of numerical simulations of stirred vessel flows and the improvement of the turbulence models used in such calculations. Progress in modern computational techniques led recently to reliable calculations of single-phase flow in stirred tank reactors (see for example Wechsler *et al.*). These developments will be supported by the detailed LDV-experiments carried out during the present study.

For this purpose a LDV-system was developed at the Institute of Fluid Mechanics in Erlangen which allows for automated angle-resolved measurements within the impeller region (i. e. between the blades) through refractive index matching of the complete measuring section. The complete set-up, the measuring equipment and the flow configuration is described in more detail in section 2. For the visualisation of the results a commercial software "TECPLOT" was used and a movie was created to animate the flow around the impeller which shows the generation, development and break down of the trailing vortices. Characteristic results are presented to show the most important flow features which are discussed in section 3. As mentioned above the energy dissipation rates within the trailing vortices are an important parameter to assess the efficiency of mixing processes. Therefore an rough estimate of the local energy dissipation rate was carried out which is described and presented in section 4. The paper ends with a summary of the main findings and some conclusions which can be drawn from the results.

2 EXPERIMENTAL SET-UP AND FLOW CONFIGURATION

A fully automated test rig for detailed LDV-measurements in stirred tank reactors has been developed at the Institute of Fluid Mechanics within the framework of several research projects. The set-up of the test rig is shown in Figure 1. The set-up included three main parts: the measuring section, the traversing equipment for automation and the LDV measurement system consisting of a diode fibre laser-Doppler-anemometer operating in backscatter mode, a traversable probe and a frequency counter.

The measuring section consisted of a cylindrical baffled vessel of diameter T = 152 mm and a four-bladed pitched blade turbine of diameter 50 mm (D = 0.329 T) installed at a clearance of $C = T/3$. Figure 2 shows the geometry of the mixing vessel and the coordinate system used. Figure 3 gives the details of the turbine. The liquid height was equal to the vessel diameter ($H = T$). The top of the vessel was closed with a lid to avoid air entrainment into the liquid from the free surface. Nouri and Whitelaw (1990) have shown that the effect of the lid on the flow field has only an influence in the immediate vicinity of the lid/free surface. Four equally spaced baffles of width B = T/10 and thickness of 3 mm were mounted along the inner wall of the cylinder at a distance of 2.6 mm. The vessel could be rotated about its axis which facilitated the adjustment of the vessel for measurements in different vertical planes.

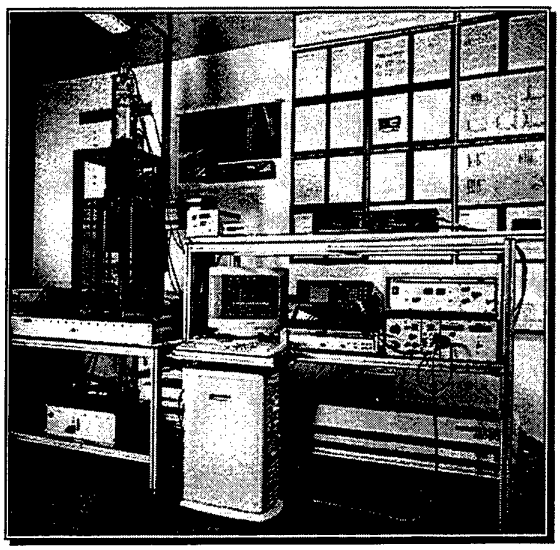


Fig. 1 Stirrer test rig at the Institute of Fluid Mechanics in Erlangen

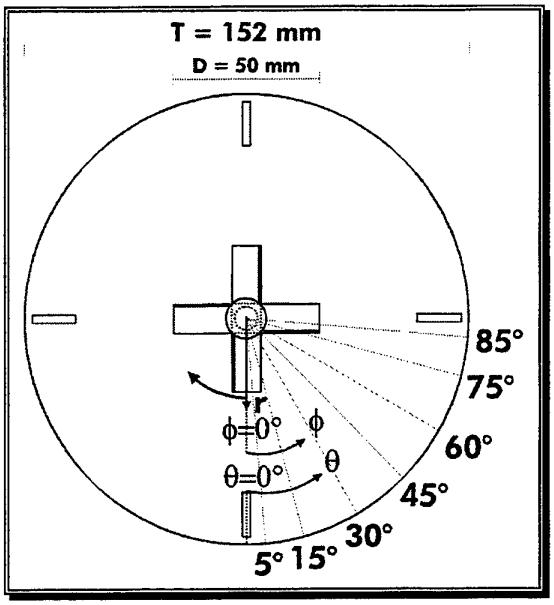


Fig. 2 Geometry of mixng vessel and coordinate system

The turbine used here was a four bladed stirrer with a blade pitch of 45°. The blade thickness was 0.9 mm and the blade height was 0.264 D (13.2 mm) corresponding to a projected height of 0.2 D. The hub in which the blades were fixed had a diameter of 12.5 mm.

The entire measuring section was refractive index matched, i.e. the walls, the baffles and the impeller blades were constructed from Duran glass that has the same refractive index as the working fluid. In addition, the tank vessel was located in a rectangular trough filled with the working fluid, in order to eliminate the distorting effect of the rounded surface of the cylindrical vessel on the path of the laser beams. The refractive index depends mainly on the molecular structure of the material/fluid, the temperature and the wave length of the light (laser beam). At the operating wave length of 832 nm of the laser system and an average temperature of 21° C during the experiments Duran glass has an refractive index of n = 1.468. Two silicone oils, from which one has an refractive index above and one below n = 1.468, were mixed in that way that the fluid matches exactly the refractive index of Duran glass at a temperature of 21° C. The kinematic viscosity of the final mixture of silicone oils was measured to $\nu = 15.3 \times 10^{-6}$ m²/s. The temperature within the vessel and the trough was controlled with a cooling coil so that the temperature was kept constant during the measurements. The full refractive index matching offered optical access to the inner part of the impeller without any distortion of the laser beams allowing for detailed studies of the flow field in the important region, where the trailing vortices are generated.

Periodic variations in the flow field were taken into account by angle resolved measurements close to the impeller. For this purpose an optical shaft encoder was used providing 1,000 pulses and a marker pulse per revolution. The marker pulse corresponded to the angle $\phi = 0°$ of the blade

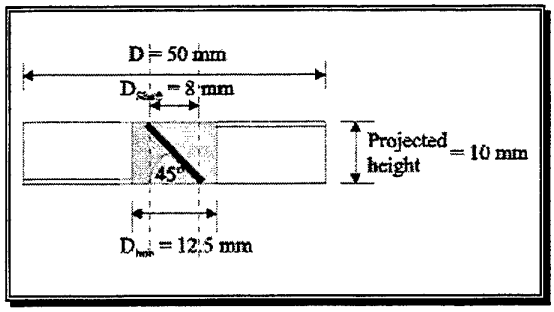


Fig. 3 Geometry of pitched blad

and was set at the middle of the blade at the radial tip with an accuracy of ± 0.36°.

For the measurements a Diode-Fiber-Laser-Doppler-Anemometer (DFLDA) was used which has been previously described in detail by Stieglmeyer and Tropea (1992). The DFLDA-system consists of a miniaturised, traversable optical probe containing transmission and receiving optics, separated mechanically from the bulky components (laser, beamsplitter, Bragg cell, fiber in coupling, avalanche photo diode (APD) for signal detection, etc.). Optical fibers connect the probe with the laser, detector and other optical components and the probe can be easily mounted on a traversing unit. The working fluid was seeded with titanium dioxide particles (3 µm mean diameter) and the scattered light was focused back to the APD. Radial and tangential velocity components were measured with the beams located in a horizontal plane and axial components were measure by rotating the optical probe 90° so that the beams are located in a vertical plane. The signal from the APD was filtered, validated and evaluated by using a frequency counter (TSI model 1980b) which was interfaced to a PC.

As the laser system used only supplies flow information at a single point, the entire flow field can only be determined rapidly if data acquisition is automated. For this purpose the optical probe was mounted on a 3-D traversing unit which was controlled via a CNC-controller by the PC. The accuracy of locating the measuring volume (i. e. the probe) was 0.1 mm.

The velocity data as well as the angular information were stored for each measuring point in a data file. Software was written to assemble all data files obtained to one input file for the postprocessor, which was the commercial software "TECPLOT".

The results which will be shown in the next section were conducted at a stirrer speed of N = 2,672 r.p.m. ($V_{tip} = \pi DN$ = 7 m/s) corresponding to a Reynoldsnumber of $Re = ND^2/\nu$ = 7,300. The stirrer speed was kept within ± 30 r.p.m (1%).

At each measuring location 10,000 single velocity data were collected for the ensemble-averaged measurements whereas this number was increased to 60,000 for the angle-resolved measurements. These numbers of velocity samples were sufficient to minimise statistical errors in the determination of mean and fluctuating flow velocities. There are further possible error sources in an LDV-system and measurement uncertainties vary with location. The accumulated

errors in mean and fluctuation (rms) velocity measurements have been estimated to be, on average, 1 -3 % and 5 - 10% of V_{tip}, respectively, with the higher errors expected in region of steep velocity gradients.

3 RESULTS

3.1 Large-Scale Flow Field

For the purpose of obtaining a better understanding of the flow generated by the pitched blade turbine throughout the whole vessel ensemble-averaged measurements and angle-resolved measurements were carried out for the complete flow field. Angle-resolved measurements were made only in those flow regions, where periodic variations in the flow variables occurred. The boundaries of this region were determined via test measurements which indicated that periodic variations are apparent beneath the impeller down to the bottom of the vessel (from z/T = 0 to z/T = 0.4). In radial direction periodic variations were obtained only close to the impeller (from the shaft up to r/T = 0.2). The measuring grid for the complete flow investigations extended in axial direction from the bottom to the top (6 mm - 150 mm or z/T = 0.039 - 0.987) and in radial direction from the shaft to the cylinder walls (6 mm - 74 mm or r/T = 0.039 - 0.487) and had a fine resolution of 4 mm (= 0.026 T) in each direction. In addition, seven different planes between the baffles were examined to resolve also the influence of the baffles on the bulk flow. In Figure 2 the locations of the planes of measurements within the stirred vessel are shown.

By way of example the flow field and the distribution of turbulence kinetic energy obtained for a vertical plane (r, z-plane) located half way between two baffles at θ = 45° before a baffle are shown in Figure 4 and Figure 5, respectively. The mean velocity components were normalised with the blade tip velocity V_{tip} and are denoted $\overline{U}$ / V_{tip}, $\overline{V}$ / V_{tip} and $\overline{W}$ / V_{tip} for the axial, radial and tangential components respectively. The turbulence kinetic energy k were calculated from the fluctuating velocity components u', v' and w' according to

$$k = \frac{1}{2}\left(u'^2 + v'^2 + w'^2\right) \qquad (1)$$

and normalised with the square of the stirrer tip velocity V_{tip}^2.

It is important to note that the velocity vectors close to the impeller (i. e. in the region, where periodic variations occur) were obtained from angle-resolved measurements, which means that they refer to a blade angle of ϕ = 45°. The vectors shown in Figure 5 reveal the characteristic flow pattern produced by a pitched blade turbine. The fluid is entrained into the stirrer element from the top and is ejected axially at axial peak velocities of 0.45 V_{tip} (at r/T = 0.125). The discharge flow becomes then increasingly more radial and reaches the bottom approximately half way between the shaft and the vessel wall. A large scale ring vortex is formed, which extends only over slightly more than half of the vessel height (z/T = 0.55 - 0.65), therefore poor mixing exists in the upper bulk flow of the tank with almost no exchange of fluid. The flow velocities in the ring vortex reach magnitudes of

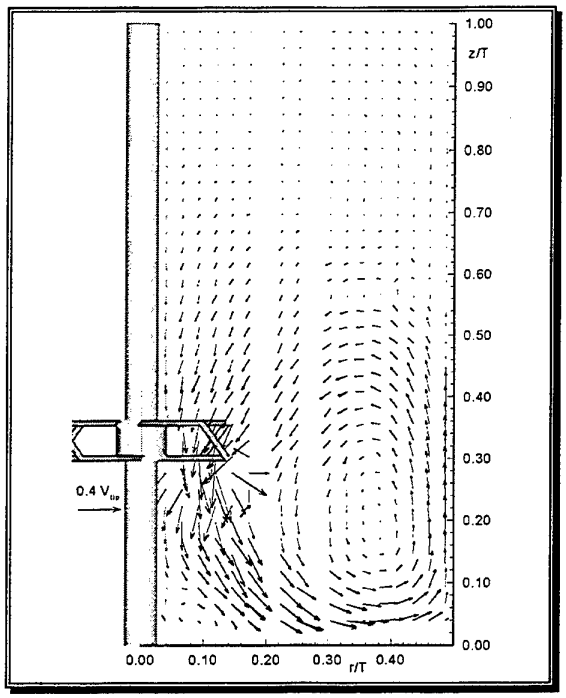


Fig. 4 Bulk flow field in a vertical plane 45° before a baffle

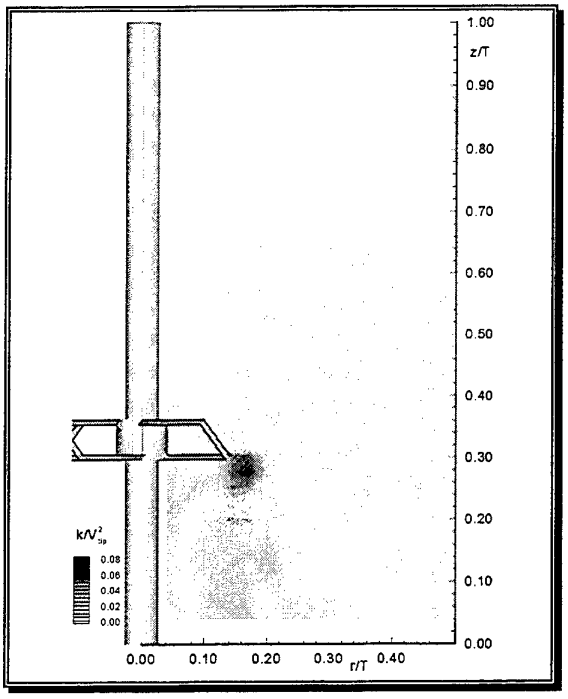


Fig. 5 Distribution of turbulence kinetic energy in vertical plane 45° before a baffle

0.2 V_{tip} close to the vessel wall whereas in the uppermost area only slow velocities below 0.05 V_{tip} were obtained. A secondary vortex is formed at the bottom close to the shaft with very low magnitudes of velocity. This may cause problems in this area in solid-liquid mixing tasks with the suspension of the solids off the vessel bottom.

It must be noted that the flow structure changes slightly for different measuring planes which are not shown here. In the vertical plane at $\theta = 5°$ the axial extension of the large ring vortex reaches 3/4 of the liquid height due to additional axial flow which results from the deflection of tangentially propelled fluid at the baffles. The extension in axial direction decreases with increasing distance from the baffles and at the plane at $\theta = 75°$ the vortex is only able to form over one half of the liquid height.

The flow field close to the impeller beneath the outer tip of the blade at around r/T = 0.16 reveals that a vortex is generated in the impeller region which is still present at $\phi = 45°$ behind the blades. As it can be seen in Figure 5 this vortex is associated with high turbulence intensity. The magnitudes of turbulence kinetic energy reach here peak values of about 0.04 - 0.085 V_{tip}^2, whereas in the bulk flow of the vessel only very little turbulence of less than 0.015 V_{tip}^2 is present.

3.2 Impeller Flow Field

Considering that for a reliable assessment of mixing processes the exact distribution of turbulence kinetic energy is required, the generation and development of the trailing vortices constitutes an important phenomenon of the flow in stirred tank reactors. In order to capture all the details of the flow in the region of the trailing vortices the resolution of the measuring grid was increased to a step width of 1 - 2 mm within and close to the impeller.

The results will be presented in form of an animation of the impeller flow field, in which planes at each degree between two blades (1° to 90°) are shown step by step lead-

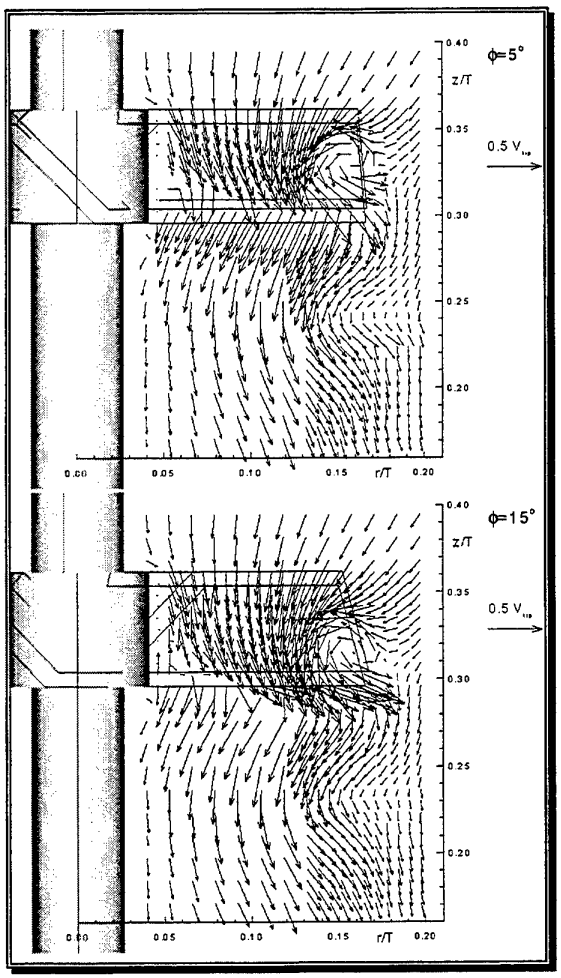


Fig. 6 Impeller flow field at $\phi = 5°$ and $\phi = 15°$

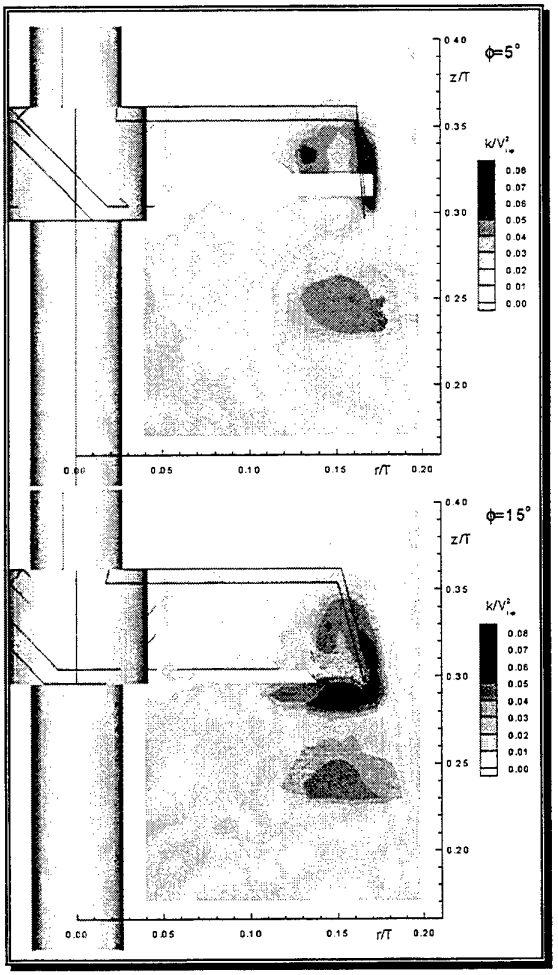


Fig. 7 Distribution of turbulence kinetic energy at $\phi = 5°$ and $\phi = 15°$

ing to a rotating impeller movie. By way of example Figures 6 and 7 show the flow field and the distribution of turbulence kinetic energy for two selected planes located at $\phi = 5°$ and $\phi = 15°$ behind the blades. The blades must be considered as moving out of the page towards the reader. It must be mentioned that the blade cuts across the measurement plane and as a result some of the vectors show the flow in front and some behind the blade.

The trailing vortex is formed by the interaction of the streams issuing from the top and side of the blade and it is fully developed at $\phi = 5°$ behind the blade with an extension of over 5 mm in diameter. The trailing vortex moves further down with increasing angular distance from the blade and reaches the lower tip at approximately $\phi = 15°$. The peak values of turbulence kinetic energy exist in the region of the trailing vortex below the impeller. It is interesting to note that above the impeller where the fluid is sucked in turbulence values are low, as indicated by the magnitudes of the turbulence kinetic energy that are similar to those in the bulk flow ($k < 0.015\ V_{tip}^2$). The second circulatory motion of the flow below the impeller at approximately $z/T = 0.25$ in the $\phi = 5°$ plane indicates the presence of the trailing vortex from the preceding blade which is still in evidence at $\phi = 15°$ or $\phi = 105°$ after that blade has crossed this plane. Also higher turbulence kinetic energy values were obtained in this region.

Although the depicted flow fields clearly show the trailing vortices and the vortex centres can be determined accurately due to the high density of the measuring grid, it is more difficult to locate exactly the vortex edges, which are needed to give a full description of the trailing vortices. As vortices are characterised the intensity of vortex motion was found to be a valuable parameter for determining the extension of the trailing vortices in a more quantitative manner. For this purpose the vorticity (ζ) in ϕ-planes were calculated using the following equation:

$$\zeta = \frac{\partial \overline{V}}{\partial z} - \frac{\partial \overline{U}}{\partial r} \qquad (2).$$

The vorticity is very intensive within and very low outside trailing vortices. A limiting value of vorticity can be found that indicates the edges of the trailing vorticity. For the present study a value of $\zeta = 330$ 1/s was determined. It was then possible to visualise the trailing vortices with a contour plot (Figure 8) in which contours lower than the limiting value of the vorticity (cut-off value) were erased.

From Figure 8 the total extent of the trailing vortices generated behind each stirrer blade can be determined. Vorticity originates at the side and upper tips of the blade. The vortex extends to around 135° behind a blade and stays in an almost constant radial position. The axial inclination of the vortex axis to the horizontal after entering the flow around the impeller is approximately 20° which remains constant up to the total dissipation of the vortex in the bulk flow. From the impeller flow movie, which gives more details of the flow than shown in the present paper, one interesting fact has to be mentioned, that with increasing diameter of the vortex the distribution of the turbulence kinetic energy along the vortex

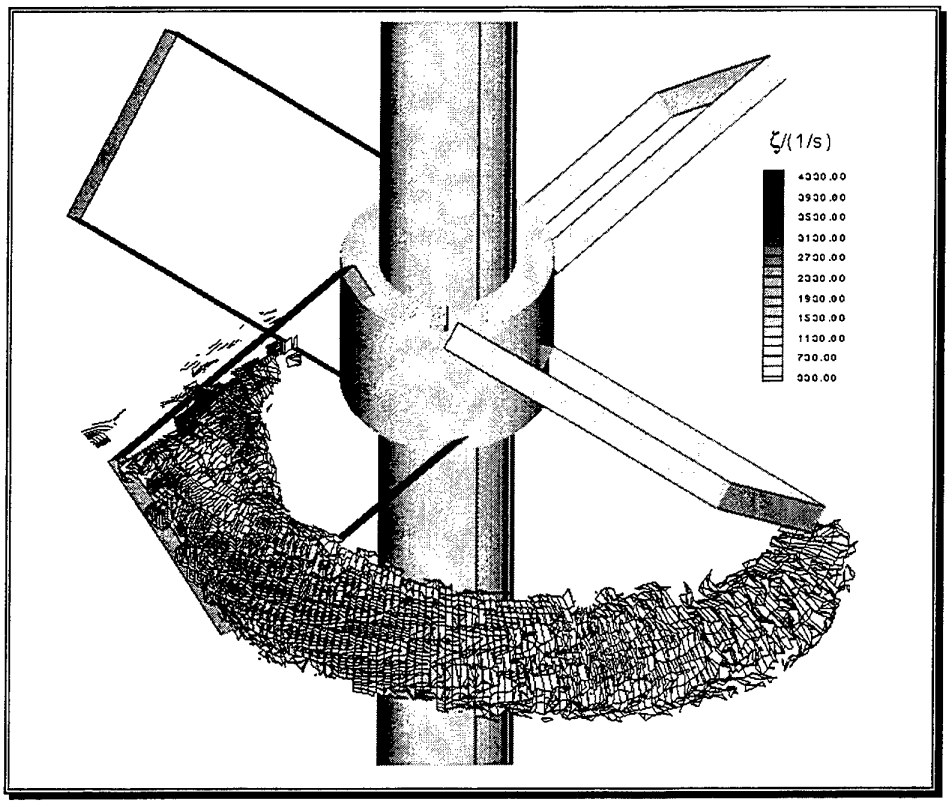


Fig. 8 Contours of Vorticity with $\zeta >= 330$ 1/s

radius becomes more uniform, which means that the difference between the peak value in the core of the vortex and the values at the vortex edges diminishes with distance from the blade.

Comparison with the results of earlier investigations on the flow field produced by pitched blade turbines (e.g. flow visualisation results of Tatterson and co-workers) show good qualitative agreement in the formation and extent of the trailing vortices. However, it is difficult to do quantitative comparisons, since there are a number of differences in the individual experiments, such as different flow configurations (geometry of turbine, vessel, etc.) and different measuring techniques (flow visualisation, ensemble-averaged LDV/angle-resolved LDV).

4 ENERGY DISSIPATION

The distribution of the local energy dissipation rate ε within the stirred vessel is an important key variable for the design of mixing processes, in which gas and/or liquid dispersion, forces on particles or micro-mixing phenomena must be considered. In the past several methods have been used to estimate energy dissipation rates in stirred tank reactors by experimental approaches (see for example Kresta and Wood (1993)). One of the most commonly used expression for ε, which was also used in the present study, is Brodkey's (1975) recommendation based on dimensional analysis:

$$\varepsilon = A\frac{u'^3}{L}, \qquad (3)$$

where u' respresents a characteristic turbulence velocity, L a characteristic length scale of the flow and A is a constant of proportionality. For the characteristic turbulence velocity the square root of measured turbulence kinetic energy k was chosen. The proportionality constant A can be set to 1 in jet flows according to Batchelor (1953). This was also assumed here by approximating the discharge of the impeller as a jet-type flow. For the characteristic length scale several methods have been applied in literature. The most accurate way is to determine the macro scale of turbulence from the autocorrelation coefficient. This method has been employed by Wu and Patterson (1989b) and Lee and Yianneskis (1998) for a Rushton turbine flow and Kresta and Wood (1993) for a pitched blade turbine flow. However, this method could not applied in the present study due to the absence of sufficient data rates provided by the instrument that is required to obtain the energy spectra. Kresta and Wood (1993) reported that the macro scale L is almost constant in the impeller discharge stream of a pitched blade turbine and that L is approximately equal to the width of the trailing vortices which were found to be of diameter D/10. It must be noted that the recent study of Lee and Yianneskis (1998) showed that this may not be valid in the discharge of a Rushton turbine.

In absence of more detailed information on the macro scale a constant length scale within the total vessel volume was assumed in the present study, but since the flow data was so detailed for the complete flow field this length scale could be determined via an energy balance calculation throughout the total volume V_{tot} of the stirred vessel:

$$L = \frac{\sum u_i'^3}{\varepsilon_{tot}}, \text{ with } \sum u_i'^3 = \frac{\sum V_i k_i^{3/2}}{V_{tot}} \qquad (4).$$

The total energy dissipation ε_{tot} was determined via an integral power measurement and introduced into the equation given above. Using this method a length scale of L = 13.2 mm = 0.264 D was calculated, which is exactly the blade height and similar to the diameter of the trailing vortex before detaching from the blade. The fact that the length scale corresponds to the diameter of the trailing vortex is in agreement with the result of Kresta and Wood, but on the other hand the magnitudes differ more than 100% from each other (0.1D compared to 0.26D).

The calculated length scale can be inserted in the above equation for calculating the local energy dissipation in each separate volume element V_i of the entire vessel. This will lead to contours which are similar to those for the turbulence kinetic energy shown in Figures 5 and 7 for the bulk flow and the impeller flow field, respectively. It must be pointed out, that although the used method for estimating the dissipation rate is very rough, it provides an approximate magnitude of local dissipation and together with the detailed flow studies presented in section 3 the regions of highest dissipation rates were resolved.

5 CONCLUDING REMARKS

The results presented here provide the most comprehensive and detailed quantitative data set that is available to date for the flow field produced by a pitched blade turbine. The trailing vortex system generated at each stirrer blade has been characterised in detail and it has been shown that the introduction of the vorticity function is a valuable tool for an accurate description of the extension of trailing vortices. The LDA-measurements confirm the findings of earlier investigations resulting from flow visualisations, but with the presented data it is now possible to give also detailed information on flow quantities within the trailing vortices, such as mean and fluctuating velocities and turbulence kinetic energy.

An estimate of the distribution of local energy dissipation rates was carried out. Although the method is rough it provides valuable information for engineers, since this parameter is essentially required for the lay-out of mixing processes like in gas and liquid dispersions.

For numerical simulations of stirred vessel flows, a data set is now available, that is required for accurate validation and improvements of the turbulence models used in such calculations. The results will therefore significantly support the ongoing developments in the field of computational fluid dynamics and chemical reactor simulation.

ACKNOWLEDGEMENTS

The authors acknowledge financial support provided by the Commission of the European Union under the BRITE EURAM Programme, Contract number BRPR-CT96-0185.

REFERENCES

Ali, A. M., Yuan, H.-H. S., Dickey, D. S. & Tatterson, G. B. 1981, Liquid Dispersion mechanisms in Agitated Tanks: Part I. Pitched Blade Turbine, Chem. Eng. Commun., vol. 10, pp. 205 - 213.

Batchelor, G. K. 1953, The Theory of Homogenous Turbulence, Cambridge University Press, Cambridge.

Brodkey, R. S. 1975, Turbulence in Mixing Operations, Academic Press, New York.

Fournier, M.-C., Falk, L. & Villermaux, J. 1996, A New Parallel Competing Reaction System for Assessing Micromixing Efficiency - Determination of Micromixing Time by a Simple Mxing Model, Chem. Eng. Sci., vol. 51, no. 23, pp. 5187 - 5192.

Günkel, A. & Weber, M. 1975, Flow Phenomena in Stirred Tanks, Part I: The Impeller Stream, AIChE-J., vol. 21, pp. 931 - 949.

Hockey, R. M. & Nouri, J. M. 1996, Turbulent Flow in a Baffled Vessel Stirred by a 60° Pitched Blade Impeller, Chem. Eng. Sci., vol. 51, no. 19 pp. 4405 - 4421.

Lee, K. C. & Yianneskis, M. 1998, Turbulence Properties of the Impeller Stream of a Rushton Turbine, AIChE-J., vol. 44, no. 1, pp. 13 - 24.

Nouri, J. M. & Whitelaw, J. H. 1990, Effect of Size and Confinement on the Flow Characteristics in Stirred Reactors, Proc. Fifth Int. Symposium on Application of Laser Techniques to Fluid Mechanics, Lisbon, Portugal, pp. 23.2.1 - 23.2.8.

Kresta, S. M. & Wood, P. E. 1993, The Flow Field Produced by a Pitched Blade Turbine: Characterisation of the Turbulence and Estimation of the Dissipation Rate, Chem. Eng. Sci., vol. 48, pp. 1761 - 1774.

Ranade, V. V. & Joshi, J. B. 1989, Flow Generated by Pitched Blade turbines I: Measurements Using Laser Doppler Anemometer, Chem. Eng. Commun., vol. 81, pp. 197 - 224.

Schäfer, M., Höfken, M. & Durst, F. 1997, Detailed LDV Measurements for Visualization of the Flow Field within a Stirred-Tank Reactor Equipped with a Rushton Turbine, Trans. I.Chem.E., vol. 75, Part A, pp. 729 - 736.

Stieglmeier, M. & Tropea, C. 1992, Mobile Fiber-Optic Laser Doppler Anemometer, Applied Optics, vol. 31, no. 21, pp. 4096 - 4105.

Stoots, C. M. & Calabrese, R. V. 1995, The Mean Velocity Field Relative to a Rushton Turbine Blade, AIChE J., vol. 41 no. 1, pp. 1 - 11.

Tatterson, G. B. Yuan, H.-H. S. & Brodkey, R. S. 1980, Stereoscopic Visualization of the Flows for Pitched Blade Turbines, Chem. Eng. Sci., vol. 35, pp. 1369 - 1375.

Van't Riet, K. & Smith, J. M. 1975, The Trailing Vortex System Produced by Rushton Turbine Agitators , Chem. Eng. Sci., vol. 30, pp. 1093 - 1105.

Wechsler, K., Breuer, M. & Durst, F. 1998, Steady and Unsteady Computations of Turbulent Flows Induced by a 4/45° Pitched Blade Impeller, submitted for publication.

Wu, H. & Patterson, G. K. 1989a, Laser-Doppler Measurements of Turbulent-Flow Parameters in a Stirred Mixer, Chem. Eng. Sci., vol. 44, no. 10, pp. 2207 - 2221.

Wu, H. & Patterson, G. K. 1989b, Distribution of Turbulence Energy Dissipation Rates in a Rushton Turbine Stirred Mixer, Exp. Fluids, vol. 8, pp. 153 - 160.

Yianneskis, M., Popiolek, Z. & Whitelaw, J. H. 1987, An Experimental Study of the Steady and Unsteady Flow Characteristics of Stirred Reactors, J. Fluid Mech., vol. 175, pp. 537 - 555.

Yianneskis, M. & Whitelaw, J. H. 1993, On the Structure of the Trailing Vortices around Rushton Turbine Blades, Trans. I.Chem.E., vol. 17, Part A, pp. 543 - 550.

MEASUREMENT OF THE MIXING CHARACTERISTICS OF A STIRRED VESSEL WITH A LIQUID CRYSTAL TECHNIQUE

K C LEE

Division of Engineering
King's College London
Strand, London
United Kingdom WC2R 2LS

ABSTRACT

A liquid crystal thermographic technique has been developed to measure mixing time in a vessel of diameter $T = 0.1$ m and liquid height $H = T$ stirred by one and two impellers. The impellers used were six-bladed Rushton turbines of diameter $D = T/3$. The technique makes use of temperature as a passive scalar. Thermochromic liquid crystals were suspended in the fluid as well as in the tracer. A small volume of tracer at a temperature a few degrees above that of the fluid in the vessel was inserted into the vessel. The transient dispersion of the tracer in the vessel was recorded on video tape and the mixing time was determined as it corresponds to the time when temperature becomes uniform across the whole vessel.

The mixing times for four rotational speeds were determined for both the single- and double-Rushton impeller configurations.

The results obtained show that the liquid crystal technique provides a rapid and accurate method of mixing time measurement and thus shows great promise for the characterisation of mixing processes in stirred reactors.

1. INTRODUCTION

During a mixing operation, a number of physical and transport processes can occur simultaneously and the main purpose of agitation is often to enhance such processes. Since turbulent flow conditions greatly increase the speed at which mixing is achieved, in most stirred vessels the aim is to generate a turbulent flow field by means of agitation to accelerate the momentum, mass and/or heat transfer processes.

The flow fields in mixing vessels are in general three-dimensional and can be very complex. Knowledge of the flow and mixing characteristics in a stirred vessel is therefore very useful, and often essential, in order to improve the understanding of the complex flow structures.

In contrast to power consumption and velocity measurement techniques, there is not a universally accepted technique suitable for the accurate determination of mixing time. The most commonly used methods for mixing time measurements make use of conductivity or thermocouple probes to detect the variation of the conductivity or temperature of the fluid in the vessel, respectively. This variation is produced by introducing a small amount of a passive scalar of different conductivity or temperature. However, both techniques can only measure the local concentration or temperature. In order to resolve the complex concentration or temperature distributions encountered in the three-dimensional flows occurring in stirred vessels, it is often necessary to make measurements in a large number of locations. This can be achieved by repeating the measurement in different locations. Nevertheless, such measurements are non-simultaneous, time-consuming and the probes used, however small, will interfere with the flows.

One technique that shows promise for temperature/mixing time measurements in stirred vessels is liquid crystal thermography. This utilises the change in colour of thermochromic liquid crystals when they are subjected to different temperatures. Liquid crystals exhibit a rapid and reversible response to dynamic temperature changes over a wide range of temperatures and they are available in sheet, paint and suspension form.

A number of applications of liquid crystal thermography techniques for the measurement of wall temperature distributions in forced convection flows have been reported, for example by Cooper *et al* (1975), Goldstein and Timmers (1982), Akino *et al* (1986), Rojas *et al* (1987), Yianneskis (1988) and Lee and Yianneskis (1993). Other applications have included the measurement of transient temperature fluctuations on surfaces, for example, Iritani *et al* (1984), and in fluids, Kuriyama *et al* (1981), Rhee *et al* (1984) and Lee and Yianneskis (1994).

The ability to suspend liquid crystal tracers in a stirred vessel can allow temperature measurements to be obtained simultaneously across the whole vessel. This renders liquid crystal thermography a very convenient and versatile technique for the measurement of mixing time in stirred tanks, using temperature as a passive scalar.

2. THERMOCHROMIC LIQUID CRYSTALS

Liquid crystals are organic materials which exhibit a phase between the boundaries of the solid phase and the conventional, isotropic liquid phase. This is termed a

mesomorphic phase, (or mesophase). There are three main types of liquid crystals: smectic, nematic and chiral nematic (cholesteric).

Thermochromic crystals used in liquid crystal thermography are mixtures of chiral nematic crystals. In the chiral nematic phase, the molecules are arranged in thin layers. Within each plane layer the molecules are aligned with their long axes parallel and have an average direction defined by a unit vector $\hat{r}$. Each layer is slightly twisted with respect to the next. The effect is cumulative and an overall helical structure is formed. The average molecular direction of each layer, $\hat{r}$, traces out a helix in space. The pitch length, P, defined as the longitudinal distance in which the direction vector, $\hat{r}$, undergoes a complete 360° revolution, is used to quantify the degree of twist. Changes in temperature affect the rotation angle between adjacent layers and hence the pitch of the helix. The mean angle between successive layers, $\bar{\theta}$, is given by (Chandrasekhar, 1992):

$$\bar{\theta} = \frac{A K_B t}{2 I \omega_o^4} \tag{1}$$

where A is the coefficient of the cubic anharmonicity term, K_B is the Boltzman constant, t is the temperature, I is the moment of inertia of the molecules and ω_o is the angular frequency. The pitch, $P \propto 1/\bar{\theta}$, decreases slightly with temperature and the characteristic wavelength at which a particular chiral nematic crystal scatters light, λ_o, is given by:

$$\lambda_o = \bar{\mu} P \tag{2}$$

where $\bar{\mu}$ is the mean refractive index. As liquid crystals do not change colour abruptly at a single temperature, but sweep through the spectral range from red to blue over a range of temperatures, the interpretation of liquid crystal images is complicated and may be made more complex by often imperfect colour response of the crystals. In order to extract the temperature information from the liquid crystal colour displays, it is necessary to calibrate the liquid crystals at the outset of an experiment so as to ascribe particular colours to temperatures over the response range of the liquid crystals. In the present work, a digital image processing system was used to carry out this task. The image processing system and the methodology of measuring colour as so to ascribe particular colours to temperatures are described in the following sections.

3. THE IMAGE PROCESSING SYSTEM

The digital image processing system used in this work to record and interpret the video images of the liquid crystal colour displays comprised a CCD colour video camera with PAL colour standard composite video signal output; a S-VHS PAL video cassette recorder with still frame facility; a *RGB* monitor; a computer; and a video frame grabber/digitiser card and associated software.

Liquid crystal colour displays were captured by the camera. The aperture of the video camera lens was kept fully open, the shutter speed used was 1/50 s and the image collecting angle was 90°±2° to the plane of illumination. The composite video signal output of the camera was input to the video cassette recorder. The signals received by the video recorder were observed on the monitor to assess the quality of the images. When satisfactory conditions were attained, the events were recorded onto video tapes at a rate of 25 frames per second.

The recorded events were then played back in a 'frame-by-frame' mode, so that the timing of the frame to be analysed could be ascertained relative to a reference frame/start of the event investigated. The composite video signal of a frame is input to the computer via the frame grabber/digitiser card. The frame grabber decodes the composite video signal and grabs the frame as a *RGB* true colour image.

The grabbed image was digitised into a 24-bit digital image composing of three planes of pixels where each pixel has a red, green and blue intensity, each coded on a 8-bit format (i.e. 256 levels). The digitised image is then stored on disk for off-line colour measurement.

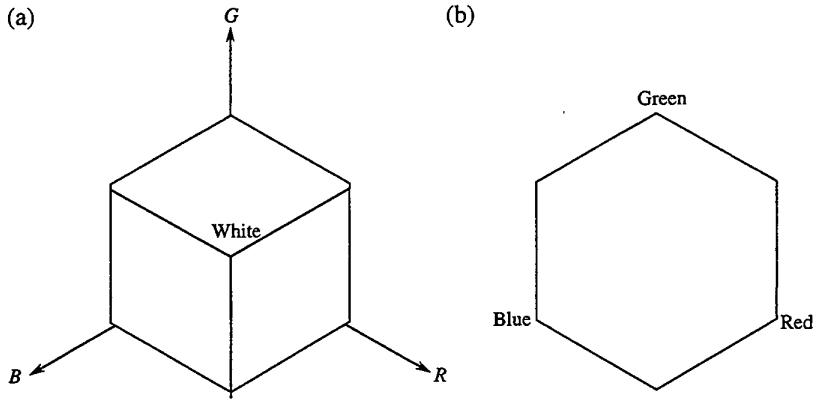


Figure 1. (a) The *RGB* colour cube and (b) when viewed along the diagonal from white to black.

4. COLOUR MEASUREMENT

Though wavelength is a physical quantity, which can be objectively measured with great accuracy, colours perceived by individuals depend on all kinds of properties of the human visual system. The determination of colours by humans is therefore very complex as it involves a subjective physiological process (Bloomer, 1990).

In order to evaluate colours quantitatively, various schemes of specifying colour have been proposed and adopted. Since the present work utilised a digital image processing system, the *HSV* (hue, saturation and value) model was used for the measurement of the colour displayed by the crystals.

The three-dimensional representation of the *HSV* model is derived from the *RGB* cube shown in Figure 1(a). By viewing the cube along the diagonal from the white vertex to the origin (black), an outline of the cube that has the hexagon shape can be seen as shown in Figure 1(b). The boundary of the hexagon represents the various hues and it is used as the top of the *HSV* hexcone shown in Figure 2. Hue is represented as an angle about the vertical axis, ranging from 0° at red through 360°. Saturation S varies from 0 to 1. It is represented in this model as the ratio of the purity of a selected hue to its maximum purity at $S = 1$. Value V varies from 0 (black) at the apex of the hexcone to 1 (white) at the top. In the present work, 8-bit integers (i.e. 0-255) were used to represent both hue and saturation measured.

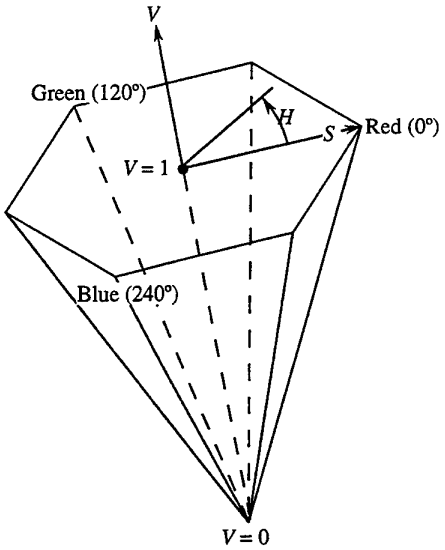


Figure 2. The *HSV* hexcone.

5. FLOW CONFIGURATION

The mixing vessel used in this investigation is shown schematically in Figure 3. It comprised a fully-baffled cylindrical vessel of internal diameter $T = 0.1$ m. Four equi-spaced baffles of width $B = T/10$ were fitted along the internal surface of the vessel. The vessel was installed inside a trough

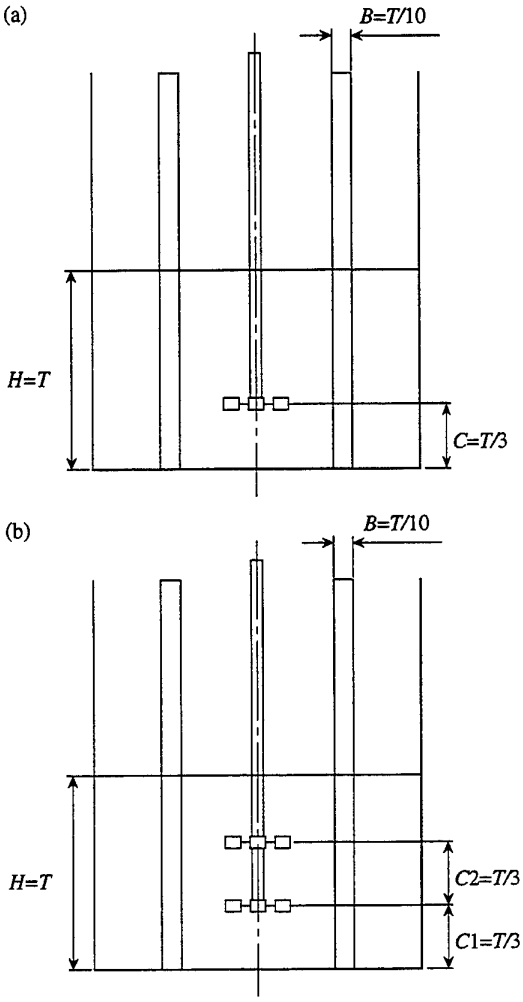


Figure 3. Schematic diagrams of the (a) Single-Rushton impeller; and (b) double-impeller systems.

of square cross-section. The gap between the vessel and the Perspex trough was filled with distilled water fed from a constant temperature water bath to dissipate the heat generated by the light source and to control the temperature of the fluid inside the vessel as well as to minimise refraction effects at the cylindrical surface of the vessel.

The working fluid inside the vessel was distilled water and a liquid column height $H = T$ was used. Thermochromic liquid crystals encapsulated as gelatine-shell microspheres of 20 μm mean diameter were suspended in the working fluid. The impellers used were six-bladed Rushton turbines of diameter $D = T/3$. A clearance $C=T/3$ was used between the bottom of the vessel and the impeller disk central plane for the single-impeller configuration. A Clearance $C1=T/3$ between the bottom of the vessel and the central plane of the lower impeller disk, and a separation $C2=T/3$ between the central planes of the two impeller disks were used for the double-impeller configuration. A lid was used to eliminate the

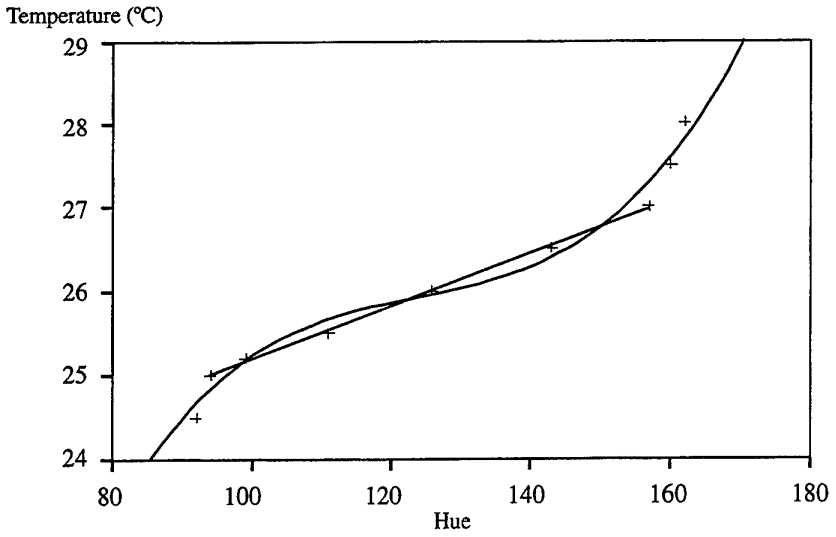


Figure 4. A typical temperature-hue calibration curve.

formation of a vortex in the free surface. Experiments were conducted at four impeller speeds of 9, 18, 27 and 36 rev·s^{-1}, corresponding to impeller Reynolds numbers, *Re* of 10000, 20000, 30000 and 40000, respectively.

The liquid crystals used in the present work displayed colours between 24°C and 29°C. Light-sheet illumination of the flow field in the vessel was provided by a 1 kW mercury lamp. A 5 cm^3 tracer of liquid crystals suspended in distilled water and, having the same crystal concentration as the fluid in the vessel was contained in a syringe-hypodermic needle assembly. The insertion of the tracer was made at $r/T = 0.25$ and $z/T = 1.0$ by means of applying a dead weight to the syringe-hypodermic needle assembly. The insertion time was kept constant at 0.4 s throughout the experiments.

6. EXPERIMENTAL PROCEDURE

At the outset of the experiments calibration of the liquid crystals was carried out so as to ascribe particular colours to temperatures, since the colour displayed by the liquid crystals depends on the lighting conditions as well as on the image collection angle. The lighting condition was optimised so that the hue of any pixel was within ±5 of the mean value of hue at any particular temperature.

To calibrate the variation of hue with temperature, the $\theta = 0°$ plane (located halfway between two baffles) was illuminated. The constant temperature water bath which fed water into the trough of the test section was set at the desired temperature. When steady state was reached in the vessel, the temperature inside the vessel was measured by a fine-wire thermocouple, and the thermal field was recorded. This process was repeated to cover the response range of the liquid crystals. The recording was then analysed using the image processing system described above to obtain the calibration curves such as that shown in Figure 4.

It can be observed from Figure 4 that, within the temperature range of 25°C to 27.5°C, small changes in temperature can be registered with a unique value of hue and inside this range the value of hue varies approximately linearly with temperature. Experiments were therefore only conducted within this temperature range.

The temperature of the working fluid inside the vessel was kept constant at 25.2°C and the temperature of the tracer was 27°C. The transient process of the mixing of the inserted tracer in the vessel was recorded onto video tape. The tracer insertion was performed after the video recording had commenced so that the beginning of the insertion could be accurately determined. A 'frame-by-frame' analysis was subsequently performed on the video recording of each of the experiments to determine the time between the frame at which the insertion of the tracer commenced and the frame at which the process was fully-mixed.

As the scattered light in the vicinity of the impeller shaft and near the vessel wall strongly affect the colour measurements, analysis of the hue of the images was not carried out in these regions. Furthermore, since imperfections in the liquid crystals used were inevitable, a process was considered to be fully-mixed when 95% of the analysed pixels in each image had the same value of hue.

7. RESULTS AND DISCUSSION

Characteristic hue contours of the images obtained with the single-Rushton configuration with an impeller Reynolds number of 20000 are shown in Figures 5(a)-(c).

The hue contour map of the image obtained 200 ms after the start of the insertion of the tracer is shown in Figure 5(a). The jet of the tracer, which was at a higher temperature than the fluid in the vessel, is indicated by the region of hue values between 120 and 150.

Figure 5(b) shows the hue contour map of the image obtained 360 ms after the start of the insertion of the tracer.

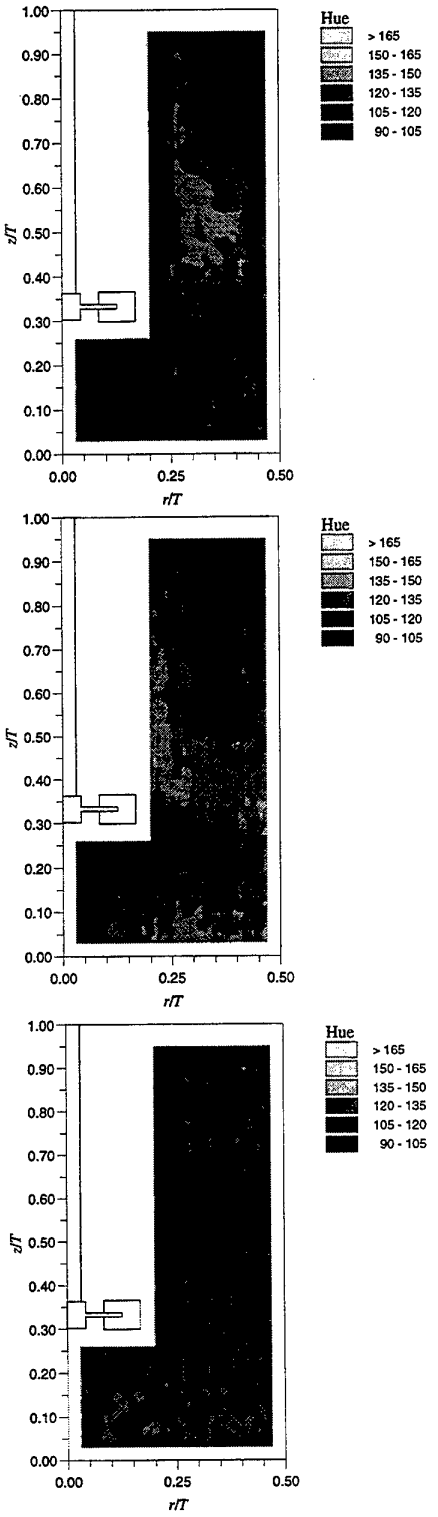


Figure 5. Hue contours of half of the flow field stirred by a single Rushton impeller at *Re*=20000 at (a) 200 ms; (b) 360 ms and (c) 1 s after the tracer insertion.

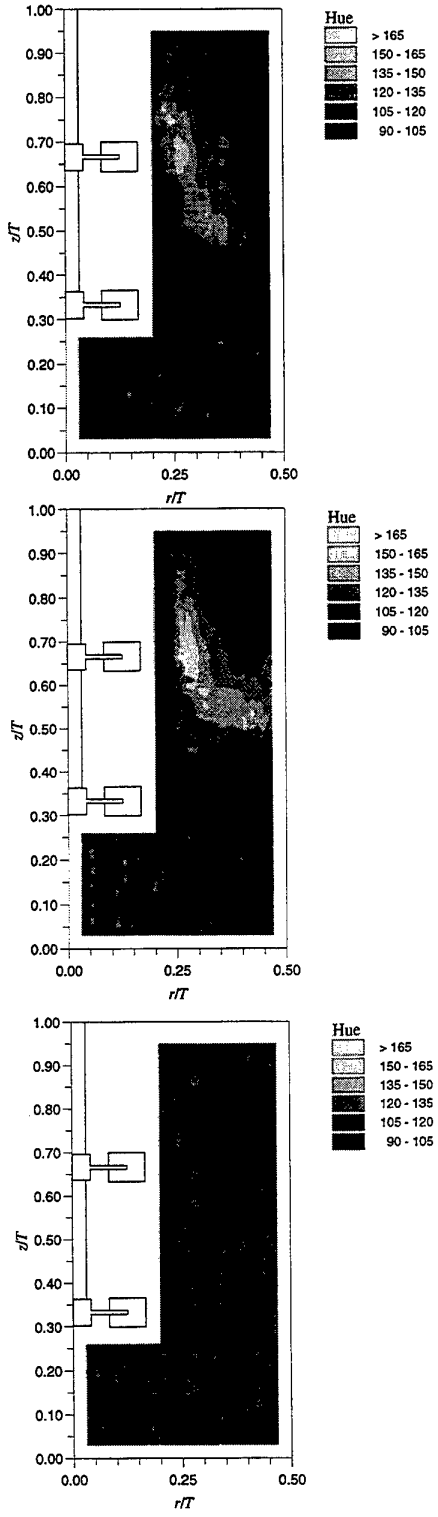
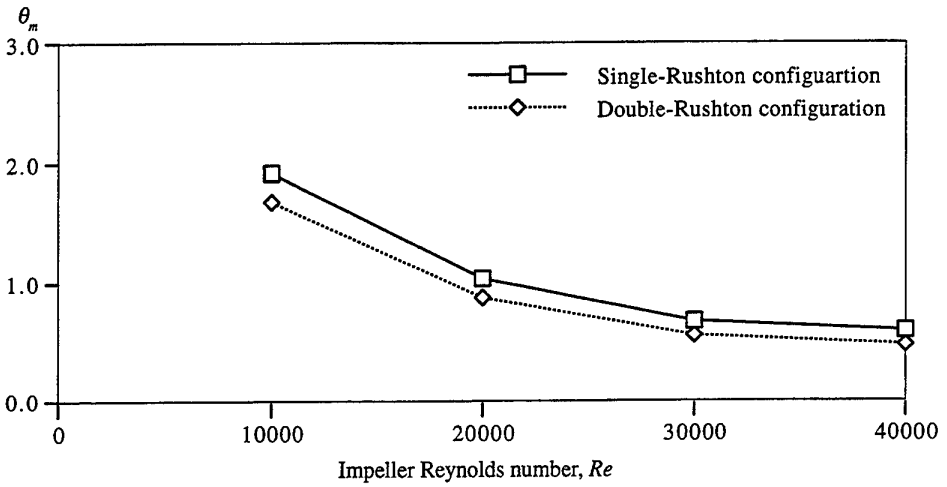


Figure 6. Hue contours of half of the flow field stirred by two Rushton impeller at *Re*=20000 at (a) 200 ms; (b) 360 ms and (c) 880 ms after the tracer insertion.

(a)



(b)

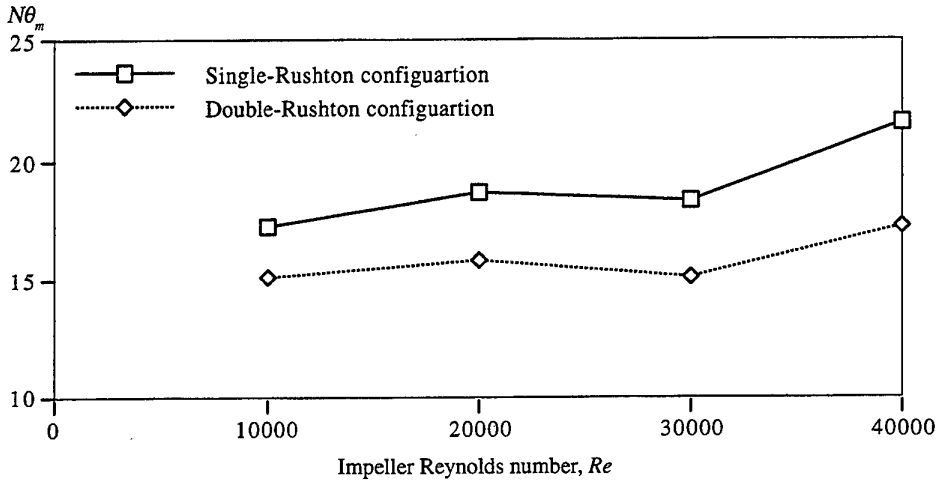


Figure 7. the variation of (a) θ_m and (b) $N\theta_m$ with impeller Reynolds number.

The region of hue values higher than 120 again indicate the jet of the tracer, which has moved further towards the vessel wall under the influence of the impeller stream and has reached the bottom of the vessel. As in Figure 5(a), locally high hue values (above 135) can be observed in the core of the tracer jet.

At 1 s after the start of the insertion of the tracer (Figure 5(c)), the hue values in most regions are between 105 and 120, indicating that the fluid inside the vessel is nearly fully-mixed.

Images obtained from the recordings made with other impeller speeds showed similar mixing behaviour to that described above. Hue analysis was performed on the images obtained with all impeller speeds investigated to determine the mixing times. The mixing times found were 1.92 s, 1.04 s, 0.68 s and 0.60 s for impeller speeds of 9, 18, 27 and 36 rev·s^{-1}, respectively.

Hue contours of the images obtained at 200 ms, 360 ms and 880 ms after the start of the insertion of the tracer for the double-Rushton configuration at an impeller Reynolds number of 20000 are shown in Figures 6(a)-(c), respectively.

The trends indicated by the double-Rushton impeller results exhibit many similarities with the single-impeller ones: 200 ms after the start of the insertion of the tracer (Fig 6(a)) the core of the tracer jet has penetrated half-way down the vessel. Subsequently the tracer is entrained into the 'merging' flow pattern (Mahmoudi, 1994) and is re-directed towards the vessel wall (Figure 6(b)). By 880 ms after the start of the tracer insertion, Figure 6(c), the near-uniform hue distribution across the vessel indicates that mixing is nearly complete.

Hue analysis of the images obtained with the double-Rushton configuration for all the impeller speeds investigated were performed to determine the mixing times. The average mixing times found were 1.68 s, 0.88 s, 0.56 s and 0.48 s for impeller speeds of 9, 18, 27 and 36 rev·s^{-1}, respectively.

Since the number of revolutions required to achieve fully mixing in an agitated tank is essentially a constant for a particular geometry (Tatterson, 1991), N and θ_m can be related by :

$$N\theta_m = \mathrm{K} \qquad (3)$$

where N is the impeller speed in rev·s^{-1}, θ_m is the mixing time in seconds, and K is a constant. The variation of θ_m and the values and of $N\theta_m$ with impeller Reynolds number is shown in Figure 7.

It can be seen from Figure 7 that the values of $N\theta_m$ for both the single-and double-impeller configurations are approximately constant up to an impeller Reynolds number of 30000. At the higher Re (40000), the values of $N\theta_m$ for both configurations are higher. These higher values can be partly attributed the comparatively long tracer insertion time. The insertion time was 0.40 s in all cases, corresponding to nearly 67% and 83% of the mixing times at 36 rev·s^{-1} for the single- and double-impeller configurations, respectively. Clearly, shorter insertion times cannot be achieved in practice and most studies to-date have employed pulse injections of tracer lasting around 0.5 – 1.0 s (for example, Armstrong and Ruszkowski, (1988) and Mahmoudi (1994)). Although this represents a limitation of mixing times studies carried out in small vessels and with high impeller speeds to achieve dynamic similarity, the average $N\theta_m$ values are not strongly affected. For example, the average values of $N\theta_m$ determined from the experiments at all four impeller Reynolds numbers are 18.99 and 15.84 for the single- and double-impeller configurations respectively. The corresponding average values for the three lower impeller Reynolds number are 17.97 and 15.36 respectively, i.e. they are smaller by only 5.4% and 3.1%, respectively.

The average $N\theta_m$ values obtained were compared with those reported in the literature. It was found that the values obtained for both the single- and double-Rushton configurations in the present work are generally lower.

There are four likely reasons for the differences between the $N\theta_m$ values determined in this work and those reported in the literature. First, the wide variation in $N\theta_m$ values obtained with the different published correlations (24.4, 34, 36 and 38.34) may be due to differences in experimental procedure and/or the definition of when the 'fully-mixed' state is achieved (e.g. 90% or 95% of the final concentration of tracer). Second, tracer insertion times have not been reported in some of the aforementioned studies, but they may affect the $N\theta_m$ value determined. Evidence for this is provided in the work of Mahmoudi (1994) who employed a single Rushton impeller in a 0.294 m diameter vessel which was otherwise identical to the 0.1 m vessel used in the present study. He reported an average mixing time of 12.8 s with an insertion time of 6.5 s. The corresponding $N\theta_m$ values are around 45 – 50 compared with the values of up to 38 reported by other investigators. Mahmoudi's results indicate, as might be expected, that comparatively longer insertion times will result in larger $N\theta_m$ values. This is in agreement with the findings at Re = 40000 compared with those at lower Re's in the present work.

A third, and more likely, reason might be the vessel size. Kramers *et al* (1953) reported that mixing times are affected by scale: a larger tank required a larger number of revolutions (i.e. a higher value of $N\theta_m$) to achieve the same degree of mixing. Fourth, impeller blade width and thickness could also affect $N\theta_m$. It has been established (Rutherford *et al*, 1996) that smaller blade thicknesses result in higher flow numbers and this might be expected to affect mixing times as well. There is also a substantial effect of blade width on mixing times (Tatterson, 1991), but as relevant values are not quoted by many investigators, it is difficult to ascertain how large this effect is.

Although θ_m values in the transition regime are different (Norwood and Metzner, 1960) the flows in all Re's studied in this work are expected to be fully-turbulent: this is indicated by the similarity of the $N\theta_m$ values determined.

8. CONCLUDING REMARKS

The work presented above has shown that the liquid crystal thermographic technique developed can be used to characterise the transient mixing state in a stirred vessel with considerable accuracy and in greater detail than it has been possible hereto. Although hue values were used to describe the mixing process here, the corresponding temperature values can be readily obtained and consequently temperature measurements can also be made.

Mixing times obtained with the double impeller configuration were on average 20% lower than with the single Rushton turbine. However, in practice this more rapid mixing must be assessed against the higher power draw of the two-impeller system (Mahmoudi, 1994).

The work has also shown that more detailed studies of mixing are required, with an aim to formulate more accurate prediction of $N\theta_m$ by taking better account the effects of impeller and vessel geometry. The rapid acquisition of data across the vessel which is possible with the present technique should prove very useful for such studies.

REFERENCES

Akino, N., Kunugi, T., Ichimiya, K., Mitsushiro, K. and Ueda, M., 1986. Improved liquid-crystal thermometry excluding human colour sensation: Part 2. Application to the determination of wall temperature distributions, in Pressure and Temperature Measurements, ed. Kim, J. H. and Moffat, R. J., pp. 63-68, ASME Fluids Eng. Div., vol. 44, and Heat Transfer Div., vol. 58.

Armstrong, S.G. and Ruszkowski, S., 1988, The flow field in the discharge stream of disk turbines, Proc 6th Eur Conf on Mixing, Pavia, Italy, pp. 1-6.

Bloomer, C.M., 1990. Principles of Visual Perception, Herbert Press, London.

Chandrasekhar, S, 1992. Liquid Crystals, 2nd Ed, Cambridge University Press.

Cooper, T.E., Woolf, R.J. and Meyer, J.F., 1975. Liquid crystal thermography and its application to the study of convective heat transfer. Transactions of the ASME, Journal of Heat Transfer, pp. 442-450.

Goldstein, R.J. and Timmers, J.F., 1982. Visualization of heat transfer from arrays of impinging jets, Int. J. Heat Mass Transfer, vol. 25, No. 12, pp. 1857-1868.

Iritani, Y., Kasagi, N. and Hirata, M., 1984. Heat transfer mechanism and associated turbulence structure in a near-wall region of a turbulent boundary layer. In Turbulent Shear Flows 4, ed. Bradbury, L.J.S., Durst, F., Launder, B.E., Schmidt, F.W. and Whitelaw, J.H., pp. 223-234. Springer-Verlag, Berlin.

Kramers, H., Baars, G.M. and Knoll, W.H., 1953, A comparative study on the rate of mixing in stirred tanks, *Chem Eng Sci*, **2**: pp. 35-42.

Kuriyama, M., Ohta, M., Yanagawa, K., Arai, K. and Saito, S., 1981. Heat transfer and temperature distributions in an agitated tank equipped with helical ribbon impeller, J. Chem. Eng. Japan., vol. 14, pp 323-330.

Lee, K.C. and Yianneskis, M., 1993. An image processing technique for the analysis of thermotic distributions utilising liquid crystals. Chapter 16 in Imaging in Transport Processes, ed. Sideman, S. and Hijikata, K. Begell House Inc. Publishers, New York.

Lee, K.C. and Yianneskis, M., 1994. Temperature measurements in stirred vessels with liquid crystal tracers. Engineering Systems Design and Analysis, ASME, PD - Volume 64, Part 5, 1994, pp. 487-494.

Mahmoudi, S.M.S., 1994. Velocity and Mixing Characteristics of Stirred Vessels with Two Rushton Impellers, PhD Thesis, King's College London, University of London.

Norwood, K.W. and Metzner, A.B., 1960, Flow patterns and mixing rates in agitated vessels, AIChE J, **6**(3): pp. 432-437.

Rhee, H.S., Koseff, J.R. and Street, R.L., 1984. Flow visualization of a recirculating flow by rheoscopic liquid and liquid crystal techniques. Exp. Fluids, vol. 2, pp. 57-64.

Rojas, J, Whitelaw, J.H. and Yianneskis, M., 1987. Forced convective heat transfer in curved diffusers. Transactions of ASME, Journal of Heat Transfer, vol. 109, pp. 866-871.

Rutherford, K., Mahmoudi, S.M.S., Lee, K.C., and Yianneskis, M., 1996, The effect of Rushton impeller blade and disk thickness on the mixing characteristics of stirred vessels. Transactions of the Institution of Chemical Engineers, Chemical Engineering Research and Design, Vol. 74, Part A, pp. 369-378.

Tatterson, G.B., 1991. Fluid Mixing and Gas Disperson in Agitated Tanks, McGraw Hill.

Yianneskis, M., 1988. Investigation of convective heat transfer in a ventilated chamber by liquid crystal thermography. Proc. 2nd UK National Heat Transfer Conference, Glasgow, 14-16 September, pp. 725-734.

LASER PULSED HOLOGRAPHY APPLIED TO THE THREE-DIMENSIONAL TWO-PHASE FLOW IN AERATED STIRRED VESSELS

O. Feldmann and F. Mayinger

Lehrstuhl A für Thermodynamik, Technische Universität München
Boltzmannstr. 15, 85748 Garching, Germany
Fax: ++49 89 289 16218, E-mail: feldmann@thermo-a.mw.tu-muenchen.de

ABSTRACT

The present paper deals with the application of the short-time holography to the three-dimensional two-phase flow in aerated stirred vessels. Two holograms of the volume of interest, the entire agitator-vessel, were taken simultaneously from two viewing directions, perpendicular to one another. Both, the information about the flow field of the generated bubbles, and about the number, the size, the location, and the velocities of the generated bubbles were recorded. The developed holograms are reconstructed and stationary images, the real images of the recorded flow-field, were formed three-dimensionally. These two three-dimensional reconstructions of the flow field, seen from different viewing-directions were scanned by means of two CCD-cameras. Computer based algorithms were developed in order to determine the quantities to be measured that are stored in the obtained video-images. By means of a stereo-matching module, both views were correlated and the position and the three-dimensional velocity-vector of each bubble were determined.

1. INTRODUCTION

An optimum design of an aerated, stirred vessel depends on the requirements in terms of parameters like generated phase interface, period of dwell of the gaseous phase, hold-up, and other quantities that may be linked. It is achieved by the correct choice of type of stirrer, rotational speed, and type and location of the gas injector. Therefore, a detailed knowledge of the number and the size of the generated bubbles and the velocity fields of both phases as a function of the different operating points is required.

In order to determine the phase interface, the information about both, the bubble size distribution, the hold-up, and the shape of the generated bubbles has to be derived from the experiments. Therefore, only unobtrousive measuring techniques can be applied. Several attempts to optically determine the dispersion characteristics in two-phase flow systems are reported in the literature.

The Phase-Doppler-Velocimetry (PDV) is a widespread measuring technique that is applied to punctually determine the velocity and the size of the particles in a dispersed flow (Durst et a. (1990), Tassin and Nikitopoulos (1995)). When applying this measuring technique to determine bubble sizes in aerated stirred vessels, the bubbles have to be spherical and their surface should not be oscillating. Otherwise the determination of the bubble size is coherent with high uncertainties.The optical analysis of the dispersion characteristics is focussed on Particle Image Velocimetry (PIV) and Particle Tracking Velocimetry (PTV) techniques (Adrian and Liu (1993), v. d. Geld et a. (1995), Merzkirch et a. (1995)). When applying these two-dimensional measuring techniques, in general a laser-light-sheet is used to illuminate a layer of the flow field which is then recorded. Only the velocity-component of the bubbles in this layer can be recorded. In order to measure the 'off-plane'-component of the bubble velocity, the light sheet has to be moved rapidly through the measuring volume, as it was reported by Brücker (1995).

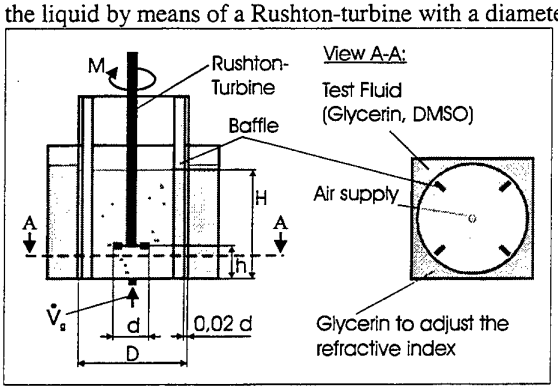
In this study, the entire agitator-vessel has been recorded unobtrusively and three-dimensionally by applying the short-time holography (Gebhard and Mayinger (1995), Mayinger (1994)) in order to provide a broad data base for the prediction of the hold-up and the phase-interface. When applying this measuring

technique, the entire agitator-vessel is recorded three-dimensionally, including every spatial and perspective effect, and the entire recorded volume is reconstructed three-dimensionally. Due to the extremely short exposure of only t = 30ns the flow field can be regarded as being 'frozen' in time, and after its reconstruction it is placed at disposal to be evaluated without any time-restriction. The velocity field of the bubbles is determined three-dimensionally by illuminating the holographic plates twice within an - adjustable - time interval of a few micro- to milliseconds.

The dispersion characteristics of a fully baffled, aerated stirred vessel agitated by a Rushton-turbine were analysed. These operating points were adjusted by varying the liquid viscosity and the agitator speed.

2. EXPERIMENTAL SETUP

The test section which has been applied to this study - shown in Fig.1 - consists of a cylindrical vessel with an inner diameter of T_i = 124 mm. In order to provide an optical access to the vessel, the vessel is made of glass and located in a rectangular glass vessel. The volume between the two vessels is filled with Glycerine, which has the same refractive index as the glass vessels. Since the test fluid has the same refractive index, the laser beams can cross the test section without being diffracted at the cylindrical surface of the agitator vessel. The vessel is equipped with four glass baffles, according to the German norm (DIN 28131) as far as their size and location is concerned. The air is supplied from a nozzle with a diameter of d_N = 0.5mm which is mounted in the centre of the flat bottom of the vessel (s. Fig.1). The air is dispersed in the liquid by means of a Rushton-turbine with a diameter of d = 40mm.



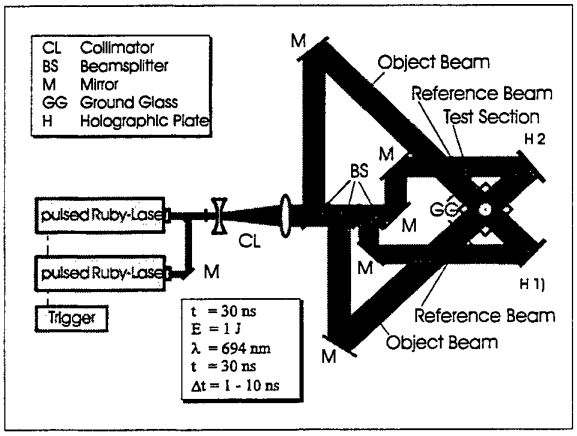
The test fluid consists of a mixture of Glycerine and Dimethylsulfoxide (DMSO). These two liquids have similar densities, they can be dissolved in one another at any ratio, and they have the same refractive index as the used glass. By varying the mixture ratio the viscosity of the test fluid can be adjusted in the range of η = 2mPas (pure DMSO) and η = 1.4Pas (pure Glycerine).

3. THE SHORT-TIME HOLOGRAPHY

The short-time holography, applied in this work, is a highly suitable non-invasive measuring technique to analyse transport phenomena, such as the heat and mass transfer, in dispersed transparent flows. When applying this measuring technique, the complete light information scattered by or reflected on an object, namely both, the amplitude and the phase distribution is recorded. Due to the short exposure time, even fast-moving particles can be imaged sharply. The entire optical information about the flow field in the test section is stored three-dimensionally on the holographic plates. The situation in the vessel can be regarded as being 'frozen' in time. It is reconstructed in form of a stationary three-dimensional image by illuminating the holographic plates with a continuous HeNe laser-beam. The reconstructed images can then be evaluated with no restriction to the time. When applying this measuring technique, particles with a diameter greater than ten times the wavelength of the laser light are imaged sharply. The principal features of this measuring technique are explained in a more detailed way in the literature (Chàvez and Mayinger (1992), Gebhard and Mayinger (1995) , Kiemle and Röss (1969), Mayinger (1994).

3.1 Recording of the holograms

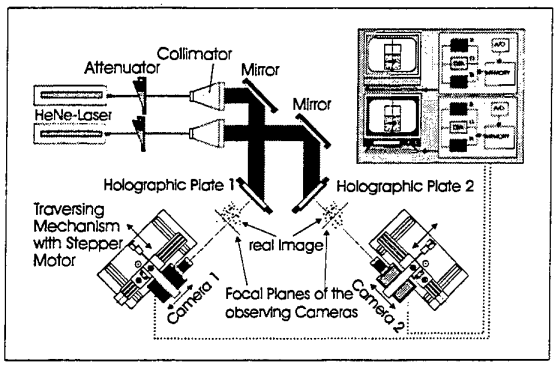
The stereoscopic optical set-up for recording two holograms simultaneously on which the situation inside the vessel is stored three-dimensionally from two different viewing directions is schematically shown in Fig.2. A pulsed ruby-laser that generates light pulses with a wavelength of $\lambda = 694$nm and an energy of E = 1Joule for the exposure time of t = 30ns has been applied as the light source. The emitted laser beam is collimated by passing two lenses (CL) and is then split into two object beams and two reference beams in the bank of beam-splitters (BS). The object beams are diverted at the mirrors (M) in such way that they cross the test section perpendicularly to one another after they have been converted into diffuse light at a plate made of ground glass (GG). Exiting the test section, the object beams fall perpendicularly onto the holographic plates (H1, H2). Contrary to that, the reference beams are diverted directly to the holographic plates (s. Fig.2). The superposition of an object beam and a reference beam results in an interference figure that contains the entire optical information of the test-section. This image is stored without being distorted on the holographic plates.



The ruby-laser can be operated either in a single-pulse or in a double-pulse mode. In a single pulse mode, the resulting holograms contain the information about both, the flow field of the bubbles, and about the number, the size and the location of the generated bubbles. In addition to that, the information of the bubbles' velocities and trajectories is obtained by operating the laser in a double-pulse mode. In this case, two successive holograms of the flow field in the vessel are recorded on each holographic plate. With the knowledge of the pulse-separation and the evaluated holographic reconstructions, the velocity field of the bubbles is determined. The pulse separation of one laser can be varied from $\Delta t = 1\mu s$ to $\Delta t = 800\mu s$. In order to provide an enlargement of the pulse-separation, a second ruby laser is coupled in the beam-path of the first laser. The second laser is fired any time after the first laser. The pulse-separation is adjusted and controlled by a trigger (s. Fig.2).

3.2 Reconstruction of the holograms

The developed holograms are reconstructed by illuminating the holographic plate with a continuous HeNe laser-beam with a wavelength of $\lambda = 632$nm. The continuous laser-beam simulates the reference beam during the exposure of the hologram with respect to its geometry and to its angle of incidence. The HeNe laser-beam is diffracted at the interference figure that is stored on the coating of the holographic plate. As a result of this diffraction, the object beam which contains the entire optical information of the test section is obtained. A stationary image, the real image of the recorded scene, is formed three-dimensionally and without being distorted in front of the holographic plate, without any time-restriction, as it is shown in Fig.3.

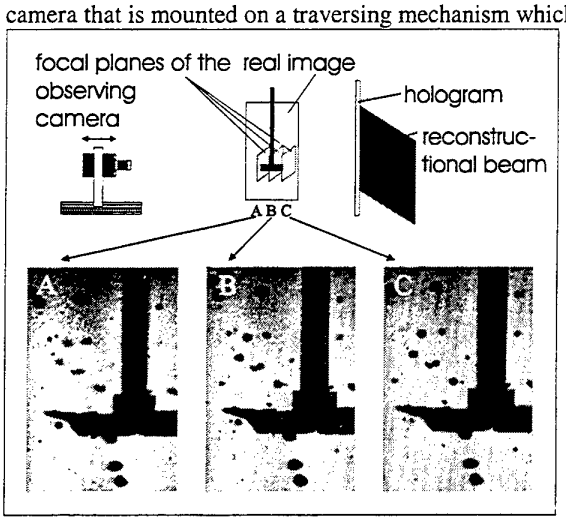


After a hologram had been recorded and reconstructed, the spatial information of the entire measuring volume is three-dimensionally placed at disposal, having a diameter of approximately d = 130mm and an infinite depth of focus. This 3-D image is scanned by means of a Newicon CCD-camera which is equipped with an objective of long focal length. Therefore, only a small fraction of the entire holographic reconstruction is imaged on each video-image. The obtained video-images are then transmitted to a digitizer and stored in the digitizer frame memory in form of an array of 512 x 512 pixels of 8 bits depth.

The camera is equipped with an objective with a small focal range, so that only a small fraction of the entire reconstruction is in focus. This is compensated by recording series of images with a translation of the camera after every acquiring process. The holographic reconstruction is mapped. By moving the camera stepwise along its depth coordinate, the entire 3-D information contained in the holographic reconstruction is scanned. It can be derived from the images in Fig.4 how the bubbles that are depicted sharply in one image move out of focus while the camera's position is changed and vice versa.

The depth coordinate of a bubble is determined from the position of the camera, but only within the accuracy of the focal range. Since the two holograms of one operating point were recorded in a stereoscopic optical set-up, the depth position of a bubble in one view is its lateral position in the second view. The depth of field is adjusted in such way, that this correlation is definite. With a depth of focus of e.g. 5 mm, the field of view of the camera is 40 x 40mm^2.

The test section then is divided into several subvolumes with the dimension of 40 x 40 x 5mm^3 which correspond to the field of view and the depth of field of the observing camera. In this manner, the 3-D holographic reconstructions are transformed into series of 2-D digital video-images (s. Fig.4). The camera that is mounted on a traversing mechanism which is controlled by a personal computer.



Both holograms of one experiment are reconstructed and scanned as described above. They represent two 3-D images corresponding to one 'frozen' scene of the test section, so that the entire 3-D information of the test section from two different views is placed at disposal in form of digital video-images to be evaluated by the image processing system.

4. DIGITAL IMAGE PROCESSING

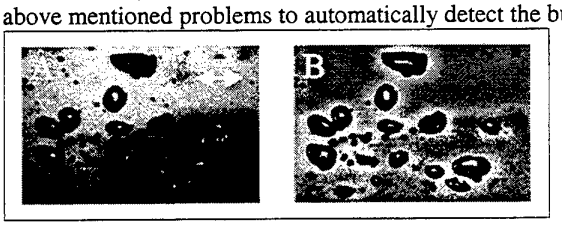
The video-images obtained from the holographic reconstructions show distinctive properties. Especially if they were recorded with a small depth of focus of the observing camera, only a small fraction of the bubbles - visible in such an image - is depicted sharply. The edges of these bubbles can be blurred by unsharply depicted bubbles that are reconstructed out of focus of the observing camera. In addition to that, the grey value of the background varies significantly due to the Gaussian intensity-profile of the laser-beam and due to defects that are inherent in the optical parts, such as the unevenness of the mirrors. Due to these peculiarities of the video-images, commercially available image processing systems could not be applied to evaluate the images. Therefore, the evaluation software be developed at the 'Lehrstuhl A für Thermodynamik'. It is based on algorithms introduced by Chàvez and Mayinger (1992) and Gebhard (1996). Implemented in this software package are tools

- to filter noisy images to remove speckles,
- to detect sharply depicted bubbles,
- to create binary images,
- to measure the size and the position of identified bubbles, and
- to determine the velocity of the bubbles.

The objective of the image processing is to obtain an image with exclusively the sharply depicted bubbles clearly separated from the background. The information about the shape, the size, and the location of the bubbles is then derived from these images. The algorithms that were developed and applied to the images are explained in the following subsections.

4.1 Single-pulsed holograms

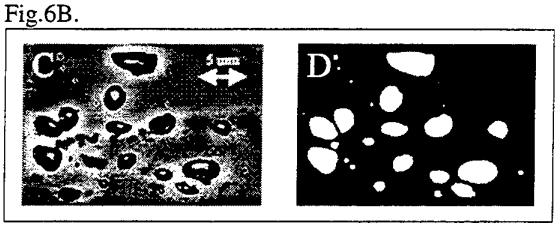
A typical image taken from the reconstruction of a single pulse hologram is shown in Fig.5A . The above mentioned problems to automatically detect the bubbles are evident in this image.



A reliable detection of the bubbles that are depicted sharply is impeded due to the substantial variations of the grey-value of the background. Therefore, after the high frequency noise had been reduced by means of a Median filter, a newly developed filter that uniforms the grey level of the background is applied to the image. No information about the sharpness of the imaged bubbles was lost by applying these two filter, but the background is substantially more uniform (s. Fig.5B). Sharply depicted bubbles can now clearly be separated from the background and detected by the edge detection algorithm. As the result of the edge detection, an image is obtained where the sharply depicted bubbles are completely or partly surrounded, as it is shown in Fig.6A.

In order to close the edges of partly closed bubbles, an additional routine was implemented. This is performed under the assumption that the bubble can be represented by an ellipsoide. The detected part of the edge of the bubble is extrapolated from its curvature. When proceeding as described, every bubble

which is depicted sharply in the image is detected and marked. The image is then binarised, as it is shown in Fig.6B.

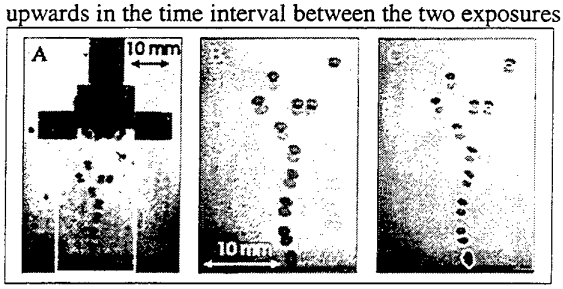


The detected bubbles are measured and sized. By recording and evaluating an image of an object with a known size, the scale of the image is determined.

4.2 Double-pulsed holograms

The flow field in an aerated stirred vessel has a highly three-dimensional character. When considering the various operating conditions, there is no preferred flow direction for the bubbles at any place inside the vessel. Since the velocities of the bubbles also have to be determined automatically, criteria were implemented in the software module, such that not only the two images of one bubble are mapped on one another, but also that its first image is distinguished from its second.

A typical image taken from a reconstructed double-pulse hologram is shown in Fig.7A. This image is included to facilitate the location of the image in Fig.7B is taken at. The brighter images of the bubbles belong to the first pulse (lower intensity), whereas the darker images belong to the second pulse (higher intensity). With this information it can be clearly derived from Fig.7B that the bubbles were moving upwards in the time interval between the two exposures to the laser beam.



In general, for the two images of one bubble obtained from reconstructions of double-pulsed holograms, three cases have to be distinguished: the images overlap partly, the images overlap completely, or the images do not overlap. The time interval between the two exposures is adjusted in such way that most of the bubble pairs partly overlap. Since the region the bubbles overlap is substantially darker than the rest of the bubble images, it is a suitable tool to map both images of one bubble on one another. If the images of one bubble overlap completely, the bubble was moving parallel to the optical axis of the observing camera. This is detected by the software, due to the very low grey value the bubble is imaged in. The vertical coordinate of the bubble is determined, which is the criterion needed to identify this bubble in the second view, where the bubble should have been moving in a horizontal direction. If a bubble is relatively small and moving fast, its images do not overlap any more, as it was sometimes observed in region next to the stirrer. In this case, a search volume around the first image of a bubble is being created in order to find its second image. The radius of this volume is calculated from the scale of imaging, the pulse separation, and the maximum occurring speed, which is the agitator's circumferential speed. The correlation of the images to the two pulses is then performed as in the described below.

Considering the original image (s. Fig.7B), identical procedures are performed as it had been in the case of single pulsed holograms, up to the point, where the edges are detected and closed and the image is

binarised. The position of the two centres of gravity of one pair of bubble images are measured and the velocity is calculated. In order to get the direction in which the bubble is moving, the binarised image is added to the original image, as it is shown in Fig.7C.

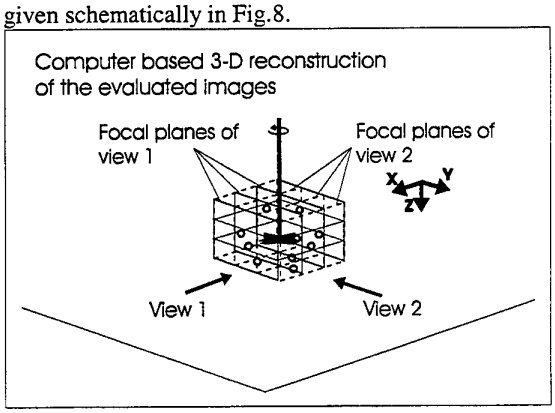
The average grey value of both images of one bubble is calculated. The brighter area with the higher average grey value belongs to the first pulse, the darker one to the second pulse, and the direction of the velocity vector in this view is determined.

4.3 Stereo matching algorithm

Two holograms were recorded simultaneously and evaluated separately from one another. The correlation of the two holograms with one another presupposes a stereoscopic optical set-up. In this set-up the optical axis of each camera is parallel to one of the axis' of a carthesian coordinate system. The cameras only can conduct translatoric movements. The parallelism of the axis is ensured by the alignment of the traversing slide and the horizontal justification of the camera by means of the regulating screw of the pitch plane.

Because of the high quality of the utilised objectives no correction of the distortion has to be performed. Since the cameras uniquely conduct movements of translation, a simplified calibration processes can be applied. The model to determine the projection equation is simplified and the number of the unknown projection parameter that have to be determined is reduced.

After both holograms that were taken at one operating point have been completely split into the series of 2-D images and evaluated as described above, the images are reset together again numerically including the obtained results. This results in two 3-D reconstructions flow field in the vessel, displaying the same scenario, but seen from two perpendicular viewing-directions. These two 3-D images are correlated with one another by applying a stereo-matching algorithm. The physical model this algorithm is based on is given schematically in Fig.8.



From one holographic reconstruction the vertical position and the lateral position of each bubble is derived. The depth position is derived from the location of the camera, but it can only be determined within the accuracy of the depth of focus of the observing camera. Since the two holographic reconstructions of one operating point display the same scenario seen from viewing directions that are perpendicularly to one another, the depth coordinate of a bubble in one holographic reconstruction is its lateral coordinate in the second holographic reconstruction. Because of this, and by considering the vertical coordinate of the bubble, the position of each bubble can be determined exactly. The correlation of the bubbles in both views is performed without considering any feature-based criterion. This is an important fact, since the shape and the size of a bubble can vary significantly between the two views. After the two views have been correlated, the determination of the sizes, the spatial locations, and, in case of a double-pulsed hologram, the velocity field of the bubbles is performed.

5. RESULTS

In the first three series of experiments, the viscosity of the liquid and the agitator speed were varied. The air flow rate was kept at a constant value of V_G = 3l/h during the experiments. A Rushton-turbine was chosen to disperse the air which was supplied from a nozzle in the centre of the flat bottom of the vessel (s. Fig.1). In these experiments,

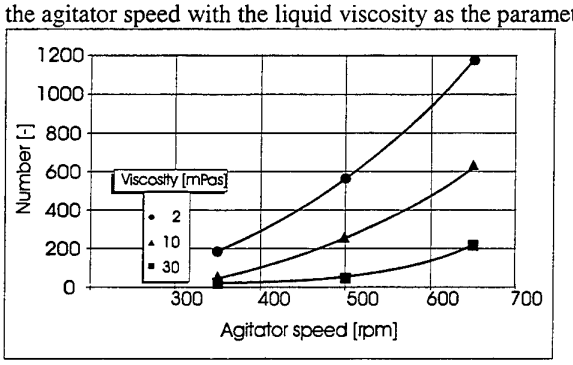
- the number and the size of the generated bubbles,
- the spatial distribution of the bubbles, and
- the velocity field of the bubbles

were analysed. In order to determine the first three values, two single pulsed holograms of each operating point were evaluated. In order to determine the velocity of the bubbles, two double pulsed holograms have been recorded and evaluated from every experiment. The matrix of the analysed operating points is given in table1.

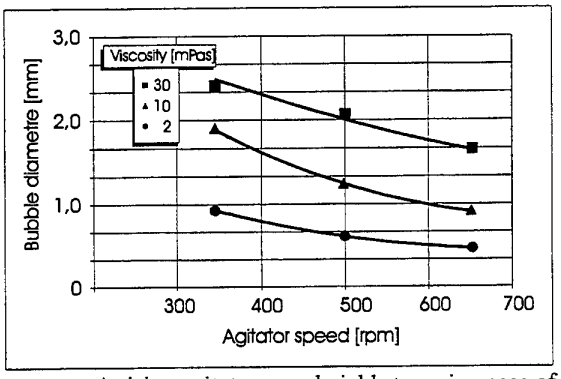
Viscosity	Agitator speed [rpm]		
	350	500	650
2 mPas	X	X	X
10 mPas	X	X	X
30 mPas	X	X	X

Table 1: Matrix of the analysed operating points

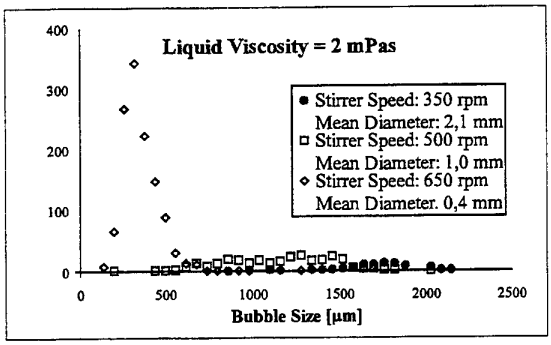
The evaluation of the three experimental runs in terms of the number of bubbles is plotted versus the agitator speed with the liquid viscosity as the parameter in Fig.9.



With the agitator speed reaching a minimum value, the first bubbles are split up due to the shear field in the liquid which is induced by the agitator. The smaller bubbles are drained back in the section below the agitator which leads to a significant increase of the number of bubbles in the vessel. In case of a low viscosity this point at an agitator speed of n = 350rpm is already exceeded. An increase of the viscosity also entails an increase of the minimum value for the speed. For this reason it is exceeded at a value of n = 500rpm at the intermediate measurement run, whereas at the lower measurement run it is not exceeded before n = 650rpm. This is due to the decrease of the Reynolds number with an increase of the viscosity which results in smaller turbulent shear forces to which the bubbles are subjected. This impact of the increase of the viscosity which reduces the dispersion is only compensated with an increase in the agitator speed.



A rising agitator speed yields to an increase of the probability that a bubble is disintegrated in the shear field of the liquid, that was induced by the stirring process. This leads to a significant decrease of the average diameter of the bubbles inside the vessel for all of the three series of measurements. This is amplified due to the fact that the surface tension of the test fluid is in the range of $\sigma = 44$mN/m and therefore, the fluid shows a low trend to coalescence effects, when compared to pure water-air systems.

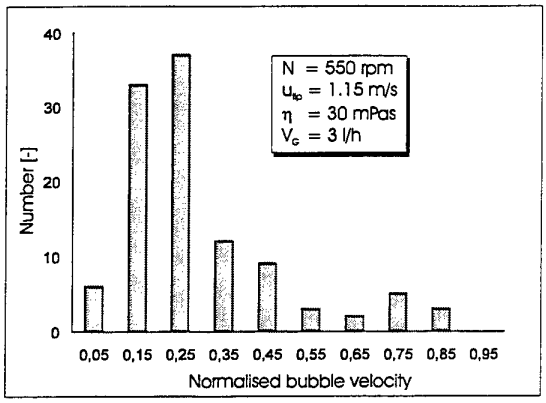


The impact of the agitator speed on the number of bubbles in the vessel is evident, as it can be derived from Fig.10. The increase of the viscosity of the liquid leads to a drastic decrease of the number of bubbles in the test section.

In Fig.11 the different size classes of the bubbles are plotted for three different agitator speeds and the viscosity $\eta = 2$mPas. In accordance with the previously mentioned results, it can be derived from Fig.11, that the increase of the stirrer speed results in an decrease of the medium bubble size. In addition to that, the increasing stirrer speed narrows the bubble size distribution significantly.

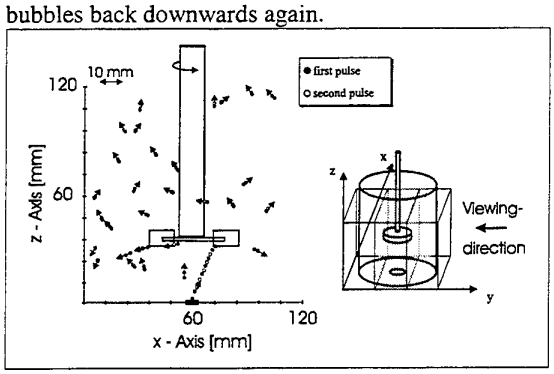
As an example for an evaluated double pulse hologram, the velocity field of the bubbles that were generated for one operating point is given. For an agitator speed of N = 550rpm, an air flow-rate of V_G = 3l/h and a liquid viscosity of $\eta = 30$mPas, and a pulse-separation of $\Delta t = 5$ms, the three-dimensional velocity field of the generated bubbles was evaluated.

The evaluation of the two double pulse holograms yielded to 110 bubble-pairs. The obtained velocity distribution of the bubbles, normalised with the circumferential agitator speed $u_{tip} = 1{,}15$m/s, is given in Fig.12.



It is striking that only those bubbles right next to the agitator move with a velocity in the range of the circumferential agitator speed. As soon as the bubbles have left the sphere of influence of the agitator, their speed is reduced significantly due to inertia effects. Regions where the bubbles have a higher velocity can be found close to the side of the baffles which is faced towards the governing liquid flow and above the nozzle. The lowest bubble velocities were found in the centres of the whirls below the agitator.

In Fig.13 both reconstructed locations of each bubble in the middle plane of the vessel are shown. Additionally, arrows are included in Fig.13 indicating the bubble velocity and flow direction. Their length is proportional to the projected velocity in this plane. A bubble whirl below the stirrer can be identified. Above the stirrer the ascent velocity of the bubbles is almost uniform. Superimposed to that velocity is the global swirling flow of the liquid. The upper liquid whirl is - as expected - not strong enough to entrain the bubbles back downwards again.



6. CONCLUSIONS

In this study, the short-time holography was applied to the analysis of the highly three-dimensional two-phase flow in an aerated stirred vessel. This measuring technique is - in combination with the evaluating algorithms - a highly valuable tool in the analysis of the flow field of the generated bubbles in aerated stirred vessels.

The drawback of this measuring technique was found to be the fact that, due to a limitation to double-pulsed holograms, the transient character of the flow field of the bubbles could not be analysed well. Therefore, a combination of the short-time holography and the high-speed cinematography in order to provide a more detailed analysis of the dispersion characteristics in aerated stirred vessels is recommended.

ACKNOWLEDGEMENTS

It is gratefully acknowledged that the work presented in this paper has been supported by the German Research Foundation (Deutsche Forschungs-gesellschaft DFG)

REFERENCES

Adrian, R. & Liu, Z.C. (1993), Simultaneous imaging of velocity fields of two phases, Particulate Two-Phase Flow, Butterworth-Heinemann Series

Brücker, C. 1995, 3-DPIV using a scanning light-sheet and stereoscopy: Study of flow development around a spherical cap, ASME FED-VOL 209, Flow visualisation and image processing of multiphase flow, pp. 497 - 505

Chàvez, À. & Mayinger, F. 1992, Measurement of direct-contact condensation of pure saturated vapour on an injection spray by applying pulsed laser holography, Int. J. Heat and Mass Transfer, Vol. 35, No. 3, pp. 691-702

Durst, F., Naqui, A. & Liu, X., 1990, Characterisation of multiphase flow using an extended PDA, Proc. 5th. Intl. Symp. On Application of Laser Techniques to Fluid Mechanics

Gebhard, P. 1996, Zerfall und Verdampfung von Einspritzstrahlen aus lamellenbildenden Düsen, Ph.D. Thesis, Technical University of Munich, Munich, Germany

Gebhard, P. & Mayinger, F. 1995, Evaluation of pulsed laser holograms of flashing sprays by digital image processing, ASME FED-VOL 209, Flow visualisation and image processing of multiphase flow, pp. 13 – 22

v. d. Geld, Meng, H. & Boot, P. (1995), High pressure optical measurements of sizes, velocities and longitudinal positions of bubbles, Int. J. of Multiphase Flow, Vol. 21, No. 1, pp. 95-105

Kiemle, D. & Röss, A. (1969), Einführung in die Technik der Holographie, Akademische Verlagsgesell-schaft, Frankfurt am Main

Mayinger, F (1994), Optical Measurements, Techniques and Applications, Springer Verlag, Berlin

Merzkirxh, W., Hilgers, S. & Wagner, T. (1995), Visualization and image processing for gas-liquid Two-Phase-Flow, ASME FED-VOL 209, Flow visualisation and image processing of multiphase flow, pp. 151-154

Tassin, A.L. & Nikitopoulos (1995), Nonintrousive measurements of bubble size and velocity, Experiments in Fluids, Vol. 19, No. 2

PHASE-RESOLVED THREE-DIMENSIONAL LDA MEASUREMENTS IN THE IMPELLER REGION OF A TURBULENTLY STIRRED TANK

J.J. Derksen, M.S. Doelman and H.E.A. van den Akker

Kramers Laboratorium voor Fysische Technologie; Delft University of Technology
Prins Bernhardlaan 6; 2628 BW Delft; The Netherlands

ABSTRACT

Predictions on the quality of mixing in a turbulently operated stirred tank ask for a detailed knowledge of the flow field, including its turbulence characteristics. In this paper we present the results of three-dimensional, angle-resolved LDA measurements in the vicinity of a Rushton turbine in a baffled tank at Re=29000. For optimal coincidence of the signals in the three velocity channels, an accurate laser beam alignment procedure was developed. The average flow field is characterized in terms of velocity and vorticity fields. In the characterization of the turbulence, the emphasis is on the anisotropy of the Reynolds stress tensor.

1. INTRODUCTION

Understanding the fluid dynamics of turbulently operated stirred tanks is inevitable for optimizing this widely used piece of process equipment. Investigations into stirred tank flow often exploit numerical (computational fluid dynamics) as well as experimental techniques. A key role for experiments is in validating simulations. With the availability of large and fast computational resources, simulations are able to resolve more and more details of the turbulent flow field (Eggels 1996, Derksen and Van den Akker 1998). As a result, the demands on the quality and resolution of the experiments increase. Not only accurate experimental data on the average flow fields, but also on turbulence characteristics, need to be available. With respect to turbulence characteristics, we have focused on the Reynolds stress tensor, and, more specifically, on the extent to which it is (an-)isotropic.

In this paper, we report on phase-resolved, three-dimensional LDA experiments in the impeller outflow region of a stirred tank at Re=29000. In a three-dimensional LDA setup, the full Reynolds stress tensor can be measured in one go. Additional advantages of a three-dimensional setup are the possibility for direct velocity bias correction, and an enhanced spatial resolution when operating the LDA equipment in an off-axis scattering mode. In a three-dimensional setup, laser beam alignment is an important and difficult issue, especially when the working fluid has an index of refraction that strongly differs from its environment. An accurate alignment procedure, based on a submerged micro-mirror system, was developed for this goal.

2. FLOW GEOMETRY

The flow geometry is depicted in figure 1. The baffled, flat-bottomed tank was filled with water up to a level H=T=288 mm. At the top level there was a free surface. The tank was entirely made of glass. To reduce refraction at the cylindrical side-wall, the tank was surrounded by a square glass box filled with water. The impeller was set to rotate with an angular velocity of $N=2\pi\Omega$ =3.138(±0.002) rev/s. The Reynolds number, which for this flow system is traditionally defined as $Re=ND^2/\nu$, amounted to $2.9\cdot10^4$. The velocities in the tank will all be scaled with the impeller tip speed $v_{tip}=\pi ND$.

The Froude number ($Fr=N^2D/g$, with g the gravitational

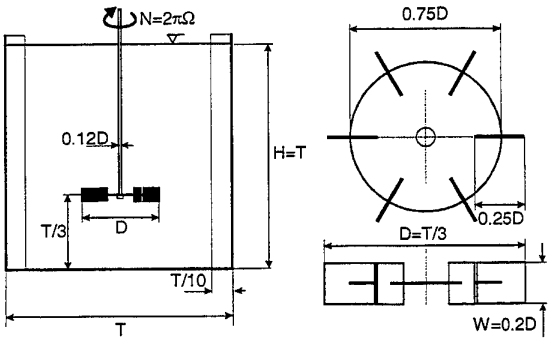


Figure 1. The flow geometry. The tank (left) is equipped with four baffles to prevent solid body rotation of the fluid. The impeller (right) is a Rushton turbine. The diameter of the tank is T=288 mm. The thickness of the disk and the impeller blades is 2 mm. The impeller was mounted on the shaft without a hub.

acceleration) was 0.1. It was observed that, under the conditions described above, the free surface was not distorted by air entrainment.

Together with each individual velocity measurement, the angular position of the impeller was recorded. This was done by resetting every impeller revolution a 16 bit clock, running at 10 kHz and writing two clock values to file. The first value represents the time since the last clock reset, the second value is the time of the last full impeller revolution. Together they determine the impeller angle at the instant of the velocity data acquisition.

3. LDA SETUP

The sending optics of the LDA setup consisted of an Ar-ion laser, operating in all-lines mode, a beam splitter system (TSI ColorBurst model 9201) and an optical fiber system that guided the beams to the flow.

The ColorBurst selected the three major wavelengths of the laser and produced three pairs of beams. One beam of each pair was given a frequency pre-shift of 40 MHz. All beams were coupled into single-mode, polarization preserving optical fibers. At the flow system, they were coupled out in two laser probes. The initial spacing between the two beams in each pair was fixed to 50 mm. From probe #1 two beam pairs emerged. They were focused by a 500 mm lens, and entered the flow through the (flat) bottom of the tank (see figure 2a). This probe allowed for measuring the radial and tangential velocity component. The axial velocity component was measured with the single beam pair emerging from probe #2, which entered the vessel through the side-wall. This probe was equipped with a 250 mm front lens. If all beams show maximum overlap, a three-dimensional measurement volume of approximately 100^3 μm^3 has been created.

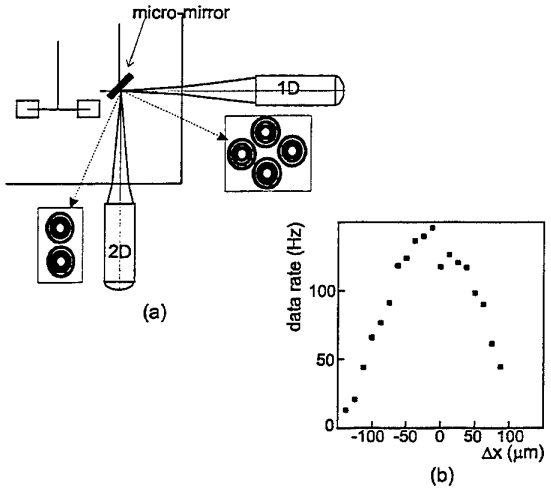


Figure 2. (a) The alignment system: two fiber optic LDA probes (a 1D probe and a 2D probe) are aligned with help of a micro-mirror. (b) Data rate in coincidence and side-scatter mode as a function of beam misalignment Δx.

Both probes contained the receiving optics as well. A lens system projected the measurement volumes onto flat, multi-mode fiber-ends. These fibers guided scattered light to three photo multiplier tubes (one for each wavelength). The signals emerging from the photo multipliers were fed into the signal processor (an IFA 750 by TSI). The LDA system was operated in side scatter mode.

The flow was seeded with aluminum coated polystyrene particles with a mean diameter of 4 μm. They were chosen because of their good light scattering properties. A disadvantage of these particles is their relatively high density ($2.6 \cdot 10^3$ kg/m^3) which forced us to keep the impeller running during the course of the experimental sessions to prevent sedimentation.

3.1 Laser Beam Alignment

Optimum overlap of the three measurement volumes is crucial for the signal quantity (in terms of the data-rate in coincidence mode) and quality (e.g. with respect to spatial resolution and geometric bias effects).

The alignment was controlled and checked by means of an aluminum micro-mirror with elliptical shape (long axis: 70 μm, short axis: 50 μm) deposited on a sheet of glass, that was placed in the tank at the measuring position (see figure 2a). Optimal alignment was achieved when all the six laser beams that were involved in the experiment, showed (in reflection) a concentric diffraction pattern. Figure 2b (the data rate in coincidence mode at a certain position in the vessel as a function of beam misalignment Δx) gives an impression of the quality and resolution of the alignment system.

3.2 Data Processing

In the vicinity of the impeller tip a measurement grid was defined in a vertical plane, midway between two baffles, see figure 3. In figure 3 the coordinate system that will be used for presenting the flow field results is defined as well. The spacing of the grid in axial and radial direction was $\Delta z = \Delta r = 2.5$ mm, i.e. $\Delta z \approx W/8$ (with W the height of an impeller blade). In tangential direction the resolution was 3° (at the inner bound of the grid this corresponds with a

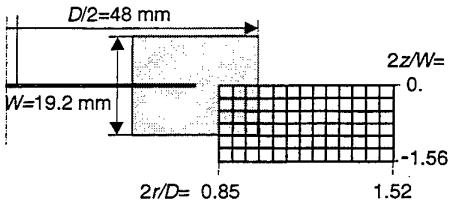


Figure 3. The measurement grid was located in a vertical plane midway between two baffles. The grid spacing is $\Delta r = \Delta z = 2.5$ mm.

spacing of 2.2 mm, at the outer bound with 3.9 mm). Per grid

point, i.e. per measurement position and tangential interval, $6 \cdot 10^3$ velocity samples were collected.

Burst type LDA data in turbulent flows are inflicted by velocity bias: the particle transfer rate through the measurement volume is approximately proportional to the absolute value of the velocity. Therefore, unweighted averaging will lead to biased results. The average data presented in this paper were all corrected for velocity bias with a velocity weighing scheme, as introduced by McLaughlin and Tiederman (1973). Note that, with this bias correction procedure, explicit use is made of the availability of three velocity components in the same sample, as the inverse of the absolute velocity is the weighing factor. In the impeller outstream, the bias corrected mean tangential and radial velocity components were significantly smaller than their unweighted equivalents. The differences amounted up to $0.1 \cdot v_{tip}$.

4. ANISOTROPY CHARACTERIZATION

The major reasons for measuring Reynolds stresses can be found in the field of turbulence modeling. An ongoing debate in the field of modeling complex turbulent flows, such as the flow under investigation, is whether second-order closure models have significant added value over first-order (e.g. k-ε) models. Since the standard k-ε model is an eddy-viscosity model, it locally assumes isotropic turbulent transport. The k-ε model is known to be inappropriate in rotating and/or highly three-dimensional flows (Wilcox 1993). Assessment of the isotropy assumptions by experiment is therefore necessary.

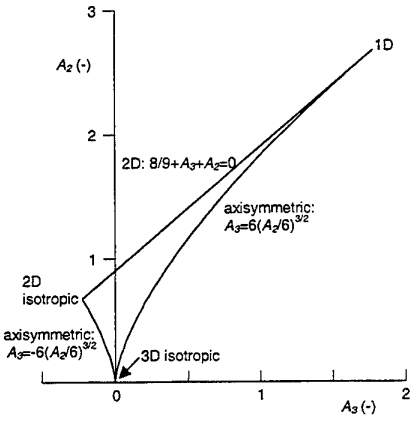


Figure 4. The plane with coordinates A_3, A_2 (i.e. the invariants of the anisotropy tensor) was used to characterize the anisotropy of the turbulence. The physically possible states are bounded by the Lumley triangle (Lumley 1978).

The Reynolds stress data will be presented in terms of the anisotropy tensor a_{ij} and its invariants (Lumley 1978). The anisotropy tensor is defined as

$$a_{ij} = \frac{\overline{u_i u_j}}{k} - \frac{2}{3}\delta_{ij} \qquad (1)$$

with k the turbulent kinetic energy: $k = \frac{1}{2}\overline{u_i u_i}$; u_i the fluctuations about the mean of the i-th velocity component (i.e. $U_i = \overline{U}_i + u_i$); and δ_{ij} the Kronecker delta. The anisotropy tensor has a first invariant equal to zero by definition. The second and third invariant respectively are $A_2 = a_{ij}a_{ji}$ and $A_3 = a_{ij}a_{jk}a_{ki}$. The range of physically allowed values of A_2 and A_3 is bounded in the (A_3, A_2) plane by the so-called Lumley triangle, see figure 4. The boundaries that appear to be most relevant in the current study are the ones associated with axisymmetric turbulence.

Axisymmetric turbulence is defined as a situation in which the kinetic energy in two orthogonal directions is equal. Hence, a_{ij} reads

$$a_{ij} = \begin{pmatrix} -\alpha & 0 & 0 \\ 0 & \alpha/2 & 0 \\ 0 & 0 & \alpha/2 \end{pmatrix} \qquad (2)$$

(the reference frame is chosen such that the axis of symmetry of the turbulence coincides with the direction of the first coordinate). The energy contained in the first coordinate direction is $\left(\frac{1}{3} - \frac{1}{2}\alpha\right)k$, in the second and third direction the energy is $\left(\frac{1}{3} + \frac{1}{4}\alpha\right)k$. As a result of equation 2, $A_2 = \frac{3}{2}\alpha^2$ and $A_3 = -\frac{3}{4}\alpha^3$. Consequently $A_3 = 6(A_2/6)^{3/2}$ if $\alpha < 0$, i.e. the energy contained in the symmetry direction is more than $k/3$. This is the right branch of axisymmetric turbulence (see figure 4). If $\alpha > 0$, then $A_3 = -6(A_2/6)^{3/2}$ This constitutes the left branch, where the energy contained in the symmetry direction is less than $k/3$.

As a reference we calculate the point on the right axisymmetric branch where the energy contained in the symmetry direction is twice the energy in the other two directions. At this point α=−1/3, and therefore A_3=1/36 and A_2=1/6.

5. RESULTS

5.1 Average Flow Field

The structure of the average flow field, relative to an impeller blade (see figure 5), qualitatively corresponds with the results presented by Stoots and Calabrese (1995) and Lee and Yianneskis (1998). The wake behind an impeller blade can be clearly observed in the top vector plot. In Lee and Yianneskis (1998) a velocity vector plot at the level $2z/W$=+0.51 (i.e. *above* the impeller disk) in the tank is presented. Their wake is somewhat larger than the wake

observed in figure 5, which can be most likely attributed to the flow's asymmetry with respect to the impeller disk. The bottom part of figure 5 shows the development and advection of a strong vortex behind the impeller blade.

The strength of the vortex can be expressed in terms of the vorticity, which could be calculated because three-dimensional velocity data on a three-dimensional grid were

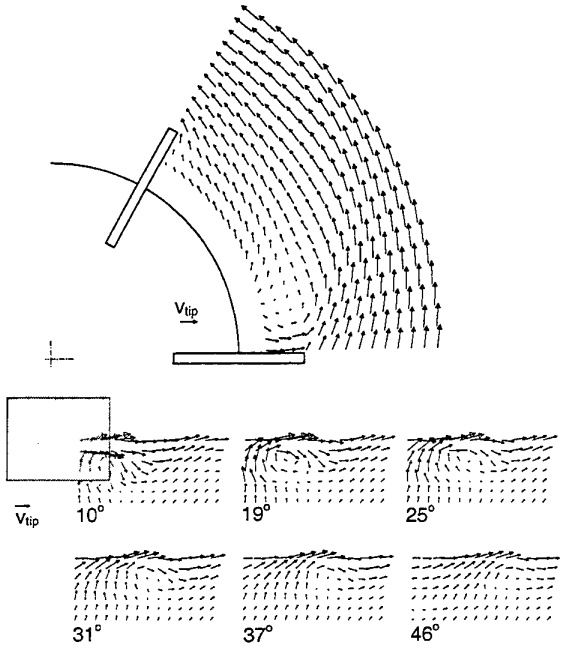


Figure 5. The average flow field. Top: velocity relative to the impeller in a horizontal plane at the level $2z/W=-0.52$. Bottom: velocity in six vertical planes at different angles with respect to the leading impeller blade. For reference, the position of the blade at the zero-angle position is drawn in the vector plot at 10°.

available. The vorticity was calculated from the average flow field with a central differencing scheme. This way, vorticity data reside on a grid that is staggered with respect to the velocity measurement grid depicted in figure 3. The vorticity field in a single horizontal plane (figure 6) shows that the trailing vortex is associated with a concentrated region of high vorticity. Note that at the lower right corner of the vector field the vortex from the preceding blade can still be distinguished.

Yianneskis *et al.* (1987) proposed to characterize the curve along which the trailing vortex is swept into the tank by connecting the points in a *horizontal* plane with a mean axial velocity component equal to zero. An assumption was that the vortex core did not move in the vertical direction. In figure 7 the curves found in literature (Yianneskis *et al.* 1987; Stoots and Calabrese 1995; Lee and Yianneskis 1998; Van 't Riet and Smith 1975) are compared with the one deduced from the present flow field. The strong deviation between curve [5] and the other curves is commonly

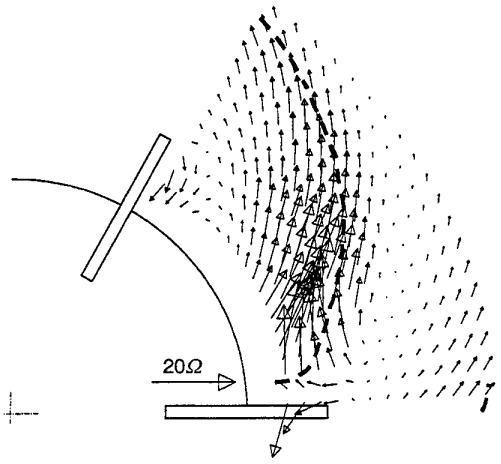


Figure 6. The vorticity field in a horizontal plane at $2z/W=-0.39$. The vorticity is scaled with the angular velocity Ω ($N=2\pi\Omega$). The dashed line is the position of the vortex core in the plane $2z/W=-0.52$.

attributed to inertia of the relatively large particles (needed for a photographic technique) used by Van 't Riet and Smith. We calculated, by linear interpolation, the position of zero axial velocity in the horizontal plane at a distance $2\cdot\Delta z$ below the impeller disk (i.e at the $2z/W=-0.52$ level). According to figure 5 this approximately was the plane in which the vortex core moved. Yianneskis *et al.* (1987) focused on the vortex that originated from the upper part of the impeller blade. They claim that its core moved in the $2z/W=1$ plane, which again clearly demonstrates the asymmetry of the flow with

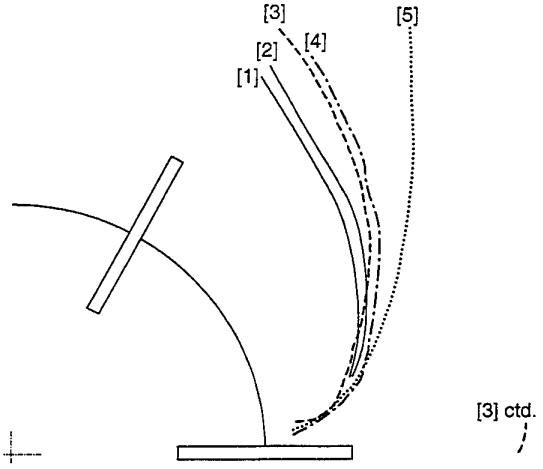


Figure 7. The vortex core position deduced from several investigations reported in literature and from the present work. [1] Lee and Yianneskis (1998); [2] Yianneskis *et al.* (1987); [3] present work; [4] Stoots and Calabrese (1995); [5] Van 't Riet and Smith (1975).

respect to the horizontal plane containing the impeller disk. The asymmetry is also reflected in the curves as given in figure 7. Curves [1] and [2] were taken form the upper vortex, curves [3] and [4] from the lower. It should also be noted, however, that Stoots and Calabrese (1995) used a flow geometry which differed quite strongly from the rest. Its disk had a diameter of 0.6·D, while in the present work it was 0.75·D; their bottom clearance was $T/2$.

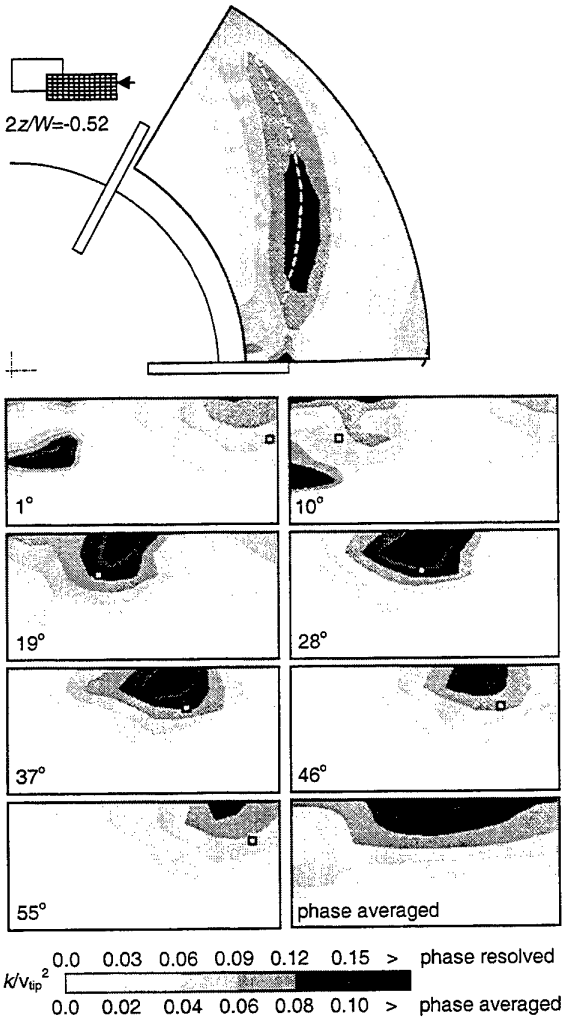


Figure 8. The distribution of the turbulent kinetic energy $k=\frac{1}{2}\overline{u_i u_i}$ in the horizontal plane at $2z/W=-0.52$ (top figure); in seven r-z planes with different angles with respect to the impeller blade; and in the r-z plane averaged over all impeller angles. The vortex core position is indicated with a dashed line in the top figure. In the r-z planes it is indicated with a small white square.

5.2 Turbulence Characteristics

First, the regions of high turbulent activity will be identified. This is done by plotting the turbulent kinetic energy $k=\frac{1}{2}\overline{u_i u_i}$ as a function of the position, see figure 8. In the horizontal plane with $2z/W=-0.52$ it can be observed that the region with high turbulent activity more or less coincides with the trailing vortex path. The vertical sections through the flow field show a concentrated region of high k just above the vortex core. We speculate that this distribution of kinetic energy is (at least partly) due to random fluctuations in the vortex core position. Combined with the steep gradients in the flow field right above the vortex core (see figure 5), erratic motion of the core position will locally lead to high levels of velocity fluctuation.

The local anisotropy of the turbulence has been characterized with the second and third invariant of the anisotropy tensor (A_2 and A_3, see section 4). Both parameters define a location within the Lumley triangle (figure 4). A subset of all measured locations has been depicted in figure 9. It can be observed that the most common situation in the present flow system is close to the right-hand-side boundary of the Lumley triangle. At this boundary the turbulence is axisymmetric, with the energy contained in the direction of the axis of symmetry being highest. Many points in figure 9 go beyond the state of anisotropy characterized by $A_3=1/36$ and $A_2=1/6$. At this latter state, the energy contained in the symmetry direction is equal to the sum of the energies contained in the other two directions (see also section 4).

From figure 9, it can be concluded that in the near wake of an impeller blade the anisotropy is strongest. Also the core of the vortex can be associated with relatively high anisotropy of the turbulence. If we focus on the horizontal plane with $2z/W=-0.52$ (i.e. the plane in which the vortex moves) and the angular positions 22° and 40°, we observe that the extreme locations of anistropy are encountered at $2r/D=1.16$ and at $2r/D=1.37$ respectively, whereas the vortex core at the corresponding lines is at $2r/D=1.13$ and $2r/D=1.33$ respectively. Away from the vortex core, the trajectories of figure 9 indicate that the turbulence tends more and more to isotropic.

6. CONCLUSIONS

Detailed data on the mean flow and the Reynolds stresses in the complex flow field in the vicinity of a Rushton turbine have been obtained. The three-dimensional setup allowed for measuring the full Reynolds stress tensor, and, as a result, an unambiguous characterization of the anisotropy of the turbulence.

Special attention was paid to beam alignment. A submerged micro-mirror system was developed to approach optimum beam overlap. Its resolution is of the order of 10 μm (i.e. about 1/10 of the width of the measurement volume). Operation of the LDA system in side scatter mode resulted in a measurement volume with a linear dimension of approximately 0.1 mm in all three coordinate directions.

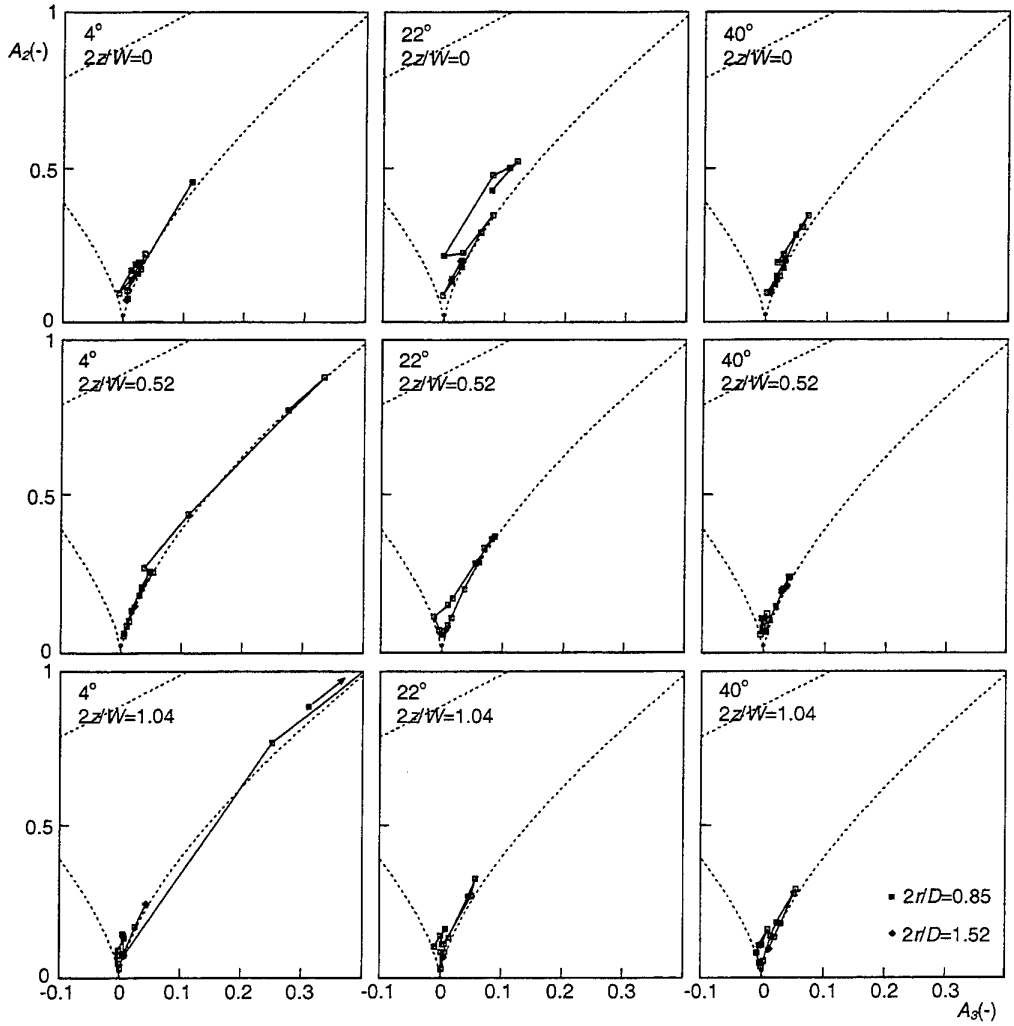


Figure 9. The locations within the Lumley triangle (the open squares) along radial trajectories in the flow field at three levels ($2z/W$=0, $2z/W$=−0.52, and $2z/W$=−1.04), and at three different angles (4°, 22°, and 40°) with respect to an impeller blade. The dotted lines denote the boundaries of the Lumley triangle. The drawn lines connect neighboring grid points. The points on the innermost radius of the measurement grid are denoted with +, the outermost points with ◆.

The average, phase-resolved flow field is characterized by a vortex that originates from the near wake of the impeller blade. This coherent structure could be clearly identified behind the blade over an angular range of more than 60°. As has been observed before (Lee and Yianneskis 1998), with the trailing vortex a region of high turbulent activity is associated. The strongest turbulent fluctuations were measured closely above the vortex core.

The turbulence in several flow regions close to the impeller was demonstrated to be anisotropic. Especially in the near wake of an impeller blade, and near the trailing vortex core the turbulence tends to a strongly anisotropic, axisymmetric state, i.e. the turbulent kinetic energy contained in two orthogonal directions is almost equal and significantly different from the energy in the third direction.

REFERENCES

Derksen, J.J. & Van den Akker, H.E.A. 1998, Parallel simulation of turbulent fluid flow in a mixing tank, Lecture Notes in Computer Science, vol. 1401, pp. 96-104.

Eggels, J.G.M. 1996, Direct and large eddy simulation of turbulent fluid flow using the lattice-Boltzmann scheme, Int. J. Heat & Fluid Flow, vol. 17, pp 307-323.

Lee, K.C. & Yianneskis, M. 1998, Turbulence properties of the impeller stream of a Rushton turbine, AIChE J., vol. 44, pp. 13-24.

Lumley, J. 1978, Computational modeling of turbulent flows, Adv. Appl. Mech., vol. 26, pp 123-176.

McLaughlin, D.K. & Tiederman, W.G. 1973, Bias correction methods for laser Doppler velocimeter counter processing, Phys. Fl., vol. 16, pp. 2082-2088.

Stoots, C.M. & Calabrese, R.V. 1995, Mean velocity field relative to a Rushton turbine blade, AIChE J., vol. 41, pp 1-11.

Van 't Riet, K. & Smith, J.M. 1975, The trailing vortex system produced by Rushton turbine agitators, Chem. Eng. Sci., vol. 30, pp. 1093-1105.

Wilcox, D.C. 1993, Turbulence modeling for CFD, La Cañada (CA), DCW Industries.

Yianneskis, M., Popiolek, Z. & Whitelaw, J.H. 1987, An experimental study of the steady and unsteady flow characteristics of stirred reactors, J. Fluid Mech., vol. 175, pp 537-555.

Turbulence Energy Dissipation Rate Estimation in Stirred Vessels

Pentti Saarenrinne, Mika Piirto, Heimo Ihalainen*, Osmo Kaleva**,

Tampere University of Technology, Energy and Process Engineering,
*Measurement and Information Technology, **Mathematics.

Abstract

The magnitude of the turbulent energy dissipation rate determines the quality and efficiency of the mixing process in stirred vessels. From the Kolmogorov length scale it can be concluded that maximum dissipation rate of the turbulent energy exists at minimum length scale. Therefore the local turbulence energy dissipation rate is in the interest of a process designer. The estimation of the turbulent dissipation energy rate is based on flow measurements made typically with LDA. The paper reviews different approaches for estimating the turbulence energy dissipation rate and studies different estimation methods for air, water and CMC-water solution flows. Different convection velocity calculation possibilities are studied. The existence and estimation of pseudo-turbulence is discussed and a notch-filter is used to eliminate peak from turbulence power spectral density function. A Particle Image Velocimeter is used to direct estimation of the turbulent kinetic energy dissipation rate in the same stirred tank as the other measurements. Different estimates calculated from PIV results are compared.

1. Introduction

The magnitude of the turbulent energy dissipation rate in different positions of a stirred vessel determines the quality and efficiency of the mixing process. From the equation of Kolmogorov length scale $\eta = \left(\nu^3 / \varepsilon\right)^{\frac{1}{4}}$ can be concluded that the maximum dissipation rate of the turbulent energy exist at minimum length scale. Therefore the local turbulence energy dissipation rate is in interest of a process designer. From the literature many different approaches to this problem can be found. The measurements are often made with a hot wire anemometer in those papers in which the turbulent dissipation rate is estimated through the spectrum of the turbulent kinetic energy. At present the estimation of the turbulent dissipation energy rate is based on flow measurements made typically with LDA. The estimates can be classified as: direct estimation from basic equations, transformation from time signal to space signal and to other from basic equations derived or phenomenological estimates. To estimate the turbulent energy dissipation rate from LDA measurements is a very demanding task. The data rate is in most cases too low for spectrum analysis and the possibility to measure derivatives of velocity fluctuations are restricted. The use of the Taylor's frozen turbulence hypothesis in time to space transformation is also doubtful in the stirred vessels. The paper reviews different approaches to estimate the turbulence energy dissipation rate and compares results for different estimation methods for air, water and CMC-water suspension flows. Different convection velocity calculation possibilities are studied. The existence and estimation of pseudo-turbulence is discussed and a notch-filter is used to eliminate peak from the turbulence power spectral density function. Particle Image Velocimetry is also applied to estimate the turbulent dissipation rate directly from basic equations. The purpose of this paper is to evaluate different estimates of turbulent kinetic energy dissipation rate by comparing different measurement methods, different estimation equations and the influence of the test setup construction.

2. Estimated equations

The turbulence energy dissipation rate ε is in average determined in an agitated tank from power input P per unit mass of fluid, $\bar{\varepsilon} = P/\rho V_T$. The local turbulence energy dissipation rate can be calculated from basic definitions. In general

$$\varepsilon = \nu \overline{\frac{\partial u_j}{\partial x_i}\left(\frac{\partial u_i}{\partial x_j} + \frac{\partial u_j}{\partial x_i}\right)} \qquad (1)$$

and for homogeneous turbulence

$$\varepsilon = \nu \overline{\frac{\partial u_j}{\partial x_i}\frac{\partial u_j}{\partial x_i}} = \nu \frac{1}{2}\overline{\left(\frac{\partial u_j}{\partial x_i} - \frac{\partial u_i}{\partial x_j}\right)\left(\frac{\partial u_j}{\partial x_i} - \frac{\partial u_i}{\partial x_j}\right)} \qquad (2)$$

In isotropic turbulence the equation is simplified to the following form

$$\varepsilon = 6\nu\left[\overline{\left(\frac{\partial u_1}{\partial x_1}\right)^2} + \overline{\left(\frac{\partial u_1}{\partial x_2}\right)^2} + \overline{\frac{\partial u_1}{\partial x_2}\frac{\partial u_2}{\partial x_1}}\right] \qquad (3)$$
$$= 15\nu\overline{\left(\frac{\partial u_1}{\partial x_1}\right)^2} = 7.5\nu\overline{\left(\frac{\partial u_1}{\partial x_2}\right)^2}$$

The turbulence energy dissipation rate ε can also be evaluated from the power spectral density of the velocity according to the equation

$$\varepsilon = 15\nu\int_0^\infty k^2 E_1(k)dk \qquad (4)$$

In this equation k = 2πf/U is the wave number. The wave number spectrum can be achieved from the one dimensional energy spectrum of velocity E_1 measured in terms of frequency by using the Taylor's frozen turbulence hypothesis.

$$E_1(k) = \frac{U_c}{2\pi}E_1(f) \qquad (5)$$

Methods to calculate the power spectrum density of the turbulent kinetic energy have been reviewed in Ihalainen et al. 1995. All of these definitions contain only at best circumstances measurable quantities, namely derivatives of the velocity fluctuations and the power spectral density of turbulence.

3. Turbulence energy dissipation rate estimation

3.1 Turbulence energy dissipation rate estimation from turbulent kinetic energy spectrum using LDA measurements

To fully resolve the small scales in the flow, high validated data rates are needed for LDA- measurements. Host-Madsen et el. 1994 provides a rule of the thumb for the maximum obtainable mean data validation rate

$$N_{\max} \approx \frac{4e^{-2}\overline{U}}{\Delta x} \qquad (6)$$

where N_{max} is the mean data validation rate (DVR) and Δx is probe volume diameter. For the used LDA and test setup this equation gives 2.7 kHz maximum DVR for liquid flows and 32 kHz for air flow. Measurements made with two different size vessels and three different fluids shows that the data rate in LDA measurements tends to remain well below these values at every point in the vessel (Appendix A). This is especially the case when liquid flows are measured in backscatter mode. Several kHz data rates can be achieved, when fluid is air and it is seeded with paraffin oil smoke.

According to Adrian et al. 1987 one should try to achieve so called high data density low burst density limit, which gives optimum conditions for the measurement of the power spectra. One should eliminate burst overlap to avoid the "phase" or "ambiguity" noise. The high data density and low burst density can occur simultaneously because the LDV measurement volume can usually be made much smaller than the scales of the motion of the fluid flow. At this high data density and low burst density, case phase noise is eliminated and replaced by step noise if one uses the sample and hold procedure. Step noise is created by the random steps that occur at the new samples. This also produces, at the same time, a low pass filtering effect caused by the information loss during the hold periods. Adrian et al. 1987 shows that the sample and hold process attenuates the spectrum with a $1/f^2$ roll-off as a first order low pass filter, and increases the energy content of the low frequencies by adding step noise as the mean data rate decreases. The roll-off occurs at a frequency equal to the mean data rate divided by 2π. The measured spectra calculated with the sample and hold procedure shows (Figure 1) the behaviour described by Adrian et al. 1987. From the spectrum can be found the roll-off at the frequency equal to the mean data rate divided by 2π. Below that there is a zone nearby -5/3 slope and at higher frequencies -2 slope. Figure 2 illustrates the dissipation rate spectra of the turbulent kinetic energy calculated from spectra in Figure 1. From Figure 2 the roll-off zone can be seen clearly. At high frequencies the dissipation rate spectrum in Figure 2 is unrealistic. In Figures 1 and 2 spectra calculated with linear interpolation are also shown. Before linear interpolation the data is pre-processed by a procedure to remove non-Gaussian "outlier's" and "double burst's", because they tend to distort the results (Benedict et al. 1998). The forms of the spectra are more realistic but there it is harder to find clear -5/3 or -2 slope zones. The roll-off frequency is also difficult to recognise. Figure 3 shows the average of ten batches of 10^5 sample spectra. The averaged power spectrum density curves do not differ remarkably from the Figure 1 spectra. The averaging process smoothens the spectrum only slightly. To further check the validity of the power spectral density estimates, we tried to measure the spectrum for different fluids with different rheological properties. Figure 4 shows the power spectrum density estimates for different fluids. The measurements are made at the same position in the same vessel and calculated with the linear interpolation sample and hold method. The uppermost curve is for 0.25-w% CMC-water solution, the second for water, third for 1.0-w% CMC-water solution and the fourth for paraffin oil. The curves are one decade shifted from the water curve and from each other. The spectra for high viscosity fluids (two lowest) shows steeper slopes at frequencies 10 to 50 Hz and at higher frequencies the slopes are unchanged. The high frequency end of the spectra is formed by the sample and hold calculation process.

To check the influence of the vessel wall curvature and the refractive index difference of fluid and wall we made further measurements. We used paraffin oil in a vessel made from Borosilicate glass (n = 1.47) to see the effect of refractive index matching and in another test we used water in a plastic cylinder made from FEP. Neither of these tests showed drastic increase in data validation rate.

According to the methods described in this chapter it is not feasible to use power spectrum density measurements for turbulence dissipation rate estimation.

3.2 Turbulence energy dissipation rate estimation from PIV measurements

Particle image velocimeter offers a new possibility for turbulence kinetic energy dissipation rate measurement. Dahm et al. (1991) used the LIF-method to estimate the dissipation rate of a conserved scalar. One can consider particles as a conserved scalar and estimate from their velocities the dissipation rate of turbulence. This method also has its own specific problems. The spatial resolution of PIV is weak. This combined with the spatial filtering effect, caused by the for velocity estimation used cross-correlation calculation method over a finite area, makes its use difficult. The second problem is related to the particles. Very small particles or particle clouds able to follow the smallest eddies must be recognised and the velocity derivatives has to be determined accurately. Technical problems also exist, the data amount of time series of images is huge. We used the smallest image area (6.25x5.00 mm^2) achievable with our objectives and we obtained a 4.9 μm resolution for a pixel in both co-ordinate directions. The spatial resolution for a 32x32 pixel interrogation area was 0.16x0.16 mm^2 , 16x16 interrogation area 0.08x0.08 mm^2 and 8x8 interrogation area 0.04x0.04 mm^2. The laser sheet thickness was 1 mm. The spatial resolution was comparable to the LDA measurements. The turbulence energy dissipation rate was then estimated with equations 2 and 3 from the time series of 30 images in a stirred tank flow field. The velocity vector field and the intensity field of the turbulence dissipation rate is shown in Figures 5 and 6. Numerical values have been computed to Table 1.

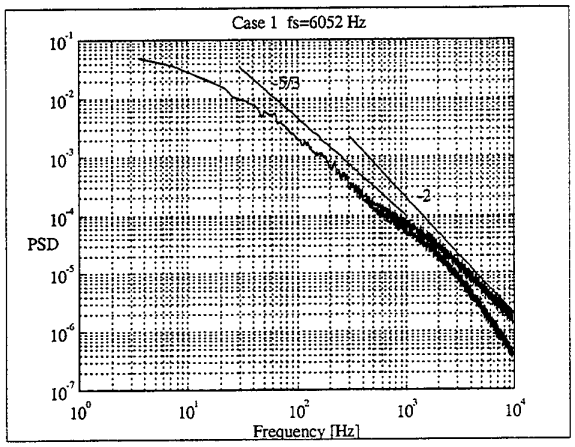


Figure 1: Power Spectral Density for Case 1, lower curve with linear interpolation. Also shown -2 and -5/3-slopes, 10^5 samples.

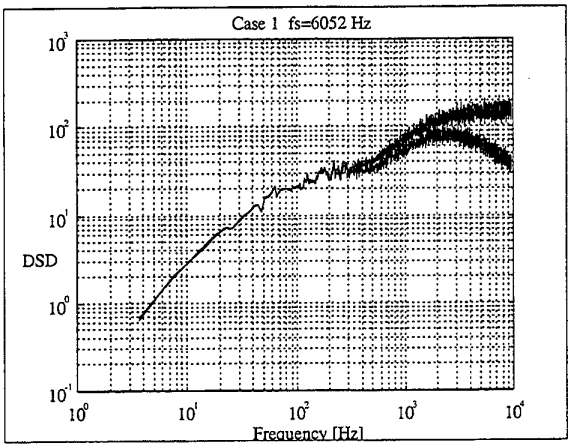


Figure 2: Dissipation spectrum for Case 1, lower curve with linear interpolation, 10^5 samples.

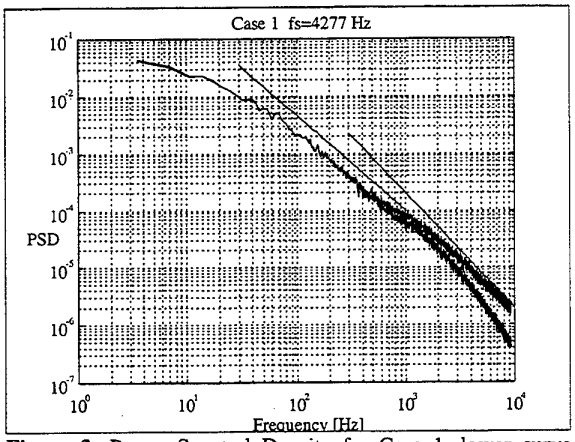


Figure 3: Power Spectral Density for Case 1, lower curve with linear interpolation. Also shown -2 and -5/3-slopes, 10^6 samples.

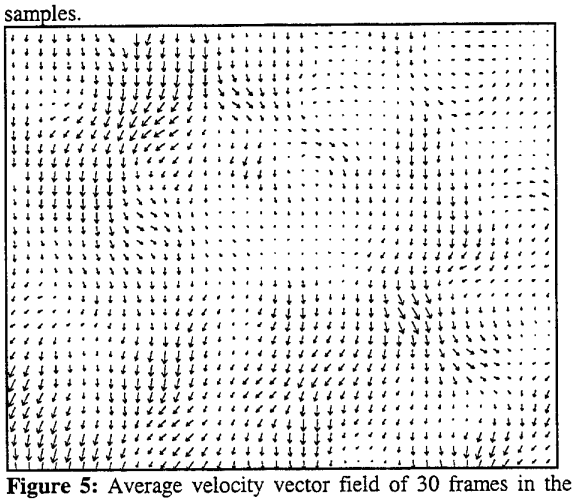


Figure 5: Average velocity vector field of 30 frames in the flocculator. 16x16 pixel interrogation area.

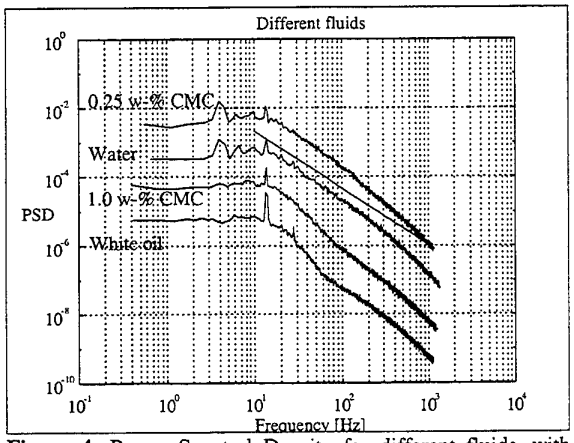


Figure 4: Power Spectral Density for different fluids, with linear interpolation. Top curve shifted a decade upwards, two bottom curves one decade down from above. Also shown -5/3-slope. 10^5 samples.

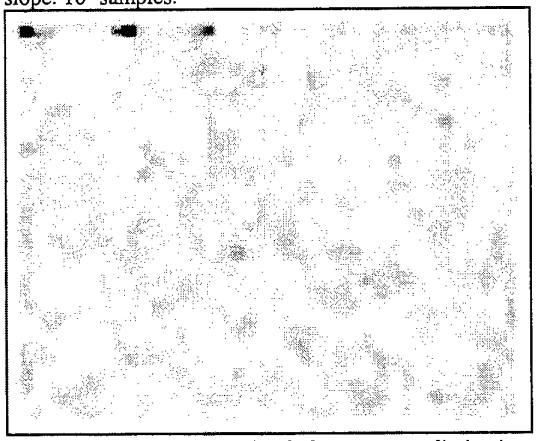


Figure 6.: Intensity map of turbulence energy dissipation rate. Low dissipation rate values denoted by light spots.

Table 1: PIV results for turbulence energy dissipation rate. Subscribt I is for isotropic turbulence estimate

Case	$\overline{U}$-mean [m/s]	$\overline{V}$-mean [m/s]	$\overline{U}$-max [m/s]	$\overline{V}$-max [m/s]	$\overline{u'}$ [m/s]	$\overline{v'}$ [m/s]	$\overline{\varepsilon}$-mean [m^2/s^3]	ε-max [m^2/s^3]	$\overline{\varepsilon'}$ [m^2/s^3]	$\overline{\varepsilon_I}$-mean [m^2/s^3]	ε_I-max [m^2/s^3]	$\overline{\varepsilon_I'}$ [m^2/s^3]
8×8	0.05	0.05	0.132	0.131	0.02	0.02	1.7	5.4	0.45	3.3	15.3	1.2
16×16	0.02	0.02	0.122	0.138	0.02	0.03	5.6	21.6	1.8	10.7	36.7	4.3
32×32	-0.003	0.08	0.166	0.139	0.05	0.06	6.4	23.0	2.5	10.8	46.6	5.1

3.3 Other turbulence energy dissipation rate estimation methods

Since the exact determination of the local turbulence energy dissipation rate is by measurements difficult, several methods of estimating the local dissipation rate have been applied to stirred tank flow fields.

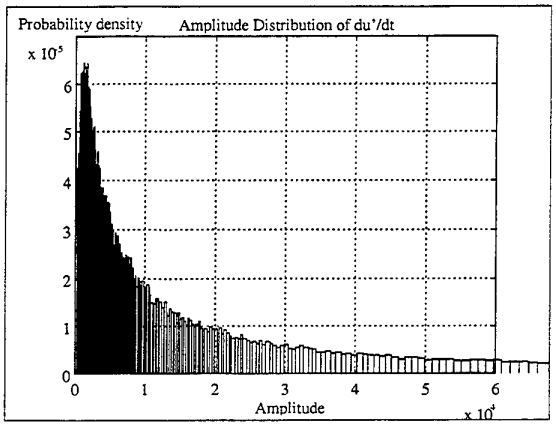


Figure 7: Probability density function of velocity time derivative. Calculated from preprosessed data.

Elsner et al. 1996 describe in their paper difficulties to measure and estimate the turbulence energy dissipation rate especially combined with the hot wire anemometer measurements. They recommend the use of the already presented equation (3) in its different forms and give some other equations which could be used for stirred tank measurements. In equation (3) the spatial derivatives are impossible to obtain by LDA without special optical arrangements. By using the Taylor's frozen turbulence hypothesis one can transform the isotropic equation (3) to the formula

$$\varepsilon = 15\nu\overline{(\frac{\partial u_1}{\partial x_1})^2} = \frac{15\nu}{\overline{U_1^2}}\overline{(\frac{\partial u_1}{\partial t})^2} \qquad (7)$$

Elsner et al. 1996 point out that the application of this equation is not straightforward, one has to consider the accuracy of differentiation of the $u_1(t)$ signal and the use of the stream wise mean velocity component U_1 as a convection velocity. Figure 7 shows the probability density of the instantaneous time derivatives for stream wise velocity fluctuations in a stirred vessel. There exist huge variations in the derivatives caused by 'outliers'. The time derivative has to be estimated carefully. Elsner et al. 1996 also recommends the use of the equation (4) because its results can be verified by equation

$$\int_0^\infty E_1(k)dk = \overline{u_1^2}. \qquad (8)$$

According Elsner et al. 1996 the turbulence energy dissipation rate may also be calculated from the energy spectrum in its inertial subrange

$$\varepsilon = \left[\frac{E_1(k)_{in}(k)_{in}^{3/5}}{\alpha_1}\right]^{3/2} \qquad (9)$$

where $(k)_{in}$ is an arbitrary value of k taken from the -5/3 wave number range. For the 'universal' constant α_1 a recommended value lies within relatively wide limit α_1 =0.45...0.57. This equation is applicable in flows of sufficiently large Reynolds number, which provoke the existence of the inertial subrange in the turbulence energy spectrum. The substantial advantage of this equation is the relative moderate wave number range up to which the spectrum has to be measured.

Cutter 1966 derived the following equation for the turbulence energy dissipation rate estimation

$$2\pi r\int_{-\infty}^{\infty}\varepsilon dz = \frac{d}{dr}\left[r2\pi\int_0^\infty\left(K^2\overline{V_z} + 2\overline{V_\theta v_r v_\theta}\right)dz\right] \qquad (10)$$

where $K^2 = \overline{V_z^2} + \overline{V_r^2} + \overline{V_\theta^2} + \overline{v_z^2} + \overline{v_r^2} + \overline{v_\theta^2}$.

Okamoto et al. 1981 integrated equation (4) for the one dimensional energy spectrum to measure the turbulence energy dissipation rate. They used a hot-film anemometer.

Costes and Coudrec 1988 measured with LDA the energy spectrum in a tank and calculated the local turbulence energy dissipation rate with equation (4).

Wu and Patterson 1989 used LDA to measure Rushton turbine flow field. They estimated the local turbulence energy dissipation rate with equation

$$\varepsilon = A\left(\frac{q^{\frac{3}{2}}}{L_{res}}\right) \qquad (11)$$

where q is the turbulent kinetic energy and L_{res} is a three dimensional resultant macro length scale. The coefficient A had a value of 0.85.

Zhou and Kresta 1996 measured the turbulence energy dissipation rate using LDA for four different impellers. They used a same form equation as Wu and Patterson 1989 to estimate the turbulence energy dissipation rate .

$$\varepsilon = A\frac{v^3}{L} \qquad (12)$$

Coefficient A had a value 1 and L was equal to D/10. The stream wise component of the fluctuating velocity is v.

Ducoste et al. 1997 measured with LDA the turbulent flow field in a flocculator for two impellers. They used a variation of equation (11). Instead of turbulent kinetic energy they calculated a mean velocity fluctuation in a new co-ordinate system, where the Taylor's frozen turbulence

hypothesis holds. They rotated the co-ordinates in every measurement point so that they found the one dimensional mean flow field. For the length scale they used a autocorrelation coefficient function in new co-ordinates and by integrating it they got a macro length scale L. Coefficient A had a value of 1.

Yianneskis et al. 1987 used an equation developed in conjunction with the k-ε -model used in CFD. This method requires the time mean measurement of turbulent kinetic energy q, Reynold's stress u_iu_j and the velocity gradient of the mean flow.

$$\varepsilon = -\frac{0.09q^2}{\overline{u_i u_j}} \frac{\partial \overline{U_i}}{\partial x_j} \quad (5)$$

3.4 Taylor's frozen turbulence hypothesis, pseudo turbulence and corrections

The need to use the Taylor's hypothesis arises, when spatial variation of the signal must be deduced from the time varying signal. The use of Taylor's frozen turbulence hypothesis has been criticised strongly in many papers (see e.g. Southerland et al. 1995). The hypothesis assumes that in low turbulence intensity flows all the vortex structure is convected downstream with the mean flow velocity U_1. It is proven that the small-scale motion is convected downstream faster than the large, energy containing eddies. The convection velocity U_{con} is always somewhat higher than the mean velocity U_1. Lumley 1965 gives a correction formula for the inertial subrange

$$\overline{U_{con}} = \overline{U_1}\left(1 - \frac{11}{3}\frac{\overline{u_2^2}}{\overline{U^2}}\right)^{-1} \quad (14)$$

Kresta at al. 1993 have reviewed several correction formulas found in literature. A correction for three dimensional highly turbulent flows can be calculated from the equation

$$\overline{U_{con}^2} = \overline{U_1^2}\left[1 + 2\frac{\overline{U_2^2}}{\overline{U_1^2}} + 2\frac{\overline{U_3^2}}{\overline{U_1^2}} + \frac{\overline{u_1^2}}{\overline{U_1^2}} + 2\frac{\overline{u_2^2}}{\overline{U_1^2}} + 2\frac{\overline{u_3^2}}{\overline{U_1^2}}\right] \quad (15)$$

If U_2=U_3~0 and the turbulence intensities are nearly equal, former expression can be reduced to

$$\overline{U_{con}^2} = \overline{U_1^2}\left[1 + 5\frac{\overline{u_1^2}}{\overline{U_1^2}}\right] \quad (16)$$

Kresta at al. 1993 still give one further estimation equation for the convection velocity

$$\overline{U_{con}^2} = \overline{U_1^2} + \overline{u_1^2} + 2\overline{u_2^2} + 2\overline{u_3^2} \quad (17)$$

Measurements in the stirred tanks are mostly made with 2D-LDA systems. This restricts the usefulness of the different dissipation rate estimation methods which use different kinds of the convection velocity approximations. The comparison of the convection velocity approximations show no benefits to justify their use. Pseudo-turbulence is considered in some papers (Elsner et al. 1996, Wu and Patterson 1989). It is difficult to make difference between coherent structures and the periodic

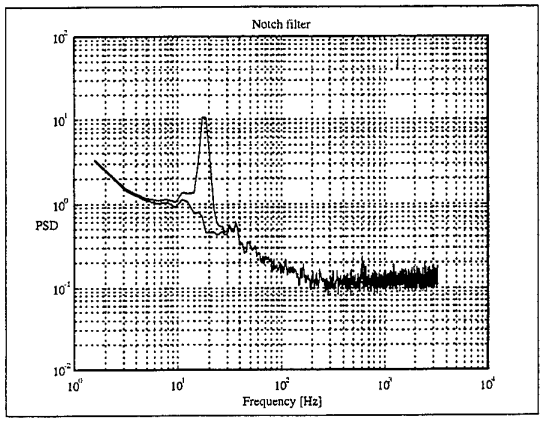


Figure 8: Peak elimination with notch-filter.

fluctuations formed in the impeller stream in a stirred vessel. In the near field of the impeller they can be clearly recognised in the spectrum of the turbulence (see figures 4 and 8). However in the propeller stream the peak is smeared quickly. In every case one must cut a narrow band of frequencies around the desired pseudo-turbulence peak. We used a notch-filter to eliminate the peak. The LDA-time series was first made evenly spaced with the sample and hold method. The results are shown in Figure 8. The arbitrariness of the width of the peak and the increase of the noise resulting from the filtering, makes the usefulness of the method doubtful.

Lumley 1965 suggest corrections to the measured dissipation rate value for high turbulence levels. Two dimensional measurement is recommended for use in following equation for correction

$$\varepsilon_{meas} = \varepsilon_{corr}(1 + 5\overline{u_2^2}/\overline{U^2}) \quad (18)$$

Elsner et al. 1996 also recommended another correction equation, which takes into account the tridimensionality of the turbulence.

$$\varepsilon = \varepsilon_{corr}\left[1 + \overline{u_1^2}/\overline{U^2} + (\overline{u_2^2} + \overline{u_3^2})/\overline{U^2}\right] \quad (19)$$

4. Conclusions

There exist many possibilities to estimate the turbulence energy dissipation rate. The difficulties in the dissipation rate estimation from LDA measurements are based on the low data rates obtained in the stirred vessel measurements. Estimation of the PSD for the turbulent kinetic energy seems to be impossible for high frequencies with the linear interpolation sample and hold procedure. Therefore to this estimation methods inherent increase of noise due to the sampling process prevents its use above the frequencies the sampling frequency divided by 2π. The low data rate is caused mainly from the long light path in the seeded flow medium. In the liquid flows the data rate remains low in spite of improvements in the model construction. The evaluation of the different dissipation rate estimates in the different measured cases shows that the direct calculation of the dissipation rate from the equation (1) or (2) is hardly ever possible. At best circumstances, when the fluid is air, their use is reasonable. The remaining question is, which of

the other approximations is most efficient for practical use. The comparison shows that the use of the equation (11) is most convenient for all cases. The use of the equation (12) is recommended in the bulk flow of the tank, where the turbulence is decaying. The equation (9) could be useful if the PSD spectrum estimation reaches the inertial subrange. The use of the time derivative equation (7) is difficult because the observed large variation of the derivative estimates. The elimination of the pseudo-turbulence is considered doubtful because of the arbitrariness of the frequency band estimation and the physical meaning of the remaining turbulence. The Particle Image Velocimetry gives promising results for the direct dissipation rate estimation, but it needs further examination.

References

Adrian R. J., Yao C. S. 1987, Power spectra of fluid velocities measured by laser Doppler velocimetry, Experiments in Fluids, Vol. 5 pp. 17-28.

Benedict L.H., Gould R. D. 1998, Concerning time and length scale estimates made from burst mode LDA autocorrelation measurements, Experiments in Fluids, Vol. 24, pp.246-253.

Costes J. , Coudrec J. P. 1988, Study by laser anemometry of the turbulent flow induced by a Rushton turbine in a stirred tank: Influence of the size of the units. Chemical Engineering Science, Vol. 43 No 10, pp. 2765-2772.

Cutter L. A. 1966, Flow and turbulence in a stirred tank, AICHE J. , Vol. 12, pp. 35-45.

Dahm W. J. A., Southerland K. B., Buch K. A., 1991, Direct high resolution, four dimensional measurements of the fine scale structure of Sc>>1 molecular mixing in turbulent flows, Phys. Fluids A. Vol. 5 No. 3, pp. 1115-1112.

Ducoste J. J., Clark M. M. 1997, Turbulence in Flocculators: Effects of Tank Size and Impeller Type, AIChE Journal, Vol. 43, No. 2, pp. 328-338.

Elsner J. W., Elsner W. 1996, On the measurement of turbulence energy dissipation, Meas. Sci. Technol., Vol. 7, pp. 1334-1348.

Guenkel A. A., Weber M. E. 1975, Flow Phenomena in Stirred Tanks, AIChE Journal, Vol. 21, No. 5, pp. 931-949.

Hinze J. O., Turbulence, McGraw-Hill, **1975**.

Hoest-Madsen A., Caspersen Chr., 1994, The Limitations in High Frequency Turbulence Spectrum Estimation using the Laser Doppler Anemometer, Proc. 7. Int. Symp. On Appl. of Laser Techn. To Fluid Mechanics, Vol. 1, Lisbon.

Ihalainen H., Kaleva O., Saarenrinne P., Soini S.,1995, Estimation of spectral power density of turbulence for flow field with Laser Doppler Velocimetry, Proc. for the Nordic Matlab conference '95, Stockholm.

Kresta S., Wood P. E., 1993, The flow field produced by a pitched blade turbine: Characterization of the turbulence and estimation of the dissipation rate, Chemical Engineering Science, Vol. 48, No. 10, pp. 1761-1774.

Lumley J. L., 1965, Interpretation of time spectra in high intensity shear flows, Phys. Fluids, Vol. 8, pp. 1056-1062.

Okamoto Y. , Nishikawa N., Hashimoto K., 1981, Energy dissipation rate distribution in mixing vessels and its effects on liquid-liquid dispersion and solid-liquid mass transfer. Int. Chem. Engng., Vol. 21, pp. 88-94.

Yianneskis M., Popiolek Z., Whitelaw J. H. 1987, An experimental study of the steady and unsteady flow characteristics of stirred reactors, J. Fluid Mech., Vol. 175, pp. 537-555.

Wu H., Patterson G. K. 1989, Laser-Doppler measurements of turbulent-flow parameters in a stirred mixer, Chemical Engineering Science, Vol. 44, No., pp. 2207-2221.

Zhou G., Kresta S. M. 1996, Impact of Tank Geometry on the Maximum Turbulence Energy Dissipation Rate for Impellers, AIChE Journal, Vol. 42, No. 9, pp. 2476-2490.

Appendix A: Experimental arrangements

MEASUREMENT DEVICES:

Laser Doppler Anemometer (DANTEC Measurement Technology A/S)

-2-D fiber optic
-PDA-processor
-measurement volume Ø75x640 μm^3
-Ar-Ion-laser (SP 164)

Particle Image Velocimeter (LaVision 2D-Messtechnik GmbH)

-CCD-camera 1280x1024 pixels
-6.7x6.7 μm^2 pixel size
-8 frames/s, Peltier cooled
-light arm, sheet optics
-Nd-YAG-laser (SP PIV400)

Stirred vessels:

Flocculator
-Ø 90mm, height 180 mm
-Borosilicate glass cylinder (n=1.47)

Mixing tank 1
-Ø 250mm, height 450 mm
-FEP cylinder

Mixing tank 2
-Ø 480mm, height 600 mm
-Plexiglass cylinder

Used Fluids:

Case	Fluid	Kinematic viscosity	Data validation rate
1	Air	1E-5	3...6 kHz
2	Water	1E-6	1082 Hz
3	CMC 1%		660 Hz
4	CMC 0.25%		912 Hz
5	White Oil	40E-6	690 Hz

SYNCHRONISED LDA AND INTERFACIAL WAVE HEIGHT AND ENTRAINMENT MEASUREMENTS IN A MODEL OF A CONTINUOUS CASTING MOULD

M. Keicher, H. Morikita* & A. M. K. P. Taylor

Mechanical Engineering Department, Imperial College of Science Technology and Medicine
Exhibition Road, London SW7 2BX, UK
*Mechanical Engineering Department, University of Tokyo
7-3-1 Hongo, Bunkyo-ku, Tokyo 113 - 8656 Japan

ABSTRACT

Eighth-scale experiments in a mould of a width of L = 23 cm simulating the continuous casting process in steel production were conducted. Water was employed as a molten steel simulant and was injected via a 'submerged entry nozzle (SEN)' into the mould where the floating semi-molten slag layer was simulated by a layer of olive oil. The flow in the mould was fully turbulent and showed transient behaviour, such as internal waves at the water/oil meniscus. The flow to each of the two nozzle ports was metered independently and the jet Reynolds numbers ranged from 10 000 to 17 500; the associated Froude numbers were from 2.58 to 4.70. A recently developed digital imaging system was applied in order to quantify instantaneous, h, and hence mean and rms internal wave heights which were complemented by laser-Doppler anemometer measurements to simultaneously obtain the associated instantaneous horizontal water (analogous to steel) velocity component, called the wave pushing velocity, u_S, just upstream of an internal wave trough. Conditions which induced the start of entrainment of the floating oil layer into the water were identified and a forced asymmetric inflow, with a ratio of bulk velocities in the two feed pipes of the nozzle of 5:7, resulted in a stabler wave shape (i. e. smaller rms wave height) in the mould and reduced the number of entrainment events per unit time by 25 % as compared to the symmetric inflow. For positions close to the narrow sidewalls, waveheight autocorrelations revealed a periodicity in waveheights of about three seconds with an integral time scale which was of the order of magnitude of one second; the wave pushing velocity autocorrelation was zero for correlation times longer than 0.1 seconds and h~u_S-cross-correlations showed that the timescales and the periodicity of the considered variables were decoupled. To identify the propensity of entrainment, previous results which presented interfacial characteristics as a function of bulk velocity in the two feed pipes of the nozzle, $v_{b,\,pipe}$, ($1.1\ m/s \le v_{b,\,pipe} \le 1.9\ m/s$) and its immersion depth, ID, ($0.22 \le ID/L \le 0.48$) were expanded. The improved criterion now incorporates the overall Froude number as well as the Weber number, $We = \rho u_S^2 h/\sigma$, which was based upon *instantaneous* wave heights and associated *simultaneously* obtained wave pushing velocities. It is proposed that slag entrainment occurs above the trendline $Fr = -0.33\ We + 7$. This criterion takes account of the considered scale of the model of the mould.

1. INTRODUCTION

In the continuous casting process in steel production, the liquid steel is injected through a nozzle which is immersed into the mould and below the interface formed by the floating semi-molten layer of slag. The flow of molten steel within the mould is fully turbulent and the characteristic flow pattern consists of two pairs of vortices - one above the exit of the submerged entry nozzle and one below - on either side of the vertical symmetry plane, see Figure 1. Their transient motion, in particular of the vortex pair near the surface, induce unsteady internal waves at the steel meniscus between the denser steel and the lighter slag. In production, the casting speed is limited in part by the fact that these waves ultimately become sufficiently strong to result in the intermittent entrainment of the slag into the steel which leads to undesirable inclusions in the final product. These must be minimised. The interfacial wave heights, and thus the onset of entrainment in

the mould, depend on the transient motion of particularly the upper vortex pair and its strength, which can be controlled by changing the flow rate in or the immersion depth of the feed pipe of the entry nozzle.

In physical modelling it has become customary to use water as a molten steel simulant, since their kinematic viscosities ν are of the same order of magnitude, and free surface fluctuations - introduced by the flow pattern below it - were studied and quantified by means of a capacitance pressure sensor, Andrzejewski (1992) *et al.*, to recommend optimum operating conditions in terms of casting rate and immersion depth for selected flow configurations. The mean wave height increased with lowering the immersion depth which also resulted in a decrease of the size of the upper vortices, Gupta and Lahiri (1994). Low buoyancy particles or liquids floating on top of water were employed to simulate the slag layer, e. g. Iguchi (1995) *et al.*, and Gupta and Lahiri (1996) stated that the internal wave amplitude was independent of both the thickness and the viscosity of the upper liquid and that the dimensionless wave amplitude was linearly related to the (modified) Froude number, $Fr_m = (V^2/gL_C)(\rho_W/\rho_W - \rho_o)$, where V is the nozzle exit velocity of the fluid, g is the gravitational acceleration, L_C represents the effect of different immersion depths, and ρ_W, ρ_o denote the density of water and the floating oil layer respectively.

Modelling of the entrainment phenomenon has considered the instability between two co-flowing stratified layers with a velocity difference across the interface for which the primary mechanism are Kelvin-Helmholtz waves, e.g. Zalosh (1976), Xiao *et al.* (1987) or Cramb and Feldbauer (1995). They identified a critical velocity difference of about 0.4 m/s (depending on fluid properties) in the horizontal direction between the two initially parallel flows for detecting the onset of a growing instability which was held to lead, ultimately, to the formation of slag globules which might lead to inclusions in the final product. However, it is unclear how relevant their findings are to a flow in which there is a large mean waveheight structure due to the presence of a vortex below the interface, Keicher (1998) and Keicher and Taylor (1998). The quantification of interfacial characteristics in an *eighth* scale mould, Christoyannis *et al.* (1998), were expanded by Keicher and Taylor (1997) who complemented this wave height measurement technique in a *quarter* scale mould with laser-Doppler measurements to simultaneously determine the associated horizontal velocity component, u_S, just upstream of an internal wave trough. In addition, Keicher (1998) found that although the model geometry and supplied flow rates were nominally symmetrical, the flow pattern was not and seemed to be bistable. The bistability was associated with the interface on one half of the vertical symmetry plane being more-or-less flat and that on the other side becoming progressively distorted, leading to intermittent entrainment eventually, before dying away. Then, the previously flat side started to distort with the previously distorted becoming calm. These transient effects promoted entrainment and as a consequence, Keicher and Taylor (1997) suggested a critical dimensionless Weber number $We_C = \rho u_S^2 h/\sigma$, of about 21, above which slag entrainment will occur {where ρ is the density of the slag, u_S is the instantaneous horizontal component of velocity in the molten steel below the interface, h is the instantaneous height of the interfacial wave and σ is the surface tension between the two liquids}. This paper is the continuation of previous work and its purposes are: (a) to simultaneously quantify velocities beneath the steel meniscus and the related interfacial wave heights in the *eighth* scale water/olive oil mould model, (b) to introduce a recently developed and faster CCD-camera-based wave height measurement technique, (c) to investigate whether a forced asymmetric inflow reduces transient effects, here in particular respect to the effects on the interfacial characteristics, and the related event of entrainment, and (d) to find the extent to which the velocity field is associated with the interfacial profile by calculating wave height and velocity auto-, and cross-correlations. The aim of research is to identify a criterion which quantifies the onset of entrainment of the floating slag layer into the lower molten steel.

The following section is concerned with the flow configuration and experimental techniques. The results are then presented and discussed, and conclusions are given in the final section.

2. FLOW CONFIGURATION AND EXPERIMENTAL TECHNIQUE

2.1 Flow Configuration

The present eighth scale configuration was based upon the dimensions of physical moulds at British Steel plc in order to aid comparisons and the interpretation of gained data. A schematic of the

flow facility is shown in Figure 1. Water was circulated, driven by a centrifugal pump, between the storage sump, where a cooling circuit was incorporated to maintain constant water temperature, and the transparent Perspex model of the mould, thus allowing optical access. It was 230 mm in width, L, had a depth, W, of 30 mm, i.e. normal to the plane of the paper, and a height, H, of 345 mm. In order to promote a uniform outflow at the bottom of the test section, a stainless steel baffle plate with 112 holes of diameter 5 mm was installed, with the holes distributed uniformly (4 by 28) across the cross-section. Water was injected through a brass model of a submerged entry nozzle (SEN) into the mould and the fluid inlet was about 80 inner diameters, D = 9 mm, of the stainless feed pipe above the nozzle exit in order to assure a fully developed flow just upstream of the nozzle to assist future numerical simulation of the flow using CFD. The two outlet ports of the nozzle were identical, within manufacturing tolerance, and 180 degrees apart, machined with a circular cross-section of 9 mm diameter and with the ports' axes inclined at 20 degrees below the horizontal.

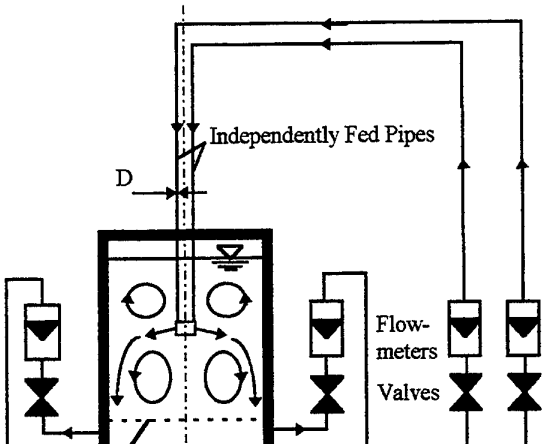


Figure 1: Schematic of the flow facility.

The immersion depth of the nozzle (ID) was defined as the distance from the meniscus to the top of the nozzle port and the casting rate was simulated by varying the water flow rate by controlling the volume flow rate through the flowmeter in the feed pipe. Each flow rate of the two nozzle exits was metered individually to be able to create and control deliberately asymmetric flow patterns in the mould which were characterised by a strong jet flow which impinged on the 'narrow' wall and then split into two wall jets which formed the upper and lower recirculation zones. The two exit pipes, connecting the mould with the storage tank, were equipped with one flowmeter each and the flows were adjusted to be the same in each. A layer of olive oil of 2 cm thickness was employed as a slag simulant as it is immiscible with, and lighter than, water, easy to procure, easy to dispose of, and causes no damage to the Perspex mould model. This led to a density ratio of $\rho_{slag}/\rho_{steel} = 0.92$ in comparison with 0.43 in the real plant thus, due to the greater ratio, permitting waves with higher amplitudes at the interface to be generated at a greater Froude number. To accomplish steady flow conditions, the entire system had to be free of air bubbles, which was achieved by using a running time of 1.5 hours before starting measurements.

In a typical steel production plant the bulk velocity in the feed pipe, $v_{b,\,pipe}$, is ranging from 0.9 to 1.56 m/s which corresponds to a range of jet Reynolds numbers leaving each nozzle port between 42 000 and 70 000 where the port cross-section diameter represents the characteristic length. In order to ensure a turbulent flow in the mould, the requirement for the scale down model was to achieve Reynolds numbers at each nozzle port greater than 10 000. Maintaining the ratio between the maximum and minimum bulk velocity in the real plant resulted in a velocity range of $1.1 \text{ m/s} \le v_{b,\,pipe} \le 1.9 \text{ m/s}$ for the eighth scale model. The overall Froude number, which is the ratio between momentum and buoyancy force and which characterises the mean interfacial wave shape, was defined as follows:

$$Fr = \frac{v_{b,pipe}}{\sqrt{(1-\frac{\rho_{slag}}{\rho_{steel}})gL}} \qquad (1)$$

which results in a range from 0.28 to 0.49 in the real plant and from 2.58 to 4.47 in the constructed model. The immersion depth (ID) of the submerged entry nozzle was normalised by the width of the mould and varied between $0.22 \le ID/L \le 0.48$ following values which represent appropriate immersion depths of the real plant and which also ensured the required bulk velocity range in the feed pipe without causing permanent entrainment of a floating olive oil layer into the water flow.

2.2 Measurement Technique and Uncertainties

The entire flow facility was enclosed in a dark room and one 150 W lamp was positioned at each of the two narrow sidewalls of the Perspex mould model to illuminate the flow which was then recorded by means of a digital image processing system. At the heart of the system was a black and white 25 Hz video frame rate CCD camera (HCS-MXR) in conjunction with a zoom lens (Nikon -AF Nikkor; 28 - 85 mm; 1:3.5-4.5) operated with an f-stop of 8 which relates to an intermediate aperture size. The camera was located perpendicular to the transparent mould model: a white background in form of a cardboard was provided. A monochrome and programmable Peripherical Component Interface (PCI) bus frame grabber board (DT3152) operated within a Pentium PC which transferred consecutive frames across the bus in real time up to the capacity of available system RAM (64 Mb). The typical image resolution was 768x512 pixels and in order to be able to transfer the acquired frames from the RAM onto the hard disk of the computer the maximum number of consecutive frames was limited to 80. Thus, the previous time consuming use of data processing based on images stored on a video tape was avoided. Another feature of the grabber board was an external trigger (see below) and thus selected images can be recorded which was achieved by means of a TTL trigger signal provided by a 20 MHz Function Generator (Datron-Wavetek Model 145). Any particular frame could be digitised into 256 (2^8) shades of grey, representing a brightness resolution. Finally, a sequence of images (up to 650 Mb) was written permanently onto CD via a Compact Disc Recorder (Plasmon CDR 480) for postprocessing and in order to free the hard disk of the PC. Figure 2 represents a typical frame of the observed flow pattern.

The algorithm for determining the interfacial wave heights was based upon the grey level contrasts observed by the camera between air, olive oil and water and in order to enhance the grey level contrasts between the 3 fluids, 37 ml black oil colour were dissolved in about 5 l of olive oil without changing any of its properties. For each frame, a digital Finite Impulse Response (FIR)-filter produced a 'binary' image, Press *et al.* (1992), to eliminate noise at low or high frequencies respectively. Every single frame was scanned, starting from the pixel in the top left corner, moving down along a vertical line and repeating this procedure by stepping one pixel in horizontal direction to the right. Each pixel of the binary image was compared with an adaptive threshold level in terms of contrast which was constant along vertical lines but varied according to the absolute light intensity in the horizontal direction above the oil layer. Thus, the number of pixels depicting the olive oil layer, as well as entrained olive oil globules and their location, could be identified and converted into interfacial wave heights where one pixel corresponded to 0.3 mm in the mould model. In order to determine mean and rms interfacial wave heights, typically thirteen sampled batches of 80 frames, i. e. in total 1040 frames, were considered.

The dual-beam laser-Doppler anemometer operated in forward scatter and made use of a 30 mW He-Ne laser at a wavelength of 632.8 nm, a diffraction grating and associated optics, and a custom-built frequency counter for the processing of the Doppler signals. Thus, horizontal (u) mean and rms velocity components, called wave pushing velocities, were measured at a position $x/(L/2) = 0.72$ and at a distance of about $y/(L/2) = 0.02$ below the calm meniscus according to the investigated immersion depth of the submerged entry nozzle, as indicated in Figure 2. Hence, the x-co-ordinate of the location for velocity measurements was constant for the investigated flow configurations and it was ensured that measurements were taken just upstream of the internal scar as suggested by Woodmansee and Hanratty (1967) to identify a critical condition above which entrainment occurs.

The synchronisation of interfacial wave height measurements and the record of the associated wave pushing velocity was realised by means of a bar-code number, seen in Figure 2, which was superimposed on the right top side of each video field, Sakakibara *et al.* (1993). Whilst the laser beam was turned on, a manual switch at the barcode generator device: (a) started to superimpose the bar-code number on each frame and thus indicated the reference time zero, (b) triggered the function generator (Datron-Wavetek Model 145) which then triggered the grabber board operating in the PC, and (c) triggered the custom built frequency counter of the laser-Doppler velocimeter and hence initiated time dependent velocity measurements starting at the reference time zero. The velocity measurements were sorted into temporal bins with duration of 1/25 s, and could then be referred to the corresponding frame identified by the inherent bar-code number.

Compared to previous work, the experimental technique described above reduced the processing time by a factor of 6 and removed

uncertainties in the method of synchronisation. More details concerning the instrumentation can be found in Keicher (1998), together with estimates of uncertainties of the measured quantities. In brief, the uncertainties associated with interfacial wave height measurements mainly originate from the non-uniform light intensity across the mould width and the accuracy in detecting the interfaces was ± 1 pixel. The overall accuracy in determining interfacial wave heights is thought to be about 2 % of the actual value and errors in measuring velocities were estimated to be less than 3 % of the bulk velocity.

3. RESULTS AND DISCUSSION

The interfacial characteristics as a function of a forced asymmetric inflow are shown in Figure 3 where (a) refers to normalised mean and (b) to normalised rms wave heights. Figures 4 to 6 show wave and velocity autocorrelations as well as the corresponding cross-correlation. Entrained olive oil globules were detected as described above and the propensity of olive oil entrainment is revealed in Figure 7 which is a scatter plot of entrainment results for the overall Froude number and the local Weber number of each measurement. The presented results build upon data obtained in the quarter and eighth scale model, Keicher and Taylor (1997) and Christoyannis *et al.* (1998). The normalised magnitude of internal mean wave heights and their rms values decreased with increasing casting speed and increasing immersion depth by about 0.1. More detailed results, including flow visualisation and velocity characteristics of the flow pattern in the mould models, are available in Keicher (1998).

In Figure 2, a representative video frame with a typical olive oil/water interface wave pattern can be seen together with the *flat* air/olive oil interface where, as indicated, the distance between two screws at the narrow sidewall amounted to 3.7 cm. Note the latter interface was always flat. For the description of the interfacial wave heights, the origin of the xy-co-ordinate system was situated on the symmetry plane of the mould at the calm meniscus. The unsteady distance between the air/olive oil and olive oil/water interfaces was defined as the instantaneous wave height, H, and to acquire the relative, i. e. with respect to the calm meniscus before water flow began, instantaneous wave height, h, the thickness of the olive oil layer was subtracted. Wave heights were determined at ten equidistant positions across the mould, every 1.73 cm, starting at ± 2.66 cm with respect to the symmetry axis of the mould, and shall be referred to as 'Pos - 5' to 'Pos 5'. For the presented results, distances in the horizontal (x) direction were normalised by half of the mould width, L/2, and wave heights by the velocity based head, $v^2_{b,\,pipe}/2g$. To distinguish between the bulk velocities in the two feed pipes, $v^+_{b,\,pipe}$ for the greater, and $v^-_{b,\,pipe}$ for the lower velocity are introduced; when the flows were equal, it shall be referred to as $v_{b,\,pipe}$.

With equal port flows, transient effects were observed and a cycle of events, such as the jet impingement point travelling up and down the vertical y-direction at the narrow side wall, was suggested, Keicher and Taylor (1998). As mentioned above, the combination of waves and flow might lead to intermittent - or eventually continuous - entrainment and these transient effects promote such entrainment events. With the current flow facility a forced asymmetric flow pattern in the tank was possible since each port of the feed pipe was metered independently. Figure 3 shows the effect of an asymmetric inflow at a normalised immersion depth of ID/L = 0.22, as compared to a symmetric inflow condition of bulk velocities in both feed pipes of 1.6 m/s (Fr = 3.7) - here, $v^+_{b,\,pipe}$ = 1.9 m/s (Fr = 4.5) was applied to the left of the nozzle and $v^-_{b,\,pipe}$ = 1.3 m/s (Fr = 3.0) to the right and vice versa, thus maintaining the overall casting rate of the initial symmetric inflow condition. It can be seen that the normalised mean wave height decreased on the side of the nozzle with the lower velocity, approximately by 0.05, and increased by about 0.02 on the side where the higher velocity was employed. For both forced asymmetric cases the normalised rms wave height decreased by about 0.015 which implies a stabilisation in the interfacial wave pattern. The higher velocity, $v^+_{b,\,pipe}$, resulted in a well defined circular upper vortex and a strong lower recirculation zone which expanded across the geometrical symmetry line. This led to an egg-shaped upper vortex to the side with the lower velocity, stretching across the plane of symmetry, Keicher (1998), and only at the position where the two upper recirculation zones turned downwards, was entrainment detected. This is in contrast to the symmetric inflow conditions where entrainment happened alternately on both sides of the nozzle. With a forced asymmetric inflow condition, the total number of entrainments per unit time was reduced by about 25 %.

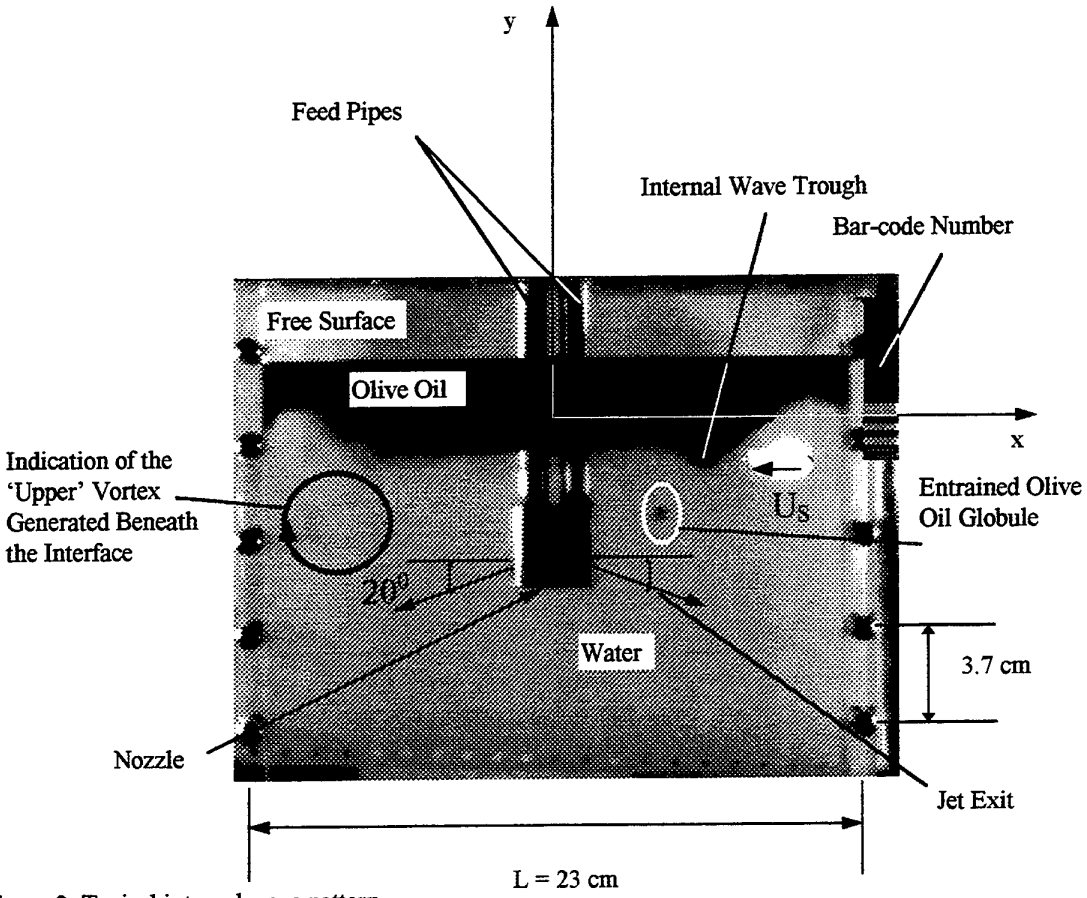
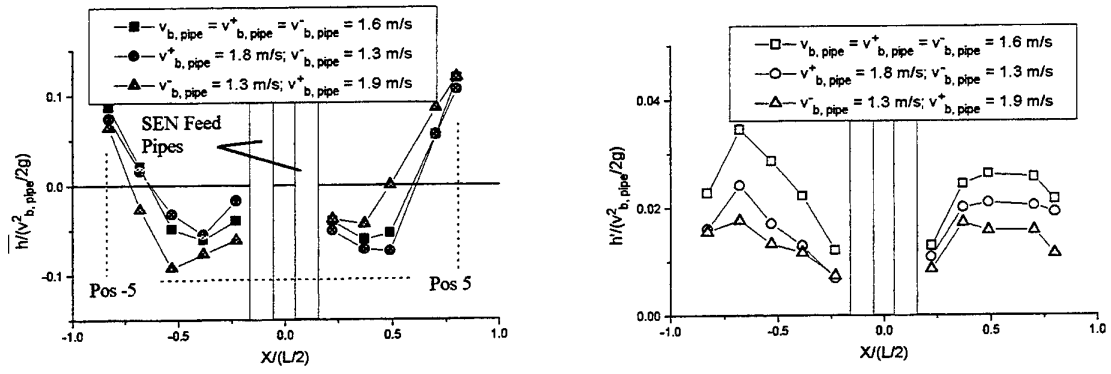


Figure 2: Typical internal wave pattern.



(a) (b)

Figure 3: Normalised mean and rms wave heights as a function of a forced asymmetric inflow (ID/L = 0.22).

In order to learn more about the flow close to the interface, wave as well as wave pushing velocity auto-, and the corresponding cross-correlations were calculated as follows, with a and b being surrogate symbols for u_S and h, measured at locations x_1 and x_2 respectively:

$$R_{a,b}(\tau) = \frac{\overline{a(x_1,t)b(x_2,t-\tau)}}{a'(x_1)b'(x_2)}, \qquad (2)$$

where

$$\overline{a(x_1,t)b(x_2,t-\tau)} =$$

$$\frac{\sum_{i=1}^{N}(a(x_1,t_i)-\overline{a(x_1)})(b(x_2,t_i-\tau)-\overline{b(x_2)})}{N} \qquad (3)$$

and

$$a'(x_1) = \sqrt{\frac{\sum_{i=1}^{N}(a(x_1,t_i)-\overline{a(x_1)})^2}{N}}. \qquad (4)$$

The overbar denotes mean values, the prime stands for rms values of the wave heights and N represents the total number of frames processed for each configuration which here amounted to 1040. Figure 4 shows representative wave height autocorrelations, $R_{h,h}(\tau)$, at two positions (Pos - 5 and Pos 4) for an inflow condition of $v_{b,\,pipe}$ = 1.1 m/s (Fr = 2.5) and a normalised immersion depth of ID/L = 0.22. The time lag was normalised by the characteristic time scale of the considered flow, T_{Flow}, which is taken as the ratio between the half mould width, L/2, and the applied casting speed. The casting speed was here defined as the volume flow rate of water through the mould (9 l/min to 15 l/min) divided by the cross-sectional area of the caster, namely 3*23 cm^2. This resulted in 5.3 s ≥ T_{Flow} ≥ 3.1 s. Position 'Pos - 5' (x/(L/2) = - 0.83) is close to the left narrow sidewall and was a weak periodic component of about three seconds with an integral time scale which is of the order of one second. In contrast, 'Pos 4' (x/(L/2) = 0.68) - close to the location of velocity measurements, see Section 2.2 - reveals a smaller periodic component, indeed close to zero, but with a comparable integral time scale. Wave pushing velocities were obtained at a vertical distance from the mean wave height of about y/(L/2) = 0.03 and sorted into temporal bins as described above. In Figure 5 a typical wave pushing velocity autocorrelation, $R_{u_S,u_S}(\tau)$, can be seen, indicating an integral timescale which is much less than a tenth of that of the wave height and with a complete lack of a periodic component. It was zero for correlation times longer than 0.1 seconds. A preliminary attempt was made to measure the cross-correlation between both variables, $R_{h,u_S}(\tau)$, and this is shown in Figure 6. The data is preliminary because the continuous length of velocity was restricted to forty seconds by the current software. So that, for example, the mean wave height recorded over forty seconds worth of data is different from the time mean value. Nevertheless, Figure 6 in conjunction with Figures 4 and 5 suggest that there is, perhaps somewhat surprisingly in view of the success of the relation presented in Figure 7 in the next paragraph, no clear correlation between wave pushing velocity and wave height. Certainly, the timescales and the periodicity governing the interfacial wave height and the flow velocity are decoupled.

Previously, a dimensionless local Weber number, $We_C = \rho u_S^2 h/\sigma$, of about 21 was proposed as the critical condition above which entrainment might happen, Keicher and Taylor (1997). This number is based upon instantaneous wave heights, h, and the associated simultaneously obtained instantaneous wave pushing velocity, u_S, in horizontal (x) direction upstream of the trough; ρ denotes the density of olive oil (918 kg/m^3) and σ is the surface tension between olive oil and water (0.02 N/m). Figure 7 illustrates the scatter plot of entrainment for each overall Froude number and the local Weber number as opposed to the number of entrainment events versus the local Weber number as in Keicher and Taylor (1997). It shows the number of entrainment events per observation time for the investigated flow configurations considered in this work and also includes some results from the quarter scale model, marked with a circle in Figure 7. A trendline, Fr = - 0.33 We + 7, was constructed and it is suggested that slag entrainment occurs above this line. This criterion takes account of the considered scale of the model of the mould.

4. CONCLUSIONS

This paper is the continuation of previous work studying the continuous casting process by means of eighth scale laboratory experiments simulating the mould by olive oil floating on water.

A recently developed multi point internal wave height measurement technique was introduced and results were complemented with simultaneously obtained wave pushing velocities just upstream of an internal trough. Measurements were taken for an asymmetric inflow condition and correlations for wave heights as well as associated wave pushing velocities were presented.

A forced asymmetric inflow with a ratio of bulk velocities in the two feed pipes 5:7 stabilised the flow pattern relative to symmetric inflow. For asymmetric inflow, olive oil entrainments only occurred to the side where the stronger bulk velocity was employed and the total number of entrainment events per unit time was reduced by 25 % as compared to a symmetric inflow.

The calculated correlations revealed a completely random behaviour for the wave pushing velocity. For positions close to the narrow sidewall, the wave height autocorrelations showed a weak periodic component of about three seconds with an integral time scale of about one second. The corresponding cross-correlations revealed that the periodicity and the timescales of the considered variables are decoupled.

To identify the propensity of entrainment previous results were expanded and an improved criterion developed. We now suggest that entrainment occurs above the trendline $Fr = -0.33\ We + 7$. The dimensionless Weber number, $We = \rho u_S^2 h/\sigma$, is based on instantaneous wave heights and associated simultaneously obtained wave pushing velocities. The advantage of the improved criterion is that it takes account of the considered scale of the model of the mould.

ACKNOWLEDGEMENTS

The authors are glad to acknowledge the support from the colleagues within the Thermofluids Section at Imperial College as well as from the British Steel Technical Teeside Laboratories, in particular Dr. R. J. Hawkins. Financial support was provided by the European Coal and Steel Community, ECSC, under the agreement number: 7210.CA/836 (C3.03d/94).

REFERENCES

Andrzejewski, P., Kohler, K.-U. & Pluschkell, W. 1992, Model Investigations on the Fluid Flow in Continuous Casting Moulds of Wide Dimensions, Steel Research, vol. 63 (6), pp. 242-246.

Christoyannis, J., Grispos, A., Keicher, M. & Taylor, A. M. K. P. 1998, Meniscus Level Measurements in a Model of Continuous Casting Moulds, Metallurgical and Materials Transactions B.

Cramb, A. W. & Feldbauer, S. 1995, Insights into Slag Entrainment in the Mould of a Continuous Caster, Proc. 13th PTD Conf., Nashville, TN, pp. 327-340.

Gupta, D. & Lahiri, A. K. 1994, Water-Modelling Study of the Surface Disturbances in Continuous Slab Caster, Metallurgical and Materials Transactions B, vol. 25B, pp. 227-233.

Gupta, D. & Lahiri, A. K. 1996, Cold Model Study of the Surface Profile in a Continuous Slab Casting Mould: Effect of Second Phase, Metallurgical and Materials Transactions B, vol. 27B, pp. 695-697.

Keicher, M. 1998, Study of Interfacial Waves in Continuous Casting Mould Models, Ph.D. thesis, University of London.

Keicher, M. & Taylor, A. M. K. P. 1997, Experimental Study of Internal Waves in the Stratified Shear Flow Between Two Immiscible Layers, Proc. 11th Symposium on Turbulent Shear Flows, Grenoble, vol. 2, pp. P2-13-P2-18.

Keicher, M. & Taylor, A. M. K. P. 1998, Visualisation in Models of Continuous Casting Moulds, Proc. 8th Int. Symposium on Flow Visualisation, Sorrento.

Press, W. H., Teukolsky, S. A., Vetterling, W. T. & Flannery, B. P. 1992, Fourier and Spectral Applications, in Numerical Recipes in C, 2nd ed., pp. 537-608, Cambridge University Press, Cambridge.

Sakakibara, J., Hishida, K. & Maeda, M. 1993, Measurements of Thermally Stratified Pipe-Flow Using Image Processing, Experiments in Fluids, vol. 16, pp. 82-96.

Woodmansee, D. E. & Hanratty, T. J. 1967, Mechanism for the Removal of Droplets from a

Liquid Surface by a Parallel Air Flow, Chem. Eng. Sci., vol. 24, pp. 299-307.

Xiao, Z., Peng, Y. & Liu, C. 1987, Modelling Study of the Entrapment Phenomena at the Slag-Metal Interface in the Gas-Stirred Ladle, Chin. J. Met. Sci. Technol., vol. 3, pp. 187-193.

Zalosh, R. G. 1976, Discretised Simulation of Vortex Sheet Evolution with Buoyancy and Surface Tension Effects, AIAA Journal, vol. 14, No. 11, pp 1517-1523.

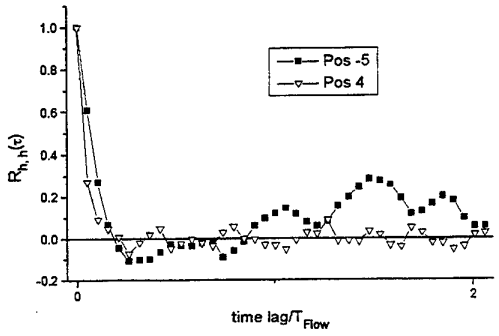


Figure 4: Wave height autocorrelation for two positions ($v_{b,\,pipe}$ = 1.1 m/s; Fr = 2.5; ID/L = 0.22).

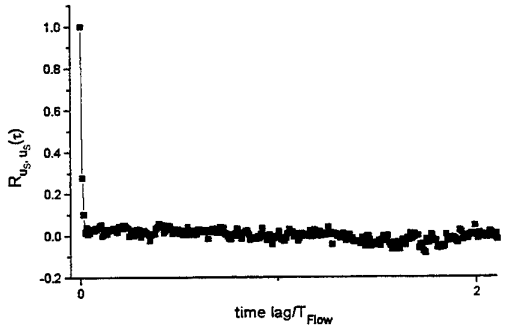


Figure 5: Wave pushing velocity autocorrelation ($v_{b,\,pipe}$ = 1.1 m/s; Fr = 2.5; ID/L = 0.22).

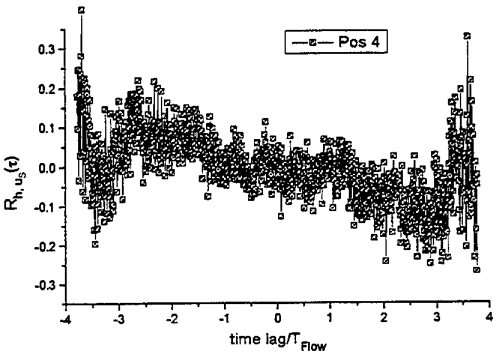
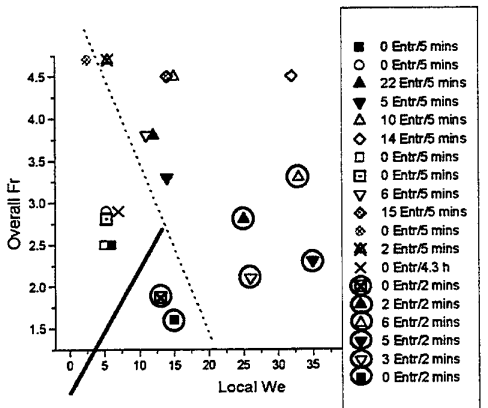


Figure 6: Cross-correlation between the wave height and the wave pushing velocity measured at $\Delta y/(L/2)$ = 0.02 below the calm interface ($v_{b,\,pipe}$ = 1.1 m/s; Fr = 2.5; ID/L = 0.22).



Trendline: Fr = - 0.33 We + 7

Figure 7: Overall Froude number versus local Weber number (○ : data from quarter scale model).

SESSION 15

LDV OPTICS 1

INVESTIGATION OF A TWO-COMPONENT LDA USING INTEGRATED OPTICAL DEVICES

C. Resagk, J. Grabow
Technische Universität Ilmenau, Fakultät für Maschinenbau,
Postfach 100565, D-98684 Ilmenau, Germany
S. Voigt
LITEF GmbH Freiburg, Lörracher Str. 18, D-79115 Freiburg, Germany

ABSTRACT

The use of a Y-fed balanced bridge modulator is suggested as a means to realise optical multiplexing in a dual beam laser Doppler anemometer (LDA). The resulting system measures two components of velocity but uses only one laser source, one integrated optical phase modulator for frequency shifting, one detector and one signal processing system. The laser, the modulator, the multiplexer and the probe are connected by single mode fibres.
In this paper a laboratory system is described and verification experiments to investigate the performance of the system are presented.

1. INTRODUCTION

A large number of integrated optical (IO) devices have been developed over recent years, most of which are used now in telecommunication applications. Many of these could potentially be used for laser Doppler anemometers (LDA) to decrease the size, the weight and the costs. Although several such systems have been proposed and demonstrated previously by Toda et al (1989), these have not found widespread use, perhaps due to the relatively low power levels admitted by the titanium diffused waveguides in Lithium Niobate ($LiNbO_3$) substrates. The more recent annealed proton exchange method of waveguides fabrication appears to be superior for high transmitted power levels reported by Rottschalk et al (1988).
A review of integrated optics in LDA applications by Pradel et al (1993) describes the fabrication of such devices and possible LDA topologies. IO devices for telecommunication are normally designed for use at a wavelengths of 1300 and 1500 nm, but are available for 800 nm as well. For this reason, laser diodes and avalanche photodiodes (APD) are particularly well suited for LDA systems incorporating IO devices. In recent investigations of IO-LDA by Resagk et al (1995) a Y-fed balanced bridge has been employed for time-division multiplexing of one beam in a dual beam LDA. A additionally IO phase modulator on the Y-fed balanced bridge chip has been tested for frequency shifting the Doppler signal by Resagk et al (1996) one year later. Similarly, the coupling into and out of the IO devices is best performed using single mode, polarization preserving glass fibres and fibre couplers or an IO beam splitter in connection with a pigtailed laser diode.
In the following work, a pigtailed laser diode, a IO-Y-junction with phase modulator and a Y-fed balanced bridge have been employed for a 2D-IO-LDA using time-division multiplexing of one beam. The system has been tested using a rotating wire.

2. CHARACTERISTICS OF THE IO DEVICES

The schematic diagrams of the Y-junction with phase modulator and the Y-fed balanced bridge are shown in the block diagram of the LDA system (Fig. 1). Both devices are fabricated on x-cut material ($LiNbO_3$ substrates) using the annealed proton exchange process. The phase modulator is a commercial product available from LITEF GmbH Freiburg (LITEF Analog-MIOC). The specifications of this device can be seen in Table 1. The phase modulator includes a Y-junction to split the incoming laser beam. A RF voltage was applied to the electrodes to control the phase shift.
The Y-fed balanced bridge is also a commercial product of United Technologies Photonics Inc. (APE FYBBM-0.8-0.6-00-02). It was controlled using a bias and an RF voltage. Table 2 shows the characteristics of the bridge.
The input power of both devices is limited by 5 mW. Above this optical power limit the light-induced refractive-index changes in the waveguide reported by Steinberg et al (1995) cause a rapid decrease of the modulation depth of the Doppler burst, resulting from a disappearing fringe pattern in the measurement volume.
Alternative materials for guiding higher optical power at a wavelength of 800 nm are MgO doped $LiNbO_3$ with at least 5 Mol% MgO in the melt and $LiTaO_3$.

Table 1. Specifications of the phase modulator.

Parameter	
Pigtailed, excess loss (dB)	3.5
Y-junction, power split ratio	47:53
Polarization extinction ratio (dB)	60
Half wave-voltage (V)	4.9
Residual intensity modulation (dB)	30

Table 2. Specification of the Y-fed balanced bridge.

Parameter	
Insertion loss (dB)	3.8
RF half-wave voltage (V)	1.4
Bias half-wave voltage	2.1
On/off extinction (dB) Output 1 Output 2	 22.2 35.3
Bandwidth (GHz)	0.9

3. LASER DOPPLER ANEMOMETER

The laboratory LDA system is pictured in Figure 1. The pigtailed laser diode operates at 790 nm. This was followed by the IO beamsplitter (Y-junction) and the IO phase modulator. The phase modulator operates at 100 kHz up to 10 MHz with a low power triangular wave signal, resulting in an effective shift frequency in the same range.

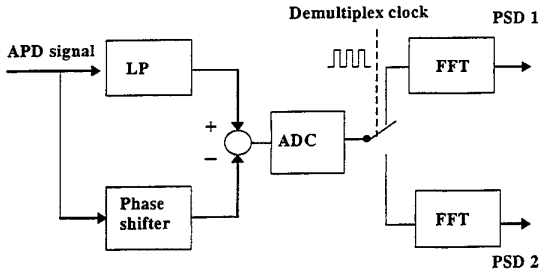


Figure 2. Block diagram of signal processor

The two resulting beams were coupled into two single mode, polarization preserving fibres, one of which was attached to the Y-fed balanced bridge, and the other leading directly to the three-beam probe. The scattering light from particles in the measurement volume was collected in backscatter through the front lens of the probe and focused onto a graded index fibre, which led

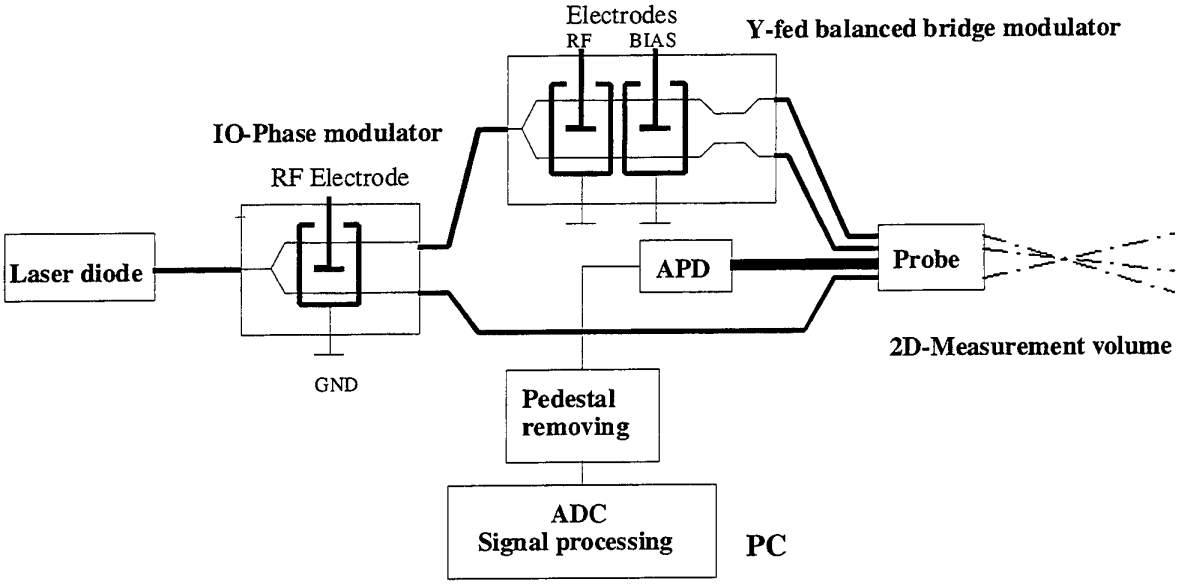


Figure 1. Block diagram of LDA system

back to an avalanche photodiode (APD). By switching the light path at the bridge modulator, one of two orthogonal measurement volumes could be activated.
The switching was performed in the present experiments with a square wave signal up to 50 MHz. Thus the signal at the APD contained information about two velocity components, multiplexed in time. Assuming a minimum required sampling rate of two samples per period, the 50 MHz multiplexing would be sufficient to detect Doppler frequencies of 25 MHz. For the resent purpose the APD signal was digitised using a fast analogue-to-digital conversion (ADC). The output clock frequency (100 MHz) of the ADC board is used to acquire the modulation signal of the Y-fed balanced bridge. It was necessary to reduce this frequency, and hence a frequency divider is inserted in the system.

All components of the IO-LDA system have been connected with optical fibres without fibre connectors. High optical stability, easy adjustment and low insertion loss are the results of this arrangement. Normally a band pass filter is used between the APD and the ADC board to remove the pedestal portion of the received signal. Some difficulties due to the filter phase shift arose in the signal processing, as discussed in a recent paper of Resagk et al (1995).
In this case of a signal consisting of two Doppler signals and the multiplex frequency, each component will experience a considerably different phase shift. This leads to a mixing of the components when demultiplexing and thus to an induced cross talk.

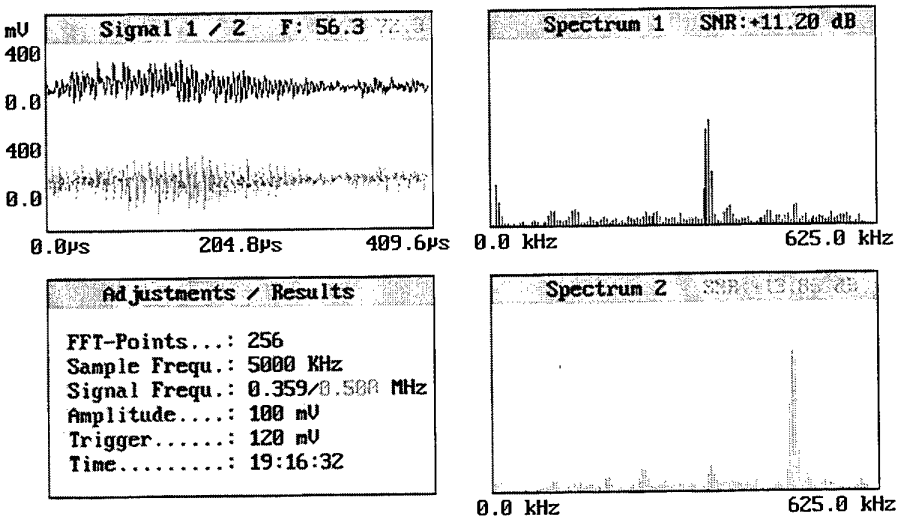


Figure 3. Example signal and signal analysis taken with rotating wire, channel 1: shift frequency of 500 kHz minus velocity component of 140 kHz, channel 2: shift frequency of 500 kHz (zero velocity), multiplex frequency 1250 kHz

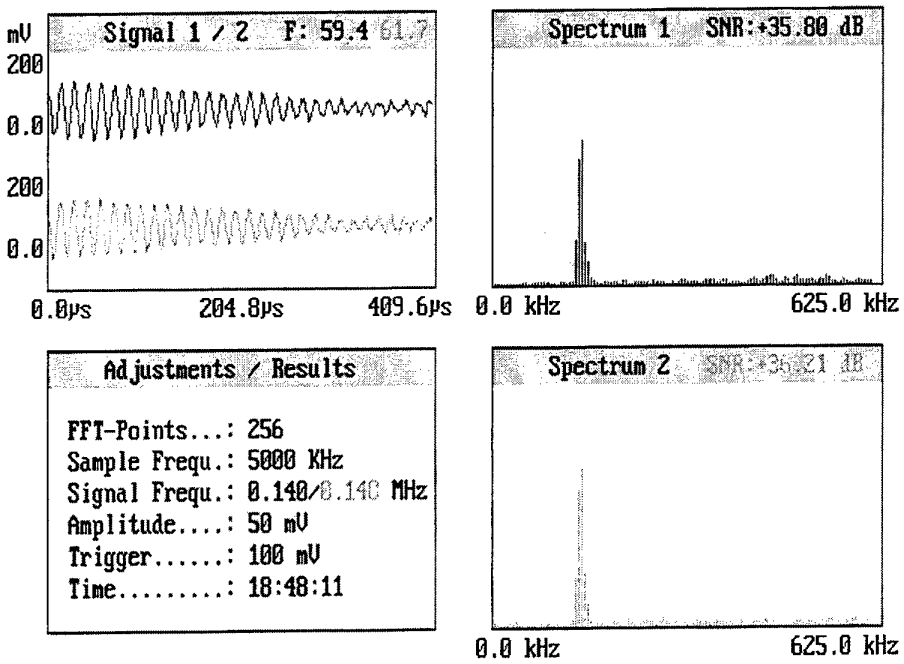


Figure 4. APD signal and power spectral density of velocity component 1 without multiplexing

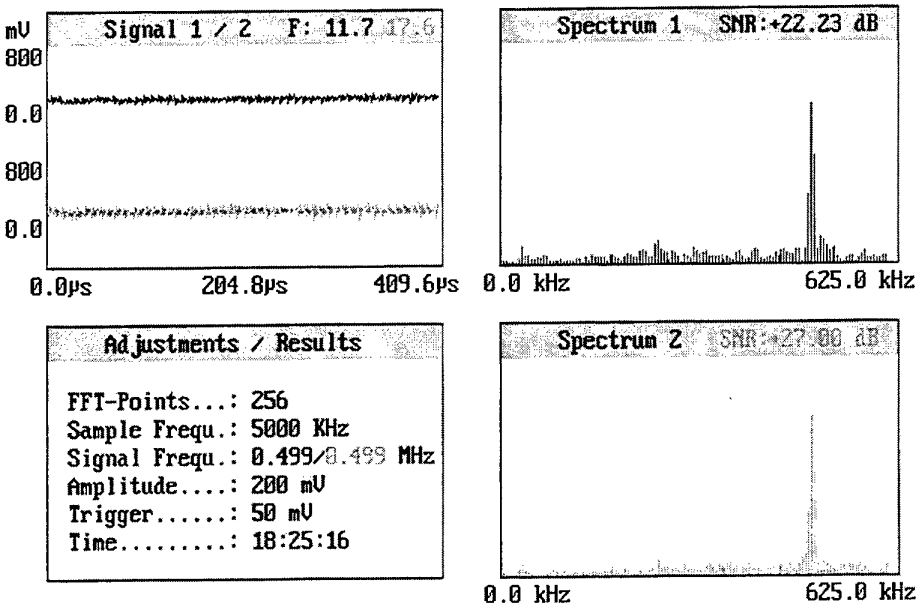


Figure 5. APD signal and power spectral density of zero velocity plus shift frequency of 500 kHz without multiplexing

To avoid this cross talk a new method has been used to remove the pedestal signal. Instead of a band pass filter a circuitry subtracted the pedestal. A block diagram is shown in Figure 2. The phase shifter has been employed to shift the APD signal in the same range as the pedestal signal was shifted passing the low pass filter (LP). Software programs were available to demultiplex the signal, to compute the power spectral density (PSD) of each of the two demultiplexed signals using FFT and to perform frequency and signal-to-noise ratio (SNR) estimations of the signals.
The multiplex frequency is only limited by the maximum sampling rate of the used ADC board (100 MHz). The IO-devices are working up to modulation frequencies of several GHz.

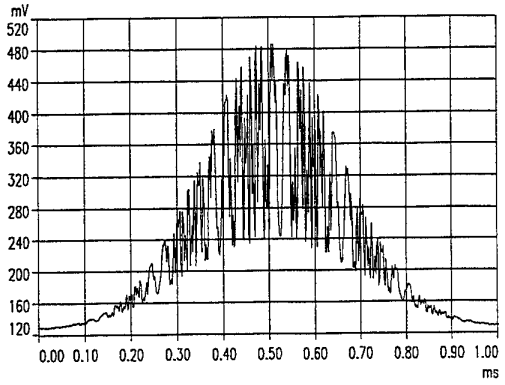


Figure 7. Multiplex burst signal with pedestal

4. RESULTS

The IO-two-component LDA has been tested using a 1 micron wire mounted on a rotating disk and aligned to rotate through the measurement volume. The velocity vector of the wire was aligned with one of the measurement volumes and at 90° (zero velocity, registering only shift frequency).
Figure 3 shows the resulting APD signal and the power spectral densities of the two demultiplexed signals. For a single detection of the LDA signals of the two components the Y-fed balanced bridge was set up to one channel (0 kHz multiplex frequency). With the bias voltage it was possible to select one velocity component time independent. Now the APD signal is not multiplexed, but it was split into two equal signals after the signal processing as shown in Figures 4 and 5.
Second experiments were performed in simple air flows with a well-known main flow direction. A smoke generator produced the necessary particles.
This test demonstrates the ability to separate the two velocity signals from the multiplex signal with a high accuracy. Also closely neighbouring frequencies were detected with a high SNR, using the optical multiplex approach together with the new filter method. Figures 6 to 8 show the results of the subtraction of the pedestal signal on the example of a generated burst signal.
The described three-beam, two component IO-LDA had a backscatter probe with a focal length of 300 mm. The resulting fringe space of about 4 microns allows, together with a sample frequency of 100 MHz and a multiplex frequency up to 50 MHz, the detection of velocities up to 100 m/s.

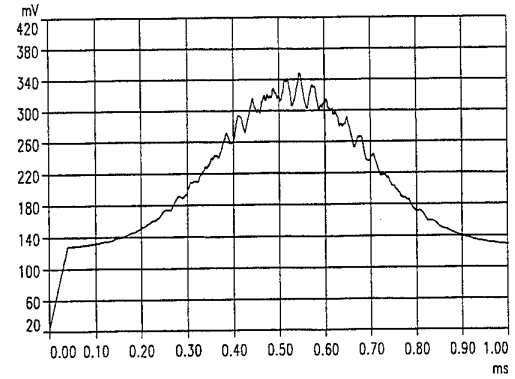


Figure 6. Pedestal signal separated with a low pass

5. CLOSING REMARKS

In summary, the feasibility of optical multiplexing in dual-beam LDA system has been demonstrated. The system offers several advantages over conventional two-component systems, in that a single wavelength, a single photodetector, a single processing electronics and a small low power integrated optical phase modulator are used.
For further integration to achieve the full miniaturization potential however, it would be useful to integrate the laser diode and the photodetector onto a single device. The integration of the beam splitter and the phase modulator onto one chip is easy realised and was published by Resagk et al (1996).
Considering the modest power levels which were used, this system would presently only be appropriate

for shorter focal ranges and in measurements where suitable particles were available. New optical materials and technologies of integrated optical devices for visible light could considerably increase the power levels.

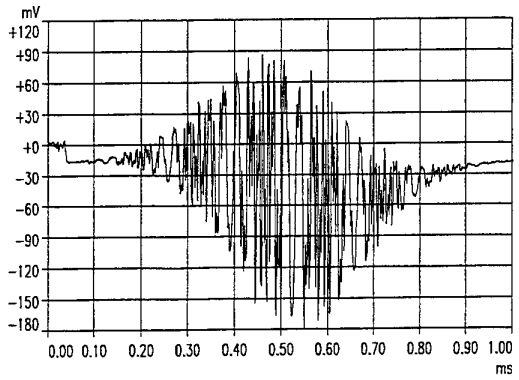


Figure 8. Burst signal without pedestal

REFERENCES

Pradel T, Rasch A, Rothhardt M, Tropea C, Varro W and Weber H 1993, Use of integrated optical devices in laser Doppler anemometry, Proc. Kongress Sensorik und Systemtechnik, Nürnberg

Resagk C, Schellenberger U, Grabow J, Tropea C and Stieglmeier M 1995, Two-component LDA using optical multiplexing, Meas. Sci. Technol., vol.6, pp.674-681

Resagk C, Schellenberger U, Rasch A and Voigt S 1996, Zweistrahl-Multiplex LDA mit integriert-optischem Schaltkreis, Proc. OPTO 96 Opt. Sensor Technol. Measuring Techn. Electronics, Leipzig, pp.315-317

Rottschalk M, Rasch A and Karthe W 1988, Electrooptic behaviour of proton exchanged $LiNbO_3$ optical wave guide, J. Opt. Commun., vol. 9, pp.19-23

Toda H, Kasazumi K, Haruna M and Nishihara H 1989, An optical integrated circuit for time-division 2-D velocity measurement, J. Lightwave Technol., vol. 7, pp.364-7

Steinberg S, Göring R, Hennig T and Rasch A 1995, Comparison of photorefractive-index changes in annealed-proton-exchanged channel waveguides in MgO-doped and congruent $LiNbO_3$, Optics Letters, vol. 20, no. 7, pp.1-3

A compact LDV system for high resolution flow measurements

Larry Berkner and Amir Naqwi

TSI Incorporated

Fluid Mechanics Instrument Division

P.O. Box 64394, St. Paul,

Minnesota 55164, USA

Abstract

The design of a compact laser diode based LDV system is described. In order to obtain high resolution flow measurements, stringent specifications of fringe uniformity and fringe stability were set out as critical criteria for the measuring volume. Frequency shifting is provided for detection of flow reversal and real-time high-speed signal processing is included to measure flow spectra.

The optical head houses the transmitting and receiving optics, while the electronics unit consists of the power supply for the laser diode and the signal processing board for data analysis.

A precise collimation of the laser diode is designed to provide a fringe spacing that is uniform to within a few tenths of a percent of its mean value. Standard deviation caused by fringe non-uniformity is expected to be smaller than 0.1%. The fringe stability was obtained by a novel design which ensures perfect matching of the optical paths of the two beams. Results have shown that the beam path matching technique provides an extremely stable fringe pattern regardless of the mode-hopping caused by aging of the laser diode or changes in its operating temperature.

Digital signal processing (DSP) chips are utilized in the signal processor, in order to obtain a design that offers unprecedented flexibility in the LDV burst detection and burst processing.

Measurements of an air jet flow were taken by the compact diode system. In terms of flow statistics and the data rate, these measurements agreed very well with a conventional argon-ion based LDV system.

1. Introduction

Miniature laser Doppler systems based on semiconductor lasers and detectors have been built and marketed for solid surface measurements for nearly 15 years. For fluid mechanics applications, such systems have been reported in literature for over 10 years, see e.g. Dopheide et al. (1988), Damp (1989) and Durst et al. (1989). Although it is straight-forward to assemble a semiconductor LDV system and obtain signals from a seeded flow, accuracy of the measurement remains questionable, unless due attention is given to the unique characteristics of diode lasers and avalanche photodiodes. The purpose of this paper is to underline the system design considerations that are important for obtaining research quality data using a semiconductor LDV system. New techniques for signal processing are also introduced. Experimental results are presented which compare the laser diode based system with a conventional LDV system, using an Argon-ion laser.

2. Design of the optical head

The design of the optical head is illustrated in Fig. 1. The laser diode has an output power of 50 mW at a wavelength of 690 nm, i.e. the light source is visible. A standard, precision beam splitter is used and one path passes through a Bragg cell which adds a 40 MHz shift, before both beams exit the probe though the focusing lens. Received light is collected in the backscatter mode along the same optical axis as the transmitted light. The signal detector is an avalanche photodiode, which is compact and offers high quantum efficiency for the above wavelength.

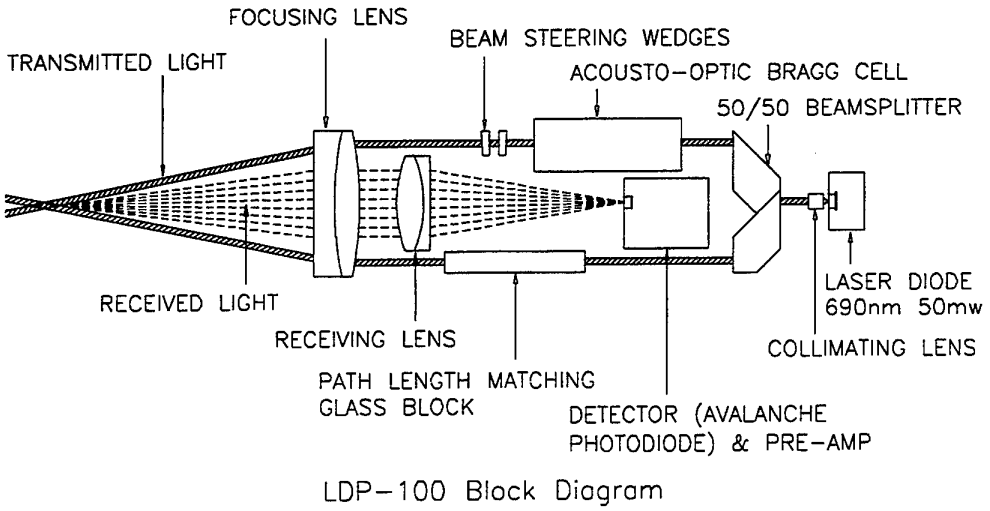


Figure 1: Optical layout of the frequency-shifted diode LDV system

3. Fringe Uniformity

Uniformity of the fringes across the measuring volume, or fringe flare, can often determine the minimum dispersion added by the LDV measurement technique. It is determined by the laser's collimation and the degree to which the beam profile is Gaussian.

Some of the accuracy-related issues were addressed by Naqwi & Durst (1990) and Durst et al. (1990). These articles were concerned with conditioning the diode laser beams, so as to obtain uniform fringes. Diode laser beams are generally astigmatic, elliptic in cross-section and have a non-Gaussian intensity distribution along the larger of the two transverse axes. Durst et al. (1990) considered two optical configurations:

1. using the wider non-Gaussian beam cross-section in the plane of the two laser beams;
2. using the narrower Gaussian beam cross-section in the plane of the diode laser beams.

It was demonstrated theoretically and experimentally that the second configuration, i.e. utilizing Gaussian distribution in the beam plane, resulted in more uniform fringes and was considered appropriate for accurate velocity measurements.

The above system did not employ frequency shifting, so the effect of a Bragg cell on the diode beam quality — and hence, on the fringe uniformity — could not be established.

The previous work is extended to a frequency-shifted system in the present system. The results of fringe uniformity measurements are given in Figure 2 which shows how the fringes are distorted by small misalignment of the lens used to collimate the diode laser beam. Differential threads are used to precisely position the collimator for minimum fringe flare. Using a focusing lens focal length of 350 mm, measuring volume width of 250 μm (as defined by the $1/e^2$ point) was obtained when fringe flare was minimized. A rotating wheel was scanned through the measuring volume to measure fringe spacing at various locations along the optical axis.

Figure 3 presents theoretical predictions of fringe spacing versus collimating lens position, assuming a Gaussian beam. The experimental results and simulations agree quite well, and show that fringe uniformity is better than 0.1% for the best alignment.

It is interesting to notice that the measuring volume width (and hence the measuring volume length) is very sensitive to micron size misalignment. As the collimator misalignment is

increased from –8.8 μm to –35.3 μm, the measuring volume width is increased from about 300 μm up to 800 μm. This causes a *reduction* in the fringe flare with increasing misalignment in the above range. This trends is verified by the results of the simulations in Fig. 3.

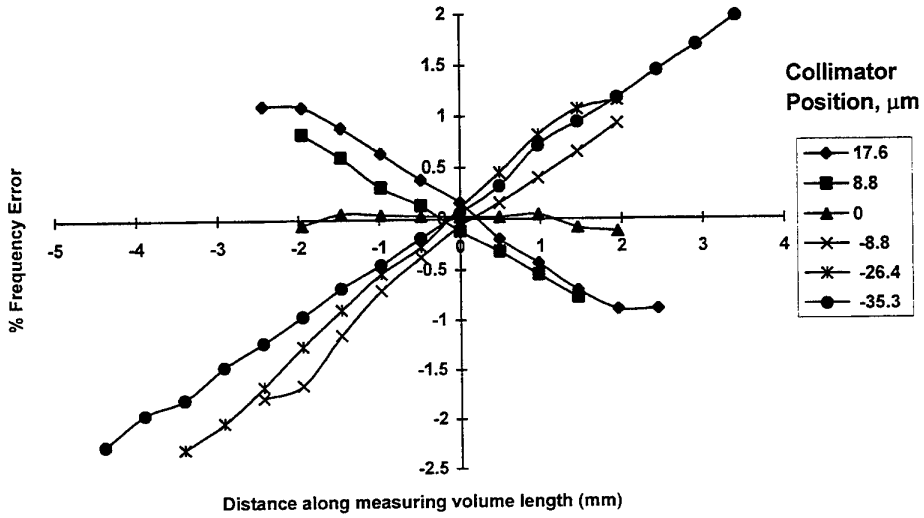


Figure 2: Measurement of fringe flare using a moving wheel

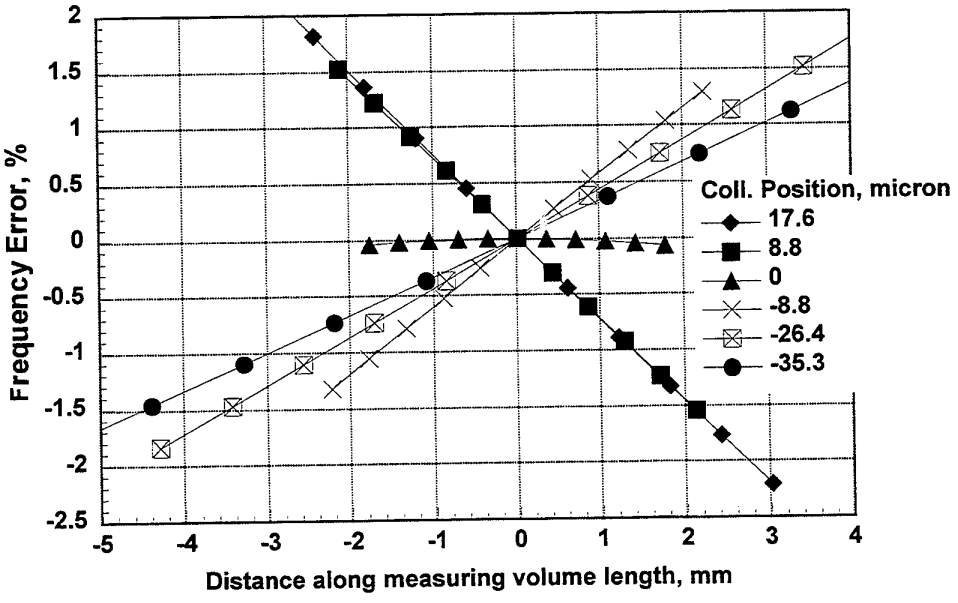


Figure 3: Simulation of fringe flare

4. Fringe Stability

Besides the uniformity of fringes, precision measurements require stable fringes that are unaffected by variations in the ambient temperature. Diode lasers are known to suffer from mode-hopping due to changes in the operating temperature. The common solution is to hold the laser diode to a fixed temperature. After a certain length of operation, the mode maps of laser diodes can drift leading to mode-hopping at the preset temperature that was initially selected for stable operation. When the laser transitions between modes, the fringes make an instantaneous shift in the same direction. This causes severe phase noise in Doppler signal which generally results in the burst not being detected with a resultant dramatic drop in data rate.

In solving the above problem it was found that if the path lengths were carefully matched, mode hopping had a negligible effect. With the mode hopping no longer a problem, other problems such as long term drift of the diode and possible lag of the temperature control circuit were no longer an issue. Typical mode hopping in laser diodes causes a wavelength change between 0.02 and 0.15%. At the maximum level of 0.15% in wavelength variation, the corresponding frequency error is still considered to be negligible.

5. Design of the Signal Processor Unit

To ensure a high measurement quality, capabilities of the signal processing scheme need to be considered. It is now well recognized that LDV signals can be processed efficiently and with a high degree of automation, provided that an SNR-based burst detector is used to identify the beginning and the ending of the bursts. Subsequently, a spectral technique (Fourier transform or autocorrelation) is used to accurately determine the frequency and isolate the signals from the noise. This approach, not only ensures accurate measurements, but also enables high data rates as detailed processing is applied only to the segments of the data stream that are already identified as bursts. High data rates are essential for measuring turbulence spectra.

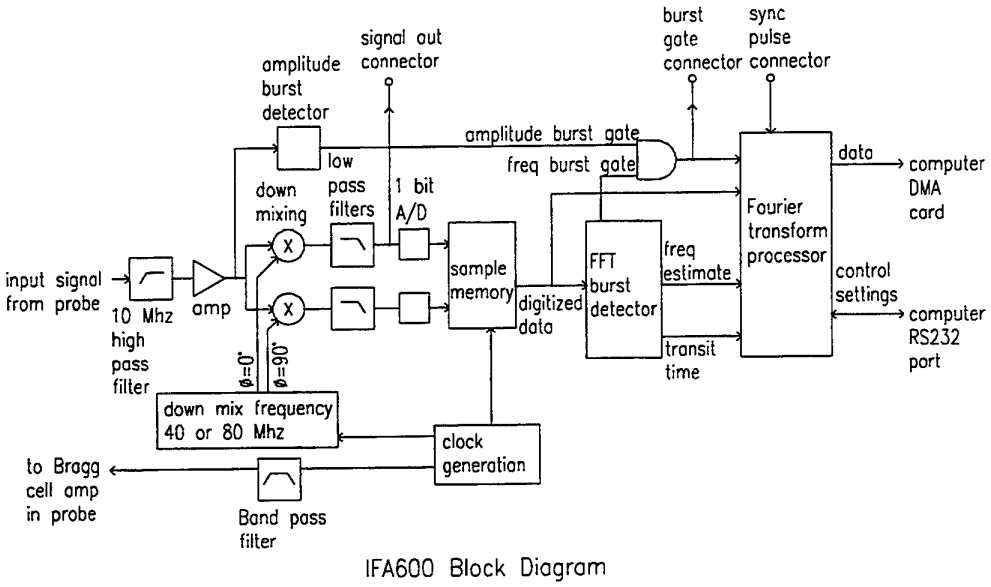


Figure 4: Schematic diagram of the signal processor

6. Burst Detection

The frequency-domain burst detector, developed by Ibrahim and Bachalo (1994), is now extended to detect not only the beginning and the ending of the bursts based on SNR, but also to obtain an estimate of the signal frequency, in a manner similar to that described by Jenson (1990).

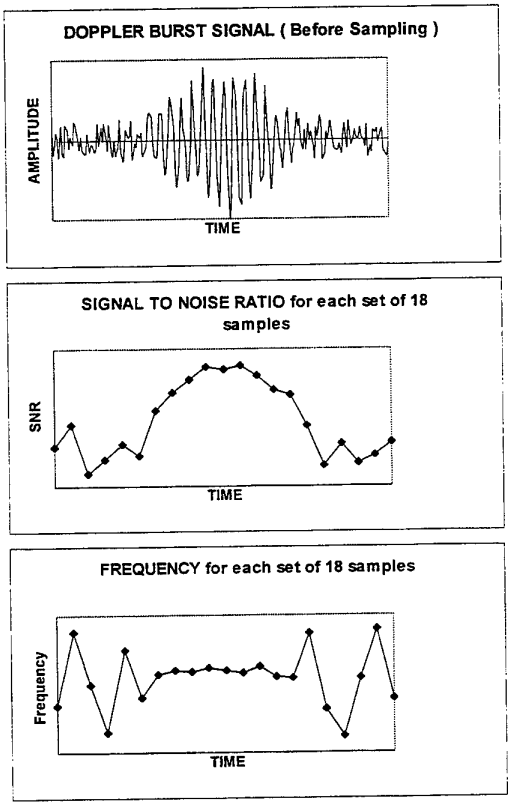


Figure 5: Processing of a noisy signal

The burst detector examines consecutive sets of 18 samples. Using a lookup table it rapidly performs a Fourier transform on these samples. This provides the dominant frequency and the height of the highest peak in the power spectrum which is a measure of SNR. By tracking both the frequency and SNR of each set of 18 samples, Doppler bursts can be reliably detected. The upper plot in Figure 5 shows a Doppler burst signal with noise. The central plot shows the SNR from each pass of 18 samples through the Fourier transform lookup table. Each new group of 18 samples is separated by 16 samples, so there is a slight overlap. The lower plot in Fig. 5 show the frequency for each set of 18 samples. It is easily seen how the presence of a single coherent frequency within the noise, i.e. a Doppler burst, is indicated by the SNR and frequency graphs.

When the burst detector logic detects a burst, it begins to accumulate a frequency average from the successive outputs from each set of 18 samples. Subsequent frequencies are compared to this running average to see if the burst is still present. Pre-set criteria determine the tolerance limits for detected frequency and the number of detections within this tolerance to validate a burst. When a burst meets the criteria, the burst detector has a reliable estimate of the burst frequency based on an average over the entire burst. This is used to optimize the second stage of processing discussed in the next section.

7. Burst Processing

Processing of Doppler burst signals using spectral techniques such as the Fourier transform is well established. When the processing is done primarily in software, the number bursts per second that can be processed is necessarily low, measured in the 100s or maybe thousands. To achieve high data rates most of the processing has been done in specifically designed electronic hardware. Continuing improvements in the speed and capabilities of digital signal processing (DSP) chips have made them a viable choice for processing Doppler burst signals. The present system employs a DSP chip to perform the final burst processing in firmware.

The burst detector hardware flags the presence of a burst and provides a frequency estimate. From there the DSP chip takes over and accurately extracts the burst frequency using a Fourier transform. By having the frequency estimate from the burst detector, software processing in the DSP chip is streamlined providing a maximum data rate of 40 thousand per second.

Doing the bulk of the signal processing in firmware, without sacrificing high data rates, has the advantages of lower cost and higher system flexibility. The flexibility emanates from being able to easily change the processing algorithm in the firmware to suit different applications. The degree of accuracy in the processing (such as samples per burst used) could be traded off with the maximum data rate required.

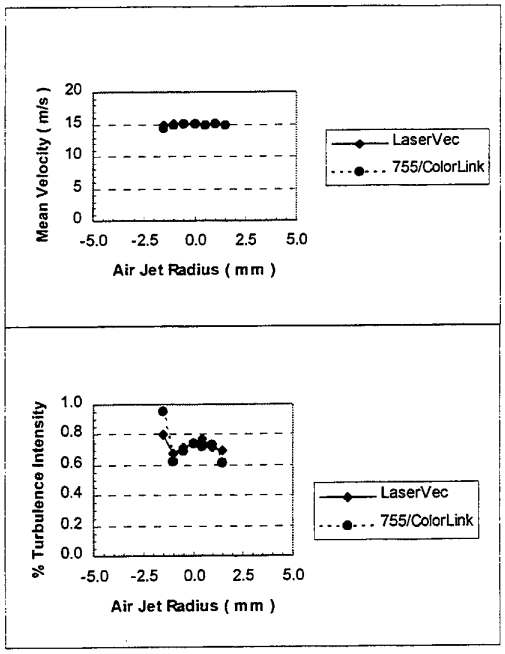


Figure 6: Flow at 1 diameter from the nozzle

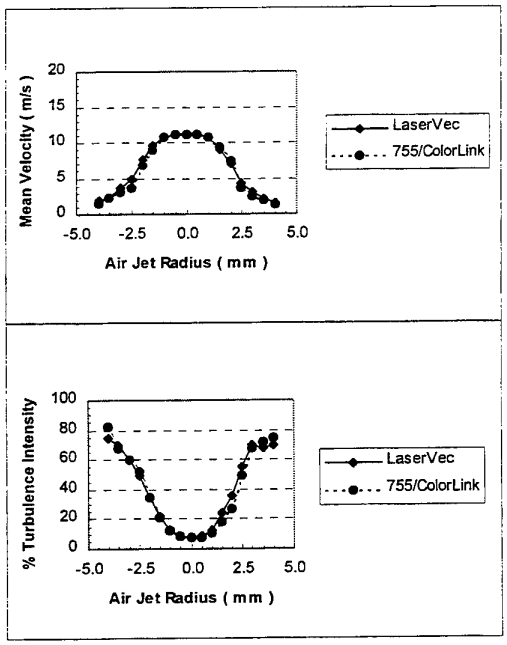


Figure 7: Flow at 5 diameters from the nozzle

8. Measurement of air jet flow

During system development, many detailed tests were performed using signal generators and noise generators to verify the theoretical operation of the signal processor. However, the critical test is the operation of the complete system — optics and signal processor — in a flow field. The present system, utilizing a laser diode probe and new signal processor, was compared experimentally with a conventional LDV system.

The conventional system consisted of an Argon-ion laser, a beam conditioning unit (TSI's ColorBurst) and fiber optic probe, detection electronics (TSI's ColorLink) and IFA755 signal processor. The 488 nm Argon-ion line was used for measurements. The TSI ColorLink uses a photomultiplier tube for a detector. Laser power densities within the measurement volume were made similar for the two systems.

Measurements were taken in an asymmetric air jet, seeded with micron-size water droplets. Due to the flow setup, the measuring volumes for the conventional LDV and the diode LDV were not completely overlapped, especially at locations close to the edge of the jet. However the comparisons still provided very useful information and also illustrated the performance of the diode system well.

Data was taken across the jet diameter at two locations, i.e., one and five nozzle diameters away from the nozzle exit. Mean velocity and turbulence intensity at each point are shown in figures 6 and 7. Although not shown, data rates were similar between the two systems. The results show that the two systems agree well.

The fact that the results agreed at the lowest turbulence intensities (0.7%) show that the spread added to the data by the laser diode system is less than a few tenths of a percent. It is also interesting to note that even at the highest turbulence intensities, which included some negative flow, the two systems agreed well even though they have two very different methods of dealing with negative flows.

The conventional TSI system typically downmixes the incoming signals with a frequency smaller than 40 MHz, so that signals received by the processor have adequate frequency offset to cover the negative flow. The new processor used with the laser diode system downmixes the incoming signals with 40 MHz to completely remove the Bragg cell's shift, but it uses quadrature mixing to obtain the flow direction. This results in two quite different sets of Doppler signals seen by the signal processors

which could make one or the other processor favor faster or slower particles. However, processor bias is minimized using effective signal validation criteria.

9. Conclusions

The design of a complete LDV system is presented, which uses semiconductor devices for both the laser source and the photodetection along with a unique combination of digital burst detection and Fourier transform analysis for signal processing. The problem of mode hopping generally seen in laser diode systems has been circumvented by accurately matching the beam path lengths. This eliminates the need for a temperature control circuit for the diode laser which can cause problems as the laser ages. The signal processor represents a unique combination of previous processor designs (IFA750 and RSA) as well as taking advantage of the latest DSP technology. The result is a very compact package that provides research quality measurements on a single component of a flow field.

Acknowledgment

The authors are grateful to Dr. M. Fingerson and Dr. W. Lai of TSI for valuable suggestions.

References

S. Bopp, F. Durst, R. Müller, A. Naqwi, C. Tropea and H. Weber, "Small laser Doppler anemometers using semiconductor lasers and avalanche photodiodes", in the book, Applications of Laser Anemometry to Fluid Mechanics (Eds. Adrian, Asanuma, Durão, Durst & Whitelaw), Springer-Verlag (1989) 315-337.

S. Damp, "Battery-driven miniature LDA-system with semiconductor laser Diode", in the book, Applications of Laser Anemometry to Fluid Mechanics (Eds. Adrian, Asanuma, Durão, Durst & Whitelaw), Springer-Verlag (1989) 338-360.

D. Dopheide, M. Faber, G. Reim and G. Taux, "Laser and avalanche diodes for velocity measurement by laser Doppler anemometry", Experiments in Fluids, 6 (1988) 289-297.

F. Durst, R. Müller & A. Naqwi, "Measurement accuracy of semiconductor laser Doppler anemometry systems", Experiments in Fluids 10 (1990) 125–137.

K. Ibrahim and W. D. Bachalo, "Method and apparatus for optimum signal burst detection", US Patent No. 5,289,391 (1994).

L. Jenson, "Coherent frequency burst detector apparatus and method", US Patent No. 4,973,969 (1990).

A. Naqwi & F. Durst, "Focusing of a laser diode beam: a simple mathematical model", Applied Optics 29 (1990) 1780–1785.

COMPACT ACHROMATIC LASER DOPPLER ANEMOMETRY EMPLOYING NOVEL POWERFUL FIBER LASERS AND DIFFRACTION OPTICS

J. Czarske, H. Zellmer, K. Plamann, H. Welling

Laser Zentrum Hannover e.V., Development Department,
Hollerithallee 8, D-30419 Hannover, Germany, email cz@lzh.de

ABSTRACT

Diode pumped fiber lasers are compact robust light sources, emitting to date up to about 30 W fundamental mode power. Hence, fiber lasers are interesting for the realization of portable LDA systems with high optical power. This contribution shows the state of art of fiber lasers and their application for a miniaturized fiber-coupled LDA system. Due to the use of diffraction gratings as laser beam splitters, the LDA system becomes achromatic, so that broadband emitting fiber lasers can be used. Furthermore, a new method for a directional discrimination of achromatic LDA systems will be presented.

1. INRODUCTION

Conventional powerful LDA systems employ Argon ion lasers, having a low efficiency and a bulky design. Hence, powerful LDA systems exhibit to date a low portability, so that such LDA systems are problematic in field applications, e.g. for aircraft flights. In order to enhance the applicability of the LDA technique, compact lasers with a high efficiency and reliability have to be employed. However, laser diodes, which fulfill these demands, emit to date only approximately 0.1W single-mode power. Master-Oscillator-Power-Amplifier (MOPA) arrangements can enhance the single-mode power up to the 1 W range, see Müller et al. (1997), but a further power scaling is very difficult. Another well-known technique is the use of diode-pumped solid-state lasers, which emit up to several 10 W fundamental mode power. However, solid-state lasers have a high technical effort. Furthermore, for fiber-based LDA systems the coupling of the high laser power in monomode fibers could be problematically.

In this contribution we propose the use of diode-pumped fiber lasers for the LDA technique. Fiber lasers have a robust, simple design and emit currently up to about 30 W fundamental mode power. Furthermore, the launching into single-mode fibers of a LDA measuring head can be saved. Thus, fiber lasers are very attractive for the LDA technique. The application of diode-pumped Nd-doped fiber lasers was already presented by Czarske et al. (1997a). In this contribution we will describe the recent achieved technical progress in fiber lasers as well as their application for miniaturized powerful LDA systems.

2. DIODE-PUMPED FIBER LASERS

Fiber lasers are well-known in several application fields, e.g. in the optical communication techniques for the amplification of fiber-guided signals. Since a few years there are also significant efforts in the realization of high-power fiber lasers, especially in order to apply them in printing techniques and material processing. As described e.g. by Zellmer et al. (1995) fiber lasers, having a high fundamental mode power can be build by the double-clad concept: The emission of a high-power laser diode array is efficiently launched into the multimode-fiber of typical 400µm diameter. Inside these pump core, a rare-earth-doped single-mode fiber core is embedded, which absorbs the pump light, so that an optical amplification along these active core results. Together with a resonator, simply given by the fiber and two mirrors at the fiber ends, the single-mode powerful fiber laser is realized. The cladding pumping of the active single-mode core provides a simple and efficient means to convert multimode pump light from high-power laser diodes into bright laser radiation. Thus, a "light funnel" for transferring the low-brightness pump light into high-brightness fiber laser output is achieved. This is a forbidden operation in the conventional (passive) optics, but the stimulated emission process in the active fiber core allows the reduction of light beam parameter product, so that a combination of a high laser power and a small laser focus, i.e. LDA measuring volume, can be achieved.

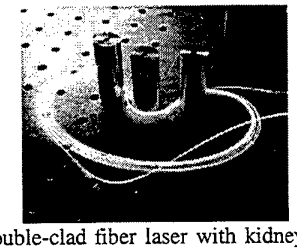


Fig. 1 Double-clad fiber laser with kidney-shaped fiber coiling for an efficient pump light absorption.

However, one assumption of a high conversion efficiency is the mixing of the cladding modes, since the also excited helix fiber modes are not fully absorbed by the doped single-mode core, see Zellmer (1996). Hence, a mode conversion from the helix modes to e.g. the meridional

modes, which cross the active core, has to arranged. Fig. 1 shows a fiber laser, where the mode conversions are based on a periodically bending of the fiber. Another method is to employ a special cladding shape, which also results in mode conversions. Both concepts are well-suited for the realization of powerful fundamental mode fiber lasers, see Fig. 2.

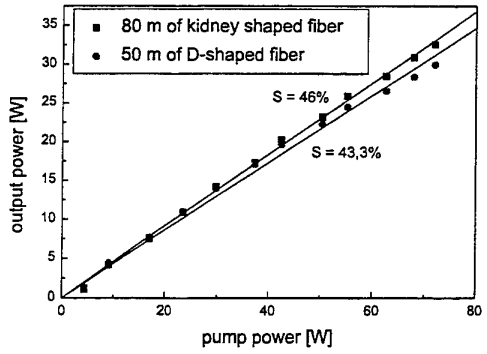


Fig. 2 Power scaling of double-clad Nd-doped fiber lasers. The kidney-shaped coiling and the D-shaped cladding of the fiber, respectively, results in a high absorption efficiency.

Up to now, the features of fiber lasers, relevant for high-power applications like material processing, were discussed. However, the application of fiber lasers for the LDA technique has further demands besides high power density. Firstly, fluctuations of the fiber laser power should be sufficiently suppressed, so that the Doppler frequency spectrum can be reliably evaluated. Unfortunately, Fabry-Perot fiber lasers usually emit in multiple longitudinal modes, resulting an electrical comb spectrum of the photo diode current, see e.g. Dopheide (1995), Tropea (1995). Assuming typical fiber lengths of about l=50 m, the mode spacing Δf yields to $\Delta f=c/(2nl)=2.05$ MHz, where c is the light velocity and n=1.46 is the refraction index of the fiber. Hence, the LDV signal spectrum has a superposed laser mode comb with about 2 MHz spacing. Due to the huge gain bandwidth of the fiber laser, the mode comb is extended over the whole photo detector bandwidth. In consequence, these mode comb has to be suppressed for reliable LDA measurements. One possibility is to suppress the reflex of one fiber end, so that the operation of amplified spontaneous emission (ASE) is achieved. This was realized by an 8^0 cut angle of the fiber end surface. The mode comb were successfully suppressed, see Fig. 3. Only small spectral distributions in the 100 Hz range occurs, caused by the power supply.

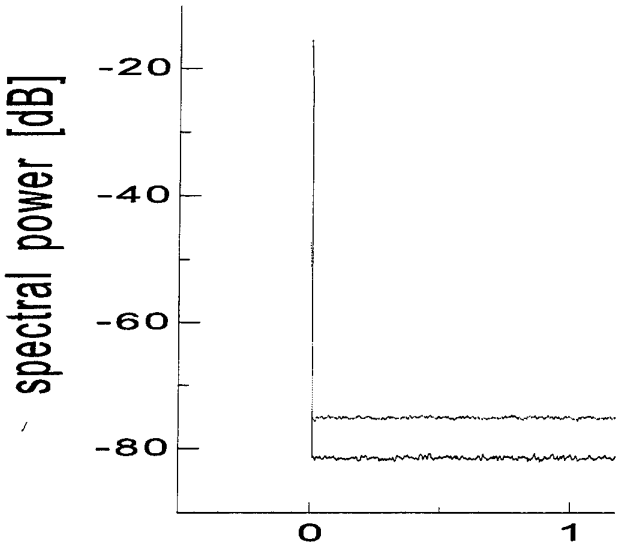


Fig. 3 Electrical spectrum of the Nd-doped silica fiber laser (30 A pump current). The enhanced spectral density for the fiber lasers results from shot noise of the APD. The straight-line spectrum demonstrates the suppressed power fluctuations.

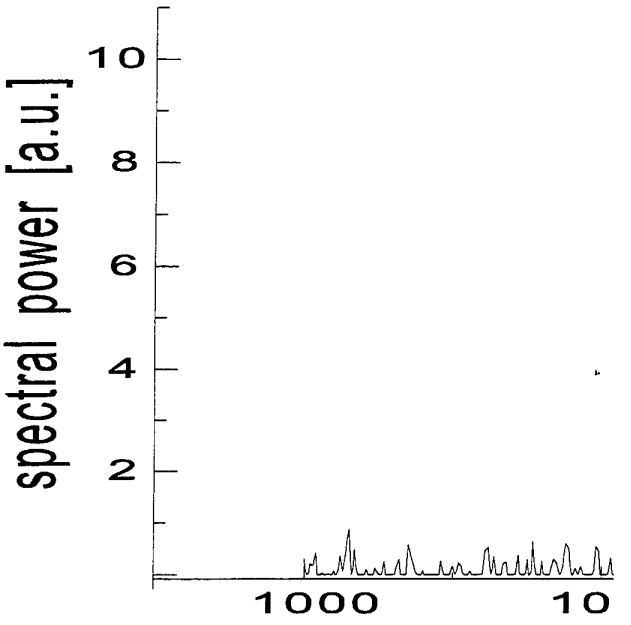


Fig. 4 Optical spectrum of the Nd-doped silica fiber laser (30A pump current, ca. 2 W ASE power).

Next, the optical spectrum of this fiber laser was measured, see Fig. 4. As can be seen, the linewidth of the fiber laser

is about 10 nm. Thus, the application of this laser type in LDA requires achromatic system properties as described by Czarske et al. (1997). In the next chapter such achromatic LDAs will be illuminated.
Although the presented properties of the Nd-doped fiber lasers are well-suited for portable powerful LDA systems, the emission wavelength around 1060 nm is not advantageously for the scattering at small particles, especially in the Rayleigh scattering regime. Visible or UV

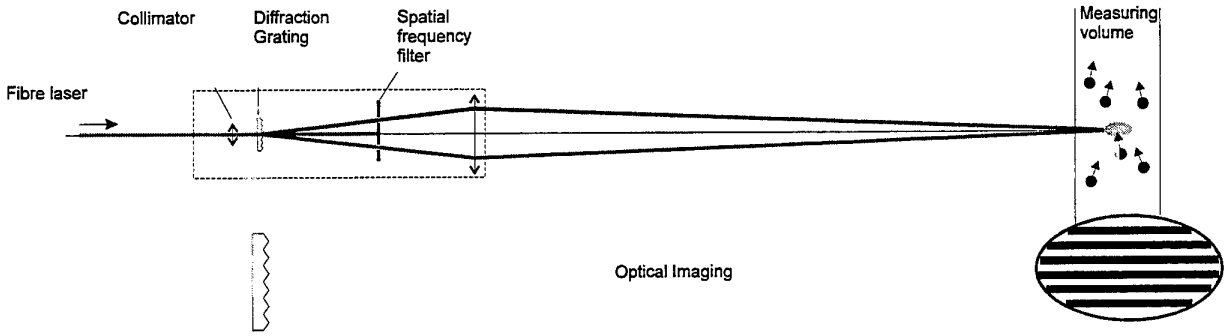


Fig. 5 Principally scheme of the achromatic LDA system.

wavelength. In consequence, an up-conversion laser, emitting e.g. at visible wavelengths can be pumped with conventional infrared pump diodes. In single-mode fibers the ESA process can be efficiently used, since high intensities and great interaction lengths are available. Currently, in the LZH powerful up-conversion fiber lasers are developed for the laser TV technique. Mainly three laser types are of interest: (i) Thulium-doped ZBLAN up-conversion fiber lasers, pumped by a three step absorption of e.g. 1122 nm Nd:YAG pump light and emitting in the blue wavelength range (e.g. at 480 nm). (ii) Erbium doped ZBLAN up-conversion fiber lasers, pumped by e.g. a two step absorption of 970nm laser diode light and emitting in the green wavelength range (e.g. at 546nm). (iii) Praseodymium/Ytterbium doped ZBLAN up-conversion fiber lasers, pumped by e.g. a two step absorption of 840nm diode laser light and emitting in the red wavelength range (e.g. 635nm). The to date achieved single-mode power is typically 100 mW (see e.g. Zellmer et al. (1997)) with optical efficiencies in the range of 20%. First applications of the up-conversion fiber laser for LDA were investigated. However, in this paper we will describe the application of Nd-doped fiber lasers for achromatic LDA systems, since these powerful laser type is today already available at low cost and high reliability.

3. ACHROMATIC LASER DOPPLER ANEMOMETRY

The linewidth of powerful fiber lasers of typically 10 nm requires an achromatic LDA system, i.e. a wavelength independent fringe spacing. As shown e.g. by Czarske et al. (1997) these achromatic properties can be achieved by the use of a diffraction grating as beam splitter, see Fig. 5. Using a lens system, the illuminated grating is imaged into emitting light sources are then required. In this section we will briefly present the diode-pumped up-conversion fiber lasers, which have the potential to fulfill the mentioned demands. Up-conversion lasers are based on the excite-state-absorption (ESA) effect, which allows the absorption of multiple pump photons and the emission of one photon at a shorter wavelength than the pump

the measuring volume. The achromatic fringe spacing can be simply understood, if one recognize that the fringe system can be view as an image of the grating structure, which is of course independent of the laser wavelength. An achromatic fiber LDA system can be realized by different techniques and elements, respectively. But the



Fig. 6 STM image of a phase grating, written by excimer laser ablation in F2 glass.

following functions are common: (i) Collimation of the fiber-guided laser wave onto a sufficient number of grating periods. Special GRIN lenses, fabricated by the University Mannheim, were used for the image of the 5µm beam waist of the fiber laser e.g. into a 90µm beam waist, which illuminates a number of 9 grating periods, assuming 10µm

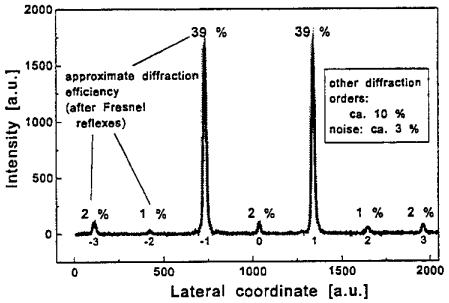


Fig. 7 Fourier spectrum of the phase grating, shown in Fig. 6. Almost 80% of the laser power is diffracted into the -1./+1. orders.

as grating constant. According to Czarske et al. (1997) this results in 18 fringes in the LDA measuring volume, which ensures a reliable signal evaluation by conventional LDA processors. (ii) Beam splitting by the diffraction grating. As described in Czarske (1996) only two diffraction orders have to be used. Holographic phase grating can achieve about 60% efficiency for the -1./+1. diffraction orders. However, besides a high diffraction efficiency, the laser power resistance is important, since fiber lasers can reach power densities in the MW/cm^2 range. In Fig. 6 such a robust phase grating is shown. It is a simple glass plate, which was structured in the LZH by an excimer laser ablation process. These rectangular phase grating has an diffraction efficiency of almost 80%, see Fig. 7. Higher efficiencies of over 90% can be achieved by thick (Bragg) holograms, which was manufactured by the RWTH Aachen. (iii) Transferring of the splitted laser beams into the LDA measuring volume. Using an imaging optic, it results a negligible path length differences between the two LDA beams, see Czarske et al. (1997). Hence a good visibility of the fringe system occurs, although the fiber laser has a small coherence length. Furthermore, the laser beams are self-aligned focused into the measuring volume. Hence, the alignment effort can be significantly reduced. Therefore the first prototype of the achromatic fiber laser Doppler anemometer was realized by the use of an imaging system, see the next chapter. (iv) Accumulation of the scattering light. As shown in the next chapter, a back-scatting optics, focusing the light into a multimode fiber can be used.

4. PROTOTYPE OF A COMPACT LDA MEASURING HEAD

In Fig. 8 the scheme of the achromatic LDA system is shown. The light from the described Nd-doped fiber laser, see chapter 2, is collimated by a apheric lens of 1.45mm focus length to about 100µm beam diameter. A holographic transmission grating of 10µm grating constant is used as beam splitter. By an AR-coated achromat the grating is imaged into the measuring volume. The back-reflected scattering light is imaged by two achromats into a multimode fiber. However, the high apertures results to a point-spreading to about 100µm. In order to accumulate the scattering light sufficiently a 250µm fiber was used, which can guide the light onto an APD.

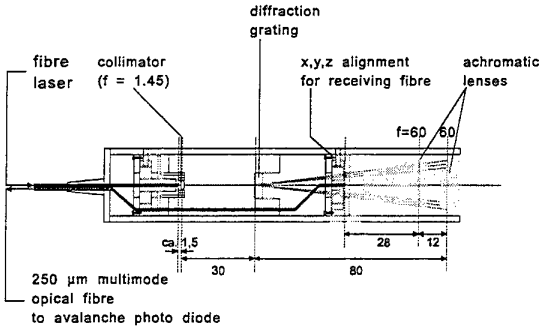


Fig. 8 Scheme of the fiber-optic achromatic LDA measuring head with a working distance of 240 mm.

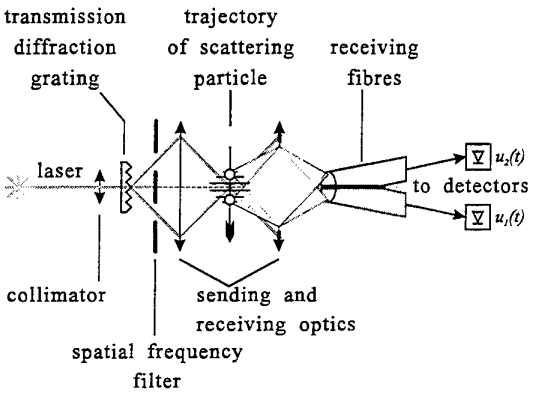


Fig. 9 Experimental arrangement of the directional LDA system.

5. ACHROMATIC DIRECTIONAL LDA SYSTEM

Directional discrimination is normally obtained by frequency shifting of the LDA beams with a Bragg cell. The technical effort of this directional technique is sometimes too high. Therefore simpler methods were developed like the use of position-sensitive detectors (PSD). By imaging of the scattering light onto the PSD element the trajectory of the scattering particle can be investigated, so that a directional discrimination was achieved without a frequency shifting technique. However, the noise properties of PSD elements are significantly worst than of conventional LDA detectors, especially APDs. In this contribution we briefly describe a new directional techniques, which overcomes the mentioned drawbacks.

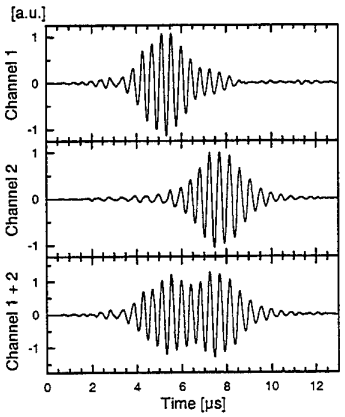


Fig. 10 High-pass filtered burst signals. The sum signal can be used for the determination of the velocity amount. The sign of the velocity vector can be determined by the time delay between channel 1 and 2, respectively.

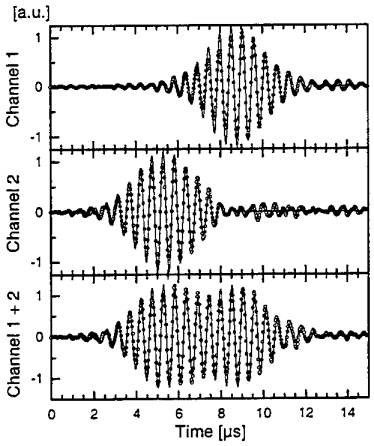


Fig. 11 High pass filtered burst signals, generated by scattering particles, passing the measuring volume from the opposite direction compared with Fig. 10.

Fig. 9 outlines the principle of the directional LDA system. The scattering light is imaged into a pair of multimode fibers, specially prepared and arranged so that their front end forms an area of approximately circular shape, where each fiber is connected to a semicircular area. Both fibers guide the launched light onto separate detectors. Fig. 9 shows that the upper half of the measuring volume is projected into the lower fiber and vice versa. Fig. 10 shows the high-pass filtered photodetector signals recorded while a stream of water droplets was directed across the measuring volume. The direction of the flow is obtained by comparing the signals on both detectors. Although the burst signals in both channels slightly overlap in time due to occurring aberrations in the imaging optics, the signal from channel one leads with respect to the other by a couple of micro seconds, which unambiguously reveals the sign of the fluid velocity, compare to Fig. 11. We underline that the concept presented here exclusively uses fiber coupled optics both in the sending and receiving parts of the LDA system. The fibers can be connected with free chosen photo detector types, e.g. APDs.

6. CONCLUSIONS

We have shown that fiber lasers have significant advantages for the LDA technique. They are robust due to the simply arrangement, exhibit a high efficiency and a small size. We have presented that fiber lasers can be used for the realization of portable powerful directional LDA systems, having a miniaturized measuring head. However, the realized achromatic fiber laser Doppler anemometers (AFLDA) have to optimized further: both from the side of the fiber lasers towards visible emission as well as of the LDA measuring head towards low measuring errors and small size. Then these AFLDA systems should be verified in special field applications.

ACKNOWLEDGEMENT

This work was partially funded by the DFG under Cz55/4-1. The authors thank J. Wais (LZH) for the realization of the power resistant phase gratings, see Fig. 7 and 8, by an excimer laser ablation process. For collaboration we thank Dr. J. Schaller (RWTH Aachen) and Prof. K.H. Brenner (University Mannheim).

REFERENCES

Czarske J 1996, Verfahren zur Messung und Auswertung der Interferenzphase in der Laser-Doppler-Velocimetrie', VDI-Fortschritt-Berichte 1996, 8, 530, VDI, Düsseldorf, Germany.

Czarske J Dölle O Freitag I Welling H Müller H 1997, Novel high-power laser Doppler anemometer using a diode-pumped fiber laser, Appl. Phys. B 64, p.119-122

Dopheide D 1995, Neue Halbleitermeßverfahren für komplexe Strömungen, Habilitationsschrift am Fachbereich Maschinentechnik der Universität-Gesamthochschule Siegen, Germany.

Müller H Dopheide D 1997, Directional 2 Watt LDA system applying MOPA lasers, Proc. 7th int. conf. on laser

anemometry - advances and applications, Karlsruhe, 8-11 September 1997, ed. B Ruck, A Leder D Dopheide, pp.3-8

Tropea C 1995, Laser Doppler anemometry: recent developments and future challenges, Meas. Sci & Tech., **6** pp.605-619

Zellmer, H., Willamowski, U., Tünnermann, A., Welling, H., Unger, S., Reichel, V., Müller, H., Kirchhof, J., Albers, P., 1995, High-power cw neodymium-doped fiber laser operating at 9.2 W with high beam quality, Opt. Lett. 20, pp.578,

Zellmer, H., 1996: Leistungsskalierung von Faserlasern, PhD. thesis, University Hannover, Germany.

Zellmer, H., Buteau, S. Tünnermann, A., Welling, H., 1997: Electron. Lett. p.1383-1384

OPTICAL PREAMPLIFICATION OF 1064 NM LDA RADIATION

H. Többen, H. Müller, D. Dopheide

Physikalisch-Technische Bundesanstalt (PTB)
Section of Fluid Flow Measuring Techniques
D-38116 Braunschweig, Bundesallee 100, Germany
Tel.: #49-531-592-1319; Fax.: #49-531-592-1305
e-mail: helmut.toebben@ptb.de

ABSTRACT

First results about the optical preamplification of LDA radiation are presented. By using a fiber amplifier in front of the photodiode of a conventional 1064 nm LDA setup burst signals of really low intensities (few nW power in cw-mode) were drastically pushed over the detection limit of the photodetector with strong improved signal-to-noise ratio.

1. INTRODUCTION

At the 8th Int. Symposium on Applications of Laser Techniques to Fluid Mechanics a new concept where fiber amplifiers are used in fiber optical LDA-systems as booster amplifier to magnify the laser power in the measuring volume as well as preamplifier to increase the sensitivity of detector units was demonstrated by Többen et al (1996). Now, first results about optical preamplification of LDA signals at a wavelength of 1064 nm are presented. At this wavelength powerful Nd:YAG lasers are available, but commonly used conventional photodiodes work with a low sensitivity.

2. FUNDAMENTALS AND THEORETICAL BACKGROUND

Fiber amplifiers magnify the power of optical signals to higher power levels with low additional noise. They can be used as (i.) booster amplifier placed behind a laser source with low output power (mW or sub-mW range) to convert pump power delivered from broadband pump sources into signal power of high precision lasers. With an Erbium doped fiber amplifier as booster amplifier a pump-to-signal conversion efficiency of 59 % was realized by Laming et al (1991). As (ii.) preamplifier in front of photo detectors fiber amplifiers can be used to increase the signal-to-noise ratio (SNR). SNR improvements up to 30 dB (factor: 1000) are calculated by Desurvire (1994). The greatest efforts in developing optical amplification have been done in the optical telecommunication technique where fiber amplifiers are used as (iii.) inline amplifiers for realizing long distance transmission systems with transmission rates of a few Gbit/s.

The basic function principle of a fiber amplifier which is placed between standard fibers is shown in figure 1. A fiber amplifier consists essentially of a pump laser diode, a fiber coupler and a short fiber doped with rare earth ions - like the well known Neodymium. The pump power of the pump laser diode supplies the amplifier with energy. The doped fiber core creates the active medium and its dopant is excited to higher energy levels by the pump power. Amplification occurs if the excited energy level of an ion is depleted by an incident photon which induces, or stimulates, the emission of a second photon. Because the stimulated photon is an exact replica of the stimulating photon, a coherent avalanche process starts. The fiber coupler combines the pump and the signal radiation.

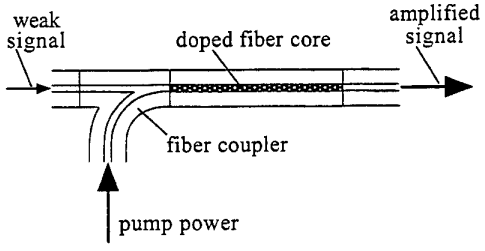


Fig. 1 Basic function principle of a fiber amplifier

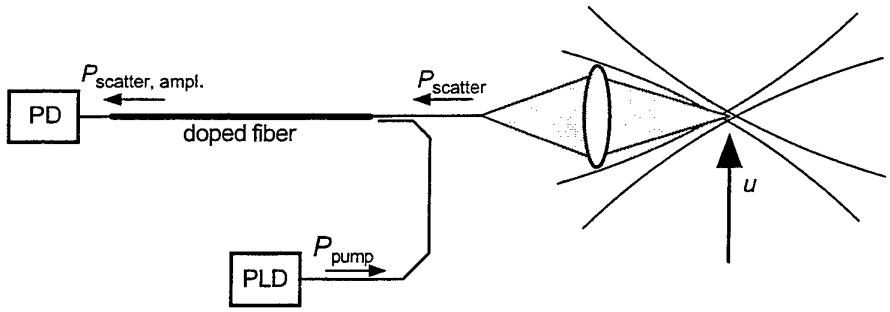


Fig. 2 Schematic diagram of the fiber amplifier receiver module for LDA scattered light

A record amplification of 54 dB (factor: 251000) and a noise figure of 3,1 dB were achieved with an Erbium-doped fiber amplifier by Laming et al (1992). The input signal had a power of 3 nW and a wavelength 1,53 µm. Therefore, the fundamental application of fiber amplifiers as preamplifier allows to improve the sensitivity of thermal noise limited receivers, which makes it possible to operate photodetectors at a performance level very close to the ideal shot noise limit.

At time, the realization of a fiber amplifier receiving module for the optical preamplification for 1064 nm LDA signals is started at the PTB. Figure 2 describes the fiber amplifier receiving module. The scattered light of tracer particles crossing the measuring volume is focused into the core of a Neodymium-doped fiber which is simultaneously pumped by a 808 nm pump laser diode (PLD). The pump diode represents the energy source for the fiber amplifier. The pump power P_{pump} and the signal power $P_{scatter}$ are combined via a wavelength selective fiber coupler. Leaving the fiber amplifier, the weak amplitude of the signal radiation is amplified up to higher power levels and the detecting photodiode (PD) delivers a photocurrent with an improved SNR.

Calculations about the SNR improvement by using the technique of optical preamplification were made by Desurvire (1994). We adapted the used formulas to our application - the optical preamplification of 1064 nm signals. The results are shown in figure 3. We assume for our calculation a signal power of 50 nW, a quantum efficiency of the photodetector of 0,4, an optical bandwidth of 1 GHz, an electrical bandwidth of 100 MHz and an incoupling efficiency of the 1064 nm scattered light into the preamplifier fiber core of 10 %.

Figure 3a shows that the total detector noise power at low gains (G < 20 dB) is dominated by the thermal noise component and at high gains (G > 20 dB) by the signal-ASE beat noise component (ASE: amplified spontaneous emission). Figure 3b demonstrates that the electrical SNR steadily

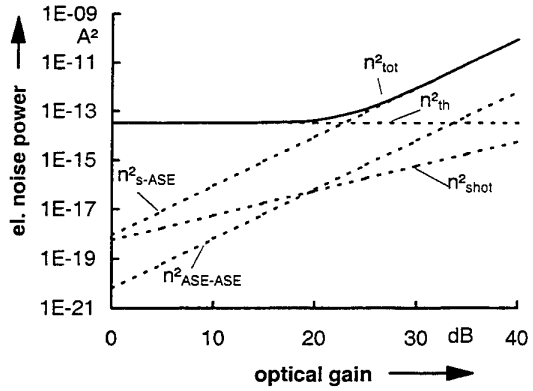


Fig. 3a Total electrical noise power n^2_{tot} depending on fiber amplifier gain; n^2_{th}: thermal noise, n^2_{shot}: shot noise, n^2_{s-ASE}: signal-ASE beat noise, $n^2_{ASE-ASE}$: ASE-ASE beat noise

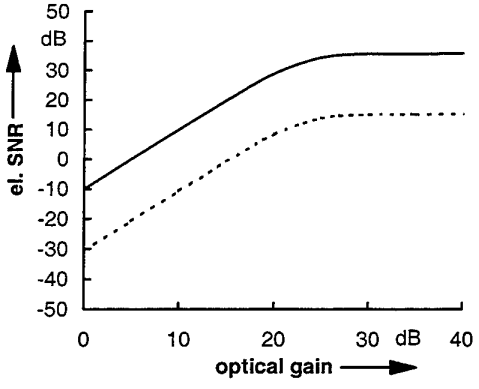


Fig. 3b Electrical signal-to-noise ratio depending on the fiber amplifier gain (dotted line) and SNR-improvement in comparison to direct detection by a PIN-photodiode (full line)

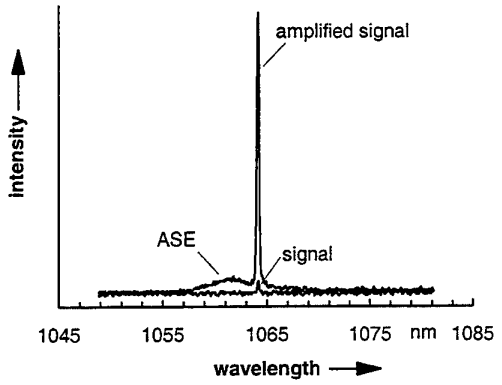


Fig. 4a Spectrum of the 1064 nm radiation with and without optical preamplification

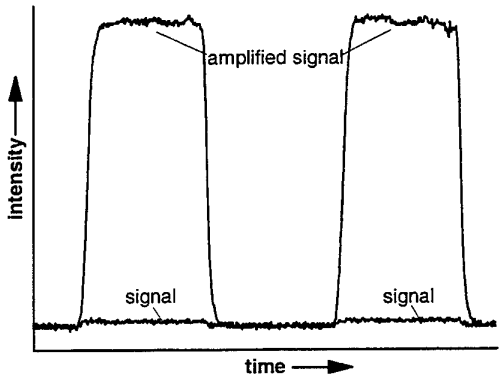


Fig. 4b Intensity of the 1064 nm radiation with and without optical preamplification in the time domain

increases with gain until the detector is in the signal-ASE beat noise regime, where the SNR reaches an upper limit.

The final SNR improvement by using 1064 nm preamplifier in front of a PIN-photodiode in comparison to the SNR which is reached by direct detection is presented by the upper curve in figure 3b. Because the calculation was made with an incoupling efficiency of only 10 %, the upper curve starts with a SNR deterioration of -10 dB. The SNR improvement becomes positive above amplifier gains greater than 5 dB. At a realistic gain value - earlier realized in a Neodym-doped fiber by Miyazaki et al (1994) - of 30 dB (factor: 1000), a SNR improvement of 35 dB (factor: 3162) can be achieved.

3. Experimental Results

Our first examinations were made by a non-optimized experimental setup. A short double clad Neodym-doped fiber was pumped by a transversal multimode emitting 808 nm laser diode. A polarizing beam splitter combines the pump and signal radiation. ASE suppression filters have not been used. Nevertheless, the obtained results were really promising for a successful realization of the fiber amplifier receiving module. Figure 4a shows the spectrum of a 2 µW-signal with and without preamplification. By the amplification process the signal was magnified up to 98 µW. This corresponds to an amplification factor of 49 (17 dB). Figure 4a shows also the broadband ASE power spectrum which decreases the gain at the signal wavelength.

The signal radiation with and without amplification in the time domain is shown in figure 4b. The combined pump and signal beam was chopped with a frequency of 37 Hz. As can seen here, the signal intensity is strongly increased by the amplification process and at the same time the high frequency noise level has not been affected. In consequence, the SNR of the amplified signal is improved. Variations in the pump power absorption process in the cladding pumped fiber cause the observed low frequency fluctuations in the amplified signal. But for most LDA applications they are out of the bandwidth of interest.

In a second experiment a Neodymium-doped standard singlemode fiber was pumped by a transversal singlemode emitting 808 nm laser diode. Neodym^{3+} doping concentration was 1300 ppm and the length of the fiber was 2 m. Between the fiber amplifier and the photodetector an optical bandpass filter (bandwidth: 4 nm) in combination with an etalon (FSR: 1034 GHz; finesse: 10) was placed to suppress the detection of ASE radiation. This setup - quite similar to the setup in figure 2 - was used to investigate the optical preamplification of LDA radiation.

With a conventional LDA setup and a 1064 nm Nd:YAG laser as LDA source a measuring volume with a fringe distance of 2 µm was created. A short piece of a fiber (outer diameter: 125 µm) acts as scatterer. It was fixed on the axis of a small motor. With a stationary fiber and 56 mW laser power in the measuring volume, 26 nW scattered light power was launched into the core of the fiber amplifier and 17 nW scattered light power in cw-mode was measured behind the amplifier/filter unit. With

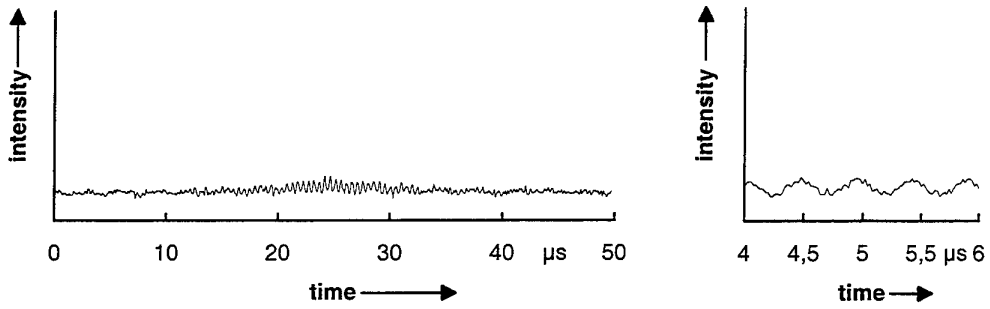


Fig. 5 Burst signals generated without optical preamplification; the right side shows a section of the center of a second non-amplified burst, measured with an expanded time resolution

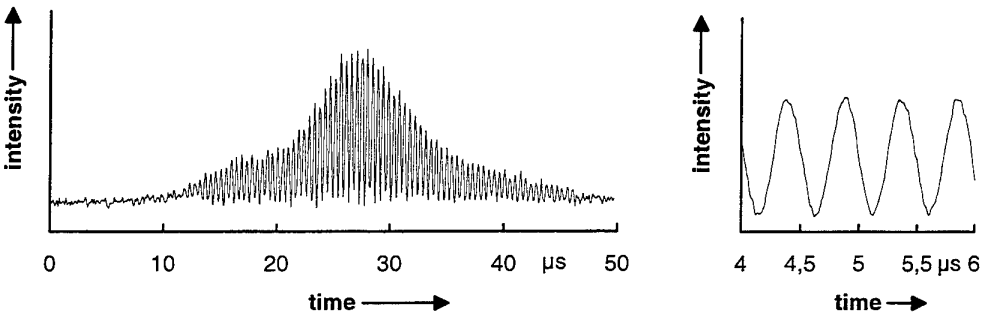


Fig. 6 Burst signals generated with optical preamplification; the right side shows a section of the center of a second amplified burst, measured with an expanded time resolution
(the scaling of intensity axes in fig. 5 and fig. 6 are the same)

59 mW launched pump power the fiber amplifier increases the cw-signal radiation up to 960 nW as measured with a power meter behind the filter unit.

With a rotating fiber LDA burst signals have been produced. An avalanche photodiode detects the burst signals that travel through the fiber amplifier receiving module and the electrical unfiltered photo currents have been plotted on a digital ocsilloscope.

A typical burst signal without optical preamplification, when the pump power is switched off, is shown in figure 5. The detected burst signal reaches with only a small part the detection limit of photodiode and exhibits a weak amplitude with only few periods. The right side of fig. 5 shows the center part of a second weak burst signal which was measured with an increased time resolution. This expanded burst signal demonstrates the noisy shape of the unamplified weak burst.

The optical preamplification process forces a strong improvement. The launched burst signals are now amplified by the fiber amplifier before the optical-electrical conversion is done in the photodiode. Figure 6 shows a pronounced increase in amplitude and in number of periods of the signal. Further, the expanded signal on the right side of fig. 6 shows a strong noise reduction. Figure 6 exhibits that the optical preamplification process allows to push the signal intensities over the detection limit of the photodetector and simultaneously improves the signal-to-noise ratio of LDA signals.

4. Conclusion and Outlook

The research and development project about the realization of a fiber amplifier receiving module for LDA radiation is supported by the Deutsche Forschungsgemeinschaft (DFG) and was started at the beginning of the year 1998. It produces really promising first results. With non-optimized experimental setups drastic improvements of burst signal quality at low power levels by using a fiber

amplifier in front of a photodetector have been demonstrated. A strong SNR improvement and, therewith, an enhancement of the detector sensitivity is obtained.

The two great claims following the presented first examinations are (i.) the increase of the amplifier gain and (ii.) the improvement of the incoupling efficiency of the scattered light into the fiber amplifier. With a two stage fiber amplifier with core pumped Neodym-doped fibers and singlemode waveguiding at pump and signal wavelength - to ensure a good overlap between the pump and the signal field distribution in the active fiber core - and further, with the inset of filters between both stages - to suppress the amplified spontaneous emission (ASE) - the optical gain at the signal wavelength will be increased and the signal-ASE beat noise will be reduced. The aim is a gain factor of 1000 (30 dB).

In comparision to the direct detection with a photodiode the concept of optical preamplification of LDA radiation with low power levels is only attractive if the incoupling losses of scattered light in the fiber amplifier are much lower (in percent or dB) than the optical gain produced by the fiber amplifier. First calculations and examinations shows an optimistic way to increase the incoupling, which will be presented in the next future.

REFERENCES

Desurvire, E., 1994, Erbium-doped fiber amplifier, pp. 167-174, John Wiley & Sons, New-York.

Laming, R.I., Townsend, J.E., Payne, D.N., Meli, F, Grasso, G. & Tarbox, E.J., 1991, High-power Erbium-doped-fiber amplifiers operating in the saturated regime, Photonics Tech. Letters, vol. 3, pp. 253-255.

Laming, R. I., Zervas, M. N. & Payne, D. N., 1992, Erbium-doped fiber amplifier with 54 dB gain and 3,1 dB noise figure, Photonics Tech. Letters, vol. 4, pp. 1345-1347.

Miyazaki, T., Karasawa, Y. & Yoshida, M., 1994, Neodym-doped fibre amplifier at 1,064 μm, Electronics Letters, vol. 30, pp. 2142-2143.

Többen, H., Müller, H., & Dopheide, D, 1994, Power and Sensitivity Improvement of LDA-systems by Fiber amplifiers. Proc. 8th Int. Symp. on Appl. of Laser Techniques to Fluid Mechanics, 8-11 July 1996, Lisbon, pp. 34.1.1-34.1.4

ANALYSIS OF THE THREE-DIMENSIONAL FRINGE PATTERNS FORMED BY THE INTERFERENCE OF IDEAL AND ASTIGMATIC GAUSSIAN BEAMS

E. B. Li and A. K. Tieu

Department of Mechanical Engineering
University of Wollongong, NSW 2522, Australia

ABSTRACT

This paper presents an analysis of fringe fields in the LDA measuring volume formed by the interference of two Gaussian beams with and without astigmatism. First the astigmatism introduced by an optical window in LDA measurements has been examined by using the q parameter of Gaussian beam and the ABCD law. The formulae for calculating the beam waist radii in both tangential and sagittal planes and the distance between the two waists have been derived and a practical example is presented. Then the phase equations for the interference of both ideal and astigmatic Gaussian beams are established and the three-dimensional fringe fields in the measuring volume are computed for different situations. It has been found that fringe gradients along the length of the measuring volume increase with an increase of the astigmatism unless the incident beams intersect at their tangential beam waists. The method introduced in this study will be useful for estimating the measurement errors caused by fringe gradients in LDA practice.

1. INTRODUCTION

The most popular optical configuration used in laser Doppler anemometry (LDA) is the well-known dual-beam differential system in which two coherent laser beams with equal intensity are focused by a positive lens and a set of interference fringe surfaces are formed in the measuring volume defined by the intersection parts of the beams. The interference fringes in the measuring volume are usually non-uniform as the result of: (a) the inherent Gaussian properties of laser beams; (b) improper optical design of the LDA; and (c) astigmatism caused by titled or curved optical surfaces where the laser beams are refracted. The non-uniformity of the fringe field or fringe gradients in the measuring volume can cause frequency bias and broadening in the produced Doppler signals and consequently will result in measurement errors in both mean velocity and turbulence intensity. It is, therefore, of vital importance to minimise or eliminate the fringe gradients for accurate measurements.

The influence of Gaussian properties on the frequency spectrum of Doppler signals and the measurement errors caused by the fringe gradients have been extensively investigated by several investigators since the early stages of LDA development (e.g. Hanson 1973, Durst & Stevenson 1979, Miles & Witze 1996) . The existing analytical models introduced in previous studies predict well for the situations where the beam waists are far away from the measuring volume. However, for the more commonly used situations where the beam waists are located at or very close to the measuring volume, the validation of the existing models decrease.

On the other hand, in previous studies only the fringe spacing along the major and minor axes were investigated. As shown below, the interfering surfaces are three-dimensional. It is, therefore, necessary to examine the three-dimensional spacing variations. Furthermore, the influence of the astigmatism introduced by the titled or curved optical surfaces in both LDA systems and experimental set-ups is also needed to be carefully examined.

In this study, we first analyse the astigmatism of a Gaussian beam introduced by a transparent window by using the q parameter of Gaussian beam and the ABCD law. Then the phase equations for the interference of both ideal and astigmatic Gaussian beams are established. The fringe fields in the measuring volume are computed for different situations.

2. EXPRESSIONS FOR GAUSSIAN BEAMS

2.1 Ideal Gaussian Beams

The wave amplitude of a fundamental mode (TEM_{00}) Gaussian beam propagating along the z-axis is described by

$$E(x,y,z)=E_0\frac{w_0}{w(z)}\exp\{-i[kz-\tan^{-1}(\frac{z}{z_0})] -(x^2+y^2)(\frac{1}{w^2(z)}+\frac{ik}{2R(z)})\}, \quad (1)$$

where E_0 is a constant; w_0 is the radius of the beam waist; $k=2\pi/\lambda$ is the propagation constant. The parameter z_0, which is known as the Rayleigh range, is defined by

$$z_0=\frac{\pi w_0^2}{\lambda}. \quad (2)$$

The beam radius $w(z)$ is given by

$$w(z)=w_0[1+(\frac{\lambda z}{\pi w_0^2})^2]^{1/2}=w_0[1+(\frac{z}{z_0})^2]^{1/2}. \quad (3)$$

$R(z)$ represents the radius of the wavefront curvature, and changes along the z-axis according to the relation

$$R(z)=z[1+(\frac{\pi w_0^2}{\lambda z})^2]=z[1+(\frac{z_0}{z})^2]. \quad (4)$$

For the convenience of our analysis, we rewrite Eq.(1) as

$$E(x,y,z)=E_0\frac{w_0}{w(z)}\exp\{-\frac{x^2+y^2}{w^2(z)}\} \cdot\exp\{-i[kz-\tan^{-1}(\frac{z}{z_0})+k\frac{x^2+y^2}{2R(z)}]\}. \quad (5)$$

According to Kogelnik & Li (1966), a complex quantity q(z) can be defined by

$$\frac{1}{q(z)}=\frac{1}{R(z)}-i\frac{\lambda}{\pi w^2(z)}. \quad (6)$$

We can rewrite Eq(6) in another form as follows

$$\frac{1}{q(z)}=\frac{1}{R(z)}-i\frac{1}{p(z)}, \quad (7)$$

where $p(z)=\pi w^2(z)/\lambda$.

It has been demonstrated that the q parameter of a Gaussian beam satisfies the ABCD law as it passing through an optical system, ie

$$q_2=\frac{Aq_1+B}{Cq_1+D}, \quad (8)$$

where, q_1 and q_2 are respectively the q parameters at the input and output planes of the optical system, and the constants A, B, C and D are the elements of ray transfer matrix. Using Eqs.(7) & (8) we can readily establish the relations between the input parameters R_1, p_1 and the output parameters R_2, p_2, which are

$$R_2=\frac{(A+B/R_1)^2+(B/p_1)^2}{(A+B/R_1)(C+D/R_1)+BD/p_1^2}, \quad (9)$$

$$p_2=\frac{(A+B/R_1)^2+(B/p_1)^2}{(AD-BC)/p_1}. \quad (10)$$

The output beam waist radius w_{20} and its location z_w can be calculated by using

$$w_{20}=(\frac{\lambda p_2}{\pi})^{1/2}\cdot[1+(p_2/R_2)^2]^{-1/2} \quad (11)$$

$$z_w=R_2[1+(R_2/p_2)^2]^{-1} \quad (12)$$

2.2 Astigmatism Caused by Tilted Refraction Surfaces

As shown in Fig.1, the laser beams in an LDA system are focused by a front lens for which only the outer part is used for transmitting. The surface where the incident beam is refracted is tilted from the optical axis of propagation. On the other hand, transparent windows have to be used in most LDA measurements to provide the optical access to the flows. The incident laser beams are, in general, inclined to the window surfaces. The tilted surfaces of both the front lens and the windows can cause astigmatism on the incident Gaussian beams. Here we only consider the influence of the optical window for which the surfaces are planar. The treatment for the front lens is more complex and will appear in other publications.

We consider a transparent window with the thickness of t and the refractive index of n_2. The refractive indexes of the medium outside the window (air, in most cases) and of the measured flow are n_1 and n_3 respectively. The incidence and refraction angles are shown in Fig1. According to the results given by Massey & Siegman (1969), for the first interface, the

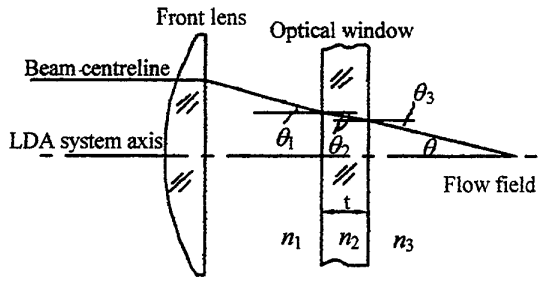


Fig. 1 Propagation of a laser beam through a front lens and a transparent window in LDA measurements

ray matrices in the tangential and sagittal planes can be written as

$$\mathbf{M}_{T1} = \begin{bmatrix} \dfrac{\cos\theta_2}{\cos\theta_1} & 0 \\ 0 & \dfrac{n_1\cos\theta_1}{n_2\cos\theta_2} \end{bmatrix}, \tag{13}$$

$$\mathbf{M}_{S1} = \begin{bmatrix} 1 & 0 \\ 0 & n_1/n_2 \end{bmatrix}. \tag{14}$$

For the second surface, we have

$$\mathbf{M}_{T2} = \begin{bmatrix} \dfrac{\cos\theta_3}{\cos\theta_2} & 0 \\ 0 & \dfrac{n_2\cos\theta_2}{n_3\cos\theta_3} \end{bmatrix}, \tag{15}$$

$$\mathbf{M}_{S2} = \begin{bmatrix} 1 & 0 \\ 0 & n_2/n_3 \end{bmatrix}. \tag{16}$$

The matrix representing the propagation of the laser beam inside the window is

$$\mathbf{M}_W = \begin{bmatrix} 1 & t/n_2\cos\theta_2 \\ 0 & 1 \end{bmatrix}. \tag{17}$$

The total matrices characterising the beam passing through the optical window, $\mathbf{M}_T$ and $\mathbf{M}_S$, can be obtained from Eqs.(13)-(17). The results are

$$\mathbf{M}_T = \mathbf{M}_{T2}\cdot\mathbf{M}_W\cdot\mathbf{M}_{T1} = \begin{bmatrix} \dfrac{\cos\theta_3}{\cos\theta_1} & \dfrac{tn_1\cos\theta_1\cos\theta_3}{n_2^2\cos^3\theta_2} \\ 0 & \dfrac{n_1\cos\theta_1}{n_3\cos\theta_3} \end{bmatrix}, \tag{18}$$

$$\mathbf{M}_S = \mathbf{M}_{S2}\cdot\mathbf{M}_W\cdot\mathbf{M}_{S1} = \begin{bmatrix} 1 & \dfrac{tn_1}{n_2^2\cos\theta_2} \\ 0 & \dfrac{n_1}{n_3} \end{bmatrix}. \tag{19}$$

Substituting the matrix elements given by Eqs.(18) & (19) into Eqs.(9) & (10), we can calculate by using Eqs.(11) & (12) the waist radii, w_{T20} and w_{S20}, and beam waist locations, z_{Tw}, and z_{Sw}, in the tangential and sagittal planes. Expressed by the input parameters, they are

$$\begin{aligned} w_{T20} &= \left[\frac{n_3\lambda}{n_1\pi}\cdot\frac{R_1^2 p_1}{R_1^2+p_1^2}\right]^{1/2}\cdot\frac{\cos\theta_3}{\cos\theta_1} \\ w_{S20} &= \left[\frac{n_3\lambda}{n_1\pi}\cdot\frac{R_1^2 p_1}{R_1^2+p_1^2}\right]^{1/2} \\ z_{Tw} &= \frac{tn_2\cos^2\theta_3}{n_2^2\cos^3\theta_2} + \frac{n_3\cos^2\theta_3}{n_1\cos^2\theta_1}\cdot\frac{R_1 p_1^2}{R_1^2+p_1^2} \\ z_{Sw} &= \frac{tn_3}{n_2^2\cos\theta_2} + \frac{n_3}{n_1}\cdot\frac{R_1 p_1^2}{R_1^2+p_1^2} \end{aligned} \tag{20}$$

Comparing w_{T20} with w_{S20}, we can find that when an ideal Gaussian beam obliquely passes through the optical window, its beam waist radius in the tangential plane will be, in general, different from that in the sagittal plane. Only when the media on both sides of the window are the same, ie $n_1 = n_3$ thus $\theta_1 = \theta_3$, the beam radii in the tangential and sagittal planes will be of the same value.

The obvious difference between z_{Tw}, and z_{Sw} indicates that the beam waists in the tangential and sagittal planes will never coincide in one plane. This means that astigmatism is introduced by the optical window. The astigmatism can be characterised by the difference between z_{Tw}, and z_{Sw}, ie

$$\begin{aligned} \Delta z = z_{Tw} - z_{Sw} &= \frac{tn_2}{n_2^2\cos\theta_2}\left(\frac{\cos^2\theta_3}{\cos^2\theta_2} - 1\right) \\ &+ \frac{n_3}{n_1}\cdot\frac{R_1 p_1^2}{R_1^2+p_1^2}\left(\frac{\cos^2\theta_3}{\cos^2\theta_1} - 1\right) \end{aligned} \tag{21}$$

The beam waist radii in both tangential and sagittal planes and the distance between the two waists can then be calculated by using Eqs.(20) & (21). Consider, for example, a He-Ne laser beam with an incidence angle of 10 degrees and beam radius of 1 mm passing through a 10 mm thick perspex window into a water flow. This implies in Eqs.(20) & (21) that λ = 633 nm, w_1 = 1 mm ($p_1 = \pi w_1^2/\lambda$), t = 10 mm, n_1 = 1, n_2 = 1.5, n_3 = 1.33 and θ_1 = 10 deg. Assuming R_1 = -0.5 m, we will have w_{T20} = 0.1164 mm, w_{S20} = 0.1156 mm and Δz = -8.9 mm. As R_1 is negative, the negative value of Δz indicates that the beam will first reach its sagittal waist then the tangential waist.

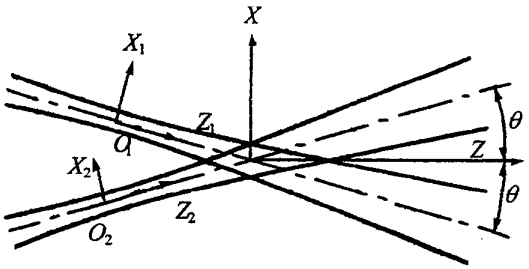


Fig. 2 Interference of two Gaussian beams and the relevant coordinate systems

3. INTERFERENCE OF TWO GAUSSIAN BEAMS WITH AND WITHOUT ASTIGMATISM

3.1 Phase Equations

For an astigmatic Gaussian beam, its phase can be expressed as

$$\phi(x,y,z) = kz - \tfrac{1}{2}\tan^{-1}(\frac{z}{z_{T0}}) - \tfrac{1}{2}\tan^{-1}(\frac{z}{z_{S0}}) + k\frac{x^2}{2R_T(z)} + k\frac{y^2}{2R_S(z)} \quad , \quad (22)$$

where, $z_{T0} = \pi w_{T0}^2 / \lambda$, $z_{S0} = \pi w_{S0}^2 / \lambda$, and $R_T(z)$, $R_S(z)$ are the wavefront radii in the tangential and sagittal planes respectively. For an ideal Gaussian beam, $z_{T0} = z_{S0} = z_0$, $R_T(z) = R_S(z) = R(z)$, $\phi(x,y,z)$ becomes the phase in Eq.(5).

Consider two laser beams intersecting with a cross-angle of 2θ in a global x-y-z coordinate system, as shown in Fig.2. The relevant coordinate systems, x_1-y_1-z_1 for Beam 1 and x_2-y_2-z_2 for Beam 2, are also shown in Fig.2. It is assumed that in the global coordinate system the tangential beam waists are located at $o_1(x_{10}, 0, z_{10})$ and $o_2(x_{20}, 0, z_{20})$ respectively. The locations of the sagittal beam waists are determined by Δz which can be calculated by using Eq.(21). The phase of each beam is expressed by Eq.(22). Interference occurs at the intersection region of the two beams and the intensity reaches a maximum when

$$\phi(x_2 y_2 z_2) - \phi(x_1 y_1 z_1) = 2n\pi \quad , \quad (23)$$

where n is an integer. The coordinates of the individual beams can be expressed with the global coordinates through the following coordinate transformations:

$$\begin{aligned} x_1 &= x\cos\theta + z\sin\theta \\ y_1 &= y \\ z_1 &= -z_{10} / \cos\theta - x\sin\theta + z\cos\theta \\ x_2 &= x\cos\theta - z\sin\theta \\ y_2 &= y - y_{20} \\ z_2 &= -z_{20} / \cos\theta + x\sin\theta + z\cos\theta \end{aligned} \quad (24)$$

In the measuring volume, if the interfering maximum occurs at a point, its coordinates x, y and z must satisfy Eqs.(23)&(24). Interfering surfaces and the fringe spacings can be obtained by directly solving these equations for x with any given y, z and n. For general cases no analytical solution can be obtained, therefore, numerical method was used and computed results for different situations are given in next section.

3.2 Fringe Patterns and Spacing Variations

Calculations were carried out for the fringe generated by the interference of both ideal and astigmatic Gaussian beams. The results shown below are all based on the following parameters: $\lambda = 0.633\mu m$, $\theta = 10^o$, $w_{T0} = w_{S0} = 50\mu m$ for both beams.

We first consider an ideal situation, ie two beams without astigmatism intersect at their waists. Shown in Fig.3 is a three-dimensional interfering surface with n = 1. It can be found that even for this ideal situation, the interfering surface is not a plane, but curved to a saddle-shape. The computed results shows that in any section of y = constant along z-direction the fringe spacing increases from the centre to the outer part of the measuring volume. Adversely, in any section of z = constant along y-direction the fringe spacing decreases from the centerlines to the outer parts. Detailed examinations show that the fringe variations along all three directions are not obvious, thus negligible for the configuration considered. However, for the situations where the beams are sharply focused and large cross-angle are used for achieving high spatial resolution, the fringe variations along all three directions, especially the z-direction may become noticeable and should be considered in LDA designs and applications.

To examine the influence of the astigmatism on the fringe patterns and spacing variations, we consider three cases: (1) the tangential beam waists are located at the origin of the global coordinate system; (2) the sagittal beam waists coincide with the origin of the

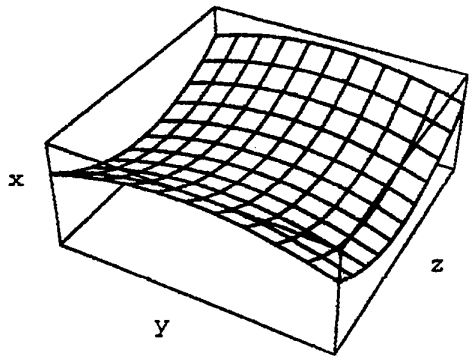


Fig. 3 Three-dimensional interfering surface (n=1) formed by two Gaussian beams without astigmatism

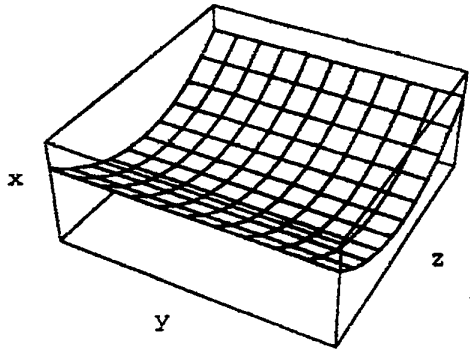


Fig. 4 Three-dimensional interfering surface (n=1) formed by two astigmatic Gaussian beams . The tangential beam waists are located at the origin of the global coordinate system, $\Delta z / w_0 = 40$

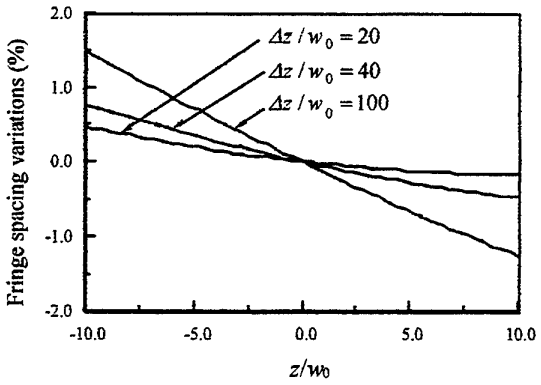


Fig. 5 Fringe spacing variations along the z-axis in a section of $y / w_0 = 0.5$ under different values of $\Delta z / w_0$

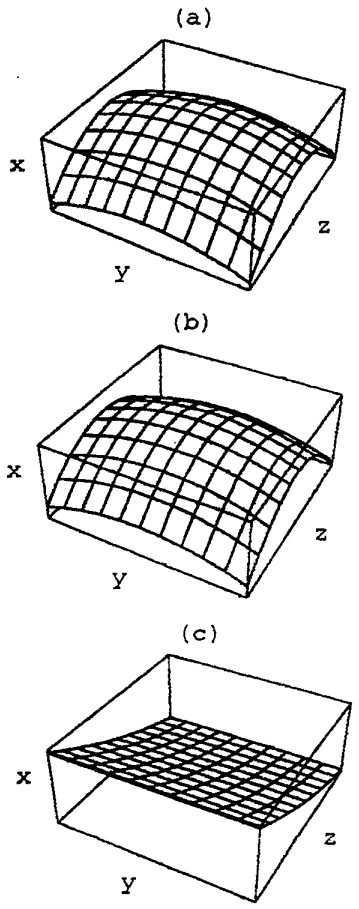


Fig. 6 Three-dimensional interfering surfaces and fringe spacing distribution. The tangential beam waist of Beam 1 and the sagittal beam waist of Beam 2 are located at the origin of the global coordinate system, (a) interfering surface of n=1; (b) interfering surface of n=2; (c) fringe spacing distribution

global coordinate system, and (3) the tangential beam waist of Beam 1 and the sagittal beam waist of Beam 2 are at the origin.

An interfering surface of Case (1) with $\Delta z / w_0 = 40$ is depicted in Fig.(4). Calculations with different Δz show that the astigmatism has little influence on the fringe patterns and spacing variations if the tangential beam waists are located at the origin of the global coordinate system.

The spacing variations in a section of $y / w_0 = 0.5$ in Case (2) with different Δz are compared in Fig.(5). It is clear that the fringe gradients along the z-axis increase when the astigmatism becomes larger. This implies that the fringe patterns and spacing variations

are sensitive to the astigmatism if the incident beams intersect at their sagittal beam waists.

The interfering surfaces with n=1 and n=2 are plotted in Fig.(6a) & (6b) respectively for Case (3). Shown in Fig.(6c) is the fringe spacing distribution. We can find from Fig.(6) that although the interfering surfaces are significantly curved along both the y- and z-axis, obvious spacing variations only happen along the z-axis.

4. CONCLUSIONS

The astigmatism introduced by an optical window in LDA measurements has been analysed by using the q parameter of Gaussian beam and the ABCD law. The formulae for calculating the beam waist radii in both tangential and sagittal planes and the distance between the two waists have been derived and a practical example is presented. With the existence of astigmatism, the shape of a wavefront of a Gaussian beam is significantly different from that of an ideal spherical Gaussian beam. Three-dimensional fringe patterns and spacing variations are computed for the interference of two Gaussian beams with and without astigmatism by numerically solving the established phase equations. It has been found that fringe gradients along the length of the measuring volume increase with an increase of the astigmatism unless the incident beams intersect at their tangential beam waists. The method introduced in this study will be useful for estimating the measurement errors caused by fringe gradients in LDA practice. Our results also suggest that attention has to be paid when one uses a magnified image of the measuring volume to determine the fringe spacings since the astigmatism introduced by the imaging lens may alter the fringe field.

ACKNOWLEDGMENTS

The financial supports from the Australian Research Council (ARC) and Illawarra Technology Corporation (ITC) are gratefully acknowledged

REFERENCES

Durst, F. & Stevenson, W. H. 1979, Influence of Gaussian Beam Properties on Laser Doppler Signals. Appl. Opt., vol. 18, pp. 516-524.

Hanson, S. 1973, Broadening of the Measured Frequency Spectrum in a Differential Laser Anemometer due to Interference Plane Gradients, J. Phys. D, vol. 6, pp. 164-171.

Kogelnik, H. & Li, T. 1966, Laser Beams and Resonators. Appl. Opt. vol. 5, pp. 1550-1567.

Massey, G. A. & Siegman, A. E. 1969, Reflection and Refraction of Gaussian Light Beams at Titled Ellipsoidal Surfaces, Appl. Opt., vol. 8, pp. 975-978.

Miles, P. C. & Witze, P. O. 1996, Evaluation of the Gaussian Beam Model for Prediction of LDV Fringe Fields, Proc. 8th Int. Symposium on Applications of Laser Techniques to Fluid Mechanics , Lisbon, pp, 40.1.1-40.1.8.

SESSION 16

HOLOGRAPHIC PIV

DECOMPOSITION OF TURBULENT FIELDS AND VISUALIZATION OF VORTICES

R. J. Adrian, K. T. Christensen, S. M. Soloff, C. D. Meinhart† and Z. C. Liu

Department of Theoretical and Applied Mechanics
University of Illinois, Urbana, IL 61801 USA

†Department of Mechanical and Environmental Engineering
University of California, Santa Barbara, CA 93106 USA

ABSTRACT

Several types of decomposition techniques exist for revealing the underlying structure in two- and three-dimensional velocity fields obtained by experiment and computation; however, it is unclear which is most appropriate. Traditionally, Reynolds decomposition and vorticity contours are used to visualize the eddies, but several other methods, including Galilean (constant convection velocity) and Large Eddy decompositions, along with swirling strength contours, are found to be superior in visualizing vortices.

1. INTRODUCTION

Reynolds decomposition into mean and fluctuating parts is the *de facto* standard method of describing turbulent fields. While Reynolds decomposition is entirely appropriate for the analysis of the statistics, it is not always the most appropriate method of visualizing the turbulent mechanics of a flow. This is especially true when the data is two-dimensional, as in Particle-Image Velocimetry (PIV), or three-dimensional, as in Direct Numerical Simulation (DNS), Large Eddy Simulation (LES) or Holographic PIV (HPIV).

The method that is best suited to a particular investigation is determined by the questions one asks. If the ultimate goal is to understand the mechanics of turbulence so as to contribute to improved Reynolds averaged Navier–Stokes models, then Reynolds decomposition is clearly the correct choice. However, if one focuses on the dynamics of small-scale vortices, or on the contribution of small structures to the stresses acting on larger structures, then Reynolds decomposition may no longer be the best choice. While these considerations may seem, after only a little reflection, to be quite apparent, the use of Reynolds decomposition is so widespread, and so ingrained in the turbulence community, that it is worthwhile to articulate the differences carefully.

In this paper, these differences will be discussed in the context of identifying small-scale vortices. Alternative methods to Reynolds decomposition include decomposition by Galilean transformation and by filtered fields, as in large eddy simulation. These particular methods are based on the scale of the fluid motions in space or time. Yet another class of decompositions is based on classifying points of the turbulent field according to a certain property (or group of properties), such as rotation. The field is then decomposed into regions depending on the magnitude of that property. A classic example of this is to separate the velocity field into toroidal and poloidal fields. Modern eddy classifiers based on the mathematics of the local velocity gradient tensor will also be discussed.

2. DECOMPOSITION BY SCALE

Decomposition by scale implies separation of the total vector field into fields having different scales of length or time. For example, let $\tilde{\boldsymbol{u}}$ be the total velocity vector and let

$$\langle \tilde{\boldsymbol{u}} \rangle = \boldsymbol{U}(\boldsymbol{x},t) \qquad (1)$$

be the mean of the total velocity, defined either by ensemble averaging, time averaging or spatially averaging in a statistically homogeneous direction. The Reynolds decomposition

$$\tilde{u} = U + u' \qquad (2)$$

can then be viewed as a scale decomposition in several ways, depending upon the definition of the mean. If the mean is determined by long time averaging, the decomposition separates the field into a component that has infinite time-scale and a fluctuation that contains all other components of lesser time-scale. If the mean is found by averaging in one or more spatial directions, then the mean may vary in time, and the decomposition separates the field into a component that has infinite scale in those spatial directions and a component that fluctuates on finite spatial scales and in time. Note that either approach is extreme, in that out of the full space-time spectrum of motions the decomposition only isolates the component that has infinite scale in space or time from all others. One can easily question the utility of this decomposition, as opposed, for example, to isolating the components that are merely large-scale in space and/or time.

Clearly, the more general approach would be to define a decomposition by separating the space-time spectrum of the field into two or more groups, each representing different aspects of the field. If the separation is done purely in space, then this is essentially the approach of large eddy decomposition. Typically, the large eddy field is defined by low-pass filtering the total velocity to obtain the filtered field, $\overline{\tilde{u}}$, and the total field is the sum of the large-scale field and the remaining small scale field

$$\tilde{u} = \overline{\tilde{u}} + u'' \qquad (3)$$

One of the main goals of scale decomposition is to make the visualization and analysis of turbulent eddies easier by removing the translation caused by the large-scale field. The simplest possible way of doing this, although not one that necessarily involves scale decomposition, is through a simple Galilean transformation. In this case, the total velocity is represented as the sum of a constant *convection velocity,* u_c, plus the deviation

$$\tilde{u} = u_c + u \qquad (4)$$

If the convection velocity is simply a freely selected constant, then there is no scale decomposition. But, if u_c is found by averaging over a local region, then the scale velocity corresponds to a moving average, which has the properties of a low-pass filter. In PIV, the measured vector field is commonly averaged over the entire field of view, and this value is then subtracted from the total field before displaying it.

As mentioned earlier, the type of decomposition used can have a dramatic effect on the visualization of the resulting fluctuation field. In the next section, we will consider the effects on the visualization of small-scale vortices.

3. VISUALIZATION OF VORTICES

A consensus definition of a vortex or an eddy has proven to be suprisingly challenging to obtain, and one can find various proposals in the recent research literature (Chong *et al.* (1990), Dallman *et al.* (1991), Jeong and Hussain (1995), and Zhou *et al.* (1998)). Some aspects of this work will be discussed in a later section. For the present, it is sufficient to use the definition offered by Robinson (1991): "A vortex exists when instantaneous streamlines mapped onto a plane normal to the core exhibit a roughly circular or spiral pattern, when viewed from a reference frame moving with the center of the vortex core." A key condition in this definition is that the velocity field must be viewed in a frame that moves at the same velocity as the core of the vortex (It is implicit in this definition that the vorticity is concentrated in a "core").

If a turbulent field consists of large-scale motion with many small-scale vortices imbedded in it, it will only be possible to recognize a vortex in terms of the foregoing definition if the velocity at the center of the vortex is removed from the field. An important function of decomposition by scale is to do exactly this.

To illustrate these ideas, we will use a typical realization of a turbulent field in the radial-streamwise plane of pipe flow at Re=50,000 measured by PIV (Meinhart (1994)) as an example. The resolution of this experiment was very high. Vectors were measured on a 0.27 mm × 0.27 mm grid with interrogation spots that were 0.454 mm × 0.454 mm. This permitted resolution of small scale vortices down to two Kolmogorov scales. Data extends nearly 500 wall units in the streamwise direction and over 250 wall units in the radial direction. A block of data in the upper left-hand corner is missing in this realization due to severe light reflections from the pipe wall.

3.1 Galilean Decomposition

In this section, we illustrate the visualization of small-scale vortices through Galilean decomposition. The aforementioned field is shown in Figure 1 with three different convection velocities removed. The

visible vortices are labeled A-I. Each value of the convection velocity corresponds to a different value of the translational velocity of groups of vortices. When the convection velocity matches the vortex translational velocity, the vortex becomes recognizable as a roughly circular pattern of vectors that fits Robinson's (1991) definition.

For u_c=3.9 m/s (Figure 1(a)), five vortices near the wall (y^+<60) are exposed (A, B, C, D, and E). The vortices in this example lie just above the interface of the buffer and logarithmic regions. In addition, a large region of relatively uniform momentum (darkened portion of the velocity map) is exposed (roughly between 100<x^+<300 and 100<y^+<250).

For u_c=5.8 m/s (Figure 1(b)), two more vortices (F, G) are revealed further away from the wall (50<y^+<150), along with vortex D, which was also seen in the previous case (although its apparent center has moved slightly further away from the wall in this frame). This particular value of convection velocity happens to correspond to the frame-averaged streamwise velocity. The Q2 events induced by these vortices near the wall are also visualized (0<x^+<470 and y^+<70). An outer region vortex (H) is somewhat evident in this frame of reference; however, its velocity vector pattern is not completely circular, implying that this is not the most appropriate frame in which to visualize it. Additionally, the uniform momentum zone in the outer region of the field discussed in the previous case is still visible at this convection velocity.

Finally, for u_c=6.2 m/s (Figure 1(c)), a new outer region (y^+>200) vortex is visualized (I), along with those already seen in Figure 1(b) (D, F, G, H). It is important to note that vortex H has now become much more circular in this reference frame as compared to the previous one. The uniform momentum zone in the outer region is less visible in this frame of reference, although the Q2 events near the wall are still quite strong. It is evident from this discussion that one must consider a range of convection velocities in order to identify **all** of the eddies imbedded in the velocity field.

3.2 Reynolds Decomposition

As mentioned previously, Reynolds decomposition is the traditional method of decomposing a turbulent field. Reynolds decomposition of our pipe flow example reveals six vortices (A, B, C, D, E, H), mostly near the wall. Reynolds decomposition tends to reveal more vortices than Galilean decomposition because, to a first approximation, the vortices in this flow are moving at the local mean velocity. Therefore, by subtracting the mean velocity profile, $U(y)$, many more vortices will be visualized than by removing a single convection velocity. Thus, one of the strengths of Reynolds decomposition is that it does a fair job of revealing the small-scale vortices.

One of the weaknesses of Reynolds decomposition is that it removes large-scale features (mechanisms) that are intimately associated with the mean flow. Thus, comparing figures 1(a, b, c, d) and 2(a), one sees large regions of relatively uniform momentum in the Galilean decomposition that are not as visible in the Reynolds decomposed field. In addition, the Q2 events associated with the vortices are less visible in the Reynolds decomposition. These regions provide important clues as to the structure of the logarithmic layer (Meinhart and Adrian (1995)).

3.3 LES Decomposition

If the small-scale vortices translate with the velocity of the larger-scale vortices in which they are imbedded, then LES decomposition should reveal all of the small-scale eddies in the field. In LES decomposition, the filtered field is defined as

$$\overline{\tilde{u}}(x) = \int_D f(x' - x)u(x')dx' \qquad (5)$$

where f is the smoothing operator (filter) and D is the domain of the velocity field. In this study, a Gaussian filter was used to compute the filtered field.

Figure 2(b) shows the LES fluctuating velocity field for the same pipe flow realization discussed earlier. It was obtained by subtracting the filtered field from the total velocity field. As expected, the LES decomposition extracts eddies from all three of the layers noted in Figure 1, indicating that it is superior to both Reynolds and Galilean decomposition as an eddy visualization tool. Note that the fluctuating field does not provide any insight into regions of constant momentum. However, the filtered field itself should show the large-scale features of the flow, i.e. the uniform momentum zones. In Figure 2(c), regions of near-constant momentum are evident for 100<x^+<375 and y^+>100. These coincide well with those seen in the Galilean decompositions, especially Figure 1(b).

3.4 Vortex Identification Based on Local Velocity Gradient Tensor

The newest method of extracting underlying structure from velocity fields involves analysis of the

local velocity gradient tensor and its corresponding eigenvalues (Chong *et al.* (1990), Dallman *et al* (1991), Jeong and Hussain (1995), and Zhou *et al.* (1998)). In three dimensions, the local velocity gradient tensor will have one real eigenvalue (λ_r) and a pair of complex conjugate eigenvalues ($\lambda_{cr} \pm \lambda_{ci}$) when the discriminant of its characteristic equation is positive. Zhou *et al.* (1998) show that the strength of any local swirling motion is quantified by λ_{ci}^2, the *swirling strength* of the vortex. This identification method is frame independent, meaning that *a priori* choice of a correct reference frame is not necessary. In addition, it does not extract regions which have vorticity but are absent of any local swirling motion (i.e., shear layers).

Since PIV fields tend to be two-dimensional, the full local velocity gradient tensor cannot be formed. However, an equivalent two-dimensional form of the velocity gradient tensor can be computed in the plane in which the PIV data lies; namely,

$$\underline{\underline{D}}_{2\text{-}D} = \begin{bmatrix} \partial u/\partial x & \partial u/\partial y \\ \partial v/\partial x & \partial v/\partial y \end{bmatrix} \qquad (6)$$

where (u, v) and (x, y) are the streamwise and wall-normal velocities and directions, respectively. In this case, $\underline{\underline{D}}_{2\text{-}D}$ will either have two real, distinct eigenvalues or a pair of complex conjugate eigenvalues. Therefore, swirling motion is easily identified by simply plotting contours of the swirling strength, λ_{ci}^2.

This analysis was performed on the same pipe flow realization presented earlier. Spatial derivatives were computed using a central difference scheme. Contours of swirling strength are shown in Figure 3(a). Swirling strength is noted at **all** locations where a vortex was identified in the various velocity decompositions (labeled A-I). Figure 3(b) shows vorticity (gray scale) and swirling strength (line) contours superimposed on one-another. Although vorticity does identify the eddies fairly well, it is much noisier than the swirling strength and it also tends to identify any local shear layers present in the field. These shortcomings of vorticity make swirling strength more appropriate as a means of identifying eddies.

The drawback of swirling strength analysis is that it does not decompose the velocity field into a portion containing the large-scale motions and a portion containing the small-scale motions. In addition, it provides no information about the motions induced by the vortices. It simply allows one to identify the locations of small-scale vortices in a velocity field.

4. CONCLUSIONS

Several methods exist for decomposing turbulent velocity fields. For statistical analysis, Reynolds decomposition is the most appropriate. However, for visualization of vortices, other decomposition methods have been shown to be superior. Galilean transformations allow one to not only to visualize the core of the small-scale vortices moving at a particular translational velocity, but also the motions these vortices induce (especially near the wall). Despite these advantages, LES decomposition is still the best method for visualizing all of the small-scale vortices in a flow. Although analysis based on the local velocity gradient tensor provides a means of extracting the small-scale vortices from the velocity field, it does not, without further development, provide a way of decomposing the total velocity field by scale.

5. ACKNOWLEDGEMENTS

This research was supported by grants NSF-ATM 95-22662 and NSF CTS 96-16219. K.T. Christensen was supported by an NSF Graduate Fellowship.

REFERENCES

Chong, M.S., Perry, A.E. & Cantwell, B.J. 1990, A General Classification of Three-Dimensional Flow Fields, Phys. Fluids, vol. A2, pp. 765-777.

Dallman, U., Hilgenstock, A., Riedelbanh, S., Schulte-Werning, B. & Vollmers, H. 1991, On the Footprints of Three-Dimensional Separated Vortex Flows Around Blunt Bodies, AGARD, CP-494.

Jeong, J. & Hussain, F. 1995, On the Identification of a Vortex, J. Fluid Mech., vol. 285, pp. 69-94.

Meinhart, C.D. 1994, Investigation of Turbulent Boundary Layer Structure Using Particle-Image Velocimetry, *Ph.D. Thesis*, University of Illinois, Urbana, Illinois.

Meinhart, C.D. & Adrian, R.J. 1995, On the Existence of Uniform Momentum Zones in a Turbulent Boundary Layer, Phys. Fluids, vol. 7, pp. 694-696.

Robinson, S.K. 1991, Coherent Motions in the Turbulent Boundary Layer, Ann. Rev. Fluid Mech., vol. 23, pp. 601-639.

Zhou, J., Adrian, R.J., Balachandar, S. & Kendall, T.M. 1998, Mechanisms for Generating Coherent Packets of Hairpin Vortices in Near-Wall Turbulence, in press.

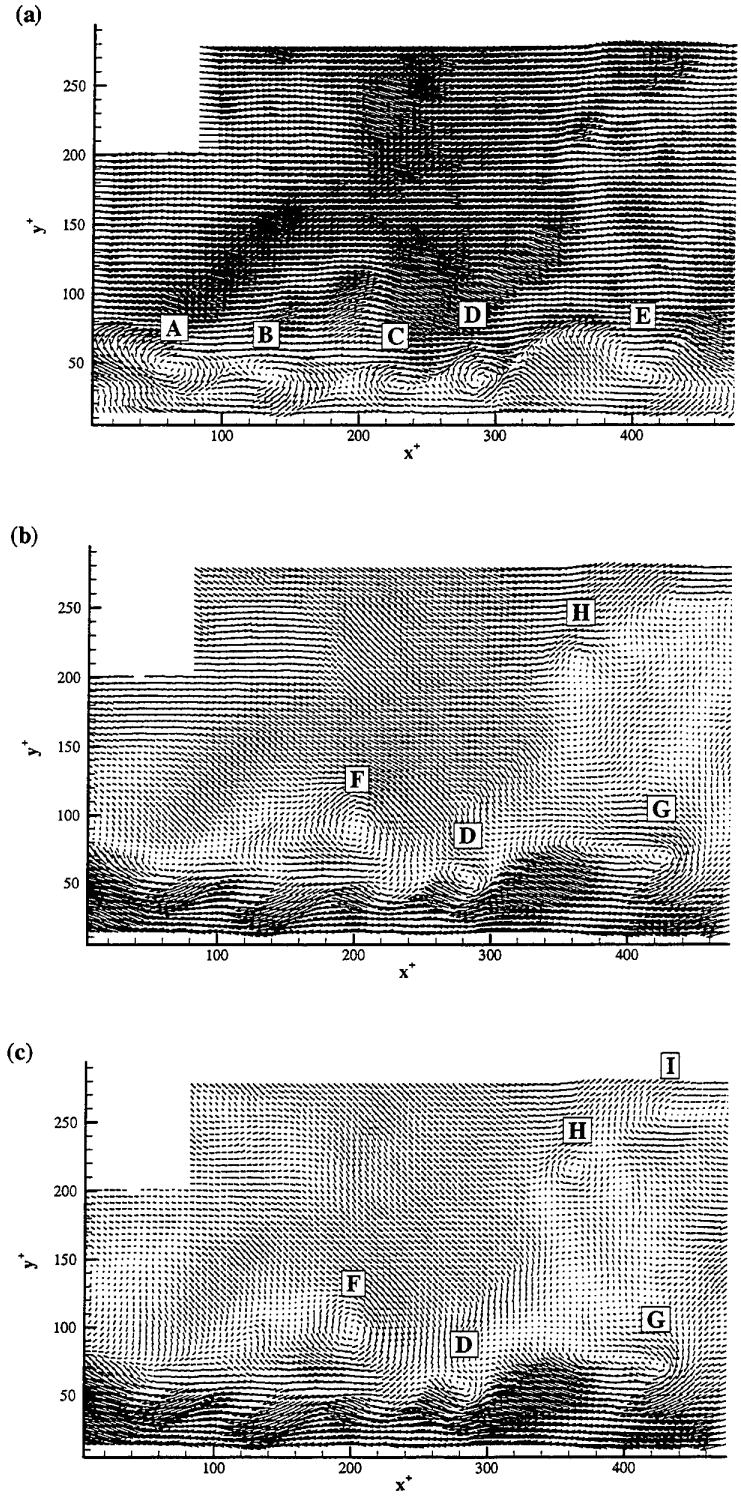


Figure 1. Fluctuating vector fields in pipe flow found by Galilean decomposition. (a) u_c=3.9 m/s ; (b) u_c=5.8 m/s ; (c) u_c=6.2 m/s. The vortices are labeled A-I.

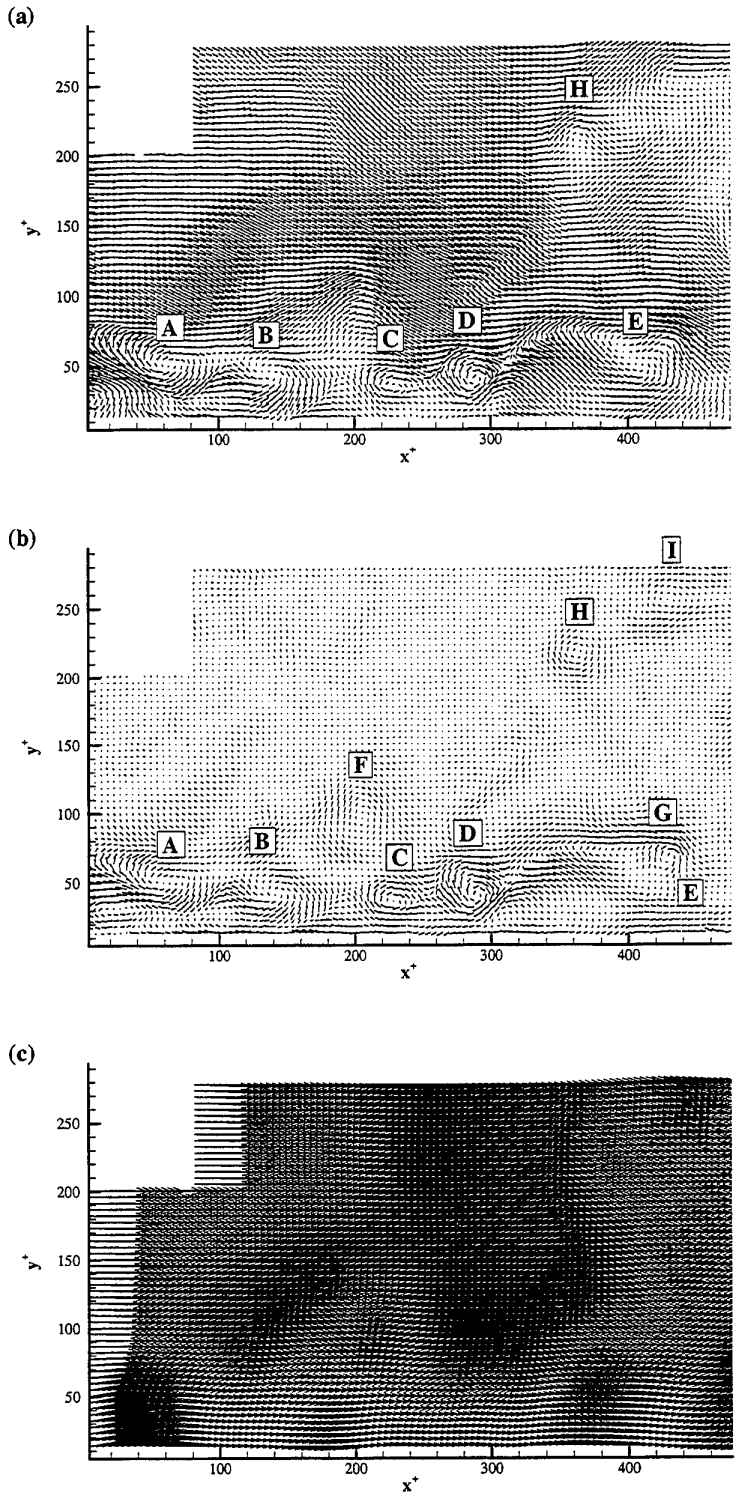


Figure 2. Pipe flow velocity fields (same data as in Figure 1) illustrating (a) Reynolds-decomposed fluctuations; (b) LES-decomposed fluctuations; (c) LES low-pass filtered field.

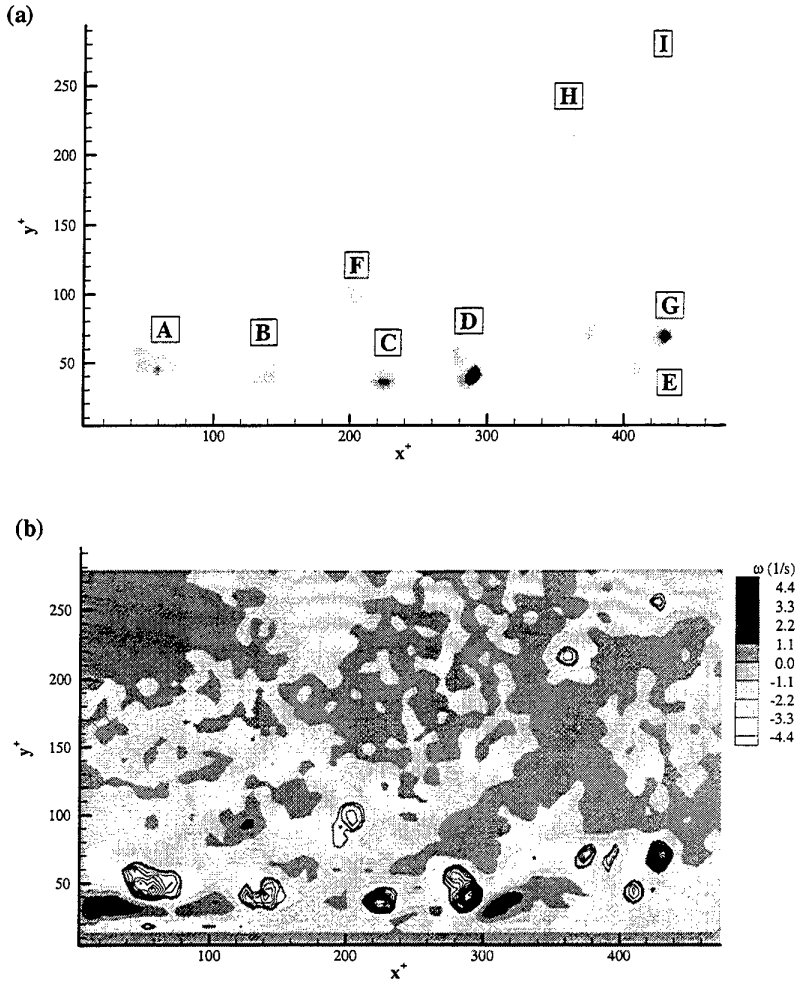


Figure 3. (a) Swirling strength contours and (b) vorticity (gray-scale) and swirling strength (line) contours for pipe flow (same data as Figure 1).

AN ADVANCED OFF-AXIS HOLOGRAPHIC PARTICLE IMAGE VELOCIMETRY (HPIV) SYSTEM

Ye Pu, Zhijian Huang and Hui Meng*
Department of Mechanical and Nuclear Engineering
Kansas State University
Manhattan, KS 66506, USA
* (785) 532-5619, meng@ksume.me.ksu.edu

ABSTRACT

Holographic PIV (HPIV) is the most promising candidate for the next generation full-field velocimetry that can measure high spatial resolution instantaneous three-dimensional (3D) velocity fields. To explore the maximum performance capabilities of HPIV including spatial resolution, off-axis-holography based HPIV has become a major direction of development. A fully automated off-axis HPIV system based on an injection-seeded dual-pulsed YAG laser and 3D data processing software has been implemented in Laser Flow Diagnostics Lab (LFD). In our system 90-degree particle scattering, dual reference beams, *in situ* reconstruction/data processing, and 3D velocity extraction based on a fast "Concise Cross Correlation" (CCC) algorithm are utilized. The off-axis HPIV system is tested for an acoustically excited air jet and the wake of a surface-mounted tab in a water channel flow, giving instantaneous 3D velocity fields for both flows. Experimental data of instantaneously measured 3D flow structures show great promise of this technique.

1. Introduction

The establishment of PIV technique marks a significant advancement in experimental fluid mechanics from single-point to multi-point velocity measurement (Adrian 1996; Adrian 1997). This progress, however, is only half way towards full-field three-dimensional (3D) measurement of turbulent flows, and by far the easier half. Attempts have been made to generalize these planar PIV techniques to 3D volumetric field measurement (Guezennec, *et al.* 1994; Bruecker 1995; Bruecker 1997). These methods are based on photographic principle and thus 2D in nature. Their spatial and time resolutions are severely limited when it comes to 3D volumetric measurement. Hence, these PIV techniques are unable to provide detailed space- and time-resolved experimental data in highly transient and three-dimensional turbulent flows needed for understanding, modeling and control of turbulent flows.

Holographic PIV (HPIV) records the instantaneous 3D information of a large quantity of tracer particles in a fluid *volume* on a hologram and then reconstructs the particle images optically. By finding the 3D displacements of the particles in the image volume between two exposures separated by a short time lapse, instantaneous volumetric 3D velocity field is retrieved. When applied in conjunction with cinematography, both time- and space-resolved measurements can be accomplished. Hence holography is the path for 3D velocimetry.

The key problems that any HPIV system faces are reduction of speckle noise, handling of huge quantities of data, extraction of 3D velocity in presence of large gradients/fluctuations, and system complexity vs. user-friendliness. While the strategies of handling all these issues make each setup unique, HPIV configurations can be broadly classified into two kinds based on the nature of the holographic scheme: "in-line", where only one beam is employed to produce both the object wave (scattered part) and the reference wave (unscattered part), and "off-axis", where separate object beam and reference beam(s) are introduced. Many variations are possible, which often blur such distinctions.

While enjoying simplicity of optical geometry, low requirements for laser coherence and energy, standard in-line method, when used in HPIV, has been proven to produce excessive intrinsic speckle noise due to the superposition of its real image,

virtual image and reference beam (Meng, *et al.* 1993). In-line Recording Off-axis Viewing (IROV) technique appears to be an efficient way to suppress the speckle noise and improve the SNR of the reconstructed particle images, while using only one beam for hologram recording. Holographic PIV based on IROV has been successfully applied to instantaneous 3D flow measurements (Meng and Hussain 1995a, b; Sheng & Meng 1998).

With the innovative IROV approach, in-line HPIV has reached a certain level of applicability. Indeed, its optical simplicity makes it attractive for many applications including holographic 3D flow visualization, and hence it is one of the major HPIV techniques this and other labs are currently pursuing (Sheng & Meng 1998; Meng, *et al.* 1998). However, at a seeding density no more than a few particles per mm^3, which is a *de facto* limitation of IROV, the achievable spatial resolution of in-line HPIV is still far from fully resolving turbulent flows, the ultimate goal of HPIV. In the pursuit of high spatial resolution 3D velocity vector field measurement, off-axis holography becomes the logical choice. With off-axis HPIV scheme, the real, virtual images and the reference beam are no longer superposed, eliminating the major source of speckle noise inherent in in-line HPIV.

2. Rationale of Off-axis HPIV System

Various off-axis methods have been proposed and reported since the early years of HPIV development (Barnhart, *et al.* 1994; Meng 1994; Liu & Hussain 1995; Zhang & Katz 1996), addressing the problem of laser energy utilization and effective N.A. Encouraged by the high scattering efficiency of the forward scattering, Zhang & Katz (1996) constructed a hybrid HPIV system, where forward scattering is combined with off-axis holography. In the configuration an optical high-pass spatial filter is utilized to avoid the directly transmitting wave in the object beam. In contrast, Barnhart, *et al.* (1994) implemented a phase conjugate HPIV system, where two separate channels of near-forward scattering are combined to achieve an effective large N.A. of particle images. To compensate for the severe optical distortion and aberration imposed by the complex optics, a phase conjugate reconstruction system is required. These two approaches exemplify compromises between the laser energy utilization and the effective N.A.

We propose to take a more practical approach to the off-axis HPIV. A high effective N.A. can be achieved by using 90-degree scattering, which provides homogeneous intensity distribution over a large solid angle, and shortening the recording distance without adding any optics between the hologram and the particle field (Meng 1994). Since 90-degree scattering is rather weak, it is essential to minimize noise introduced by reflection of laser light on walls and optical components. The short recording distance also increases the efficiency of the laser energy utilization. To further increase particle image SNR, we reduce aberration by *in-situ* reconstruction, which involves the use of both the same laser source and the same reference-beam optics for recording and reconstruction.

In this paper we describe our new off-axis HPIV system developed in the Laser Flow Diagnostics Lab, and show its preliminary applications in 3D turbulent and vortical flows.

3. System Description

Based on off-axis holographic principle, we implemented a fully automated experimental off-axis HPIV, which employs 90-degree scattering, dual reference beams, *in-situ* reconstruction, and novel 3D data processing algorithms. In this section we describe the system in details.

Recording

Recording is the first step in HPIV measurement. Illustrated in Fig. 1 is the optical configuration for off-axis HPIV recording. An injection-seeded dual Nd:YAG laser (Spectra-Physics PIV-400) is employed as the light source, which gives a pair of temporally and spatially separated laser pulses, each of 8ns duration, at a repetition rate of 10Hz. Like in regular PIV applications, the double pulse separation Δt is adjusted according to the estimated flow speed. The two laser units contained in the dual YAG laser system are fired by a multi-channel digital delay generator. The addition of injection seeding to the standard PIV-400 laser guarantees sufficient coherence length (over a meter), which otherwise would be less than 1cm.

Each laser head emits a beam, which, after passing through a shutter and a couple of high-energy mirrors (HEM), is split into two parts by a partial reflection mirror which works as a beam splitter (BS). The majority of the energy (80%) from each beam is reflected and used for illumination. The two illuminating beams, very close to each other, are combined at a common receiving HEM. The slight angular misalignment between the two beams becomes negligible after they pass through the illuminating beam expander. The transmitting part of each laser beam through the BS is further manipulated by a variable beam splitter (VBS), which consists of a pair of half-wave plates (WP)

and a polarizing beam splitter (PBS). With the two VBS, it is possible to adjust the intensity of the reference beams and thus the reference-to-object intensity ratio. Evidently, the beam handling unit (enclosed by dashed line on the bottom-right corner of Fig. 1) produces three output beams: two separate reference beams (Reference 1 and 2) and one combined illuminating beam. It actually works as a multiplexer during double exposure: the illuminating beam is double pulsed, while the two reference beams are alternately single pulsed. This dual-reference-beam design provides angular separation of the reference beams for the double-exposure hologram, so that the two holographic images can be

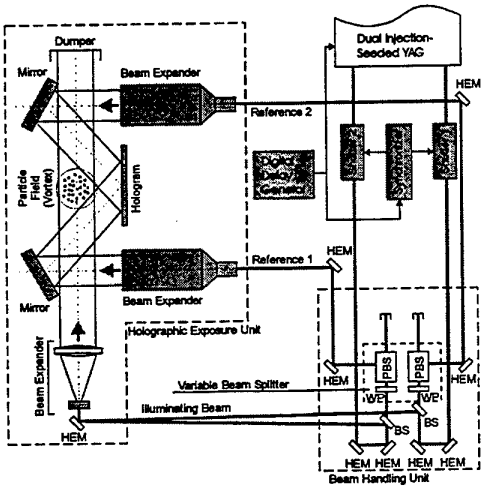


Fig. 1. Schematic of off-axis HPIV recording.

reconstructed alternately in time.

The 90-degree scattered light from the particle field interferes with the reference beams, and the resultant interference pattern is recorded by the holographic plate. In this way a 90-degree scattering dual-reference off-axis HPIV recording scheme is created.

Reconstruction

To reduce aberrations as much as possible (important for achieving high SNR), the hologram is reconstructed *in situ*, where exactly the same laser and reference beams for recording are employed. As shown in Fig. 2, the hologram reconstruction system shares the same optics as the recording system, except that the object illustrating beam is blocked since it is no longer needed during reconstruction. The light paths for the two reference beams are identical to those in the recording stage. The developed hologram containing interference fringes is now placed back at the original position, albeit with the film emulsion facing opposite to that of recording, such that each reference beam incident on the hologram becomes the complex conjugate of that used in recording. In this way, an unscrambled real image of the 3D particle field is reconstructed on the emulsion side, *i.e.,* on the opposite side to the flow field.

The laser shutters are kept open at all times to pass every laser pulse for continuous hologram reconstruction and image acquisition. The two laser units are fired alternately, each at 10Hz, to produce the two reference beams corresponding to those used for double-exposure recording. This way, the hologram reconstructs alternately the particle field recorded before and after the Δt.

Now that a frozen 3D particle field from each exposure is reconstructed continuously, it can be interrogated with a planar imaging device to be converted into digital form. A high-resolution digital CCD camera (KODAK ES1.0, 1k×1k, 30fps) mounted on a 3D traversing system (Daedal-Parker) is employed to capture the reconstructed holographic image. The camera sees only a small area of a thin slice at a time. The 3D image is interrogated slice by slice, and area by area. The entire particle field is thus decomposed into many 3D Interrogation Cells (IC), similar to the 2D Interrogation Spots (IS) in planar PIV. The pitch in depth direction, *i.e.* the distance between adjacent slices must be small enough to resolve particle images along the depth.

Data acquisition and processing is fully automated and administered by a PC. A PCI digital image framegrabber is hosted in the computer to perform image capturing, and a motion controller is also installed to position the camera through the 3-axis traverse system. Image acquisition and camera movement are synchronized with the laser pulses to ensure data integrity. Data processing is completed on-the-fly on the basis that the processing is fast enough to follow the image acquisition and camera positioning. A speed of approximately one pair of image planes per second is achieved by the system. Most of the time is consumed by particle centroid finding.

4. Data Processing

Demonstrated in Fig. 3 is a schematic diagram of data processing in our off-axis HPIV system. Digital image captured by the CCD camera is transferred into the system memory in the host computer via the framegrabber. Because of the tremendous amount of data, it is impractical to compress and store the raw 3D image, even with state-of-the-art image compression algorithms. Therefore the centroid locations of particles are extracted from the raw image for further data

processing, while the raw image is discarded. The centroid finding process not only reduces the amount of data by 4 to 5 orders of magnitudes (depending on the seeding density), but also enables the application of the novel CCC algorithm.

during reconstruction.

Larger viewing area means faster processing speed since there are less image data to be processed. However, as the viewing area increases, the accuracy of particle centroid decreases. Therefore to obtain reasonable precision at relatively large viewing area, subpixel resolution is used.

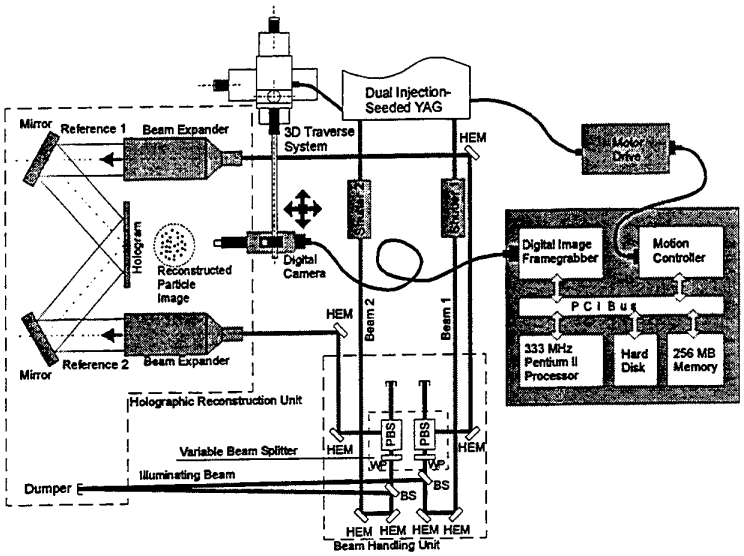


Fig. 2. The schematic of off-axis HPIV reconstruction.

4.1Centroid finding

The centroid finding is critical to processing efficiency. Since intensity peak of a particle image is typically located at its geometric centroid, a simple thresholding and binarization procedure provides the centroid pixel, whose 3D location is recorded. It has been well recognized that the centroid finding process is the bottleneck of the processing speed, since the enormous image data have to be processed pixel by pixel before anything is discarded. Due to the high image quality (i.e. the high image SNR) of off-axis holography, no de-noising operation is involved in the centroid finding process in our system. This greatly improves the overall processing speed. In addition, adaptive thresholding is utilized to reduce the influence of the laser energy fluctuation

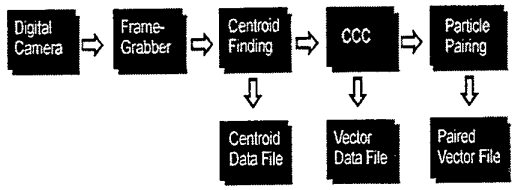


Fig. 3. Data acquisition and processing.

4.2 CCC algorithm

Conventional FFT-based correlation has been the norm for velocity field extraction in planar PIV. For holographic PIV, where 3D velocity components are extracted in a 3D volume, generally it is assumed that this standard correlation method can be directly extended to 3D by either working with a 3D matrix (Gray and Created 1993; Huang, K., *et al.*, 1993) or two stereo 2D matrices (Barnhart *et al.* 1994; Meng

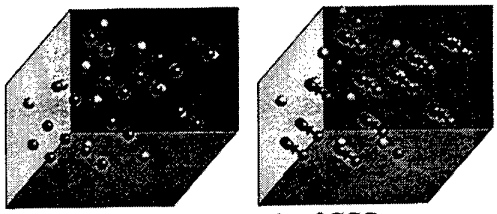


Fig. 4. Principle of CCC.

1994). Direct 3D FFT correlation appears impractical for high-resolution, large-volume off-axis HPIV measurement, since there are usually over 100 GB of 3D image data per hologram, which, with FFT-based algorithms, can easily take thousands of hours to process. On the other hand, working with

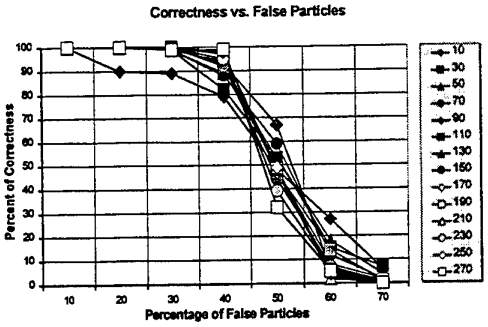


Fig. 5. Correctness of CCC vs. false

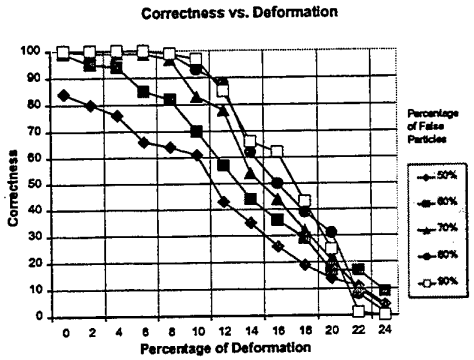


Fig. 6. Correctness of CCC vs. deformation

two stereo 2D matrices does provide relatively fast processing speed, but it suffers from an inherent low accuracy in depth direction and, more critically, requires a large viewing angle of the hologram to fit in two cameras. This often imposes difficulties on the holographic scheme (Meng 1994). Besides, due to its FFT-based nature it cannot handle low seeding densities.

We recognize that since only the displacements of particle images or at most their locations carry the information needed for velocity field measurement, it is unnecessary to store and handle the entire image data (which include redundancies such as particle sizes, shapes, intensities, background conditions etc.). Hence a correlation procedure can be applied directly to the 3D locations of particles. This is implemented in the novel Concise Cross Correlation algorithm, which yields a compression ratio of 4 to 5 orders and an increase in processing speed of 3 orders of magnitude.

In our implementation of correlation, we take two groups of particle centroids, whose 3D coordinates are extracted from a pair of images in the double exposure. Keeping one of them fixed in its original place, we translate the other one in the 3D space and compute their correlation intensity. The displacement yielding the highest correlation peak is considered the displacement of the particle group and is the correlation output. Fig. 4 illustrates how CCC works. Depicted in Fig. 5 and 6 is the correctness of CCC vs. number of false particles and morphological deformation, respectively, based on Monte Carlo simulations.

Higher spatial resolution and accuracy can be further achieved by pairing individual particles after CCC finds the mean displacements of particle groups. In each Interrogation Cell, after the three components of the resultant vector are obtained through CCC, the second set of particle centroids is shifted in 3D along the vector. Now that there is no net displacement of the particle group but only net deformation between the two particle groups, pairing is accomplishable on the basis of closest distance.

5. Experimental Results

5.1Measurement of a vortex ring in air

The off-axis HPIV system described above has been tested with measurement of a forced jet. The airflow, generated by a fan, is seeded with water droplets 5μm in size. It enters a chamber with a loud speaker mounted on the bottom and passes through a honey- comb, a contraction, and a circular nozzle, as depicted in Fig. 7. At 1-in. downstream of the jet exit, a vortex ring is formed, which travels at ~ 2m/s. The acoustic forcing is synchronized with the 10Hz laser pulses, producing a stationary vortex ring located in the center of illumination. The dispersion of droplets in the 3D vortex ring is rather inhomogeneous. The average seeding density is

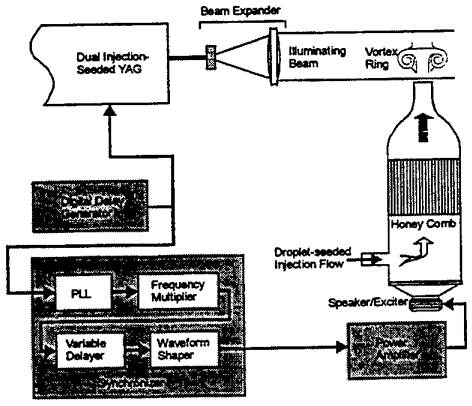
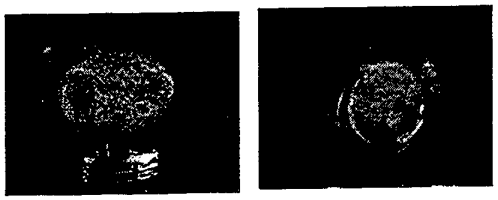


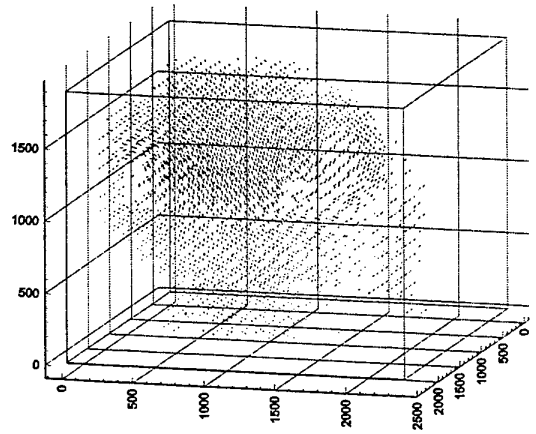
Fig. 7. Schematic of vortex ring generator

around 30 particles per mm^3, which produces excellent image quality for data processing.

The R-O intensity ratio used to record the hologram is around 4:1. Depth of focus of particle images in this experiment ranges from 0.3mm to 0.5mm, for which a pitch distance of 0.1mm is chosen for depth interrogation. A 4× microscope objective is mounted on the CCD camera to obtain a 2×2mm viewing area, and with 20 image planes in each IC, the IC size is 2×2×2mm. Therefore in the whole image volume, 50 (width) × 40 (height) × 50 (depth) = 12500 interrogation cells are acquired and processed, containing 250000 planar interrogation spots. With the CCD resolution of 1k x 1k, this corresponds to 250 Gbytes of data.



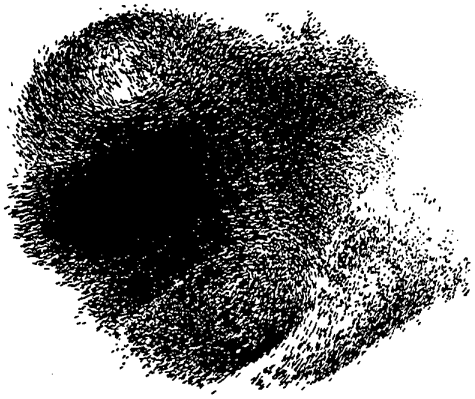
(a) (b)



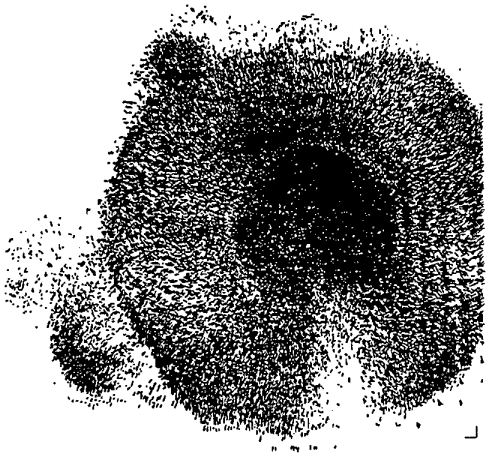
(c)

Fig. 8. The vortex ring and its measured velocity field: (a) side view. (b) top view. (c) The instantaneous 3D velocity field of the vortex ring.

Shown in Fig. 8 are 3D vectors in the flow volume directly extracted with CCC algorithm. This instantaneous 3D snapshot of the test flow consists of approximately 6000 vectors. Since the particle distribution is inhomogeneous, at some test points there are no data. Out of the total number of vectors produced by CCC, only about 5% are bad vectors, which can be easily identified and eliminated based on their lower correlation peak values. After bad-vector elimination, the residual bad vectors are well below 1%.



(a)



(b)

Fig. 9. Velocity field after pairing: (a) side view. (b) top view.

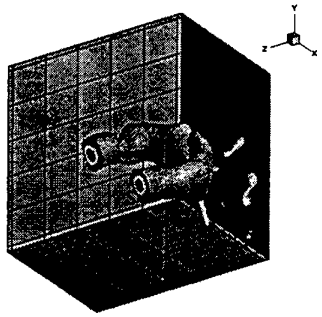


Fig. 10. 3D vorticity iso-surface

The 3D vortex ring structure can be identified from this preliminary 3D vector map. To increase spatial resolution, particle pairing is further performed on individual particles, with the average vectors generated by CCC as references. After the particle pairing process, the spatial resolution is increased by two orders of magnitude. The resulting raw velocity field is shown in Fig. 9, where the vectors are irregularly distributed in the 3D space.

From the dense version of the 3D velocity vector field, 3D vorticity field is calculated. To deal with missing data points and achieve higher accuracy, the velocity vectors are interpolated on a regular grid prior to the vorticity calculation. Illustrated in Fig. 10 is a vorticity iso-surface created from the computed vorticity field. Clearly, it depicts the 3D topology of the vortex ring measured.

5.2 3D velocity field in a surface-tab water channel flow

To test the feasibility of the off-axis HPIV technique for water flows, it is applied to a water channel flow with a tapered passive mixing tab mounted on the wall. The wake of such a tab is known to produce complex 3D vortical motions (Yang & Meng 1998; Gretta & Smith 1993) and thus the tab is often called vortab. The free-stream flow rate is approximately 16cm/s, corresponding to Re ~ 12000 based on the channel height, and 2040 based on the tab height.

The holographic recording geometry of this flow is depicted in Fig. 11. The optical configuration is identical to the one employed in the air jet

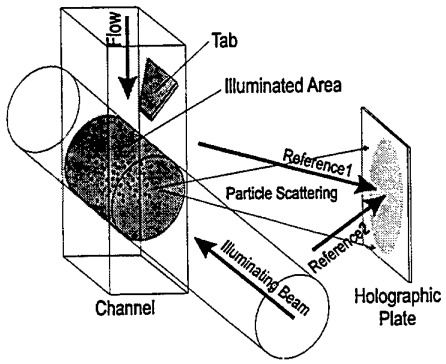


Fig. 11. Vortab flow measurement using

measurement. Hollow glass beads sized around 9μm are illuminated by the volumetric laser beam at the test section. In this experiment, higher processing speed is achieved by adopting a large aperture objective lens with a low magnification. As a result the viewing area (IC size) is increased to 4mm×4mm. Figure 12 shows the 3D snapshot of the velocity field measured in a volume of 52mm × 60mm × 36mm. For clarity only those vectors on the outer surfaces are plotted. Approximately 400,000 vectors have been extracted using CCC and particle pairing algorithms. In this figure, the mean velocity averaged over all the vectors in the volume has been subtracted.

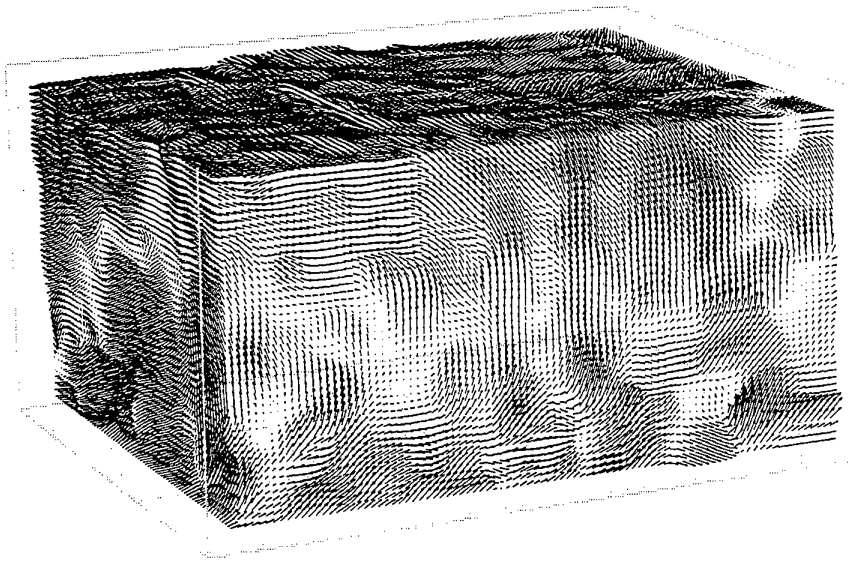


Fig. 12. The instantaneous 3D velocity field obtained from the vortab flow.

6. Summary

In this paper we describe an advanced off-axis HPIV system with fully automated data processing. It is distinguished by the use of 90-degree scattering, dual reference beam structure, *in situ* reconstruction, on-the-fly processing, and a novel CCC algorithm based on particle centroids. Our off-axis HPIV configuration offers superior image SNR at relatively high seeding density, alleviating the need for de-noising in data processing and enabling the use of CCC algorithm. A great gain on processing speed and data compression ratio is achieved over traditional methods by using CCC. This innovative correlation approach also makes particle pairing possible, which increases the spatial resolution by two orders of magnitudes. This technique has been successfully tested on two flows including an acoustically excited air jet seeded with water droplets and a surface-tab water channel flow.

REFERENCE

Adrian, R. J. 1996, Strategies for Imaging Flow Fields with PIV, AIAA 96-1988.

Adrian, R. J. 1997, Dynamic ranges of velocity and spatial resolution of particle image velocimetry, Meas. Sci. Technol. 12, pp. 1393-1398.

Adrian, R. J., Soloff, S. M., Liu, Z. C., Meinhart, C. D., and Lai, W. 1997, Stereoscopic PIV Applications to the Study of Turbulence, Workshop on PIV-Fukui, July 8-11, 1997, Fukui, Japan.

Barnhart, D. H., Adrian, R. J., Meinhart, C. D. and Papen, G. C., 1994, Phase-conjugate holographic system for high-resolution particle image velocimetry, Appl. Opt., vol. 33, pp.7159-7169.

Bruecker, Ch. 1995, 3-D DPIV using a scanning light-sheet and stereoscopy: study of flow development around a spherical cap, ASME FED 229, pp. 497-503.

Bruecker, Ch. 1997, 3D scanning PIV applied to an air flow in a motored engine using digital high-speed video, Meas. Sci. Technol. 12 pp. 1480-1492.

Cha, S., *et al.* 1993, Double-reference beam off-axis holographic particle image velocimetry, Holographic Particle Image Velocimetry (ed: E. P. Rood), ASME FED 148, pp. 23-32.

Gray, C. and Greated, C. A. 1993, Processing system for the analysis of particle displacement holograms, SPIE 2005, San Diego, pp. 636-647.

Gretta, W. J. and Smith, C. R. 1993, Flow structure and statistics of a passive mixing tab, J. Fluids Eng., Trans. ASME 2 pp. 255-263.

Guezennec, Y. G. Zhao, Y. and Gieseke, T. J. 1994, High-speed 3-D scanning particle image velocimetry (3-D SPIV) technique, Proc. Laser Symp., Lisbon, paper26.1.

Hinsch, K. D., Hinrichs, H., Roshop, A. and Dreesen, F. 1993, Holographic and stereoscopic advances in 3D PIV, Holographic Particle Image Velocimetry (ed: E. P. Rood), ASME FED 148, pp. 33-36.

Huang, K., Slepicka, J. and Cha, S. S. 1993, Cross-correlation of three-dimensional images for three-dimensional three-component fluid velocity measurements, SPIE 2005, pp. 655-666.

Hussain, F., Liu, D., Simmons, S. and Meng, H. 1993, Holographic particle velocimetry: prospects and limitations, Holographic Particle Image Velocimetry (ed: E. P. Rood), ASME FED 148, pp. 1-11.

Meng, H., Anderson, W. L., Hussain, F., and Liu, D. 1993, Intrinsic speckle noise in in-line particle holography, J. Opt. Soc. of Am 10 pp. 2046-2058.

Meng, H. 1994, Development of holographic particle velocimetry techniques for three-dimensional vortical flows, Ph.D. thesis, University of Houston, Houston, TX.

Meng, H. and Hussain, F. 1995a, In-line Recording and Off-axis Viewing (IROV) technique for holographic particle velocimetry, Appl. Opt. 34, pp. 1827-1840.

Meng, H. and Hussain, F. 1995b, Instantaneous flow field in a circular vortex ring captured by innovative holographic particle velocimetry, Phys. Fluids vol.7, pp. 9-11.

Meng, H., Estevadeordal, J., Gogeneni, S., Goss, L., and Roquemore, W. M. 1997, Holographic flow visualization as a tool for studying 3D coherent structures and instabilities, Proc. 2nd Int. Workshop on Particle Image Velocimetry, Vis. Soc. of Japan, Fukui, Japan, July 9-11.

Prasad, K. and Adrian, R. J. 1993, Stereoscopic particle image velocimetry applied to liquid flows, Exp. Fluids 15, pp. 49-60.

Sheng, J., and Meng, H. A Genetic Algorithm approach for 3D velocity field extraction in holographic particle image velocimetry, accepted by Exp. Fluids.

Yang, W. and Meng, H. Regeneration of hairpin vortices in the wake of a surface-mounted mixing tab, accepted by J. Fluid Mech.

Zhang, J. and Katz, J. 1996, Three dimensional velocity measurements using hybrid HPIV, Proc. 8th Int. Sym. on Appl. Laser Technol. to Fluid Mech., Lisbon, pp. 4.3.1-8.

HOLOGRAPHIC INTERFEROMETRY AND DIGITAL SPECKLE PATTERN INTERFEROMETRY vs STEREOSCOPIC PIV FOR MEASURING OUT-OF-PLANE VELOCITY FIELDS

V. Palero, N. Andrés, I.J. Sola, M.P. Arroyo and M. Quintanilla

Dpto. Física Aplicada. Facultad de Ciencias.
Universidad de Zaragoza. SPAIN

ABSTRACT

Holographic interferometry and digital speckle pattern interferometry as techniques for measuring out-of-plane velocity fields are described and compared with stereoscopic PIV. Special attention is paid to the specific problems encountered in confined flows. Experiments have been carried out in a small Rayleigh-Bénard convective cell

1. INTRODUCTION

Particle image velocimetry (PIV) is a well known technique for the measurement of in-plane velocity components in a whole-fluid plane (Grant, 1997). Some efforts have been made to extend PIV to the measurement of the full velocity vectors. The most straightforward approach is based on a stereoscopic viewing of the fluid plane, being the most popular configuration known as translational or angular displacement methods (Gauthier and Riethmuller, 1988). This stereoscopic PIV works well for not confined gaseous flows in both methods although the out-of-plane velocity component is always obtained with less accuracy than the in-plane components (Gauthier and Riethmuller, 1988; Arroyo and Greated, 1991). However, its application to liquid flows is not so straightforward due to the aberrations introduced by the liquid layer that lay between the fluid plane and the image plane (Prasad and Adrian, 1993; Prasad and Jensen, 1995). These aberrations are bigger in the angular displacement method. In the case of confined flows, a new difficulty arise when the whole area of the confinement needs to be measured, due to the non orthogonal viewing of the plane. The main advantage of stereoscopic PIV remains that it can be done digitally (Willert, 1997) and uses essentially the same software as standard PIV.

Holographic interferometry (HI) is another whole-field velocimetry technique for the measurement of the full velocity vectors (Andrés et al. 1997; Andrés et al. 1998). HI shares with PIV the same optical setup for fluid illumination and differs from it in the type of recording (holographic instead of video or photographic). Besides, HI is more sensitive to the out-of-plane velocity component than to the in-plane components, although the three of them can be measured. HI does not store the velocity information on particle images but on the interferometric comparison of two light beams coming from the fluid plane in two different times. The reconstruction of the hologram produces an image of the fluid plane overlaid by interference fringes, i.e., an interferogram. The interferogram fringes represent lines of constant velocity component. HI has none of the problems pointed out for stereoscopic PIV such as aberration in liquid flow experiments and difficulty of observing the whole fluid plane in confined flows. The main drawbacks of HI are related with the holographic recording: superior laser light quality and power may be needed for HI as compared with stereoscopic PIV. Besides, the holographic plate processing, which is a non real time process, can prevent HI from being regularly used in fluid mechanics laboratories.

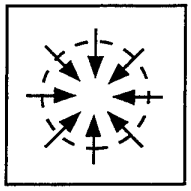
An alternative interferometric technique, that is very widely used in solid mechanics for the measurement of deformations and displacements, is speckle pattern interferometry (Ennos, 1975). In this case, the speckle produced on the solid object surface is made to interfere with a reference beam (plane wave or another speckle). This interference is recorded twice, one before and another after the solid

object is deformed or displaced. A comparison of both recordings produces an image very much like the interferograms obtained with HI. The advantage of speckle interferometry is that the recording can be made with a CCD camera. In this case, the technique is called digital speckle pattern interferometry (DSPI). DSPI shares with HI most of the experimental setup, the analysis software and its sensitivity to out-of-plane velocity components. However, only one component can be obtained with this technique.

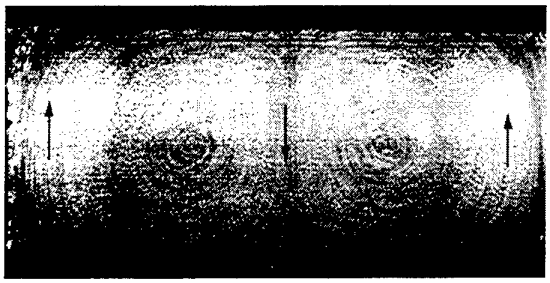
This paper presents the basic principles and experimental implementations of the three techniques (stereoscopic PIV, HI and DSPI) that have been investigated, after describing the Rayleigh-Bénard convective flow where they have been demonstrated. It also includes a discussion and comparison of the results obtained with the different techniques.

2. RAYLEIGH-BENARD CONVECTIVE FLOW

The Rayleigh-Bénard cell is a square plexiglass frame placed between two cooper plates. The inside dimensions are L_X = 25 mm, L_Y = 25 mm and L_Z = 12.5 mm, yielding aspect ratios of 2.0 for both horizontal dimensions. The plexiglass walls are 20 mm thick while the cooper plates are 10 mm thick. The cell is filled with an aqueous glycerol solution that contains 20% in volume of water, being its Prandtl number 500 at 25°C. Refractive index is measured to be n=1.450. The fluid is seeded with 5 μm diameter latex particles.



a)



b)

Fig. 1 Rayleigh-Bénard convective flow in a small field. a) Sketch of the velocity field at a XY plane: $z > L_Z/2$ (the dashed line represents the line of null vertical velocity); b) Multiple exposure PIV image of a XZ plane: y = 6 mm.

The upper cell boundary is kept at 25°C while the lower boundary is kept at a slightly higher temperature, just above the threshold that triggers the fluid motion. The flow has been observed to have a toroidal shape (Fig. 1), with the fluid going down along the cell centre and going up near the lateral walls.

A continuous Argon laser beam, with 60 mW output power, has been shaped into a 15 mm high and 1 mm wide light sheet. This light sheet is used to illuminate the fluid in all the techniques described in the following. An electromechanical shutter, EMS, is used to control each exposure time, t, and the interval time between the exposures, ΔT.

Figure 1b shows a typical PIV image with eight exposures obtained from standard digital PIV. It corresponds to a XZ plane but it might as well represents an YZ plane. It shows a two-roll pattern, being the flow direction indicated by the superposed black arrows. By measuring the roll centers on different XZ planes, the dotted line of figure 1a has been obtained.

3. STEREOSCOPIC PIV

As it is well known, stereoscopic PIV is based on simultaneously viewing the fluid plane from two different directions. This produces two images, each of which is a two-dimensional projection of the full three-dimensional velocity vector field. The correlation of this two different projections permit to extract the out-of-plane component, at the same time as the correct in-plane components. There are two basic configurations of stereoscopic PIV: the translational and the angular displacement methods. In the translational method, the image planes of the cameras are placed parallel to the fluid plane while in the angular method they are placed perpendicular to the main viewing directions. In each method, the cameras can be placed both on the same side of the flow or each on a different side. Besides, in a totally confined flow, we can consider viewing the flow through the walls parallel to the fluid plane or through the perpendicular wall (output wall).

In our experiments, neither viewing through the output wall nor the angular displacement method are feasible due to the aberrations introduced in the images by the liquid flow. Furthermore, viewing from

the same side is not convenient not only because the forward scattered light is more intense than the backscattered light but also because the area of the fluid plane blocked by the lateral walls due to the non orthogonal viewing will not overlap. Thus the common field of view will be much reduced.

For all the above reasons, a translational method with each of the two cameras on each side of the fluid plane has been used (Fig. 2). Two identical macro lenses (IL_1, IL_2) are used to image the fluid plane at unity magnification. They are placed such that the mean viewing directions are at about 20^o from the normal to the fluid plane. This gives an effective angle of working of 15^o, when viewed from inside the fluid. Thus, the out-of-plane velocity component, V_y, is expected to be measured with an error at least three times bigger than the in-plane components, V_x and V_z (Arroyo and Greated, 1991).This is obvious in figure 3, where the results obtained from the y = 6 mm plane are shown. Figure 3c shows no measurement in the right upper corner of the plane. This is because a filling hole was in one of the lateral walls, blocking one of the views. At the same time, the maximum area blocked by the lateral walls in one of the views was 5 mm. Thus no V_y can be obtained for x > 20 mm. However, V_x and V_z can be obtained in most of the fluid plane, because only 1.5 mm are blocked in one of the views. V_z is not influenced by the stereoscopic arrangement, so accuracy should be quite good. V_x data should be less accurate than in a standard PIV system in the areas where there are no V_y data.

4. HOLOGRAPHIC INTERFEROMETRY

Holographic interferometry as a velocimetry technique is based on the same principle as PIV: the velocity is inferred from the light scattered by particles (tracers) in an illuminated fluid sheet, which is recorded at least twice at fixed time intervals, ΔT. While using the same optical illumination setup as classical PIV, holographic (instead of photographic or video) recordings are taken (Fig. 4). Velocity is inferred from the interferometric comparison of at least two holographically reconstructed object waves. The object wave is formed by the light that reaches

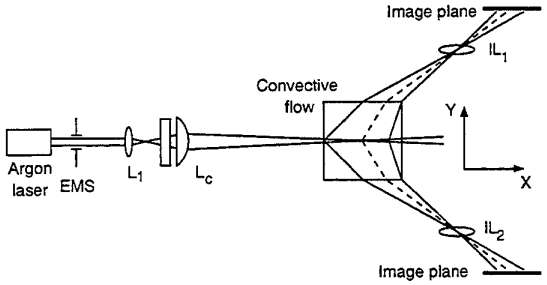
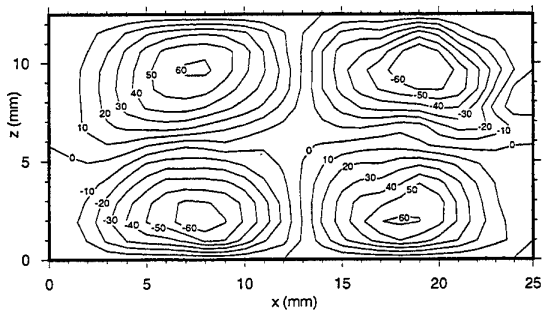


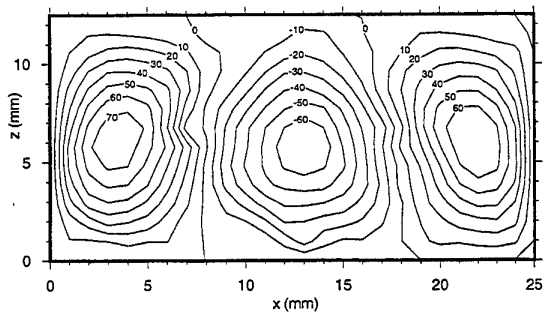
Fig. 2 Experimental stereoscopic PIV setup (top view).

the hologram after being scattered by the tracers in the fluid. Differences between these two object waves come from the local displacement **d** of the tracers during the time interval ΔT, with **d** related to the local velocity **V** in the usual way: $\mathbf{d} = \mathbf{V}\,\Delta T$.

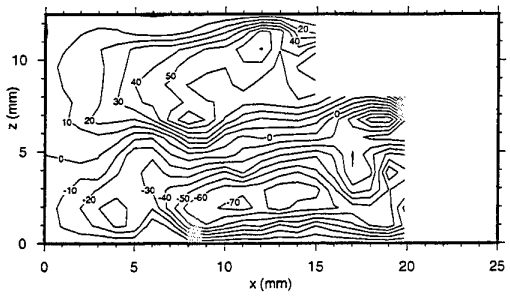
A reconstruction of the hologram using a pointwise beam produces a real image of the fluid plane overlaid by interference fringes. This image is known as interferogram (Fig. 5a). It can be shown (Andrés et al, 1997 and 1998) that each fringe corres-



a)



b)



c)

Fig. 3 Results from the y = 6 mm plane using stereoscopic PIV. a) Horizontal in-plane velocity, V_X; b) vertical velocity, V_Z, c) out-of-plane velocity, V_Y.

ponds to the points where the velocity V is such that

$$\mathbf{K}\cdot\mathbf{V}\,\Delta T = 2\pi\, m, \quad m = 0, \pm1, \pm2, ... \qquad (1)$$

where the integer m is known as the fringe order and $\mathbf{K} = (2\pi/\lambda)\,[\,\mathbf{u_o} - \mathbf{u_i}]$ is the sensitivity vector, being $\mathbf{u_o}$ and $\mathbf{u_i}$ unity vectors in the observation and illumination directions respectively (Fig. 4). Thus the brightest fringes correspond to velocities such that

$$V_K = m\,2\pi / (|\mathbf{K}|\,\Delta T) \qquad (2)$$

where V_K means the projection of **V** along the direction of **K**.

In general, $\mathbf{u_i}$ will be the same in the whole fluid plane while $\mathbf{u_o}$ can change over the plane. If the hologram-fluid plane distance is much larger than the fluid plane dimensions, $\mathbf{u_o}$ will be constant and the interferogram will represent an isovelocity component map. The velocity component selected is the projection of **V** along the direction of **K**. Obviously **K** is never in the illuminated plane.

It is clear that only one velocity component can be inferred from one interferogram. For measuring all the three components, at least three interferogram with different **K** are needed. This can be obtained from one hologram by changing the position of the reconstructing beam, if the hologram is big enough.

Figure 4 shows the experimental setup used for the present experiments. The holographic plate has been placed in such a way that the mean observation direction is at an angle of 20° from the illumination direction. Thus the setup is mainly sensitive to the V_y field. This configuration also has the advantage of collecting the forward scattered light that is much more intense than the light scattered at 90°. Thus, the smaller sensitivity of holographic plates vs photographic film is compensated in some extent.

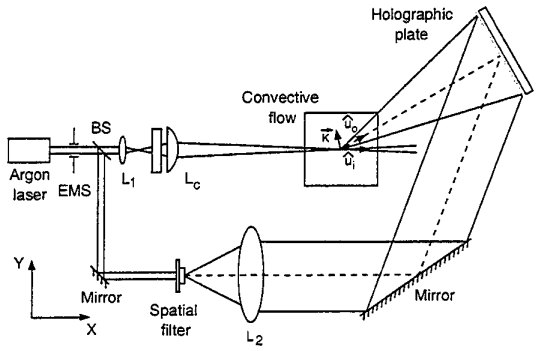
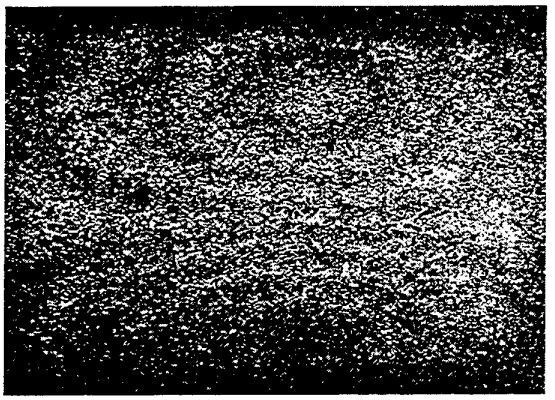
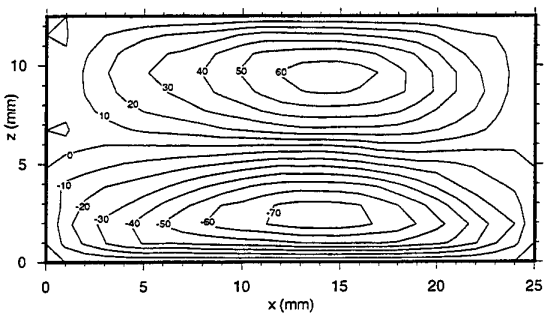


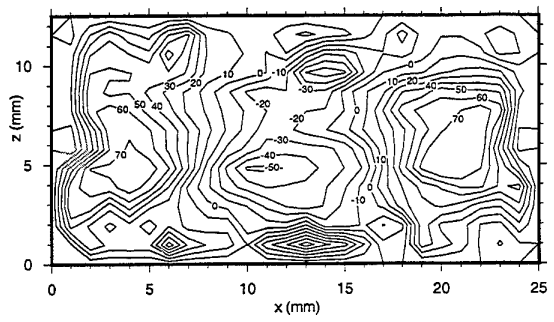
Fig. 4 Experimental holographic interferometry setup (top view).



a)



b)



c)

Fig. 5 Results from the y = 6 mm plane using holographic interferometry. a) Interferogram; b) V_y-field; c) V_z-field.

Figure 5a shows a typical interferogram obtained from the same y = 6 mm plane used in the stereoscopic PIV experiments. It directly gives a clear idea about the spatial pattern of the V_y field. The quantitative V_y data are shown in figure 5b. The smoothness of the isolines gives an idea about the accuracy of the data. Figure 5c shows the V_z field inferred from two interferograms obtained by reconstructing the same hologram from two different points that are 10 mm apart in vertical. This is the maximum possible distance between the reconstructing points if the blockage of the fluid plane by the upper and lower cell plates is to be avoided.

5. DIGITAL SPECKLE PATTERN INTERFEROMETRY

In DSPI, like in HI, the light scattered by the tracers in the fluid plane is made to interfere with a reference beam. This interference pattern, that we will call specklegram, is recorded at least twice at fixed time intervals, ΔT. Again, the differences between the two specklegrams come from the local displacement of the tracers during the time interval ΔT.

The specklegram is a field of speckles whose size and intensity varies randomly across the field. This is so because, at least, the object beam is also a speckle field. The characteristics of the specklegram are related to the characteristics of the object beam. Thus, if the phase of the object beam locally changes by $2\pi m$ due to the tracer motion the intensity of each speckle at that point will remain unchanged. But if the phase changes by $(2m+1)\pi$, the intensity of each speckle will differ randomly. As a result, the correlation of speckle intensities between two specklegrams will change between 0 and 1, depending on the phase change introduced by the tracer displacements. It can be shown (Ennos, 1975) that this change in phase is, like in HI, $\mathbf{K}\cdot\mathbf{V}\,\Delta T$. By correlating the two specklegrams, an interferogram (or a field of speckle pattern correlation fringes) is obtained. Fringes correspond to the same velocities as in HI, as determined by equation (2).

There are, at least, three different ways of determining the correlation of the specklegrams. In the most commonly used, the two specklegrams are just subtracted. In this case, minimum speckle intensity is obtained where the correlation is high and

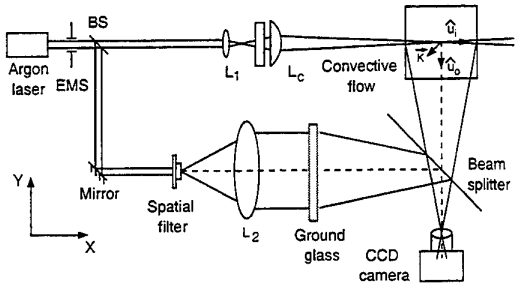


Fig. 6 Experimental DSPI setup (top view).

maximum where the correlation is low. This means that equation (2) corresponds to the darkest fringes.

Another technique consists on adding up the two specklegrams. In this case, we have the opposite situation and, thus, equation (2) will correspond to the brightest fringes (like in HI). The disadvantage of this technique is that the fringe contrast is very poor. The advantage is that the two specklegrams could be recorded in the same CCD frame. Another technique has been recently proposed (Schmitt and Hunt, 1997), where the correlation coefficient is directly calculated. In this case, equation (2) corresponds also to the brightest fringes, like in the addition procedure, but the contrast is at least as good as in the subtraction procedure. The main advantage of this technique is that the fringe contrast is not anymore dependent on the local mean intensity of the specklegram.

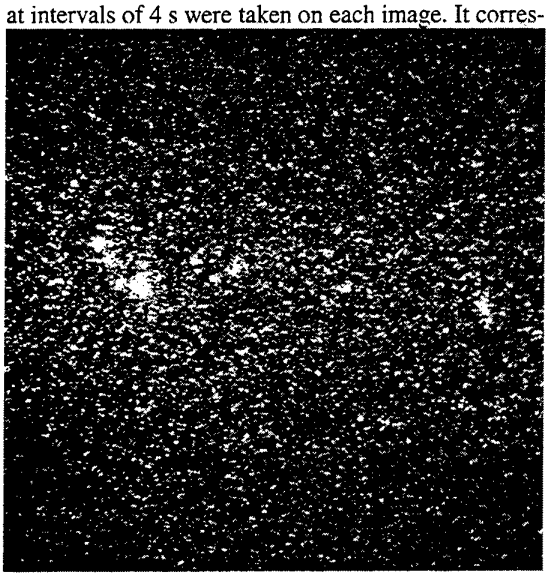
Figure 6 shows the experimental setup used for DSPI in our experiments. A speckled beam, produced by the light passing through a ground glass plate, has been used as reference beam. Both reference and object beam has been combined by means of a beam splitter placed in front of the CCD camera lens. Care has been taken as to locally have both beams at angles very close to zero. This is obtained by having both the fluid plane and the ground glass imaged on the CCD sensor. The lens aperture has been chosen to match the mean speckle size with the CCD pixel size. This corresponds to f/8 or f/11. Both beam intensities have been matched as much as possible. As seen in figure 6, the sensitivity vector is at 45° with the

illumination direction. We believe that no other direction can be selected in fluid velocimetry.

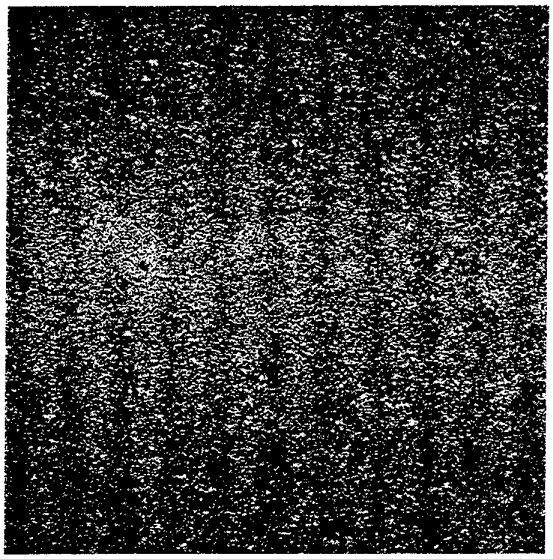
The specklegram shown in figure 7a correspond to a 25x25 mm^2 area of a solid object made to simulate the fluid plane. It is a 15 mm thick transparent plastic with small particles embedded in it. The brightest particles are clearly seen in the figure but there are more small particles not visible in the figure. The object can be rotated a small amount along the vertical axis. Figure 7b show the speckle correlation fringes that are obtained for a rotation of 0.75'. Fringe spacing is about 2.5 mm/fringe and maximum displacement along the sensitivity vector direction is of the order of 5 μm. The correlation fringes have been obtained using the subtraction technique.

6. DISCUSSION

Stereoscopic PIV images were recorded on Kodak Technical Pan film. Eight exposures of 200 ms at intervals of 4 s were taken on each image. It corresponds to maximum in-plane and out-of-plane displacements of 0.25 mm. As expected, figure 3 shows that in-plane components are measured with higher accuracy than the out-of-plane component. The reason is that the out-of-plane component is inferred by comparing two vectors, where the changes in the vector are not too big in comparison with the vector itself. Figure 3 also shows that there are problems for measuring the whole plane in a confined flow.



a)



b)

Fig. 7 Results from DSPI. a) Specklegram; b) speckle pattern correlation fringes.

The hologram in HI was recorded on Kodak 131 plates. Two exposures of 6 ms at an interval of 54 ms were taken. It corresponds to maximum displacements of 3.6 μm. This is an important difference between PIV and HI: the order of magnitude of the detected displacements is between 50 and 100 times smaller in HI than in PIV. Figure 5b shows that the measured out-of-plane component agree on the whole with the data obtained with stereoscopic PIV. However, the HI data are more accurate than the PIV data for this component. Now, there are the in-plane components the ones that are measured with less accuracy. Again the reason is that the in-plane components are obtained by comparing two data (fringe orders in this case) where the changes are smaller than the absolute data. Besides, a big source of error is the correct point to point matching of the two interferograms. Since no fixed reference lines have been used in these experiments, V_Z data are less accurate than in previous experiments (Andrés et al, 1997). In any case, the pattern and order of magnitude of the V_Z field agree

with the PIV data. Since PIV and HI are sensitive to different velocity components, it seems as if the combination of PIV with HI should be more accurate than stereoscopic PIV for the measurement of the full velocity vector field.

The DSPI experiments present here are the first ones carried out with the purpose of measuring fluid velocity fields. So far, we have been able of demonstrating the technique using a simulated fluid-like object. We have used a standard analog camera running at 30 Hz or a cheap digital camera that only allows to take two frames/sec. We have checked that exposure times and interval times of the order of the ones used in HI are also needed for DSPI. Those times are not possible with our cameras since the analog one has a too long exposure time while the digital camera has a too long interval time. However, we believe that DSPI would work with the digital cameras that are routinely used now for PIV in many laboratories (and that will be more easily available in the near future).

From the experiments on the solid object, we have checked out that DSPI works as expected, i.e. like the digital version of HI. DSPI shares with HI most of the optical setup, the types of images (interferograms), the way these interferograms are related to tracer displacements, and thus, its relative sensitivity to the different velocity components. DSPI has the advantage over HI of being a digital technique and the drawback of being able of measuring only one component in one plane. However, it seems the perfect technique to be combined with digital PIV. This combination would require also two cameras like in stereoscopic PIV, but non-orthogonal viewing is not required which removes most of the problems encountered in confined liquid flows.

7. CONCLUSIONS

Three different techniques for measuring out-of-plane velocity fields have been described. Stereoscopic PIV has been shown not to be able of measuring the whole fluid plane in confined flows due to blockage by the lateral walls because of the non orthogonal viewing. In any case, the non orthogonal viewing requires either two opposites windows or one bigger window, which may be a problem in some cases. Holographic interferometry has been shown to be able of measuring the out-of-plane velocity fields more accurately than stereoscopic PIV and in the whole plane. However, the need of a holographic recording is a drawback for its extensive use in fluid mechanics laboratories. Digital speckle pattern interferometry has been shown to be a promising digital alternative to holographic interferometry.

ACKNOWLEDGMENTS

This research was partially supported by the University of Zaragoza under the Research Support Programme, by the CICYT under grants AMB96-0427 and by DGES under grant PB96-0739-C03-02.

REFERENCES

Andrés, N., Arroyo, M.P. & Quintanilla, M. 1997, Velocity measurements in a convective flow by holographic interferometry, Appl. Opt., vol. 36, pp. 6997 - 7007.

Andrés, N., Arroyo, M.P., Hinrichs, H., Hinsch, K. & Quintanilla, M. 1998, Holographic interferometry as a velocimetry technique in gaseous flows, IMechE 1998, C451, pp.1 - 9.

Arroyo, M.P. & Greated, C.A. 1991, Stereoscopic particle image velocimetry, Meas. Sci. Technol., vol. 2, pp. 1181 - 1186.

Ennos, A.E. 1975, Speckle interferometry, in *Laser speckle and related phenomena*, J. C. Dainty ed. Topics in Applied Physics, vol. 9 (Springer-Verlag, Berlin), Chap. 6.

Gauthier, V. & Riethmuller, M.L. 1988, Application of PIDV to complex flows: measurement of the third component, VKI Lecture Series on Particle Image Displacement Velocimetry (Brussels) .

Grant, I. 1997, Particle image velocimetry: a review, Proc. Instn. Mech. Engrs., vol. 211 part C, pp. 55 - 76

Prasad, A.K. & Adrian, R.J. 1993, Stereoscopic particle image velocimetry applied to liquid flows, Exp. Fluids ,vol. 15, pp. 49 - 60.

Prasad, A.K. & Jensen, K. 1995, Scheimpflug stereocamera for particle image velocimetry in liquid flows, Appl. Opt., vol. 34, pp. 7092 - 7099.

Schmitt, D.R. & Hunt, R.W. 1997, Optimization of fringe pattern calculation with direct correlations in speckle interferometry, Appl. Opt., vol. 36, pp. 8848 - 8857.

Willert, C. 1997, Stereoscopic digital particle image velocimetry for application in wind tunnel flows, Meas. Sci. Technol., vol. 8, pp. 1465-1479.

DEVELOPMENT AND APPLICATION OF A DEFOCUSING THREE DIMENSIONAL DPIV TECHNIQUE FOR THE MAPPING OF TWO-PHASE BUBBLY FLOWS

M. Gharib, D. Modares, D. Dabiri, F. Pereira, F. Taugwalder

CALIFORNIA INSTITUTE OF TECHNOLOGY
Center for Quantitative Visualization
Pasadena, California 91125

ABSTRACT

The assembly and real-time acquisition system of a unique three-dimensional imaging system for the purpose of mapping two-phase bubbly flows is presented. A unique defocusing optical setup was used to generate images with imbedded information on the spatial position of bubbles. A novel approach was used to overcome the overcrowding of bubble images within a single CCD, which had previously inhibited the practical application of this technique. Special software was developed to measure bubble sizes and map the bubbles' velocity field. Sample results are presented herein.

1. INTRODUCTION

Despite the progress made in the area of bubble acoustics and cavitation inception, there remains a deep gap in our understanding of the nature of coupling between the bubbles and the turbulent shear flows. This is crucial for understanding the complex phenomenon of bubble interaction with the turbulent wake of surface ships. At the heart of the problem lies the understanding of the effect of shear flow on bubbles and vice versa. In a ship wake, for example, bubbles are introduced into the wake through cavitation and/or by surface entrainment through wave breaking and free surface breakage near solid boundaries. The entrained bubbles are then subject to the underlying flow dynamics which consists of mixed boundary shear layers and free shear flows in the wake.

It is the lack of a comprehensive understanding of the nature of the origin of the entrained air and collective bubble dynamics, of its interaction with the underlying flow and the process of bubble convergence and change of size due to the imposed flow structures such as vortices in boundary layers and wakes, that has impaired our flow prediction capabilities. Such difficulties have negative impact on the design of surface ships and overall viability of such systems.

In this respect, it is important to understand the dynamics of bubbles in the presence of vortical shear flows. Crucial to this understanding is the knowledge of the underlying transient 3D-flow field. The complexity of the situation has imposed severe limitations in computational approaches for tackling this problem. Therefore, experimental approaches in free surface water tunnels and tow tanks have played a critical role in the development of current state of knowledge for bubbly flow dynamics. However, the turbulent, multi-phase and three-dimensional nature of the bubbly flow field demands measurement and instrumentation capabilities beyond standard and conventional single point LDA or existing planar imaging systems.

This entails the use of a non-intrusive diagnostic instrument capable of mapping the flow field within a reasonably large volume and tracking the history and size of bubbles and the surrounding flows simultaneously in three dimensions. Furthermore, the instrument should have sufficient sensitivity to locate and identify each and all of the bubbles with sufficient spatial resolution in all three dimensions to accurately estimate the void fraction. Finally, the instrument should be simple, easy to use and portable between different flow facilities such as tow tanks. Currently, such a flow mapping system is not available. Furthermore, state-of-the-art in the field, which is mainly in the academic groups, has not produced a general-purpose system capable of delivering the expected performance.

Recent works in imaging bubbly systems have been limited to two-dimensional mapping of the flow and bubble fields [1]. Size and void fraction measurements have been performed and limited, but useful flow information has been obtained within the confine of two-dimensional space. However, it is crucial that the temporal and spatial history of bubble trajectory as well as its dynamics be mapped within a

volume of fluid along with the underlying three-dimensional.

The available three-dimensional systems such as holography, stereo images or scanning systems suffer from extreme complexity or lack of spatial or temporal resolution to be useful or practical for the above-mentioned purpose. In this paper, we introduce a novel three-dimensional imaging system with flexibility and capability for adoption in various experimental facilities such as tow tanks and water tunnels. The system is capable of real-time digital imaging of the bubbly flows and its underlying flow field in three dimensions with a combined dynamic range, resolution and reliability that surpasses alternative systems.

2. DEFOCUSING DPIV (DDPIV)

This technique uses a special defocusing mask placed in front of the camera lens to obtain three images for each scattering center. This allows for accurate determination of the position of the scattering centers in three dimensions along with its size estimate [2].

To fully describe the technique, a set of imaging lenses with different apertures is represented in Figure 1.

In Figure 1a, a small aperture within the lens shows a solid angle of light rays emanating from a point source *B*, which is reduced to its blurred image *B'*. In this case, the location of the bubble *B* is identified only in two directions and the information regarding the depth is lost. If the aperture is shifted away from the centerline, a proportional shift is observed for the images of point sources that are not on the reference plane. This is a direct result of the modified viewing angle of these point sources.

Defocusing DPIV uses the image shift caused by an off-axis aperture for the measurement of the depth location of the bubble. By using three equally spaced apertures, all located near the edge of the imaging lens, this results in the projection of three images from one point source *B* as shown in Figure 1b. The separation *b* of the images *B'* can be directly related to the distance *Z* away from the reference plane, whereas the size of the individual image is proportional to *Z*, the size of the apertures and the size of the point source.

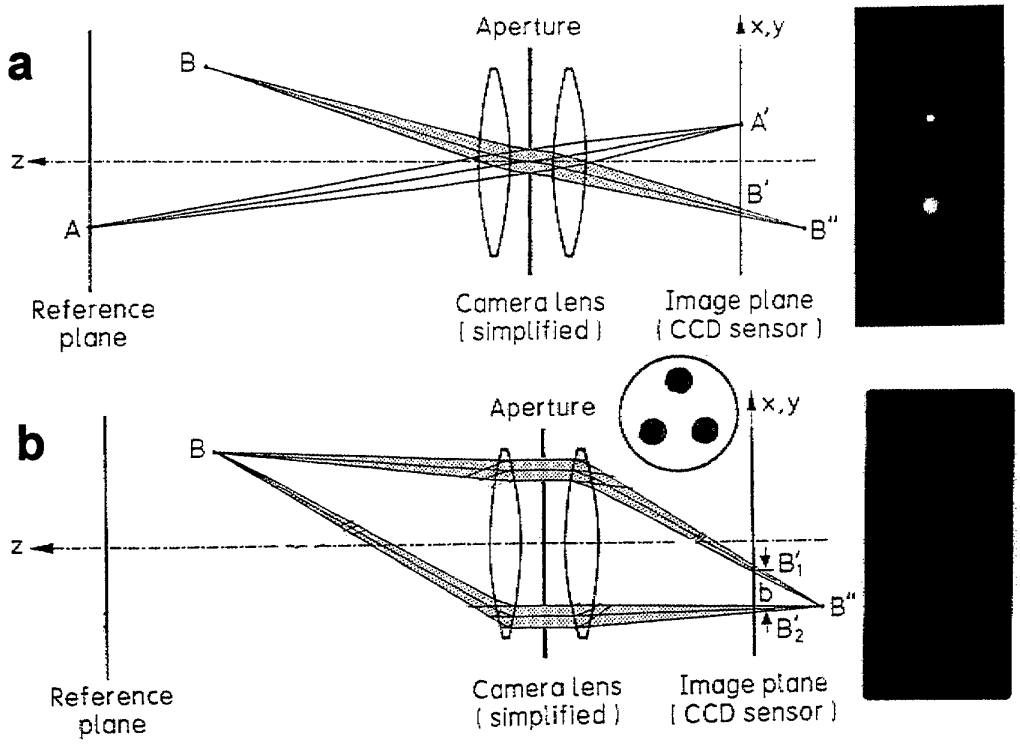


Fig. 1: Defocusing principle

Essential to the recovery of three component spatial data is the measurement of the separation b to recover the Z component (depth) and of the location of the self-similar image set to find the in-plane components X and Y. The corresponding geometrical analysis is shown in Figure 2 in which the camera lens of focal length f is located at $Z = 0$. Within the lens, two small apertures are separated a distance $d/2$ away from the centerline (here we have used two pinholes for simplicity, the theory for three apertures is similar). Using the well-known lens law and self-similar triangle relationships, the spatial coordinates of a point source (X, Y, Z) (not necessarily on the reference plane) can be calculated using only a few easily determined constants:

$$Z = \frac{1}{L^{-1} + Kb} \qquad 1$$

where

$$K = \frac{L - f}{fdL} \qquad 2$$

The remaining two coordinates X and Y are found from the geometrical center (x_o, y_o) of the image pair B' using:

$$x = \frac{-x_0 Z(L - f)}{fL} \qquad 3$$

$$y = \frac{-y_0 Z(L - f)}{fL} \qquad 4$$

Solving (1) for the image separation b reveals several interesting performance characteristics of the lens/aperture system:

$$b = \frac{1}{K}\left[\frac{1}{Z} - \frac{1}{L}\right] \qquad 5$$

Three operating regimes can be distinguished: if the object distance Z is less than the reference plane distance L, the separation b is greater than zero and a non-inverted image is formed on the focal plane. If on the other hand, Z exceeds L, i.e. the object is not located in the region between the reference plane and the lens, an inverted image is formed. A mask with an equilateral triangular pinhole arrangement will exhibit a flipping of the triangular bubble image pattern as the bubble passes through the reference plane (Z=0). Between these two regimes, lies a region where the separation b becomes too small to be resolved because the images blur into each other, i.e. b tends to 0 with $|Z\text{-}L|$. It is important to note that the pinhole diameter has no bearing on either the gain or the image separation b and is only responsible for the blurriness of the individual images.

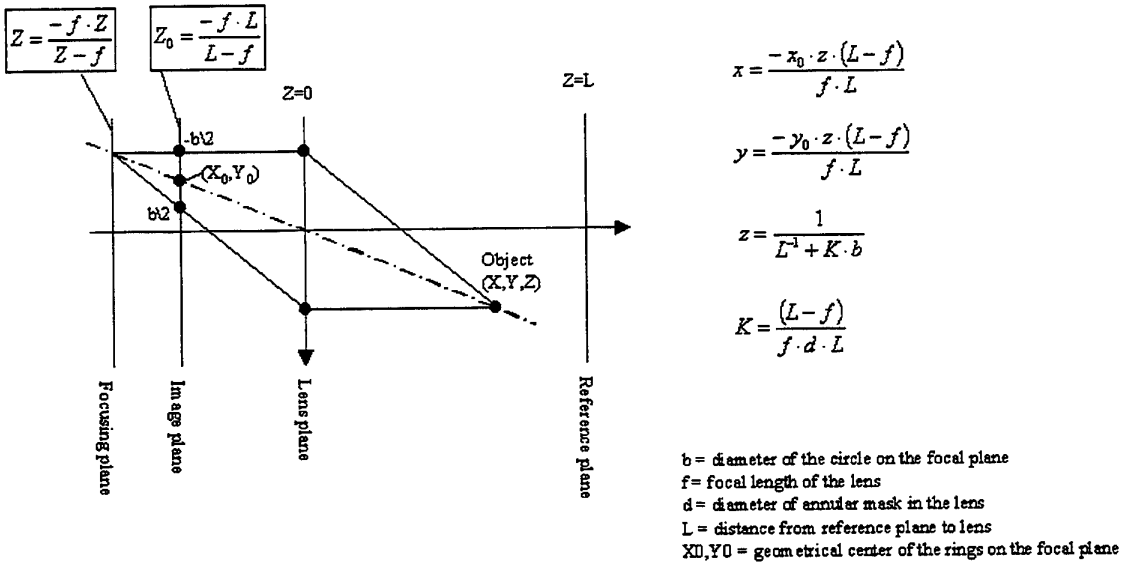


Fig. 2: Geometrical analysis of the DDPIV camera system

3. ADVANTAGES / DISADVANTAGES

There are several advantages of this technique that make it superior to other methods. First, it uses a single optical axis resulting in very simple aligning procedures. Also, it eliminates all problems associated with the motion (vibration) of cameras with respect to each other that are found in stereoscopic techniques and that would otherwise produce erroneous results [1, 3, 4, 5]. Second, this technique provides these measurements at 30 frames/sec. Holographic techniques, though capable of 3 component velocity measurements within a volume, cannot provide such data rates [6]. Third, the DDPIV technique incorporating a 1K x 1K camera provides a high resolution of 0.05% of its full scale in all three components. Fourth, this technique naturally blurs bubbles by up to 3.5 pixels beyond its focused image that provides the advantage of imaging and sizing bubbles as small as 15 micrometers within the full volume. Investigations of smaller bubbles are achievable by reducing the size of the interrogation volume.

One apparent disadvantage of this technique is that it exposes three times as many pixels, as compared with other three-dimensional techniques due to the triple exposure of each bubble. This would imply that the capacity of the technique (in terms of number of bubbles and/or particles) is reduced at least by a factor of 3. However, this problem was overcome by using a separate CCD for capturing each of the pinhole images. The three images are then recorded simultaneously with a real-time digital storage unit. The use of the recording system along with our specially designed camera provides a large bandwidth to insure 24-bit/pixel digital recording of bubbles images, and therefore accurate velocity derivations from the bubble images.

4. SYSTEM DESCRIPTION

The system is composed of a camera, a PC-based data acquisition and processing system, an illumination unit, and the data processing software.

Camera

Figure 3 shows the camera schematic. A three-pinhole mask in the shape of an equilateral triangle is placed directly behind the camera lens. The pinhole mask is oriented in such a way so that bubbles between the focal plane and the camera will be inverted equilateral triangles. Immediately behind each of the pinholes is a prism which turns the light directly into three 1024^2 CCDs, which are equally spaced at 120 degrees apart on a concentric circular mount. The CCDs are aligned so that they see the same field of view to within ¼ of a pixel.

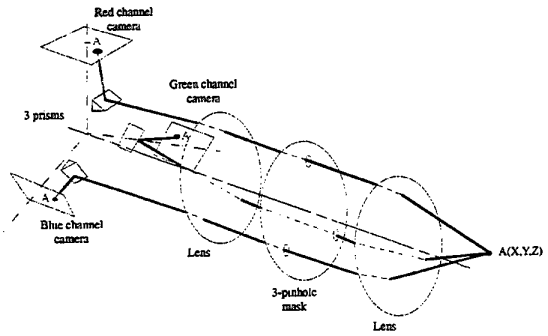


Fig. 3: DDPIV camera schematic

Acquisition System

The images acquired by the custom-made camera are recorded using a high-bandwidth data acquisition system. This system can store images at 30 frames per second at a 1024^2*3 pixel^2 CCD resolution for a minimum of one minute. This is equivalent to storing a minimum of 5.4 Gbytes of memory at 90 Mbytes per second.

Illumination System

Unlike planar PIV, where the area of interest is a plane, DDPIV's area of interest is a volume, and therefore requires much more light to illuminate. Also, since flows of relatively high velocities are to be observed, it is required that our light source be pulsed rather than continuous. Furthermore, it is important to note that for water applications, since different wavelengths have different absorption rates, a single wavelength light source with the least absorption is required. Therefore, a frequency-doubled 300 mJ dual YAG laser is used to satisfy all these criteria.

Data Processing

In order to obtain velocity vector fields within a volume, processing of the images is done in the following steps. The first step is to identify the X, Y and Z coordinates of every bubble. Since the mask pinholes are in the shape of an inverted equilateral triangle, first, a search is done for the pinhole image forming the upper left corner of the triangle on the first CCD. Once one is found, a search is done for the second pinhole image on the second CCD. Due to the shape of the triangle, this image should be located horizontally to the right of the first pinhole. Once this is found, the search is completed by

finding the third pinhole image on the third CCD that completes the shape of the equilateral triangle. If it is not found, then it is known that the second pinhole image found is not correct, and the search for it begins anew. Once a complete set is found, the X and Y position of the bubble is found from the centroid of the triangle using equations 3 and 4, while its Z position is determined from equation 1. This process is repeated until all possible bubbles and their positions are extracted from the images.

The second step is to determine the bubble displacements between sequential images. A small interrogation volume sub-samples and interrogates the same position within two sequential volume pairs. A three-dimensional cross-correlation is then performed on the bubbles within the sub-sampled volumes to give an average three-dimensional displacement of all bubbles within these volumes. This interrogation window is then marched through the whole volume to produce three-dimensional velocities distributed within the imaged volume.

Lastly, the pixel displacements are converted to real space domain to provide three-component velocity vectors.

5. EXPERIMENTAL SET-UP

A Plexiglas water tank with dimensions 0.9x0.9x1.5 m^3 is used for the laboratory experiments. The tank is fitted within a metallic frame on which the camera and the illumination system can be rigidly fixed and aligned with the flow system.

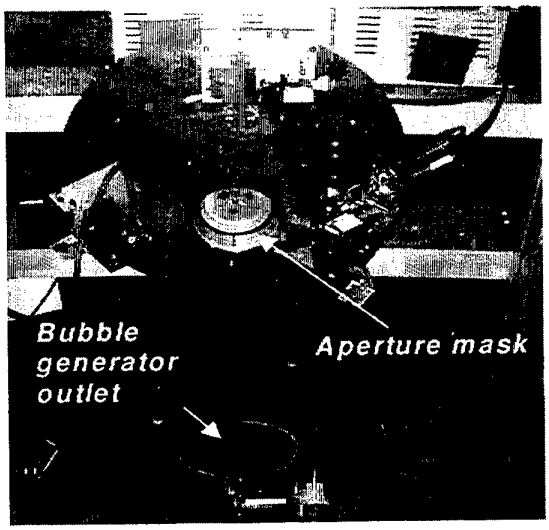


Fig. 4: Experimental set-up

A bubble generator is placed at the bottom of a tube, generating different bubble size and density distributions. The camera observes the flow at the outlet of the tube, as shown in Figure 4. The flow of interest is located in between the camera and the reference plane in such a way that all triangles have the same orientation, i.e. they are always inverted.

The laser illuminating system is placed ninety degrees relatively to the optical axis. The laser beam is enlarged by a lens in order to illuminate a measurement volume of 5 * 5 * 5 cm^3. The YAG lasers are each pulsed at 15 Hz with a time difference of 800 μs. The images from the three CCDs are captured simultaneously at 30 frames per second with the real-time data.

6. RESULTS AND DISCUSSION

A typical pair of images taken at 800 μs apart is shown in Figure 5. Each of the figures shown in Figure 5 is a super-position of the images from all three CCDs, which are color-coded in red, green, and blue for easy identification: red is the upper left corner of the inverted equilateral triangle, green is the upper right and blue is the lower corner of the triangle.

Figure 6 shows the identification of the bubbles corresponding to the first image of the pair shown in figure 5. Each of the inverted equilateral triangles corresponds to a bubble, where the size of the triangle corresponds to its depth location in Z, and its lateral and vertical positions correspond to its location in X and Y. Based on former simulations, our calculations show a 95% success rate in identifying correct bubbles. The remaining 5% rejection is due to incomplete triangles, this occuring when the corresponding bubble is close to the boundary of the volume being observed. Because optical distortions and misalignment cannot be totally avoided, triangles may not be perfectly equilateral. The processing software is given a tolerance to take into account this disturbance parameters.

Figure 7 shows a histogram plot of the bubble size distribution. The mean bubble size is 40 μm with a standard deviation of 0.02 μm. We should emphasize that the bubble size is not measured from the bubble image, rather, this value should be corrected by taking into account the image magnification and the bubble scattering properties as well. These correction factors have to be included in the size determination procedure by means of a calibration, using a known size and density distributions of bubbles.

Figure 8 shows the velocity plot corresponding to the bubble displacements carried out from the image pair of figure 5. The colors of the vectors correspond to the magnitude of the velocity vectors. The color spectrum starts at red, which corresponds to the minimum velocity amplitude, and ends at blue, which corresponds to the maximum velocity amplitude. Note that the bubble motion is generally vertical, and is indicated mostly by the green vector and blue vectors.

7. CONCLUSION

This paper has introduced a novel imaging technique for three-dimensional mapping of two-phase bubbly flow, based on a defocusing technique. The technique is shown to be suitable for the determination of both the velocity field and the size and density distributions of bubbles, with a resolution on the bubble position below 0.05% of the full-scale volume. A camera based on this technique has been successfully assembled and used to image rising bubbles in a water tank. Specific hardware has been assembled to allow real-time and high-resolution acquisition. Dedicated software has been developed to calculate the bubble size distribution as well as the three-component velocity vectors within a three-dimensional domain of 5x5x5 cm^3. Sizes down to 20 μm have been measured.

Improvements are foreseen that will give the system the capability of mapping volumes of 30x30x30 cm^3 in real-time. Moreover, the bubble sizing procedure has to be calibrated to relate the optical image of bubbles with their real size.

ACKNOWLEDGEMENT

The work was sponsored under the ONR program, contract number N00014-97-1-0303, under the direction of Dr. E. P. Rood.

The Defocusing Digital Particle Image Velocimetry (DDPIV) system is protected under a U.S. pending patent filed by California Institute of Technology.

REFERENCES

[1] Oakley, R. T., Loth, E., Adrian, R. J., 1995, FED-Vol. 209, Flow Visualization and Image Processing of Multi-Phase Systems, ASME, 123-130.

[2] Willert, C.E.; Gharib, M. 1992: Three-dimensional particle image with a single camera, *Exp. Fluids*, 12, 353-358

[3] Prasad, A.K.; Adrian, R.J. 1993: Stereoscopic particle image velocimetry applied to liquid flow, *Exp. Fluids*, 15, 49-60.

[4] Nishino, K.; Kasagi, N.; Hirata, M 1989: Three-Dimensional Particle Tracking Velocimetry Based on Automated Digital Image Processing, *Journal of Fluids Engineering*, 111, 384-391.

[5] Maas, H.G.; Gruen, A; Papantoniou, D; 1993: Particle Tracking Velocimetry in Three-Dimensional Flows, *Exp. Fluids*, 15, 133-146.

[6] Barnhart D.H., Adrian, R.J. and Papen G.C., Phase-conjugate holographic system for high-resolution particle-image velocimetry, *Applied Optics,* Vol. 33, No. 30, pp. 7159 to 7170, 1994.

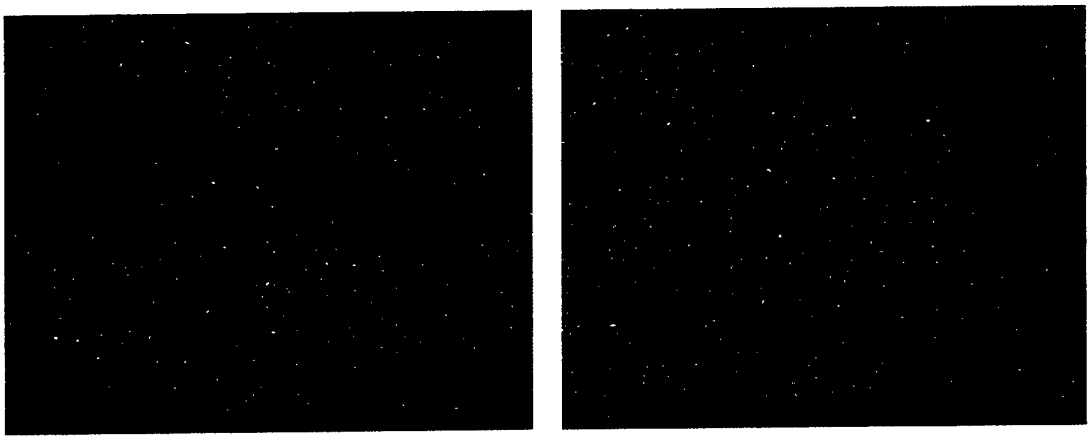


Fig. 5: Image pair 800 μs apart

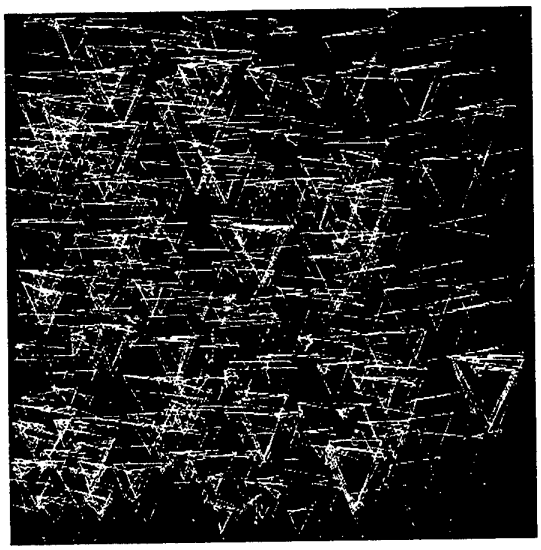


Fig. 6: DDPIV Bubble identification

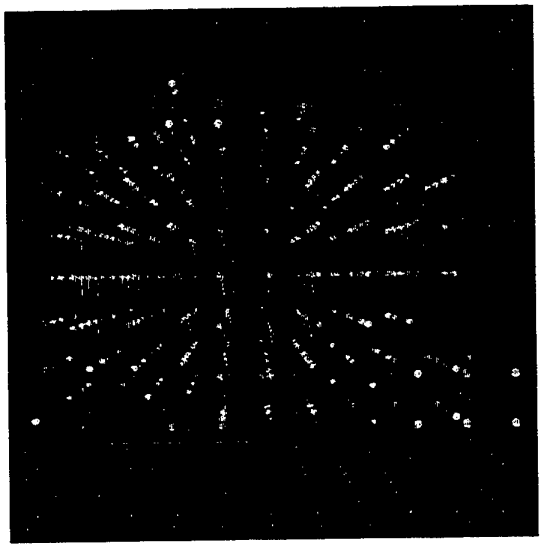


Fig. 8: Velocity field

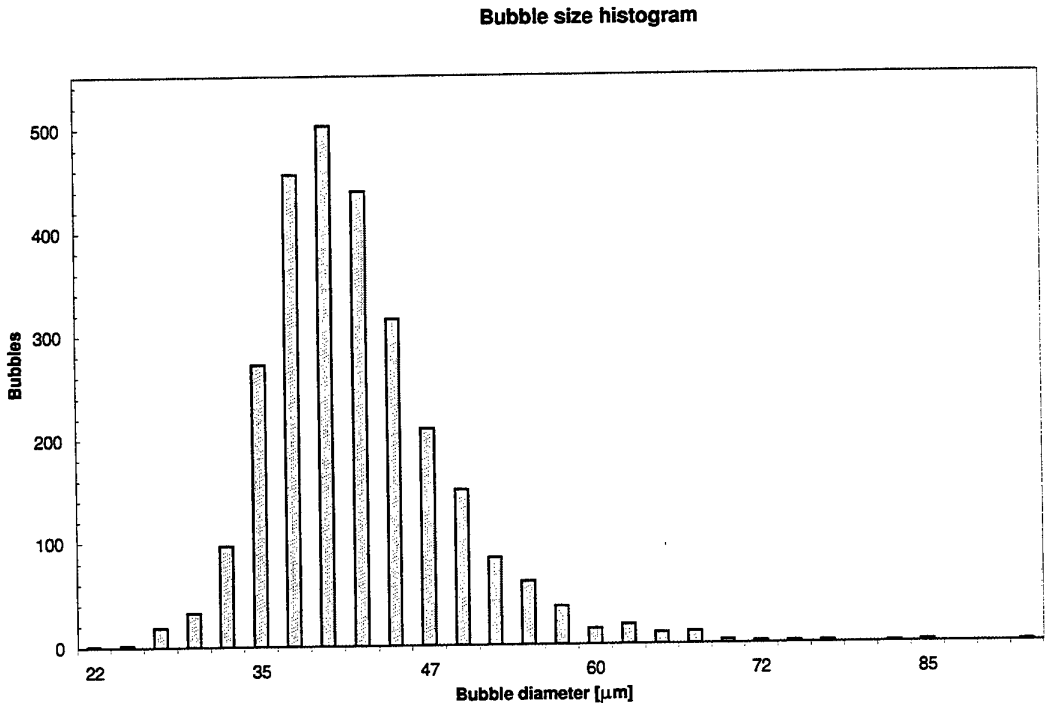


Fig. 7: Histogram plot of bubble size distribution

SESSION 17

FREE Flows I

A PIV STUDY OF COMPRESSIBLE SHEAR LAYERS

W. D. Urban and M. G. Mungal

Mechanical Engineering Department
Stanford University, Stanford, CA 94305-3032 USA

ABSTRACT

Planar, two-component velocity measurements are performed using PIV in gaseous shear layers of varying compressibility. Instantaneous side-view velocity fields display interfacial features similar to those previously observed using scalar visualizations, while the corresponding vorticity maps provide new information about the kinematic state within the layer. The disappearance of the two-dimensional scalar structures ('rollers') with increasing compressibility is seen to correspond with a shift from large regions of vorticity spanning the transverse extent of the layer to smaller, segregated 'sheets' of vorticity within the layer. This change in the vorticity field suggests an impairment of cross-stream communication, with the well-known macroscopic result of impaired mixing-layer growth rate. Large-ensemble turbulence quantities based on the instantaneous planar data show sharp decreases in transverse velocity fluctuation and primary Reynolds stress with increasing compressibility, in accord with previous pointwise measurements.

1. INTRODUCTION

High-Mach number aerospace propulsion applications require rapid molecular mixing between gaseous streams in the presence of compressibility effects. The two-stream plane shear layer has served as an important model for this family of flows; its relatively simple initial and boundary conditions and well-defined parameter space facilitate numerical and experimental studies alike. The primary variables are compressibility, parametrized by the convective Mach number M_c, the density and velocity ratios s and r, and the degree of heat release due to chemical reaction; the relevant Reynolds number is $Re_\delta \equiv \Delta U \delta / \nu$. Early experimental studies (Papamoschou & Roshko 1988; Clemens & Mungal 1995) using planar scalar imaging techniques have documented significant suppression of mixing layer growth and change in large-scale structure with increasing compressibility, while pointwise velocity measurements (Elliott & Samimy 1990; Goebel & Dutton 1991; Debisschop & Bonnet 1993) have revealed the associated alteration of turbulence quantities. Other studies have sought to measure mixing efficiency (Hall 1991, Messersmith & Dutton 1992, Island et al. 1996, Island 1997) and to explore enhancement strategies (Gutmark et al. 1995). The present effort seeks to complement this work with planar velocity measurements via PIV, permitting structural interpretation of the kinematic behavior of the layer. Previous work (e.g. Kompenhans & Höcker 1988; Crisler et al. 1994) has demonstrated the utility of PIV in supersonic flows, in addition to identifying and addressing experimental issues related to these applications.

2. EXPERIMENTAL APPARATUS AND TECHNIQUE

2.1 Flow Facility

A two-stream blowdown wind tunnel (Figure 1) is used to generate a plane shear layer for experiments of 30 s typical duration. The test section is 10 cm wide, 8 cm high and 48 cm long, and operates at 0.6–0.8 atm. Table 1 summarizes the experimental conditions; cases of negligible (M_c = 0.25), moderate (M_c = 0.63), and high compressibility (M_c = 0.76) are presented here. M_c is varied by changing the exit Mach number of the upper, supersonic stream; the lower stream is subsonic in all cases. For the M_c = 0.76 case, pure argon is used for the subsonic stream in order to maximize compressibility. The test section walls are normally adjusted to eliminate any streamwise pressure gradient; however, in the M_c = 0.25 case the walls are deliberately diverged in order to accelerate both streams, minimizing compressibility. Solid titanium dioxide (TiO_2) particles are seeded into both streams using fluidized bed seeders. In order to address the particle agglomeration which plagues velocimetry with solid seeds, hydrodynamic cyclones and impactors are placed between the seeder outlets and the injection point; these are designed for an effective diameter cutoff around 0.4 μm.

2.2 PIV System

The PIV data acquisition system appears in Figure 2. Illumination is provided by a two-cavity Quanta-Ray PIV-400 pulsed Nd:YAG laser delivering collinear beams of 532 nm light at up to 400 mJ per laser per 8 ns pulse. Short values of the pulse separation, typically 200 ns, are required in order to prevent the spanwise motions which characterize compressible mixing layers from conveying particles out of the imaging plane between the two realizations. Scattering from the

particles is collected at 90° from a 23 mm square region of the flow by a 2000 x 2000 pixel Kodak Megaplus 4.2 CCD camera equipped with a Nikkor 200 mm lens normally set to *f*/16. Both realizations occupy a single digital image, and velocity vectors are calculated by means of an FFT-based autocorrelation whose peaks are localized using a Gaussian curve fit. Interrogation regions are 80 pixels square, yielding spatial resolution of 0.9 mm. Since there are no velocity reversals in the lab frame in this flow, no biasing or tagging is necessary to resolve directional ambiguity. However, in compressible cases the short pulse separation demands the use of a rotating mirror in the imaging path to add a positive bias to the particle image displacements at the imaging plane. This is crucial since the presence of a central peak in the autocorrelation function enforces a strict minimum value for the particle-image displacement.

2.3 Seeding Considerations

Since PIV measures the velocity of the tracer particles rather than the fluid itself, the measurement accuracy is critically dependent on the flow-following ability of the particles, particularly in supersonic flows where large velocity gradients exist. The effectiveness of a given seed particle is a composite effect of the inherent particle size, the tendency of the particles to agglomerate, the capability of the seeding system to deagglomerate and deliver the particles, and the response of the imaging system to the particles when they are illuminated.

Therefore, *in situ* measurements of the characteristic particle response time τ_p have been carried out in order to provide seed particle selection and validation data. The high-speed stream of the mixing layer facility is used to provide a supersonic (M = 2.2) approach flow, and an oblique shock is generated by a two-dimensional 10° wedge mounted on the top wall of the tunnel. Representative particle images using two candidate seeds appear in Figure 3; the wedge appears at the top of the images and flow is from left to right. The mixing layer, which forms the lower boundary of the high-speed freestream, is visible at the bottom of the images. The particles are solid Al_2O_3 and TiO_2 with fundamental particle sizes quoted by the manufacturers of 0.3 μm and 0.02 μm respectively.

Several qualitative features of these images suggest the superiority of the TiO_2 seed. First, we note that the Al_2O_3 image contains a greater number of vertical, dagger-like particle images. These 'bloomed' particle images result when overflowing charge due to saturation bleeds among adjacent pixels during readout of the CCD array; the saturation in turn results from the high signal returned by oversized particles in the flow. Thus, the readout blooming is an indication of the dispersion of the Al_2O_3 seed to larger sizes than the TiO_2. Another qualitative observation is that the TiO_2 seed visualizes the oblique shock, while the Al_2O_3 seed does not. Since rapid, small-scale particle motion is required for a fluid density change to be reflected as a seeding density change, this suggests that the TiO_2 particles more faithfully follow the flow across the shock.

Analysis of the wedge-flow particle images leads to measurements of cross-shock velocity profiles for the two seeds (Figure 4). By transforming the spatial coordinate to time and applying exponential fits, we estimate τ_p to be 20–28 ms for the Al_2O_3 seed and 3.5 ms for the TiO_2 seed, translating to effective diameters of 1.2 and 0.4 μm respectively. These results agree well with the scattering-based measurements of Crosswy (1985), and the degree to which they differ from the advertised fundamental particle diameters emphasizes the importance of *in situ* particle-dynamic measurements. These measurements lead us to select the TiO_2 particle for use in the present experiments, where it delivers an estimated Stokes number of 0.06 at the measurement station.

3. RESULTS

3.1 Particle Images

Typical side-view particle images for three shear-layer cases appear in Figure 5. Flow is from left to right, and the high-speed stream is at the top. The field of view has been set to coincide with the transverse extent of the mixing layer in order to maximize relative spatial resolution. Seeding has been set with the goal of equalizing the tracer particle densities of the freestreams, minimizing measurement biases associated with seed origin. The M_c = 0.63 and M_c = 0.76 cases are significantly affected by compressibility; previous studies have shown growth-rate suppression to begin around M_c = 0.3 and to saturate as M_c approaches unity (Papamoschou & Roshko 1988).

3.2 Velocity Fields

Use of the rotating mirror permits analysis yields exceeding 99%, minimizing or obviating the need for interpolation. Velocity fields corresponding to the images in Figure 5 appear in Figure 6. Interrogation regions are non-overlapping, yielding fields of 25 x 25 vectors. We notice that the instantaneous transverse velocity profiles for the compressible cases exhibit significant excursions from the average, including local extrema and regions of near-freestream velocity values penetrating well into the envelope of the time-averaged layer thickness. This intermittency, along with meandering patterns of v velocity, has spatial scales similar to those of the large-scale structures observed in scalar visualizations (Clemens & Mungal 1995) of the flow, and decreases in definition with increasing compressibility as the scalar structures do.

Contour plots of velocity magnitude (Figure 8) provide another useful view of the data. Regions of large instantaneous velocity gradients may be readily seen along the boundaries of the structures, suggesting further that interaction with the large-scale structures drives momentum exchange between entrained fluid and the layer. Furthermore, the steep gradients associated with the low-speed edges of the structures coincide with the local sonic velocity. This is particularly evident in the M_c = 0.63 case, for which the two freestreams have equal specific heat ratios. Although in principle a free-shear flow, in which compressibility effects are defined in a convecting frame, the layer demonstrates here a sensitivity to lab-frame effects as well. Indeed, small sub-boundary layer disturbances have been shown to be highly effective in promoting layer growth rate (Island et al. 1997).

The structural features of the velocity field are rendered more readily when the vectors are displayed in a frame of reference convecting downstream at $U_c = (a_2U_1 + a_1U_2)/(a_1 + a_2)$ (Figure 8). In this frame, we observe significant

transverse excursion of the $U = U_c$ line at higher M_c, further evidence of the rapid distortion of large-scale structure common to compressible layers. Figure 8 also presents contours of vorticity magnitude derived from the velocity fields presented above. In the incompressible case, the vorticity is seen to reside in a large structure spanning the transverse extent of the layer, corresponding to the 'roller' familiar from scalar visualizations. However, in the compressible layers, the vorticity is seen to reside in thinner 'sheets,' oblong in the streamwise direction and possessing little transverse connectivity. Since scalar visualizations of compressible layers exhibit a diffuse, disorganized appearance, direct measurement of the velocity field was necessary to reveal these features of the vorticity. The lack of cross-stream communication between regions of high spanwise vorticity in the compressible cases is reminiscent of the 'co-layer' structures disclosed by stability analyses (Day et al. 1997) under certain conditions of compressibility and heat release, and related to growth-rate suppression in those cases.

3.3 Large-Ensemble Statistics

Turbulence statistics for the mixing layer are obtained by using the multiple transverse profiles present in each PIV image, and expanding the ensemble through the acquisition of multiple images. Typical profiles reflect 5000–10000 independent measurements at each point. Velocity, velocity fluctuation, and Reynolds stress profiles for the three cases appear in Figures 9–12. The highly variable instantaneous u profiles of Figure 6 are seen to relax to smooth, well-behaved curves. Also, the decrease in Reynolds stress and transverse velocity fluctuation with increasing compressibility revealed in LDV studies (Elliott & Samimy 1990; Goebel & Dutton 1991) is clear in our PIV result, while the streamwise velocity fluctuations show little change. These trends in the turbulence quantities are central to models for the mechanism behind the growth rate suppression in compressible layers (Freund et al. 1997, Sarkar 1995).

4. SUMMARY AND CONCLUSIONS

This study has produced high-yield, well-resolved planar velocity measurements in the gaseous mixing layer at three compressibility levels. The side-view velocity fields show structural effects of compressibility similar to those derived from scalar studies. However, details of the vortical structure, particularly in the compressible case, are revealed through direct velocity measurement. At high M_c, thin sheets of vorticity appear within the layer thickness, a situation predicted by linearized stability analysis (Day et al. 1997) and potentially related to growth-rate suppression. Steep velocity gradients exist at the local sonic speed in the lab frame, suggesting a sensitivity to wall disturbances. Finally, large-ensemble turbulence statistics are gathered, and trends established by previous pointwise studies are borne out.

ACKNOWLEDGMENTS

This work was supported by the National Science Foundation. WDU is supported by an AFOSR AASERT grant.

REFERENCES

Clemens, N. T. & Mungal, M. G. 1995, Large-Scale Structure and Entrainment in the Supersonic Mixing Layer, *J. Fluid Mech.*, vol. 284, pp. 171–216.

Crisler, W., Krothapalli, A. & Lourenço, L. 1994, PIV Investigation of High Speed Flow Over a Pitching Airfoil, AIAA paper 94-0533, 32nd Aerospace Sciences Meeting, Reno, NV.

Crosswy, F. L. 1985, Particle Size Distributions of Several Commonly Used Seeding Aerosols, in *NASA CP 2393: Wind Tunnel Seeding Systems for Laser Velocimeters*, ed. W. W. Hunter & C. E. Nichols, pp. 53–75.

Day, M. D., Reynolds, W. C. & Mansour, N. 1997, Linearized Stability Analysis and Structure of the Compressible Reacting Mixing Layer, AIAA paper 97-0761, 35th Aerospace Sciences Meeting, Reno, NV.

Debisschop, J. R. & Bonnet, J. P. 1993, Mean and Fluctuating Velocity Measurements in Supersonic Mixing Layers, in *Engineering Turbulence Modelling and Experiments 2*, ed. W. Rodi & F. Martelli, pp. 467–478.

Elliott, G. S. & Samimy, M. 1990, Compressibility Effects in Free Shear Layers, *Phys. Fluids A*, vol. 2, pp. 1231–1240.

Freund, J. B., Moin, P. & Lele, S. 1997, Compressibility Effects in a Turbulent Annular Mixing Layer, Flow Physics and Computation Division Report TF-72, September.

Goebel, S. G. & Dutton, J. C. 1991, Experimental Study of Compressible Turbulent Mixing Layers, *AIAA J.*, vol. 29, pp. 538–546.

Gutmark, E. J., Schadow, K. C. & Yu, K. H. 1995, Mixing Enhancement in Supersonic Shear Flows, *Ann. Rev. Fluid Mech.*, vol. 27, pp. 375–417.

Hall, J. L. 1991, *An Experimental Investigation of Structure, Mixing and Combustion in Compressible Turbulent Shear Layers*, Ph.D. thesis, California Institute of Technology, Pasadena, CA.

Island, T. C. 1997, *Quantitative Scalar Measurements and Mixing Enhancement in Compressible Shear Layers*, Ph.D. thesis, Stanford University, Stanford, CA.

Island, T. C., Urban, W. D. & Mungal, M. G. 1996, Quantitative Scalar Measurements in Compressible Mixing Layers, AIAA paper 96-0685, 34th Aerospace Sciences Meeting, Reno, NV.

Island, T. C., Urban, W. D. & Mungal, M. G. 1997, Small-Perturbation Mixing Enhancement in Compressible Shear Layers, AIAA paper 97-0395, 35th Aerospace Sciences Meeting, Reno, NV.

Kompenhans, J. & Höcker, R. 1988, Application of Particle Image Velocimetry to High Speed Flows, in *Particle Image*

Velocimetry, pp. 67–84, von Karman Institute for Fluid Dynamics.

Messersmith, N. L. & Dutton, J. C. 1992, Laser-Induced Fluorescence Measurements of Scalar Transport in Compressible Mixing Layers, AIAA paper 92-3547, 28th Joint Propulsion Conference, Nashville, TN.

Papamoschou, D. & Roshko, A. 1988, The Compressible Turbulent Shear Layer: An Experimental Study, *J. Fluid Mech.*, vol. 197, pp. 453–477.

Sarkar, S. 1995, The Stabilizing Effect of Compressibility in Turbulent Shear Flow, *J. Fluid Mech.*, vol. 282, pp. 163–186.

Table 1: Mixing layer conditions

Case	$M_c = 0.25$		$M_c = 0.63$		$M_c = 0.76$	
Stream	1	2	1	2	1	2
Bulk gas	Air	Air	Air	Air	Air	Ar
$\dot{m}$ [kg/s]	1.4	1.2	2.1	0.72	1.7	0.57
M	1.64	0.97	2.22	0.54	2.17	0.37
U [m/s]	441	296	525	175	522	111
T [K]	176	227	136	255	139	258
P [kPa]	64	65	67	70	58	58
r	0.67		0.33		0.21	
s	0.77		0.53		0.77	
$x_{imaging}$ [cm]	38		24		24	
δ_{visual} [cm]	1.8		2.5		2.5	
$Re_\delta/1000$	150		400		1000	

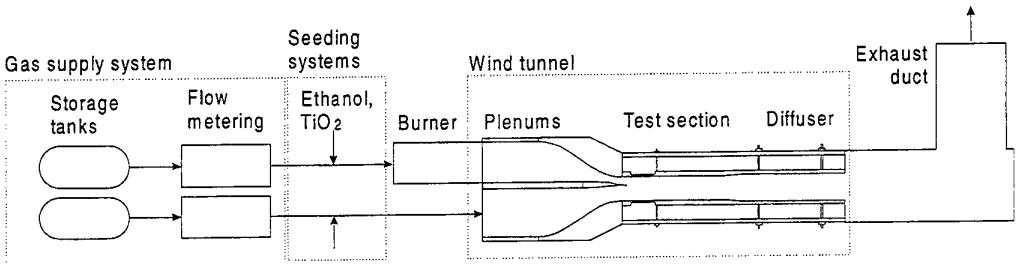


Fig. 1: Compressible mixing layer facility. Vitiation heater (burner) in high-speed stream is not used in the present experiments.

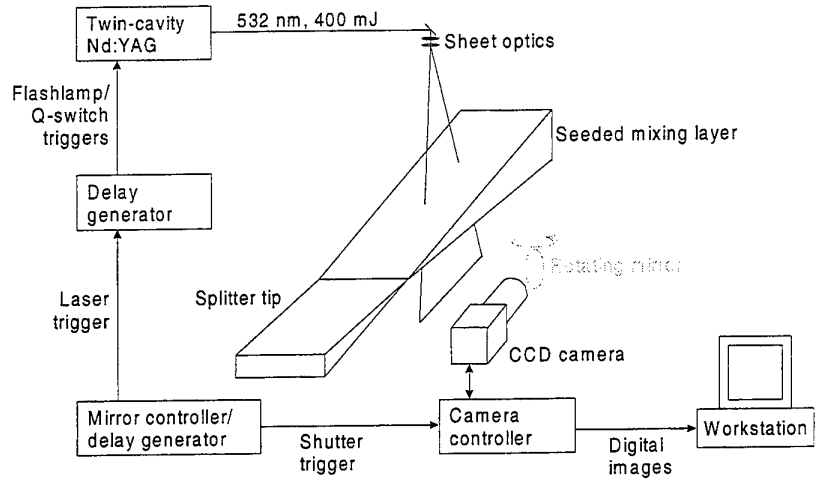


Fig. 2: PIV data acquisition system

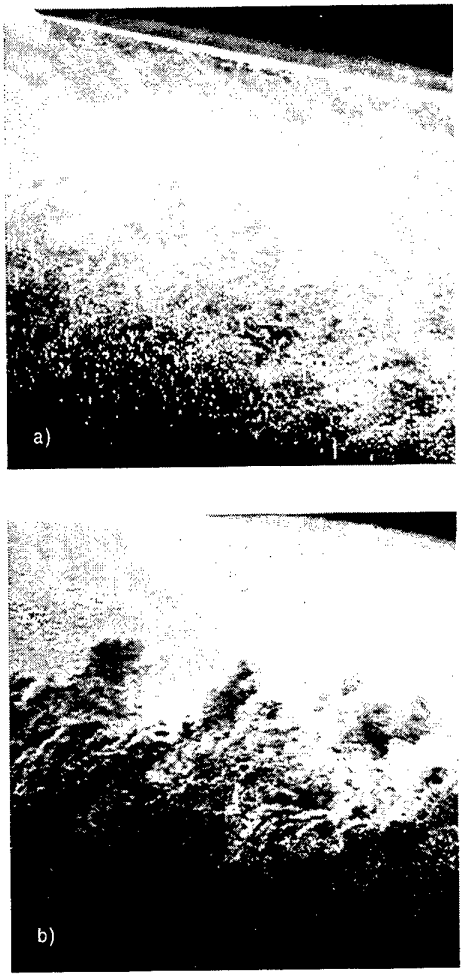


Fig. 3: Wedge-flow particle images for (a) Al_2O_3 and (b) TiO_2 seed particles

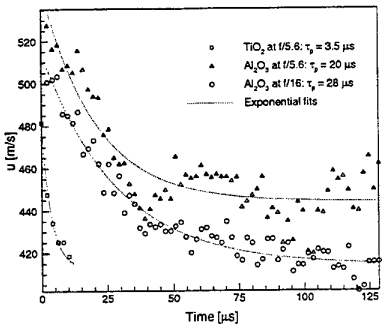


Fig. 4: Wedge-flow velocity relaxation traces for three candidate seed particles

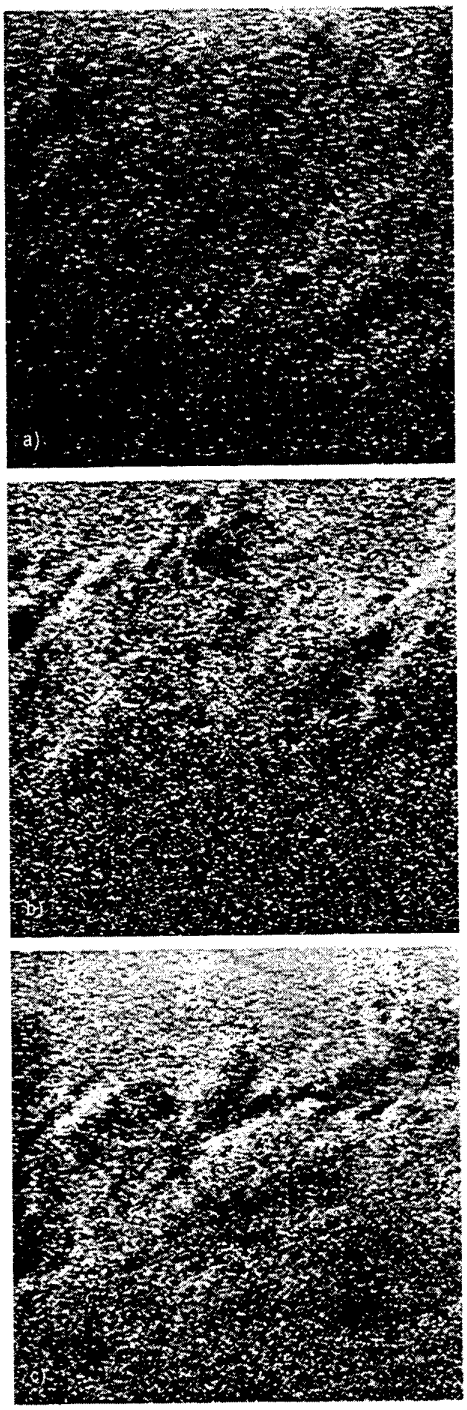


Fig. 5: Mixing layer particle images for (a) $M_c = 0.25$, (b) $M_c = 0.63$, and (c) $M_c = 0.76$

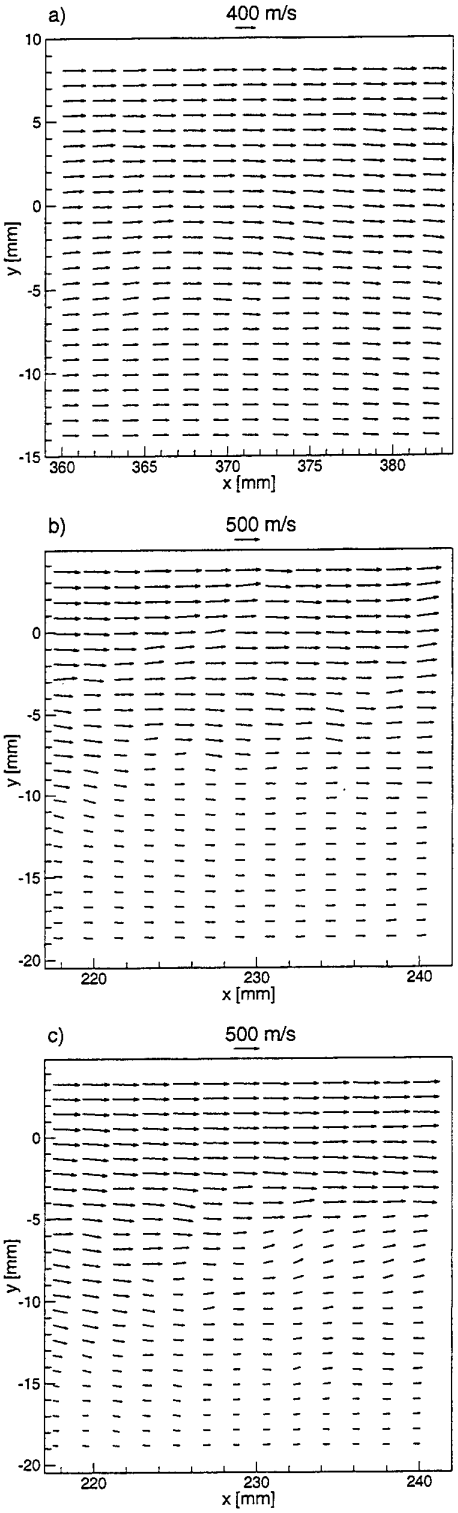


Fig. 6: Velocity vector fields for (a) $M_c = 0.25$, (b) $M_c = 0.63$, and (c) $M_c = 0.76$

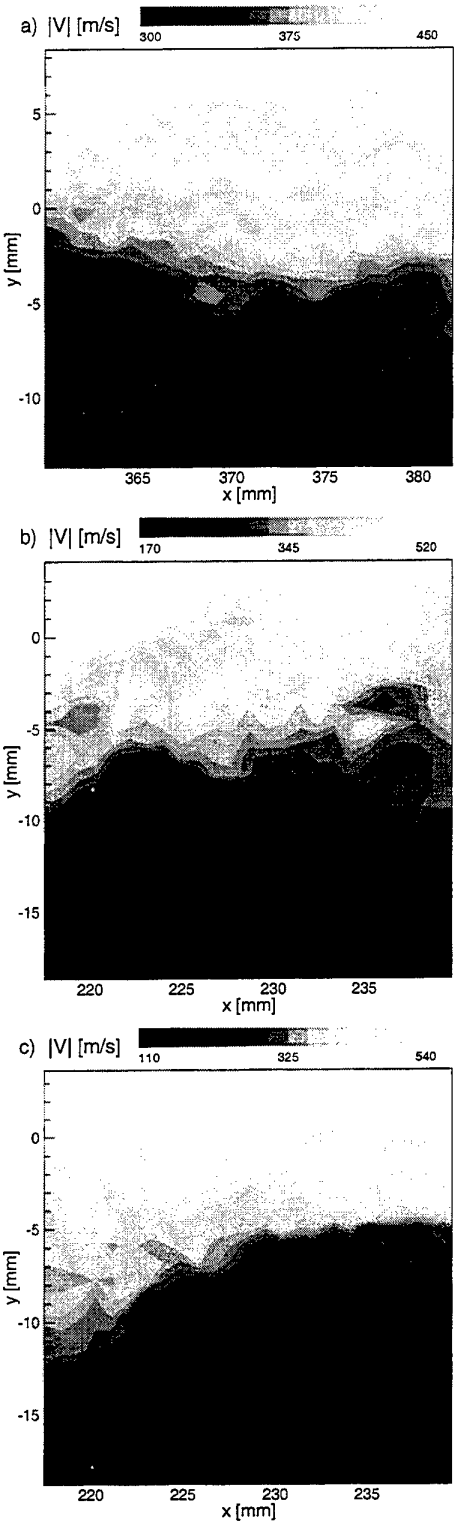


Fig. 7: Velocity magnitude fields for (a) $M_c = 0.25$, (b) $M_c = 0.63$, and (c) $M_c = 0.76$

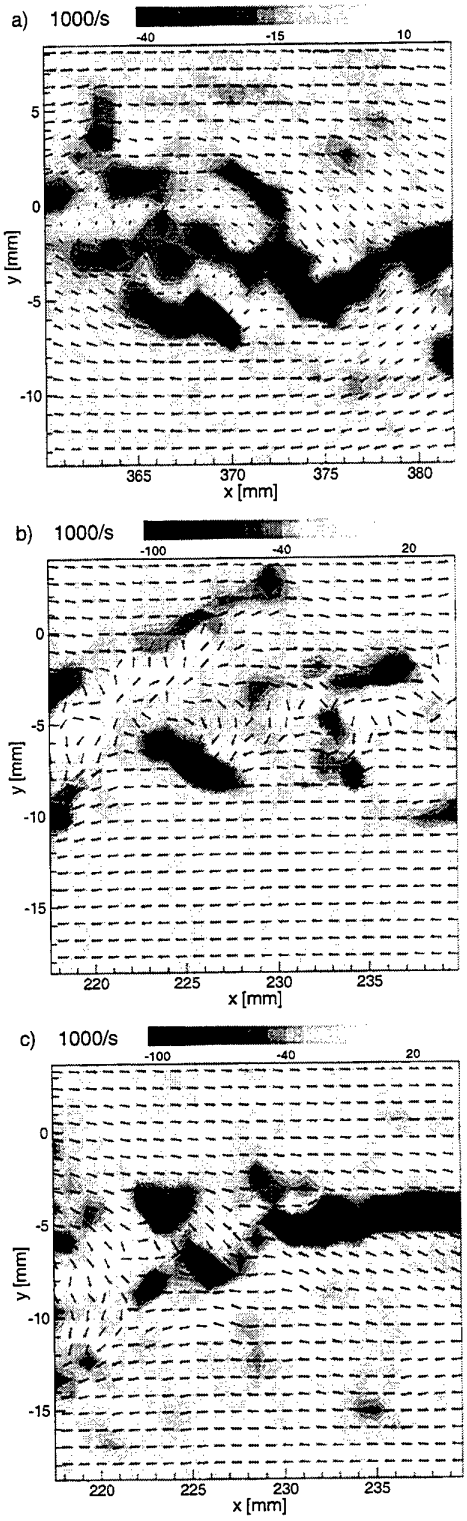


Fig. 8: Vorticity magnitude fields for (a) $M_c = 0.25$, (b) $M_c = 0.63$, and (c) $M_c = 0.76$; velocity vectors presented in convective frame

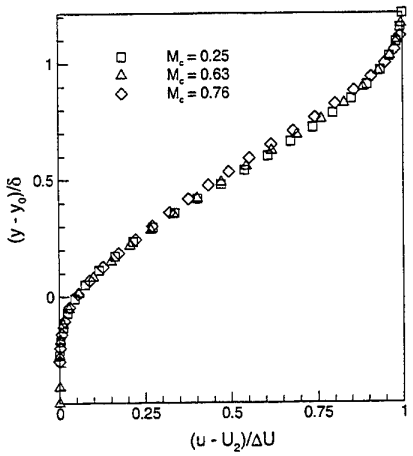


Fig. 9: Ensemble-averaged streamwise velocity profiles

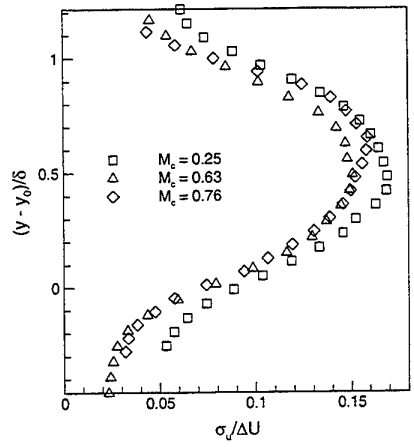


Fig. 10: Ensemble-averaged streamwise velocity fluctuation profiles

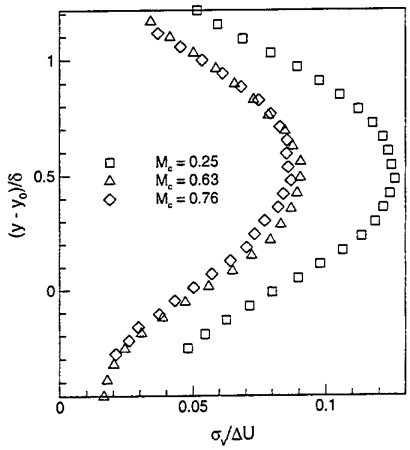


Fig. 11: Ensemble-averaged transverse velocity fluctuation profiles

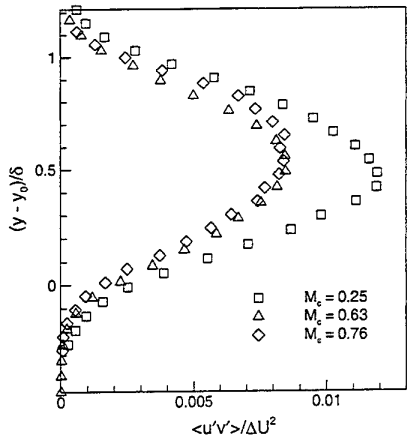


Fig. 12: Ensemble-averaged Reynolds stress profiles

EXPERIMENTAL DETERMINATION OF THE TURBULENT KINETIC ENERGY AND THE DISSIPATION RATE IN VARIABLE DENSITY TURBULENT JETS

J. PAGÉ, B. SARH and I. GÖKALP

Laboratoire de Combustion et Systèmes Réactifs

Centre National de la Recherche Scientifique

1C, avenue de la Recherche Scientifique

45071 Orléans Cedex 2, France

ABSTRACT

The experimental determination of centerline evolution of the turbulent kinetic energy k and axial component of the dissipation rate ε_u is conducted with variable density turbulent axisymmetric jets. Helium, methane, air and CO_2 are exhausting vertically into a coflowing air stream. The density ratio $R_\rho = \rho_e/\rho_j$ varies between 7.2 (helium in air) to 0.66 (CO_2 in air). The experiments are conducted with a constant velocity ratio $m = U_e / U_j = 0.075$.

Velocity field measurements are performed using a two-component laser Doppler anemometer. The purpose of this paper is to document the centreline evolution of k and ε_u in the near and the far fields.

1. INTRODUCTION

The objective of this study is to gain a better understanding of the influence of density variations on the structure of turbulence in jets, and therefore on turbulent mixing of variable density jets. An experimental investigation of variable density turbulent axisymmetric jets is presented, where the velocity field measurements are performed using two-component laser Doppler anemometry. Helium, methane, air and CO_2 jets exhausting into a coflowing air are investigated.

Different strategies are applied in the literature when experimental studies on variable density turbulent jets are performed. Of particular importance is to decide which parameters should be kept constant when comparing two jets of different mean densities. Parameters such as momentum flux (Amielh *et al.*, 1996), Reynolds number (Sarh, 1990) and velocity ratio (Antonia and Bilger, 1973 ; Panchapakesan and Lumley, 1993) have been selected in the literature for this purpose. In this study, we decided to maintain constant the Reynolds number and the velocity ratio for each jet.

In this paper, the centreline evolution of the turbulent kinetic energy, k, is presented for each jet. This result is compared to the experimental results of Sautet (1992) and Djeridane (1994), and also to the numerical predictions of Ruffin *et al.*, 1994 ; Harran et al., 1996 ; and Sanders et al., 1997.

We also present the centreline evolution of the dissipation rate of the turbulent kinetic energy, ε. This result is compared to those of Antonia and Satyaprakash (1979) for circular jets, obtained by hot wire anemometry, The variable density effects on both results are discussed.

2. EXPERIMENTAL SET-UP

The flow configuration is schematised on Figure 1. Experiments are performed in a 2 m high vertical wind tunnel. This enclosure has a square cross- section, with a width of 300 mm and a length of 1300 mm. This rectangular chamber houses the experimental configuration as shown in Figure 2a. The experimental conditions explored are summarised on Table 1.

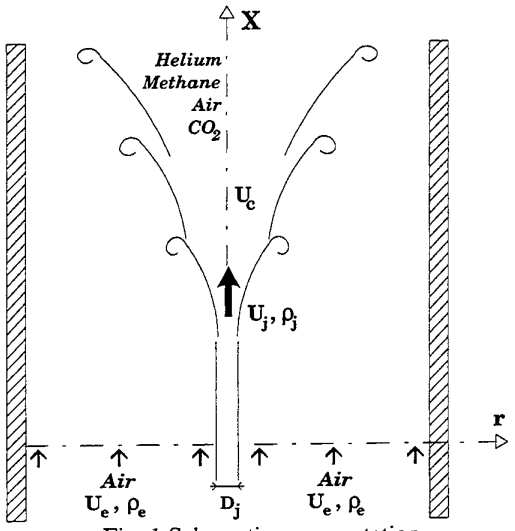


Fig. 1 Schematic representation of the flow configuration.

Optical access is allowed by large optical quality glass windows (for laser beam transmission and light collection). A turbulent vertical pipe flow (with mean longitudinal velocity U_j at the exit section) of helium, methane, air and CO_2 discharges into the chamber. The diameter Dj of this pipe is 7 mm (giving a L/D_j ratio of 80). This pipe is positioned in the centre of the chamber.

The Reynolds number, based on the pipe diameter D_j, is $Re = U_j D_j/\nu_j$, where ν_j is the kinematic viscosity at the exit section. The Froude number is egal to $Fr^2 = U_j^2 / g D_j |R_\rho - 1|$. The coflowing stream of air is generated by a fan and the mean longitudinal velocity is U_e. To homogenise the coflow, air coming from the fan passes trough a settling section and honeycomb structures

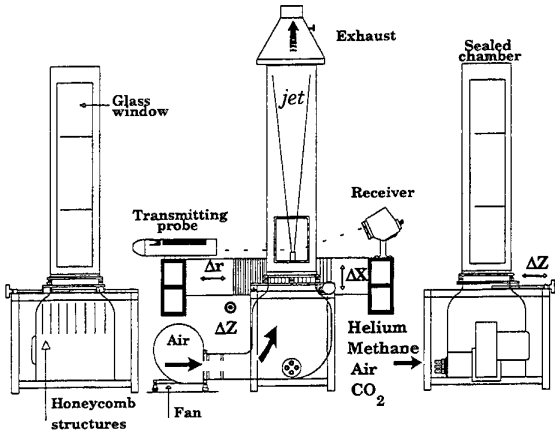


Fig. 2a Details of the experimental set-up.

Table 1. Experimental conditions.

Gas	*Helium*	*Methane*	*Air*	CO_2
U_j (m/s)	40	40	40	40
U_e (m/s)	3	3	3	3
ρ_j (kg/m^3)	0.167	0.667	1.202	1.815
D_j (mm)	7	7	7	7
$R_\rho = \rho_e/\rho_j$	7.2	1.8	1	0.66
m	0.075	0.075	0.075	0.075
Re	2400	18400	19200	34500
Fr	61	170	---	262

3. LASER VELOCIMETRY

The complete determination of the flow field velocity characteristics (Pagé *et al.*, 1997a and 1997b, 1998 are measured by a two-color laser Doppler anemometer, consisting of a 7 W Argon-ion laser source, Colorburst beam separator, a transmitting probe. The scattered light is collected by a receiver and treated by IFA 755 (Figure 2b).

A coincidence mode time of 10 μs is used for both component measurements. The measuring volume is located 350 mm from the transmitting probe head. This displacement of the measurement volume is performed by moving both the transmitting probe and the receiver with the same 2D traversing mechanism driven by a step motor. Seeding of the jet is achieved by injecting a mist of olive oil particles upstream of the jet flow, with mean diameter of 1.5 μm (determined by Phase Doppler Anemometry). We try to keep a constant coincidence rate about 15 kHz to obtain representative information for spectral analysis.

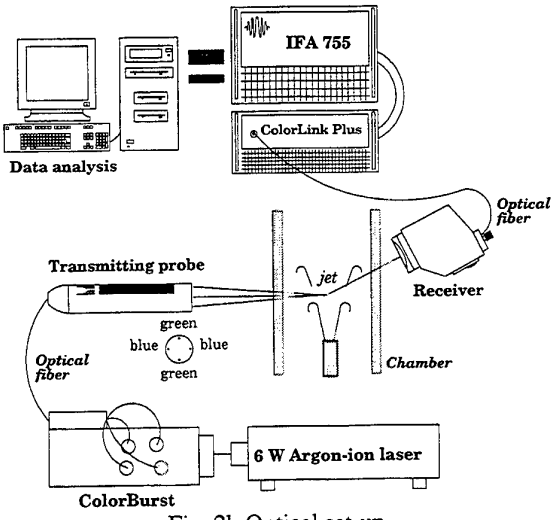


Fig. 2b Optical set-up.

4. TURBULENT KINETIC ENERGY

For symmetry reasons in axisymmetric jets ($\langle v^2\rangle^{1/2} \approx \langle w^2\rangle^{1/2}$), turbulent kinetic energy can be defined as :

$$k \approx 0.5\ (\langle u^2\rangle + 2.\langle v^2\rangle) \qquad (1)$$

The centerline variation of the turbulent kinetic energy normalized by the excess exit velocity (U_j - U_e) is presented in Figure 3. The influence of density is obvious, showing that light gases tend to mix more quickly with the coflowing stream than heavy gases. We note a rapid increase of k from the exit section, then k reaches a maximum which depends on the density ratio. The higher value is for light gases (He and CH_4), the lower for heavy gases (CO_2).

For light gases, this position is near the exit section of the jet ($X_{kmax}/D_j = 5$ and $X_{kmax}/D_j = 8$ for helium and methane respectively). For air and CO_2, this maximum is located further downstream (respectively, $X_{kmax}/D_j = 10$ and $X_{kmax}/Dj = 12$). A comparison between these results and other experimental results (Sautet, 1992 ; Djeridane, 1994) is presented in Figure 4. In addition, we also show a comparison between experimental results and numerical results of Harran *et al.* (1996), for which $0 \le X/D_j \le 50$. There is a good agreement between experiments and this numerical prediction with the exception of lightest gases, where X_{kmax} is over estimated ($X_{kmax} = 7$ for helium). Note, however, that the Reynolds number of the experiments with Helium is much lower than for other gases.

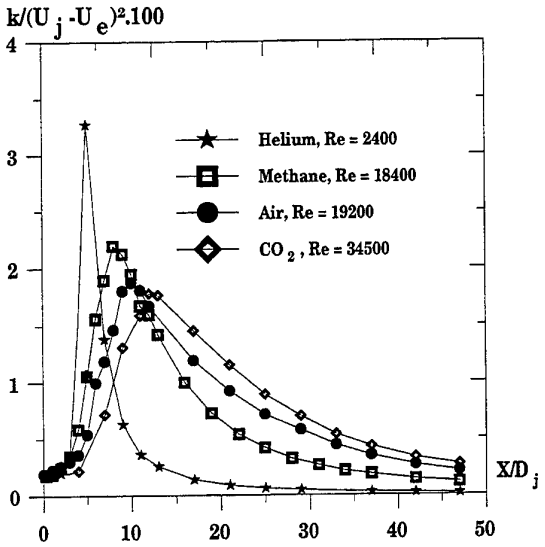


Fig. 3 Centerline evolution of the turbulent kinetic energy.

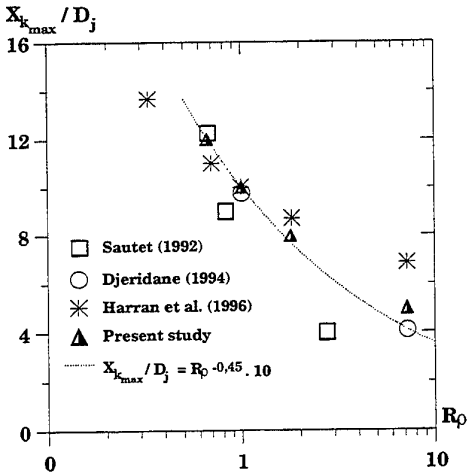


Fig. 4 Axial localisation of the maximum turbulent kinetic energy.

The dependence between density and the maximum location of the kinetic energy is also verified experimentally by Pitts (1991). This maximum corresponds to the end of the potential core of the jet, and also to a location where longitudinal and transversal turbulence intensities are maximum (Pagé, 1997b).

From our results, we have established a law (see also Sautet, 1992) which gives the maximum axial location of the energy according to the density ratio, R_ρ :

$$X_{kmax}/D_j = 10.R_\rho^{-0.45} \qquad (2)$$

5. METHODOLOGY TO CALCULATE ε

The U-component spectrum density functions (not presented in this paper), are used to obtain ε. The corresponding dissipation rate (with the locally isotropic turbulence hypothesis, Batchelor, 1953) is calculated as :

$$\varepsilon = 30\nu\left(\frac{2\pi}{\overline{U}}\right)^2 \int_{f\min}^{f\max} n^2 E_u(n)dn \qquad (3)$$

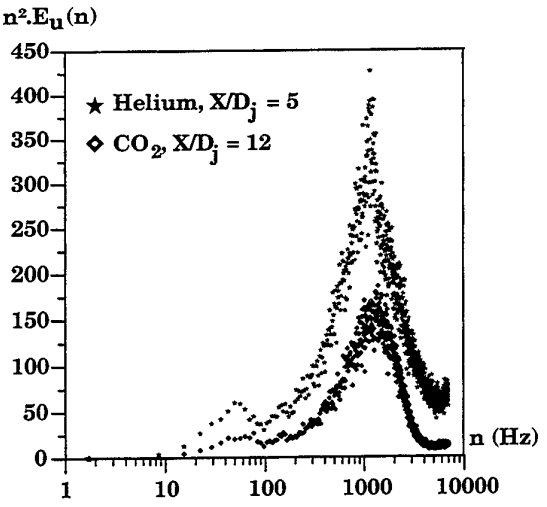


Fig. 5 Dissipation spectra for helium and CO_2.

Figure 5 presents the dissipation spectra $n^2.E_u(n)$ for the lightest and the heaviest gases at centerline positions were the kinetic energy k peaks. Due to the correct spectral representation of the total frequency range by the LDA measurements, they show the expected behavior, so that their integration provides the correct dissipation rates.

However, it is important to remind that the estimation of the dissipation rate of the turbulent kinetic energy is directly related to the *data rate*, i.e. the rate of seeding particles which pass through the probe volume. The higher the data rate is, better is the estimation of ε.

6. CENTERLINE EVOLUTION OF ε_u

The centreline evolution of $\varepsilon_u D_j/U_j^3$ using logarithmic scales is presented in Figure 6 for all the gases. For the near-field region (X/D_j>10) a rapid increase from the exit level is observed. The dissipation rate presents a maximum located at the same X/D_j values noticed for k. Throughout the jet, ε is higher for lightest gases. We notice also power law evolution when X/D_j > 10. This region is explored below.

In Figure 7, for X/D_j > 10, $\varepsilon_u D_j/U_j^3$ presents two slopes: -1, $X/D_j \in [10;40]$ and -3, X/D_j > 40.

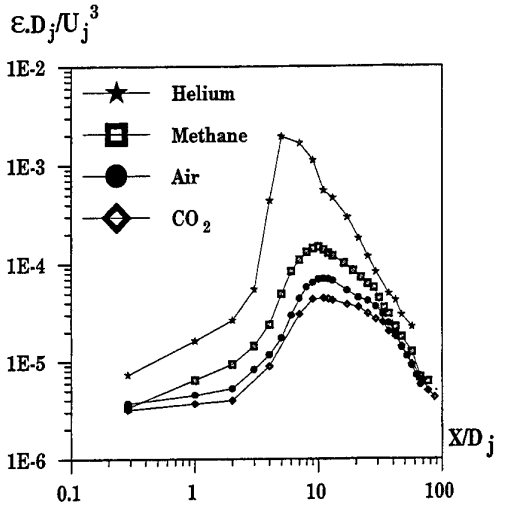


Fig. 6 Centreline evolution of the dissipation rate of u'^2.

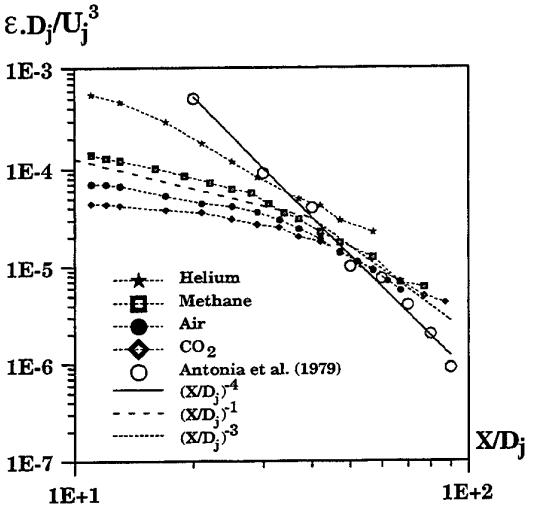


Fig. 7 Comparison of the centreline variation of ε_u with Antonia *et al.* work (1979).

Theoretically, in the far-field of an axisymmetric jet we have :

$$\varepsilon \propto (X/Dj)^{-4} \qquad (4)$$

The dissipation rate is related to the integral turbulent length scale l_o by : $\varepsilon = C.U_c^3 / l_o$ (C is a constant). In the self-preserving region, the jet local half-width is $L_{u/2} \propto (X-X_o)$. Therefore, we indeed obtain :

$$\varepsilon.D_j/U_j^3 = C_1 (X/D_j)^{-4} \qquad (5)$$

The experimental results of Antonia *et al.* (1979) confirm the -4 slope, whereas we determine a -3 slope. The reason of this discrepancy is not clear yet. The Centreline evolution of the non-dimensional

dissipation rate $\varepsilon.D_j/U_c^3$ is given in Figure 8. We observe the same axial evolution observed for turbulent intensities $\langle u^2\rangle^{1/2}$ and $\langle v^2\rangle^{1/2}$ (not presented here, see Pagé *et al.*, 1997b). After a rapid increase, more quick for light gases, there is a trend for the non-dimensional dissipation rate to reach an asymptotic value.

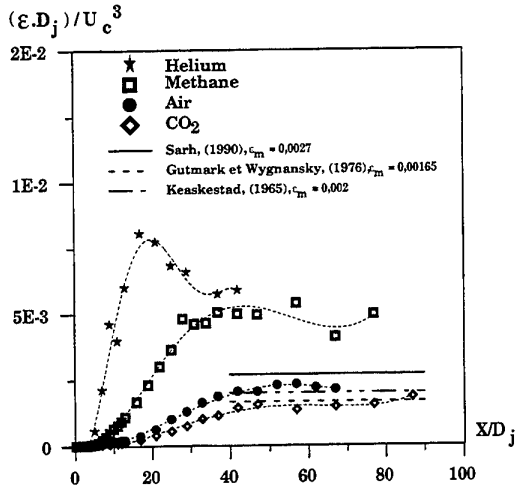


Fig. 8 Centreline evolution of the dissipation rate ε_u

The only comparable experimental results in the literature are those for isothermal (Heakstead, 1965; Gutmark and Wygnanski, 1976; Sarh, 1990;) and heated air jets (Sarh, 1990).

7. THE EFFECT OF THE EQUIVALENT DIAMETER

The equivalent diameter D_e is frequently used for variable density experiments in order to take into account the density effects, namely on the centerline decay rates of the longitudinal velocity (U_c) and the mass fraction (Y_c). Its introduction is based on the idea that the jet with variable density should have the same momentum flux than a jet with constant density, issuing from the same pipe ($D_e = D_j$), in order the two jets to be comparable.

The equivalent diameter concept has been used by many researchers (Thring and Newby, 1953 ; Becker *et al.*, 1967 ; Dahm and Dimotakis, 1987 ; Pitts, 1991). The equivalent diameter D_e (Thring and Newby, 1953) is defined as :

$$D_e = D_j R_\rho^{-1/2} \qquad (4)$$

In the present study we have used this equivalent diameter D_e to know if it has an influence on the kinetic energy and the dissipation rate of the kinetic energy. Figure 9 shows the centerline evolution of the ratio k / k_{max} versus axial coordinate normalised by the equivalent diameter, where k_{max} is the maximum of the kinetic localized at X_{kmax} .

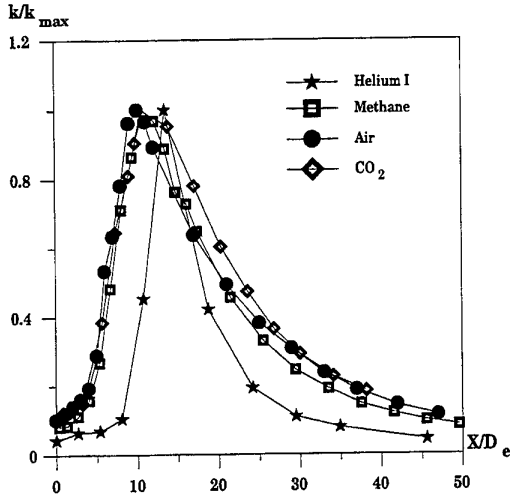


Fig. 9 Centreline evolution of k / k_{max} vs X/D_e.

The uniformisation of each curve is excellent both for the near and the far fields, except however for the helium experiments, but note again the low value of the corresponding Reynolds number (2400). The equivalent diameter seems therefore to take into account the density variation effects on the centreline variation of the turbulent kinetic energy.

We present the centreline evolution of $(\varepsilon_u D_e/U_j^3)/R_\rho$ versus X/D_e on Figure 10. The uniformisation of each curve is again excellent when $X/D_e \geq 10$. Moreover, the -1 et -3 slopes are clearly observed. On the other hand, the curves do not collapse in the near-field ($X/Dj < 10$). A good collapse of these curves in the near field is obtained if $\varepsilon.D_j/U_j^3$ is plotted against X/D_e for each gas (Figure 11). We notice a +2.2 slope in the near filed, again except for the Helium case.

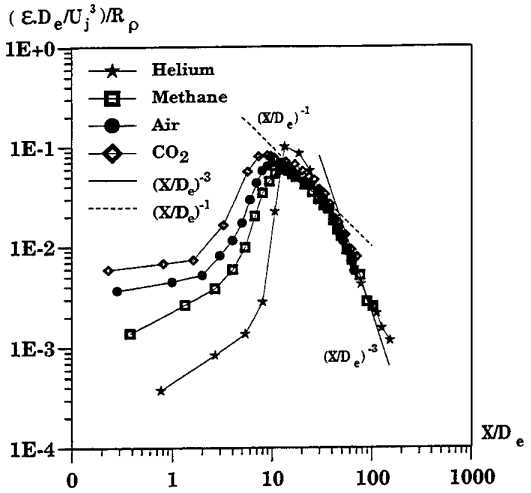


Fig. 10 Centreline evolution of the normalised ε_u versus X/D_e

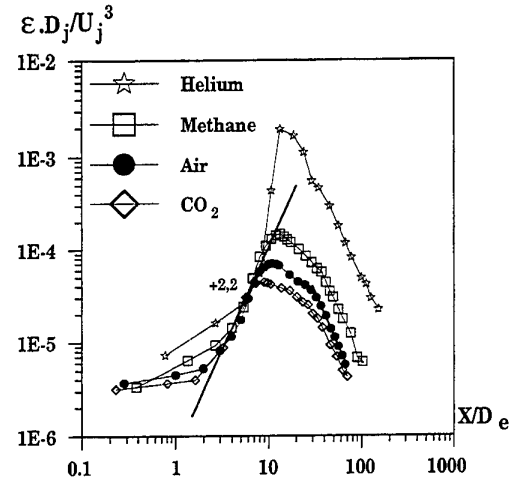


Fig. 11 Centreline evolution of normalised ε_u versus X/D_e

8. CONCLUSIONS

We have presented experimental results on variable density turbulent axisymmetric jets with a density ratio R_ρ varying between 7.2 (helium jet in air coflow) to 0.66 (CO_2 jet in air coflow). After the determination of the velocity field by two-component laser Doppler anemometry, we have obtained the dissipation rate of the u component turbulent kinetic energy, ε_u, from the spectral density functions. The adequate coincidence *data rate* (around 15 kHz) and the good spectral resolution (1 to 7500 Hz) allowed us to estimate ε_u all along the jet (with local isotropy hypothesis). We found that ε_u has a rapid increase in the near field and reaches a maximum peak value for each gas, related to the end of the potential core and to the peaks of the turbulent kinetic energy. The dissipation rate is higher in light gases than in heavier ones.

In the far field, $\varepsilon_u D_j/U_j^3$ follows a power law. We found a -3 slope when $X/D_j > 10$. This slope is not exactly the same given by the theory (-4) and the experimental results from Antonia *et al.* (1979). Inlet characteristics, and the presence of a coflow may explain such a difference. Finally, the use of an equivalent diameter based on the density ratio R_ρ permits to collapse the centreline evolutions of the turbulent kinetic energy and the dissipation rate for each gas.

ACKNOWLEDGEMENTS

This work is supported by the CNRS and the *Conseil Régional du Centre*. JP is supported by a grant from the *Conseil Régional du Centre*.

REFERENCES

Amielh, M., Djeridane, T., Anselmet, F. & Fulachier, L., 1996, Velocity near-field of variable density turbulent jets, Int. J. Heat Mass Transfer, vol. 39, pp. 2149-2164.

Antonia, R. A. & Bilger, R. 1973, An experimental investigation of an axisymmetric jet in a co-flowing air stream, J. Fluid Mech., vol. 61, pp. 805-822.

Antonia, R. A., Satyaprakash, B. R. & Hussain, A. K. M. F. 1979, Measurements of dissipation rate and some other characteristics of turbulent plane and circular jets , Phys. Fluids, vol. 23, pp. 695-700.

Batchelor, G. K. 1953, The Theory of Homogeneous Turbulence. Cambridge University Press, New York.

Becker, H. A., Hottel, H. C. & Williams, G. C., 1967, The nozzle-fluid concentration field of the round, turbulent, free jet, J. Fluid Mech., vol. 30, pp. 285-303.

Dahm, W. A. and Dimotakis, P. E., 1987, Measurements of entrainment and mixing in turbulent jets, AIAA J., pp. 1216-1223.

Djeridane, T. 1994, Contribution à l'étude expérimentale de jets turbulents axisymétriques à densité variable. Thèse de docteur, université d'Aix-Marseille II.

Doudou, A. 1990, Étude des techniques pour l'analyse des autocorrélations, des échelles et des spectres en turbulence à partir des données de la vélocimétrie laser. Thèse de docteur, université de Rouen.

Gutmark, E. & Wygnanski, I. 1976, The planar turbulent jet , J. Fluid Mech., vol. 73, pp. 465-495.

Harran, G., Chassaing, P., Joly, L. & Chibat, M. 1996, Étude numérique des effets de densité dans un

jet de mélange turbulent en microgravité, Revue Générale de Thermique, 35, pp. 151-176.
Heskestad, G. 1965, Hot-wire measurements in a plane turbulent jet, Journal of Applied Mechanics, Trans. ASME, 32, pp. 721-735.
Pagé, J., Haidous, Y., Sarh, B. & Gökalp, I. 1997a, Détermination expérimentale des échelles de tubulence dans les jets axisymétriques à masse volumique variable, 13ème Congrès Français de Mécanique, Poitiers, ENSMA, pp 139-142.
Pagé, J., Haidous, Y., Sarh, B. & Gökalp, I. 1997b, Experimental determination of some characteristics scales in variable density turbulent jets , Proc. 11th Symposium on Turbulent Shear Flow, Institut National Polytechnique, Université Joseph Fourier, Grenoble, vol. 2, pp. 12-12/12-17, 8-11/9.
Pagé, J., 1998, Contribution à l'étude des jets turbulents axisymétriques à masse volumique variable. Thèse de docteur de l'université d'Orléans.
Pitts, W. M., 1991, Effects of global density and Reynolds number variation on mixing in turbulent axisymmetric jets, Exp. in Fluids, vol. 11, pp. 125-134.
Ruffin, E., Schiestel, R., Anselmet, F., Amielh, M. & Fulachier, L., 1994, Investigation of characteristics in variable density turbulent jets using a second-order model, Phys. Fluids, vol. 6, pp. 2785-2799.
Sanders, J. P. H., Sarh, B. & Gökalp, I., 1997, Variable density effects in axisymmetric isothermal turbulent jets : a comparison between a first- and a second-order turbulence model, Int. J. Heat Transfer, vol. 40, pp. 823-842.
Sarh, B. 1990, Contribution à l'étude des jets turbulents à masse volumique variable et des flammes de diffusion turbulentes . Thèse de doctorat d'État, université Pierre et Marie Curie, Paris.
Sautet, J. C. 1992, Effets de densité sur le développement scalaire et dynamique des jets turbulents. Thèse de doctorat, université de Rouen.
Thring, M. W. & Newby, M. P. 1953, Combustion length of enclosed turbulent jet flames. Fourth (Intl) Symp. Combust., pp. 789-796. The William & Wilkins Co.

ON THE ANALYSIS OF TURBULENT SCALAR MIXING IN COAXIAL JET FLOWS

F. Caldas, P. Ferrão, M.V. Heitor and M. de Matos
Instituto Superior Técnico
Mechanical Engineering Department
Technical University of Lisbon
PORTUGAL

ABSTRACT

The turbulent characteristics of the developing region of coaxial jet flows are studied making use of velocity and concentration measurements obtained in axisymmetric jet flows of CO_2 (Re_i=15000) and air (Re_o=50000). Laser Doppler velocimetry and Rayleigh scattering are used for point measurements of time-resolved velocity and concentration distributions, while the instantaneous velocity field was analysed with double-exposure photographic particle image velocimetry. The results identify local peaks in Reynolds shear stresses associated with local maxima in vorticity maps, which are related with large scale motions that contribute to turbulent diffusion.

1. INTRODUCTION

This paper is concerned with the experimental analysis of turbulent scalar mixing in coaxial jet flows, as a critical step to improve understanding of mixing in highly turbulent reacting flows, which normally involve turbulent mixing of fuel and air. Variable density effects are a consequence of heat release due to reaction, which have shown to alter turbulent mixing in flames (e.g. Bray et al., 1985; Starner and Bilger, 1986; Heitor et al., 1987; Ferrão and Heitor, 1998).

In this context, our approach is to consider a comparatively simple flow in the form of two co-flowing jets of different gases, without the inherent complexities of chemical reaction. The primary interest is in the developing region of the coaxial jet, where most of the mixing takes place and the characteristic turbulent processes are well known (e.g. Ribeiro and Whitelaw, 1980).

Axisymmetric coaxial turbulent jets at various velocity ratios have been widely studied, but most of the research have been limited to time-averaged velocity and turbulence quantities and pressure spectra (e.g. Champagne and Wygnanski, 1971; Durão and Whitelaw, 1973; Ribeiro and Whitelaw, 1980; Takahashi et al., 1992; Rehab et al., 1997). Ribeiro and Whitelaw (1980) have provided the experimental evidence that turbulent diffusion is dependent on the surrounding field where both the Reynolds stresses and their gradients can change. This has been assessed in term of asymmetric probability density functions of velocity fluctuations, which are associated with the occurrence of large eddies. However, such large scale motions, or any vortex structures of the flow field which ultimately determines turbulent mixing, have not been experimentally identified. Chan and Ko (1978) and Ko and Chan (1979) attempt to infer the near-field vortex structure of an annular jet based on pressure and velocity measurements. More recently, Dahm et al. (1992) presented a physical picture of the vortex structure in the near field of a coaxial jet with low velocities, for different ratios of the outer-to-inner mean velocity, where vortex patterns were visualised by means of laser-induced-fluorescence. However, no quantitative direct measurements of large-scale motions of the flow field have been presented.

In addition to the analysis above, the continuos research on coaxial jets during the last two decades have also shown features that cannot be represented by conventional turbulent mechanisms. One is the occurrence of vortex shedding and flow instabilities in the wake of the inner pipe, as identified by Ribeiro and Whitelaw (1980). Gladnick et al. (1990) have reported instabilities in the annular shear layer between the two flows of different velocities, in that the shear instability, for a velocity ratio different than unity, is that of an annular mixing layer and corresponds to vortex rings, which interact and become unstable, leading to a fully developed turbulent flow far downstream of the jet exit plane.

The present work is intended to improve understanding of these processes, which ultimetly influence turbulent mixing in variable-density coaxial jets. The following section describes the diagnostics used, which include laser Doppler velocimetry, laser Rayleigh light scattering and particle image velocimetry. The results are presented in section 3 and briefly discussed in section 4. The final section presents the main conclusions of the work

2. EXPERIMENTAL METHOD

2.1 Flow Configuration

The flow rig includes 3 concentric stainless steel ducts where CO_2 flows in the inner duct and is surrounded by two different annular air flows. The inner tube has an inside diameter, d=2mm and 1211mm in length and is 1-mm-thick. The two air jets are generated by a primary annulus which is D=24mm in diameter, and a secondary annulus of 150mm in diameter. The coaxial jet develops downstream of the tip of the inner and the primary annulus, which is 2mm thick and has a total length of 1125mm. Both tubes are tapered at 7 degrees over their final length to a knife-edge at the exit. The external air jet is intended to provide well-defined boundary conditions, which are defined by a low air velocity (0.5m/s), and avoids the entrainment of external air in the initial developing region. The total length of the outermost 2mm-thick-tube is 1000mm.

The rig was designed and built in order to obtain fully developed turbulent flows at the exit plane.The annuli formed by the innermost and the middle tube is equipped with 3 honeycomb with 50mm-length each one. A thin metal net, with a ratio of free area bigger than 57%, was introduced 24 diameters upstream the jet-exit to remove any swirl component of the flow.

The coannular tubes are mounted on a three-dimensional traverse, which has a resolution of 0.2mm in all three directions. The entire rig is orientated such that the coaxial jet issue vertically upwards, as in Fig.1.

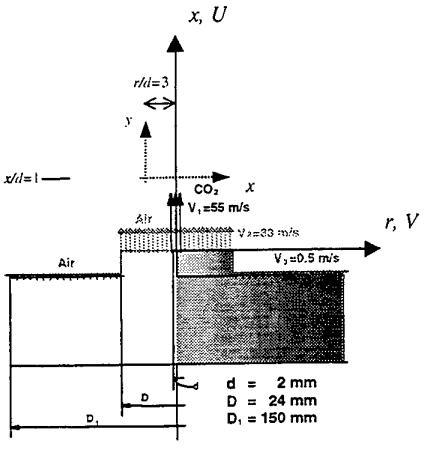


Figure 1- Flow geometry and boundary conditions for the regime studied (dashed co-ordinates were used for P.I.V. measurements).

The density ratio of the inner jet to the outer coaxial jet is about 1.5, while the ratio of the bulk mean axial velocity in the coannular air jet to the central jet at the exit plane is 0.6. This is associated to an average velocity of 55m/s in the central jet and 33 m/s in the outer jet, which correspond to a Reynolds number characteristic of the air jet based on the equivalent diameter (D-d) of Re=50000, and a Reynolds number characteristic of the CO_2 jet and based on the inner diameter, of 15000.

The CO_2 is supplied to the inner jet from a 99.5% pure gas pressurised cylinder, while the air is supplied from a fan and is filtered by means of an 1μm particle filter. Both the CO_2 and air are passed through pressure regulators to maintain constant flow rates, which are monitored by individual flowmeters.

2.2 Single-Point Measurements

The instrumentation used throughout this work for the time-resolved measurements consists on a combined LDV/LRS system, which was based on a single laser light source (5W argon-ion laser). The system has derived from that described by Duarte et al. (1995) and Almeida et al. (1996) and has been optimised, as the main data acquisition system includes a 16 bits analogue/digital converter, in place of the 12 bits data acquisition board previously used, in order to increase the accuracy of the scalar measurements.

The velocimeter was based on the green light (514.5nm) of the laser and was operated in dual-beam, forward-scatter mode with sensitivity to the flow direction provided by a rotating diffraction grating. The calculated dimensions of the measuring volume at the e^{-2} intensity locations were 606μm in length and 44μm in diameter. The velocity results were obtained by seeding the flow with 1μm-diameter aluminium oxide particles, which are introduced upstream of the ducts by a set of cyclones.

The Rayleigh scattering system was operated from the blue line of the same laser source, which was made to pass through a 5:1 beam expander. The light converged in a beam waist of 50μm diameter was collected at 90° from the laser beam direction with a magnification of 1, and passed through a slit of 1mm length. The collected light was filtered by a 1nm-bandwidth interference filter and a polariser, in order to optimise the signal-to-noise ratio. The signal was amplified and low pass filtered at 10kHz before digitalisation. The temporal resolution of the system depends on the integration time associated with this filter, which is quantified to be 50μs.

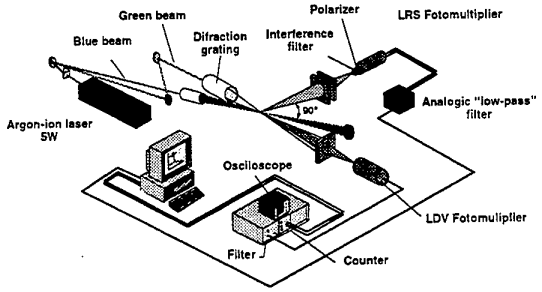


Figure 2- Combined L.D.V./L.R.S. system.

2.3 Multi-Point Measurements

Double-exposure photographic particle image velocimetry was used together a spatial autocorrelation technique, following the main procedures given by Adrian (1986), and reviewed by Adrian (1991) and more recently by Grant (1997).

In the present work, the coaxial jet flow field was illuminated from a Q-switched double-pulsed Nd:YAG laser (Spectra Physics Pulsed Nd:YAG laser GCR-130) with an output energy of approximately 0.2J per pulse. The 6mm diameter laser beam was expanded by a divergent cylindrical lens and collimated by a plan-convex lens (f#7) that focuses the beam in the test section, giving rise to a light sheet, 145mm in height and 0.2mm minimum thickness.

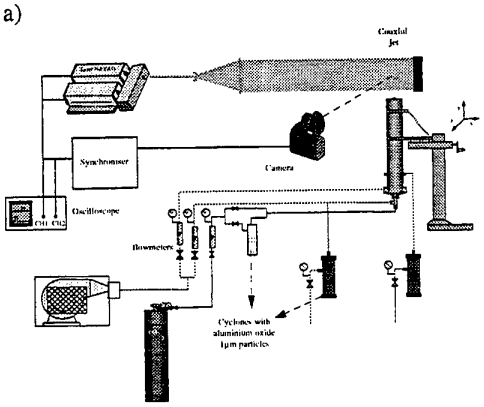
The flow was seeded with 1μm diameter Al_2O_3 particles, which allow for accurate photographic recording of particle images. The seeding concentration was approximately 25 to 30 particles/mm3, in both the inner CO_2 jet and in the outer air jet.

The coaxial jet flow field was photographed using a 60mmx70mm-view camera, making use of a macro M140mm high quality lens, using an aperture of f#16 at unit image magnification, in order to minimise lens aberrations.

A synchroniser based on an electric pulse generator was developed to provide the appropriate trigger control of the camera and the firing of the lasers. Analysis showed that the maximum power in the laser beam is obtained when the Q-switch delay is about 170μs for both laser cavities, which is a longer period than the time required to open completely the camera shutter (0.1ms). According to the flow velocities and the magnification of the camera, the synchroniser receives a manual trigger by the operator, which turns on immediately the lamp of one of the pulsed lasers (L.P.1) and simultaneously the camera. After a certain delay, an electric pulse generator generates an appropriate electric pulse that turns on the lamp of the second pulsed laser (L.P.2). This time delay determines the time between consecutive pulses, and the correct choice of the camera shutter speed stops the image acquiring after exactly two light pulses. Figure 3 shows a schematic time diagram, together with a scheme of the system set-up, where the use of an electric pulse generator is justified by the accuracy of the delay in firing the second laser cavity.

Images of the flow were recorded at independent instants in Kodak TMax400 films, which were processed using Kodak D19 developer to produce high-contrast negative image fields of the jet flow. Two sets of P.I.V. photographs were taken in a x-y plane, centred with the jet axis, and refer to the flow regions of interest from x=d to x=48d. Two flow zones are considered throughout this paper with an area of 48mm(=24d)x12mm(6d). The first zone is referred as zone A and extends from d=1 to 24d, while zone B extends from x=24d up to x=48d in the axial direction.

a)



b)

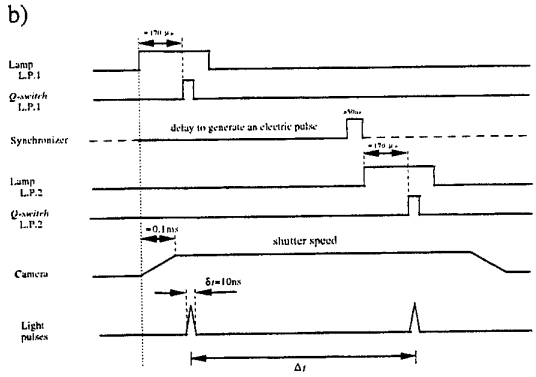


Figure 3- Experimental rig and image acquisition system.

a) Schematic diagram of the flow rig and the multi-point measuring technique

b) Measuring time diagram.

The double-exposure PIV photographs were analysed on a T.S.I. interrogation system (Model 6000), based on two-dimensional autocorrelation processing techniques, which has shown to be appropriate for the flow studied, Menon and Kronewetter (1992).

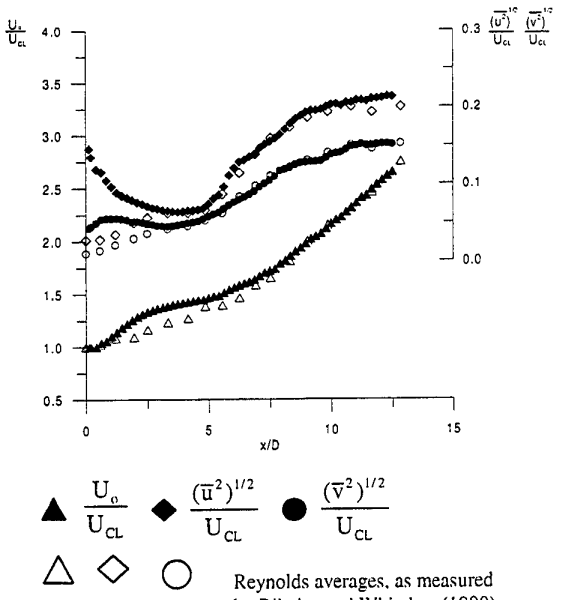
The coaxial jet double-exposure P.I.V. photographs were evaluated using an interrogation spot size of 1.5mm×1.5mm, giving rise to a measuring volume of 1.5×1.5×0.2=0.45mm3. The interrogation spots were overlapped by 50% in order to enable image reconstruction, as defined by the Nyquist's theorem. Each photograph yielded instantaneous two-dimensional data sets of the axial and radial velocities at 1100 points separated by 0.75mm.

Data validation procedures has shown spurious measurements always under 10% of the total number of velocity vectors presented herein. Following this operation, an interpolation operation by multiple linear regression is performed on the vector map to replace the removed vectors with estimates of local velocity.

3. EXPERIMENTAL RESULTS

Figure 4 shows centreline distributions of the inverse of the mean velocity and of the Reynolds normal stresses, which show that the annular flow does not influence the mean velocity at the centreline only up to x/D≈1, but it does, however, affect the Reynolds stresses. Between 1 and 7 diameters downstream of the jet tip, the centreline decay of mean velocity asymptotes to a value which is inversely proportional to the distance from the inlet. Downstream of x/D=7, the profiles of $\overline{u}^2$ and $\overline{v}^2$ follow a trend towards self-similarity, which is reached at approximately x/D=13. Then the behaviour of the mean flow and of the Reynolds stresses is no longer dependent on the initial conditions.

This description of the flow is typical of coaxial turbulent jets, in that the mean and turbulent flows downstream of the jet duct tend to self similarity. In particular, the present results are consistent with those of Ribeiro and Whitelaw (1980) downstream of x/D=4, although the near tip zone is influenced by variable density effects and the flow boundary conditions, apart from the spatial resolution of our measuring system. This is particularly important in the vicinity of the jet tip, as the inner jet diameter is considerably small, when compared with the shear layer thickness.



Reynolds averages, as measured by Ribeiro and Whitelaw (1980) in uniform density coaxial jets for similar velocity ratio.

Figure 4 – Centreline distributions of Favre-average velocity and axial and radial turbulence intensities.

Figures 5 and 6 show radial distributions of mean and rms axial and radial velocities and shear stresses, which identify the central jet up to x/D=4.17, as also quantified in figure 7 in terms of the time-averaged CO_2 concentration.

The results quantify the process of turbulent diffusion along the flow and identify zones of outward turbulent transport of momentum, with $\overline{uv}$ >0, where the inner jet is accelerating the annular jet and in the outer shear layer, as well as an intermediate zone of inward turbulent transport of momentum up to x/D=2.92, where $\overline{uv}$ <0. The shear stress is zero at locations of zero mean axial velocity gradient, as expected by turbulent viscosity models. Also, the local peaks in shear stress correspond to maxima of the normal stresses, which are associated to annular clockwise rotating vortices. This is consistent with the development of a single peak in the radial distribution of normal stresses downstream of x/D=3.33 and, again, agrees with the analysis of Ribeiro and Whitelaw (1980), in that the diffusive flux of energy is proportional to energy times a diffusive velocity characteristic of the large scales of motion. In that case, the diffusive velocity may be taken proportional to the square root of the average Reynolds shear stress across the flow field, based on the fact that the latter determines the production of the large eddies (e.g. Bradshaw et al., 1967).

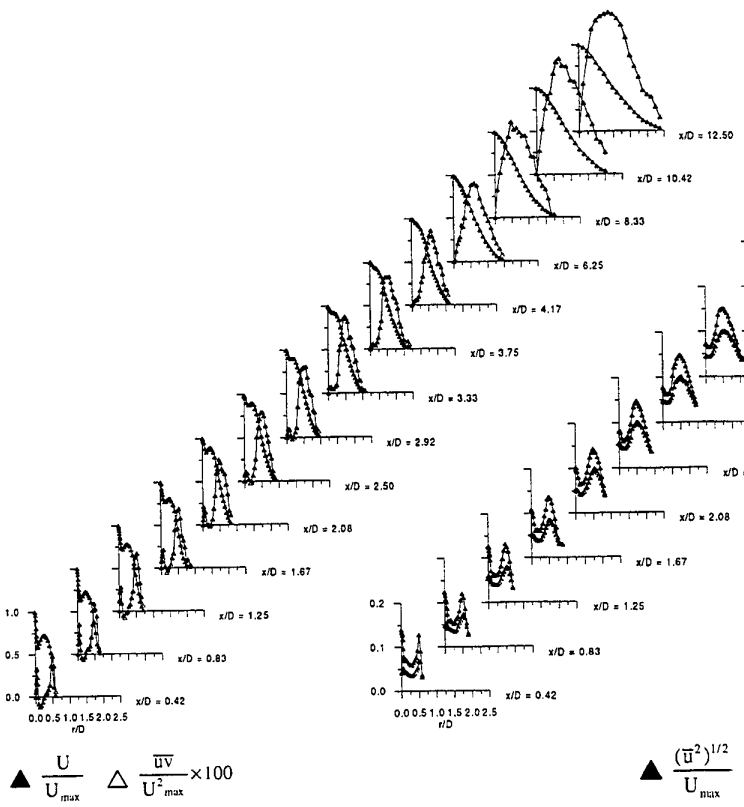


Figure 5 – Radial distribution of mean axial velocity and Reynolds shear stresses

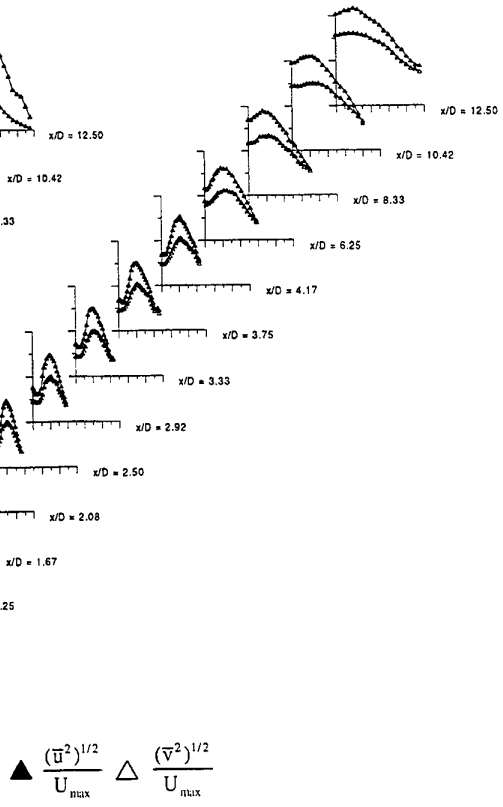


Figure 6 – Radial distributions of axial and radial turbulence intensities

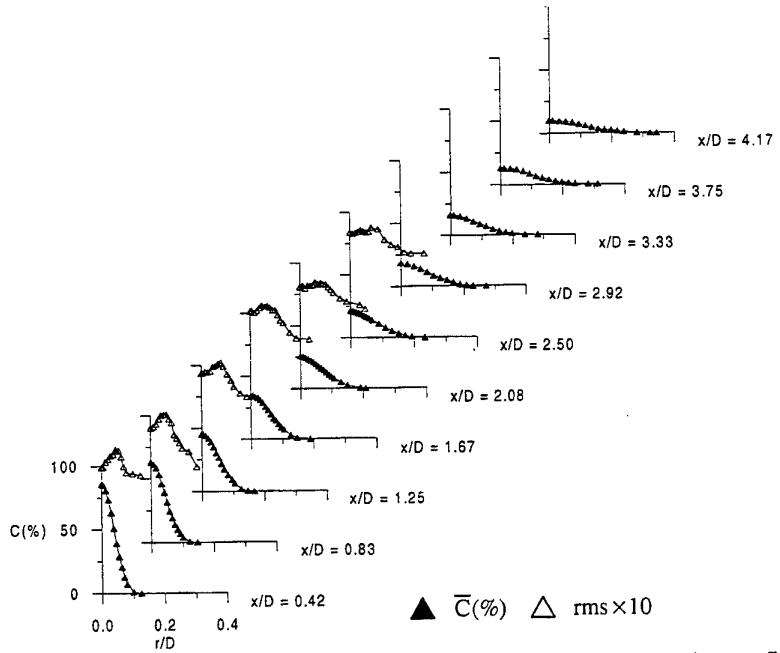
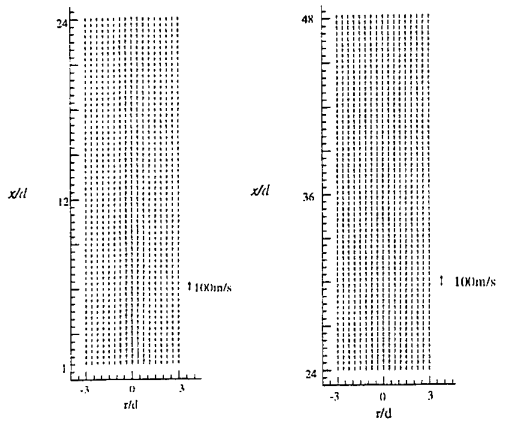


Figure 7- Radial distribution of time-averaged and turbulent concentration profiles

The present results also show that the axial and radial normal stresses exhibit a double peak while the inner jet is identified (i.e., x/D<4.17), with $\overline{u^2}$ always higher than $\overline{v^2}$ and following the trend to be expected from the evolution of the Reynolds shear stress. These considerations can be extended to the scalar characteristics of figure 7, in that the radial distributions of the CO_2 concentration fluctuations exhibit a local minimum at the centreline and a peak at the maximum radial gradient of mean concentration. Also, it should be noted that the profiles of mean concentration are well fitted by a gaussian curve.

Figure 8 shows vector maps of the velocity field u(r,x) corresponding to instantaneous images and covering the flow regions A and B identified above. The measured axial velocity ranges from 30.0m/s to 59.0m/s in zone A and from 32.4m/s to 46.9m/s in zone B, while the radial velocities range from -5.3m/s to 4.4m/s in zone A and from -3.8m/s to 3.8m/s in zone B. The results clearly identify the inner jet pattern on the vicinity of the jet tip (in zone A), which is surrounded by the shear flow described above.



Zone A Zone B

Figure 8– Instantaneous velocity fields of the coaxial jet for different axial locations.

a) Zone A: near tip zone
b) Zone B: far tip zone

The vorticity structure of the coaxial jet can be determined when each velocity field is spatially differentiated to obtain maps of the out-of-plane component of the vorticity, w_z. The vorticity values are found at each point in the vector map by computing the circulation around a closed contour surrounding the point, and invoking Stoke's theorem to relate the circulation per unit area to w_z (Landreth and Adrian, 1990).

In addition, the components of the rate of strain tensor are calculated from second order finite differences of the velocity components at each point in the flow. Figure 9 shows sample results for our 2-D flow field, where the out-of-plane component of vorticity is given by (following the system of Fig.1):

$$w_z = \left(\frac{\partial u}{\partial x} - \frac{\partial v}{\partial y} \right) \quad (1)$$

The results obtained have shown that $\partial u/\partial x$ is the main component to the final value of vorticity over the measured zone in the coaxial jet mixing layer. The largest values of the vorticity are noted in the inner-to-outer jet mixing layer on the initial merging zone, where large velocity gradients exist. In agreement with the previous description of the present shear layer, the results show three zero-vorticity lines, namely along the centre of the jet up to x=48d, and limiting two outer small vorticity zones of opposite sign (Fig.9a-ii).

4. DISCUSSION

The analysis above has been presented in terms of the turbulence structure of coaxial jet flows, and particularly on the effect of large-scale motions on turbulent mixing. The present single-point measurements follow previous trends reported in the literature for the developing zone of turbulent jets and provide new information on the scalar mixing pattern. In addition, the use of particle imaging technique that yields large numbers of instantaneous velocity vectors from which flow structures can be visualised and quantified has allowed identifying those structures in relation to the single-point measurements.

The evidence is that the positive local peaks in the distribution of shear stress for r/d≈1 correspond to an annular vortex structure, as defined in the vorticity maps of figure 9. This annular vortex dominates turbulent mixing and (for the co-ordinates system used here) is related with positive vorticity on the left side of the flow represented in figure 9 and negative vorticity (clockwise rotation) otherwise, which in turn corresponds to a positive axial-to-radial velocity correlation on the right side of the figure. The single peaks in the turbulent radial velocity profiles downstream of the edge of the central jet tube and the corresponding maxima of vorticity measured in the same region, are also consistent with this pattern for the initial developing region of the jet.

Although the direct observation of the velocity maps of figure 8 does not identify any coherent structure in the flow field, these structures can be easly

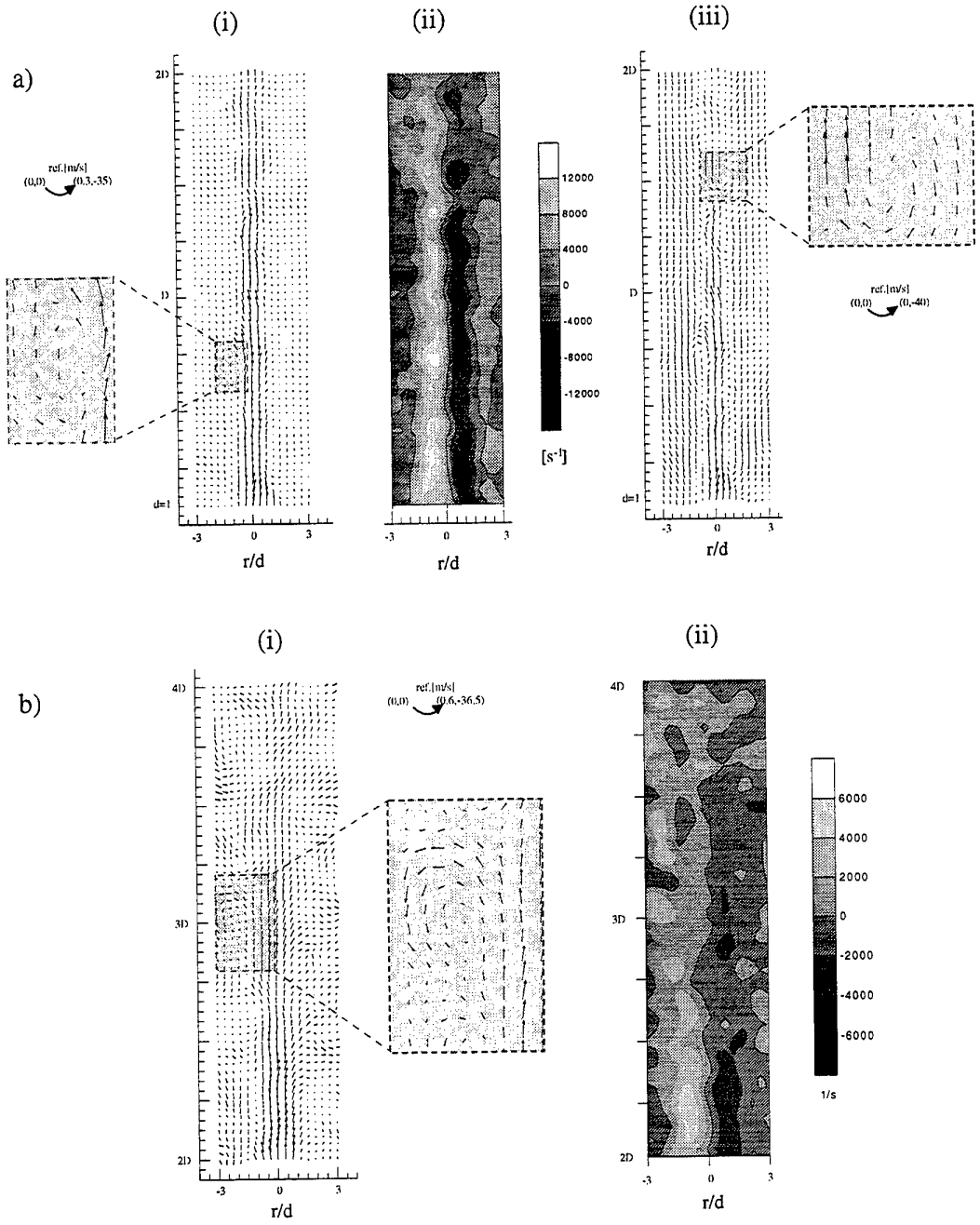


Figure 9- Sample PIV measurements in coaxial jet

a) Zone A:
- i) Sample results in a frame of reference convecting at u(-0.3,35) m/s, with identification of large-scale motion around x=0.75D=9d
- ii) Instantaneous vorticity map
- iii) Sample results obtained in a frame of reference convecting at u(0,40) m/s, with identification of large-scale motion around x=1.5D=18d

b) Zone B:
- i) Sample results obtained in a frame of reference convecting at u(-0.6,36.5) m/s, with identification of large-scale motion around x=3D=36d
- ii) Instantaneous vorticity map

visualised by subtracting an appropriate value to the velocity in each point of the vectorial map (e.g., Keane et al., 1995). This can be achieved by changing the frame of reference of the instantaneous velocity map by the convective transport velocity of the fluid surrounding a particular vortice. The sample results of figure 9 quantify the propagation of coherent structures that occurs in the locus of maximum vorticity and correspond to the flow region where the Reynolds shear stresses are maxima. In addition, the analysis show that the turbulent structures that occur in the mixing layer of the coaxial jet tend to grow for downstream locations in the plane of the measurements. Also, large-scale structures which occur due to shear instability in the wake of the inner pipe wall have a clockwise sense of rotation to the right of the central jet flow and an opposite sign otherwise, as represented in figure 9. Following the results of Ko and Kwan (1976), the different forms of vortices identified are typical of the complex structures within coaxial jets, being associated to Strouhal number between 0.3 and 0.7, as the jet tip is approached.

5. CONCLUSIONS

Laser Doppler velocimetry and laser Rayleigh scattering are used together with a particle imaging technique to improve understanding of turbulent mixing downstream of co-flowing jets of CO_2 and air. Attention is focused on the evidence that turbulent diffusion is dependent on the surrounding field, being determined by the occurrence of large-scale motions. The results quantify the propagation of coherent structures that occurs in the locus of maxima vorticity and the shear stress distribution, and provide reliable information on the variable length scales typical of coaxial jet flows.

REFERENCES

Adrian R.J. (1986): Multi-point Optical Measurements of Simultaneous Vectors in Unsteady Flow - a review; Int. J. Heat and Fluid Flow, Vol.7, N°2.

Adrian R.J. (1991): Particle-Imaging Techniques for Experimental Fluid Mechanics; Annu. Rev. Fluid Mech. 23, pp261-304.

Almeida P., Ferrão P. and Heitor M.V. (1995): The Effect of Swirl on the Interaction between Pressure Gradients and Density Fluctuations in Baffle-Stabilised Flames, Proc. of 10th Symposium on Turbulent Shear Flows, Vol.2, pp16-7 to 16-12.

Bradshaw P., Ferriss D.H. and Atwell N.P. (1967): calculations of Boundary-layer Development using the Turbulence Energy Equation; J. Fluid Mech., Vol.28, p593.

Bray K.N.C., Libby P. and Moss J.H. (1985): Unified Modelling Approach for Premixed Turbulent Combustion – Part I: General Formulation; Combustion and Flame, 61, pp87-102.

Champagne F.H. and Wygnanski I.J. (1971): An Experimental Investigation of Coaxial Turbulent Jets; Int. J. of Heat and Mass Transfer, Vol.14, pp1445-1464.

Chan W.T. and Ko N.M.W. (1978): Coherent Structures in the Outer Mixing Region of Annular Jets; J. Fluid Mech., Vol.89, pp515-533.

Dahm W.J.A., Frieler C.E. and Tryggvason G. (1992): Vortex Structure and Dynamics in the Near Field of a Coaxial Jet; J. Fluid Mech., Vol.241 pp371-402.

Duarte D., Ferrão P. and Heitor M.V. (1996): Flame Structure Characterisation based on Rayleigh Thermometry and Two-point Laser Doppler Measurements; in Developments in laser Techniques and Application to Fluid Mechanics, Eds. Adrian et al., Springer Verlag, pp185-249.

Durão D. and Whitelaw J.H. (1973): Turbulent Mixing in the Developing Region of Coaxial Jets; J. of Fluids Engr., pp467-473.

Ferrão P. and Heitor M.V. (1998): Simultaneous Measurements of Velocity and Scalar Characteristics in Premixed Recirculating Flames, Experiments in Fluids (to appear).

Gladnick P.G., Enotiadis A.C., Larue J.C. and Samuelsen G.S. (1990): Near-Field Characteristics of a Turbulent Coflowing Jet; AIAA Journal, Vol.28, N°8, pp1405-1414.

Grant I. (1997): Particle Image Velocimetry: a Review; Proc. Instn. Mech. Engrs., Vol.211, Part C; pp55-76.

Heitor M.V., Taylor A.M. and Whitelaw J.H. (1987): The Interaction of Turbulence and Pressure Gradients in Baffle-Stabilised Premixed Flames; J. Fluid Mech., Vol.181, pp387-413.

Keane R.D., Adrian R.J. and Zhang Y. (1995): Super-resolution Particle Imaging Velocimetry, Meas. Sci. Techn., 6, pp754-768.

Ko N.M.W. and Chan W.T. (1979): The Inner Region of Annular Jets; J. Fluid Mech., Vol.93, pp549-584.

Ko N.W. and Kwan A.S.H. (1976): The Initial Region of Subsonic Coaxial Jets; J. Fluid Mech., Vol.73, pp305-332.

Landreth C.C. and Adrian R.J. (1990): Impingement of a Low Reynolds Number Turbulent Circular Jet onto a Flat Plate at Normal Incidence; Experiments in Fluids 9, pp74-84.

Menon R. and Kronewetter H. (1992):Quantitative Flow Measurement System Using the PIV Technique; in 'Combusting Flow Diagnostics', pp325-338; ed. Durão et al.; Kluwer Academic Publishers; Netherlands.

Rehab H., Villermaux E. and Hopfinger E.J. (1997): Flow Regimes of large-velocity-ratio coaxial jets; J. fluid Mech., Vol.345, pp357-381.

Ribeiro M.M. and Whitelaw J.H. (1980): Coaxial Jets with and without Swirl; J. Fluid Mech., Vol.96, pp769-795.

Starner S.H. and Bilger R.W. (1986): Joint Measurements of Velocity and Scalars in a Turbulent Diffusion Flame with Moderate Swirl; 21th Symp. (Intl.) on Combustion, The Combustion Institute, pp1569-1577.

Takahashi F., Vangsness M.D. and Belovich V.M. (1992): Conditional LDV Measurements in Swirling and Non-swirling Coaxial Turbulent jets for Model Validation; 30th Aerospace Sciences Meeting & exhibit, Reno, NV, Jannuary 6-9.

PIV AND PLIF INVESTIGATION OF BIOMIXING BY MODEL FILTER-FEEDERS

U.Ullum, R.J.Adrian* and P.S.Larsen

Dept. of Energy Engineering, Fluid Mechanics Section, Building 404
Technical University of Denmark, DK-2800 Lyngby, Denmark
* Department of Theoretical and Applied Mechanics
University of Illinois, Urbana, IL 61801, USA

ABSTRACT

A regular array of pairs of sources and sinks in the form of flush-mounted holes in the bottom plate of an aquarium tank simulate the flow generated by filter feeding worms burried in the sediment of a quiescent marine area. Starting from a uniform concentration of dye simulating food particles, sink flows are 100% filtered before returned at sources. The resulting flow and transient concentration distribution near the bottom are studied by PIV and PLIF in terms of mean and rms fields of two velocity components and the concentration. The fields may be interpreted as low-Reynolds number, large scale, high intensity turbulence, and fluxes and the effective diffusivity for vertical scalar transport are estimated from the data in selected vertical planes.

1. INTRODUCTION

Benthic filter feeders such as the worm *Nereis diversicolor* may have a significant impact on the phytoplankton concentration in many marine areas. The animals, typically 100-200 ind/m^2 in the field, pump water continuously. Inhalant water, essentially 100% filtered and subsequently exhaled, represents a net drain of phytoplankton at the bottom. Exhalant jets provide momentum sources responsible for the associated biomixing causing the development of a phytoplankton depleted boundary layer near the bottom. Estimated values of an equivalent effective diffusivity $D_e(z)$ in otherwise stagnant water was inferred (Larsen and Riisgaard, 1997) by comparing transient concentration profiles measured in earlier laboratory experiments (Riisgaard *et al.*, 1996b) with solutions to a transient convection-diffusion problem. Field experiments (Riisgaard *et al.*, 1996b) related the animal growth rate at various heights above the bottom to the concentration of phytoplankton and it was found that near-bottom depletion had a significant impact on the growth rate of the animals.

It is the purpose of the present study to determine directly the distribution of an effective diffusivity $D_e(z)$ resulting from the action of an array of model filter-feeders in an otherwise stagnant pool of water using optical diagnostics. PLIF has been used earlier to study the concentration boundary layer under flow conditions in a laboratory flume with a bed of simulated bivalves (O'Riordan *et al.*, 1993), but the effective diffusivity was not inferred. Presently, in order to get detailed information of the mixing and transport processes induced by filter-feeders, it is desirable to obtain accurate data on both concentration and velocity fields in the vicinity of the animals. This is done by using a 3-frame PIV technique and a reference camera PLIF technique.

2. EXPERIMENT

2.1 Flow System

Fig. 1 is a schematic of the experimental setup showing the 330×330×500 *mm* perspex test section with 4×4=16 pairs of flushmounted inlets and outlets. Each pair represents the inhalant and exhalant openings of one individual of *Nereis diversicolor*. Pairs of 4 *mm* diameter inlets and outlets are arranged on a monospaced grid of spacing Δ=73 *mm*, and the distance between coherent inlets or outlets is 50 *mm*. All inlets and all outlets, respectively, were connected, through

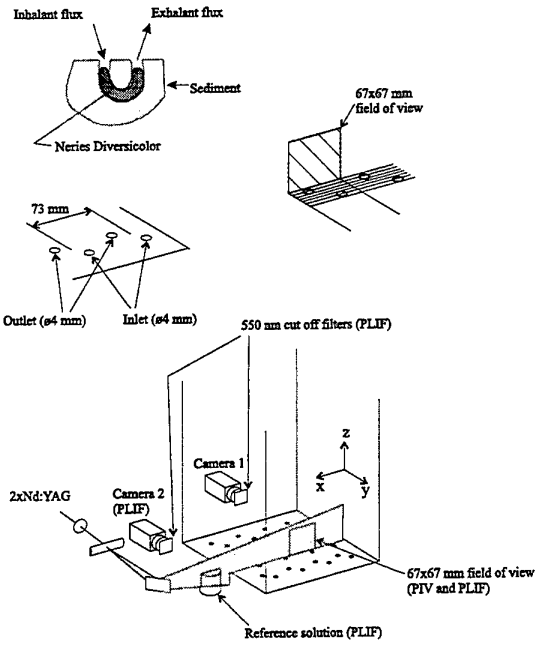


Figure 1: Schematic of the experimental setup.

equal length tubing, to its own manifold. For PIV measurements, one metered pump delivered the desired steady volume flow from one manifold to the other. The water was seeded with 15 μm particles. For PLIF measurements, first the test section was filled with pure water mixed with the flourescent tracer Rhodamine 6G to an initial concentration C_0 = 0.1 mg/l and left to reach a quiescent state. A sample of the inital mixture, the reference solution (see Fig. 1), was continually monitored for aging of the flourescence. At time t = 0, an open circuit flow was initated by pumping pure water from a reservoir to the manifold for inlets, while another pump drained the same metered volume flow of contaminated water from the manifold of outlets to a dump. The flowrate per opening was $\approx 2.1ml/s$ at all experiments, yielding $Re = 40$ based on mean inlet velocity and inlet diameter but variations between individuals occurred.

2.2 PIV System and Processing

The apparatus consisted of a 1k×1k TSI PIVCAM 10-30 cross-correlation camera and a TSI synchronizer controlled by TSI Insight software. Illumination was provided by a NewWave 2×Nd:YAG laser with a maximum energy of 50 mJ per pulse. Particle images of size 67×67 mm were recorded in 7 vertical x, z-planes covering the area of one unit cell of side length Δs = 73 mm (see Fig. 1). Now let the origin be the corner of the unit cell closest to the sink. The 7 planes are located at: $y/\Delta s$ = 0.14, 0.26, 0.39, 0.50, 0.61, 0.74, 0.86 - where plane 2 ($y/\Delta s = 0.26$) contains the sink and plane 6 ($y/\Delta s$ = 0.74) contains the source.

Because of the high velocity gradients occuring in the nearfield of the source, a 3-frame approach was applied in 1 of the 7 investigated planes, that is, the plane above the source. Acquisition of 3 frames, namely at $t_0 = 0$, $t_1 = 20$ and $t_2 = 200$ ms, and subsequent cross-correlation of frame 0 with frame 1 and 2, respectively, yields 2 vector plots of the same flowfield. This method ensures that displacements measured in the jet region are below 1/4 times the interrogation area side length (Keane and Adrian, 1990). The two vector plots were combined by substituting spurious vectors in plot 2 (Δt=200 ms) with vectors from plot 1 (Δt=20 ms). All images were processed using 64×64 pixels interrogation areas with 50 % overlap and a gaussian subpixel interpolation. Each vector field consist of 30×30 vectors with a spacing of 2.1 mm.

A total of 50 instantaneous vector fields were acquired within 25 min. from each plane and ensemble averaged velocity and rms fields were extracted from the vector fields. In addition the data provided information of the degree of anisotropy w_{rms}/u_{rms} and a measure for the agitaion level α, defined by

$$\alpha = \sqrt{\frac{\overline{u^2} + \overline{w^2}}{\overline{U}^2 + \overline{W}^2}} \tag{1}$$

2.3 PLIF System and Processing

The transient concentration development was measured by PLIF using the flourescent tracer Rhodamine 6G ($C_0 = 0.1$ mg/l). The apparatus consisted of two 1k×1k TSI PIVCAM 10-30 cross-correlation cameras and a TSI synchronizer. Illumination was provided by a NewWave 2×Nd:YAG emitting 532 nm green light. The maximum absorption wave length of Rhodamine 6G is 530 nm and the emmission spectrum is 540 to 660 nm with a peak at 560 nm. A 550 nm cutoff filter was used in front of each camera to filter out ligth scattered from surfaces and particles in the test section. The light sheet was directed into both the test section and the reference solution enabling coincident image acquisition on camera 1 and 2.

Now, let $\theta_r = \int\int I_{cam2}(i,j,t = 0)didj$ and $\theta(t) = \int\int I_{cam2}(i,j,t)didj$, where I_{cam2} denotes the pixel intensities on camera 2. The concentration dis-

tribution on one image from camera 1 can now be calculated as

$$\frac{C(i,j,t)}{C_0} = \frac{\theta_r}{\theta(t)} \frac{I_{cam1}(i,j,t)}{I_{cam1}(i,j,t=0)} . \quad (2)$$

The use of the reference parameter $\theta_r/\theta(t)$ provides a correction for fluctuations in pulse energy and also for a possible aging of the flourescent dye, as described by Arcoumanis *et al.* (1990). Before the flow was initiated 10 calibration images were aquired on each of the two cameras. The ensemble average of images from camera 1 gave the distribution of $C_0(i,j)$ i.e. the calibration image and θ_r was inferred from 250×250 pixels on the ensemble average from camera 2.

PLIF measurements were conducted in the same 7 vertical planes as the PIV measurements and, in each plane, acquisition of 10 images on both cameras took place at each of seven time delays after start of the experiment, marked by switching on the pumps, t=5,10,20,40,60,90 and 120 minutes. After having deduced $\theta(t)$ from the coincident camera 2 image the instataneous concentration distribution C/C_0 from each image were calculated according to (2).

3. DIFFUSION MODEL

Defining the spatial average, $< \phi >= \int_0^{L_z} \int_0^{L_y} \phi dxdy$, the instantaneous flux through a horizontal plane xy is modeled by gradient diffusion as

$$J_c = \langle wc \rangle = -D_e \frac{d\langle c \rangle}{dz} . \quad (3)$$

For turbulent transport the quantity $< wc >$ can only be deduced from data of coincident concentration and velocity mesurements, as done by Atmane and George (1997). They investigated a similar flow field but at a significantly higher Reynolds number, $Re > 3500$, and they state that the vertical mass transport was mainly due to turbulent fluctuations and not due to mean fields. Since presently $Re = 40$, it is assumed that the vertical mass transfer is dominated by the mean fields and a conservative estimate of $D_e(z)$ can be calculated.

Since the velocity field does not depend on the concentration field, then at any vertical plane within the unit cell region studied there will be a constant mean field of flow. This follows from the fact that there is a steady mean flow from sources to sinks. However, experimental results show that both velocity and concentration fields vary in time in a random manner in time at any location. Here, concentration fluctuations are a result of velocity fluctuation.

It is the conjecture - in view of the observed spatial and temporal variations - that the time-dependent process of concentration depletion may be viewed as a stochastic process when considering a full unit cell. Hence, the process may be treated by the concepts and tools used for turbulent transport. Thus, velocity and concentration at any point is expressed as $W = \overline{W} + w$ and $C = \overline{C} + c$, where $\overline{W}$ and $\overline{C}$ denotes the ensemble average at the point.

Specifically, we may attempt to model the mass transport by (3), involving an effective average diffusivity defined by

$$D_e = -\langle \overline{WC} \rangle / \frac{\partial \langle \overline{C} \rangle}{\partial z}, \quad (4)$$

hence the net flux is to be understood as contributions from both steady and fluctuating fields.

In any horizontal plane covering many unit cells the mean flow in the vertical direction is zero. Hence, a phenomenological continuum model for the vertical mass transport should involve no convective transport on the average, but only diffusive terms. These include 'turbulent' transport in the above sense and molecular transport, where the latter is negligible.

Decomposing the flux terms in (4) gives

$$-\langle \overline{WC} \rangle = -\langle \overline{W}\ \overline{C} \rangle - \langle \overline{wc} \rangle. \quad (5)$$

Here the last term, requiring simultaneous velocity and concentration measurements, has not been measured. However, an upper limit for its magnitude can be estimated from

$$-\langle \overline{wc} \rangle < -\langle w_{rms} c_{rms} \rangle. \quad (6)$$

Experiments have shown that - in a given plane involving spatial averages along horizontal lines - the last term on the right of (5) is non-zero, but much smaller than the first term, hence may be neglected. Then (4) becomes

$$D_e = -\langle \overline{W}\ \overline{C} \rangle / \frac{\partial \langle \overline{C} \rangle}{\partial z}, \quad (7)$$

which can be computed from the experimental results.

4. RESULTS

Concentration and velocity fields at each of 7 planes were recorded in different experiments owing to instrument limitations. After pumps were

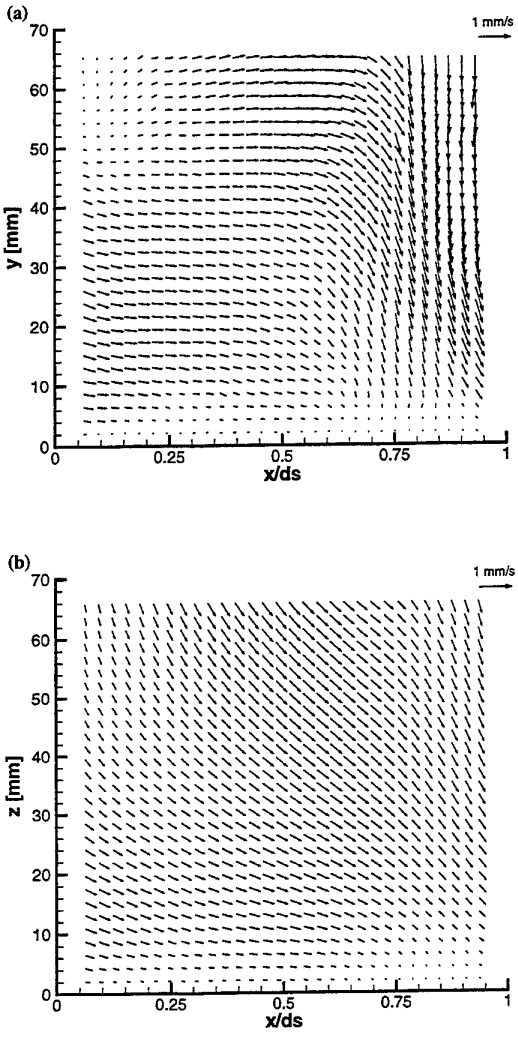


Figure 2: Velocities measured in plane 4 ($y/\Delta s = 0.50$). *(a)* Instantaneous velocity field. *(b)* Ensemble average of 50 instantaneous measurements.

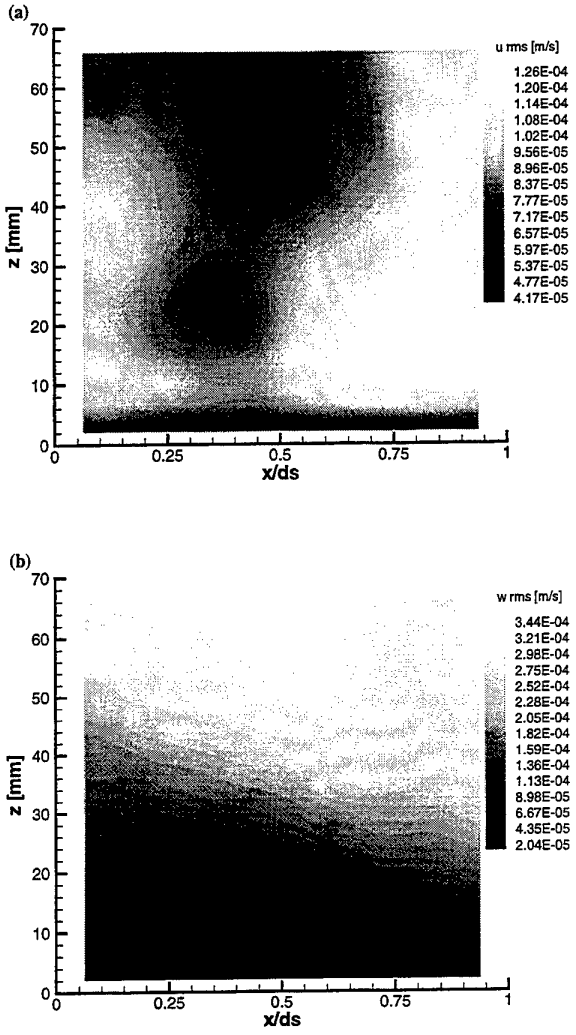


Figure 3: Rms values of fluctuating velocity components measured in plane 4 ($y/\Delta s = 0.50$). *(a)* u_{rms}. *(b)* w_{rms}.

switched on the characteritic random flow structure was established within a few minutes, although transport times from inlet to outlet could be as high as 8-9 min.

Visual observations showed that after 5-10 min a rather sharp horizontal boundary emerged in the PLIF study, about 105-115 mm above the bottom. Above this boundary, the concentration of tracer remained virtually unchanged. Below the boundary the concentration gradually became uniformly lighter as time progressed. Apparently, mixing was relatively uniform and high up to a certain vertical penetration. Typical transient boundary layer penetration of depletion was only visible during the first about 40 min. In this regard the results resembled more those from the laboratory experiments (Riisgaard *et al.*, 1996a) on *Ciona intestinalis* populations than those of *Nereis diversicolor* populations.

4.1 Velocity fields

Fig. 2a shows an instantaneous velocity field acquired in plane 4 which is the plane in the mid-

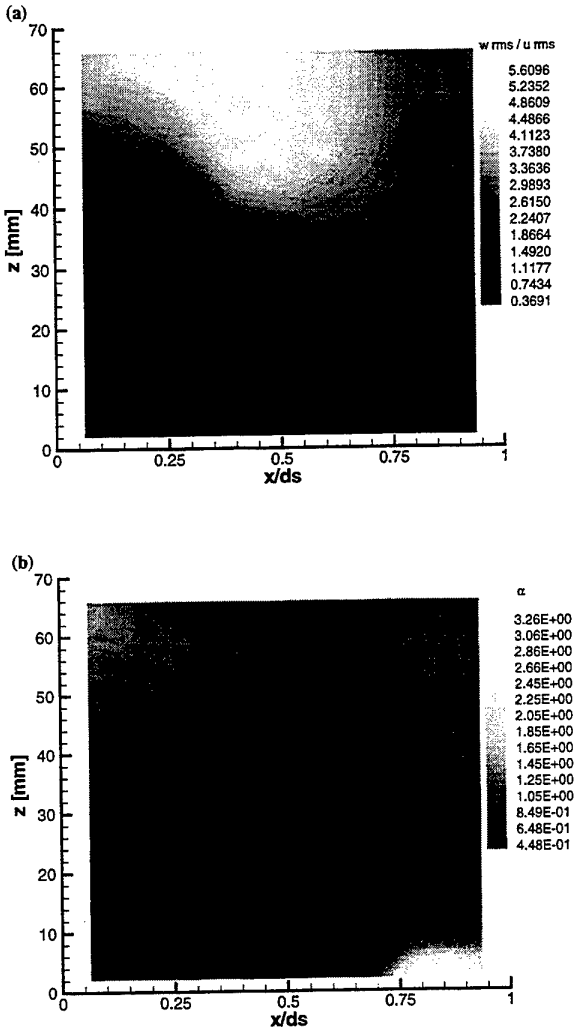


Figure 4: *(a)* Degree of anisotropy w_{rms}/u_{rms} in plane 4 ($y/\Delta s = 0.50$). *(b)* Agitation level in plane 4 ($y/\Delta s = 0.50$) computed from (1).



Figure 5: Single, instantaneous image (*upper*) and ensemble average of 10 images (*lower*) from PLIF recording in plane 4 ($y/\Delta s = 0.50$) at time $\Delta t = 20$ min.

dle between the inlet and outlet. Considering only the vertical velocity, a current towards the bottom seems to be dominating and keeping in mind the relatively high inlet velocities this seems plausible since conservation of mass requires $\langle W \rangle$ to be zero. The ensemble average field computed in plane 4 is shown in Fig. 2b. Comparing the ensemble velocity field to the instantaneous field reveals remarkable differences in the flow pattern although it is obvious that the down current is persistent. Evidently the flow can not be characterized as stationary and since no periodicity has been observed the flow is moreover chaotic.

The rms-values u_{rms} of horizontal velocity are depicted in the contour plot Fig. 3a. Close to the bottom fluctuations are damped by the wall but about 6-8 mm above the bottom the values increase significantly and larger values appear particularly in the region of strong down flow.

As expected, the damping effect of the bottom is stronger for the vertical velocity fluctuations w_{rms} shown in Fig. 3b. Values continues to increase in a regular manner with increasing height above the

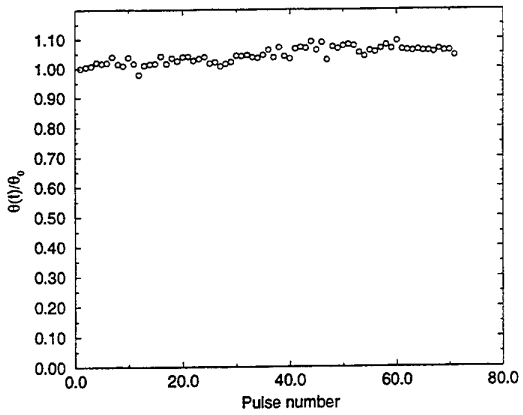


Figure 6: Reference parameter $\theta(t)/\theta_r$ from acquisition in plane 2.

bottom. The somewhat higher values of w_{rms}, as compared to u_{rms}, is not surprising since agitation is a result of vertical sources of momentum.

Fig. 4 shows the ratio w_{rms}/u_{rms} which expresses the degree of anisotropy. Throughout the domain the vertical fluctuations of are higher than the horizontal ones, except for a narrow region in the vicinity of the bottom. The high degree of anisotropy (with values approaching 6) is a result of energy being supplied to the vertical component and it is responsible for the strong vertical mixing.

Finally, the velocity field may be characterized by the agitation level α, defined by (1) (a two component turbulence intensity) shown in Fig. 4b. Except for the high values of α seen in the lower right corner (probably due to very low mean velocities) α values are of the order of unity. Hence, the fluctuating components of velocities are comparable to mean values. Again this suggest that the flow has a chaotic character.

4.2 Concentration fields

Fig. 5 for plane 4 at time $\Delta t = 20$ min. shows a single image and the ensemble average of 10 images, respectively. Time between individual images in the ensemble was $\approx$ 5sec. Visually, images were largely statistically independent, yet from Fig. 5 some correlation is visible.

Fig. 6 shows a typical series of intensity measurements from the reference solution used to normalize each PLIF image. The signal proved to increase slightly with time as the pulsed laser heated

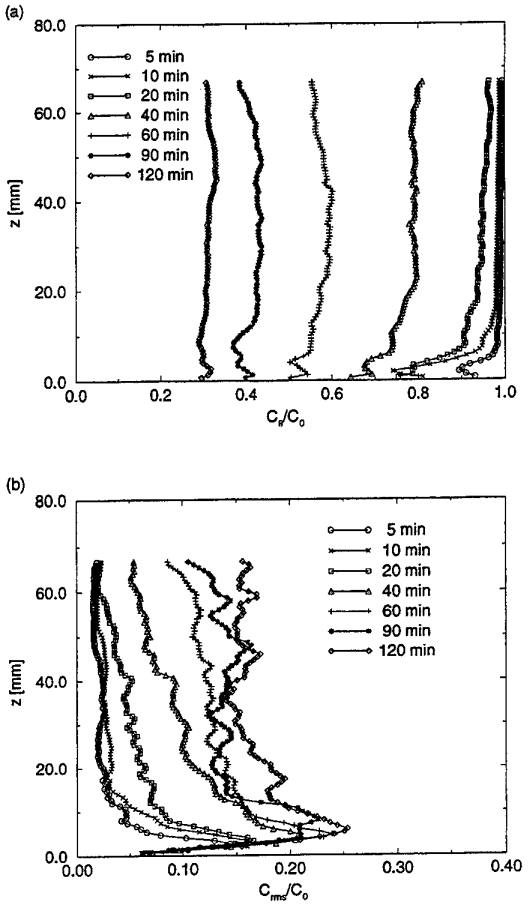


Figure 7: Mean and rms profiles derived from ensembles of PLIF images from all planes at a given time delay Δt. Each point is an average of 10 horizontal pixel-planes. *(a)* Mean concentration profiles $\langle C/C_0 \rangle$ at 7 investigated time delays. *(b)* Rms profiles of the concentration fluctuations $c_rms/\langle C/C_0 \rangle$ at 7 investigated time delays. .

up. The random fluctuations in intensity about the mean could suggest the level of experimental uncertaincy on concentrations to be about $\pm 5\%$.

Fig. 7a shows overall characteristics of the concentration field in terms of vertical distributions of ensemble averages of all planes along horizontal lines of the 7 times recorded. Results from each plane has been given the same weight. The distributions of mean concentration show typical transient boundary layer penetration of depletion at the bottom only during the first about 40 min. Later, distributions are almost uniform while decreasing with time, suggesting a uniform and high level of agitation. These

levels appear to be nearly uniform above z = 10-20 mm and decreasing with time, in agreement with the visual observations that showed mixing to be relatively uniform and high up to a vertical penetration of about z_1 = 105-115 mm.

Assuming the existence of a fluctuating velocity field, an increase in rms-concentration requires that depletion occurs. This is evident from Fig. 7b showing $c_{rms}/\langle C/C_0\rangle$ versus vertical height. At small times, there is essentially no depletion above about z = 10 mm where $c_{rms}/\langle C/C_0\rangle$ shows consistent low values, most likely representing the noise level of about 2-3 %. As time proceeds, Fig. 7b shows the build up of nearly uniform and high levels (about 15%) of $c_{rms}/\langle C/C_0\rangle$.

4.3 Downward flux

Fig. 8 shows how the flux $\langle \overline{W}\ \overline{C}\rangle$ varies with height above the bottom at 4 times for the representative plane 4 which excludes inlets and outlets. Being only a single plane in the unit cell, clearly the variation with height includes contributions to mass transfer in and out of the plane associated with redestribution in horizontal planes. As a main feature, the magnitude of the flux decreases with time. In this plane the flux also appears to approach zero at the wall. Other planes not containing the inlet show similar trends of downward fluxes, while plane 6 containing the inlet shows high upward fluxes.

To estimate the net flux, reconsider Fig. 7a showing average concentration distributions for the unit cell. Aside from some features of conventional boundary layer penetration near the bottom at small times the main feature is the consistent decrease of a nearly uniform plateau of concentration extending over the full height investigated by PLIF. As observed visually and recorded at the time of the experiments, the plateau in fact extended to a height of about z_1 = 110 mm, above which there was no reduction in concentration. This behavior is similar to that observed for *Ciona intestinalis* and analyzed by a simple lumped formulation (Larsen and Riisgaard, 1997). The behavior implies that there existed a fairly uniform and high level of mixing in this region, that the layer did not receive any flux from above, but was drained from the bottom with a certain net flux. Denoting this flux by F_w, the mean concentration in the well mixed layer of height z_1 by C_1, a simple lumped conservation analysis for the layer gives

$$d(C_1 z_1)/dt + F_w C_1 = 0\,, \qquad (8)$$

subject to $C_1(0) = C_0$. The exponential solution

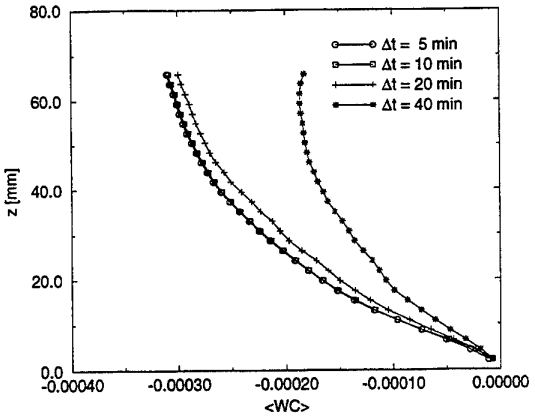


Figure 8: Vertical flux $\langle \overline{W}\ \overline{C}\rangle$ in plane 4 at time delays Δt = 5, 10, 20 and 40 min.

is characterized by the time constant z_1/F_w, from which the flux may be estimated. Following the initial phase of the transient, data from Fig. 7 show exponential decay of C_1 and we find the estimate $F_w \approx 20\times10^{-6}\ m/s$. This value is of the same order of magnitude as the flux computed near the bottom in plane 4. The higher values further up are associated with redistribution.

Now, using the above value of F_w and distributions of mean concentration at small times the effective diffusivity has been estimated to be of the order $D_e \approx 10^{-6}\ m^2/s$, which is comparable to the value $0.3 \times 10^{-6}\ m^2/s$ found by Larsen and Riisgaard (1997) for *Nereis intestinalis*. However, the present result is associated with considerable uncertainty.

5. CONCLUSIONS

The present study has provided detailed data on distributions of mean and fluctuating velocity and concentration during a transient process of concentration depletion in a model of a biomixing process. The data were collected by PIV and PLIF at 7 planes covering af unit cell in an array of such cells, which represent filter-feeders burried below the bottom.

The data show the process to have unsteady features that when considered over time and space for a unit cell suggest chaotic behavior such that the process could be studied by use of statistical tools and concepts that are used for turbulence. It is shown

that the net mass transfer can be attributed primarily to mean fields, and the resulting downwards flux can thus be computed even though velocity and concentration fields were measured separately. In addition to calculating fluxes, the data have been analyzed to give an estimate of an effective diffusivity on the assumption that the process could be modeled by gradient diffusion. The observed high and uniform levels of agitation, being limited to a certain height above the bottom, leads to a layer of finite thickness in which the nearly uniform mean concentration decreased exponentially with time.

ACKNOWLEDGEMENTS

The study was partially supported by 'Civilingeniør Kristian Rasmussen og hustru Gunild Katrine Rasmussens Fond' and the Danish Technical Research Council under grant STVF 5.26.16.31.

REFERENCES

Arcoumanis, C., McGuirk, J. J., and Palma, J. M. L. M. (1990). On the use of flourescent dyes for concentration measurements in water flows. *Exp. in Fluids*, **10**, 177–180.

Atmane, M. A. and George, J. (1997). Energetic and Scalar Measurements Beneath a Shear-Free Interface. In K. Hanjalic and T. W. J. Peeters, editors, *2nd Int. Symposium on Turbulence, Heat and Mass Transfer*. Delft University Press.

Keane, R. D. and Adrian, R. J. (1990). Optimization of particle image velocimeters. Part I: Double pulsed systems. *Meas. Sci. Technol.*, pages 1202–1215.

Larsen, P. S. and Riisgaard, H. U. (1997). Biomixing generated by benthic filter feeders: a diffusion model for near-bottom phytoplankton depletion. *J. Sea Res.*, **37**, 81–90.

O'Riordan, C. A., Monismith, S. G., and Koseff, J. R. (1993). A study of concentration boundary-layer formation over a bed of model bivalves. *Limnol. Oceanogr.*, **38**, 1712–1729.

Riisgaard, H. U., Jørgensen, C., and Clausen, T. (1996a). Filter-feeding ascidians (Ciona intestinalis) in a shallow cove: implications of hydrodynamics for grazing impact. *J. Sea. Res.*, **35**, 293–300.

Riisgaard, H. U., Poulsen, L., and Larsen, P. S. (1996b). Phytoplankton reduction in near-bottom water caused by filter-feeding Neries Diversicolor - implications for worm growth and population impact. *Mar. Ecol. Prog. Ser.*, **141**, 47–54.

SESSION 18

2-PHASE FLOWS
INSTRUMENTATION 3

PLANAR PARTICLE IMAGE ANALYZER

Cecil F. Hess
MetroLaser, Inc.

ABSTRACT

A technique that is capable of simultaneously sizing multiple transparent droplets on a plane from scattered light features that are independent of laser beam intensity and obscuration is presented. Light scattered by reflection and refraction from droplets immersed in a laser sheet is recorded either holographically or photographically. The holographic recording requires the addition of a reference beam. Each droplet image is characterized by either a unique set of fringes or by two spots. Both the number of fringes in each image and the separation between the refraction and reflection spots yield particle size information. The holographic recording allows image reconstruction and analysis anywhere; from the particle image to the far field. This added flexibility can be valuable in the measurement of dense sprays since interference of far field features from multiple particles can be avoided. The principles and operating envelope of the technique are discussed in this paper and experimental data for droplets between about 2 and 150 μm are discussed. The technique showed good accuracy when measuring known size droplets produced by a monodisperse droplet generator. Measurements made on droplets produced by an ultrasonic humidifier yielded a reasonable size distribution. Modeling showed that the technique is capable of measuring droplets of 1 μm in diameter and larger and particle concentrations in excess of $10^5/cm^3$.

1.0 INTRODUCTION

Global measurements of a spray would provide needed information of spray structure, spatial distribution of droplet diameter and mass concentration, and large scale variations that cannot be measured with existing point measurement techniques. This measurement capability will augment current point measurement techniques in the same way that Particle Image Velocimetry (PIV) augments the capability of laser Doppler velocimetry (LDV). That is, the technique represents a logical evolution of two-phase flow diagnostics. Previous attempts to measure particle size on a plane have had marginal success due to the non-uniformity of the laser sheet intensity (typically Gaussian), the oscillating nature of the scattered light intensity (Mie scattering), and signal obscuration due to particles along the beam and signal trajectories. Planar Particle Image Analysis (PPIA) overcomes these problems by imaging intensity-independent features of the scattered light from which the particle size may be obtained. PPIA uses a pulsed laser sheet to illuminate the particles and a recording medium to collect the scattered light. This technique was originally developed by Glover et al (1995), who analyzed the far field features of the scattered light and applied it to the measurement of sparse sprays. We show in this paper that measurements of the near field features of the scattered light can also yield particle size information, thus extending the technique to the measurement of denser sprays. König et al (1986), presented a related fringe measurement strategy and discussed its inherent high accuracy. They focused a laser beam to illuminate single droplets and measured the resulting fringe pattern in the very far field. Their technique has been successfully used to measure evaporation of monodisperse droplets. The PPIA technique may, in principle, be extended to measure droplet size and velocity by double-pulsing the laser. In this paper we emphasize the sizing features of the technique.

2.0 PRINCIPLES OF THE PPIA TECHNIQUE

Following the discussion about large particles (large relative to the illumination wavelength) presented in van de Hulst (1981), a non-opaque particle will refract (p=1) and reflect (p=0) light. At off-axis angles both the refracted and reflected components of the scattered light appear to emanate from small spots (small relative to the particle size). In PPIA the angle of collection, θ, is judiciously chosen to balance the intensity of the refracted and reflected spots to maximize fringe contrast and optimize the resolution of the two spots. Two measurement strategies are presented: 1) the two-spot, and 2) the fringe mode. The two-spot strategy requires analyzing the scattered light in the immediate vicinity of the particle while the fringe mode requires allowing the interference between the refracted and reflected components of the scattered light. Both of these strategies can be implemented with a single hologram since the hologram records amplitude and phase information that would subsequently permit the

reconstruction of the scattered light features anywhere from the particle image to the far field. In contrast, the photographic recording can only be made one plane at the time.

Figure 1 illustrates the geometry of PPIA. A pulsed laser beam formed into a sheet illuminates a particle field and imaging optics placed at the collection angle θ image the scattered light onto film or a detector array. A reference beam is added to yield a holographic recording. A possible implementation of this technique is digital recording and numerical reconstruction as discussed by Schnars et al (1996). The numerical holography method offers the potential of fast data recording and reconstruction but it imposes limitations due to the coarse resolution of CCD detectors (i.e., 100 lines/mm).

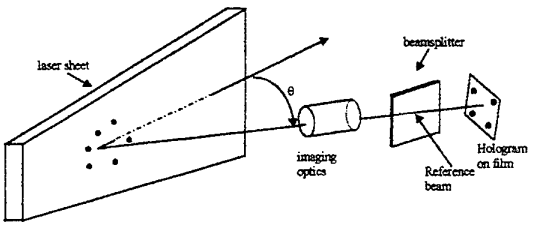


Figure 1. Geometry of PPIA system

Figure 2 shows a spherical particle that bends the light by refraction and reflection. The reflection emanates from the spot L which lies at an angle τ_L from the horizontal while the refraction emanates from the exit refraction spot R_E which lies at an angle $-\tau_1$ from the vertical.

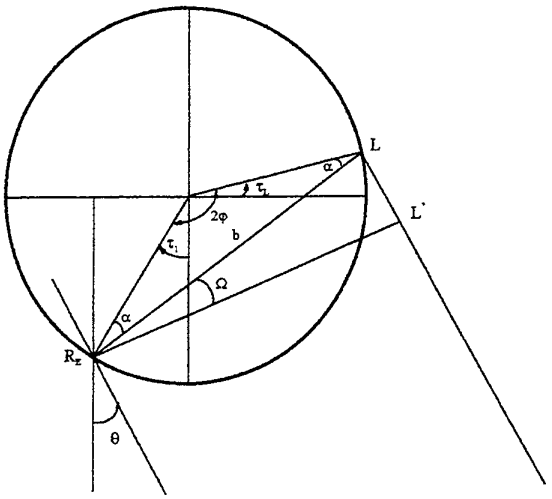


Figure 2. Particle scattering refracted and reflected light into angle θ.

τ_L is the input angle of reflection that causes the incident light to be deflected by an angle θ (defined as collection angle). It is given by:

$$\tau_L = \frac{\theta}{2}, \tag{1}$$

while τ_1 is given by:

$$\tau_1 = \frac{\pi}{2} - \theta - \tau_R, \tag{2}$$

where τ_R is the input angle of refraction that causes the incident light to be deflected by an angle θ. It can be calculated from the following implicit relationship:

$$\tau_R = \cos^{-1}\left(\frac{n_1 \cos\tau_R}{n_2}\right) - \frac{\theta}{2}, \tag{3}$$

where $0 \le \theta \le \pi$, n_1 is the index of refraction of the medium and n_2 is the index of refraction of the particle.

The spacing between the exit refraction and reflection spots is given by:

$$R_E L = d \sin\varphi, \tag{4}$$

where d is the particle diameter and φ is given by:

$$\varphi = \tfrac{1}{2}[\pi - \theta - \tau_R + \tau_L]. \tag{5}$$

The projected spacing between R_E and L in the θ direction is given by:

$$R_E L' = R_E L \cos\Omega, \tag{6}$$

$$\text{where } \Omega = \tfrac{1}{2}[\tau_R + \tau_L - \theta]. \tag{7}$$

The fringe angle resulting from the interference between light emanating from L and R_E in the θ direction is given approximately by:

$$\sin\delta^\circ = \frac{\lambda}{R_E L'}. \tag{8}$$

Figure 2 shows the relevant reflection and refraction rays and the various angles and other parameters needed to derive the equations above. Additional details are given in Hess and Wood (1994).

The fringe angle computed by Eqn. 8 was compared to the result of a full Mie scattering computation for various size water droplets at an angle $\theta = 58°$. These results are shown in Table 1.

Table 1. Fringe angle computed by Eqn. 8 and by Mie scattering computer program.

$\theta = 58°$	$\theta = 58°$	$\theta = 58°$	$\theta = 58°$
$n_1 = 1$	$n_1 = 1$	$n_1 = 1$	$n_1 = 1$
$n_2 = 1.33$	$n_2 = 1.33$	$n_2 = 1.33$	$n_2 = 1.33$
$\lambda = 0.5145$ μm	$\lambda = 0.5145$ μm	$\lambda = 0.5145$ μm	$\lambda = 0.5145$ μm
d = 82 μm	d = 10 μm	d = 5 μm	d = 2 μm
$\delta°$(Eq. 2) = 0.39°	**$\delta°$(Eq. 2) = 3.2°**	**$\delta°$(Eq. 2) = 6.4°**	**$\delta°$(Eq. 2) = 16.2°**
$\delta°$(Mie) = 0.378°	**$\delta°$(Mie) = 3.175°**	**$\delta°$(Mie) = 6.3°**	**$\delta°$(Mie) = 16.8°**

Figure 3 shows some of the selected Mie scattering computations used in Table 1.

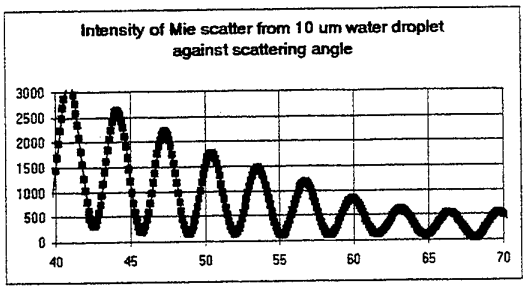


Figure 3. Selected Mie scattering computations.

Note the excellent behavior of the signal and the high contrast afforded by the S polarization intensity. In contrast, the signal in the vicinity of the rainbow is characterized by a more complicated structure although useful size and velocity information has been obtained by van Beeck et al (1996).

Assuming a constant fringe angle between the particle image and the far field, the fringe spacing at any position Z is the product of the fringe angle ($\delta°$) times the distance between the analysis plane and the image plane accounting for magnification ($S_2 - Z$). The diameter of the scattered image at the analysis plane (D) should be smaller than the spacing between particle images to avoid confusion due to multiple particles. Referring to Figure 4 where the analysis plane is positioned at Z from the collecting lens with diameter D_L, the following formulae apply:

$$D = \frac{D_L(S_2 - Z)}{S_2} = \frac{S_2 - Z}{Mag\, f\#}, \qquad (9)$$

where Mag = $\frac{S_2}{S_1}$ is the magnification and $f\# = \frac{S_1}{D_L}$. The fringe spacing on the analysis plane is:

$$\delta = (S_2 - Z)\tan\delta_2^\circ, \qquad (10)$$

where $$\tan\delta_2^\circ = \frac{S_1}{S_2}\tan\delta_1^\circ . \qquad (11)$$

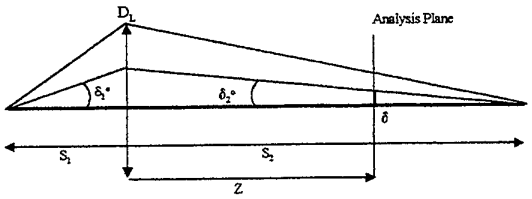


Figure 4. Schematic of imaging system for PPIA

The fringe spacing given by Eqn. 10 may be rewritten as:

$$\delta = \frac{(S_2 - Z)\lambda}{(R_E L')Mag}. \qquad (12)$$

Alternatively,

$$\delta = \frac{S_1}{D_L} D \tan\delta_1^\circ. \qquad (13)$$

The number of fringes on the analysis plane is:

$$\#\text{fringes} = \frac{D}{\delta} = \frac{D_L}{S_1 \tan\delta_1^\circ} = \frac{D_L R_E L'}{S_1 \lambda} = \frac{R_E L'}{f\#\lambda}. \qquad (14)$$

Note that the number of fringes anywhere in the reconstruction is only function of the receiver f-number (f#) and the fringe angle, δ_1° from which the droplet size is obtained.

By way of example, for a collection angle $\theta = 68°$ and an index of refraction $n_2 = 1.33$ the refraction and reflection spots have nearly the same intensity.

For these conditions $\tau_R = 7.86°$ and $R_E L' = 0.91$ d. Therefore from Eqn. 14,

$$\#\text{ fringes} = \frac{R_E L'}{f\#\lambda} = \frac{0.91d}{f\#\lambda}. \qquad (15)$$

For example, if we use a f/2 collection system, magnification of 2.5, illumination wavelength $\lambda = 0.5$ μm, and reconstruct the image at 1 mm from the image point, that is $S_2 - Z_{film} = 1$ mm, we can create the following table for different size particles:

Table 2. Number of fringes as a function of particle diameter.

d (μm)	1	3	10	30	100
$R_E L'$ (μm)	.91	2.73	9.1	27.3	91
δ (μm) Eq. 12	220	73	22	7.3	2.2
#fringes Eq. 14	0.9	2.7	9.1	27.3	91

The scattered light image on the analysis plane (D) will have a diameter of about 200 μm in all of the above cases (see Eqn. 9). In terms of particle number density this is close to assuming that the distance between particles at the image plane could be about 200 μm. Since the magnification of the above example is 2.5, this corresponds to an average particle separation of about 80 μm. If we further assume that the laser sheet thickness is 200 μm, the corresponding particle number density referenced to the object plane could be higher than $10^5/cm^3$.

The minimum particle size that can be measured with the fringe mode could be established if we require collecting at least one fringe. Thus, from Eqn. 15,

$$d_{min} = \frac{f\#\lambda}{0.91} = 1.1 f\#\lambda .$$

3.0 EXPERIMENTAL VERIFICATION.

Experiments were conducted using photography and holography. Monodisperse droplets produced by a Berglund-Liu generator and a mist of droplets produced by an ultrasonic humidifier were measured with PPIA. The photographs were obtained with a pulsed YAG laser operating at 532 nm, sheet forming optics, a camera with a near f/2 collection lens, 4 x 5 inch Polaroid film, film holder and a device to position and angle the film. The holograms were obtained with a dye laser operating at 589 nm, Agfa film 8E75 placed at 45 degrees to the object and reference beams and an f/2 receiving lens. Both the holographic and photographic data showed various imaging regimes from which particle size information can be derived. The data presented in this paper is all photographic.

The collection angle was varied between 50 and 70 degrees with most of the data collected at 68° where the brightness of the refraction and reflection spots is balanced for water droplets. Image magnification varied at 8.9, 11, and 11.6 and the film was perpendicular to the receiving optical axis, yielding images of various sizes and complexity depending on the position of the particle on the laser sheet. Another set of experiments was conducted with a magnification of 2.5 and the film oriented at 45° to the receiving optical axis in order to yield images of almost uniform magnification across the entire film.

Four imaging regimes of the scattered light are discussed and illustrated with experimental data below.

1. **Focused image.** Here two well-defined spots whose separation is a function of droplet size and magnification characterize the droplet.
2. **Near field.** Here the droplet is characterized by the two spots and curved fringes around them. Both the separation between spots and the number of fringes yield droplet size.
3. **Middle field.** Here the droplet is characterized by a set of fringes with a small curvature. The number of fringes contained in each image field is a function of droplet size.
4. **Far field.** Here the droplet is characterized by a set of reasonably straight fringes whose pitch may change across the scattered image. The number of fringes contained in each image field is a function of droplet size.

In terms of complexity the first and fourth imaging regimes are the simplest to analyze, the third requires more advanced image processing, and the second is the most complex.

3.1 Focused Image Regime

Figure 5 shows a string of monodisperse droplets produced by a Berglund-Liu generator. The Berglund-Liu generator was operated with a pinhole of 50 μm. The flow rate was 1 ml/min and the frequency was around 10 kHz (Note: the precise frequency was not recorded for this case, instead the operator was shopping for a stable frequency in the vicinity of 10 kHz). These conditions yielded monodisperse droplets of about 147 μm in diameter. The receiving collection angle was 59°. The film was placed near the image plane of the laser sheet so that each droplet clearly shows a pair of spots; the refraction and reflection spots. The magnification for this set of data was 8.9. After accounting for magnification the spot separation R_EL' was 135 μm. The diameter of 145 μm is obtained by dividing the spot separation by 0.93. Note that the two spots are aligned on a slightly slanted trajectory. This is the trajectory of the laser sheet.

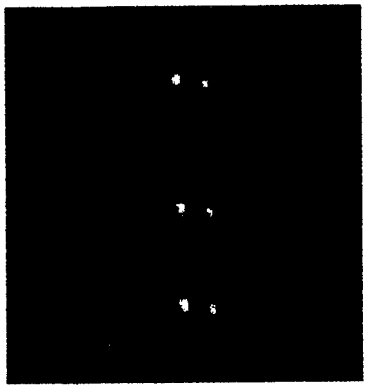


Figure 5. String of monodisperse droplets showing the refraction and reflection spots.

3.2 Far field imaging regime

Here the collection angle was changed to 68° to optimize fringe contrast, the magnification was 11.6, and the Berglund-Liu generator was configured to produce smaller droplets. Figure 6 shows a string of monodisperse droplets produced by the Berglund-Liu generator. The Berglund-Liu generator was operated with a pinhole of 25 μm, the flow rate was 0.2 cc/min, and the frequency was 25 kHz. These conditions yielded monodisperse droplets of 63 μm in diameter. The film in this case was placed away from the image plane to allow the refraction and reflection light to interfere. Each droplet is clearly defined by a set of 55 reasonably straight fringes. Referring to Eqn. 15, for a receiver f# = 1.97, a collection angle θ= 68, and wavelength λ = 0.532, *d = 1.15 x number of fringes.* This yields d = 63 microns. This measured diameter agrees very well with the generated droplet size.

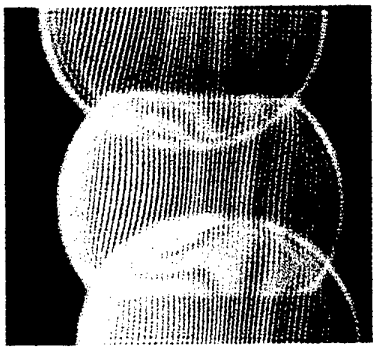


Figure 6. String of monodisperse droplets characterized by a set of interference fringes.

3.3 Near field imaging regime.

The droplets whose scattering signatures are shown in Figure 7 were generated with an ultrasonic humidifier. The magnification measured at the image point (S_2/S_1, see Figure 4) was about 11. The image point lies on the receiver optical axis. The film was perpendicular to the receiver optical axis. The film was first positioned so that the image point fell on the center of the film. The film was then moved away from this central position to allow the interference between refracted and reflected light. Since the laser sheet is 68° to the receiver axis, the film will record across its length light corresponding to drops that are nearly in focus as well as drops that are out of focus.

Note that many of the images obtained at this *near field* condition show rounded fringes emanating from two spots. We attempted to measure the droplet diameter from both the spot separation and the number of fringes on each image. Referring to Eqn. 15, $d = R_EL'/0.91$ and d = 1.15 x #fringes.

We measured the spot separation with a 10X eyepiece and a reticule. This method limited the measurement to spot separations on the order of 100 microns with an error of about 25 microns. Table 3 shows typical measurements made on images of Figure 7.

Table 3. Particle diameter measured from the spot separation and the number of fringes.

R_EL' = Spot separation/11	d = R_EL'/0.91	#fringes	d = 1.15 x #fringes
8	8.8 μm	8	9.2 μm
11	12 μm	12	13.8 μm

The agreement in the diameter measured by the two methods is within the experimental error associated with measuring the spot separation with the eyepiece. Furthermore, a diameter around 12 to 14 microns is representative of the largest particles produced by an ultrasonic humidifier.

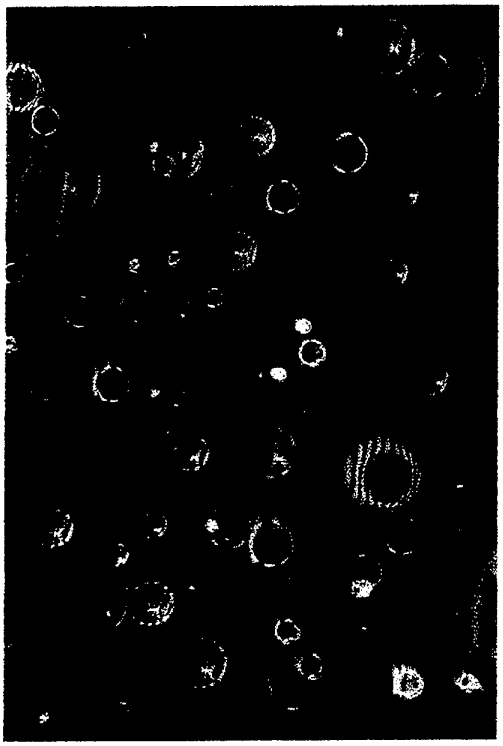


Figure 7. Near field images of droplets produced by an ultrasonic humidifier.

3.4 Middle field imaging regime

The magnification for this set of experiments was changed to 2.5 and the film was tilted by 45° to the receiver optical axis so that every point on the laser sheet had a corresponding focused image on the film when the film was placed at the focal point. The film was moved away from the focal point by a few millimeters to record the interference of the refracted and reflected scattered light. The images are oval in shape with dimensions of about 1200 μm x 1700 μm. To avoid particle overlap at this condition, the maximum number density is about $5x10^3/cm^3$ which is rather small. It was, however, a very convenient recording condition that lent itself well to image analysis with a simple eyepiece. Note that this is the same general condition run by Glover et al (1995), that led them to conclude that the technique is useful in the measurement of sparse sprays. Figure 8 shows some of the data corresponding to this set of experiments. An ultrasonic humidifier generated the droplets. The number of fringes in each individual image varied between 2 and 12, corresponding to diameters between 2 μm and 14 μm. Note that the images with more fringes tend to be brighter as one might expect from larger particles; however, one can find images with the same number of fringes (i.e., same diameter) and different brightness which is the result of intensity variation (Gaussian) across the laser sheet.

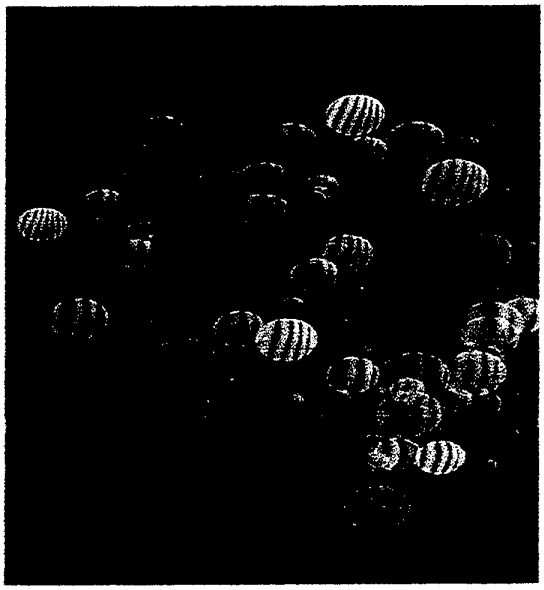


Figure 8. Middle field images of droplets produced by an ultrasonic humidifier.

4.0 OBSERVATIONS REGARDING PARTICLE NUMBER DENSITY.

For the small droplets produced by the ultrasonic humidifier, the smallest images corresponding to the "middle field imaging regime" were about 500 x 700 μm which are equivalent to objects of 200 x 350 μm. The maximum number density for these images is about 2.3 x $10^5/cm^3$. Considerably more research is necessary to establish minimum image dimensions as a

function of particle size for the different imaging regimes. Smaller images with concomitant larger number densities are obtained in the "near field regime". Unfortunately, data analysis for this condition is far more complex due to the shape of the fringes. The smallest image and associated largest number density can be obtained in the "focused image regime" where the analysis is rather simple; measure spot pairs. Photographic recording of the two-spot droplet image requires very high film resolution and/or magnification. Holographic recordings could be effected at virtually any distance from the focused image and reconstructed at virtually any other distance, thus tailoring the measurements to the particular spray number density.

5.0 SUMMARY AND CONCLUSIONS

This paper discusses a technique, PPIA, which is capable of measuring the size of droplets on a plane from scattered light features that are independent of laser beam intensity and obscuration. The light scattered from droplets immersed in a laser sheet can be recorded either holographically or photographically. Each droplet image is characterized by a set of fringes and/or by two spots. The number of fringes in each image or the separation between the two spots yields particle size. Droplets from about 2 to 150 μm in diameter were measured with PPIA. The smallest droplet that can be measured with PPIA was estimated to be about 1 μm while the largest has no clear limit. The technique showed remarkable accuracy when measuring known size droplets produced by a monodisperse droplet generator. Measurements made on droplets produced by an ultrasonic humidifier yielded a reasonable size distribution although an independent measurement was not made.

5.0 ACKNOWLEDGMENTS

The author wishes to acknowledge the skillful experimental work performed by Robert Nichols who built the experimental breadboard and recorded the data. Dr. Stefan Martin performed the Mie scattering computations shown on this paper.

5.0 REFERENCES:

Glover, A.R., Skippon, S.M., and Boyle, R.D., 1995, Interferometric laser imaging for droplet sizing: a method for droplet-size measurement in sparse spray systems, Applied Optics, Vol. 34, No. 36, pp. 8409-8421.

Hess, C.F. and Wood, C.P. 1994, The Pulse Displacement Technique-A Single Particle Counter With A Size Range Larger Than 1000:1, Part Syst Charact, 11, pp. 107-113.

König, G., Anders, K., and Frohn, A. 1986, A new light-scattering technique to measure the diameter of periodically generated moving droplets, J. Aerosol Sci., Vol. 17, No. 2, pp. 157-167.

Schnars, U., Kreis, T.M., Jüpner, W.P.O. 1996, Digital recording and numerical reconstruction of holograms: reduction of the spatial frequency spectrum, Optical Engineering, 35 (4) pp. 977-982.

van Beeck, J.P.A.J. and Riethmuller, M.L. 1996, A Single Beam Velocimeter Based On Rainbow-Interferometery, Paper Number 9.1.1, Eighth International Symposium On Applications Of Laser Techniques To Fluid Mechanics, July, 1996, Lisbon, Portugal.

van de Hulst, H.C. 1981, "Light Scattering By Small Particles", Chapter 12, Dover Publications, Inc. New York.

DROPLET SIZING BY INTERFEROMETRIC METHOD BASED ON MIE SCATTERING IN AN I.C. ENGINE.

O. Pajot and C. Mounaïm-Rousselle

Laboratoire de Mécanique et d'Energétique
E.S.E.M. / Université d'Orléans
45072 Orléans cédex 2, France

ABSTRACT

The global aim of this work is to estimate the fuel droplets diameter distribution in an Internal Combustion engine. The limited optical accesses have induced the application of a technique based on the Mie Scattering Interferometry (M.S.I.), obtained by defocusing collecting optics. The originality of this study is the development of this droplet sizing method by planar laser light scattering with a collecting angle range around 90°. In this paper, we firstly remind theoretical basements of the technique. After some practical details, the results obtained in the combustion chamber of the Spark Ignition engine, near the spark plug, prior to ignition and for different injections timing are shown and discussed.

It can be concluded that the implementation of the M.S.I. method in our experimental set-up has been realised successfully to provide droplets distribution in engine. To get an easier use of the technique, image processing software will be developed.

1. INTRODUCTION

To reduce Spark Ignition engine fuel consumption and pollutants emissions, one working mode can be the lean burn one. Unhappily, it induces more misfires. To inhibit this drawback, the air-fuel mixture must be carefully prepared around the spark plug. For a better understanding of the mixture preparation effect, it needs to provide experimental data. One way is to determine the influence of the fuel droplets presence inside the combustion chamber before the ignition. Indeed, it has been shown by Ballal and Lefebvre (1980), and, Singh and Polymeropoulos (1986), that the spark ignition of vapor fuel flow is sharply affected by the presence of fuel droplets. They have studied the ignition phenomena for different droplets diameters and different liquid/vapor fuel ratios. Moreover, this spark ignition affects strongly flame kernel initiation, propagation and finally pollutants formation. Therefore the knowledge of the droplets life near the spark plug and prior to ignition in engines is relevant.

To achieve experimental data, in engine environment, is relatively difficult and needs to choose the more appropriate technique. Firstly, the advantage of the optical diagnostics is evident due to the non-intrusivity but also because they provide spatial evolution of droplet distribution with good time resolution. In the other hand, in S.I. engines, the droplet population, spatially near the spark ignition does not form a dense core spray but sparse distribution one. In fact, this aspect is important due to the limited application of few techniques in dense liquid jets. The measurement based on scattered light from droplets in an incident laser beam are generally much faster and more convenient than the use of pure imaging techniques. Peters (1982) has firstly estimated droplets size distribution during intake and compression strokes with a technique based on light Mie scattering : to estimate droplet diameter, it needed to assume on numerical droplet density and

size range. Moreover, the analysis was not so evident due to some out-of-focus droplets. Kadota *et al.* (1990) have successfully shown the feasibility of local fuel droplet diameter measurements in engine by using laser Mie scattering. One HeNe laser beam was focused inside the chamber and the scattered light due to the interaction between the ray and a droplet was collected via a photomultiplier placed at 90°. The limitation was that to size fuel droplets, a calibration is required or even complex Mie theory simulation. The great evolution of these diagnostics is the Phase Doppler Particle Anemometer. Vannobel *et al.* (1993) and Posylkin *et al.* (1994) have done few studies on optical accesses engine with PDPA. It seems to be attractive due to simultaneous droplet size and velocity measurements. Unhappily, this technique needs a collection optics location around 30° and provides temporal data but not spatial one. Finally Skippon *et al.* (1996) have applied a recent technique, the interferometry based on Mie scattering, in an optical engine. Glover *et al.* (1995) have firstly well developed this method to characterize sparse sprays. One of the advantages is the independence on the absolute scattering intensities : out-of-focus images of laser scattering droplets from the 45° direction consist of a set of lighting spots with fringes. They shown that due to geometrical analysis, diameter can be easily determined from the number of fringes.

The aim of this study is to get at droplets sizing and repartition data in a S.I. engine but with an unique possible collecting scattering angle of 90°. In this case, geometrical analysis must be used carefully and the scattering intensity is relatively low. Ragucci *et al.* (1990) have tested the Inteferometric Mie Scattering method in this particular case with one drop : their conclusion was very promising. It seems possible to develop it in planar configuration. Therefore, the emphasis of the paper is on the development of this suitable diagnostic technique. So we will firstly remind some theoretical basements to express clearly the relation between number of fringes and droplets diameter by using geometrical hypothesis. Then the experimental setup will be described. The final section shows and discusses results of preliminary experiments in different engine working cases during the compression stroke, prior to ignition and near the spark plug.

2. THEORETICAL BACKGROUND

In this part, basis phenomena and hypothesis will be clearly described in order to get the simple relation between the number of fringes and the droplet diameter.

Van de Hulst (1957) has demonstrated that, for large size parameter, i.e. $x = \pi d/\lambda$, with d, droplet diameter and λ incident light wavelength, the scattering of light by a spherical particle illuminated by plan wave fronts can be simply described by geometrical optics rules, simpler than the complex Mie theory equation. In our case, droplet diameters lie within a range from a few micrometers up to 100 µm. So for a 532 nm wavelength, x is ranging from 5.9 to 590. Ungut *et al.* (1981) have shown that this approximation is valid for droplet as small as 1 µm but for forward scattering angle (0-20°). The geometrical analysis can be contested in our application due to the 90° scattering angle but provides simple relation to estimate droplet size.

All droplets are considered perfectly spherical and homogeneous. The interaction between a light ray (i.e. here a laser beam) and a droplet can be schematised as on Figure 1. The scattering light intensity is due to reflection and successive refractions. For the interferometry Mie scattering method, only the reflection and first refraction rays are useful. The reflected one is not attenuated by absorption but the first refracted one is : the difference of both optical paths, which form dark and bright fringes, is due to the absorption, function of the droplet diameter. The advantage is that this sizing method is totally independent of the intensity of the illuminating light source. The droplet itself acts as an interferometer.

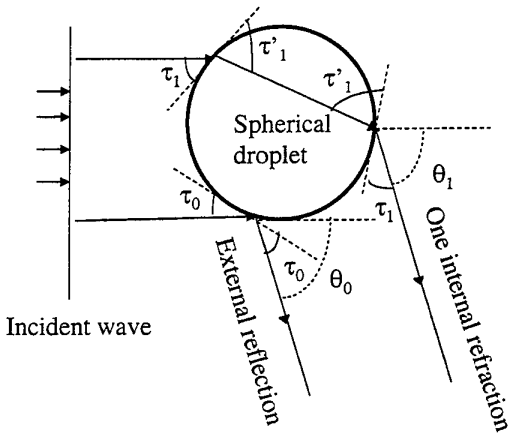


Figure1. Laser light pattern through a droplet.

τ_0 and τ_1 are the incidence angles of reflected and refracted beams respectively and τ'_1 the refraction angle. By the Snell's law, the relation between τ'_1 and τ_1 can be expressed as below, with m real part of the refractive index:

$$\cos\tau_1' = \frac{1}{m}\cos\tau_1 \qquad (1)$$

The scattering angle from the incident ray is, for pure reflection, $\theta_o=2\tau_o$ and for one refraction, $\theta_1=2\tau_1'-2\tau_1$. It exists only two rays for that the scattering angles are the same : for example for $\theta=90°$, $\tau_o=45°$, and $\tau_1\approx1°$ and $\tau_1'\approx44°$. So the phase difference between both rays can be easily expressed via the phase term determined by simple geometry :

$$\delta_0-\delta_1=\frac{2\pi d}{\lambda}\sin\tau_0-\frac{2\pi d}{\lambda}(\sin\tau_1-m\sin\tau_1') = \frac{2\pi d}{\lambda}(\sin\frac{\theta}{2}-\sqrt{m^2+1-2m\cos\frac{\theta}{2}}) \qquad (3)$$

As Ungut *et al.* have shown, the phase difference is taken account into total scattered light intensity expression via a cosine. Therefore, an infinitesimal variation of the scattering angle induces a maximum or minimum light intensity variation and occurs when an infinitesimal phase difference is equal to 2π. These considerations allow to write :

$$\Delta(\delta_0-\delta_1)=\frac{\pi d}{\lambda}(\cos\frac{\theta}{2}+\frac{m\sin\frac{\theta}{2}}{\sqrt{m^2+1-2m\cos\frac{\theta}{2}}})\Delta\theta=2\pi \qquad (4)$$

So as Van de Hulst (1951) and Roth *et al.* (1991) notified, the angular inter-fringe spacing $\Delta\theta$ is linked to the droplet diameter by :

$$\Delta\theta=\frac{2\lambda}{d}\frac{1}{\cos\frac{\theta}{2}+\frac{m\sin\frac{\theta}{2}}{\sqrt{m^2+1-2m\cos\frac{\theta}{2}}}} \qquad (5)$$

This relation can be simplified only when the experimental set-up allows a relatively low scattering angle as Glover *et al.* configuration. We will discuss during the following part about the experimental feature of the Planar Mie Scattering Interferometry (P.M.S.I.).

3. EXPERIMENTAL CONSIDERATIONS

The Planar Mie Scattering Interferometry set-up is simple : as it can be seen on Figure 2, a laser sheet illuminates the droplets area and an imaging lens collects the droplet image on a CCD camera for example. To visualise the fringes inside the droplet it needs to focus out the collecting system : indeed, at the focusing plane, the fringes are superimposed so only uniformly lighted droplets are obtained. For a scattering plane at 90°, the main drawback is the low scattered intensity, but in fact, even with a classical CCD camera, intensifier is not essential. In previous work, Mounaïm-Rousselle and Pajot (1997) have verified the good accuracy obtained by this technique in calibrated sprays.

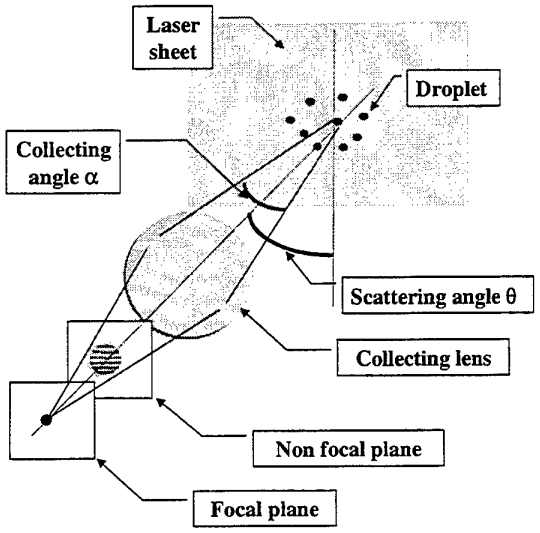


Figure 2. The PMSI experimental set-up.

One experimental important parameter is the collecting angle α : it must allow to get a number of fringes sufficiently high to distinguish them : α is equal to the number of fringes N multiplied by the angular fringe spacing $\Delta\theta$. This angle can be also approximated as function of the magnification ratio G and the number of aperture N.A. :

$$\alpha\approx 2\arcsin(G/2NA) \qquad (6)$$

Finally the droplet diameter can be expressed as :

$$d=\frac{\lambda N}{\arcsin(\frac{G_t}{2N.A.})}\frac{1}{\cos\frac{\theta}{2}+\frac{m\sin\frac{\theta}{2}}{\sqrt{m^2+1-2m\cos\frac{\theta}{2}}}} \qquad (7)$$

The importance of this collecting angle is shown on Figure 3 where the number of fringes is plotted versus the droplet diameter for different collecting angles. It can be concluded that for a given diameter, more this angle is great more the number of fringes will be important. Therefore, for example a collecting angle of 20° allows a good estimate of droplet diameters range of 5-20 µm, which generates a number of fringes from 3 to 11.

Experimentally, around a device, as an engine for example, collecting angles are relatively limited. If one considers again the equation (6), to collect the maximum of light with a classical objective lens, for

instance, an objective aperture of 4 and a collecting lens diameter of 50 mm, with a magnification ratio of 1:1, the laser sheet – objective lens must be 200 mm. In the other hand, current CCD size is not more than 100 mm^2, so it implicates that the image area will be sharply restricted. So to have few possibilities, the best way is the using of an objective which enables a large aperture with a large lens diameter.

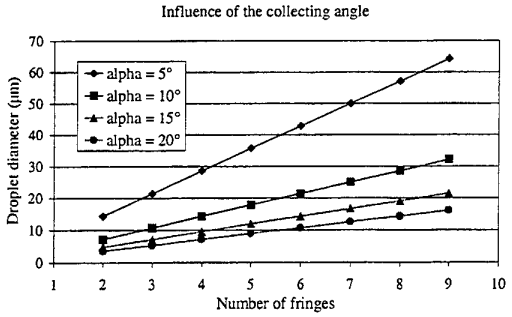


Figure 3. Effect of the collecting angle on droplet diameter estimate.

We have underlined above that to image fringes on the CCD pixels, the camera must be defocused. In fact, this defocusing distance must not be too large to allow a sufficient visualisation area. It is evident also that the maximum droplet size determinable is limited by the minimum distinguishable angular inter-fringe spacing. This problem can be seen on Figure 4 where an example of PMSI image is presented : the biggest droplet, i.e. most brightness can not be sized due to the too large number of fringes. In the other hand, droplets with one fringe are also difficult to evaluate : it is not possible to know if they are really only one fringe or if they are not totally into the laser sheet. As underlined Glover et al., this technique allows only droplet sizing in relatively sparse sprays due to the overlapping of droplets.

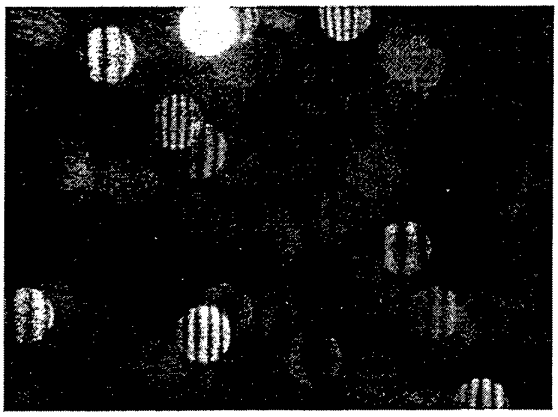


Figure 4. An example of the image achieved by PMSI.

The last important parameter which must be considered is the refraction index. As all techniques based on Mie scattering, the refraction index change plays an important role on the droplet sizing. Via equation (7), one can evaluate that refraction index variation of 6% induces number of fringes variation of 0.07 % ! For example, if iso-octane droplets refraction index varies from 1.39 to 1.49, due to the temperature or pressure field, the number of fringes passes from 5.6 to 5.595 for 10 µm droplet diameter and 10° collecting angle. So with this technique, it can be considered that the refraction index variation does not affect sharply the droplet sizing.

4. EXPERIMENTAL SET-UP

Optical engine. The global arrangement of the engine is shown below on Figure 5. This optical accesses spark-ignition is derived from a standard 4 cylinders 2 litres engine. An one-cylinder head is mounted on the top of an elongated crankcase. This raised cylinder houses a piston with a quartz transparent crown, allowing an optical access below the combustion chamber. Two quartz windows enable an access through the cylinder head which is 4 valves pentroof shaped.

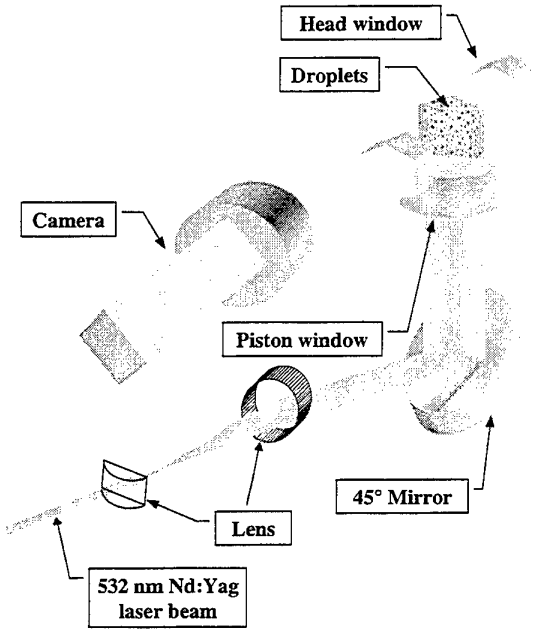


Figure 5. Global view of the experimental set-up.

An optical shaft encoder with 3600 pulses per revolution provides crank angle to a timer card, which

generates pulses for injection, ignition, laser triggering and video capture.

The engine is driven at 2000 revolutions per minute by an electrical engine and is fed with iso-octane as fuel. The mean admission pressure is fixed at 500 mbar and the injection duration at 5 ms. The global equivalence ratio of air/fuel mixture is maintained for all cases at stoichiometric level. The timing of the different injections and spark ignition are represented on Figure 6 (crank angles are referenced to cross-flow TDC).

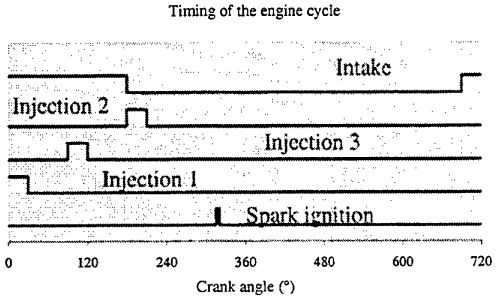


Figure 6. Timing of the engine working.

Planar Mie Scattering Interferometry set-up. To implement this technique, a frequency doubled YAG laser beam (532 nm) passes through a set of cylindrical and spherical lenses to form a sheet with a minimum thickness of 0.5 mm (the sheet thickness must be larger than maximum droplet diameter). This vertical sheet goes in the combustion chamber via the transparent piston head as it can be seen on Figure 5.

The detailed view of Figure 7 gives an idea of the visualised droplets location inside the combustion chamber : just below the spark plug. At each laser pulse, triggered once per engine cycle, the scattered light by the fuel droplets is collected at 90° via a KPM2 Hitachi CCD camera. The CCD resolution is 768 by 568 pixels and its size 6.47mm by 4.83 mm. In fact, due to the asynchronous trigger, it has been used only 768 by 284 pixels. In fact, the camera is turned in order to have the maximum pixels number in the direction of the number of fringes detection. The resolution seems to be too low as underlined Glover *et al.* Indeed, they have used firstly a photographic film to get larger resolution by scanning. But high resolution is not essential to provide quantitative results, it depends on the diameter resolution and the diameter range required. In our case, the knowledge of diameter with a 1µm precision is widely sufficient.

To get a good collecting angle, few classical types of objectives have been tested. The best choice in our configuration is the Nikkor AF80-200f/2.8 : it allows large aperture with a non usual lens diameter of 77 mm. For this study, the visualisation area at the focal plane is : 10 mm by 13 mm which gives a magnification ratio (for largest dimension) of 1:2 and the distance between the laser sheet and the objective lens is 150 mm at 80 mm macro position. To achieve sufficient distinguishable fringes, the out-of-focus distance used is about 11 mm, for instance, about 7% of the objective-object distance. In this case, the size of the area visualised becomes 9 mm by 12 mm.

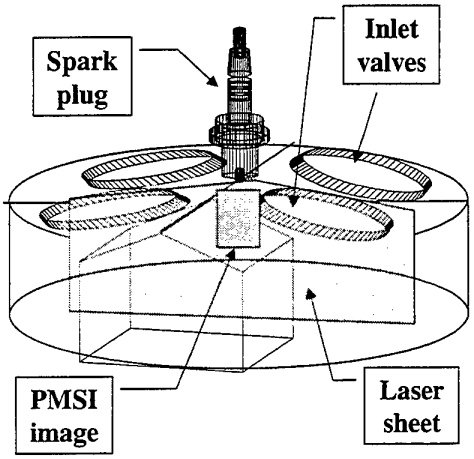
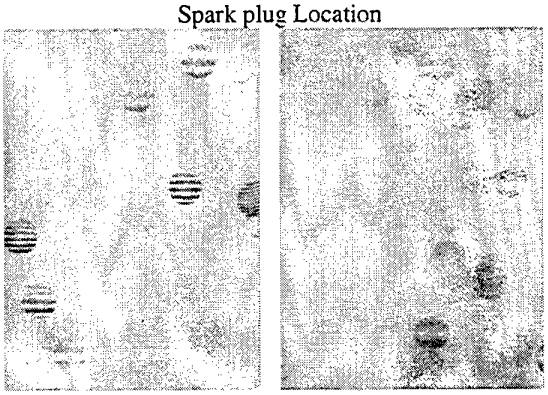


Figure 7. Detailed view of the set-up.

5. RESULTS AND DISCUSSION

Firstly we have studied the droplets presence and diameter distribution for the injection case 1, i.e. the injection is made at the beginning of the intake valve opening. Few instantaneous images are shown on Figure 8. They are resized and negative to have a better contrast.



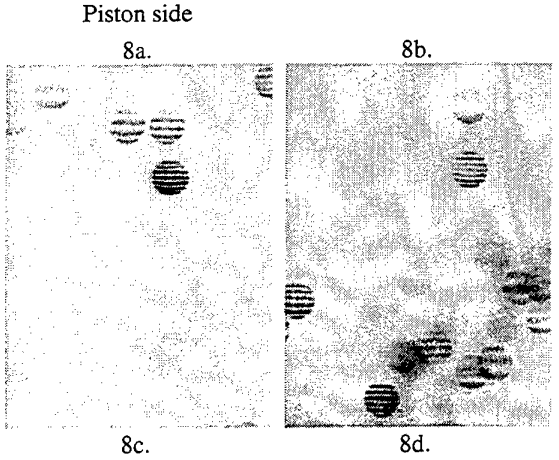


Figure 8. Instantaneous images for injection 1, 5° before start of ignition (S.I.).

Some of them do not allow the fringe detection certainly due to too small droplets and also droplets out of the field of view (see on Fig.8b). So few images are not considered : in average, in this study, about 75 images for 100 taken images are validated.

The droplet diameter distribution achieved in this case, for one hundred and two hundred images is plotted below on Figure 9. The droplet number parameter is the number of droplets at this diameter normalised by the total validated droplets number. To obtain droplet size from the images, we have only counted the integer number of fringes. We have verified that this approximation provides a good idea of the droplet size distribution.

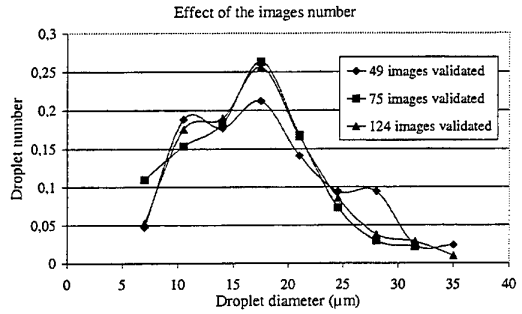


Figure 9. Effect of the number of images on the droplet size distribution.

The images on figure 10 have been taken at different crank angles around the ignition timing (which is 45° before T.D.C.) but not during the same cycle. It is not easy to conclude about droplets field : it can be noted firstly that 15° before start of ignition droplets are more at the top of the image so nearer the spark plug location. Indeed, during this compression stroke, droplets are pushed by the piston itself. We can see, also that 5° after the ignition, droplets are still present in this area.

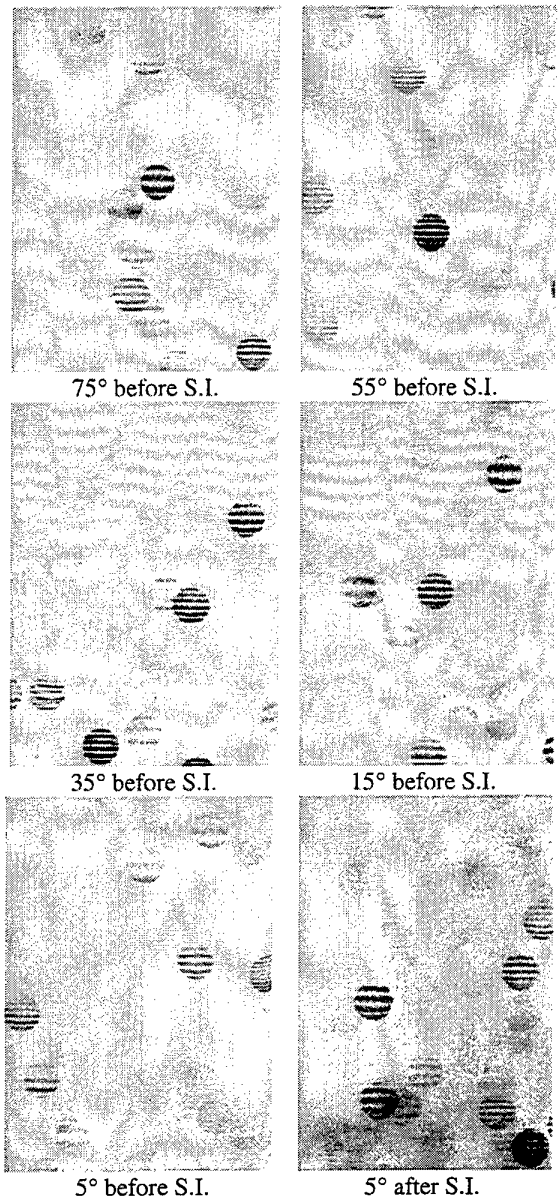


Figure 10. P.M.S.I. images at different crank angles

To analyse the droplet diameter is not also evident, as it can be seen on Figure 11. It seems that just after the start of ignition, few large droplets exist, certainly due to the piston rise.

An interesting parameter can be used to understand better the liquid process, is the mean number of droplets found on the total validated image number. On table 1 below, this average and the mean Sauter diameter are reported. It can be concluded that

larger droplets number is far from the ignition due the piston rise and also liquid deposit on the piston head. During the rise, with pressure and temperature effects, these droplets due to the deposit vaporise and less droplets are found just prior to ignition. After ignition, certainly larger droplets at spark plug location have been pushed away by the flame kernel and they appear on the image area. The mean Sauter diameter is about 20 µm in this small area and for the injection case.

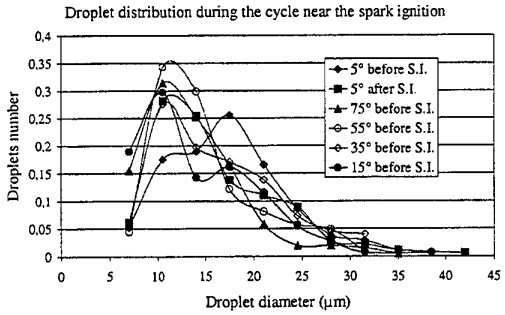


Figure 11. Size distribution at few crank angles.

	Droplets number average	Mean Sauter diameter (µm)
75° before S.I.	2.72	18.16
55° before S.I.	3.22	19.03
35° before S.I.	2.11	21.01
15° before S.I.	2	19.6
5° before S.I.	1.72	20.3
5° after S.I.	2.26	22.9

Table 1. Droplets number average and mean Sauter diameter for injection mode 1.

To emphasise the feasibility of the Planar Mie Scattering Interferometry technique, we have visualised droplets for two other injection modes, 5° prior to ignition. As it is explained on Figure 6, the mode 2 corresponds to an injection when the valves are closed at the beginning of the compression stroke so the liquid droplets stay in the intake pipe during 540°. In the mode 3, the injection is done 120° after the beginning of intake valves opening.

The droplets size distribution for the three modes are plotted on Figure 12. In fact, in the mode 2, usually called closed valve injection mode, only two images contain one discernible droplet. This result can be explained by the vaporisation process occurring in the intake pipe itself.

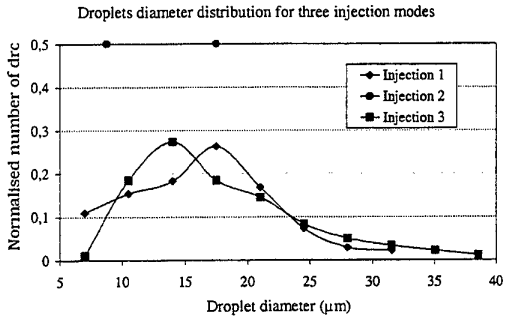


Figure 12. Influence of injection modes

For mode 3, the average number of droplets per image is higher than for case 1 : 2.26 and 1.72 respectively and also the mean Sauter diameter, 23 µm. In fact, for the mode 1, the intake flow velocity is lower at the beginning of the intake, then it can be expected that deposits on the intake wall are more important, inducing less droplets in the combustion chamber. Moreover, the injection is done during the exhaust gases back flow, which induces an increase of temperature and so an earlier droplets vaporisation.

6. CONCLUSION AND PERSPECTIVES

Planar Mie Scattering Interferometry has been applied in an engine environment where optical accesses are limited inducing a collecting plane perpendicular to the laser sheet. The theoretical basis of this technique were clearly written to remind fundamental concepts and assumptions. The experimental arrangement for P.M.S.I. was described and all technical problems for implementing it discussed in detail. This technique was used successfully to investigate iso-octane droplets presence as function of crank angles during the compression stroke around the spark ignition and just below the spark plug. Three injection modes were also improved to achieve an idea of the droplets life in this area. These results will be used to study the earliest flame kernel in Spark Ignition engine.

It can be concluded from this work that the Planar Mie Scattering Interferometry technique is an easy optical diagnostic. It can provide good resolved spatial information about droplet location and droplet size. The simple geometrical analysis is sufficient to establish the relation between optical characteristics of the collecting system, number of fringes detected and droplet diameter. Compromise must be chosen in terms of droplets size range, maximum distinguishable number of fringes, image area and also the required diameter precision. In our future

work, we will develop an image processing software to avoid the manual fringes count.

ACKNOWLEDGMENTS

The authors wish to thank G. Grehan, CORIA Rouen, for his theoretical help and C. Preterre, Renault S.A., for providing access to a transparent engine during this work.

REFERENCES

Ballal D.R., Lefebvre A.H., 1981, A General Model of Spark Ignition for Gaseous and Liquid Fuel-Air Mixtures, Eighteen Symposium (International) on Combustion, pp. 1737-1776.

Glover A.R., Skippon S.M., Doyle R.D., 1995, Interferometric Laser Imaging for Droplet Sizing : A Method for Droplet-Size Measurement in a Firing Lean Burn Engine, Applied Optics, vol.34 n°36, pp. 8409-8421.

Kadota T., Mizutani S., Wu C.Y., Hoshino M, 1990, Fuel Droplet Size Measurements in the Combustion Chamber of a Motored SI Engine via Laser Mie Scattering , SAE paper 900477.

Mounaïm-Rousselle C., Pajot O., 1997, Droplet Sizing by Interferometric Mie Scattering in Engine Environment, Optical Technology in Fluid, Thermal and Combustion III, ed.SPIE, vol. 3172, pp. 700-707.

Peters B.D., 1982, Fuel Droplets Inside the Cylinder of a Spark Ignition Engine with Axial Stratification, SAE paper 820132.

Posylkin M., Taylor K.P., Vannobel F. and Whitelaw J.H., 1994, Fuel Droplets Inside a Firing Spark-Ignition Engine, SAE paper 941989.

Ragucci R., Cavaliere A., Massoli P., 1990, Drop Sizing by Laser Light Scattering Exploiting Intensity Angular Oscillation in the Mie Regime, Part. Part. Syst. Charact. 7, pp. 221-225.

Roth N., Anders K., Frohn A., 1991, Refractive-Index Measurements for Correction of Particle Sizing Methods, Applied optics, Vol 30 n°33, pp. 4960-4965.

Ungut A., Grehan G. and Gouesbet G., 1981, Comparisons Between Geometrical Optics and Lorenz-Mie Theory, Applied Optics, Vol. 20 n°17, pp. 2911-2918.

Vannobel F., Dementhon J.B., Robard D., 1993, Phase Doppler Anemometry Measurements on a Gasoline Spray Inside the Inlet Port and Downstream of the Induction Valve ; Steady and Unsteady Conditions, Applications of laser techniques in fluid mechanics, Edited by Adrian R J, Durao D F G, Durst F, Heitor M, Maeda M and Whitelaw J H,6, 507, Springer Verlag.

Van de Hulst H.C., 1957, Light Scattering by Small Particles, Willey, New York.

Smith A.K., Polymeropoulos C.E., 1987, Spark Ignition of Aerosols, Twenty-first Symposium (International) on Combustion, pp. 513-519.

AEROSOL SIZE MEASUREMENT USING A LASER DOPPLER PROBE AND ACOUSTIC EXCITATION OF THE FLUID FLOW

V. Strunck, H. Müller, G. Grosche, D. Dopheide

Section of Fluid Flow Measuring Techniques, Physikalisch-Technische Bundesanstalt
D-38116 Braunschweig, Bundesallee 100, Germany
tele #49-531-592-1311, fax #49-531-592-1305
e-mail: volker.strunck@ptb.de

ABSTRACT

In laser Doppler anemometry the reliability of the measurement in a flow depends upon the fidelity of the tracer particles in following the fluid motion. To estimate the particle lag in a flow the size distribution of the tracers have to be known. Moreover, it is the size distribution visible to the laser probe that is the important parameter.

The method applied is to superpose a known oscillatory fluid velocity field to the flow by an acoustic excitation of the medium. At several discrete frequencies simultaneously the medium is excited with an acoustic radiator. The frequency response of the suspended particle is measured by the laser probe to be investigated to obtain the dynamic relaxation times and the sizes of the particles as seen by the probe. Aerosol sizes from 0,1 µm to 20 µm can be measured by simply applying a loudspeaker with a multi-frequency generator to the LDA set-up.

1. THEORY

The equation of motion of a small spherical particle in a uniform acoustic field follows from the Stokes fluid resistance law:

$$\tau(\frac{dv}{dt}) + v = u \sin \omega t \qquad \text{(i)}$$

τ is the dynamic relaxation time of the particle, v is the particle velocity, u the velocity of the medium and ω the angular frequency of the acoustic excitation. The dynamic relaxation time τ is a function of the particle diameter d, the viscosity η of the medium and the density difference ρ between particle and medium:

$$\tau = \rho d^2 / 18\eta \qquad \text{(ii)}$$

The ratio of the velocity amplitudes of the medium and the particle is obtained from Eq. (i), see Hinze (1959):

$$\left|u^2 / v^2\right| = 1 + \omega^2\tau^2 \qquad \text{(iii)}$$

Mazumber and K.J. Kirsch (1975) have done recent investigations by using this ratio to measure aerosol size spectra. By using two or more different frequencies with known velocity amplitudes in the medium (say calibrated with c that $u_1 = cu_2$) , Eq. (iii) can be simplified to

$$c^2\left|v_2^2 / v_1^2\right| = c^2\left|a_2^2 / a_1^2\right| = (1 + \omega_1^2\tau^2) / (1 + \omega_2^2\tau^2) . \qquad \text{(iv)}$$

If the velocity amplitudes or the amplitudes of oscillation a_1 and a_2 of the particle at both frequencies are measured, the dynamic relaxation time of the particle can be determined from Eq. (iv). The aerodynamic diameter then follows from Eq. (ii).

By using the ratio of amplitudes of the particle oscillations at two ore more frequencies instead of a single frequency, some advantages can be shown: Once the loudspeaker is calibrated in the frequency range applied, the absolute excitation levels of the medium are of no more interest, because the ratios at different frequencies are important. Thus, variations of distance, inclination and level of excitation in the laser probe volume have less influence.

If the probe is excited with white noise, the ratio of power of oscillation of the particle to the power of oscillation of the medium is just one half at the frequency $\omega = 1/\tau$ (see iii). A disadvantage of exciting the flow with white noise is that the excitation power of the acoustic radiator has to be distributed equally to the bandwidth of interest. Forcing the excitation to a set of discrete frequencies thus allows higher excitation levels at these frequencies. The half value of the power ratio of particle and medium oscillation amplitudes then has

to be interpolated and the particle diameter can be evaluated from (ii).

2. EXPERIMENTAL SET-UP

A differential LDA single laser diode set-up and a differential LDA set-up with two MOPA lasers to obtain a frequency shift in the measuring volume has been used as probe to measure the effect of acoustic excitation on aerosols suspended in an air flow. The loudspeaker was aligned to the direction of the sensitive component of the laser probe, see Fig. 1. In case of the LDA without frequency shift, the particles to be investigated have to move towards to the loudspeaker to obtain Doppler frequencies modulated by the acoustic excitation. In case of the frequency shifted LDA the direction of the mean particle movement is of no importance.

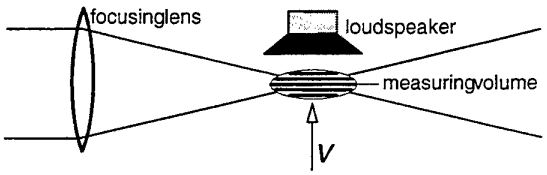


Fig. 1 LDA system to measure aerosol size by using acoustic excitation

The analysis of the LDA signals has been performed using one and two channel transient recorders connected to a computer to allow real time measurements of particle size. The central idea of the analysis is to observe the particle oscillation due to an observer moving with the flow but not imposed by the oscillatory acoustic field. Hence, in case of moving with the flow towards the loudspeaker, the particle moves back and forth to the observer. For this purpose, the location of the particle has to be determined at each time during the passage through the measuring volume.

Quadrature analysis is a well-suited tool for this task. For the LDA system without frequency shift a quadrature signal has to be calculated from the acquired Doppler signal by applying a Hilbert transform, see Strunck at al. (1996). This presents a certain restriction to the acoustic excitation levels in the measuring volume. They should not be as large as to produce velocity oscillations higher than the mean flow, because the sign of velocity is not measurable in a LDA without frequency shift. Quadrature signal generation in a frequency shift LDA is easy, when the signals are shifted down to the baseband by mixing the LDA signal with the shift frequency signal to obtain the inline signal, and, by mixing the LDA-signal by a 90° phase shifted shift frequency signal to obtain the quadrature signal. The arc tangent of the inline and quadrature signal directly gives the relative position of the scatterer in the measuring volume. To obtain the movement of particle due to an observer moving with the fluid flow, the position calculated from the mean flow velocity is subtracted.

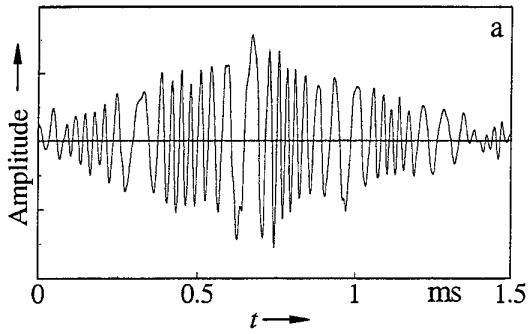


Fig. 2a Doppler signal out of an oscillating flow

Fig. 2a shows a typical LDA signal of a particle moving through a fringe system in a flow with a superposed oscillatory flow. When the frequency is high, the scatterer is accelerated. When the frequency is low, the scatterer is retarded.

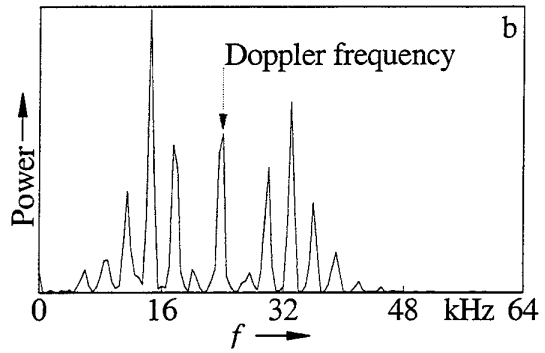


Fig. 2b Power spectrum of Doppler signal from 2a.

In the power spectrum in Fig. 2b there are multiple peaks symmetrically distributed around the central peak of the Doppler frequency. Due to the acoustic excitation with two frequencies, several higher products of the participating frequencies are produced.

Applying quadrature analysis and removing the mean velocity of the scatterer, the spatial amplitude oscillation of the scatterer can be extracted. The amplitude of oscillation of the medium is always constant, but visible only at the time of passage of a scatterer through the measuring volume. Because the visibility in the measuring volume is a function of the light intensity, the squared envelope of the Doppler signal is taken as a weight and was multiplied with the oscillation amplitude, see Fig. 3a.

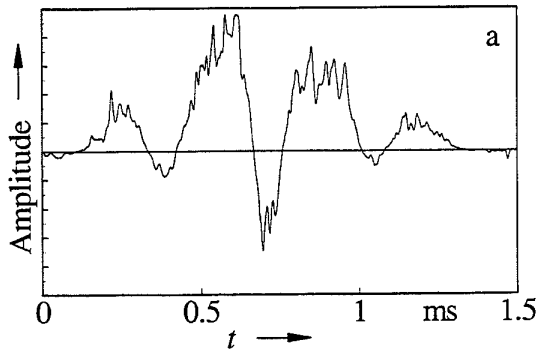


Fig. 3a Extracted oscillation amplitude from the signal in Fig. 2a

Therefore, the oscillation function of the scatterer location artificially has the shape of the Doppler signal, which performs well when the power spectrum of this oscillation has to be analyzed in Fig. 3b

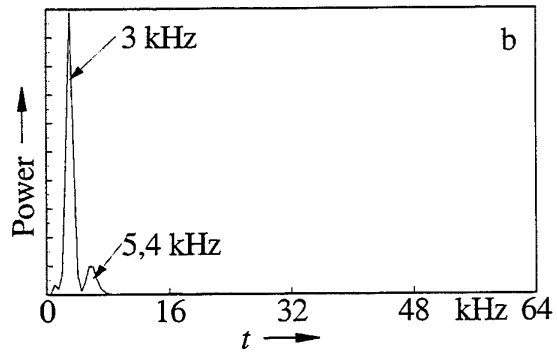


Fig. 3b Power spectrum of the extracted oscillation amplitude of Fig. 3a

As expected, only the excitation frequencies in the power spectrum in Fig. 3b have been left. Now the squared amplitudes (power) at the applied frequencies are read out and the particle diameter can be calculated using Eq. (iv) and (ii). In case of Fig. 2 and Fig. 3, the velocity of the mean flow was 0,12 m/s equivalent to a Doppler frequency of 24 kHz. The excitation frequencies have been 3 kHz and 5,4 kHz, the calibration coefficient c was 8/3. The particle diameter of the water droplet was calculated to be 6,7 µm.

3. MULTI FREQUENCY EXCITATION

To generate a set of discrete frequencies, a simple synthesized function generator has been built (Figure 4).

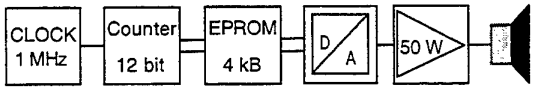


Fig. 4 Synthesized function generator to drive the acoustic radiator

The binary counter following the clock generates the addresses for the EPROM. The digitized signal in the EPROM is converted to an analog signal. The high output of the power amplifier is neccessary to have acoustic excitation levels of more than 100 dB at the piezo loudspeeker. The 'tweeter' has been calibrated to correct the power of the set of six discrete frequencies. Water droplets in a flat plate boundary layer moving at velocities of 0,05 m/s (to have a long transit time during the passage of the measuring volume) have been excited acoustically.

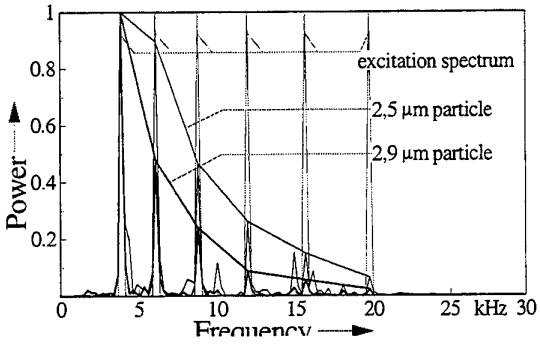


Fig. 5 Oscillation power spectra of the excited medium and of two different particles.

The oscillation spectra in figure 5 show the power of oscillation (dotted line) of the air, and two power distributions of particles of different diameters show the decay towards higher frequencies.

The power spectra have been obtained from a non-shift LDA system. In this case we applied the Hilbert transform to get a quadrature signal. The excitation

has been very moderate in order to have local velocities in the measuring volume not less than the lowest frequency that can be resolved by spectral methods. In case of frequency shift LDAs, no restrictions on excitation levels and velocities would have to be made to the passage of a particle through the measuring volume.

4. CONCLUSION

Two methods of measuring the aerodynamic size of solid or liquid scatterers from 0,1 μm to 20 μm in diameter with standard LDAs has been outlined. One method is to apply a two frequency excitation and to measure the oscillation amplitudes. The second method is in consequence to use a multi frequency excitation to read out directly the relaxation time of the particle to analyse from the oscillation power spectrum.

No special assumptions on the shape, refractive index, coagulation etc. of scatterers have to be done using these methods. Additional merits of the methods are that the particle distribution visible to the LDA performing measurements is acquired without changing the apparatus. The only supplement in an existing LDA set-up for this method is a loudspeaker and a frequency generator.

REFERENCES

J.O. Hinze 1959, Turbulence, McGraw-Hill, New York, p. 357

M.K. Mazumder and K.J. Kirsch 1975; Flow Tracing Fidelity of Scattering Aerosol in Laser Doppler Velocimetry, Appl. Optics, Vol. 14, No. 4, April, p. 894-901

K.J. Kirsch and M.K. Mazumder 1975; Aerosol size spectrum analysis using relaxation time measurement, Appl. Phys. Letters, Vol. 26, No. 4, 15 February, p. 193-195

V. Strunck, H. Müller, D. Dopheide; Time domain single tone analysis using quadrature algorithm 1996, Proc. of the Eighth International Symposium on Applications of Laser Techniques to Fluid Mechanics, Lisbon, Portugal, July 8th to 11th , 6.61-6.64

MEASUREMENT OF SIZE AND VELOCITY OF PARTICLES BY OPTICAL BASED SPATIAL FILTERING TECHNIQUE

D. Petrak, K. Rosenfeld and E. Przybilla

Department of Technical Thermodynamics
University of Technology Chemnitz, Germany

ABSTRACT

This paper describes size and velocity measurement of solid particles by fibreoptical-based spot scanning combined with fibreoptical spatial filtering velocimetry. Main part of the measuring system is a robust probe, which can provide spatially and temporally in situ readings of size and velocity of a single particle. In this work, glass beads and limestone particles were measured to evaluate the sizing range and the influence of particle concentration. Different kinds of optical set-up in relation to the illumination of the particles were investigated. The results were compared with simultaneous laser diffraction measurements.

It was found that the measuring ranges are 10...1000 µm for the particle size and 0.01...50 m/s for the particle velocity. The data rate of the present signal analysis set-up is limited to ≈ 200/s. It was also found that the spatial filter method was suitable to measure size and velocity of crystals in solutions and bubbles in liquids.

1. INTRODUCTION

Sizing of particles in industrial processes is of technical interest and different laser-based techniques have been developed such as the phase Doppler anemometry (PDA) for sizing of optically homogeneous spheres with known complex refractive indices. There is a lot of work to develop the PDA in relation to inhomogeneity and absorptivity of the particle medium. New results show that the PDA requires a priori knowledge of optical properties (Wriedt et al 1993, Köser and Wriedt 1996, Schneider and Hirleman 1994, Onofri et al 1996). Naqwi and Fandrey (1997) have developed a PDA technique to measure the size of irregular particles smaller than 20 µm.

The diffraction amplitude method or the light scattering are suitable instruments for the determination of the equivalent particle diameter but require large effort in industrial process application (Witt and Röthele 1998). For sizing of irregular shaped particles imaging techniques have an advantage. Two applicable methods are the focused beam reflectance measurement (Reichel et al 1998) and the shadow Doppler technique.

Hardalupas et al (1994), Morikita et al (1994, 1995) and Morikita (1996) have developed the shadow Doppler velocimetry (SDV) to measure the size of irregular, opaque particles. The SDV is based on the combination of a particle imaging technique and the well known laser Doppler velocimetry (LDV). Morikita and Taylor (1998) have shown the ability of the SDV technique to size optically inhomogeneous particles of a water-based paint spray, as used in industrial coating processes. The application of the SDV is limited to measurements in processes with a small particle number density. Another disadvantage of the SDV is the forward scattering technique.

In-line measurement techniques for size and velocity of particles in industrial processes are of great interest since these provide further understanding of the phenomena and improve the control of processes. Sachweh et al (1998) have developed a new light scattering method for in-line measurement of mean particle sizes in suspensions.

The purpose of the present work is to demonstrate the ability to measure size and velocity of solid particles by fibreoptical-based spot scanning combined with fibreoptical spatial filtering velocimetry. A first presentation of this technique was given by Petrak et al (1996). Now the work was

concentrated on the limitation of the instrument in relation to the size range and the number density. Different kinds of the illumination set-up were used.

2. MEASURING PRINCIPLE

The principle of the fibreoptical spot scanning (FSS) is based on the fibreoptical spatial filtering velocimetry (FSFV). Therefore the instrument can determine velocity and size of a single particle. The basic operation of the FSS is to observe the shadow image of a moving particle through a single optical fibre with diameter d. When the shadow image passes through the single optical fibre, an impulse is generated which width depends on the particle size x, the particle velocity v and the location of particle and fibre. The composition of the total impulse width is shown in Figure 1. The total time Δt of the impulse is:

$$\Delta t = (t_2-t_1) + (t_3-t_2) + (t_4-t_3) = (x/v) + ((d-x)/v) + (x/v) \quad (1)$$

and the particle size is then

$$x = v\,(t_2-t_1) = v\,(t_4-t_3) \quad (2)$$

or

$$x = v\cdot\Delta t - d\ . \quad (3)$$

Equations (2-3) are valid too, if the particle is larger than the diameter d of the single fibre. In every case the result is the distribution of chord lengths of the shadow image of the particle, if the particle is a sphere.

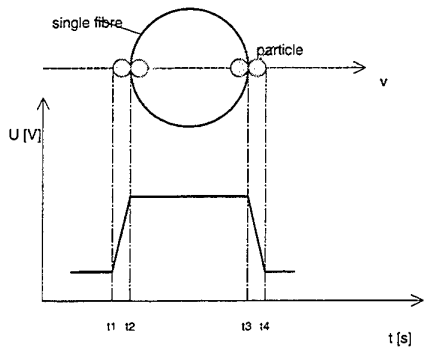


Fig. 1 Fibreoptical spot scanning of the shadow image of a particle by single fibre

The FSFV is used to determine the unknown particle velocity v. Details of FSFV are given in the review by Aizu and Asakura (1987). The basic operation of spatial filtering velocimetry is to observe the optical image of a moving object through a spatial filter placed in front of a photodetector. The output signal of the photodetector contains a frequency f_0 related to the object velocity v:

$$v = f_0 \cdot g/M\ , \quad (4)$$

where g is the interval of the spatial filter and M is the magnification of the imaging system. Various types of spatial filtering velocimeter are mainly characterised by the types of the spatial filter: transmission grating type, detector type, optical fibre type, and special grating type. The optical fibre type was investigated by Hayashi and Kitigawa (1982).

Our instrument of the fibreoptical spot scanning uses the fibroptical configuration which is demonstrated in Figure 2. The single fibre for spot scanning and a fibreoptical spatial filter are arrayed together. Optical fibres of diameter a are linearly arrayed at intervals of g/2. The shadow of a moving particle is formed at the entrance faces of a differential-type optical fibre spatial filter with the interval g. The output light from every other fibre is collected, and an output signal is obtained by taking the difference between them to eliminate the pedestal frequency around zero spatial frequency. The power spectrum $H(\mu,\nu)$ of the spatial filter function represents the selective characteristic in the spatial frequency domain. It can be obtained by Fourier transforming after weighting ± 1 at the end faces of uniform optical fibres:

$$|H(\mu,\nu)|^2 = \pi^2 a^4 (\sin \pi g\mu/2)^2 \times \left(\frac{\sin N\pi g\mu}{\sin \pi g\mu}\right)^2 \left(\frac{J_1(\pi a\sqrt{\mu^2+\nu^2})}{\pi a\sqrt{\mu^2+\nu^2}}\right)^2, \quad (5)$$

where μ and ν are the spatial frequencies in the x and y directions, respectively, J_1 is the Bessel function of the first order, and 2N is the total number of the fibres. According to equation (5), the optical fibre array selects a narrowband spatial frequency around $\mu = 1/g$ and acts as a filtering function on the input function $F_p(\mu, \nu)$ in the space domain. The spatial power spectral density function $G_p(\mu, \nu)$ is given by:

$$G_p(\mu,\nu) = F_p(\mu,\nu)\left|H(\mu,\nu)^2\right|, \quad (6)$$

where $F_p(\mu,\nu)$ stands for the Fourier transform of the

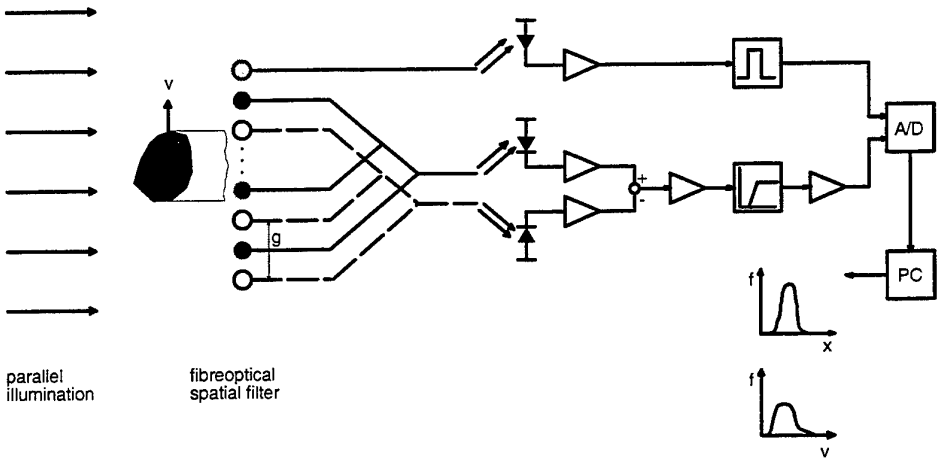


Fig. 2 The optical and electronic arrangement of fibreoptical spot scanning combined with fibreoptical spatial filtering velocimetry

image intensity f (x, y). The temporal power spectral density function $G_p(f)$ is given by integrating (6) with respect to the spatial frequency ν:

$$G_p(f) = \frac{1}{v} \int_{-\infty}^{\infty} F_p\left(\frac{f}{v}, \nu\right) \left|H\left(\frac{f}{v}, \nu\right)\right|^2 d\nu \quad (7)$$

where a relation of $\mu = f/v$ has been used. The temporal power spectrum G_p (f) may have a peak at $f = f_o = v/g$. By measuring the frequency f_o, the particle velocity v can be determined from equation (4).

The spatial filter should be constructed to have the appropriate filtering characteristics by choosing the following parameters: transmittance, interval of filter elements, number of filter elements. A systematic deviation smaller than 1 % of the central frequency f_o is almost negligible for the number of filter elements N>5. The visibility of the output signal depends on ratio shadow size x to interval g. A high visibility is obtainable for x/g less than 0.5. The optical fibres have an insufficiently long aperture size in the direction perpendicular to the spatial filter axis. Therefore, the proposed method is not qualified for chaotic particle movement.

Various signal-analysing techniques used in laser Doppler anemometry can also be used in spatial filtering velocimetry: spectrum analysis, correlation, frequency counting, and frequency tracking.

3. INSTRUMENTATION AND EXPERIMENTAL APPARATUS

3.1 Fibreoptical Spot Scanning (FSS)

The optical unit and signal processing are illustrated in Figure 2. The illumination unit, the fibreoptical unit and the electronics are arrayed in a measuring probe with a cylindrical measuring pipe made by stainless steel (Figure 3).

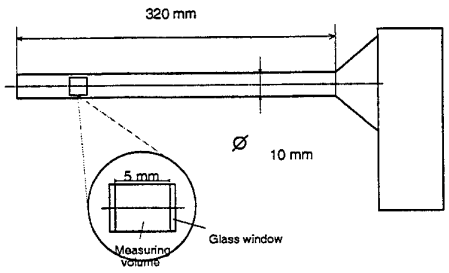


Fig. 3 Schematic view of the measuring probe

The measuring pipe has a diameter of 10 mm and the measuring volume is arrayed at a distance of 32 mm from the top. The illumination unit is located left from the measuring volume and the fibreoptical unit right. Both optical units are protected by special glass windows.

Two different illumination units are used to

generate a parallel light beam with high optical power. The first illumination unit contains a high-performance LED coupled with a short fibre and a graded index lens. The second illumination unit is a laser diode module combined with an objective. Both units are illustrated in Figure 4.

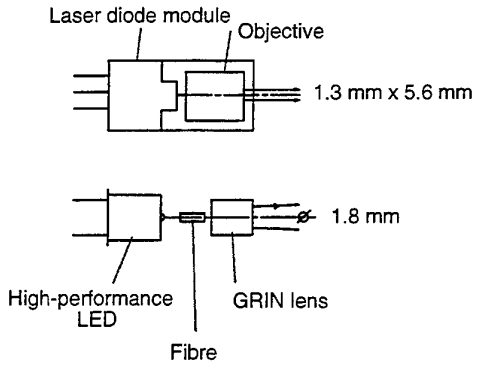


Fig. 4 Schematic view of both illumination units

The characteristics of these illumination units are listed in table 1 together with the data of the fibres. The photodetectors are Si-PIN-photodiodes with 1 mm^2 photosensitive area. Signal processing is realized by a two-channel 40 MHz transient recorder card T 3240 in connection with a PC. In order to obtain the central frequency f_o in equation (4), the Fast Fourier Transform (FFT) was applied. The magnification M = 1 is valid for the particle shadow projection with a parallel light beam. Using a trigger unit to get a TTL-impulse in the single size channel, the total time in equation (3) was determined by counting the number of samples. In order to obtain a high accuracy, the sampling frequency of the size channel is much higher than the sampling frequency of the velocity channel. The first part of the signal processing is the signal validation to select a valid particle event. The measurement begins with a particle event in the size channel and after that, the validation of the velocity signal follows. The result is a table with the velocity and size values for each measured particle. These values are used for statistical analysis: number size distribution, volume size distribution, velocity distribution.

3.2 Experimental Apparatus

Two different experimental configurations were used to generate a particle flow. In the coarse size range the particles are in a vessel and flow out through a nozzle to generate a particle free jet. In the fine size range the particles are dispersed by a powder disperser. The setup for the fine size range is shown in Figure 5. In order to determine the size range, different seave classes of glass beads and limestone particles from type ESKAL are used in the total size range from 2.5 µm to 1000 µm. A comparison was done by simultaneous measurements with a HELOS laser diffraction system.

Table 1. Characteristics of the FSS system

High-performance LED	
Wavelength (nm)	810
Fibre-coupled power (µW)	150
in graded index fibre	
Lens diameter (mm)	3
Divergent angle	0.5°
Laser diode module	
Wavelength (nm)	670
Output power (mW)	3
Divergent angle	0.021°
Spatial filter: Step index fibres	
Core diameter (µm)	125
Cladding (µm)	140
Interval (µm)	280
Total number 2N	18
Single size fibre: step index	
Core diameter (µm)	28
Cladding (µm)	30
Measuring volume: 5 mm x 0.14 mm x 2.52 mm = 1.76 mm^3	

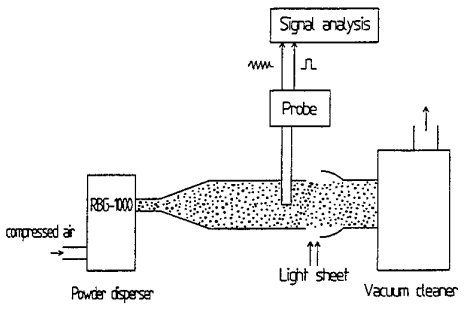


Fig. 5 Schematic view of the apparatus for the fine size range

The measuring range of the laser diffraction system was 0.1 µm – 875 µm and the dry dispersion was realized by the RODOS equipment.

4. RESULTS

4.1 Particle Size and Velocity Ranges

The measuring range in relation to the particle size lies between 10 µm and 1000 µm. For smaller particles the signal amplitude is not high enough for safe triggering. Larger particles generate bursts with a small modulation and a complicated structure.

The velocity measuring range is 0.01 m/s to 50 m/s. The upper limit is caused by the maximum of the sampling frequency and the lower limit depends on the frequency range of the probe electronics. The Figures 6 and 7 show two output signals and the Figures 8 and 9 two volume size distributions for different particle sizes.

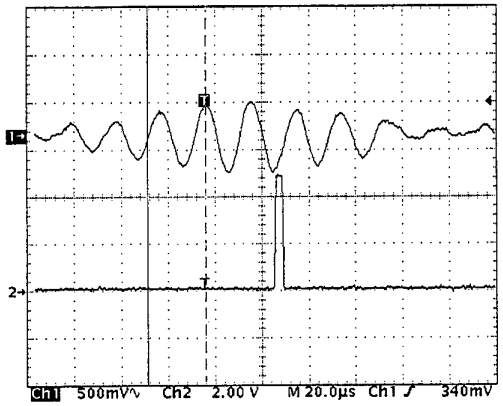


Fig. 6 Output signals of a single limestone particle, probe with laser diode module, upper signal: burst with v = 14 m/s, lower signal: size impulse with x = 26 µm

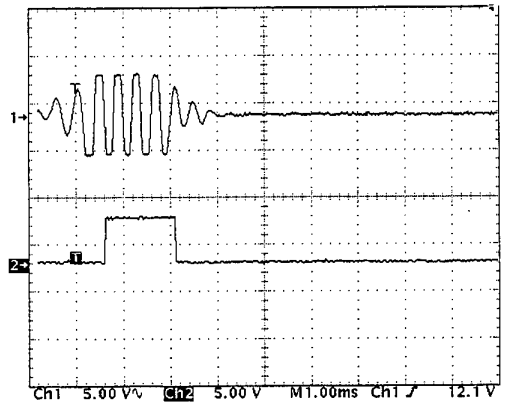


Fig. 7 Output signals of a single glass bead, probe with LED system, upper signal: burst with v = 0.68 m/s, lower signal: size impulse with x = 930 µm

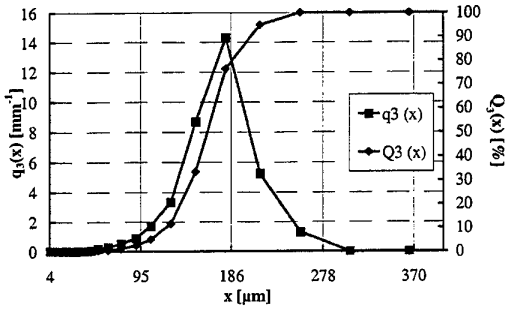


Fig. 8 Volume size distributions for glass beads seave class 125 µm – 160 µm, x_{50} = 167 µm, probe with laser diode

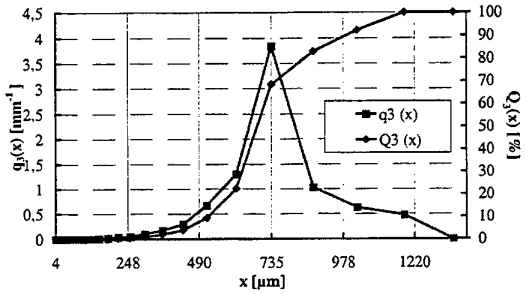


Fig. 9 Volume size distributions for glass beads seave class 630 µm – 800 µm x_{50} = 687 µm, probe with laser diode

The volume size distributions of Figure 8, 9 show, that the small chord lengths, -caused by the statistical positions of the particles to the single size fibre-, are supressed. On the other hand, the volume size distributions are sensitive to few measured large particles caused by coincidences in the measuring volume at local high particle concentrations. The total number of measured particles is 5000 for every size distribution. The reproducibility is satisfied as it can be shown in Figure 10.

The upper limit of the data rate "particles per time" was 200/s measured by a PCI card.

4.2 Particle Concentration

In order to determine the influence of the number density on the size distribution, the powder disperser was used with different rate of feed. The results are illustrated in Figure 11 and Figure 12. The parameter rate of feed was converted into the particle number

density considering the particle velocity in the horizontal particle-gas flow.

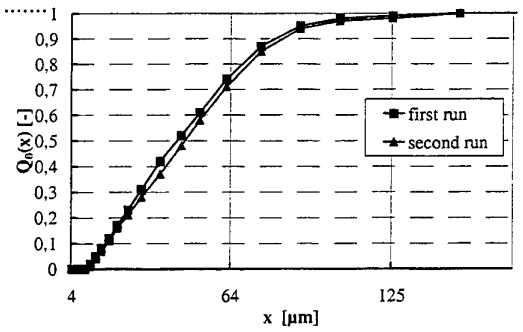


Fig. 10 Number size distributions for limestone particles with $x_{50,1}$ = 46.8 µm and $x_{50,2}$ = 45 µm, probe with laser diode

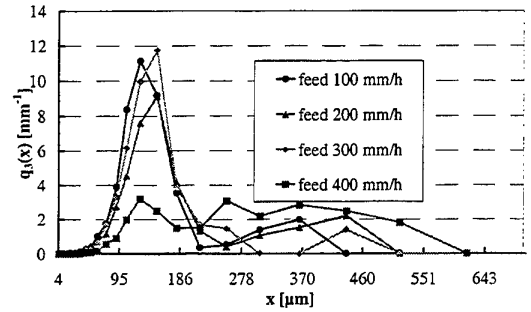


Fig. 11 Volume size distribution for limestone particles with x_{50} = 70 µm at different rate of feed, probe with laser diode

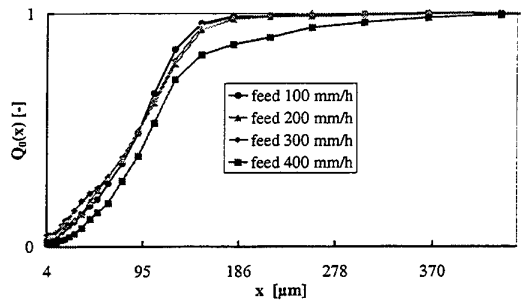


Fig. 12 Number size distribution for limestone particles with x_{50} = 70 µm at different rate of feed, probe with laser diode

The results of Figure 11 and 12 show that the volume size distribution is more sensitive to the particle number density than the number size distribution. The high sensivity of the volume size distribution is caused by the influence of a few measuring events with large particles. Thr rate of feed of 400 mm/h corresponds to a particle number density of about 100 /cm^3 for a particle size of 70 µm.

4.3 Comparison with laser diffraction

In order to compare the two sizing methods, the measured number size distributions of FSS have to be converted to volume size distributions. The comparison is illustrated for the probe with the LED illumination system. The mesurements werde done simultaneously at the free falling particles. Figure 13 and 14 demonstrate the results for different sizes of glass beads.

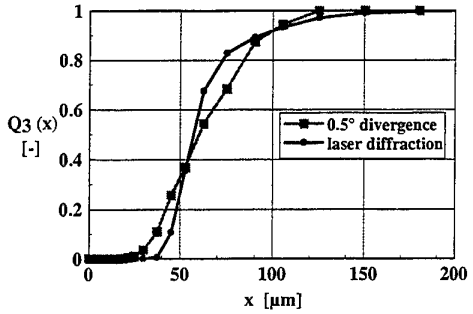


Fig. 13 Volume size distributions of glass beads, seave class 40 µm – 63 µm, FSS probe with LED and HELOS system

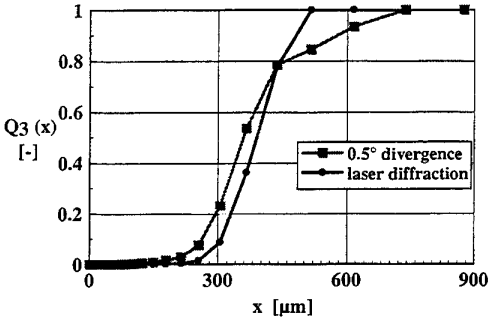


Fig. 14 Volume size distributions of glass beads, seave class 420 µm – 590 µm, FSS probe with LED and HELOS system

By using the results with different seave classes, a calibration function for the special FSS probe with a LED illumination can be calculated. Reference points are the x_{50}-values measured with both methods as it is shown in Figure 15. The theoretical curve was calculated only by considering the divergence effects and without of the effects of chord lengths.

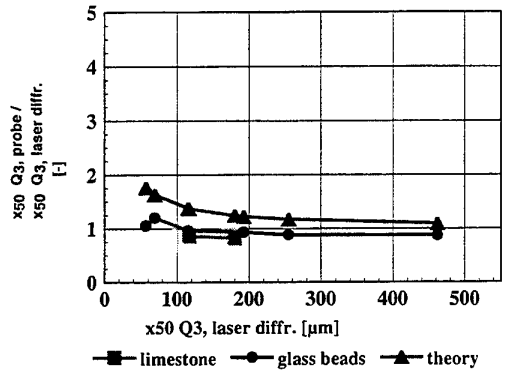


Fig. 15 Comparison of FSS with laser diffraction with x_{50}–values of different size classes, probe with LED

4.4 Application

The fibreoptical spot scanning combined with fibreoptical spatial filtering velocimetry was tested with different particle-laden flows. Successful measurements were done with solid particles in gases and in liquids and with bubbles in liquids.

An example of the measuring record for the first ten particles is illustrated in Table 2.

Table 2. First part of a measuring record

No.	Velocity [m/s]	Diameter [µm]
1	9,10E-01	120
2	1,21E+00	64
3	1,44E+00	119
4	1,11E+00	27
5	1,28E+00	80
6	1,17E+00	77
7	1,39E+00	296
8	1,20E+00	104
9	1,14E+00	40
10	1,20E+00	51

The main advantage of the FSS system is the applicability to in-line measurements. Examples are the controlling of the crystallization process or the controlling of powder products in combination with the reactors.

5. CONCLUSIONS

The fibreoptical spot scanning combined with fibreoptical spatial filtering velocimetry was developed to measure size and velocity of solid particles in flows by using a probe-based measuring system. Two different kinds of illuminations were realized. By using a laser diode module, the probe has the highest sensivity for small particle sizes.

The measuring system was tested with different seave classes of limestone particles and glass beads. Under the present configuration the FSS system can measure solid particles in the size range of 10...1000 µm and in the velocity range of 0.01 ... 50 m/s with data rates up to 200/s.

In order to compare the FSS results with laser diffraction values, a calibration function can be calculated. In the case of process control it should be used mainly the number size distributions.

Acknowledgment

The authors are grateful to Mr. R. Loos (student of the TU Chemnitz) for his extensive measurements.

REFERENCES

Aizu, Y. & Asakura, T. 1987, Principles and Development of Spatial Filtering Velocimetry, Appl. Phys., vol. B 43, pp. 209-224.

Hardalupas, Y., Hishida, K., Maeda, M. & Morikita, H. 1994, Shadow Doppler Technique for Sizing Particles of Arbitrary Shape, Appl. Opt., vol. 33, pp. 8417-8426.

Hayashi, A. & Kitigawa, Y., Image Velocity Sensing Using an Optical Fiber Array, Appied Optics, vol. 21, no. 8, pp. 1394-1399.

Köser, O. & Wriedt, T. 1996, Iterative Inversion of Phase-Doppler-Anemometry Size Distributions from Sprays of Optically Inhomogeneous Liquids, Appl. Opt., vol. 35, pp. 2537-2543.

Morikita, H., Hishida, K. & Maeda, M. 1995, Measurement of Size and Velocity of Arbitrarily Shaped Particles by LDA Based Shadow Image Technique, in Developments in Laser Techniques and Applications to Fluid Mechanics, Berlin, Springer-Verlag, pp. 354-375.

Morikita, H., Hishida, K. & Maeda, M. 1994, Simultaneous Measurement of Velocity and Equivalent Diameter of Non-spherical Particles, Part. Part. Syst. Charact., vol. 11, pp. 227-234.

Morikita, H. 1996, Ph. D. thesis, Keio University, Japan (in Japanese).
Morikita, H. & Taylor, A. M. K. P. 1998, Application of Shadow Doppler Velocimetry to Paint Spray: Potential and Limitations in Sizing Optically Inhomogeneous Droplets, Meas. Sci. Technol., vol. 9, pp. 221-231.

Naqui, A. A. & Fandrey, C. W. 1997, Phase Doppler Measurement of Irregular Particles and Their Inversion to Velocity-resolved Size Distributions, Proc. Fluids Engineering Division Summer Meeting, Vancouver, Canada.

Onofri, F., Blondel, D., Grehan, G. & Gousbet, G. 1996, On the Optical Diagnosis and Sizing of Spherical Coated and Multilayered Particles with Phase-Doppler Anemometry, Part. Part. Syst. Charact., vol. 13, pp. 104-111.

Petrak, D., Rosenfeld, K. & Przybilla, E. 1996, Optical Sizing of Particles for Measurements in Processes, Proc. 5th GALA Conference Laser Based Methods of Flow Measuring Technique, Berlin, pp. 32.1-32.5.

Reichel, A., Gerber, M., Schwartz, F. H. & Waggeling, R. 1998, In-Situ Particle Measurements in High Concentrations-a Novel Approach for Particle Measurement, Proc. 7th European Symposium Particle Characterization, Nürnberg, vol. II, pp. 561-570.

Sachweh, B., Heffels, C., Polke, R. & Rädle, M. 1998, Light Scattering for In-Line Measurement of Mean Particle Sizes in Suspensions, Proc. 7th European Symposium Particle Characterization, Nürnberg, vol. II, pp. 635-644.

Schneider, M. & Hirleman, E. D. 1994, Influence of Internal Refractive Index Gradient on Size Measurement of Spherically Symmetric Particles by Phase Doppler Anemometry, Appl. Opt., vol. 33, pp. 2379-2388.

Witt, W. & Röthele, S. 1998, In-line Laser Diffraction with Innovative Sampling, Proc. 7th European Symposium Particle Characterization, Nürnberg, vol. II, pp. 611-624.

Wriedt, T., Manasse, U. & Bauckhage, K. 1993, Deconvolution of PDA Size Distributions from Sprays of Optically Inhomogeneous Liquids, Proc. SPIE, vol. 2052, pp. 137-143.

A NEW LASER METHOD FOR AEROSOL CONCENTRATION MEASUREMENTS

G. Cognet* - P. Falgayrettes** - Y. Brenier*

*CEA
(Atomic Energy Commission)
DRN/DER - Bât. 212
CEA Cadarache - 13108 St. Paul Lez Durance - FRANCE
**CEM2 / Lincs - Case courrier 083
Université Montpellier II
Place E. Bataillon 34095 Montpellier

ABSTRACT

The classical optical methods for « in-situ » concentration measurements of aerosols are often limited to a narrow aerosol diameter range and are difficult to use in extreme or industrial conditions. Based on MIE scattering, these methods (diffraction or phase Doppler analysis) consist of diameter measurements by assuming that the aerosols are spherical. Then concentration calculations sometimes induce great inaccuracy. Moreover, to use such methods, at least two windows are needed.
In some specific applications such as nuclear safety, it is difficult and sometimes impossible to use these techniques. Therefore, we here propose a new measurement method based on the LIDAR technique coupled with Laser Induced Fluorescence (LIF).
This method offers some advantages :

- The chemical compound whose concentration is interesting, can be selected in the flow;
- Only one window is required;
- Resolution can be high as they only depend on laser characteristics;
- Instantaneous measurements are obtained on a line (1D);
- Extension to 2D and 3D measurements is easy.

This paper describes the basis and the limits of the method, the experimental set-up and the tests conducted to confirm the validity of the method.

1. INTRODUCTION

Due to the increase of pollution and industrial risks, the request for concentration field measurements is currently very strong. Therefore, various industries (chemistry, thermal and nuclear energy production, transport, insulation products, waste,...) are trying to develop measurement methods to improve their fabrication processes or to reach the authorized levels.
As regards nuclear engineering, in the event of a highly unlikely core melt-down accident in Pressurized Water Nuclear Reactor (PWR), scenarios in which the reactor pressure vessel fails and the core melt mixture (called corium and essentially composed of molten UO_2, ZrO_2, Zr, Fe and fission products) relocates into the reactor cavity cannot be excluded. In this context, large R&D efforts within the European Union are currently directed towards ex-vessel corium behaviour with particular emphasis on long-term corium retention and coolability in order to keep it in the containment. There are various so-called core-catcher concepts for future reactors under investigation in order to prevent basemat erosion and to stabilize and control the corium within the containment.
Whatever the concept, the interaction between corium and substratum materials induces aerosol release which can promote or inversely limit thermal radiation and consequently play an important role in ablation process.

The Reactor Studies Department (DRN/DER) of the French Atomic Energy Commission (CEA) has undertaken an experimental program, named AEROSTAT, in order to study corium thermal radiation through aerosols under representative conditions. A pool of a small amount of corium (< 3

kg) composed of real materials : depleted UO_2, ZrO_2, Zr and Fe reacts with a substratum composed of concrete. The high corium temperature (up to 3000K) induces strong thermal radiation and the release of aerosols.
To improve the understanding of the key phenomena, « in-situ » aerosol concentration measurements are needed.

The classical optical methods (see for example : Levy (1990), Martin et al. (1990), Ibrahim & Bachalo (1994), Brenn et al. (1994)) for such measurements are often limited to a narrow size range and difficult to use in extreme or industrial conditions. Based on MIE scattering, these methods (diffraction or phase Doppler analysis) consist of diameter measurements by assuming that the aerosols are spherical; then concentration is calculated sometimes inducing great inaccuracy. Moreover, to use such methods, at least two windows are needed.
Therefore, we here propose a new measurement method based on the LIDAR technique coupled with Laser Induced Fluorescence (LIF) which can potentially give the concentration of a constituent whatever their number and the phase (liquid or gas).

2. PRINCIPLE

The developed method is based on the LIDAR technique and laser induced fluorescence (LIF) used together in a special arrangement.
An ultra-short laser pulse is used to induce the fluorescence of the chosen compound. As in the LIDAR technique, it is possible to determine the position and the concentration of different samples in the flow.

Figure 1 shows the theoretical diagram of the method.

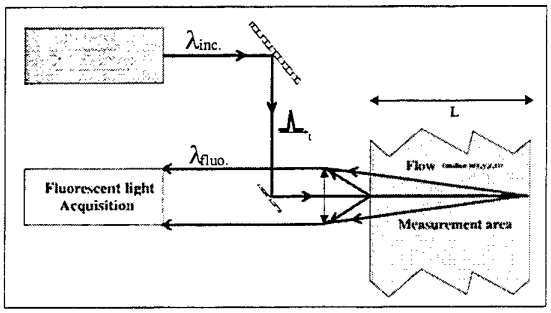


Figure 1 : Principle of the developed method.

To obtain a measurement, a tunable laser pulse is sent through the flow. All the molecules of the selected constituent which are on the laser path are excited at different times. These times obviously depend on the spatial location of the molecules, thereby the energy of the light fluoresced by each molecule is time shifted.
Therefore, in the case of a measurement of the concentration of a dispersed phase in a multiphase flow with a classical Lidar configuration, the signal given by a detector located besides the laser is composed of bursts due to the fluorescence of the dispersed constituent. The magnitude and the time location of these bursts represent the concentration of the dispersed constituent in a specific location of the flow.
With only one pulse, the system gives the concentration of the dispersed component all along pulse travel.
The sampling rate of the signal determines the spatial resolution/accuracy of the measurement. To obtain a high resolution (one millimeter) the sampling rate must be increased ($3.3\ 10^{-12}$ s / sample). A standard LIDAR set-up is limited by the electronic characteristics of detectors and by maximum sampling speed (resolution : 1 sample / 100 meter).
To overcome this problem, an optical-electronic sampling method has been developed by Falgayrettes (1996).

If we consider that e(t) is a time varying optical signal of duration T that represent the fluorescent signal :

$$e(t) = \begin{cases} 0 & if \quad t < 0 \\ e(t) & if \quad 0 \le t \le T \\ 0 & if \quad t > T \end{cases}$$

Δt is the sampling rate needed to determine the signal $e(t)$. The number of samples N that have to be acquired is :

$$N = \frac{T}{\Delta t}$$

As used in the standard Lidar, a single detector can be used, but the rising and falling edge of this detector limits the sampling frequency.
Another solution consists of employing N similar detectors in which the sampling time is shifted by Δt for each detector. Because it is not easy to make such a device when N is large, it seems more interesting to use a linear Charge Coupled Device (CCD) which has many similar detectors. The main difficulty of the classical linear array is that it is impossible to acquire

the signal on each photodetector at different times. The order of exposure control, or shuttering, is the same for all the photodetectors.

Given the constraints of a standard linear CCD, we need to modify the previous acquisition scheme by using a set of optical delay lines as shown in Fig. 2. The input light is simply integrated for different duration at each photodetector (Fig. 3).

A photodetector *'i'* receives an amount of energy equal to :

$$E_i = \int_{-\infty}^{\tau} e_i(t).dt \qquad with\ \tau = i.\Delta t$$

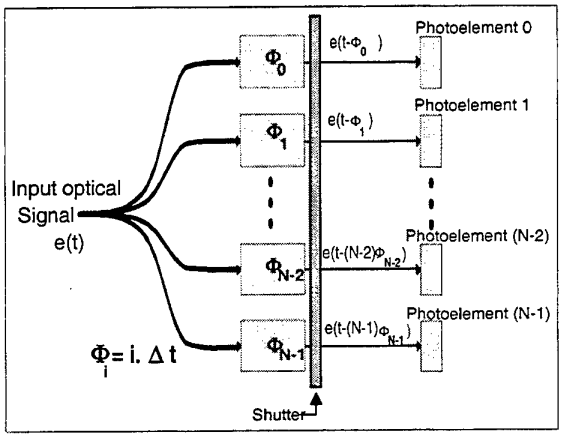


Figure 2 : Time/spatial domain conversion by adding different delays to the signal received by each detector.

Now, it is possible to write the time evolution of the energy received on the i^{th} photodetector as :

$$e_i(t) = e(t - i.\Delta t)$$

All the detectors are exposed for the same duration θ. In theory, θ may be equal to the input signal duration T (see Fig. 3).

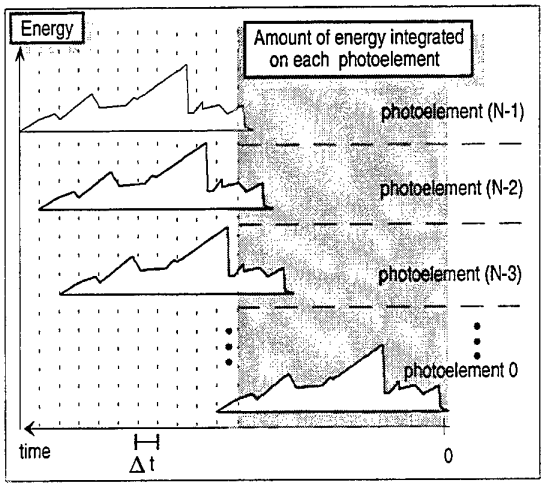


Figure 3 : Different parts of light signal integrated by each photodetector.

For the first photodetector *'0'*, which has no delay :

$$E_0 = \int_0^{\theta=T} e_0(t).dt = \int_0^{T} e(t).dt$$

For the second photodetector *'1'* with a delay of Δt :

$$E_1 = \int_0^{\theta=T} e_1(t).dt = \int_0^{T} e(t - \Delta t).dt$$

For the i^{th} photodetector with a delay of $i.\Delta t$:

$$E_i = \int_0^{\theta=T} e_i(t).dt = \int_0^{T} e(t - i.\Delta t).dt$$

And for the last photodetector *'N-1'*, with a delay of $(N\text{-}1).\Delta t$:

$$E_{N-1} = \int_0^{\theta=T} e_{N-1}(t).dt = \int_0^{T} e\big(t - (N-1).\Delta t\big).dt$$

Thus, on each photodetector the energy recorded represents the input light integrated for different duration. To find the input signal simply requires calculating the difference between the energy recorded by two successive photodetectors, as shown in Fig. 4.

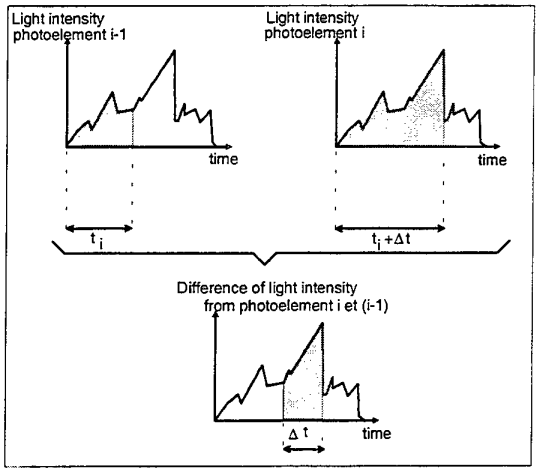


Figure 4 : Difference in energy integrated between adjacent detectors.

It is possible to write this as :

$$\Delta E_k = E_{k-1} - E_k = \int_0^{\theta=T} \left[e_{k-1}(t) - e_k(t)\right].dt$$

$$\Delta E_k = \int_0^{(k+1).\Delta t} e(t).dt - \int_0^{k.\Delta t} e(t).dt = \int_{k.\Delta t}^{(k+1).\Delta t} e(t).dt$$

In this way, all the samples of the incident light signal are known, and the input signal can be rebuilt.

3. TIME/SPACE DOMAIN CONVERSION

The optical sampling system is composed of three distinct parts (see Fig. 1) : a series of detectors, a shutter and a set of optical delay lines.
The CCD has a good sensitivity, a large number of photodetector, a good uniformity of light response, and has an integrated electronic shutter.
The optical delay lines can be made by various methods.
The solution used in the present work consists of using different lengths of optical fiber. The difference in length between adjacent fibers creates the delay and represents the sampling rate. By using a difference in length between neighboring fibers of between *1 mm* and *10 mm*, a variable resolution sampling system was obtained (of *5 ps* to *50 ps*).
All the optical fibers receive the signal to be analyzed at their inputs. The output is imaged onto a photodetector of the CCD as shown in Fig. 5. The main advantage of these delay lines is that it is possible to obtain any duration of analysis. For example, we have reached an analysis duration of *4.15 ns*, which corresponds to a total difference in fiber length of *90 cm*.

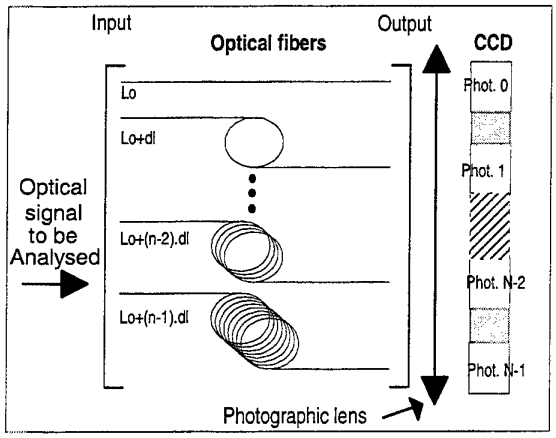


Figure 5 : Delay lines with optical fibers.

In the prototype converter developed, the delay set consists of 43 optical fibers and a 2048 photodetectors CCD (each element being *13x500µm* in size). The optical fibers have a core diameter of *500 µm* and are mounted in line without space between them. The outputs of the optical fibers are imaged onto the CCD through a *28 mm* photographic lens (See Fig. 5). The image of one fiber end covers 7 photoelements. The inputs of the optical fibers are grouped together in concentric circles (starting from one end of the array) to form a disc like the surface of a single detector (*10 mm* diameter).
The electronic shutter integrated on the CCD provides an exposure of *40 ns*, with a fall time of *3 ns*.

The following equation gives the energy of the fluorescent light received by the N detectors corresponding to the analysis length :

$$E_{\text{received}}(t) = \sum_{i=0}^{N-1} dE_{\text{received } z_i}(t)$$

$$E_{\text{received}}(t) = \sum_{i=0}^{N-1} \pi\left(t - \frac{z_i}{\bar{v}_i}\right) \otimes c_{z_i}\left(t - \frac{z_i}{\bar{v}_i}\right)$$

in which $\pi(t)$ is the shape of the laser pulse and $c_z(t)$ is the concentration of the fluorescent compound in

the flow. z_i is the location of the "i" burst in the analysis length. $\overline{v}_i$ is the average light speed in the flow.
Thanks to N subtractions between the signals recorded by the detectors "i" and"$i+1$", the energy corresponding to the "i" burst $dE_{recieved\ z_i}(t)$ is deduced.
Then, the inversion of the equation gives the concentration field.

The main features of the method are :

- non-intrusive;
- non-dependent on aerosol shapes;
- only one window is needed;
- a analysis depth of about one meter with a resolution of one millimeter if a saphir-titan laser is used;
- potentiality of measuring the concentrations of several constituents of the same flow.
- potentiality of 3D measurement.

However, this method requires a tunable laser which delivers extremely short pulses.

4. RESULTS

Because we used a YAG laser whose pulse length is 30 ns, the first experiments were carried out with an experimental set-up enabling an analysis depth of 20 m.
The objective of such a set-up was only to check the theoretical basis of the method and to qualify it with an available laser.
With such a laser, whose pulses have a rising edge equal to 7.8 ns, the resolution is 2.34 m. Therefore, to have a significant number of measurements, it is necessary to increase the analysis depth.
The experimental setup (see figure 5) is composed of 40 aerosol generation nozzles fed in water with a pressurized tank and located at equal distances along the feeding tube. Fluoresceine was added to water.

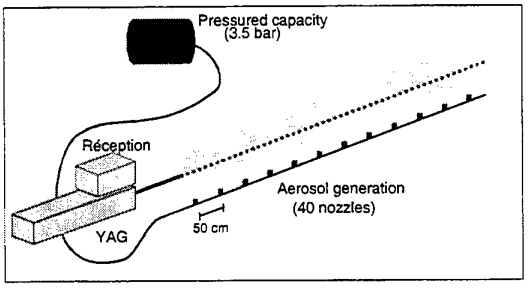


Figure 5 : Experimental set-up

The experiments were performed outside and only at night to minimize the error term due to the fluorescent light resulting from daylight excitation.

Two kind of results are presented :

- Measurements performed when all the nozzles are active;
- Measurements performed when only some nozzles are inactive.

Measurements with uniform concentration :
Figure 6 shows the fluorescent energy received when the nozzles are active on the whole analysis depth (20 meters).

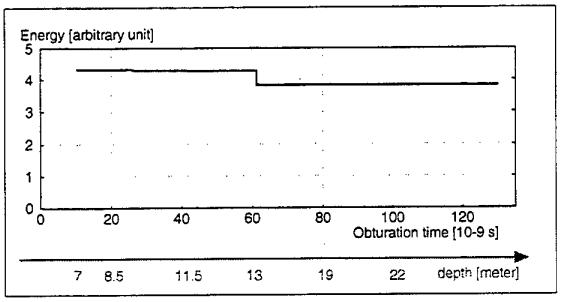


Figure 6 - Concentration evolution versus analysis depth (all nozzles active).

Measurements with variable concentration :
The curve represents the energy of fluorescent light. A hole 2 meters long appears and corresponds to the area inside closed nozzles n°5 to n°8 (See Fig. 7).

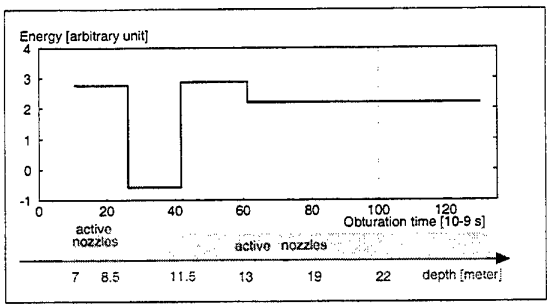


Figure 7 - Concentration evolution versus analysis depth (nozzles n° 5 to n° 8 closed).

These results show that it is possible to determine the location of the area without aerosols.
The two curves exhibit an energy variation at about 13 m which does not correspond to a variation in

aerosol concentration. This seems due to the compensation of the angle under which measurement volumes are viewed; at such distances, this compensation should be improved.
The spatial accuracy for the positioning of the bursts is satisfactory.

5. CONCLUSIONS

The concentration measurement method developed in this work gives very satisfactory results. The experimental set-up and the laser used are not the best choice to obtain high spatial resolution, nevertheless the validity of the method has been demonstrated.
Other tests are needed, they will be performed with a more convenient laser in order to reach the resolution given by theory (picosecond or femtosecond laser like MIRA 900 Coherent SA).
After this development phase, this method should be used in the AEROSTAT facility to measure the aerosol concentration due to corium concrete interaction.

ACKNOWLEDGMENTS:

The authors wish to acknowledge Mr J-L Tapie (Coherent SA France) and J. Stefanini (Imagine Technologie France) for their contribution to this work.

REFERENCES

G. Brenn & al. : «Investigation of polydisperse spray interaction using an extended phase Doppler anemometer» 7th International Symposium on applications of laser techniques to fluid mechanics. Lisbonne 1994.

K.M. Ibrahim & W.D. Bachalo : «Time-Frequency analysis and measurement accuracy in laser Doppler and phase Doppler Signal Processing Applications. 7th International Symposium on applications of laser techniques to fluid mechanics. Lisbonne 1994.

Y. Levy :«Back scattered phase Doppler anemometry (PDA) for spray diagnostics» Symp. on applications of laser techniques to fluid mechanics. Lisbonne 1990.

S.R. Martin & al. : «Resolution limits of the phase Doppler technique and its extension to monitor non ideal particles in two phase flows» Symp. on applications of laser techniques to fluid mechanics. Lisbonne 1990.

P.Falgayrettes : «Elaboration d'une méthode de mesure de champs de concentrations instantanés». PhD Thesis of the University of Aix-Marseille II may 1996.

RAINBOW THERMOMETRY WITH A PULSED LASER

J.P.A.J. van Beeck and M.L. Riethmuller

von Karman Institute for Fluid Dynamics
Chaussée de Waterloo 72, B-1640 Rhode-Saint-Genèse, BELGIUM
(32) 2-359.96.11 (Phone) (32) 2-359.96.00 (Fax)

ABSTRACT

Rainbow thermometry with a pulsed laser is presented. Like classical rainbow thermometry, it is a non-intrusive technique able to measure simultaneously droplet size and temperature of a spherical transparent particle. The problem of signal blurring due to droplet oscillation during the acquisition time is solved by replacing a CW laser by a pulsed one. It strobes the droplet with one short pulse of laser light and therefore freezes the vibrating rainbow pattern, thus ensuring a detection of clear rainbow interference structures. Preliminary experiments on a single falling droplet and on a water spray have been performed and optimum signal quality is obtained. As a result, measurement precision is enhanced.

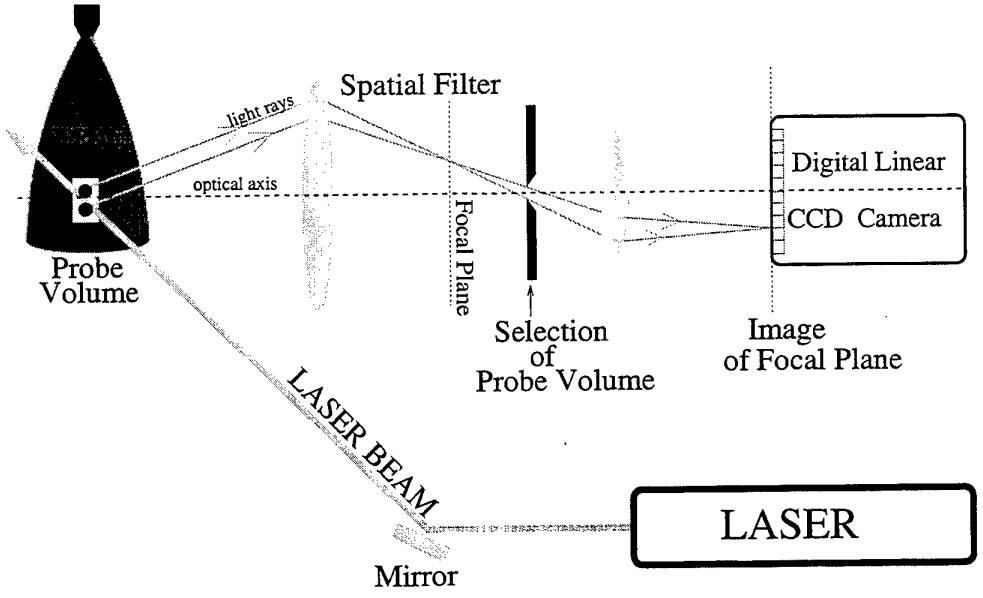


Fig. 1 Outline of the optical configuration for classic rainbow thermometry for measuring droplet size and temperature in a liquid spray. The spatial filter selects a measurement volume containing a single droplet. The second lens assures that the position of the rainbow on the sensitive area of the camera does not depend on the position of the droplet in the measurement volume.

1. CLASSIC RAINBOW THERMOMETRY

Since several years, experimental results on classic rainbow thermometry have been reported by Roth et al. (1988, 1991), Sankar et al. (1993) and Van Beeck and Riethmuller (1994a, 1995). Rainbow thermometry has already been applied with success to fuel combustion research by Sankar et al. (1996).

Classic rainbow thermometry is a non-intrusive technique for measuring simultaneously size and refractive index of a single droplet, a transparent particle or cylinder. From the refractive index, the temperature can be derived provided the empirical relationship between both quantities is known. The development of the rainbow technique is placed at the forefront of innovation in optical diagnostics of particles and droplets.

Classic rainbow thermometry (or shortly the rainbow technique) is based on the detection of laser light scattered by a single transparent scatterer. An outline of a conventional experimental setup is given in Figure 1. A CW laser beam illuminates an ensemble of droplets (in case of a liquid spray). A spatial filter selects a single droplet, alike in e.g. LDV. By placing a (linear) CCD camera at focal distance of the lens system, one observes the angular scattered light distribution coming from this one selected droplet. Provided the range of scattering angles is well chosen, a part of the primary rainbow can be seen, corresponding to the rainbow that is normally seen in the sky. In fact, because the particle is illuminated by laser light, only one coloured band corresponding to the colour of the laser beam is detected. Figure 2 shows such a monochromatic primary rainbow. Because this rainbow was originated by a water droplet, the camera was focused around a scattering angle of 138°.

1.1 Airy Fringes

A 2D monochromatic rainbow pattern reveals various supernumerary bows, also known as Airy fringes. These fringes originate from optical interference between rays having experienced one internal reflection inside the droplet. The bows are rarely visible in the rainbow in the sky due to four reasons. First of all, the sun beams have a range of incidence angles of about 0.5°, simply because of the finite size of the sun with respect to the distance sun-earth. This counteracts the visibility of the fringes. Secondly the diffraction of the imaging system is a disadvantage for signal clearness. The third reason is the superposition of the different colours and the fourth one is the fact that the droplet size distribution in a rain shower is poly-disperse. The latter reason implies that the distance between the various bows is a function of droplet diameter. By employing a collimated laser beam as light source and by recording a single droplet at the same time, one should normally avoid all the problems that are associated with the detection of the supernumerary bows in the sky.

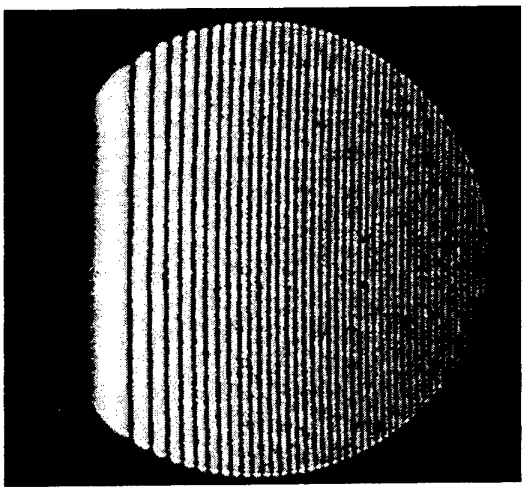


Fig. 2 A monochromatic primary rainbow pattern coming from a single water droplet, illuminated by a CW laser beam. The picture is taken by an ordinary camera having a finite shutter time. The supernumerary bows (Airy fringes) are clearly visible.

Because the pattern of Figure 2 is quasi mono-dimensional, it is logical to analyze it along one cross section. Figure 3 shows such a cross section which is used for signal processing.

Van Beeck and Riethmuller (1994a, 1995) explains that from the Airy fringe spacing the droplet diameter can be derived without preliminary knowledge of the refractive index. Therefore, the Airy theory for the rainbow is employed, developed by G.B. Airy (1838). In fact, the so-called Airy diameter D_{Airy} is proportional to the Airy fringe-spacing to the power -3/2. Once the droplet size is know, the refractive index is determined from the absolute angular position of the interference pattern, again using the theory of G.B. Airy (1838).

This pattern shifts uniformly for about 1.5° when the refractive index changes by 0.1. Knowing the relationship between refractive index and temperature, the latter can be deduced subsequently. In particular, the angular shift of the rainbow equals 1° when the water temperature changes 40°C. For fuel droplets, the 1° angular shift is already observed for a temperature difference of 20°C.

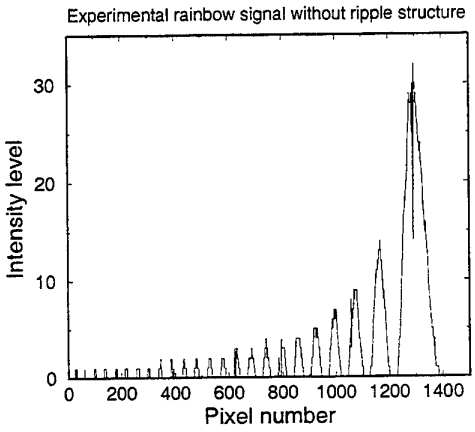


Fig. 3 A typical 1D rainbow signal (recorded by a digital linear CCD camera) showing the Airy fringes. No fine structure are superimposed on these fringes.

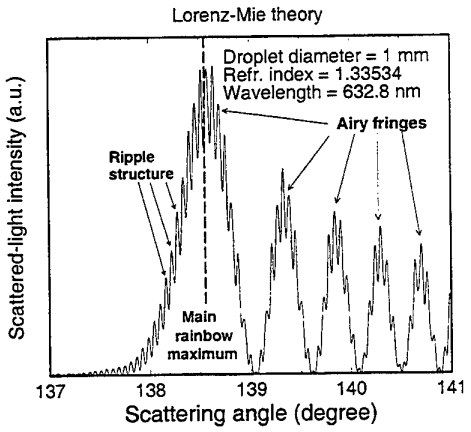


Fig. 4 Simulation by Lorenz-Mie theory of a 1D monochromatic rainbow signal. A ripple structure is superimposed on the Airy rainbow pattern.

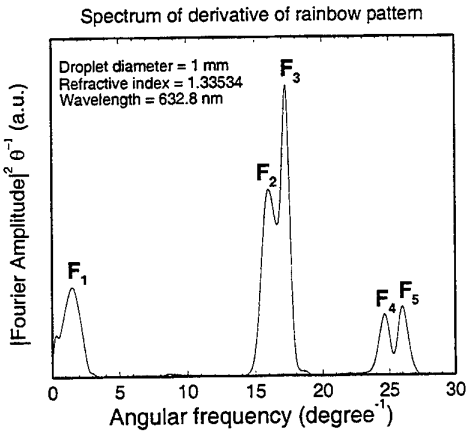


Fig. 5 Derivative of the spectrum of the simulated rainbow pattern shown in Figure 4. Peak F_1 corresponds to the Airy fringes. The ripple structure is represented by peaks F_2 and F_3 . The peaks F_4 and F_5 are not considered in the present paper.

1.2. Ripple Structures inside the Rainbow

A signal like that of Figure 3 can be simulated by the Lorenz-Mie theory (G. Mie 1908). The result is presented in Figure 4. The derivative of the spectrum is shown in Figure 5. The fact that the derivative is presented, is only to bring the amplitudes of the peaks in the same order of magnitude; there is no effect on the frequency of the spectrum. The various peaks are labeled from F_1 to F_5. As the experimental signal, the simulation contains Airy fringes (i.e. supernumerary bows), labeled by F_1 in the power spectrum. But in addition to those fringes, a ripple structure is seen that was not visible in the experimental rainbow pattern (Figure 3). This ripple structure is represented in the spectrum by the peaks labeled from F_2 to F_5. Peaks F_2 and F_3 are the result of optical interference between external and internal reflection of the laser light that was scattered by the droplet surface. Peaks F_4 and F_5 are not discussed here.

As for the Airy fringes, the ripple structure can be related to the droplet diameter. Consequently, a so-called ripple diameter, D_{ripple}, can be deduced and appears to be almost proportional to the reciprocal of the spacing between the ripple fringes, as described by Van Beeck and Riethmuller (1994b, 1996b). The

additional manner for droplet sizing through the ripple structure improves both size and temperature determination following Van Beeck and Riethmuller (1996a). But in order to achieve this improvement, one has to be able to detect this fine structure, requiring optimum signal visibility. This is also a necessity to establish advanced validation criteria in order to recognize a proper rainbow signature.

2. WHY USING A PULSED LASER?

Often the ripple structure, and sometimes even the Airy fringes in the rainbow pattern are blurred, even when optimum conditions for laser illumination are assured. Signal blurring decreases the accuracy in size and temperature measurement by rainbow thermometry.

2.1. Transient Events

The reasons for signal blurring are the transient events occurring when the droplet traverses the laser beam. A transient event is for example the rapid evaporation of a fuel droplet in a combustion spray, causing a rapid decrease in droplet diameter. Another transient event is droplet oscillation, causing a rapid change is droplet shape; it is this event that has to be considered in the experiments presented here, all carried out at ambient temperature.

One has to realize that the phase of the ripple structure changes already 90^{o} when the surface of the droplet deviates from the spherical shape only by a fraction of the wavelength of the laser light. Therefore, it is plausible to believe that the ripple structure will disappear when the rainbow pattern vibrates due to droplet oscillation. Because of the finite shutter time of the CCD camera, the interference structures will simply be averaged out in a certain extent, depending on the shutter time, the droplet oscillation time and amplitude.

2.1. Overcoming Transient Events

Van Beeck and Riethmuller (1997a) first proposed a solution to the signal blurring by attacking the problem on the side of the detector. The CCD camera is replaced by a photomultiplier that is positioned, out of focus, directly behind an additional pin hole. Consequently, a time-varying rainbow signal is detected because the rainbow interference structures move in front of this second pin hole when the droplet traverses the laser beam. Experimental rainbow signals in a full-cone water spray have been recorded, always showing the ripple structure. In spite of this positive result, signal processing appears to be complicated because in this configuration the fringe spacing does not only depend on droplet size but also on the droplet velocity, thus reducing the measurement accuracy.

J.P.A.J. van Beeck (1997b) describes an alternative solution to the signal visibility problem. It tackles the visibility problem from the emitter side, leaving the rainbow receiver unchanged. By strobing the droplet by pulsed instead of C.W. laser light, one freezes the rainbow pattern at one instant of time provided the pulse duration is much shorter than the characteristic time constant of the transient event. A frozen rainbow pattern means that, in theory, the signal visibility should be optimum. In the following section preliminary results are presented showing the success of the proposed alternative solution to the visibility problem.

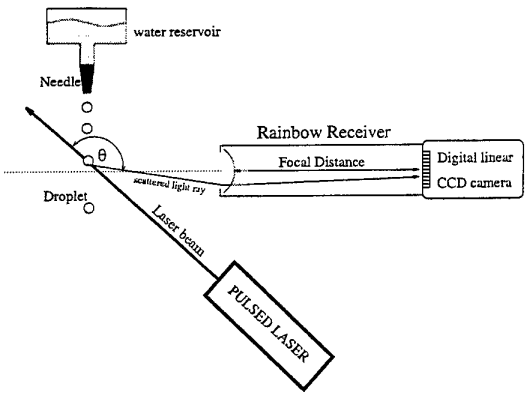


Fig. 6 Experimental layout for the preliminary rainbow experiments with a pulsed laser. The liquid used is water at ambient temperature. The needle produces single falling droplets by hydrostatic pressure.

3. EXPERIMENTAL RESULTS

Preliminary experiments have been carried out with the simplified setup depicted in Figure 6. The spray in the setup, that was introduced in

Figure 1, is replaced by a simple needle generating a stream of falling droplets by a certain hydrostatic pressure. As a consequence, a single droplet crosses the laser beam at the same time, enabling the omission of the spatial filter. The linear CCD camera is placed at the focal distance of a single plano-convex lens, making the position of the rainbow at the camera independent of the position of the droplet in the laser beam. The experiments are carried out with water at ambient temperature.

Another difference between the setup of Figure 1 and that of Figure 6 is the laser. A Ruby laser is used generating laser pulses of 30 ns at a wavelength of 694 nm. The energy per pulse is 100 mJ for a beam diameter of 40 mm. This energy is largely sufficient for a proper detection of the rainbow pattern with an ordinary CCD camera even when the droplet diameter is much smaller than 100 μm. Moreover, it is important to realize that the absorption of the Ruby laser light by the water droplet heats up the droplet by only a negligible fraction of a degree Kelvin.

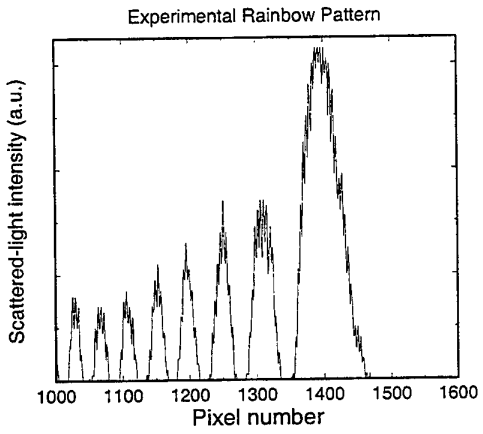


Fig. 7 Experimental rainbow pattern detected by the setup with the pulsed laser depicted in Figure 6.

3.1 Experiments with a Single Falling Droplet

Figure 7 shows an experimental rainbow signal resulting from pulsed laser-light illumination of a single falling water droplet. The signal is recorded by the digital linear CCD camera IDC100 (company I2S). The Airy fringes and the ripple structure are clearly visible. From the power spectrum (Figure 8), taken over the first three Airy fringes, it is shown that the high frequency component in the rainbow signal indeed resembles the ripple structure because two closely-spaced peaks appear that compare well with the peaks F_2 and F_3 of the theoretical predictions (Figure 5).

These experiments are the first of its kind and show that the use of a pulsed laser is a solution to the visibility problem.

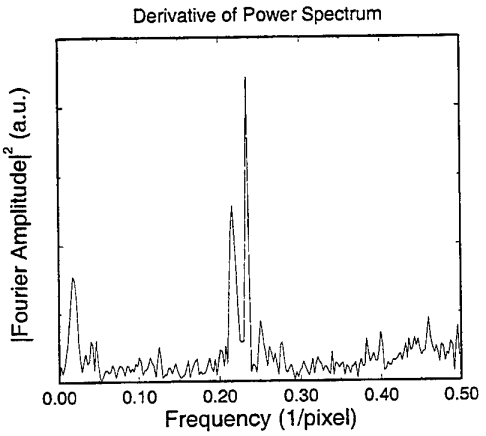


Fig. 8 Derivative of the spectrum of the rainbow pattern shown in Figure 7. Three peaks are visible, corresponding to the Airy fringes and the ripple structure.

3.2 Preliminary Experiments in a Water Spray

Additional preliminary experiments in a water spray were performed with the experimental setup of Figure 1, except that the CW laser was replaced by a pulsed one. Moreover, the camera IEC800 BC (company I2S), having a 2D CCD array, was employed. The purpose of these experiments was to examine whether the ripple structure is visible for a rainbow in a water spray. The result is shown in Figure 9. It depicts a beautiful primary-rainbow pattern, showing clearly the Airy fringes and the ripple structure. A rainbow signal of such quality has never recorded before as far as an isolated droplet in a liquid spray is concerned. It opens new ways to define validation criteria and therefore reveals a enormous potential for increasing precision in droplet size and temperature measurements and thus for establishing confidence in the rainbow technique.



Fig. 9 A 2D image of the rainbow pattern coming from a droplet inside a spray, illuminated by a pulsed laser. The image is recorded by a 2D CCD camera. Airy fringes and ripple structure are well visible.

4. CONCLUSIONS

It has been shown that the use of a pulsed laser in rainbow thermometry has solved the problem of signal blurring due to transient events, such as droplet oscillation and/or deformation. The laser-light pulse freezes the vibrating rainbow pattern. This ensures optimum visibility for all rainbow interference structures provided the light flash is much shorter than the characteristic time constant of the transient event. Consequently, the finite integration time of the CCD camera will no longer deteriorate the signal quality.

Experimental evidence has been given by recording the primary rainbow by a linear and a 2D CCD camera, for a single falling water droplet and a spray, respectively. Unique signal clearness has been obtained. This should improve the measurement accuracy and provide new possibilities for signal validation.

In the future, validation experiments will be carried out by a novel rainbow apparatus, constructed at the von Karman Institute for Fluid Dynamics. The droplet size measurements will be compared to those of a phase-Doppler anemometer and the measured temperature has to be the ambient one.

ACKNOWLEDGMENTS

The authors thank F. Giuliani for carrying out most of the experiments presented in this paper.

REFERENCES

N. Roth, K. Anders, and A. Frohn 1988, Simultaneous measurement of temperature and size of droplet in the micrometer range, 7th International Congress on Optical Methods in Flow and Particle Diagnostics ICALEO 88, L.I.A. (Sunnyvale U.S.A.), vol. 67, pp. 294-304.

N. Roth, K. Anders, and A. Frohn 1991, Refractive-index measurements for the correction of particle sizing methods, Applied Optics, vol. 30, no. 33, pp. 4960-4965.

S.V. Sankar, K.H. Ibrahim, D.H. Buermann, M.J. Fidrich, and W.D. Bachalo 1993, An integrated phase doppler/rainbow refractometer system for simultaneous measurement of droplet size, velocity, and refractive index, The Third International Congress on Optical Particle Sizing (Yohokama, Japan), August 1993, pp. 275-284.

J.P.A.J van Beeck and M.L Riethmuller 1994a, Simultaneous determination of temperature and size of droplets from the rainbow using Airy theory, Proc. of the 7th International Symposium on Applications of Laser Techniques to Fluid Mechanics (Lisbon, Portugal), vol. 2, pp. 21.5.1-21.5.6., also in "Developments in Laser Techniques and Applications to Fluid Mechanics", R.J. Adrian et al. (eds.), Springer, pp. 330-339.

G.B. Airy 1838, On the intensity of light in the neighbourhood of a caustic, Trans. Camb. Phil. Soc., vol. 6, pp. 379-402.

G. Mie 1908, Beitrage zur Optik Trueber Medien speziell kolloidaler Metalloesungen, Ann. Phys., vol. 25, pp. 377-445.

J.P.A.J. van Beeck and M.L. Riethmuller 1995, Nonintrusive measurements of temperature and size of single falling raindrops, Applied Optics, vol. 34, no. 10, pp. 1633-1639.

S.V Sankar, D.H. Buermann, and W.D. Bachalo 1996, An advanced rainbow signal processor for improved accuracy in droplet temperature measurements, 8th International Symposium on Applications of Laser Techniques to Fluid Mechanics (Lisbon, Portugal) vol. 1, pp. 9.3.1.-9.3.9.

J.P.A.J. van Beeck and M.L. Riethmuller 1994b Détermination non-intrusive de la dimension et de la température des gouttes dans une pulvérisation, Recueil des actes du 4e Congrès francophone de Vélocimétrie Laser, Poitiers, France, pp. 2.2.1-2.2.8.

J.P.A.J. van Beeck and M.L. Riethmuller 1996a, Rainbow phenomena applied to the measurement of droplet size and velocity and to the detection of nonsphericity, Applied Optics, vol. 35, no. 13, pp. 2259-2266.

J.P.A.J van Beeck and M.L. Riethmuller 1996b, A single-beam velocimeter based on rainbow-interferometry, Proc. of the 8th International Symposium on Applications of Laser Techniques to Fluid Mechanics, (Lisbon, Portugal), vol. 1, pp. 9.1.1-9.1.6, also in "Developments in Laser Techniques and Applications to Fluid Mechanics", R.J. Adrian et al. (eds.), Springer.

J.P.A.J. van Beeck and M.L. Riethmuller, 1997a, Particle and Particle Systems Characterization, vol. 14, pp. 186-192.

J.P.A.J. van Beeck 1997b, Rainbow phenomena: development of a laser-based, non-intrusive technique for measuring droplet size, temperature and velocity, Ph.D. thesis, Eindhoven University of Technology, The Netherlands.

SESSION 19

AERODINAMIC FLOWS

LDV-MEASUREMENTS ON A HIGH-LIFT CONFIGURATION WITH SEPARATION CONTROL

F. Tinapp, W. Nitsche

Department of Aeronautics and Astronautics
Technische Universität Berlin, Germany

ABSTRACT

The flow field around a 2D-high-lift con Figuration with active separation control has Been investigated by using LDV. The test Models a two element high-lift configuration, was equipped with an excitation mechanism inside the trailing edge flap to generate periodical flow excitation near the flap leading edge. A reattachment of the flow was achieved at various excitation frequencies and amplitudes.

1. INTRODUCTION

Modern transport aircraft wings have to provide very high lift-coefficients in low speed flight during take-off and landing. This leads to good payload/range capabilities for a given field length and a reduction of the noise footprint in the airport area. Therefore high-lift systems are of complex mechanics, generally consisting of a combination of leading-edge slats and multiple trailing-edge flaps. At high angles of attack the flow over high lift wings may separate, resulting in a lift reduction and in an increase of drag. If the onset of separation could be delayed towards a higher angle of attack, it will either be possible to achieve a higher lift or to reduce the complexity of the high-lift system (Fig. 1).

Recent investigations showed clearly that periodic excitation of the separated shear layer results in a partial reattachment and therefore in an increase of lift and decrease of drag (Hsiao et a.(1990), Dovgal (1993) and Seifert et a.(1996)). The present paper investigates this problem and deals with experiments aimed on the separation control via excitation of the separating boundary layer on the flap.

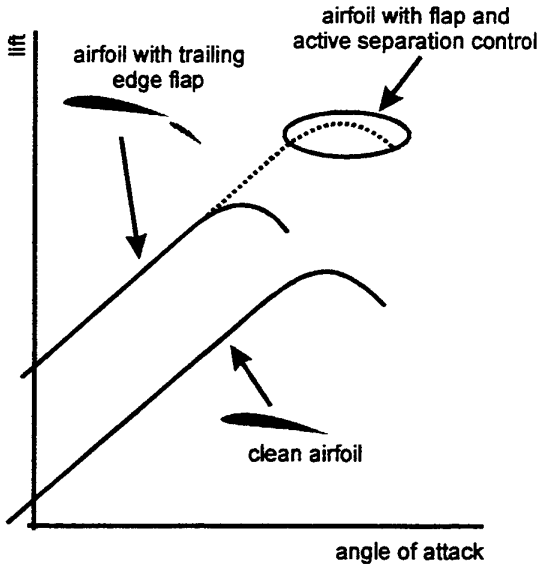


Fig 1: Schematic behaviour of the lift against angle of attack with and without active separation control

2. EXPERIMENTAL APPARATUS

The test model was a generic two element high-lift configuration, consisting of a 100 mm chord length NACA 4412 main airfoil and a NACA 4415 flap with 40 mm chord length. The flap was mounted at a fixed position underneath the trailing edge of the main airfoil, thus forming a gap of 3.5 mm height with an overhang of 2.8 mm (Fig. 1a). In accordance with the experiments made by Adair & Horne (1989), the angle of attack of the main airfoil was chosen to be fixed at 8° while the flap-angle α_{Flap} could be varied from 20° to 50°. With this configuration the flow over the main airfoil was still completely attached but separated over the flap at higher flap angles. To ensure turbulent separation of the flow, turbulators were placed close to the leading edge of the main airfoil and the flap.

For dynamic excitation of the separated shear layer over the flap, a pressure chamber was installed inside, with a 0.3 mm wide slot at 3.5% chord length (Fig. 1b).

A water cooled rotating valve was propelled by a electrical drive and was connected to a high-pressure pump. With this excitation apparatus it was possible to generate pressure pulses of varied frequency and amplitude. These externally generated pressure pulses were fed into the flap of the test model by pressure tubes, resulting in flow

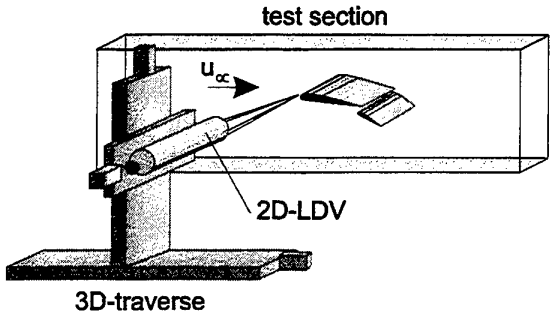


Fig. 3: 2D-Laser-Doppler-Velocimeter mounted on a 3D-traverse system

oscillations emanating vertically from the narrow slot near the leading edge of the flap.

All experiments were carried out in a closed water tunnel, equipped with a test section made of glass with the dimensions (l x h x w) 1250 x 330 x 255 mm. The maximal achievable flow speed was 6 m/s and the mean level of turbulence was about 4%. Flow field measurements were made by means of a two component laser doppler system (Polytec LDV-580), connected with two fast fourier real-time analysers (Aerometrics RSA-1000). To allow automatic measurements of the complete flowfield, the laser optic was mounted on a 3D computer controlled traverse system (Fig. 3).

The flow speed of the present test was 1.5 m/s, resulting in a chord Reynolds number of 150.000, calculated with the flap chord of 100 mm as characteristical length.

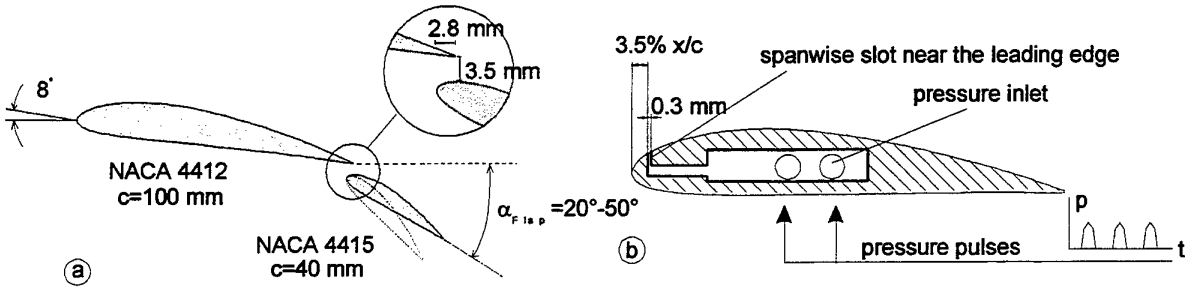


Fig.2: a) Two element high-lift configuration with fixed gap geometry
b) Flap, equipped with a pressure chamber and a narrow slot near the leading-edge

3. EXPERIMENTS

3.1 Mean Flow

For a general investigation of the flow field around the high-lift configuration at different flap deflections, extensive laser doppler measurements were undertaken. The flap deflection was varied between 20° and 50° in order to proof the separation behaviour of the configuration. Here the flow separated at α_{Flap} of about 30° forming a very small recirculation area near the trailing edge of the flap. With an increase of the flap angle, the separation point moved upstream and the flow separated at the leading edge of the flap, resulting in a big recirculation area. As an example of these measurements the velocity vector plots are shown in figure 4. In fig 4a and 4b the velocity field around the complete configuration can be seen while the fig 4c and d present the obtained results near the flap. In case of the α_{Flap}=27° (fig 4a, 4c) the flow over the flap remained attached over the flap while the flow near the trailing edge of the main airfoil tended to separate. The Increase of the flap deflection angle to α_{Flap}=32° (fig 4b, 4d), resulted in a flow separation near the leading edge of the flap. The strong shear layer between the free jet and the recirculation area can clearly be seen.

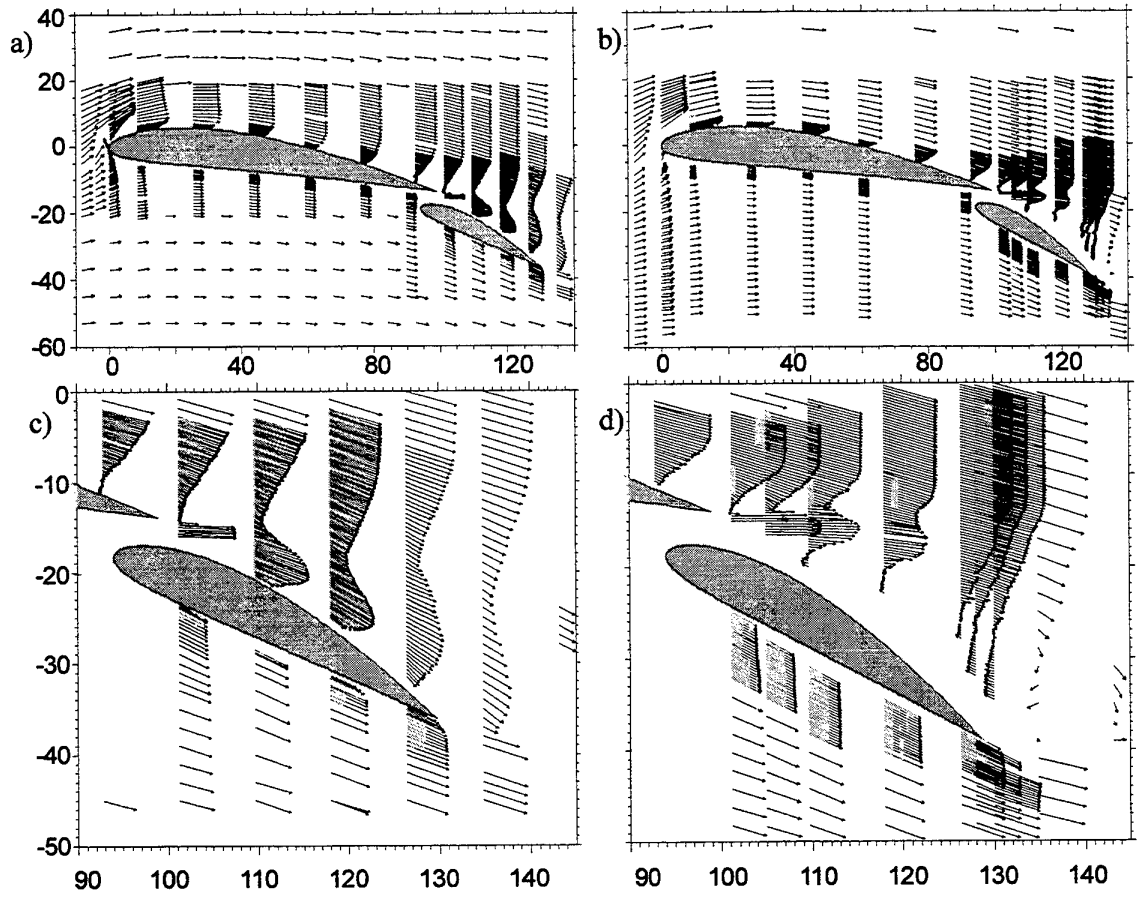


Fig 4: Mean flow field at two different flap angles around the high-lift configuration and in the vicinity of the flap: a)&c) 27°, flow remained completely attached, b)&d) 31°, flow over the flap separated at the leading edge forming a closed area of recirculation (LDA results)

3.2 The Excitation

As seen in figure 4d, the flow over the flap for $\alpha_{Flap}>30°$ separated near the leading edge. To obtain the reattachment of the flow which leads to higher lift coefficients, a periodical excitation of the free shear layer between the main airfoil and the flap was realised. This was done using a pulsed jet which was emanating perpendicularly to the flap surface next to the leading edge.

To verify the jet characteristics, velocity measurements were made in the region of the jet-slot (figure 5). Using phase-averaged laser doppler measurements, the time dependent characteristic of the jet was investigated. As can be seen in figure 5 the jet velocity was pulsating and in good agreement with the corresponding state of the rotating valve.

Phase averaged velocity measurements of the jet flow field were made for three different excitation angles Φ (fig 6). These excitation angles correspond to the three valve positions: closed, opening and opened.

For three different exciting angles the corresponding velocity distributions over the slot are plotted in figure 6a-c. At Φ=175°

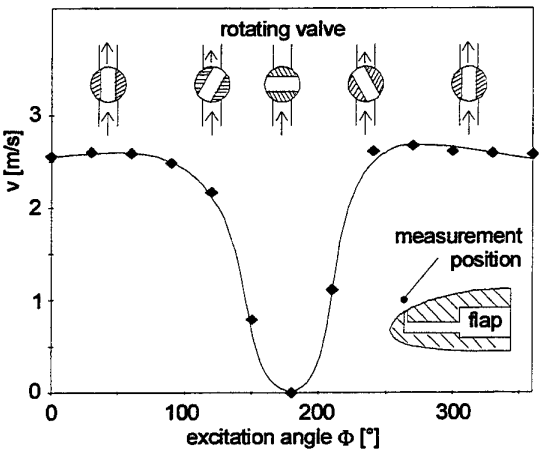


Fig 5: Vertical jet velocity at the slot exit in relation to the valve position

(a: closed valve) a very weak velocity field, which was caused by the residual impulse, can be detected, while at 225° (b: opening valve) a strong jet occurred, emanating vertically from the slot. Figure 6d shows the velocity field around the exciting slot in the moment of maximum excitation (valve open). Downstream and upstream of the jet two strong vortices, induced by the jet can be recognised. Because of the relatively long measurement time window (260°-290° equals 3.3 ms at 25 Hz) the single vortices are not clearly visible.

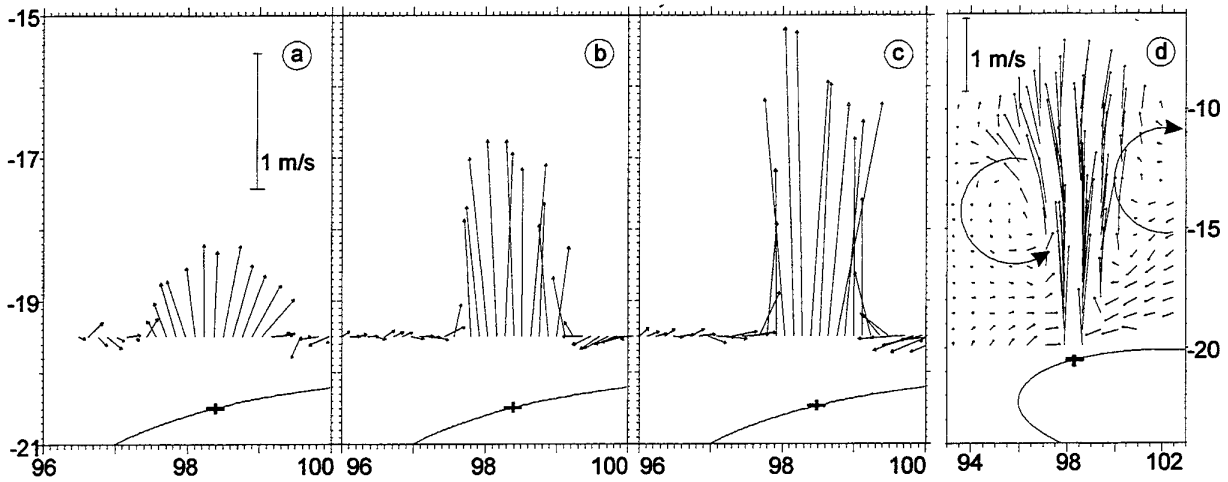


Fig 6: Velocity distribution over the slot at different exciting angles, F=25 Hz, u_μ=0 m/s (LDA results), (a) closed valve, F=175°, (b) opening valve, F=225°, (c) open valve, F=275°, (d) velocity field around the slot at open valve, F=275° (different scale) The cross marks the slot outlet

3.3 Reattachment Due to Flow Excitation

Due to the used excitation mechanism, the net momentum introduced into the flow was not zero. However steady blowing did not achieve reattachment.

Exciting the separated shear layer by a periodic jet may cause a reattachment of the flow over the flap. As an example, the velocity field over the flap at α_{Flap}=34° without excitation is plotted in fig 7a. The flow separated at the leading edge of the flap and formed a recirculation area. By activating the excitation mechanism a complete reattachment of the flow occurred, eliminating the recirculation area over the flap (fig 7b).

To get detailed information about the influence of the pulsed jet on the separated shear layer, detailed laser doppler measurements in the region over the flap were made. It was found, that at relatively high flap angles (α_{Flap}=30°-36°) the flow reattached completely, while at angles higher than 36°, the reattachment was only partly achieved. Several measurements were made, investigating the dependence of reattachment on the excitation parameters such as frequency and excitation amplitudes. Reattachment occurred in a frequency band around Strouhal number St=1 ($St=F*c_{Flap}/u_\infty$). Fig.8 depicts the development of reattachment in

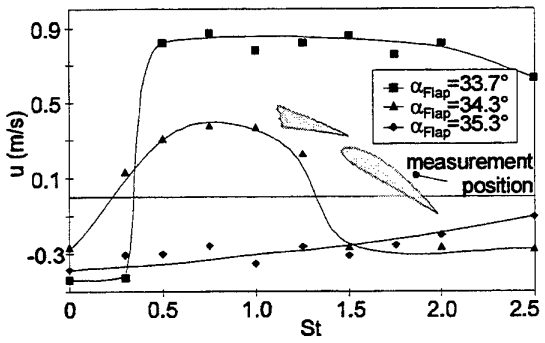


Fig. 8: Influence of the excitation frequency on reattachment at different angles of flap deflection (fixed excitation amplitude)

dependence of the excitation frequency. To illustrate this, the x-component of the flow velocity at a fixed position over the flap is plotted over the excitation frequency for different flap angels. The positive x-component of the flow velocity for the case of α_{Flap}=34.3°, at an excitation frequency between St=0.5 and St=1.5 indicates the transition from the separated to the reattached flow. A reseparation was found when increasing the excitation frequency to a value higher than St=1.5.

In order to investigate the dependency of reattachment on the excitation amplitude, figure 9 shows some of the results at the same fixed measurement position near the

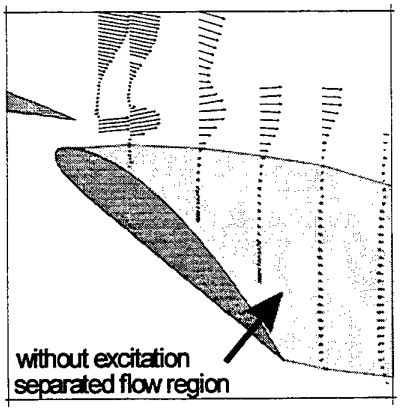


Fig. 7a: Separated flow at 34° flap angle with no excitation (LDA results)

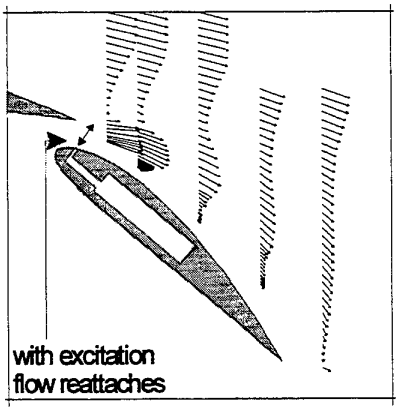


Fig. 7b: Reattachment of the flow at 34° flap angle by excitation (LDA results)

flap, as described in fig 8. The x-component of the flow velocity is plotted versus the excitation frequency for two different flap angles and two different excitation intensities. The lines marked by triangles symbolise the higher flap angle at different excitation intensities (open symbols = weak excitation, closed symbols = strong excitation). As can be seen in the graphic, the reattachment occurred in a frequency band around St=1 for all excitation intensities, but the width of the usable frequency band depended strongly on the intensity of excitation. The more intensive the excitation was, the more frequencies achieved a reattachment of the flow. Increasing the excitation intensity also resulted in a better reattachment, that means higher velocity components in the vicinity of the flap surface.

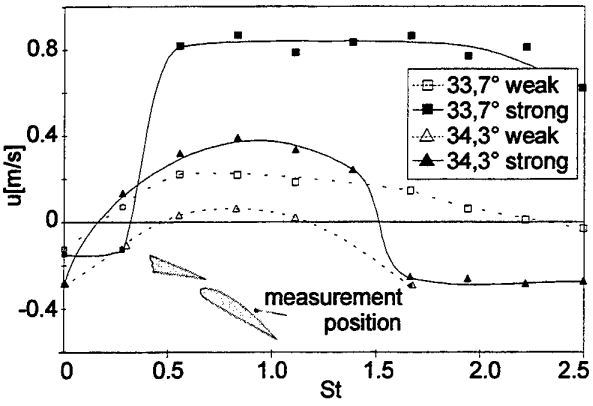


Fig 9: Dependency of reattachment on excitation intensity

For three different excitation intensities c_μ the velocity profiles in a vertical slice at 75% flap chord length are plotted in figure 10 ($c_\mu = 2 H/c (u'/u_\infty)^2$, H=slotwidth, c=chordlength, u'=RMS excitation velocity, u_∞=freestream velocity). The dotted line represents the velocity profile of the separated flow for the case of no excitation. It can be seen that a weak excitation (a) was not able to completely suppress the recirculation area close to the flap surface. A stronger excitation (b) resulted in a complete reattachment with totally absence of negative velocity components. Increasing the excitation intensity (c) did not change the fluid behaviour

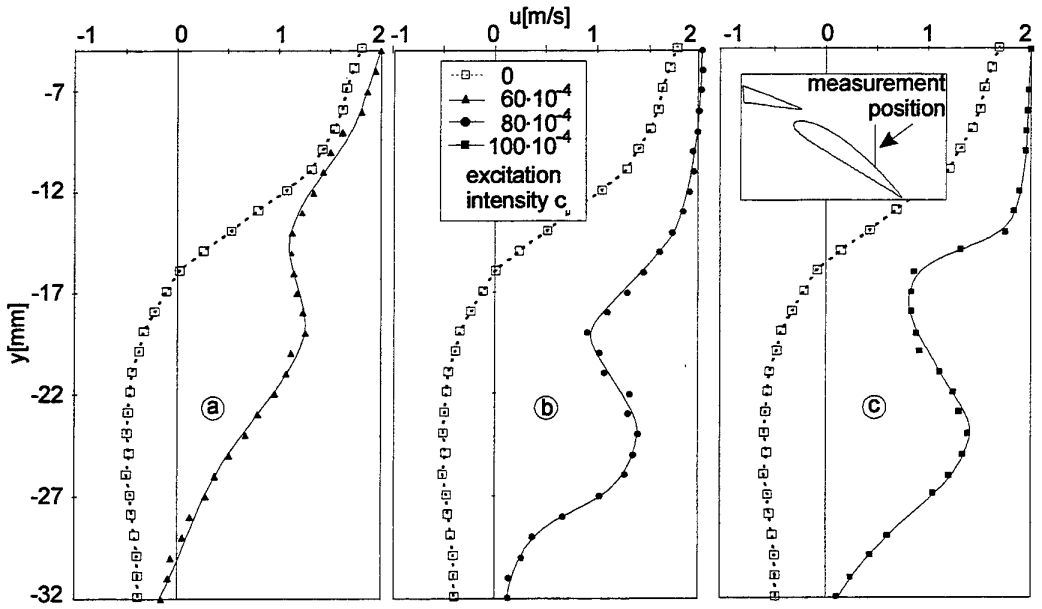


Fig 10: Mean velocity profiles over the flap at 75% x/c_{Flap} for different excitation intensities, α_{Flap}=34,5°, excitation frequency = 20 Hz ≅ 0,75 St,
a) $c_\mu = 60 \cdot 10^{-4}$, b) $c_\mu = 80 \cdot 10^{-4}$, c) $c_\mu = 100 \cdot 10^{-4}$

remarkably but still enhanced the velocity profile close to the flap surface.

Phase averaged flow field measurements in the flap region were undertaken to understand the mechanism of reattachment. In fig. 11a the time averaged separated flow at α_{Flap}=35.5° is plotted. Graphic 11b shows the results of the phase averaged measurements with activated excitation. The flow reattached, forming a small separation bubble downstream of the flap leading edge. To visualise the changes in the flow field due to excitation, the velocities of graphic b are subtracted from those of graphic a and plotted in graphic 11c. Here a transport of momentum from the outer flow into the former

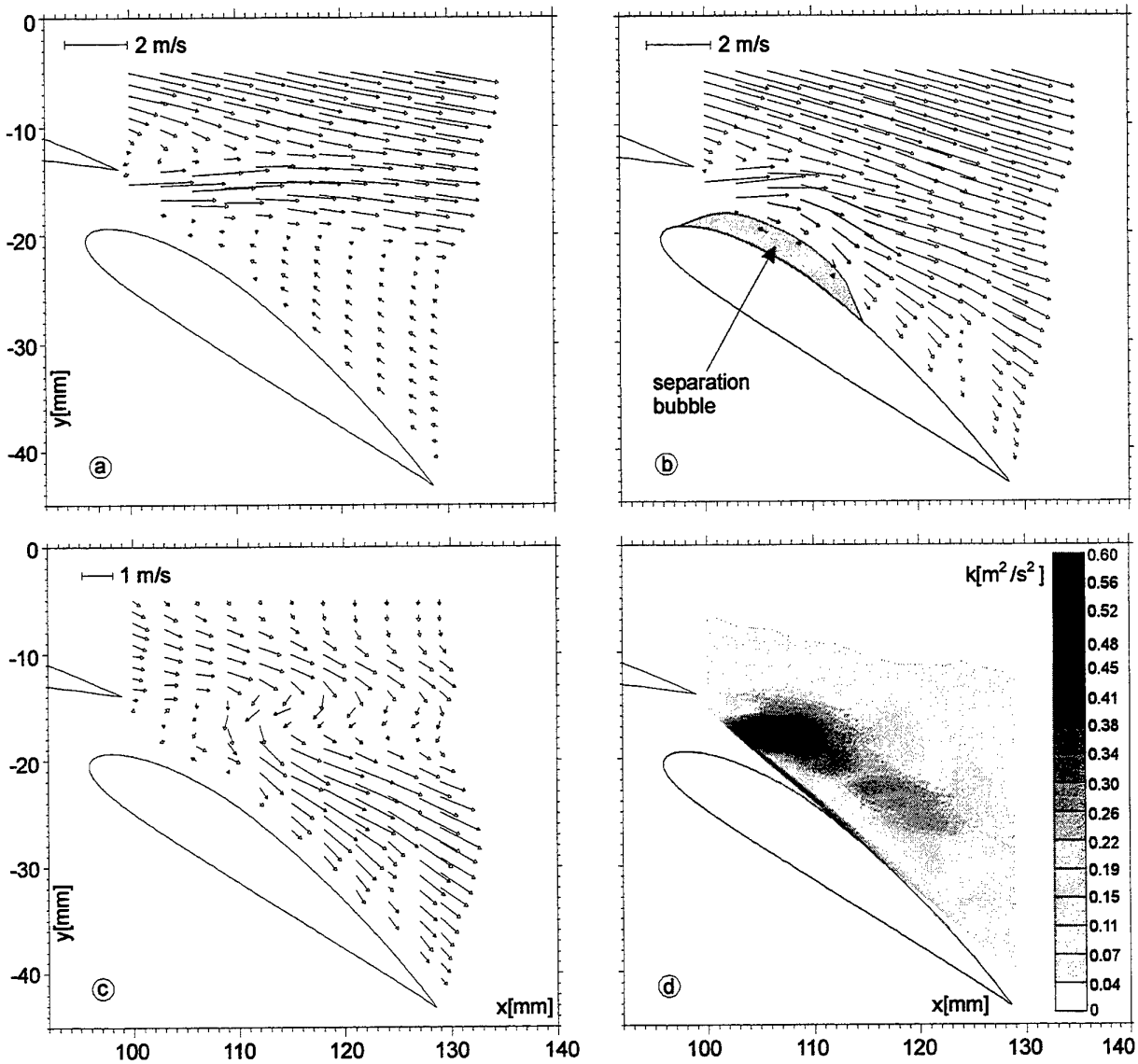


Fig 11: a) separated flow at α_{Flap}=35.5° without excitation, b) reattachment due to excitation (St=0.75, $c\mu=80\cdot10^{-4}$) at F=225° (opening valve) with formation of separation bubble near the leading edge, c) subtraction of both flow fields (b-a) showing a vortice structure in the shear layer induced by periodic excitation, d) turbulent kinetic energy shows a maximum near the excitation point and further downstream in the reattached flow (LDA Results)

separated flow region can be seen. To depict the amount of turbulence in the flow field due to the excitation, the turbulent kinetic energy $k=1/2\cdot(u'^2+v'^2)$ is plotted as isolines in graphic 11d. The dark colours symbolise high degree of turbulence. It can be recognised that the maximum peaks of turbulent energy were located close to the excitation point and further downstream in the shear layer of the reattached flow. This emphasises the fact of enhanced momentum transport from the outer flow into the separated flow area due to periodic excitation, which results in the reattachment of the flow.

4. CONCLUSIONS

The reattachment of separated flow on a simple high-lift configuration by internal periodic excitation near the leading edge of the flap was investigated by using phase averaged LDV. It was shown that it is possible to achieve a reattachment of a separated flow by exciting the separated shear layer. It also exists a strong influence of excitation frequency and intensity, showing clearly a favourite frequency of $St \cong 1$. The increase of the excitation intensity results in a widening of the usable frequency band. Phase averaged LDV measurements showed a enhanced transport of momentum from the outer flow into the separated region near the flap surface.

REFERENCES

Adair, D., Horne, W.C. 1989, Turbulent Separating Flow Over and Downstream of a Two-Element Airfoil, Experiments in Fluids, Vol. 7, pp. 531

Dovgal, A. 1993, Control of Leading-Edge Separation on an Airfoil by Localized Excitation, DLR-Forschungsbericht DLR-FB-93-16

Hsiao, F.B., Liu, C.F., Shyu, L.Y. 1990, Control of Wall-Separated Flow by Internal Acoustic Excitation, AIAA Journal, Vol. 28, No.8, pp. 1440

Seifert, A., Darabi, A., Wygnanski, I. 1996, On the Delay of Airfoil Stall by Periodic Excitation, Journal of Aircraft 33, No.4, pp. 691

FLOW MEASUREMENTS ON A LARGE DELTA WING USING PARTICLE IMAGE VELOCIMETRY (PIV)

L. Dieterle, J. Raffel, K. Ehrenfried and J. Kompenhans

DLR, Deutsches Zentrum für Luft- und Raumfahrt (German Aerospace Center)
Institut für Strömungsmechanik, Göttingen, Deutschland (Germany)

ABSTRACT

The vortex structures on the leeward side of a large delta wing have been investigated by means of digital particle image velocimetry. The measurements were carried out in a plane crosswise to the main flow direction. The large spatial dimensions of the interesting flow structure required a special technical solution: Two CCD cameras were employed to record neighboring regions of the flow field simultaneously. A combination of four single-pulsed laser oscillators, in which two of them fired simultaneously, generated an extended light sheet of sufficiently high intensity in order to image micron particles added to the flow. In this way, the whole vortex system could be observed at Reynolds numbers $Re > 10^7$.

1. INTRODUCTION

A joint research project of three German Collaborative Research Centers (SFB 253, 255 and 259) and the German Aerospace Center deals with the experimental investigation of a large model of the hypersonic research configuration ELAC-1 (Elliptical Aerodynamic Configuration). ELAC-1 represents a space transporter for horizontal take off and landing. It is a delta wing with an elliptical cross-section, rounded leading edges and integrated winglets in the afterbody. The ELAC-1 configuration was designed by the Institute of Aeronautics and Astronautics (ILR) at the Technical University (RWTH) of Aachen and described in detail by Neuwerth and Staufenbiel (1990).

In order to study the low-speed aerodynamics at high Reynolds numbers, a 1:12-scale model was built exclusively for tests in the Large Low-speed wind tunnel Facility (LLF) of the German-Dutch Wind tunnel (DNW) in Emmeloord, The Netherlands. The test program comprised six-component force and moment, pressure and velocity distribution as well as boundary layer measurements. Therefore, the model was equipped with an internal six-component strain gage balance and a total of 150 pressure holes. The boundary layer transition was determined by use of multisensor hotfilms, its separation by means of surface oil flow patterns. Mean velocity profiles and the skin friction were measured with a single hot wire and a Preston tube, respectively. The vortex structures on the leeward side of the delta wing have been investigated utilizing laser sheet imaging and particle image velocimetry.

The measurements took place in the autumn of 1997 and since then, a number of papers have been published about the different experiments and their results: Jacob *et al* (1998) and Neuwerth *et al* (1998) reported on the force and moment and the pressure distribution, Fühling and Abstienz (1998) on the boundary layer measurements. A comparative depiction of the laser sheet imaging and the particle image velocimetry is in preparation by Dieterle *et al* (1998). The results of the PIV measurements are described in detail by Dieterle and Peiter (1998) and Neuwerth *et al* (1998) as well.

The present paper is directed to the special experimental problems the PIV technique has been faced with in this particular application.

2. EXPERIMENTAL SET-UP

2.1 Wind Tunnel and Delta Wing Model

The experiments were carried out in the LLF's closed test section of 6 x 8 m^2. The model of the delta wing configuration ELAC-1, adapted in scale to this

particular surrounding, has a total length of $l = 6$ m; its sweepback angle of the leading edge is 75° and, consequently, the full span 3.2 m. The model is supported by a rear sting.

The PIV measurements had to be carried out in the cross section $x/l = 0.6$ on the port side of the delta wing. The area of interest was expected to be about 0.3 m^2 in size. Due to the high running costs of the wind tunnel facility, the PIV measurements – excluding system installation – were limited to the period of about one working day. During this time 15 different flow conditions had to be investigated: The main flow velocity v varied between 15, 20, 30, 50 and 70 m/s, the angle of attack α between 12°, 18° and 21°.

2.2 Measuring Technique

In order to manage the extensive test program within the provided time, the measurement data had to be checked on-line and high data rates had to be achieved. This could only be accomplished by using a digital PIV system instead of a photographic one: For instance, it was not reasonable to stop the wind and to enter the test section each time a complete photographic film had been recorded and to be replaced by a new one.

Unfortunately, common CCD cameras are still inferior to photographic films in so far as sensitivity and resolution are concerned. Particularly, the comparatively low sensitivity of CCD cameras turned out to be a serious problem in this special application: In order to get digital particle images as bright as photographic ones, the energy of the light scattered by the tracer particles or the intensity of illumination, respectively, must be increased. Additionally, in the present case the light sheet has to be much more extended in height and thickness compared with common applications because (i) the observation area is larger than normal and (ii) the light sheet is placed crosswise to the main flow direction causing a considerable out-of-plane motion of the particles; in order to avoid the loss-of-pairs effect, described by Keane and Adrian (1990), the light sheet thickness must be increased. A high light intensity I over an extended cross section area of the light sheet requires light pulses of particularly high energy E according to

$$I \propto \frac{E}{t_p z \delta}, \qquad (1)$$

where t_p is the pulse duration, z the height and δ the thickness of the light sheet.

While deciding on a digital PIV system, other problems arose: How to illuminate the object plane with sufficiently high intensity and how to resolve digitally an observation area of about 0.3 m^2 in order to investigate flow structures down to a few centimeters in size? A feasible solution was (i) to combine four single-pulsed laser oscillators in which two of them fire simultaneously, generating light pulses of sufficiently high energy and (ii) to employ two identical CCD cameras, which simultaneously take pictures of neighboring regions of the flow field, capturing a total area of the size required but without a considerable loss in resolution.

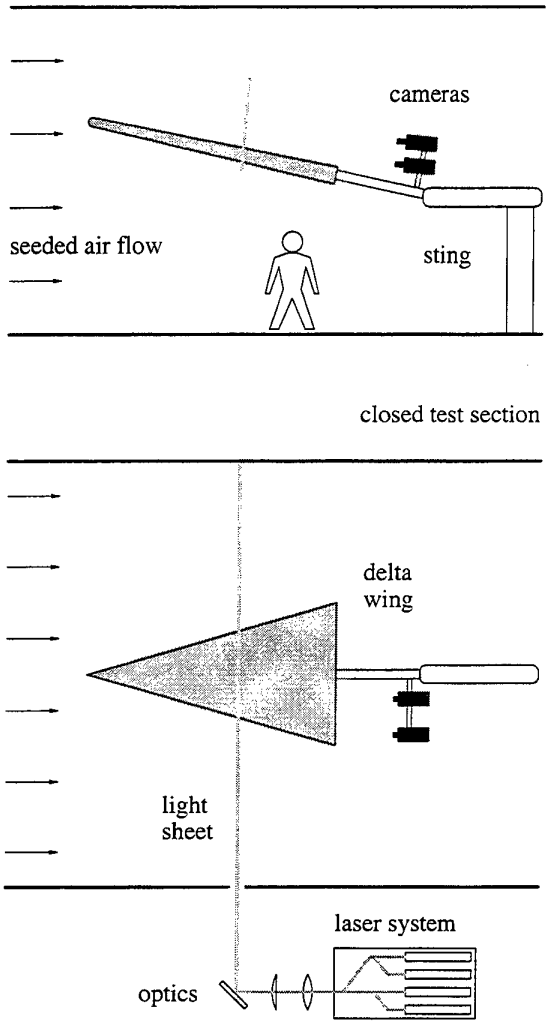


Fig. 1 Schematic view of the experimental set-up in the 8 x 6 m^2 test section of DNW-LLF

The experimental set-up can be seen in Figure 1. The cameras were arranged in pilot's view on the port side of the delta wing at a working distance of about

4 m and directly mounted on the model sting. Their position relative to the model was fixed and they did not need to be rearranged when changing the angle of attack. The laser system was placed beside the closed test section. A combination of spherical and cylindrical lenses formed the laser beam into a light sheet, which entered the test section through a small opening in the wall. The light sheet illuminated the cross section $x/l = 0.6$ of the model. In order to be able to observe the flow region close to the rounded leading edge of the delta wing from the cameras' position, their image planes as well as the light sheet were not perpendicular to the surface of the model but slightly tilted by an angle of 7°. The light sheet optics had to be readjusted when changing the angle of attack.

Light source. The laser system (Quantel) contains four single-pulsed and frequency-doubled Nd:YAG lasers, Figure 2. Their beams are combined by use of their different directions of polarization: Oscillators (1) and (3) generate vertically polarized light, oscillators (2) and (4) horizontally polarized light. The infra-red beam released by a resonator becomes visible behind the frequency doubler (F). Vertically polarized light is reflected, horizontally polarized light is transmitted by the Brewster windows (B). The Q-switches of oscillator (1) and (4) are connected each with one of the Pockels cells (P). When oscillator (1) or (4) fires, the corresponding Pockels cell is switched simultaneously and turns the direction of polarization of the incident beam by an angle of 90°. For example, the beam of oscillator (1) is frequency-doubled by (F), reflected by the first (B) and, after its direction of polarization has been turned by (P), transmitted by the second (B). The beam of oscillator (2), the polarization of which is not changed by (P), passes through both Brewster windows.

Because the beams of oscillator (1) and (2) or (3) and (4), respectively, take the same path behind the first Brewster window, but need different modes of (P) for exit, they can not fire simultaneously. So the first light pulse is generated by oscillator (2) and (3), the second one by oscillator (1) and (4). A single light pulse originating from two oscillators has the following specifications:

wavelength:	$\lambda = 532$ nm
energy:	$E = 600$ mJ
pulse duration:	$t_p = 6$ ns

The laser system creates double pulses with a repetition rate of 10 Hz and is triggered externally.

Optics. The laser beam is slightly focused by combining a spherical biconcave and biconvex lens and spread to a light sheet by two cylindrical lenses (Spindler & Hoyer). The light sheet thickness δ depends on the distance between the two spherical lenses and can be adjusted continuously. Choosing an appropriate value for δ means fulfilling competing requirements: On the one hand δ should not exceed the objective's depth of field in order to avoid defocused particle images. Additionally, it must be taken into account that the intensity of illumination is inversely proportional to δ, see Equation (1). On the other hand δ should be as large as possible in order to minimize the loss-of-pairs effect mentioned above: In case of an out-of-plane motion, particles enter or leave the light sheet during the period Δt between the two light pulses – they are illuminated and imaged only once and do not contribute to a successful image evaluation. The number of 'lost' particles depends on their out-of-plane velocity, the light sheet thickness and the separation time Δt. The larger δ, the larger the feasible separation time or the feasible particle image displacement, respectively, resulting in a higher resolution of the measured velocity. So the light sheet thickness strongly impinges on the quality of the particle images and the velocity data.

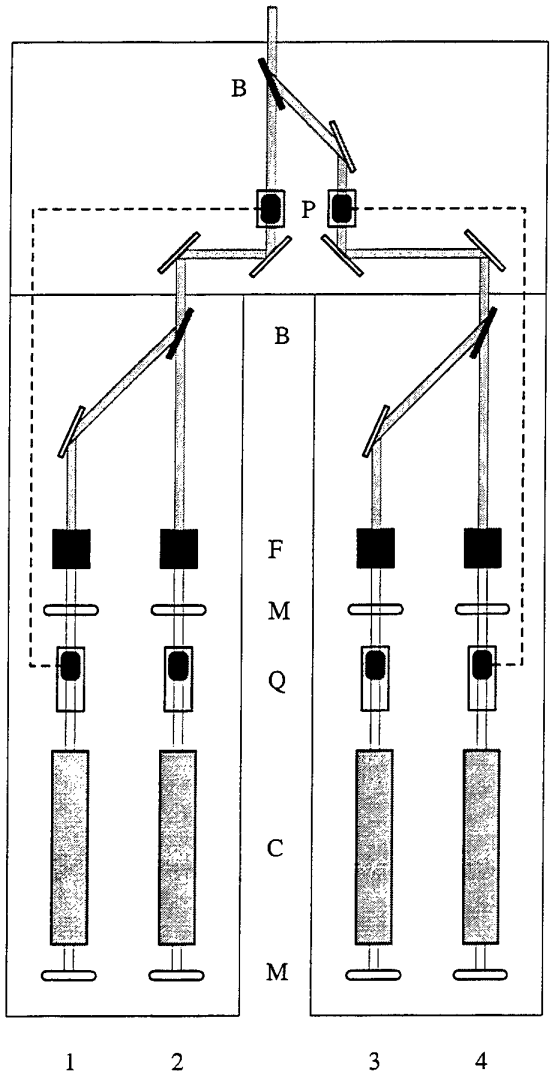


Fig. 2 Beam combination of four single-pulsed and frequency-doubled Nd:YAG lasers. (M) mirrors of the resonator, (C) cavity, (Q) Q-switch, (F) frequency doubler, (B) Brewster window, (P) Pockels cell

Seeding. A seeding system consisting of two aerosol generators and a movable, remote-controlled seeding rake are placed in the settling chamber. The air-operated aerosol generators produce olive oil droplets of about 1 μm in size by means of so-called Laskin nozzles, see Echols and Young (1963). The seeding rake connected to the aerosol generators releases the tracer particles and disperses them over a cross section of about 1 m^2 in the test section. In this way the air flow is seeded locally around the delta wing.

The relaxation time of the olive oil droplets ($\rho = 874$ kg/m^3, $d = 1$ μm) in air ($\bar{\lambda} = 66$ nm, $\eta = 1.82$ kg/m s) is, see e.g. Hinds (1982),

$$\tau = \frac{\rho d^2 Cu}{18\eta} \approx 3\ \mu s\,, \qquad (2)$$

were ρ is the density and d the size of the particle,

$$Cu = 1 + 2.52\frac{\bar{\lambda}}{d} \qquad (3)$$

the Cunningham correction factor, $\bar{\lambda}$ the mean free path and η the dynamic viscosity of air. τ is a measure for the particle's ability to follow an accelerated flow and should be small compared to the separation time.

Particle imaging. The tracer particles are imaged by objectives (Zeiss) with a focal length $f = 100$ mm and an f-number $f_\# 2.8$. Working at a distance of 4 m their magnification is $M = 0.023$ and their depth of field according to Adrian (1991)

$$\Delta l = 4\left(1 + M^{-1}\right)^2 f_\#{}^2 \lambda \approx 30\ \text{mm}\,. \qquad (4)$$

Inside of this range the diameter of the blurred particle image is increased by less than 20 % compared with the in-focus diameter. The objective's focus adjustment is motor-driven and remote-controlled.

Two identical CCD cameras (Kodak) with full-frame interline transfer sensors take single-exposed double images of the tracer particles at an interval of a few microseconds each. The cameras have the following specifications:

resolution:	1024 x 1024 pixels
sensor area:	9 x 9 mm^2
digital output:	8 bits
frame rate:	≤ 7.5 Hz

They are triggered synchronously by an external source and therefore take pictures of neighboring regions of the flow field at the same time.

The perspective projection of three-dimensional particle displacement onto the image plane induces a perspective error of the measured image displacement, as described by Raffel *et al* (1998). Following their remarks, the error relative to a pure in-plane displacement is

$$\varepsilon = \frac{s_z}{s_{xy}} \cdot \frac{r_i}{z_i}\,, \qquad (5)$$

where s_z is the particle's out-of-plane displacement, s_{xy} its in-plane displacement, r_i the distance between the particle image and the optical axis and

$$z_i = f(M+1) \qquad (6)$$

the distance between the lens and the image plane. In the present case the in-plane and the out-of-plane flow velocity or particle displacement, respectively, are expected to be in the same order of magnitude, that means $s_z/s_{xy} \approx 1$. The size of the CCD sensor limits r_i to a maximum of about 6 mm. z_i slightly exceeds 100 mm resulting in a maximum error of approximately 6 %. It should be emphasized that this estimation is vague concerning the ratio s_z/s_{xy} which changes considerably in space and depends on the angle of attack, see Decker (1997). The only way to quantify accurately and – at the same time – to eliminate the perspective error is to apply a stereoscopic PIV system – but this would go beyond the technical and financial scope of the project.

Operating. After system installation and adjustment, the laser system beside the test section, the seeding rake in the settling chamber and the objectives and cameras within the test section can be operated via remote control, see Figure 3. The laser system and the cameras are triggered and synchronized by a so-called 'sequencer', consisting of a 10 Hz trigger source and a programmable, PC-controlled delay generator. Because the cables for image data transfer between the cameras and their acquisition PCs are limited in length, the PCs are placed close to the test section and equipped with keyboard extensions. The operator can check on-line the quality of the digital particle pictures and if necessary focus the objectives and change the position of the seeding rake in the settling chamber.

Oscillator 2 and 3 or 1 and 4, respectively, get the same trigger (TTL) in order to fire simultaneously. Starting the sequencer they are triggered continuously at 10 Hz. The common trigger line of the cameras is interrupted by a logical AND. The trigger (TTL) coming from the sequencer can be released by a continuous signal (TTL) at the second input of the logical AND. So, setting the cameras in a state ready for image recording – i. e. waiting for a trigger –, the measurements can be started and stopped interactively by switching the AND. Because the frame rate of the cameras is less than or equal to 7.5 Hz, they ignore each second trigger and take double images with a 5 Hz frame rate.

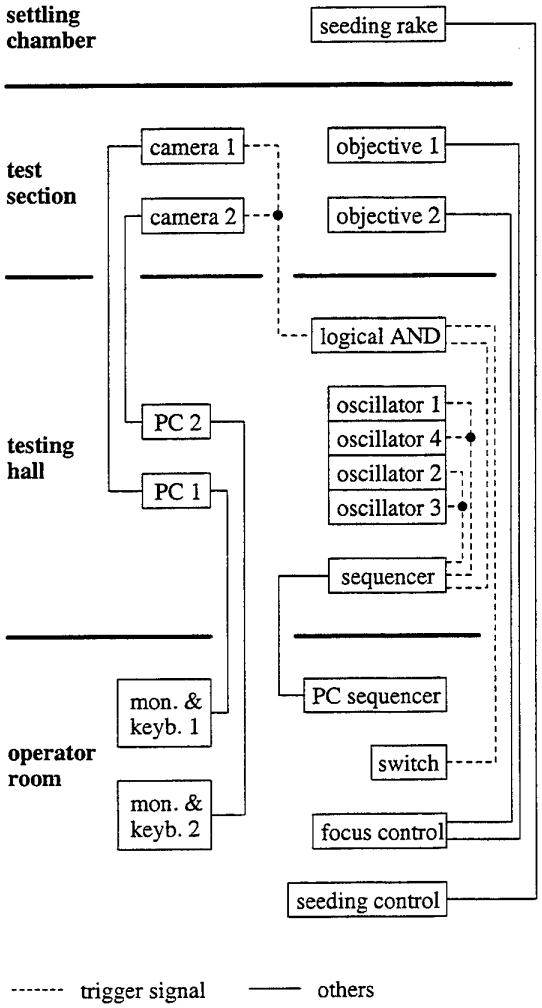


Fig. 3 PIV operation scheme

3. TEST PROCEDURE

First, appropriate values of the parameters δ and Δt, the latter in dependence on the main flow velocity, had to be determined in pre-tests. Due to the comparatively large depth of field of the objectives, see Equation (4), δ was restricted by the required intensity of illumination only, see Equation (1). A light sheet thickness of about 2 mm turned out to be an acceptable compromise: The objectives just created particle images of sufficient brightness and contrast and the loss of image pairs could be reduced to a minimum – but at the expense of small separation times or image displacements, respectively: Δt varied between 13 µs at $v = 70$ m/s and 100 µs at $v = 15$ m/s resulting in image displacements up to a maximum of

about 6 pixels near the vortex' center, see Chapter 5. However, for all cases Δt is large compared to the relaxation time of the particles, see Equation 2. For this reason particle slip as a potential source of error in PIV caused by an accelerated flow can be neglected.

Because the light sheet optics had to be readjusted when changing the angle of attack, the measurements were divided into three recording sessions corresponding to three different angles of attack. Each session comprised five successive runs corresponding to five different main flow velocities, see Section 2.1. During a session the wind did not need to be stopped. A session including data acquisition as well as image and displacement data check took about 30 minutes. After each session a calibration grid fitting to the model's surface was placed in the object plane as can be seen in Figure 4 in order to determine the magnification of the objectives and the cameras' position relative to each other and to the model as well. Installing the calibration grid and readjusting the light sheet optics for the next session turned out to be the most time-consuming work.

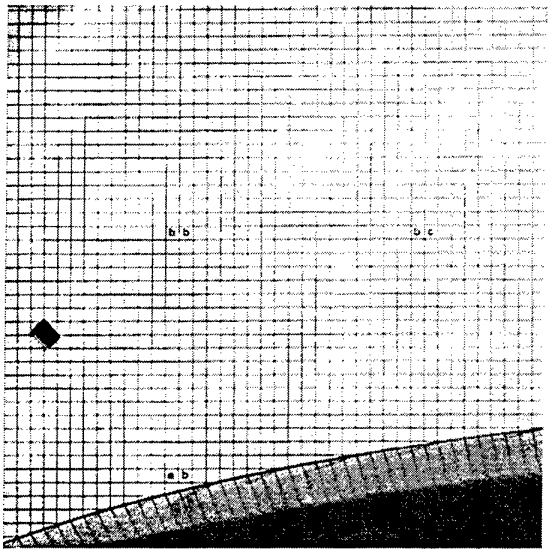


Fig. 4 Calibration grid fitting to the model's surface in the object plane as seen by the inboard camera. The distance between two grid points is 10 mm.

The cameras took 2 x 40 image pairs per run resulting in 168 Mbytes image data per run, 838 Mbytes per session or more than 2.5 Gbytes for the whole campaign. As an example, a single-exposed frame taken by the inboard camera at $v = 50$ m/s and $\alpha = 21°$ is shown in Figure 5. The picture has been inverted and modified in brightness and contrast for the sake of a better presentation in this print.

The picture shows the particle-laden flow on the leeward side of the delta wing configuration ELAC-1 in the cross section $x/l = 0.6$. Strands of particles and a bare core indicate a clockwise rotating vortex on the port side of the model. The obviously inhomogeneous distribution of the tracers and the quite poor contrast of the original makes the image processing difficult.

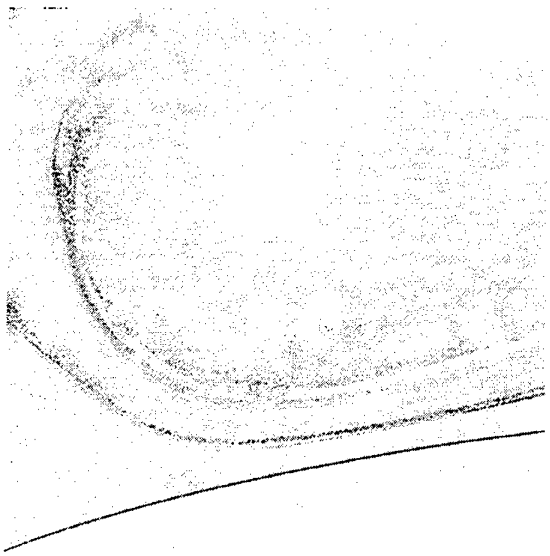


Fig. 5 Single-exposed frame taken by the inboard camera at $v = 50$ m/s and $\alpha = 21°$

4. IMAGE PROCESSING

Due to their moderate quality the particle images had to be preconditioned prior to the evaluation: In order to reduce the background noise, the average of the 40 images taken by the same camera and exposed by the same, that means the first or the second, scattered light pulse during a single run was subtracted from each of these images. Other preprocessing tools described by Willert (1997), e.g. a highpass filter which removes a non-uniform background level caused by diffused reflections on the model's surface, have been applied as well.

The single-exposed and preconditioned double images were evaluated by means of digital cross-correlation following the remarks of Raffel *et al* (1998). Interrogation took place in windows of 32 x 32 pixels in size without an off-set between the two corresponding windows of a double image. Cen-

ters of neighboring windows were spaced by 16 pixels yielding about 4000 interrogations per frame. A three-point estimator introduced by Willert (1991) determined the position of the cross-correlation peak or the particle image displacement, respectively, with subpixel accuracy.

In order to detect and replace automatically spurious displacement vectors, the dynamic mean value operator described by Raffel *et al* (1998) was applied: The operator compares each calculated vector with the average of its eight adjacent vectors. If the difference in magnitude between this average and the considered vector exceeds a certain value depending on the displacement gradient in the 3 x 3 neighborhood, the considered vector is removed and replaced by the average. Vectors calculated in the area below the visible contour of the model do not have a physical meaning and therefore are removed without substitution.

The objective's magnification and the model's contour were derived from the pictures of the calibration grid in order to convert displacement data into velocity data and to determine their location in space relative to the model's surface. In the same way the velocity plots generating from the two cameras could be combined.

The image processing yielded a series of 40 combined fields of instantaneous velocity per run measured within a period of 8 s each. Additionally, a combined field of the averaged velocity has been derived from each series resulting in a total of 615 velocity fields.

5. RESULTS

As an example, the combined field of instantaneous velocity on the leeward side of the delta wing at $v = 50$ m/s, corresponding to $Re \approx 2 \cdot 10^7$, and $\alpha = 21°$ is shown in Figure 6. The inboard camera captured an observation area of 400 x 400 mm^2, the outboard camera an additional area of about 270 x 230 mm^2. So the outboard camera's field of view was not fully used for the measurements. A total flow field of 0.22 m^2 size has been investigated with the digital PIV system. The individual vectors in Figure 6 represent the local mean flow velocity within an area of 12.5 x 12.5 mm^2 in the object plane. Their length corresponds with the magnitude of velocity.

The contour of the model is also drawn in Figure 6, even though in a shape as it is not seen by the outboard camera: The view on the port leading edge from the camera's position is blocked by the broadening cross section of the arrow-shaped wing. This is the reason for the bare region near the leading edge in Figure 6; despite the inclined light sheet and image plane, see Section 2.2, the flow field very close to the leading edge was not accessible for observation.

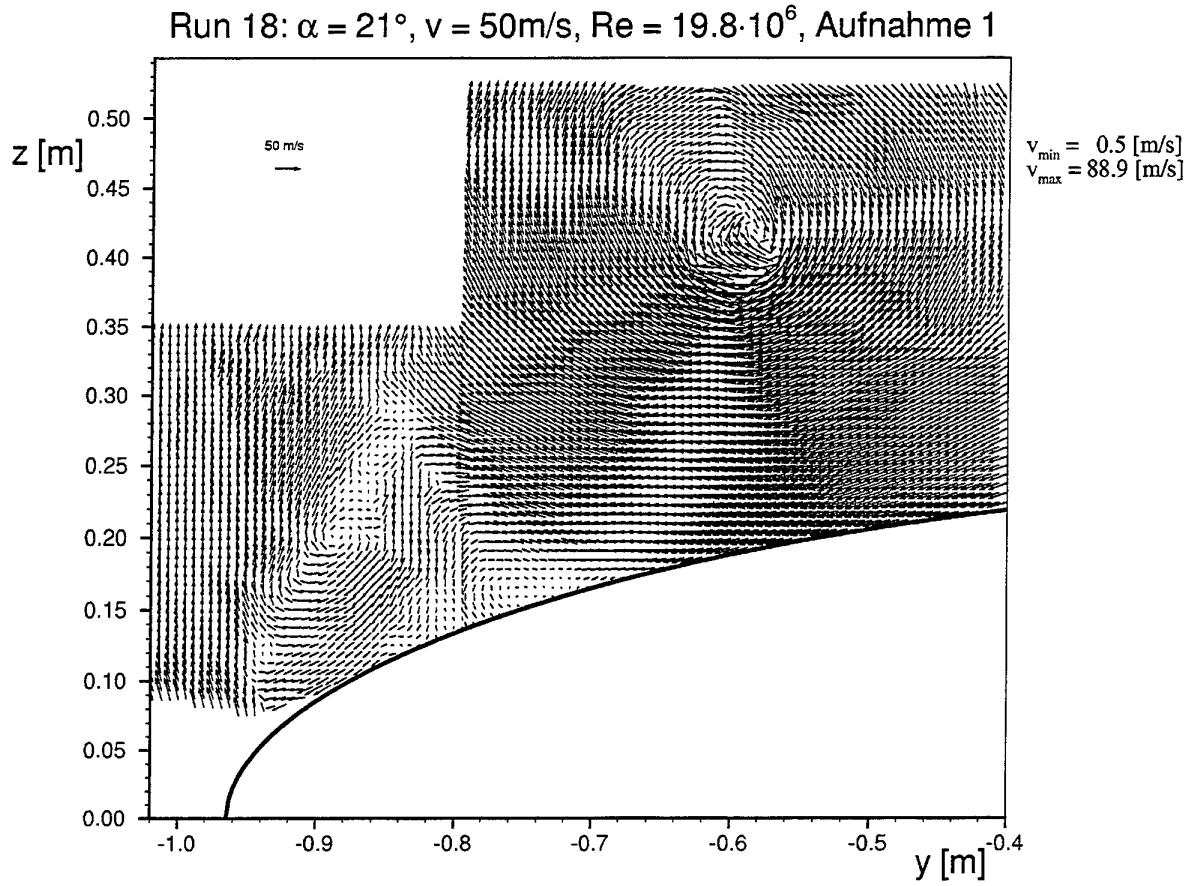


Fig. 6 Instantaneous velocity field on the leeward side of the delta wing configuration ELAC-1 derived from the pictures of two CCD cameras placed in pilot's view on the port side of the model as shown in Figure 1

The vector plot shows on the left – in the outboard camera's field of view – a shear layer apparently separating from the rounded leading edge of the delta wing. Small vortices are arranged on the shear layer, each of them clockwise rotating. The shear layer rolls up to the big primary vortex, clockwise rotating as well, which covers almost completely the inboard camera's field of view. Obviously, the flow on the leeward side of the delta wing separates a second time creating a small counterrotating secondary vortex close to the model's surface, centered at $y = -0.75$ and $z = 0.16$. The maximum velocity $v_{max} \approx 90$ m/s occurs below the center of the primary vortex.

The velocity data are interpreted in detail and compared with results of pressure distribution measurements and surface oil flow patterns by Neuwerth *et al* (1998). Some specific features of the flow around the large model of the ELAC-1 configuration have been discovered exclusively by the PIV technique: The existence of shear layer instabilities or vortex layers, respectively, the structure of the secondary vortex (The primary vortex' one could also be determined by laser sheet imaging, see Dieterle *et al* (1998)), the local distribution of vorticity and the unsteady behaviour of the flow.

6. CONCLUSIONS

A digital PIV system has been successfully applied to the flow around the 1:12-scale model of the ELAC-1 configuration. The goal was to gain comprehensive knowledge about the vortex structures on its leeward side within a stringently limited test time. This has been accomplished by extending the applicability of digital particle image velocimetry to large observation areas: Combining four single-pulsed high-energy laser oscillators provides an extended light sheet of sufficiently high intensity in order to illuminate and image particles of negligible inertia. Employing two CCD cameras which simultaneously

take pictures of neighboring flow regions makes it possible to observe total areas of about 0.3 m^2 in size (In the present application this capability was not fully used), resolving flow structures down to 12.5 x 12.5 mm^2. Operating the devices via remote control and checking on-line the image data enables one to carry out a tight test program and, consequently, to reduce the test time in a large wind tunnel and the costs of the research project, respectively.

ACKNOWLEDGEMENTS

B. Bretthauer, M. Raffel, H. Vollmers, C. E. Willert (all DLR, arranged in alphabetical order) assisted the PIV measurements. S. Haverkamp (RWTH Aachen) carried out the image processing using DLR's software. K. Pengel and his colleagues (DNW) supported the PIV measurements, especially by providing the second Nd:YAG laser system and the beam combination optics. Both, the laser system and the optics are part of DNW's PIV system as developed by the DLR and now being fully operational at the DNW.

REFERENCES

Adrian, R. J. 1991, Particle-Imaging Techniques for Experimental Fluid Mechanics, Annu. Rev. Fluid Mech., vol. 23, pp. 261-304.

Decker, F. 1997, Experimentelle und theoretische Untersuchungen zur Aerodynamik der Hyperschallkonfiguration ELAC-1 im Niedergeschwindigkeitsbereich; pp. 31-37, Cuvillier Verlag, Göttingen.

Dieterle, L., Kompenhans, J., Peiter, U. & Pengel, K. 1998, Flow Field Investigations on a Large Delta Wing Using Laser Sheet Imaging and Particle Image Velocimetry, accepted to the 8th Int. Symp. Flow Visualization, Sorrento.

Dieterle, L. & Peiter, U. 1998, ELAC-1: Experimental Investigation of Vortex Structures Using PIV, Proc. Ann. Sci. Conf. GAMM (Gesellschaft für Angewandte Mathematik und Mechanik), Bremen (to be published).

Echols, W. H. & Young, J. A. 1963, Studies of Portable Air-Operated Aerosol Generators, NLR (Naval Research Laboratory) Report 5929, Washington.

Fühling, S. & Abstienz, R. 1998, Boundary Layer Measurements on the ELAC-1 Configuration at $Re = 4 \cdot 10^7$, Proc. Ann. Sci. Conf. GAMM, Bremen (to be published).

Hinds, W. C. 1982, Aerosol Technology, pp. 44-47 and 104-105, John Wiley & Sons, New York.

Jacob, D., Neuwerth, G. & Peiter, U. 1998, High Reynolds Number Wind Tunnel Tests with an ELAC-Model in the DNW, Proc. Ann. Sci. Conf. GAMM, Bremen (to be published).

Keane, R. D. & Adrian, R. J. 1990, Optimization of Particle Image Velocimeters. Part I: Double Pulsed Systems, Meas. Sci. Technol., vol. 1, pp. 1202-1215.

Neuwerth, G., Peiter, U., Decker, F. & Jacob, D. 1998, Reynolds Number Effects on the Low-Speed Aerodynamics of the Hypersonic Configuration ELAC-1, AIAA 8th Int. Space Planes Hypersonic Sys. Techn. Conf., Norfolk, Paper No. AIAA-98-1578.

Neuwerth, G. & Staufenbiel, R. 1990, Geometrie der Konfiguration ELAC-1, Internal Paper A-90-1 SFB 253, Institut für Luft- und Raumfahrt (ILR), Rheinisch-Westfälische Technische Hochschule (RWTH) Aachen.

Raffel, M., Willert, C. E. & Kompenhans, J. 1998, Particle Image Velocimetry – A Practical Guide, pp. 46-47, 117-134 and 153-154, Springer-Verlag, Berlin.

Willert, C. E. & Gharib, M. 1991, Digital Particle Image Velocimetry, Exp. Fluids, vol. 10, pp. 181-193.

Willert, C. E. 1997, Stereoscopic Digital Particle Image Velocimetry for Application in Wind Tunnel Flows, Meas. Sci. Technol., vol. 8, pp. 1465-1479.

FLOW FIELD IN THE VICINITY OF A THICK CAMBERED TRAILING EDGE

G. Pailhas[1], Ph. Sauvage[2], Y. Touvet[1] & E. Coustols[1]

[1] ONERA/DMAE, Department of Modelling for Aerodynamics and Energetics, Toulouse, FRANCE
[2] presently AEROSPATIALE A/SW/SF, Toulouse, France

ABSTRACT

The aim of this experimental study is to scrutinize the flow in the vicinity of a non zero thickness trailing edge, i.e. just upstream and downstream of the base, using Laser Doppler Anemometry. Indeed, boundary layer surveys as well as wake surveys have been performed for different thicknesses and shapes of trailing edges. Experiments have been conducted with two-dimensional trailing edges in both two- and three-dimensional flows. Much of the discussion presented in this paper is relevant to flow field modification induced by thick cambered trailing edges.

1. INTRODUCTION

The aerodynamical characteristics of an airfoil are strongly dependent on the geometry of the trailing edge vicinity. Rather recent interest has suggested that trailing edge thickness could be a key feature for aerodynamical purpose [1]. For transonic applications, the interest of the namely D.T.E. (Divergent Trailing Edge) concept has arisen because when considering relatively high values of the lift coefficient of supercritical airfoils, the total drag could then be reduced [2]. Such a "DTE" concept has been mainly developed through computational tools, but there is very little published experimental results. As the physical aspects induced by such unconventional trailing edge geometries are identical whatever the flow regime, a complete experimental program has been elaborated at ONERA/CERT for several years.

Thus, a study has been launched successively at the hydrodynamic tunnel of ONERA/CERT for two two-dimensional (2D) thick trailing edges set in a 2D incompressible flow and at the F2 atmospheric wind tunnel of ONERA/Fauga-Mauzac for a single 2D thick trailing edge set in a three-dimensional (3D) incompressible flow. Apart from static pressure measurements, a 2D or 3D Laser Doppler Anemometry system has provided velocity measurements in the vicinity of the trailing edge, for the 2D and 3D configurations, respectively.

Results for two thick cambered trailing edges are mainly discussed in the present paper.

A Navier-Stokes solver has been recently applied to the airfoil equipped with these different geometries of trailing edges, for the afore-mentioned experimental conditions [3,4].

2. EXPERIMENTAL SET-UP

2.1 THALES Water Tunnel

The experimental study has been carried out in the T.H.A.L.E.S. water tunnel; it is essentially of a recirculating type and resembles a conventional closed circuit wind tunnel. Water runs into the loop by the way of a motor driving a simple impeller situated in the low corner of the tunnel. Water velocities in the working section are infinitely variable from 0.1 ms^{-1} to 7.0 ms^{-1}. The velocity variations at the test section entrance are lower than 1% of the mean velocity, whatever the value of the free-stream velocity, after an effective contraction ratio of 10:1.

The horizontal test section is 0.5 m large, 0.3 m high and 3 m long; the four walls are made of glass or plexiglass, which provides good optical access for flow visualization.

A heat exchanger, located in the lower part of the circuit, allows the temperature of the water to vary. The pressure inside the loop can be adjusted in order to avoid eventual cavitation problems. The main parameters (velocity, pressure and temperature) governing the flow are constantly controlled and adjusted by a micro computer via an automaton.

The tunnel is fitted with a displacement mechanism controlled by a computer allowing linear displacements of the optical probe of the Laser Doppler Anemometry system and measurements at any location in the test section volume. The traversing unit contains step

by step motors which permit remote movement of the probe in the streamwise and vertical directions. The probe location is determined with the aid of encoders allowing position resolution of 0.01 mm per encoder pulse.

Model. The reference model for the present investigation is an OAT15A airfoil having a maximum thickness ratio of 12.3% and a chord length C (or c on some figures) of 400 mm; the upper surface contour is constrained to be the same as the original OAT15A whereas the airfoil geometry is modified on the lower surface. The airfoil is manufactured in such a way that the rear part (last 19% and 15% chord length of the upper and lower sides, respectively) be removable allowing to mount rather easily the three following 2D trailing edges (figure 1):

- the reference trailing edge, referred to as RTE, having a base thickness of 0.5% C;
- two increased cambered trailing edges with the same trailing edge angle, but different incremental base thicknesses, either 0.2%C (CTE 1) or 0.5%C (CTE 2).

These geometries were defined from Euler computations performed at transonic conditions.

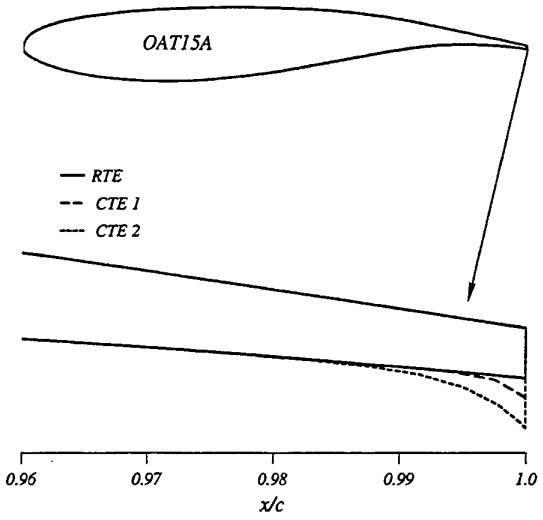


Figure 1. Trailing Edge Geometries

The model, with the reference trailing edge (RTE), is fitted with 64 static pressure taps located on its suction and pressure sides, with one on the base. The others geometries involve one or two supplementary pressure taps on their base, according to their thickness.

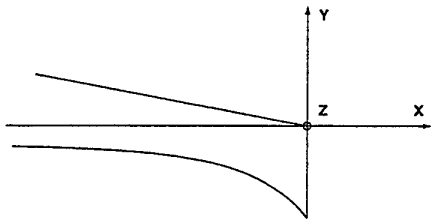
The wing model is mounted vertically between the top and the bottom walls of the test section; using a turntable, it could be manually rotated through a ±5° range in angle of attack by step of 0.25°.

Test conditions. The experiments are conducted for a constant tunnel water speed of 2 ms^{-1} and a practically constant water temperature of 293K. This leads to a free stream Reynolds number based on the model chord length of about 800,000.

Transition is tripped on the lower and upper sides of the model by a 0.2 mm diameter trip wire stuck parallel to the leading edge, at about 3% of chord length downstream of it.

Measurements in the wake and in the boundary layer are performed in a plane located at one third of the span airfoil from the upper test section wall.

Measurement technique. In the present experimental study, measurements include essentially pressure distribution and flow scrutinizing in the vicinity of the trailing edge airfoil through Laser Doppler Anemometry system. The sketch below shows the system of coordinates used for the present study: the X(or x)-axis is along the mean flow direction, Z is parallel to the airfoil trailing edge and Y is in the transverse direction, perpendicular to both X- and Z-axis. X=0 refers to the airfoil leading edge, Z=0 corresponds to the test section centre-line, while Y=0 is the point located at the intersection line between the suction side of the airfoil and its base.



Co-ordinate system for wake surveys.

A two-dimensional component Laser Doppler Anemometer is used to measure the magnitude and direction of the velocity vector and elements of the Reynolds stress tensor in the X-Y plane. The L.D.A. system uses a coherent argon ion laser operating with a power of about 1.5W.

The light beam from the laser is split into two components: one green (λ=5.14 nm) and the other blue (λ=488 nm). Each color component of the laser is further split into two beams, one relating to the green and the other one relating to the blue passed through a Bragg cell containing a 40MHz transducer.

The L.D.A. system is used in a backward scattering mode; the four beams probe is located in such a way that its axis is perpendicular to the upper wall of the test section. So, the probe produces convergent beams that enter the water tunnel through one of its upper glass wall. The front lens of the optical system has a focal length of 480 mm in air and the laser beam pairs are focused down to a diameter of about 180 µm at the measuring point which has a length of 4 mm at an

intersection angle of 5.4°. The two beams are inclined at 45° with respect to the main flow direction.

The seeding of the flow is made by means of iriodine powder (particles with a mean size of 2 μm) added to the circulating water in the tunnel. Light scattered by particles travelling through the intersection volume is collected by the probe's lens and then focuses into a receiver fiber optic cable which carries it to the output which feeds the light to the photomultiplier.

Data acquisition is done by means of Burst Spectrum Analyzers used in master-master configuration; frequencies and arrival times of particles in the B.S.A. output buffers are transferred to a Macintosh computer. A post processing of these data information validates the measured values related to the two B.S.A. counters for which the arrival time differences are within a certain preset coincidence time window.

Positioning of the measuring point in the X and Y directions is done by steps motors under computer control. Time for traversing is used for displaying mean value, standard deviation and correlation of the two velocity components at the point measured just before. Mean and fluctuating quantities are obtained from average over 2000 samples and standard statistic treatment, respectively.

The task of the LABVIEW data acquisition system is also to provide continually on a graphical display the main elements of the data processing (instantaneous velocity signals, velocity histograms, arrival times comparison, number of validated data) allowing the permanent control of the validity of the L.D.A. measurements.

Generally speaking, boundary layer measurements have been performed as close as 0.2 mm to the wall; however, the measurement volume has not been approached to the model base closer than its diameter thickness.

Measurement uncertainties, mainly attributable to the optical system, include the uncertainty in the measurement of the cross beam angles of laser beam orientation and in the misalignement of laser beams at probe volume. If so, the fringe pattern is either diverging or contracting along the optical axis and its spacing variation yields different signals frequencies for the same velocity depending where the particle passes through the sample volume. Bias errors in instantaneous velocity component may also arise as a result of a velocity lag between particles and flow, noise in signals... and so forth.

The optical probe makes an angle of 1.5° with the Z-axis direction to insure that there is no interference of the beams (at the measurement volume) with the model when measurements are being made close to the model surface in its trailing edge region. Bias error is unavoidably introduced when the laser probe axis is not perpendicular to the wall glasswindow; this bias error is increased when the environment through which the laser beam is passing changes which is the case with the present experiment. However, the measurement method with the inclined laser beam did not point out a significant deviation in data as compared with the reference ones obtained when the probe axis is normal to the window.

A systematic analysis of the bias errors has not been performed. Nevertheless, some previous experiments conducted by letting vary the laser beam orientation and the preset coincidence time window gave us some useful information about errors occurring in velocity measurement.

2.2 F2 Wind Tunnel

Experiments concerning the same as above reference and increased cambered trailing edges set in 3D turbulent flows have been conducted in the F2 atmospheric wind tunnel of ONERA-Fauga. The test section ($1.80 \times 1.40 m^2$) is fitted with a mechanism allowing the displacement of the optical probes of the three-dimensional L.D.A. system at any location in the test section volume.

Model. The model is a cylindrical wing 400 mm chordlength and 1505 mm span; the aspect ratio being about 7. In fact, the model consist of three elements: the profile of the central element is the one previously used for the 2D analysis in the water tunnel. Measurements are made only in the wake of this central element. However, the trailing edge has the same geometry in any spanwise section of the wing.

The model is fixed with a sweep angle of 20° on a turntable (inserted in the test section floor) allowing its rotation.

Test conditions. Experiments are conducted for a constant velocity of 32 ms^{-1} leading to the same free stream Reynolds number (based on the model chord and on the velocity normal to the leading edge direction) of 800 000 obtained in 2D configuration at the water tunnel. Transition tripping is exactly the same as the one considered in 2D flows.

Measurement technique. Laser measurements are performed in a forward scattering mode. The emission heads are located in such a way that each plane formed with two beams is parallel to the model trailing edge. The focal distance of the optic laser heads is inclined at about 20° related to the horizontal reference is 1500 mm. The measurement volume has a diameter of 0.30 mm and a fringe separation of 15 μm.

From photomultipliers, signals are directed on three Dantec counters through analogic pass-band filters. A preset coïncidence time (1ms) forced the counter to detect the same particle.

3. ANALYSIS AND RESULTS

3.1 Two-dimensional Flow

Pressure Distributions. The streamwise pressure distributions obtained for the RTE, CTE 1, CTE 2 trailing edges, for the same value of the lift coefficient (nominal value: Cl=0.47), are plotted in figure 2.

The pressure coefficient has been corrected from wall effects using empirical formulae [4]. As expected, the important effect attributed to the cambered lower side and divergence angle is clearly evidenced: the airfoil loading near the trailing edge is substantially modified.

The lower and upper surfaces appear to be uncoupled, that is to say that the pressure level on the upper side differs tremendously from the one recorded on the lower side. This uncoupling effect is rather more important for the CTE 2 trailing edge than for the CTE 1 one.

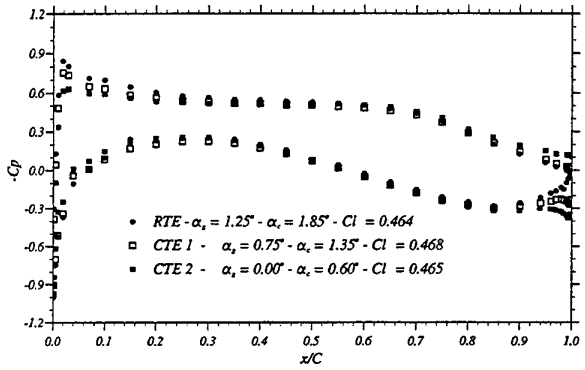


Figure 2. Streamwise Pressure Distribution

Another important feature of these increased trailing edges results is a rather large pressure gradient modification on the last 10% of chord length (figure 3):

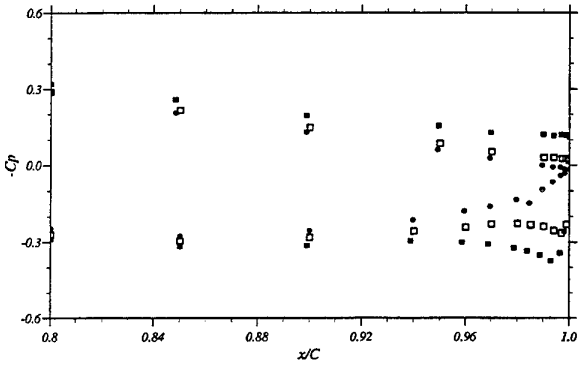


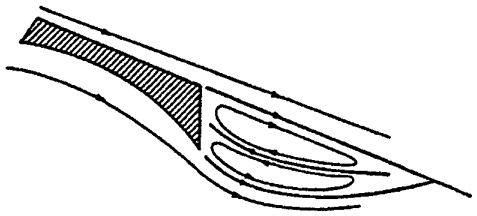
Figure 3. Streamwise Pressure Distribution (Zoom)

- on the upper surface the existing adverse pressure gradient for the standard trailing edge is reduced when considering the CTE 1 geometry; the decrease is even larger with the thickest base (CTE 2).

- on the lower surface, the pressure gradient is always negative for the OAT15A airfoil; on the other hand, this gradient is slightly positive down to x/C=0.99 and then negative again. Thus, there will be a rather small surface exposed to great acceleration.

An interesting feature to point out is that the rear loading effect does not seem to evolve too much with the angle of attack of the model, at least for the considered incidence variation.

Flow field in the vicinity of the trailing edge. One objective of the experimental programme was to scrutinize the flow just downstream of the increased trailing edges. The idea being to verify the hypothesized flow field pattern suggested by Henne et al. for the flow closure downstream of a Divergent Trailing Edge airfoil [2]. For that specific purpose, the 2D L.D.A. system has been considered.



Hypothesized Flow Closure for Divergent Trailing Edge Airfoil

For all trailing edges, boundary layer surveys in the last 6.25% of chord length of the upper and lower sides as well as surveys in the near wake (towards 6.5% chord length downstream of the trailing edge) have been performed, allowing to catch a very precise description of the flow. This represents approximately an amount of 2,500 survey points.

It has to be recalled that boundary layer and wake surveys are performed with and without inclination angle of the laser beams, respectively. In any case, it allows to go as close as 0.2 mm to the wall.

Thus, for the RTE, CTE 1, CTE 2 trailing edge airfoils, set at the right incidence which corresponds to the nominal value of the lift coefficient (Cl=0.47), a very complete data base has been generated; it comprises the two components of the mean velocity, U and V, as well as the turbulent intensity and shear stress components in the close vicinity of the trailing edge.

Velocity profiles in the boundary layer are expressed in the (X,Y) cartesian frame linked to the tunnel test section. Then, knowing the geometry of the trailing edge airfoil, projection has been carried out in order to express the velocity components in directions parallel to the wall and normal to the wall, U and V respectively. However, in the last percent of chord length along the lower side, where a divergence angle is present, such a projection cannot be correctly applied.

Illustration of some boundary layer surveys is only detailed at a given location: x/C=96.25%, i.e. 15mm

upstream of the trailing edge base; indeed, such a streamwise location is rather well representative of the flow modification.

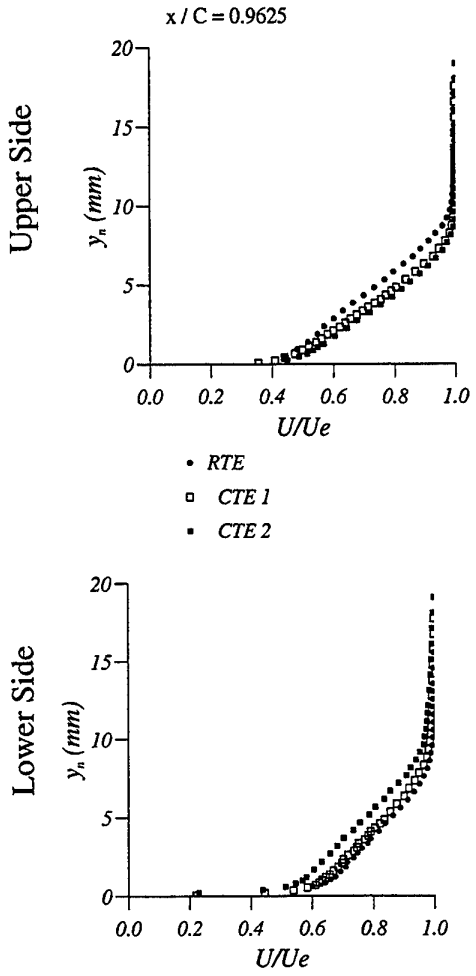


Figure 4. Mean Streamwise Velocity Profiles

For both upper and lower surfaces, mean velocity profiles, non-dimensionalized by the outer edge velocity Ue, are plotted versus y_n in figure 4; y_n is the distance normal to the wall. Being able to go as close as 0.2 mm to the wall allows to start with values of U/Ue as low as 0.4.

Considering the upper side of any airfoil model, the RTE trailing edge presents a stronger adverse pressure gradient, which explains a greater thickening of the viscous layer than that obtained from the CTE 1 and CTE 2 geometries (figure 4).

On the lower side of the airfoil, the behaviours are completely inverted: the RTE trailing edge has the most favourable pressure gradient at this measurement station compared to the CTE 1 and CTE 2 shapes and, as a consequence, the thickening of the boundary layer is less important. Whatever geometry of the trailing edge, the V-component is either negative or almost zero due to the acceleration of the flow.

The normal and cross components of the Reynolds stress tensor are plotted in figure 5, at the same station (x/C=96.25%), for both the upper and lower sides of the three trailing edge geometries: RTE, CTE 1 and CTE 2. The profiles of u'^2, v'^2 and u'v' exhibit a classic evolution versus y_n. Indeed, the streamwise turbulent intensity profile presents a peak close to the wall, the level of which increases for positive pressure gradients. On the other hand, the profile of velocity fluctuations normal to the wall has a maximum at about 20-25% of the boundary layer thickness, which moves away from the wall as the pressure gradient increases.

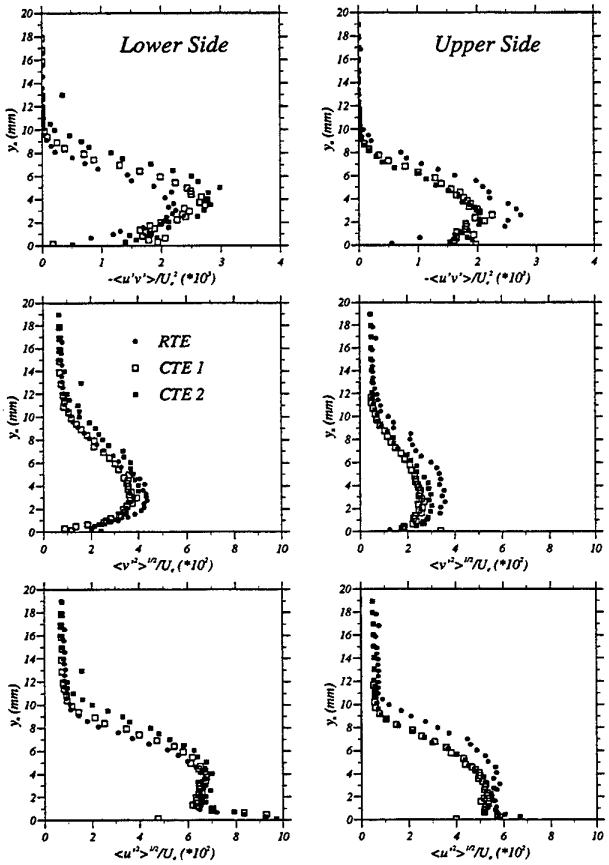


Figure 5. Components of the Reynolds Stress Tensor

One of the most evident feature concerns the shear stress profile, for which the maximum value for the upper surface (or lower one) increases (or decreases) with the adverse (or favourable) pressure gradient. That maximum shear stress is larger than the wall shear stress.

At the edge of the boundary layer the profiles of the velocity fluctuations tend towards a very weak turbulent value close to 1%; it represents the free stream

turbulence rate that has been measured previously in the water tunnel for this free stream velocity.

The knowledge of the velocity field in the vicinity of the various trailing edges allows to plot the streamline pattern; in order to compare the flow field downstream of these thick cambered trailing edges, an enlargement has been produced downstream of any trailing edge, over about 3% of chord length in the streamwise as well as transverse directions.

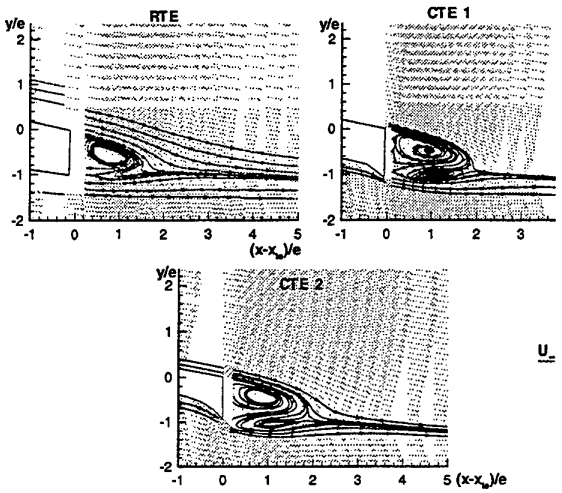


Figure 6. Streamline Pattern

Figure 6 refers to the streamline pattern of the OAT15A-RTE, CTE 1 and CTE 2 trailing edges, respectively. For every configuration, two vortices are recorded in a confined area, downstream of the base. The dimensions of the recirculating area is tightly related to the base height or thickness, e: indeed, it is about (2e x e) in the streamwise x transverse directions. The grid refinement is even such that the location of the re-attachment point can be estimated.

However, when looking at these streamline patterns downstream of such airfoils, one could question the two-dimensionality of the vortex flow, since some streamlines seem to wrap around one point while others do not. In order to try to analyse such an observation, the dW/dZ component has been derived from the continuity equation and plotted in the near wake. Although, no drawing is given in the present paper, there has been no sufficient variation in the modulus of that derivative to explain that the flow was moving inwards or outwards the (X,Y) plane.

A first numerical approach has been recently conducted, aiming at testing the behaviour of different turbulence models for such boundary and wake flows [3,4]. Several one-equation and two-equation models have been implemented in the Navier-Stokes solver, originally developed at ONERA [5]. Some turbulence models provide a correct prediction of the measured viscous flow behind such cambered trailing edges, but others do not [4]. An example of rather good agreement between experiments and calculation is given in figure 7, using the Spalart-Allmaras model [6].

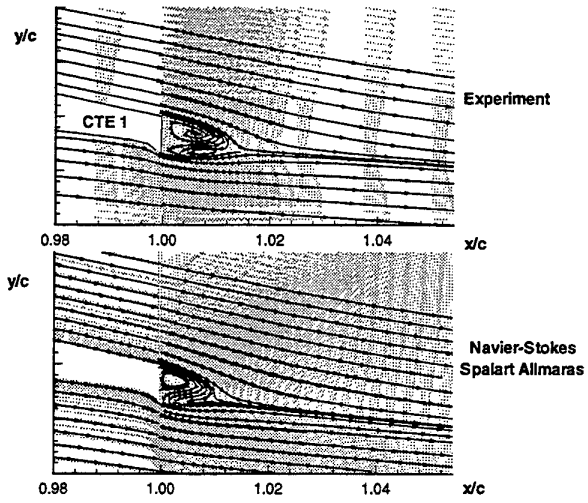


Figure 7. Computed and measured near-wake flows

3.2 Three-dimensional Flow

Pressure measurement. Pressure measurements obtained for the model equipped with the thicker cambered trailing edge (CTE 2) have given, as expected, comparable distributions with the ones obtained for 2D flow conditions.

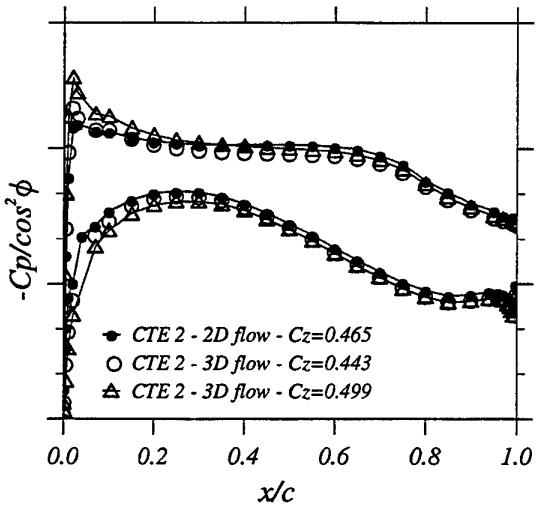


Figure 8. Pressure Distribution

With the infinite swept wing hypothesis, the pressure coefficient can be expressed in a direction normal to the leading edge. Figure 8 gives a comparison of the pressure distribution for CTE 2 (for three values of Cl surrounding the nominal value of 0.47) obtained in 2D and 3D flows. Some deviations are notable on the upper and lower side in the vicinity of the leading edge whereas on the rear part of the model, the evolutions of the pressure coefficient are very close to each other.

Flow field in the vicinity of the trailing edge. Near wake surveys with the 3D Laser Anemometer have been made in two planes P1 and P2, aligned with the free-stream direction; the distance in the transverse direction (Z) between these two planes is equal to 100mm. Results obtained then would allow to verify the invariance of mean and turbulent quantities in the Z-direction in accordance with the uniform repartition of the local lift coefficient in spanwise direction, resulting from Euler computations.

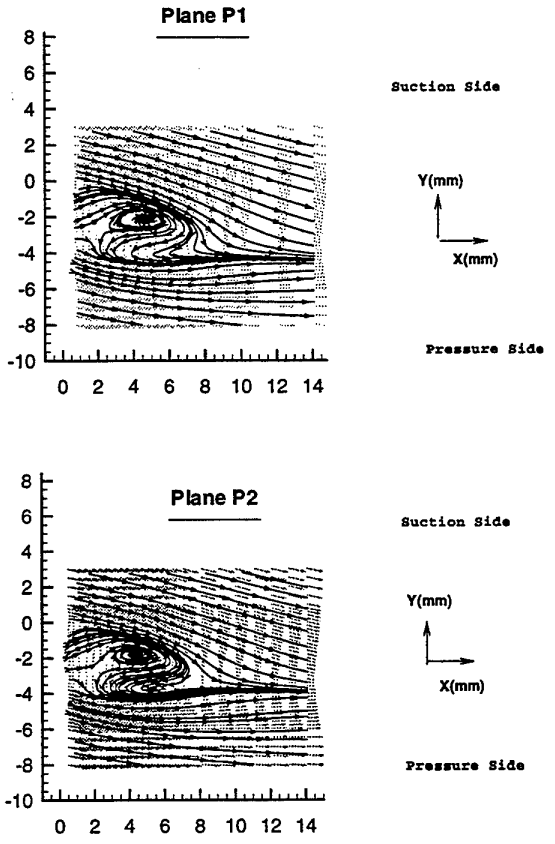


Figure 9. Streamline pattern downstream of the CTE 2 trailing edge; Check for two-dimensionality

From a good refinement of the survey grid, it has been possible to catch a very precise description of the flow. Figure 9 shows a comparison of the streamline pattern in the two above mentioned planes. This comparison reveals a good agreement on the topologic structure of the flow downstream of the CTE 2 trailing edge. It should be noticed that the flow pattern just downstream of the base is correctly reproduced from P1 to P2. The two-dimensionality of the flow does not seem to be questionable regarding the location and the size of the vortices in the two measurement planes.

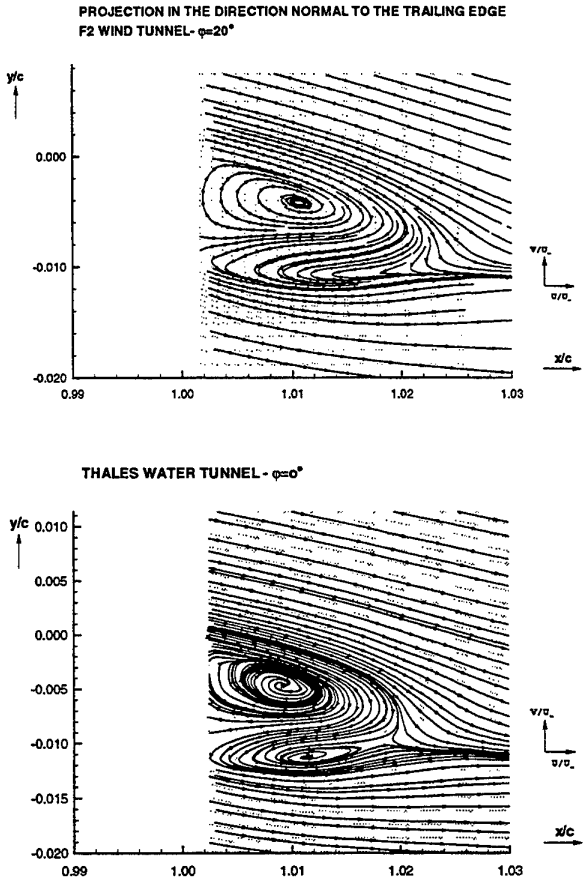


Figure 10. Comparisons of the flow field pattern downstream of the CTE 2 in 2D and 3D flows

Projecting the velocities in a plane perpendicular to the trailing edge, the flow field pattern in the near wake can be compared to the one observed in two-dimensional case (figure 10).

In a general way, behind 2D thick cambered trailing edges, 3D flow does not exhibit a topological structure far away from the one evidenced in 2D flow.

Nevertheless, the rolling motion of the fluid in the lower side of the wake has disappeared. Setting the model at a given sweep angle of 20° seems to slightly modify the streamwise position of the upper vortex and of the reattachment point.

4. CONCLUSION

Some interest has been recently devoted to the Divergent Trailing Edge concept, following up research that has been undertaken at McDonnell Douglas Corporation. When looking at literature, there is very little published work from either an experimental or numerical point of view, as regards flow modification induced by such non-conventional trailing edge geometries.

An experimental programme has thus been carried out in order to characterize the potential and viscous flows in the vicinity of different thick cambered trailing edges in both two- and three-dimensional flows.

The two increased cambered trailing edges have induced a rather important pressure gradient modification on the last 10% chord length of both upper and lower sides of the airfoil. The effect of the cambered lower side and of the divergence angle of the trailing edge results in an increase of rear airfoil loading.

In two-dimensional configuration, a lot of boundary layer and wake surveys have been performed on both sides of the trailing edges geometries, providing with a very precise description of the flow. A consistent data base, for mean and fluctuating quantities, has been obtained even though the laser beam orientation has been changed in some areas in order to go as close as possible to the wall.

Just downstream of each increased base thickness, a recirculation area has been captured, including two contra-rotating vortices, the dimensions of which are tightly related to the base height.

The behaviour of non-conventional two-dimensional shapes of trailing edges has thus been looked at in three-dimensional turbulent flows putting the model with 20° sweep angle. Near wake surveys have also revealed a recirculation area corresponding to negative streamwise velocities. However, the topological structure is slightly modified from the one obtained for two-dimensional flow conditions.

Thus, a very complete data base has been generated and will be (hopefully) used for subsequent code validation. Indeed, boundary layer and wake surveys in the immediate vicinity of the trailing edge have provided mean and fluctuating quantities as well as integral parameters, for various geometries of trailing edges. The recorded flow field pattern downstream of such base shapes should help for validating and/or improving the existing Navier-Stokes codes for future optimisation of thick cambered trailing edges.

Acknowledgements

GP and EC are very grateful to the whole team from the ONERA/Fauga F2 wind tunnel (MM. D. Afchain, M. Deluc, R. Johannel and Ph. Loiret).

The authors wish also to acknowledge Airbus Industrie and the Service des Programmes Aéronautiques (SPAé) for supporting these studies.

REFERENCES

[1] Liebeck R.H. 1978, Design of subsonic airfoils for high lift. Journal of Aircraft, vol. 15, N°9, pp. 547-561.

[2] Henne P.A. and Gregg R. D. 1991, A new airfoil design concept. Journal of Aircraft, vol 28, N°5, pp. 333-345.

[3] Sauvage Ph, Pailhas G., Coustols E. 1997, Detailed flow pattern around thick cambered trailing edges. Seventh Asian Congress of Fluid Mechanics, Chennai Madras.

[4] Sauvage Ph. 1998, Etude expérimentale et numérique des écoulements potentiels et visqueux dans le voisinage d'un bord de fuite épais cambré, Ph. D Thesis, ENSAE, Toulouse, France.

[5] Vuillot A.M., Couailler V. and Liamis N. 1993, 3D turbomachinery Euler and Navier-Stokes calculations with a multi-domain cell-centered approach, AIAA-93-2576.

[6] Spalart P.R. and Allmaras S.R. 1994, A one-equation turbulence model for aerodynamics flows. La Recherche Aerospatiale, pp. 5-21.

RECONSTRUCTION OF 3-D STEADY INCOMPRESSIBLE FLOW FIELD OUT OF 2-D PIV MEASUREMENTS IN WIND TUNNELS

N. Lang and W. Limberg

Aerodynamisches Institut of Rheinisch-Westfälische-Technische-Hochschule Aachen
Wüllnerstr. zw. 5 u. 7, D-52062 Aachen, Germany

ABSTRACT

Particle image velocimetry was applied to the flow over the leeward side of the delta wing configuration ELAC. A set of measurements were taken in parallel planes at different positions in spanwise direction. The whole three-dimensional structure of the flow was gained by application of continuity equation and integration of the out-of-plane velocity component. Dependant on the spatial resolution of the measurements even small flow structures as the area of secondary separation were detected. Accuracy of the so constructed third velocity component was investigated by application of the reconstruction procedure to a numerically obtained dataset of the flow field. An improvement of the calculation of derivatives and integration results in a small error. The influence of the different methods is examined and compared by statistical analysis.

1. INTRODUCTION

The experimental investigation of three-dimensional flow structures with particle image velocimetry (PIV) has gained rising importance in experimental flow examination during the past. Aim of the efforts is a timeresolved measurement of all velocity components in a 3D observation volume.

An extension to the classical PIV, which enables the measurement of the 2D velocity components within a plane, is stereoscopic PIV. The information on the depth of particles is gained by recording the particle images in different views so that the velocity distribution is measured in all three dimensions within a plane. The different styles of stereoscopic PIV are subdivided by the viewing direction. It is the governing factor for the accuracy of measurement of the out-of-plane component. Due to the required depth of focus big tracer particles of 30 µm and more are required. This is adverse to the velocity lag of particles versus fluid flow.

Dual-plane PIV enables the detection of the third velocity component by taking particle images at different light-sheet positions. Two exposures are taken at the same light sheet position, a third is taken at a light-sheet position, which is shifted by a certain distance. The velocity component normal to the light sheets is computed by an evaluation of the height of the cross-correlation peak. This method is limited by the requirement of a uniform intensity profile of the different light-sheets and a constant loss of particles due to in-plane motion. The aspects of stereoscopic and dual-plane PIV are explained in Raffel et al. (1997).

With help of holographic PIV all velocity components can be measured in a three-dimensional domain. The area of interest of the flow field is illuminated by an expanded light sheet. A holographic plate records the superimposed wave of the scattered light and a reference wave. Subsenquently a virtual image of the flow field is constructed with the help of a reconstruction laser. Then the velocities can be evaluated by taking exposures of this virtual image with e.g. stereoscopic PIV. The holographic PIV requires a very high output energy of the laser. Furthermore vibrations have a disastrous effect on the quality and finally the measurement of the velocity component in viewing direction is limited by pulse duration and laser wavelength. The different set-ups are explained e.g. in Hinsch (1995) or Royer (1997).

Other methods are also subject to restrictions. For the resolution of 3D particle tracking see e.g. Choi et al. (1996) and for the flow velocity at scanning PIV, which also yields the velocity distribution in a 3D area, see Brücker (1997).

All the described methods have a complex experimental set-up in common. Therefore an applica-

tion to wind tunnel flows is difficult, because limited optical access and vibrations, which were caused by test facilities, represent strong restrictions. In order to cope with these problems in small test facilities for 2-D PIV the recording system can be mounted outside the test section. Due to the small depth of focus and the required small out-of-plane component a light sheet orientation in streamwise direction is advisable. For the case of measurements being taken at different planparallel positions of the light sheet in incompressible flow, continuity equation can be applied to the in-plane components. Then the out-of-plane component can be integrated starting at the symmetry plane. According to Nyquist criterion the distance between the discrete positions of the different measurements must be chosen carefully so that small flow structures can be resolved. A combination of the method suggested by Robinson and Rockwell (1993) for numerical calculation of derivatives with the numerical integration with Simpson's resp. Bode's rule minimizes the computational error and provides the velocity distribution in all three dimensions over the model.

2. APPARATUS

The velocity distribution was measured using PIV. It is suited to measure in a 2D observation area the in-plane velocities. This is attained by illuminating a particle laden flow with a pulsed light sheet. Usually in wind tunnel experiments photographs of this light sheet are taken. The experiments were carried out with a model of the hypersonic configuration ELAC in a low speed wind tunnel in Eiffel configuration. The pulsed light sheet for the PIV photographs was generated by a ruby laser and an appropriate optic. The photographs were evaluated with autocorrelation using a semi-optical system. All these components are described in the following.

2.1 Experimental Set-up and Test Conditions

The hypersonic configuration ELAC is a two-stage-to-orbit system (TSTO), which was developed in the Collaborative Research Center "Grundlagen des Entwurfs von Raumflugzeugen" (SFB 253) of the German Research Association DFG, fig 1a. A 1:240th scale model of the first stage was used for the experiments. It is a delta shaped lifting body with rounded leading edges and semi-elliptic cross-sections, fig. 1b. The model was mounted on a traverse which enabled a movement in spanwise direction.

A low-speed wind tunnel was used for the measurements. It was driven in Eiffel configuration. The free stream velocity can be varied from 0 m/s to 34 m/s with a turbulence level less than 0.4%. The cross-section is 0.5x0.5 m^2 and the contraction ratio of the nozzle is 5.7:1. The test conditions were an angle of attack of 10° and 20°, the Reynolds number was 300 000, corresponding to a free-stream velocity of 11 m/s. Oil aerosol with a mean diameter of 1.97 µm was used as tracer particles. It was produced with the use of Laskin nozzles as described in Echols and Young (1963).

The pulsed light sheet for the single-frame double-exposed photographs was generated with a pulsed ruby system with 400 mJ pulse energy at a wavelength λ of 694 nm and 30 ns pulse duration. With help of a cylindrical lense, a telescopic optic and a convex focussing lense a light sheet was formed over the model of 50 mm in width and 0.5 mm in height, Prenel et al. (1989). In order to minimize the loss of particles due to out-of-plane motion the time delay Δt between the light pulses was adapted to the position of the light sheet in spanwise direction. It was shortened from 81 µs to 50 µs in the area of maximum out-of-plane motion, which is situated in the area of primary vortex. The photographs were taken with a 35 mm high-resolution technical pan film and a Makro-Elmarit 1:2.8/60 mm lens.

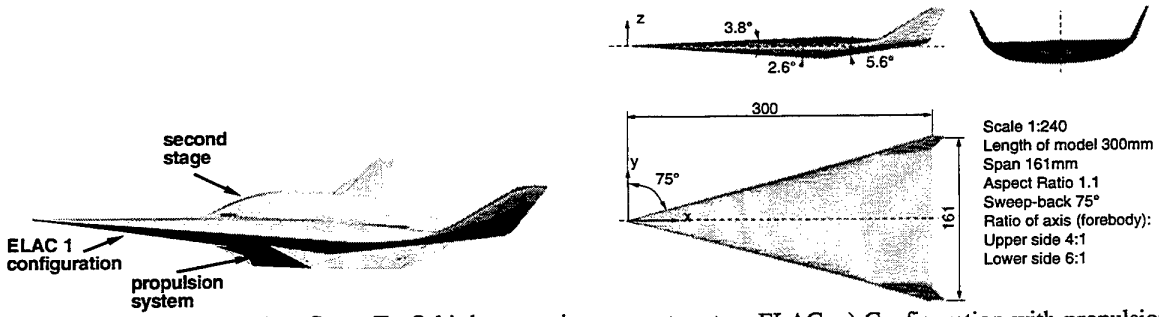


Fig. 1a,b Sketch of the Two-Stage-To-Orbit hypersonic transport system ELAC. a) Configuration with propulsion system and second orbital stage. b) Used model of ELAC for experiments without second stage or propulsion system.

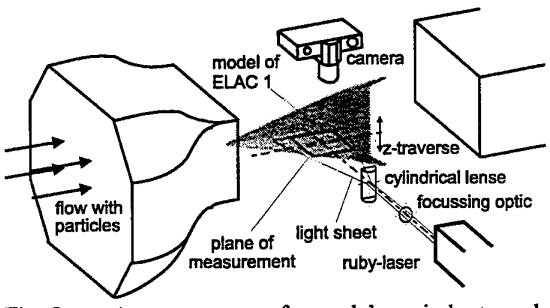


Fig. 2 Arrangement of model, wind tunnel, camera and laser sheet optic. The model is mounted on a z-traverse.

2.2 Evaluation of Photographs

The evaluation of the double exposed PIV photographs was realized by a semi-optical system as e.g. explained in Molezzi and Dutton (1993). The negatives were mounted on a PC driven traverse so that small interrogation areas could be stepwise illuminated by a He-Ne laser. Resultant from a stepwidth of 0.3 mm the overlap was 50%. The so produced Young's fringes were digitized with help of a frame grabber and a CCD camera. The average displacement of the particles was obtained by an inverse fourier transform of the fringe pattern. Then the velocity was computed with help of the magnifaction factor M and the time delay Δt between the pulses.

16 data planes were obtained at an angle of attack of 10°, the distance between the several light sheet positions h was 4 mm. At 20° angle of attack h was reduced to 2 mm resulting in 31 data planes with the velocity distribution of u and v. Every velocity map in x,y-direction contains 31x57 vectors. The evaluation error of 3% was decreased by averaging the datas over five measurements. Figure 3 shows the orientation of model and three already evaluated velocity maps at different positions in spanwise direction.

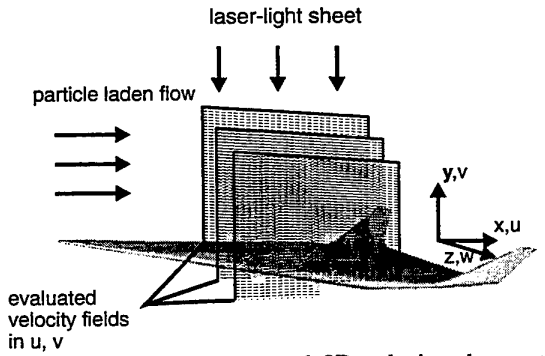


Fig. 3 Different measured 2D velocity planes at three positions in spanwise direction over ELAC.

3. DESCRIPTION OF RECONSTRUCTION PROCEDURE

The construction of the out-of-plane velocity component w is based on application of continuity equation for steady incompressible flows., eqn 1.

$$div\,\vec{u} = \frac{\partial u}{\partial x} + \frac{\partial v}{\partial y} + \frac{\partial w}{\partial z} = 0 \qquad (1)$$

The derivative of the out-of-plane velocity can then be computed in the x,y-planes of measurement by eqn. (2).

$$\frac{\partial w}{\partial z}(x_i,y_j,z) = -(\frac{\partial u}{\partial x}+\frac{\partial v}{\partial y})(x_i,y_j,z) \qquad (2)$$

Thus the velocity w can be integrated starting at the symmetry plane by applying eqn. (3) with the initial value in the symmetry plane $w(z_0=0) = 0$.

$$w(x_i,y_j,z) = w(x_i,y_j,z_0=0) - \int_{z_0}^{z}(\frac{\partial u}{\partial x}+\frac{\partial v}{\partial y})(x_i,y_j,z')dz' \qquad (3)$$

The numerical calculation of derivatives and integrals has a leading effect on the quality of reconstruction. In the following an improved procedure for this is worked out.

3.1 Computation of Derivatives and Integrals

First an averaging filter was applied to all velocities in the x,y-planes according to Spedding et al. (1987), eqn. (4).

$$g(x_i,y_j) = \frac{1}{4}[g(x_{i-1},y_j)+g(x_{i+1},y_j) + g(x_i,y_{j-1})+g(x_i,y_{j+1})] \qquad (4)$$

The computation of the in-plane velocity derivatives was improved by applying the adaptive Richardson extrapolation scheme. In comparison to central differences the truncation error ε_T is decreased while the expermimental ε_{ex} error remains in the same order of magnitude. Equation 5 describes the errors.

$$\varepsilon_T = a_0h^2 + a_1h^2 + \ldots; \quad \varepsilon_{ex} = \frac{\varepsilon}{h} \qquad (5)$$

The adaptive scheme combines values of derivatives calculated on different grids. A coarser grid leads to an increasing truncation error and a decreasing experi-

mental error. Equations 6 and 7 show the values for the derivatives f_1 and f_2 on a h and $2h$ spaced grid in dependance of the exact derivative f_{ex} and the appropriate errors as descirbed in Lourenco and Krothapalli (1995).

$$f_1 = \frac{u_{i+1} - u_{i-1}}{2h} = f_{ex} + \frac{\varepsilon}{h} + a_0 h^2 + a_1 h^4 + \ldots \quad (6)$$

$$f_2 = \frac{u_{i+2} - u_{i-2}}{4h} = f_{ex} + \frac{\varepsilon}{2h} + 2^2 a_0 h^2 + 2^4 a_1 h^4 + \ldots \quad (7)$$

A better estimate of f_{ex} can be gained by f_{d1} in eqn. 8, which combines the values f_1 and f_2. The second order term of the truncation error is eliminated while the experimental error keeps the size of magnitude.

$$f_{d1} = \frac{4f_1 - f_2}{3} + \frac{7}{6}\frac{\varepsilon}{h} + 4a_1 h^4 + \ldots \quad (8)$$

Applying the same procedure to the values of a $2h$, $4h$ and $8h$ spaced grids results in the values f_{d2} and f_{d4}.

$$f_{d2} = \frac{4f_2 - f_4}{3} + \frac{7}{12}\frac{\varepsilon}{h} + 64a_1 h^4 + \ldots \quad (9)$$

$$f_{d4} = \frac{4f_4 - f_8}{3} + \frac{7}{24}\frac{\varepsilon}{h} + 1024a_1 h^4 + \ldots \quad (10)$$

The fourth order truncation error is then eliminated by combination of f_{d1} and f_{d2} and f_{d2} and f_{d4}. Combining these results the sixth order truncation error can also be deleted. This is shown in equations 11 and 12.

$$f_{dd1} = \frac{16f_{d1} - f_{d2}}{15} + \frac{217}{180}\frac{\varepsilon}{h} + 64a_2 h^6 + \ldots \quad (11)$$

$$f_{ddd1} = \frac{64f_{dd1} - f_{dd2}}{63} + \frac{3937}{3240}\frac{\varepsilon}{h} + 4096a_3 h^8 + \ldots \quad (12)$$

On the initial grid with spacing h f_{dd1} and f_{ddd1} can be computed by the values of the different grid size as follows:

$$f_{dd1} = \frac{64f_1 - 20f_2 + f_4}{45} \quad (13)$$

$$f_{ddd1} = \frac{4096f_1 - 1344f_2 + 84f_4 - f_8}{2835}. \quad (14)$$

The integration of equation 3 is realized with help of Simpson's and Bode's rule, see Press et al. (1992). The simple trapezoidal rule is based on the calculation of the integral of a function by approximating the function with two points. The resultant error is of order $g^{(2)}h^3$. The value g stands for the derivative $\partial w/\partial z$ in equation 2.

$$\int_{z_0}^{z_1} g(z')dz' = \frac{h}{2}(g_1 + g_2) + O(g^{(2)}h^3) \quad (15)$$

Following the same principle as already described for Richardson extrapolation, the order of error is decreased by three-point formulas (Simpson's rule, eqn. 16) and five-point formulas (Bode's rule, eqn 17).

$$\int_{z_0}^{z_2} g(z')dz' = \frac{h}{3}(g_1 + 4g_2 + g_3) + O(g^{(4)}h^5) \quad (16)$$

$$\int_{z_i}^{z_{i+4}} g(z')dz' = \frac{h}{45}(14g_i + 64g_{i+1} + 24g_{i+2} + 64g_{i+3} + 14g_{i+4}) + O(g^{(6)}h^7) \quad (17)$$

4. STATISTICAL ANALYSIS OF THE RECONSTRUCTION PROCEDURE

The accuracy of the construction procedure of the out-of-plane velocity component was investigated by the use of a numerically obtained dataset of the compressible flow around the ELAC configuration. Details about the computation can be found in Henze et al. (1996). Density and velocity distribution of a solution of the parabolized Navier-Stokes equations was interpolated on a three-dimensional grid appropriate to the evaluation of the experiments. In this way 31 data planes according to the experiment at an angle of attack of 20° were extracted.

A 3% relative error was superimposed on the extracted distribution of ρu and ρv in all x,y-planes. It is the estimated averaged relative error of the used PIV system. Then the construction procedure for the out-of-plane velocity was carried out using Robertson's extrapolation and Simpson's and Bode's rule. Table 1 shows the improvement by application of these methods in comparison to central differences and the trapezoidal rule. Accuracy of reconstruction is shown for 0% and 3% noise level. The uncertainty of 3% noise level on ρu and ρv represents a maximum value for the reconstruction error, because the experimental

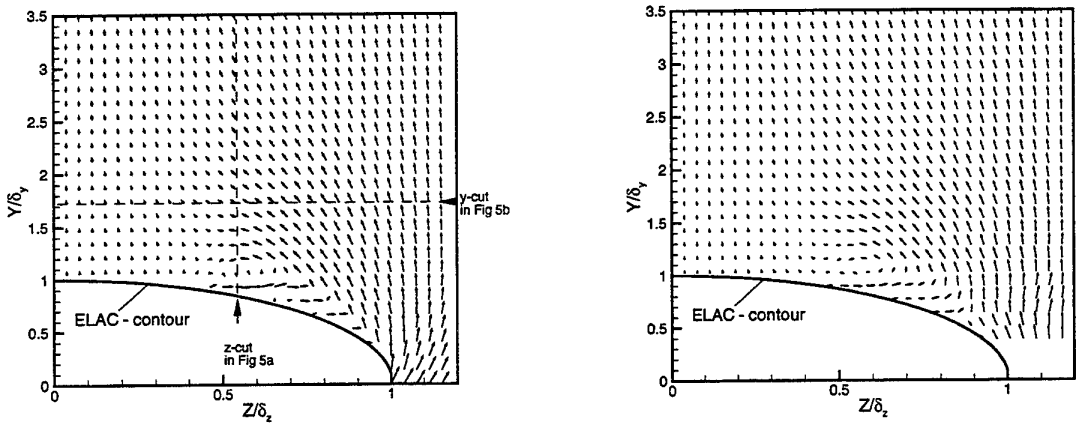


Fig. 4a,b Vector plots of ρw and ρv in a z,y-plane. a) Crossflow field of the numerical solution of the Navier-Stokes equations interpolated on a grid according to the measurements. b) Reconstructed flow field out of the extracted in-plane components of the numerical solution with 3% noise level and the reconstructed momentum ρw.

uncertainty was reduced by an averaging over five measurements.

The error of reconstruction was investigated by statistical analysis. The variability of the reconstructed component in comparison to the expected value of ρw is represented by the ***RMS*** value, also known as standard deviation. It was computed as shown in equation 17.

$$RMS = \sqrt{\frac{1}{(NM)-1} \sum_{i=1}^{N} \sum_{j=1}^{M} \left(\rho w_{i,j} - \rho w_{i,j,theor} \right)^2} \quad (17)$$

A statement concerning the asymmetry of data can be achieved by computing the third moment or skewness S of a distribution, eqn. 18. A positive value signifies a too large estimate relative to the theoretical data. The fourth moment or kurtosis K was computed by application of equation 19. It is a value for the latitude of the data. A large value K means a smaller distribution. The third and the fourth moment are both nondimensional quantities.

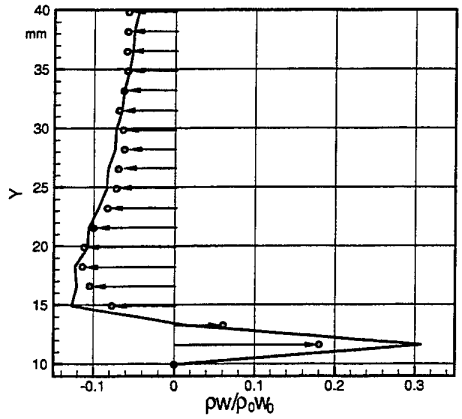
$$S = \frac{1}{NM} \sum_{i=1}^{N} \sum_{j=1}^{M} \left[\frac{\rho w_{i,j} - \rho w_{i,j,theor}}{\sigma} \right]^3 \quad (18)$$

$$K = \left\{ \frac{1}{NM} \sum_{i=1}^{N} \sum_{j=1}^{M} \left[\frac{\rho w_{i,j} - \rho w_{i,j,theor}}{\sigma} \right]^4 \right\} - 3 \quad (19)$$

Table 1 ***RMS*** error, skewness S and kurtosis K of constructed momentum ρw with Robertson's scheme and Bode's rule in comparison to central differences and trapezoidal rule. 3% noise level corresponds to the uncertainty of the used PIV system. Four-neighbour averaging filter in b), c), d) and e). Robertson's scheme in d) and e). Bode's rule in c) and e).

noise level		a)	b)	c)	d)	e)
	RMS[%]	5.13	4.55	4.42	2.82	2.81
0%	S	-6.90	-6.60	-6.57	3.49	4.48
	K	50.7	46.1	45.7	94.5	122
	RMS[%]	5.17	4.54	4.42	3.56	3.52
3%	S	-6.92	-6.58	-6.66	2.36	2.59
	K	51.0	46.0	47.2	50.1	54.0

Table 1 illustrates that the best estimate of the reconstructed momentum ρw with 3.52% ***RMS*** is achieved by using Robertson's scheme and Bode's rule. It is less than the theoretically expected value of the investigation of Robinson and Rockwell (1993). The skewness S and the kurtosis K also prove a better perfomance of the reconstruction procedure in comparison to central differences and trapezoidal rule



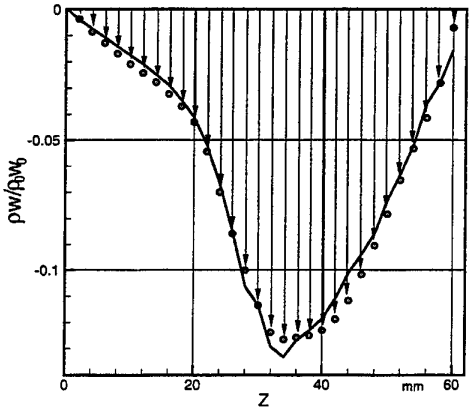


Fig. 5a,b Cut through the area of primary vortex as shown in fig. 4a. o - numerical data of momentum ρw, — - constructed data of ρw.

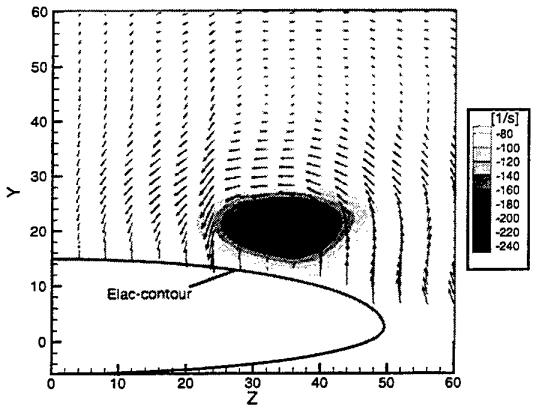


Fig.6 Crossflow field over the halfspan of ELAC at 10° angle of attack, u_∞ = 11 m/s at a relative chord length of x/l = 61.7%. The distribution of vorticity is shown in a colour-coded contour plot.

because of the lower absolute value of S and the larger value of K.

Vector plots of the theoretical and reconstructed crossflow velocity planes are shown in figures 4a and b. The constructed field is in good accordance to the exact solution. The positive value for the skewness S indicates larger estimated values of w, which can be seen in the area of primary vortex at large values of z. For a small y reconstruction leads to a smaller w. The development of the constructed momentum ρw is shown in cuts through the area of primary vortex in y and z direction in figures 5a and 5b. Both figures represent an accurate reproduction. Only in figure 5a the value near to the model gives a too large estimate.

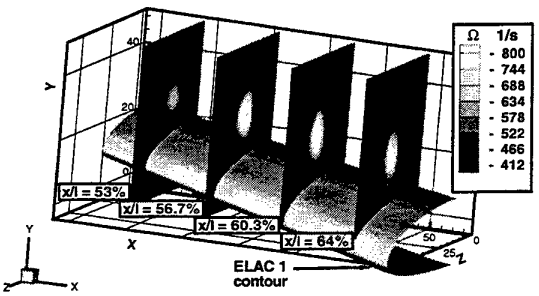


Fig. 7 Colour-coded vorticity distribution at 20° angle of attack and u_∞ = 11m/s.

5. EXPERIMENTAL RESULTS

The experiments were carried out with a free stream velocity of u_∞ = 11 m/s and angles of attack of 10° and 20°. The corresponding Reynolds number was 300 000. At angles of attack larger than 6° flow separates near to the leading edge and rolls up into the vortices over the leeward side of the model.

At an angle of attack of 10° 16 measurements in spanwise direction were taken to obtain the velocity distribution in all three dimensions. Vorticity was computed by use of Robertson's extrapolation. To resolve even smaller structures as secondary vortices the number of measurements was increased to 31 positions in spanwise direction at 20° angle of attack. This enabled observation of secondary separation. Comparing figures 6 and 7 vorticity increases with increasing angle of attack. The streamlines in figure 8 demonstrate the helical structure of the flow in the

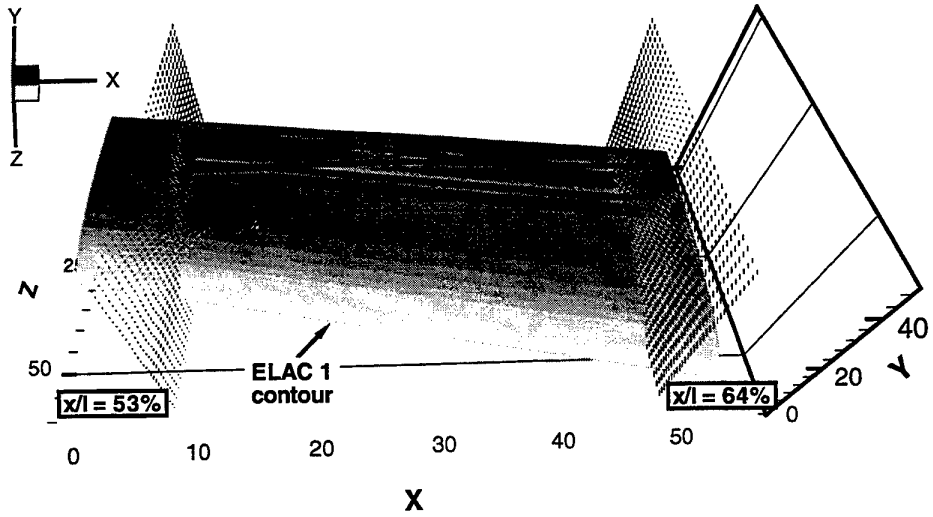


Fig. 8 Velocity distribution of w and v in two selected crossflow planes and four streamlines in the spiral vortex sheet of primary vortex over the halfspan.

primary vortex sheet. Figure 9 shows the non-conical velocity distribution of the crossflow velocities w and v at x/l = 62.7% relative chord length. The non-conical velocities were calculated with help of equations 20 and 21. Figure 1b shows the position of the corresponding origin.

$$v_{nk} = v - u\frac{y}{x} \tag{20}$$

$$w_{nk} = w - u\frac{z}{x} \tag{21}$$

Reconstruction capabilities are demonstrated because

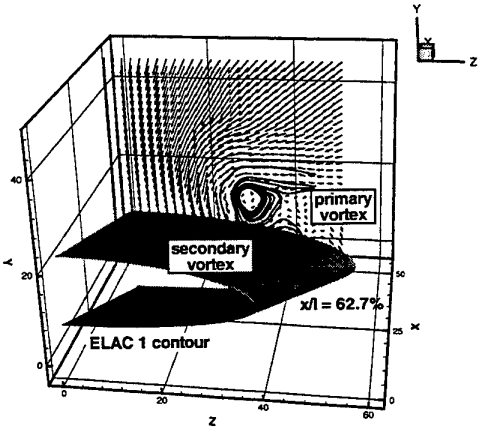


Fig. 9 Vector plot of the non-conical crossflow velocities w and v at x/l = 62.7%. Streamlines illustrate roll-up of the flow into primary and secondary vortex.

both spiral vortex sheets of primary and secondary separation over the delta wing are visualized. According to former investigations by Lang and Jacobs (1996) the corresponding vortex topology is shown in figure 10. At 20° angle of attack existance of a tertiary vortex is supposed, but due to the distance between the planes of measurements it was not to be detected.

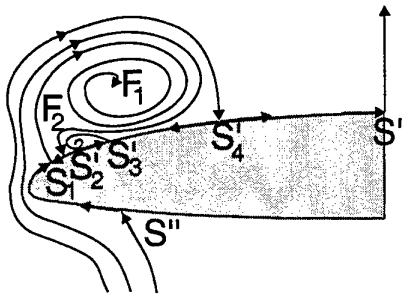


Fig. 10 Estimated vortex topology with primary and secondary vortex over the halspan.

6. CONCLUSION

The steady flow field over the delta wing configuration ELAC 1 has been measured using a set of 2D PIV measurements. The velocity component in spanwise direction z was constructed by use of continuity equation for steady incompressible flow. It was integrated starting at the symmetry plane with the initial value of $w_{z=0} = 0$. The influence of several

different derivation and integration schemes was investigated. The smallest uncertainty of reconstruction has been established to a RMS error of 3.52% using Robertson's scheme for differentiation and Simpson's rule for integration. This applied method yields the whole three-dimensional structure with all velocity components of a steady incompressible flow field while using the less complex set-up of classical PIV.

ACKNOWLEDGEMENTS

These investigations were supported by the Graduiertenkolleg "Transportvorgänge in Hyperschallströmungen" of the German Research Association DFG.

REFERENCES

Brücker, C. 1997, 3D scanning PIV applied to an air flow in a motored engine using digital high-speed video, Meas. Sci. Technol., vol. 8, pp. 1480-1492.

Choi, W.-C. & Guezennec, Y.G. & Jung, I.-S. 1996, Rapid evaluation of Variable Valve Lift Strategies using 3-D In-Cylinder Flow Measurements, SAE paper no. 960951.

Echols, W.H. & Young, J.A. 1963, Studies of Portable Air-Operated Aerosol Generators, NRL Report 5929.

Henze, A. & Houtmann, E.M. & Jacobs, M. & Vetlutsky, V.N. 1996, Comparison between experimental and numerical heat flux data for supersonic flow around ELAC 1, Z. Flugwiss. Weltraumforsch., vol. 20, pp. 61-70.

Hinsch, K.D. 1995, Three-dimensional particle velocimetry, Meas. Sci. Technol., vol. 6, pp. 742-753.

Lourenco, L. & Krothapalli, A. 1995, On the accuracy of velocity and vorticity measurements with PIV, Exp. Fluids, vol. 18, pp. 421-428.

Lang, N. & Jacobs, M. 1996, Flow visualization and application of Particle Image Velocimetry to the hypersonic configuration ELAC 1, Notes on Num. Fluid Mech., vol. 60, pp. 213-220.

Molezzi, M.J. & Dutton J.C. 1993, Application of particle image velocimetry in high-speed separated flows, AIAA Journal, vol. 31, no. 3, pp. 438-446.

Prenel, J.P. & Porcar, R. & El Rhassouli, A. 1989, Three-dimensional flow analysis by means of sequential and volumic laser sheet illumination, Exp. Fluids, vol. 7, pp. 133 - 137.

Press, W.H. & Teukolsky, S.A. & Vetterling, W. T. & Flannery, B. P. 1992, Numerical Recipes in FORTRAN, Cambridge Univ. Press, New York.

Raffel, M. & Willert, C.E. & Kompenhans, J. 1997, Particle Image Velocimetry: A practical Guide, Springer-Verlag, Berlin.

Robinson, O. & Rockwell, D. 1993, Construction of three-dimensional images of flow structure via particle tracking techniques, Exp. Fluids, vol. 14, pp. 257 - 270.

Royer, H. 1997, Holography and particle image velocimetry, Meas. Sci. Technol., vol. 8, pp. 1562-1572.

Spedding, G.R. & Maxworthy, T. & Rignot, E. 1987, Unsteady vortex flows over delta wings, Proc. 2nd AFSOR Workshop on Unsteady and Separated Flows, Colorado Springs, pp. 283-288.

EMBEDDED LDV METHODOLOGY FOR BOUNDARY-LAYER MEASUREMENTS ON OSCILLATING OR ROTATING MODELS

C. Allain, M. Deparis, E. Berton, M. Nsi Mba, D. Favier , C. Maresca

IRPHE/ASI Laboratory, UMR 6594 of CNRS, University of Aix-Marseille I & II
163 Avenue de Luminy, case 918, 13288 Marseille Cedex 09, FRANCE

ABSTRACT

The Embedded Laser Doppler Velocimetry (ELDV) methodology has been shown to be an efficient tool for investigating nonsteady flows near moving surfaces. The present study gives some examples of application of this methodology for velocity profiles measurements across the boundary-layer on different geometrical oscillating models (flat plate, airfoil, half wing, considered in 2D and in 3D flow configurations) or on rotary wings. The paper presents some typical steady (model at rest) and unsteady (oscillating model and helicopter rotor blade in hover) data sets illustrating different aspects of the ELDV capability for determining the instantaneous velocity field within the boundary-layer and in the imediate vicinity of a moving surface.

In each flow configuration (2D, 3D and 3D + centrifugal effects), a common measurement principle has been developped and based on an optical fibres option using an optical head wich is either embedded inside the moving model (**ELDV-method 1 and 3**) or installed outside the model but always linked with the oscillating frame and thus with the motion of the model (**ELDV-method 2**). In both cases, the result is a direct instantaneous velocity measurement in a reference frame linked to the moving wall.

The present paper presents a detailed description of these three ELDV measurement methods and gives some examples of typical features concerning the boundary-layer response to unsteadiness for oscillating and rotating models.

1. INTRODUCTION

Understanding of rotary wings aerodynamics for a better efficiency in terms of their performances have been strongly developed during the past decades. In a wide range of aeronautical applications, a better knowledge of the boundary-layer response to forced unsteadiness produced by oscillating or rotating models is of major interest. For example, one of the main effects of unsteadiness on the boundary-layer behavior is to produce a significant change in its transition location from laminar to turbulent and thus to generate a strong modification of the turbulent separation process (Cousteix et a. (1988), Favier et a. (1992), Simpson (1989), Swales et a. (1994), Telionis (1981)). A proper simulation of the complex blade sections environment requires to consider the influence of several parameters, including simultaneous variations of both angle-of-attack $\alpha=\alpha(\omega t)$ and local flow velocity $V=V(\omega t)$, compressibility, blade tip and centrifugal effects, wake generation, separation phenomena, BVI, ...

However, due to the complex nature of these 3D unsteady phenomena, previous works in this domain have generally tackled the problem by means of simplified flow configurations, which are simulated to specifically dissociate the different parameters, in order to analyze separately their respective influence. Within this scope, the present study is more specially focused on the application of the ELDV method for studying the boundary-layer behavior and the associated specific local phenomena on rotating surfaces and on models oscillating in different kinds of motion : pitch, translation and combined translation/pitch motion. Unsteady boundary-layer characteristics are then deduced from measurements of the instantaneous velocity components. As described below, the measurement principle basically consists in using a specific arrangement of the ELDV optical fibres option, installed inside or outside the models but always linked with the moving frame and thus with the motion of the model.

From the present study, the ELDV methodology appears currently to be a very efficient tool for detailed nonsteady flow measurements near moving surfaces. Using this methodology, the boundary-layer behavior can be directly analysed in a frame linked to the wall. The following sections gives a detailed description of the experimental ELDV

approach together with results concerning the boundary-layer on oscillating and rotating lifting surfaces.

2. EXPERIMENTAL SET-UP AND ELDV MEASUREMENT METHODS

2.1 Experimental Set-Up (ELDV-Methods 1 and 2)

As sketched in Figure 1, experiments are conducted at ASI laboratory in the S2-Luminy subsonic wind-tunnel (rectangular cross section : 0.5 x 1.0 m2 ; length : 3m ; velocity $U_\infty \leq 25$ ms^{-1}), by means of an oscillating device located beneath the wind-tunnel test section. The tested model is supported in a vertical position and attached to the oscillating frame by means of a support shaft located at the quarter chord axis. Different kinds of model motions can be simulated : translation, plunging, pitching and translation combined with pitching (Maresca et a. (1981), Favier et a. (1992), Pascazio et a. (1994)).

The present study concerns more specifically unsteady boundary-layer measurements on a flat plate and on an airfoil model which oscillate according to the following motions :

- Pitching motion (instantaneous incidence variation around a mean incidence) : $\alpha(t) = \alpha_0 + \Delta\alpha\cos\omega t$,
- Translation motion (instantaneous velocity variation) : $U_{rel}(t) = U_\infty + A\omega\cos\omega t$,
- Combined translation/pitch motion: $\alpha(t) = \alpha_0 + \Delta\alpha(\cos\omega t + \phi)$, $U_{rel}(t) = U_\infty + A\omega\cos\omega t$.

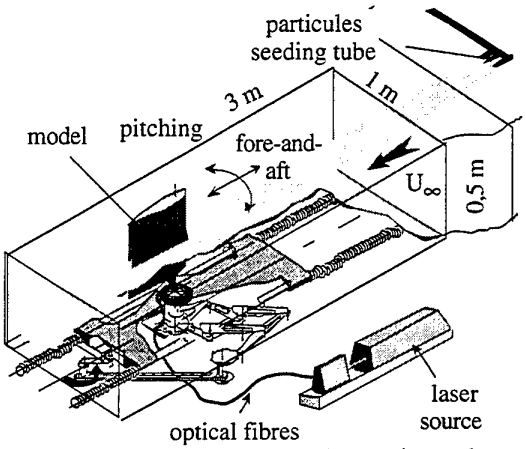


Fig. 1 S2 Luminy wind-tunnel-Experimental set-up

In order to simulate a 2D flow configuration around the model, the flat plate is 37 cm in chord, 49.5 cm in span (spanning the entire test section) and 3.6cm in thickness. As shown in Figure 2, the leading edge and the trailing edge consist respectively of an elliptical nose of 1/3 ratio, and a wedge at 30° of incidence. The same characteristics are considered for the flat plate model in the 3D flow configuration, except for the span which is limited to 40 cm (half flat plate). The NACA0012 airfoil considered in a 2D flow configuration is 30 cm in chord, 49.5 cm in span (see Figure 3). The upstream Reynolds number is fixed here at $Re=10^5$. Steady and unsteady measurements of the velocity profiles have been performed at different chordwise locations s/C along the upper-side of the model and at different spanwise section z/h in the 3D flow configuration (only the middle span section was investigated in the 2D flow configuration). The two ELDV-methods used with this experimental set-up are described below.

2.2 ELDV-Method 1

As shown in Figure 2, inside the flat plate, a 2D teledriven-gearframe supports the optical head of the LDV system, the optical fibres and a 45° mirror. The laser beams are focused in the boundary-layer through the wall equipped with an optical quality glass window. The measurement volume can be displaced along the direction perpendicular to the wall (along a distance of 1.5cm with an accuracy of 1µm) and the displacement along the chord is about 15cm.

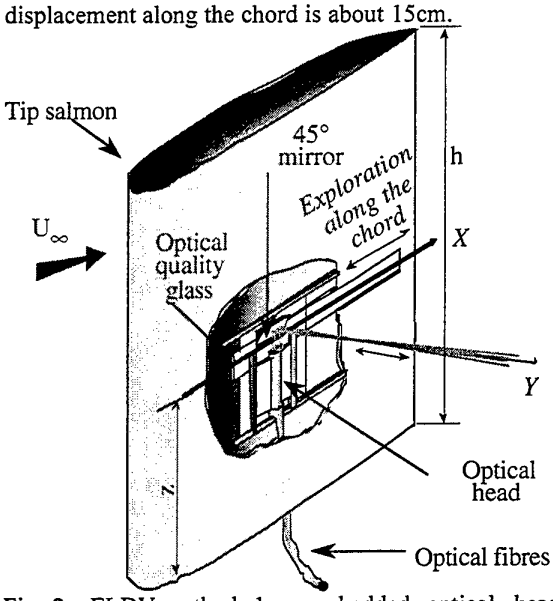


Fig. 2 ELDV-method 1 : embedded optical head inside the model

The optical head is characterized by a focal length f=50 mm with a beam separation distance on front lens D=8mm providing an interfringe i=3.23µm corresponding to the wavelength : 514.5nm (green colour) and i=3.06µm for the wavelength : 488 nm (blue colour). On the blue colour, the dimension of the measurement volume is 0.11 x 0.11 x 1.44 mm3 ; and on the green colour the measurement volume is 0.12 x 0.12 x 1.52 mm3.

2.3 ELDV-Method 2

The optical head is mounted in this case on a supporting turntable which is attached to the oscillating frame as shown in Figure 3. The optical head is equipped with a beam-expander to increase the focal distance up to 400 mm, so that the laser beams are focusing at mid-span of the airfoil in the boundary-layer through a 45° mirror. Due to the fact that the supporting turntable is linked with the oscillating frame, the u and v (tangential and normal) velocity components are also directly measured in the reference frame in relative motion.

Moreover, the optical head is also installed on an automatized 2D-displacement device mounted itself on the circular turntable. This teledriven system allows the adequate positioning of the measurement volume at any point of the airfoil surface (30 cm in chordwise displacement). An angular sector (from 0° to 360° by step of 0.1°) provides the selection of the surveying normal direction to the surface, and the laser measurement volume can then be displaced along the local normal to the surface from y=0.2 mm to y=145 mm with a displacement accuracy of 0.1 mm. The main characteristics of such an ELDV system are as follows : on the blue colour (wavelength : 488 nm), the measurement volume is 0.23 x 0.23 x 5.74 mm3 and the interfringe is i=6.10 µm ; on the green colour (wavelength : 514.5 nm), the measurement volume is 0.24 x 0.24 x 6.08 mm3 and the interfringe is i=6.44 µm.

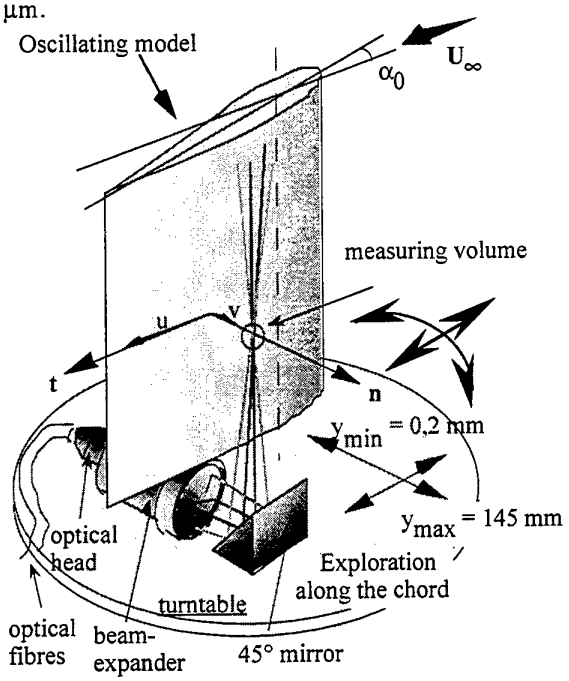


Fig. 3 ELDV-method 2 : embedded optical head linked with the oscillating model

2.4 Data Acquisition and Reduction Procedures (ELDV-Methods 1 and 2)

Figure 4 scketches the acquisition chain of the bidimensional ELDV system operating in the back scatter mode. This chain includes the Argon laser source (5 W), the beam splitter and the transmitter block where the four beams (2 blue for the u-component, 2 green for the v-component) are connected by means of four optical fibres to the optical head linked with the airfoil motion (either outside or inside the model). The light reception is realised through additional optical fibres connected to a beam splitter and two photomultipliers PM1 and PM2 (see Figure 4).

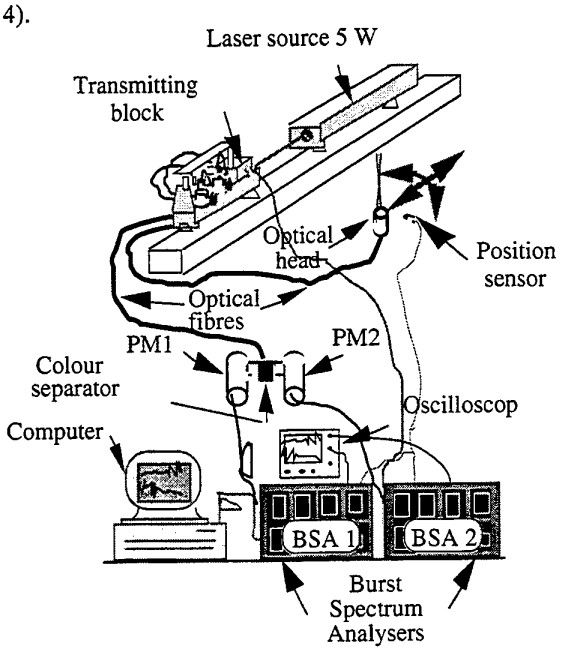


Fig. 4 ELDV data acquisition chain

Data acquisition is made on a micro-computer from two Burst Spectrum Analysers delivering for each velocity component the Doppler frequencies and the arrival validation time for each frequency measurement (Figure 4). The arrival validation times are counted from a time origin delivered by a photoelectric cell mounted on the oscillating device and providing the model position at each phase of the oscillation. The software (COMBSA) used for acquisition and data reduction has been developed at ASI Laboratory under Apple-LabVIEW system. The unsteady data reduction technique is made using an ensemble average procedure suited for periodic flows investigation.

Due to the periodicity of the flow, each period is considered as a specific sample of the same phenomenon, so that each velocity component, can be obtained at each phase angle ωt as the averaged value of the velocity samples recorded at the same given

phase angle and over a large number of oscillations (higher than 150). The simultaneousness of the 2D measurement is then obtained from a synchronization procedure of the acquisition chain, providing the phase averaged value of the mean velocity components and their associated turbulent quantities.

Concerning the seeding of the flow, rates of data validation of about 500 Hz are obtained using a mixture of alcohol and glycerine producing particles of about 1 μm in diameter. As shown in Figure 1 the freestream flow is seeded by means of streamlined tubes located in the suction chamber of the wind-tunnel.

2.5 Experimental Set-Up (ELDV-Method 3)

A two bladed rotor (b = 2) of simplified geometry is set up on the hovering test rig of the S1-Luminy wind tunnel (Ramos, (1996)) and has been designed according to requirements prescribed by centrifugal forces, masses of the embedded components, rigidity of the structures, fiability of beams alignment, etc. One of the blade is equiped with the ELDV, in the other is mounted an adjustable mass in order to perfectly balance the weight repartition of the first blade. The untwisted blades (length R = 0.845m) have a symmetrical constant spanwise profile of chord c = 0.133m and maximum thickness e = 0.02m (e/c = 0.15), located at x/c = 0.25. The blades have been designed and manufactured by DEI (Dynamics Engineering Incorporated) to be run at rotational speeds up to 3000rpm, producing a velocity of 226m/s at r/R = 0.8. The net weight of the blade is about 0.12Kg with 30% corresponding to embedded LDV components.

2.6 ELDV-Method 3

The ELDV prototype, manufactured in collaboration with DANTEC/MT, is schematically shown in Fig. 5 (see Favier et a. (1997)). The different components A, B, C, D, E, are described as follows:

Components embedded inside the blade (Figs. 5, 6)

A1. Emission and reception optical head located near the hub to avoid strong centrifugal effects. DANTEC/MT have designed these components to support acceleration up to 5000 g.

A2. Converging lens mounted at the end of the traversing mechanism (see Fig.6).

A3. Lens traversing mechanism (Fig. 6).

A4. Fixed 45 deg mirror (Fig. 6).

A5. Glass window mounted flush to the blade surface allowing the exit and the focusing of the beams at r/R=0.80.

The lens displacement with respect to the fixed mirror results in a displacement of the measurement volume ranging from 0.25mm to 22mm above the surface by step of 1/8mm given by a displacement screw (see Fig. 6). As the motion of the measuring volume is not motorized, the rotor has to be stopped before changing the volume position in the boundary-layer with an accuracy of 0.05mm.

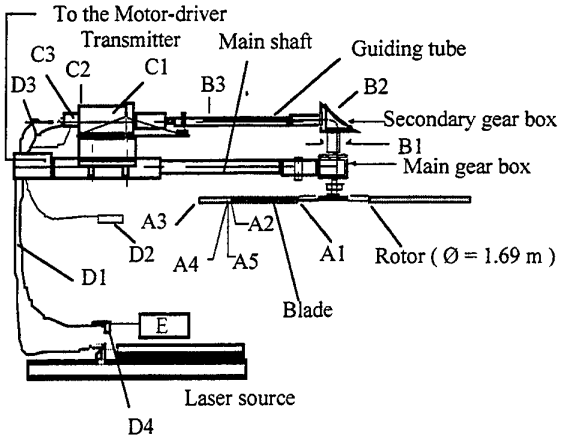


Fig. 5 Components of the ELDV-method 3

Guiding of rotating fiber optic cables between the blade and the transmitter (Fig. 5)

B1. Guiding tube for fibre optic cables coming from the blade to the secondary gear box trough the main gear box.

B2. Secondary gear box.

B3. Guiding tube for fibre optic cables between the secondary gear box and the rotating part of the transmitter.

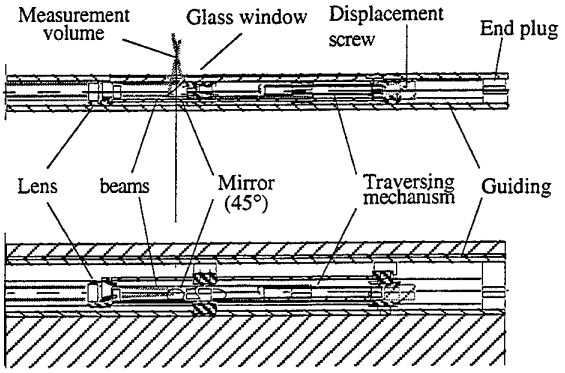


Fig. 6 Scheme of the instrumented blade

Transmitter coupling rotating and fixed components (Figs. 5, 7)

C1. Rotating part synchronous with the blade. This part includes Bragg cell, optics and fibre optics for emission and reception.

C2. Rotating optic collector for back scattered light and rotating multitrack electrical connector for

power supply of rotating part and connexion with fixed part.

C3. Fixed part supporting the multimode fibre to the photomultiplier.

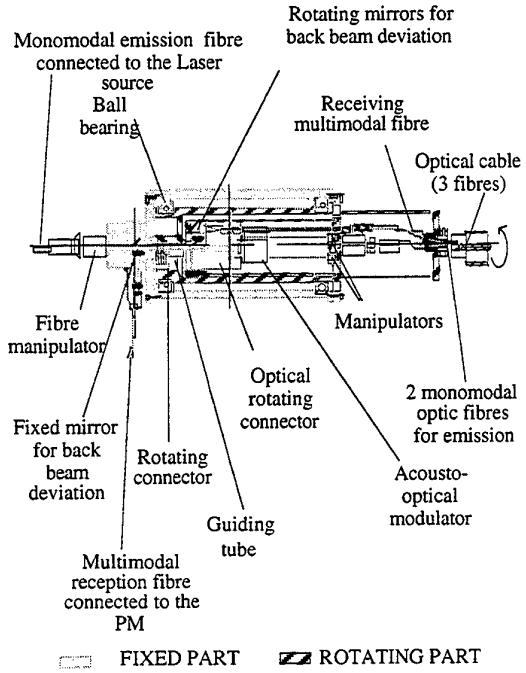


Fig. 7 Transmitter : coupling between fixed and rotating components

Fixed components of the ELDV (Fig. 5)

D1. Monomode fibre optic cable from the fibres manipulator to the fixed part of the transmitter.

D2. Power supply of the Bragg cell.

D3. Multimode fibre optic cable between the fixed part of the transmitter and the photomultiplier.

D4. The photomultiplier equiped with a preamplifier.

The source is a 6 watts Coherent Ion Argon laser.

Processing system (Fig. 5)

E. Signals are analysed through a Burst Spectrum Analyser coupled to a micro-computer.

Allowing to the characteristics of the components listed above, the main specifications of ELDV are summarized as follows in Table 1.

Table 1 Main specification of the ELDV method 3

	Specification	Units
Velocity component	1D*: tangential Vt or spanwise Vr	m/s m/s
Focal lens	50	mm
Laser source wave length	514,5	nm
Measurement volume	dx=0.041 dz=0.510	mm mm
Fringe spacing	0.032	mm
number of fringes	13	
Axial working length	46	mm
maximum rotating freq.	3000	rpm
Maximum Doppler freq.	70	MHz
Maximum velocity	226	m/s
Spanwise position of measurement volume r/R	0.8	
Chordwise position of measurement volume x/c	0.25	

The seeding of the flow is realized by emitting particles of incense or oil mixture in the room where the rotor is run. The concentration of particles (0.1µm to 0.3µm in diameter) is about $3.10^3/cm^3$. However, such a good seeding of the flow induces stains on the optics that have to be cleaned up about every 30 hours of running.

Calibration and accuracy of the measurement

The first step of the calibration has consisted in testing the ELDV when the blade is fixed and close to a rotating disk as shown in Fig. 8 (rotating frequency varying between 600t/mn and 2400t/mn). A hole located at r/R = 0.95 on the disk allows the measurement of the tangential velocity from the signal delivered by the ELDV at each revolution of the disk. The data are averaged over an acquisition time of about 1mn. The tangential velocity is also deduced in an other way from the frequency given by a slot on the disk crossing a photoelectrical cell.

In order to test the stability of the optical components, the same fixed blade measurement has been performed after a 40mn rotation on the rotor at 3000rpm. Fig. 9 shows the tangential velocities of the disk compared to those obtained by the ELDV before and after the rotation of the rotor. It can be noticed that the deviation of measurements from the disk tangential velocity is less than 2% and that the ELDV remains insensitive to rotational effects after 40mn running.

Moreover, it has been possible to estimate, based on previous experiments in laser velocimetry from the present group (Favier et a. (1992, 1997)), the total error made on each velocity component, tangential

Vt and spanwise Vr, within the boundary-layer. Accuracy results are summarized in Table 2.

Table 2 Accuracy of velocity component measurements

Flow region	region close to the wall		region far from the wall	
Compnent	Vt	Vr	Vt	Vr
Accuracy	<2.6%	<4.1%	<2.0%	<6%

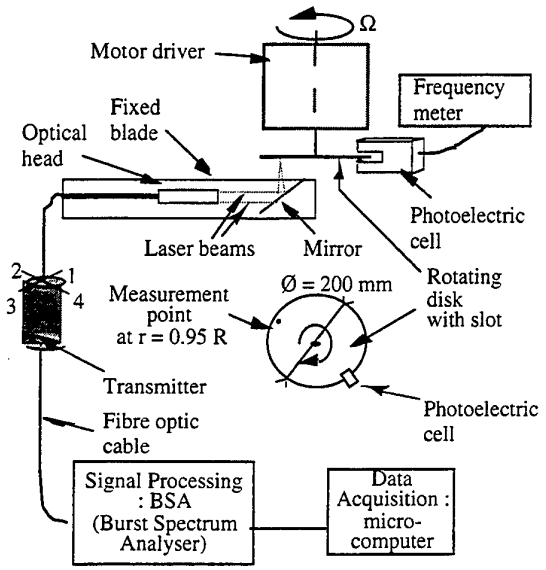


Fig. 8 Calibration : rotating disk test.

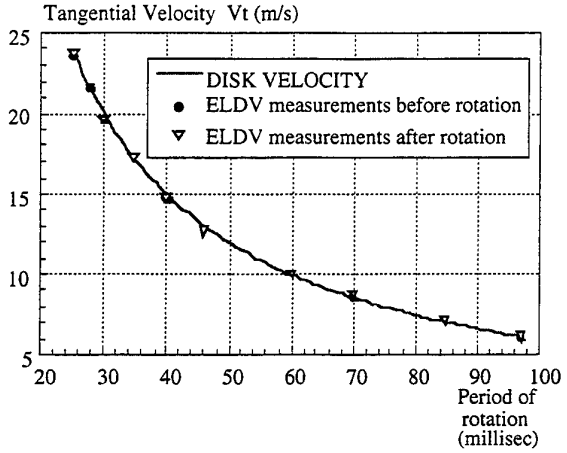


Fig. 9 Calibration measurement

3. RESULTS AND DISCUSSION

The following data sets are given to illustrate different aspects of the steady and unsteady boundary-layer behavior on oscillating and rotating models (flat plate, NACA0012 airfoil and rotating blade) in steady and unsteady 2D/3D flow configurations.

3.1 Steady Flow Configuration (ELDV-Methods 1 and 2)

Considering first the flap plate model in a steady 2D and 3D flow configurations, Figure 10 shows the evolution of the mean tangential velocity components u/Ue=u/Ue(η) measured as a function of η (Blasius normal distance to the surface) at the reduced abscissa along the chord x/c=0.37, for a mean incidence $\alpha_0=0°$ and a freestream velocity $U_\infty=5$ m/s. Figure 10 compares the evolution of the boundary-layer profiles measured both in a 2D flow configuration (flat plate) and in a 3D flow configuration (half-flat plate) at the same spanwise altitude z/h=0.47. Velocity measurements obtained in these cases, are shown to be well matched by theoretical velocity profiles corresponding to a laminar boundary-layer (Pohlhausen law). The effects of the finite span is shown to be quite small at the span altitude z/h=0.47 of the half-flat plate.

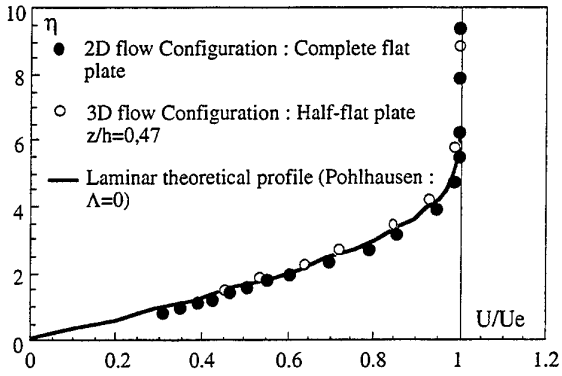


Fig. 10 Mean Tangential velocity profiles U/Ue in steady flow as a function of η.

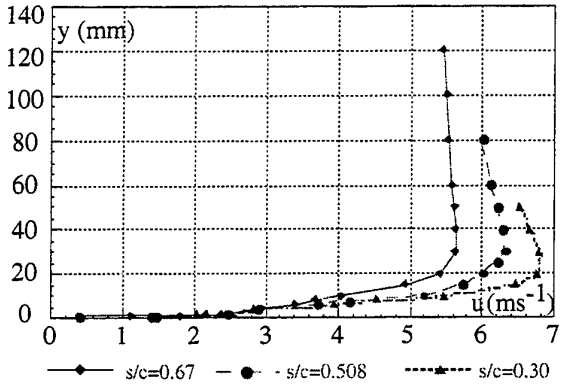


Fig. 11 NACA0012 -Tangential velocity profiles in steady flow as a function of s/c.

The development of the steady boundary-layer along the upper-surface of the NACA0012 airfoil, is

shown in Figure 11 at a fixed incidence $\alpha_0=12°$, $Re=10^5$. For 3 values of the reduced abscissa s/c (s/c=0.3 ; 0.508 ; 0.67), Figure 11 presents the evolution of the velocity profiles as a function of y. They indicate that for a fixed value of y, the tangential velocity u increases as s/c is decreasing, as a result of the boundary-layer thickening and the development of the turbulent regime.

3.2 Unsteady Flow Configuration (ELDV-Method 2)

The effect of the translation motion on the boundary-layer behavior along the upper-surface of the NACA0012 airfoil has been investigated through oscillating conditions which involve instantaneous velocity variations with $\alpha_0=6°$, $Re=10^5$, $\lambda=0.251$, $k=0.188$. The corresponding evolutions of u=u(y) and v=v(y) during the oscillation, are plotted in Figure 12 for three reduced abscissa values (s/c=0.3 ; 0.508 ; 0.67).

As for the steady flow case, Figure 12 shows that the mean local external velocity U_e is higher at the reduced abscissa located near the leading edge of the airfoil (s/c=0.3) when compared with the U_e value relative to s/c=0.508 and 0.67. It can also be noted that all along the oscillation cycle, this decrease in U_e is linked with the increase of the boundary-layer thickness δ. This phenomenon is the result of the decrease of the pressure gradient due to the local airfoil curvature along its chord. Moreover, considering the entire oscillation cycle, it appears clearly that the velocity components (u, v) reach their minimal values at nearly the same phase of oscillation ($\omega t=180°$).

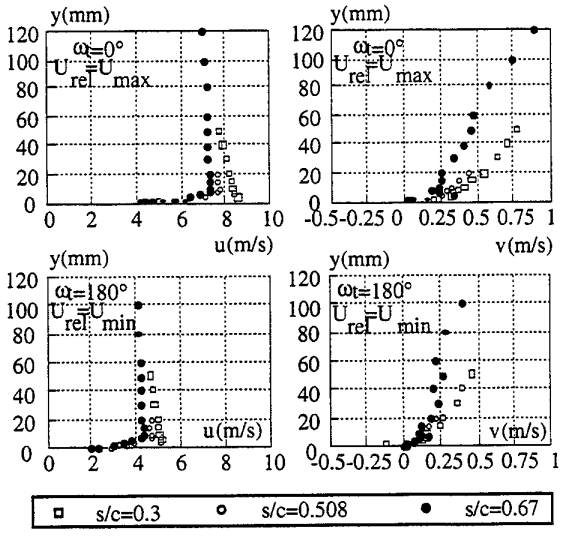


Fig. 12 NACA0012-Tangential and normal velocities (u,v) in translation motion as a function of y and ωt.

3.3 Rotating blade Configuration (ELDV-Method 3)

The following results concern measurements of tangential Vt and spanwise Vr velocity components in the boundary-layer of the rotating blade at r/R = 0.8 and x/c = 0.25. The measurement of the two components is not performed simultaneously as already mentioned, and the displacement z of the measurement volume along a perpendicular to the blade surface requires to stop the rotor. The value of each component at a fixed z is averaged over Ne = 2500 samples of the azimuthal position ψ of the blade ($0deg \leq \psi \leq 360$ deg). Although the rotor can be run up to 3000 rpm, the rotational frequency has been limited between 300 rpm and 1200 rpm, and the collective pitch angle θ between 8 deg and 12 deg, in order to obtain a boundary layer that is between 1 and 2mm thick, allowing about 20 velocity measurements in z.

The boundary-layer profiles of Vt and Vr concern three values of θ = 8, 10, 12deg, and three values of N = 300, 600, 1200rpm, in Fig. 13, 14. Fig. 13 presents the profiles relative to the higher value of the collective pitch angle and N= 300rpm, i.e. Ωr = 21.23m/s. It can be observed on the Vt component a marked overspeed in the region close to the wall when compared to the value of Ωr. The flow is accelerated due to the upperside succion region of the profile. It is worthy of note that Vt is the chordwise component in the rotating plane. When z becomes very high, particles are at rest, and the measurement volume will give Vt = Ωr when crossing such particles. It can also be observed in Fig. 13 that the Vr component is orientated from the tip to the hub (centripetal), with an amplitude of about 5% of Vt .

When θ is decreased to 10deg (see Fig. 14), the profiles of Vt relative to N = 300 and 600 rpm, exhibit the same acceleration of the flow due to the succion region. The ratio of the spanwise component to the tangential one is in this case of the same order than the previous one (5%), with the same centripetal effect.

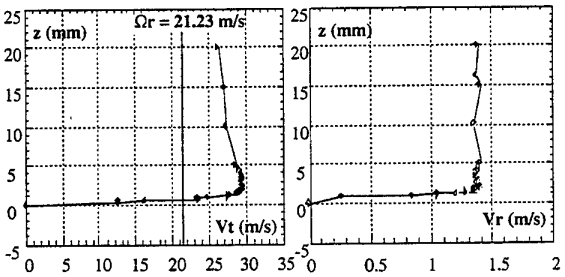


Fig. 13 Rotating blade-velocity profiles (Vt, Vr) in the boundary-layer, b = 2 ; θ = 12° ; N = 300 rpm.

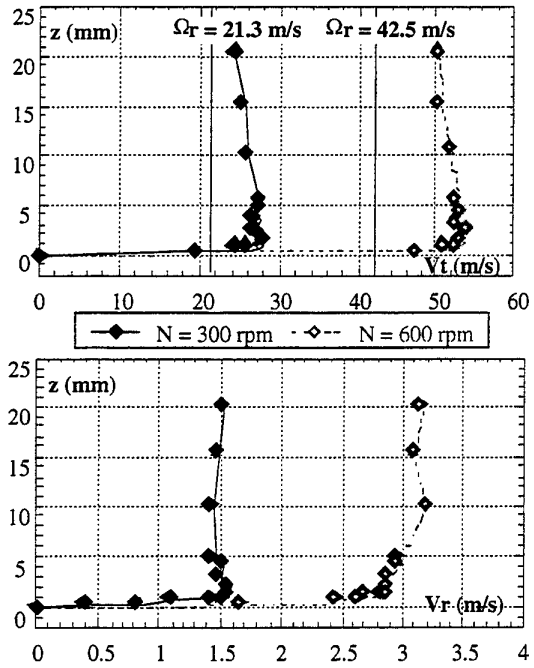


Fig. 14 Evolution of the velocity profile (Vt,Vr) in the boundary-layer as function of the frequency rotation, b = 2 ; θ = 10° ; r/R = 0.8

4. CONCLUSIONS

In the present study, three ELDV measurement methods have been successfully developped and applied to the determination of the 2D velocity field close to the wall, both in the steady flow case and around moving models (flat plate or airfoil oscillating in pitch, translation, and translation/pitch combined motions and rotating blades). As shown by the present results, the boundary-layer behavior and the associated specific local phenomena can be fully investigated and analysed in a frame linked to the wall, when using such ELDV measurement methods.

It has been also shown that ELDV was able to perform accurate 2D measurements in the boundary-layer of rotary wings. Although in the present study it has been tested in a flow with no time dependent variations (symmetry of revolution for the rotor in hover), it may be extended to phase dependent rotating flows using statistical phase averaging procedures. Moreover the capability to measure instantaneous velocity and to phase average the unsteady data also make available the turbulence quantities investigation.

Some improvements will be given in the near future to the present ELDV methods. They concern more specifically : the measurement of the third component, the automatisation of the measurement volume displacement, the reduction of wall light reflexion to allow measurements closer to the moving surface.

5. ACKNOWLEGMENTS

The present results are part of a contract wich has been financially supported by "Direction des Recherches Etudes et Techniques ", from the Délégation Générale à l'Armement. The ELDV prototype has been developed in collaboration with DANTEC/MT, as part of this contract.

6. REFERENCES

Cousteix, J. & Houdeville, R., 1988, Effects of Unsteadiness on Turbulent Boundary-Layers, Fluid Dynamics Lecture Series of V.K.I.

Favier, D., Maresca, C., Renon, P. and Autric, J.M., 1992, Boundary-Layer Measurements on Oscillating Models Using an Optical Fibre LDA Technique, Proc. 6th Int.Symp. on Applications of Laser Techniques to Fluid Mechanics, Lisbon.

Favier, D., Maresca, C., Nsi Mba, M., Berton, E., Agnes, A., 1997, New Type of Embedded Laser Doppler Velocimeter (ELDV) for Measurement of Rotary Wings Boundary-Layer, The Review of Scientific Instruments, Vol. 66, n° 6, pp. 2447-2455.

Maresca, C., Favier, D., Rebont, J., 1981, Unsteady aerodynamics of an airfoil at high angle of incidence performing various linear oscillations in a uniform stream, Journal of American Helicopter Society, Vol. 26, n° 2, pp. 40-45.

Pascazio, M., Favier, D., Maresca, C., 1994, Embedded LDA Technique Applied to the Boundary-Layer Separation Measurement on Oscillating Airfoils, Proc. 7th Int.Symp. on Applications of Laser Techniques to Fluid Mechanics, Lisbon.

Ramos, J., Nsi Mba, M., Favier, D., Berton, E., 1996, Near Wake L.V. Investigation on Hovering Rotor Blades, Proc. 8th Int.Symp. on Applications of Laser Techniques to Fluid Mechanics, Lisbon.

Simpson, R.L. 1989: "Turbulent Boundary-Layer Separation.", Ann. Rev. Fluid Mech., 21, pp 205-234.

Swales, C., Richards, J., Lowson, M.V., Barret, R.V., 1994, Development of an Advanced LDA Technique for the Determination of Boundary-Layer Profiles on a Rotor, Proc. 7th Int.Symp. on Applications of Laser Techniques to Fluid Mechanics, Lisbon.

Telionis, D.P., 1981, Unsteady Viscous Flow, Springer Verlag Editor, N.Y.

INSTANTANEOUS FLOW FIELD MEASUREMENTS FOR PROPELLER AIRCRAFT AND ROTORCRAFT RESEARCH

M. Raffel[1], F. De Gregorio[2], K. Pengel[3], C. Willert[4], C. Kähler[1], K. Ehrenfried[1], J. Kompenhans[1]

[1] DLR, Bunsenstraße 10, 37073 Göttingen, Germany.
[2] CIRA, Via Maiorise, 81043 Capua (CE), Italy.
[3] DNW, Forsterweg 31, 8316 PR Marknesse, the Netherlands.
[4] DLR, Linder Höhe, 51147 Köln, Germany.

ABSTRACT

This paper illustrates results of instantaneous flow field measurements which were performed by the PIV group of DLR Göttingen during test campaigns in three different wind tunnel facilities of the Dutch-German Wind Tunnel foundation (DNW). The test results described first were obtained in the low speed tunnel LST in order to obtain detailed flow field information about the wake of a new high speed propeller model. The second test was performed in the transonic wind tunnel TWG in the frame of a German helicopter research project. Here the flow field above a pitching airfoil equipped with a flap driven by an integrated piezoelectric actuator has been observed with high spatial resolution. During the third test, stereoscopic flow field measurements were performed in the wake of a rotorcraft model in order to characterize the blade tip vortices at different flight conditions. The test was conducted in the 6 x 8 m^2 open jet test section of the large low speed facility LLF which required observation distances exceeding 9 meters between camera and light sheet.

1 INTRODUCTION

The increasing demand of air transport, the strong competition between the different airline companies and the competition with other transport systems like high speed trains - especially in Europe where the travel time between the centers of the cities can be comparable - as well as a strong interest in the protection of the environment led the propeller aircraft and rotorcraft manufactures to intensify their investigations on the efficiency and noise emission of their products.

Current testing techniques on airframe/propeller engine integration and rotorcraft research for performance enhancement and noise reduction deliver mainly test data on overall aerodynamic forces, moments, and surface pressure distributions. More detailed investigations are required for an improved CFD modelling for a better understanding of the aerodynamic phenomena in general. The instationary complex flow structures, especially the vortices above and behind rotor blades require detailed instantaneous flow field mapping to get insight into the physics. The improvement and reliability of particle image velocimetry (PIV) applied to high speed air flows in large industrial wind tunnel facilities play a key role in today's aircraft development.

2 PIV UTILITIES FOR WIND TUNNEL TESTS

In large scale industrial wind tunnels one of the main requirements is to obtain a relatively large observation area. This requires a recording system with a high spatial resolution as well as a high light sensitivity. Through the use of single-exposure photo cameras or high resolution digital cameras large acquisition areas can be achieved but usually require complex additional hardware to resolve e.g. the directional ambiguity. The rapid development of full-frame interline transfer solid state sensor architectures during the past years made a new generation of cameras available which are ideally suited for PIV applications in industrial wind tunnels. The limited present resolution of approximately one million pixels is partly compensated by the fact that cross-correlation of separately-recorded single-exposed images with full frame resolution shows a principally superior SNR compared to other correlation techniques, and therefore allows smaller interrogation areas that can be used for a reliable velocity estimation (Keane and Adrian 1992).
Another set of requirements arises from the fact that nearly all our applications of PIV take place in air, from moderate to high speed velocities, and sometimes with high centrifugal forces: small seeding particles are needed to accurately follow the flow which in turn requires the use of high powered lasers in conjunction with high quality imaging equipment. This holds in particular in large facilities where distances between observation area and recording equipment can be considerable. In order to fulfill all these requirements we chose the following subsystems for our wind tunnel tests.

2.1 Recording

In recent years cameras incorporating progressive scan, full-frame interline CCD technology have become available which, contrary to the more common interline transfer CCD sensors, are capable of shuttering (exposing) and storing the entire array of pixels, not just every other line. Thus, these sensors immediately offer the full vertical resolution when the CCD is used in the shuttered mode. A standard (TV) resolution camera of this type was first used for high-speed PIV measurements in air at the California Institute of Technology as part of the collaboration in the Center of Quantitative Visualization (Vogt et al. 1996).

Following this general approach, the present PIV camera systems additionally feature a non-standard, high resolution, digital video format consisting of 1008 by 1018 pixels and 1024 by 1280 pixels respectively. Using a 32^2 pixel interrogation window, this translates to a spatial resolution of up to 32 by 40 discrete vectors. standard 35 mm photographic film in comparison, digitized at 100 pixels per millimeter, yields about 56 by 37 discrete vectors at a comparable measurement uncertainty (a 64^2 pixel interrogation window is required (Willert 1996)). As the digital video signals of these cameras cannot be viewed using a standard video monitor a PC-interface card is necessary which transfers the digital data directly into the computer's memory (RAM) and thereby allows a continuous sequence of frames to be captured and viewed. An enormous advantage of these cameras is that they are offered with both high resolution and sensor cooling which reduces the black current and increases the dynamic range to 12 bit. A fibre optic transmission link allows for very long distances between camera and frame grabber.

One major drawback of these cameras and subject of investigations (Westerweel 1998, Ronneberger et al. 1998) arises through the regular arrangement and response characteristics of picture elements on the sensor. It was found that a decrease of the particle image size to cover only a few pixels was associated with an increased systematic bias error towards integer displacement values, generally referred to as "peak locking". Since air flow PIV applications require diffraction limited imaging of very small particles this effect can cause severe problems and requires detailed studies to be able to make reliable statements about the obtained measurement accuracy. In the case of the test results presented here a significantly enhanced data quality could be achieved by applying improved correlation algorithms as presented by Ronneberger et al. (1998).

2.2 Flow Seeding

The most common seeding particles for PIV investigation of gaseous flows are oil droplets which are generated by means of Laskin nozzles. Pressurized air, injected in olive oil, leads to the formation of small oil droplets. The aerodynamic diameter of the olive oil particles is about 1µm. In wind tunnel flows the supply of tracers is often difficult. The particles, which are mostly used, are not easy to handle because many droplets formed from liquids tend to evaporate rather quickly and solid particles are difficult to disperse and very often agglomerate. Therefore, the particles cannot simply be fed preceding the measurement, but must be injected during the test into the flow upstream of the test section. The injection has to be done without disturbing the flow significantly, but also in a way and at a location that ensures homogenous distribution of the tracers. Since the existing turbulence in many test facilities is not strong enough to sufficiently mix the fluid with particles, the particles have to be supplied through a large number of openings. Distributors like rakes consisting of many small pipes with a large number of small holes are often used. This requires particles which can be transported inside small pipes without agglomeration. The following section gives a description of an atomizer which generates suitable particles and has been used for most of our PIV measurements in air flows. The particles generated by this device are non-toxic, stay in air at rest for hours, and do not significantly change in size under various conditions.

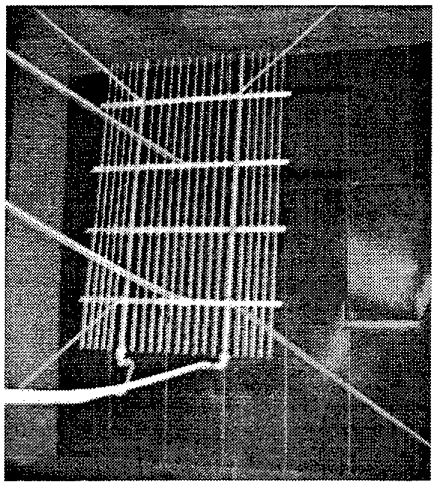


Fig. 1 Seeding rake

In closed circuit wind tunnels these micron-sized oil droplets can be used for a global seeding of the complete volume, as done in the TWG. Alternatively a local seeding of a stream tube can be achieved by a seeding rake with a few hundred small holes such as the 2.5 x 2 m^2 rake which was mounted in the settling chambers upstream the honeycombs and screens of the low speed wind tunnels LST and LLF (Fig. 1).

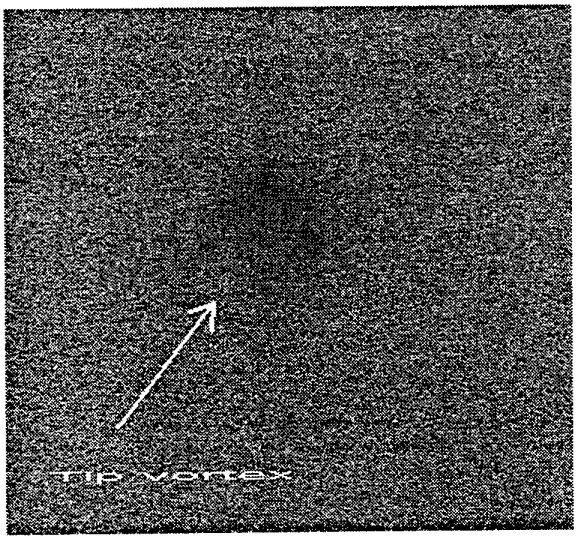


Fig. 2 Typical PIV recording

The goal is, to obtain an high uniform seeding density in the region of interest (at least 15 pairs of particles per interrogation window (Keane and Adrian 1990)) in order to apply statistical evaluation methods also in the region where strong recirculation or velocity gradients are present. Figure 2 shows a PIV image portion with reduced seeding density due to the velocity lag (integrated from the blade tip to the observation area) and due to the reduced air density inside the vortex core. Because of the size of the rake, three aerosol generators, each containing 40 Laskin nozzles, are used. Each generator consists of a closed cylindrical container with five air inlets and one aerosol outlet. Several Laskin nozzles, 1 mm in diameter, are radially spaced in the inlet pipes. A horizontal circular impactor plate is placed inside the container, so that a small gap of about 2 mm is formed by the plate and the inner wall of the container. Compressed air with 0.5 to 1.5 bar pressure difference against the outlet pressure is applied to the Laskin nozzles and creates air bubbles within the liquid. Due to the shear stress induced by the tiny sonic jets, small droplets are generated and carried inside the bubbles towards the oil surface. Big particles are retained by the impactor plate; small particles escape through the gap and reach the aerosol outlet. The amount of particles can be controlled by switching four valves at the nozzle inlets. The particle concentration can be decreased by an additional air supply via the second air inlet. The mean size of the particles generally depends on the type of liquids being atomized but is only slightly dependent on the operating pressure of the nozzles. Vegetable oil and Di-2-Ethylhexyl-Sebacat (DEHS) are the most commonly used liquids since they are said to be less unhealthy than many other liquids. However, any kind of seeding particles, which can not be dissolved in water, should not be inhaled. DEHS and most vegetable oils lead to polydisperse distributions with mean particle diameters of approximately 1 µm or less and therefore can agglomerate within the lungs.

2.3 Laser

The light sources used were pulsed Nd:YAG lasers with two independent oscillators. They were driven at repetition rates of 10 Hz, the pulse energy at λ = 532 nm was 2 x 320 mJ and 2 x 150 mJ in case of the TWG test respectively. PIV measurements over long distances do not only require powerful lasers but also excellent characteristics of spatial intensity distribution (hole-free without hot spots especially in the midfield where it is most difficult to get), excellent co-linearity, beam pointing stability (< 100 µrad) and energy stability (< 5 %). To obtain a thin light sheet, typically with a thickness in the order of 1 mm, the laser beam passed a set of coated spherical and cylindrical lenses optimized for a homogenous light intensity distribution versus the light sheet thickness and height. A small "misalignment" of the combination optics has partly been used in order to obtain light sheet positions which were slightly displaced in mean flow direction for enhanced correlation strength during evaluation.

3 PROPELLER INVESTIGATIONS

The request to reduce the fuel consumption and the pollution emission of the propulsion systems has forced the aircraft manufactures to investigate and install new ultra high by-pass ratio engines, and, in case of smaller aircrafts, high speed open rotors. Furthermore, these requirements have led the manufactures to renew their interest towards propeller driven aircrafts in order to develop a new generation of commuter aircrafts with the same operational capacities and comfort as regional jets with reduced emission, cost and noise.

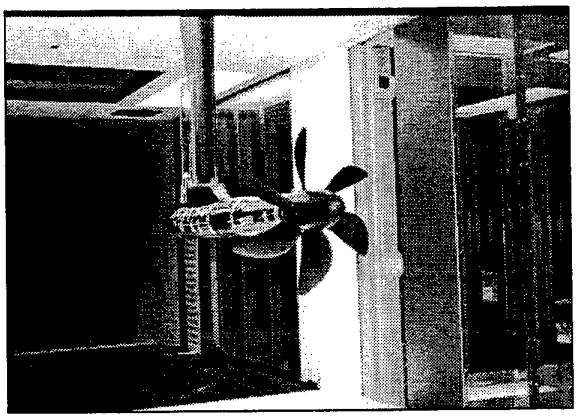


Fig. 3 The isolated test rig

To develop such a propeller, it is mandatory to study the slip stream behavior and the propeller and airframe integration in order to come to higher efficiency and performance. The highly unsteady phenomena require new experimental tools in order to analyze the flow field characteristics. In parallel, the new measurement techniques should also allow to reduce the wind tunnel time in order to minimize the development cost.

In order to study the high speed propellers behavior an experimental campaign on an isolated propeller test rig (Fig. 3) has been carried out in the LST facility by means of PIV. For the first time, this allows one to obtain quantitative information about these unsteady and partly non-periodic flow fields for CFD code validation experimentally.

A large number of images was acquired for each different test condition in order to also allow a statistical evaluation of the wake downstream of the propeller plane. The instantaneous results and the mean results obtained by averaging over a large number of PIV data sets were compared such that the difference between the time-averaged and unsteady flow could be studied. The dependence between blade position and wake flow could be investigated by simultaneously storing the azimuth angle of each PIV recording.

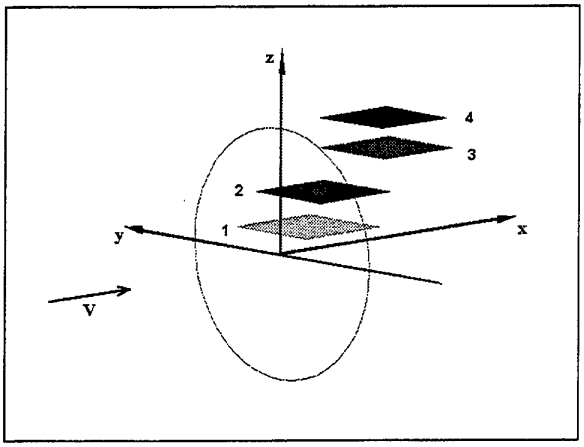


Fig. 4 Reference system and investigated areas

The LST is a continuous atmospheric wind tunnel with closed walls, a test section of 3 m width and 2.25 m height, maximum air velocity of 80 m/s, and powered by a 700 kW fan. The measurements have been carried out downstream of an isolated propeller test rig. The propeller model, including an internal six component rotating balance, has been mounted on the external force balance of the tunnel as shown in Figure 3. The model represents a new type of high speed propeller (Mach 0.7-0.8), and which is composed of six blades, which has a diameter of 500 mm. All tests were performed at the same wind tunnel velocity (80 m/s) with the same blade angle of 40.4° but with different propeller rotational speed (8000 and 8650 rpm). This permitted the investigation of the influence of the advance ratio on the slip stream under various different incidence and jaw angles (0°, +10°,-10°) of the propeller.

The reference system is related to the model and defined as follows: the plane $z = 0$ is a horizontal plane containing the axis of rotation, the plane $y = 0$ is a vertical plane containing the axis of rotation and the plane $x = 0$ is a vertical plane containing the trailing edge of the blade profile. The measurements were performed for different horizontal planes (Fig. 4), starting from the axial plane until to the z-position of 70 % of the blade radius.

The Nd:YAG pulse laser was mounted at the outer sidewall of the test section above a 2D traversing system in order to be able to easily change the light sheet position. The whole laser system and light sheet optics was constructed on an optical bench using commercially available X-95 elements. This results in a stable and still very variable and compact set up. Two DC gear motors, connected to the alignment screws of the laser's second harmonic generators, allowed the phase-matching to be optimized remotely from the wind tunnel control room during the tunnel run. The light sheet formed by a 500 mm spherical and 200 mm cylindrical lens, was 300 mm wide and 2 mm thick. The flow field of the propeller slipstream presents a strong 3-D behavior. Therefore, the pulse delay time was reduced to 10 µs in order to reduce the strong out-of-plane loss of correlation.

The digital camera was located above the test section, mounted on the support of the external balance so that a realignment and a re-calibration of the camera was not necessary when changing the incidence and the jaw angles of the propeller. Calibration was done with a calibration grid inserted in the test section at the position of the light sheet as shown in Figure 5.

The measurement planes, dimension about 20 x 20 cm^2 , have been acquired, by the digital camera, from a distance of 1.5 m, using a 100 mm lens with f-number of 2.8. Remotely focusing of the lens was achieved with a self made focusing system.

To correlate the propeller blade position to the acquired vector field a custom Propeller Angle Measurement device (PAM) has been designed and built. A reset signal per each propeller revolution and a Q-switch signal from the laser were used by the PAM system to evaluate the propeller position. This information was stored in the first two bytes of the image file.

In total about 1700 image pairs, related to 28 different test conditions, were acquired. For each test condition 50 pairs of images were taken in order to investigate the instantaneous flow condition and, by

averaging over all the instantaneous measurements, the mean flow field. In one test condition, more than 400 image pairs have been acquired so that the influence of the blade position on the slipstream could be investigated. The images have been evaluated by means of cross-correlation method using interrogation windows of 32 x 32 pixels, the interrogation windows have been overlapped 50 % providing a matrix of 61 x 62 displacement vectors. To improve the signal/noise ratio the multi pass algorithm described by Willert (1997) has been used. The spatial resolution of the vector matrix is better than 3 mm. A filter algorithm (Raffel et al. 1993) to remove to faulty vectors and a filter pass to replace the hole with vectors evaluated from the average of the neighbor's values were applied. After that the displacement vector matrix was converted in the velocity matrix and the new origin of the reference system was determined (Fig. 5).

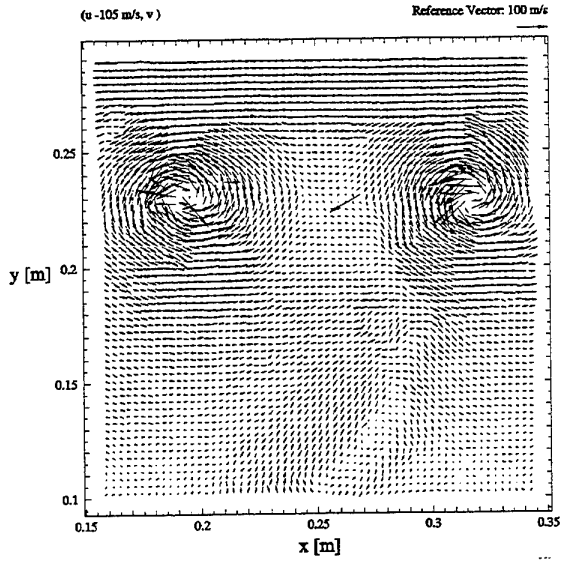


Fig. 5 Instantaneous velocity field

These vortical structures can also be observed in Figure 6, which represents the out-of-plane component of the vorticity as isolevel lines. Continuous contours indicate positive and dashed contours negative values of vorticity. The contour levels are spaced at 1500/s.

PIV measurements in the plane z = 0 were performed, and 40 instantaneous vector fields are taken. The measured plane covers the area from 155 mm to 350 mm along the x-direction and from 97 mm to 292 mm along the y-direction (Area 1 in Fig. 4). In Figure 5 the instantaneous velocity field for 0 degree of incidence and jaw angles is shown. The mean component of the velocity has been subtracted in order to highlight the vortical structures. Figure 7 clearly presents two sequential blade tip vortex in the measurement plane. Furthermore the shear layer of one of the blades can clearly be seen as it rolls up in to its tip vortex.

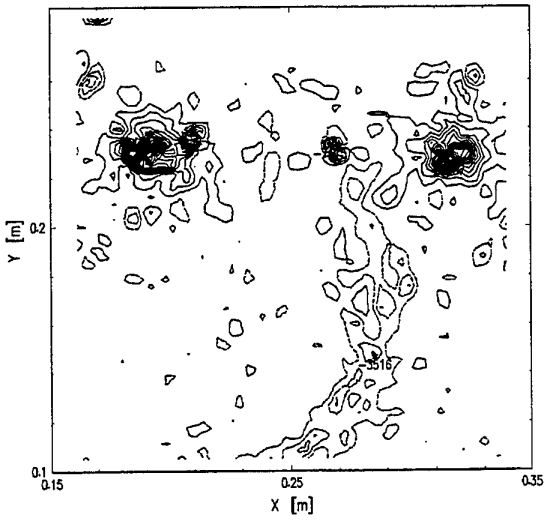


Fig. 6 Isolines of the (1d) vorticity field

Furthermore from our results it is possible to determine the trajectory of the tip vortex. In this case the vortex moves on a straight line nearly parallel to the free stream velocity direction of the wind tunnel at a distance of y = 227 mm from the x-axis, showing a contraction of the slip stream downstream the propeller disc. The distance between each vortex core is 120 mm.

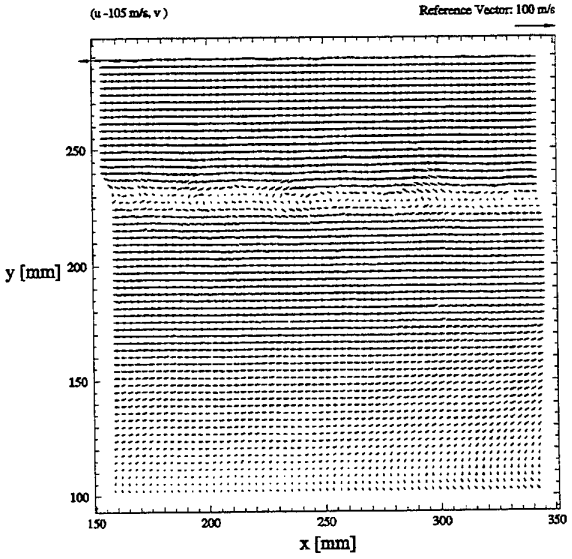


Fig. 7 Averaged velocity field (50 PIV data sets)

For each test condition, the average of the flow field has been evaluated on the basis of 50 instantaneous

velocity fields. The obtained flow field is shown in Figure 7. Also in this case the mean velocity is subtracted to highlight the vortical structures but only the shear layer is visible. These averaged flow fields are the typical output of pointwise measuring techniques like laser Doppler velocimetry, pressure probes or by hot wire anemometry, if no conditional sampling has been applied. This is also the case for most of the stationary CFD codes.

In order to investigate the influence of the blade position in more detail, more than 400 image pairs were recorded for one case. The chosen test condition is more critical than the others because the propeller had an incidence angle of 10° with respect to the wind tunnel system. In this condition the out-of-plane velocity is larger and the measurement is affected by an higher noise error. Conditional averaging was performed with reference to the position of the propeller.

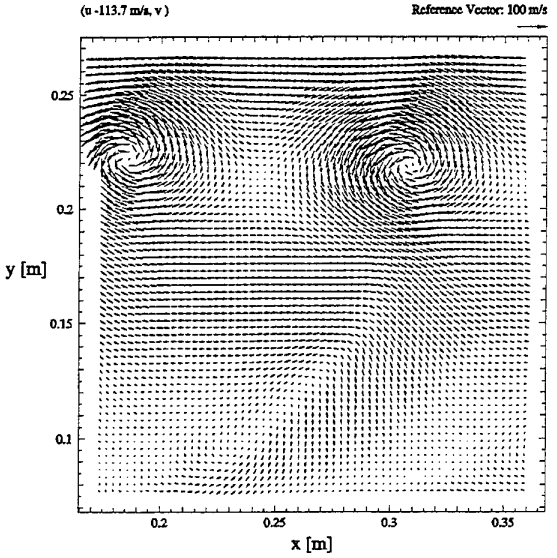


Fig. 8 Phase averaged flow field at 30° incidence angle

In Figure 8, the conditionally averaged velocity field at the blade position of 30° is presented. The blade position is counted starting from the positive z-axis in clock-wise direction. About 40 instantaneous velocity maps, taken all at the same angular position, were averaged. Also here the mean value of the x-component of the velocity is subtracted to highlight the vortical structures.

By averaging the flow fields the noise errors can significantly be reduced, the vortical structures appear more homogeneous, and the comparison with results of other numerical or experimental techniques, which do not resolve the cycle-to-cycle variations but the periodic flow phenomena becomes easier.

This can also be seen in the vorticity map (Fig. 11), where the isolevel contour are smoother and homogeneous with respect to the vorticity contour of an instantaneous measurement (Fig. 9).

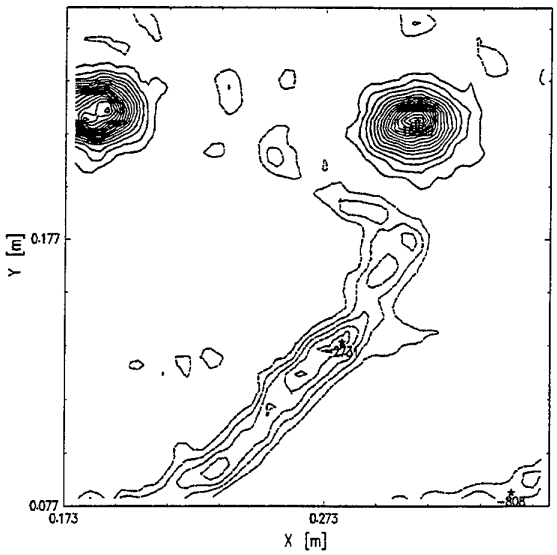


Fig. 9 Isolevel contour map of the vorticity of a phase-averaged flow field at 30° incidence angle

4 HIGH RESOLUTION FLOW FIELD MAPPING ON AN ADAPTIVE HELICOPTER BLADE MODEL

Adaptive helicopter rotor blades are assumed to be one of the key technologies for helicopter performance enhancement for the oncoming decade. In a national project (AROSYS), the German industry (ECD and Daimler Benz Forschung) and the German Aerospace Research Establishment (DLR) combined their efforts to reach reliable solutions for adaptive rotor systems. One of the first promising results was a piezoelectric actuator small enough to be integrated into a full-scale rotor blade and strong enough to drive a servo flap at the trailing edge of the outer blade area (Fig. 10). Since performance estimations and blade

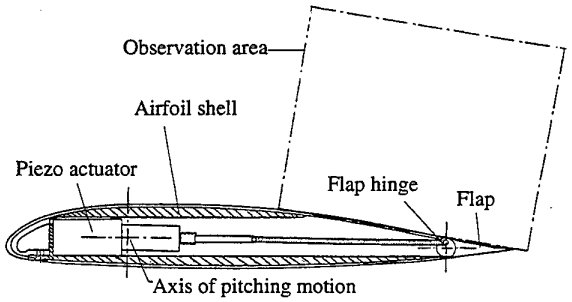


Fig. 10 Helicopter blade model and observation area.

profile optimization can efficiently be obtained by instationary Navier-Stokes simulations (see e.g. Wernert et al. 1996) there is a great interest in validating these codes and to subsequently apply them to adaptive blade geometries and concepts. For this purpose a wind tunnel test was recently performed in the transonic wind tunnel TWG in. Forces, moments and surface pressure distributions were measured dynamically for different Mach numbers, pitching amplitudes, and frequencies. The tests were performed at different flap frequencies and phase relations by the Institute for Aeroelasticity of DLR. In order to complete this information, PIV measurements of an area above the trailing edge flap, which was pitching in phase with the airfoil frequency, were performed.

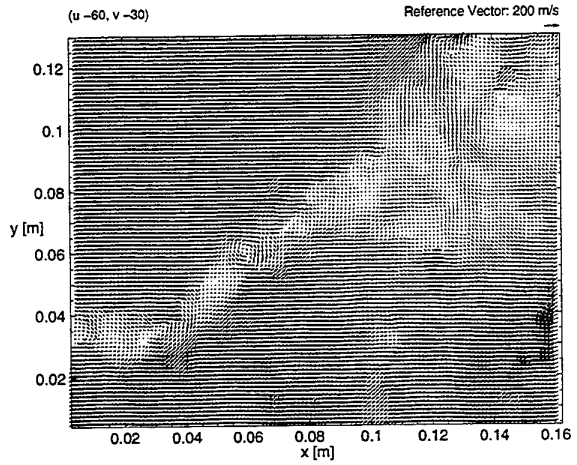


Fig. 11 Instantaneous flow velocity field above the adaptive blade at a Mach number of 0.33, pitching at 7 Hz (14.5° +/- 5°), with a flap motion of 14 Hz, +/- 3°.

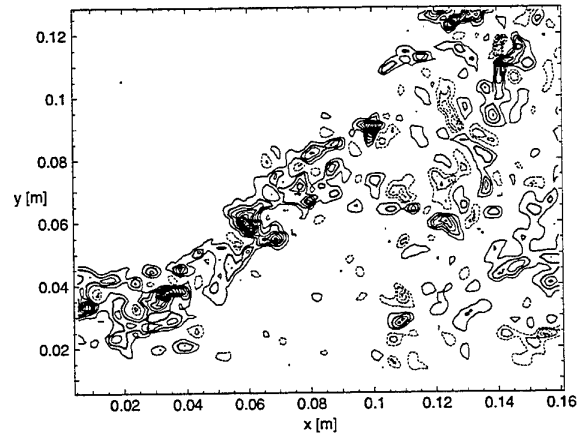


Fig. 12 Instantaneous out-of-plane component of vorticity computed from flow velocity data shown in figure 11.

First results of these measurements at a phase angle of 320° are shown in Figure 11 and its vorticity distributions in Figure 12. A shear layer between the separated flow area and the mean flow and the influence of the dynamically pitching flap can be seen. The flap angle varied by +/- 3° at a frequency of 14 Hz and the airfoil was operated at a mean angle of attack of 14.5° with 5° amplitude at 7 Hz. Laser and camera were phase locked with the pitching motion at pre-selected phase angle. The chord length of the blade was 0.3 m, the span 1m. High The quality schlieren windows gave optical access to the perforated transonic test section of the tunnel. Due to the high camera resolution, the high seeding density and homogeneity, and improved correlation algorithms described by Ronneberger et al. (1998) up to 125 by 100 velocity vectors could be measured with an overlap of 50 %.

5 STEREOSCOPIC ROTOR MEASUREMENTS IN A LARGE LOW-SPEED WIND TUNNEL

Detailed investigations employing PIV, surface pressure and acoustic measurements at an 1:4 scaled rotor were conducted in the large low-speed facility (LLF) of DNW. The successful PIV measurements on rotors in a large scale facility such as LLF are based on continual efforts over the past three years to resolve a number of special problems such as long observation distances, seeding problems, and the robustness and remote control capabilities of the systems. At this point it can be said that all technically relevant problems, even for stereoscopic measurements, can be solved and that additional efforts to employ this technique on a routine base in near future are justified. The main motivation for this is, that in spite of all its advantages, the PIV method underlies some shortcomings that make further developments on the basis of instrumentation necessary. One of these disadvantages is the fact that the 'classical' PIV method is only capable of recording the two-dimensional projection of the velocity vector. A variety of approaches capable of recovering the complete set of velocity components have been described in the literature (Hinsch 1995, Royer and Stanislas 1996). The most straightforward, but not necessarily easily implemented, method is the additional PIV recording from a different viewing axis using a second camera, which can be generally referred to as stereoscopic PIV recording (Westerweel and Nieuwstadt 1991, Prasad and Adrian 1993, Gaydon et al. 1997). Stereoscopic recording can also be achieved with a single camera by placing a set of mirrors in front of the recording lens (Arroyo and Greated 1991). To adapt the stereoscopic approach to an industrial wind tunnel environment, a number of additional developments are necessary. First of all the optical access in wind tunnels rarely permits the imaging configuration to be symmetric as given in all of the previous implementations. Another

requirement is that the small, micron sized, seeding particles, have to be imaged over large distances at up to 10 meters. This makes the use of large focal length lenses with large light collecting capability (i.e. small $f_{\#}$-numbers) necessary. Since the measurement precision of the out-of-plane component increases as the opening angle between the two cameras reaches 90°, it is not always possible to mount the cameras onto a common base, much less to provide a symmetric arrangement.

In the following a description of our generalized, that is, non-symmetric, set up for stereoscopic PIV imaging is given. The feasibility of this approach was demonstrated in an actual experiment with the unsteady flow field of a rotorcraft model blade tip vortex. In the final configuration, the recording parameters were optimized such that a pulse delay of 20 μs resulted in a particle displacement of 3-4 mm normal to the light sheet (approximately 10 mm thickness) with a maximum in-plane displacement on the order of 3 mm. With an observation area of 25 by 30 cm^2 this translated to displacements in the order of 10 pixels on the digital sensor which still provides at least a factor 100 of dynamic range (the noise level in the recovered displacement data is in the order of 0.1 to 0.05 pixel). The seeding particles were illuminated by a dual oscillator, frequency doubled Nd:YAG laser with 320 mJ per pulse. The observation area was imaged by two high resolution digital cameras using two 300 mm $f_{\#}$ 2.8 lenses at an observation distance of 9.5 meters each. The large observation distances were chosen to reduce any blockage effects imposed by the imaging equipment.

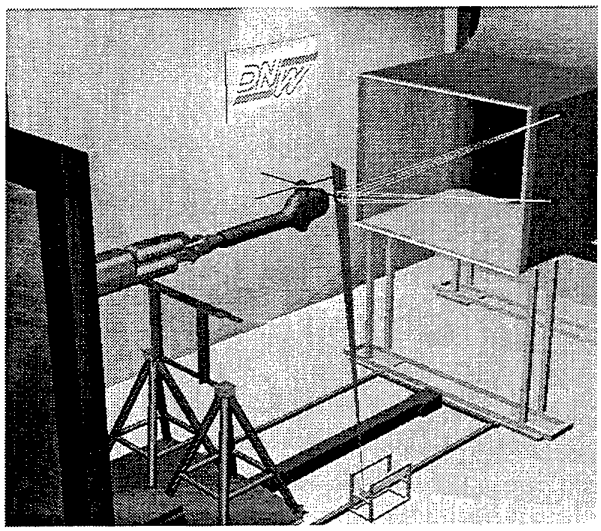


Fig 13: Experimental arrangement of the stereoscopic PIV measurement of a rotorcraft flow in the large wind tunnel of DNW.

The experimental configuration used two sensitive (12-bit converter, cooled sensor) and high spatial resolution CCD cameras to image the experimental region of interest, an area approximately 25 by 30 cm^2 over 9.5 m from each camera (see Fig. 2). The cameras were located at the side of the nozzle of the open jet test section, and were placed in a vertical plane intersecting the observation area. The angle between the camera axes and the normal of the observation area was approximately 12°. Figures 14 and 15 show the first preliminary results taken from a series of measurements performed at the DNW-LLF on a rotorcraft model. The diagrams were turned by 90° anticlockwise in order save space. The resulting vector maps, while taken at subsequent azimuth angles have clear differences. The rotor blade tip, which had just passed the observation area in out-of-plane direction when the first recordings were made, had given rise to the vortices present in the velocity vector maps. The out-of-plane velocity component represented graylevel coded in Figure 14b shows strong spatial gradients between the wake of the blade and the tip vortex center (compared Fig. 14 and 14b).

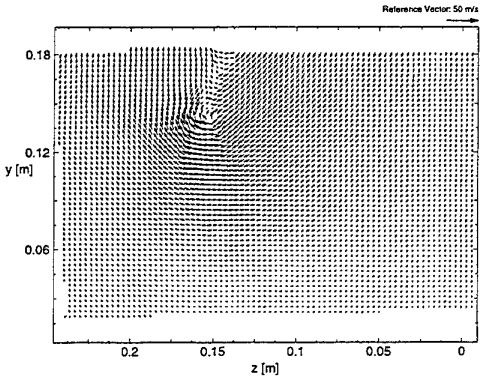


Fig. 14 In plane velocity components of the tip vortex and the wake of the blade. (The diagrams (14 and 14b) are turned by 90° anticlockwise with respect to Fig. 13.)

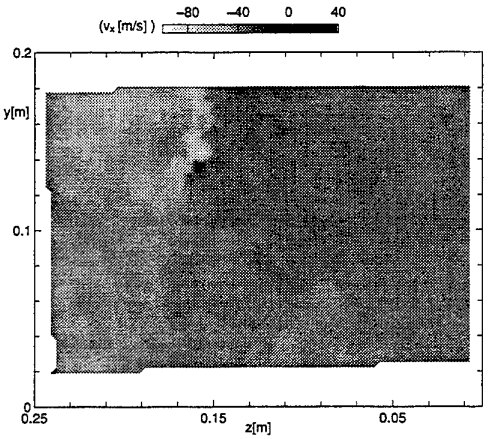


Fig. 14b Out-of-plane velocity components

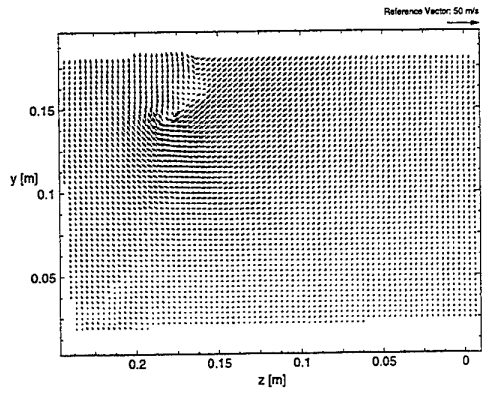


Fig. 15 In plane velocity components of the tip vortex and the wake of the blade. (The diagrams (15 and 15b) are turned by 90° anticlockwise with respect to Fig. 13.) The azimuth angle during recording was 10° larger than during the recording of the data set shown in Fig. 14.

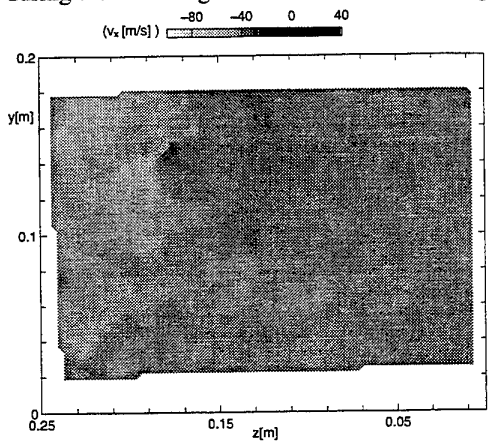


Fig. 15b Out-of-plane velocity components

The following velocity maps were recorded at slightly higher azimuth angles when the advancing blade has moved further upstream. Therefore, the vortex roll-up and the development of the axial velocity component can be investigated in detail.

6 CONCLUSIONS AND OUTLOOK

High resolution cross-correlation cameras fill the gap in spatial resolution between the high-speed video camera and photographic 35 mm PIV recording. The high-speed data transfer (up to 40 MByte/s) allows a large number of PIV recordings to be recorded in a short time. The acquisition software was devised in such a manner that captured image pairs could be interrogated within 30 seconds allowing the camera's observation area to be shifted to the area of interest during the operation of the tunnel. This procedure was exercised during the rotor studies in mid-scale as well as in large-scale facilities at moderate and high velocities.

The seeding particles used for these investigations were oil and DEHS droplets, which were generated by means of Laskin nozzles. The aerodynamic diameter of the particles was about 1 µm or smaller. The particles have been used for a global seeding of the complete volume in the transonic wind tunnel TWG and for a local seeding of a stream tube by a seeding rake with a few hundred small holes like the rake used in the mid-scale low speed wind tunnel LST and in the large low speed facility LLF. In all cases the injection was done without significantly disturbing the flow, but also in a way and at a location that guaranteed homogenous distribution of the tracers. The fluid mechanical properties of the seeding particles have been checked in order to avoid large discrepancies between fluid and particle motion. The diameter of the particles was small enough in order to ensure a good tracking of the fluid motion and a sufficient particle density inside the tip vortices to be measured.

The current development efforts regarding PIV systems DLR Göttingen are now focused on oblique as well as stereoscopic imaging arrangements. Aside from providing image access in areas that cannot be viewed in a classical PIV imaging configuration, the oblique viewing geometry can greatly improve the sensitivity of the system especially in a forward scattering configuration. Ultimately this also permits the imaged area to be increased without a need to further increase the laser power. The large angle (30°) between the viewing axis and the normal of the light sheet in conjunction with long focal length lenses (= narrow viewing angle) no longer permits the imaging plane to be parallel to the light sheet (translation imaging geometry). Rather, the lens, image and light sheet planes are tilted with respect to each other such that they intersect in a common line (angular displacement or Scheimpflug imaging geometry). This arrangement produces images with a varying magnification factor across them, which can be accounted for by de-warping the image. By adding a second camera with a different viewing angle all three velocity components have been retrieved simultaneously. Initial experiments (Willert 1997) and our first tests in a large wind tunnel both using two digital cameras, have demonstrated the feasibility of this approach.

ACKNOWLEDGMENT

The investigations of the propeller flow field were performed in the frame work of a Brite Euram Project, a research project denominated APIAN (Advanced Propulsion Integration Aerodynamics and Noise), in the collaboration between CIRA and DLR.

The tests in the transonic wind tunnel in Göttingen (TWG) were performed in the frame of the national AROSYS project. Special thanks to Dr. Schewe, Dr. Wendt, Dr. Schimke, and Mr. Jänker for the fruitful cooperation during the tests. The high motivation of the wind tunnel teams in LLF, LST, and TWG is greatly appreciated.

REFERENCES

Arroyo M.P., Greated C,A., 1991: Stereoscopic particle image velocimetry. Meas. Sci. Technol., Vol 2, 1181-6.

Gaydon M., Raffel M., Willert C., Rosengarten M. and Kompenhans J., 1997: Hybrid stereoscopic particle image velocimetry. Exp. Fluids, Vol 23, 331-334.

Hinsch K.D. 1995: Three-dimensional particle velocimetry. Meas. Sci. Technol., Vol 6, 742-53.

Keane R D, Adrian R J 1990: Optimization of particle image velocimeters. Part I: Double pulsed systems. Meas. Sci. Technol. 1, pp. 1202-1215.

Keane R D, Adrian R J 1992: Theory of cross-correlation analysis of PIV images. Appl. Sci. Res. 49, pp. 191-215.

Lowson M.V., 1991: Progress towards quieter civil helicopters. Proceedings of the 17th European Rotorcraft Forum, paper 91-59, Berlin, Germany.

Prasad A.K. and Adrian R.J., 1993: Stereoscopic particle image velocimetry applied to liquid flows. Exp. Fluids, Vol 15, 49-60.

Raffel M, Leitl B, Kompenhans K, 1993: Data validation for particle image velocimetry, in 'Laser Techniques and Applications in Fluid Mechanics', Eds. R.J. Adrian et al., Springer-Verlag, 210 - 226.

Raffel M., Seelhorst U., Willert C., Vollmers H., Bütefisch K.A., Kompenhans J., 1996: Measurement of vortical structures on a helicopter rotor model in a wind tunnel by LDV and PIV. Proc. 8th Intl. Symposium on Appl. of Laser Techniques to Fluid Mechanics, Lisbon, paper 28.1.

Ronneberger O, Raffel M., Kompenhans J., 1998: Advanced evaluation algorithms for standard and dual plane particle image velocimetry. Proc. 9th Intl. Symposium on Appl. of Laser Techniques to Fluid Mechanics, Lisbon, paper 10.1.

Royer H. and Stanislas M., 1996: Stereoscopic and holographic approaches to get the third velocity component in PIV. von Karman Institute for Fluid Dynamics, Lecture Series 1996-03, Particle Image Velocimetry.

Vogt A., Baumann P., Gharib M., Kompenhans J., 1996: Investigations of a wing tip vortex in air by means of DPIV. Proc. 19th AIAA Advanced Measurement and Ground Testing Technology, New Orleans, LA., 17-20 June 1996.

P. Wernert, W. Geißler, M. Raffel, J. Kompenhans, 1996: Experimental and numerical investigations of the dynamic stall process on a pitching NACA 0012 airfoil. AIAA Journal, Vol. 34 No. 5, 982-989.

Westerweel J. and Nieuwstadt F.T.M., 1991: Performance tests on 3-dimensional velocity measurements with a two-camera digital particle-image velocimeter. Laser Anemometry Advances and Applications, Vol. 1, ed. Dybbs A and Ghorashi B (New York: ASME) pp. 349-55.

Willert C., 1996: The fully digital evaluation of photographic PIV recordings. Appl. Sci. Res., Vol. 56, pp. 79-102.

Willert C, 1997: Stereoscopic digital particle image velocimetry for application in wind tunnel flows. Meas. Sci. and Techn., Vol. 8, No. 12.

SESSION 20

COMPLEX FLOWS 2

THREE-DIMENSIONAL EFFECTS OF TURBULENT FLOW IN AN IN-LINE TUBE BUNDLE

K. E. Meyer

Department of Energy Engineering, Technical University of Denmark
DK-2800 Lyngby, Denmark

ABSTRACT

Velocities have been measured with laser Doppler anemometry between tubes in cross-flow in a small in-line tube bundle with longitudinal to transverse pitches of $1.5D \times 1.8D$ and a Reynolds number based on mean velocity in minimum flow section of $Re = 30\,000$. At most locations a single recirculation zone is found behind each tube. However, the direction of circulation changes sign along the tube with a period of about 2 tube diameters. Three different patterns of such recirculation zones have been observed. Each pattern is very stable and does not change under undisturbed flow conditions.

1. INTRODUCTION

Recently, several detailed measurements have been performed on the local flow and local heat transfer in tube bundles in cross flow, e.g. Simonin and Barcouda (1988), Meyer and Larsen (1994) and Meyer (1995). Such experimental results are valuable for deriving improved correlations for pressure drop and heat transfer used for the design of heat exchangers, as well as for the experimental verification of numerical calculations of flow in tube bundles. The latter is important since tube bundle flows are complex and therefore challenging test cases for turbulence models.

While most available data concern staggered tube bundles the present study deals with an in-line tube bundle. Preliminary data for the local heat transfer in this tube bundle was obtained by Jørgensen and Larsen (1997) using the same gold-foil technique as developed earlier, Meyer (1995). The measurements showed that the local heat transfer was *not* symmetrical for any given tube. This is in contrast with the traditionally assumed distribution, see e.g. Žukauskas and Ulinskas (1988).

Researchers working with in-line tube bundles do sometimes refer to "problems" with asymmetrical flow. However, only a few detailed studies seem to have been made of this type of flow. Cheng and Moretti (1989) found by visualization 9 different flow asymmetric patterns in in-line tube bundle with pitches $1.25D \times 1.25D$. Groehn and Scholz (1972) found a highly non-uniform velocity profile behind a tube bundle with longitudinal to transverse pitches $1.38D \times 2.06D$. This non-uniformity could be explained by asymmetric flow conditions inside the tube bundle. In a later investigation Heinecke and van der Decken (1974) found that the non-uniform velocity profile behind an in-line tube bundle is limited to bundles with longitudinal pitches smaller than two diameters.

The purpose of the present study is to provide detailed LDA-data on the three-dimensional flow in a small in-line tube bundle subject to controlled uniform inlet conditions, jet manifesting naturally occuring asymmetrical flow.

2. EXPERIMENTAL SETUP

Figure 1 shows the experimental tube bundle mounted 400 mm downstream of the inlet contraction in the 300×300 mm test section of a closed-loop wind tunnel. The tube bundle consists of seven rows of tubes with diameter $D = 40$ mm mounted with longitudinal and transverse pitches $1.5D \times 1.8D$. Each row has three full tubes and two half tubes mounted on a thin metal plate. There is a 6 mm spacing between the metal plate and the top and bottom walls of the wind tunnel. Tube ends are mounted on windows of transparent acrylic plates. The length of the tubes are $7.3D$. The coordinate system has the x_1-axis in the main flow direction, the x_3-axis along the tube axes and the x_2-axis perpendicular to both flow and tubes. The origin is at the center of the center tube in row 1 and at the side window closest to the LDA optics.

Two designs of the tube bundle were used. The first tube bundle was used for prelimiary studies and employed PVC tubes. Control measurements showed

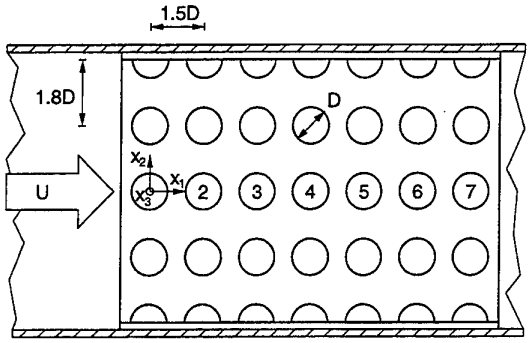


Figure 1: Tube bundle in wind tunnel test section and with indication of row numbers.

that the PVC tubes were not straight showing deviations up to 0.5 mm. This was clearly unsatisfactory and a second tube bundle was made with precision steel tubes. This tube bundle has a geometrical accuracy better than 0.1 mm and has been used for all the presented measurements, unless otherwise noted.

The mean velocity in the smallest cross section between two tubes in a row was $U_m = 11.5$ m/s, giving a Reynolds number $Re = 30\,000$ based on U_m and the diameter D. The volume flow of air was found by a measurement of the pressure drop over the contraction upstream of the test section of the wind tunnel. The mean velocity was kept constant within $\pm 1\%$. LDA measurements in the empty wind tunnel with the upstream velocity that was to be used for the tube bundle showed that the mean velocity profile here is uniform within $\pm 1\%$. A cooling system kept the air temperature constant at 20 °C ± 0.1 °C. The test section of the wind tunnel is slightly diverging. Each wall in the test section forms an angle of 1 degree with the direction of the main flow. During the measurements the tube bundle was aligned with the bottom wall and the side window in the positive x_3-direction.

The local velocity components U_1 and U_2 in the x_1- and x_2-directions, respectively, were measured with a four-beam, two component laser Doppler anemometer from Dantec Measurement Technology A/S. The LDA-system consisted of a 5 W Argon-ion laser, an optical probe (FiberFlow 60X81) fitted with a 1.98:1 beam expander and connected to the laser and the photomultipliers with fiber optics. The signals were processed with a Flow Velocity Analyser (FVA 58N20) connected to a personal computer. The computer also controlled the three-axes traversing bench that positioned the optical probe. The accuracy of the positioning is estimated to be about 0.1 mm. The focal length of the front lens was 310 mm, yielding a measuring volume with a diameter of about 0.07 mm and a length of about 2.5 mm. The flow was seeded with 2–3 μm droplets of atomized glycerol. To maintain a high signal/noise ratio window surfaces in the test section were frequently cleaned for deposited seeding.

Before the final measurements time series at 10 representative locations in the flow were taken. The time series were used to estimate integral time from auto-correlation for the two velocity components. The maximum integral times were about 10 ms and were found in the low velocity region downstream of a tube. During the measurements a "dead-time" of 10 ms was used in these low velocity regions and a "dead-time" of 5 ms was used in the rest of the flow. A "dead-time" of 10 ms ensures that the minimum time between samples is 10 ms. For most measurements 1000 samples were used to estimate each local velocity using residence time weighted averaging. However, at a few points near walls bad optical conditions caused low data rates and the sampling process was therefore interrupted by a timeout after 5 minutes. Turbulence intensities based on U_m were in general below 30% and combined with the variation of U_m it is estimated that most of the measured mean values of the velocity components are within $\pm 2\%$ of actual values.

3. RESULTS

The measurements show that the flow in the tube bundle consists of high velocity regions between longitudinal planes of tubes and a low velocity region behind each tube. In the low velocity region one or more recirculation zones are present. Several flow patterns with different distributions of these recirculation zone was found.

3.1 Flow patterns

In the case of a single recirculation zone behind a tube a high U_2 velocity component is found in front the following tube. The flow patterns can therefore be illustrated by a profile of the velocity component U_2 along a line in the x_3-direction located just upstream of a tube. This is done in figure 2 for three different patterns in the second tube bundle.

In the first tube bundle (with PVC tubes) only one flow pattern of changes in direction of net flow was found. This is probably because the geometrical imperfections favor a certain pattern. In the second tube bundle (with steel tubes) several different flow patterns were found.

The first pattern is almost symmetrical along the centre plane between side windows. There is a positive velocity peak at the centre plane and two negative velocity peaks placed symmetrically with a distance of

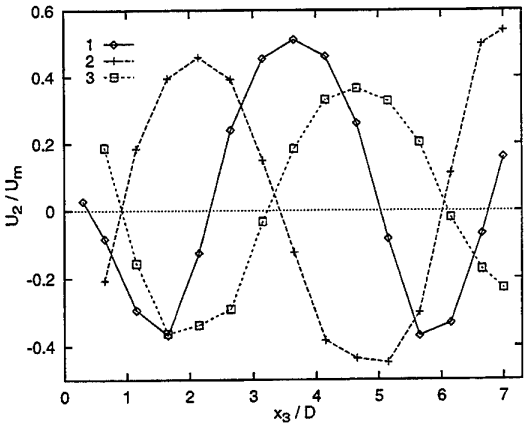


Figure 2: The U_2 velocity component along a line in the x_3-direction through $(x_1, x_2) = (5.45D, 0)$ for the three different flow patterns.

two tube diameter from the centre plane. Small regions with positive velocities are found close to the side windows.

The second flow pattern is close to being anti-symmetrical with zero velocity near the centre plane, two velocity peaks, one negative and one positive, located symmetrically at a distance $0.75\,D$ in the x_3-direction from the point of zero velocity. Close to the the side windows two additional velocity peaks with opposite directions were found. The third flow pattern is similar to a mirror image of flow pattern 2. Compared to flow pattern 2 the third flow pattern has a point of zero velocity a bit further away from the center plane and has velocity peaks of smaller magnitude.

When the wind tunnel was turned on a flow pattern would be established within the first few minutes. The flow pattern would then remain stable and only in a few cases was it observed that the flow pattern changed under stable running conditions. It was, however, possible to change the flow pattern by moving a rod with a cloth on (used for cleaning the windows) between the tubes. The rod was inserted manually through a hatch downstream of the tube bundle. In order to change the flow pattern the cloth had to be placed between the first couple of tube rows.

In order to monitor which flow pattern was present in the tube bundle the tube in the middle of the seventh row was equipped with small tufts of rabbit wool. The tufts were 10 mm long and were taped on to the front side of the tube along the line with $(x_1, x_2) = (8.5D, 0)$. The distance between two tufts was 20 mm and a total of 14 tufts were used. The tufts made small rapid movements due to turbulence, but most of the tufts generally pointed either up or down depending on the flow pattern. The pattern seen on the tufts was found to match very well with measurements like the ones shown in figure 2. During all measurements the tufts were checked regularly to ensure that the measurements were performed on the desired flow pattern.

3.2 Flow details

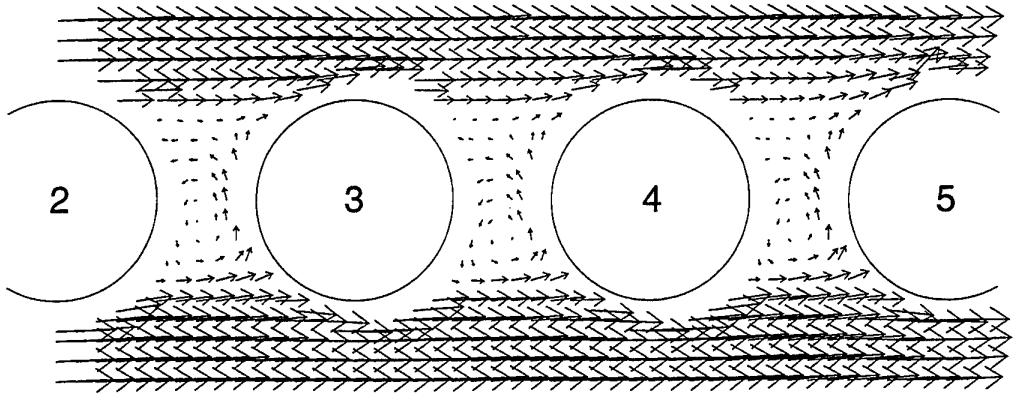
The general features of the flow for flow pattern 1 is illustrated by the vector plots shown in figure 3. The plots show the U_1 and the U_2 velocity components as vectors in a plane with constant x_3. In figure 3, plot (a) show the velocities at the centre plane between side windows ($x_3 = 3.65D$). Here, a single counter-clockwise recirculation zone is found behind each tube. All the way along the front side of a tube velocity vectors with a positive and quite large U_2 velocity composant is found. This clearly creates a net flow in the positive x_2-direction between two tubes.

Plot (c) in figure 3 shows the velocity vector at $x_3 = 1.65D$, i.e. in the plane where the largest negative U_2 velocity component was found for flow pattern 1 in figure 2. The velocity distribution found here are almost a mirror image of the velocity distribution found at plot (a). There is a clockwise recirculation zone and a net flow in the negative x_2-direction. Due to better optical access some of the velocity vectors in plot (c) are located closer to the tube wall than it was possible to do for the velocity vectors in plot (a).

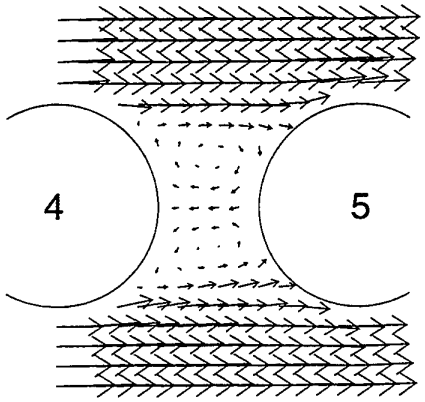
Plot (b) in figure 3 shows the velocity vector at $x_3 = 2.3D$, i.e. in the plane where the U_2 velocity component was found to be approximately zero for flow pattern 1 in figure 2. Here the velocity vectors show two recirculation zones and a flow that is symmetrical along a line in the x_1-direction through the tube axes.

An overview of flow pattern 1 is shown in figure 4. Here, the distribution of the U_2 velocity component between the center line tubes (i.e. $x_2 = 0$) is shown as a contour plot. Between row 1 and 2 there appears to be 5 regions with positive or negative U_2 velocity component near row 2. The direction of the U_2 velocity component seems to be the opposite of all the subsequent distributions of U_2. Between row 2 and 3 three main regions are found with two small extra regions at the side windows. Subsequent rows have the same flow pattern with a tendency towards larger regions downstream in the tube bundle. The mean values of U_2 between each pair of rows are found by integration of the measurements shown in figure 4 to be less than 1% of U_m. The total net flow through the low velocity region is therefore very small.

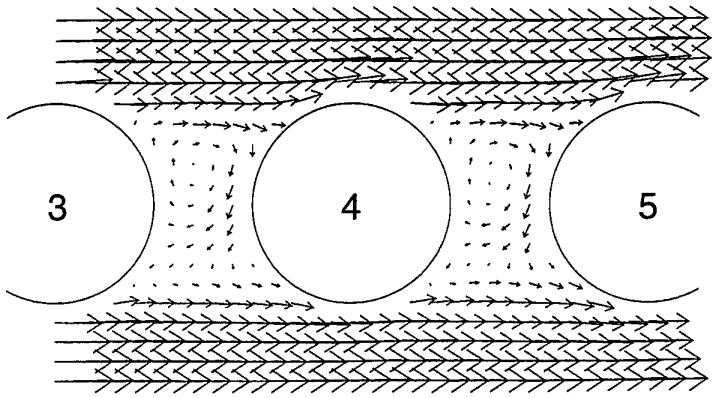
Spectrum analysis of the times series mentioned in section 2. did not find any characteristic frequencies in the flow. Histograms of the distribution of the



(a) Centre plane ($x_3 = 3.65D$) between rows 2–5



(b) Plane at $x_3 = 2.3D$ between rows 4–5



(c) Plane at $x_3 = 1.65D$ between rows 3–5

Figure 3: Velocity vector plots for flow pattern 1 shown in the interval $-0.9D \leq x_2 \leq 0.9D$.

velocity components of the samples in a local velocity measurement has been generated. At most points a normal Gaussian-like distribution was found. However at points close to the front side of a tube (e.g. the points shown in figure 2) where the U_2 velocity component was close to zero, the velocity distribution had two velocity peaks, one positive and one negative. A similar observation was done for the tufts. A tuft located between a region with tufts pointing upwards and a region with tufts pointing downwards would often flip randomly between the downward and upward direction.

3.3 Velocities between tubes

Profiles of the U_1 velocity component between two tubes are shown in figure 5 for row 3, 4 and 5. The U_1 velocity is shown as a function of the distance from the nearest tube surface in negative x_2-direction. Measurements taken in the same row are almost identical, while there is a general development in the velocity profile through row 3 to 5.

The velocity profiles shown in figure 5 can be integrated to estimate the mean velocity U_m. These estimates have been calculated from measurements done in all the three x_3 positions shown in figure 3. For the third row the estimates gave the same value within a margin of 1%. The mean value of the U_m estimates was 1% lower that the U_m value found from the measurement of the pressure drop over the contraction upstream of the wind tunnel test section. For row 4 and even more for row 5 a decrease of the estimated U_m was found at $x_3 = 3.65D$ and $x_3 = 1.65D$ while an increase of the estimated U_m was found at $x_3 = 2.3D$. These differences was 2%–3% of the U_m at the 5th row.

Measurements of the U_2 velocity component in the low velocity region between two tubes are shown in figure 6. Profiles have been measured between row 3 and 4 and between row 4 and 5 at $x_2 = 0$. In addition the profile between row 4 and 5 has also been measured for $x_2 = 1.8D$, i.e. between two tubes above the center line

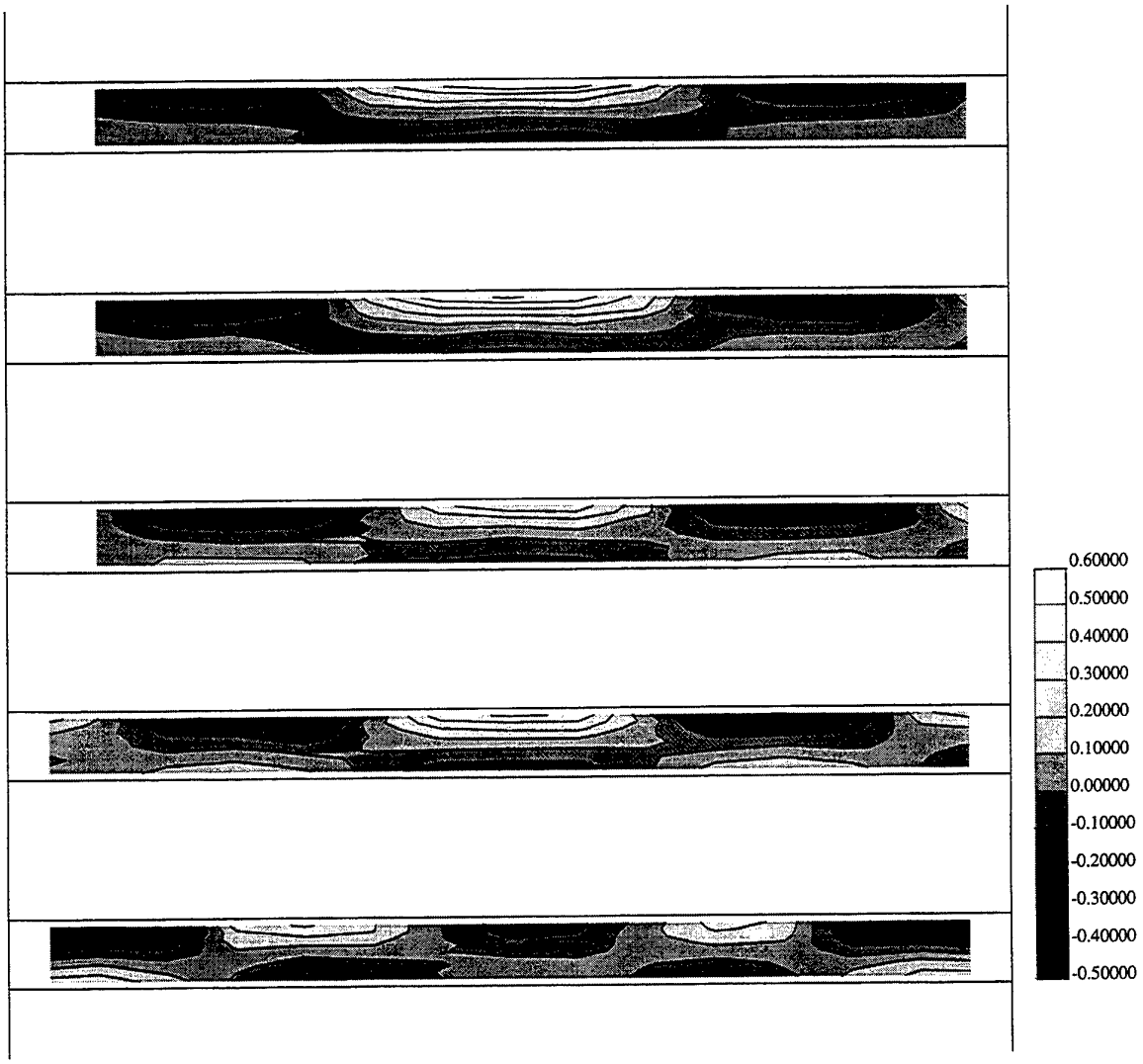


Figure 4: Contours of the U_2/U_m at the x_1–x_3 plane at $x_2 = 0$ for flow pattern 1.

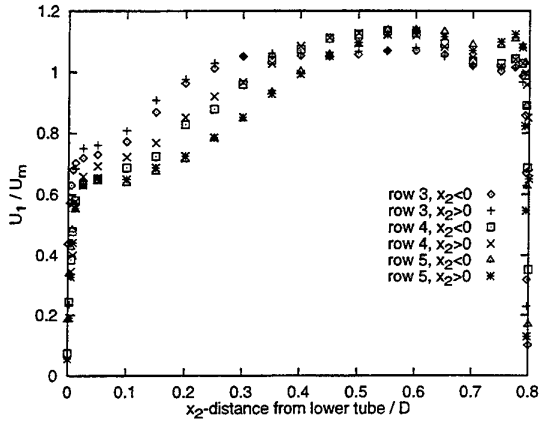


Figure 5: U_1 velocity component between tubes in a row for flow pattern 1.

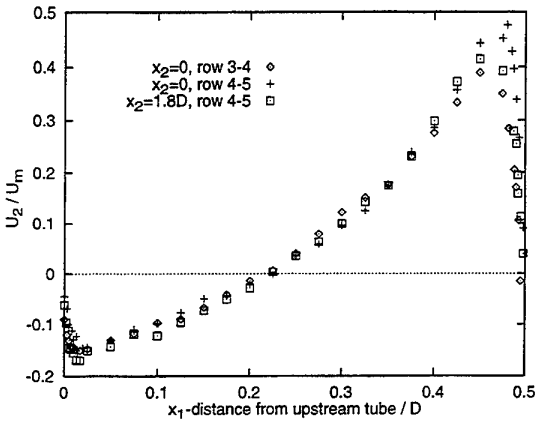


Figure 6: U_2 velocity component in low velocity region between tubes for flow pattern 1.

tubes. All three profiles are almost identical.

3.4 Dependency of tube length

In order to investigate the influence of distance between side windows, a thin "baffle" plate (a 2 mm metal plate) was placed at different locations parallel to the side window. This investigation was carried out in the first tube bundle (with PVC tubes). With the baffle plate in distances $2D$, $3D$ and $4D$ from the side window, there appears to be two distinct flow regions: The region close to the window (low values of x_3) with net negative flow and the region close to the baffle (high values of x_3) with net positive flow. For the baffle plate placed in distances $5D$, $6D$ and $7.3D$ from the side window, three flow regions were found: The central part has a net positive flow while the regions near the sides have net negative flows.

A measurement in the second tube bundle with the baffle wall in a distance $4D$ from the side wall showed distributions of U_2 similar to the corresponding part of flow pattern 3 in the full bundle. Tuft studies indicated that several flow patterns were possible here.

4. DISCUSSION

The measurements have shown flow patterns in a small in-line tube bundle that are quite different from the two-dimensional, symmetric flow suggested in traditional literature by e.g. Žukauskas and Ulinskas (1988). At most locations a single recirculation zone was found in the low velocity region between two tubes causing a locally asymmetrical flow. The direction of rotation of this recirculation zone changed along a tube. The change from counter-clockwise to clockwise circulation takes place with a distance of approximately 2 tube diameters. It seems likely that the change of direction of circulation keeps the net flow through the planes shown in figures 4 and 7 close to zero. The local mean velocity between tubes in the high velocity region, hence the pressure drop, is therefore reasonably constant.

The flow patterns were found to be very stable. After a large disturbance was introduced shortly in the downstream part of the tube bundle, the original flow pattern would usually be reestablished. In order to change the flow pattern a disturbance had to be introduced upstream of the tube bundle or between the first couple of rows. It is therefore reasonable to assume that the tufts mounted on a tube in the seventh row did not influence the flow patterns. Spectral analysis of time series did not find any dominating frequencies. This indicates that regular vortex shedding is not an important feature of the flow.

Three different patterns of the distribution of the direction of circulation along the tubes were found. One might argue that additional patterns could be expected in a symmetrical geometry, e.g. a pattern similar to flow pattern 1, but where zones with positive and negative circulation had switched direction. Due to the tube bundle's small misalignment with the main flow direction the present experimental setup might favor only some of the possible patterns. On the other hand, in a more symmetrical flow geometry the flow patterns might be significantly more unstable and thereby more difficult to measure.

It is clear from the measurements shown in figures 5 and 4 that the flow does not become fully developed during the seven rows. The flow in a large tube bundle with more tubes in the transverse and longitudinal directions and with longer tubes could be very different from the present small tube bundle. The measurements in figures 5 and 6 indicate that flow pattern 1

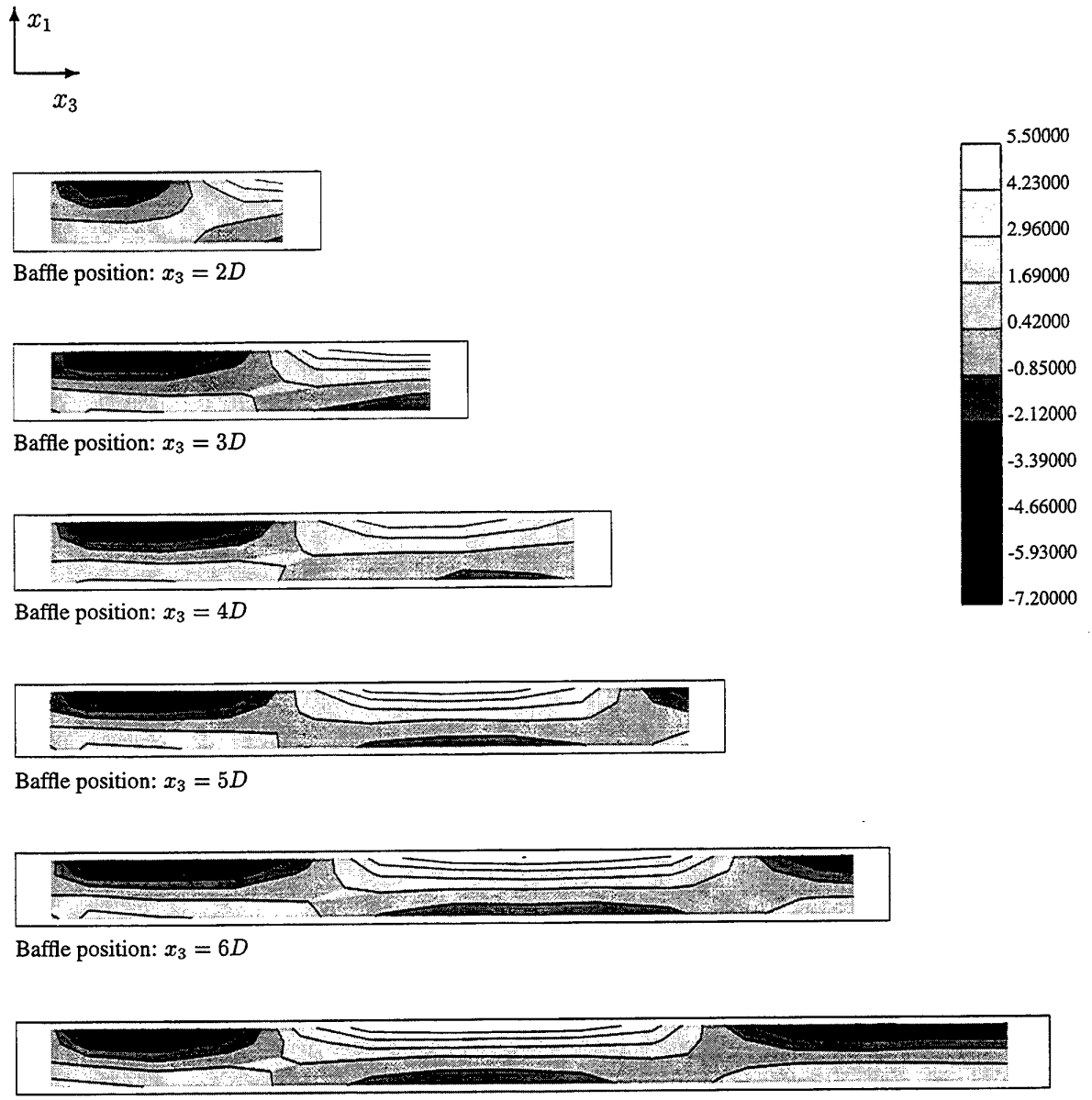


Figure 7: Contours of U_2 for the x_1–x_3 plane at $x_2 = 0$ between the central tubes in the 4th and 5th row in the first tube bundle. The positions of the tube, side window (left) and baffle plate (right) are shown as a rectangular box.

could exist in a larger tube bundle. However, it is possible that the presence of top and bottom walls prevents more complicated flow patterns from developing.

5. CONCLUSIONS

Measurements have shown that inside a small in-line tube bundle with small longitudinal pitch complex, three-dimensional and stable flow patterns can exist. The patterns consist of cells of a single recirculation zones behind each tube. The direction of circulation changes along a tube with a distance between regions of different direction of circulation of about 2 tube diameters. Three different patterns of distributions of these recirculation zones have been observed. Each pattern was very stable and did not change under stable flow conditions. It was also observed that the flow does not become fully developed even at the 7th row in the tube bundle.

Further study is needed to investigate the influence of changes in the geometrical parameters, particularly the longitudinal pitch and the number of transverse tubes in a row. Measurements of the local heat transfer coefficient, now in progress, have already confirmed asymmetrics, and will constitute an important experimental tool in further studies.

ACKNOWLEDGEMENTS

The study was partially supported by the Danish Technical Research Council under grant STVF 9502261 and the Danish Agency for Trade and Industry. Valuable comments and suggestions from P. S. Larsen are acknowledged.

REFERENCES

Cheng, M. and Moretti, P. M. (1989). Flow instabilities in tube bundles. In M. K. Au-Yang, S. S. Chen, S. Kaneko, and R. Chilukuri, editors, *Flow-Induced Vibration 1989*, pages 11–15. ASME.

Groehn, H. G. and Scholz, F. (1972). Investigations on steam generator models of in-line tube arrangement in pressurized air and helium. In *Symposium on Component Design for High Temperature Reactors using Helium as Collant*, London.

Heinecke, E. and van der Decken, C. B. (1974). Steady and unsteady flow phenomena in and behind staggered and in-line tube banks. In *Heat Exchangers: Design and Theory Source Book*, pages 663–671. McGraw-Hill.

Jørgensen, T. A. and Larsen, T. L. (1997). *Eksperimentel og numerisk undersøgelse af rørvarmeveksler (Experimental and numerical investigation of tube heat exchanger)*. Master's thesis, Department of Energy Engineering, Technical University of Denmark. In danish.

Meyer, K. E. (1995). Local heat transfer from a tube in a staggered tube bundle. In B. Sundén, E. Blums, and A. Zukauskas, editors, *Advances in Engineering Heat Transfer*, pages 289–298. Computational Mechanics Publications.

Meyer, K. E. and Larsen, P. S. (1994). LDA study of turbulent flow in a staggered tube bundle. In *Proceedings of the 7th International Symposium on Applications of Laser Techniques to Fluid Mechanics*, pages 39.4.1–39.4.7, Lisbon, Portugal.

Simonin, O. and Barcouda, M. (1988). Measurements and prediction of turbulent flow entering a staggered tube bundle. In *Proceedings of the 4th International Symposium on Applications of LDA to Fluid Mechanics*, pages 5.23.1–5.23.6, Lisbon, Portugal.

Žukauskas, A. and Ulinskas, R. (1988). *Heat Transfer in Tube Banks in Crossflow*. Hemisphere Publishing Corporation.

DETAILED LDV FLOW FIELD MEASUREMENTS ON A MODEL OF BAYONET TUBE EQUIPPED WITH HEAT TRANSFER AUGMENTING DEVICES

A. Cattanei (*), N. Elia (**), S. Razore (**), A. Sciacchitano (**), M. Ubaldi (*), P. Zunino (*)

(*) Università di Genova, Istituto di Macchine e Sistemi Energetici - V. Montallegro, 1 I-16145 Genova, ITALY
(**) Ansaldo Ricerche S.r.l., Laboratorio di Termofluidodinamica - C.so Perrone, 25 I-16161 Genova, ITALY

ABSTRACT

Using a laser-Doppler anemometer detailed velocity and turbulence measurements have been done on a model of bayonet tube heat exchanger. The model consists in a high aspect ratio rectangular channel with a wall provided with square ribs periodically spaced. Detailed velocity and Reynolds stress distributions are shown and analyzed. Highly unsteady, separated flow regions are present in front, over, and downstream of the rib. The flow field is analyzed and compared to the ones of classic separating and reattaching flows; similarities with those cases have been found.

1. INTRODUCTION

The present work stems from the study of heat exchanger tubes to be used in externally fired gas turbine plants and is part of a wider research project oriented towards the development of such kind of plants.

In order to limit the exchanging surfaces extent the tubes are equipped with annular square section ribs which enhance the heat transfer. From a thermo-fluid-dynamic point of view the design of the exchanger tube consists in determining the optimum values of rib height, pitch, and number.

The LDA measurements presented in the paper have been taken on a plain model of the tube; they provide an accurate knowledge of the flow field within the tube necessary for the heat exchanger design.

The flow around a square obstacle belongs to the category of turbulent separating and reattaching flows typical of many thermally highly loaded gas turbine components: diffusers, blade internal and external passages, combustors. Furthermore such kinds of flows are present in many other technical problems.

The present geometry is rather simple and has already been studied by several authors; see for instance Arts et a. (1997), Okamoto et a., (1993), Zhang et a. (1994). Nevertheless, due to the large number of parameters involved, it is difficult to find a case which can be easily compared to the present one.

A strong similarity exists with the backward-facing step case or other typical separated flows which have been widely studied; see for instance Eaton and Johnston (1981) or Simpson (1989). Nevertheless differences with present case exist which are mainly due to three effects: the remarkable acceleration caused by the obstraction, the existence of a big separation zone over it, and the spacial periodicity of the geometry.

While a normal boundary layer is usually present on the backward-facing step upstream the separation point, in present case the flow at the rib trailing edge is strongly unsteady and turbulence is higher and with a different structure. Thus the large quantity of results available in literature on the backward-facing flow is not easily transposable to the present case and it has to be specifically investigated.

Beyond their purpose these results may be interesting for both improving the knowledge on the specific flow and validating numerical codes and turbulence models.

2. EXPERIMENTAL APPARATUS AND MEASUREMENT TECHNIQUE

The experiment was done on the plain model of the bayonet tube which is shown in fig. 1 and is fed with cold air by a blower.

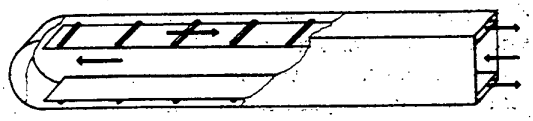


Fig. 1. View of the bayonet tube model.

The model is composed by an inner square section tube 1 800 mm long with a side of length 180 mm. Air enters the model through the tube, at the end of it the flow undergoes a 180° deflection and is splitted in two channels parallel to the internal tube. The channels have the same height as the tube but width H = 25 mm. Eight square ribs of height h = 9.6 mm and length l = 180 mm are placed on the internal wall of each channel with a pitch p = 244.4 mm; the air is descharged in the atmosphere; in the real tube the external wall is the heat exchanging surface. The main proportions are the expansion ratio $H/(H-h)$ = 1.623 and the pitch to height ratio p/h = 25.46; the large value of the aspect ratio (l/H = 18.75) assures that three dimensional effects due to the endwalls do not influence the flow at midspan. Various configurations (with different values of h and p) have been tested but the configuration described in present work is the one studied in detailed way.

The investigated flow field region is shown in fig. 2 together with the coordinate system. Measurements have been taken by means of a two-components laser-Doppler anemometer in the region between the last but one couple of ribs in the midspan plane. Only the components of velocity lying in this plane have been measured. In order to have reference profiles of mean and fluctuating quantities velocity has been measured in the traverses corresponding to inlet and outlet of flow field, with the same value of mass flow rate and in absence of ribs. Flow periodicity in space has been checked.

Probe positioning has been realized by means of an automatic traversing system allowing movements with a minimum step of 0.002 mm. Measurements have been done in 25 traverses at the axial locations x/h reported in table 1; (traverses 1 through 5 and 25 are located over the rib).

Table 1. Axial traverses locations.

n	x/h	n	x/h	n	x/h
1	-1.021	10	2.083	19	20.313
2	-0.781	11	3.125	20	22.188
3	-0.521	12	3.750	21	22.917
4	-0.260	13	4.063	22	23.781
5	-0.021	14	5.208	23	23.958
6	0.104	15	6.458	24	24.292
7	0.260	16	8.125	25	24.417
8	0.542	17	12.188		
9	1.042	18	16.250		

Typically 53 measuring points per traverse have been used between the ribs and 49 in the throat over them; the first and last points were located at the nominal distance of 0.050 mm from each wall thus resulting in two points in the laminar sublayers at least.

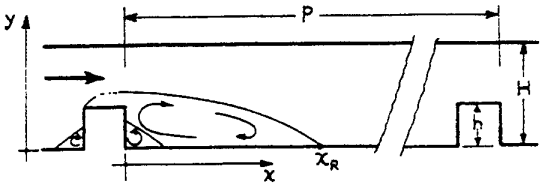


Fig. 2. Flow field and coordinate system.

The bulk velocities in the throat over a rib U_b = 6.694 m/s and in the channel between the ribs U_B = 4.124 m/s have been calculated from the mass flow rate. The correspondent Reynolds numbers are $Re_h = U_b h/\nu = 4280$ and $Re_H = U_B H/\nu = 6865$; Re_h and Re_H may be used for comparisons with the backward-facing step flow and with the fully developed turbulent flow in rectangular channels respectively.

The two-components LDA system employs a 4 W Argon-Ion laser with wave lengths 514.5 nm and 488 nm as laser source; signals have been acquired and processed by means of a DANTEC fiber flow 60x system. Access to the channel is provided by a window of optical glass placed on the model end-wall. The front lens has a focal length of 150 mm and a beam separation of 15 mm resulting in a measurement volume of 69 μm diameter and 1.380 mm length. The flow has been seeded with mineral oil by means of a TSI 6 jets atomizer realizing particles of 2 μm mean diameter.

30 000 samples have been collected for each location with data rates between 100 and 1000 samples per second. Reynolds shear stress has been computed using a coincidence window of 0.2 ms. Mean values have been calculated with residence time weighted average in order to compensate velocity bias.

3. MEAN VELOCITY FIELD

The profiles of the mean velocity streamwise component U in traverses n = 1÷25 are reported in fig. 3; there is no correspondence between the position on the plot and the real one. The flow field in the rib zone is reported in the vector plot of fig. 4. The time averaged streamlines separating the ricirculation zones downstream of the rib have been calculated by means of continuity equation and under the assumption of flow two-dimensionality; they are represented in fig. 4.

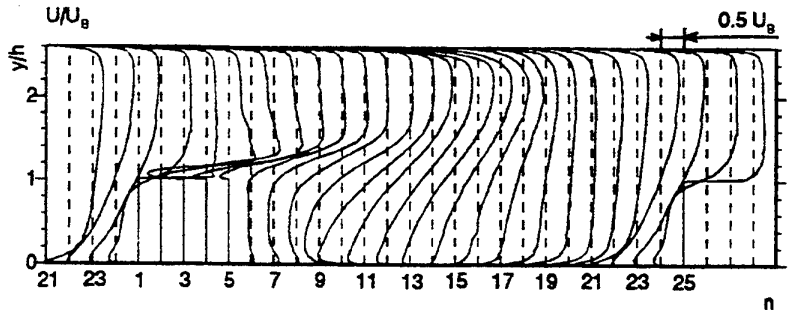


Fig. 3. Streamwise component of mean velocity.

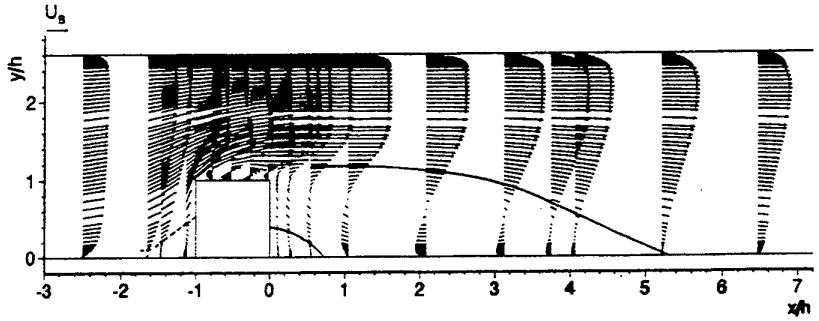


Fig. 4. Flow field in the rib zone.

The analysis of the mean velocity field may be done with reference to three zones of the flow field: upstream and over the rib, downstream of it, and on the external wall.

3.1 Region upstream and over the obstacle

The details of the flow field around the rib are reported in the vector plot of fig. 5. The sudden flow deviation caused by the rib creates a separation bubble in front of it which occupies a region extending for lengths of about $0.5h$ in both the x and y directions. Infact also in last but two traverse upstream the rib (x/h = -1.635) very small negative values of U may be observed in the points closer to the wall; this could suggest that the recirculation bubble extends even further upstream. A careful observation of the velocity profile shows that velocity is approximately parallel to the wall (that is the y-component V of mean velocity is almost zero); this is in contrast with the fact that in the last but one traverse (x/h = -1.458) the U inversion of sign takes place in stations where V is positive (that is velocity is perpendicular to the wall). Thus flow in proximity of the wall probably belongs to an upstream recirculation bubble which has not been resolved due to insufficient number of traverses in this zone.

Martinuzzi and Tropea (1993) proposed several models for flows around square ribs and cubes at Reynods numbers higher than in the present case (Re_h = 80000÷115000); a possible flow structure, similar to those ones, is represented by the lines drawn in fig. 5 and is composed by three different recirculation regions joining in a saddle point S. The same authors also observed that the flow in front of the rib does not preserve two-dimensionality even with aspect ratios as large as the present one. Instead the flow presents a cellular structure in the spanwise direction; the cells would influence the flow over the obstacle too.

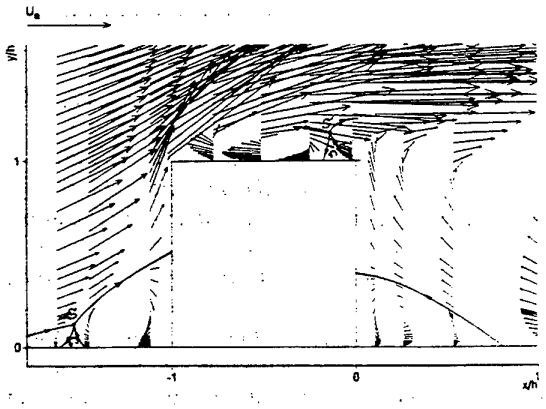


Fig. 5. Flow field around the rib.

The obstacle upper surface is completely occupied by a big recirculation zone starting from the leading edge and extending for a height of about 0.2 h in the y direction. The presence of a reversed velocity profile on all of the traverses on the rib could suggest that a whole separation bubble is present both on the rib and in the downstream region. A careful comparison of the velocity direction and modulus in the two last traverses upstream of the rib trailing edge (x/h = -0.260 and x/h = -0.021) shows inconsistency between the two velocity profiles. This suggests that also here a more complex flow structure is probably present with a saddle point S' located between the two traverses. Thus the reverse flow on the last traverse (x/h = -0.021) likely belongs to the main downstream separation bubble while the flow in the upstream traverses belongs to the bubble on the rib; the flow is probably three-dimensional.

An interesting consequence of this is that the flow leaving the rib does not separate from the rib trailing edge as in the case of the backward-facing step. Instead, considering the time averaged dividing streamline, the separation point coincides with the saddle point S' whose position probably varies in the spanwise direction and, due to the high unsteadiness, also fluctuates in time.

Kiya and Sasaki (1983) studied the flow over a blunt flat plate at Re_h = 26000; they found a large-scale unsteadiness in the bubble superposed to large-scale vortices shed downstream at different frequencies. Although present geometry and flow are different some analogies exist and the description done for the flow over the rib is probably over-simplified.

3.2 Downstream separation and recovery zones

The main separation bubble occupies the region extending downstream of the obstacle with a calculated height of about 1.10÷1.18 h within a distance x = 2.2 h from the rib trailing edge. For the backward-facing step case, in the same locations, the bubble has a height approximately equal to the step one.

Downstream of x = 2.2 h the separating streamline curves towards the reattachment point located at x_R = 5.32 h. Kasagi and Matsugana (1995) measured the flow downstream of a backward-facing step with geometry and flow similar to the ones of present case (expansion ratio 1.504, step height based Reynolds number 5540); the reattachment length value was x_R = 6.51 h. The difference in the x_R/h value in the two cases could be connected to the high unsteadiness present at the rib trailing edge; this is in agreement with findings of Ötüngen (1991) about the effects of expansion ratio and turbulence at separation point of backward-facing steps.

In the lower corner downstream of the rib a counter rotating bubble is present which extends for a length of about 0.6÷0.8 h with a height of about 0.4 h.

Downstream of the reattachment point velocity becomes positive and gradually increases. In spite of the apparently high value of the pitch to height ratio (p/h = 25.46) the profile in the further downstream traverses does not reach the the fully developed one. In fig. 6 the comparison between the velocity profile in absence of ribs (for same mass flow rate) and the one in traverse x/h = 20.313 is reported. In case of presence of ribs the velocity profile is lower and flatter in the central zone, rather higher in the external side and only slightly higher on the rib side; differences are smaller than 10%. This fact is in agreement with Eaton and Johnson (1981), Simpson (1989), and other authors who report that, for backward-facing step flows, the characteristics of the free-shear layer flow are still present 50 step heights downstream of reattachment.

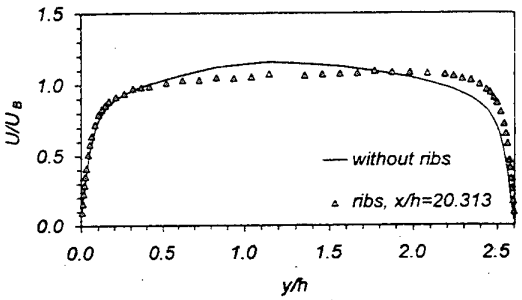


Fig. 6. Mean velocity profiles with and without ribs.

3.3 External wall

The flow on the external wall is influenced by the rib obstruction through the acceleration upstream and over of the rib (x/h = -5÷0) and the deceleration coming after (x/h = 0÷6.5); a new acceleration caused by the further rib takes place from traverse x/h = 20.313 on. A favourable pressure gradient first and an adverse one later are associated to this process; as a consequence the boundary layer on the external wall becomes thinner in the traverses where acceleration is positive and grows fastly in the others. This phenomenon is clearly detectable in fig. 7 where the external wall friction velocity $u_\tau = \sqrt{\tau_w / \rho}$ (non dimensionalized with U_B) is reported versus x/h. The continuous line u_τ = 0.06 U_B represents the value in

absence of ribs. u_τ strongly decreases with a linear trend from the rib trailing edge to traverse x/h=4.063; then u_τ increases until x/h=8.125 and decreases until x/h = 20.313 towards the value relative to the absence of ribs; after this locations u_τ increases again approaching the following rib. This trend indicates a boundary layer laminarization over the rib zone and a transition to turbulence over the riattachment zone.

Since heat transfer is strictly connected to the value of u_τ this diagram provides information on the improvement in efficiency of the exchanger due to the presence of the ribs.

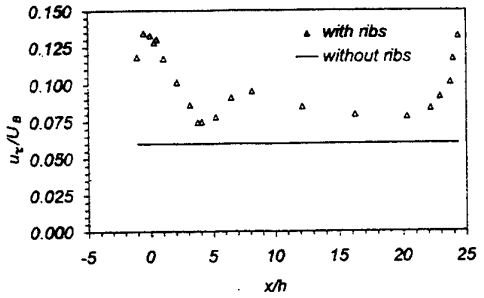


Fig. 7. Friction velocity on the external wall.

4. VELOCITY FLUCTUATIONS AND REYNOLDS SHEAR STRESS

In fig. 8-9 root-mean-squares of velocity fluctuations u' and v', non-dimensionalized with U_B, are shown; the Reynolds shear stress $\overline{u'v'}$ is shown in fig. 10 non-dimensionalized with U_B^2. The turbulent quantities are analysed with reference to the same zones employed for mean velocity and their values upstream of the throat may be assumed as reference ones. Typical values of u', v' and $u'v'$ are 0.15 U_B , 0.12 U_B, and 0.01 U_B^2 respectively.

4.1 Region upstream and over the obstacle

Upstream and within the throat u', v', and $-\overline{u'v'}$ decrease moving downstream due to the mean flow acceleration. This is consistent with the possibility of relaminarization of the boundary layer on the external wall.

Instead, in the recirculation zone in front of the obstacle, both u' and v' increase; $-\overline{u'v'}$ first increases and then decreases with a plateau in x/h = -1.458 extending from the wall until about y/h = 1.5 (fig. 10b).

Over the rib all the Reynolds stress components reach their maximum values ($-\overline{u'v'}$ shows two sharp negative and positive peaks respectively) and then start decreasing going downstream in the free shear layer. The very high values reached by both u' and v' (of the order of 0.75 U_B = 0.46 U_b) support the assumption of presence of organized unsteady structures in the separated zone which has been done during discussion of the mean velocity flow.

4.2 Downstream separation and recovery zones

Downstream of the rib edge, for a length of about 6 h, a zone with y/h ranging from 0.6 to 1.4 exists where all the Reynolds stresses present a plateau with values smaller but still comparable to the ones reached over the rib. This region is approximately coincident with the free shear-layer and is similar to a plane mixing-layer. In the first part (x < 3.5 h) it is centered on the separating streamline; then the separating streamline curves toward the reattachment point and the plateau is located over it. This trend of the locations of maximum Reynolds stresses is similar to the one observed by Ruderich and Fernholz (1986) downstream of a flat plate normal to the flow.

As in the case of the backward-facing step, high turbulence is present on the low speed side of the shear-layer while in a plane mixing-layer on the same side, turbulence is low Eaton and Johnston (1981), Simpson (1989).

In the reversed flow zone both u' and v' are smaller than in the free shear-layer, but their level is of the order of 0.2 U_B thus still considerably higher than the reference ones upstream of the throat; in the region of the counter rotating vortex their value is low. Instead $-\overline{u'v'}$ is low: it has values of the order of 0.01 U_B^2, same as the reference one. This effect becomes stronger in the near-wall layer region of the reversed flow; it is in agreement with Adams and Johnston (1988) who made a deep study of this flow in the backward-facing step case and found very low values of $-\overline{u'v'}$ despite the high unsteadiness evidenced by u' value.

Downstream of the reattachment point all Reynolds stress components decrease towards the values typical of the fully developed channel flow; anyway, as in the case of the mean velocity, these values are not reached because the distance between the ribs is not sufficient. Evidence of this is given by fig. 11 where u', v', and $-\overline{u'v'}$, non-dimensionalized by means of U_B and U_B^2 respectively, are reported versus y/h; these distributions are relative to traverse x/h = 20.313 (same as in the case of mean velocity).

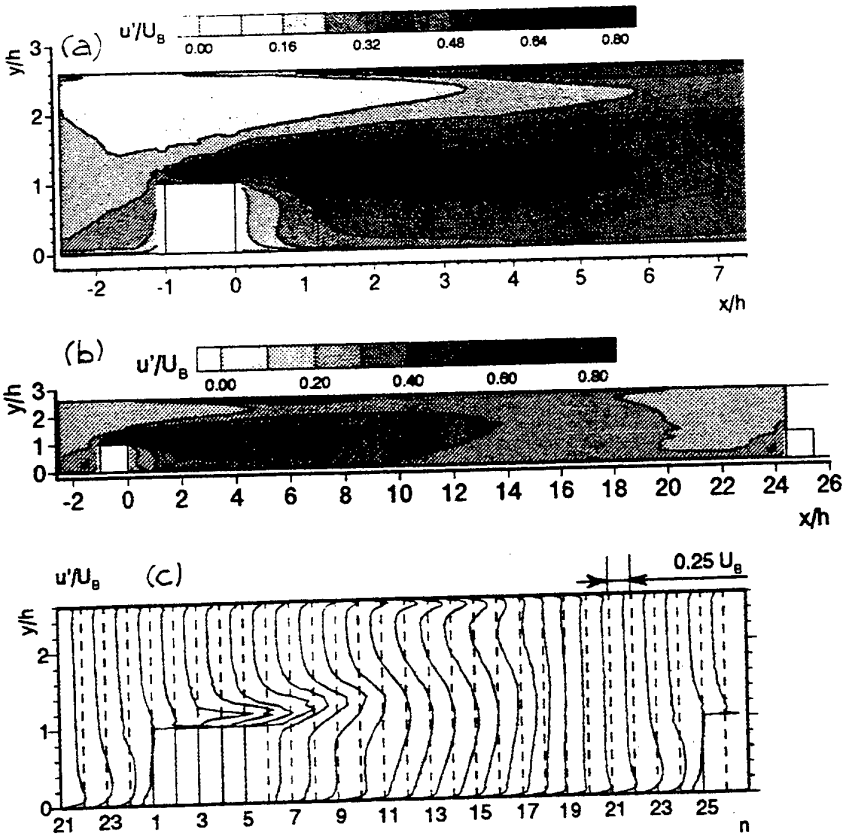


Fig. 8. Fluctuations of x-component of velocity: (a) hill diagram around the rib. (b) whole flow field hill diagram. (c) y-distributions.

The distributions of the three Reynolds stresses give evidence of the upstream free shear-layer flow. Infact in the center of the channel both u' and v' have very high level, which, for u', is comparable to the peaks close to the wall; the average values are about 3 times as much as in the case of absence of ribs.

The $-u'v'$ profile is very distorted: within a distance of 0.8 h from the internal wall $-u'v'$ has a round profile instead of the typical linear one; it reaches 0 at y/h = 20. On the external wall the two profiles are more similar and the maxima have close locations. The flatness of the profile in the range y/h = 2.5÷12.5 implies that very low shear stress unbalance exists in this zone according with the flat profile of U (see fig. 6).

4.3 External wall

As well as mean velocity, turbulence on the external wall is mainly influenced by acceleration and deceleration of the mean flow and the correspondent pressure gradients. Since v' and $u'v'$ have similar trends the analysis may be done with reference to u' (hill diagrams and distributions of fig 8). From traverse x/h = 20.313 to the rib leading edge the u' peak value decreases due to mean flow acceleration; then it starts increasing from the locations where the friction velocity u_τ decreases (see fig. 7) reaching the maximum in traverse x/h = 4.063 where u_τ is minimum. Downstream the peak decreases but the profile becomes rounder until traverse x/h = 8.125. Going further downstream u' peak values slowly decrease towards the values typical of the fully developed channel flow; then a new rib is encountered and the process repeats.

The most interesting part of the process takes place between the rib trailing edge and traverse x/h = 20.313. The trend until x/h = 4.063 is typical of laminar boundary layers approaching separation which does not take place due to transition to turbulence; the boundary layer grows rapidly until x/h = 8.125 and then becomes turbulent.

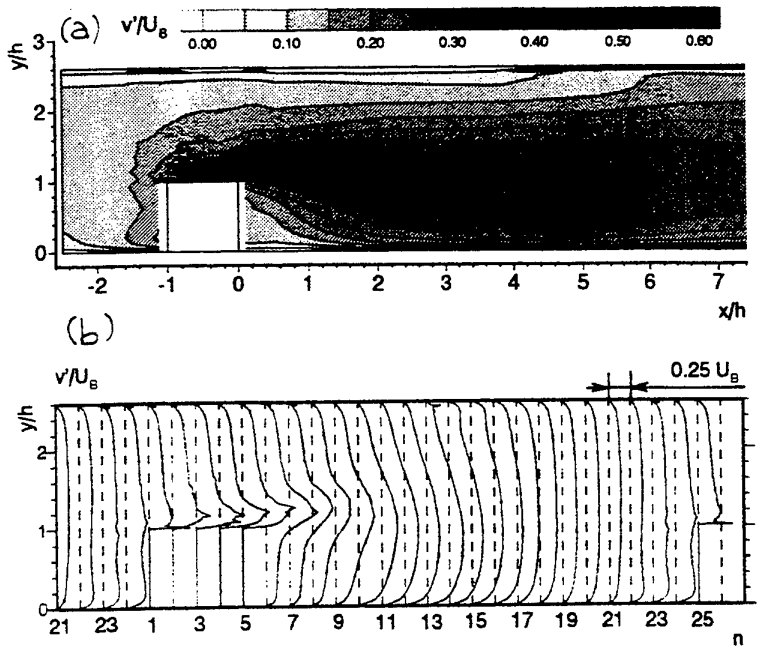


Fig. 9. Fluctuations of y-component of velocity: (a) hill diagram around the rib, (b) y-distributions.

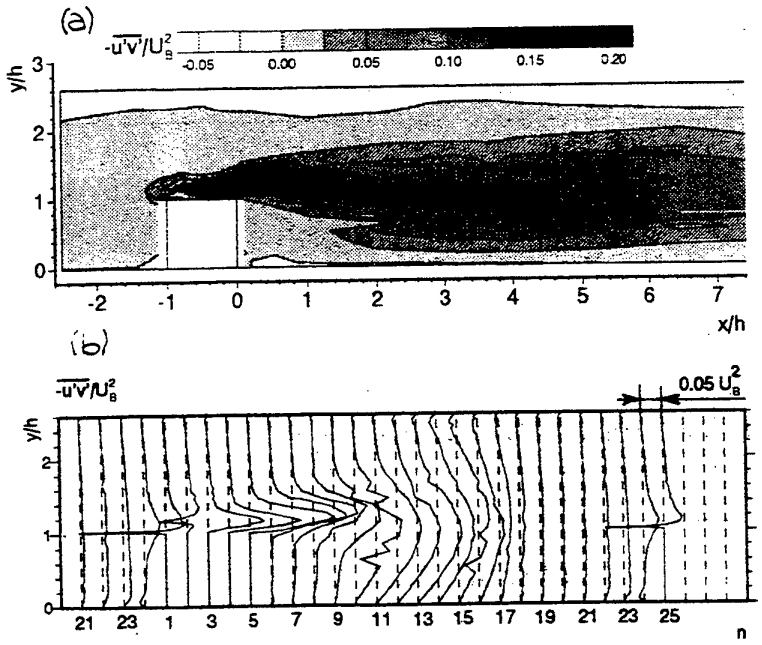


Fig. 10. Reynolds shear stress: (a) hill diagram around the rib, (b) y-distributions.

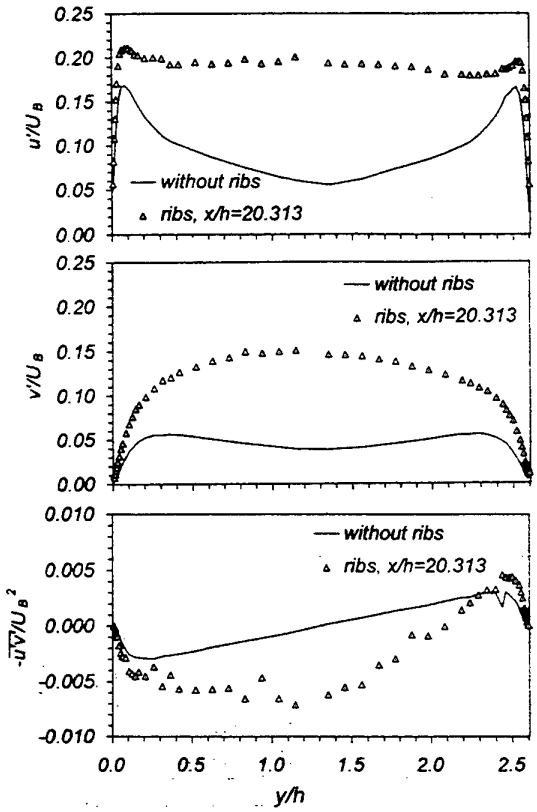


Fig. 11. Turbulent quantities with and without ribs.

CONCLUSIONS

The quantitative trend of the friction velocity, required for the study of the heat exchanger, has been determined.

The results improve the knowledge of present flow field and demonstrate a qualitative analogy of with typical separated and reattaching flows. In spite of the geometry simplicity, the flow field is extremely complex due to both the presence of zones with organized unsteadiness and the probable three-dimensionality of the mean flow.

The extreme detail of the measurements allows using the present results for validation of numerical codes and turbulence models.

REFERENCES

Adams, E. W. & Johnston, J. P., 1988, Flow structure in the near-wall zone of a turbulent separated flow, AIAA J.,
vol. 26, no. 8, pp. 932-939.

Arts, T., Rau, G., Cakan, M., Vialonga, J., Fernandez, D., Tarnowski, F. & Laroche, E., 1997, Experimental and numerical investigation on flow and heat transfer in large scale, turbine cooling representative, rib roughened channels, Proc. 2nd European Conf. on Turbomachinery, Fluid Dynamics, and Thermodynamics, Antwerpen,
pp. 453-461.

Eaton, J. K. & Johnston, J. P., 1981, A review of research on subsonic turbulent flow reattachment, AIAA Journal,
vol. 19, no. 9, pp. 1093-1100.

Martinuzzi, R. & Tropea, C., 1993. The flow around surface-mounted, prismatic obstacles placed in a fully developed channel flow, ASME J. of Fluids Eng.,
vol. 115, pp. 85-92.

Kiya, M. & Sasaki, K., 1981, Structure of a turbulent separation bubble, J. of Fluid Mechanics,
vol. 137, pp. 83-113.

Kasagi, N. & Matsugana, A., Three-dimensional particle-tracking velocimetry measurements of turbulence statistics and energy budget in a backward-facing step flow, Int. J. of Heat and Fluid Flow,
vol. 16, no. 6, pp. 477-485.

Okamoto, S., Seo, S., Nakaso & K., Kawai, I., (1993), Turbulent shear flow and heat transfer over repetead two-dimensional square ribs on ground plane, ASME J. of Fluids Engineering,
vol. 115, pp. 631-638.

Ötüngen, M. V., 1991, Expansion ratio effects on the separated shear layer and reattachment downstream of a backward-facing step, Experiments in Fluids,
no. 10, pp. 273-280.

Ruderich, R. & Fernholz, H. H., 1986, An experimental investigation of a turbulent shear flow with separation, reverse flow, and reattachment, J. of Fluid Mechanics,
vol. 163, pp. 283-322.

Simpson, R. L., 1989, Turbulent boundary-layer separation, Annual Review of Fluid Mechanics,
pp. 205-234.

Zhang, Y. M., Gu, W. Z. & Han, J. C., (1994), Heat Transfer and Friction Rectangular Channels with ribbed or ribbed-grooved walls, ASME J. of Heat Transfer,
vol. 116, pp. 58-65.

LDA- AND PIV-MEASUREMENTS ON THERMAL CONVECTION IN SPHERICAL SHELLS

C. Böhm, C. Egbers, H.J. Rath

ZARM, Center of Applied Space Technology and Microgravity,
University of Bremen, Germany

ABSTRACT

Investigations on thermal convection in spherical gaps are of importance in various technical applications such as thermal storage systems; in the case of solid body rotation it represents a model of large-scale geophysical flows. We report on a study of LDA- and PIV-measurements on the flow in a gap between two concentric spheres by heating the inner one. The dynamics and the flow structures occurring by increasing the Rayleigh number $Ra = g\alpha d^3 \Delta T / \nu\kappa$ depend strongly on the aspect ratio $\beta = (R_2 - R_1)/R_1 = d/R_1$. The first instability in narrow gaps leads to stationary rolls whereas in wider gaps the basic flow turns into a time dependent state with pulsating vortices in the pole region. In dependence on these two parameters we investigated the velocity and vorticity field in a meridional plane for the first time with PIV and analyzed the time series of the velocity components by LDA. The PIV data are in a very good agreement with numerical results. The linear analysis of the LDA data describes the dynamics of the flow. The transition from the basic flow to the pulsating vortex flow in the wide gap ($\beta = 0.5$) was characterized in the form of a bifurcation diagram.

1. INTRODUCTION

Recent experimental and numerical work on thermal convection in spherical gaps can be classified in investigation on flow with or without rapid rotation of the spheres. The geophysical convection problem in the presence of Coriolis forces was investigated theoretically and numerically by Glatzmaier & Roberts (1995), Busse (1994), Zhang (1991), Cardin & Olson (1994) and Kida (1997). Glatzmaier & Roberts as well as Kida also considered the influence of a magnetic field on the convection in spherical shells. Experimental work was done by Cardin & Olson (1994) and by Cordero & Busse (1992). Cardin & Olson visualized the flow pattern for increasing Rayleigh number in a geometry of the Earth's core ($\beta = 2$) by cooling the inner sphere and rapid solid body rotation to generate a central force field and compared them with their own numerical results. They found a small transition regime with cellular structures between the basic state and the chaotic regime.

In the technical relevant case without rotation of the spheres most of the investigations were restricted to the flow in narrow gaps. Liu et al. (1997) considered the convective flow field under an axial and central force field in narrow spherical gaps numerically. Under an axial force field they found flow patterns with a large number of banana type cells, oriented in north-south direction and aligned in the azimuthal direction, when the flow becomes unstable at a critical Rayleigh number of 2000 for $\beta = 0.08$. As the Rayleigh number is increased, the flow becomes less ordered. Laboratory experiments by Egbers et al. (1995) confirm these results. Further experimental data for convection in narrow spherical gaps have been provided by Bishop et al (1966), Scanlan et al. (1970), Yin et al. (1973) and Nagagawa et al. (1992) for a very wide range of Rayleigh and Prandtl numbers. Mack & Hardee (1968) presented results obtained by a perturbation solution of the axisymmetric steady state for small Rayleigh numbers. Garg (1992) first investigated the flow pattern in a wide gap with $\beta = 1$ numerically with a finite difference method. For high Rayleigh numbers he found a break-up in multi-cellular flow.

In this paper we report on recent experiments on thermal convection without rotation especially in

wide gaps. First we characterize the dynamic behaviour and the bifurcation diagram obtained by measuring one velocity component as a time series with Laser Doppler Anemometry (LDA). Furthermore we got the velocity field in a meridional plane by Particle Image Velocimetry (PIV) and could calculate the vorticity distribution from these data. Measurements are carried out for $\beta = 0.33$ and 0.5 in a wide range of Rayleigh numbers. The results can be compared with numerical predictions.

2. EXPERIMENTAL PROCEDURE

The experimental apparatus (Figure 1) consists of two concentric spheres. The outer sphere is made of transparent acrylic plastic and has a diameter of 80mm. Due to five exchangeable inner spheres, which differ in their diameter, we can vary the aspect ratio between $\beta = 0.08$ and $\beta = 0.5$. The gap is filled with silicon oil M3 suspended with hollow glass spheres (10μm in diameter).

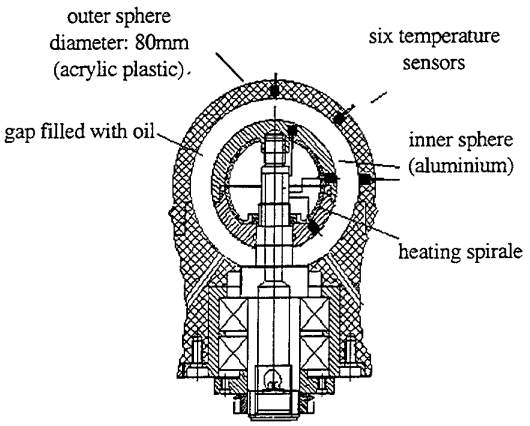


Fig. 1 Schematic view of the spherical setup

LDA-measurements are carried out with a 10 mW one component laser optic in a back scattering set-up (DANTEC BSA). The LDA optic probe is mounted on a special traversing system, so that we can measure the time series of the meridional or azimuthal velocity component at different radial and angular positions and make a linear analysis of them to obtain the frequency spectrum and the autocorrelation function. Measurements were made for increasing Rayleigh number. By determination of the dominating frequencies for each we can characterize the flow in a bifurcation diagram, which shows the dependence of the frequencies and their amplitudes on the Rayleigh number. For PIV-measurements the outer sphere was included in a rectangular cavity filled with silicon oil to reduce optical refraction. We used the PIV-system and software of the DLR Göttingen (Willert et al. 1991). With an 1W Argon-Ion-Laser we produced a meridional light sheet through the sphere's center and evaluated the video frames taken by a 25Hz CCD-camera by cross correlation:

$$\Phi_{fg}(m,n) = \sum_{k=0}^{M} \sum_{l=0}^{N} f(k+m, l+n) g(k,l)$$

As a result we obtain the displacement field averaged over 40ms every 80ms. After conversion of the displacement vectors in a velocity field, the z-component of vorticity ω_z and divergence η were computed:

$$\omega_z = \frac{\partial v}{\partial x} - \frac{\partial u}{\partial y} \text{ and } \eta = \frac{\partial u}{\partial x} + \frac{\partial v}{\partial y}$$

Experiments were carried out for $\beta = 0.08,\ 0.33,\ 0.5$ and $10^3 \le Ra \le 1.2 \cdot 10^6$ by increasing the Rayleigh number slowly.

3. RESULTS

Figure 2 shows the stability diagram and the according flow structures we obtained by flow visualization. In narrow gaps stationary rolls aligned in the azimuthal direction occur after exceeding the critical Rayleigh number. The number of these cells depends on the aspect ratio and the Rayleigh number. These flow structures were investigated numerically by Liu et al. (1997) and are in good agreement with the experimental results. Whereas in the wider gaps ($\beta \ge 0.33$) the basic flow turns into a time dependent state directly at the critical Rayleigh number with a pulsating vortex in the pole region. Numerical investigation of this transition only exists for $\beta = 1$ from Garg (1992).

In order to quantify the results from flow visualization and to compare streamlines, velocity and vorticity with the existing numerical results, we measured the velocity and vorticity field in a meridional plane through the sphere's center for the wide gaps with PIV and LDA. The averaged velocity data from PIV and LDA were compared.

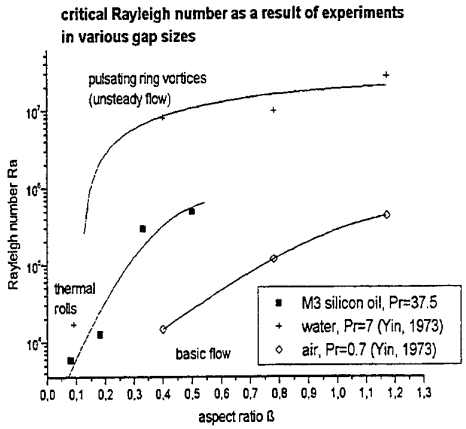




Fig. 2 Stability diagram of thermal convection in spherical shells and photographs of the different flow structures : *top:* stationary rolls (side view) at $\beta = 0.18, Ra = 15700$; *bottom:* pulsating vortex (top view) at $\beta = 0.5$, $Ra = 5 \cdot 10^5$

Figures 3-5 show the velocity field for $\beta = 0.5$ for the basic flow ($Ra = 10^5$, $\Delta T = 1° C$). obtained by PIV and LDA measurements. The streamlines which result from the velocity field shown in Figure 3 and the derived vorticity distributions (Figure 4) are in good qualitative agreement with numerical calculations by Garg (1992) for $\beta = 1$. As well the ratio of the upward flow at the inner and the downward flow at the outer sphere in the basic flow is nearly 2 as predicted theoretically (Mack & Hardee, 1968). As seen in the radial profiles of the two measured velocity components (Figure 5), the merdional velocity for $\theta = 30°, 40°$ is 0.12 cm/s upward near the inner sphere at $r = 2.8$ cm and 0.6 cm/s downward near the outer one at $r = 3.9$ cm. In the middle of the gap there is only a small area ($3.25 \le r \le 3.35$) with zero velocity. For $\theta = 80°$ there is a wide area with upstream flow. From the profile of the radial velocity component we can localize the vortex core at about 45°. Figure 4 presents the averaged meridional velocity component measured by LDA. The quantitative agreement is good especially for the pole region (0.03 cm/s upward and 0.012 cm/s downward velocity).

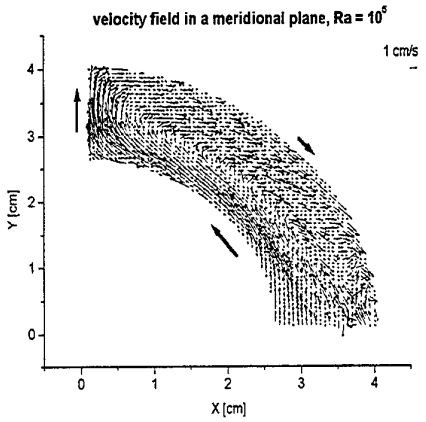


Fig. 3 Velocity vector field in a meridional plane for $\beta = 0.5, Ra = 10^5$ as a result of the PIV-measurements

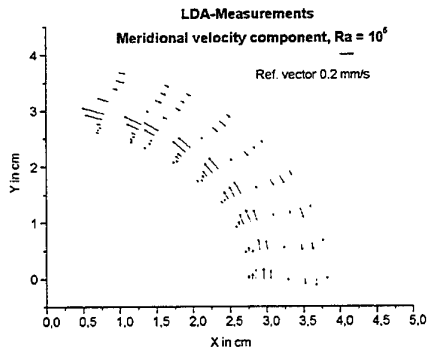


Fig. 4 Time averaged meridional velocity component in a meridional plane as a result of LDA-measurements for $\beta = 0.5, Ra = 10^5$

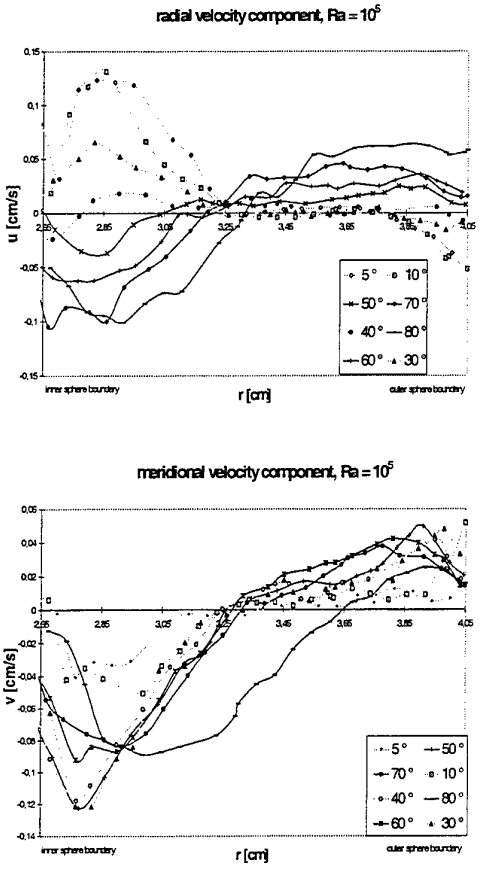


Fig. 5 Radial profile of radial (top) and meridional (bottom) velocity component for different angular positions for $\beta = 0.5, Ra = 10^5$

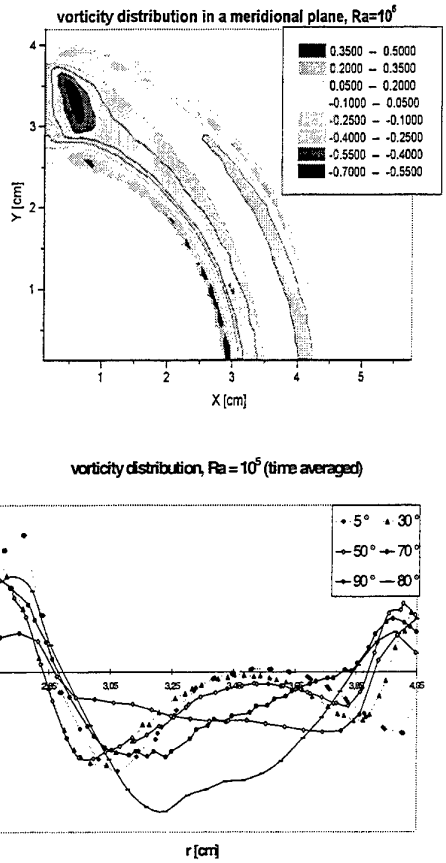


Fig. 6 Vorticity distribution determined out of the PIV measurements for $\beta = 0.5, Ra = 10^5$, shown in a contour plot in the meridional plane (top) and in a radial profile for different angular position (bottom)

In Figure 6 the time averaged vorticity (ω_z) distribution in the basic flow is represented in a contour plot (upper picture) and in a radial profile for different angular positions. We found homogeneous distributed vorticity in the pole region ($|\omega_{z,\max}| = 0.5$) and one extremum ($|\omega_{z,extr}| = 0.3$) at the outer sphere otherwise.

By increasing the Rayleigh number the pulsating vortex flow occurs at the north pole and for $Ra > 10^6$ there are additional falling vortices at higher latitude near the outer sphere as seen very well in the vorticity field as a second extremum at the outer sphere (Figure 10).

Figures 7-9 present the velocity field for the time dependent state at $\beta = 0.5$, $Ra = 1.2 \cdot 10^6$ ($\Delta T = 8{,}5°C$), this is the maximal Rayleigh number we can reach in the experiments. Like in the numerical results from Garg (1992) for $\beta = 1$, the streamlines derived from the velocity field in a meridional plane exhibit a vortex near the north pole. Figure 7 shows such a field for a given time t, the vortex is pulsating with time and grows and fades away. The velocity increases up to 0.25 cm/s radial outward flow at the pole, 0.3 cm/s upward flow at the inner sphere and 0.15 cm/s downward flow at the outer sphere. Figure 8 presents the accordant time averaged meridional velocity component measured by

LDA for different radial and angular positions. We can not see the vortex from these data but we can compare them with time averaged data from the PIV measurements for validation. The discrepancy is less than 10%. From the radial profile of the two velocity components we can detect a smaller range of upward flow near the inner sphere (with an extremum at $r = 2.7$ cm) and a wider stagnation area with zero velocity in the middle of the gap ($3 \le r \le 3.8$) as in the case of basic flow. Due to the pole vortex we found in the pole region ($\theta = 5°, 10°$) a distinctive extremum further away from the inner sphere boundary at $r = 2.85$ cm. The falling vortices near the outer sphere cause a second smaller extremum of upward flow for $10° \le \theta \le 30°$.

The contour plot and radial profile of vorticity distribution for these parameters as shown in Figure 10 confirm the appearance of the pole vortex and the falling vortices. We found higher vorticity at the north pole ($|\omega_{z,\max}| = 2$) and additional to the extremum at the inner sphere a second smaller one at the outer sphere ($|\omega_{z,extr,i}| = 2$; $|\omega_{z,\text{extr,o}}| = 1.2$). The area with zero vorticity in the middle of the gap became bigger, too.

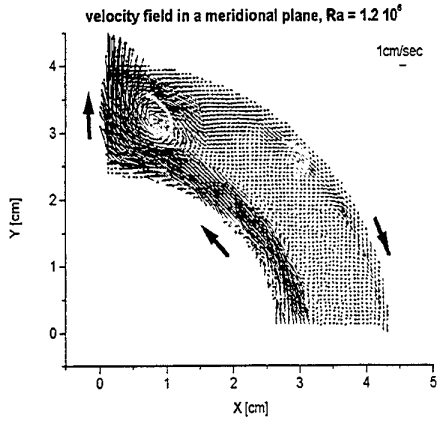


Fig. 7 Velocity vector field in a meridional plane as a result of the PIV-measurements for $\beta = 0.5, Ra = 1.2 \cdot 10^6$ (time dependent)

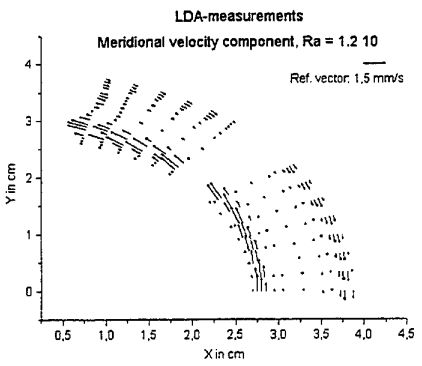


Fig. 8 Time averaged meridional velocity component in a meridional plane as a result of LDA-measurements for $\beta = 0.5, Ra = 1.2 \cdot 10^6$

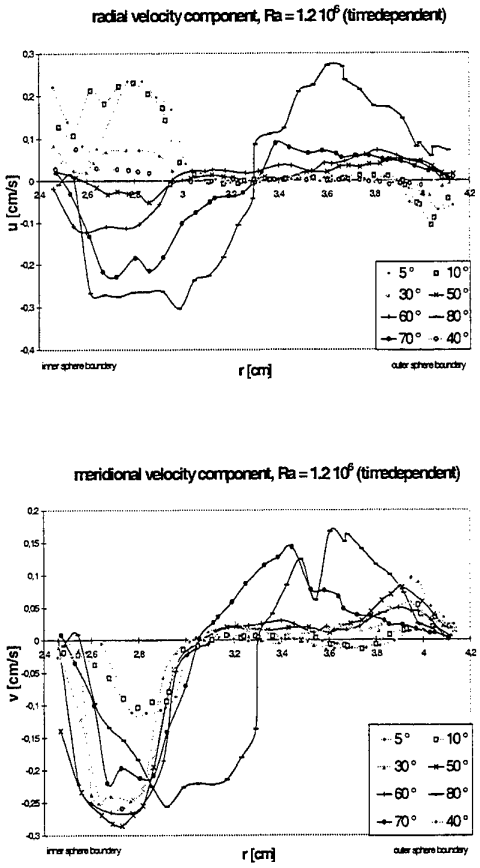


Fig. 9 Radial profile of meridional (top) and radial (bottom) velocity component for $\beta = 0.5, Ra = 1.2 \cdot 10^6$

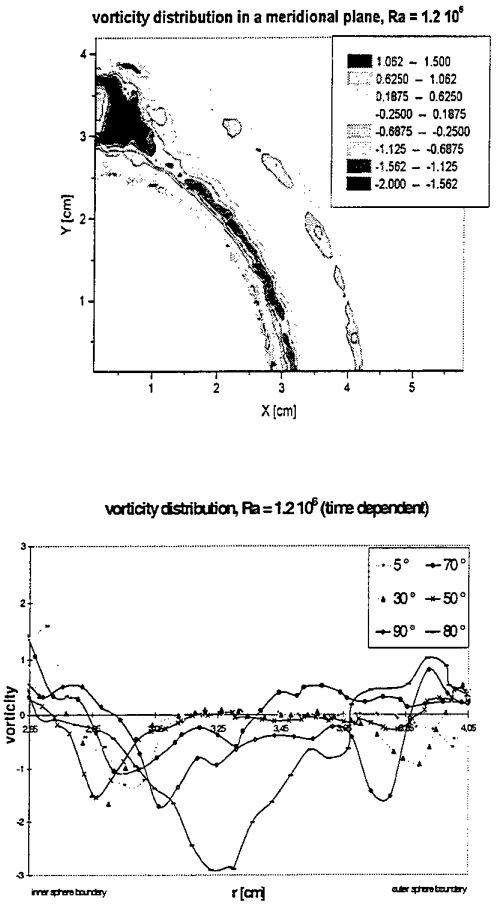


Fig. 10 Vorticity distribution determined from the PIV measurements for $\beta = 0.5, Ra = 1.2 \cdot 10^6$, shown in a contour plot in the meridional plane (top) and in a radial profile for different angular position (bottom)

Figure 11 shows the result we got by LDA measurement for $\beta = 0.5$. We measured the time series of the meridional velocity component for increasing Rayleigh number. Figure 11 represents the dominating frequencies in dependence on the Rayleigh number. For $Ra > 3 \cdot 10^5$ we got periodical motion with $f_{d,Ra=4\cdot10^5,pol} = 0.05Hz$, the frequency is increasing logarithmic with increasing Rayleigh number whereas the amplitude remains nearly constant. For $Ra > 7 \cdot 10^5$ periodical motion occurs for $20 \le \theta \le 60$ near the outer sphere ($r = 3.85$ cm) with $f_{d,Ra=4\cdot10^5,os} = 0.15Hz$.

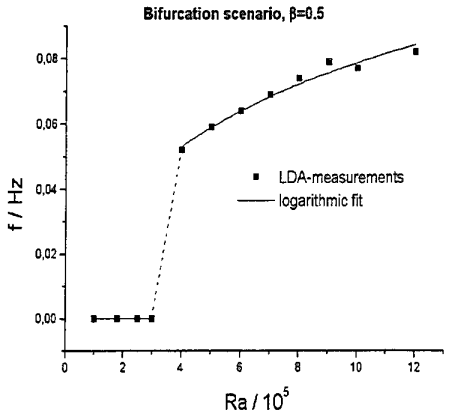


Fig. 11 Bifurcation diagram for $\beta = 0.5$, the dominating frequencies are plotted vs. the Rayleigh number

For the medium gap with $\beta = 0.33$ we made adequate measurements with PIV and LDA, but in both cases we didn't find periodic motion. But the velocity values are in good agreement.

One further aim is to compare the quantitative experimental results with own numerical solution for the same aspect ratio.

ACKNOWLEDGEMENTS

The financial support from the Deutsche Forschungsgemeinschaft (DFG) is gratefully acknowledged. The PIV measurements were carried out at the DLR Göttingen. Thanks are due to Dr. J. Kompenhans, Dr. M. Raffel and Hughes Richard.

REFERENCES

Bishop, E.H., Mack, L.R., Scanlan, J.A. 1966, Heat Transfer by natural convection between concentric spheres, Int. J. Heat Mass Transfer, vol. 9, pp. 649-662.

Busse, F.H. 1994, Convection driven zonal flows and vortices in the major planets, CHAOS, vol. 4, no. 2, pp. 123-134.

Cardin, P. & Olson, P. 1994, Chaotic thermal convection in a rapidly rotating spherical shell: consequences for flow in the outer core, Physics of the Earth and Planetary Interiors, vol. 82, pp. 235-259.

Carrigan, C. R. & Busse, F.H. 1983, An experimental and theoretical investigation of the onset of convection in rotating spherical shells, J. Fluid Mech., vol. 126, pp. 287-305.

Cordero, S. & Busse, F.H. 1992, Experiments on convection in rotating hemispherical shells: Transition to a quasiperiodic state, Geophysical Research Letters, vol. 19, no.8, pp. 733-736.

Glatzmaier, G.A. & Roberts, P.H. 1995, A three-dimensional convective dynamo solution with rotating and finitely conducting inner core and mantle, Physics of the Earth and Planetary Interiors, vol. 91, pp. 63-75.

Egbers, C. & Rath, H. J 1995, Thermal convective instabilities in spherical Couette flow, Proc. of 9th Couette-Taylor Workshop, Boulder, Colorado, USA

Garg, V.K. 1992, Natural convection between concentric spheres, Int. J. Heat Mass Transfer, vol. 35, no.8, pp. 1935-1945.

Kida, S., Araki, K., Kitauchi, H. 1997, Periodic Reversals of Magnetic Field Generated by Thermal Convection in a Rotating Spherical Shell, Journal of the Physical Society of Japan, vol. 66, no. 7, pp. 2194-2201.

Liu, M., Egbers, C., Rath, H. J.; 1997, Three-dimensional natural convection in a narrow spherical shell. J. Fluid Mech., submitted.

Mack, L.R. & Hardee, H.C. 1968, Natural convection between concentric spheres at low Rayleigh numbers, Int. J. Heat Mass Transfer, vol. 11, pp. 387-396.

Nakagawa, T., Zierep, J., Bühler, K., Wimmer, M., Kirchartz, K.R. 1992, Thermal convection between two concentric spheres, Proc. 2nd JSME-KSME thermal engineering conference, pp. 13-18.

Scanlan, J.A., Bishop, E.H., Powe, R.E. 1970, Natural convection heat transfer between concentric spheres, Int. J. Heat Mass Transfer, vol. 13, pp. 1857-1872.

Willert, C. & Gharib, M. 1991, Digital Particle Image Velocimetry, Exps. Fluids, vol. 10, pp. 181-183.

Yin, S.H., Powe, R.E., Scanlan, J.A., Bishop, E.H. 1973, Natural convection flow patterns in spherical annuli, Int J. Heat Mass Transfer, vol 16, pp. 1785-1795.

Zhang, K. 1991, Convection in a rapidly rotating spherical shell at infinite Prandtl number: steady drifting rolls, Physics of the Earth and Planetary Interiors, vol. 68, pp. 156-169.

STUDY OF HAIRPIN VORTEX DYNAMICS AND TURBULENCE STATISTICS OF A SURFACE-MOUNTED MIXING TAB WAKE USING PIV

Wenming Yang, Jian Sheng and Hui Meng*
Department of Mechanical and Nuclear Engineering
Kansas State University, Manhattan, KS 66506, USA
*(785) 532-5619, meng@ksume.me.ksu.edu

ABSTRACT

In this work, we apply time-series PIV measurement in a surface-mounted mixing tab wake and obtain a total of over 1000 instantaneous velocity fields in several regions in a streamwise wall-normal plane and a streamwise spanwise plane. Time-series velocity/vorticity fields clearly show the generation and growth of hairpin vortices, which are shed from the tab tip and enhanced by near-wall flow. Secondary hairpin vortices are observed and their generation mechanism is attributed to a viscous-inviscid interaction process. Time-series PIV also reveals the pairing process of a secondary hairpin vortex head with its trailing hairpin vortex head. Furthermore, another type of offspring with opposite-sign vorticity is frequently observed underneath the normal hairpin vortices. The large number of PIV realizations are averaged to give turbulence statistics including mean velocity profiles, Reynolds stresses and turbulent kinetic energy dissipation rate. These statistical quantities clearly reveal imprints of the vortex structures.

1. INTRODUCTION

A surface-mounted trapezoidal tab is known to shed hairpin-like vortices and produce a pair of counter-rotating streamwise vortices (Fig. 1). It can be used to artificially create a turbulence-like flow to enhance mass and heat transfer or control boundary layer separation (Yang & Meng 1998, Gretta & Smith 1993). In particular, it is used for efficiency static mixers in process industries. However, the dynamics of the vortex-induced mixing and thus the rationale for the successful mixer design are not well understood. On the other hand, hairpin vortices are fundamental coherent structures in a turbulent boundary layer. They can be studied in controlled experiments so that the evolution, regeneration, and interaction of these vortex structures can be studies without influence of background turbulence. Thus, the study of the vortex structures in the wake of a mixing tab is of interest to both industrial applications and fundamental understanding of turbulence.

The major limitation of the past experimental investigations on the development of hairpin vortex structures lies in the dependency on flow visualization of a passive scalar, *e.g.* dye concentration (Haidari & Smith 1994, Acarlar & Smith 1987, Head & Bandyopadhyay 1981). It is well known that dye concentration cannot truly represent vortex dynamics, primarily due to lack of the vortex-stretching term in the scalar transport equation. Therefore, the dynamics of hairpin vortices cannot be adequately and accurately understood from flow visualization. Since vortex structures are inherently related to the coherent vorticity distribution, quantitative full-field measurements of the velocity and vorticity fields are necessary to explore the topology and dynamics of hairpin vortices. In this study, using the time-series particle image velocimetry (PIV) in the wake of a passive mixing tab, we investigate the dynamics and regeneration mechanism of the hairpin vortices. Furthermore, turbulent mixing by the tab is quantitatively assessed by evaluating turbulent characteristics such as Reynolds stress, dissipation rate and turbulent kinetic energy distributions on 2D planes obtained from a large quantity of PIV realizations (over 1000 snapshots). The assessment of relationship between turbulence statistics and dynamics of coherent structures is also attempted.

2. EXPERIMENT SETUP

2.1 Test Flow Setup

Measurements of a mixing tab wake are conducted in a closed plexiglas channel system at the Laser Flow Diagnostic Laboratory (LFD) at Kansas State University. The water channel system has a working section 123cm long (x), 7.62cm high (y) and 7.62cm wide (z). The channel has double inlets and outlets, 3.2 cm in diameter, all of which are located on the side walls (Fig. 2). A symmetric tapered mixing tab is mounted at the center on the surface of the channel bottom 61.5cm (about 20 inlet diameter) away from the inlets. The geometry of the tab is shown in Fig 3. This flow is an elementary model of the flow in a High Efficiency Vortab (HEV) mixer (Chemineer, Inc.), a novel low-pressure-drop static mixer with arrays of tabs on the inner wall of a pipe or a square channel.

In this paper, all distances are referenced to the tab tip location at the wall (O in Fig. 3) in terms of the non-dimensional tab height, h_{tab}, where h_{tab} = 1.3cm. Water flow is driven by the 2.7m water head of a 15-gallon reservoir. The free-stream flow velocity is 16cm/s, which gives a $Re = 1.21 \times 10^4$ based on channel height and $Re_{h_{tab}} = 2{,}080$ based on mixing tab height. Mean velocity profiles in the test section, without the presence of the mixing tab, are obtained by averaging 100 instantaneous PIV realizations. They display the

characteristics of a fully developed turbulent channel flow pattern. Free-stream turbulence intensity at the test section is less than 2%. Boundary layer thickness δ based on $U=0.99U_0$ (where U is mean velocity and U_0 is free-stream velocity) is approximately 0.7 h_{tab}.

2.2. PIV Experiment Setup

PIV measurements are performed using our in-house developed time-series cross-correlation digital PIV system. The channel flow is illuminated with a 0.5mm-thick light sheet in double pulses produced by a pair of digitally sequenced Nd:YAG lasers. Distilled water is used as the test fluid, which is fully seeded with 9μm hollow glass beads. Seeding density of the flow is about 30 particles/mm^3. A series of single-frame single-exposure image pairs formed by 90° side scattering of seeding particles are recorded by a digital CCD camera providing 1K × 1K resolution and 30 frames/s data transfer speed. The PIV system has the capability of acquiring double images at a 10 Hz repetition rate. PIV measurements are applied both in a streamwise wall-normal (x-y) plane (tab center plane) and in a streamwise spanwise (x-z) plane (1.46 h_{tab} away from the bottom wall). To resolve detailed flow structures in a large enough velocity vector fields, the viewing area of the CCD camera is set as 5cm × 5cm in the flow. A cross-correlation method is applied to extract 1024 velocity vectors from each PIV image pairs with maximum less than 5% "bad" vectors. The spatial resolution of the PIV measurements is about 3.1mm×3.1mm.

For the tab wake, PIV measurements are conducted in three partially overlapping near-tab regions starting from the tip of tab, shown as Regions I, II, and III in Fig. 3. Based on Yang and Meng's (1998) studies of this flow, the hairpin vortex shed from the mixing tab are most active in these regions, where the regeneration and interaction of hairpin vortices mostly happen. Therefore, in this study, we focus our discussions on these three regions.

3. RESULTS AND DISCUSSION

3.1 Observations of Hairpin Vortex Dynamics

EVOLUTION OF HAIRPIN VORTICES. Figure 4 shows a typical time series of instantaneous velocity fields measured by PIV on the center streamwise wall-normal (x-y) plane in Region I, i.e. immediately downstream of the tab. The velocity fields are viewed with the advection velocity (62.5% U_0) of the vortices contained in this region and are superposed with the calculated vorticity (ω_z) fields. The four pictures (a-d) are in Eulerian view (fixed window) and separated in time by 0.1 sec. In the first snapshot (a), after the flow passes the tab tip (at x = 0) boundary-layer separation is evident. A shear layer with negative vorticity ($\omega_z < 0$) grows spatially and rolls up into a clockwise-rotating vortex centered at $x \approx 3h_{tab}$. Such a vortex pattern has the signature of a hairpin vortex with the cross-section of its head (arch) showing roughly circular motion, a Q2 ejection of near-wall, low-speed fluid below and upstream of the head, forming a shear layer inclined by roughly 45°, and entrainment of free-stream, high-speed fluid. Upstream at $x \approx 1.5h_{tab}$ a new hairpin vortex (marked by a white arrow), now still relatively small and weak, is beginning to roll up. In the next snapshot (b), this vortex head is fully rolled up and evidently bigger, higher, and stronger. Noticeably, an additional packet of high-vorticity region is attached to the hairpin vortex head. In the subsequent pictures from (b) to (d), this additional mass of fluid merges with the vortex head, and the resulted elongated vortex cross-section turns clockwise while continuing to rise in height.

By inspecting many time-sequences of PIV data taken in different regions of the tab wake, it is found that the vortex enhancement process is most prominent between $2h_{tab}$~ $4h_{tab}$ downstream of the tab. When hairpin vortices advect further downstream, due to the induction of legs, the hairpin vortex heads are gradually lifted away from the wall and thus the pumping of the near-wall, low-speed fluid becomes weaker and weaker. Therefore, the enhancement process of the hairpin vortices gradually diminishes.

REGENERATION OF VORTICES. Figure 5 shows a time series of instantaneous PIV measurements (velocity fields superposed with vorticity fields) taken in Region II in the center streamwise wall-normal plane, with the velocity reference frame set roughly equal to the advection velocities of the vortices. The head of hairpin vortex A enters the viewing window in (a). Subsequently a new vortex R with opposite-sign vorticity ($\omega_z > 0$) is formed below A (b and c). Furthermore, a secondary hairpin vortex S is generated in the wake of A (c), interacts with the trailing vortex B (d and e), and finally merges with B (f). Both the reverse vortices and secondary hairpin vortices were observed by Yang and Meng (1998) in single PIV snapshots. The current study, for the first time, provides the temporal processes of the velocity and vorticity fields related to these vortices.

Yang and Meng speculated that secondary hairpin vortices in the wake of a surface-mounted mixing tab are generated by a viscous-inviscid interaction mechanism, in much the same way as the regeneration of hairpin vortices in a natural turbulent boundary layer (Smith et al. 1991). According to this mechanism, the ejection effects of both the legs and head of primary hairpin vortex A lead to a local breakdown of the near-wall viscous flow and lift up of the low-speed fluid away from the wall. This low-speed fluid interacts with the incoming high-speed fluid from the top to produce a shear layer, whose vorticity has the same sign as vortex A. This unstable shear layer subsequently rolls up into a secondary hairpin vortex S with $\omega_z < 0$. This explanation is consistent with the PIV measurement shown in Fig. 5, except that in this particular example the regeneration process is complicated by the simultaneous generation of the reverse vortex R.

From Fig. 6 (c) to (d), the secondary vortex S appears intensified. Again, there must be a stretching mechanism along z axis accordingly. Consistent with the 3D structure of hairpin vortex, the two legs of vortex A (not seen in the x-y plane) must induce opposite fluid motion or stretching at the location of vortex head S. This stretching intensifies the vorticity magnitude of S. Meanwhile, the core size of S is increased from (c) to (d), which could be the consequence of continued rollup of the shear layer. In (d), the loci of parent hairpin vortex A, secondary hairpin B and trailing primary

hairpin vortex C form a typical triangle described by Yang and Meng (1998).

The reverse vortex is not known to exist in a natural turbulent boundary layer, but is not a rare phenomenon in the wake of the surface-mounted tab. According to Yang and Meng (1998), the generation of this opposite-sign vortex is a result of the interaction of the decelerated fluid directly below the parent hairpin head and the packet of fluid further underneath. This interaction produces a reversed shear layer that rolls up into the opposite-sign vortex. The vortex head must be sufficiently strong and far enough away from the wall for this process to happen. In the example shown in Fig. 5, reverse vortex R appears to be already formed before the parent vortex A enters the scene. Vortex R also appears to have been decelerated by A before the moment (a). However, continued deceleration by its parent seems to be prohibited as soon as the vortex S is born just upstream, whose Q4 sweeping action acts to counter the deceleration of R. In moment (d), the reverse vortex R (positive vorticity) is seen to be dissipating, but a new vortex with clockwise rotation (negative vorticity) is born immediately downstream. Tracing back to (c), we notice that this new-born vortex originates from a shear layer with $\omega_z < 0$, which is evidently generated by the Q1 induction of vortex R and unstable.

After secondary hairpin vortex S is formed, it advects at a lower speed than both its preceding (A) and its trailing (B) hairpin vortices, apparently due to the deceleration by these two primary vortex heads, which are located higher than S. It is finally caught up by the trailing vortex B, and these two co-rotating vortices quickly approach each other (e) and merge through pairing/viscous diffusion (f). In Fig. 5(f), another hairpin vortex head C, trailing B, comes into view.

OBSERVATIONS IN STREAMWISE SPANWISE PLANE. Figure. 6(a) shows a typical time-sequenced instantaneous velocity fields measured on the x-z plane (1.46 h_{tab} from bottom) in Region II, viewed with 66% U_0 and superposed with their vorticity fields. The two pairs of counter-clockwise rotating vortices, A and B, are identified as the cross-sections of the legs (L-left, R-right) of two successive hairpin vortices. The hairpin vortices are asymmetric about the center plane. Vortex A is displaced to -z so much that the right leg is crossing the centerline of the tab, which represents a rare case.

Notice in Fig. 6(b) that the strip of low-speed fluid between the two legs of vortex B extends into the wake or upstream region of the hairpin vortex. Where it interfaces with the high-speed flow on both sides, new shear layers are generated with vorticity signs corresponding to those of B-L and B-R. In the next two instants (c) and (d), these two shear layers develop into a pair of counter-rotating vortices, S-L and S-R. Consistent with the 3D hairpin vortex structure, we think S-L and S-R are the left and right legs of a new-born secondary hairpin vortex, S. This dynamic process shows that the legs of a secondary hairpin vortex is also generated through viscous-inviscid interaction process, that is, the interaction between the ejected low-speed near-wall fluid (the long low-speed strip between B-L and B-R) and the free-stream high-speed flow. This is consistent with our explanation of the generation of a secondary hairpin vortex head in the x-y plane.

3.2 Observation of Turbulence Statistics

It is well known that coherent structures are responsible for mass and momentum transport and turbulent macro-mixing. So is the case for the tab wake, where large-scale structures such as hairpin vortices and a pair of pressure-driven counter-rotating vortices account for the mechanism of passive mixing. A first look at the turbulence statistics (such as mean velocity profiles, Reynolds shear stresses, turbulent kinetic energy and its dissipation rate) can reveal the characteristics of this flow from a Reynolds-average point of view. These conventional statistical quantities render themselves more familiar to the process designer in assessing the transport effects. Furthermore, correlation of the dynamical events of the coherent structures with the turbulence statistics can unveil the effects of vortex dynamics on the time-averaged flow characteristics, point to valuable causality relations in the flow, and provide guidance for design improvement. From a large number of PIV measurement realizations (135 in Region I of x-y plane, 189 in Region II of x-y plane, 216 in Region II of x-z plane, and 243 in Region III of x-y plane) in short time sequences that are independent from each other, we obtain ensemble-average statistics, which roughly approximates turbulence statistics.

Mean Velocity Profiles. Mean velocity profiles of streamwise component were obtained by averaging instantaneous velocity fields. Figure 7 shows mean velocity profiles of two measurement regions in streamwise wall-normal (x-y) plane and two regions in streamwise spanwise plane (x-z). Profiles were fitted by high-order polynomial curve. Inflection points ($d^2U/d^2y = 0$ or $d^2U/d^2z = 0$) and indent points ($dU/dy = 0$ or $dU/dz = 0$) were calculated from the fitted curves. From Fig. 7(a,b), each U(y) profile in Region I and Region II exhibits two different infection points. The locations of these inflection points roughly match the locations of the passing hairpin vortex heads (upper inflection) and the reverse vortex heads (lower inflection). Two lines from linear regression were fitted to the traces of the inflection points. From $x \approx h_{tab}$ on, two indent points, one below each inflection point, are also seen to develop on these profiles. The indents reach their maximum degrees at downstream location $x \approx 4h_{tab}$, after which the profiles start to flatten out and gradually recover to the normal channel flow profile.

	Region I	Region II
Upper Inflection	10.6°	6.9°
Upper Indent	8.2°	5.3°
Lower Inflection	6.9°	3°
Lower Indent	1.2°	1.8°

Table 1. Inclination angles of the inflection and indent points on mean profile U(y) with respect to the wall

It is obvious that with the increasing downstream distance, the inflection points and indent points move away from the wall. The inclination angles of the inflection and indent points are given in Table 1. By observing the temporal instantaneous PIV velocity fields in the x-y plane and distribution of instantaneous loci of the vortices, it is suggested that the inflectional mean velocity profiles shown in Fig. 7(a,b) actually represent the imprints of the heads of hairpin vortices

(upper inflections in profile) and the imprints of the secondary, reverse vortices (lower inflections). The rising inflection points indicate the time-average effect of the rising hairpin vortices as well as of the reverse vortices, whose heights from the wall increase with downstream distance. The different inclination angles in Region I and Region II reflect different vortex dynamics in the two regions. The larger lifting angle of the indent and inflection points caused by the ordinary hairpin heads in Region I in the x-y plane can be explained by the existence of a pair of common-up, counter-rotating streamwise vortices, which help to elevate the tab-shed hairpin vortex heads before ~$2h_{tab}$ but quickly dissipate afterwards. These profiles also seem to suggest that hairpin vortex heads (clockwise rotation) and reverse vortex heads (counter-clockwise rotation) are located in different regions along the wall-normal direction. This is confirmed by the segregation of the loci of the respective vortices found from instantaneous PIV measurements. The flattening of the profiles at large downstream locations suggests weaker presence of the vortices there.

Figures 7(c,d) shows the U(z) profiles in measurement regions II and III at downstream locations from 3 to 9.8 h_{tab} in the streamwise spanwise (horizontal) plane that is 1.46 h_{tab} from the bottom wall. Although above the tab, the mean flow shows a distinct "wake" or low-speed indent region near z =0, centerline of the tab. On both sides of a profile there are two inflection points, whose distances from the centerline increases with x in Region II. Two straight lines from linear regressions are fitted to the inflection points in Region II. In Region III, some intermittent fluctuations of the traces can be noticed. Relating to the instantaneous velocity fields, it is not difficult to infer that the inflection points are imprints of the two hairpin vortex legs, and the centerline fluid deceleration is caused by the common backward induction of the legs, a manifestation of the low-speed strip. At x =3.2 h_{tab} the curvature of U(z) profile reaches its peak value (most severe deceleration). The indents in velocity profiles gradually flatten out, approaching the free-stream velocity.

Distribution of Reynolds Stresses. Reynolds shear stresses, $\langle u'v' \rangle$ and $\langle u'w' \rangle$ were measured in the aforementioned regions and are plotted as 2D contour lines in Fig. 8. The Reynolds stress $\langle u'v' \rangle$ shown in Fig. 8(a, b) as distribution in the x-y plane. Comparing with inflection point in Fig. 7(a, b), we find a correspondence between the core of the negative Reynolds stress region, defined with the maximum value of -0.1 normalized with free-stream velocity, and the upper inflection point line, which is considered the statistical path of hairpin vortex heads. The negative Reynolds stress indicates strong Q2 and Q4 momentum transport between free-stream and near-wall fluids. It is noticeable that a large negative stress region starts from $0.8h_{tab}$ downstream. It is restricted within a layer of width $0.5h_{tab}$ initially, but then after reaching $x \approx 3.0h_{tab}$ it suddenly expands to the wall. Moreover, a region with concentrated positive Reynolds stress (0.05 maximum value) is observed below the negative stress region from x = 0~$2.5h_{tab}$. The singular distribution of positive Reynolds stress is found related to the Q1 activities of a pair of short-live, counter-rotating streamwise vortices. Figure 9(c,d) shows the distribution of Reynolds stress at Region II and III in the streamwise spanwise (x-z) plane. The cores of the regions with strong negative and positive Reynolds stresses, again, match with their corresponding inflection lines in Fig. 7(c,d) very well. This indicates that the formation of these two strong Reynolds stress regions is caused by hairpin legs.

Distribution of Turbulence Dissipation Rate. The dissipation rate ε of turbulent kinetic energy is an important indication of turbulent micro-mixing and thus important for the process designer. A partial representation of ε is computed from spatial derivative from the large number of instantaneous PIV realizations. Figure 9 shows its distribution in Region I (a) and II (b) on the x-z plane. A region with concentrated dissipation rate extends from the wall to 1.2 h_{tab} just after the tab and from the wall to $2.5h_{tab}$ at $x/h_{tab} \approx 6$. It is found that 85% of total turbulent kinetic energy is dissipated in this region. Further examination of the dissipation rate in the x-z plane (not shown here) reveals that after x/h_{tab}= 8.5, dissipation rate decreases to a small fraction of the total value. Therefore, it may suggest that high mixing efficiency is achieved within a certain region ($x/h_{tab}<8.5$, $y/h_{tab}<2.5$, and $z/h_{tab}<1.6$). Since this is where most of the hairpin vortices and counter-rotating vortices are active, we infer that these vortices are responsible for the turbulent mixing in this concentrated region. Since only hairpin vortices persist beyond x ~$2.5h_{tab}$, the tab-shed hairpin vortices are thus the major contributor for mixing enhancement. About 45% of turbulent kinetic energy are dissipated in the region where hairpin heads pass by.

4. REFERENCE

Acarlar, M. S. & Smith, C. R. 1987 A study of hairpin vortices in a laminar boundary layer. Part 1. Hairpin vortices generated by a hemisphere protuberance, J. Fluid Mech., 175, 1-41.

Gretta, W. J. & Smith, C. R. 1993 The flow structure and statistics of a passive mixing tab, J. Fluid Engg., 115, 255.

Haidari, A. H. & Smith, C. R. 1994 The generation and regeneration of single hairpin vortices, J. Fluid Mech., 277, 135-161.

Head, M. R. & Bandyopadhyay, P. 1981 New aspect of turbulent boundary-layer structure. J. Fluid Mech., 107, 297-337.

Meinhart, C. D. & Adrian, R. J. 1995, Measurement of the zero-pressure gradient turbulent boundary layer using particle image velocimetry, 33rd Aerospace Science meeting and exhibit, Reno, NV.

Smith, C. R., Walker, J. D. A., Haidari, A.H., & Sobrun, U. 1991 On the Dynamics of Near-Wall Turbulence, Phil. Trans. Roy. Soc. Lond. A., 336, pp.131-175.

Yang,W. & Meng, H. 1998, Regeneration of hairpin vortices in the wake of a surface-mounted mixing tab, J. Fluid Mech., (submitted)

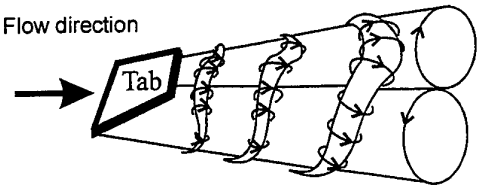


Fig. 1 Conceptual model of 3D flow structures in the wake of a tapered, symmetric mixing tab, with periodically shed hairpin vortices and a pair of counter-rotating vortices produced by pressure difference (proposed by Gretta and Smith 1993). The current study suggests that this model should be further refined.

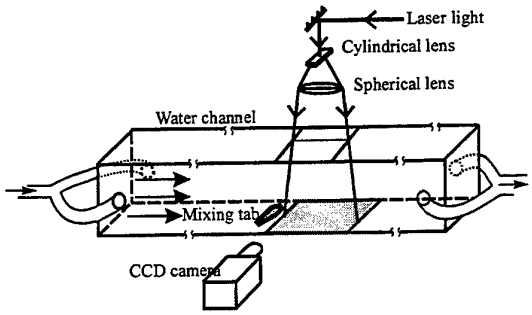
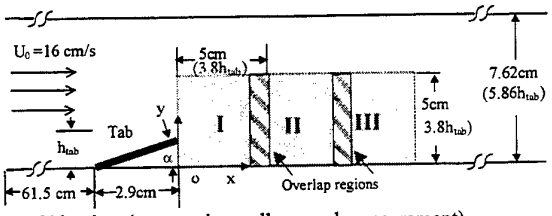
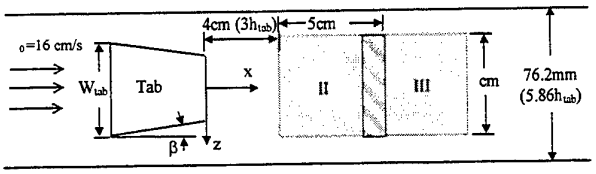


Fig. 2 PIV experiment setup, with the light sheet (0.5 mm thick) illuminating the center streamwise wall-normal plane. For streamwise spanwise measurements (not shown), the light sheet is horizontal and the camera is mounted vertically.



Side view (streamwise wall-normal measurement)



Top view (streamwsie spanwise measurement)

Fig. 3 Schematic of the mixing tab geometry, α=24.5°, β=12°, h_{tab}=1.3cm, W_{tab}=2.2cm. Each PIV image corresponds to the viewing area of the camera $3.8h_{tab} \times 3.8h_{tab}$=5cm× 5cm. The horizontal image plane is 1.9 cm (1.46 h_{tab}) from channel bottom.

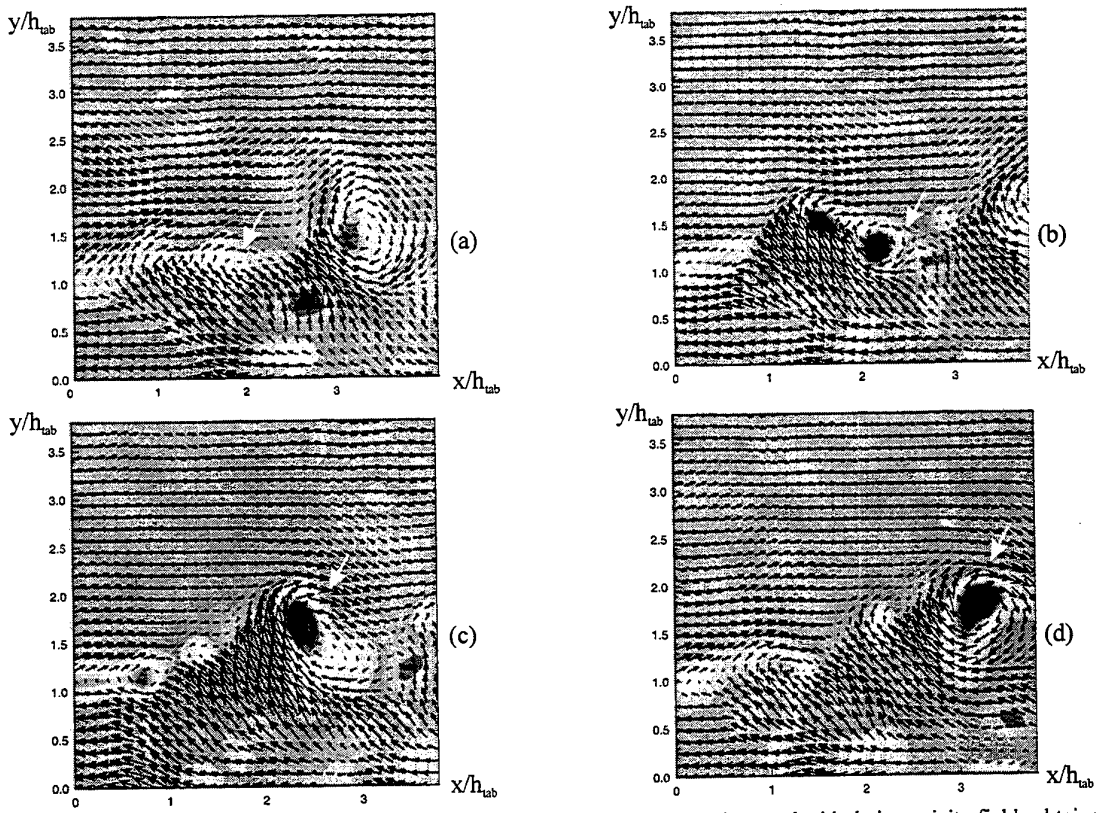


Fig. 4 A time series of instantaneous velocity fields (separated by 0.1s) superimposed with their vorticity fields obtained in Region I in the center x-y plane, showing evolution of the hairpin vortex head.

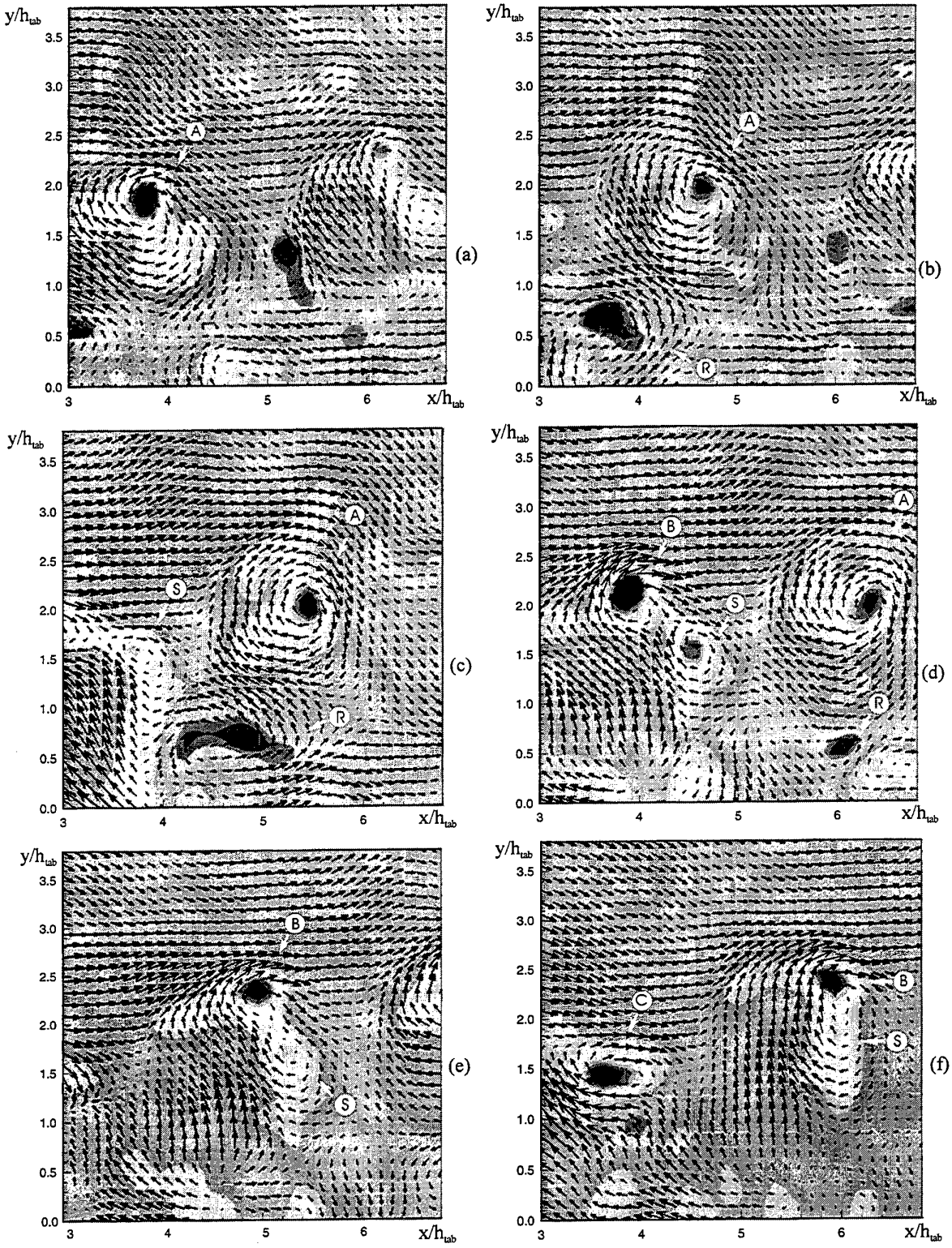


Fig. 5 A time series of instantaneous velocity fields (separated by 0.1s) superimposed with their vorticity fields obtained in Region II in the center x-y plane, demonstrating hairpin vortex regeneration and post-regeneration. A, B, C are periodically shed primary hairpin vortex heads. S is a secondary hairpin vortex head and R a reverse (opposite sign) vortex, both produced by vortex A.

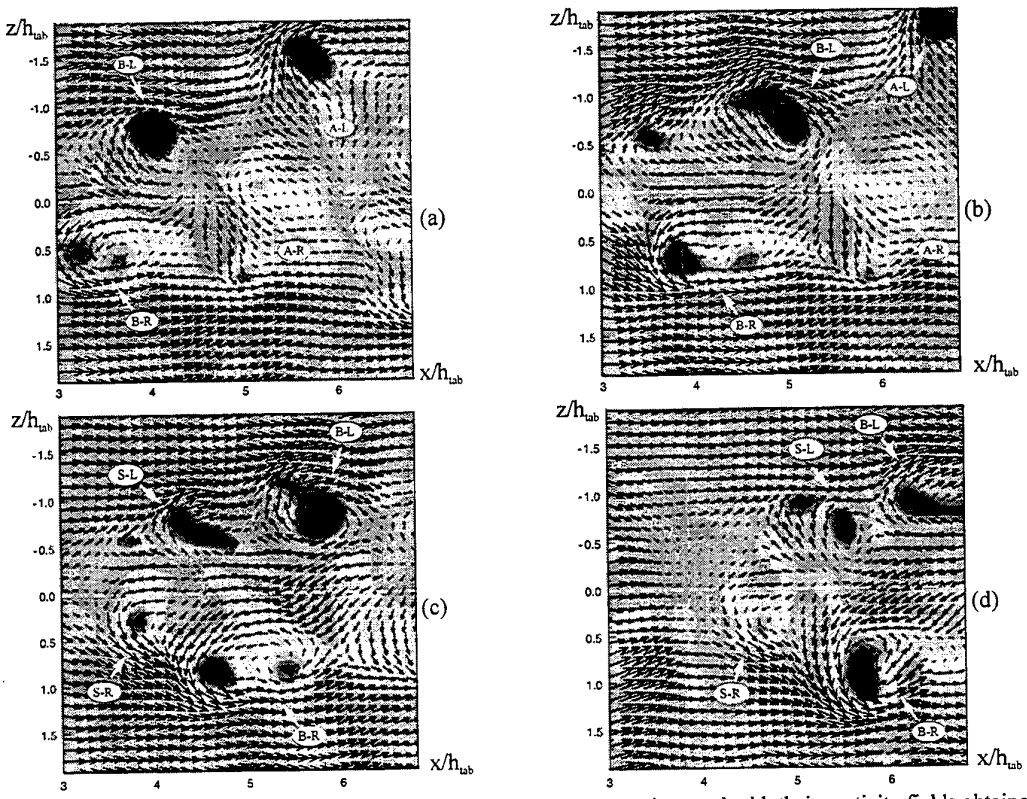


Fig. 6 A time series of instantaneous velocity fields (separated by 0.1s) superimposed with their vorticity fields obtained in Region II in x-z plane. A and B are two primary hairpin vortices and S a secondary hairpin vortex produced by B. L and R denote left and right leg, respectively.

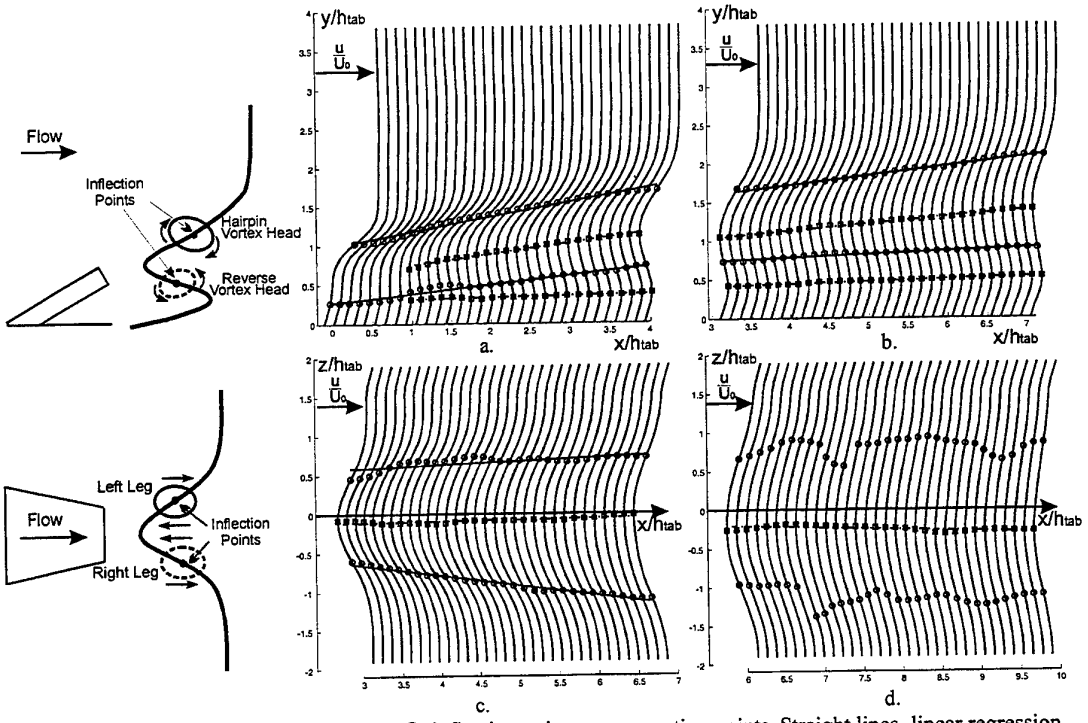


Fig. 7 Mean profiles of streamwise velocity. O-inflection points. -separation points. Straight lines–linear regression. (a) Region I of x-y plane. (b) Region II of x-y plane. (c) Region II of x-z plane. (d) Region III of x-z plane.

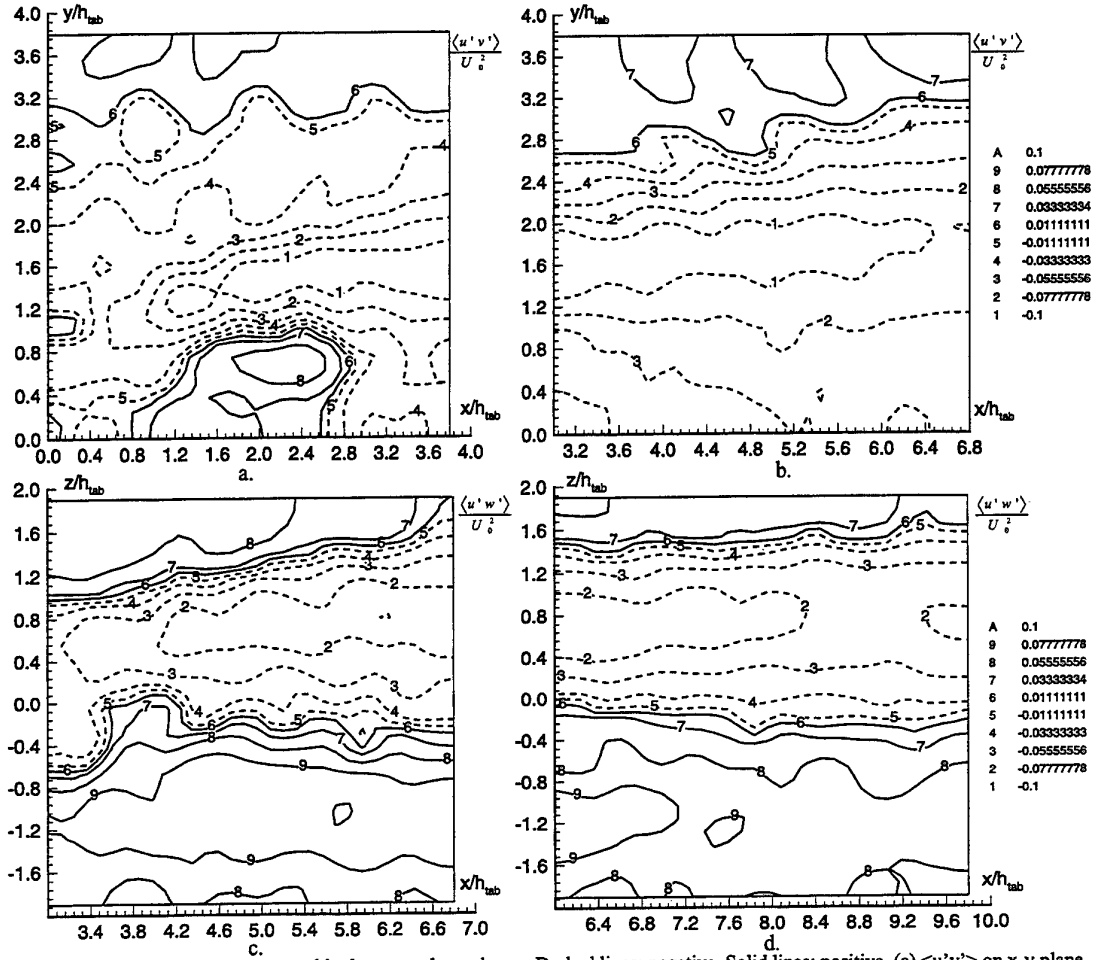


Fig. 8 Reynolds shear stresses measured in the x-y and x-z planes. Dashed lines: negative. Solid lines: positive. (a) <u'v'> on x-y plane in Region I. (b) <u'v'> on x-y plane in Region II. (c) <u'w'> on x-y plane in Region II. (d) <u'w'> on x-y plane in Region III.

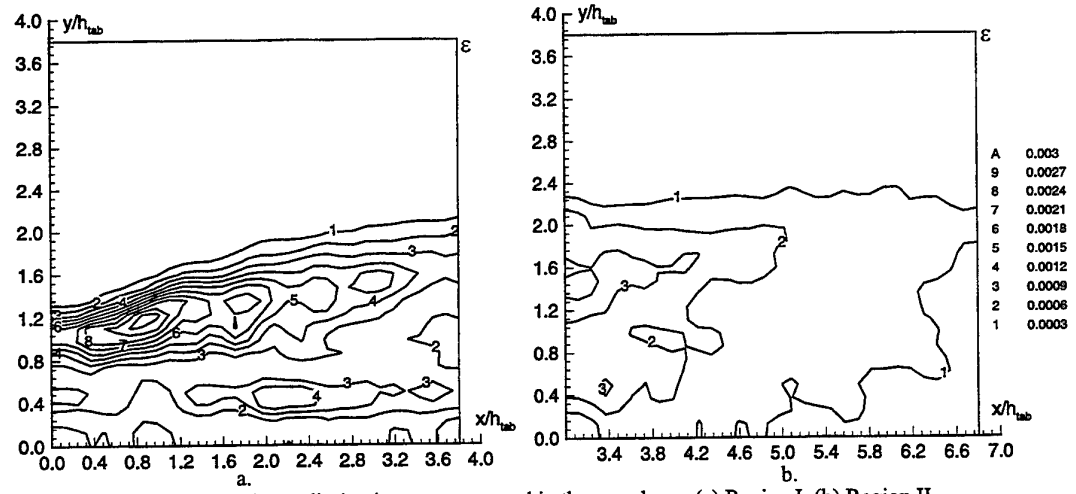


Fig. 9 Turbulence dissipation rate measured in the x-y plane. (a) Region I. (b) Region II.

A FENCE FLOW WITH CROSS-FLOW FORCING

H.A. Siller and H.H. Fernholz

Technische Universität Berlin
Hermann-Föttinger-Institut für Strömungsmechanik

ABSTRACT

The flow over a fence has a complex topology: the boundary layer separates upstream of the fence and at the tip of the fence, forming separation regions up- and downstream of the fence. The separation zones and the associated shear layers interact with each other and with the wall. Especially the large separation zone downstream of the fence sheds large vortices. If this flow is perturbed by an oscillating cross-flow with a suction and a blowing phase, the vortices in the downstream separation bubble grow very large in size. They enhance mixing processes that decrease the size of the separation bubble.

This paper describes velocity measurements taken with an LDA system in a perturbed fence flow. Two velocity components were measured along the centre axis of the test section and the data were phase averaged with respect to the excitation signal. The data reveal the dynamics of the flow: large vortices increase the mixing in the flow and reduce the length of the separation bubble.

1 INTRODUCTION

Previous investigations of fence flows (e.g. Castro & Fackrell (1978), Durst & Rastogi (1980), Dimaczek et al. (1989) and Martinuzzi & Tropea (1993)) have mainly been concerned with global features of the flow like the lengths of the separation regions and the influence of Reynolds number, blockage, aspect ratio of the fence and the ratio of boundary layer to fence height. The first field measurements in a fence flow were presented by Good & Joubert (1968).

Active control of separated flows has emerged recently. It has been applied to a number of flows: Sigurdson (1995) presents an overview of experiments with flow-control on separated turbulent flows together with his own results on the separation bubble at the leading edge of a blunt cylinder aligned with the flow. The control methods used in the literature are either acoustically generated disturbances (Sigurdson (1995) or Erk (1997)) or oscillating mechanical devices, as in the work of Miau, Chen & Chou (1995), who used an os-

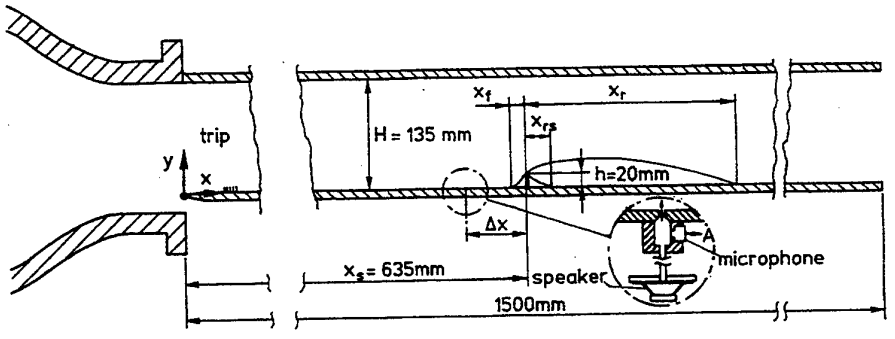


Figure 1: Experimental set-up

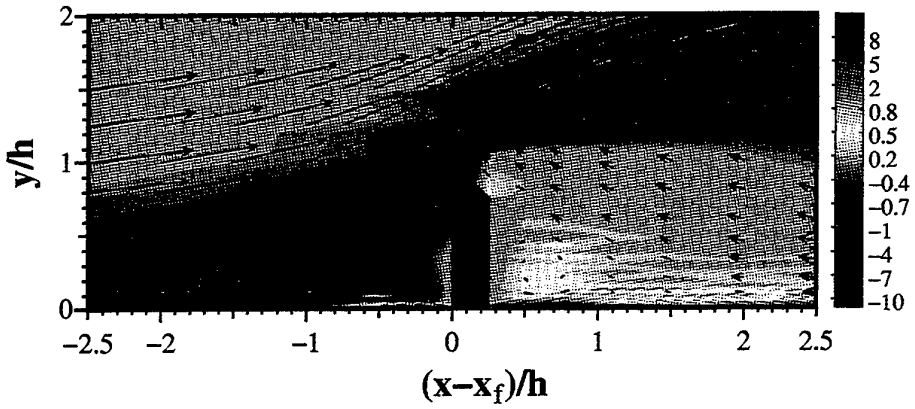


Figure 2: Velocity and vorticity field near the fence

cillating vertical plate. The physical mechanisms by which separated regions are reduced in size rely either on the excitation of shear layer instabilities (e.g. Huppertz & Janke (1996)) or the vortex shedding type instability described by Sigurdson (1995).

Siller & Fernholz (1996) present earlier experiments with the set-up described here. The paper gives further details on the wind-tunnel, wall shear-stress field up- and downstream of the fence and flow visualisations. Two manipulation devices were used: an oscillating spoiler and the periodic suction and blowing mechanism described here. The maximum reduction of the downstream separation bubble was achieved with periodic suction and blowing and amounted to 50%. The experiments described here were made with the parameter settings for this optimised case: Reynolds number $\mathrm{Re}_h = 10500$, distance slot–fence: $\Delta x/h = 1.75$, Strouhal number: $\mathrm{St}_h = (fh)/U_\infty = 0.05$ and amplitude: $v_{max}/U_\infty = 2.1$.

2 EXPERIMENTAL SET-UP AND MEASUREMENT TECHNIQUES

The experiment was set up in a blower-type wind tunnel with a rectangular test-section that is spanned by a fence about half-way down its length (see figure 1). A turbulent boundary layer develops along the floor of the test section, such that the boundary layer thickness at the fence position, measured with the fence removed, reaches 80% of the fence height.

Upstream of the fence, a periodic cross flow in the y-direction is introduced through a slot in the floor, oriented parallel to the fence. A loudspeaker system connected to the pressure chamber under the slot produces a periodic flow with a suction and a blowing phase, i.e. an oscillating jet with zero net mass flow. A large, oscillating vortex is produced upstream of the fence that leads

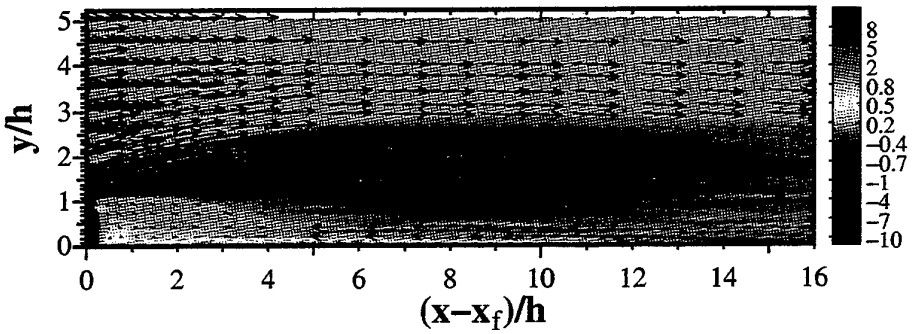


Figure 3: Velocity and vorticity field downstream of the fence

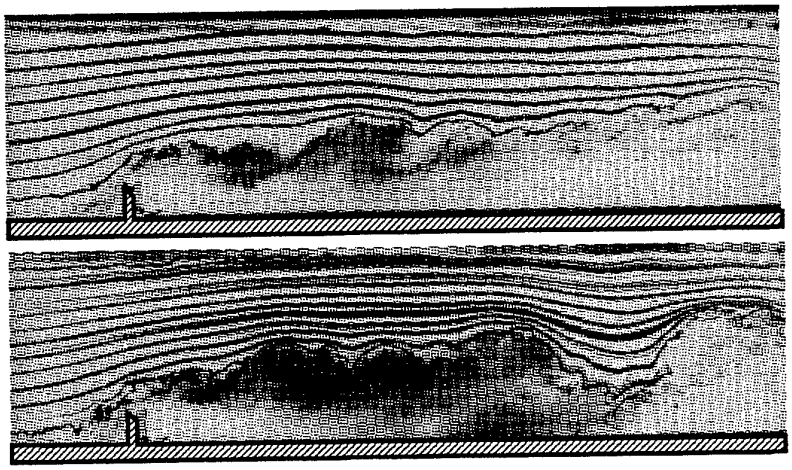


Figure 4: Smoke-wire flow visualisations of the fence flow

to the formation of large vortices in the downstream recirculation zone. Mixing processes are enhanced and the time mean reattachment length downstream of the fence is reduced.

Laser-Doppler measurements of boundary-layer profiles and two-dimensional fields were performed using a Dantec BSA system. The u and v velocity components were measured in backscatter mode. The system consisted of two standard Dantec BSA modules (type 57N10 master and 57N25 slave), a 2D-Fiberflow probe with a focal length of 600 mm, a Dantec transmitter box with four fibre manipulators and a 300 mW argon-ion laser. The BSA units were operated in continuous mode and coincidence checking was performed in private/private mode.

The measuring volume was an ellipsoid of revolution with a length of 1.4 mm and a diameter of 88 μ. The probe was inclined by an angle of approximately 6° towards the horizontal plane in order to be able to measure close to the wall. For measurements near the fence (in the range of ± 0.75 fence heights), the probe was also tilted by $\pm 4.5°$ with respect to the vertical axis.

The data acquisition and the two-dimensional traversing system were controlled by a 486 personal computer, using the Burstware 3.11 software from Dantec.

The flow was seeded using a Pallas AGF 10 cyclone seeder. It created a fine mist of DEHS particles with particle sizes under 1μ that was introduced at the inlet of the wind-tunnel. The surface of the plate was covered with black PVC foil, because prior test had shown that this coating had good properties regarding the reflection of laser light when the measuring volume was close to the wall.

The wall distance was estimated by monitoring the rms-output of the photo-multipliers with a digital multimeter while approaching the wall with the measuring volume. It was assumed that the maximum output voltage occurs when the centre of the measuring volume touches the wall, i.e. that the photo-multipliers detect the directly reflected light. With this procedure, the wall distance could be adjusted to an accuracy of 50μ.

The data were processed on a workstation with software developed at our institute (for details see Sonnenberger (1997)). Phase averaging was applied to the data by sorting the samples into 24 different intervals depending on their arrival time relative to the excitation signal.

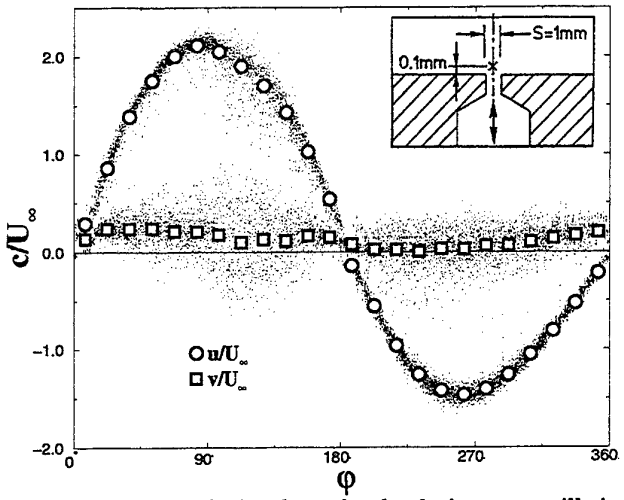


Figure 5: Phase averaged velocity above the slot during one oscillation period

3 EXPERIMENTAL RESULTS

A number of boundary layer profiles were measured along the centre axis of the test-section. Each profile was measured twice: in the unperturbed flow and with the oscillating cross flow.

3.1 The Undisturbed Flow Field

Figure 2 shows a close-up view of the velocity vector field in the vicinity of the fence together with the vorticity calculated from the velocity field. Upstream of the fence, the boundary layer separates at $(x - x_f) = 0.65h$. A shear layer separates at the sharp tip of the fence. Initially, the shear layer is oriented upward at an angle of $\alpha > 45°$, but the angle is reduced as the flow moves downstream. A secondary separation bubble is visible at the downstream foot of the fence, it is $(x - x_f) = 1.6h$ long.

Figure 3 shows the velocity and vorticity fields for the flow downstream of the fence. The main feature of this flow is the curved shear layer that reattaches to the wall at $(x - x_f) = 13.5h$.

However, the data shown in figures 2 and 3 represent only the time averaged flow field. Flow visualisations in figure 4 show that the instantaneous flow field is dominated by large vortical structures in the shear layer.

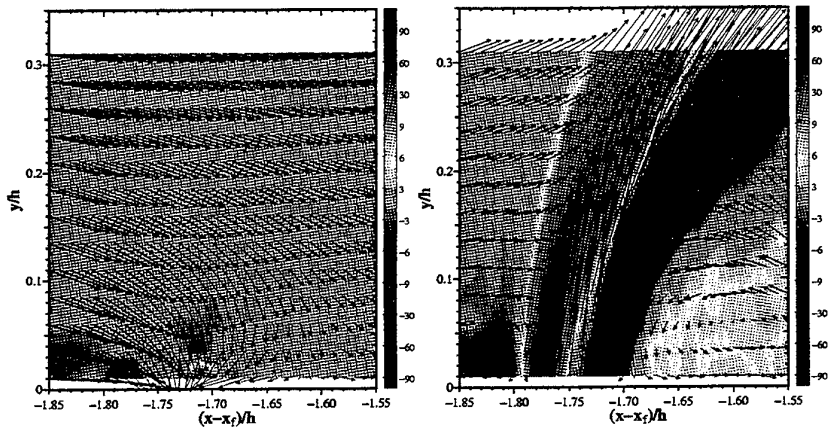


Figure 6: Velocity and vorticity fields over the slot during maximum suction and blowing phase

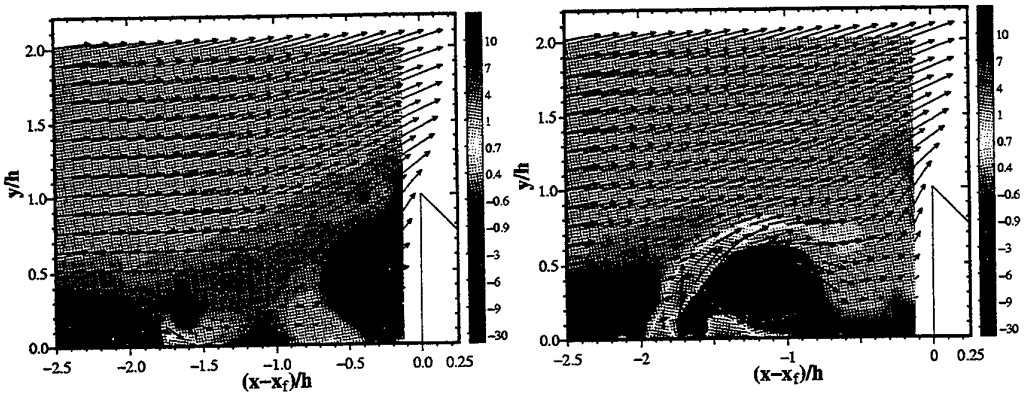


Figure 7: Velocity and vorticity fields upstream of the fence during maximum suction and blowing phase

3.2 Field Measurements With the Oscillating Cross Flow Upstream of the Fence

Figure 5 shows phase averaged velocity measurements in the centre axis of the slot and 0.1 mm above it. The maximum blowing velocity is higher than the maximum inflow velocity. These values are asymmetric, because the flow is directed upward during the blowing phase, while fluid enters the slots from all directions during the suction phase.

In order to obtain a better understanding of the dynamics of the flow in the vicinity of the slot, the velocity field was measured in a two dimensional field of 6 × 6 mm that was oriented parallel with the flow and perpendicular to the plate. The phase averaged results are shown in figure 6. The two images have a phase difference of 180°, the one to the left corresponds to the suction peak, the other on the right-hand side to the maximum blowing phase. When the boundary layer is sucked into the slot, vorticity levels are very low except for the region immediately up- and downstream of the slot. During the maximum blowing phase of the cycle, a strong jet is ejected from the slot. Vorticity levels in the shear layers at the edges of the jet are very high and a counter-clockwise rotating vortex forms downstream of the jet.

Figure 7 shows the phase averaged velocity and vorticity fields measured in a rectangular grid of 47.5 × 40 mm. This field covers the area upstream of the fence from $2.5h$ upstream of the fence to the fence itself. The two images, again, correspond to the maximum suction and blowing phase. The location of the field shown in figure 6 is marked with a dashed rectangle. During the suction phase, a large vortex is visible at the fence that has already detached from the bottom wall. This vortex will be convected over the fence. During the maximum blowing phase, there is no vortex directly at the fence. The jet rolls up into a large vortex as it is deflected by the boundary layer. This vortex is then convected by the flow towards the fence.

3.3 Boundary Layer Profiles Measured With the Oscillating Cross Flow

Boundary layer profiles in the flow field further away from the fence and downstream of the fence were measured at the same locations as the reference profiles shown in figures 3 and 2.

Figure 8 shows the phase averaged velocity and vorticity field calculated from a group of boundary layer profiles measured up- and downstream of the fence for four different phase angles with a phase difference of 90°. During the blowing phase ($0° \leq \varphi \leq 180°$), a large vortex develops downstream of the slot and is convected by the flow towards the fence. During the suction phase, this vortex dissipates until it has almost disappeared. Downstream of the fence, a large vortex develops after the upstream vortex has reached the fence. This vortex then grows larger and convects downstream.

Figure 9 gives a better view at the field downstream of the fence, again at four different phase angles. At every phase angle, the region downstream of the fence contains two large vortices. These vortices bring fluid from above the shear layer down to the wall and reduce the time mean reattachment length.

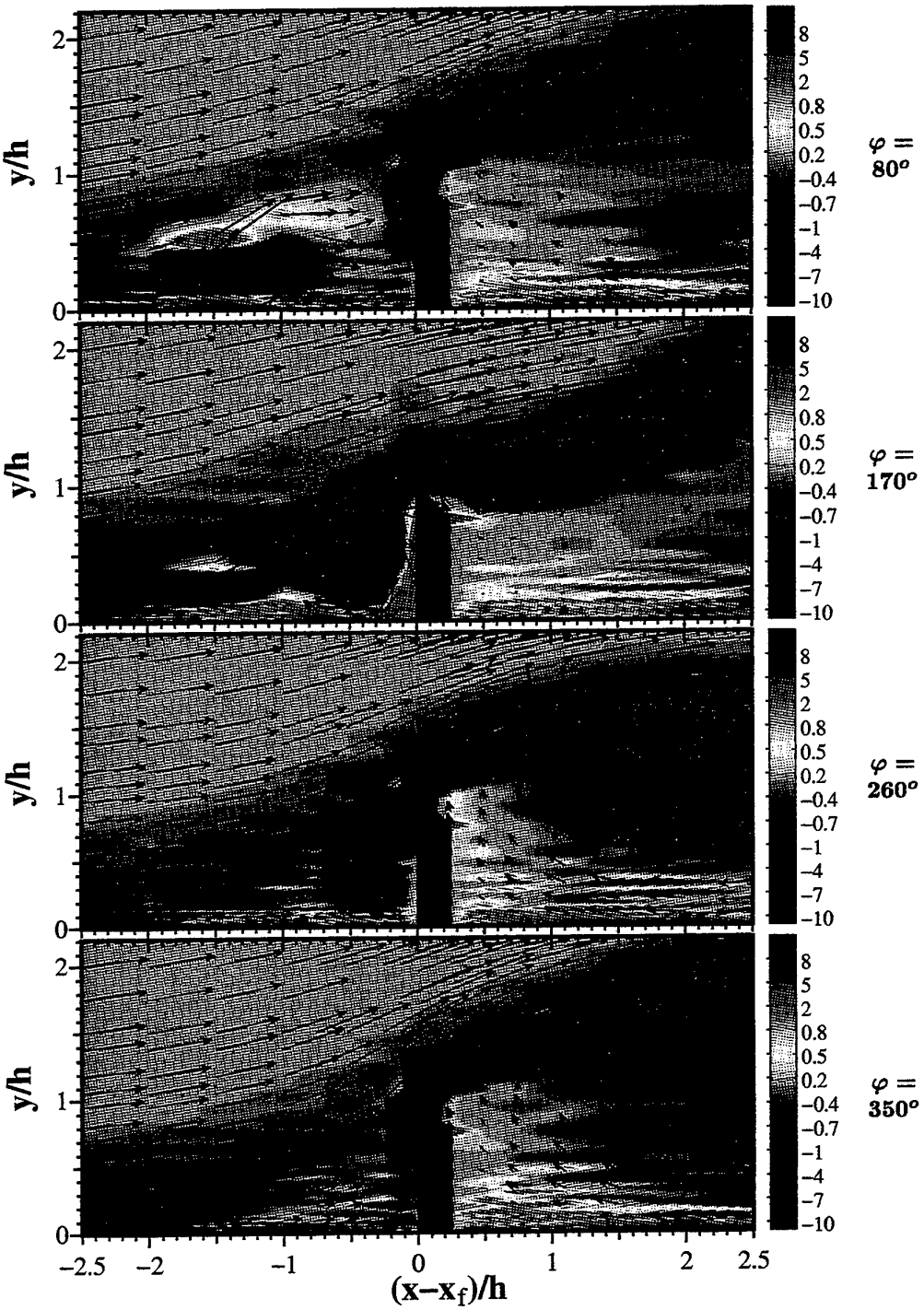


Figure 8: Velocity and vorticity fields near the fence

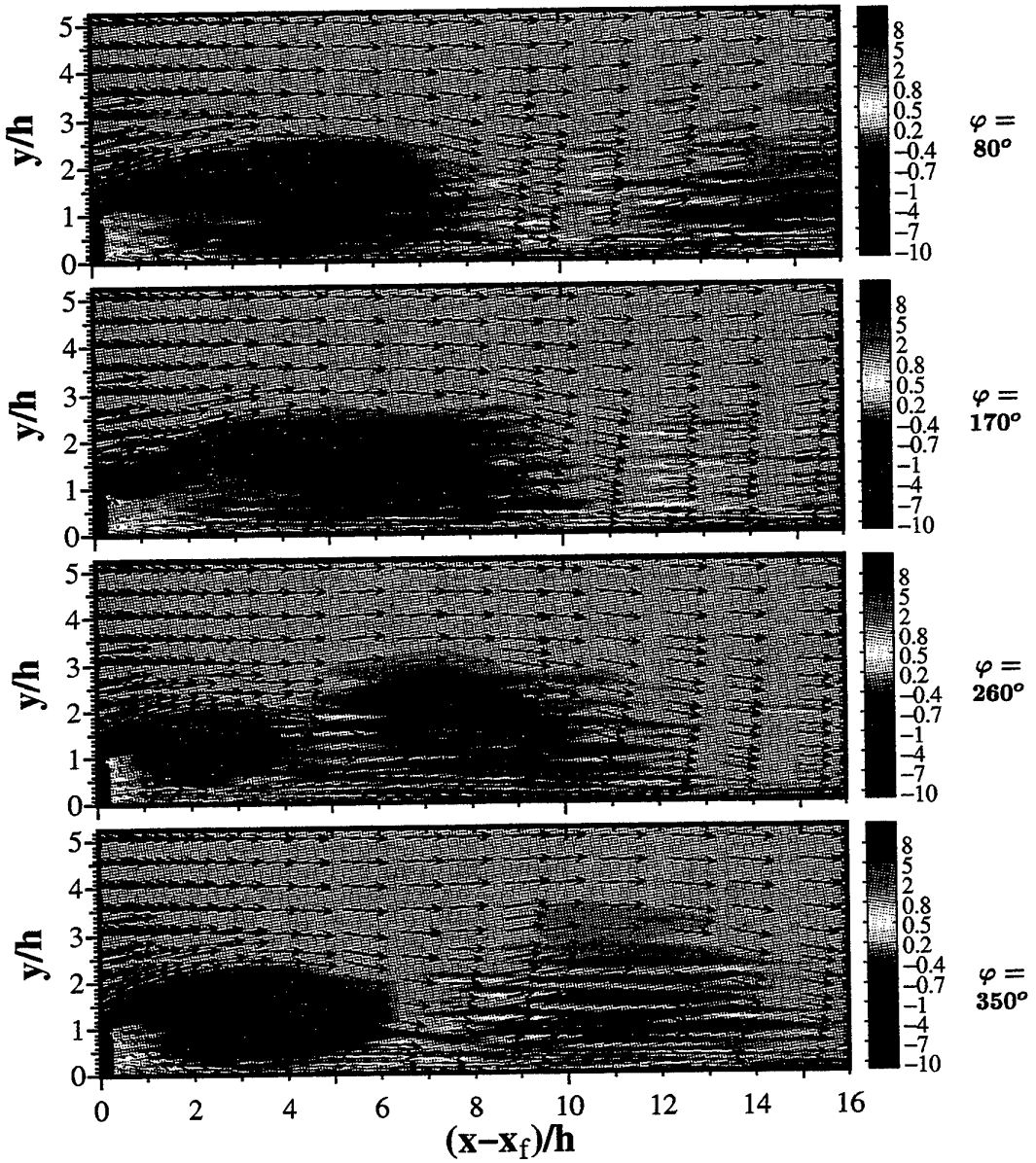


Figure 9: Velocity and vorticity fields downstream of the fence

4 CONCLUSIONS

Phase averaged two dimensional velocity-field measurements in a fence flow show how the separation bubble downstream of the fence is shortened. Large vortices form downstream of the fence and grow in size as they convect with the flow. These vortices mix the flow inside the separation bubble with fluid from above. The reattachment line oscillates up- and downstream in such a way that the time mean reattachment length is about half the size as for the unperturbed case. However, phase averaging over one period of the loudspeaker signal reveals only the dominant features of the flow that occur at the same location during every cycle. Structures that are associated with the sub-harmonic of the excitation signal have been shown to have an effect on the flow by Siller & Fernholz (1996). Such processes cannot be resolved with the methods applied here.

REFERENCES

CASTRO, I. & FACKRELL, J., 1978. A note on two-dimensional fence flows, with emphasis on wall constraints. *Journal of Industrial Aerodynamics* **3**, 1–20.

DIMACZEK, G., KESSLER, R., MARTINUZZI, R. & TROPEA, C., 1989. The flow over two-dimensional, surface mounted obstacles at high reynolds numbers. In *Proc. 7 th Symposium on Turbulent Shear Flows* (Stanford, CA, 1989), 10.1.1–10.1.6.

DURST, F. & RASTOGI, A., 1980. Turbulent flow over two-dimensional fences. In *Turbulent shear flows II* (1980), L. Bradbury, F. Durst, B. Launder, F. Schmidt, & J. Whitelaw, Eds., Springer, 218–232.

ERK, P., 1997. *Separation control on a post-stall airfoil using acoustically generated pertubations*. No. 328 in Fortschrittberichte, Reihe 7: Strömungstechnik, VDI-Verlag.

GOOD, M. C. & JOUBERT, P. N., 1968. The form drag of two-dimensional bluff-plates immersed in turbulent boundary layers. *J. Fluid Mech.* **31**, 3, 547–582.

HUPPERTZ, A. & JANKE, G., 1996. Preliminary experiments on the control of three-dimensional modes in the flow over a backward-facing step. In *Advances in turbulence VI* (1996), 461–464.

MARTINUZZI, R. & TROPEA, C., 1993. The flow around surface-mounted, prismatic obstacles placed in a fully developed channel flow. *Journ. Fluids Eng.* **115**, 85–92.

MIAU, J. J., CHEN, C. R. & CHOU, J. H., 1995. A vertically oscillating plate disturbing the development of a boundary layer. *J. Fluid Mech.* **298**, 1–22.

SIGURDSON, L. W., 1995. The structure and control of a turbulent reattaching flow. *J. Fluid Mech.* **298**, 139–165.

SILLER, H. & FERNHOLZ, H., 1996. Turbulent separation regions in front and downstream of a fence. In *Advances in turbulence VI* (1996), S. Gavrilakis, L. Machiels, & P. Monkewitz, Eds., Kluwer Academic Press, 487–490.

SONNENBERGER, R., 1997. Laser doppler measurements of oscillatory flow at high frequencies. Diplomarbeit, TU-Berlin.

MEASUREMENTS IN THE SHEAR-LAYER BEHIND A SURFACE-MOUNTED OBSTACLE FOR THE DETERMINATION OF COHERENT STRUCTURES

T. Baur and J. Köngeter

Institute of Hydraulic Engineering and Water Resources Management,
Aachen University of Technology, Germany

ABSTRACT

In the present investigation attention is given to determining and evaluating, under experimental conditions, the flow characteristics of the structures of turbulence in the shear-layer behind a surface-mounted obstacle. Turbulence in the given flow condition can cause unexpected cavitation inception for which physical explanations have to be found. The reason must be seen in coherent turbulent motion with the occurrence of local pressure reductions in the cores of time-dependent vortices. The elements of coherent motion are expected to have a three-dimensional horseshoe-shaped behavior as it is known from previous studies. This behavior cannot be proved by time-averaged LDV-measurements for the given flow configuration. The time-averaged flow field is indeed three-dimensional, but represents the macro scale of the recirculation zone. The statistical theory of turbulence is applied and results in the presence of ordered structures. Detailed quantitative information will be obtained from PIV-measurements. High flow velocities and the restrictions concerning the use of artificial particles in the flow cause several difficulties in the approach of this latter technique with the given equipment. The disadvantages can be overcome by applying the technique of temporal smoothing. An optimization of the measurement technique is a step forward to find physical explanations of the observed cavitation inception in the future.

1. INTRODUCTION

Dealing with non-streamlined test bodies, in a water-flow configuration low pressure conditions can cause vortex cavitation. The motivation for the examinations presented in this paper is the occurrence of cavitation inception at very low system pressure conditions which does not correspond to the prediction by the characteristic cavitation-number. The cavitation-number predicts the critical system pressure for a given inflow velocity so that cavitation occurs. From its definition the dimensionless cavitation-number should be independent from the inflow velocity. But, as it could be observed, at very low inflow velocities cavitation in the shear-layer is caused at a system-pressure which is higher than it should be according to the cavitation number. The discrepancies must be seen in the existence of coherent turbulent motion.

As it is generally stated in cavitation research, the inception of cavitation arises due to a pressure reduction in the core of time-dependent vortices. This pressure reduction reaches the critical vapor pressure of the fluid so that cavitation bubbles can be observed. The initiating effect is vortex motion - a hydrodynamic effect. The unsteady flow phenomena causing cavitation are expected to be bursting events with the roll-up of coherent structures in the shear-layer behind the test body. The bursting events cause extreme flow phenomena which yield critical pressure reductions.

The aim of the approach is to investigate the turbulent flow field by means of Laser Doppler Velocimetry (LDV) and a statistical analysis of the recorded time-series. On this basis a detailed investigation of the unsteady flow characteristics in predefined flow planes with Particle Image Velocimetry (PIV) can be undertaken. Previous studies have been carried out by Leucker (1995). But the results could not yet prove the occurrence of cavitation due to a critical pressure reduction in the time-dependent flow field and thus were not completely satisfying.

Only with the understanding of the turbulent phenomena and the coherent structures in the flow field insight into a reliable prediction of cavitation inception can be provided. This starts with an appropriate approach for the investigation of time-dependent flow phenomena. The results will later correct the definition

of the characteristic cavitation-number for inception if the outer variables like the inflow velocity can be proved to scale the occurrence of the mentioned phenomena.

2. THEORY OF COHERENT TURBULENCE

The effect of unsteady phenomena on the flow conditions is not only important in studies on cavitation inception but also e.g. for the turbulence phenomena in open-channel flows in general. In the boundary layer of turbulent flows unsteady vortices are induced which severely effect the flow characteristics. The occurring effects are described by e.g. Nezu and Nakagawa (1993). As a general observation it can be said that unsteady vortices occur quite periodically in laminar and transitional flows whereas they occur randomly in turbulent shear flows.

The coherent motion can be defined as it was done by Blackwelder (1987) as a parcel of vortical fluid occupying a confined spatial region such that a district phase relationship is maintained between the flow variables associated with its constituent components.

Coherent structures can be subdivided into bursting phenomena and large-scale vortical motion. Large-scale vortical motion occurs in the outer flow field, whereas the bursting phenomena mainly appear close to the surface. Since bursting phenomena are very similar to the cavitation process, this effect is focused on in detail.

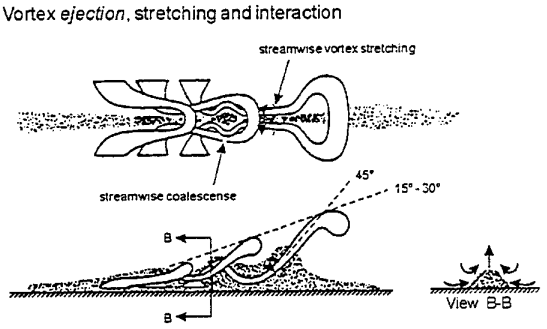


Fig. 1 Physical model of horseshoe-vortices during bursting processes in open-channel flow by Smith (1984)

In the model of Smith (1984) horseshoe-vortices are taken as the governing motion in bursting events. These vortices are not two-dimensional, they have a three-dimensional shape. The life-cycle of a structure consists of lift-up, oscillation, ejection and sweep. The process of ejection including the stretching and interaction of the vortices is demonstrated in Figure 1, indicating the Ω-shape or horseshoe-shape. These structures grow from the laminar boundary layer in channel flows and have a three-dimensional horseshoe-shape. The legs of the horseshoe-vortices are oriented in the general direction of the flow and pointing upstream. Similar three-dimensional structures are expected to exist in the turbulent flow field behind the obstacle and maintain their identity within the free sheer-layer.

3. FLOW CONFIGURATION

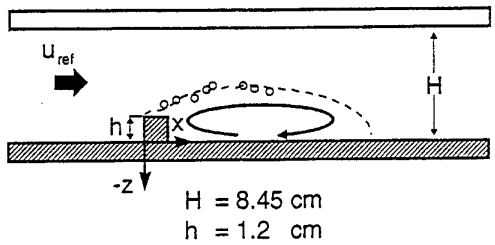


Fig. 2 Flow configuration for the experiments

The examined test configuration is characterized by the flow over a rectangular obstacle of height h = 1.2 cm fixed on the surface of the channel with rectangular cross-section and pipe flow conditions. The channel width is B = 12 cm and the height H = 8.45 cm. The medium of flow is water. According to the geometry, vortex cavitation occurs randomly in the shear layer and is not fixed to one exact location (Fig 2) as it would be in the case for streamlined test bodies. The components of the three-dimensional velocity vector in x-, y-, z-direction are u, v, w.

4. LDV-MEASUREMENTS

4.1. Measurement set-up

For the laser measurements two single-component Laser-Doppler-Velocimeters are used and installed according to Fig. 3. The first system by TSI works in the forward-scatter mode. Due to the transparent channel walls this approach is possible. The system allows measurements of the flow velocities in the x- and z-direction alternatively. The system axis is installed perpendicular to the xz-plane. The received signals are evaluated by a counter. The second LDV-system is a DANTEC Laser-Doppler-Velocimeter (DANTEC, 1993a+b) which is working in backscatter-mode. Since the system is installed in a vertical optical axis to measure the third velocity-component in y-direction and the surface is not transparent, a backward-scatter laser is used. The received signals are in this case evaluated by a

burst spectrum analyser (BSA), based on a Fast Fourier Transformation. To analyze the data the evaluated signals of both systems are transmitted to a conventional PC. The Laser-probes are adjusted by two computer controlled traversions. For all measurements the inflow velocity is u_{ref} = 3.0 m/s resulting in a Reynolds-Number Re_h = 36.000 (h is the obstacle height).

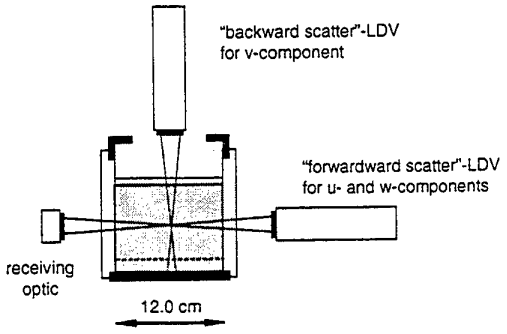


Fig. 3 Measurement set-up with two LDV-systems

In order to investigate the turbulent flow conditions, two approaches are followed. In the first one it is tested if even the time-averaged velocities indicate a three dimensional character of the flow field behind the obstacle. In the second one the flow is investigated by its statistical parameters. For both approaches LDV-measurements with the explained experimental set-up are carried out.

The measurement grid covers a xz-plane with the coordinates $0 < x < 12.0$ cm and $0 < z < 6.0$ cm. The distance between the measuring points is 5 mm maximum and smaller close to the surface and the obstacle edges. This allows for an exact determination of flow velocities in the highly complex flow. The xz-plane is measured not only in the symmetric axis y = 6.00 cm but in the positions y = 3.33; 4.66; 6.00; 7.33 and 8.66 cm. So a three-dimensional grid with 5 x 425 = 2,125 measuring points is produced.

The number of velocity data to be recorded for every measuring point by the TSI system is set to 1,000. With the DANTEC system 10,000 bursts are collected with a maximum duration of 60 seconds. Due to the relatively high flow velocities it is not necessary to use any seeding. The measurements are taken for all velocity components of the three-dimensional velocity vector. They result in time series of the fluctuating velocities u, v and w and its mean values. To visualize the results of the LDV-measurements the software packet MATLAB by *The MathWorks, Inc.* is used.

4.2. Three-dimensional time-averaged velocity field

The combination of two velocity components results in a vector field of time-averaged velocities. The vector plot in Fig. 4 is taken from the xz-plane in the middle of the channel. Dimensionless coordinates are used. The recirculation zone can be clearly noticed. The u- and w-components of the velocity are the main acting directions of the flow.

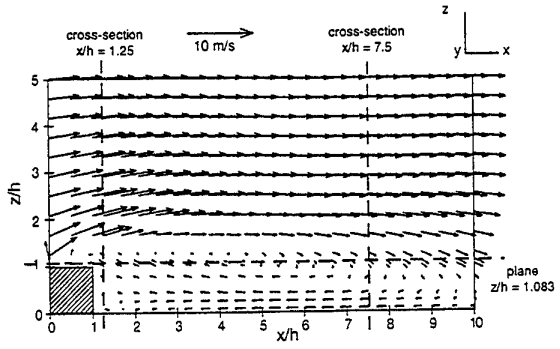


Fig. 4 Vector plot of time-averaged velocities in the recirculation zone and indication of vector planes

A full two-dimensional behavior with no contribution of the transverse velocity-component v is not present, as it can be seen in Fig. 5 representing a horizontal plane directly above the obstacle. In the region x/h = 6 the u-component of the velocity vector tends to zero and the transverse velocity is dominant. It is the region in the recirculation zone of Fig. 4 where the sign changes from negative to positive.

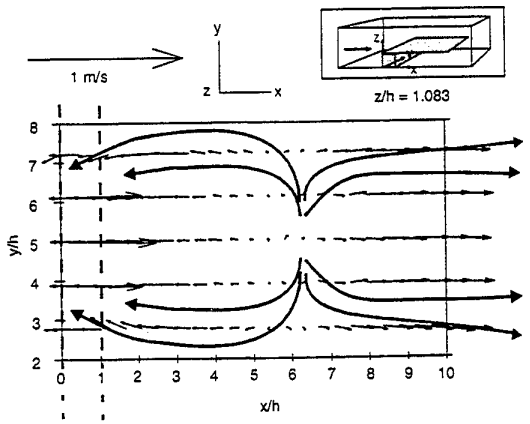


Fig. 5 Horizontal xy-plane directly above the obstacle (Δh = 1 mm)

The transverse velocity is directed to the channel walls, whereas close to the obstacle edge at x/h = 1 it is in opposite direction to the middle.

For two vertical cross-sections the vector plots with dimensionless coordinates are given in Fig. 6. The cross-sections are two yz-planes, one directly behind the obstacle (x/h = 1.25) and another one in the recirculation zone (x/h = 7.50). The vector plots indicate the existence of a 3D-secondary current. It can be observed that close to the surface the downward flow in the recirculation zone is directed to the channel walls. Following the recirculation upstream back to the obstacle the streamlines are directed into the middle. The transverse velocities in the outer measurement planes have the order of 0.50 m/s which is about 0.5/3.0 = 16.7 % of the mean inflow velocity. This is valid only in the region close to the surface at z/h < 1.0, whereas in the region above the obstacle at z/h > 3.0 the averaged transverse velocity is about 0.08 m/s (=2.7 %).

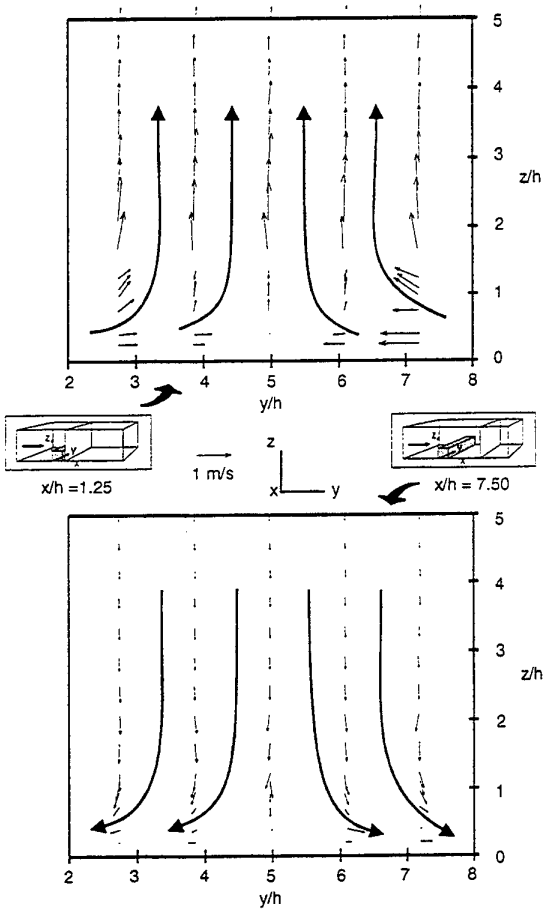


Fig. 6 Secondary currents in two planes behind the obstacle

The behavior of the secondary current is proved to be symmetric. This yields a xz-plane in the symmetric axis of the channel where the transverse velocities are expected to be zero. The recirculation is clearly three-dimensional and forms two loops at both sides of the symmetric axis. The mainly vertical loops are bent close to the surface in a horizontal plane. The measured three-dimensional time-averaged flow field is of macro scale and does not correspond to the classical shape of coherent structures of Fig. 1. This shows the expected effect that she unsteady flow conditions in the shear-layer are without severe contribution to the time-averaged flow field.

4.3. Statistical parameters of turbulence

Besides the mean velocities of the unsteady, turbulent flow, the variance of velocity fluctuations representing the intensity of turbulence is determined for the x-direction. Fig. 7 shows that in the given flow configuration the shear-layer forms a zone of high turbulence. The free inflow velocity is again $u_{ref} = 3.0$ m/s. The maximum value is located in the region $6.0 < x/h < 8.0$ and corresponds to a RMS-value of $\overline{u'} = 1.2$ m/s which is 40 % of the free inflow velocity.

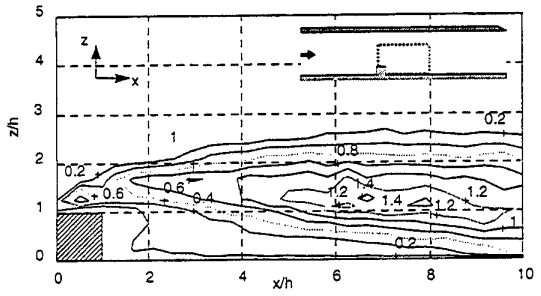


Fig. 7 Contour plot of turbulence variance of the horizontal velocity component

Additionally, third-order moment (skewness) calculations are carried out in order to obtain more detailed information concerning turbulence. This latter parameter is taken as additional information to describe the characteristics of the observed turbulent flow field. The skewness indicates the departure of the fluctuations from a normal Gaussian distribution around the mean value due to bursting events.

Fig. 8 shows the skewness of the velocity-component u in x-direction. It is given for the plane y = 6.00 cm in the symmetric axis of the flow configuration since there the maximum values can be determined. The contour plot demonstrates that the shear-layer consists of a well developed skewness. The skewness is negative in the region with positive u and positive in the region with negative u. Speculating that the basic structural elements

of the turbulent shear-layer are similar to the horseshoe-vortices, one expects within the vortex a negative u-correlated with a positive v-component. The positive v corresponds to the direction away from the surface. The existence of the measured positive skewness indicates that the passage of the vortices is followed by a strong acceleration in the flow by the overlying free stream.

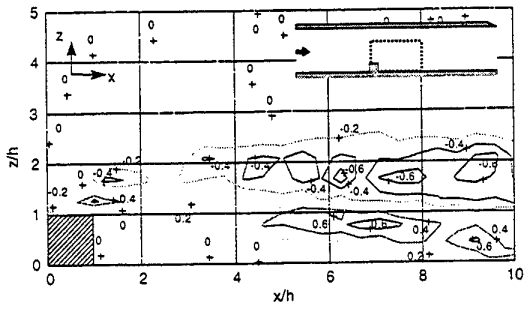


Fig. 8 Contours of skewness of the horizontal velocity component

The area behind the obstacle, where the maximum values of skewness of the turbulent fluctuations in the mean flow direction is expected, lies between x/h = 6.0 and x/h = 9.0 according to Fig. 8. This corresponds well with the results from the turbulence variance determination.

It is obvious that the shear layer behind the obstacle produces high turbulence levels and a concentration of bursting events. Though, the statistical analysis of the recorded LDV-data is not sufficient enough to define parts of the observed turbulent motion as the life-cycles of coherent structures. The turbulence variance and the higher-order moment are not a sufficient parameter to give evidence about the quality of the arising coherent structures of the time-dependent turbulent motion. Nevertheless, the data can be used to define spatial areas of interest where detailed measurements of the instantaneous flow field are required.

5. PIV-MEASUREMENTS

5.1. Preceding Investigations

For the purpose of measuring the unsteady flow field, the video-based Particle Image Velocimetry (PIV) is used. With this optical measurement system the time-dependent velocity vectors in a two-dimensional area of flow can be determined. For the given flow configuration measurements have been carried out already by Leucker (1995). The studies were performed at the same test rig with free surface flow conditions.

The examined area of flow had the dimensionless coordinates in x-direction $1.0 < x/h < 5.0$ since there the inception of cavitation nuclei was observed and consequently the extreme flow events causing critical pressure reductions were expected. Leucker (1998) calculated the time-dependent pressure by using the Navier-Stokes-Equations. He could verify that the calculated pressure shows a minimum in the vortex cores. Thus the conclusion was proved that cavitation inception starts in the center of time-dependent vortices. But nevertheless, even by using unsteady velocity data from the PIV-measurements the resulting pressure conditions in the shear-layer did not result in the critical vapor pressure necessarily, although cavitation inception was observed.

There must be reasons for this discrepancy between calculation and observation. Following this theory, the recorded flow conditions in the used video images did not represent extreme flow events but unfortunately only slow vortical motion. Additionally, it might be possible that the temporal resolution of the used camera with 1,000 frames per second was not sufficient enough to capture the bursting phenomena in detail. With mean velocities in the shear-layer up to 4.5 m/s the coherent structures still might show a shorter temporal resolution which can only be investigated with a recording technique of higher temporal resolution.

5.2. Improvements in the measurement-technique

Due to high flow velocities the recording for the PIV-measurements in this new approach is done with a high-speed video-camera of *type KODAK Ektapro* at a temporal resolution of 9,000 frames per second of size 256 x 128 pixel.

With this approach the turbulent phenomena can be recorded with a high temporal resolution on a digital memory. To store the data a video-recorder is required and analog data produced. The digitalization of the analog images is finally carried out by a PC-mounted frame-grabber after the images have been recorded (see Fig. 9).

The illumination of the flow is done by a 3 W-Argon-Ion Laser in continuous mode with fiber optics and a prismatic lens.

The region of interest is a vertical xz-plane in the symmetric axis of the channel. The recorded frame size is 8.3 x 4.15 cm^2 which results in a spatial resolution of the region of interest of t = 0.324 mm for a pixel height and width respectively.

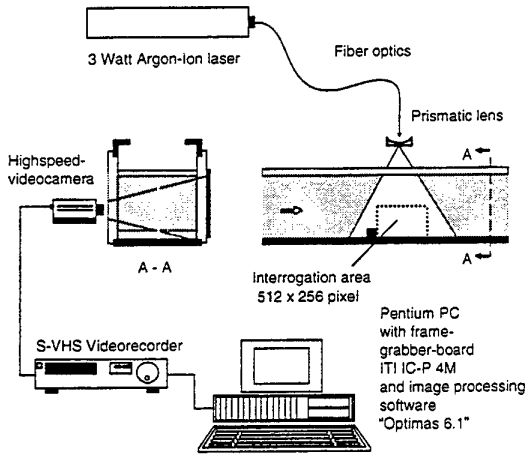


Fig. 9 Measurement set-up with PIV-system

In order not to influence the channel facilities for the investigation of cavitation inception which is highly sensitive on the fluid quality an artificial seeding is not used. The recorded particles are nuclei of the undissolved gas present in the system. It was proved that the nuclei are an adequate tracer which represent the unsteady flow field very well (Leucker, 1995).

For the processing of velocity data the cross-correlation technique is applied. After the data has been stored on the video-recorder and digitized again with the frame-grabber, the spatial resolution of the frames is doubled. So the digital image processing correlates regions of 64 x 64 Pixels. The spatial step width is 16 Pixel. For every time step 551 vectors are calculated for one data-set.

The processing yields vector plots which are poor in validity. The reason must be seen in the used light source and the illumination time of $\Delta t = 1/9{,}000 = 0.11$ ms which is too short to transfer enough light energy on the CCD-ship of the camera. The laser light efficiency is reduced to ~60 % due to the use of the fiber optics, so that in the frame margins information about the velocities is lost. The restriction concerning the use of tracer particles are a supporting factor for the lack of data.

This disadvantage can be overcome by applying the technique of temporal smoothing to the data sets: Introducing a characteristic time scale t* for the description of the unsteady flow phenomena with $t^* = h/u_{ref} = 4$ ms, a comparison with the time difference of two successive frames becomes possible. At a recording velocity of 9,000 frames per second the time difference is $\Delta t = 0.11$ ms. Since the temporal resolution of 9,000 Hz of the used camera is relatively high, the development with time of the recorded flow phenomena between the data sets is quite small. By temporal smoothing, which is enabled by the determination of temporal moving average for every single point in the flow field, the quality of the data set can be improved. For the present study the number of frames for the temporal smoothing is chosen to $n = 9$ corresponding to a time interval of $\Delta t = 1$ ms for time-averaging. This yields $t^*/\Delta t = 4$. With this approach the time-averaged flow field within 1 ms can still be taken as a result which represents the time-dependent flow field.

5.4. Results of PIV-measurements

In Fig. 10 the time-dependent velocity vectors of the flow in the recirculation zone behind the obstacle obtained by using PIV are presented for one time step. The unsteady velocities, which differ distinctively from the time-averaged flow velocities gained with the LDV-System (Fig. 4), can be used to identify vortex cores.

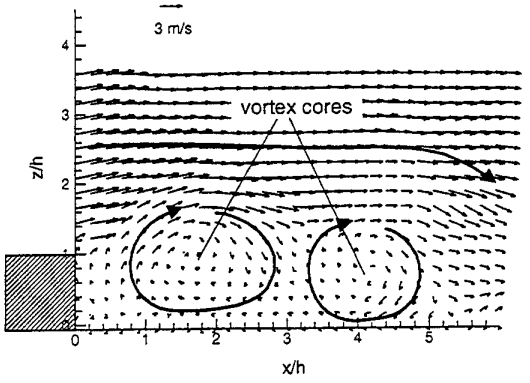


Fig. 10 Result of PIV-measurement behind the obstacle with vortex cores

So the zones of local pressure reductions can be defined qualitatively. The exact calculation of the unsteady pressure distribution demands for a velocity-measurement of high quality. Furthermore, a data base has to be obtained in order to cover all flow phenomena including the extreme flow events which lead to cavitation inception. Although the area of maximum turbulence can be defined in the given flow configuration to be at $6.0 < x/h < 8.0$, the PIV-measurements presented here concentrate on the area directly behind the obstacle. Further recordings have to be carried out, especially to focus on other regions of interest.

CONCLUSIONS

Both measurement techniques show that the instantaneous flow field behind the obstacle is not independently random but contains deterministic vortices which can be described as coherent motion.

The PIV-technique is an appropriate approach to quantify the influence of bursting phenomena on the pressure conditions in the flow which can initiate cavitation inception. From the PIV-measurements by Leucker (1995), who used the Navier-Stokes-Equations, the occurrence of a local pressure reduction in a vortex core by coherent motion could be proved. But the critical vapor pressure could not yet been calculated for flow fields where cavitation inception has been observed.

For this discrepancy the reason has to lie in the fact that the extreme flow events have not been recorded. Three approaches should be followed in order to solve for this problem:

1. The region of interest for the PIV-measurement has to correspond with the region where the maximum statistic parameters of the turbulent flow field can be determined. This disagrees with the position in the flow field where cavitation inception was observed.

2. The orientation of the measurement plane (xz-plane) does not contain the extreme flow events which are responsible for the critical pressure reductions. So other measurement planes have to be chosen, e.g. the horizontal xy-plane.

3. The experimental set-up with very low light efficiency has to be further optimized by using a stronger light source.

It can be stated that the shown PIV-technique is a powerful tool for the purpose of calculating unsteady pressure fields after the optimization has been performed.

For the used system restrictions are given which are probably not present in other investigations. Due to the actual need for the use of a camera of higher temporal resolution the improvement of data post-processing was required. The method of temporal smoothing is a contribution to the optimization of the measurement techniques. With respect to the made approaches detailed investigations of the time-dependent velocities can be carried out in the future.

ACKNOWLEDGEMENTS

The project was funded by the German Research Foundation (DFG) with project number Ko 1573/4-1.

REFERENCES

Blackwelder, R. F. 1987, Coherent structures associated with turbulent transport, Proc. of 2nd Int. Symp. on Transport Phenomena in Turbulent Flows. Tokyo, pp. 1-20.

DANTEC 1993a, Burstware-Installation and users guide, Manual.

DANTEC 1993b, FLOWLITE- Installation and users guide, Manual.

Leucker, R. 1995, Analyse instationärer Strömungsphänomene zur Vorhersage des Kavitationsbeginns (Analysis of unsteady flow phenomena to predict cavitation inception), Ph.D. thesis, Instituts für Wasserbau und Wasserwirtschaft, RWTH Aachen.

Leucker, R. 1998, Influence of large-scale vortices on cavitation inception in steady, turbulent flows, in MICHEL, J.M.; H. KATO (ed.): Proceedings of the 3rd International Symposium on Cavitation: Grenoble, France, 7.-10. April 1998, pp. 123 - 128.

Nezu, I. & Nakagawa, H. 1993, Turbulence in open-channel flows, IAHR Monograph Series, Balkema, Rotterdam/Brookfield.

Smith, C.R. 1984, A synthesised model of the near-wall behaviour in turbulent boundary layer, Proc. of 8th Symposium of Turbulence, University of Missouri-Rolla, USA, pp. 299-327.

MEASUREMENTS OF THE SPATIAL COHERENCE OF THE FLOW AROUND TWO CYLINDERS

J.A.Fitzpatrick & V.Valeau*

Department of Mechanical Engineering
Trinity College, Dublin 2, Ireland.
(* on leave from LAUM, Le Mans, France.)

ABSTRACT

The spatial coherence of the flow around a configuration of two cylinders in tandem has been investigated using a laser Doppler anemometer together with hot film and microphone probes. The single component LDA system was used to monitor the velocity in the wake of the upstream cylinder and hot film and microphone probes were used to examine the coherent structure of the flow between the cylinders using the LDA measurement as a reference. Results presented for a specific velocity show a so called phase locked condition with harmonics of the vortex shedding frequency observable in the auto spectra. A technique for identifying non-linear interactions is used to show that the harmonics are most likely generated by vortex impingement at the downstream cylinder together with non-linear turbulent interactions in the wake region.

1. INTRODUCTION

The sound generated by flow/structure interactions is of considerable interest for many applications in the transport field where an understanding of the mechanisms of noise generated is required to reduce or control community noise levels. The study of two tandem cylinders (i.e. one behind the other) in a cross flow provides a useful vehicle to develop an understanding of the mechanisms of flow/acoustic interactions. Although the noise generated by groups of cylinders in cross flow has been investigated by numerous authors, there has been little reported on the noise emanating from smaller groups of cylinders particularly in unbounded flows. The noise generated by a single cylinder has been investigated by numerous authors since the empirical work of both Strouhal (1878) and Rayleigh (1896) in the last century. Theoretical analysis was developed by Curle (1955) who demonstrated that the sound is a dipole type source generated principally by the unsteady pressure interaction with the cylinder surface as summarised more recently by Powell (1990). The interactions between two cylinders in cross flow has been extensively reviewed by Zdravkovich (1977) who has shown that vortex formation in the inter cylindrical space is only present when the non-dimensional spacing is greater than approximately four diameters. Mahir and Rockwell (1996) have reported on an extensive study of the effect of vibration on the flow around two cylinders in tandem. Their work focused on the ability of the vibration to "lock on" to the vortex shedding systems but indicated an absence of vortex shedding for small inter cylinder spacing. The noise generated by impingement on a body in the wake of vortex dominated flow has been reported by, for example, Ziada and Rockwell (1982) for a wedge downstream of a jet.

A recent paper by Fitzpatrick & Nitti (1997) has shown that hot wire and microphone measurements along the nominal free shear layer between two cylinders at a non-dimensional spacing (L/d) of both 4 & 5 show clear evidence of non-linear interactions giving rise to secondary peaks in both the turbulence spectrum and the near field pressure spectrum. It was suggested that this was a consequence of both acoustic feed back and non-linear shear layer dissipation between the two cylinders. It was also observed that the harmonics were suppressed when the hot wire was located close to the upstream cylinder. In order to eliminate the suppression of the non-linear interactions, measurements have now been made using a laser Doppler anemometer together with a hot film and a microphone on a similar configuration. The objective was to examine the non-linear interactions which give rise to the harmonic

development along the nominal free shear layer between the two cylinders. The non-linear interactions are examined using a spectral technique proposed by Rice & Fitzpatrick (1988) to identify the quadratic correlation between two measurements .

2. EXPERIMENTAL SET-UP & ANALYSIS

2.1 Rig & Instrumentation

The experiments were performed in a low turbulence wind tunnel with a velocity range from 15 to 35 m/s. Two cylinders of 8 mm diameter were mounted between two parallel plates with an inter cylinder spacing of five diameters in the direction of flow. The expected vortex shedding frequencies were not coincident with tunnel resonance frequencies. The tunnel velocity was monitored using a Pitot static tube together with a Furness control micro manometer type FCO510. A single channel laser Doppler system using a 32mW He-Ne laser in forward scatter mode was used in conjunction with a TSI 1980B counter interfaced to a Pentium type pc through a DMA board. Dantec hot film probes were used with 55MO1 anemometer modules as required. A B&K microphone type 4138 with a nose cone was used to monitor the fluctuating pressure in the vicinity of the two cylinders (near field). Measurements with the hot film and the microphone were obtained along the nominal free shear layer between the cylinders.

Experiments were conducted in which measurements were obtained using laser Doppler anemometer together with both the hot film anemometer and the microphone to investigate the correlation between the pressure and the velocity fluctuations. A schematic of the set up and measurement positions is shown in figure 1.

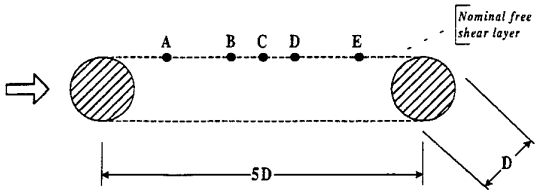


Fig. 1 : Schematic of test set up

The LDA was located along the nominal free shear layer at one diameter downstream of the first cylinder and the hot film was traversed along the nominal free shear layer between the two cylinders. The microphone was traversed with its centreline some 2 mm above the nominal free shear layer.

2.2 Data Acquisition & Analysis

The LDA data was acquired in the usual way of validated velocity and time from the counter. The hot film and microphone data was acquired at the same time as the validated LDA data by using a trigger pulse from the counter to activate the A to D board and sample the hot film and microphone signals. This method was used as it has been shown by Scholten et al. (1996) that serious bias errors are experienced when cross spectra are calculated using irregularly sampled LDA data with regularly sampled data. For analysis using only the hot film and the microphone, the data was acquired using normal equispaced acquisition procedures with suitable anti-aliasing filters.

Time domain reconstruction of the irregularly sampled data required for cross spectral analysis was effected using a linear interpolation (first order) method as described by Scholten et al. (1996). The data was corrected for the low pass filter effect but no other corrections were implemented. It has also been shown by Scholten et al. (1996) that the same step noise will be introduced to both data sequences by irregular simultaneously sampling and, hence, coherence estimates will be biased upwards. The degree of bias was shown to depend on the signal to step noise ratio and on the coherence of the original data. This bias is evident for much of the data presented in this paper.

The signal processing to yield auto and cross spectra were implemented using spectral analysis software written in MATLAB. The mean data rate for the LDA acquisition was 5 kHz. After reconstruction by either sample & hold or linear interpolation at time intervals equivalent to 100 kHz, the data was low pass filtered using an 8 pole Butterworth filter and resampled at 10 kHz with spectra computed up to 4 kHz. The hot film data was linearised using a 4th order polynomial before any spectral calculations were performed. Auto and cross spectra were calculated for 30 ensemble averages of 1024 data points.

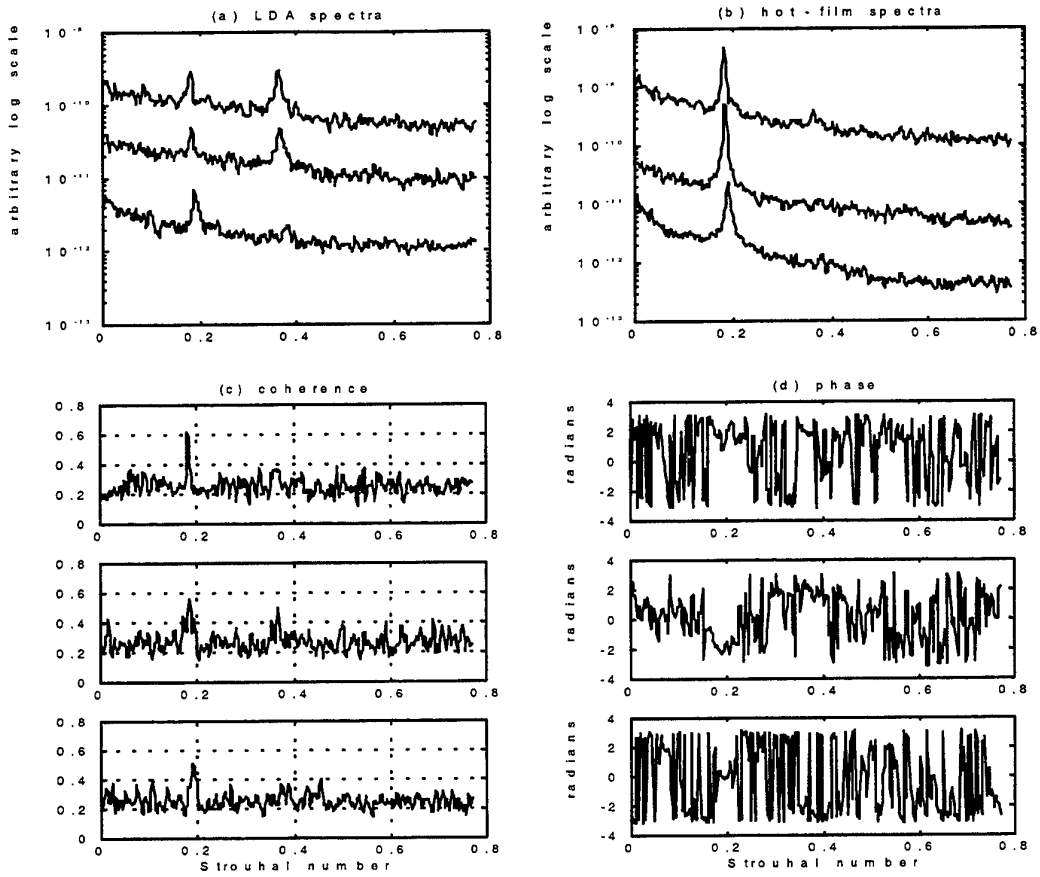


Fig. 2 : Results for LDA/hot film measurements (x/d = 1.- lower , 2.5 - mid, 4. - upper)

3. TEST PROCEDURES & RESULTS

Simultaneous measurements from the LDA system and the hot film and microphone were obtained at the five positions shown in figure 1 for a velocity of 35 m/s. The results at this velocity are of most interest as it was at this speed that the vortex impingement on the downstream cylinder generates a pressure which feeds back in phase to the vortex generation process at the upstream cylinder. The tests were then repeated traversing the microphone probe with respect to the LDA and finally, a series of tests were conducted using the hot film and the microphone in order to assess errors inherent in the LDA signal processing system.

The auto spectra, coherence and phase for the LDA./hot film measurements at 1, 2.5 and 4 diameters downstream of the leading cylinder are shown in figure 2. For the hot film probe located at 1D, it can be seen from figure 2 that there is a clear peak in both auto spectra at the vortex shedding frequency with a coherence of 0.6. The low coherence is a result of poor signal to noise ratios for these results as a consequence of the random sampling. As the hot film probe is moved downstream, a second peak becomes evident in the LDA auto spectrum. This peak is not all obvious in the hot film spectra, but some measure of coherence between the LDA and hot film results is evident at 2.5 diameters. The suppression of this second peak in the auto spectrum when a hot film probe was located at the rear of the upstream cylinder was also reported by Fitzpatrick & Nitti (1997). The results for phase show that this is only measurable at the vortex shedding frequency where a reasonably high coherence is measured.

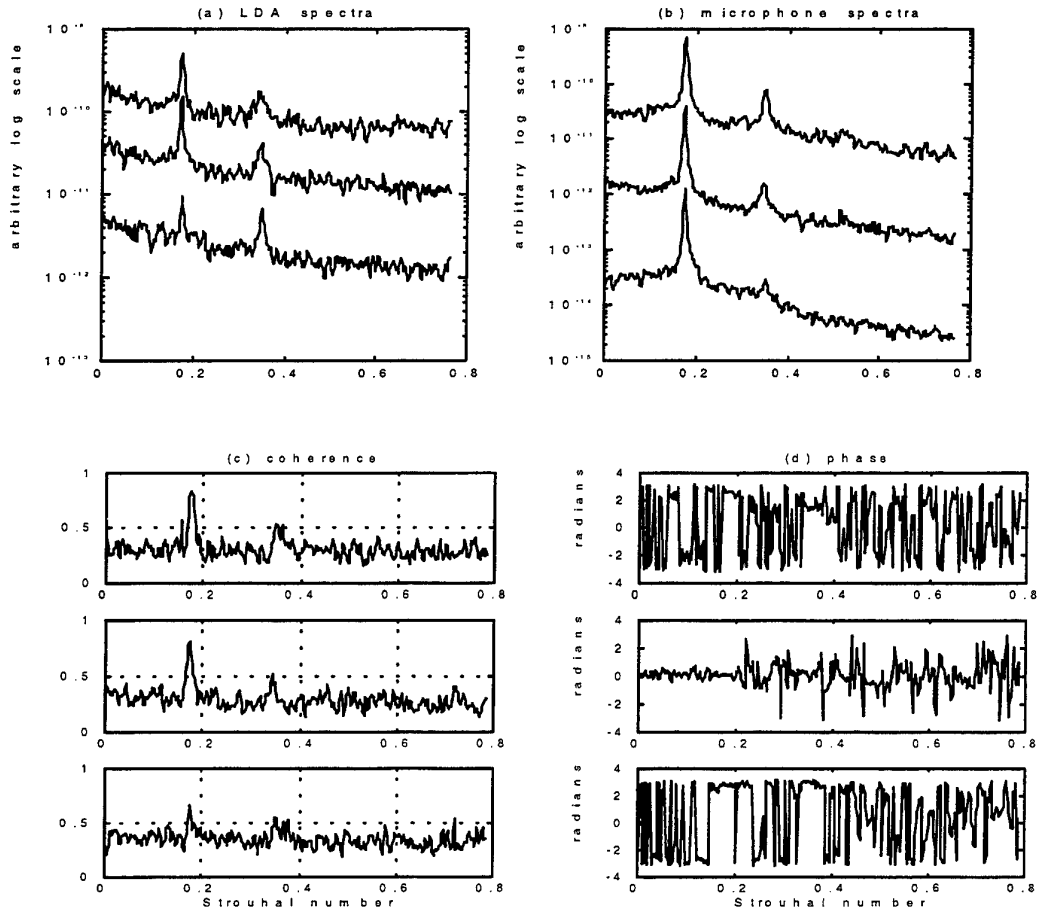


Fig.3 : Results for LDA/microphone measurements (x/d = 1- lower , 2.5 - mid, 4 - upper)

The results for the LDA/microphone tests are shown in figure 3. Here, the second peak in the auto spectrum for the LDA data is evident in all the measurements. For the microphone measurements, the peak at twice the vortex shedding frequency is just discernible at 1D and grows as the microphone is traversed towards the downstream cylinder. However, there is evidence of some coherence at this frequency at all measurement locations. It is interesting to note that the background level of coherence for all these results is quite high. This is a result of the common noise introduced to the data when the simultaneous sampling and subsequent interpolation process is applied. The level is about 20% for the LDA/hot film data and some 30% for the LDA/microphone data indicating a high noise to signal ratio at frequencies other than that of the vortex shedding and its first harmonic. Figure 4 shows a composite plot of the results for the phase between the LDA and the hot film and microphone measurements at the vortex shedding

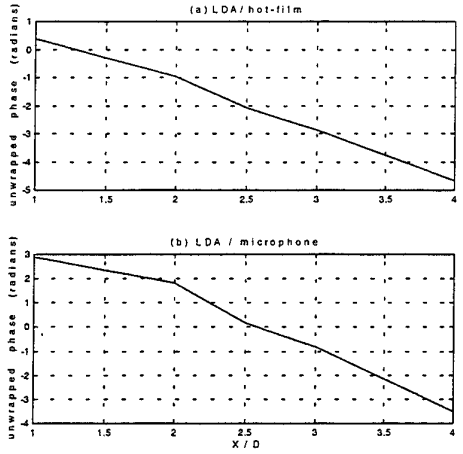


Fig.4 : Phase at vortex shedding frequency

frequency. This data was extracted from the results for the phase at the vortex shedding frequency. For the LDA/hot film results, the results show clearly that

the vortex pattern is one of in phase to out of phase to in phase demonstrating a "standing" pattern of vortices in the wake region with a vortex impinging on the downstream cylinder as the next is being shed from the upstream cylinder. This is confirmed by the microphone measurements where the phase moves from out of phase in the wake of the upstream cylinder to in phase at the centre of the two cylinders to out of phase again at the downstream cylinder. The potential for feedback for two cylinders in cross flow can be examined by considering the generation by vorticity shedding of a fluctuating pressure at the upstream cylinder. This disturbance is convected downstream where it impinges on the downstream cylinder. This impingement then radiates upstream at the local relative velocity of sound and causes a further fluctuating pressure on the upstream cylinder. If this is in phase with the original unsteady pressure fluctuation, then positive feedback occurs and a standing pattern of vortices exists in the inter cylinder region. This so called "phase-locking" process has been reported for other flow configurations (e.g. Kwon (1996). The measurements of phase for the velocity show that the vortex is being convected downstream at about 0.8 of the mainstream velocity whereas those for the pressure show a slightly higher values for phase than for pure convection indicating that the velocity/pressure interactions are not one of simple convection but more probably a mixture of convection and acoustic feed back.

4. NON-LINEAR INTERACTIONS

The appearance of a significant peak in the LDA auto spectrum at twice the vortex shedding frequency requires some thought as to its origin. Fitzpatrick & Nitti (1997) observed multiple peaks in the turbulence spectrum for two cylinders in cross flow and also noted that the sound generated at the second harmonic was a maximum at the downstream cylinder. The measurements obtained here show an even more dominant second harmonic has been measured by the LDA. At 1D downstream, some influence of the vortices being shed from the other side of the cylinder would be observed by the LDA which measures the streamwise component of velocity and this will appear as a second harmonic in the data. However, it is unlikely that, at the nominal free shear layer, this would be at the same amplitude as the fundamental.

Non-linear interactions in the free shear layer bounding a vortex street have been studied both theoretically and experimentally. The instability of a shear layer under the influence of vorticity and its capacity to produce harmonics due to non-linear interactions has been predicted by Stuart (1967) and has been observed by Ziada & Rockwell (1983) for a jet impinging on a wedge. Fitzpatrick & Nitti (1997) reported that the generation of harmonics for two cylinders in cross flow was dependent on flow velocity, incident turbulence and the capacity of a system for acoustic type feedback. The results obtained in this study have shown the presence of a second harmonic close to the upstream cylinder where non-linear shear layer instability would be unlikely. The auto spectrum for the unsteady pressure would seem to indicate that the second harmonic is being generated at the downstream cylinder perhaps as a consequence of vortex deformation. This deformation would then radiate upstream and enhance any potential for non-linear instability.

A number of methods have been proposed for analysis of non-linear interactions in flows. The most common has been the use of the bispectrum which seeks to determine the degree of quadratic interaction for a specific variable and between variables (e.g. Hajj et al., 1997). However, Fitzpatrick & Rice (1988) showed that, due to multiple interactions, it is difficult to obtain quantitative information from bispectral analysis and they proposed an alternative technique to investigate non-linear interactions. This approach can be used to investigate the non-linear interactions associated with the two cylinder system.

In most fluid flow systems, non-linearity arise from velocity product terms in the governing equations which give rise to quadratic interactions. In order to investigate this mechanism as a potential source for the generation of the second harmonic in the LDA auto spectrum, consider the schematic shown in figure 5.

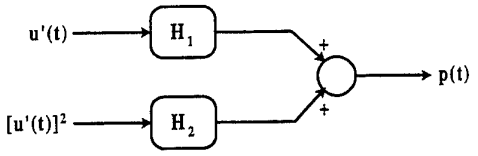


Fig.5 : Non-linear velocity/pressure interaction

Here, the system is represented as two inputs and an output. The inputs are considered as the turbulent velocity and the square of this and the output can be velocity or pressure measured separately. Thus, linear source terms are governed by the relationship between u' and the output and quadratic sources are determined from the relationship between u'^2 and the output. The degree of correlation or coherence can be determined for both the "linear" and "non-linear"

elements using the technique. The method is based on conditioned spectral analysis which eliminates any possible correlation between u' and u'^2. The degree of correlation between the uncorrelated "inputs" and the conditioned output is then assessed using a partial coherence function in the same manner one uses a coherence function to assess the degree of interdependence between two variables. The procedures have been given in detail by Bendat & Piersol (1994) and applied to two input non-linear system by Rice & Fitzpatrick (1998).

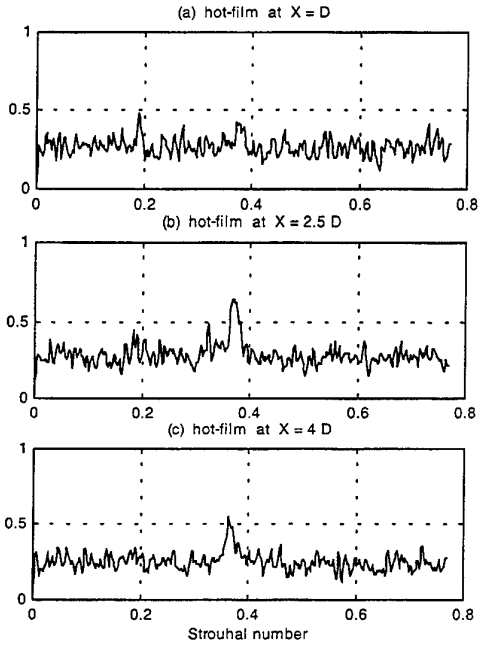


Fig.6: Quadratic coherence for hot film/LDA data

This approach was then used to investigate potential quadratic interactions in the results obtained for the two cylinder system in cross flow. In the first instance, the input was considered to be the LDA measurements obtained in shear layer near the upstream cylinder and the output the hot film as it was moved along the shear layer to the rear cylinder. This would then show if the non-linearity was due to shear layer instability as this would originate in the near wake region and the interactions would grow in the direction of flow. This was not the case and there was no measurable quadratic interaction using the LDA data as the input. Since the pressure data seemed to suggest that the source of the second harmonic was at the downstream cylinder, the hot film data for the downstream cylinder was then used as the input for the analysis and the LDA measurements as the output. The results from this are shown in figure 6 and it can be seen that there is a high coherence between the downstream quadratic term and upstream measurement at twice the vortex shedding frequency. This shows that the source for the perturbation which leads to the generation of a second harmonic of the vortex shedding frequency is most likely a consequence of non-linear deformation arising from vortex impingement at the downstream cylinder. This was confirmed by further analysis using the pressure data from which it was observed that the non-linear source was of the quadratic type originating at the downstream cylinder. Further analysis was undertaken using the hot film data and determining the degree of correlation between u' and u'^2 using an auto quadratic coherence function as this is a measure of the quadratic interactions in a process.

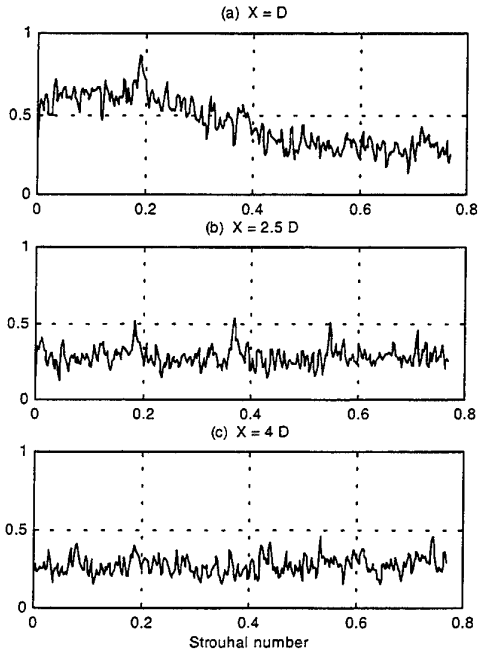


Fig.7 : Auto-quadratic coherence for hot film data

From figure 7, it can be seen that the quadratic interactions for the turbulence measurements are strongest at 2.5D where up to the fourth harmonic is observable. Finally, figure 8 shows the results using the hot film data as input and the microphone measurement from the downstream cylinder as output. For these cases, the data was equispaced and the errors associated with the random sampling have been eliminated. From this, it can be seen that the origins of the harmonic instability arise due to velocity/velocity interactions in the mid-wake region

and these are being amplified by pressure feedback due to vortex distortion at the downstream cylinder.

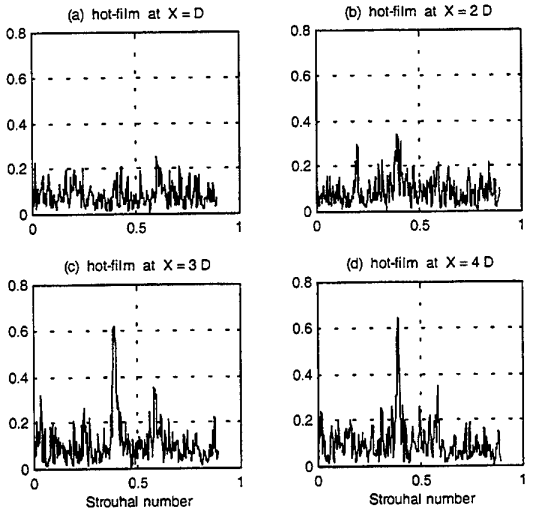


Fig.8 : Quadratic coherence for hot film/microphone data

5. CONCLUSIONS

A series of tests have been conducted using a laser Doppler anemometer to investigate the spatial correlation of turbulence for two cylinders in cross flow. From the results presented here, the following conclusions can be drawn.

- Phase locking has been observed for the configuration tested at 35 m/s and confirmed by the LDA/hot film and LDA/microphone measurements.
- A novel approach to determine the quadratic interactions between the measured variables has shown that harmonics of the vortex shedding frequency have been generated by a combination of vortex deformation at the downstream cylinder and turbulent interactions in the mid wake region.
- Further analysis is required to quantify these initial findings and to examine the implications of the results.

6. REFERENCES

Bendat, J.S. & Piersol, A. 1980, Engineering Applications of Correlation and Spectral Analysis. Wiley Interscience, New York.

Curle, N., 1955, The Influence of Boundaries Upon Aerodynamic Sound, Proceedings of the Royal Society, vol.A 231, pp. 505-514.

Fitzpatrick, J.A. & Nitti, F. 1997, Flow/Acoustic Interactions for Two Cylinders in Cross Flow, Flow Induced Vibration & Noise, ASME AD-vol.53-1, pp.463-470.

Hajj, M.R., Miksad,R.W. & Powers,E.J. 1997, Perspective: Measurements and Analyses of Nonlinear Wave interactions with Higher Order Spectral Moments, Trans. ASME, Journal of Fluids Engineering, vol.119, pp.3-13.

Kwon, Y-P. 1996, Phase-Locking Condition in the Feedback Loop of Low-Speed Edge Tones", Journal of the Acoustical Society of America, vol. 100, pp. 3028-3032.

Mahir,N. & Rockwell, D. 1996, Vortex Shedding from a Forced System of Two Cylinders. Part I: Tandem Arrangement, Journal of Fluids and Structures, vol. 10, pp. 473-489.

Powell, A. 1990, Some Aspects of Aeroacoustics: from Rayleigh until Today, Trans.ASME, Journal of Vibrations & Acoustics, vol. 112, pp. 145-159.

Rayleigh, Lord 1896, The Theory of Sound - Vol. II, MacMillan & Co. Ltd., London.

Rice,H.J. & Fitzpatrick,J.A. 1988, Spectral Analysis of Non-Linear Systems, Mechanical Systems & Signal Processing, vol.2, pp.195-207.

Rice, H.J. & Fitzpatrick, J.A. 1991, The Measurement of Non-Linear Damping in Single Degree of Freedom Systems, Trans. ASME, Journal of Vibration & Acoustics, vol.114, pp.132-140.

Strouhal, V. 1878, Ueber eine Besondre Art der Tonnerung, Annals der Physik, vol. 5, pp. 216-251.

Scholten, J., Dawson, S., Fitzpatrick, J.A. & Simon,L. 1996, Minimising Errors for Cross Spectral Analysis using Laser Doppler Anemometer Measurements, Proc. 8th Int. Symp. on Applications of Laser Techniques to Fluid Mechanics, Lisbon, paper 36.5.

Stuart, J.T. 1967, On Finite Amplitude Oscillations in Laminar Mixing Layers, Journal of Fluid Mechanics, vol. 29, pp. 417-440.

Ziada, S. and Rockwell, D. 1982, Oscillations of an Unstable Mixing Layer Impinging upon a Wedge, Journal of Fluid Mechanics, vol. 124, pp. 307-334.

Zdravkovich, M.M. 1977, Review of Flow Interference Between Two Circular Cylinders in Various Arrangements, Trans. ASME, Journal of Fluids Engineering, vol. 99, pp. 618-633.

AUTHORS' INDEX

Abe, M., 6.1.1
Adrian, R.J., 6.4.1, 6.6.1, 11.1.1, 14.1.1, 16.1.1, 17.4.1
Ajayi, K.T., 22.1.1
Akamatsu, F., 35.3.1
Alkislar, M.B., 13.5.1
Allain, C., 19.5.1
Allen, J.T., 23.3.1
Alvarez, M.P., 16.4.1
Anacleto, P., 25.7.1
Andrés, N., 16.4.1
Antonia, R.A, 2.1.1
Aoki, T., 4.5.1
Araneo, L., 7.4.1
Aroussi, A., 33.4.1
Arregle, J., 7.6.1
Arroyo, M.P., 16.4.1
Arsié, A., 39.2.1
Augenstein, E., 2.3.1
Auger, P.L., 28.4.1
Azzazy, M., 23.1.1, 34.3.1

Baetz, W., 6.2.1
Barreras, F., 2.5.1, 24.2.1
Barrientos, A., 33.5.1
Barros, A.N., 21.3.1
Bar-Ziv, E., 35.5.1
Batliwala, F., 34.1.1
Baur, T., 20.6.1
Beale, A., 3.5.1
Becker, J., 34.5.1
Belghit, A., 31.2.1
Bélorgey, M., 39.2.1
Bench, P., 28.4.1
Benedict, L., 32.5.1
Bergounoux, L., 9.2.1
Berkner, L., 15.2.1
Berry, J.D., 1.1.1
Berton, E., 19.5.1
Bettis, R.J., 23.3.1
Beylich, A.E., 23.4.1
Bjorkquist, D.C., 6.5.1
Böhm, C., 20.3.1
Bolcs, A., 8.2.1
Bolinder, J., 29.2.1
Boree, J., 24.4.1
Borg, A., 29.2.1
Brehm, C., 7.2.1
Brenier, Y., 18.5.1
Brenn, G., 21.1.1
Britan, A.B., 26.5.1
Bröder, D., 27.2.1
Brücker, Ch., 27.4.1
Brun, M., 7.5.1
Buckberry, C.H., 12.5.1, 31.5.1
Burnett, M., 36.3.1
Bütefisch, K.A., 24.6.1

Caldas, F., 17.3.1
Carlier, J., 11.2.1
Carlomagno, G. 38.3.1
Cartallier A., 28.4.1
Carter, C.D., 35.1.1
Carvalho, I.S., 24.1.1
Cater, J., 4.2.1
Cattanei, A., 20.2.1, 36.4.1
Catton, I., 23.1.1, 34.3.1
Cenedese, A., 38.3.1
Cessou, A., 25.3.1
Champagne, J.Y., 36.2.1
Changsong, G., 29.1.1
Charbonnier, J.M., 2.6.1
Chiné, B., 33.5.1
Christensen, K.T., 16.1.1
Christnacher, F., 2.3.1
Coghe, A., 7.4.1
Cognet, G., 18.5.1
Cossali, G.E., 7.4.1
Coustols, E., 19.3.1
Cross, P.B., 36.3.1
Czarske, J.W., 15.3.1, 32.3.1

Da Costa, G., 26.4.1
Dahoe, A.E., 35.6.1
Dakemoto, Y., 21.4.1
Dam, N., 37.3.1
Damp, S., 2.3.1
Dawson, J.R., 3.3.1, 3.5.1, 3.6.1
Day, S., 29.3.1
De Angelis, G., 38.3.1
De Gregorio, F., 19.6.1
Delfos, R., 24.3.1
Deljouravesh, R., 18.7.1
Derksen, J.J., 4.3.1, 14.5.1
Desantes, J.M., 7.6.1
Dias, I., 12.1.1
Diertele, L., 19.2.1
Dinkelacker, F., 25.4.1, 25.6.1
Djenidi, L., 2.1.1
Doelman, M.S., 14.5.1
Dölle, O., 32.3.1
Domnick, J., 21.1.1
Donbar, J.M., 35.1.1
Dopazo, C., 2.5.1
Dopheide, D., 15.4.1, 18.3.1
DrBarber, P.A., 34.1.1
Duarte, D., 25.5.1
Dullenkopf, K., 1.3.1, 31.3.1
Dupont, P., 4.1.1, 11.2.1
Duport, I.S., 28.4.1
Durst, F., 9.1.1, 11.3.1, 14.2.1, 21.1.1, 22.1.1

Ebner, J., 1.3.1
Egbers, C., 4.6.1, 20.3.1, 28.2.1
Ehrenfried, K., 19.2.1, 19.6.1
Einav, S., 29.4.1
El Hajem, M., 36.2.1
Elia, N., 20.2.1
Elsässer, A., 1.3.1
Elvarasan, R., 2.1.1
Entwistle, J.D., 6.3.1
Escudier, M.P., 8.3.1

Falgayrettes, P., 18.5.1
Fandrey, C., 9.3.1
Fanouille, P., 24.4.1
Favier, D., 19.5.1
Feldmann, O., 14.4.1
Fernandes, E.C., 3.3.1
Fernholz, H.H., 20.5.1
Ferrão, P., 17.3.1, 25.5.1
Fick, W., 3.2.1
Fiechtner, G.J., 35.1.1
Firpo, J.L., 9.2.1
Fischer, M., 11.3.1, 8.1.1
Fitzpatrick, J.A., 3.6.1, 20.7.1
Flack, R.D., 8.1.1
Fleming, G.A., 1.1.1
Foucaut, J.M., 11.2.1
Four, I., 24.4.1
Freek, C., 4.4.1, 13.1.1, 22.4.1
Fuchs, L., 29.2.1
Funke, S., 12.3.1
Furuichi, N., 22.2.1

Garib, M., 13.6.1
Gentner, C. 36.5.1
Geropp, D., 2.2.1
Gharib, M., 16.5.1
Gicquel, P., 8.6.1
Gindele, J., 31.1.1
Girardot, L., 36.7.1
Göde, E., 36.5.1
Gökalp, I., 17.2.1
Golovanevsky, B., 34.7.1
Gomes, F.V., 39.1.1
Góngora, H.G.C., 7.5.1
Gonzalez, U., 7.6.1
Gord, J.R., 35.1.1
Gorton, S.A, 1.1.1
Gougat, P., 39.3.1
Gouldson, I.W., 8.3.1
Grabow, J., 15.1.1
Grad, Y., 29.4.1
Greated, C.A., 6.3.1
Griffths, A.J., 3.2.1
Grosche, G., 18.3.1
Gui, L., 10.5.1

Hachiga, T., 22.2.1
Hackert, G., 35.4.1
Hand, D.P., 6.3.1
Hanson, R.K., 25.2.1

Hardalupas, Y., 3.4.1
Hargrave, G.K., 9.4.1
Hart, D.P., 13.3.1, 37.4.1
Hassan, Y.A., 27.5.1
Hasselbrink, E.F., 25.2.1
Havermann, M., 23.4.1
Heath, J., 9.4.1
Hein, D., 23.2.1
Heitor, M.V., 3.3.1, 17.3.1, 24.1.1, 25.7.1
Hentschel, W., 13.1.1
Hess, C., 18.1.1
Hino, M., 26.3.1
Hishida, K., 6.1.1, 16.2.1, 22.2.1, 26.6.1
Hoekstra, A.J., 4.3.1
Holler, V., 25.6.1
Holzapfel, W., 6.2.1
Honore, D., 25.1.1
Hsu, C.T., 9.5.1
Huang, Z., 20.4.1
Hubner, W., 13.2.1
Huckle, E., 34.3.1

Ikeda, Y, 12.2.1, 12.6.1, 21.5.1
Immohr, J., 28.2.1
Ishima, T., 7.1.1, 24.4.1

Ismailov, M., 7.1.1
Israel, A.T., 4.3.1

Jackson, D.A., 29.5.1
Jaffre, D., 25.1.1
Javanovic, J., 11.3.1
Jingui, C., 29.1.1
Jones, J., 6.3.1

Kadambi, J.R., 12.4.1
Kähler, C., 11.1.1, 19.6.1
Kantorovich, I., 35.5.1
Karatekin, Ö., 2.6.1
Karl, J., 23.2.1
Kataoka, K., 4.5.1
Katayama, K., 10.3.1
Katsuki, M., 35.3.1
Kawaguchi, T., 26.6.1
Kawahara, N., 12.2.1
Keicher, M., 14.7.1
Keller, J., 31.4.1
Kerrigan, S., 6.6.1
Kim, J.H., 21.5.1
Kim, K.C., 14.1.1
Kim, M.S., 2.2.1
Kobayashi, K., 7.1.1
Kobayashi, T., 13.4.1, 13.6.1
Kockx, J.P., 24.3.1
Kompenhans, J., 10.1.1, 13.6.1, 19.2.1, 19.6.1
Köngeter, J., 20.6.1, 33.1.1
Korenaga, K., 28.3.1
Kowalewski, T.A., 34.7.1, 39.3.1
Kozlov, P.V., 26.5.1
Kremer, H., 35.4.1
Kuhn, A., 6.3.1
Kumada, M., 22.2.1
Kuzmanovski, A., 10.4.1

Lai, J.C.S., 38.1.1, 38.4.1
Lai, W., 6.6.1
Lam, D.H., 10.2.1
Lang, N., 19.4.1
Lanzetta, F., 36.7.1
Larsen, P.S., 17.4.1
Lawes, M., 35.2.1
Le Coz, J.F., 7.3.1
Le Mironet, S., 4.1.1
Lee, K.C., 14.2.1
Lee, W.K., 36.3.1
Lehmann, P., 32.3.1, 33.2.1
Lein, G., 36.5.1
Leipertz, A., 25.4.1, 25.6.1
Leopold, F., 2.3.1
Levin, V.A. 26.5.1
Levy, Y., 34.7.1
Li, E.B., 15.5.1
Lim, T.T., 4.2.1
Limberg, W., 19.4.1
Liu, Z.C., 6.6.1, 16.2.1
Liubao, Z., 29.1.1
Lixin, Y., 29.1.1
Löber, W., 6.2.1
Lourenco, L.M., 13.5.1
Lozano, A., 2.5.1, 24.2.1

Lu, D., 38.4.1
Lund, C., 2.4.1
Luxton, R.E., 3.1.1

Madarame, H., 26.1.1
Maeda, M., 6.1.1, 16.2.1, 26.6.1
Maia, R., 8.4.1
Maison, L., 39.2.1
Maresca, C., 19.5.1
Martin, W.T., 12.4.1
Matos, M., 17.3.1
Matsumoto, K., 4.5.1
Maurey, C., 25.3.1
Mayinger, F., 14.4.1
McCluskey, D.R., 8.5.1
McCusker, S., 38.2.1
Meerts, W., 37.3.1
Meinhart, C.D., 6.4.1, 16.2.1
Melling, A., 9.1.1
Mendoza, J., 23.1.1
Meng, H., 16.3.1, 20.4.1
Menon, R., 36.1.1, 36.7.1
Merzkirch, W., 10.5.1, 13.1.1
Meyer, K.E., 20.1.1
Meyers, J.F., 1.1.1
Miles, P., 37.2.1
Miranda, P., 8.4.1
Mitichkin, S.Y., 26.5.1
Modares, D., 16.5.1
Mok, K.M., 39.2.1
Möller, T.J., 24.6.1
Moreira, A.L.N., 21.3.1
Morel, R., 36.2.1
Morikita, H., 14.7.1
Most, D., 25.6.1
Mounaïm-Rousselle, C., 18.2.1
Mouqallid, M., 31.2.1
Muller, E., 32.1.1
Muller, H., 18.3.1, 15.4.1
Mungal, M.G., 17.1.1, 25.2.1

Nakajima, T., 12.6.1, 21.5.1
Nakatani, N., 34.6.1
Naqwi, A., 9.3.1, 15.2.1
Nasr, A., 38.1.1
Nath, B., 6.2.1
Nathan, G.L., 3.1.1
Nijenboer, F.J., 32.2.1
Nino, E., 11.4.1
Nishio, S., 13.4.1
Nishiyama, M., 28.3.1
Nitsche, W., 19.1.1
Nobach, H., 32.1.1
Nonn, T.I., 27.3.1

Obermayer, K., 10.4.1
Obokata, T., 7.1.1
O'Doherty, T., 3.2.1, 3.5.1
Ohba, K., 21.4.1, 28.3.1
Ohmi, K., 10.2.1
Ohmura, N., 4.5.1
Okamoto, K., 10.6.1, 13.4.1, 26.1.1
Oliemans, R.V.A., 24.3.1
Onofri, F., 9.2.1, 24.5.1
Oschwald, M., 23.5.1
Ottmann, M., 23.2.1

Pagé, J., 17.2.1
Pailhas, G., 19.3.1
Pajot, O., 18.2.1
Pallacin, I.G., 24.2.1
Pantaloni, J., 24.5.1
Pastor, J.V., 7.6.1
Pekalski, A.A., 35.6.1
Pengel, K., 19.6.1
Pereira, A.S., 22.3.1
Pereira, F., 16.5.1, 22.4.1, 33.3.1,
Perrin, M., 25.1.1
Petrak, D., 18.4.1
Pickering, S.J., 33.4.1
Pinho, F.T., 8.4.1, 22.3.1
Pinto, F.T., 39.1.1
Pitz, R.W., 34.1.1
Plamann, K., 15.3.1
Podoleanu, A.G., 29.5.1
Posylkin, M., 7.2.1
Prenel, J.P., 36.7.1
Proença, M.F., 8.4.1, 39.1.1
Przybilla, E., 18.4.1
Pu, Y., 20.4.1

Qiu, H., 9.5.1, 21.2.1
Quénot G., 39.3.1

Raffel, M., 10.1.1, 19.2.1, 19.6.1
Raimann, J., 21.1.1
Rambert, A., 39.3.1
Ramuzat, A., 29.3.1
Raposo, J.M.F., 13.1.1, 33.3.1
Rasmussen, J.J., 8.5.1
Rath, H.J., 28.2.1, 20.3.1
Razore, S., 20.2.1
Reeves, M., 12.5.1, 31.5.1
Resagk, C., 15.1.1
Reuber, J., 33.1.1
Reuss, D.L., 37.1.1
Ribarov, L.A., 34.1.1
Riethmuller, M.L., 12.1.1, 18.6.1, 22.5.1, 29.3.1
Ripault, J.M., 9.2.1
Rogers, J.A., 29.5.1
Röhle, I., 33.2.1, 34.2.1
Rolon, J.C., 35.1.1
Romano, G.P., 32.4.1
Rona, A., 11.5.1
Ronneberger, O., 10.1.1
Rosalik, M., 37.1.1
Rosenfeld, K., 18.4.1
Rottenkolber, G., 31

Saarenrinne, P., 14.6.1
Saga, T., 13.4.1
Samenfink, W., 1.3.1
Santiago, J.G., 6.4.1
Santos, D., 24.1.1
Sarh, B., 17.2.1
Sato, Y., 26.3.1
Sauvage, P., 19.3.1
Savory, E., 38.2.1
Scaramo, F., 22.5.1
Scarlett, B., 35.6.1
Schabacker, J., 8.2.1
Schafer, M., 14.2.1
Scheuerpflug, W., 12.3.1
Schik, A., 23.5.1
Schmidt, W.D., 27.5.1
Schneider, G.M., 3.1.1
Schodl, R., 34.2.1
Schoepf, G., 3.2.1
Sciacchitano, A., 20.2.1
Selbach, A., 3.4.1
Sellens, R., 18.7.1
Sen, R., 13.5.1
Serio, C., 11.4.1
Servouze, Y., 8.6.1
Sharp, K., 6.6.1, 14.1.1
Sheng, J., 16.3.1
Sheppard, C.G.W., 35.2.1, 35.7.1
Siller, H.A., 20.5.1
Sitte, B., 4.6.1
Skarman, B., 34.5.1
Soika, A., 25.4.1, 25.6.1
Sola, I.J., 16.4.1
Sollows, K.F., 33.6.1
Soloff, S.M., 16.2.1
Sommerfeld, M., 27.2.1
Son, P.H., 21.4.1
Soria, J., 4.2.1
Sousa, J.M.M., 4.4.1, 13.1.1, 22.4.1
Spaanjaars, C., 37.3.1
Spettel, F., 36.2.1
Spicher, U., 31.1.1
Stahlecker, D., 36.5.1
Stanislas, M. 4.1.1, 11.2.1, 13.6.1
Stefanini, J., 36.7.1
Stenum, B., 8.5.1
Stenzel, O., 2.4.1
Stepowski D. 25.3.1
Stoffels, G., 37.3.1
Strunck, V., 18.3.1
Susset, A., 25.1.1
Syred, N., 3.1.1, 3.5.1

Tadrist, L., 24.5.1
Tanaka, G., 26.1.1
Tanguy, B., 8.6.1
Tarr, S., 33.4.1
Taugwalder, F., 16.5.1
Taylor, A.M.K.P., 14.7.1
Teng-Yang, R., 33.6.1
Ter Meulen, J.J., 37.3.1
Testov, V.G., 26.5.1
Thirouard, B., 37.4.1
Tieu, A.K., 15.5.1
Tinapp, F., 19.1.1

Tobben, H., 15.4.1
Tomkins, C., 6.6.1
Tosiyasu, T., 10.3.1
Touvet, Y., 19.3.1
Towers, D.P., 12.5.1, 31.5.1
Toy, N., 38.2.1
Trinite, M., 25.1.1, 31.2.1
Tropea, C., 13.2.1, 31.4.1, 32.1.1, 32.5.1
Tsukagoshi,M., 7.1.1
Tsushima, S., 35.3.1
Tujeehut, T.D., 24.3.1

Ubaldi, M., 20.2.1, 36.4.1
Udrea, D., 36.3.1
Uemura, T., 10.3.1
Ullmun, U., 17.4.1
Urban, W.D., 17.1.1

Valeau, V., 20.7.1
Van Beeck, J.P.A.J., 18.6.1
Van den Akker, H.E.A., 4.3.1, 14.5.1
Van den Boom, E., 37.3.1
Van den Konijnenberg, J.A., 8.5.1
Van den Moortel, T., 24.5.1
Van Maanen, H.R.E., 32.2.1
Venart, J.E.S., 33.6.1
Villafuerte. J.O., 27.5.1
Voigt, S., 15.1.1, 26.2.1
Volkert, J., 13.2.1, 31.4.1
Volkholz, P., 9.1.1

Wachter, P., 14.2.1
Wang, F.Y., 2.6.1.
Wehrmeyer, J.A., 34.1.1
Welling, H., 15.3.1
Wereley, S.T., 6.4.1
Wernet, M.P., 12.4.1
Werquin, O., 4.1.1
Westerweel, J., 1.2.1
Whitelaw, J.H., 3.4.1, 7.2.1
Wigley, G., 9.4.1
Wiles, D.P., 6.3.1
Willert, C.E., 11.1.1, 19.6.1, 34.2.1
Wirtz, S., 35.4.1
Wittig, S., 1.3.1, 31.3.1
Wolf, G., 21.1.1
Woolley, R., 35.2.1
Wozniak, G., 27.1.1, 34.5.1
Xianqiu, Y., 29.1.1

Yamada, N., 12.2.1, 12.6.1
Yamaguchi, K., 16.2.1
Yang, W., 20.4.1
Yates, A., 2.5.1
Yeh, H., 39.2.1
Yeung, Y.F., 21.2.1
Yianneskis, M., 14.2.1
Yongda, S., 29.1.1
Yoshida, N., 6.1.1

Zellmer, H., 15.3.1
Zevenbergen, J.F., 35.6.1
Zhang, X., 11.5.1
Zhao, B., 35.5.1
Zijl, J.L.J., 24.3.1
Zunino, P., 20.2.1, P., 36.4.1